ACCSCIENCE PUBLISHING

International Journal of BIOPRINTING



ACCSCIENCE PUBLISHING
Volume 10 Issue 5, 2024
ISSN: 2424-8002 (Online) ISSN: 2424-7723 (Print)

ACCSCIENCE PUBLISHING

International Journal of Bioprinting

Print ISSN: 2424-7723

Online ISSN: 2424-8002

International Journal of Bioprinting is an international journal covering the technology, science and clinical application of the broadly defined field of Bioprinting. Bioprinting is defined as the use of 3D printing technology with materials that incorporate viable living cells or biological elements to produce tissue or biotechnological products. We are interested in the scientific topics spanning all stages of bioprinting process from concept creation to fabrication and beyond.



Scan to access website:

Scan to submit papers:

About the Publisher

AccScience Publishing is a publishing company based in Singapore. We publish a range of high-quality, open-access, peer-reviewed journals and books from a broad spectrum of disciplines.

Contact Us

Managing Editor
ijb.office@accscience.sg

AccScience Publishing
8 Burn Road, #15-03 Trivex, Singapore 369977.

Volume 10 • Issue 5 • October 2024
ISSN 2424-7723 (print) ISSN 2424-8002 (online)

INTERNATIONAL JOURNAL OF BIOPRINTING

Editor-in-Chief
Chee Kai Chua
Singapore University of Technology and Design, Singapore

ACCSCIENCE PUBLISHING
Access Science Without Barriers

Full issue copyright © 2024 AccScience Publishing
All rights reserved. Without permission in writing from the publisher, this full issue publication in its entirety may not be reproduced or transmitted for commercial purposes in any form or by any means, electronic or mechanical, including photocopying, recording, or any information storage and retrieval system. Permissions may be sought from ijb.office@accscience.sg.

Article copyright © Respective Author(s)
See articles for copyright year. All articles in this full issue publication are open-access. There are no restrictions in the distribution and reproduction of individual articles, provided the original work is properly cited. However, permission to reuse copyrighted materials of an article for commercial purposes is applicable if the article is licensed under Creative Commons Attribution-NonCommercial License. Check the specific license before reusing.

INTERNATIONAL JOURNAL OF BIOPRINTING

ISSN: 2424-7723 (print)
ISSN: 2424-8002 (online)

Editorial and Production Credits

Publisher: AccScience Publishing
Managing Editor: Cathy Huang
Editorial Assistants: Puva Ramakrishnan, Flora Kang
Production Editor: Puva Ramakrishnan Special Issue
Commissioning Editors: Shirley Song, Terra Shi
Article Layout and Typeset: Bsmart Publishing (India)

For all advertising queries, contact ijb.office@accscience.sg.

Supplementary file

Supplementary files of articles can be obtained at https://accscience.com/journal/IJB/10/5.



Disclaimer

AccScience Publishing is not liable to the statements, perspectives, and opinions contained in the publications. The appearance of advertisements in the journal shall not be construed as a warranty, endorsement, or approval of the products or services advertised and/or the safety thereof. AccScience Publishing disclaims responsibility for any injury to persons or property resulting from any ideas or products referred to in the publications or advertisements. AccScience Publishing remains neutral with regard to jurisdictional claims in published maps and institutional affiliations.

International Journal of Bioprinting

Editorial Board

Editor-in-Chief

Chee Kai Chua
Singapore University of Technology and Design, Singapore

Associate Editors

Maling Gou
Sichuan University, China

Jiankang He
Xi'an Jiaotong University, China

Liliang Ouyang
Tsinghua University, China

Wai Yee Yeong
Nanyang Technological University, Singapore

Editorial Board Members*

Jason A. Burdick, *USA*

Shweta Agarwala, *Denmark*

Eben Alsberg, *USA*

Anthony Atala, *USA*

Douglas B. Chrisey, *USA*

Amit Bandyopadhyay, *USA*

Andrea Barbetta, *Italy*

Mikhael Bechelany, *France*

Martin Birchall, *UK*

Paulo J.D.S. Bártolo, *Singapore*

Christian Celia, *Italy*

Boris Chichkov, *Germany*

Gianluca Ciardelli, *Italy*

Jeremy Crook, *Australia*

Rui Domingues, *Portugal*

Dennis Douroumis, *UK*

Tal Dvir, *Israel*

Eleonora Ferraris, *Belgium*

Gunter Finkenzeller, *Germany*

Sanjay Garg, *Australia*

Manuela Gomes, *Portugal*

Brunella Grigolo, *Italy*

Yongqiang Hao, *China*

Charlotte Hauser, *Saudi Arabia*

Mei He, *USA*

Dong Nyoung Heo, *Korea*

Geun Hyung Kim, *Korea*

Richard James Bibb, *UK*

Jingchao Jiang, *China*

Qing Jiang, *China*

Hyun-Do Jung, *Korea*

Ali Khademhosseini, *USA*

Dimitrios A. Lamprou, *UK*

Khoon Lim, *Australia*

Fengyuan Liu, *UK*

Veronica MacChi, *Italy*

Elena Martínez Fraiz, *Spain*

Laurence Meagher, *Australia*

Nikolaos Michailidis, *Greece*

Joaquim Miguel Oliveira, *Portugal*

David K. Mills, *USA*

Vladimir Mironov, *Russia*

Mario Moisés Alvarez, *Mexico*

Maurice N Collins, *Ireland*

Makoto Nakamura, *Japan*

Roger Narayan, *USA*

Insup Noh, *Korea*

Ali Nokhodchi, *UK*

Aleksandr Ovsianikov, *Austria*

Sang-Hyug Park, *Korea*

Alokesh Pramanik, *Australia*

Aldo R. Boccaccini, *Germany*

Michael Raghunath, *Switzerland*

Shinji Sakai, *Japan*

Thomas Scheibel, *Germany*

Cijun Shuai, *China*

Swee Leong Sing, *Singapore*

Kedong Song, *China*

Jie Sun, *China*

Ergün Süleyman, *Germany*

Ibrahim Tarik Ozbolat, *USA*

Savas Tasoglu, *Turkey*

S. Vijayavenkataraman, *UAE*

Giovanni Vozzi, *Italy*

Liqiang Wang, *China*

Seung-Schik Yoo, *USA*

Barbara Zavan, *Italy*

Yi Zhang, *China*

Yu Shrike Zhang, *USA*

Assistant Editor

Jia An, *Singapore*

Youth Editorial Board

Yiting Lei, *China*

Lan Li, *China*

Huixin Liang, *China*

Wei Long Ng, *Singapore*

Yogendra Pratap Singh, *USA*

Thiago Domingues Stocco, *Brazil*

Hui Zhu, *China*

*Editorial Board Members as of February 28, 2024

ACCSCIENCE PUBLISHING

Volume 10 | Issue 5 | October 2024 | Page 1 – 573 |

International Journal of Bioprinting

https://accscience.com/journal/IJB

CONTENTS

REVIEW ARTICLES

1 **Advancements in 3D bioprinting for nanoparticle evaluation: Techniques, models, and biological applications**
Moon Sup Yoon, Jae Min Lee, Min Jeong Jo, Su Jeong Kang, Myeong Kyun Yoo, So Yeon Park, Ji-Hyun Kang, Chan-Su Park, Chun-Woong Park, Jin-Seok Kim, Andrea Bernardos, Vicente Martí-Centelles, Ramón Martínez-Máñez, Dae Hwan Shin

31 **Bioprinting of tumor immune microenvironment for immunotherapy**
Sein Kim, Seokgyu Han, Jaehyun Lee, Chanyang Lee, Sungsu Park

47 ***In situ* bioprinting: Tailored printing strategies for regenerative medicine**
Chengwei Hu, Chenmin Wang, Shaoquan Bian, Weichen Qi, Bo Liu, Liangliang Wang, Chunyi Wen, Jun Wu, William W. Lu, Xiaoli Zhao

68 **Emerging frontiers in 3D bioprinting: Harnessing decellularized matrix bioink for advancements in musculoskeletal tissue engineering**
Peilin Li, Xixin Li, Guosheng Tang, Zongke Zhou, Zeyu Luo

97 **Advancements in 3D bioprinting for precision medicine: Enhancing patient-derived organoids and extracellular vesicle applications in inflammatory diseases**
Hyun Sung Park, Jae Han Park, Mi-Kyung Oh, Kyung-Rok Yu

120 **The application of 3D bioprinting technology in liver manufacturing: Progress, challenges, and prospects**
Yifan Hou, Xin Liu, Xinhuan Wang, Shen Ji, and Qi Gu

RESEARCH ARTICLES

152 **Experimental and numerical approaches for optimizing conjunction area design to enhance switching efficiency in single-nozzle multi-ink bioprinting systems**
Mitsuyuki Hidaka, Masaru Kojima, Colin Zhang, Yasunori Okano, Shinji Sakai

168 **Manipulating fungal growth in engineered living materials through precise deposition of nutrients**
Jia Heng Teoh, Eugene Soh, Hortense Le Ferrand

183 **Biomimetic structural design and performance study of 3D-printed graded minimal surface bone scaffolds with enhanced bioactivity**
Tang Liu, Yuxin Lin, Lin Sang, Fei Wang, Jiawei Hu, Kun Guo, Shanglian Ju, Yiping Zhao, Xiaohong Shu

198 **Spatiotemporal delivery of BMP-2 and FGF-18 in 3D-bioprinted tri-phasic osteochondral scaffolds enhanced compartmentalized osteogenic and chondrogenic differentiation of mesenchymal stem cells isolated from rats with varied organizational morphologies**
Weiwei Su, Shiyu Li, Panjing Yin, Weihan Zheng, Ling Wang, Zhuosheng Lin, Ziyue Li, Zi Yan, Yaobin Wu, Chong Wang, Wenhua Huang

217 **A preliminary investigation on the effect of ingredient flow speed in extrusion-based printing through experimental and theoretical approaches**
Phoebe Xin Ni Leam, Aakanksha Pant, Jia An, Chen Huei Leo, U-Xuan Tan, Chee Kai Chua

232 **3D-printed Mg-substituted hydroxyapatite/gelatin methacryloyl hydrogels encapsulated with PDA@DOX particles for bone tumor therapy and bone tissue regeneration**
Shangsi Chen, Yue Wang, Junzhi Li, Haoran Sun, Ming-Fung Francis Siu, Shenglong Tan

256 **A functionally graded gyroid-type three-periodic minimal surface framework applied to implant-supported fixed complete dentures**
Jiwei Ren, Renkai Huang, Linqing Huang, Shaoying Yang, Chunrong Pan, Yuchun Sun, Sukun Tian, Xuehua Wu, Dongsheng Wang, Youwen Yang

276 **A study on the synergistic chondro-inductive effects of collagen II and its high-resolution 3D-printed scaffolds**
Kaixuan Li, Hanxiao Huang, Cailiang Shen

293 **Double-protein-loaded 3D-printed polyetheretherketone cage for promoting interbody fusion via osteogenic differentiation**
Feng Zheng, Xiaoqiang Gao, Sheng Chai, Haibin Lin, Huan Liu

307 **Amphiphobic encapsulation for biodegradable electronics**
Daeun Sung, Yerim Lee, Seunghun Han, Sumin Kim, Bon Jekal, Minki Hong, Keunhong Jeong, Jahyun Koo

320 **3D-Printed mesoporous bioglass/polycaprolactone scaffolds induce macrophage polarization toward M2 phenotype and immunomodulates osteogenic differentiation of BMSCs**
Weihua Huang, Shuai Huang, Xitao Linghu, Wei-Chih Chen, Yang Wang, Jingjie Li, Huinan Yin, Hang Zhang, Weikang Xu, Qingde Wa

340 **3D bioprinting of colon organoids in ultrashort self-assembling and decorated peptide matrices**
Jiayi Xu, Rosario Pérez-Pedroza, Manola Moretti, Dana Alhattab, Alexander Valle-Pérez, Jezabel García-Parra, Antonio Cárdenas-Calvario, Diana Eveline Sanchez-Amador, Charlotte A. E. Hauser

363 **Design and fabrication of anisotropic SiO_2 gyroid bioscaffolds with tunable properties**
Ka-Wai Yeung, Chi-Yeung Mang, Quan-Jing Mei, Chi Ho Wong, Chak-Yin Tang, Xin Zhao, Wing-Cheung Law, Gary Chi-Pong Tsui, Zhenjia Huang

383 **Dexamethasone-loaded PLGA porous microspheres used as 3D-bioprinted bioink promote tissue-engineered cartilage regeneration**
Zhuoqi Chen, Yanjun Feng, Yuchen Wang, Tianfeng Zheng, Jinshi Zeng, Wenshuai Liu, Yue Ma, Xiaowei Yue, Tian Li, Luosha Gu, Qinghua Yang, Haiyue Jiang, Xia Liu

406 **The effect of manufacturing method; direct compression, hot-melt extrusion, and 3D printing on polymer stability and drug release from polyethylene oxide tablets**
Nour Nashed, Barnaby W. Greenland, Mridul Majumder, Matthew Lam, Taravat Ghafourian, Ali Nokhodchi

425 **Bioprinting with superelastic and fatigueresistant bioinks for large-sized tissue delivery**
Ruoyu Chen, Yijun Su, Dazhi Chen, Yinying Lu, Jinghua Zhao, Yali Zhang, Quan Yuan, Mingen Xu, Rui Yao

444 **3D-printed devices for optimized generation of cold atmospheric plasma to improve decontamination of surfaces from respiratory pathogens**
Asma Bouazizi, Klára Obrová, Eva Vaňková, Anna Machková, Josef Khun, Romana Hadravová, Jan Hodek, Lucie Ulrychová, Abdelhalim Trabelsi, Jan Weber, Leonardo Zampieri, Fabio Avino, Ivo Furno, Vladimír Scholtz, Thomas Lion

462 **3D printing of retainer for post-otoplasty morphology preservation**
Peixu Wang, Di Wang, Wenshuai Liu, Litao Jia, Bo Pan, Xiaobo Yu, Yiwen Deng, Xia Liu, Haiyue Jiang, Lin Lin

477 **Development of a biocompatible radiotherapy spacer using 3D printing and microcellular foaming process for enhanced prostate cancer treatment**
DongHwan Lim, DoKun Yoon, JaeHoo Kim, KiHoon Sung, YoungEun Choi, HeeSoon Sheen, Han-Back Shin, Sung Woon Cha

487 **3D bioprinting of in vitro full-thickness skin model with a rete ridge structure**
Ilho Jang, Jae-Hun Kim, Misun Kim, Paulo Andre Marinho, Younhwa Nho, Seunghyun Kang, Won-Soo Yun, Jin-Hyung Shim, Songwan Jin

502 **3D-bioprinted model of adult neural stem cell microenvironment in Alzheimer's disease**
Natalia Dall'Agnol Ferreira, Paula Scanavez Ferreira, Cristina Pacheco Soares, Marimelia Aparecida Porcionatto, Geisa Rodrigues Salles

526 **Mechanism study of structural functional dual biomimetic composite bone scaffold for repair of mandibular defects in rabbits**
Jiaqi Hu, Hong Zhu, Chongqing He, Xiaochuan Liu, Kenny Man, Shanqin Liang, Jingying Zhang

542 **Methacrylic anhydride-assisted one-step *in situ* extrusion 3D bioprinting of collagen hydrogels for enhanced full-thickness skin regeneration**
Xiaxia Yang, Linyan Yao, Wenhua Li, Xiaodi Huang, Na Li, Jianxi Xiao

560 **Machine learning-generated compression modulus database for 3D printing of gelatin methacryloyl**
Shiue-Luen Chen, Manisha Senadeera, Kalani Ruberu, Johnson Chung, Santu Rana, Svetha Venkatesh, Chong-You Chen, Guan-Yu Chen, Gordon Wallace

ACCSCIENCE PUBLISHING

International Journal of Bioprinting

REVIEW ARTICLE

Advancements in 3D bioprinting for nanoparticle evaluation: Techniques, models, and biological applications

Moon Sup Yoon[1†], Jae Min Lee[1†], Min Jeong Jo[2], Su Jeong Kang[1], Myeong Kyun Yoo[1], So Yeon Park[1], Ji-Hyun Kang[3], Chan-Su Park[1], Chun-Woong Park[1], Jin-Seok Kim[4], Andrea Bernardos[5,6,7,8], Vicente Martí-Centelles[5,6,8*], Ramón Martínez-Máñez[5,6,7,8,9*], and Dae Hwan Shin[1,5,10*]

[1] College of Pharmacy, Chungbuk National University, 28160 Cheongju, Republic of Korea

[2] Department of Oncology Science, University of Oklahoma, Oklahoma City, 73104 Oklahoma, United States of America

[3] Institute of New Drug Development and Respiratory Drug Development Research Institute, School of Pharmacy, Jeonbuk National University, 54896 Jeonju, Republic of Korea

[4] Drug Information Research Institute (DIRI), College of Pharmacy, Sookmyung Women's University, 04310 Seoul, Republic of Korea

[5] Instituto Interuniversitario de Investigación de Reconocimiento Molecular y Desarrollo Tecnológico (IDM), Universitat Politècnica de València, Universitat de València, Camino de Vera, s/n, 46022 Valencia, Spain

[6] CIBER de Bioingeniería Biomateriales y Nanomedicina (CIBER-BBN), Instituto de Salud Carlos III, 46026 Madrid, Spain

[7] Unidad Mixta UPV-CIPF de Investigación en Mecanismos de Enfermedades y Nanomedicina, Universitat Politècnica de València, Centro de Investigación Príncipe Felipe, Avenida Eduardo Primo Yúfera, 3, 46012 Valencia, Spain

[8] Departamento de Química, Universitat Politècnica de València, Camino de Vera s/n, 46022 Valencia, Spain

[9] Unidad Mixta de Investigación en Nanomedicina y Sensores, Universitat Politècnica de València, Instituto de Investigación Sanitaria La Fe (IISLAFE), Avenida Fernando Abril Martorell, 106, 46026 Valencia, Spain

[10] Chungbuk National University Hospital, Chungbuk National University, 28644 Cheongju, Republic of Korea

†These authors contributed equally to this work.

***Corresponding authors:**
Vicente Martí-Centelles (vimarce1@upv.es)

Ramón Martínez-Máñez (rmaez@qim.upv.es)

Dae Hwan Shin (dshin@chungbuk.ac.kr)

(This article belongs to the Special Issue: *Advances in Bioprinting and Organ-on-a-chip and Applications for Precision Medicine*)

Citation: Yoon MS, Lee JM, Jo MJ, et al. Advancements in 3D bioprinting for nanoparticle evaluation: Techniques, models, and biological applications. *Int J Bioprint.* 2024;10(5):4273. doi: 10.36922/ijb.4273

Received: July 17, 2024
Revised: August 6, 2024
Accepted: August 7, 2024
Published Online: August 9, 2024

Copyright: © 2024 Author(s). This is an Open Access article distributed under the terms of the Creative Commons Attribution License, permitting distribution, and reproduction in any medium, provided the original work is properly cited.

Publisher's Note: AccScience Publishing remains neutral with regard to jurisdictional claims in published maps and institutional affiliations.

Abstract

Three-dimensional (3D) bioprinting technology has opened new possibilities for nanoparticle evaluation. This review discusses the latest research trends using various disease models created through 3D bioprinting for the biological evaluation of nanoparticles. The focus is on tumor models, vascular models, and skin models. In tumor models, evaluations include antitumor effects, gene expression analysis, and cytotoxicity comparisons between 2D and 3D models. Vascular models are used to assess restenosis prevention, ischemic repair, and vascular regeneration. Skin models are employed to investigate nanoparticle toxicity, drug release, and transdermal penetration. These studies highlight the versatility of 3D bioprinting in replicating complex biological environments, enabling more accurate nanoparticle testing. The use of various bioinks and cell types enhances the relevance of *in vitro* findings. The integration of nanoparticles with 3D-bioprinted models shows significant potential

in advancing therapeutic strategies, including cancer treatment, vascular repair, and drug delivery systems. Overall, by providing selected examples to illustrate the concepts, this comprehensive review underscores the importance of 3D bioprinting as an innovative platform for nanoparticle research, bridging the gap between traditional 2D cell cultures and *in vivo* studies, and contributing to the development of nanomedicines and personalized medical treatments.

Keywords: 3D bioprinting; Nanoparticles; Disease models; Antitumor effects; Drug delivery

1. Introduction

In recent years, particularly since the early 2000s, three-dimensional (3D) bioprinting technology has achieved significant advancements in the fields of life sciences and medicine. This technology, which can precisely mimic the complex structures and functions of biological tissues, is garnering considerable attention. Unlike traditional 2D cell culture methods, 3D bioprinting creates constructs that more accurately recapitulate the actual human body environment.[1,2] 2D cell culture methods are known for their simplicity and reproducibility, but they fall short in replicating the complex cell-to-cell interactions and tissue structures that occur *in vivo*. This limitation often undermines the reliability of experimental results in drug development and nanoparticle (NP) evaluation. In contrast, 3D bioprinting addresses these issues by stacking cells and biomaterials layer by layer to form 3D structures that closely resemble actual tissues.[3–6] For instance, a research team at Utrecht University has developed a novel volumetric 3D bioprinting technique to rapidly produce high-resolution liver tissues. This method, which projects 2D light patterns onto photoresponsive hydrogels containing cells, allows for the quick formation of tissues. This research has made significant strides in enhancing the detoxification function of liver tissues, contributing substantially to the development of patient-specific models and new drug research.[7]

Three-dimensional bioprinting technology can precisely replicate the form and function of tissues using bioinks with various biological and physical properties. This capability holds significant potential, particularly in NP research. NPs play a crucial role in diverse biomedical applications, including drug delivery, diagnosis, and therapy, and yet more accurate models are needed to evaluate their efficacy and safety.[8–10] Compared to 2D systems, 3D culture systems offer several important advantages for NP research. In 2D cultures, cells grow attached to a flat surface, limiting cell-cell interactions. In contrast, 3D cultures provide an environment where cells can grow and interact in all directions, better replicating the complex, physiologically relevant microenvironments found *in vivo*.[11–13] The spatial arrangement in 2D cultures restricts cell interactions, affecting cell morphology, growth patterns, and signaling pathways. Conversely, 3D environments allow for more natural and complex cell signaling interactions.[14,15] Additionally, in 2D cell cultures, drug or NP penetration is straightforward and typically contacts only one side of the cells, limiting the depth and distribution of penetration. In 3D cultures, however, drugs or NPs can be distributed throughout the entire cell structure, reflecting the drug distribution patterns in actual human tissues. This enables more accurate assessments of drug efficacy and toxicity.[16,17]

Recent studies indicate that 3D bioprinting can be used to develop various disease models, including tumor models, vascular models, and multifunctional models, to evaluate the effectiveness and safety of NPs. For example, in tumor models, the efficacy of NPs can be assessed through the evaluation of anti-tumor effects, gene expression analysis, and cytotoxicity comparisons between 2D and 3D models.[18–20] In vascular models, the technology can be used to evaluate vascular regeneration through targeted drug delivery, the prevention of restenosis, and the repair of ischemic injuries.[21–23] Furthermore, 3D bioprinting can enhance the relevance of *in vitro* studies by utilizing various types of bioinks and cells to mimic specific tissues and diseases.[24] The integration of NPs with 3D-bioprinted models shows significant potential for advancements in therapeutic strategies, such as cancer treatment, vascular repair, and drug delivery systems.[1–3,5,6,25]

In summary, 3D bioprinting technology has established itself as a crucial tool in NP research, providing new directions and applications for future studies. The continued development and application of 3D bioprinting are poised to significantly advance the development of safe and effective NP-based therapies.

In this review, we focus on the recent advancements in 3D bioprinting technology for NP evaluation. Specifically, we cover progress achieved in the last decade, providing selected references to highlight the main concepts and significant developments. The review is structured into several sections: first, an overview of the current state of 3D bioprinting technology; second, detailed applications in disease models such as cancer, skin, vessel, and bone; and third, an exploration of the integration of NPs with these bioprinted models (Tables 1–3). Each section aims

Table 1. Bioprinted tumor models for evaluation of various chemotherapeutic nanoparticles.

Printed model	Used NPs	Used drug	Cell line	Main materials of bioink	Bioprinting method	NPs evaluation study	Ref.
Tumor models	Poly(ethylene glycol)poly(ω-pentadecalactone-co-N-methyldiethyleneamine-co-3,3′-thiodipropionate) (PEG-PPMT)	Docetaxel	MCF-7	dECM (adECM), and GelMA	Extrusion-based 3D bioprinting	Cellular uptake, cytotoxicity	[33]
	Pluronic® F127	Curcumin	MDA-MB-231	Sodium alginate, gelatin, and nanoclay	Extrusion-based bioprinting	Cytotoxicity	[36]
	Keratin-coated gold NP	N/A	U87-MG	Gelatin, GelMA, alginate	Inkjet bioprinting	Immunofluorescence study	[37]
	Gold NP	N/A	MCF-7	hDAT	Suspended layer additive manufacturing	Cytotoxicity test, H&E staining	[38]
	Glyceryl monoolein/ Pluronic® F127 mixed)	Meloxicam	MCF-7, MDA-MB-231	Poly (ε-caprolactone), 25 kDa	Extrusion-based bioprinting	Cell viability, cytotoxicity study	[40]
	Cetyl palmitate-based PEGylated solid lipid NP	Paclitaxel, sorafenib	U87-MG	Nanoshuttle-PL (Nano3D Biosciences)	Magnetic bioprinting	Cellular uptake, cytotoxicity study	[44]
	DSS lignin NP	Benzazulene	PC3-MM2, MDA-MB-231, A549	Nanoshuttle-PL (Nano3D Biosciences)	Magnetic bioprinting	Cellular uptake, cytotoxicity study	[46]

Abbreviations: adECM: Adipose-derived decellularized extracellular matrix; dECM: Decellularized extracellular matrix; DSS: Dentin phosphophoryn-derived peptide; GelMA: Gelatin methacryloyl; hDAT: Human decellularized adipose tissue; NP: Nanoparticle.

to illustrate the innovative approaches and breakthroughs that have improved the evaluation methods for NP-based therapies (Figure 1).

2. Three-dimensional bioprinted cancer models

Three-dimensional bioprinting technology has emerged as an innovative tool for developing and evaluating NP-based therapies used in cancer research.[26,27] Recent studies have proposed methods to create models that mimic actual tumor tissues using 3D bioprinting, thereby enabling a more accurate assessment of the efficacy and safety of NPs. This approach provides insights that are difficult to obtain from traditional 2D cell culture methods and plays a crucial role in maximizing the effectiveness of drug delivery systems.[28–31]

2.1. Three-dimensional bioprinted tumor models using adipose decellularized extracellular matrix-enhanced bioinks for evaluating PEG-PPMT nanoparticles

Chen et al.[33] developed a sophisticated 3D-bioprinted tumor model using an extracellular matrix (ECM)-enhanced hybrid bioink, which significantly improves the evaluation of NPs for cancer treatment. The traditional evaluation methods for NPs, such as 2D cell culture and animal models, often fail to accurately replicate the human tumor microenvironment and the complex transportation mechanisms of NPs within it. This limitation hinders the translation of nano-drug formulations from preclinical studies to clinical applications. To address these challenges, the researcher team leveraged the capabilities of 3D bioprinting to create a more realistic and functional tumor model and utilized adipose-derived decellularized ECM (adECM) to enhance the bioink's properties. This hybrid bioink, combining adECM and gelatin methacryloyl (GelMA), provides a scaffold that closely mimics the natural ECM in tumors. This bioink was carefully optimized to ensure excellent printability, cytocompatibility, bioactivity, and mechanical support, which are essential for maintaining cell viability and function in 3D culture. The bioprinting process involved a modified extrusion-based 3D printer that accurately deposited the hybrid bioink layer by layer to form complex 3D tumor structures. One of the significant advantages of using this ECM-enhanced bioink is its ability to replicate key characteristics of the tumor microenvironment, including ECM remodeling and epithelial-mesenchymal

Table 2. Bioprinted organ models for evaluation of nanoparticles.

Printed model	Used NPs	Used drug	Cell line	Main materials of bioink	Bioprinting method	NPs evaluation study	Ref.
Skin models	Hydroxyl, amine, sulfate, polystrene NP	N/A	3T3	Collagen (rat rail, type I)	Extrusion-based bioprinting	Penetration	[56]
	PLGA 50:50, lecithin NP	Quinizarin	NHEK, HDF, ADSCs	Collagen, pectin	Suspended layer additive manufacturing	Permeation	[57]
Ear model	Compritol 888 ATO NP	Cyclosporine A, co-enzyme Q10	NIH-3T3	Alginate, polyylactic acid, polyvinyl alcohol	Extrusion-based bioprinting	Cell viability	[62]
Vascular models	Mesoporous silica NP	Rapamycin	EPC	Sodium alginate/ atelocollagen/ alginate	Extrusion-based bioprinting	*In vivo* evaluation of 3D-bioprinted artificial blood vessels containing NPs	[71]
	Superparamagnetic iron oxide NP (SPIONs)	Rapamycin	HUVECs	GelMA	Laser-assisted bioprinting	Evaluation of endothelial cell response to targeted delivery of NPs	[75]
	Mesoporous silica NP	Curcumin, atorvastatin	EPC	Neutralized atelocollagen, alginate	Extrusion-based bioprinting	*In vivo* evaluation of 3D-bioprinted artificial blood vessels containing NPs	[76]
	Gold NP, PEG-*b*-PLA	miRNA	Human aortic valve interstitial cells	GelMA, HAMA, LAP	Extrusion-based bioprinting	Cellular uptake, functionality evaluation	[79]
Bone models	Bioglass NP (molar ratio of SiO_2:CaO:P_2O_5 of 55:40:5)	N/A	SaOS-2	Alginate/gelatin	Extrusion-based bioprinting	Influence of the polymers on biomineralization	[92]

Abbreviations: ADSCs: Adipose-derived stem cells; EPC: Endothelial progenitor cells; GelMA: Gelatin methacryloyl; HAMA: Methacrylated hyaluronic acid; HDF: Human dermal fibroblasts; HUVEC: Human umbilical vein endothelial cell; LAP: Lithium phenyl-2,4,6-trimethylbenzoylphosphinate; miRNA: MicroRNA; NHEK: Normal human epidermal keratinocytes; NP: Nanoparticle; PLGA: Poly(L-lactic acid-co-glycolic acid).

transition.[32] These features are critical for studying how NPs interact with the tumor environment.

In Chen et al.'s study,[33] the 3D-printed tumor models exhibited multicellular spheroids that closely resemble real tumors in terms of protein expression, gene expression, and tumorigenicity both *in vitro* and *in vivo*. This level of biomimicry is crucial for evaluating the efficacy and safety of NPs, as it provides a more accurate representation of how these particles would behave in human tumors. Specifically, they evaluated the transport and efficacy of poly(ethylene glycol)-poly(ω-pentadecalactone-co-N-methyldiethyleneamine-co-3,3'-thiodipropionate) (PEG-PPMT) NPs, demonstrating the model's capability in assessing such advanced nano-drug formulations. The research demonstrated that the cellular uptake efficiency of NPs was significantly lower in the 3D-printed tumor model compared to traditional 2D cultured cells. This finding suggests that the ECM barrier in the 3D model affects NP permeability, highlighting the importance of including ECM components in *in vitro* models to better predict NP behavior *in vivo*. Additionally, the study observed higher drug resistance in the 3D model, further emphasizing the model's potential to provide more clinically relevant data for NP evaluation. Chen et al.'s work underscores the benefits of using 3D bioprinting for creating tumor models. The enhanced ECM bioink not only supports the growth and maintenance of tumor cells in a 3D structure but also allows for the study of dynamic interactions between NPs and the tumor microenvironment. This approach offers a more detailed understanding of NP transport processes and pathophysiological barriers within tumors, which is essential for designing more effective nano-drug delivery systems.[33]

Table 3. Bioprinted models for inflammatory disease, toxicity, drug release, and tissue engineering.

Printed model	Used NPs	Used drug	Cell line	Main materials of bioink	Bioprinting method	NPs evaluation study	Ref.
Inflammatory disease	Albumin NPs	Roxadustat, caffeic acid phenethyl ester	Caco-2, HT29	Polysaccharide components, alginate, hydrated cellulose nanofibrils	Extrusion-based bioprinting	Transepithelial electrical resistance	[101]
Toxicity	Copper oxide NP coated with bovine serum albumin	N/A	Human iPSCs	Porcine gelatin, methacrylic anhydride	μCOP system	Gene expression related to mitochondrial biogenesis, cell viability	[112]
	Polydispersity colloidal silver NP, atoxic carboxyl-modified fluorescent NP	N/A	Calu-3	Alginate/gelatin/ Matrigel	Extrusion-based bioprinting	Toxicity	[115]
Drug release	Dextran sulfate, magnesium ions	Minocycline hydrochloride	L929 fibroblast	GelMA	Extrusion-based bioprinting	Drug release	[123]
Tissue engineering and regenerative medicine	*N*-vinylcaprolactam, 2-hydroxyethyl methacrylate	Catechol	L929	CMCh, HAox	Extrusion-based bioprinting	Cell viability	[131]

Abbreviations: CMCh: Carboxymethyl chitosan; GelMA: Gelatin methacryloyl; HAox: Oxidized hyaluronic acid; NP: Nanoparticle; μCOP: Micro-continuous optical printing.

2.2. Three-dimensional printed tumor models with alginate-gelatin-nanoclay scaffolds for evaluating curcumin-loaded nanoparticles in breast cancer therapy

The study by Su et al.[36] presents an innovative approach that combines curcumin-loaded NPs (CurNPs) with 3D-printed bionic tumor models to evaluate and enhance breast cancer treatment. The researchers utilized 3D cell culture models to create a more realistic tumor microenvironment, thereby addressing the limitations of conventional 2D culture methods. To synthesize CurNPs, the researchers encapsulated curcumin, a traditional anticancer agent, in a polymer (Pluronic® F127) using the nanoprecipitation method.[34] This process produced NPs with excellent water solubility and biocompatibility. CurNPs demonstrated significant anticancer effects against breast cancer cells (MDA-MB-231), showing high internalization and excellent cytotoxicity.

To create realistic 3D tumor models, Su et al.[36] prepared hybrid scaffolds using sodium alginate, gelatin, and nanoclay. These materials were selected for their printability and mechanical properties, crucial for maintaining the structure and function of the 3D models. The printed scaffolds exhibited strong mechanical properties through rapid crosslinking, making them suitable for long-term cell culture. Experimental results showed that CurNPs had a higher release rate in acidic conditions, which is characteristic of the tumor microenvironment.[35] This pH-responsive drug release enhances the targeting efficiency of the NPs, potentially leading to better therapeutic outcomes with reduced side effects. The researchers also demonstrated that CurNPs exhibited significant cytotoxicity against breast cancer cells in the 3D tumor models. The 3D models supported cell proliferation and more accurately reflected the characteristics of tumor cells, providing high reliability in drug screening and therapeutic efficacy evaluation. This study indicates that the combination of CurNPs with 3D-printed tumor models presents a novel approach to breast cancer treatment, overcoming the limitations of traditional therapies and contributing to the development of more effective treatment strategies. Thus, Su et al.[36] have shown that merging NPs with 3D bioprinting technology opens new possibilities for breast cancer treatment evaluation.

2.3. Three-dimensional bioprinted GelMA constructs for photothermal therapy with keratin-coated gold nanoparticles in glioblastoma treatment

Chirivì et al.[37] conducted an innovative study integrating biomimetic keratin-coated gold NPs (Ker-AuNPs) with advanced 3D bioprinting technology to develop a glioblastoma tumor model for photothermal therapy (PTT) (Figure 2). This approach offers a compelling alternative to traditional 2D culture systems, enabling more realistic tumor models that better mimic the complex

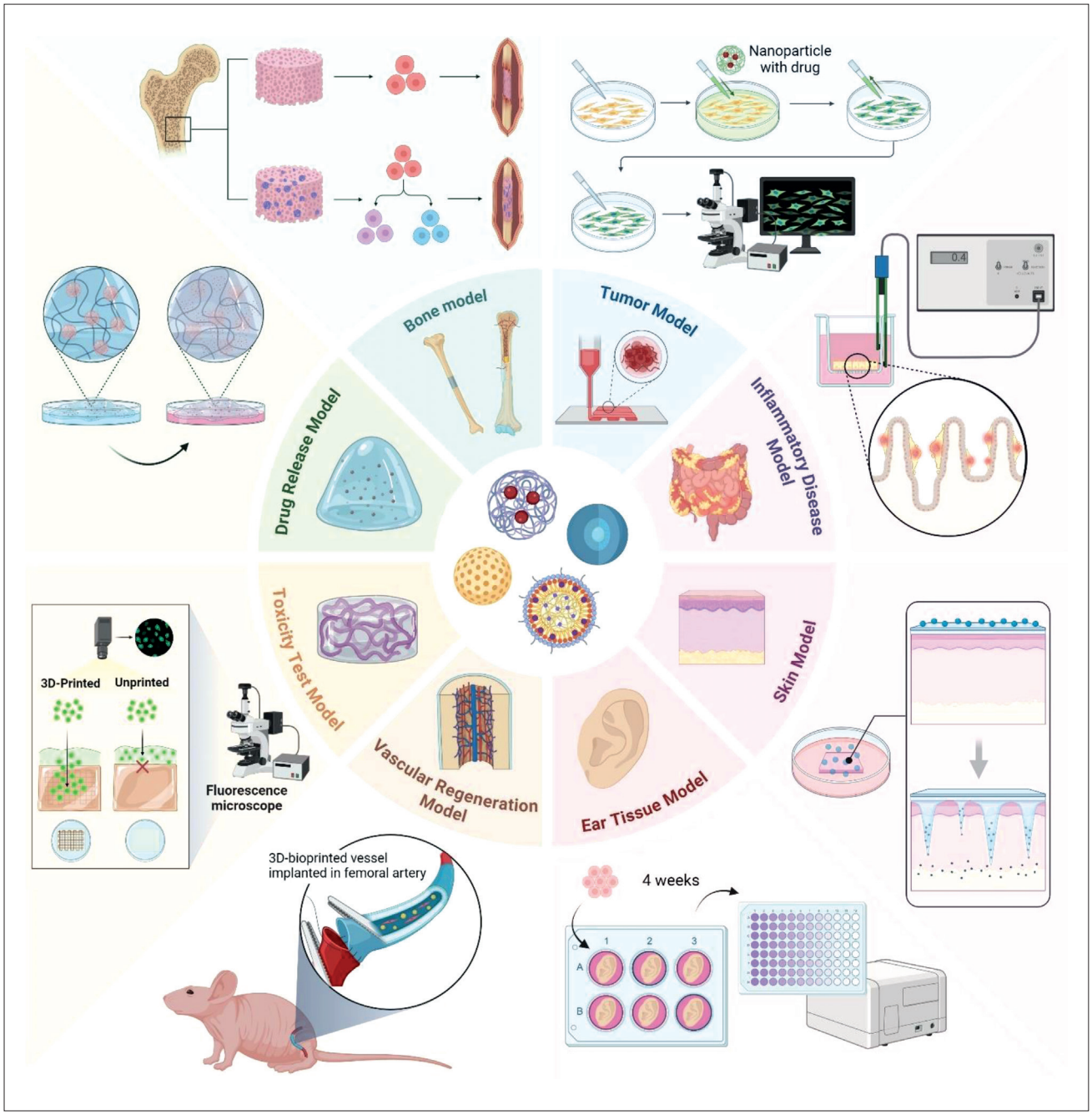


Figure 1. Schematic diagram of 3D bioprinting for nanoparticle evaluation.

microenvironment of glioblastomas. The researchers used U87-MG glioblastoma cells combined with GelMA bioink and Ker-AuNPs to create 3D-bioprinted constructs. The Ker-AuNPs serve as photothermal agents due to their strong plasmonic resonance, which generates localized heating when exposed to specific wavelengths of light (532 nm in this study). This method allows for targeted thermal ablation of cancer cells, presenting a minimally invasive treatment option. The bioprinting process was meticulously designed to ensure uniform cell distribution within the constructs, with subsequent proliferation and alignment along the bioprinted fibers observed over time. Immunofluorescence assays confirmed that Ker-AuNPs were effectively localized within the cells and did not leak from the constructs, even after 56 hours of culture. This stability is crucial for ensuring that the therapeutic agents remain within the tumor site for effective treatment. The study demonstrated that the Ker-AuNPs, besides

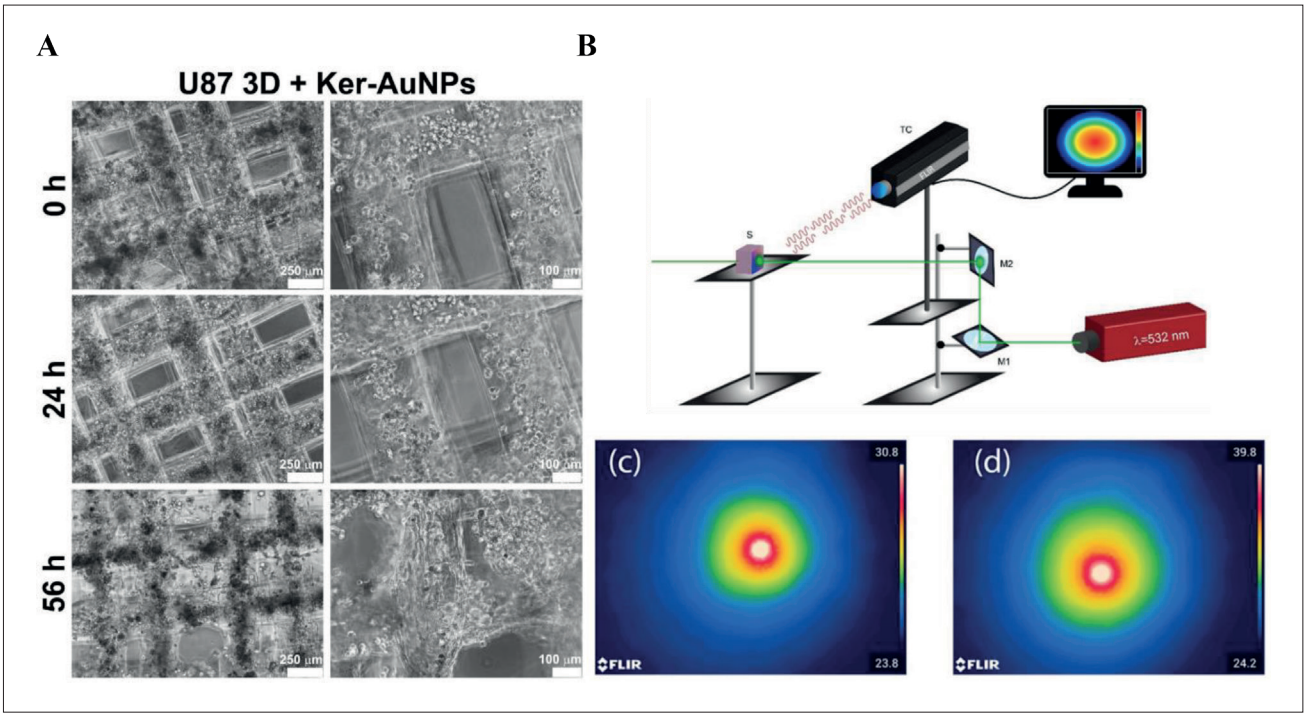


Figure 2. Efficacy evaluation of nanoparticle (NP) formulations using 3D-bioprinted cancer models.[37] (A) Micrographs of 3D-bioprinted structures coupled with U87-MG glioblastoma cells and ker-AuNPs. (B) Schematic of the experimental optical setup used to investigate the photothermal properties of the 3D-bioprinted structures and thermal images.

being highly biocompatible, did not adversely affect cell viability. This was validated through FACS analysis, which showed comparable cell viability in 3D constructs with and without Ker-AuNPs, though a slight reduction was noted compared to 2D cultures. The internalization of Ker-AuNPs by glioblastoma cells was confirmed via transmission electron microscopy (TEM), showing that the NPs were enclosed within endosomal structures without causing morphological damage to the cells. Laser-assisted PTT experiments highlighted the extraordinary capability of Ker-AuNPs to produce significant heating. The temperature within the 3D constructs increased by approximately 16 °C after 56 hours of culture, followed by 120 seconds of laser irradiation, showcasing the potential of Ker-AuNPs for effective thermal ablation of cancer cells. This heating effect was more pronounced in the 56-hour cultured samples compared to those cultured for 24 hours, indicating that a longer incubation time enhances the accumulation and effectiveness of the Ker-AuNPs within the tumor model. Chirivì et al.'s research[37] emphasizes the advantages of using 3D bioprinting for developing more accurate tumor models. The integration of Ker-AuNPs with 3D bioprinting technology not only allows for the creation of complex tumor architectures but also provides a robust platform for testing the efficacy of NP-based therapies. The study opens up new avenues for exploring multi-modality treatments and the synergistic effects of combining PTT with other therapeutic approaches, such as chemotherapy and immunotherapy, in a controlled *in vitro* environment that closely mimics *in vivo* conditions.[37]

2.4. Bioprinting 3D tissue constructs for evaluating gold nanorods in breast cancer photothermal therapy

In a recent study, Nam et al.[38] developed an innovative 3D-bioprinted complex tissue construct to evaluate the photothermal properties of gold nanorods (AuNRs) for early-stage breast cancer therapy. This advanced tissue model replicates the structural and compositional characteristics of human breast tissue and it was designed to provide a realistic environment for assessing the efficacy of plasmonic photothermal therapy (PPTT). The bioprinting process involves multiple materials, including thermal plastic polymers and hydrogels, to create a multi-layered construct that mimics the breast tissue's complexity. The construct includes a layer of human decellularized adipose tissue (hDAT) and a layer containing MCF-7 breast cancer cells. The hDAT provides a supportive matrix while the cancer cells form a realistic tumor environment. A mold printed with polycaprolactone supports the structure during gelation, ensuring precise layering and structural integrity. To evaluate the viability and response of the

cancer cells within the bioprinted construct, a live/dead cell assay was employed using ethidium homodimer and calcein AM. Confocal microscopy allowed for detailed visualization of cell viability, highlighting the effectiveness of the bioprinting method in maintaining a viable and functional tissue model. The core of this research focuses on the thermal properties and heat generation of AuNRs embedded within the bioprinted constructs. When irradiated with a near-infrared (NIR) laser, the AuNRs generate localized heat, which is critical for PPTT. The study utilized infrared (IR) microthermography to measure the temperature distribution across the tissue construct. This non-contact method provides high-resolution thermal maps, essential for understanding the thermal behavior of AuNRs within the complex tissue environment.

One of the significant advantages of this bioprinted model is its ability to simulate various depths and layers of human tissue, providing a comprehensive analysis of heat distribution and thermal damage. The model enables precise control over the AuNRs' depth, allowing for detailed studies on how depth affects heat generation and cancer cell viability. The results indicated a sharp decrease in temperature variation with increasing depth, emphasizing the need for precise control in clinical settings to avoid damage to surrounding healthy tissues. Nam et al.[38] proposed a thermal prediction equation to estimate temperature variations based on laser power density and AuNR concentration. This predictive model is instrumental for optimizing PPTT parameters, ensuring effective and selective thermal damage to cancer cells while minimizing harm to normal tissues. This highlights significant progress in tissue engineering and demonstrates the benefits of using bioprinted models for evaluating NP-based treatments.[38]

2.5. Three-dimensional printed acrylamide-based scaffolds for evaluating meloxicam-loaded nanostructured colloidal self-assemblies in breast cancer

The study conducted by Rarokar et al.[40] focuses on evaluating the antitumor and anti-inflammatory efficacy of meloxicam-loaded nanostructured colloidal self-assembly (MLX-NCS) using 3D-printed scaffolds.[39] This research emphasizes the use of nanostructured colloidal self-assembly (NCS) as a promising drug delivery carrier in cancer treatment, enhancing drug circulation half-life and cellular internalization. The formulation of NCS involved glyceryl monoolein and Pluronic® F127, optimized through quality-by-design experiments. The resulting NCS demonstrated an average particle size of 185.5 nm, high meloxicam (MLX) encapsulation efficiency of 94.74%, and sustained drug release over 24 hours. *In vitro* cytotoxicity tests on MCF-7 and MDA-MB-231 cell lines revealed lower cell viability and higher cell growth inhibition rates, confirming the dual antitumor and anti-inflammatory activities of the MLX-NCS. This dual functionality is particularly significant in highly invasive estrogen-dependent MDA-MB-231 cells, attributed to the high expression of cyclooxygenase-2 (COX-2). This study utilized 3D bioprinting technology to evaluate the nanostructured particles, and the researchers used acrylamide and bis-acrylamide hydrogels combined with MCF-7 cells to print 3D scaffolds, which were then used to assess the cell growth inhibition efficacy of MLX-NCS. The 3D-printed cell cultures exhibited distinct drug release and cytotoxicity profiles compared to 2D cultures. MLX-NCS demonstrated more sustained and controlled MLX release, beneficial for maintaining therapeutic drug levels over extended periods. The study showed that NCS releases MLX with an initial burst followed by sustained release, helping maintain the minimum therapeutic concentration required for effective treatment. Furthermore, the study's findings indicate that MLX-NCS can exert antitumor effects in 3D-printed scaffolds without relying on the COX-2 enzyme. This suggests that MLX can have antitumor effects independent of COX-2 expression. In summary, the research by Rarokar et al.[40] demonstrates the potential of MLX-loaded NCS as an effective cancer drug delivery system. By utilizing 3D bioprinting technology, the study provides a robust tool for evaluating the antitumor efficacy of MLX-NCS in a 3D environment that reflects the stability and sustained release characteristics of the NPs.[40]

2.6. Three-dimensional bioprinted glioblastoma models for paclitaxel- and sorafenib-loaded solid lipid nanoparticles

In the study conducted by Arduino et al.,[44] the use of solid lipid NPs (SLNs) for drug delivery in glioblastoma models was explored by leveraging 3D bioprinting technology. The authors utilized SLNs as they offer numerous advantages over other colloidal systems.[41] SLNs provide a stable matrix that can encapsulate both hydrophobic and hydrophilic drugs, ensuring controlled and sustained release while minimizing systemic toxicity.[42] Despite these benefits, traditional bulk methods of SLN production face significant challenges in terms of reproducibility and scalability, limiting their clinical translation. To address these challenges, the study employed a microfluidic technique for the preparation of SLNs. This method allows for continuous, controlled synthesis of NPs with a narrow size distribution and high batch-to-batch reproducibility.[43] By optimizing microfluidic parameters, the researchers were able to produce SLNs with an average diameter of approximately 100 nm, a size conducive to effective cellular uptake and drug delivery. The study conducted

various experiments to assess the impact of SLNs on glioblastoma treatment. The SLNs were loaded with the model anticancer drugs paclitaxel and sorafenib, and their cellular uptake and penetration were confirmed through fluorescence microscopy analysis. Notably, the SLNs were effectively delivered to tumor cells, significantly reducing cell viability and demonstrating superior results compared to free drugs.

A key aspect of the study was the use of 3D bioprinting technology to create glioblastoma models.[44] The researchers used a human glioblastoma cell line (U87-MG) to produce 3D tumor spheroids. This was achieved by magnetizing the cells, then placing them in ultra-low attachment 96-well plates, and using a magnetic drive to aggregate the cells into spheroids. To evaluate the penetration of SLNs into the tumors, the NPs were labeled with a fluorescent dye (DiA) and observed using confocal fluorescence microscopy. The researchers incubated the DiA-labeled SLNs with the 3D spheroids for 6 and 24 hours, capturing images at each time point to visualize the extent and depth of SLN penetration into the tumor spheroids. Cytotoxicity assays showed that SLNs loaded with paclitaxel and sorafenib reduced cell viability more effectively than the free drugs. This indicates that SLNs are more efficiently delivered to tumor cells, maximizing the therapeutic efficacy of the drugs. The effectiveness of SLNs in drug delivery was particularly evident in the 3D spheroid models, where the penetration and therapeutic impact of the SLNs were significantly greater compared to free drugs, demonstrating the ability of SLNs to deliver drugs deep into the tumor tissue. The study by Arduino et al.[44] demonstrates that SLNs produced via microfluidics, evaluated in sophisticated 3D-bioprinted tumor models, hold great promise for the effective delivery of anticancer drugs.

2.7. Evaluating nanoparticle uptake in bioprinted tumor spheroids using functionalized lignin nanoparticles

Figueiredo et al.[45] explored the application of bioprinting techniques to develop a 3D tumor spheroid model for evaluating the cellular uptake and efficacy of functionalized lignin NPs (LNPs). These LNPs are functionalized with a dentin phosphophoryn-derived peptide (DSS) to enhance cellular uptake, particularly for cancer treatment applications. The study begins with the synthesis of carboxylated lignin to prepare the LNPs using a solvent exchange method.[45] The LNPs are characterized by their size, polydispersity index, and zeta potential, demonstrating stable spherical NPs suitable for biological applications. EDC/NHS coupling chemistry was then used to functionalize the LNPs with DSS, resulting in DSS-functionalized LNPs (LNP-DSS). The researchers prepared both 2D cell models and 3D tumor spheroids to evaluate how the modifications to the LNPs affected their *in vitro* cytocompatibility.

The bioprinted tumor spheroids were generated using magnetized cancer cells (PC3-MM2, MDA-MB-231, and A549) that aggregate under a magnetic drive. During this process, cells were magnetized using NanoShuttle-PL and cultured in ultra-low attachment 96-well plates to form spheroids via the magnetic drive. For cytotoxicity evaluation, various human cancer cell lines (PC3-MM2, MDA-MB-231, and A549) were used as the 2D cell models, being exposed to LNPs at concentrations up to 500 μg mL^{-1} for 24 hours. In the 3D spheroid model, the cells were exposed to LNPs at concentrations up to 100 μg mL^{-1} for 48 hours to assess cytotoxicity. The results showed that LNP-DSS significantly increased cellular uptake compared to non-functionalized LNPs and LNPs functionalized with 9-amino acid cyclic peptide (iRGD). The cellular uptake rates differed between the 2D and 3D models. In the 2D cell model, sedimentation and diffusion effects led to higher cellular uptake rates, whereas, in the 3D spheroid model, stronger and more realistic cell-cell interactions resulted in lower uptake rates. This difference is attributed to the 3D model's ability to better replicate the realistic tumor microenvironment, thereby providing a more accurate representation of NP-cell interactions.[46]

3. Three-dimensional bioprinted skin tissue models

Skin tissue models are essential tools in dermatological research and pharmaceutical development, providing a means to study skin physiology, disease mechanisms, and the efficacy of topical treatments.[47,48] These models range from simple 2D cell cultures to more complex 3D constructs that better replicate the structural and functional properties of human skin.[12,49,50] Advanced models can include multiple cell types and layers, mimicking the epidermis and dermis to offer more accurate predictions of skin responses.[47,51,52] Such models are crucial for evaluating transdermal drug delivery systems, cosmetic products, and therapeutic NPs, helping to reduce the reliance on animal testing and accelerate the development of new treatments.

3.1. Utilization of 3D bioprinting for evaluating transdermal nanoparticle penetration

Xu et al.[56] presented a groundbreaking study on the use of 3D bioprinting technology to construct an artificial skin model for assessing the transdermal penetration capabilities of NPs. This innovative approach aims to overcome the limitations of traditional methods, which often rely on scarce human skin tissues or costly and time-consuming animal models, particularly porcine

models. The artificial skin model is developed through a meticulous layer-by-layer bioprinting process, involving the alternate deposition of collagen hydrogels and fibroblast cells (Figure 3A). The researchers utilized a 3D Discovery Instrument that allows precise control over the printing parameters, such as valve on-time ratio, air pressure, and nozzle diameter. This control is critical for creating well-defined, consistent 3D structures that closely mimic the natural architecture of human skin. One of the significant advantages of this bioprinted skin model is its ability to maintain cell viability and structural integrity over an extended period.

Xu et al.[56] demonstrated that their construct, composed of multiple layers of collagen and fibroblasts, remained stable and functional for at least 14 days in culture. The cells within the construct exhibited high viability rates, indicating effective nutrient diffusion and a conducive environment for cellular activities. To validate the model's efficacy for NP screening, the research team tested the penetration abilities of polystyrene NPs with different surface charges. The study focused on hydroxyl, amine, and sulfate-modified polystyrene NPs, which possess varying surface chemistries and, consequently, different penetration efficiencies (Figure 3B). The bioprinted skin model revealed that amine-modified NPs, which are positively charged, penetrated the collagen layers more effectively than their negatively charged counterparts. This finding is consistent with previous studies involving living skin tissues, suggesting that the bioprinted model accurately replicates the behavior of natural skin. The bioprinting technique employed not only facilitates rapid screening of NPs but also offers a scalable and ethically sound alternative to animal testing.[53,54] By enabling the precise control of cell placement and scaffold structure, bioprinting allows for the creation of complex tissue models that can be tailored to specific research needs. This flexibility is particularly beneficial for exploring the mechanisms of transdermal drug delivery and optimizing NP formulations for therapeutic applications.[55] Overall, the study by Xu et al.[56] highlights the potential of 3D bioprinting technology to revolutionize the field of transdermal drug delivery and NP evaluation. The artificial skin model they developed serves as a powerful platform for rapid, cost-effective screening, and providing valuable insights into the interactions between NPs and skin tissue.[56]

3.2. Quinizarin-loaded nanocapsules and 3D-bioprinted skin model for photodynamic therapy evaluation

Amaral et al.[57] developed an approach for evaluating photodynamic therapy (PDT) using quinizarin-loaded nanocapsules (QZ/NC) within a 3D-bioprinted skin model. This study focuses on the application of these nanocapsules in addressing the inflammatory processes in skin diseases through PDT. The research presents a comprehensive evaluation of the physicochemical properties, stability, cytotoxicity, permeation, and cytokine modulation of QZ/NC. The QZ/NCs were prepared using the nanoprecipitation method, with a polymer coating composed of poly(L-lactic acid-co-glycolic acid) (PLGA) and lecithin. These nanocapsules demonstrated excellent compatibility, as evidenced by cytotoxicity tests on HaCaT cells, showing no significant toxicity at lower concentrations. The permeation studies utilized a sophisticated 3D-bioprinted skin model, designed through suspended layer additive manufacturing, which mimics the epidermal and dermal layers of human skin. Fluorescence analysis confirmed the successful permeation of QZ/NCs across all skin layers, highlighting their enhanced bioavailability and permeability in the stratum corneum.

The bioprinted skin model can simulate the *in vivo* environment, thereby providing a reliable platform for evaluating the therapeutic efficacy of QZ/NCs in PDT. This model was created using a bioink composed of pectin and collagen, which mimic the polysaccharides and proteins, respectively, found in native ECM. The suspended layer additive manufacturing method involved using computer-aided design (CAD) to accurately replicate the complex structure of human skin, layer by layer. This precise bioprinting technique allowed for the creation of a skin model that closely resembles the actual human skin, both structurally and functionally, enabling accurate assessment of nanocapsule permeation and intracellular incorporation. PDT and QZ/NCs were tested on this model, revealing significant enhancement in drug delivery efficiency and effective intracellular drug accumulation. Further experiments involved inducing an inflammatory process in HaCaT cells using bacterial lipopolysaccharide (LPS) and subsequently treating them with QZ/NC and PDT. The cytokine modulation was analyzed through enzyme-linked immunosorbent assay (ELISA), which showed a notable reduction in pro-inflammatory cytokines (interleukin [IL]-1β, IL-8, and monocyte chemoattractant protein-1 [MCP-1]) after PDT treatment. This anti-inflammatory effect was significantly more pronounced compared to treatments with QZ/NCs or LED light alone. The integration of 3D bioprinting and nanotechnology in this study underscores the potential for developing advanced therapeutic modalities that overcome the limitations of current treatments for skin inflammation.[57]

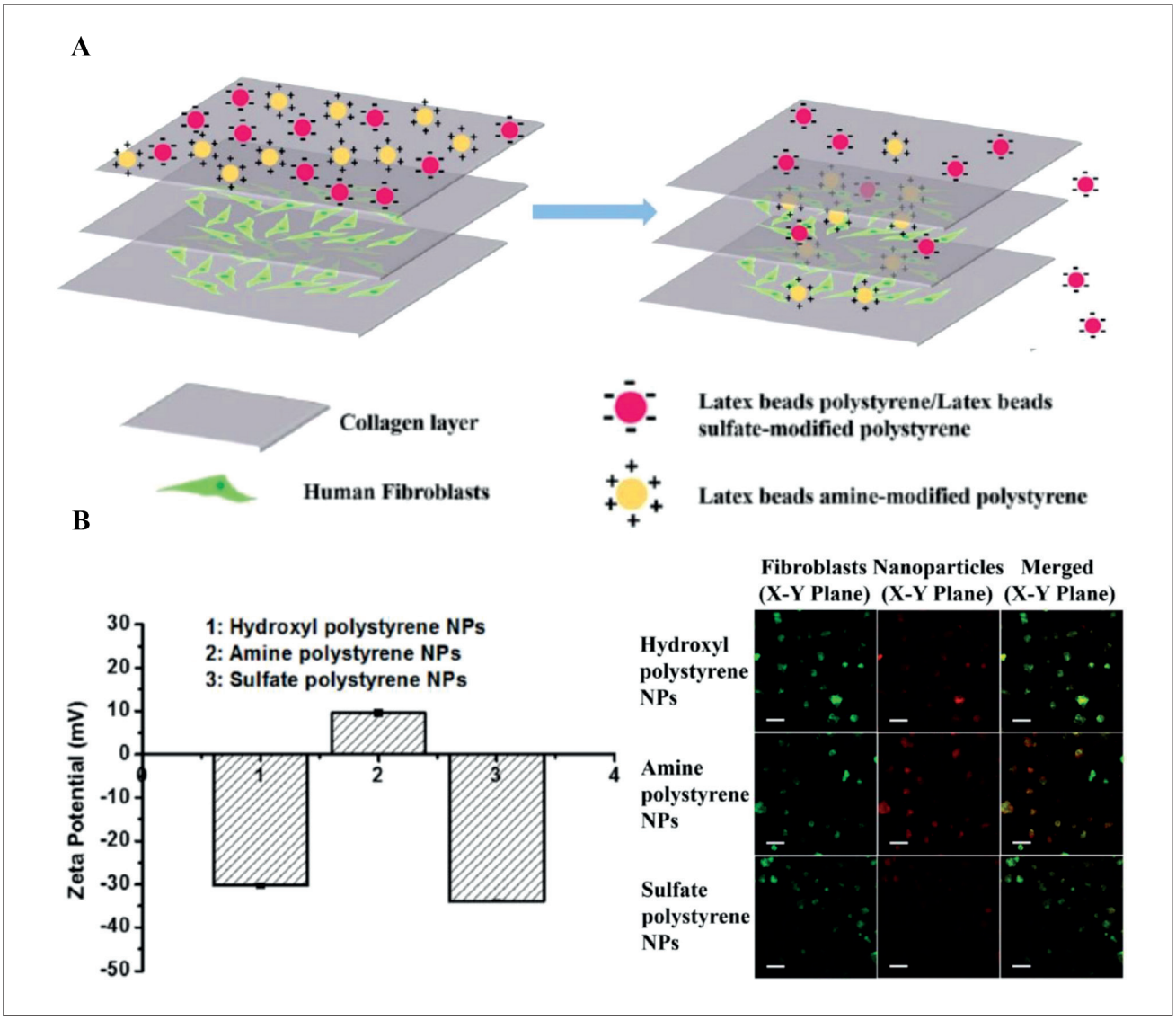


Figure 3. Layer-by-layer 3D skin model for evaluation of skin penetration efficacy of nanoparticles (NPs) with different charges. (A) Three-dimensional skin model fabricated through layer-by-layer deposition of collagen and fibroblasts. (B) Amine-modified positively charged polystyrene NPs penetrate collagen layers more effectively than hydroxyl and sulfate-modified negatively charged polystyrene NPs. Reproduced with permission from Hou et al.[56] Copyright © 2017 Society for Laboratory Automation and Screening.

4. Three-dimensional bioprinted ear models

Three-dimensional bioprinting technology has significantly advanced the development of ear models for tissue engineering and regenerative medicine. This technology allows for the precise deposition of cells and biomaterials, enabling the creation of complex structures that closely mimic the natural architecture of human tissues. The printing of ear constructs, in particular, uses patient-specific imaging data to achieve high accuracy, incorporating the patient's own cartilage cells for better integration and functionality post-implantation.[58,59] Recent studies have successfully integrated microvascular networks within these bioprinted ear models, enhancing tissue viability by mimicking natural nutrient and oxygen supply. Additionally, 3D bioprinting has shown potential in incorporating therapeutic agents into the printed structures, improving treatments for conditions such as cartilage damage and ear deformities. These technological advancements have revolutionized ear model fabrication, offering robust and customizable solutions that enhance

patient outcomes through personalized and precise medical interventions.[60,61]

4.1. Three-dimensional bioprinted human auricular model for cyclosporine A- and coenzyme Q10-loaded solid lipid nanoparticles

The study by Yalgın et al.[62] used 3D bioprinting technology to develop human auricular models for evaluating the effects of SLNs loaded with cyclosporine A (CycA) and coenzyme Q10 (Q10) on cell growth. The authors employed biocompatible materials such as alginate, polylactic acid (PLA), and polyvinyl alcohol (PVA) using an Ultimaker-2 3D printer to create models that mimic human ear structures (Figure 4A). The primary goal is to assess the suitability of these 3D-printed models for NIH-3T3 fibroblast growth in the presence of CycA and Q10 SLNs. The 3D printing process involves creating precise, layer-by-layer models from these biocompatible materials. Alginate, PLA, and PVA were tested for their ability to serve as scaffolds for cell growth. However, due to mechanical instability, alginate hydrogels were less suitable, while PLA provided a stable scaffold conducive to NP incorporation. The study utilized a high-shear homogenization technique to prepare the SLNs, which were then incorporated into the PLA models. The incorporation of SLNs into the 3D-printed PLA models allowed for a controlled release of CycA and Q10, enabling a detailed evaluation of their effects on cell viability and growth. MTT assays were used to measure cell viability, showing that Q10-SLNs significantly enhanced cell proliferation and mitigated the cytotoxic effects of CycA. Specifically, while CycA-SLNs alone resulted in lower cell viability, the addition of Q10-SLNs to the PLA models improved cell viability to a substantial degree (Figure 4B). Three-dimensional bioprinting offers significant advantages for tissue engineering, particularly in creating patient-specific models with complex geometries. This study demonstrates that 3D-printed PLA auricular models effectively support fibroblast growth and NP delivery, providing a stable environment for evaluating SLNs.[62]

5. Three-dimensional bioprinted cardiovascular and vascular models

Recent advancements in 3D bioprinting technologies have significantly propelled the field of cardiovascular and vascular regeneration. These cutting-edge techniques enable the fabrication of complex, functional blood vessel structures, which are crucial for treating various vascular conditions.[63–66] Key studies have demonstrated the potential of integrating drug-loaded NPs within 3D-bioprinted constructs to enhance therapeutic outcomes. The incorporation of rapamycin-loaded NPs into artificial blood vessels shows promise in improving ischemic repair. Meanwhile, the use of magnetic NPs for targeted drug delivery effectively addresses stenosis in blood vessels. Furthermore, the development of cell-laden blood vessels with dual drug delivery systems represents a significant leap forward, offering comprehensive solutions for vascular regeneration. These interdisciplinary approaches underscore the transformative potential of combining 3D bioprinting with nanotechnology in the field of regenerative medicine.

5.1. Bioprinting of artificial blood vessels with rapamycin-loaded nanoparticles for vascular regeneration

The study by Choi et al.[71] explored an approach using 3D bioprinting technology to fabricate artificial blood vessels loaded with rapamycin-loaded NPs. This method aims to address significant clinical challenges posed by vascular diseases, such as restenosis following interventions like stent placement.[67–69] The researchers utilized 3D bioprinting to create artificial blood vessels that closely mimic natural vascular architecture. This technique allowed for precise control over the dimensions and structure of the vessels, ensuring they were tailored to the specific needs of the patient. The customization capabilities of 3D printing are crucial for creating patient-specific solutions, which are more effective and less likely to be rejected by the body. One of the significant advancements in this study was the integration of NPs within the 3D-printed vessels. These NPs were made from mesoporous silica, characterized by their small size and porous nature, which allowed for efficient drug loading and controlled release. The study focused on rapamycin, a drug known for its potent ability to prevent restenosis by inhibiting smooth muscle cell proliferation. By encapsulating rapamycin in NPs, the authors aimed to achieve sustained and localized drug delivery, thereby enhancing its therapeutic efficacy while minimizing systemic side effects. The bioprinting process involved creating a bioink composed of a mixture of sodium alginate and atelocollagen, which was used to print the vessel's structure. The core material, a sacrificial substance made from Pluronic® F-127, was used to create the lumen of the blood vessels. Endothelial progenitor cells (EPCs) were also incorporated into the bioink to promote re-endothelialization, a critical process for long-term vessel functionality and integration into the host tissue.[70] To evaluate the effectiveness of the 3D-printed vessels, Choi et al. included both *in vitro* and *in vivo* experiments. *In vitro*, the researchers assessed the stability and drug release profile of the rapamycin-loaded NPs. The NPs demonstrated a slow and controlled release of rapamycin, maintaining its concentration at therapeutic levels over an extended period. This controlled release is essential for preventing

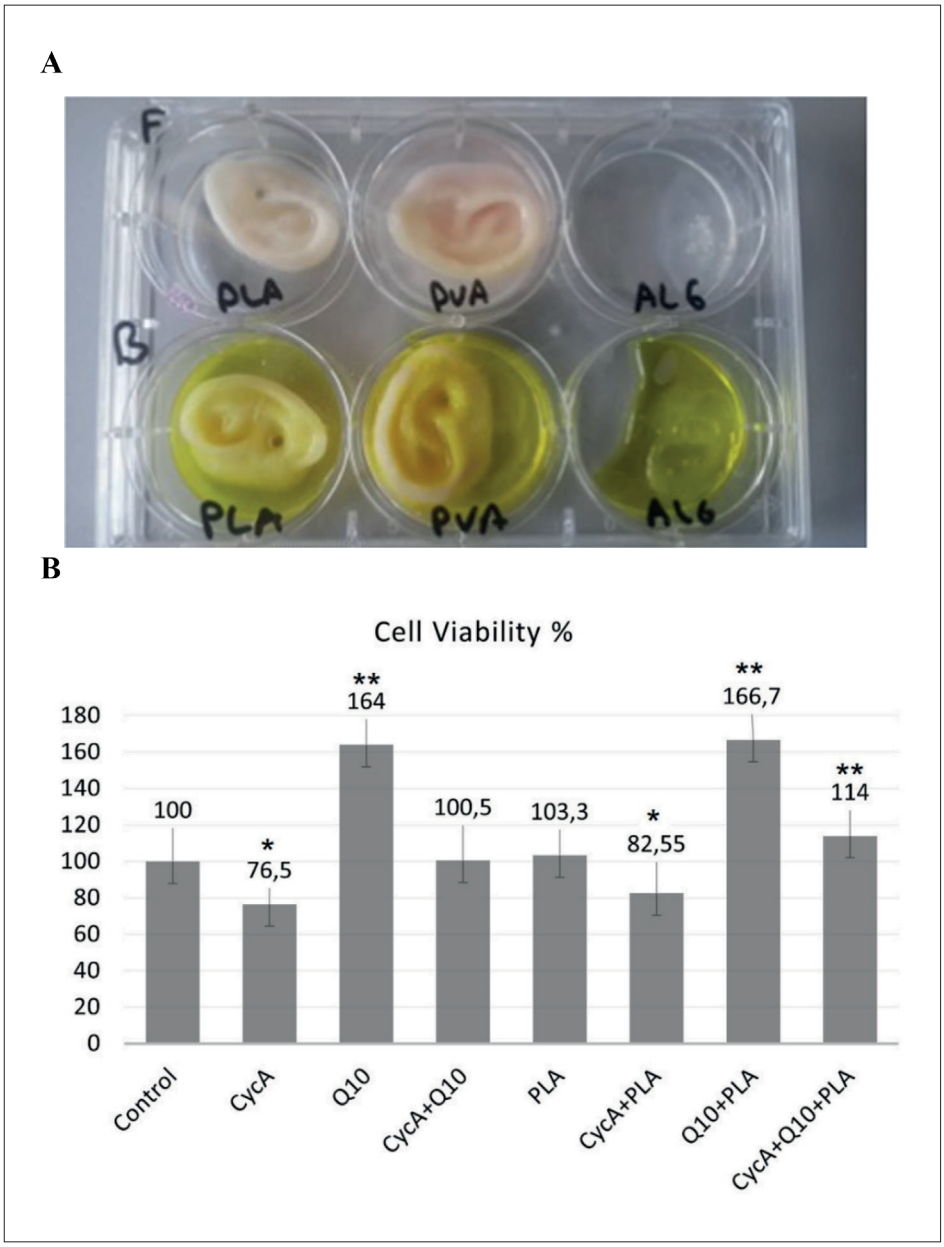


Figure 4. Evaluation of drug loading solid lipid nanoparticles (SLNs) using ear tissue model. (A) Polylactic acid (PLA), polyvinyl alcohol (PVA), and alginate ear models were cultured with fibroblast cells for 4 weeks, showing shrinkage and deterioration in alginate, swelling and disintegration in PVA, while maintenance of its initial hardness in PLA. (B) Coenzyme Q10-SLNs mitigated cyclosporine A (CycA) cytotoxicity and improved cell viability in PLA Models. Reproduced with permission from Yalgın et al.[62] Copyright © 2022 Elsevier B.V.

restenosis, as it ensures the drug remains effective at the site of the blood vessel over time. *In vivo* experiments involved a murine hind limb ischemia model to test the regenerative capabilities of the bioprinted vessels. The results showed that the vessels loaded with rapamycin-NPs and EPCs significantly improved blood flow and reduced tissue necrosis compared to control groups (Figure 5A). Histological analysis further confirmed enhanced capillary and arterial formation, as well as reduced inflammatory responses in the tissues surrounding the implanted vessels. The study by Choi et al.[71] highlights several key advantages of using 3D bioprinting combined with NP technology for vascular regeneration. Firstly, the precise fabrication of vessels with patient-specific dimensions ensures better integration and functionality. Secondly, the controlled release of rapamycin from the NPs effectively prevents restenosis, a common issue in vascular interventions. Finally, the incorporation of EPCs supports the

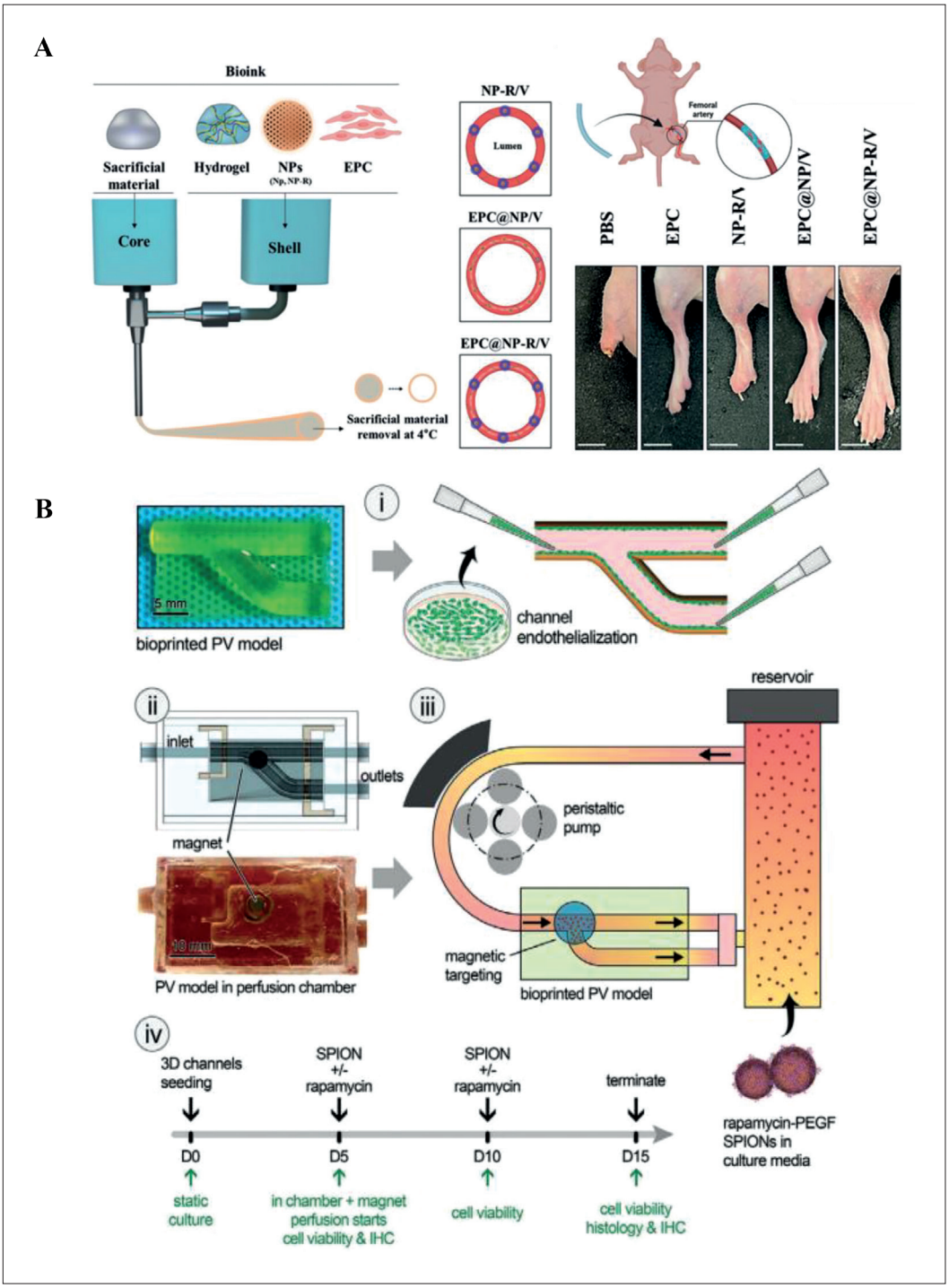


Figure 5. Schematic Illustration of a 3D Artificial Blood Vessel Model and Nanoparticle Evaluation. (A) 3D artificial blood vessels and evaluation of rapamycin nanoparticles (NPs) for restenosis control.[71] (B) Evaluation of rapamycin-conjugated superparamagnetic iron oxide NPs using a bifurcated 3D pulmonary vein stenosis model closely mimicking human pulmonary vein anatomy.[75]

regeneration of endothelial cells, crucial for the long-term success of the implanted vessels.[71]

5.2. Three-dimensional bioprinted pulmonary vein stenosis models for targeted nanoparticle delivery

Ning et al.[75] developed an *in vitro* model of pulmonary vein stenosis (PVS) using 3D bioprinting technology (Figure 5B). This study aims to address the limitations of the current PVS treatments, particularly issues of restenosis and off-target effects, by creating a precise and controllable model for studying disease mechanisms and potential therapies. The research team employed digital light processing-based 3D bioprinting to fabricate bifurcated pulmonary vein (PV) constructs that closely mimic the anatomical features of human pulmonary veins. These constructs were seeded with human umbilical vein endothelial cells (HUVECs) and maintained in a perfusion bioreactor system, which simulates a dynamic flow environment similar to physiological conditions. This setup enabled the formation of a uniform and viable endothelium within the PV constructs. The study used superparamagnetic iron oxide NPs (SPIONs) conjugated with rapamycin, a potent mTOR inhibitor effective in reducing vascular cell proliferation.[72–74] The SPIONs were designed to be magnetically guided to specific regions of the bioprinted PV constructs using an external magnetic field. Computational modeling identified the bifurcation points within the PV constructs as high-risk areas for endothelial cell overgrowth, making them ideal targets for NP delivery. The application of an external magnetic field effectively concentrated the rapamycin-loaded SPIONs at the bifurcation points, significantly reducing endothelial cell proliferation. This targeted approach minimized adverse side effects associated with systemic drug delivery, such as immunosuppression and endothelial damage. Magnetic targeting allowed for precise localization of therapeutic NPs, enhancing treatment efficacy. The mechanical properties and structural fidelity of the bioprinted PV constructs were thoroughly characterized, demonstrating high precision and reproducibility. The porous structure facilitated nutrient and oxygen exchange, which is essential for maintaining cell viability over extended culture periods. The 3D bioprinting technology also enabled the production of patient-specific models, increasing the relevance and applicability of the *in vitro* system for PVS research.[75]

5.3. Three-dimensional bioprinting of dual drug-loaded artificial blood vessels for enhanced vascular regeneration

In the study conducted by Lee et al.[76] the innovative use of 3D bioprinting technology to fabricate artificial blood vessels incorporating NPs loaded with atorvastatin and curcumin, aimed at enhancing vascular regeneration, was explored. This approach leverages the synergistic effects of these drugs on EPCs to address challenges in cardiovascular therapy, particularly in the context of ischemic diseases. The core of the study revolves around the encapsulation of atorvastatin and curcumin into NPs. Atorvastatin is known for its ability to lower cholesterol and enhance nitric oxide production, promoting vasodilation and anti-inflammatory effects. Curcumin, a potent antioxidant, combats reactive oxygen species (ROS), which are typically elevated in ischemic conditions and transplantation scenarios. The dual-drug-loaded NPs (NPSC) are designed to provide controlled, sustained release of the drugs, enhancing their therapeutic efficacy and reducing potential side effects.

To create the artificial blood vessels, the researchers employed a bioprinting technique using bioink composed of EPCs isolated from umbilical cord blood, combined with the NPSC. The bioprinting process allowed for precise control over the size and shape of the blood vessels, accommodating various anatomical requirements. This customization is critical for ensuring the successful integration and function of the transplanted vessels within the host's circulatory system. The characterization of the NPs revealed consistent spherical shapes and sizes, confirming the stability and reproducibility of the fabrication process. The sustained release profiles of statin and curcumin from the NPs were validated using liquid chromatography/mass spectrometry (LC/MS), ensuring that the therapeutic agents were available over extended periods. Additionally, the biocompatibility assessments indicated that the NPs were non-toxic to EPCs even at high concentrations, supporting their safe application *in vivo*. Upon transplantation into a mouse model of hindlimb ischemia, the NPSC-loaded artificial blood vessels demonstrated significant improvements in vascular regeneration. The *in vivo* studies showed enhanced blood flow recovery and reduced tissue necrosis in the treated groups compared to controls. Histological analyses confirmed increased expression of vascular markers, such as CD31 and alpha-smooth muscle actin (α-SMA), indicating successful angiogenesis and vascular repair.

The study highlights several advantages of using 3D-bioprinting for vascular regeneration.[76] The ability to customize artificial blood vessels ensures better anatomical fit and integration, while the incorporation of NPs allows for localized, sustained drug delivery. This approach minimizes systemic side effects and provides a targeted therapeutic effect, crucial for treating complex vascular diseases. The combination of atorvastatin and curcumin within the NPs leverages their complementary mechanisms, enhancing cell function and survival

in oxidative stress environments typical of ischemic tissues. Lee et al.'s research demonstrates the potential of 3D-bioprinted artificial blood vessels loaded with dual-drug NPs as a promising strategy for vascular regeneration. This method not only provides a customizable and efficient means of restoring blood vessel functionality but also offers a novel approach to localized and sustained drug delivery, paving the way for advancements in regenerative medicine and cardiovascular therapy.[76]

5.4. Evaluation of gold nanoparticle-coupled microRNA therapeutics using a 3D-bioprinted model of calcific aortic valve disease

Van der Ven et al.[79] investigated the use of 3D bioprinting to create a model of calcific aortic valve disease (CAVD) for evaluating the efficacy of gold NP (AuNP)-coupled microRNA (miRNA) therapeutics.[77,78] This research utilizes a novel bioprinting technique to develop a realistic human tissue model that can mimic the complex biological environment of CAVD. The bioprinted constructs were produced using a hydrogel blend of GelMA and hyaluronic acid methacrylate (HAMA), facilitating the precise deposition of cells and ECM components to replicate the calcified tissue found in CAVD. The process involved printing a cylindrical mold using Pluronic gel and then infilling it with a pre-polymer hydrogel solution, which was subsequently crosslinked with ultraviolet light to form stable hydrogel discs.

The primary innovation in this study lies in the use of an injectable, shear-thinning, self-healing hydrogel system to deliver AuNP-miRNA therapeutics within the bioprinted CAVD model. The hydrogels were prepared from HPMC-C12 and PEG-*b*-PLA NPs, which provide a biocompatible and responsive environment for sustained miRNA release. The miRNA molecules were conjugated to AuNPs to enhance their stability and delivery efficacy, with additional functionalization using influenza hemagglutinin (HA1) peptide to promote endosomal escape and intracellular release. The hydrogel's shear-thinning properties allow for minimally invasive injection, making it a practical solution for *in vivo* applications. The study demonstrated a linear release profile of the AuNP-miRNAs over several days, with the particles maintaining their functional activity *in vitro* as evidenced by successful transfection and gene knockdown in HEK293 cells. This research highlights the potential of combining advanced bioprinting techniques with smart hydrogel systems to develop effective and targeted therapies for cardiovascular diseases.[79]

6. Three-dimensional bioprinted bone model

In the realm of biomedical research and tissue engineering, the development of accurate and functional bone models is essential for the evaluation of new therapeutic approaches and materials.[80,81] Three-dimensional bioprinting technology has emerged as a powerful tool in this field, offering unparalleled precision in creating complex bone tissue constructs.[82–85] These models closely mimic the natural extracellular matrix and mechanical properties of bone, providing a realistic environment for studying cell behavior, disease progression, and the efficacy of various treatments.[85] By incorporating different biomaterials and bioactive molecules, bioprinted bone models can enhance cell proliferation, differentiation, and mineralization, which are critical for successful bone regeneration and repair.[86–88]

6.1. Bioprinted SaOS-2 cell model for evaluating nanoparticles via bioglass-enhanced biomineralization

The study conducted by Wang et al.[92] delves into the effects of bioglass on the growth and biomineralization of SaOS-2 cells encapsulated within a bioprintable hydrogel composed of alginate and gelatin. The bioprinting technology is pivotal for creating complex, 3D tissue models that accurately mimic the ECM of bone tissues, thus providing a robust platform for evaluating the efficacy of NPs in biomedical applications. The bioprinting process involved encapsulating SaOS-2 cells, a type of osteosarcoma cell line, within an alginate/gelatin hydrogel matrix. This matrix was enhanced with various additives, including polyphosphate (polyP), administered as polyP together with $CaCl_2$ (polyP·Ca^{2+}-complex), silica, and enzymatically prepared biosilica. These components were chosen for their known biological activities that support cell growth and mineralization. The bioprinted constructs were designed using computer-aided techniques to ensure precise architecture and consistency in scaffold production (Figure 6A).

One of the key findings was that the inclusion of bioglass NPs significantly promoted the mineralization capacity of the encapsulated SaOS-2 cells.[89–91] Bioglass particles, approximately 55 nm in size, were added to the hydrogel, and their impact on cell proliferation and mineralization was assessed. The study revealed that the bioglass did not adversely affect cell growth; instead, it enhanced the mineralization activity of the cells. When combined with polyP·Ca^{2+}-complex, silica, or biosilica, the bioglass particles increased the mineral deposition by up to 6.8-fold compared to the controls without bioglass (Figure 6B). The primary advantage of using bioprinting in this context lies in its ability to create a highly controlled environment that mimics the natural ECM, thereby providing a more accurate assessment of NP efficacy. The bioprinted hydrogel scaffolds not only supported cell viability but also facilitated enhanced biomineralization, which is crucial for bone tissue engineering. The use of bioglass

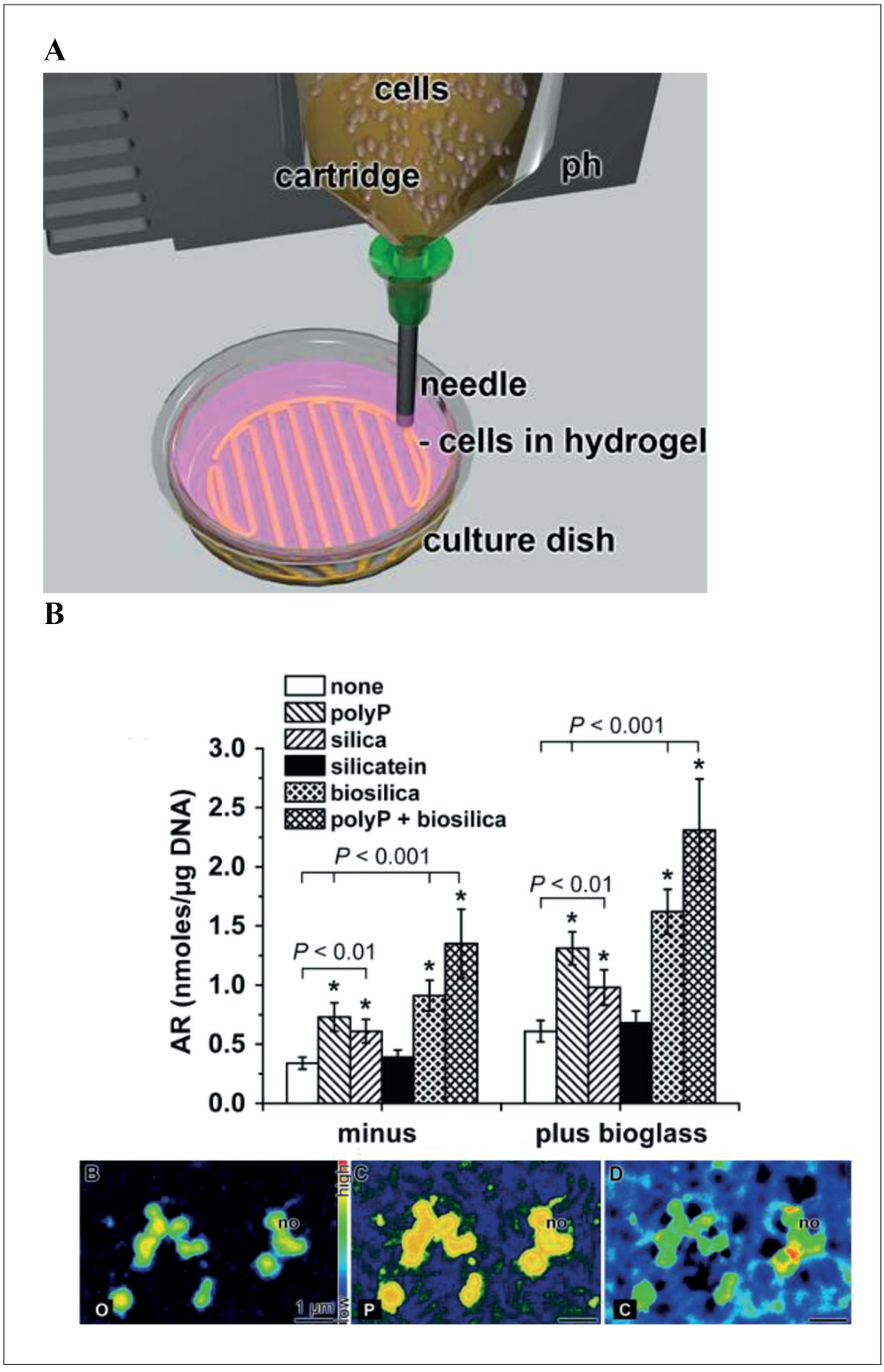


Figure 6. Effect of bioglass on the growth and biomineralization of SaOS-2 cells (an osteosarcoma cell line) encapsulated in hydrogel after 3D cell bioprinting.[92] (A) Three-dimensional bioprinting structure encapsulating SaOS-2 cells in alginate/gelatin hydrogel matrix. (B) Evaluation of the mineralization promoting ability of encapsulated SaOS-2 cells with the inclusion of bioglass (nano) particles.

in the outer matrix of these scaffolds provided additional mechanical support and bioactivity, leading to improved outcomes in terms of cell proliferation and mineralization. By incorporating bioglass into the bioprinted scaffolds, the study demonstrates a significant enhancement in the biomineralization capabilities of SaOS-2 cells, providing a valuable strategy for the development of advanced, biocompatible implants.[92]

7. Three-dimensional bioprinted inflammatory disease model

Three-dimensional bioprinting technology has emerged as a crucial tool in the study of inflammatory diseases.[93–95] This technology enables the creation of models that surpass traditional 2D culture systems by replicating the complex structures and environments of actual human tissues.[96] Such models allow for a more precise analysis of inflammatory responses and interactions between immune cells. They are particularly useful in studying inflammatory bowel diseases, Crohn's disease, colitis, and other related conditions, facilitating the evaluation of new anti-inflammatory treatments.[97–99] By accurately mimicking the pathological features of inflammatory diseases, 3D bioprinting enhances the preclinical testing phase, providing reliable data on the efficacy and safety of drugs before they enter clinical trials.

7.1. Three-dimensional bioprinted colitis-mimicking model for evaluation of albumin nano-encapsulated anti-inflammatory drugs

Almutary et al.[101] conducted an insightful study leveraging 3D bioprinting technology to develop a colitis-mimicking model, aiming to assess epithelial barrier function using albumin nano-encapsulated anti-inflammatory drugs. The research addresses a significant gap in drug development: the lack of effective preclinical models that accurately replicate the physiological conditions of the human intestine, which often leads to poor predictions of drug efficacy and toxicity. The study utilized 3D bioprinting to create a model that closely mimics the intestinal environment under colitis conditions. The authors employed Caco-2 and HT-29 colon cancer cell lines, which are standard in studies of intestinal function. These cells were incorporated into a bioink and bioprinted using the INKREDIBLE bioprinter, which offers precise control over the printing process. The bioprinter used pneumatic pressure to extrude cell-laden hydrogel strands, creating a layered structure that closely resembles the architecture of the intestinal epithelium. One of the key advantages of 3D bioprinting highlighted in the study is its ability to control cell shape and spatial organization, which are crucial for accurate physiological modeling.[100] Traditional 2D cell cultures fail to replicate the complex interactions and 3D structure of tissues, leading to less reliable data. In contrast,

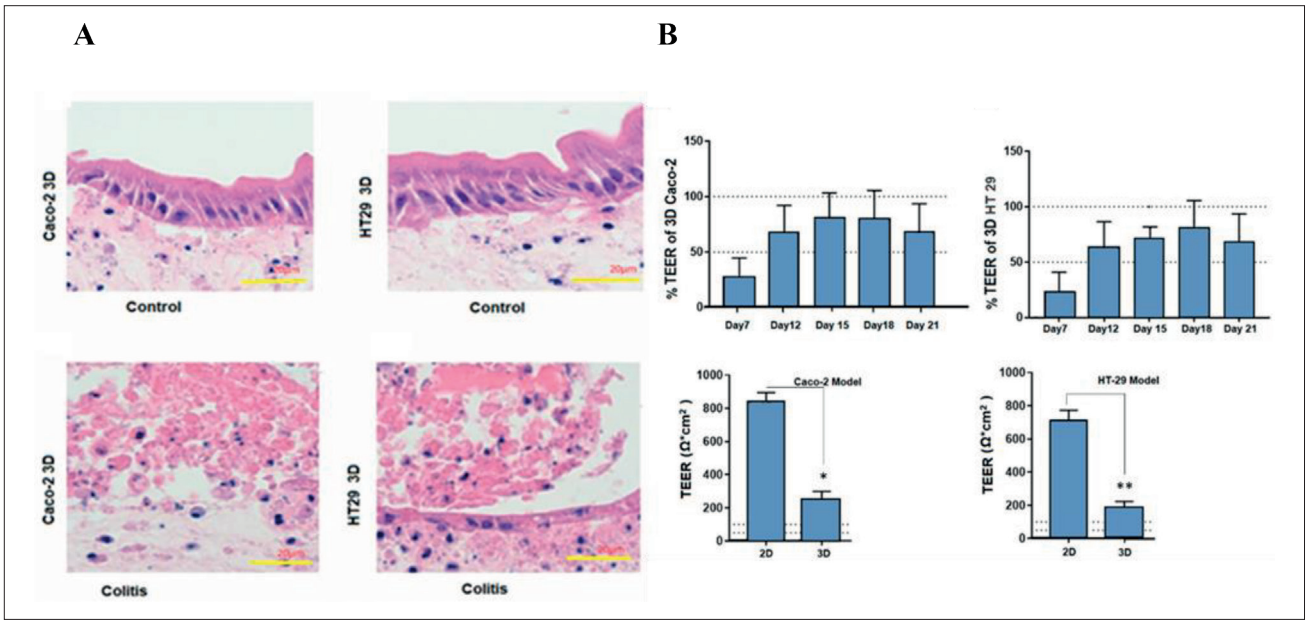


Figure 7. Evaluation of nanoparticles (NPs) using inflammatory disease model.[101] (A) Comparison of hematoxylin & eosin (H&E) staining between a 3D colon model and a 3D colitis model induced by dextran sodium sulfate (DSS). (B) Comparison of transepithelial electrical resistance (TEER) values between 2D and 3D models.

the 3D-bioprinted model allows for the creation of more physiologically relevant structures, which can provide more accurate assessments of drug effects.

The authors also demonstrated the induction of a colitis-like condition in their 3D-printed model by treating it with dextran sodium sulfate (Figure 7A).[101] Histological analysis showed significant epithelial disorganization, indicative of colitis, thereby validating the model's ability to mimic disease conditions accurately. This is crucial for studying the efficacy of anti-inflammatory drugs in a controlled, reproducible environment. Furthermore, the study compared the barrier function of the 3D-printed constructs with traditional 2D monolayer cultures. The transepithelial electrical resistance (TEER) measurements revealed that the 3D-printed models provided more reliable data on barrier function, maintaining higher physiological relevance over time compared to 2D cultures (Figure 7B). This is a significant finding, as barrier integrity is a critical factor in evaluating the therapeutic potential of anti-inflammatory drugs. The researchers also assessed the impact of albumin nano-encapsulated drugs, specifically roxadustat and caffeic acid phenethyl ester, on the barrier function of the 3D-printed colitis model. They observed that these nano-encapsulated drugs were effective in maintaining barrier integrity, as indicated by stable TEER values. This suggests that the 3D-printed model can be an effective tool for evaluating the efficacy of nano-encapsulated therapies, which are increasingly important in the treatment of inflammatory diseases.[101]

8. Three-dimensional bioprinted toxicity models

Understanding the toxicity of NPs is crucial to ensuring their safe application in biological systems.[102–104] Toxicity studies investigate how NPs interact with cellular environments, affecting cell survival, proliferation, and function. Nanoparticle toxicity can lead to cell damage, inflammatory responses, and long-term biocompatibility issues.[105–107] Three-dimensional bioprinting technology offers a novel method for toxicity evaluation by mimicking more realistic tissue structures compared to traditional 2D cultures.[108] This approach allows for a more accurate analysis of the long-term effects and bioaccumulation of NPs.[109,110]

8.1. Three-dimensional bioprinted human cardiac tissue model for evaluating copper oxide nanoparticle toxicity

The study by Miller et al.[112] utilized advanced bioprinting technology to create human-induced pluripotent stem cell (iPSC)-derived cardiac microtissues for evaluating the toxicity of copper oxide (CuO) NPs. This research focused on assessing the dose-dependent toxicity of CuO NPs by examining cell viability, contractile function, and gene expression related to mitochondrial biogenesis and apoptosis pathways. The 3D bioprinting process was used to construct cardiac microtissues that closely mimic the structural and functional properties of human heart tissue. The bioprinted tissues included iPSC-derived cardiomyocytes and human cardiac fibroblasts, creating a complex tissue environment. CuO NPs were coated with bovine serum albumin to simulate protein adsorption *in vivo*, which stabilizes the NPs and enhances the reliability of experimental results.[111] CuO NP exposure resulted in significant cytotoxicity in the bioprinted cardiac tissues. Viability assays indicated a median lethal dose (LD_{50}) of 7.176 μg/mL, with complete cell death observed at 100 μg/mL. Notably, the contractile force of the tissues significantly decreased at 10 μg/mL after 48 hours, highlighting the impact of CuO NPs on cardiac function. Interestingly, the beating frequency of the tissues was not significantly affected up to the 10 μg/mL dose, suggesting that the electrical signaling pathways related to contraction remained intact at lower NP concentrations. Gene expression analyses provided further insights into the mechanisms of CuO NP toxicity. The study found dose-dependent increases in markers of mitochondrial biogenesis, such as peroxisome proliferator-activated receptor gamma coactivator 1-alpha (PCG-1α) and NADH dehydrogenase 1 (NDI), indicating mitochondrial damage. Additionally, significant upregulation of caspase 3 and caspase 8 suggested that apoptosis in the cardiac tissues was mediated primarily through the extrinsic death receptor pathway. The use of 3D-bioprinted cardiac tissues offers several specific advantages over traditional models. For example, it allows for more accurate replication of cell-cell and cell-matrix interactions, providing a realistic assessment of cellular behavior and response. Additionally, the integration of force measurement capabilities enables direct evaluation of changes in tissue contractility, which is crucial for understanding the impact of toxicants on cardiac health. Miller et al.'s study presents significant methodological advancements in utilizing bioprinting technology to evaluate NP toxicity. This approach provides a robust tool for precisely assessing the effects of NPs on human tissues and establishes a solid foundation for future toxicological research.[112]

8.2. Organoid-based bioprinting for toxicological evaluation of silver nanoparticles

Gerbolés et al.[115] studied the application of 3D bioprinting to create organoid-based scaffolds for long-term toxicological investigations of NPs (Figure 8). This approach aims to simulate the exposure of lung cells to NPs, providing a more accurate model for nanotoxicological studies

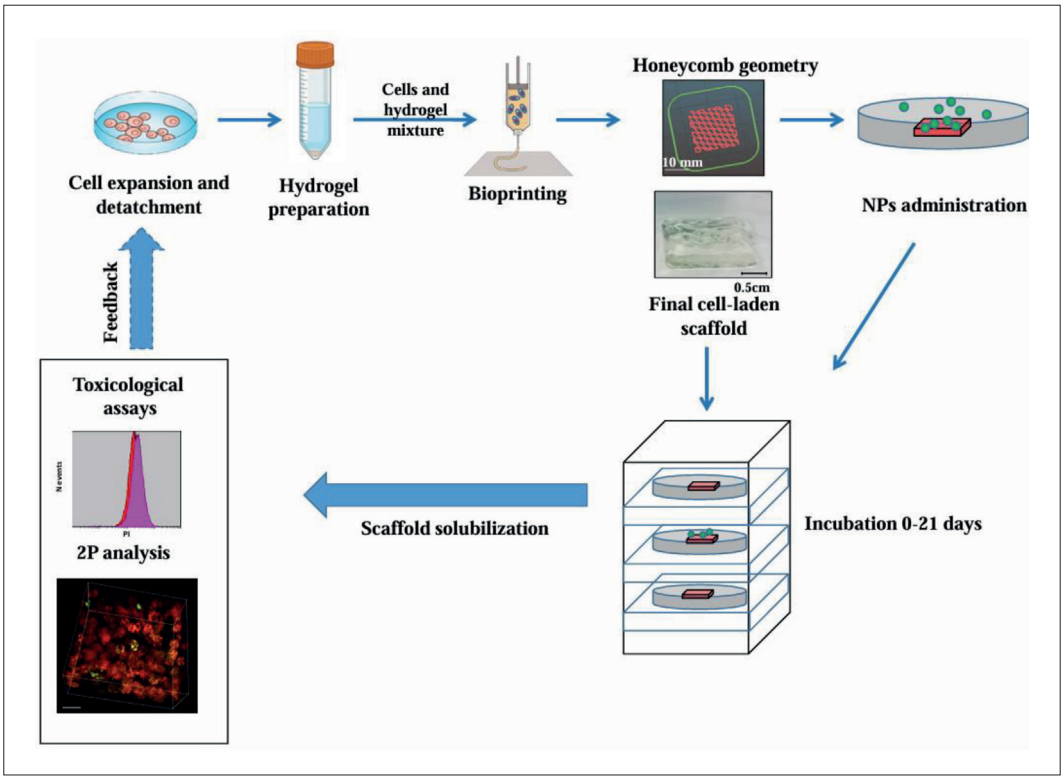


Figure 8. Three-dimensional bioprinted matrix model that closely mimics real tissue environments, providing a more realistic assessment of nanoparticle (NP) toxicity.[115]

compared to conventional 2D cell cultures. The researchers used a customized 3D bioprinter to print viscous cell-laden hydrogels. These hydrogels were composed of a mixture of alginate, gelatin, and Matrigel, optimized to support cell viability and structural integrity.[113] The printed scaffolds were then used to culture immortalized lung cell lines over extended periods, specifically to observe the interaction with NPs such as 40 nm latex-fluorescent and 11–14 nm silver NPs (AgNPs).

One of the significant findings of this study is the enhanced cell proliferation within the 3D-printed scaffolds. Over 14 days, the cell count increased from 5×10^5 to 1.27×10^6, demonstrating a conducive environment for cell growth. Furthermore, the lipid peroxidation levels were reduced by 91%, indicating a decrease in oxidative stress, which is a common response to NP exposure. The 3D environment also showed minimal cell death over a 21-day period, highlighting the protective nature of the bioprinted scaffolds. The diffusion of NPs within the 3D scaffolds was another critical observation. Fluorescent NPs were able to spread throughout the scaffolds, unlike in the unprinted environments. This characteristic is vital for mimicking *in vivo* conditions where NPs interact with cells in a more complex 3D space. Additionally, cell viability in 3D cultures exposed to AgNPs was significantly higher compared to 2D cultures, suggesting that the 3D-bioprinted models better replicate the *in vivo* responses to NP exposure.

The study also emphasizes the advantages of using 3D bioprinting for nanotoxicology investigations.[115] Firstly, it allows for the creation of more physiologically relevant models that can maintain cell viability over longer periods without frequent passages. Secondly, the ability of NPs to diffuse and interact with cells in a 3D matrix closely mimics real tissue environments. Thirdly, the 3D-printed scaffolds provide a more realistic assessment of NP toxicity, showing similar toxicological responses to those observed in *in vivo* studies, such as those with zebrafish, insects, and rodents.[114] In summary, the research conducted by Gerbolés et al.[115] demonstrates that 3D bioprinting of organoid-based scaffolds presents a promising advancement for the long-term investigation of NP toxicology. This method not only improves the accuracy of *in vitro* models but also reduces the use of animals in experiments, aligning with the principles of the 3Rs (Replacement, Reduction, and Refinement) in toxicological research. The findings suggest that 3D bioprinting could be a vital tool for future nanotoxicology and nanomedicine research, providing more reliable and ethically sound alternatives to traditional methods.[115]

9. Three-dimensional bioprinted drug release model

The evaluation of drug release profiles and their impact on cellular environments is crucial for developing effective therapeutic strategies.[116–118] This section explores various methodologies used to study drug release from NP-based systems within 3D-bioprinted models. Advanced bioprinting techniques enable the creation of complex *in vitro* environments that closely mimic *in vivo* conditions. Specifically, 3D bioprinting excels in replicating cell-cell and cell-matrix interactions, allowing for more accurate assessments of NP drug release and cellular responses.[119–121] These studies highlight the importance of optimizing bioprinting parameters and materials to advance preclinical drug testing and therapeutic applications.

9.1. GelMA bioinks for evaluating nanoparticle-based minocycline release and cellular protection

Fu et al.[123] conducted a study utilizing bioinks to develop a 3D-bioprinted model for evaluating the release and protective effects of minocycline (MH)-loaded NPs under oxidative stress conditions. This research underscores the significant potential of 3D bioprinting in creating *in vitro* models that closely mimic the *in vivo* environment for more accurate NP evaluation. The study focused on leveraging the thermoresponsive and photocrosslinking properties of GelMA to create a suitable bioink for extrusion bioprinting. The primary challenge addressed was the time- and temperature-dependent flow behavior of GelMA, which affects its printability and cell viability. By optimizing the extrusion printing process, the researchers successfully printed GelMA constructs with high fidelity and cell survival rates. They determined the optimal GelMA concentrations and printing conditions to achieve this balance.

Minocycline, known for its anti-inflammatory and neuroprotective properties, was incorporated into dextran sulfate (DS)-based NPs (MH-DS complexes) to overcome the issues of burst release and lack of sustained drug delivery commonly seen with direct MH incorporation.[122] The MH-DS complexes were then encapsulated within the GelMA bioink (Figure 9A). The resulting 3D-printed constructs demonstrated significantly reduced initial burst release and prolonged drug release over several days, as compared to directly mixed MH in GelMA. The researchers utilized a dual-nozzle extrusion bioprinter to create a two-layered *in vitro* model. The bottom layer consisted of fibroblasts printed with 5% GelMA, while the top layer was printed with 10% GelMA containing the MH-DS complexes. This model was subjected to oxidative stress using hydrogen peroxide to simulate cellular damage. The study found that the released MH from the NPs significantly enhanced fibroblast viability and provided protection against oxidative stress, with optimal results at specific MH loading concentrations.

Scanning electron microscopy (SEM) was employed to visualize the internal microstructure and distribution of the MH-DS NPs within the GelMA matrix. The NPs formed clusters within the GelMA network, ranging in size from 50 to 120 nm. The controlled release profile was attributed to the interactions between the MH-DS complexes and the charged networks within the GelMA, which facilitated sustained release by reducing the initial burst effect observed with directly mixed MH (Figure 9B). The study conducted by Fu et al.[123] showcases the versatility and efficacy of GelMA bioinks in 3D bioprinting applications. The ability to control the release kinetics of MH through NP encapsulation and optimize printing parameters for high cell viability underscores the potential of this approach for developing advanced *in vitro* models for cancer research and NP evaluation. The findings indicate that GelMA-based bioprinted constructs can provide a more accurate representation of the *in vivo* environment, thus improving the reliability of preclinical evaluations of NP-based therapies.[123]

10. Three-dimensional bioprinting in tissue engineering and regenerative medicine

The field of tissue engineering and regenerative medicine has experienced significant advancements, particularly through the integration of nanotechnology and 3D bioprinting. These innovations have paved the way for the development of complex, functional tissues and organs that can potentially replace damaged or diseased ones.[124,125] Nanoparticles have become a cornerstone in this field due to their unique properties, such as high surface area, tunable size, and the ability to carry therapeutic agents.[126] When combined with 3D bioprinting, NPs can be precisely incorporated into biocompatible scaffolds, enhancing their structural and functional capabilities.[127] This synergy between nanotechnology and bioprinting not only improves the efficacy of tissue regeneration but also allows for the creation of customized, patient-specific implants and wound dressings.[128–130] The ongoing research focuses on optimizing the synthesis and functionalization of NPs, developing novel bioinks, and refining bioprinting techniques to achieve better integration and performance of engineered tissues.

10.1. Bioprinted hydrogel scaffolds for evaluating the efficacy of catechol-functionalized nanoparticles in wound healing

Puertas-Bartolomé et al.[131] developed catechol-functionalized NPs and applied them in 3D bioprinting

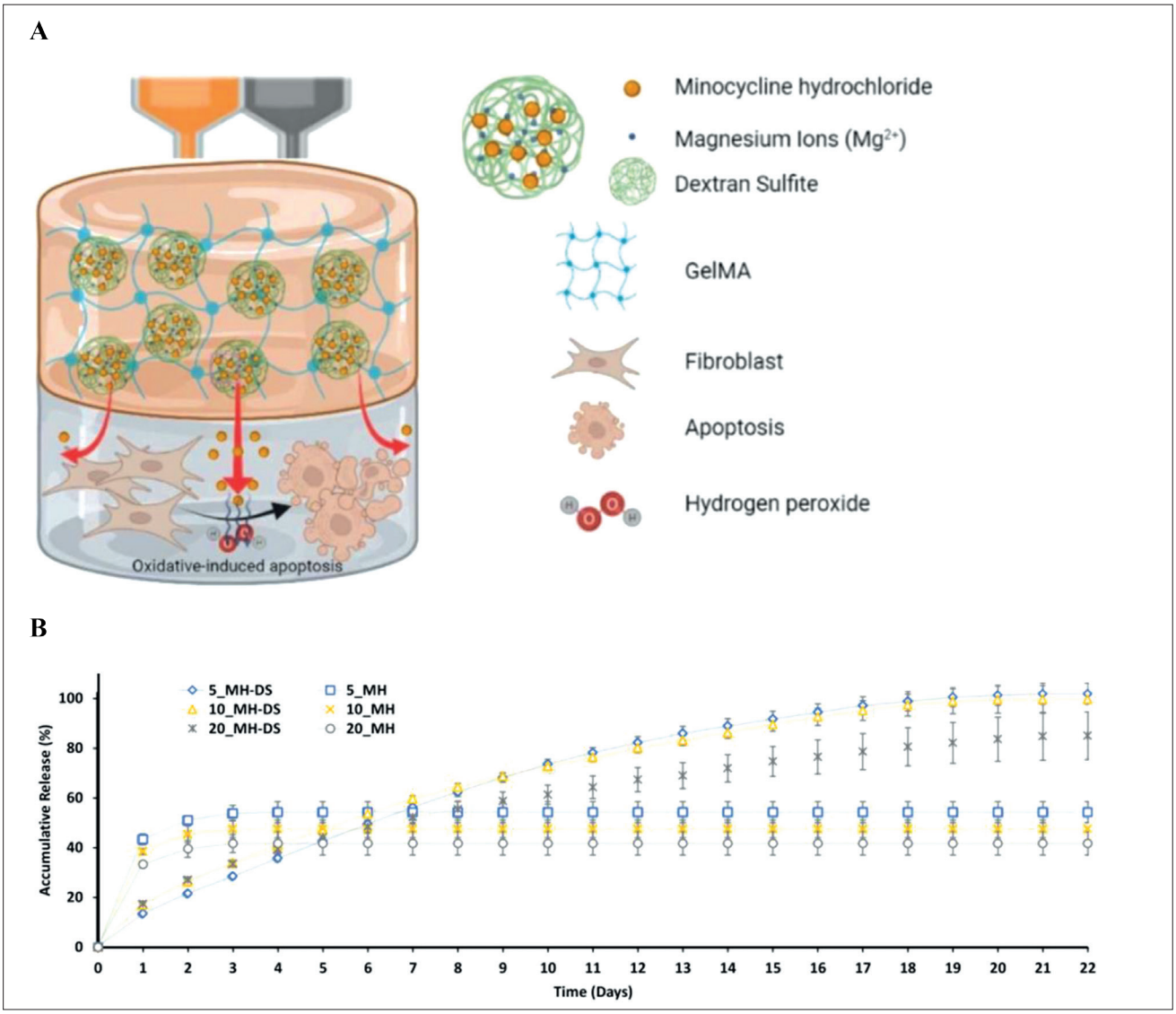


Figure 9. Drug release model of drug-loaded nanoparticles (NPs).[123] (A) Three-dimensional bioprinted model for evaluating the release and protective effects of minocycline (MH)-loaded NPs under oxidative stress conditions. (B) Controlled release of MH from MH-DS (dextran sulfate-based NPs incorporated with MH) nanocomplexes in gelatin methacryloyl (GelMA).

with the aim of enhancing wound healing. This study explored the synthesis, characterization, and biological evaluation of these NPs, focusing on their integration into hydrogel bioinks for fabricating cell-laden 3D scaffolds. The primary objective is to utilize catechol-bearing polymeric NPs to improve wound healing. These NPs were synthesized using a nanoprecipitation method, and two types of NPs with varied catechol content (2% and 29%, named NP2 and NP29) were created, exhibiting hydrodynamic diameters of 100 and 75 nm, respectively. These NPs were tested for their ability to encapsulate the hydrophobic compound coumarin-6, achieving an encapsulation efficiency of approximately 70%.

The catechol-functionalized NPs demonstrated several promising biological properties. In cell culture studies, NP2 and NP29 protected RAW 264.7 macrophages from oxidative stress induced by ROS and modulated inflammatory responses. Additionally, they promoted the upregulation of vascular endothelial growth factor (VEGF) in fibroblasts and endothelial cells, crucial for angiogenesis and wound healing. These NPs were incorporated into a hydrogel bioink formulation composed of carboxymethyl

chitosan and hyaluronic acid, using a reactive mixing bioprinting approach. The resulting NP-loaded hydrogel scaffolds exhibited good structural integrity, shape fidelity, and homogeneous NP dispersion. The scaffolds supported the viability and proliferation of encapsulated L929 fibroblasts over a 14-day period, highlighting their potential as effective wound dressings. The bioprinting process itself offers several advantages. The *in situ* crosslinking during bioprinting provides appropriate structural integrity without the need for additional cytotoxic crosslinkers, reduces post-printing steps, and allows the use of low-viscosity starting solutions, minimizing shear stress on encapsulated cells. The sustained release profile of catechol NPs from the printed scaffolds ensures prolonged bioactivity at the wound site, contributing to the regulation of ROS production, control of inflammatory responses, and facilitation of neovascularization.

Overall, the study by Puertas-Bartolomé et al.[131] presents a significant advancement in the use of bioactive catechol-functionalized NPs for 3D bioprinting in wound healing. The integration of these NPs into hydrogel scaffolds not only supports controlled drug release and enhances bioactivity but also provides a versatile platform for developing customized wound dressings tailored to patient-specific needs.[131]

11. Conclusions and future perspectives

Three-dimensional bioprinting technology has made significant strides in NP evaluation and biomedical research. This technology offers substantial advantages over traditional 2D cell culture methods, as it creates constructs that more accurately mimic the complex structures and functions of human tissues. By recreating multicellular structures, 3D bioprinting provides more reliable results in drug efficacy and toxicity testing.

Current research demonstrates the potential of 3D bioprinting across various applications. In cancer research, bioprinted tumor models have been used to more accurately assess the effectiveness of NP-based therapies by closely mimicking the tumor microenvironment. In vascular regeneration, studies have shown that bioprinted artificial blood vessels loaded with drugs like rapamycin can open new avenues for treating vascular diseases. Toxicity studies using 3D-bioprinted tissues, such as iPSC-derived cardiac microtissues, have yielded more realistic data on NP-induced cytotoxicity compared to traditional 2D cultures.

The implications of these advancements are profound. Three-dimensional bioprinting technology overcomes the limitations of traditional methods, enhancing the reliability of experimental results and contributing significantly to the development of nanomedicines. This technology also holds immense potential in personalized medicine and regenerative medicine. Personalized disease models, created using patient-derived cells, can reflect individual pathological and genetic characteristics, enabling more tailored and effective treatments.

Future research should focus on developing advanced bioinks and innovating printing technologies. Improvements in mechanical properties, biocompatibility, and controlled degradation rates of bioinks will expand the application range of 3D bioprinting. Innovations such as multi-material and multi-cell printing can further enhance the complexity and functionality of printed tissues. Integrating real-time imaging and monitoring technologies into the printing process can improve precision and reproducibility.

In clinical applications, 3D bioprinting offers vast possibilities. Personalized tumor models can be used to test the efficacy of NP-based therapies, leading to more effective and customized treatment plans. In regenerative medicine, bioprinted tissues and organs can reduce the need for donor organs and improve patient outcomes. Additionally, bioprinted skin models can be utilized for testing transdermal drug delivery systems and studying skin diseases, reducing reliance on animal testing.

Addressing regulatory and ethical issues is crucial for the widespread adoption of 3D bioprinting. Ensuring the safety and efficacy of bioprinted tissues through rigorous preclinical and clinical testing is essential. Developing regulatory frameworks to oversee the production and use of bioprinted tissues will ensure they meet established medical standards. Ethical considerations, particularly regarding the use of human cells and tissues in bioprinting, must also be addressed to gain public trust and acceptance.

In conclusion, 3D bioprinting is poised to revolutionize NP evaluation and biomedical research. This technology bridges the gap between *in vitro* and *in vivo* studies, providing a more accurate and reliable platform for drug testing and disease modeling. Future research should continue to advance bioink development, printing technologies, and regulatory frameworks to fully harness the potential of 3D bioprinting. This technology is expected to play a crucial role in the advancement of nanomedicine and the development of personalized medical treatments.

Acknowledgments

Figure 1 was created with Biorender.com. This work was conducted during the research year of Chungbuk National University in 2024.

Funding

This research was supported by "Regional Innovation Strategy (RIS)" through the National Research Foundation of Korea (NRF) funded by the Ministry of Education (MOE) (2021RIS-001); and the Basic Science Research Program through the National Research Foundation of Korea (NRF), funded by the Ministry of Education (grant number NRF-2022R1C1C1007107). This research was supported by project PID2021-126304OB-C41 funded by MICIU/AEI/10.13039/501100011033/ and by European Regional Development Fund—A way of doing Europe.

Conflict of interest

The authors declare no conflicts of interest.

Author contributions

Conceptualization: Dae Hwan Shin
Funding acquisition: Dae Hwan Shin
Supervision: Chan-Su Park, Chun-Woong Park, Jin-Seok Kim, Vicente Martí-Centelles, Ramón Martínez-Máñez, Dae Hwan Shin
Visualization: Myeong Kyun Yoo, So Yeon Park, Su Jeong Kang
Writing–original draft: Moon Sup Yoon, Jae Min Lee, Min Jeong Jo, Dae Hwan Shin
Writing–review & editing: Su Jeong Kang, Ji-Hyun Kang, Andrea Bernardos, Vicente Martí-Centelles, Ramón Martínez-Máñez, Dae Hwan Shin

Ethics approval and consent to participate

Not applicable.

Consent for publication

Not applicable.

Availability of data

Not applicable.

References

1. Jamieson C, Keenan P, Kirkwood D, et al. A review of recent advances in 3D bioprinting with an eye on future regenerative therapies in veterinary medicine. *Front Vet Sci*. 2020;7:584193. doi: 10.3389/fvets.2020.584193
2. Ricci G, Gibelli F, Sirignano A. Three-dimensional bioprinting of human organs and tissues: bioethical and medico-legal implications examined through a scoping review. *Bioengineering (Basel, Switzerland)*. 2023;10(9):1052. doi: 10.3390/bioengineering10091052
3. Yaneva A, Shopova D, Bakova D, et al. The progress in bioprinting and its potential impact on health-related quality of life. *Bioengineering (Basel, Switzerland)*. 2023;10(8):910. doi: 10.3390/bioengineering10080910
4. Cheng Y, Hu H, Dong X, Hao X, Li Y. Exploring transformer model in longitudinal pharmacokinetic/pharmacodynamic analyses and comparing with alternative natural language processing models. *J Pharm Sci*. 2024;113(5):1368-1375. doi: 10.1016/j.xphs.2024.02.008
5. Migulina N, de Hilster RHJ, Bartel S, et al. 3-D culture of human lung fibroblasts decreases proliferative and increases extracellular matrix remodeling genes. *Am J Physiol Cell Physiol*. 2024;326(1):C177-C193. doi: 10.1152/ajpcell.00374.2023
6. Nizamoglu M, Alleblas F, Koster T, et al. Three dimensional fibrotic extracellular matrix directs microenvironment fiber remodeling by fibroblasts. *Acta Biomater*. 2024;177:118-131. doi: 10.1016/j.actbio.2024.02.008
7. Bernal PN, Bouwmeester M, Madrid-Wolff J, et al. Volumetric bioprinting of organoids and optically tuned hydrogels to build liver-like metabolic biofactories. *Adv Mater*. 2022;34(15):2110054. doi: 10.1002/adma.202110054
8. Muthusamy S, Kannan S, Lee M, et al. 3D bioprinting and microscale organization of vascularized tissue constructs using collagen-based bioink. *Biotechnol Bioeng*. 2021;118(8):3150-3163. doi: 10.1002/bit.27838
9. Jia W, Gungor-Ozkerim PS, Zhang YS, et al. Direct 3D bioprinting of perfusable vascular constructs using a blend bioink. *Biomaterials*. 2016;106:58-68. doi: 10.1016/j.biomaterials.2016.07.038
10. Zhu J, Wang Y, Zhong L, Pan F, Wang J. Advances in tissue engineering of vasculature through three-dimensional bioprinting. *Dev Dyn*. 2021;250(12):1717-1738. doi: 10.1002/dvdy.385
11. Farouk SM, Khafaga AF, Abdellatif AM. Bladder cancer: therapeutic challenges and role of 3D cell culture systems in the screening of novel cancer therapeutics. *Cancer Cell Int*. 2023;23(1):251. doi: 10.1186/s12935-023-03069-4
12. Jensen C, Teng Y. Is it time to start transitioning from 2D to 3D cell culture? *Front Mol Biosci*. 2020;7:33. doi: 10.3389/fmolb.2020.00033
13. Abuwatfa WH, Pitt WG, Husseini GA. Scaffold-based 3D cell culture models in cancer research. *J Biomed Sci*. 2024;31(1):7. doi: 10.1186/s12929-024-00994-y
14. Centeno EGZ, Cimarosti H, Bithell A. 2D versus 3D human induced pluripotent stem cell-derived cultures for neurodegenerative disease modelling. *Mol Neurodegener*. 2018;13(1):27. doi: 10.1186/s13024-018-0258-4

15. Khafaga AF, Mousa SA, Aleya L, Abdel-Daim MM. Three-dimensional (3D) cell culture: a valuable step in advancing treatments for human hepatocellular carcinoma. *Cancer Cell Int*. 2022;22(1):243.
doi: 10.1186/s12935-022-02662-3

16. Badr-Eldin SM, Aldawsari HM, Kotta S, Deb PK, Venugopala KN. Three-dimensional *in vitro* cell culture models for efficient drug discovery: progress so far and future prospects. *Pharmaceuticals (Basel)*. 2022;15(8):926.
doi: 10.3390/ph15080926

17. Belfiore L, Aghaei B, Law AMK, et al. Generation and analysis of 3D cell culture models for drug discovery. *Eur J Pharm Sci*. 2021;163:105876.
doi: 10.1016/j.ejps.2021.105876

18. Parodi I, Di Lisa D, Pastorino L, Scaglione S, Fato MM. 3D bioprinting as a powerful technique for recreating the tumor microenvironment. *Gels*. 2023;9(6):482.
doi: 10.3390/gels9060482

19. Germain N, Dhayer M, Dekiouk S, Marchetti P. Current advances in 3D bioprinting for cancer modeling and personalized medicine. *Int J Mol Sci*. 2022;23(7):3432.
doi: 10.3390/ijms23073432

20. Bojin F, Robu A, Bejenariu MI, et al. 3D bioprinting of model tissues that mimic the tumor microenvironment. *Micromachines (Basel)*. 2021;12(5):535.
doi: 10.3390/mi12050535

21. Di Marzio N, Eglin D, Serra T, Moroni L. Bio-fabrication: convergence of 3D bioprinting and nano-biomaterials in tissue engineering and regenerative medicine. *Front Bioeng Biotechnol*. 2020;8:326.
doi: 10.3389/fbioe.2020.00326

22. Richards D, Jia J, Yost M, Markwald R, Mei Y. 3D bioprinting for vascularized tissue fabrication. *Ann Biomed Eng*. 2017;45(1):132-147.
doi: 10.1007/s10439-016-1653-z

23. Chen EP, Toksoy Z, Davis BA, Geibel JP. 3D bioprinting of vascularized tissues for *in vitro* and *in vivo* applications. *Front Bioeng Biotechnol*. 2021;9:664188.
doi: 10.3389/fbioe.2021.664188

24. Yang Q, Gao B, Xu F. Recent advances in 4D bioprinting. *Biotechnol J*. 2020;15(1):e1900086.
doi: 10.1002/biot.201900086

25. Phogat S, Thiam F, Al Yazeedi S, Abokor FA, Osei ET. 3D *in vitro* hydrogel models to study the human lung extracellular matrix and fibroblast function. *Respir Res*. 2023;24(1):242.
doi: 10.1186/s12931-023-02548-6

26. Vakhshiteh F, Bagheri Z, Soleimani M, et al. Heterotypic tumor spheroids: a platform for nanomedicine evaluation. *J Nanobiotechnology*. 2023;21(1):249.
doi: 10.1186/s12951-023-02021-y

27. Chia SL, Tay CY, Setyawati MI, Leong DT. Biomimicry 3D gastrointestinal spheroid platform for the assessment of toxicity and inflammatory effects of zinc oxide nanoparticles. *Small*. 2015;11(6):702-712.
doi: 10.1002/smll.201401915

28. Kim D, Jo S, Lee D, et al. NK cells encapsulated in micro/macropore-forming hydrogels via 3D bioprinting for tumor immunotherapy. *Biomater Res*. 2023;27(1):60.
doi: 10.1186/s40824-023-00403-9

29. Sun S, Wang YH, Gao X, et al. Current perspectives and trends in nanoparticle drug delivery systems in breast cancer: bibliometric analysis and review. *Front Bioeng Biotechnol*. 2023;11:1253048.
doi: 10.3389/fbioe.2023.1253048

30. Chakraborty A, Roy A, Ravi SP, Paul A. Exploiting the role of nanoparticles for use in hydrogel-based bioprinting applications: concept, design, and recent advances. *Biomater Sci*. 2021;9(19):6337-6354.
doi: 10.1039/d1bm00605c

31. Datta P, Dey M, Ataie Z, Unutmaz D, Ozbolat IT. 3D bioprinting for reconstituting the cancer microenvironment. *NPJ Precis Oncol*. 2020;4:18.
doi: 10.1038/s41698-020-0121-2

32. Cho ES, Kang HE, Kim NH, Yook JI. Therapeutic implications of cancer epithelial-mesenchymal transition (EMT). *Arch Pharm Res*. 2019;42(1):14-24.
doi: 10.1007/s12272-018-01108-7

33. Chen Y, Xu L, Li W, et al. 3D bioprinted tumor model with extracellular matrix enhanced bioinks for nanoparticle evaluation. *Biofabrication*. 2022;14(2):025002.
doi: 10.1088/1758-5090/ac48e4

34. Tomeh MA, Hadianamrei R, Zhao X. A review of curcumin and its derivatives as anticancer agents. *Int J Mol Sci*. 2019;20(5):1033.
doi: 10.3390/ijms20051033

35. Gu X, Gao Y, Wang P, et al. Nano-delivery systems focused on tumor microenvironment regulation and biomimetic strategies for treatment of breast cancer metastasis. *J Control Release*. 2021;333:374-390.
doi: 10.1016/j.jconrel.2021.03.039

36. Su Y, Hu X, Kang Y, et al. Curcumin nanoparticles combined with 3D printed bionic tumor models for breast cancer treatment. *Biofabrication*. 2022;15(1):014105.
doi: 10.1088/1758-5090/aca5b8

37. Chirivì M, Bearzi C, Rosa P, et al. Biomimetic keratin-coated gold nanoparticles for photo-thermal therapy in a 3D bioprinted glioblastoma tumor model. *Int J Mol Sci*. 2022;23(17):9528.
doi: 10.3390/ijms23179528

38. Nam KH, Jeong CB, Kim H, et al. Quantitative photothermal characterization with bioprinted 3D complex tissue constructs for early-stage breast cancer therapy using gold nanorods. *Adv Healthc Mater*. 2021;10(18):e2100636.
doi: 10.1002/adhm.202100636

39. Dong X, Li R, Xiu P, et al. Meloxicam executes its antitumor effects against hepatocellular carcinoma in COX-2- dependent and -independent pathways. *PloS One*. 2014;9(3):e92864.
doi: 10.1371/journal.pone.0092864

40. Rarokar N, Ravikumar C, Gurav S, Khedekar P. Meloxicam encapsulated nanostructured colloidal self-assembly for evaluating antitumor and anti-inflammatory efficacy in 3D printed scaffolds. *J Biomed Mater Res A*. 2021;109(8):1441-1456.
doi: 10.1002/jbm.a.37135

41. Kaur IP, Bhandari R, Bhandari S, Kakkar V. Potential of solid lipid nanoparticles in brain targeting. *J Control Release*. 2008;127(2):97-109.
doi: 10.1016/j.jconrel.2007.12.018

42. Rohit B, Pal Kaur I. A method to prepare solid lipid nanoparticles with improved entrapment efficiency of hydrophilic drugs. *Current Nanosci*. 2013;9(2):211-220.
doi: 10.2174/1573413711309020008

43. Liu D, Cito S, Zhang Y, Wang CF, Sikanen TM, Santos HA. A versatile and robust microfluidic platform toward high throughput synthesis of homogeneous nanoparticles with tunable properties. *Adv Mater*. 2015;27(14):2298-2304.
doi: 10.1002/adma.201405408

44. Arduino I, Liu Z, Rahikkala A, et al. Preparation of cetyl palmitate-based PEGylated solid lipid nanoparticles by microfluidic technique. *Acta Biomater*. 2021;121:566-578.
doi: 10.1016/j.actbio.2020.12.024

45. Figueiredo P, Lintinen K, Kiriazis A, et al. *In vitro* evaluation of biodegradable lignin-based nanoparticles for drug delivery and enhanced antiproliferation effect in cancer cells. *Biomaterials*. 2017;121:97-108.
doi: 10.1016/j.biomaterials.2016.12.034

46. Figueiredo P, Sipponen MH, Lintinen K, et al. Preparation and characterization of dentin phosphophoryn-derived peptide-functionalized lignin nanoparticles for enhanced cellular uptake. *Small*. 2019;15(24):e1901427.
doi: 10.1002/smll.201901427

47. Ahn M, Cho WW, Park W, et al. 3D biofabrication of diseased human skin models *in vitro*. *Biomater Res*. 2023;27(1):80.
doi: 10.1186/s40824-023-00415-5

48. Cho SW, Malick H, Kim SJ, Grattoni A. Advances in skin-on-a-chip technologies for dermatological disease modeling. *J Invest Dermatol*. 2024;144(8):1707-1715.
doi: 10.1016/j.jid.2024.01.031

49. Scheurer J, Sauer B, Focken J, et al. Histological and functional characterization of 3D human skin models mimicking the inflammatory skin diseases psoriasis and atopic dermatitis. *Dis Model Mech*. 2024;17(1):dmm050541.
doi: 10.1242/dmm.050541

50. Nuwayhid R, Schulz T, Siemers F, et al. A platform for testing the biocompatibility of implants: silicone induces a proinflammatory response in a 3D skin equivalent. *Biomedicines*. 2024;12(1):224.
doi: 10.3390/biomedicines12010224

51. Randall MJ, Jüngel A, Rimann M, Wuertz-Kozak K. Advances in the biofabrication of 3D skin *in vitro*: healthy and pathological models. *Front Bioeng Biotechnol*. 2018;6:154.
doi: 10.3389/fbioe.2018.00154

52. Zoio P, Oliva A. Skin-on-a-chip technology: microengineering physiologically relevant *in vitro* skin models. *Pharmaceutics*. 2022;14(3):682.
doi: 10.3390/pharmaceutics14030682

53. Mukhopadhyay C, Paul MK. Organoid-based 3D *in vitro* microphysiological systems as alternatives to animal experimentation for preclinical and clinical research. *Arch Toxicol*. 2023;97(5):1429-1431.
doi: 10.1007/s00204-023-03466-8

54. Marano F. Les méthodes alternatives à l'expérimentation animale, présent et futur [Alternative methods to animal testing, present and future]. *Biol Aujourdhui*. 2023;217(3-4):199-205.
doi: 10.1051/jbio/2023035

55. Gao C, Lu C, Jian Z, et al. 3D bioprinting for fabricating artificial skin tissue. *Colloids Surf B Biointerfaces*. 2021;208:112041.
doi: 10.1016/j.colsurfb.2021.112041

56. Hou X, Liu S, Wang M, et al. Layer-by-layer 3D constructs of fibroblasts in hydrogel for examining transdermal penetration capability of nanoparticles. *SLAS Technol*. 2017;22(4):447-453.
doi: 10.1177/2211068216655753

57. do Amaral SR, Amantino CF, Atanasov A, et al. Evaluation of photodynamic therapy as a new therapeutic approach using quinizarin-loaded nanocapsules: *in vitro* cytotoxicity, permeation in 3D bioprinted skin equivalent and *in vitro* cytokines modulation. Preprints; 2024.
doi: 10.20944/preprints202405.1323.v1

58. Bhamare N, Tardalkar K, Khadilkar A, Parulekar P, Joshi MG. Tissue engineering of human ear pinna. *Cell Tissue Bank*. 2022;23(3):441-457.
doi: 10.1007/s10561-022-09991-7

59. Bos EJ, Doerga P, Breugem CC, van Zuijlen PP. The burned ear; possibilities and challenges in framework reconstruction and coverage. *Burns*. 2016;42(7):1387-1395.
doi: 10.1016/j.burns.2016.02.006

60. Abaci A, Camci-Unal G, Guvendiren M, Guest E. Three-dimensional bioprinting for medical applications. *MRS Bulletin*. 2023;48(6):624-631.
doi: 10.1557/s43577-023-00546-z

61. Bernal PN, Delrot P, Loterie D, et al. Volumetric bioprinting of complex living-tissue constructs within seconds. *Adv Mater*. 2019;31(42):1904209.
doi: 10.1002/adma.201904209

62. Yalgın A, Köse FA, Gökçe EH. The effect of cyclosporine A and co-enzyme Q10 loaded solid lipid nanoparticles on 3D printed human auricular model: evaluation of cell growth. *J Drug Deliv Sci Technol*. 2023;79:104087. doi: 10.1016/j.jddst.2022.104087

63. Fang Y, Ouyang L, Zhang T, Wang C, Lu B, Sun W. Optimizing bifurcated channels within an anisotropic scaffold for engineering vascularized oriented tissues. *Adv Healthc Mater*. 2020;9(24):e2000782. doi: 10.1002/adhm.202000782

64. Gao Q, Liu Z, Lin Z, et al. 3D bioprinting of vessel-like structures with multilevel fluidic channels. *ACS Biomater Sci Eng*. 2017;3(3):399-408. doi: 10.1021/acsbiomaterials.6b00643

65. Zhou X, Gao Q, Yu D, et al. 3D-bioprinted vascular scaffold with tunable mechanical properties for simulating and promoting neo-vascularization. *Smart Mater Med*. 2022;3:199-208. doi: 10.1016/j.smaim.2022.01.003

66. Gold KA, Saha B, Rajeeva Pandian NK, et al. 3D bioprinted multicellular vascular models. *Adv Healthc Mater*. 2021;10(21):2101141. doi: 10.1002/adhm.202101141

67. Boada C, Zinger A, Tsao C, et al. Rapamycin-loaded biomimetic nanoparticles reverse vascular inflammation. *Circ Res*. 2020;126(1):25-37. doi: 10.1161/CIRCRESAHA.119.315185

68. Betala J, Bae S, Langan III EM, LaBerge M, Lee JS. Combinatorial therapy of sirolimus and heparin by nanocarrier inhibits restenosis after balloon angioplasty *ex vivo*. *Nanomedicine*. 2020;15(12):1205-1220. doi: 10.2217/nnm-2020-0028

69. Rosner D, McCarthy N, Bennett M. Rapamycin inhibits human in stent restenosis vascular smooth muscle cells independently of pRB phosphorylation and p53. *Cardiovasc Res*. 2005;66(3):601-610. doi: 10.1016/j.cardiores.2005.01.006

70. Hauser PV, Chang H-M, Nishikawa M, Kimura H, Yanagawa N, Hamon M. Bioprinting scaffolds for vascular tissues and tissue vascularization. *Bioengineering*. 2021;8(11):178. doi: 10.3390/bioengineering8110178

71. Choi J, Lee EJ, Lim HJ, et al. Development of 3D-bioprinted artificial blood vessels loaded with rapamycin-nanoparticles for ischemic repair. *Int J Bioprin*. 2024;10(2):1465. doi: 10.36922/ijb.1465

72. Ge G, Wu H, Xiong F, et al. The cytotoxicity evaluation of magnetic iron oxide nanoparticles on human aortic endothelial cells. *Nanoscale Res Lett*. 2013;8:1-10. doi: 10.1186/1556-276X-8-215

73. Wu X, Tan Y, Mao H, Zhang M. Toxic effects of iron oxide nanoparticles on human umbilical vein endothelial cells. *Int J Nanomedicine*. 2010;5:385-399. doi: 10.2147/ijn.s10458

74. Nemmar A, Beegam S, Yuvaraju P, et al. Ultrasmall superparamagnetic iron oxide nanoparticles acutely promote thrombosis and cardiac oxidative stress and DNA damage in mice. *Part Fibre Toxicol*. 2015;13:1-11. doi: 10.1186/s12989-016-0132-x

75. Ning L, Zanella S, Tomov ML, et al. Targeted rapamycin delivery via magnetic nanoparticles to address stenosis in a 3D bioprinted *in vitro* model of pulmonary veins. *Adv Sci (Weinh)*. 2024;11(26):e2400476. doi: 10.1002/advs.202400476

76. Lee EJ, Choi J, Lim HJ, et al. 3D-bioprinted cell-laden blood vessel with dual drug delivery nanoparticles for advancing vascular regeneration. *Int J Bioprint*. 2024;10(2):1857. doi: 10.36922/ijb.1857

77. Song R, Fullerton DA, Ao L, et al. Altered micro RNA expression is responsible for the pro-osteogenic phenotype of interstitial cells in calcified human aortic valves. *J Am Heart Assoc*. 2017;6(4):e005364. doi: 10.1161/JAHA.116.005364

78. Voicu G, Mocanu CA, Safciuc F, et al. Nanocarriers of shRNA-Runx2 directed to collagen IV as a nanotherapeutic system to target calcific aortic valve disease. *Mater Today Bio*. 2023;20:100620. doi: 10.1016/j.mtbio.2023.100620

79. van der Ven CFT, Tibbitt MW, Conde J, et al. Controlled delivery of gold nanoparticle-coupled miRNA therapeutics via an injectable self-healing hydrogel. *Nanoscale*. 2021;13(48):20451-20461. doi: 10.1039/d1nr04973a

80. Ning L, Gil CJ, Hwang B, et al. Biomechanical factors in three-dimensional tissue bioprinting. *Appl Phys Rev*. 2020;7(4):041319. doi: 10.1063/5.0023206

81. Byambaa B, Annabi N, Yue K, et al. Bioprinted osteogenic and vasculogenic patterns for engineering 3D bone tissue. *Adv Healthc Mater*. 2017;6(16):1700015. doi: 10.1002/adhm.201700015

82. Gonzalez-Fernandez T, Tenorio AJ, Campbell KT, Silva EA, Leach JK. Alginate-based bioinks for 3D bioprinting and fabrication of anatomically accurate bone grafts. *Tissue Eng Part A*. 2021;27(17–18):1168-1181. doi: 10.1089/ten.TEA.2020.0305

83. Fischetti T, Di Pompo G, Baldini N, Avnet S, Graziani G. 3D printing and bioprinting to model bone cancer: the role of materials and nanoscale cues in directing cell behavior. *Cancers*. 2021;13(16):4065. doi: 10.3390/cancers13164065

84. Holmes B, Bulusu K, Plesniak M, Zhang LG. A synergistic approach to the design, fabrication and evaluation of 3D printed micro and nano featured scaffolds for vascularized bone tissue repair. *Nanotechnology*. 2016;27(6):064001. doi: 10.1088/0957-4484/27/6/064001

85. Baino F, Minguella-Canela J, Korkusuz F, et al. *In vitro a*ssessment of bioactive glass coatings on alumina/zirconia composite implants for potential use in prosthetic applications. *Int J Mol Sci*. 2019;20(3):722. doi: 10.3390/ijms20030722

86. Chen YW, Shen YF, Ho CC, et al. Osteogenic and angiogenic potentials of the cell-laden hydrogel/mussel-inspired calcium silicate complex hierarchical porous scaffold fabricated by 3D bioprinting. *Mate Sci Eng C, Mater Biol Appl*. 2018;91:679-687. doi: 10.1016/j.msec.2018.06.005

87. Yang Z, Yi P, Liu Z, et al. Stem cell-laden hydrogel-based 3D bioprinting for bone and cartilage tissue engineering. *Front Bioeng Biotechnol*. 2022;10:865770. doi: 10.3389/fbioe.2022.865770

88. Zhang J, Eyisoylu H, Qin X-H, Rubert M, Müller R. 3D bioprinting of graphene oxide-incorporated cell-laden bone mimicking scaffolds for promoting scaffold fidelity, osteogenic differentiation and mineralization. *Acta Biomaterialia*. 2021;121:637-652. doi: 10.1016/j.actbio.2020.12.026

89. Zhang X, Cui J, Cheng L, Lin K. Enhancement of osteoporotic bone regeneration by strontium-substituted 45S5 bioglass via time-dependent modulation of autophagy and the Akt/mTOR signaling pathway. *J Mater Chem B*. 2021;9(16):3489-3501. doi: 10.1039/d0tb02991b

90. Souza L, Lopes JH, Encarnação D, et al. Comprehensive *in vitro* and *in vivo* studies of novel melt-derived Nb-substituted 45S5 bioglass reveal its enhanced bioactive properties for bone healing. *Sci Rep*. 2018;8(1):12808. doi: 10.1038/s41598-018-31114-0

91. Bellucci D, Cannillo V, Sola A, Chiellini F, Gazzarri M, Migone C. Macroporous Bioglass®-derived scaffolds for bone tissue regeneration. *Ceramics international*. 2011;37(5):1575-1585. doi: 10.1016/j.ceramint.2011.01.023

92. Wang X, Tolba E, Schröder HC, et al. Effect of bioglass on growth and biomineralization of SaOS-2 cells in hydrogel after 3D cell bioprinting. *PLoS One*. 2014;9(11):e112497. doi: 10.1371/journal.pone.0112497

93. Raveendran N, Vaswani K, Han P, Basu S, Moran CS, Ivanovski S. Modeling inflammatory response using 3D bioprinting of polarized macrophages *Int J Bioprint*. 2024;10(2):2116. doi: 10.36922/ijb.2116

94. Roh TT, Chen Y, Paul HT, Guo C, Kaplan DL. 3D bioengineered tissue model of the large intestine to study inflammatory bowel disease. *Biomaterials*. 2019;225:119517. doi: 10.1016/j.biomaterials.2019.119517

95. Torras N, Zabalo J, Abril E, Carré A, García-Díaz M, Martínez E. A bioprinted 3D gut model with crypt-villus structures to mimic the intestinal epithelial-stromal microenvironment. *Biomater Adv*. 2023;153:213534. doi: 10.1016/j.bioadv.2023.213534

96. Murphy SV, De Coppi P, Atala A. Opportunities and challenges of translational 3D bioprinting. *Nat Biomed Eng*. 2020;4(4):370-380. doi: 10.1038/s41551-019-0471-7

97. Dickman CTD, Russo V, Thain K, et al. Functional characterization of 3D contractile smooth muscle tissues generated using a unique microfluidic 3D bioprinting technology. *FASEB J*. 2020;34(1):1652-1664. doi: 10.1096/fj.201901063RR

98. Maes L, Szabó A, Van Haevermaete J, et al. P035 3D bioprinting of gelatin derivatives: towards novel small intestinal *in vitro* models. *J Crohns Colitis*. 2024;18(Supplement_1):i293-i293. doi: 10.1093/ecco-jcc/jjad212.0165

99. Mon A, Gervacio S, Aidnik H, Oxford S, Rosette C, Piu F. Evaluation of the clinical stage FXR Agonist FXR314 in human primary cell 3D models of Crohn's disease and ulcerative colitis. *Inflamm Bowel Dis*. 2024;30(Supplement_1):S59-S59. doi: 10.1093/ibd/izae020.121

100. Lee JM, Yeong WY. Design and printing strategies in 3D bioprinting of cell-hydrogels: a review. *Adv Healthc Mater*. 2016;5(22):2856-2865. doi: 10.1002/adhm.201600435

101. Almutary AG, Alnuqaydan AM, Almatroodi SA, Bakshi HA, Chellappan DK, Tambuwala MM. Development of 3D-bioprinted colitis-mimicking model to assess epithelial barrier function using albumin nano-encapsulated anti-inflammatory drugs. *Biomimetics (Basel)*. 2023;8(1):41. doi: 10.3390/biomimetics8010041

102. Garcés M, Cáceres L, Chiappetta D, Magnani N, Evelson P. Current understanding of nanoparticle toxicity mechanisms and interactions with biological systems. *New J Chem*. 2021;45(32):14328-14344. doi: 10.1039/D1NJ01415C

103. Abbasi R, Shineh G, Mobaraki M, Doughty S, Tayebi L. Structural parameters of nanoparticles affecting their toxicity for biomedical applications: a review. *J Nanopart Res*. 2023;25(3):43. doi: 10.1007/s11051-023-05690-w

104. Buzea C, Pacheco I. 28 – Toxicity of nanoparticles. In: Pacheco-Torgal F, Diamanti MV, Nazari A, Granqvist CG, Pruna A, Amirkhanian S, eds. *Nanotechnology in Eco-Efficient Construction (Second Edition)*. Sawston, UK: Woodhead Publishing; 2019:705-754. doi: 10.1016/B978-0-08-102641-0.00028-1

105. Egbuna C, Parmar VK, Jeevanandam J, et al. Toxicity of nanoparticles in biomedical application: nanotoxicology. *J Toxicol*. 2021;2021(1):9954443. doi: 10.1155/2021/9954443

106. Ajdary M, Moosavi MA, Rahmati M, et al. Health concerns of various nanoparticles: a review of their *in vitro* and *in vivo* toxicity. *Nanomaterials*. 2018;8(9):634. doi: 10.3390/nano8090634

107. Wang M, Yang Q, Long J, et al. A comparative study of toxicity of TiO2, ZnO, and Ag nanoparticles to human aortic smooth-muscle cells. *Int J Nanomedicine*. 2018: 8037-8049. doi: 10.2147/IJN.S188175

108. Sanches PL, Geaquinto LRdO, Cruz R, et al. Toxicity evaluation of TiO2 nanoparticles on the 3D skin model: a systematic review. *Frontiers in Bioengineering and Biotechnology*. 2020;8:575. doi: 10.3389/fbioe.2020.00575

109. Dubiak-Szepietowska M, Karczmarczyk A, Jönsson-Niedziółka M, Winckler T, Feller KH. Development of complex-shaped liver multicellular spheroids as a human-based model for nanoparticle toxicity assessment *in vitro*. *Toxicol Appl Pharmacol*. 2016;294:78-85. doi: 10.1016/j.taap.2016.01.016

110. Chen L, Wu M, Jiang S, et al. Skin toxicity assessment of silver nanoparticles in a 3D epidermal model compared to 2D keratinocytes. *Int J Nanomedicine*. 2019:9707-9719. doi: 10.2147/IJN.S225451

111. Gelamo EL, Tabak M. Spectroscopic studies on the interaction of bovine (BSA) and human (HSA) serum albumins with ionic surfactants. *Spectrochim Acta Part A Mol Biomol Spectrosc*. 2000;56(11):2255-2271. doi: 10.1016/S1386-1425(00)00313-9

112. Miller KL, Sit I, Xiang Y, et al. Evaluation of CuO nanoparticle toxicity on 3D bioprinted human iPSC-derived cardiac tissues. *Bioprinting*. 2023;32:e00284. doi: 10.1016/j.bprint.2023.e00284

113. Saufi SASA, Zuhri MYM, Dezaki ML, et al. Compression behaviour of bio-inspired honeycomb reinforced starfish shape structures using 3D printing technology. *Polymers*. 2021;13(24):4388. doi: 10.3390/polym13244388

114. Bilberg K, Hovgaard MB, Besenbacher F, Baatrup E. *In vivo* toxicity of silver nanoparticles and silver ions in zebrafish (danio rerio). *J Toxicol*. 2012;2012:293784. doi: 10.1155/2012/293784

115. Gerbolés AG, Galetti M, Rossi S, et al. Three-dimensional bioprinting of organoid-based scaffolds (OBST) for long-term nanoparticle toxicology investigation. *Int J Mol Sci*. 2023;24(7):6595. doi: 10.3390/ijms24076595

116. Hossen S, Hossain MK, Basher M, Mia M, Rahman M, Uddin MJ. Smart nanocarrier-based drug delivery systems for cancer therapy and toxicity studies: a review. *J Adv Res*. 2019;15:1-18. doi: 10.1016/j.jare.2018.06.005

117. Kashkooli FM, Soltani M, Souri M. Controlled anti-cancer drug release through advanced nano-drug delivery systems: static and dynamic targeting strategies. *J Control Release*. 2020;327:316-349. doi: 10.1016/j.jconrel.2020.08.012

118. Hussain Z, Arooj M, Malik A, et al. Nanomedicines as emerging platform for simultaneous delivery of cancer therapeutics: new developments in overcoming drug resistance and optimizing anticancer efficacy. *Artif Cells Nanomed Biotechnol*. 2018;46(sup2):1015-1024. doi: 10.1080/21691401.2018.1478420

119. Ahmad J, Garg A, Mustafa G, Mohammed AA, Ahmad MZ. 3D printing technology as a promising tool to design nanomedicine-based solid dosage forms: contemporary research and future scope. *Pharmaceutics*. 2023;15(5):1448. doi: 10.3390/pharmaceutics15051448

120. Chakka JL, Salem AK. *3D Printing in Drug Delivery Systems*. Taylor & Francis; 2019:59-62. doi: 10.2217/3dp-2019-0005

121. Staros R, Michalak A, Rusinek K, Mucha K, Pojda Z, Zagożdżon R. Perspectives for 3D-bioprinting in modeling of tumor immune evasion. *Cancers*. 2022;14(13):3126. doi: 10.3390/cancers14133126

122. Garrido-Mesa N, Zarzuelo A, Gálvez J. Minocycline: far beyond an antibiotic. *Br J Pharmacol*. 2013;169(2):337-352. doi: 10.1111/bph.12139

123. Fu Z, Hai N, Zhong Y, Sun W. Printing GelMA bioinks: a strategy for buildingin vitromodel to study nanoparticle-based minocycline release and cellular protection under oxidative stress. *Biofabrication*. 2024;16(2):025040. doi: 10.1088/1758-5090/ad30c3

124. Zhu H, Monavari M, Zheng K, et al. 3D bioprinting of multifunctional dynamic nanocomposite bioinks incorporating Cu-doped mesoporous bioactive glass nanoparticles for bone tissue engineering. *Small*. 2022;18(12):2104996. doi: 10.1002/smll.202104996

125. Zhu W, Cui H, Boualam B, et al. 3D bioprinting mesenchymal stem cell-laden construct with core–shell nanospheres for cartilage tissue engineering. *Nanotechnology*. 2018;29(18):185101. doi: 10.1088/1361-6528/aaafa1

126. Rizzi F, Castaldo R, Latronico T, et al. High surface area mesoporous silica nanoparticles with tunable size in the sub-micrometer regime: insights on the size and porosity control mechanisms. *Molecules (Basel, Switzerland)*. 2021;26(14):4247. doi: 10.3390/molecules26144247

127. Theus AS, Ning L, Kabboul G, et al. 3D bioprinting of nanoparticle-laden hydrogel scaffolds with enhanced antibacterial and imaging properties. *Iscience*. 2022;25(9):104947. doi: 10.1016/j.isci.2022.104947

128. Cleetus CM, Alvarez Primo F, Fregoso G, et al. Alginate hydrogels with embedded ZnO nanoparticles for wound healing therapy. *Int J Nanomedicine*. 2020: 5097-5111.
doi: 10.2147/IJN.S255937

129. Li Z, Zheng A, Mao Z, et al. Silk fibroin–gelatin photo-crosslinked 3D-bioprinted hydrogel with MOF-methylene blue nanoparticles for infected wound healing. *Int J Bioprint*. 2023;9(5):773.
doi: 10.18063/ijb.773

130. Su Y, Liu Y, Hu X, et al. Caffeic acid-grafted chitosan/sodium alginate/nanoclay-based multifunctional 3D-printed hybrid scaffolds for local drug release therapy after breast cancer surgery. *Carbohydr Polym*. 2024;324:121441.
doi: 10.1016/j.carbpol.2023.121441

131. Puertas-Bartolomé M, Włodarczyk-Biegun MK, del Campo A, Vázquez-Lasa B, San Román J. Development of bioactive catechol functionalized nanoparticles applicable for 3D bioprinting. *Mater Sci Eng C*. 2021;131:112515.
doi: 10.1016/j.msec.2021.112515

ACCSCIENCE PUBLISHING

International Journal of Bioprinting

REVIEW ARTICLE

Bioprinting of tumor immune microenvironment for immunotherapy

Sein Kim[1†], Seokgyu Han[2†], Jaehyun Lee[3], Chanyang Lee[2], and Sungsu Park[1,2*]

[1]Department of Biomedical Engineering, Institute for Cross-disciplinary Studies (ICS), Sungkyunkwan University (SKKU), Suwon, Republic of Korea

[2]Department of Mechanical Engineering, School of Mechanical Engineering, Sungkyunkwan University (SKKU), Suwon, Republic of Korea

[3]Department of Bio-Integrated Science and Technology, College of Life Sciences, Sejong University, Seoul, Republic of Korea

(This article belongs to the Special Issue: *Advances in Bioprinting and Organ-on-a-chip and Applications for Precision Medicine*)

Abstract

Accurately simulating the tumor immune microenvironment (TIME), which consists of a tumor, extracellular matrix (ECM), vascular network, and a variety of stromal and immune cells, is crucial for advancing and testing immunotherapies such as checkpoint inhibitors, chimeric antigen receptor-T (CAR-T) cells, and cancer vaccines. Traditional models, such as animal models, are limited by their differences from human immune environments. Bioprinting addresses these limitations by incorporating tumors, immune cells, and vascular cells within an ECM, thereby reflecting the complex interactions, including trafficking, between cancer and immune cells. These models provide better predictive accuracy for human immune responses, reducing translational failures and improving preclinical testing. While bioprinting methods for simulating the tumor microenvironment, where cancer cells form spheroids surrounded by blood vessels, are well reviewed, bioprinting methods for recapitulating the TIME are not as thoroughly explored. This review aims to fill this gap by exploring the development, application, and potential of bioprinted TIME models in enhancing the study and efficacy of immunotherapies, ultimately offering a more realistic and personalized approach to cancer treatment.

Keywords: Tumor; Immune microenvironment; Bioprinting; Immunotherapy; Efficacy

1. Introduction

With the rise in novel tumor immunotherapies, such as checkpoint inhibitors, chimeric antigen receptor (CAR)-T, and cancer vaccines, the importance of accurately simulating the tumor immune microenvironment (TIME) has increased. Simulating the TIME is crucial as it provides insights into the complex interactions between the immune system and tumor cells. This understanding aids in predicting how tumors evade immune detection and respond to various immunotherapies. It also facilitates the development and optimization of these therapies, enhancing their efficacy and safety, and ultimately leading to more personalized and effective treatment options

†These authors contributed equally to this work.

***Corresponding author:**
Sungsu Park
(nanopark@skku.edu)

Citation: Kim S, Han S, Lee J, Lee C, Park S. Bioprinting of tumor immune microenvironment for immunotherapy. *Int J Bioprint*. 2024;10(5):3988. doi: 10.36922/ijb.3988

Received: June 19, 2024
Revised: August 7, 2024
Accepted: August 13, 2024
Published Online: August 15, 2024

Copyright: © 2024 Author(s). This is an Open Access article distributed under the terms of the Creative Commons Attribution License, permitting distribution, and reproduction in any medium, provided the original work is properly cited.

Publisher's Note: AccScience Publishing remains neutral with regard to jurisdictional claims in published maps and institutional affiliations.

for patients. However, traditional animal models and two-dimensional (2D) cultures, which have long been used in tumor immunotherapy research, presenting a significant limitation due to difference in circulating immunosuppressive cytokines like Interleukin-10 (IL-10) and transforming growth factor (TGF)-β.[1] To overcome these limitations, the *in vitro* simulation of the TIME can facilitate the study of the immune response in tumor models and the interaction between tumor and immune cells and can aid in the exploration of the effectiveness of immunotherapeutic drugs and their mechanisms of action.[2–4]

TIME models, especially those created using bioprinting technology, offer enhanced fidelity and are closer to the *in vivo* TIME than traditional 2D culture models.[5] This is because bioprinting, an advanced form of three-dimensional (3D) modeling, allows for the precise placement of cells, extracellular matrix (ECM), and bioactive molecules to create complex structures that closely mimic the human microenvironment *in vitro*.[6] This capability addresses the limitations seen with animal models and conventional 2D cultures, enhancing our understanding of cancer pathophysiology and metastasis.[7] By accurately arranging cells and ECM, bioprinting provides a realistic representation of the TIME, invaluable for advancing cancer therapies, including drug screening, high-throughput analysis,[8] personalized treatment research,[9] and the study of cancer metastasis mechanisms.[10] The ability to replicate the intricate interactions within the TIME makes bioprinting a particularly useful technology for exploring the effectiveness of various immunotherapies and their mechanisms of action.

The tumor microenvironment (TME) primarily focuses on the interactions between cancer cells and various stromal components, including fibroblasts and the ECM, as well as the formation of blood vessels. In contrast, the TIME includes not only these elements but also the dynamic interactions with immune cells. These interactions are critical for understanding how tumors evade immune detection and how immunotherapies can be optimized. Existing studies have mainly focused on bioprinting the TME, with limited reviews on using bioprinting to simulate the TIME.[11–13]

This review intends to conduct an in-depth exploration of the TIME, focusing on how bioprinting methods and design considerations can significantly advance our understanding and manipulation of these complex systems. The following sections will be covered: immunotherapy, physiological factors in TIME for bioprinting including immune cells and their social interactions, and ECM. Additionally, this paper reviews the components essential for bioprinting the TIME, including the sources of immune cells, bioink formulations, and the required structural complexity. The development of bioprinted TIME (bTIME) models will be detailed, with a focus on their creation and the evaluation of immunotherapeutic drug efficacy within these models.

2. Immunotherapy

Immunotherapy is a type of cancer treatment that harnesses the body's immune system to fight cancer. Unlike traditional therapies that directly target tumor cells, immunotherapy stimulates or enhances the natural ability of the immune system to recognize and destroy cancer cells. This approach can provide long-lasting protection against cancer by creating an immune memory, which helps prevent the recurrence of cancer. Immunotherapeutic drugs are represented by immune modulators, checkpoint inhibitors, CAR-T cells, cancer vaccines, etc.

Immune modulators are drugs that modify the immune response to enhance anti-tumor activity. Their mode of action involves targeting various pathways to modulate the immune system and improve its ability to fight cancer. Examples of immune modulators include pexidartinib (Turalio), which targets the colony-stimulating factor 1 (CSF-1) pathway.[14]

Checkpoint inhibitors are drugs that block proteins used by cancer cells to evade detection by the immune system.[15] Checkpoint inhibitors work by targeting checkpoint proteins such as programmed cell death protein 1 (PD-1), programmed death-ligand 1 (PD-L1), and cytotoxic T-lymphocyte-associated protein 4 (CTLA-4).[16]

CAR-T cell therapy involves modifying the T cells of patients to express CARs on their surface. These receptors are designed to recognize specific proteins on cancer cells, enabling the T cells to target and kill the cancer cells.[17,18] However, the success of CAR-T therapy is largely limited to non-solid tumors such as leukemia and lymphoma. It has not been proven effective against solid tumors such as breast, lung, and pancreatic cancers, where numerous hurdles, including trafficking and immune suppression, are known to interfere with the therapy. These challenges underscore the need for advanced bioprinted models to study and overcome the barriers to CAR-T therapy in solid tumors.

Cancer vaccines are designed to stimulate the immune system to recognize and attack cancer cells.[19] These vaccines introduce tumor-specific antigens to the immune system, prompting it to mount an immune response against cells bearing these antigens. This can involve either stimulating T cells to attack cancer cells or enhancing the production of antibodies against cancer cells.[20]

3. Immune cells and their social interactions in TIME

TIME consists of a tumor, ECM, vascular network and a variety of stromal cells and immune cells (Figure 1).[21] The main immune cells involved in the TIME are cytotoxic T lymphocytes (CTLs), dendritic cells (DCs), macrophages, and natural killer (NK) cells, which interact with each other within this complex environment (Table 1). T cells play a critical role in the immune response against various cancers.[22] Notably, CTLs can kill cancer cells directly when properly activated. Upon recognizing a tumor cell, CTLs release perforin and granzymes, which induce apoptosis in the tumor cell.[23] Additionally, T cells secrete cytokines such as interferon-gamma (IFN-γ) and tumor necrosis factor alpha (TNF-α), which not only have direct anti-tumor effects but also recruit and activate other immune cells.[24] DCs are key antigen-presenting cells that play a crucial role in initiating and regulating immune responses.[25] Macrophages are frequently observed in several solid tumors, making them a common choice for modeling bTIME.[26] NK cells secrete cytokines such as IFN-γ, which have anti-tumor effects and can modulate the activity of other immune cells, enhancing the overall immune response against the tumor.[27]

However, tumors secrete various immunosuppressive cytokines, which interfere with the normal activity of immune cells. For example, these cytokines inhibit the differentiation of DCs.[28,29] This leads to impaired antigen presentation and consequently reduces T cell activation.[30] Immunosuppressive cytokines can induce the conversion of macrophages from anti-tumor (M1-like) to pro-tumor (M2-like) phenotypes, thereby supporting tumor growth and metastasis.[26] M2 macrophages also express checkpoint molecules such as PD-L1, which can bind to PD-1 on T cells, leading to T cell exhaustion and reduced anti-tumor activity.[31]

4. Bioprinting the TIME

4.1. Components for bioprinting the TIME

4.1.1. Source of immune cells

Immune cells can be derived from commercial sources, patient biopsies, or generated from induced pluripotent stem cells (iPSCs) to model specific immune responses.

Immune cells extracted from mice or humans are widely used in research to study immune responses in the TIME *in vitro*.[37] Mouse-derived immune cells, such as those from the spleen, lymph nodes, or bone marrow, have been utilized extensively in preclinical models. However, there are species-specific differences in immune responses that may not fully replicate human immune responses due to differences in immune system architecture and function between species.[38,39] Human-derived immune cells offer high authenticity for modeling human diseases and testing therapies. Variability among donors can

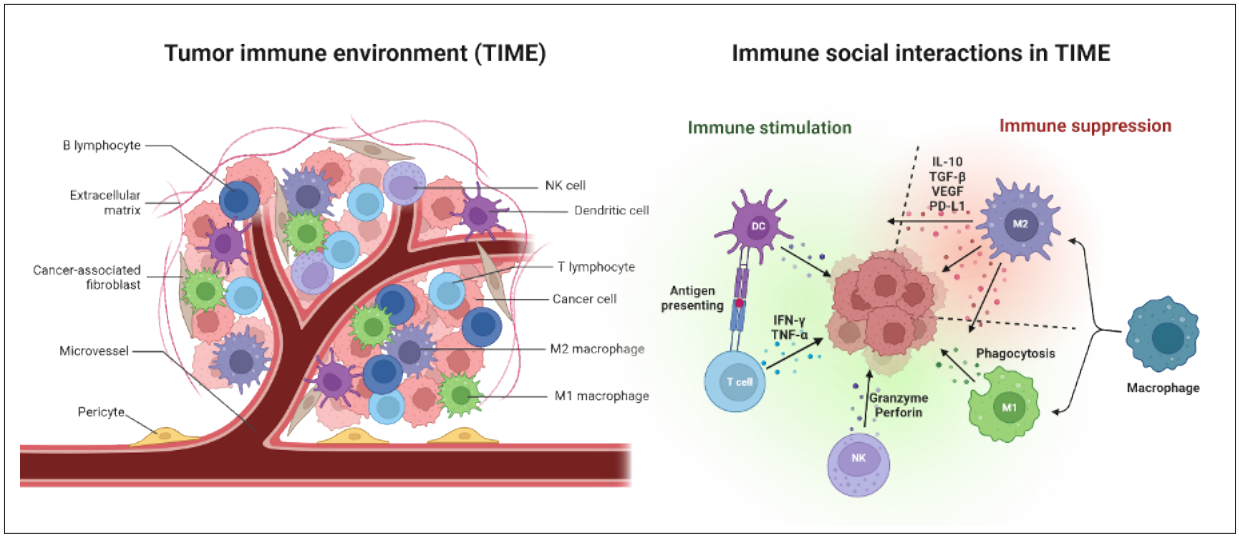


Figure 1. Components of tumor immune microenvironment (TIME) and immune-related interactions. TIME consists of cancer cells, extracellular matrix, microvessels, various stromal cells and immune cells. T cells, natural killer (NK) cells, and M1 macrophages activate each other through cytokines like tumor necrosis factor alpha (TNF-α), interferon gamma (IFN-γ), and interleukin (IL)-6. On the other hand, cancer cells and M2 macrophages inhibit the cytotoxic effects of other immune cells by secreting IL-10, transforming growth factor beta (TGF-β), vascular endothelial growth factor (VEGF), and programmed death-ligand 1 (PD-L1). Modified from Mou et al.[21] published under the terms of the Creative Commons CC BY 4.0 license and created with Biorender.com.

Table 1. Comparison of immune cell activity in normal and cancer conditions.

Cell type	Normal activity	Cancer-associated activity
CTLs	Directly kill infected cells and pathogens by releasing perforin and granzymes to induce apoptosis; secrete cytokines (IFN-γ, TNF-α) to recruit and activate other immune cells[32]	Directly kill cancer cells by releasing perforin and granzymes to induce apoptosis[23]; secrete cytokines (IFN-γ, TNF-α) to recruit and activate other immune cells, aiding in anti-tumor responses[24]
DCs	Capture and present antigens to T cells, activating them; maintain immune surveillance[33]	Present tumor antigens to T cells, activating them and initiating anti-tumor immune responses[25]; impaired by tumor-secreted immunosuppressive cytokines, reducing effectiveness in T cell activatio[n3]4
Macrophages	Phagocytose pathogens and dead cells; secrete cytokines to regulate immune responses; promote tissue repair and remodeling[35]	M1 macrophages exhibit anti-tumor activity; tumors induce M2 phenotype, supporting tumor growth and metastasis[26]; M2 macrophages express PD-L1, leading to T cell exhaustion[31]
NK cells	Directly kill infected or stressed cells by releasing cytotoxic granules (perforin, granzymes); secrete cytokines (IFN-γ) to modulate the activity of other immune cells[36]	Directly kill tumor cells by releasing cytotoxic granules (perforin, granzymes); secrete cytokines (IFN-γ), enhancing anti-tumor immune response[27]

Abbreviations: CTLs, cytotoxic T lymphocytes; DCs, dendritic cells; IFN-γ, Interferon gamma; PD-L1, programmed death-ligand 1; TNF-α, tumor necrosis factor alpha.

affect the consistency of responses, but this variability also provides a comprehensive understanding of human immune responses.[40]

Stem cell-derived immune cells offer a renewable and scalable source for research and therapeutic applications. Immune cells derived from iPSCs can differentiate into various types, such as iPSC-NK or iPSC-T cells, exhibiting functional properties similar to their primary counterparts, including cytotoxicity, cytokine production, and target recognition.[41,42] These cells can be genetically modified to enhance specific functions or to express CARs for targeted therapies.[43,44]

Cell line-derived immune cells, such as Jurkat (T cells),[45] NK-92 (NK cells),[46] and THP-1 (monocytes/macrophages),[47] provide consistent and reproducible models for *in vitro* studies. The stem cell-derived and cell line-derived immune cells should be selected distinguishably in the bTIME model. For example, when using NK cells, NK-92 or iPSC-derived NK cells can be used. NK-92 cells, which do not express killer cell immunoglobulin-like receptors (KIRs), are advantageous for attacking cancer cells because they remain active even when cancer cells have low MHC class I expression, which normally inhibits NK cell activity.[48] However, due to their cancerous origin, they require irradiation prior to use, and their lack of CD16 expression limits their effectiveness in antibody-dependent cellular cytotoxicity (ADCC)-mediated cancer models.[49] Conversely, iPSC-derived NK cells offer a renewable and scalable source, with the ability to be genetically engineered to enhance specific functions, making them ideal for personalized immune response studies.[50] iPSC-derived NK cells often require careful differentiation protocols. Thus, depending on the research objective, both different cell-derived immune cells should be selected.

4.1.2. Bioinks

ECM provides a physical scaffold that not only supports but also influences the behavior of tumor cells. Changes in the composition and organization of the ECM can promote cancer cell motility and invasiveness.[51–53] Components like collagen, fibronectin, and laminins interact with cell surface receptors on cancer cells (e.g., integrins), activating pathways that promote tumor growth and metastasis.[54] The ECM can act as a barrier, and its composition and density can dictate the extent and effectiveness of immune cell infiltration. A denser and more crosslinked ECM can hinder the mobility of T cells and NK cells.[55] ECM secretes or presents chemokines and cytokines that attract immune cells to the tumor site, essential for initiating an immune response.[56] Certain ECM components promote an immunosuppressive environment by supporting cell types such as regulatory T cells and myeloid-derived suppressor cells, which can inhibit effector immune cells.[57]

When selecting bioinks for encapsulating immune cells and cancer cells, it is essential to consider both physical properties of the hydrogels and their interactions with the immune system. The following sections describe the characteristics and immune responses associated with various hydrogels, including alginate, gelatin, hyaluronic acid (HA), collagen, chitosan, and gelatin methacryloyl (GelMA) (Table 2).

Table 2. Summary of hydrogels for bioprinted tumor immune microenvironment.

Hydrogel	Source	Key properties	Immune response
Alginate	Brown seaweed	Biocompatible, gelation with divalent cations	Triggers innate immune responses through macrophage receptors, activates macrophages via the NF-κB pathway, produces IL-6, IL-12, IL-1β, and TNF-α[58,59]
Gelatin	Derived from collagen	Biocompatible, biodegradable, easy to use in bioprinting	Minimal immune response, suitable for bioinks with minimal immune interaction; requires crosslinking with other polymers[60,61]
HA	Connective tissues	Excellent hydration, supports cell proliferation and migration	Interacts with HA-binding receptors (TLR-2, TLR-4); triggers pro-inflammatory responses; modulates immune environment; regulates T cell recruitment[62–65]
Collagen	The most abundant protein in humans	Supports cell adhesion, migration, and differentiation	Immune response varies by species; high density reduces T cell proliferation and infiltration, affecting immunomodulation[66–68]
Chitosan	Exoskeletons of crustaceans	Biodegradable, biocompatible, antimicrobial	Activates macrophages (anti-inflammatory) and dendritic cells (pro-inflammatory), influences cytokine secretion (TNF-α, IL-12/23)[69–71]
dECM	Derived from tissue/organ	Preserving organ-specific ECM properties	Immune response can be varied depending on the decellularization method[72]

Abbreviations: dECM, decellularized extracellular matrix; ECM, extracellular matrix; HA, hyaluronic acid; IL, interleukin; NF-κB, nuclear factor kappa B; TLR, toll-like receptor; TNF-α, tumor necrosis factor alpha.

Alginate is a naturally occurring polysaccharide derived from brown seaweed, which is known for its biocompatibility and gelation capabilities in the presence of divalent cations like calcium ions.[58] Alginate can trigger innate immune responses through macrophage receptors.[59] Yang et al.[59] showed that alginate activated macrophage-like cells via the nuclear factor kappa B (NF-κB) pathway, leading to the production of pro-inflammatory cytokines such as interleukin (IL)-6, IL-12, IL-1β, and TNF-α.

Gelatin is derived from collagen and is widely used due to its excellent biocompatibility, biodegradability, and ease of use in bioprinting applications.[60] Pure gelatin does not elicit a significant immune response, making it a suitable material for bioinks where minimal immune interaction is desired.[61] However, since gelatin does not crosslink, it is difficult to create a 3D structure on its own when making bioink. Therefore, it is necessary to mix polymers that can be crosslinked or made to crosslink through additional chemical bonding.

Hyaluronic acid (HA) is a naturally occurring glycosaminoglycan present in connective tissues.[62] It has excellent hydration properties and the ability to support cell proliferation and migration. HA can interact with HA-binding receptors, such as toll-like receptor (TLR)-2 and TLR-4, recognizing HA fragments that trigger pro-inflammatory responses and thus contribute to the modulation of the immune environment.[63] HA also serves as a ligand for cell surface receptors such as CD44, which can regulate the recruitment of T cells, neutrophils, and monocytes.[64,65]

Collagen is the most abundant protein in the human body and a key component of the ECM, providing support for cell adhesion, migration, and differentiation.[66] The immune response to collagen varies depending on the species from which the collagen is derived and the species of cells being cultured with it.[67] Tumors tend to remodel the surrounding ECM, resulting in a collagen-rich structure with increased stiffness. Kuczek et al.[68] showed that a high density of collagen matrices reduced T cell proliferation and infiltrating CD8+ T cells indicating an immunomodulatory effect depending on collagen matrix density. This property is crucial for designing bioinks that aim to study immune cell interactions within a controlled environment.

Chitosan, derived from chitin found in the exoskeletons of crustaceans, is known for its biodegradability, biocompatibility, and antimicrobial properties.[69] Chitosan activates both macrophages and DCs, eliciting different responses. Oliveira et al.[70] showed that macrophages tend towards an anti-inflammatory phenotype, while DCs exhibit pro-inflammatory attributes. Additionally, the cytokine secretion profile of human monocytes/macrophages cultured on chitosan scaffolds indicates enhanced TNF-α secretion, with scaffold geometry influencing the quantities of TNF-α and IL-12/23 released, which is particularly relevant for applications requiring specific immune responses.[71]

GelMA is a modified form of gelatin with methacryloyl groups that allow photo-crosslinking.[73] It combines the biocompatibility of gelatin with the tunable mechanical properties of synthetic polymers. GelMA, like gelatin,

generally exhibits low immunogenicity. However, when lipopolysaccharide was used to stimulate a pro-inflammatory immune response, it was found that TNF-α expression was suppressed in GelMA culture conditions when culturing human primary peripheral blood mononuclear cells.[74] Thus, GelMA had immune-modulatory properties and might reduce the pro-inflammatory response.

Decellularized extracellular matrix (dECM) refers to the extracellular matrix that remains after the removal of cells from a tissue or organ. Considering the role of foreign cells in graft rejection, decellularization significantly attenuates the host's immune response against transplants.[72] Various decellularization methods contribute to the immunogenicity of the ECM. For example, ionic detergents like sodium dodecyl sulfate (SDS) are highly effective in removing protein antigens, especially in dense tissues, but can expose hidden antigenic sites.[75]

4.1.3. Structural complexity

For the investigation of immune–tumor interaction using bTIME, structural complexity, particularly spatial heterogeneity, is crucial for accurately modeling the migration behavior of immune cells interacting with tumor sites (Figure 2A).[76] Reynolds et al.[77] bioprinted melanoma model in helix shape, and CD8+ T cells were shown to migrate within the matrix to the tumor site (Figure 2B). Morley et al.[78] spatially defined the distributions of glioma cells, hematopoietic stem cells (HSCs), and T cells using bioprinting, and observed that tumor spheroids containing HSCs recruited T cells more rapidly due to cytokine diffusion. Mazzaglia et al.[79] introduced deployable extrusion bioprinters to create compartmentalized tumoroids with cancer-associated fibroblasts (CAFs), embedded in an immune cell-laden collagen matrix, which facilitated the tracking of immune–tumor interactions and revealed enhanced cellular proliferation. Flores-Torres et al.[80] bioprinted gastric cancer patient-derived organoids and tumor infiltrated lymphocytes (TILs), using an alginate, gelatin, and basal membrane mix designed to present physical barriers, and facilitated detailed analysis of TIL migration and activation dynamics (Figure 2C). These studies collectively underscore the significance of spatial heterogeneity in 3D bioprinting for studying immune cell migration and interactions within the TIME, providing valuable insights for developing effective immunotherapies.

4.2. Development of bioprinted tumor immune microenvironment

In order to bioprint tumors, early studies focused on creating a bTME that primarily includes cancer cells, fibroblasts, and the ECM, along with synthetic blood vessels to simulate the vascular network of the tumor.[76,81] These models typically use methods to achieve precise spatial arrangement of cells and materials, such as extrusion-based and inkjet bioprinting. They are designed to closely mimic the 3D structure of actual tumors, facilitating detailed studies of tumor growth, metastasis, and drug response in a controlled environment.[82] However, a significant limitation of these traditional bTME models is the exclusion of immune cells, which are crucial for accurately simulating the interactions within the TIME.[83] This omission restricts the ability of these models to fully replicate the complex dynamics of tumor–immune system interactions and may impact the evaluation of immunotherapeutic agents.[84]

In recent years, efforts have been made to include immune cells in bioprinted tumor models. These models not only simulate interactions between cancer and immune cells but also broader TME. The results obtained by these models such as cytokine profiling and drug response are highly consistent with real tumors. However, optimizing culture conditions for multiple cell types remains challenging, requiring high-resolution and accurate bioprinting method. The following section explains the research on simulating TIME using bioprinting, categorized by the complexity of the models.

4.2.1. Bioprinting immune cells with tumor

Bioprinting immune cells with tumor cells enable the study of direct cytokine and chemokine-mediated interactions. Constructing TIME using various bioprinting techniques involves encapsulating immune cells, such as macrophages, and tumor cells within a bioink, provides a more favorable environment for immune cell culture and activation,[85–87] which is crucial for simulating TIME. Not only can the tumor cytotoxicity effects be observed, but also the specific tumor-supporting effects of immune cells, such as M2 macrophages. For example, Li et al.[88] printed a cholangiocarcinoma (bile duct cancer) cell line RBE in a square structure and arranged macrophages around the square like a fence using extrusion-based bioprinting (Figure 3A). Bioprinting RBE cells and macrophages cells separately in this configuration could evade the contact inhibition during cell growth and ensure better viability than direct mixing. RBE cells bioprinted with macrophages showed higher proliferation and expression in tumor-related genes like epithelial cell adhesion molecule (*EPCAM*), N-cadherin, and matrix metalloproteinase-9 (*MMP9*).

Heinrich et al.[76] printed a miniature brain shape using mouse macrophage-encapsulated GelMA leaving a cavity for the tumor site. Subsequently, glioblastoma (GBM) cells were injected into the cavity. Thus, the bioprinting method offered the cellular position between GBM cells and macrophages, enabling the study of cell–cell interactions such as migration and invasion. The expression of glioma-

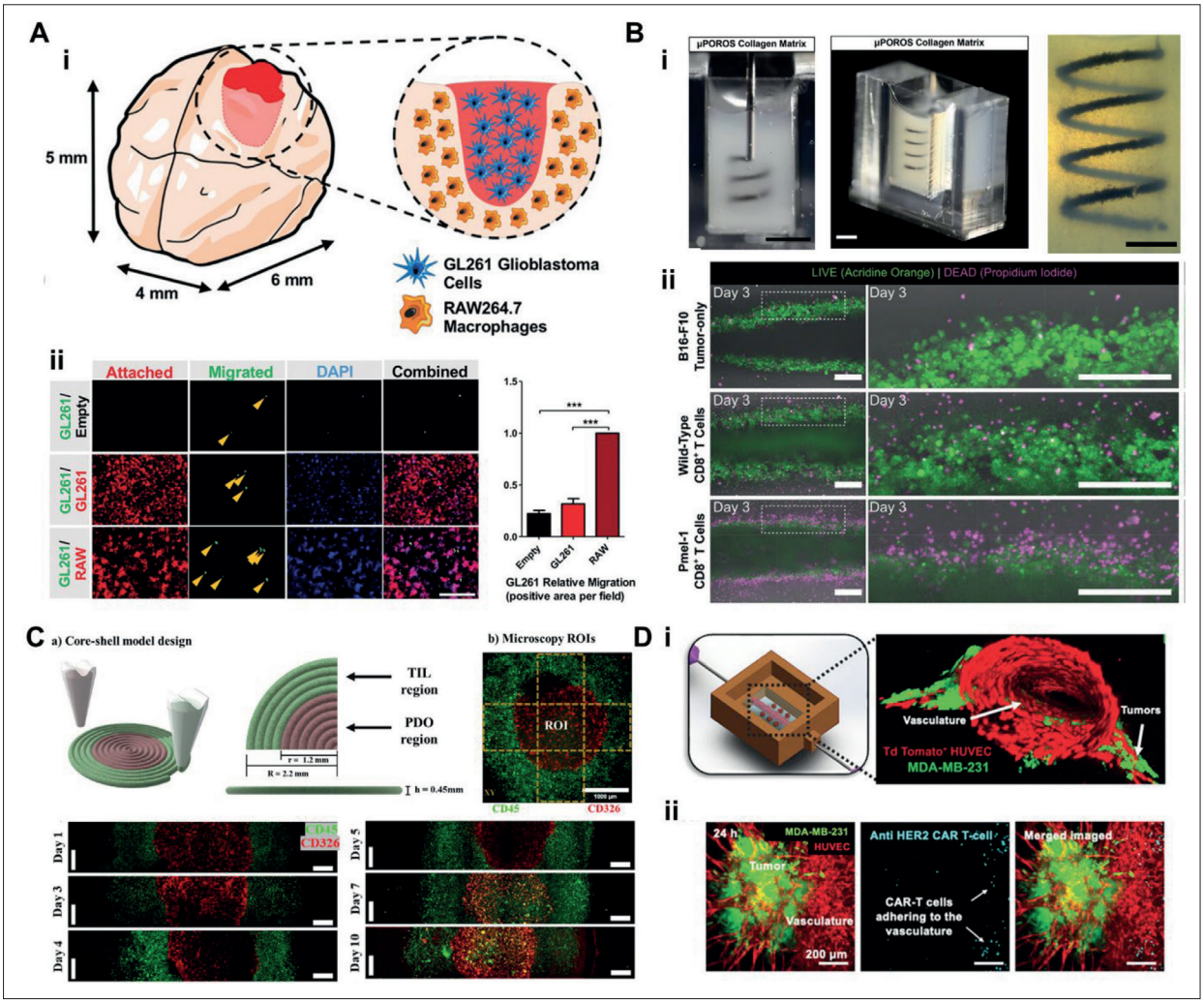


Figure 2. Design considerations for fabricating bioprinted tumor immune microenvironment (bTIME). (A) Incorporation of macrophage in bioprinted mini brain for modeling interactions between glioblastoma (GBM) and glioblastoma-associated macrophages (GAMs).[76] (i) Bioprinted mini brain consisted of GL261 GBM cells and RAW264.7 macrophages with well-defined locations. (ii) Higher migration of GBM cells towards macrophages in mini brain. Scale bar: 200 μm. Reprinted with permission granted by John Wiley & Sons. Copyright © 2019 WILEY-VCH Verlag GmbH & Co. KGaA, Weinheim. (B) Incorporation of T cells in bioprinted melanoma tumor model printed within microporogen-structured (μPOROS) collagen matrix for evaluating T cell-mediated tumor killing effect.[77] (i) Deposition of melanoma cell ink in μPOROS collagen (left image), 3D-bioprinted B16-F10 murine melanoma model within μPOROS collagen in helix shape (middle image), and side view of printed helix (scale bars: 4 mm [left and middle images]; 2 mm [right image]). (ii) Live/dead images of bioprinted melanoma model treated with wild-type CD8+ T cells and pmel-1 CD8+ T cells on day 3. Scale bar: 250 μm. Reprinted with permission granted by John Wiley & Sons. Copyright © 2023 Wiley-VCH GmbH. (C) Spatially well-defined gastric tumor organoid and tumor-infiltrated lymphocyte (TIL) model for assessing TIL migration and activation.[80] Scale bar: 500 μm. Reprinted with permission granted by American Chemical Society. Copyright © 2023 American Chemical Society. (D) Bioprinted vascularized breast cancer for assessing CAR-T efficacy.[96] (i) Construction of tumor angiogenesis connected to a dynamic flow-based culture. (ii) Culture of engineered CAR-T cells in a 3D-bioprinted perfusable and vascularized tumor spheroids. Scale bar: 200 μm. Reprinted with permission granted by John Wiley & Sons.

associated microglia/macrophages (GAM)-specific markers and matrix remodeling markers increased in macrophages, while glioblastoma-specific markers increased in GBM compared to those cultured alone. The upregulated genes in each cell type were consistent with patient data.

Grolman et al.[89] co-axially printed a channel structure with adenocarcinoma cells on the shell and the macrophages on the core to simulate the interaction between macrophages and adenocarcinoma cells. Notably, by varying the extrusion speeds of the alginate and $CaCl_2$ solutions, the macrophage tube could be

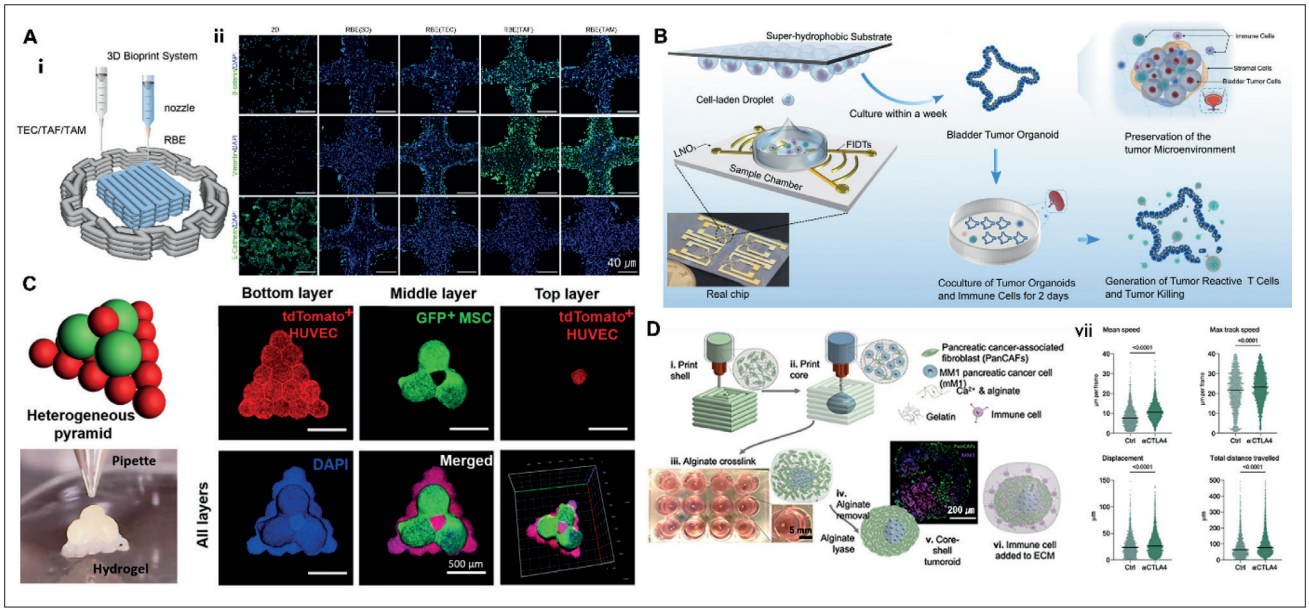


Figure 3. Various bioprinting methods used to reproduce tumor immune microenvironment (TIME). (A) Bioprinted cholangiocarcinoma TIME.[88] (i) A schematic image of printing RBE cholangiocarcinoma TIME. (ii) Immunofluorescence images of tumor-related markers in two dimensions, solely printed RBE, and tumor-associated endothelial cells (TEC)/tumor-associated fibroblasts (TAF)/tumor-associated macrophages (TAM) co-printed RBE models. Scale bars: 40 μm. Reprinted and adapted under the terms of the Creative Commons CC BY 4.0 license. (B) Acoustic droplet printing (ADP) to rapidly culture organoids containing tumor cells, stromal cells, and immune cells.[90] Reprinted with permission granted by John Wiley & Sons. Copyright © 2021 Wiley-VCH GmbH. (C) Aspiration-assisted bioprinting (ABP) used for printing spheroids of different sizes in a complex structure.[94] Scale bars: 500 μm. Reprinted with permission granted by AAAS. Copyright © 2020 Ayan et al. (D) Extrusion-based printing of gelatin-alginate ink mixed with pancreatic cancer cells and cancer-associated fibroblast cells (i–vi).[79] Activities and directions of immune cells with and without anti-CTLA-4 in bioprinted pancreatic TIME (vii). Scale bars: 5 mm in (iii); 200 μm in (v). Reprinted under the terms of the Creative Commons CC BY 4.0 license.

printed in various shapes, such as serpentine and helically packed structures, which enlarged interaction area. When flowing epithelial growth factor receptor (EGFR) inhibitors through the serpentine structure, migration of macrophage was reduced due to the enhanced diffusion, indicating that the interaction between tumor cells and immune cells can be affected by the geometry. However, extrusion-based methods for constructing bTIME models are limited to using cell lines, as the high shear stress of bioprinting can damage fragile primary or patient-derived cells.

Gong et al.[90] printed single cells dissociated from bladder tumor tissue using acoustic droplet printing (ADP), preserving the tumor immune environment including cancer cells, and immune cells such as T cells, macrophages, and CD19+ B cells *in vitro* (Figure 3B), which can be used for high-throughput screening. In ADP, cells encapsulated in bioink were ejected upwards as a droplet (0.1–0.2 μL) by acoustic force and deposited onto a substrate. Although ADP is limited to low-viscosity bioinks and cannot print large structures, it is suitable for cells that are difficult to obtain in large quantities due to the small amount of ink used and minimizes the shear stress on the cells lower than 1 Pa, allowing fragile cells to be printed. The bioprinted droplet could preserve immune cells, especially endogenous infiltration T cells, and the immune population in the droplet is consistent with that of *in vivo* tissue.

Reynolds et al.[77] utilized embedded bioprinting, a technique where cells and biomaterials are printed within a hydrogel support to minimize gravitational effects to print melanoma cells in a helical shape embedded within a cytotoxic T-cell-encapsulated collagen matrix. In this complex structure, T cells in the matrix migrated and infiltrated the printed melanoma structure. Although not yet applied, hydroelectric bioprinting methods, such as electrospinning, also offer advantages for modeling TIMEs. Electrospinning uses a high-voltage electric field to produce extended nanometer to micrometer-scale fibers from polymer solutions, which have the advantage of high surface area.[91] By printing fibers that have been surface-modified with immunomodulatory cytokines, researchers can co-culture cancer cells and immune cells to observe the impact of cytokine-mediated cancer–immune cell interactions in detail.

However, these models are still insufficient for fully simulating the TIME. To accurately mimic TIME in the

future, it is essential to include other stromal cells, as they aid tumor growth and create an immunosuppressive environment, significantly influencing immune cell activity *in vivo*.

4.2.2. Bioprinting immune cells with tumor and stromal cells

Efforts to address the lack of stromal cells in tumor models have led to recent advancements in bioprinting. These developments have allowed for the creation of more sophisticated models that include not only tumor and immune cells but also stromal cells, which play an immunosuppressive role in the TME. For example, Tang et al.[92] fabricated GBM tumor models with glioblastoma stem cells, macrophages, and stromal cells such as astrocytes, and neural progenitor cells using digital light processing bioprinting (DLP). The DLP method enabled the adjustment of stiffness by varying the exposure time, allowing the mimicry of the peripheral region stiffness of the brain (~1 kPa). Macrophages cultured in the bioprinted model showed more immunosuppressing RNA profiles than 2D-cultured macrophages, including upregulation of M2-related markers such as CD163 and IL-10. Dey et al.[93] printed 3D models of breast cancer with precise positioning using aspiration-based bioprinting (ABB), a technique that harnesses aspiration forces to pick and bioprint biologics in three dimensions (Figure 3C).[94] When combined with microvalve bioprinting, ABB is uniquely capable of printing spheroids of different sizes. They studied the effect of localization of engineered T cells and breast cancer/human dermal fibroblasts (HDF) spheroids on immune response. They observed that closer proximity between T cells and breast cancer/HDF spheroids slowed tumor invasion and enhanced secretion of granzymes, IFN-γ, and XXX (CCL2), indicating paracrine interactions between tumors and T cells. These studies highlight the critical role of stromal cells in creating more advanced and accurate tumor models, which can provide deeper insights into tumor biology and immune responses.

4.2.3. Integrated bioprinted tumor immune microenvironment with vascular system

The creation of vascularized models is also crucial for studying the interactions between immune cells and cancer cells within the TIME. These models can include blood or lymphatic vessels, which are essential for mimicking physiological conditions and enabling the study of immune cell migration towards cytokine-producing cancer cells.[95,96] One method involves dynamic flow-based 3D bioprinting to create a vascularized model that responds to chemo- and immuno-therapies. For instance, a breast tumor model demonstrated that heterotypic tumors bioprinted at predefined distances from perfused vasculature exhibited tumor angiogenesis and cancer cell invasion (Figure 2D).[96] Furthermore, perfusing human epidermal growth factor receptor 2 (HER2)-targeting CAR-modified CD8+ T cells through the channels resulted in significant T cell activation, infiltration, and up to 70% reduction in tumor volumes. This illustrates the potential of these vascularized models for preclinical testing and personalized medicine.

Combining 3D bioprinting with microfluidic technology also enhances the physiological relevance of these models. A bladder cancer-on-a-chip was developed to mimic the TIME using the bladder cancer cells along with the lung fibroblast cells, human umbilical vein endothelial *cells* (HUVECs), and human leukemia monocytic cells.[97] The study found that the bioprinted structure integrated with the microfluidic chip enhanced cell proliferation and allowed detailed tracking of monocyte migration and cytokine concentration changes. These examples demonstrate how vascularization and perfusion system achieved through 3D bioprinting can be leveraged to model complex tumor–immune interactions and develop effective immunotherapies. The advantages and limitations of various methods introduced in this review are summarized in Table 3.

4.2.4. Efficacy of immunotherapeutic drugs in bioprinted tumor immune microenvironment

The evaluation of immunotherapeutic drugs using bTIME models is promising but is still in preliminary phases. Here, we discuss how bTIME models are uniquely suited to testing immunotherapeutic drugs, such as immune modulators, checkpoint inhibitors, CAR-T cells, and cancer vaccines.

bTIME models can accurately replicate the interactions between cancer cells and immune cells, including T cells and macrophages. Therefore, they offer a sophisticated platform to evaluate the effectiveness of immune modulators and checkpoint inhibitors in a controlled reproducible environment. Heinrich et al.[76] evaluated the effects of immune modulators, such as CSF-1 inhibitor and the signal transducer and activator of transcription 6 (STAT6) inhibitor, in bioprinted miniatured brains with macrophages and glioblastoma cells. The CSF-1 inhibitor BLZ945 is known to inhibit the growth of tumor cell lines both *in vitro*[99] and *in vivo*, and the same result was observed in this bioprinted model. Notably, the STAT inhibitor AS1517499 has been shown to reduce tumor growth and metastasis in mouse tumor models,[100] but no direct effects on GBM models have been reported in *in vitro* experiments. However, in glioblastoma within the AS1517499-treated bTIME, a decrease in the expression of SPP-1, a GBM marker related to macrophage recruitment, was observed.[76]

Table 3. Advantages and limitations of bioprinting tumir immune microenvirornment.

Type	Description	Advantages	Limitations
Extrusion bioprinting	Uses continuous flow of bioink extruded through a nozzle to create structures	– Precise control over cancer and immune cell positioning and quantity – Usage of a wide range of biomaterials for ECM	– Lower resolution than other methods – Shear stress can affect immune cell viability[89]
Acoustic droplet printing	Utilizes sound waves to precisely place droplets of bioink	– Low shear stress for fragile immune cells – Capable of printing with a small amount of ink	– Limited to low-viscosity bioinks[90] – Cannot print large structures
Aspiration-assisted bioprinting	Uses aspiration forces to pick up and place bioink droplets	– Allows printing various sizes of spheroids in precise positions	– Unable to print cells in a distributed manner – Specific self-healing bed conditions is needed[94]
Digital light processing bioprinting	Uses light to polymerize a photosensitive bioink layer by layer	– Capable of printing multiple identical structures simultaneously	– Limited to photopolymerizable bioinks – Potential cytotoxicity caused by photoinitiators and ultraviolet light[98]
Embedded printing	Print cells and biomaterials within a hydrogel support	– Minimizes the effects of gravity – Allows precise stacking of complex 3D structures along the *Y*-axis	– Supporting matrix is required – Limited supply of oxygen and nutrient in the matrix[77]

Mazzaglia et al.[79] simulated a complex TIME by bioprinting with GelMA-alginate ink to create tumor core–shell constructs containing pancreatic ductal adenocarcinoma cells, CAFs, splenocytes, T cells, and NK cells (Figure 3D). The study demonstrated that anti-CTLA-4 treatment resulted in enhanced migration speed and directionality of immune cells. To our knowledge, there are currently no reports on the interaction between immune cells and tumor cells treated with anti-CTLA-4 in a 2D culture environment, making comparisons impossible. The efficacy of anti-CTLA-4 is primarily studied using mouse models. In these studies, it is challenging to directly observe the interaction between immune cells and tumors posttreatment, leading to a focus on the changes in tumor or analyzing immune cells separately *in vitro* before injecting them into mouse models.[101] The results from the research team suggest that the bTIME model can be used to directly evaluate the impact of immune cell changes on tumors within the same model. Incorporated with key immune interactions (e.g., CSF-1, STAT6, PD-1/PD-L1, and CTLA-4), these models allow for the precise assessment of checkpoint inhibitors in a realistic TIME.

The bTIME models allow detailed evaluation of CAR-T/NK cell cytotoxicity, proliferation, and persistence within the TME (Table 4). Particularly in solid tumors, CAR-T/NK cells have shown disappointing efficacy due to the ECM blocking their infiltration.[102,103] bTIME models can simulate these essential challenges for CAR-T/NK cells that cannot be replicated by 2D or conventional spheroid models. Grunewald et al.[104] encapsulated neuroblastoma cells in GelMA, which acts as the ECM, and bioprinted them for CAR-T screening using stereolithographic bioprinting. Using the bioprinted model, they are able to distinguish the more effective CAR-T between the two different types of L1 cell adhesion molecule (L1CAM) CAR-T, short spacer or long spacer, and the results were consistent with *in vivo* findings. CAR-T cells showed higher activation in the bioprinted model compared to the 2D model, but their cytotoxicity was lower due to fewer CAR-T cells reaching the tumor, as the bioink hinder CAR-T cell movement, mimicking the ECM in the TIME environment, which impedes CAR-T cell infiltration.[105] This highlights the need for the development and refinement of experimental protocols tailored for 3D-bioprinted models, distinct from those used in traditional 2D experiments.

Cancer vaccines and bi-specific antibodies are relatively new immuno-oncologic agents and, unlike other immuno-oncologic agents, have not been tested with bTIME. Given that cancer vaccines work by activating T cells in the body,[106] it is essential to test them in a TIME containing T cells. bTIME can effectively simulate the complex tumor immune environment in a controlled and reproducible setting. Researchers can evaluate the activation and proliferation of T cells in response to the vaccine, as well as the subsequent tumor cell killing.[93] bTIME models can be used to test bi-specific antibodies that simultaneously target tumor antigens and engage T cells. This setup allows for the evaluation of the crosslinking efficiency of bi-specific antibodies and their ability to recruit and activate T cells in the proximity of cancer cells. These models enable the testing of bi-specific antibodies in combination with other immunotherapeutic drugs, providing a comprehensive understanding of synergistic effects and the potential of combination strategies to enhance anti-tumor responses.

Table 4. Immunotherapy outcomes in bioprinted tumor immune microenvironment model.

Immunotherapy	bTIME construct	Cells	Bioink	Outcome
CSF-1 inhibitor (BLZ945)[76]	Miniatured brains	Macrophages and glioblastoma cells	GelMA	Inhibition of tumor cell growth
STAT6 inhibitor (AS1517499)[76]				Decreased macrophage recruitment marker, SPP-1
Anti-CTLA-4[79]	Core–shell	Pancreatic ductal adenocarcinoma cells, CAFs, splenocytes, T cells, and NK cells	GelMA, alginate	Enhanced migration speed and directionality of immune cells
L1CAM CAR-T[104]	Disk with channel	Neuroblastoma cells in	GelMA	CAR-T cells showed higher activation in the bioprinted model compared to the 2D model

Abbreviations: CAFs, cancer-associated fibroblasts; CAR-T, Chimeric antigen receptor-T cells; CSF-1, colony-stimulating factor 1; CTLA4, Cytotoxic T-lymphocyte-associated protein 4; GelMA, gelatin methacryloyl; L1CAM, L1 cell adhesion molecule; STAT6, signal transducer and activator of transcription 6.

5. Conclusion

In this paper, we review the critical aspects of bTIME for immunotherapy research. Several key areas warrant further investigation and development. 3D bioprinting plays a crucial role in the development of immunotherapies. Considering the advantages, limitations, and areas requiring optimization of this technology, significant advancements can be made in the efficacy evaluation and personalized design of immunotherapies.

One of the main advantages of 3D bioprinting is its ability to accurately model the TIME. To create the TIME model, it is essential to control the positions of tumor cells, immune cells, and stromal cells accurately. In the TIME, these cells exhibit heterogeneity and distinct regions while being closely associated. This heterogeneity allows the observation of cancer and immune cells' migration. This capability is particularly useful in observing CAR-T cell infiltration, specific targeting, and tumor mass changes, helping to overcome the disappointing efficacy of CAR-T/NK cells in solid tumors. Additionally, bTIME can recapitulate immunosuppressive environment with the tumor-protective ECM and immunosuppressive stromal cells, which are challenging in 2D or conventional 3D spheroid models. These advantages position 3D bioprinting as a crucial predictive model in the development of immunotherapies. They provide promising results in screening CAR-T cell candidates, more accurately predicting their efficacy and safety. Detailed studies of immune–tumor interactions in a controlled environment promote more effective immunotherapy development and reduce dependence on animal models.

However, 3D bioprinting faces several limitations. First, high-resolution imaging is challenging in thick bioprinted TIME structures, making it difficult to accurately observe cell and tissue interactions. Second, analyzing the vast amounts of data generated from complex 3D structures is challenging. Third, reproducing tissue-level cell density and stiffness is difficult because bioprinted tissues lack the microvasculature to supply nutrients, leading to necrosis at high cell densities. Additionally, degradation proteins from cells can dissolve the bioink, making it hard to maintain the structure and stiffness of the tissue.

Several approaches are proposed to address these issues. First, imaging challenges can be tackled using advanced imaging technologies like CLARITY,[107] optical coherence tomography (OCT),[108] and photoacoustic imaging.[109] CLARITY makes tissues transparent to enable visualization of 3D structure, while OCT provides high-resolution real-time imaging of tissue microstructures, and photoacoustic imaging allows for deep tissue imaging. Second, analysis challenges can be addressed using artificial intelligence (AI), which can quickly analyze large, complex datasets to identify patterns and provide insights into cell behaviors and therapeutic responses.[110] Finally, the difficulties in reproducing tissue-level cell density and stiffness can be resolved by optimizing bioinks or introducing new materials.

In conclusion, 3D bioprinting shows great potential for immunotherapy development. By accurately modeling TIME, it enables precise evaluation of CAR-T cell efficacy in tumors. With the inclusion of stromal cells, bTIME can replicate an immunosuppressive environment. In-depth study to overcome immunosuppressive effect on immune cells such as cell trafficking can be carried out in the bTIME. Advancements in imaging, AI integration, and bioink optimization address current challenges in bioprinting, making 3D bioprinting an essential tool for creating personalized and effective immunotherapies.

Acknowledgments

None.

Funding

This work was supported by the National Research Foundation (NRF) of Korea grants funded by the Korea government (MSIT; No. RS-2023-00242443, RS-2023-00218543).

Conflict of interest

The authors declare they have no competing interests.

Author contributions

Conceptualization: Sungsu Park
Formal analysis: Sein Kim
Investigation: Jaehyun Lee, Chanyang Lee
Methodology: Seokgyu Han
Writing–original draft: Sein Kim, Seokgyu Han
Writing–review & editing: Sein Kim, Seokgyu Han, Chanyang Lee, Sungsu Park

Ethics approval and consent to participate

Not applicable.

Consent for publication

Not applicable.

Availability of data

Not applicable.

References

1. Yaddanapudi K, Mitchell RA, Eaton JW. Cancer vaccines: looking to the future. *Oncoimmunology.* 2013;2(3):e23403. doi: 10.4161/onci.23403

2. Flores-Torres S, Jiang T, Kort-Mascort J, et al. Constructing 3D in vitro models of heterocellular solid tumors and stromal tissues using extrusion-based bioprinting. *ACS Biomater Sci Eng.* 2023;9(2):542-561. doi: 10.1021/acsbiomaterials.2c00998

3. Zhou Z, Pang Y, Ji J, et al. Harnessing 3D in vitro systems to model immune responses to solid tumours: a step towards improving and creating personalized immunotherapies. *Nat Rev Immunol.* 2024;24(1):18-32. doi: 10.1038/s41577-023-00896-4

4. Zhang Z, Chen X, Gao S, et al. 3D bioprinted tumor model: a prompt and convenient platform for overcoming immunotherapy resistance by recapitulating the tumor microenvironment. *Cell Oncol.* 2024;47:1113-1126. doi: 10.1007/s13402-024-00935-9

5 Staros R, Michalak A, Rusinek K, et al. Perspectives for 3D-bioprinting in modeling of tumor immune evasion. *Cancers.* 2022;14(13):3126. doi: 10.3390/cancers14133126

6 Parodi I, Di Lisa D, Pastorino L, et al. 3D bioprinting as a powerful technique for recreating the tumor microenvironment. *Gels.* 2023;9(6):482. doi: 10.3390/gels9060482

7 Voskoglou-Nomikos T, Pater JL, Seymour L. Clinical predictive value of the cell line, human xenograft, and mouse allograft preclinical cancer models. *Clin Cancer Res.* 2003;9(11):4227-4239.

8 González-Callejo P, García-Astrain C, Herrero-Ruiz A, et al. 3D bioprinted tumor-stroma models of triple-negative breast cancer stem cells for preclinical targeted therapy evaluation. *ACS Appl Mater Interfaces.* 2024;16(21):27151-27163. doi: 10.1021/acsami.4c04135

9 Augustine R, Kalva SN, Ahmad R, et al. 3D bioprinted cancer models: revolutionizing personalized cancer therapy. *Transl Oncol.* 2021;14(4):101015. doi: 10.1016/j.tranon.2021.101015

10 Zhu W, Holmes B, Glazer RI, Zhang LG. 3D printed nanocomposite matrix for the study of breast cancer bone metastasis. *Nanomed Nanotechnol Biol Med.* 2016; 12(1):69-79. doi: 10.1016/j.nano.2015.09.010

11 Bae J, Han S, Park S. Recent advances in 3D bioprinted tumor microenvironment. *Biochip J.* 2020;14:137-147. doi: 10.1007/s13206-020-4201-8

12 Zhang YS, Duchamp M, Oklu R, et al. Bioprinting the cancer microenvironment. *ACS Biomater Sci Eng.* 2016;2(10): 1710-1721. doi: 10.1021/acsbiomaterials.6b00246

13 Shukla P, Yeleswarapu S, Heinrich MA, et al. Mimicking tumor microenvironment by 3D bioprinting: 3D cancer modeling. *Biofabrication.* 2022;14(3):Article 032002. doi: 10.1088/1758-5090/ac6d11

14 Monestime S, Lazaridis D. Pexidartinib (TURALIO): the first FDA-indicated systemic treatment for tenosynovial giant cell tumor. *Drugs R D.* 2020;20(3):189-195. doi: 10.1007/s40268-020-00314-3

15 Pardoll DM. The blockade of immune checkpoints in cancer immunotherapy. *Nat Rev Cancer.* 2012;12(4):252-264. doi: 10.1038/nrc3239

16 Topalian SL, Drake CG, Pardoll DM. Immune checkpoint blockade: a common denominator approach to cancer therapy. *Cancer Cell.* 2015;27(4):450-461. doi: 10.1016/j.ccell.2015.03.001

17 June CH, O'Connor RS, Kawalekar OU, et al. CAR T cell immunotherapy for human cancer. *Science.* 2018;359(6382):1361-1365. doi: 10.1126/science.aar6711

18 Gross G, Waks T, Eshhar Z. Expression of immunoglobulin-T-cell receptor chimeric molecules as functional receptors with antibody-type specificity. *Proc Natl Acad Sci U S A.* 1989;86(24):10024-10028.
doi: 10.1073/pnas.86.24.10024

19. Schlom J. Therapeutic cancer vaccines: current status and moving forward. *J Natl Cancer Inst.* 2012;104(8):599-613.
doi: 10.1093/jnci/djs033

20 Finn OJ. Cancer vaccines: between the idea and the reality. *Nat Rev Immunol.* 2003;3(8):630-641.
doi: 10.1038/nri1150

21 Mou P, Ge QH, Sheng R, et al. Research progress on the immune microenvironment and immunotherapy in gastric cancer. *Front Immunol.* 2023;14:1291117.
doi: 10.3389/fimmu.2023.1291117

22 Chen C, Liu X, Chang CY, et al. The interplay between T cells and cancer: the basis of immunotherapy. *Genes.* 2023;14(5):1008.
doi: 10.3390/genes14051008

23. Cullen SP, Brunet M, Martin SJ. Granzymes in cancer and immunity. *Cell Death Differ.* 2010;17(4):616-623.
doi: 10.1038/cdd.2009.206

24. Navasardyan I, Bonavida B. Regulation of T cells in cancer by nitric oxide. *Cells.* 2021;10(10):2655.
doi: 10.3390/cells10102655

25. McDonnell AM, Robinson BW, Currie AJ. Tumor antigen cross-presentation and the dendritic cell: where it all begins? *J Immunol Res.* 2010;2010(1):539519.
doi: 10.1155/2010/539519

26. Chen Y, Song Y, Du W, et al. Tumor-associated macrophages: an accomplice in solid tumor progression. *J Biomed Sci.* 2019;26(1):78.
doi: 10.1186/s12929-019-0568-z

27. Yu Y. The function of NK cells in tumor metastasis and NK cell-based immunotherapy. *Cancers.* 2023;15(8):2323.
doi: 10.3390/cancers15082323

28. Gabrilovich D. Mechanisms and functional significance of tumour-induced dendritic-cell defects. *Nat Rev Immunol.* 2004;4(12):941-952.
doi: 10.1038/nri1498

29. Melief CJ. Cancer immunotherapy by dendritic cells. *Immunity.* 2008;29(3):372-383.
doi: 10.1016/j.immuni.2008.08.004

30. Shurin GV, Ma Y, Shurin MR. Immunosuppressive mechanisms of regulatory dendritic cells in cancer. *Cancer Microenviron.* 2013;6(2):159-167.
doi: 10.1007/s12307-013-0133-3

31. Cess CG, Finley SD. Multi-scale modeling of macrophage—T cell interactions within the tumor microenvironment. *PLoS Comp Biol.* 2020;16(12):e1008519.
doi: 10.1371/journal.pcbi.1008519

32. Ito H, Seishima M. Regulation of the induction and function of cytotoxic T lymphocytes by natural killer T cell. *J Biomed Biotechnol.* 2010;2010:641757.
doi: 10.1155/2010/641757

33. Zanna MY, Yasmin A, Omar AR, et al. Review of dendritic cells, their role in clinical immunology, and distribution in various animal species. *Int J Mol Sci.* 2021; 22(15):8044.
doi: 10.3390/ijms22158044

34. Xiao Z, Wang R, Wang X, et al. Impaired function of dendritic cells within the tumor microenvironment. *Front Immunol.* 2023;14:1213629.
doi: 10.3389/fimmu.2023.1213629

35. Lendeckel U, Venz S, Wolke C. Macrophages: shapes and functions. *ChemTexts.* 2022;8(2):12.
doi: 10.1007/s40828-022-00163-4

36. Vivier E, Tomasello E, Baratin M, et al. Functions of natural killer cells. *Nat Immunol.* 2008;9(5):503-510.
doi: 10.1038/ni1582

37. Mu P, Zhou S, Lv T, et al. Newly developed 3D in vitro models to study tumor–immune interaction. *J Exp Clin Cancer Res.* 2023;42(1):81.
doi: 10.1186/s13046-023-02653-w

38. Zschaler J, Schlorke D, Arnhold J. Differences in innate immune response between man and mouse. *Crit Rev Immunol.* 2014;34(5):433-454.
doi: 10.1615/CritRevImmunol.2014011600

39. Bjornson-Hooper ZB, Fragiadakis GK, Spitzer MH, et al. A comprehensive atlas of immunological differences between humans, mice, and non-human primates. *Front Immunol.* 2022;11(13):867015.
doi: 10.3389/fimmu.2022.867015

40. Zhao Z, Zhang S, Jiang N, et al. Patient-derived immunocompetent tumor organoids: a platform for chemotherapy evaluation in the context of T-cell recognition. *Angew Chem Int Ed.* 2024;63(9): e202317613.
doi: 10.1002/anie.202317613

41. Goldenson BH, Hor P, Kaufman DS. iPSC-derived natural killer cell therapies-expansion and targeting. *Front Immunol.* 2022;3(13):841107.
doi: 10.3389/fimmu.2022.841107

42. Minagawa A, Yoshikawa T, Yasukawa M, et al. Enhancing T cell receptor stability in rejuvenated iPSC-derived T cells improves their use in cancer immunotherapy. *Cell Stem Cell.* 2018;23(6):850-858.e4.
doi: 10.1016/j.stem.2018.10.005

43. Li Y, Hermanson DL, Moriarity BS, Kaufman DS. Human iPSC-derived natural killer cells engineered with chimeric antigen receptors enhance anti-tumor activity. *Cell Stem Cell.* 2018;23(2):181-192.e5.
doi: 10.1016/j.stem.2018.06.002

44. Zhou Y, Li M, Zhou K, et al. Engineering induced pluripotent stem cells for cancer immunotherapy. *Cancers.* 2022;14(9):2266. doi: 10.3390/cancers14092266

45. Abraham RT, Weiss A. Jurkat T cells and development of the T-cell receptor signalling paradigm. *Nat Rev Immunol.* 2004;4(4):301-308. doi: 10.1038/nri1330

46. Klingemann H, Boissel L, Toneguzzo F. Natural killer cells for immunotherapy–advantages of the NK-92 cell line over blood NK cells. *Front Immunol.* 2016; 14(7):91. doi: 10.3389/fimmu.2016.00091

47. Chanput W, Mes JJ, Wichers HJ. THP-1 cell line: an in vitro cell model for immune modulation approach. *Int Immunopharmacol.* 2014;23(1):37-45. doi: 10.1016/j.intimp.2014.08.002

48. Gong J-H, Maki G, Klingemann HG. Characterization of a human cell line (NK-92) with phenotypical and functional characteristics of activated natural killer cells. *Leukemia.* 1994;8(4):652-658.

49. Laskowski TJ, Biederstadt A, Rezvani K. Natural killer cells in antitumour adoptive cell immunotherapy. *Nat Rev Cancer.* 2022;22(10):557-575. doi: 10.1038/s41568-022-00491-0

50. Zhu H, Blum RH, Bjordahl R, et al. Pluripotent stem cell-derived NK cells with high-affinity noncleavable CD16a mediate improved antitumor activity. *Blood.* 2020;135(6):399-410. doi: 10.1182/blood.2019000621

51. Lu P, Weaver VM, Werb Z. The extracellular matrix: a dynamic niche in cancer progression. *J Cell Biol.* 2012;196(4):395-406. doi: 10.1083/jcb.201102147

52. Mai Z, Lin Y, Lin P, et al. Modulating extracellular matrix stiffness: a strategic approach to boost cancer immunotherapy. *Cell Death Dis.* 2024;15(5):307. doi: 10.1038/s41419-024-06697-4

53. Park Y, Lee D, Lee JE, et al. The matrix stiffness coordinates the cell proliferation and PD-L1 expression via YAP in lung adenocarcinoma. *Cancers.* 2024;16(3):598. doi: 10.3390/cancers16030598

54. Hynes RO. The extracellular matrix: not just pretty fibrils. *Science.* 2009;326(5957):1216-1219. doi: 10.1126/science.1176009

55. Joyce JA, Fearon DT. T cell exclusion, immune privilege, and the tumor microenvironment. *Science.* 2015; 348(6230):74-80. doi: 10.1126/science.aaa6204

56. Madsen CD, Sahai E. Cancer dissemination—lessons from leukocytes. *Dev Cell.* 2010;19(1):13-26. doi: 10.1016/j.devcel.2010.06.013

57. Noy R, Pollard JW. Tumor-associated macrophages: from mechanisms to therapy. *Immunity.* 2014;41(1):49-61. doi: 10.1016/j.immuni.2014.06.010

58. Lee KY, Mooney DJ. Alginate: properties and biomedical applications. *Prog Polym Sci.* 2012;37(1):106-126. doi: 10.1016/j.progpolymsci.2011.06.003

59. Yang D, Jones KS. Effect of alginate on innate immune activation of macrophages. *J Biomed Mater Res.* 2009;90(2):411-418. doi: 10.1002/jbm.a.32096

60. Alipal J, Pu'Ad NM, Lee T, et al. A review of gelatin: properties, sources, process, applications, and commercialisation. *Mater Today: Proc.* 2021;42(1):240-250. doi: 10.1016/j.matpr.2020.12.922

61. Elalouf A. Immune response against the biomaterials used in 3D bioprinting of organs. *Transpl Immunol.* 2021;69:101446. doi: 10.1016/j.trim.2021.101446

62. Necas J, Bartosikova L, Brauner P, Kolar J. Hyaluronic acid (hyaluronan): a review. *Vet Med.* 2008;53(8):397-411. doi: 10.17221/1930-VETMED

63. Haas A. The phagosome: compartment with a license to kill. *Traffic.* 2007;8(4):311-330. doi: 10.1111/j.1600-0854.2006.00531.x

64. Johnson P, Ruffell B. CD44 and its role in inflammation and inflammatory diseases. *Inflamm Allergy Drug Targets.* 2009;8(3):208-220. doi: 10.2174/187152809788680994

65. Assmann V, Fieber C, Herrlich P, et al. CD44 is the principal mediator of hyaluronic-acid-induced melanoma cell proliferation. *J Invest Dermatol.* 2001;116(1):93-101. doi: 10.1046/j.1523-1747.2001.00236.x

66. Avila Rodríguez MI, Rodríguez Barroso LG, Sánchez ML. Collagen: a review on its sources and potential cosmetic applications. *J Cosmet Dermatol.* 2018;17(1):20-26. doi: 10.1111/jocd.12450

67. Lynn A, Yannas I, Bonfield W. Antigenicity and immunogenicity of collagen. *J Biomed Mater Res B Appl Biomater.* 2004;71(2):343-354. doi: 10.1002/jbm.b.30096

68. Kuczek DE, Larsen AMH, Thorseth M-L, et al. Collagen density regulates the activity of tumor-infiltrating T cells. *J Immunother Cancer.* 2019;7(1):68. doi: 10.1186/s40425-019-0556-6

69. Kou SG, Peters LM, Mucalo MR. Chitosan: a review of sources and preparation methods. *Int J Biol Macromol.* 2021;169:85-94. doi: 10.1016/j.ijbiomac.2020.12.005

70. Oliveira MI, Santos SG, Oliveira MJ, et al. Chitosan drives anti-inflammatory macrophage polarisation and pro-inflammatory dendritic cell stimulation. *Eur Cell Mater.* 2012;24(136):133-136. doi: 10.22203/ecm.v024a10

71. Almeida CR, Serra T, Oliveira MI, et al. Impact of 3-D printed PLA-and chitosan-based scaffolds on human monocyte/macrophage responses: unraveling the effect of 3-D structures on inflammation. *Acta Biomater.* 2014;10(2):613-622.
doi: 10.1016/j.actbio.2013.10.035

72. Kasravi M, Ahmadi A, Babajani A, et al. Immunogenicity of decellularized extracellular matrix scaffolds: a bottleneck in tissue engineering and regenerative medicine. *Biomater Res.* 2023;27(1):10.
doi: 10.1186/s40824-023-00348-z

73. Yue K, Trujillo-de Santiago G, Alvarez MM, et al. Synthesis, properties, and biomedical applications of gelatin methacryloyl (GelMA) hydrogels. *Biomaterials.* 2015;73:254-271.
doi: 10.1016/j.biomaterials.2015.08.045

74. Donaldson AR, Tanase CE, Awuah D, et al. Photocrosslinkable gelatin hydrogels modulate the production of the major pro-inflammatory cytokine, TNF-α, by human mononuclear cells. *Front Bioeng Biotechnol.* 2018;6:116.
doi: 10.3389/fbioe.2018.00116

75. Chakraborty J, Roy S, Ghosh S. Regulation of decellularized matrix mediated immune response. *Biomater Sci.* 2020;8(5):1194-1215.
doi: 10.1039/c9bm01780a

76. Heinrich MA, Bansal R, Lammers T, et al. 3D-bioprinted mini-brain: a glioblastoma model to study cellular interactions and therapeutics. *Adv Mater.* 2019;31(14):1806590.
doi: 10.1002/adma.201806590

77. Reynolds DS, de Lázaro I, Blache ML, et al. Microporogen-structured collagen matrices for embedded bioprinting of tumor models for immuno-oncology. *Adv Mater.* 2023;35(33):e2210748.
doi: 10.1002/adma.202210748

78. Morley CD, Flores CT, Drake JA, et al. Spatiotemporal T cell dynamics in a 3D bioprinted immunotherapy model. *Bioprinting.* 2022;28:e00231.
doi: 10.1016/j.bprint.2022.e00231

79. Mazzaglia C, Sheng Y, Rodrigues LN, et al. Deployable extrusion bioprinting of compartmental tumoroids with cancer associated fibroblasts for immune cell interactions. *Biofabrication.* 2023;15(2):025005.
doi: 10.1088/1758-5090/acb1db

80. Flores-Torres S, Dimitriou NM, Pardo LA, et al. Bioprinted multicomponent hydrogel co-culture tumor-immune model for assessing and simulating tumor-infiltrated lymphocyte migration and functional activation. *ACS Appl Mater Interfaces.* 2023;15(28):33250-33262.
doi: 10.1021/acsami.3c02995

81. Datta P, Dey M, Ataie Z, et al. 3D bioprinting for reconstituting the cancer microenvironment. *NPJ Precis Oncol.* 2020;4(1):18.
doi: 10.1038/s41698-020-0121-2

82. Langhans SA. Three-dimensional in vitro cell culture models in drug discovery and drug repositioning. *Front Pharmacol.* 2018;9:6.
doi: 10.3389/fphar.2018.00006

83. Jenkins RW, Barbie DA, Flaherty KT. Mechanisms of resistance to immune checkpoint inhibitors. *Br J Cancer.* 2018;118(1):9-16.
doi: 10.1038/bjc.2017.434

84. Cattaneo CM, Dijkstra KK, Fanchi LF, et al. Tumor organoid-T-cell coculture systems. *Nat Protoc.* 2020;15(1):15-39.
doi: 10.1038/s41596-019-0232-9

85. Jin Z, Li X, Zhang X, et al. Engineering the fate and function of human T-Cells via 3D bioprinting. *Biofabrication.* 2021;13(3):035016.
doi: 10.1088/1758-5090/abd56b

86. Kim D, Jo S, Lee D, et al. NK cells encapsulated in micro/macropore-forming hydrogels via 3D bioprinting for tumor immunotherapy. *Biomater Res.* 2023;27(1):60.
doi: 10.1186/s40824-023-00403-9

87. Xu Y, Zhu W, Wu J, et al. 3D-printed dendritic cell vaccines for post-surgery cancer immunotherapy. *Adv Funct Mater.* 2024;34(33):2400507.
doi: 10.1002/adfm.202400507

88. Li C, Jin B, Sun H, et al. Exploring the function of stromal cells in cholangiocarcinoma by three-dimensional bioprinting immune microenvironment model. *Front Immunol.* 2022;13:941289.
doi: 10.3389/fimmu.2022.941289

89. Grolman JM, Zhang D, Smith AM, et al. Rapid 3D extrusion of synthetic tumor microenvironments. *Adv Mater.* 2015;27(37):5512.
doi: 10.1002/adma.201501729

90. Gong Z, Huang L, Tang X, et al. Acoustic droplet printing tumor organoids for modeling bladder tumor immune microenvironment within a week. *Adv Healthc Mater.* 2021;10(22):2101312.
doi: 10.1002/adhm.202101312

91. Xu Y, Saiding Q, Zhou X, et al. Electrospun fiber-based immune engineering in regenerative medicine. *Smart Med.* 2024;3(1):e20230034.
doi: 10.1002/SMMD.20230034

92. Tang M, Xie Q, Gimple RC, et al. Three-dimensional bioprinted glioblastoma microenvironments model cellular dependencies and immune interactions. *Cell Res.* 2020;30(10):833-853.
doi: 10.1038/s41422-020-0338-1

93. Dey M, Kim MH, Nagamine M, et al. Biofabrication of 3D breast cancer models for dissecting the cytotoxic response of human T cells expressing engineered MAIT cell receptors. *Biofabrication.* 2022;14(4):044105.
doi: 10.1088/1758-5090/ac925a

94. Ayan B, Heo DN, Zhang Z, et al. Aspiration-assisted bioprinting for precise positioning of biologics. *Sci Adv.* 2020;6(10):eaaw5111.
doi: 10.1126/sciadv.aaw5111

95. Cao X, Ashfaq R, Cheng F, et al. A tumor-on-a-chip system with bioprinted blood and lymphatic vessel pair. *Adv Funct Mater.* 2019;29(31):1807173.
doi: 10.1002/adfm.201807173

96. Dey M, Kim MH, Dogan M, et al. Chemotherapeutics and CAR-T cell-based immunotherapeutics screening on a 3D bioprinted vascularized breast tumor model. *Adv Funct Mater*. 2022;32(52):2203966.
doi: 10.1002/adfm.202203966

97. Kim JH, Lee S, Kang SJ, et al. Establishment of three-dimensional bioprinted bladder cancer-on-a-chip with a microfluidic system using Bacillus Calmette–Guérin. *Int J Mol Sci.* 2021;22(16):8887.
doi: 10.3390/ijms22168887

98. Goodarzi Hosseinabadi H, Dogan E, Miri AK, Ionov L. Digital light processing bioprinting advances for microtissue models. *ACS Biomater Sci Eng.* 2022;8(4):1381-1395.
doi: 10.1021/acsbiomaterials.1c01509

99. El-Gamal MI, Al-Ameen SK, Al-Koumi DM, et al. Recent advances of colony-stimulating factor-1 receptor (CSF-1R) kinase and its inhibitors. *J Med Chem.* 2018;61(13): 5450-5466.
doi: 10.1021/acs.jmedchem.7b00873

100. Binnemars-Postma K, Bansal R, Storm G, Prakash J. Targeting the Stat6 pathway in tumor-associated macrophages reduces tumor growth and metastatic niche formation in breast cancer. *FASEB J.* 2018;32(2): 969-978.
doi: 10.1096/fj.201700629R

101. Wang W, Wang X, Yang W, et al. A CTLA-4 blocking strategy based on Nanoboby in dendritic cell-stimulated cytokine-induced killer cells enhances their anti-tumor effects. *BMC Cancer.* 2021;21(1):1029.
doi: 10.1186/s12885-021-08732-5

102. Terren I, Orrantia A, Vitalle J, et al. NK cell metabolism and tumor microenvironment. *Front Immunol.* 2019;10:2278.
doi: 10.3389/fimmu.2019.02278

103. Kankeu Fonkoua LA, Sirpilla O, Sakemura R, et al. CAR T cell therapy and the tumor microenvironment: current challenges and opportunities. *Mol Ther Oncolytics.* 2022;25:69-77.
doi: 10.1016/j.omto.2022.03.009

104. Grunewald L, Lam T, Andersch L, et al. A reproducible bioprinted 3D tumor model serves as a preselection tool for CAR T cell therapy optimization. *Front Immunol.* 2021;12:689697.
doi: 10.3389/fimmu.2021.689697

105. Nguyen DT, Ogando-Rivas E, Liu R, et al. CAR T cell locomotion in solid tumor microenvironment. *Cells.* 2022;11(12):1974.
doi: 10.3390/cells11121974

106. Morse MA, Gwin III WR, Mitchell DA. Vaccine therapies for cancer: then and now. *Target Oncol.* 2021;16(2):121-152.
doi: 10.1007/s11523-020-00788-w

107 Langer EM, Allen-Petersen BL, King SM, et al. Modeling tumor phenotypes in vitro with three-dimensional bioprinting. *Cell Rep.* 2019;26(3):608-623. e6.
doi: 10.1016/j.celrep.2018.12.090

108. Huang Y, Wang S, Guo Q, et al. Optical coherence tomography detects necrotic regions and volumetrically quantifies multicellular tumor spheroids. *Cancer Res.* 2017;77(21):6011-6020.
doi: 10.1158/0008-5472.CAN-17-0821

109. Park J, Park B, Kim TY, et al. Quadruple ultrasound, photoacoustic, optical coherence, and fluorescence fusion imaging with a transparent ultrasound transducer. *Proc Natl Acad Sci U S A.* 2021;118(11):e1920879118.
doi: 10.1073/pnas.1920879118

110. Gao Q, Yang L, Lu M, et al. The artificial intelligence and machine learning in lung cancer immunotherapy. *J Hematol Oncol.* 2023;16(1):55.
doi: 10.1186/s13045-023-01456-y

ACCSCIENCE PUBLISHING

International Journal of Bioprinting

REVIEW ARTICLE

In situ bioprinting: Tailored printing strategies for regenerative medicine

Chengwei Hu[1,2], Chenmin Wang[1], Shaoquan Bian[1], Weichen Qi[3,4], Bo Liu[1], Liangliang Wang[1], Chunyi Wen[5], Jun Wu[3,6*], William W. Lu[1,3], and Xiaoli Zhao[1,2*]

[1]Research Center for Human Tissues and Organs Degeneration, Institute of Biomedicine and Biotechnology, Shenzhen Institute of Advanced Technology, Chinese Academy Sciences, Shenzhen, Guangdong, China

[2]University of Chinese Academy of Sciences, Beijing, China

[3]Department of Orthopaedics and Traumatology, Faculty of Medicine, The University of Hong Kong, Hong Kong, China

[4]Department of Orthopedics, Shanghai Key Laboratory for Prevention and Treatment of Bone and Joint Diseases, Shanghai Institute of Traumatology and Orthopedics, Ruijin Hospital, Shanghai Jiao Tong University School of Medicine, Shanghai, China

[5]Department of Biomedical Engineering, Faculty of Engineering, The Hong Kong Polytechnic University, Hong Kong, China

[6]Shenzhen Key Laboratory for Innovative Technology in Orthopaedic Trauma, Guangdong Engineering Technology Research Center for Orthopaedic Trauma Repair, Department of Orthopaedics and Traumatology, The University of Hong Kong-Shenzhen Hospital, Shenzhen, Guangdong, China

***Corresponding authors:**
Xiaoli Zhao
(zhao.xl@siat.ac.cn)

Jun Wu
(wuj7@hku-szh.org)

Citation: Hu C, Wang C, Bian S, et al. *In situ* bioprinting: Tailored printing strategies for regenerative medicine. *Int J Bioprint*. 2024;10(5):3366. doi: 10.36922/ijb.3366

Received: April 4, 2024
Accepted: May 17, 2024
Published Online: July 24, 2024

Copyright: © 2024 Author(s). This is an Open Access article distributed under the terms of the Creative Commons Attribution License, permitting distribution, and reproduction in any medium, provided the original work is properly cited.

Publisher's Note: AccScience Publishing remains neutral with regard to jurisdictional claims in published maps and institutional affiliations.

Abstract

In recent years, three-dimensional (3D) bioprinting has emerged as a revolutionary biological manufacturing technology. Despite significant progress, current bioprinting technologies face critical barriers, such as the need for *in vitro* maturation of printed tissues before implantation and challenges of prefabricated structures not matching the defect shapes. *In situ* bioprinting has been introduced to address these challenges by printing customized structures to the wound shape via direct deposition of biological inks at the tissue interface. This paper reviews strategies to optimize printing performance for enhanced tissue repair and analyzes the advantages, challenges, and future directions of *in situ* bioprinting technologies.

Keywords: Bioprinting; *In situ* bioprinting; Tissue regeneration; Bioinks; Handheld bioprinter

1. Introduction

Over the past decade, bioprinting has gained widespread attention as a powerful tool to precisely control the spatial placement of cells and biomaterials.[1] Bioprinting refers to the bottom-up automated fabrication of scaffolds, containing living cells, drugs, and growth factors, with the aid of additive manufacturing technology in a computer-aided manner.[2-4]

Bioprinting is increasingly demanded due to conditions such as osteosarcoma,[5,6] osteoporosis,[7,8] and skin burns.[9–11] Given the complex hierarchical architectures of human organs and the individual differences among patients, conventional tissue engineering strategies fail to fabricate scaffolds with controlled surface chemistry and complex microstructure.[12,13] Bioprinting can construct artificial tissue grafts with precise cell and regenerative factor placements, overcoming the limitations of donor availability.[14] Bioprinting is also widely used to create tissue models for drug testing[15–18] and disease modeling.[19–22] However, there are still limitations that hinder its development: (i) conventional bioprinting strategies require a computer-aided design (CAD) model, generated by magnetic resonance imaging (MRI) or X-ray computed tomography (CT), before printing and transplantation to the wound site, but the time-consuming nature of MRI or CT scanning makes this approach challenging for time-sensitive clinical cases[23]; (ii) the printed scaffolds may deform or contract after implantation, making it challenging to precisely match the defects[2]; (iii) before surgical implantation, the scaffold requires *in vitro* maturation that lasts several weeks.[24] Hence, it is necessary to overcome these barriers in 3D bioprinting to meet the needs of emergency clinical applications.[25]

Conversely, *in situ*, bioprinting, introduced in 2007 as an emerging strategy for clinical translation of bioprinting, has recently gained traction.[26,27] This technology, also called intraoperative bioprinting, directly prints biomaterials inside tissue defects.[28,29] *In situ* bioprinting bypasses *in*

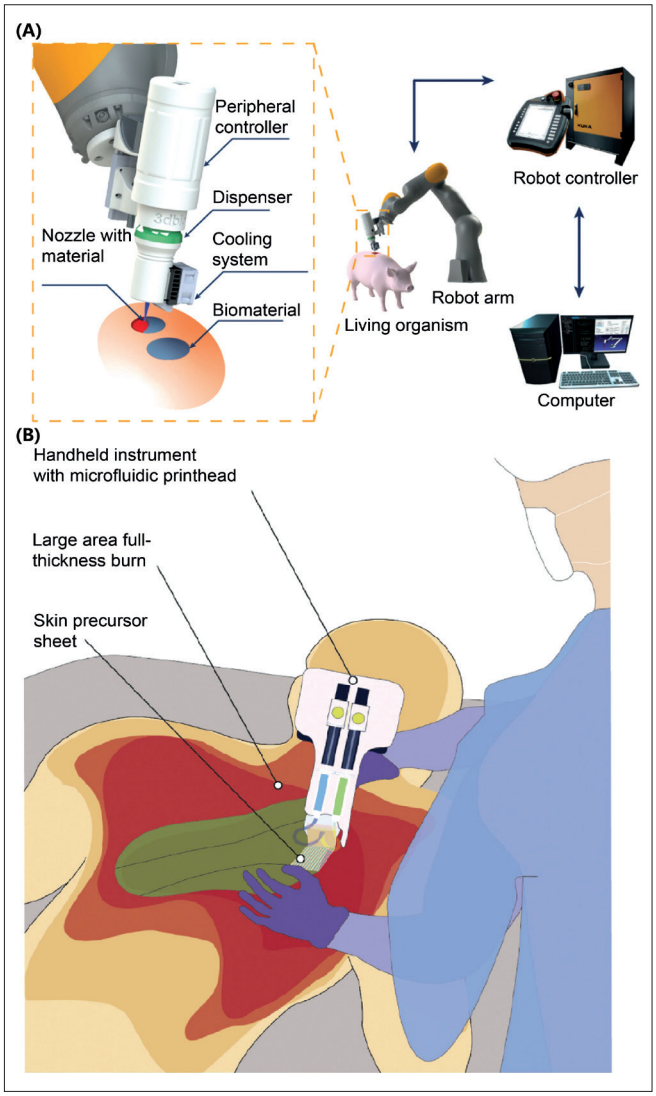


Figure 1. Schematic diagrams of (A) robotic-assisted *in situ* bioprinting system (RASBS) and (B) handheld *in situ* bioprinting system (HISBS). Adapted, with permission, from Levin et al.[34] (A) and Cheng et al.[9] (B).

vitro pre-printing and incubation requirements, reduces contamination risks, and enables real-time adjustments according to the printed structures. Compared with conventional bioprinting, the strategy can precisely match the shape of the wound, crosslink *in situ* for adhesion without *in vitro* culture, facilitate rapid repairment, and minimize fibrosis.[30–32] Furthermore, *in situ* bioprinting can exploit the human body's regenerative potential, providing the physiological environment required for scaffold culture.[33] *In situ* bioprinting systems can be divided into two major categories: robotic-assisted *in situ* bioprinting system (RASBS) (Figure 1A) and handheld *in situ* bioprinting system (HISBS) (Figure 1B). RASBS can be programmed by computer-aided manufacturing (CAM) and usually be used in less mobile environments. This strategy has many advantages, such as high precision,[35,36] multi-material *in situ* printing for significant composite defects,[37] and compatibility with minimally invasive surgery,[38] but is also time-consuming and requires sophisticated equipment. HISBS is an alternative strategy for *in situ* bioprinting that is easy to use without the need for complex equipment and expertise. Although HISBS has a relatively lower printing resolution and limited multi-material processing ability due to the compromise for portability, it has the potential to meet specific requirements of emergency clinical applications. Minimally invasive *in situ* bioprinting combines robotic assistance and human control for non-invasive printing *in vivo*.

In situ 3D bioprinting has been demonstrated to effectively repair tissue defects, addressing the problems of mismatched structures from conventional 3D bioprinting and reducing infection risks, while simplifying the surgical procedure. Despite existing reviews on *in situ* 3D bioprinting technology, recent research has reported new advancements in this technology, highlighting its potential to enhance tissue repair and better promote its clinical application. These studies focus on ensuring the precise fit and mechanical integrity of structures for irregularly shaped wounds, optimizing the printing path, real-time monitoring of the printing process, and accurately positioning and curing bioinks in deep tissues *in vivo*. Herein, this article reviews the utilization of *in situ* bioprinting in real-time monitoring and the optimization of printing performance in terms of automatic printing, handheld printing, human-controlled machine assisted in situ bioprinting and bioinks.

2. Strategies of *in situ* bioprinting

The bioprinting techniques used for *in situ* bioprinting include inkjet bioprinting,[37,39] laser-assisted bioprinting (LAB),[40,41] extrusion bioprinting,[42,43] stereolithography-based (SLA) bioprinting,[44,45] and electrospinning.[46,47] A concise comparison of these techniques is provided in Table 1. Herein, we shall compare the two aforementioned *in situ* bioprinting systems (i.e., RASBS and HISBS) in detail across multiple aspects (Table 2).

2.1. Robotic-assisted *in situ* bioprinting system

2.1.1. System setup

Robotic-assisted *in situ* bioprinting systems (RASBS) are an emerging method for fabricating 3D structures using software codes, reducing human intervention and ensuring higher printing accuracy. The key factors affecting the quality of the printed structure include printing speed, stability, and repeatable positioning accuracy. The printing speed encompasses both the moving speed of the printhead and the extrusion speed of the material, and these parameters require optimization based on the rheological properties of the material.[60] For example, a high moving speed and low extrusion speed will produce discontinuous lines; a low moving speed and high extrusion speed will produce clustered lines. The stability of the printing structure mainly depends on the physical and chemical properties of the material, highlighting the importance of selecting the appropriate bioink.[61] Repeatable positioning accuracy sets high requirements for *in situ* bioprinting systems, necessitating robot-assisted positioning combined with computer vision and sensors to further improve positioning accuracy.[62]

Nonetheless, RASBS offers a range of advantages, such as: (i) superior printing accuracy and dexterity[24] that are crucial for achieving a precise fit with the exact shape of the wound; (ii) rapid production of complex multi-material structures,[63,64] especially in critical situations that necessitate emergency treatment, such as in battlefield or accident scenarios; (iii) reduced human intervention,[65] as RASBS can automate the bioprinting process using computer-aided robotic arms and digital models; (iv) seamless integration with minimally invasive surgical techniques,[29] including endoscopy, facilitating inside body printing; (v) compatibility with process monitoring systems and machine learning techniques,[65–67] contributing to error reduction during the printing process; and (vi) enhanced cell viability by minimizing the exposure of printed cells to external environmental conditions, while the complex topological structures aid in regulating the spatial distribution and growth of cells.

Most reported RASBS are made up of robotic arms,[65,68–71] but some automated *in situ* bioprinting platforms are made up of framework-based systems.[32,72] The *in situ* printing system based on the robotic arm can utilize either multi-axis rigid robot arms[38,73] or flexible robot arms.[74] During the printing process, the structure is printed by computer-

Table 1. Comparison of different bioprinting methods

Parameter	Bioprinting method				
	Inkjet[37,48]	**LAB**[40,41,49]	**Extrusion**[29,50,51]	**SLA**[44,45]	**Electrospinning**[46,47]
Print speed	Fast	Medium	Slow	Fast	Fast
Resolution	High	High	Moderate	High	High
Bioink material	Fibrin/collagen; PEGDA	Collagen; hydroxyapatite	GelMA; Alginate/ gelatin; GelMA/ Laponite/ methylcellulose	GelMA; HCC-PEG; HCC-gelatin	PCL; PLA
Applications	Vessels; skin	Bone	Stomach; skin	Skin; muscle	Skin

Abbreviations: GelMA, gelatin methacryloyl; HCC, 7-hydroxycoumarin-3-carboxylate; LAB, laser-assisted bioprinting; PCL, poly(caprolactone); PEG, poly(ethylene glycol); PEGDA, poly(ethylene glycol diacrylate); PLA, poly(lactic acid); SLA, stereolithography.

Table 2. Comparison between robotic-assisted *in situ* bioprinting systems (RASBS) and handheld *in situ* bioprinting systems (HISBS)

Feature	RASBS	HISBS
Requirements of expertise	Operators require certain professional knowledge and operating experience	Simple and intuitive interface; easy-to-use
Key components	Robotic controller; 3D scanner; CAD/CAM	Rollers, ink cartridges, and print heads the parts are usually integrated into a single unit
Resolution	High	Low
Printed scaffold	Instant production according to the condition of the wound	Instant production according to the condition of the wound
Complexity of scaffold	High	Low
Application	Skin[37,52], bone[1,40], cartilage[1], brain[45], and muscle[44]	Skin[9], skeletal muscle[53,54], cartilage[55,56,57], bone[58], and dental[59]

Abbreviations: CAD, computer-aided design; CAM, computer-aided manufacturing.

aided robot positioning and path planning. The geometry of the defect could be obtained using a high-definition scanner with computer assistance. Slicing software then programs the printing path, which is subsequently executed by the robotic arm comprising a multi-axis movable bioprinting unit.[2]

However, the printing environment of RASBS can be suboptimal, featuring challenges such as wet, irregularly shaped, and potentially moving surfaces (due to patient breathing and twitching), which can cause printed scaffolds to deviate from the wound area and lead to structural weakness.[28] Addressing this issue requires improvements in the fidelity of the printed structure and real-time monitoring of the printing process.[35,50]

2.1.2. Strategies to improve the fidelity of printed structures

A decrease in the fidelity of printed structures results in a mismatch between the structure and defect shape, which can lead to inadequate mechanical support. Achieving accurate *in situ* printing of structures on non-planar surfaces is a challenge. Conventional planar slicing can create a stepped arrangement on inclined surfaces, potentially compromising the mechanical integrity of the structure. Adaptive slicing and multidirectional slicing techniques are employed to reduce this step effect and improve printing precision. Chaudhry et al.[62] presented a print path-planning strategy based on a free-form surface-slicing design. Using this approach, they designed a three-layered skin implant with customizable porosity and mechanical strength. To ensure that the printed structure has a smooth surface, RASBS can also be integrated with sensors and computer vision to improve positioning accuracy, as well as the use of robotic arms with higher degrees of freedom (DOF).[62] Fortunato et al.[71] developed a five-axis *in situ* bioprinting platform to deposit ink via pneumatic injection for simulating skull defect repair. The *in situ* printing system with higher DOF can improve the printing accuracy and enable the deposition of bioink on the curved surface.[68] Ma et al.[66] introduced an extrusion-based six-DOF robotic-assisted 3D bioprinting technology for cartilage regeneration using a fast tool center point calibration method to significantly enhance printing accuracy. This study demonstrated that the robotic system could improve the rate and recovery performance.

Similarly, Zhao et al.[65] developed a six-DOF bioprinting system (Figure 2A), integrating a 3D scanner and a closed-loop visual system to facilitate rapid healing and high-precision printing. The authors further proposed a seven-axis bioprinting system for *in vivo* underwater bioprinting, specifically designed to operate within the limited space inside the amniotic sac.[38] This seven-axis robot has redundant properties, ensuring high-precision printing with minimal intrusion. The redundant properties of the robot means that the total freedom of each joint is greater than the freedom of the end-effector, and the redundant freedom enables obstacle avoidance and enhances flexibility during the printing process.

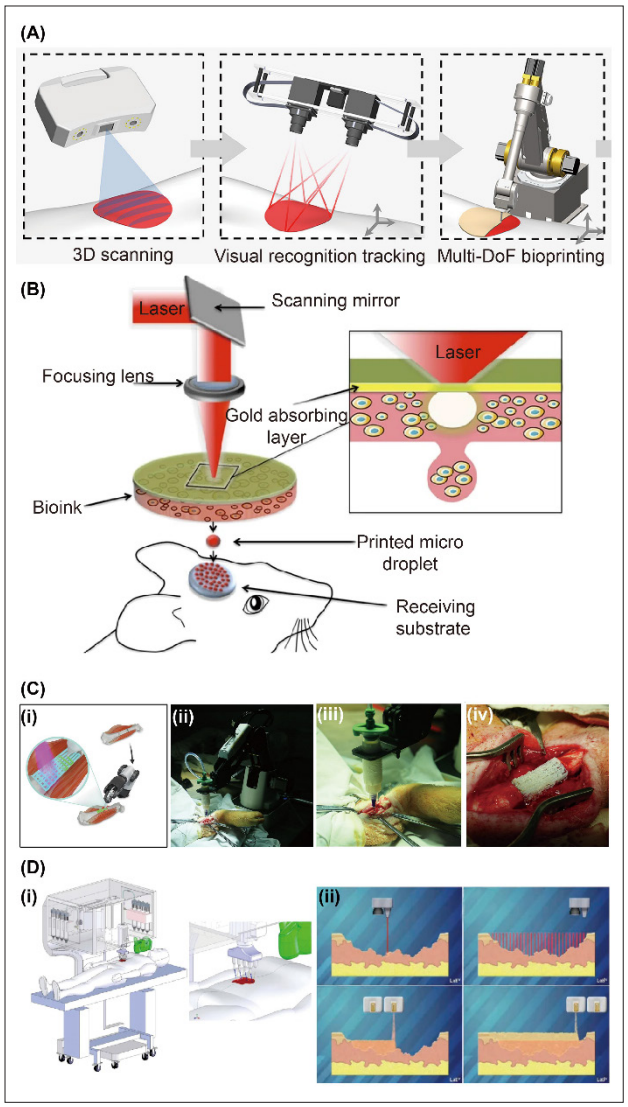


Figure 2. Robotic-assisted *in situ* bioprinting system (RASBS). (A) Schematic of the multi-degree-of-freedom (DoF) bioprinting system. (B) Application of laser-assisted bioprinting (LAB) to directly deposit bioink-encapsulated cells in mice models. (C) The process of *in situ* 3D bioprinting. (C, i) Extruded hybrid hydrogel is photo-polymerized by the ultraviolet (UV) lamp; (C, ii) view of the 3D bioprinting system; (C, iii) the bioprinting process; and (C, iv) the printed scaffold. (D) Treatment of large burn wounds. (D, i) Prior to *in situ* bioprinting, the wound topography was obtained using a handheld 3D scanner; (D, ii) the printhead deposits regenerative materials to specified locations under the guidance of the wound model. Adapted with permission from Zhao et al.[65] (A), Keriquel et al.[40] (B), Li et al.[35] (C), and Albanna et al.[37] (D).

The printing accuracy can also be enhanced using flexible robotic arms, which offer the advantages of not being limited to the DOF of rigid robotic arms and using fewer motors, resulting in smaller robotic arm volumes. Shi et al.[74] developed a flexible soft robotic arm for *in situ* bioprinting, whereby the manipulator can move freely in 3D space along Cartesian and curvilinear coordinates. Moreover, this innovation facilitates the printing of complex structures on curved wounds. For *in situ* printing on a curved surface, the ink is required to be crosslinked immediately. However, optical crosslinking may clog the printhead during printing, which is the primary cause of errors during the printing process.[35] Therefore, achieving instant control of the exposure direction is essential to mitigate this issue. Fortunato et al.[75] developed an *in situ* printing system that is integrated with an automatically activated optical crosslinking system to control the exposure direction according to the print path, ultimately avoiding the risk of needle clogging. Additionally, the potential for printhead blockage also depends on the rheological properties of the bioink. To minimize printhead blockage, selecting a material with shear-thinning characteristics can be advantageous.

2.1.3. Real-time tracking of the printing process

Imaging the tissue defect area is essential to determine the wound structure and construct a model of the implant, prior to printing with the computer-assisted RASBS. The accuracy of the model based on pre-print imaging data directly affects the degree of coincidence between the structure and the target region. During the printing process, mismatches between the printhead ink extrusion and movement speeds can result in deposition errors, thereby reducing the fidelity of the printed structure. Furthermore, correction errors of the print head, instability in the rheological characteristics of the bioink, and control errors stemming from environmental factors can also affect the fidelity of the structure. Hence, it is essential to monitor and implement feedback control mechanisms in the printing process for accuracy and consistency.

The printing procedure would make real-time adjustments according to the printed structures under predefined 3D geometries through CAD and/or CAM to regulate the spatial distribution of all regenerative biomaterials. The calibration process is necessary to reduce

printing errors. In error compensation, a new G-code is generated by comparing the printed structure and the 3D geometry for subsequent modification to the bioprinting process.[28] However, this compensation cannot be adjusted in real time according to the printing condition, especially on wet or deformable surfaces. The lack of process monitoring and immediate feedback adjustment are the main reasons for low structure fidelity. For example, when bioprinting on the surface of the human body, human breathing may cause the movement of the printing base, resulting in an error in the printed structure. Zhu et al.[50] introduced an adaptive 3D bioprinting method that can compensate for the motion of the target surface. The method integrates scanning and *in situ* bioprinting systems, allowing real-time correction of any printing errors based on feedback from the scanning system. Zhao et al.[65] introduced a closed-loop feedback system that enables real-time motion tracking of defects. In this system, the camera identifies the location of the wound and provides feedback to the robotic arm. Kucukdeger et al.[76] proposed a closed-loop control path planning method for micro-extrusion 3D printing based on the real-time perception of local nozzle offset, without pre-characterization of object geometry.

In addition to adaptive *in situ* 3D bioprinting, Yang et al.[77] combined optical coherence tomography (OCT) with *in situ* 3D bioprinting to detect defects layerwise. This approach aims to achieve process monitoring and ensure high structural fidelity. Several common methods used to reconstruct 3D images, such as confocal and multi-photon microscopes, are slow and require additional custom equipment.[78] OCT imaging can be efficiently integrated into *in situ* 3D bioprinting systems to enable real-time and rapid analysis of the printing process. This integrated OCT imaging system can detect print channel blockage, uniformity of printed structures, and defects caused by bubbles.[79] Yang et al.[78] developed a large-field, full-depth imaging system based on OCT. The system features a pre-established feedback control mechanism to perform secondary printing repairs on identified defects. This strategy of *in situ* defect detection and timely repair enhances the fidelity of printed structures improves printing efficiency, and ensures the consistency of the printed structure. Results of finite element analysis revealed that this approach significantly improved the compression modulus of the multi-layer scaffold.

Although OCT imaging features high resolution, it can only scan a depth of 1–2 mm below the surface of biological tissues. In addition to online monitoring of the quality of the printed structure, it is also necessary to track printed cells for bioinks that contain cells, such as using MRI to visualize specific cells deep inside the body. Keriquel et al.[40] demonstrated that LAB can directly deposit collagen/nano-hydroxyapatite loaded with mesenchymal stromal cells inside a murine calvaria defect model (Figure 2B). They also reported that the geometries of the printed cell scaffolds can impact the therapeutic effect in promoting bone regeneration *in vivo*.[80]

2.1.4. Applications

Robotic-assisted *in situ* bioprinting systems (RASBS) are typically utilized in less mobile environments, such as surgical operating rooms, primarily due to their considerable size and limited mobility. Various studies have demonstrated the successful printing of diverse tissues and organs, including skin,[37,50] bone,[40,41,49] and cartilage.[66] Among various *in situ* bioprinting methods, extrusion-based bioprinting stands out as the most widely researched strategy due to its extensive selection of bioinks, low-cost equipment, and versatility.[28,43,81] Li et al.[35] presented an extrusion-based 3D bioprinting system featuring a robotic manipulator to treat the swine's bone defects. The hybrid hydrogel, consisting of sodium alginate, poly(ethylene glycol diacrylate) (PEGDA), and gelatin methacryloyl (GelMA), was extruded directly onto the defect area and photo-polymerized with an ultraviolet (UV) lamp (Figure 2C).

Inkjet bioprinting has also been employed as a strategy for *in situ* bioprinting. Inkjet bioprinting can deposit droplets in predetermined locations,[37,82] facilitating the creation of gradients in cell concentrations.[39,83] Albanna et al.[37] developed an inkjet skin bioprinter for the reconstruction of full-thickness wounds. The bioprinter system comprises two principal components (Figure 2D): (i) a 3D wound scanner and (ii) a printhead. The former can generate a wound map in a single continuous scan that is subsequently compiled with additional wound maps to form a wound model. Likewise, the printhead consists of the *X*-, *Y*-, and *Z*-axis, with the wound area divided into several layers on the *Z*-axis. They printed a fibrin/collagen hydrogel in both murine and porcine total thickness wound models. Their results indicated that combining wound scanners with inkjet bioprinting improves the rate and quality of wound healing. However, as a sequential deposition strategy, inkjet bioprinting requires precise control over the deposition location, which is challenging and time-consuming. Building on inkjet bioprinting, Christensen et al.[39] developed an intersecting jets approach that enables control over the proportion of deposited material at any point in the structure. However, due to inherent spray inconsistencies between reactive hydrogel solutions and suspensions, the printed structures lack shape fidelity. To overcome this hurdle, integrating diverse bioprinting strategies offers a promising approach for achieving *in situ* printing. Moncal et al.[36] proposed a hybrid

extrusion/inkjet-based bioprinting methodology for the reconstruction of intricate craniomaxillofacial defects. In this approach, they employed extrusion bioprinting to directly print an osteogenic hard tissue bioink, while inkjet bioprinting was utilized for the deposition of a soft tissue bioink with lower viscosity. Remarkably, their findings demonstrated approximately 80% skin reconstruction within 10 days and 50% bone regeneration after 6 weeks.

2.1.5. Challenges

While RASBS has demonstrated promise for achieving complex *in situ* bioprinting, there are still some challenges that need to be addressed:

(i) The limited workspace and large setup volume make it difficult to use for internal tissue repair.

(ii) The process requires complex equipment and is time-consuming, as it involves scanning, 3D geometry construction, printing path optimization, and error compensation.

(iii) Higher criteria for bioinks are required, as not all materials are suitable for *in situ* bioprinting. New materials that are compatible with this technique must be developed, e.g., bioinks for printing on non-planar wounds require a higher viscosity to match the wound shape.

(iv) For successful tissue regeneration, the printed tissue must be able to integrate with the host tissue.

(v) Improving the automation and scalability of *in situ* bioprinting systems can reduce the cost and increase the speed of tissue production. This effort may involve developing new software for designing and printing tissues, as well as creating systems capable of printing multiple tissues simultaneously.

In response to these challenges, artificial intelligence (AI) technology has displayed great application potential in the field of bioprinting. New biomaterials and structural design can be developed through AI and machine learning to be compatible with printing technologies and application environments. Limon et al.[84] established a prediction model of key process parameters of extrusion-based *in situ* 3D bioprinting using machine learning method, and the accuracy of the model to predict the printing wire width was 85%. Qiao et al.[85] used a machine learning model to predict the effect of cryoprotectant formulations on cryoprotected bioinks. Additionally, researchers could predict the number of cells in the printed droplet through machine learning algorithms, achieving real-time evaluation of the number of printed cells during the printing process.[86] AI-mediated real-time monitoring and feedback systems can also improve the degree of automation and printing accuracy of *in situ* bioprinting systems. In the future, advancements are anticipated in remote-controlled robotic surgery, where doctors can program surgical procedures based on patient data and remotely operate robots to perform repairs or treatment.

2.2. Handheld *in situ* bioprinting system

2.2.1. System setup

Handheld *in situ* bioprinting systems (HISBS), also known as hand devices, can be easily manipulated by operators without a professional background. Unlike RASBS, the positioning and movement of the setup during the printing process are typically controlled by operators. HISBS is particularly suitable for minor wounds as it is more flexible, can print structures of any shape, and can adjust the print path in real time. Furthermore, HISBS has a shorter print response time since it does not require prior preparation, such as scanning wound shapes or calibrating path errors.[55,87]

In the actual *in situ* bioprinting process, an initial debridement step is often required, which can result in a mismatch between the prefabricated construct and the defect. To address this challenge, handheld bioprinters have been developed for *in situ* bioprinting applications.

HISBS offers several advantages, including manual control of the printing position and speed, low-cost,[42] portability, lack of computer-aided requirements,[34] ease of sterilization,[66] and suitability for hard-to-reach and non-flat wounds.[24] Handheld printers can directly deposit biomaterials inside the defect to build a tissue scaffold. Handheld bioprinting does not require a high-definition 3D scanner to scan the defect, unlike automated systems. Additionally, handheld devices can be easily operated without requiring specialized knowledge, enabling operators to build constructs using hand movements and adjust the printing strategy in real-time.

2.2.2. Performance optimization strategy of the printed structure

Portable bioprinters, also known as hand bioprinters, have successfully fabricated various types of tissues, including skin,[9] muscle,[53,54] cartilage,[55,56,57] bone,[58] and dental tissue,[59] with most handheld bioprinting utilizing extrusion-based methods. Other bioprinting methods, such as droplet and laser-assisted, are challenged by nozzle clogging and miniaturization. Russell et al.[53] developed a hand bioprinter (Figure 3A) to treat a murine volumetric muscle loss (VML) injury. The hand bioprinter directly printed gelatin-based hydrogels, which were crosslinked *in situ* under UV light. The results indicated that this device could maintain the viability of muscle cells and promote cell proliferation. Using the same printing method, Quint et al.[54] presented a growth factor-eluting bioink to treat

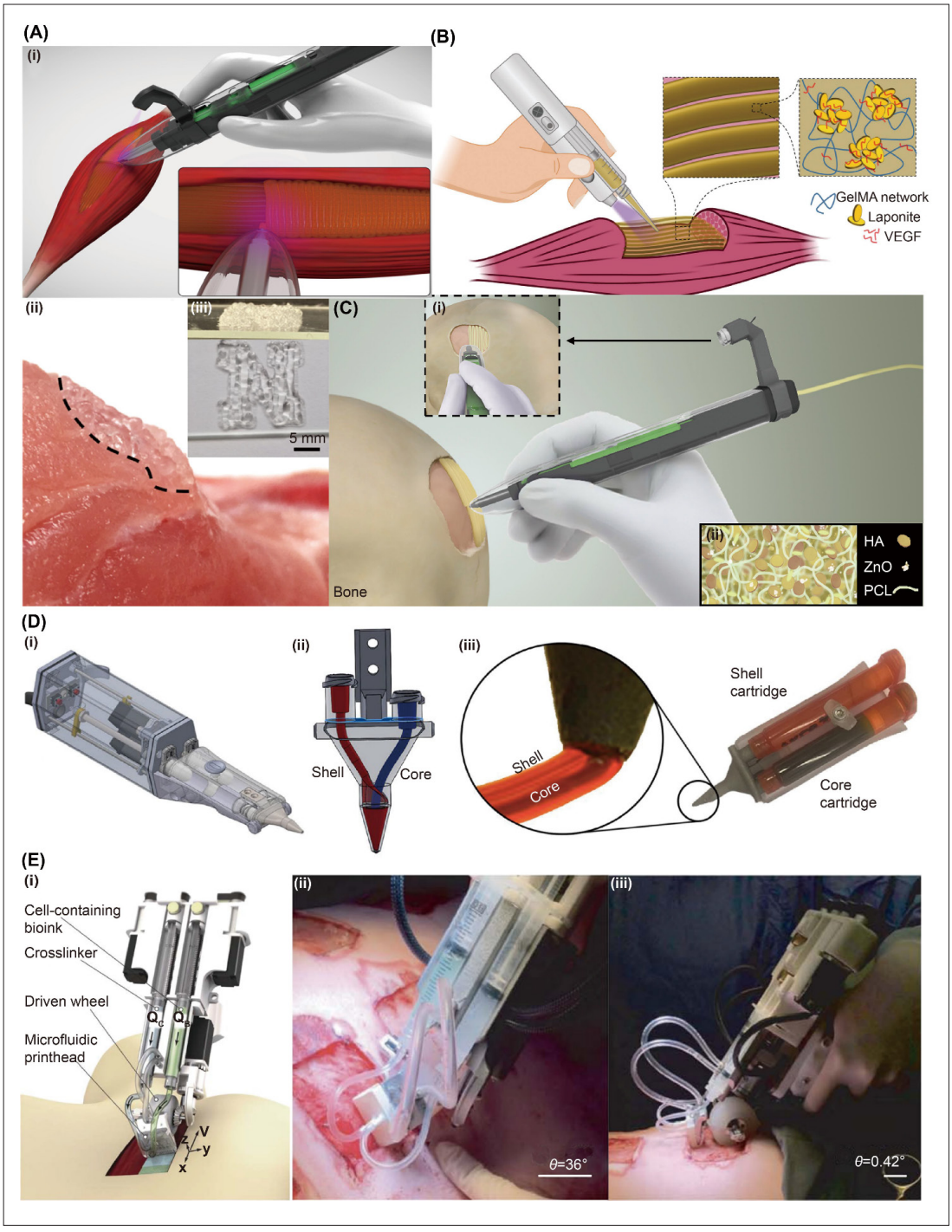


Figure 3. Applications of handheld *in situ* bioprinting systems (HISBS). (A) Utilization of a handheld bioprinter for *in situ* bioprinting of scaffolds. (A, i) Schematic of the *in situ* bioprinting of cell-laden gelatin methacryloyl (GelMA) hydrogels for the treatment of volumetric muscle loss (VML). (A, ii) Photograph of a typical scaffold printed on a non-flat porcine skeletal muscle. (A, iii) Photograph of an N-shaped scaffold (three layers thick). (B) Conceptual diagram of organized scaffold deposition directly into a wound using a handheld printer. (C) Schematic illustration of *in vivo* printing of composite scaffolds. (C, i) Schematic view of an integrated camera on the printing pen. (C, ii) Schematic of the material composition. (D) Core/shell-3D printing via co-axial extrusion. Schematic representation of the (D, i) 3D co-axial handheld printer and the (D, ii) co-axial nozzle. (D, iii) Cartridges for core/shell-loading in the printer. (E) *In situ* formation of precursor skin tissue. (E, i) Image of the handheld device. (E, ii) Isometric view of the handheld instrument during the deposition process. (E, iii) Side view of the handheld device. Scale bars: 5 mm (A, iii); 2.5 cm (E, ii and iii). Abbreviations: HA, hydroxyapatite; PCL, poly(caprolactone); VEGF, vascular endothelial growth factor. Adapted with permission from Russell et al.[53] (A), Quint et al.[54] (B), Mostafavi et al.[58] (C), Duchi et al.[56] (D), and Cheng et al.[9] (E).

VML injuries (Figure 3B). They used laponite nanoclay to control the release of vascular endothelial growth factor. The *in vivo* experimental results suggested that the bioink can promote functional muscle recovery and reduce fibrosis. Mostafavi et al.[58] introduced a hand bioprinter that can deposit melt-spun materials directly within the bone defect site (Figure 3C). The printed scaffolds displayed promising adhesion and biocompatibility in mouse models. To improve the effect of tissue repair, it is generally necessary to add bioactive factors and cells to the bioink. In the case of photo-crosslinked bioinks, the handheld printer deposits the bioink and cells into the tissue defect, and the photoinitiator reduces the activity of the cells. To address this issue, current handheld printers typically use a core-shell structure that is coaxially extruded from the bioink and cell components, isolating the photoinitiator from the cell. Duchi et al.[56] reported a co-axial core-shell handheld device to repair cartilage defects (Figure 3D). Moreover, this strategy maintains high cell viability and has great potential for *in situ* surgical cartilage engineering. Di Bella et al.[55] also introduced a handheld bioprinter featuring a core-shell structure. Their experiment using a full-layer cartilage injury model in sheep demonstrated the feasibility of printing cartilage scaffolds using this device. In addition to reducing the toxicity of the photoinitiator to the cell, the core-shell structure of the handheld printer can also be used to construct multi-layer structures with gradient properties. Besides photo-crosslinked bioinks, there have also been reports utilizing ion-[88] and enzyme-crosslinked[9] bioinks (Figure 3E). Hakimi et al.[88] reported a similar design, but their device incorporates a microfluidic printhead, enabling rapid repair of large skin defects. In addition, the roller is also installed to enhance the stability of the printing process and improve the printing efficiency, and the flow rate of the two ink tanks can be controlled separately. However, this device has its limitations. For instance, it utilizes a pneumatic extrusion, whereby changes in bioink or ambient temperature will affect the rheological properties of the material, necessitating immediate adjustments to the extrusion pressure to maintain a constant flow rate. Therefore, the incorporation of an active temperature control device should be considered. Pagan et al.[87] used a hydraulic-driven injection pump that is separate from the device to maintain constant extrusion flow.

Handheld *in situ* bioprinting systems (HISBS) can be loaded with functional modules, such as a UV light source, positioning device, and ultrasound, to improve the adhesion of printed structures and tissues. Zhou et al.[89] introduced an ultrasound module into HISBS and reported significantly enhanced bio-adhesive performance of the bioink in a diabetic wound model. Their handheld *in situ* bioprinter utilizes a coaxial extrusion strategy, but the method does not guarantee uniform mixing of the bioink. Ultrasound can enhance ink adhesion and facilitate instant mixing of two inks when deposited, thereby ensuring the mechanical strength of the printed structure.

The tissue repair ability of the printed structure can be enhanced by improving its mechanical strength and ensuring that the structure possesses a certain level of porosity. Optimal porosity facilitates efficient transport of nutrients and metabolic waste, thereby promoting improved cell activity. Ying et al.[90] developed an aqueous two-phase emulsion bioink to produce microscale pores via *in situ* photo-crosslinking. Mostafavi et al.[91] prepared a porous bioink by high-speed stirring foaming and reported significantly enhanced viscosity of the bioink for promoting skeletal muscle regeneration in a rat VML model.

2.2.3. Challenges

While HISBS is appropriate for regenerating superficial trauma and minor damage, handheld devices are limited in treating more severe damage and accessing internal trauma. This limitation can potentially increase the risk of infection.[24] Furthermore, several challenges still need to be addressed, such as low resolution, poor repeatability, high dependence on operator skills, and difficulty in rapidly covering large areas of tissue defects. Notably, most handheld printers only have simple extrusion and coating functions. For repairing tissue defects, the accurate construction of scaffolds is essential for wound healing and functional recovery. To address these challenges, several strategies can be employed. For example, reducing the speed of the printhead movement and using thinner print needles can improve resolution. Introducing programmed design and stepper motors enables controlled movement of the printhead, reducing reliance on human influence. Additionally, multi-channel printhead enables rapid coverage of large wounds. Taken together, HISBS has significant potential for further development in addressing these challenges.[55,91]

2.3. Minimally invasive *in situ* bioprinting

Minimally invasive *in situ* bioprinting utilizes human-controlled robotic systems for *in vivo* tissue repair. Automated *in situ* bioprinting systems can be combined with minimally invasive surgery to enhance printing accuracy and flexibility. Minimally invasive *in situ* bioprinting is crucial as it can mitigate the risk of infection associated with traditional surgical procedures.[60] Minimally invasive bioprinting can be achieved by integrating non-invasive surgical tools with automated strategies, such as extrusion bioprinting[29,60,51] and SLA.[44,45] To clinically apply minimally invasive *in situ* bioprinting, two issues need to

be addressed: (i) delivery and curing of scaffolds in deep tissue and (ii) real-time monitoring of the printing process.

2.3.1. Delivery and curing of scaffolds in deep tissue

Minimally invasive *in situ* bioprinting combines automated printing systems with human control for *in vivo* printing. This approach demands high flexibility and miniaturization of the printing system. However, a key challenge that needs to be addressed is accurately transporting the material to the designated area in the body. Zhao et al.[29] incorporated a micro-bioprinting platform into an endoscope and demonstrated the feasibility of *in situ* 3D printing at a specified location. The printing platform consists of a fixed base with three actuators and a laminated mobile platform that accurately deposits the bioink to the damaged area of the stomach wall via extrusion (Figure 4A). The study

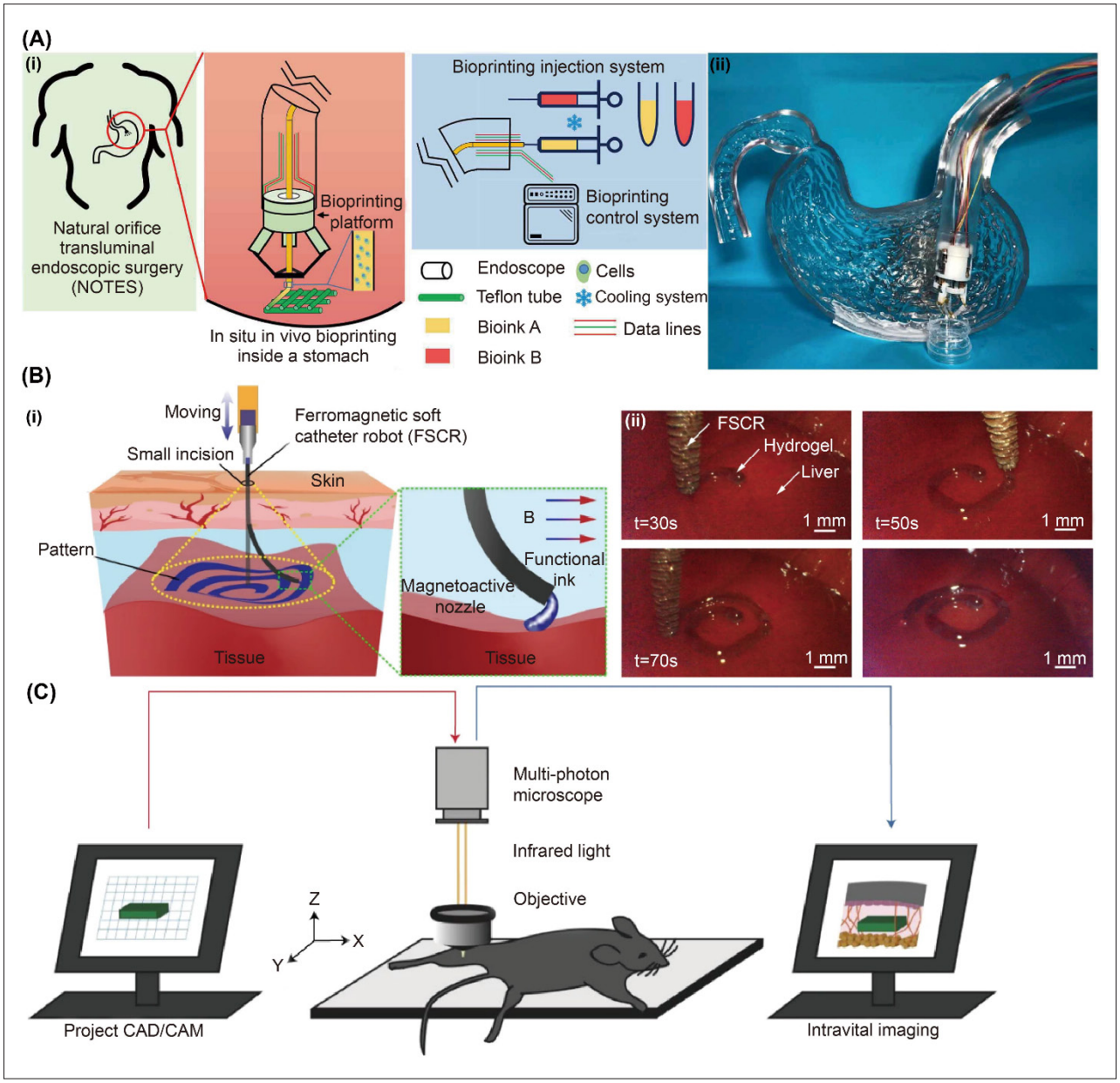


Figure 4. Minimally invasive *in situ* bioprinting combined with automated systems. (A) Schematic illustration of *in situ* bioprinting inside a stomach. (A, i) Schematic of the bioprinting and injection system. (A, ii) A bioprinting platform installed in a curved pipe mimicked an endoscope to perform bioprinting inside a stomach model. (B) Minimally invasive surgery controlled by a ferromagnetic soft catheter robot. (B, i) Schematic illustration of *in situ* bioprinting with functional bioinks under a magnetic field through a small incision. (B, ii) Photographs illustrating the minimally invasive bioprinting process on the liver surface at different times. (C) Implementation of bio-orthogonal two-photon photo-polymerization of polymers. Abbreviations: CAD/CAM, computer-aided design/computer-aided manufacturing. Adapted with permission from Zhao et al.[29] (A), Zhou et al.[60] (B), Urciuolo A et al.[45] (C).

used a stomach model to demonstrate the feasibility of the printing system and indicated further optimization of the printing platform is necessary to achieve better *in vivo* bioprinting. Several optimization strategies have been proposed, such as reducing the platform size to match the size of the endoscope before integrating into the endoscope and *in situ* real-time monitoring system. In addition, the alginate/gelatin bioink can only form stable structures at low temperatures; the use of Ca^{2+} as a crosslinking agent can affect cell activity; and other gel systems should be explored for repairing gastric wall damage. Shi et al.[92] added magnetic complexes to gelatin/sodium alginate hydrogels, which have the opposite charge to gastric juices. This approach increased the curing in the acidic environment of gastric juices without requiring external conditions. By dispersing magnetic complexes in the hydrogel, an external magnetic field can be applied to precisely locate and control the position of the hydrogel, thereby achieving the sealing of gastric perforations. The practicability of the printing method was validated in a pig model with an artificially perforated stomach, while the biosafety of the ink was confirmed in a rat model. Zhou et al.[60] developed a ferromagnetic soft catheter robotic system for minimally invasive *in vivo* printing with a magnetic drive and assessed its performance in a pig tissue model and a live rat liver (Figure 4B). Nonetheless, the minimally invasive surgical method is still in its early stages. It is necessary to miniaturize the device to fit narrow spaces in the body and develop closed-loop systems for real-time imaging combined with machine vision and structured light to enhance the accuracy of printed structures. Yang et al.[93] integrated micro-CT into a ferromagnetic soft catheter robot for printing path scanning and planning, as well as printing irregular complex structures. Electroactive bioinks were printed in a living rat model of partial hepatectomy, and the results demonstrated that the printed scaffolds significantly promoted tissue regeneration. However, the equipment used in this ferromagnetic soft catheter robot is complex and expensive. Based on simple mechanical engineering design principles, Shi et al.[74] developed a flexible robotic arm for *in vivo* bioprinting. However, the disadvantage of this flexible robot arm is its requirement for complex control and software tracking to effectively plan the printing path.

In vivo scaffold printing typically involves light-based non-invasive polymerization, but this approach is mainly limited to superficial tissues. Chen et al.[44] developed a minimally invasive *in situ* printing system based on digital near-infrared light polymerization, demonstrating the ability to construct auricle structures *in vivo*. Similar to UV and blue light, near-infrared light can also induce photo-polymerization. The system uses near-infrared light for digital light-processing *in situ* 3D bioprinting, leveraging its high penetration to induce photo-crosslinking and *in situ* polymerization of the bioink. In another study, Urciuolo et al.[45] implemented bio-orthogonal two-photon photo-polymerization of polymers (Figure 4C). They demonstrated that photosensitive biopolymers, consisting of cell-laden branched polyethylene glycol (PEG) and gelatin, can generate newly formed myofiber bundles in mice, compatible with a functional vascular network. Notably, minimally invasive *in situ* bioprinting employing SLA is constrained by the requirement of photo-crosslinkable bioinks and the effects of printing depth on the printing process. Another strategy of *in situ* bioprinting involves external ultrasound-mediated sound-sensitive bioink polymerization to achieve high-resolution, non-invasive *in situ* printing deep within the body.[94] The ultrasound-induced polymerization process does not damage the body, and ultrasound can also control the microstructure and pore size of the scaffold. Moreover, the system can also be used to achieve continuous drug release by regulating the induction time.

2.3.2. Real-time monitoring of the printing process

In minimally invasive surgery, the patient's anesthetized deep breathing can cause incision displacement, potentially leading to misalignment with the robot's remote motion center. This misalignment can increase tissue stress and the risk of postoperative hernia. Therefore, it is necessary to monitor and adjust the small incision on the patient's body in real time. In an earlier study, Zhao et al.[38] developed a seven-axis robot-assisted bioprinting system that can actively control the alignment of the remote motion center with the incision. On this basis, an adaptive closed-loop minimally invasive *in vivo* 3D printing strategy based on precise incision positioning is proposed, incorporating accurate positioning and attitude estimation through binary color ring array labeling.[95] This strategy enables notch sensing and robot printing to constitute a closed-loop control system, facilitating adaptive calibration.

2.4. Vascularization of bioprinted structures

Adequate vascularization is essential for promoting tissue defect repair, as the microvasculature provides nutrients and oxygen to tissues and promotes metabolism.[96,97] For *in situ* 3D-bioprinted structures, there are currently two ways to induce vascular tissue formation: (i) growth factor-induced vascularization and (ii) microporous structure-guided vascularization. Some studies have demonstrated that copper-epigallocatechin gallate (Cu-EGCG) promotes the secretion of growth factors from vascular endothelial cells. Hu et al.[98] prepared an extracellular matrix (ECM)-based 3D-bioprinted scaffold loaded with Cu-EGCG to promote diabetic wound healing. The ECM scaffold has

good mechanical properties and pore size distribution, but it is not sufficient to control the position and geometry of the microvascular network. To improve vascularization, it is necessary to form a predetermined microchannel in the printed structure. Mostafavi et al.[91] used high-speed stirring to control the pore size and distribution of bioinks. Coaxial printing, used to fabricate hollow structures and predetermined microchannels, has the disadvantage of low resolution. There are studies using sacrificed-template to print structures with submicron-sized capillaries. This method leverages the different solubility or temperature sensitivity of two bioinks, such as GelMA/poly(ethylene oxide)[99] or GelMA/gelatin[100] bioinks. After printing the bioinks side by side, the sacrificial bioink is removed, retaining the desired structure. However, this method is insufficient to develop complex structures. Enrico et al.[97] proposed a method of cavitation molding using femtosecond infrared laser pulses to generate cavitation bubbles in the bioink to form microchannels, subsequently filling them with endothelial cell suspension to form continuous cell layers after cell culture.

3. Bioinks for *in situ* bioprinting

3.1. Performance requirements

Bioinks, containing active biomaterials and cells, serve as scaffolds to accelerate wound or defect recovery, playing an essential role in driving biological interactions. Bioinks should meet specific essential characteristics to address the challenge of complex tissue regeneration effectively. Traditional biomaterials have been biocompatible but often lack the ability to effectively promote interactions between cells, materials, and tissues.[101] Similarly, bioinks used for *in situ* bioprinting should essentially possess remarkable rheological properties to enhance the resolution of the printing structure and maintain a specific mechanical strength. Other critical factors include rapid gelation, mechanical properties, shape fidelity, biocompatibility, and biofunctionality.[43,63] In some personalized medicine applications, bioinks should contain autologous bioactive factors from the patients. Hydrogels have been widely used as matrices for *in situ* bioprinting due to their excellent biocompatibility, ability to encapsulate cells, high permeability, large water content, and similarity to native ECM.[102–106] The *in situ* formation of hydrogels has significant advantages over traditional pre-formed hydrogels, such as being minimally invasive, excellent adaptation to wound margins, accurate filling of defects, and simple cell encapsulation.[101,103] Current research primarily focuses on meeting specific characteristics, such as electroconductivity,[103,107] physiological stimulus-responsive ability,[43] and shear-thinning ability.[81,105] Shear-thinning hydrogels are ideal for maintaining cell viability after injection.[81] Some materials, such as platelet-rich plasma (PRP), have been investigated for hydrogel integration. Zhao et al.[63] incorporated PRP into sodium alginate/gelatin bioink for repairing skin defects by releasing various growth factors and active ingredients. However, PRP degrades rapidly in the wound environment and cannot sustainably release growth factors. Lai et al.[108] prepared a dressing with three layers of core-shell fiber through coaxial 3D printing and fixed PRP in the core layer of the fiber to achieve continuous release of growth factors. By optimizing bioink characteristics, *in situ* bioprinting can be further developed and expanded for various applications in tissue engineering and regenerative medicine. The bioinks currently used for *in situ* bioprinting and their specific applications in tissue engineering are summarized in Table 3. Based on the bioink sources, the materials reported for *in situ* bioprinting can be divided into either natural or synthetic polymers.

3.2. Challenges

Current bioink research faces challenges such as viscosity,[121] rheological properties,[73,81] and the difficulty of producing intricate pores. High-viscosity bioinks can significantly improve the mechanical strength of printed structures, leading to a higher extrusion pressure and lower cell viability. Although a larger diameter nozzle can be used, the printing accuracy will be reduced. Thermo-sensitive bioinks are required to crosslink at body temperature for *in situ* bioprinting. Crosslinked bioinks should have low mechanical strength to protect cell activity, but simultaneously require high mechanical strength to maintain shape and match the defect. Rheological properties require optimization according to the properties of the material itself, the loaded cells, the bioprinting approach, bioprinting conditions (e.g., temperature, pH, and crosslinking mode), and other factors.[43,63,122] Some inks, such as gelatin, have problems creating complex pores due to their high water content and thermal sensitivity.[42]

3.3. Optimization of cellular compatibility and mechanical strength

The performance of bioinks varies according to the *in situ* bioprinting technology applied. For example, inkjet-based *in situ* bioprinting utilizes bioinks with low viscosity or shear-thinning characteristics to ensure the smooth formation of droplets, thereby limiting material selection.[37,39] Hydrogels with high water content are widely used in inkjet-based *in situ* bioprinting. Additionally, photo-crosslinked bioinks, such as GelMA, have reportedly been used in inkjet bioprinting but are prone to nozzle clogging. A multiple-nozzle system can be designed to separate the photoinitiator from the ink, or a coating can be applied to the nozzle surface to reduce clogging and adhesion.

Table 3. Bioink materials utilized for *in situ* bioprinting

Source	Materials	Category	Gelation mechanism	Bioprinting approach	Advantages	Disadvantages	Applications
Natural	Collagen	Natural proteins	pH and temperature-induced	Extrusion, LAB, and inkjet	Highly bioactive	Uncrosslinked solution lacks stability	Bone[41,105], dermis[109], skin[37,34], and cartilage[4] defect repair
	Gelatin		Enzyme-induced	Extrusion	Facilitate cellular attachment and growth	Poor mechanical properties	Muscle tissue engineering[110]
	GelMA		Photo-induced	Extrusion and SLA[111]	Fast gelation; biocompatible	Poor mechanical properties at low concentrations	Muscle[112], cartilage[56], bone[35,113], and skin[69,90] tissue engineering
	Fibrin		Photo-induced	Extrusion	Biocompatible; nanofibrous structural properties	High viscosity hindering extrusion	Cartilage[114] defect repair
	PRP		Enzyme-induced	Extrusion	Rich in growth factors and active ingredients	Rapid degradation	Skin repair[63,108]
	Silk fibroin		Enzyme-, ultrasound-, and photo-induced	Extrusion	Excellent mechanical and biological properties	Poor cell attachment	Tendon[115] repair
	HA/HAMA	Natural polysaccharides	Chemical-induced	Extrusion	Biocompatible	Slow gelation	Cartilage[66,55,116] and bone[1] regeneration"
	Alginate		Chemical-induced	Extrusion and LAB[117]	Biocompatible; fast gelation	Poor cell attachment; low mechanical strength	Bone[118] and skin[88] defect repair
Synthetic	PCL	Synthetic polymer-based hydrogel	Temperature-induced	Extrusion	Biocompatible; low melting temperature	Not bioactive	Bone repair[58]
	PLA		Temperature-induced	Electrospinning	Excellent mechanical properties	Poor cell attachment	Skin repair[46]
	PEGDA		Photo-induced	Extrusion and SLA[111]	Biocompatible; hydrophilic	Poor cell attachment	Cartilage[119] and bone[120] tissue engineering

Abbreviations: GelMA, gelatin methacryloyl; HA, hyaluronic acid; HAMA, hyaluronic acid methacrylate; LAB, laser-assisted bioprinting; PCL, poly(caprolactone); PEGDA, poly(ethylene glycol diacrylate); PLA, poly(lactic acid); PRP, platelet-rich plasma; SLA, stereolithography.

Bioinks used in extrusion-based *in situ* bioprinting require specific printability, i.e., to possess viscosity that supports the maintenance of extrusion line shape. Photo-crosslinked bioinks, such as GelMA, often employ pre-crosslinking strategies to achieve suitable viscosity. Conversely, the viscosity of bioinks should be reduced when printing to improve the biocompatibility of bioinks, which compromises the mechanical strength required to maintain the support structure. At present, microgels have garnered attention due to their good rheological properties and biocompatibility. Xie et al.[73] developed a microgel-based bioink, consisting of (i) a GelMA microgel to load cells and (ii) a GelMA precursor solution with a photoinitiator to ensure fluidity and provide mechanical strength. The pore morphology of bioinks is essential for many biological processes, such as cell migration, infiltration, printability,[123] and tissue vascularization.[77,102] Porous scaffolds can also be printed by customizing the stiffness and composition of microgels. Jalandhra et al.[113] developed a porous microgel scaffold to control the direction of stem cell differentiation by adjusting the microgel stiffness and gap-filling hydrogel volume. Other researchers have used lyogels, or freeze-dried hydrogels, to introduce microchannel structures. Lyogels offer an advantage over conventional hydrogels in that they can be stored in a dry state and used readily.[102] The pore morphology of lyogels is

determined by the size and shape of the ice crystals during the freeze-drying process. Notably, the pores of the printed structure affect tissue repair because scaffolds with good porosity are conducive to oxygen transport and promote cell adhesion and proliferation. Several studies have reported oxygen supply strategies for adding inorganic peroxides to scaffolds, but these oxygen supply systems are limited in their ability to provide sufficient oxygen. Wang et al.[124] developed a self-supplying oxygen system that prints photosynthetic microalgae *in situ* at the wound site, thereby providing continuous oxygen for wound healing. The system could also promote cell proliferation, migration, and differentiation under hypoxic conditions and accelerate wound healing in chronic diabetic wounds.

3.4. Intelligent materials for 4D bioprinting

Different soft tissue injuries require specific complex structures for repair. For *in situ* bioprinting, the surgical site is often exposed to unavoidable damage, and cells are lost during the implantation process.[125] Therefore, 4D printing technology, which allows structures to be implanted into the damaged site in a compact form, has garnered significant attention. 4D printing technology combines smart materials (i.e., stimuli-responsive materials) with 3D printing technology to compress 3D structures into 1D or 2D structures *in vitro* and implant them in the body to restore programmable shapes under specific stimuli (temperature, humidity, magnetic field, pH, etc.).[126] Shi et al.[92] developed a magnetic hydrogel for treating stomach injuries that control bioink delivery through a gastroscope nozzle. The magnetic bioink accumulates at the damaged site under the influence of an external magnetic field, facilitating sutureless tissue sealing. Compared to external stimuli, such as magnetic fields and high temperatures, endogenous stimuli in response to body temperature or body fluids are more convenient and biofriendly. Hydrogels expand due to water absorption, making them the preferred material for 4D printing. Using water-induced programmable deformation, Joshi et al.[126] prepared hydrogels using alginate and methylcellulose at specific ratios for different expansion rates. The hydrogels were then used to construct 4D-printed catheters for repairing peripheral nerves. Liu et al.[127] developed an amphiphilic dynamic thermosetting polyurethane that transitions from 2D to 1D structures in a body temperature environment and programmatically transforms into 3D structures upon exposure to water after implantation *in vivo*. Furthermore, the material has water-hardening properties, suggesting good mechanical properties. The structure is printed using melt deposition modeling, employing a layer-by-layer printing strategy that can lead to weak interlayer bonding in the printed structure. Thermally reversible dynamic covalent bonds were subsequently introduced to enhance the adhesion between the component layers. Luo et al.[128] introduced cinnamic acid groups to a polylactic acid/PEG-copolyester blend to induce photo-crosslinking, enhancing interlayer bonding, and thereby improving the printing accuracy and stability of the structure.

Overall, 4D-printed dynamic scaffolds are still in the early stages of development, with a key challenge being the design of materials that are both programmable and biocompatible. Future advancements are expected to integrate AI or machine learning techniques to develop new materials, design functional structures, and optimize printing parameters.

4. Future perspectives

While notable advancements have been made in *in situ* bioprinting, several challenges remain in promoting vascularization within printed structures, automating RASBS procedures, developing highly modular designs for HISBS, and optimizing the bioink system. Printed structures for tissue repair should promote vascularization, and *in situ* 3D bioprinting technology can combine multiple materials and cells to print complex structures, creating microchannels that promote vascularization. Microfluidic technology can also be integrated, such as using a microfluidic chip needle to mix multiple bioinks and cells and print a scaffold with a specific concentration gradient.

For RASBS, incorporating AI could enhance path planning to achieve more detailed and automated *in situ* bioprinting. For *in situ* bioprinting on curved and inclined planes, flexible robotic arms may represent the future direction of development. These arms offer higher degrees of freedom compared to rigid robotic arms, effectively mitigating the step effect caused by printing on curved structures. In addition, machine learning algorithms can optimize non-planar automatic segmentation, reconstruct defects in damaged parts, and obtain print paths. *In situ* bioprinting platforms can also be integrated with machine vision and depth cameras to improve recognition accuracy. Traditional bioprinting technology can print *in vitro* and perform print quality checks, capabilities that are currently limited with *in situ* bioprinting strategies. Therefore, achieving *in situ* quality inspection and control of printed structures is also a future development trend. There have been studies using MRI to track printed cells and assess the healing process.[80] For evaluating the quality of printed scaffolds, OCT can be used for rapid real-time imaging and process feedback control according to the monitoring data.[79]

Considering the portability of handheld bioprinters, such devices should be designed to be highly modular

and easy to disassemble, clean, and disinfect to meet the operational requirements of surgical procedures. Handheld *in situ* bioprinters are typically used in emergency trauma scenarios (e.g., car accidents, battlefields), where users are generally non-professionals. A smartphone can be combined with a handheld *in situ* bioprinter, and the smartphone's high-definition camera and computing power can be used to scan the damaged area and plan the print path.[129] Deep learning can also be combined with cloud computing to monitor and calibrate printhead movements in real time, improving print accuracy. In the future, the handheld *in situ* bioprinter may become an essential tool for astronauts during space emergencies, such as the extraction and storage of biological products containing blood or stem cells before astronauts embark on missions.[130]

At present, a few studies are focusing on real-time monitoring of *in situ* printing processes, utilizing large imaging devices and complex equipment. In the future, it is necessary to miniaturize imaging detection systems to integrate them with minimally invasive printing platforms to enhance the fidelity of printed structures. The use of external magnetic fields to control the precise positioning of magnetic bioinks in the body is a promising technology, and this strategy does not require complex minimally invasive printing robotic arms. Technical validation and optimization for more complex geometric defect printing is also required in the future. To further reduce the volume of the minimally invasive printing platform, the injection device can also be placed outside the body and connected to the pipe through the dispensing nozzle to achieve *in situ* printing. However, the effect of the material temperature at the dispensing nozzle and the ambient temperature on the printing performance of the material will be a challenge.[131] For *in vivo* bioprinting, the selection of suitable bioink depends on the specific tissue repair area. For example, in the acidic environment of the stomach, polyelectrolytes with opposite charges can be added to the bioink to achieve instant curing, without the need for external conditions, such as near-infrared light or ultrasound, to mediate polymerization.

Hydrogels, including collagen, gelatin, and alginate, have been widely used for *in situ* bioprinting. Most of these materials have excellent biocompatibility and low toxicity, but a single biomaterial cannot meet the requirements of tissue repair. Therefore, developing a multi-material *in situ* bioprinting system could expand its applications significantly. For photocured hydrogels, near-infrared light is required to induce bioink polymerization for minimally invasive bioprinting *in vivo*. Hence, it may be crucial to optimize the type and concentration of photoinitiator, light wavelength, and irradiation time. For minimally invasive printing *in vivo*, ultrasound can be used to mediate *in situ* curing of sound-sensitive inks. In this regard, other sound-sensitive materials with good biocompatibility may be developed to enhance tissue regeneration on printed scaffolds. *In situ*-bioprinted tissue scaffolds require uniform pore structure and mechanical strength, both of which share an inverse correlation. Therefore, alternative pore-forming methods need to be developed, such as optimizing microgels to serve as porous scaffolds.[113]

5. Conclusion

In this review, we introduced 3D *in situ* bioprinting to fabricate complex structures for tissue regeneration. Conventional 3D bioprinting strategies require a long incubation period for pre-printed structures in a large working space, potentially leading to a mismatch in the shape of the wound. *In situ* bioprinting can compensate for these deficiencies by using the recipient body as a bioreactor where living biomaterials and cells of scaffolds can be further cultured. The *in situ* bioprinting approach can be divided into three types: RASBS, HISBS, and minimally invasive *in situ* bioprinting. RASBS has higher printing accuracy with less human intervention and can adjust printing models and paths according to the actual printing conditions. Furthermore, combined with minimally invasive tools, RASBS can achieve *in situ* deposition of bioinks without open wounds. Driven by human hand movement, handheld bioprinters are easier to operate but are limited in their application to internal trauma and complex structures. Bioinks normally contain living biomaterials and cells as a matrix to rearrange regenerative factors. Bioinks should have optimal rheological properties for *in situ* bioprinting, ensuring sufficient mechanical strength and printing resolution. Overall, *in situ* bioprinting holds great promise as an emerging technology for tissue repair. This technology is expected to make significant progress in the coming years with technological advances in AI, medical robotics, and biomaterials.

Acknowledgments

None.

Funding

This work was supported by the National Key Research and Development Program of China (2018YFA0703100), Guangdong Basic and Applied Basic Research Foundation (2021A1515110902, 2021A1515110794), Shenzhen Science and Technology Funding (JCYJ20220530142206014), and the Shanghai Municipal Health Commission Health Industry Clinical Research Program for Youth (20224Y0184).

Conflict of interest

The authors declare no conflicts of interest.

Author contributions

Conceptualization: Xiaoli Zhao, Chengwei Hu, Jun Wu, Liangliang Wang, William W. Lu
Investigation: Chengwei Hu, Chenmin Wang, Shaoquan Bian, Bo Liu, Chunyi Wen
Writing – original draft: Chengwei Hu
Writing – review & editing: Xiaoli Zhao, Chengwei Hu, Jun Wu, Weichen Qi

Ethics approval and consent to participate

Not applicable.

Consent for publication

Not applicable.

Availability of data

Not applicable.

References

1. Li L, Yu F, Shi J, et al. In situ repair of bone and cartilage defects using 3D scanning and 3D printing. *Sci Rep.* 2017;7(1):9416. doi: 10.1038/s41598-017-10060-3
2. Singh S, Choudhury D, Yu F, Mironov V, Naing MW. In situ bioprinting—bioprinting from benchside to bedside? *Acta Biomater.* 2020;101:14-25. doi: 10.1016/j.actbio.2019.08.045
3. Ozbolat IT. Bioprinting scale-up tissue and organ constructs for transplantation. *Trends Biotechnol.* 2015;33(7): 395-400. doi: 10.1016/j.tibtech.2015.04.005
4. Gatenholm B, Lindahl C, Brittberg M, Simonsson S. Collagen 2A type B induction after 3D bioprinting chondrocytes in situ into osteoarthritic chondral tibial lesion. *Cartilage.* 2021;13(2_SUPPL):1755S-1769S. doi: 10.1177/1947603520903788
5. Yang BW, Yin JH, Chen Y, et al. 2D-black-phosphorus-reinforced 3D-printed scaffolds: a stepwise countermeasure for osteosarcoma. *Adv Mater.* 2018;30(10):1705611. doi: 10.1002/adma.201705611
6. Chow T, Wutami I, Lucarelli E, et al. Creating in vitro three-dimensional tumor models: a guide for the biofabrication of a primary osteosarcoma model. *Tissue Eng Part B Rev.* 2021;27(5):514-529. doi: 10.1089/ten.teb.2020.0254
7. Li ZH, Zhao Y, Wang ZH, et al. Engineering multifunctional hydrogel-integrated 3D printed bioactive prosthetic interfaces for osteoporotic osseointegration. *Adv Healthc Mater.* 2022;11(11):e2102535. doi: 10.1002/adhm.202102535
8. Yvanoff C, Willaert RG. Development of bone cell microarrays in microfluidic chips for studying osteocyte-osteoblast communication under fluid flow mechanical loading. *Biofabrication.* 2022;14(2):025014. doi: 10.1088/1758-5090/ac516e
9. Cheng RY, Eylert G, Gariepy J-M, et al. Handheld instrument for wound-conformal delivery of skin precursor sheets improves healing in full-thickness burns. *Biofabrication.* 2020;12(2):025002. doi: 10.1088/1758-5090/ab6413
10. Jiao T, Lian Q, Lian W, et al. Properties of collagen/sodium alginate hydrogels for bioprinting of skin models. *J Bionic Eng.* 2023;20(1):105-118. doi: 10.1007/s42235-022-00251-8
11. Liu J, Zhou Z, Zhang M, et al. Simple and robust 3D bioprinting of full-thickness human skin tissue. *Bioengineered.* 2022;13(4):10087-10097. doi: 10.1080/21655979.2022.2063651
12. Mandrycky C, Wang Z, Kim K, Kim D-H. 3D bioprinting for engineering complex tissues. *Biotechnol Adv.* 2016;34(4):422-434. doi: 10.1016/j.biotechadv.2015.12.011
13. Sithole MN, Kumar P, du Toit LC, et al. A 3D bioprinted in situ conjugated-co-fabricated scaffold for potential bone tissue engineering applications. *J Biomed Mater Res Part A.* 2018;106(5):1311-1321. doi: 10.1002/jbm.a.36333
14. Kilian D, Sembdner P, Bretschneider H, et al. 3D printing of patient-specific implants for osteochondral defects: workflow for an MRI-guided zonal design. *Bio-Des Manuf.* 2021;4(4):818-832. doi: 10.1007/s42242-021-00153-4
15. Kurzyk A, Szumera-Cieckiewicz A, Miloszewska J, Chechlinska M. 3D modeling of normal skin and cutaneous squamous cell carcinoma. A comparative study in 2D cultures, spheroids, and 3D bioprinted systems. *Biofabrication.* 2024;16(2):025021. doi: 10.1088/1758-5090/ad2b06.
16. Fu Z, Hai N, Zhong Y, Sun W. Printing GelMA bioinks: a strategy for building in vitro model to study nanoparticle-based minocycline release and cellular protection under oxidative stress. *Biofabrication.* 2024;16(2):025040. doi: 10.1088/1758-5090/ad30c3
17. Shukla P, Bera AK, Yeleswarapu S, Pati F. High throughput bioprinting using decellularized adipose tissue-based hydrogels for 3D breast cancer modeling. *Macromol Biosci.* 2024;24:2400035. doi: 10.1002/mabi.202400035
18. Wu D, Pang S, Berg J, et al. Bioprinting of perfusable vascularized organ models for drug development via

sacrificial-free direct ink writing. *Adv Funct Mater*. 2024:2314171.
doi: 10.1002/adfm.202314171

19. Gvaramia D, Fisch P, Flegeau K, et al. Evaluation of bioprinted autologous cartilage grafts in an immunocompetent rabbit model. *Adv Ther*. 2024;7(6):2300441.
doi: 10.1002/adtp.202300441

20. Bhar B, Das E, Manikumar K, Mandal BB. 3D bioprinted human skin model recapitulating native-like tissue maturation and immunocompetence as an advanced platform for skin sensitization assessment. *Adv Healthc Mater*. 2024;13(15):e2303312.
doi: 10.1002/adhm.202303312

21. Di Buduo CA, Lunghi M, Kuzmenko V, et al. Bioprinting soft 3D models of hematopoiesis using natural silk fibroin-based bioink efficiently supports platelet differentiation. *Adv Sci*. 2024;11(18):2308276.
doi: 10.1002/advs.202308276

22. Edri S, Frisch AN, Safina D, et al. 3D bioprinting of multicellular stem cell-derived constructs to model pancreatic cell differentiation. *Adv Funct Mater*. 2024;34:2315488.
doi: 10.1002/adfm.202315488

23. Li H, Cheng F, Orgill DP, Yao J, Zhang YS. Handheld bioprinting strategies for in situ wound dressing. In: Jang J, ed. *Essays in Biochemistry. Vol. 65*. London: Portland Press; 2021:533-543.
doi: 10.1042/EBC20200098

24. Thai MT, Phan PT, Tran HA, et al. Advanced soft robotic system for in situ 3D bioprinting and endoscopic surgery. *Adv Sci*. 2023;10(12):2205656.
doi: 10.1002/advs.202205656

25. Agostinacchio F, Mu X, Dire S, Motta A, Kaplan DL. In situ 3D printing: opportunities with silk inks. *Trends Biotechnol*. 2021;39(7):719-730.
doi: 10.1016/j.tibtech.2020.11.003

26. Akilbekova D, Mektepbayeva D. Chapter 5-patient specific in situ 3D printing. In: Kalaskar DM, ed. *3D Printing in Medicine*. Cambridge: Woodhead Publishing; 2017:91-113.
doi: 10.1016/b978-0-08-100717-4.00004-1

27. Campbell PG, Weiss LE. Tissue engineering with the aid of inkjet printers. *Expert Opin Biol Ther*. 2007;7(8):1123-1127.
doi: 10.1517/14712598.7.8.1123

28. Samandari M, Mostafavi A, Quint J, Memic A, Tamayol A. In situ bioprinting: intraoperative implementation of regenerative medicine. *Trends Biotechnol*. 2022;40(10): 1229-1247.
doi: 10.1016/j.tibtech.2022.03.009

29. Zhao W, Xu T. Preliminary engineering for in situ in vivo bioprinting: a novel micro bioprinting platform for in situ in vivo bioprinting at a gastric wound site. *Biofabrication*. 2020;12(4):045020.
doi: 10.1088/1758-5090/aba4ff

30. Nuutila K, Samandari M, Endo Y, et al. In vivo printing of growth factor-eluting adhesive scaffolds improves wound healing. *Bioact Mater*. 2022;8:296-308.
doi: 10.1016/j.bioactmat.2021.06.030

31. Wu Y, Ravnic DJ, Ozbolat IT. Intraoperative bioprinting: repairing tissues and organs in a surgical setting. *Trends Biotechnol*. 2020;38(6):594-605.
doi: 10.1016/j.tibtech.2020.01.004

32. Chen H, Zhang Y, Zhou D, et al. Mechanical engineering of hair follicle regeneration by in situ bioprinting. *Biomater Adv*. 2022;142:213127.
doi: 10.1016/j.bioadv.2022.213127

33. Gaharwar AK, Singh I, Khademhosseini A. Engineered biomaterials for in situ tissue regeneration. *Nat Rev Mater*. 2020;5(9):686-705.
doi: 10.1038/s41578-020-0209-x

34. Levin AA, Karalkin PA, V. Koudan E, et al. Commercial articulated collaborative in situ 3D bioprinter for skin wound healing. *Int J Bioprint*. 2023;9(2):380-393.
doi: 10.18063/ijb.v9i2.675

35. Li L, Shi J, Ma K, et al. Robotic in situ 3D bio-printing technology for repairing large segmental bone defects. *J Adv Res*. 2021;30:75-84.
doi: 10.1016/j.jare.2020.11.011

36. Moncal KK, Gudapati H, Godzik KP, et al. Intra-operative bioprinting of hard, soft, and hard/soft composite tissues for craniomaxillofacial reconstruction. *Adv Funct Mater*. 2021;31(29):2010858.
doi: 10.1002/adfm.202010858

37. Albanna M, Binder KW, Murphy SV, et al. In situ bioprinting of autologous skin cells accelerates wound healing of extensive excisional full-thickness wounds. *Sci Rep*. 2019;9(1):1856
doi: 10.1038/s41598-018-38366-w

38. Zhao W, Hu C, Xu T, et al. Subaqueous bioprinting: a novel strategy for fetal membrane repair with 7-axis robot-assisted minimally invasive surgery. *Adv Funct Mater*. 2022;32(51):2207496.
doi: 10.1002/adfm.202207496

39. Christensen K, Compaan A, Chai W, Xia G, Huang Y. In situ printing-then-mixing for biological structure fabrication using intersecting jets. *ACS Biomater Sci Eng*. 2017;3(12):3687-3694.
doi: 10.1021/acsbiomaterials.7b00752

40. Keriquel V, Oliveira H, Remy M, et al. In situ printing of mesenchymal stromal cells, by laser-assisted bioprinting, for in vivo bone regeneration applications. *Sci Rep*. 2017;7(1):1778.
doi: 10.1038/s41598-017-01914-x

41. Kerouredan O, Hakobyan D, Remy M, et al. In situ prevascularization designed by laser-assisted bioprinting: effect on bone regeneration. *Biofabrication*. 2019;11(4):045002.
doi: 10.1088/1758-5090/ab2620

42. Ding H, Chang RC. Simulating image-guided in situ bioprinting of a skin graft onto a phantom burn wound bed. *Addit Manuf*. 2018;22:708-719. doi: 10.1016/j.addma.2018.06.022

43. Liu Y, Luo X, Wu W, et al. Dual cure (thermal/photo) composite hydrogel derived from chitosan/collagen for in situ 3D bioprinting. *Int J Biol Macromol*. 2021;182:689-700. doi: 10.1016/j.ijbiomac.2021.04.058

44. Chen Y, Zhang J, Liu X, et al. Noninvasive in vivo 3D bioprinting. *Sci Adv*. 2020;6(23):eaba7406. doi: 10.1126/sciadv.aba7406

45. Urciuolo A, Poli I, Brandolino L, et al. Intravital three-dimensional bioprinting. *Nat Biomed Eng*. 2020;4(9):901-915. doi: 10.1038/s41551-020-0568-z

46. Chen H, Zhang H, Shen Y, et al. Instant in-situ tissue repair by biodegradable PLA/gelatin nanofibrous membrane using a 3D printed handheld electrospinning device. *Front Bioeng Biotechnol*. 2021;9:684105. doi: 10.3389/fbioe.2021.684105

47. Tianyuan Y, Yi Z, Zhian J, Yuanyuan L. A novel handheld device: application to in situ bioprinting compound dressing for the treatment of wound. Paper presented at: *Journal of Physics: Conference Series*; 2021. doi: 10.1088/1742-6596/1965/1/012059

48. Li X, Lian Q, Li DC, Xin H, Jia SH. Development of a robotic arm based hydrogel additive manufacturing system for in-situ printing. *Appl Sci*. 2017;7(1):73. doi: 10.3390/app7010073

49. Keriquel V, Guillemot F, Arnault I, et al. In vivo bioprinting for computer-and robotic-assisted medical intervention: preliminary study in mice. *Biofabrication*. 2010;2(1):014101. doi: 10.1088/1758-5082/2/1/014101

50. Zhu Z, Guo S-Z, Hirdler T, et al. 3D printed functional and biological materials on moving freeform surfaces. *Adv Mater*. 2018;30(23):e1707495. doi: 10.1002/adma.201707495

51. Adib AA, Sheikhi A, Shahhosseini M, et al. Direct-write 3D printing and characterization of a GelMA-based biomaterial for intracorporeal tissue engineering. *Biofabrication*. 2020;12(4):045006. doi: 10.1088/1758-5090/ab97a1

52. Skardal A, Mack D, Kapetanovic E, et al. Bioprinted amniotic fluid-derived stem cells accelerate healing of large skin wounds. *Stem Cells Transl Med*. 2012;1(11):792-802. doi: 10.5966/sctm.2012-0088

53. Russell CS, Mostafavi A, Quint JP, et al. In situ printing of adhesive hydrogel scaffolds for the treatment of skeletal muscle injuries. *ACS Appl Bio Mater*. 2020;3(3):1568-1579. doi: 10.1021/acsabm.9b01176

54. Quint JP, Mostafavi A, Endo Y, et al. In vivo printing of nanoenabled scaffolds for the treatment of skeletal muscle injuries. *Adv Healthc Mater*. 2021;10(10):e2002152. doi: 10.1002/adhm.202002152

55. Di Bella C, Duchi S, O'Connell CD, et al. In situ handheld three-dimensional bioprinting for cartilage regeneration. *J Tissue Eng Regen Med*. 2018;12(3):611-621. doi: 10.1002/term.2476

56. Duchi S, Onofrillo C, O'Connell CD, et al. Handheld co-axial bioprinting: application to in situ surgical cartilage repair. *Sci Rep*. 2017;7(1):5837. doi: 10.1038/s41598-017-05699-x

57. Onofrillo C, Duchi S, O'Connell CD, et al. Biofabrication of human articular cartilage: a path towards the development of a clinical treatment. *Biofabrication*. 2018;10(4):045006. doi: 10.1088/1758-5090/aad8d9

58. Mostafavi A, Abdullah T, Russell CS, et al. In situ printing of scaffolds for reconstruction of bone defects. *Acta Biomater*. 2021;127:313-326. doi: 10.1016/j.actbio.2021.03.009

59. Campos DFD, Zhang S, Kreimendahl F, et al. Hand-held bioprinting for de novo vascular formation applicable to dental pulp regeneration. *Connect Tissue Res*. 2020;61(2):205-215. doi: 10.1080/03008207.2019.1640217

60. Zhou C, Yang Y, Wang J, et al. Ferromagnetic soft catheter robots for minimally invasive bioprinting. *Nat Commun*. 2021;12(1):5072. doi: 10.1038/s41467-021-25386-w

61. Abdelrahim AA, Hong S, Song JM. Integrative in situ photodynamic therapy-induced cell death measurement of 3D-bioprinted MCF-7 tumor spheroids. *Anal Chem*. 2022;94(40):13936-13943. doi: 10.1021/acs.analchem.2c03022

62. Chaudhry MS, Czekanski A. Surface slicing and toolpath planning for in-situ bioprinting of skin implants. *Biofabrication*. 2024;16(2):025030. doi: 10.1088/1758-5090/ad30c4

63. Zhao M, Wang J, Zhang J, et al. Functionalizing multi-component bioink with platelet-rich plasma for customized in-situ bilayer bioprinting for wound healing. *Mater Today Bio*. 2022;16:100334. doi: 10.1016/j.mtbio.2022.100334

64. Liu X, Wang X, Zhang L, et al. 3D liver tissue model with branched vascular networks by multimaterial bioprinting. *Adv Healthcare Mater*. 2021;10(23):e2101405. doi: 10.1002/adhm.202101405

65. Zhao W, Chen H, Zhang Y, et al. Adaptive multi-degree-of-freedom in situ bioprinting robot for hair-follicle-inclusive skin repair: A preliminary study conducted in mice. *Bioeng Transl Med*. 2022;7(3):e10303. doi: 10.1002/btm2.10303

66. Ma K, Zhao T, Yang L, et al. Application of robotic-assisted in situ 3D printing in cartilage regeneration with HAMA hydrogel: an in vivo study. *J Adv Res*. 2020;23:123-132. doi: 10.1016/j.jare.2020.01.010

67. Al-Kharusi G, Dunne NJ, Little S, Levingstone TJ. The role of machine learning and design of experiments in the advancement of biomaterial and tissue engineering research. *Bioengineering (Basel)*. 2022;9(10):561. doi: 10.3390/bioengineering9100561

68. Albouy M, Desanlis A, Brosset S, et al. A preliminary study for an intraoperative 3D bioprinting treatment of severe burn injuries. *Plast Reconstr Surg Glob Open*. 2022;10(1):e4056. doi: 10.1097/GOX.0000000000004056

69. Chen H, Ma X, Gao T, et al. Robot-assisted in situ bioprinting of gelatin methacrylate hydrogels with stem cells induces hair follicle-inclusive skin regeneration. *Biomed Pharmacother*. 2023;158:114140. doi: 10.1016/j.biopha.2022.114140

70. Simeunovic A, Wolf K, Tierling K, Hoelzle DJ. A surgical robot for intracorporeal additive manufacturing of tissue engineering constructs. *IEEE Rob Autom Lett*. 2022;7(3):7495-7502. doi: 10.1109/LRA.2022.3183752

71. Fortunato GM, Sigismondi S, Nicoletta M, et al. Analysis of the robotic-based in situ bioprinting workflow for the regeneration of damaged tissues through a case study. *Bioengineering (Basel)*. 2023;10(5):560. doi: 10.3390/bioengineering10050560

72. Colosi C, Costantini M, Barbetta A, Dentini M. Microfluidic bioprinting of heterogeneous 3D tissue constructs. *Methods Mol Biol*. 2017;1612:369-380. doi: 10.1007/978-1-4939-7021-6_26

73. Xie M, Shi Y, Zhang C, et al. In situ 3D bioprinting with bioconcrete bioink. *Nat Commun*. 2022;13(1):3597. doi: 10.1038/s41467-022-30997-y

74. Shi E, Lou L, Warburton L, Rubinsky B. Three-dimensional printing in combined cartesian and curvilinear coordinates. *J Med Device*. 2022;16(4):044502. doi: 10.1115/1.4055064

75. Fortunato GM, Batoni E, Pasqua I, et al. Automatic photo-cross-linking system for robotic-based in situ bioprinting. *ACS Biomater Sci Eng*. 2023;9(12):6926-6934. doi: 10.1021/acsbiomaterials.3c00898

76. Kucukdeger E, Johnson BN. Closed-loop controlled conformal 3D printing on moving objects via tool-localized object position sensing. *J Manuf Processes*. 2023;89:39-49. doi: 10.1016/j.jmapro.2023.01.020.

77. Yang S, Wang L, Chen Q, Xu M. In situ process monitoring and automated multi-parameter evaluation using optical coherence tomography during extrusion-based bioprinting. *Addit Manuf*. 2021;47:102251. doi: 10.1016/j.addma.2021.102251

78. Yang S, Chen Q, Wang L, Xu M. In situ defect detection and feedback control with three-dimensional extrusion-based bioprinter-associated optical coherence tomography. *Int J Bioprint*. 2023;9(1):47-62. doi: 10.18063/ijb.v9i1.624

79. Tashman JW, Shiwarski DJ, Coffin B, et al. In situ volumetric imaging and analysis of FRESH 3D bioprinted constructs using optical coherence tomography. *Biofabrication*. 2023;15(1):014102. doi: 10.1088/1758-5090/ac975e

80. Kerouredan O, Ribot E, Fricain J-C, Devillard R, Miraux S. Magnetic resonance imaging for tracking cellular patterns obtained by laser-assisted bioprinting. *Sci Rep*. 2018;8(1):15777. doi: 10.1038/s41598-018-34226-9

81. Zhou Y, Liao S, Chu Y, et al. An injectable bioink with rapid prototyping in the air and in-situ mild polymerization for 3D bioprinting. *Biofabrication*. 2021;13(4):045026. doi: 10.1088/1758-5090/ac23e4

82. Kotlarz M, Ferreira AM, Gentile P, Russell SJ, Dalgarno K. Droplet-based bioprinting enables the fabrication of cell-hydrogel-microfibre composite tissue precursors. *Bio-Des Manuf*. 2022;5(3):512-528. doi: 10.1007/s42242-022-00192-5

83. Zhao D-k, Xu H-q, Yin J, Yang H-y. Inkjet 3D bioprinting for tissue engineering and pharmaceutics. *J Zhejiang Univ Sci A*. 2022;23(12):955-973. doi: 10.1631/2023.A2200569

84. Limon SM, Quigley C, Sarah R, Habib A. Advancing scaffold porosity through a machine learning framework in extrusion based 3D bioprinting. *Front Mater*. 2024;10:1337485. doi: 10.3389/fmats.2023.1337485

85. Qiao Q, Zhang X, Yan Z, et al. The use of machine learning to predict the effects of cryoprotective agents on the GelMA-based bioinks used in extrusion cryobioprinting. *Bio-Des Manuf*. 2023;6(4):464-477. doi: 10.1007/s42242-023-00244-4

86. Huang X, Ng WL, Yeong WY. Predicting the number of printed cells during inkjet-based bioprinting process based on droplet velocity profile using machine learning approaches. *J Intell Manuf*. 2023;35(5). doi: 10.1007/s10845-023-02167-4

87. Pagan E, Stefanek E, Seyfoori A, et al. A handheld bioprinter for multi-material printing of complex constructs. *Biofabrication*. 2023;15(3):035012. doi: 10.1088/1758-5090/acc42c.

88. Hakimi N, Cheng R, Leng L, et al. Handheld skin printer: in situ formation of planar biomaterials and tissues. *Lab Chip*. 2018;18(10):1440-1451. doi: 10.1039/c7lc01236e.

89. Zhou FY, Xin LJ, Wang SY, et al. Portable handheld "SkinPen" loaded with biomaterial ink for in situ wound healing. *ACS Appl Mater Interfaces*. 2023;15(23):27568-27585. doi: 10.1021/acsami.3c02825

90. Ying G, Manriquez J, Wu D, et al. An open-source handheld extruder loaded with pore-forming bioink for in situ wound dressing. *Mater Today Bio*. 2020;8:100074. doi: 10.1016/j.mtbio.2020.100074

91. Mostafavi A, Samandari M, Karvar M, et al. Colloidal multiscale porous adhesive (bio)inks facilitate scaffold integration. *Appl Phys Rev*. 2021;8(4):041415. doi: 10.1063/5.0062823

92. Shi Y, Tang S, Yuan X, et al. In situ 4D printing of polyelectrolyte/magnetic composites for sutureless gastric perforation sealing. *Adv Mater*. 2023;36:2307601. doi: 10.1002/adma.202307601

93. Yang Y, Yu Z, Lu X, et al. Minimally invasive bioprinting for in situ liver regeneration. *Bioact Mater*. 2023;26:465-477. doi: 10.1016/j.bioactmat.2023.03.011

94. Debbi L, Machour M, Dahis D, et al. Ultrasound mediated polymerization for cell delivery, drug delivery, and 3D printing. *Small Methods*. 2024:2301197. doi: 10.1002/smtd.202301197

95. Zhao W, Hu C, Lin S, et al. A closed-loop minimally invasive 3D printing strategy with robust trocar identification and adaptive alignment. *Addit Manuf*. 2023;73:103701. doi: 10.1016/j.addma.2023.103701

96. Goker M, Derici US, Gokyer S, et al. Spatial growth factor delivery for 3D bioprinting of vascularized bone with adipose-derived stem/stromal cells as a single cell source. *ACS Biomater Sci Eng*. 2024;10(3):1607-1619. doi: 10.1021/acsbiomaterials.3c01222

97. Enrico A, Voulgaris D, Ostmans R, et al. 3D microvascularized tissue models by laser-based cavitation molding of collagen. *Adv Mater*. 2022;34(11):e2109823. doi: 10.1002/adma.202109823

98. Hu Y, Xiong Y, Zhu Y, et al. Copper-epigallocatechin gallate enhances therapeutic effects of 3D-printed dermal scaffolds in mitigating diabetic wound scarring. *ACS Appl Mater Interfaces*. 2023;15(32):38230-38246. doi: 10.1021/acsami.3c04733

99. Lu S, Wang X, Li W, Zu Y, Xiao J. Injectable 3D-printed porous scaffolds for adipose stem cell delivery and endometrial regeneration. *Adv Funct Mater*. 2023;33(34): 2303368. doi: 10.1002/adfm.202303368

100. Ouyang L, Armstrong JPK, Chen Q, Lin Y, Stevens MM. Void-free 3D bioprinting for in situ endothelialization and microfluidic perfusion. *Adv Funct Mater*. 2020;30(1):1908349. doi: 10.1002/adfm.201908349

101. Muhammad M, Willems C, Rodriguez-Fernandez J, Gallego-Ferrer G, Groth T. Synthesis and characterization of oxidized polysaccharides for in situ forming hydrogels. *Biomolecules*. 2020;10(8):1185. doi: 10.3390/biom10081185

102. Baptista M, Joukhdar H, Alcala-Orozco CR, et al. Silk fibroin photo-lyogels containing microchannels as a biomaterial platform for in situ tissue engineering. *Biomater Sci*. 2020;8(24):7093-7105. doi: 10.1039/d0bm01010c

103. Chen X, Ranjan VD, Liu S, et al. In situ formation of 3D conductive and cell-laden graphene hydrogel for electrically regulating cellular behavior. *Macromol Biosci*. 2021;21(4):e2000374. doi: 10.1002/mabi.202000374

104. Li C, Faulkner-Jones A, Dun AR, et al. Rapid formation of a supramolecular polypeptide-DNA hydrogel for in situ three-dimensional multilayer bioprinting. *Angew Chem Int Ed*. 2015;54(13):3957-3961. doi: 10.1002/anie.201411383

105. Moeinzadeh S, Park Y, Lin S, Yang YP. In-situ stable injectable collagen-based hydrogels for cell and growth factor delivery. *Materialia (Oxf)*. 2021;15:100954. doi: 10.1016/j.mtla.2020.100954

106. Alruwaili M, Lopez JA, McCarthy K, Reynaud EG, Rodriguez BJ. Liquid-phase 3D bioprinting of gelatin alginate hydrogels: influence of printing parameters on hydrogel line width and layer height. *Bio-Des Manuf*. 2019;2(3):172-180. doi: 10.1007/s42242-019-00043-w

107. Handral HK, Natu VP, Cao T, et al. Emerging trends and prospects of electroconductive bioinks for cell-laden and functional 3D bioprinting. *Bio-Des Manuf*. 2022;5(2): 396-411. doi: 10.1007/s42242-021-00169-w

108. Lai S, Wu T, Shi C, et al. Triple-layered core-shell fiber dressings with enduring platelet conservation and sustained growth factor release abilities for chronic wound healing. *Regener Biomater*. 2024;11:rbae034. doi: 10.1093/rb/rbae034

109. Kang MS, Kwon M, Lee SY, et al. In situ crosslinkable collagen-based hydrogels for 3D printing of dermis-mimetic constructs. *ECS J Solid State Sci Technol*. 2022;11(4): 045014. doi: 10.1149/2162-8777/ac6897

110. Kang MS, Kang JI, Thi PL, et al. Three-dimensional printable gelatin hydrogels incorporating graphene oxide to enable spontaneous myogenic differentiation. *ACS Macro Lett*. 2021;10(4):426-432. doi: 10.1021/acsmacrolett.0c00845

111. Miri AK, Nieto D, Iglesias L, et al. Microfluidics-enabled multimaterial maskless stereolithographic bioprinting. *Adv Mater*. 2018;30(27):e1800242. doi: 10.1002/adma.201800242

112. Hwangbo H, Lee H, Jin E-J, et al. Bio-printing of aligned GelMa-based cell-laden structure for muscle tissue regeneration. *Bioact Mater*. 2021;8:57-70. doi: 10.1016/j.bioactmat.2021.06.031

113. Jalandhra GK, Molley TG, Hung T-t, Roohani I, Kilian KA. In situ formation of osteochondral interfaces through "bone-ink" printing in tailored microgel suspensions. *Acta Biomater*. 2023;156:75-87. doi: 10.1016/j.actbio.2022.08.052

114. de Melo BAG, Jodat YA, Mehrotra S, et al. 3D printed cartilage-like tissue constructs with spatially controlled mechanical properties. *Adv Funct Mater*. 2019;29(51):1906330. doi: 10.1002/adfm.201906330

115. Li C, Wang J, Yang W, et al. 3D-printed hydrogel particles containing PRP laden with TDSCs promote tendon repair in a rat model of tendinopathy. *J Nanobiotechnol*. 2023;21(1):177. doi: 10.1186/s12951-023-01892-5

116. Li J, Huang Y, Song J, et al. Cartilage regeneration using arthroscopic flushing fluid-derived mesenchymal stem cells encapsulated in a one-step rapid cross-linked hydrogel. *Acta Biomater*. 2018;79:202-215. doi: 10.1016/j.actbio.2018.08.029

117. Blaeser A, Million N, Campos DFD, et al. Laser-based in situ embedding of metal nanoparticles into bioextruded alginate hydrogel tubes enhances human endothelial cell adhesion. *Nano Res*. 2016;9(11):3407-3427. doi: 10.1007/s12274-016-1218-3

118. Khoshnood N, Shahrezaee MH, Shahrezaee M, Zamanian A. Three-dimensional bioprinting of tragacanth/hydroxyapaptite modified alginate bioinks for bone tissue engineering with tunable printability and bioactivity. *J Appl Polym Sci*. 2022;139(36):e52833. doi: 10.1002/app.52833

119. Bandyopadhyay A, Mandal BB, Bhardwaj N. 3D bioprinting of photo-crosslinkable silk methacrylate (SilMA)-polyethylene glycol diacrylate (PEGDA) bioink for cartilage tissue engineering. *J Biomed Mater Res Part A*. 2022;110(4):884-898. doi: 10.1002/jbm.a.37336

120. Zhang M, Qian T, Deng Z, Hang F. 3D printed double-network alginate hydrogels containing polyphosphate for bioenergetics and bone regeneration. *Int J Biol Macromol*. 2021;188:639-648. doi: 10.1016/j.ijbiomac.2021.08.066

121. Koo Y, Kim G. New strategy for enhancing in situ cell viability of cell-printing process via piezoelectric transducer-assisted three-dimensional printing. *Biofabrication*. 2016;8(2):025010. doi: 10.1088/1758-5090/8/2/025010

122. Krishnadoss V, Kanjilal B, Masoumi A, et al. Programmable bio-ionic liquid functionalized hydrogels for in situ 3D bioprinting of electronics at the tissue interface. *Mater Today Adv*. 2023;17:100352. doi: 10.1016/j.mtadv.2023.100352

123. Yin J, Zhao D, Liu J. Trends on physical understanding of bioink printability. *Bio-Des Manuf*. 2019;2(1):50-54. doi: 10.1007/s42242-019-00033-y

124. Wang X, Yang C, Yu Y, Zhao Y. In situ 3D bioprinting living photosynthetic scaffolds for autotrophic wound healing. *Research (Wash D C)*. 2022;2022:9794745. doi: 10.34133/2022/9794745

125. Hann SY, Cui H, Esworthy T, Zhang LG. 4D thermo-responsive smart hiPSC-CM cardiac construct for myocardial cell therapy. *Int J Nanomed*. 2023;18:1809-1821. doi: 10.2147/IJN.S402855

126. Joshi A, Choudhury S, Baghel VS, et al. 4D printed programmable shape-morphing hydrogels as intraoperative self-folding nerve conduits for sutureless neurorrhaphy. *Adv Healthcare Mater*. 2023;12(24):e2300701. doi: 10.1002/adhm.202300701

127. Liu B, Li H, Meng F, et al. 4D printed hydrogel scaffold with swelling-stiffening properties and programmable deformation for minimally invasive implantation. *Nat Commun*. 2024;15(1):1587. doi: 10.1038/s41467-024-45938-0

128. Luo K, Wang L, Wang M-X, et al. 4D printing of biocompatible scaffolds via in situ photo-crosslinking from shape memory copolyesters. *ACS Appl Mater Interfaces*. 2023;15(37):44373-44383. doi: 10.1021/acsami.3c10747

129. Li W, Wang M, Mille LS, et al. A smartphone-enabled portable digital light processing 3D printer. *Adv Mater*. 2021;33(35):2102153. doi: 10.1002/adma.202102153

130. Warth N, Berg M, Schumacher L, et al. Bioprint FirstAid: a handheld bioprinter for first aid utilization on space exploration missions. *Acta Astronaut*. 2024;215:194-204. doi: 10.1016/j.actaastro.2023.11.033

131. Tomooka Y, Spothelfer D, Puiggali-Jou A, et al. Minimally invasive in situ bioprinting using tube-based material transfer. *at - Automatisierungstechnik*. 2023;71(7):562-571. doi: 10.1515/auto-2023-0060

ACCSCIENCE PUBLISHING

International Journal of Bioprinting

REVIEW ARTICLE

Emerging frontiers in 3D bioprinting: Harnessing decellularized matrix bioink for advancements in musculoskeletal tissue engineering

Peilin Li[1†], Xixin Li[1†], Guosheng Tang[2], Zongke Zhou[3], and Zeyu Luo[3*]

[1]State Key Laboratory of Oral Diseases, National Center for Stomatology, National Clinical Research Center for Oral Diseases, Department of Orthodontics, West China Hospital of Stomatology, Sichuan University, Chengdu, Sichuan, China

[2]Guangzhou Municipal and Guangdong Provincial Key Laboratory of Molecular Target and Clinical Pharmacology, the NMPA and State Key Laboratory of Respiratory Disease, School of Pharmaceutical Sciences and the Fifth Affiliated Hospital, Guangzhou Medical University, Guangzhou, Guangdong, China

[3] Department of Orthopedics, West China School of Medicine, West China Hospital, Sichuan University, Chengdu, Sichuan, China

(This article belongs to the *Special Issue: Advancements in 3D Printing, Microfluidics, and their Integrated Applications*)

Abstract

The musculoskeletal system plays a pivotal role in maintaining posture, safeguarding organs, facilitating flexible movement, and supporting cellular metabolic functions, thereby enabling active participation in various aspects of life. Conventional treatment modalities, such as autologous and allogeneic transplantation, face significant challenges, including donor scarcity, complications, rejection, and infection. The emergence of three-dimensional (3D) bioprinting technology, coupled with bioink sourced from the decellularized extracellular matrix (dECM), offers a promising approach for repairing and regenerating musculoskeletal tissue. This article meticulously examines common methods of musculoskeletal tissue bioprinting, the properties and functions of dECM, techniques for preparing dECM bioinks, recent advancements, and applications of dECM bioinks in 3D printing of musculoskeletal tissues (e.g., heart, skeletal muscle, tendon, interfaces between tissues, bone, and cartilage). The review concludes by delineating current research limitations, aiming to catalyze future investigations in this domain.

Keywords: 3D bioprinting; Decellularized extracellular matrix; Bioink; Musculoskeletal; Tissue engineering

†These authors contributed equally to this work.

***Corresponding author:**
Zeyu Luo (luozy@wchscu.edu.cn)

Citation: Li P, Li X, Tang G, Zhou Z, Luo Z. Emerging frontiers in 3D bioprinting: Harnessing decellularized matrix bioink for advancements in musculoskeletal tissue engineering. *Int J Bioprint.* 2024;10(5):3418. doi: 10.36922/ijb.3418

Received: April 13, 2024
Accepted: June 24, 2024
Published Online: August 21, 2024

Copyright: © 2024 Author(s). This is an Open Access article distributed under the terms of the Creative Commons Attribution License, permitting distribution, and reproduction in any medium, provided the original work is properly cited.

Publisher's Note: AccScience Publishing remains neutral with regard to jurisdictional claims in published maps and institutional affiliations.

1. Introduction

The musculoskeletal system, encompassing bones, muscles, cartilage tissue (articular cartilage, intervertebral discs, meniscus), tendons, ligaments, and blood vessels, is crucial for maintaining posture, protecting organs, facilitating flexible movement, and supporting cellular metabolic functions. Maintaining good musculoskeletal health is essential for people to move with flexibility, work efficiently, and participate actively in all aspects of life.[1,2] The World Health Organization (WHO) reports that musculoskeletal

diseases affect approximately 1.71 billion people globally, highlighting it as one of the most commonly impacted systems in cases of trauma. Musculoskeletal disorders can significantly impair mobility and flexibility, resulting in decreased fitness levels, premature retirement, and reduced engagement in social activities. Autologous and allogeneic transplantation methods have been widely used to replace damaged or lost musculoskeletal tissue due to trauma or other pathologies. However, the utilization of autografts faces constraints due to issues such as donor site morbidity and scarcity of donor tissue. Furthermore, autologous and allogeneic transplantation methods present notable drawbacks, including donor-related complications, rejection, and the risk of infection.[1,3,4]

To address these challenges, tissue engineering (TE) has garnered considerable attention for its potential to restore the structure and function of tissues and organs affected by injury or disease.[5–9] Nevertheless, conventional scaffold-based TE faces limitations in accurately replicating the intricate microstructure and natural functions of biological tissues. Additionally, it lacks the ability to identify specific spatial locations.[10] Advancements in 3D bioprinting technology offer new opportunities to customize personalized TE scaffolds for specific affected areas. Artificial multicellular tissues and organs can be engineered by precisely organizing cells and biomaterials within a 3D structure.[11]

Bioink is a crucial component in bioprinting technology, comprising biological substances (e.g., cells), base-building materials, and other essential components.[12] Notably, bioinks are typically composed of soft materials, and they are required to have favorable biocompatibility, high porosity, and suitable mechanical qualities, along with other biomechanical and biochemical features, for enhancing organ function and tissue structure.[13,14] For secure clinical application, bioinks must be biocompatible, non-toxic to cells, and avoid triggering a strong immune response.[15,16] Bioinks should also facilitate cell adhesion and migration, as well as provide biochemical signals necessary for processes such as differentiation and proliferation.[17–19] Simultaneously, bioinks should offer physical support for cells and possess sufficient mechanical stability for high-resolution printing.[20,21] As scaffolds degrade, most of the bioink is replaced by tissue endogenesis, while a portion of it can be incorporated into the host tissues.[13,22]

Bioinks are normally composed of a combination of cells, extracellular matrix (ECM) proteins, and growth factors (GFs).[23] Pati et al.[24] highlighted that many biomaterials utilized in bioprinting do not fully replicate the complexity of the local ECM, thereby failing to maintain natural cellular function and morphology. A highly promising alternative is decellularized ECM (dECM), which retains the main structure and functionality of the native ECM.[24–26] In 2014, Pati et al. demonstrated the bioprinting of cell-laden structures using cartilage dECM bioink.[24] The printed dECM structure exhibited desirable cell viability and functionality. Furthermore, additional studies have revealed that using dECM bioinks on various tissues, such as the heart,[27,28] muscle,[29,30] cartilage,[31,32] pancreas,[8,33] cornea[8,34], and skin[8,35], yields beneficial effects on cell survival, growth, migration, and differentiation.

However, the decellularization and solubilization process involved in creating dECM bioink can disrupt the ultrastructure of natural ECM, resulting in a significant reduction of ECM components, as well as diminished mechanical properties and biological activity.[36,37] Consequently, the 3D-printed constructs produced with dECM bioinks exhibit inferior mechanical strength compared to native musculoskeletal tissue, potentially leading to tissue integrity damage and mechanical failure.[6] Several studies have incorporated a range of polymers, such as poly(ethylene-co-vinyl acetate) (PEVA) scaffolds[38] and poly(caprolactone) (PCL),[39] and nanoparticles, such as hydroxyapatite[40] and graphene oxide (GO),[41] into dECM bioinks via covalent bonds, as well as hydrophobic and hydrophilic interactions. This process has improved the mechanical and biological properties of the bioink, enabling it to achieve strengths comparable to natural tissue and retain a stable 3D structure. Nevertheless, there are considerable obstacles to overcome in the creation of large-scale tissues and organs. Furthermore, the lack of validation of therapeutic effects in large animal models hinders the clinical application of dECM bioinks.

This review begins with examining the features of dECM biomaterials, detailing the preparation strategy for these biomaterials, and explicating the process of integrating them into 3D bioprintable bioinks. Following this, the review delves into the current progress and applications of dECM bioink in 3D bioprinting of musculoskeletal tissue. Finally, the review addresses current limitations and offers perspectives on potential directions for future research and development.

2. Bioprinting technologies for decellularized extracellular matrix bioinks

Decellularized ECM (dECM) bioink-based bioprinting can be classified according to the working principle into inkjet-based bioprinting, extrusion-based bioprinting, laser-assisted bioprinting (LAB), and stereolithography apparatus (SLA)/digital light processing (DLP)-based bioprinting (Figure 2).[42] Each strategy has its advantages, disadvantages, and limitations (Table 1).

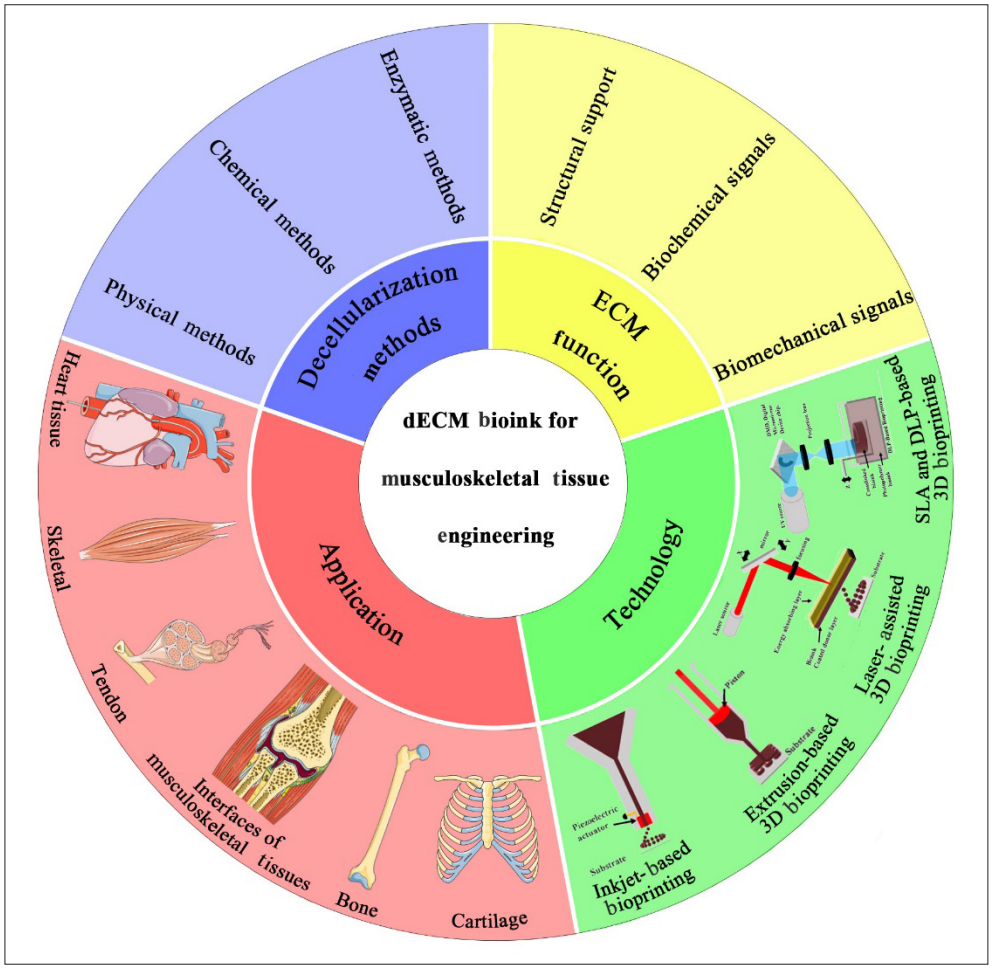


Figure 1. Decellularized extracellular matrix (dECM) bioinks for musculoskeletal tissue engineering. Abbreviations: DLP, digital light processing; ECM, extracellular matrix; SLA, stereolithography apparatus.

2.1. Inkjet-based bioprinting

Inkjet-based bioprinting is derived from conventional two-dimensional (2D) inkjet printing technology.[43,44] In the bioprinting process, the print head, which holds bioinks, is controlled using piezoelectric or digital thermal actuation. This control induces the extrusion of droplets of varying sizes, which are then deposited onto the platform layer-by-layer, facilitating the assembly of the desired 3D structures.[44–46] Inkjet-based bioprinting offers the advantages of high throughput capability, high resolution, relatively low reproducibility cost, and relatively high cell viability (>90%).[46,47] However, inkjet-based bioprinting also has its disadvantages. Thermal inkjet printing can face issues such as nozzle clogging and inconsistent droplet sizes, particularly when using high-viscosity or high-density bioinks.[48] Conversely, piezoelectric bioprinting can disrupt the structure of cell membranes and biomolecules due to the vibration frequency and power level involved.[49]

2.2. Extrusion-based bioprinting

Extrusion-based bioprinting technology is divided into two types: (i) pneumatic and (ii) mechanical systems. The latter can be further categorized into piston or screw types. The bioprinting process utilizes a system to continuously extrude bioink that flows out through a nozzle, forming a filament. Under the control of an automation system, the filament is precisely fabricated into the desired 3D structure.[29,50] Extrusion-based technology has an edge over inkjet printing as it allows for a broader range of biomaterials with different viscosities to be printed. High-viscosity materials provide structural support to printed structures, while low-viscosity materials aid in preserving cell viability and function.[51] However, a potential drawback of extrusion-based bioprinting is the exposure of encapsulated cells to greater shear stress during printing, potentially resulting in poor cell viability and relatively low printing resolutions (i.e., 200–1000 μm).[11,20,52]

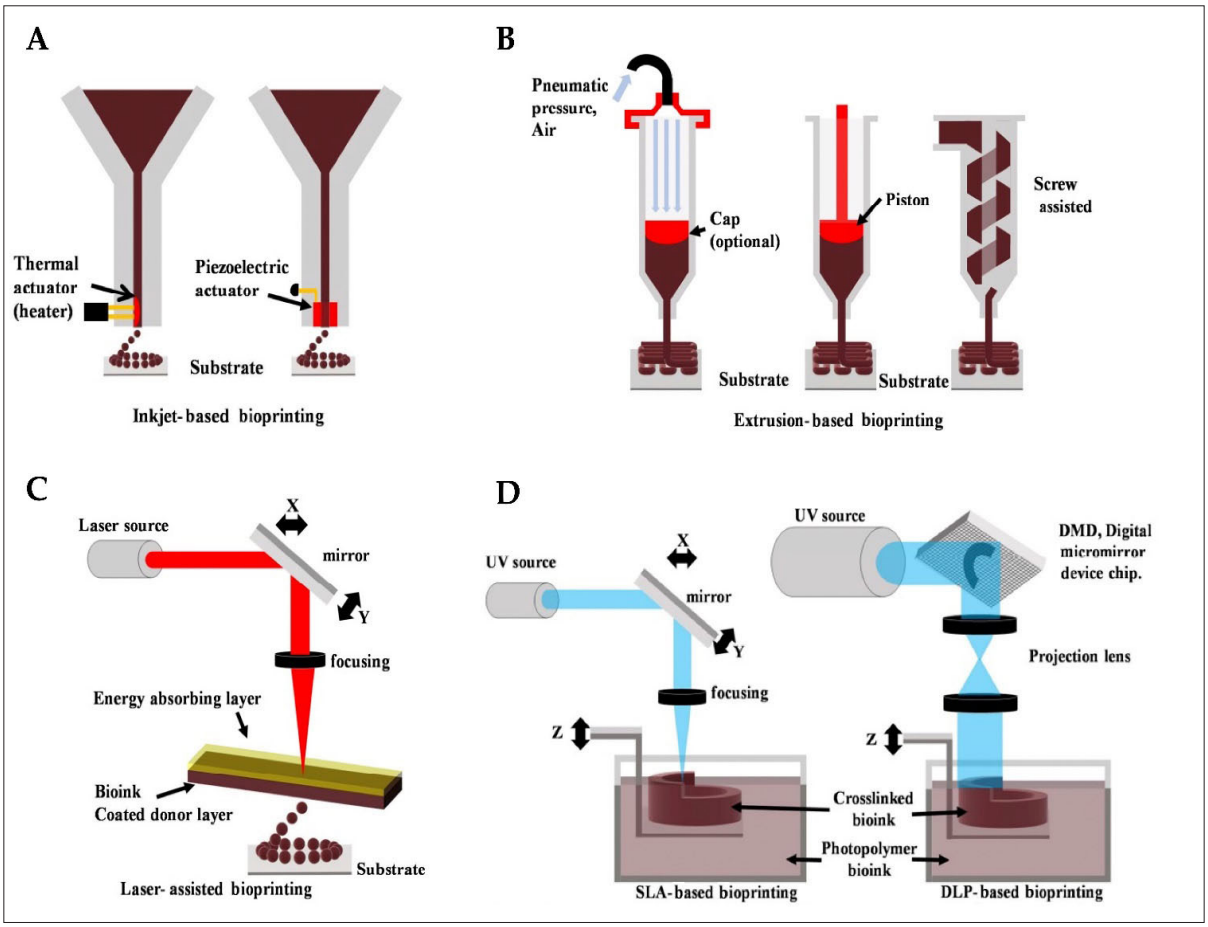


Figure 2. Schematic representations of different 3D bioprinting techniques: (A) inkjet-based bioprinting. (B) Extrusion-based bioprinting strategies. (C) Laser-assisted bioprinting. (D) Stereolithography apparatus (SLA)/digital light processing (DLP)-based bioprinting systems. Abbreviations: digital micromirror device chip (DMD), UV, ultraviolet. Adapted with permission from Matai et al.[11]

2.3. Laser-assisted bioprinting

Laser-assisted bioprinting (LAB) uses laser direct writing[53] or laser-induced forward transfer techniques[54] to print biological materials, such as cells, nucleic acids, and peptides.[55–57] When an incident laser beam is used to apply the energy-absorbing layer at the desired position, it vaporizes the corresponding donor layer below, forming high-pressure bubbles. Subsequently, these bubbles result in material ejection and droplet deposition onto the receiving plate, and the entire process of fabricating the desired 3D structure is regulated by a control system.[11] An advantage of this process is that the bioink and dispenser do not make direct contact with each other. Hence, the cells are not subjected to high shear stress, thereby preventing cellular stress and improving cell viability (>95%).[20] In addition, LAB is a cutting-edge technology that is compatible with various bioinks, accommodating a wide range of viscosities (1–300 mPa/s). Moreover, LAB features automation, reproducibility, and high-throughput capabilities. Nonetheless, the high cost of developing LAB systems, and the complexity of laser printing control systems limit the widespread application of LAB.[58]

2.4. Stereolithography apparatus/digital light processing-based bioprinting

Stereolithography apparatus (SLA)/digital light processing (DLP)-based vat-polymerization techniques use the same layer-by-layer process as traditional 3D bioprinting. The bioprinting process utilizes laser energy to cure bioink by forming covalent bonds between adjacent polymer chains. The laser scans through each layer in a 2D mode, generating complex 3D structures without moving the print head in the *x*–*y* direction. This renders it faster than other nozzle-based bioprinters and is capable of generating intricate structures with high resolution.[59,60] In addition, this technique maintains high cell viability (>85%) by avoiding shear stress on cells.[59,61] A major disadvantage of this approach is the requirement for transparent

Table 1. Advantages and disadvantages of different bioprinting techniques

3D bioprinting technique	Advantages	Disadvantages
Inkjet-based[46-49,63]	Simple; low-cost; high throughput; high resolution (10–100 μm); high cell viability (>90%)	Low cell density; low-viscosity bioinks (3.5–12 mPa/s)
Extrusion-based[38,64,65]	Printable with high-viscosity bioinks (6–30 × 10^7 mPa/s); applicable for multi-material bioprinting; simple	Low printing speed; low printing resolution (200–1000 μm)
Laser-assisted[20,58,66,67]	High cell viability (>95%); wide viscosity range (1–300 mPa/s); high-throughput	High-cost; complex system
Stereolithography apparatus (SLA) and digital light processing (DLP)-based[68,69]	High cell viability (>85%); wide variety of bioinks; high resolution	Bioink must be transparent; complex system

bioinks to ensure uniform crosslinking.[8] Furthermore, bioprinting accuracy and precision depend on factors such as laser power, exposure time, scanning speed, and laser wavelength.[62]

3. Extracellular matrix composition and function

3.1. Components

The tissue's cellular and noncellular components interlace to form a durable composite structure.[70,71] The ECM is densely concentrated with biomacromolecules synthesized and secreted by cells, including collagen, laminin (LN), elastin, glycosaminoglycan, and a variety of cytokines. These ECM components collectively or individually influence cellular behavior. The ECM forms a 3D polymer network on cell surfaces and between cells, facilitating cell interactions through membrane receptors like integrins.[72,13] ECM features high biodegradability, minimal immunogenicity, excellent biocompatibility, and a moderating effect on inflammatory responses. Moreover, ECM is commonly used as a scaffold material in regenerative medicine for its ability to support tissue regeneration and guide tissue repair effectively.[73–76]

3.2. Biological roles of the extracellular matrix

3.2.1. Structural support

The ECM provides cells with a porous 3D structure for cell adhesion, growth, and differentiation.[77] Collagen and fibronectin (FN) in the ECM provide the necessary physical strength and elasticity for cells to maintain their morphology and facilitate migration.[78] The stiffness, porosity, and insolubility of ECM largely determine the tissue structure and integrity and cell behavior within it. Studies have indicated that the ultrastructure and mechanics of the ECM can affect cell behavior, migration, and differentiation. Tightly woven fibrin networks, such as basement membranes, form an apparent barrier for cell migration. Additionally, structural remodeling of ECM can form orientation or "highways" to facilitate cell movement and subsequently affect cell migration. In skeletal muscles, the ECM plays a crucial role by providing a fundamental framework that supports muscle fibers, capillaries, and nerve supplies. Likewise, the ECM's structural integrity is essential for the optimal functioning of muscle tissue.[79]

3.2.2. Biochemical signals

The ECM affects various cellular life activities, such as adhesion, proliferation, migration, differentiation, and homing, by binding and interacting with transmembrane receptors.[80–82] ECM proteins, such as FN, collagen, and proteoglycan (PG), can enhance the binding between cellular receptors and their growth factor ligands.[83,84] For instance, myogenic cells multiply and remain undifferentiated when exposed to FN. Conversely, these cells differentiate and fuse to form myotubes when exposed to LN.[85]

3.2.3. Biomechanical signals

Under different developmental and physiological conditions, the biomechanical properties of the ECM vary greatly depending on its composition and topography. Elasticity of the ECM can vary widely, ranging from soft and pliable to stiff and rigid. This variability significantly impacts cell behavior and tissue function. For example, adipose tissue is soft; muscles are relatively compliant; and bones are stiff and rigid.[86] The ECM can transmit mechanical signals by direct cellular binding or regulating GFs and cytokines.[87,88] Likewise, an increase in matrix stiffness tends to enhance the osteogenic differentiation of mesenchymal stem cells (MSCs), whereas soft matrices tend to induce chondrogenesis and adipogenesis.[89] Studies have demonstrated that applying cyclic uniaxial and circumferential tensile strains to derivatives of human pluripotent stem cells-vascular smooth muscle cells (hPSCs-vSMCs) can induce cell alignment and impact the expression of ECM genes *in vitro*.[90]

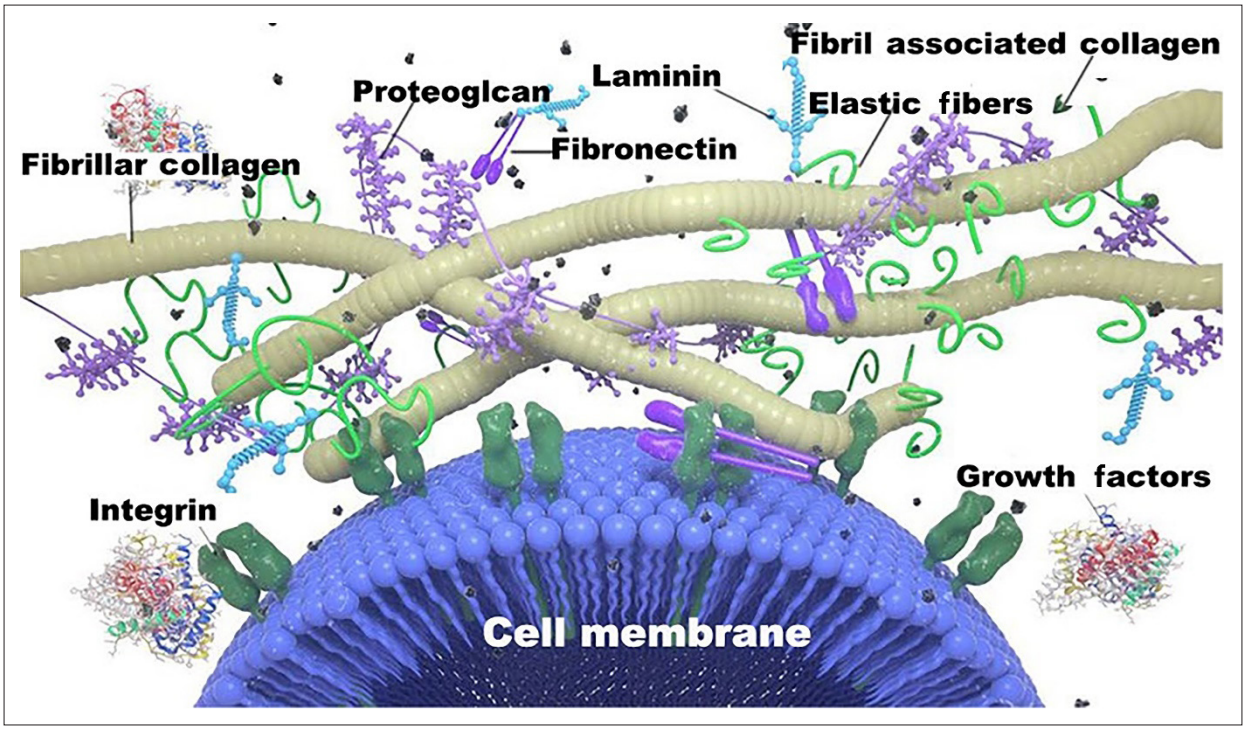


Figure 3. Representative illustration of the composition and cellular interactions of the extracellular matrix (ECM). Adapted with permission from Aamodt and Grainger.[71]

4. Decellularization methods

The decellularization process eliminates cellular and nuclear remnants that may trigger an immune response while preserving inherent ECM components to create a microenvironment suitable for cell development and function.[91] The dECM must fulfill specific requirements for effective migration: <50 ng DNA/mg ECM dry weight; <200 bp DNA fragment length.[91–93] Additionally, the decellularization conditions should be mild to prevent excessive damage to other intrinsic components in the ECM. The dECM can be produced using various decellularization techniques, depending on the tissue type, cell composition, thickness, density, and lipid content. Currently, the commonly used methods can be classified into three categories: physical, chemical, and enzymatic methods.[70] Other procedures, like ultrasound, heating, pressurization, and electroporation, can also be used to achieve decellularization.[94] In this section, we detail the three main decellularization strategies, highlighting the factors that influence the decellularization process, as well as the advantages and disadvantages compared to other methods.

4.1. Physical methods

The basic principle of physical decellularization is to mechanically destroy the cell membrane structure in tissues, resulting in cell death and rupture. Common physical decellularization methods include freeze-thaw cycles, mechanical force, osmosis, high hydrostatic pressure, nonthermal irreversible electroporation (NTIRE), and supercritical fluid extraction.[95–97] Physical decellularization is often unable to completely eliminate cellular and nuclear components following cell destruction, necessitating the washing of tissue to eliminate cell structure and genetic material. Although mechanical techniques have successfully decellularized certain tissues, they are often combined with enzymatic or chemical methods to effectively remove genetic material residues from the scaffold.[95,96,98]

Freeze-thaw cycles are usually used for the decellularization of ligament, tendon tissue, and nerve tissue. Rapid freezing induces the formation of cytoplasmic crystals in cells, leading to cell membrane destruction and lysis.[96,99] Multiple freeze-thaw cycles are necessary for optimal results, with precise regulation of temperature change rates to avoid damaging the ECM's ultrastructure due to freezing.[99] High hydrostatic pressure can also be used to decellularize tissues by directly disrupting the cell membrane, but it is only effective for soft tissues, such as the liver, cornea, lung, and blood vessels.[101,102]

In NTIRE, small electrical pulses are applied to the entire tissue and cells. This process induces potential instability and micropore formation in the cell membrane, leading to the release of intracellular components.[103] While NTIRE is effective in preserving the morphology and integrity of the ECM network, its limited probe size restricts its suitability for decellularizing large tissues or organs.[99]

4.2. Chemical methods

Chemical decellularization is commonly achieved by using chemical agents, such as acids, bases, ions, or non-ionic detergents. These agents promote the hydrolytic degradation of biomolecules and destroy the cell membrane.[96,104] The effectiveness of chemical decellularization depends on factors such as chemical concentration, exposure time, and tissue type.[105]

4.2.1. Acids and bases

Acid–base treatments decellularize the ECM by dissolving cytoplasmic components and degrading nucleic acids (e.g., RNA and DNA). Additionally, acid–base treatments have sterilizing capabilities.[92,96] Acid decellularization agents mainly include acetic acid, peroxyacetic acid (PAA), sulfuric acid, hydrochloric acid, and deoxycholic acid.[92,106,107] Acid decellularization is typically employed to denature ECM proteins, including GAG, collagen, and GFs, resulting in reduced ECM strength. Conversely, the commonly used alkaline reagents are sodium hydroxide, ammonium hydroxide, sodium sulfide, and calcium hydroxide.[92,108] These reagents can denature chromosomal and plasmid DNAs, disrupt the crosslinking of collagen fibers, and completely remove essential biomolecules (e.g., GFs) from the matrix during decellularization, resulting in a significant reduction in mechanical properties of ECM.[20,109]

4.2.2. Detergents

Detergents can be characterized into ionic, nonionic, and zwitterionic types. Ionic detergents efficiently lyse cytoplasmic and nuclear membranes and DNA by disrupting protein–protein junctions.[107] They are commonly used for the decellularization of tissues and organs, including heart,[110] liver,[111] kidney,[112] ovary,[113] and skeletal muscle,[114] with sodium dodecyl sulfate (SDS) being the most frequently used. Although SDS is a very effective decellularizing agent, it may also disrupt the internal structure of the ECM, reduce the content of GAG and essential GFs, and disrupt collagen integrity.[115,116] In contrast, non-ionic detergents (e.g., Triton X-100) destroy inter-lipid and inter-lipid–protein connections while maintaining the integrity of protein–protein connections, making them suitable for maintaining the internal structure of the ECM.[99] Nonionic detergents are more suitable for thinner tissues, and they are often combined with other chemical decellularization protocols to achieve efficient decellularization while preserving biochemical and biomechanical properties.[96,110]

4.3. Enzymatic methods

Enzymatic decellularization involves using proteases (e.g., trypsin), nucleases (e.g., RNase and DNase), lipases, and collagenases to selectively cleave cell adhesion proteins, detach and lyse cells from the surrounding matrix, and disrupt cell adhesion to the ECM.[92,115] Nucleases catalyze the hydrolytic cleavage of deoxyribonucleotides and ribonucleotide chains, fragment RNA or DNA sequences, and facilitate the removal of nucleotides after cell lysis.[92,99]

Although enzymatic treatments are effective in removing cells or cells, they tend to destroy ECM structures, thereby affecting their inherent mechanical strength. Additionally, it is challenging to completely remove cellular components with enzymes. Any residual enzymes in the dECM can hinder cell revascularization, leading to adverse immune responses, such as inflammation and apoptosis.[99] Therefore, enzymes are often used in combination with chemical methods to enhance decellularization efficiency. Yang et al. used a combination of 0.25% trypsin-EDTA and collagenase type II for the initial treatment of cartilage. The treated cartilage was then immersed in a hypotonic buffer, containing 0.5% Triton X-100 and ammonium hydroxide, for effective decellularization, while preserving the bioactive factors.[118]

5. Strategies for preparing decellularized extracellular matrix-based bioinks

The preparation of dECM-based bioinks involves a three-step process: (i) tissue preparation, (ii) tissue decellularizing, and (iii) post-decellularization processing. Tissue preparation involves removing connective tissue, large blood vessels, fat, and other impurities and dividing the tissue into smaller portions. Thereafter, decellularization methods are selected based on tissue characteristics to remove native cells, while preserving the ECM's internal structure and bioactive components. After decellularization, the remaining toxic decellularization agents were removed, and the dECM was subjected to component analysis to verify the absence of cellular components. Subsequently, sterilization was performed to prevent adverse immune reactions.[116,138] Depending on the biochemical and physical properties of dECMs, a variety of sterilization methods can be employed. Peracetic acid and/or ethanol are commonly used for sterilizing dECMs. Alternatively, ultraviolet (UV) light, ethylene oxide, and gamma radiation can also be employed, but they may alter the structure and properties of the dECM.[139] Once the residual reagents are removed and the dECM is sterilized,

the tissues are lyophilized with an instrument, followed by crushing into a powder with a pestle. The final dECM powder is then dissolved and digested in pepsin or urea solution to form a gel for 3D bioprinting.[8,140] Figure 4 illustrates the decellularization of native heart and cartilage tissues into biocompatible bioinks.

Enhancing the functionality of dECM in 3D printing to promote cell function and regeneration involves modifying the dECM bioink to enhance its mechanical strength and biological activity. This is a primary focus in current 3D bioprinting research, typically achieved through chemical and biological crosslinking methods. Many studies have combined dECM bioinks with polymers, such as PCL, polylactic acid-co-glycolic acid (PLGA), poly-L-lactic acid (PLLA), and gelatin methacryloyl (GelMA), to create bioinks with adjustable mechanical properties, strength, and structural stability.[132,137,141,142] In a recent study, researchers prepared a bioink composed of polyvinyl alcohol (PVA) and dECM (PVA/dECM) for meniscal repair. The results indicated an elastic modulus of 0.49 MPa and a stress limit of 2.9 MPa. Compared with traditional dECM bioinks, the bioink composition exhibited superior mechanical properties and printability.[137] GFs (e.g., vascular endothelial growth factor [VEGF]) are added to dECM bioinks to enhance cell adhesion and migration, creating an ideal environment for cell proliferation and differentiation.[36,132] In another study, infrapatellar fat pad adipose-derived stem cells (IPFP-ADSCs) were extracted, and decellularized cartilage ECM (dcECM) was isolated. These were then combined with a temperature-responsive hydrogel to create a bioink. Utilizing this 3D dcECM in combination with an IPFP-ADSC-loaded scaffold has been demonstrated to foster an optimal setting for stem cell proliferation and promote chondrogenic differentiation. This approach significantly enhanced the effectiveness of repairing cartilage defects in rabbits.[143]

6. Application of decellularized extracellular matrix-based bioinks in the bioprinting of musculoskeletal tissue

The morphogenetic factors, cytokines, and GFs in dECM have important functions in dynamic tissue remodeling. Moreover, the unique biochemical properties of tissue-specific dECM make it a highly desirable bioink for the 3D printing of organs and tissues. This technology presents an exciting avenue for tissue and organ regeneration, allowing for the reconstruction of natural tissue structures and the restoration of physiological function.[116]

Therefore, the creation and application of dECM-based bioinks have become a significant focus of research. These bioinks have demonstrated effective implementation in numerous 3D bioprinting applications to produce tissue and organ substitutes. In this section, we outline the progress and various applications of dECM-based bioinks, specifically within the field of 3D bioprinting of musculoskeletal tissues.

6.1. Heart tissue

The heart is a sophisticated organ with a complex structure and regular ejection. In recent years, there has been a yearly increase in the incidence of heart attacks and heart failure, significantly affecting patients' quality of life. Due to the heart's considerable mechanical strength and elasticity, traditional surgical treatments often struggle to fully restore it to its original state. Therefore, TE and 3D bioprinting have become the focus of cardiac regeneration, as they offer new avenues for repairing damaged hearts.[28,144–146]

Pati et al.[24] first investigated decellularized heart extracellular matrix (hdECM) hydrogels as a 3D bioprinting bioink that can be printed without a supporting framework. The expression levels of cardiomyocyte-specific genes, such as fast myosin heavy chain (Myh6) and α-actin (Actn1), validated the positive effect of the hdECM construct on the functional maturation of myoblasts (Figure 5A). However, due to the inadequate mechanical properties of the dECM construct for heart tissue applications, researchers have employed chemical crosslinking and polymer blending to enhance the mechanical properties of dECM bioinks.[120,147,148] Jang et al. explored the curing of hdECM bioinks by vitamin B2- and thermal gelation-induced UV-A (UVA)-crosslinking. The findings demonstrated that the hardness of the construct was significantly enhanced by vitamin B2 and UVA irradiation, resulting in a mechanical strength (15.74 kPa) similar to that of actual heart tissue (10–15 kPa) (Figure 5B).[147] Based on these results, researchers created a 3D-printed pre-vascularized stem cell patch for cardiac repair using dECM bioink loaded with stem cells. In a rat myocardial infarction model, it was observed that this patch facilitated the growth of new muscles and capillaries, thereby enhancing cardiac function (Figure 5C).[120] Yu et al. used GelMA and dECM-based bioinks in DLP-based bioprinting to adjust their mechanical properties. Through modulation of the exposure time to UV light, they were able to fabricate a heart structure that emulated the mechanical properties of native heart tissue, demonstrating superior cardiomyocyte maturation in comparison to a collagen/GelMA hydrogel blend with analogous mechanical properties.[68]

Table 2. Decellularization and digestion strategies used to produce decellularized extracellular matrix (dECM)

Tissue	Subject	Decellularization method	Digestion method	Ref.
Heart	Porcine	SDS; Triton-X 100; deoxycholate	Acetic acid; pepsin	[119]
	Porcine	1% SDS; 1% Triton-X 100	Acetic acid; pepsin	[120, 38, 121]
	Porcine	1% ABAM; 0.01 mM PMSF	DNase; 0.25% trypsin-EDTA	[68]
	Human	HSS; hypotonic solution; 1% SDS	Acetic acid; pepsin	[122]
	Porcine	1% SDS; 1% Triton-X100	5 M Urea; 2 M thiourea; 50 mM DTT; 0.1% SDS in PBS	[41]
	Porcine	1% SDS; 1% DNase; 1 U/mL RNase; Tris-HCl	Pepsin; acetic acid	[123]
	Porcine	1% SDS; 50 U/mL DNase; 1 U/mL RNase A; Tris–HCl; 0.5% Triton X-100; 1% peracetic acid; 4% ethanol	10% Pepsin; 0.5 M acetic acid	[124]
	Porcine	1% SDS; 1% Triton X-100; DPBS containing 1% antibiotic/antimycotic; DNase	0.1% Pepsin; 0.5 M acetic acid	[125]
Skeletal muscle	Porcine	0.25% Trypsin-EDTA; 2% SDS	3 mg/mL Pepsin; 0.1 M HCl	[126]
	Porcine	0.25% Trypsin-EDTA; 0.5% SDS; 0.5% TritonX-100; 0.1% peracetic acid; 4% ethanol	3 mg/mL Pepsin; 0.5 M AA; 0.1 or 0.02 M HA	[127]
	Porcine	0.25% Trypsin; PBS; 50 U/mL type I DNase; 1 U/mL RNase; 10 mM Tris–HCL	0.25% Trypsin; PBS; vigorous agitation	[128]
Tendon	Porcine	0.05% Trypsin; 0.02% EDTA	0.01 M HCl; pepsin; 15% (w/v) NaCl	[129]
Skeleton	Human	0.05% trypsin; 0.02% EDTA; 5% CO_2; 100 IU/mL DPBS-containing penicillin; 100 μg/mL streptomycin	1 mg/mL Pepsin; 0.01N HCl	[130]
	Goat	3.5% PMSF; 1% Triton X-100; protease inhibitor cocktail (0.1% EDTA; 3.5% PMSF; Tris–HCl)	50 U/mL DNase; 1 U/mL RNase; 0.1 mol HCl; 1 mg pepsin; 1 mol NaOH	[131]
	Porcine	0.05% Trypsin; 0.02% EDTA	0.01 M HCl; 1 mg/mL pepsin; 15% (*w/v)* NaCl	[132]
	Rabbit	Freeze-thaw cycles; 0.1% SDS; 0.1% EDTA; DNase I; Tris–HCl; 50 mg/mL BSA buffer	-	[64]
	Porcine	Freeze-thaw cycles; 1% Triton X-100; 1% SDS	200 U/mL DNase I; 0.5 M acetic acid; 30 mg pepsin	[133]
Cartilage	Porcine	Freeze-thaw cycles; 0.25% trypsin-PBS; 3% sodium deoxycholate; 50 U/mL DNase	0.5 M Acetic acid; pepsin; 10 M NaOH	[134]
	Calf	Freeze-thaw cycles; HSS; 0.01% (v/v) Triton X-100; 1% (v/v) SLS; 40% (v/v) ethanol	0.1 M HCl; 1 mg/mL pepsin; 1 M NaOH	[135]
	Porcine	Freezing-thaw cycles; 1% Triton X-100; protease inhibitor; HBSS; 200 U/mL DNase	10 mM Tris–HCL; 1 mM EDTA	[136]
	Goat	0.1% (w/v) EDTA; 3.5% (w/v) PMSF; 1% Triton X-100; Tris–HCl; protease inhibitor cocktail	50 U/mL DNase; 1 U/mL RNase for 12 h; 0.1 mol HCl; 1 mg pepsin; 1 M NaOH	[25]
	Rat	1:1 of 0.25% trypsin to 0.2% type I collagenase; 0.05% EDTA; 3% SDS; 3% Triton X-100	-	[65]
	Rabbit	1% (w/v) SDS/PBS; 0.1% (w/v) EDTA/PBS	Pepsin; 0.01 M HCl; 0.1 M NaOH	[137]

Abbreviations: AA, acetic acid; ABAM, antibiotic-antimycotic; BSA, bovine serum albumin; DPBS, Dulbecco's phosphate-buffered saline; DTT, Dithiothreitol; EDTA, ethylenediamine tetra acetic; HA, hydrochloric acid; HBSS, Hank's balanced salt solution; HSS, hypertonic salt solution; PBS, phosphate-buffered saline; PMSF, phenylmethylsulphonyl fluoride; SDS, sodium dodecyl sulfate; SLS, sodium lauroyl sarcosine.

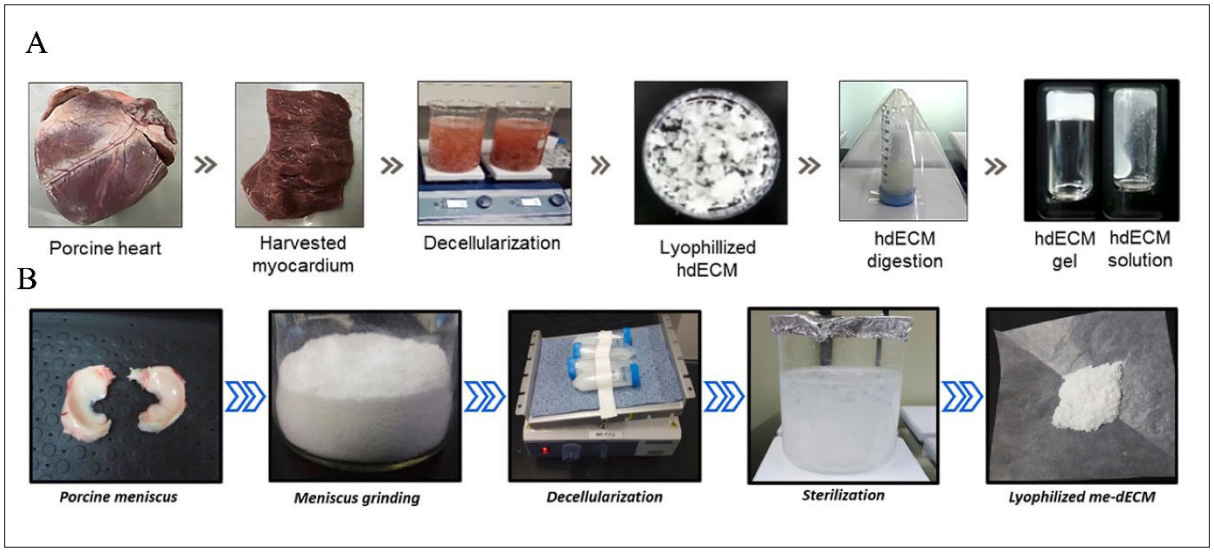


Figure 4. Strategies for preparing decellularized extracellular matrix (dECM) bioinks. (A) Decellularization process of meniscus. Adapted with permission from Das et al.[38] (B) Development of the hdECM bioink. Adapted with permission from Chae et al.[134] Abbreviation: hdECM, decellularized heart extracellular matrix; me-dECM, decellularized meniscus extracellular matrix.

In another study, Shin et al. developed a bioink composed of partially digested hdECM, laponite nanoclay, and poly(ethylene glycol)-diacrylate (PEGDA). The prepared dECM biochain exhibited varying modulus (13.4–89 kPa), viscosity at rest and under flow, extrudability, shape fidelity, and stackability.[27] Sanz-Fraile et al. developed a hydrogel patch (without additional crosslinkers or enhancers) by optimizing ECM digestion, and the patch displayed cell activity in preliminary studies, but its biological effects were not validated in animal models.[149]

The matrix microenvironment and culture conditions play a pivotal role in determining the interactions between cells and the matrix. Das et al. utilized extruded PEVA structures to print hdECM and applied external stimuli outside the engineered heart tissue (EHT) to promote the maturation of encapsulated cardiomyocytes. The results revealed that under dynamic stimulation, the expression of myogenesis-related genes increased, and the cardiomyocytes displayed maturation with improved morphology (Figure 5D).[38]

The electrical properties of scaffolds are as important as their mechanical strength. Tsui et al. developed a hybrid bioink using porcine myocardial dECM, reduced GO (rGO), and liquid polydimethylsiloxane (PDMS).[41] The bioink composition included ECM-based hydrogels for biological signaling, combined with a blend of liquid PDMS and graphite sheets for enhanced electrical conductivity. This results in a hydrogel with electrical conductivity levels 3–10 times greater than those found in native myocardium. Such conductivity can foster cell functionalization and tissue maturation, making it an ideal candidate for cardiovascular drug screening purposes (Figure 5E).[41]

6.2. Skeletal muscle

Skeletal muscle fibers are arranged uniaxially to ensure optimal delivery of nutrients and oxygen for maintaining muscle cell growth and alignment.[150] Despite the remarkable self-repair capacity of skeletal muscles, trauma-induced permanent volume and functional loss can lead to functional impairment, disability, and chronic pain.[8] To treat irreversible muscle damage due to exercise, aging, and disease, a large supply of biocompatible muscle tissue is required. Recently, research on 3D printing technology and decellularized skeletal muscle ECM (mdECM) bioink has attracted much attention. Engineered skeletal muscle tissue that mimics the structure and function of native muscle has been proposed as a viable treatment option for a range of muscle-related ailments and injuries.

Recent advances in 3D bioprinting have facilitated the development of highly ordered biological scaffolds for muscle TE. The capacity to regulate fiber alignment and orientation during the printing process paved the way for the development of functional muscle tissue constructs. Skeletal muscle is constantly contracting and expanding, and the structure should have realistic mechanical properties and anisotropy. Choi et al. utilized an mdECM bioink with encapsulated C2C12 myoblasts to print various types of 3D muscle structures, constraint by PCL at the end of the construct. PCL tension acts as a geometric

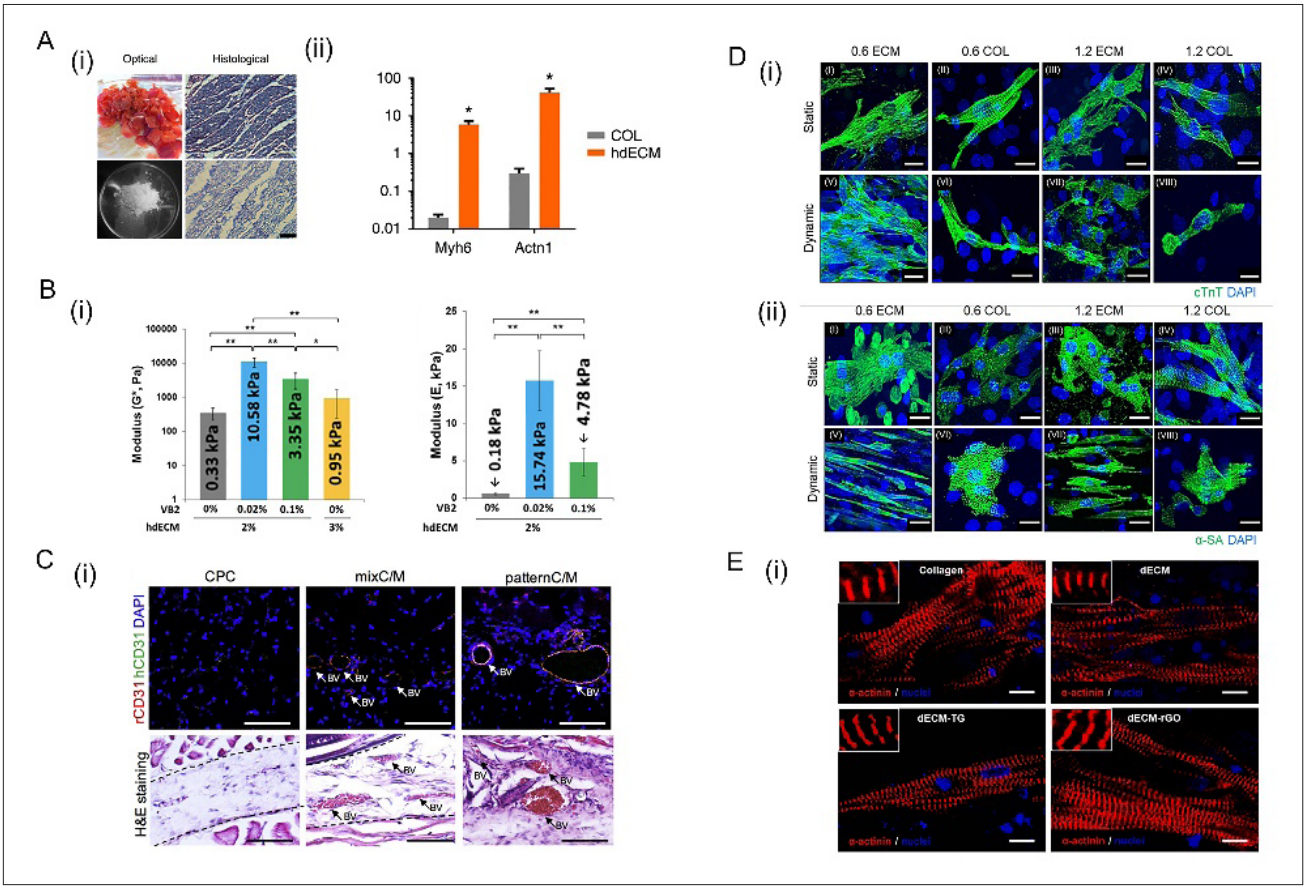


Figure 5. Advancements of the decellularized matrix bioink in heart tissue repairing. (A) Decellularized heart extracellular matrix (hdECM) preparation and its positive effect on the functional maturation of myoblasts: (A, i) decellularization of native heart tissue; (A, ii) gene expression level of fast myosin heavy chain (Myh6) and α-actin (Actn1) in COL and hdECM constructs. Adapted from Pati et al.[24] (B) Mechanical strength of vitamin B2- and thermal gelation-induced ultraviolet A (UVA)-crosslinked hdECM. Adapted with permission from Jang et al.[147] (C) 3D-printed pre-vascularized patch formulation; histological analysis, and immunofluorescence staining results 4 weeks after implantation. Adapted with permission from Jang et al.[120] (D) Expression of myogenic genes in engineered heart tissue (EHT): (D, i) Immunostaining of cardiac troponin T (cTnT) and α-actin (α-SA), synthesized by 0.6% ECM- and 1.2% COL-cultured cardiomyocytes on day 14 of static and dynamic culture. Adapted with permission from Das et al.[38] (E) Sarcomere development in dECM-reduced graphene oxide (rGO) and other hydrogels. Adapted with permission from Tsui et al.[41] Abbreviations: COL, control; (i) only CPCs (CPC, cardiac progenitor cell), (ii) randomly mixed of both CPCs and MSCs (mesenchymal stem cells) with VEGFs (vascular endothelial growth factor) (mixC/M), or (iii) generated patches by patterning of CPCs and MSCs with VEGFs alternatively (patternC/M). H&E, hematoxylin and eosin.

constraint to induce cell alignment in the muscle structure; cell alignment was regulated by changing the printing parameters to adjust the linewidth of the structure. The outcomes of the study demonstrate that mdECM bioink has the potential to offer an optimal myogenic environment for the 3D printing of muscle tissues, promoting myotube formation, differentiation, and maturation.[39]

The fabrication of large tissue structures remains a significant challenge due to the low viscosity, resolution, and mechanical properties of bioink. To address this issue, Choi et al. developed a granule-based printing reservoir for 3D cell printing to enhance the mechanical properties of soft dECM bioinks, while ensuring robust regeneration performance for creating large-volume muscle constructs using soft dECM bioink. They also fabricated a pre-vascularized muscle structure that mimicked the layered structure of vascularized muscle, demonstrating the formation of muscle fibers, vascularization, and enhanced innervation, particularly for treating volumetric muscle loss (VML) (Figure 6A).[124] In another study, researchers utilized a mdECM-methacrylate (MA) bioink along with PVA fibrillation/leaching to develop a tissue construct that mimics cellular skeletal muscle. This unique approach incorporates both biochemical and topographical cues, synergistically enhancing the alignment and differentiation of C2C12 myoblasts into myotubes. This promotes effective

recovery of diseased skeletal muscle tissue with highly consistent myogenic characteristics (Figure 6B).[125]

Additionally, several studies have focused on improving 3D printing and scaffold manufacturing technology to meet clinical needs.[30,151] Researchers have developed a technology for the specific treatment of VML by combining freeform reversible embedding of suspended hydrogels (FRESH) 3D bioprinting with computed tomography (CT), utilizing dECM and collagen-type I bioink to construct large-volume dECM patches with precise control of fiber arrangement (Figure 6C).[151]

6.3. Tendon

The tendon tissue is composed of various cell types, including a dense collagen ECM that connects skeletal muscle to bone and transmits tension during movement. The most dominant cells in the tendon tissue are tenocytes, i.e., specialized fibroblasts that regulate tendon ECM remodeling through their mechanosensory and collagen secretion functions.[152,153] The collagen ECM of tendon tissue is assembled in a layered manner, contributing to its high tensile properties with an ultimate tensile strength of 50–150 MPa.[29,152] Minor tendon fiber ruptures can often heal naturally, but larger injuries require graft implantation for repair or regeneration. Moreover, the regeneration capability of autologous or donor graft implantation repair may be limited with a high risk of re-fracture.[154,155] Despite advancements in regenerative techniques, such as cell therapy, biomaterials, and fine scaffold design, there remains a challenge in achieving artificial tendons with mechanical properties comparable to natural tissues.[156–160] Herein, we review the novel application of tendon dECM bioinks in the 3D printing of tendon tissue for tendon regeneration.

Toprakhisar et al. employed optimized tissue decellularization and solubilization methods to extract a biocompatible dECM bioink with rapid gel kinetics from a bovine Achilles tendon.[161] Studies have demonstrated

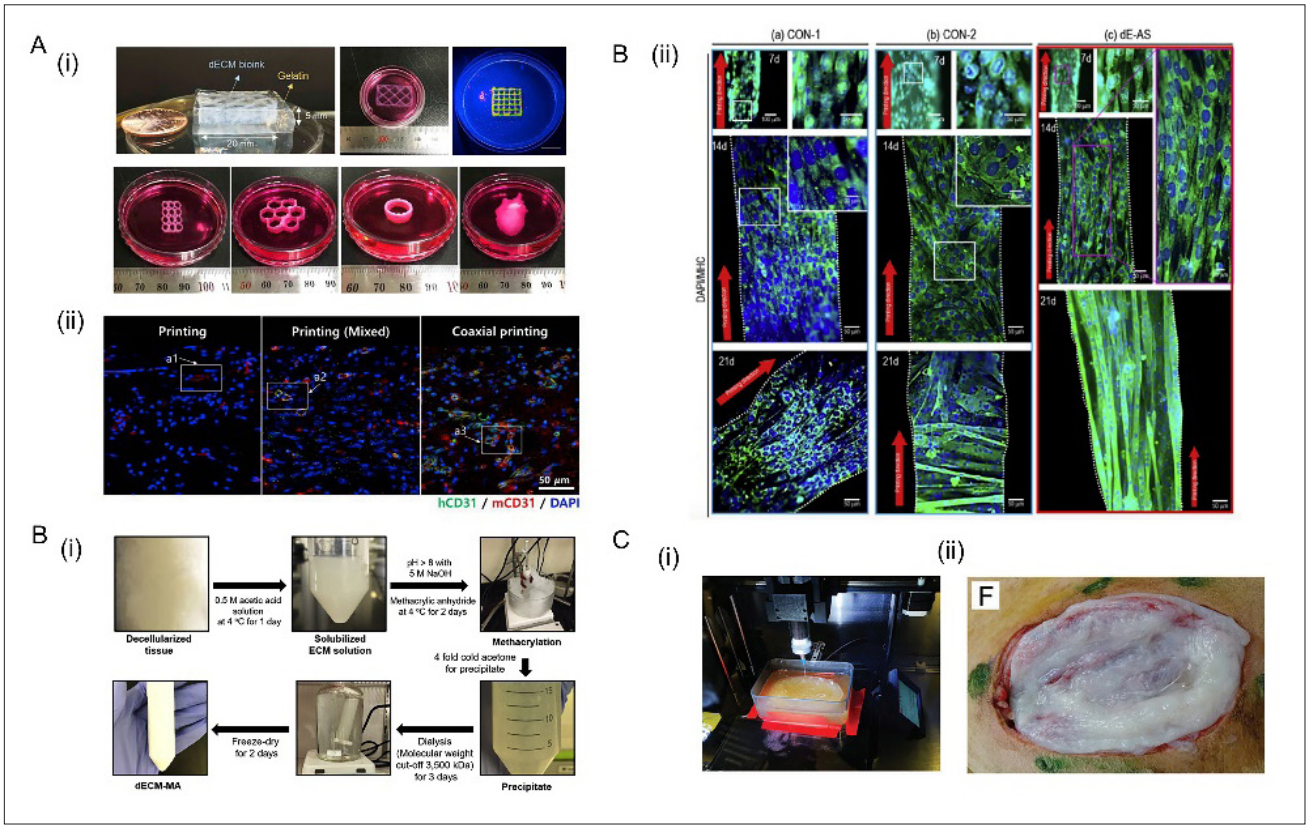


Figure 6. Engineered skeletal muscle tissue with decellularized extracellular matrix (dECM) bioink. (A) 3D cell printing of skeletal muscle construct: (A, i) 3D cell printing of large-volume tissue constructs; (A, ii) vascularization of TA muscles. Adapted with permission from Choi et al.[124] (B) Development of cell-laden dECM-methacrylate (MA) having the aligned structure and *in vitro* myotube formation, and gene expression of cell-loaded structures: (B, i) dECM-MA-based bioink preparation; (ii) DAPI (blue) and MHC (green) images of C2C12 cells in the CON-1, CON-2, and DE-AS group at days 7, 14, and 21. Adapted with permission from Kim et al.[125] (C) Production (C, i) and implantation (C, ii) of 3D-printed freeform reversible embedding of suspended hydrogel (FRESH) dECM patches. Adapted from Pati et al.[24] Abbreviations: DE-AS group, dECM-MA having the aligned structure; MHC, major histocompatibility complex; TA, tibialis anterior.

that the mechanical strength of dECM bioink is affected by its concentration and digestion time. Moreover, the mechanical strength of dECM bioink is reduced at lower dECM concentrations and longer digestion time at 5–10 mg/mL. Researchers have also fabricated tendon structures from tendon dECM bioinks through a unique process involving piston-driven microcapillary extraction-extrusion. This process relied on precise control of temperature and gelatinization time to achieve rapid gel kinetics, without the need for cross-linking agents or scaffolds. Despite exhibiting inferior mechanical properties in comparison to the native tendon tissue, the encapsulated fibroblasts demonstrated lineage-specific morphology. Additionally, it was observed that the application of tendon-derived dECM bioink facilitated the process of tendon-specific differentiation, subsequently promoting tendon tissue regeneration.[161]

To enhance the printability of dECM bioink, Zhao et al. investigated the association between the digestion degree of decellularized tendon ECM (tdECM), obtained from porcine tendons, and bioink printability. The results indicate that the viscosity of tdECM reduces progressively as the digestion time increases. In its less digested form (high-viscosity slurry state), the dECM bioink exhibits superior shape fidelity, stacking accuracy, printability, and cell viability compared to the over-digested dECM bioink (low-viscosity slurry).[126] Additionally, the researchers compared the performance of tdECM bioinks for 3D cell printing using three common acidic solutions (0.5M acetic acid, 0.1M hydrochloric acid, and 0.02M hydrochloric acid). The results revealed that tdECM hydrogels were softer after hydrolysis with 0.1 M hydrochloric acid, which was conducive to the spread, proliferation, and tendon differentiation of the encapsulated stem cells. However, the hydrogels would contract over time and become unstable.[127]

In another study, Chae et al. used tdECM bioink containing MSCs to print implantable tendon structures without a supporting frame in a gelatin granule-based supporting bath. At *in vitro* maturation, tissue-specific dECM promoted long-term preservation of cell viability and tendon production by enhancing cellular/structural anisotropy. The mature 3D-printed tendon tissue structure exhibited excellent regenerative ability after implantation under the skin in nude mice, and the mechanical properties and functions of the new tendon were significantly improved.[162] In another study, researchers proposed a new 3D bioprinting method, using human adipose stem cell (hASC)-laden tdECM bioink, to successfully manufacture cell structures with excellent mechanical stability and complete arrangement of cells. This advancement holds promise as an efficient platform for manufacturing tendon tissues.[163]

6.4. Musculoskeletal tissue interfaces

The musculoskeletal interface is the transition between bone, cartilage, tendons, ligaments, and muscles. The interface is critical for load absorption or metastasis and is susceptible to musculoskeletal disorders.[164,165] Traditional treatments to replace or enhance interfaces through autologous or allogeneic tissue transplantation face challenges such as donor scarcity, disease infection, and immune rejection. Therefore, 3D printing TE has the potential to become a promising and effective alternative for interface regeneration.[164,166,167]

The body's natural ability to self-heal at the bone-tendon/ligament interface is limited, posing a significant clinical challenge for repairing injuries in this area. To address this issue, Liu *et al.* created a biomimetic composite scaffold that mimics the random arrangement of tendons in soft tissue–bone junctions. Their research suggests that this scaffold can enhance the expression of cartilage formation and osteogenesis-related genes (e.g., Jmjd1c, Kdm6b) and promote the formation of both interface bone and fibrocartilage in a rabbit model of anterior cruciate ligament reconstruction (Figure 7A), highlighting the potential of dECM in repairing the bone-tendon interface.[168] However, the tendon-bone interface (TBI) presents structural and compositional gradients through fibrocartilage transition, which has unique structural properties. 3D printing technology offers a promising solution to customize composite scaffolds for different specific positions within this interface.[166,168,169]

Researchers have also used MSC-loaded tdECM and bone dECM (bdECM) bioink to create a spatially graded TBI patch, which reported significantly accelerated and promoted TBI healing in the rat chronic tear model.[166] Chae et al. prepared a heterogeneous structure mimicking TBI to treat rotator cuff (RC) injuries by using pure tdECM, bdECM, and hybrid bioinks (of pure tdECM and bdECM). After implantation, the complex RC regeneration process was observed *in vivo* in real-time by non-destructive, tissue-targeted near-infrared fluorescence imaging (Figure 7B). The results indicate that the implant facilitates efficient recuperation of shoulder motor function and expedites the healing process of TBI *in vivo*. Nonetheless, these studies are constrained by the lack of understanding of the fundamental mechanisms and crucial signaling pathways of ECM bioink for restoring TBI structure and function, as well as the absence of *in vivo* application in large animal models.[166,167]

The muscle-tendon interface plays a crucial physiological function by transmitting the force generated by muscles through tendons to the bone via the muscle-tendon junction (MTJ) to guide movement.[170] However, there is limited research on the use of 3D bioprinting technology to repair the muscle-tendon interface. Kim et al. utilized core collagen hydrogel, collagen bioink, muscle and tendon-derived dECM, and hASC bioinks to fabricate *in vitro* MTJ constructs via modified core-sheath nozzles for 3D bioprinting (Figure 7C). The *in vitro* 3D MTJ models displayed good morphological structure and biochemical characteristics, warranting subsequent developments of MTJ tissue interfaces *in vivo*.[171]

The bone–cartilage interface is often damaged in osteochondral defects, and osteochondral tissue has poor regenerative capacity and is difficult to repair.[40,131,172,173] Yang et al. used decellularized cartilage ECM (cdECM)/alginate and alginate/hydroxyapatite bioinks to reproduce a biphasic graft consisting of cartilage and subchondral bone. *In vitro* tests have reported good fusion between the cartilage and subchondral bone layers for a complete structure. However, the efficacy of *in vivo* implantation has not been verified, and the anisotropic structural properties are lacking.[40] Zhang et al. developed a double-layer scaffold printed from TGF-β1-loaded cartilage dECM/SF (silk fibroin) and BMP-2-loaded bone dECM/SF bioinks. The scaffold reportedly promoted the differentiation of bone marrow MSCs and osteochondral regeneration in rabbit knee joint models (Figure 7D), addressing most of the aforementioned issues except the low mechanical strength.[131] Since the osteochondral interface contains vascularized and avascular zones, the directional establishment of vascularization remains a challenge in osteochondral defect repair. To tackle this issue, Terpstra et al. developed human umbilical vein endothelial cell (HUVEC)-loaded pro-angiogenic and meniscal progenitor cell (MPC)-loaded anti-angiogenic bioinks combined with cartilage dECM and other microfibers (MFs), partitioned through 3D printing, to achieve spatial confinement of new blood vessels. This approach provides a new perspective on anisotropic vascular repair of the osteochondral interface.[174]

6.5. Bone

Bone tissue is composed of different cells, such as bone progenitors, osteoblasts, osteocytes, and osteoclasts. It also contains a rich ECM that provides excellent tensile strength and elasticity to support the body's mechanical activities. In recent years, surgical procedures, such as bone resection, bone grafting, and fracture repair, have made bone tissue the second most transplanted tissue.[1] Bone tissue grafts must possess mechanical strength and biocompatibility to effectively integrate with surrounding natural bone tissues.[4] 3D bioprinting of artificial bones holds great promise for bone TE. The bdECM bioink is highly biocompatible, capable of stimulating osteogenesis differentiation, and can mimic the intricate microenvironment of natural bone tissue. However, this biomaterial faces challenges such as its insufficient mechanical strength, limited vascularization, and susceptibility to degradation, which can result in tissue collapse.[64,130,131,175,176]

Parthiban et al. developed a photo-crosslinked methacrylate bone ECM hydrogel-derived biomaterial (boneMA), which has the ability to promote endothelial cell vasculogenesis, enhance the vascularization function for bone regeneration, and improve bioprintability and mechanical strength. These attributes highlight the potential of boneMA as a promising bioink for 3D printing applications.[130] Lee et al. prepared an alginate (Alg)/MA-dECM composite bioink and optimized its printability and capacity to support cell viability. Compared with pure Alg bioink, the expression levels of the cells loaded with structural osteogenic genes (*ALP*, *BMP2*, *OCN*, and *OPN*) printed by the composite bioink were markedly increased (Figure 8A). However, its mechanical strength (90.4 ± 14.9 MPa) is still lower than that of natural bone tissue.[129] To address this issue, the researchers combined bdECM with various reinforcement substances (e.g., gelatin [GEL],[64] PCL,[177] PLLA,[132] nano-hydroxyapatite [nHAP][178]) for 3D printing to prepare reinforced composite scaffolds (Figure 8B–D).

To improve osteogenic performance, Kang et al. utilized extrusion-based 3D printing to design a hybrid scaffold rich in microchannel network, consisting of dECM, gelatin (Gel), quaternized chitosan (QCS), and nHAP (the scaffold hereafter termed as dGQH). Exosomes (Exos) isolated from human ADSCs were subsequently loaded into the scaffold. The researchers verified the biocompatibility and osteogenic characteristics of the scaffolds with various amounts of nHAP (0%, 20%, 30%, and 40%). The $dGQH_{20}$ scaffold significantly increased the expression of *ALP*, *RUNX2*, and *OCN*. In addition, the $dGQH_{20}$@Exo group also displayed a stronger angiogenic effect than other groups and had good bacteriostatic activity. The dGQH20@Exo scaffold also demonstrated good bone regeneration and vascularization levels in rat models of skull defects. These findings indicate that the composite scaffold has great potential to treat craniofacial bone defects.

6.6. Cartilage

Cartilage is a type of tissue that lacks blood vessels, lymphatics, and nerves. It is mainly composed of

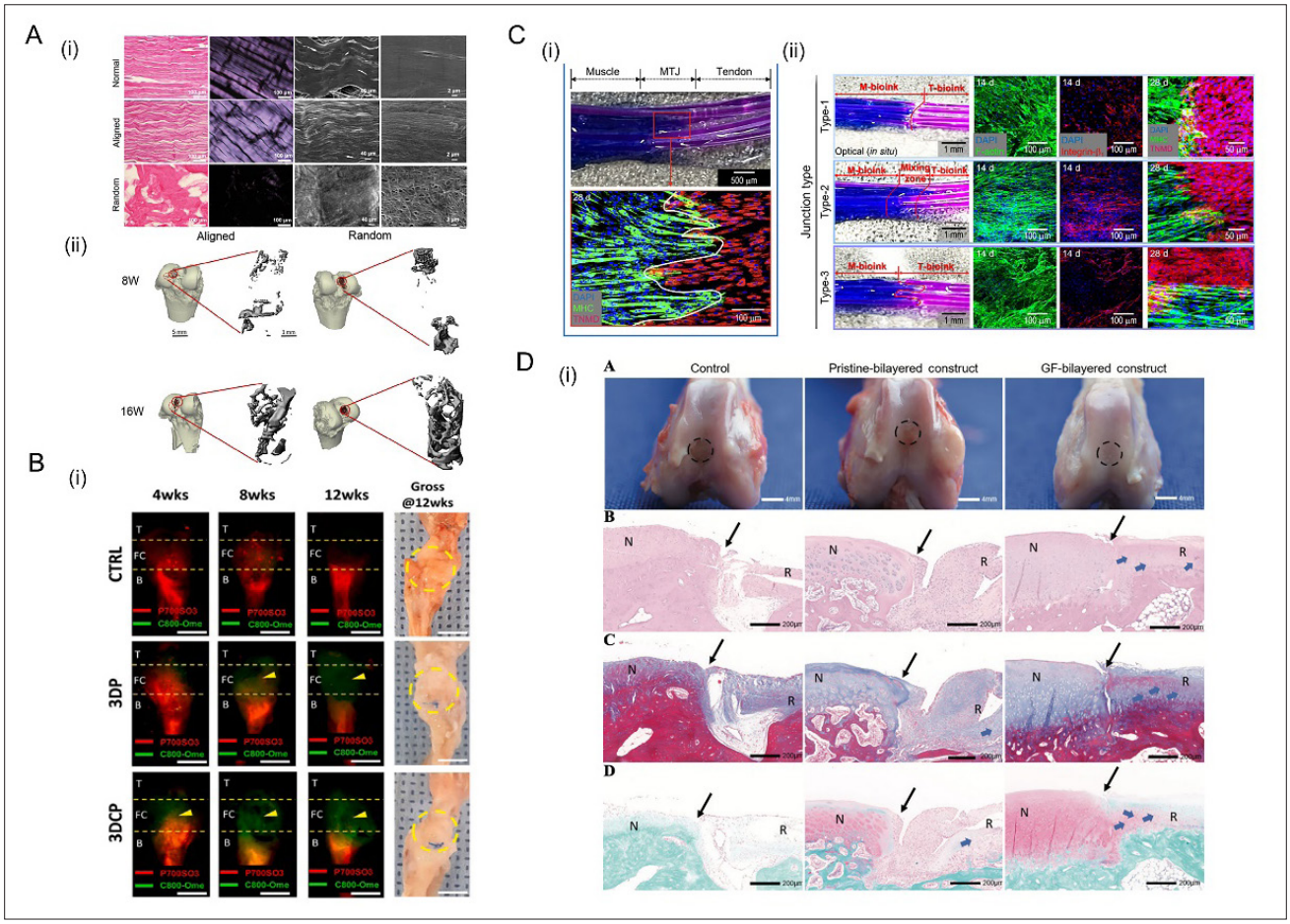


Figure 7. Regeneration of musculoskeletal tissue interfaces with decellularized extracellular matrix (dECM) bioink. (A) Biomimetic random-arranged-random decellularized tendon ECM (tdECM) composite scaffolds: (A, i) Structure of normal tdECM, permutated tdECM, and random tdECM; (A, ii): 3D-reconstruction of the femur after 8 and 16 weeks of scaffold implantation. Adapted with permission from Liu et al.[168] (B) Heterogeneous structure mimicking the tendon-bone interface (TBI): dual-channel near-infrared (NIR) and color images of repaired rotator cuffs in the CTRL, 3DP, and 3DCP groups at 4, 8, and 12 weeks post-operation. Adapted from Chae et al.[167] (C) Construction and characterization of the *in vitro* 3D muscle-tendon junction (MTJ) model[173]: (C, i) optical and DAPI (blue)/myosin heavy chain (MHC; green)/tenomodulin (TNMD; red) images of the bioprinted MTJ unit; (C, ii) optical, F-Actin, integrin-β1, and DAPI/MHC/TNMD (at 14 and 28 days) images for the three types of MTJ interfaces. Adapted from Kim et al.[171] (D) Double-layer scaffold printed from TGF-β1-loaded cartilage dECM/SF and BMP-2-loaded bone dECM/SF bioinks promote osteochondrogenic regeneration in rabbit knee joint models: (D, i) Gross observations (A), H&E staining (B), Masson staining (C), and Safranin-O/fast green staining (D) at 3 months for the control, pristine-bilayered construct (without bioactive growth factors [GFs]), and GF-bilayered construct groups. Adapted from Zhang et al.[131] Abbreviations: no implants (CTRL group), 3D bioprinted construct implantation (3DP group), and 3D cell-printed construct with BMMSCs implantation (3DCP group). Abbreviations: H&E, hematoxylin and eosin; N, normal cartilage; R, repair cartilage.

chondrocytes, which produce ECM, and collagen.[29,179] Trauma, sports injuries, and degenerative joint diseases can cause the cartilage tissue to be damaged and worn. Unfortunately, due to its vascular and neurological properties, cartilage has a very limited ability for self-repair.[24,29] Surgical treatment of cartilage lesions also poses complications such as decreased function and graft failure.[180] The advancement of TE and 3D printing has generated optimism for the restoration and regeneration of cartilage tissue.[133,134] Cartilage-derived dECM (cdECM) bioink is derived from autologous tissue and can regulate cell proliferation, migration, and differentiation, displaying great potential in cartilage tissue repair.[99,181] Herein, we review the recent applications of cdECM bioink in the restoration of cartilage tissue.

Pati et al. developed a cdECM bioink encapsulated with human lower turbinate tissue-derived mesenchymal cells (hTMSCs) and employed PCL as a support material for 3D printing the cartilage tissue structure. Studies have demonstrated that hTMSCs embedded in cdECM bioinks exhibited higher type II collagen and SOX9 expression

compared to the control group of hTMSCs embedded in collagen (Figure 9A). Although the mechanical strength and biological behavior of the constructs were not measured, the potential of cdECM bioinks for cartilage tissue regeneration has been validated.[24,182] Chae et al. developed a computer-aided design (CAD)-based 3D-printed meniscus structure using a blend of polyurethane (PU)-PCL cell-laden meniscal dECM (me-dECM) bioink. The printed constructs displayed excellent mechanical properties and good biocompatibility, promoting the formation of fibrocartilage via proliferation and differentiation. To enhance cell viability, bioprintability, and mechanical properties, researchers have developed various composite dECM bioinks (PVA-A/SDCM [solubilized decellularized cartilage matrix] bioink,[135] cdECM-MA bioinks,[136,183] aptamer-GE [GelMA/DCECM] bioink,[184] PVA/dECM bioink,[137] GelHACS [hyaluronic acid and chondroitin sulfate]-MA bioink[32]) for cartilage bioprinting (Figure 9B).

To mitigate the potential toxicity from bioink crosslinking (ion crosslinking, photocrosslinking, enzyme crosslinking) and preserve cell viability,[147] Yang et al. developed silk fibroin (SF)-dECM bioinks that do not require crosslinkers. Instead, they utilized a method involving PEG to avoid crosslinking agents and leaching processes. The scaffolds prepared from SF-dECM bioink

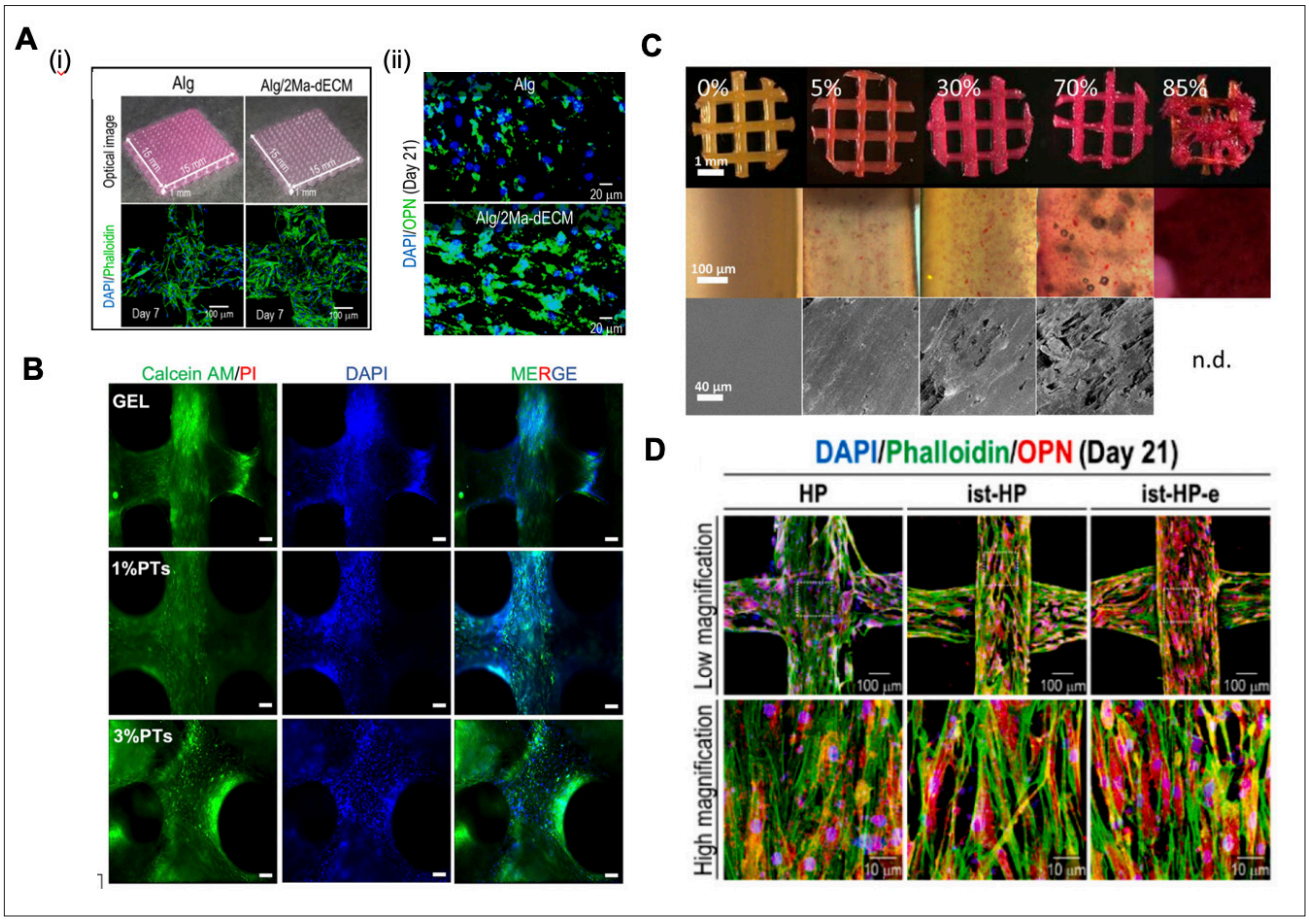


Figure 8. Bone regeneration with decellularized extracellular matrix (dECM) bioink. (A) Alg/MA-dECM composite bioink for bone tissue engineering. (A, i) Optical and DAPI/phalloidin fluorescence images of the Alg and Alg/2Ma-dECM scaffolds after 7 days; (A, ii) Immunofluorescence images of osteopontin in Alg and Alg/2Ma-dECM cells after 21 days of culture. Adapted with permission from Lee et al.[129] (B) GEL composite scaffolds: fluorescence microscopy images of MC3T3 cells cultured for 14 days. Adapted from Kara et al.[64] (C) Images of the 3D-printed hybrid scaffolds comprised of decellularized bone matrix particles combined with poly(caprolactone) (PCL). Adapted from Huang et al.[177] (D) DAPI/phalloidin/OPN staining of hASCs cultured on mixed scaffolds of decellularized bone ECM (dbECM) and HA/PLLA. Adapted with permission from Hwangbo et al.[132] Abbreviations: Alg/MA-dECM, alginate and methacrylated dECM (Ma-dECM) ; GEL, gelatin; HA/PLLA, hydroxyapatite (HA) Poly (L-lactic acid) (PLLA); n.d., no data; HP: HA/PLLA *n situ* plasma-treated nHA/PLLA (is-HP); *In situ* plasma/thermal annealed nHA/PLLA (ist-HP).

have a porous structure, suitable mechanical properties, and degradation properties. Additionally, these scaffolds can promote MSC proliferation, significantly increase the expression of osteogenesis-related genes (Figure 9C), and support cartilage regeneration.[25] However, the local immune response presents a challenge that hinders tissue regeneration. To address this issue, Zhu et al. developed a PEGDA/ECM scaffold containing the natural compound honokiol (Hon). After lipopolysaccharide (LPS) treatment, the PEGDA/ECM/Hon scaffold significantly inhibited the release of pro-inflammatory cytokines (TNF-α, IL-1β, and IL-6) from macrophages compared to the control group with PEGDA/ECM scaffolds. Animal studies demonstrated that PEGDA/ECM/Hon scaffolds significantly enhanced cartilage regeneration.[133] Due to concerns over potential pathogens in animal-derived dECM, researchers have developed a new composite bioink named dSCECMMA. This bioink utilizes decellularized sturgeon cartilage ECM (dSC-ECM), which is highly similar to human collagen. Modified with methacrylate and combined with sericin methacrylate (SerMA), dSCECMMA exhibits good printability and forms a porous structure after light curing. *In vivo* experiments have reported that it effectively promoted the regeneration of cartilage tissue.[185]

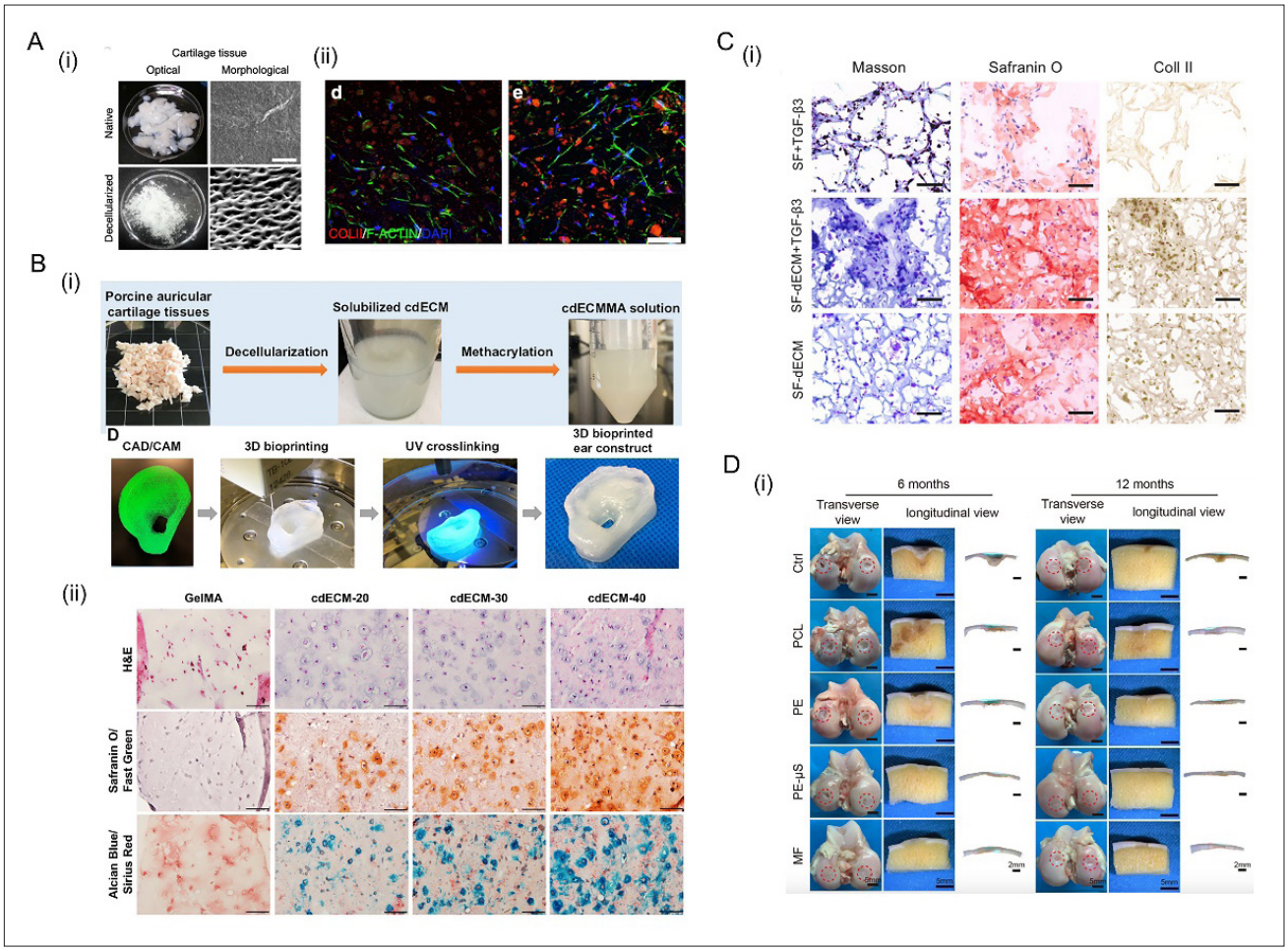


Figure 9. Cartilage regeneration with decellularized extracellular matrix (dECM) bioink. (A) cdECM preparation and positive effect on the functional maturation of hTMSC: (A, i) decellularization of cartilage tissues; (A, ii) immunofluorescence images of human lower turbinate tissue-derived mesenchymal cells (hTMSCs) in COL and decellularized cartilage extracellular matrix (cdECM) constructs. Adapted from Pati et al.[24] (B) Modified composite bioink: (B, i) 3D bioprinting of ear structures using cdECM-methacrylate (MA) bioinks for personalized ear reconstruction; (B, ii) Cartilage tissue formation of cdECM-MA constructs containing rabbit auricle chondrocytes at 28 days after the experiment. Adapted with permission from Visscher et al.[136] (C) Silk fibroin (SF)-dECM bioink without crosslinker: Histological staining and immunohistochemical analysis of collagen type II in the constructs after 28 days of culture. Adapted with permission from Zhang et al.[25] (D) Microenvironment-optimized 3D-printed TGF-β-functionalized scaffolds: histological and immunohistochemical evaluation of the repaired tissues at 6 and 12 months after surgery. Adapted with permission from Yang et al.[186] Abbreviations: H&E, hematoxylin-eosin stainin; CAD/CAM, computer-aided design (CAD) and computer-aided manufacturing (CAM); GelMA, methacrylate gelatin; MF, microfracture; PCL, poly(ε-caprolactone); PLGA, polylactic-coglycolic acid; TGF-β3, transforming growth factor-β3; UV: ultraviolet.

In another study, researchers proposed that healthy regeneration of cartilage relies on dynamic multidimensional microenvironment regulation. They developed a microenvironment-optimized scaffold by using 3D printing inks (i.e., containing cdECM, GelMA, and TGF-β3-embedded microspheres) and PCL. The sustained release of TGF-β3 from the scaffold facilitates cell migration and differentiation, promotes cartilage formation, and demonstrates effective repair in sheep animal models (Figure 9D). However, there is limited research on the regulatory processes and regulators of the cartilage repair process, with current research only focusing on promoting cartilage differentiation and regeneration.[186]

7. Challenges and future perspectives

Based on the biocompatibility of dECM and similarity in composition to natural tissues, dECM-based bioinks have demonstrated outstanding potential in TE of musculoskeletal tissues. Despite advancements in this field, significant challenges and limitations persist that need to be addressed to facilitate their widespread clinical application.[1,140,145,187,188]

7.1. Optimization of decellularized extracellular matrix-based bioinks preparation process

Both decellularization and solubilization processes damage the ultrastructure of the native ECM, significantly reducing its mechanical properties[92,116] and increasing its sensitivity to toxicity and adverse reactions.[25,189] Heterologous dECM contains a variety of bioactive components. However, during the decellularization process, residual cell components, nucleic acids, and decellularizing reagents may cause adverse immune reactions and damage the ECM ultrastructure, resulting in local/systemic reactions.[99,109,115] Conversely, maximum removal of antigens will inevitably lead to ultrastructural damage of the ECM, and the inflammatory response triggered by cell residues, within a certain range, can accelerate tissue repair.[187] Therefore, decellularization techniques should be carefully selected and refined. This involves understanding the composition and structural properties of ECM from different tissue sources, striking a balance between removing cellular components and preserving the ECM structure, and developing standardized decellularization evaluation criteria.[187,190]

In addition, allogically derived dECMs must be sterilized to avoid adverse immune responses, but inappropriate sterilization methods can affect the nature of dECMs, disrupting the structure of tissues and scaffolds.[139,191] For example, ethylene oxide can affect the mechanical properties of dECM and is harmful to cells,[192] while antimicrobial sterilization is difficult to remove and may affect cell behavior.[193,194] Addressing the immunogenicity of dECM, researchers have proposed a series of measures such as crosslinked antigen masking and genome editing.[115] Nevertheless, there remains a need for extensive research to explore suitable sterilization and decellularization protocols tailored to different dECM bioinks.

7.2. Improvement of mechanical properties and printability

Researchers have investigated various techniques to improve the mechanical properties of dECM bioinks, including adding support materials (e.g., PEVA scaffolds,[38] PCL[39]) or crosslinking with other molecules (e.g., vitamin B2,[147] GelMA[68]). Furthermore, the high miscibility of bioinks allows for the incorporation of various nanoparticles, such as hydroxyapatite,[40] GO,[41] cells, GFs,[131] and more, into dECM bioinks through covalent bonding, hydrophobic, and hydrophilic interactions, resulting in enhanced mechanical and biological characteristics. Ongoing research has successfully achieved stable 3D structures. However, challenges still exist in addressing issues such as vascularization, recovery of soft and hard interface partitions, and the precise arrangement of muscle fibers when repairing and regenerating large musculoskeletal tissue defects.[178,195–197]

The regulation of ECM scaffold degradation remains a significant challenge. Rapid degradation can lead to tissue collapse and hinder regeneration. Given the unique nature of the musculoskeletal system, implants are susceptible to degradation and failure, especially under prolonged fatigue stress conditions like exercise.[8] Ongoing research has successfully decreased the degradation rate of dECM by crosslinking it with other substances.[25,178,198] Future studies should focus on extrapolating the findings from implanted scaffolds by assessing the degradation rate of the scaffold over time for further improvement.

To enhance the printability of bioinks, researchers can alter their rheological properties by increasing the dECM concentration or through chemical modification. However, higher bioink viscosity can reduce cell activity due to low oxygen permeability and high shear stress.[187] Therefore, some researchers have explored gelatinized dECM with tissue-specific rheology adjustment, maintaining its flexibility while ensuring printability and shape fidelity.[199] Future research should explore new composite materials to balance the above conflicting needs. In addition to improving bioinks, some researchers have also made advancements in printing techniques and have employed dynamic photoinitiation systems to enhance the printability of low-concentration bioinks.[200]

7.3. Improvement of biological properties and vascular regeneration

To promote the differentiation and regeneration of musculoskeletal tissue, it is crucial to optimize the decellularization process of dECM to preserve the active ingredients. Additionally, the biological properties of dECM bioinks can be improved by crosslinking GFs, adding stem cells, and other methods. Insulin GF-1 (IGF-1) and hepatocyte GF (HGF) are commonly employed to stimulate myogenic differentiation,[201,202] with IGF-1 also demonstrating some capacity to promote chondrogenesis.[203] However, due to the complexity of ECM components and the instability of GFs, it is difficult to determine the impact of the addition of GFs on cell behavior and the specific mechanisms involved.[187] To enhance the differentiation potential of musculoskeletal tissue, MSCs, known for their high self-renewal and differentiation capabilities, are often added to dECM bioinks.[204–206] Likewise, increasing the concentration of dECM bioink improves printability but decreases cell activity. Therefore, it is vital to conduct further research to ensure the preservation of cell activity throughout the bioink printing process.

A poor blood supply restricts essential nutrients and waste products from entering and leaving cells, inhibiting tissue and organ repair and regeneration. The formation and regeneration of blood vessels are particularly important for the repair of VML. However, studies have indicated that the pro-vascularization effect of ECM is weak and cannot meet the needs of regeneration.[207] Combining bioink with angiogenic factors can effectively promote vascularization.[208] However, building functional vascular networks remains a major challenge for 3D printing of musculoskeletal tissues, thereby limiting its clinical application.

8. Conclusion

Based on recent advancements in preparing dECM bioinks and their potential applications in the 3D printing of musculoskeletal tissues, this paper provides a comprehensive review of the research progress in this field in recent years. The discussion encompasses the unique capabilities of dECM bioinks in simulating natural tissues, modulating cell functions, and promoting tissue regeneration through 3D printing techniques. Despite the promising features of dECM bioinks, certain challenges persist in their utilization, including inconsistent decellularization standards, inadequate biological property, and limited vascularization abilities. This review aims to highlight these current challenges with the anticipation that it will stimulate innovative ideas for the refinement and design of dECM bioinks, ultimately enhancing their efficacy in 3D printing musculoskeletal tissues.

Over the past decade, the field of 3D bioprinting has experienced rapid development. The outlook for the future envisions a greater concentration of scientific efforts on integrating advanced and high-end technologies, fostering multidisciplinary collaboration. This collaborative approach, coupled with the utilization of dECM bioinks, is anticipated to facilitate the creation of more intricate and finely-tuned artificial musculoskeletal tissues. Furthermore, the evolution of 3D bioprinting is expected to progress from microscale to macroscale applications, better meeting clinical requirements and enhancing therapeutic outcomes.

Acknowledgments

None.

Funding

This work was supported by the National Natural Science Foundation of China (82302786 and 62306193), the China Postdoctoral Science Foundation (BX20230245 and 2023M742478), the Sichuan Science and Technology Program (2023YFH0068), the Sichuan Province Innovative Talent Funding Proiect for Postdoctoral Fellows(BX202203), the Sichuan University Postdoctoral Interdisciplinary Innovation Fund (JCXK2226), and the Postdoctor Research Fund of West China Hospital, Sichuan University (2023HXBH012).

Conflict of interest

The authors declare they have no competing interests.

Author contributions

Conceptualization: Guosheng Tang, Zongke Zhou, Zeyu Luo
Funding acquisition: Guosheng Tang, Zongke Zhou, Zeyu Luo, Peilin Li
Investigation: Peilin Li, Xixin Li
Supervision: Guosheng Tang, Zongke Zhou, Zeyu Luo
Visualization: Peilin Li, Xixin Li
Writing - Original Draft: Peilin Li, Xixin Li
Writing - Review & Editing: Guosheng Tang, Zongke Zhou, Zeyu Luo

Ethics approval and consent to participate

Not applicable.

Consent for publication

Not applicable.

Availability of data

Not applicable.

References

1. Potyondy T, Uquillas JA, Tebon P, Byambaa B. Recent advances in 3D bioprinting of musculoskeletal tissues. *Biofabrication*. 2021; 13(2):2-3. doi: 10.1088/1758-5090/abc8de
2. Briggs AM, Woolf AD, Dreinhöfer K, et al. Reducing the global burden of musculoskeletal conditions. *Bull World Health Organ*. 2018;96(5):366-368. doi: 10.2471/BLT.17.204891
3. Shibuya N, Jupiter DC. Bone graft substitute: allograft and xenograft. *Clin Podiatr Med Surg*. 2015;32:21-34. doi: 10.1016/j.cpm.2014.09.011
4. Wang MO, Vorwald CE, Dreher ML, et al. Evaluating 3D-printed biomaterials as scaffolds for vascularized bone tissue engineering. *Adv Mater*. 2015;27(1):138-144. doi: 10.1002/adma.201403943
5. Hoffman T, Khademhosseini A, Langer R. Chasing the paradigm: clinical translation of 25 years of tissue engineering. *Tissue Eng Part A*. 2019;25:679-687. doi: 10.1089/ten.TEA.2019.0032
6. Golebiowska AA, Intravaia JT, Sathe VM, Kumbar SG, Nukavarapu SP. Decellularized extracellular matrix biomaterials for regenerative therapies: Advances, challenges and clinical prospects. *Bioact Mater*. 2023;32:98-123. doi: 10.1016/j.bioactmat.2023.09.017
7. Zorlutuna P, Vrana NE, Khademhosseini A. The expanding world of tissue engineering: the building blocks and new applications of tissue engineered constructs. *IEEE Rev Biomed Eng*. 2013;6:47-62. doi: 10.1109/RBME.2012.2233468
8. Zhe M, Wu X, Yu P, et al. Recent advances in decellularized extracellular matrix-based bioinks for 3D bioprinting in tissue engineering. *Materials (Basel)*. 2023;16(8):3197. doi: 10.3390/ma16083197
9. Tao O, Kort-Mascort J, Lin Y, et al. The applications of 3D printing for craniofacial tissue engineering. *Micromachines (Basel)*. 2019;10(7):480. doi: 10.3390/mi10070480
10. Mao AS, Mooney DJ. Regenerative medicine: current therapies and future directions. *Proc Natl Acad Sci U S A*. 2015;112(47):14452-14459. doi: 10.1073/pnas.1508520112
11. Matai I, Kaur G, Seyedsalehi A, McClinton A, Laurencin CT. Progress in 3D bioprinting technology for tissue/organ regenerative engineering. *Biomaterials*. 2020;226: 119536. doi: 10.1016/j.biomaterials.2019.119536
12. Luo Z, Tang G, Ravanbakhsh H, et al. Vertical extrusion cryo(bio)printing for anisotropic tissue manufacturing. *Adv Mater*. 2022;34(12):e2108931. doi: 10.1002/adma.202108931
13. Hospodiuk M, Dey M, Sosnoski D, Ozbolat IT. The bioink: a comprehensive review on bioprintable materials. *Biotechnol Adv*. 2017;35(2):217-239. doi: 10.1016/j.biotechadv.2016.12.006
14. Zhang J, Wehrle E, Adamek P, et al. Optimization of mechanical stiffness and cell density of 3D bioprinted cell-laden scaffolds improves extracellular matrix mineralization and cellular organization for bone tissue engineering. *Acta Biomater*. 2020;114:307-322. doi: 10.1016/j.actbio.2020.07.016
15. Dzobo K, Thomford NE, Senthebane DA, et al. Advances in regenerative medicine and tissue engineering: innovation and transformation of medicine. *Stem Cells Int*. 2018;2018:2495848. doi: 10.1155/2018/2495848
16. Radhakrishnan J, Subramanian A, Krishnan UM, Sethuraman S. Injectable and 3D bioprinted polysaccharide hydrogels: from cartilage to osteochondral tissue engineering. *Biomacromolecules*. 2017;18(1):1-26. doi: 10.1021/acs.biomac.6b01619
17. Ahlfeld T, Mateo NC, Cometta S, Guduric VTN. A novel plasma-based bioink stimulates cell proliferation and differentiation in bioprinted, mineralized constructs. *ACS Appl Mater Interfaces*. 2020;12:12557-12572. doi: 10.1021/acsami.0c00710
18. Cheng L, Yao B, Hu T, et al. Properties of an alginate-gelatin-based bioink and its potential impact on cell migration, proliferation, and differentiation. *Int J Biol Macromol*. 2019;135:1107-1113. doi: 10.1016/j.ijbiomac.2019.06.017
19. Ding S, Feng L, Wu J, et al. Bioprinting of stem cells: interplay of bioprinting process, bioinks, and stem cell properties. *ACS Biomater Sci Eng*. 2018;4(9):3108-3124. doi: 10.1021/acsbiomaterials.8b00399
20. Murphy SV, Atala A. 3D bioprinting of tissues and organs. *Nat Biotechnol*. 2014;32:773-785. doi: 10.1038/nbt.2958
21. Zheng Z, Wu J, Liu M, et al. 3D bioprinting of self-standing silk-based bioink. *Adv Healthc Mater*. 2018;7(6): e1701026. doi: 10.1002/adhm.201701026
22. Rutz AL, Hyland KE, Jakus AE, Burghardt WR, Shah RN. A multimaterial bioink method for 3D printing tunable, cell-compatible hydrogels. *Adv Mater*. 2015;27:1607-1614. doi: 10.1002/adma.201405076

23. Gungor-Ozkerim PS, Inci I, Zhang YS, Khademhosseini A, Dokmeci MR. Bioinks for 3D bioprinting: an overview. *Biomater Sci.* 2018;6:915-946. doi: 10.1039/c7bm00765e

24. Pati F, Jang J, Ha DH, et al. Printing three-dimensional tissue analogues with decellularized extracellular matrix bioink. *Nat Commun*. 2014;5:3935. doi: 10.1038/ncomms4935

25. Zhang X, Liu Y, Luo C, et al. Crosslinker-free silk/decellularized extracellular matrix porous bioink for 3D bioprinting-based cartilage tissue engineering. *Mater Sci Eng C Mater Biol Appl*. 2021;118:111388. doi: 10.1016/j.msec.2020.111388

26. Pati F, Cho DW. Bioprinting of 3D tissue models using decellularized extracellular matrix bioink. *Methods Mol Biol.* 2017;1612:381-390. doi: 10.1007/978-1-4939-7021-6_27

27. Shin YJ, Shafranek RT, Tsui JH, Walcott J, Nelson A, Kim DH. 3D bioprinting of mechanically tuned bioinks derived from cardiac decellularized extracellular matrix. *Acta Biomater*. 2021;119:75-88. doi: 10.1016/j.actbio.2020.11.006

28. Oropeza BP, Adams JR, Furth ME, Chessa J, Boland T. Bioprinting of decellularized porcine cardiac tissue for large-scale aortic models. *Front Bioeng Biotechnol.* 2022;10: 855186. doi: 10.3389/fbioe.2022.855186

29. Park W, Gao G, Cho DW. Tissue-specific decellularized extracellular matrix bioinks for musculoskeletal tissue regeneration and modeling using 3D bioprinting technology. *Int J Mol Sci.* 2021;22(15):7837. doi: 10.3390/ijms22157837

30. Lee J, Lee H, Jin EJ, Ryu D, Kim GH. 3D bioprinting using a new photo-crosslinking method for muscle tissue restoration. *NPJ Regen Med.* 2023;8:18. doi: 10.1038/s41536-023-00292-5

31. Zhu W, Cao L, Song C, Pang Z, Jiang H, Guo C. Cell-derived decellularized extracellular matrix scaffolds for articular cartilage repair. *Int J Artif Organs*. 2021;44(4):269-281. doi: 10.1177/0391398820953866

32. Sang S, Mao X, Cao Y, et al. 3D bioprinting using synovium-derived MSC-Laden photo-cross-linked ECM bioink for cartilage regeneration. *ACS Appl Mater Interfaces.* 2023;15(7):8895-8913. doi: 10.1021/acsami.2c19058

33. Hwang DG, Jo Y, Kim M, et al. A 3D bioprinted hybrid encapsulation system for delivery of human pluripotent stem cell-derived pancreatic islet-like aggregates. *Biofabrication*. 2021;14(1):1-3. doi: 10.1088/1758-5090/ac23ac

34. Kim H, Park MN, Kim J, Jang J, Kim HK, Cho DW. Characterization of cornea-specific bioink: high transparency, improved in vivo safety. *J Tissue Eng*. 2019; 10:2041731418823382. doi: 10.1177/2041731418823382

35. Kim BS, Kwon YW, Kong JS, et al. 3D cell printing of in vitro stabilized skin model and in vivo pre-vascularized skin patch using tissue-specific extracellular matrix bioink: a step towards advanced skin tissue engineering. *Biomaterials*. 2018;168:38-53. doi: 10.1016/j.biomaterials.2018.03.040

36. Yeleswarapu S, Dash A, Chameettachal S, Pati F. 3D bioprinting of tissue constructs employing dual crosslinking of decellularized extracellular matrix hydrogel. *Biomater Adv.* 2023;152:213494. doi: 10.1016/j.bioadv.2023.213494

37. Xu P, Kankala RK, Wang S, Chen A. Decellularized extracellular matrix-based composite scaffolds for tissue engineering and regenerative medicine. *Regen Biomater.* 2014;11:rbad107. doi: 10.1093/rb/rbad107

38. Das S, Kim SW, Choi YJ, et al. Decellularized extracellular matrix bioinks and the external stimuli to enhance cardiac tissue development in vitro. *Acta Biomater*. 2019;95:188-200. doi: 10.1016/j.actbio.2019.04.026

39. Choi YJ, Kim TG, Jeong J, et al. 3D cell printing of functional skeletal muscle constructs using skeletal muscle-derived bioink. *Adv Healthc Mater*. 2016;5(20):2636-2645. doi: 10.1002/adhm.201600483

40. Yang SS, Choi WH, Song B, Jin H. Fabrication of an osteochondral graft with using a solid freeform fabrication system. *Tissue Eng Regener Med.* 2015;12:239-248. doi: 10.1007/s13770-015-0001-y

41. Tsui JH, Leonard A, Camp ND, et al. Tunable electroconductive decellularized extracellular matrix hydrogels for engineering human cardiac microphysiological systems. *Biomaterials*. 2021;272:120764. doi: 10.1016/j.biomaterials.2021.120764

42. Heinrich MA, Liu W, Jimenez A, et al. 3D bioprinting: from Benches to translational applications. *Small*. 2019;15(23):e1805510. doi: 10.1002/smll.201805510

43. Tuan RS, Boland G, Tuli R. Adult mesenchymal stem cells and cell-based tissue engineering. *Arthritis Res Ther*. 2003;5(1):32-45. doi: 10.1186/ar614

44. Singh M, Haverinen HM, Dhagat P, Jabbour GE. Inkjet printing-process and its applications. *Adv Mater.* 2010;22:673-685. doi: 10.1002/adma.200901141

45. Stringer J, Derby B. Formation and stability of lines produced by inkjet printing. *Langmuir.* 2010;26:10365-10372. doi: 10.1021/la101296e

46. Roth EA, Xu T, Das M, Gregory C, Hickman JJ, Boland T. Inkjet printing for high-throughput cell patterning. *Biomaterials*. 2004;25(17):3707-3715. doi: 10.1016/j.biomaterials.2003.10.052

47. Cui X, Gao G, Qiu Y. Accelerated myotube formation using bioprinting technology for biosensor applications. *Biotechnol Lett*. 2013;35:315-321. doi: 10.1007/s10529-012-1087-0

48. Gao Q, He Y, Fu JZ, Liu A, Ma L. Coaxial nozzle-assisted 3D bioprinting with built-in microchannels for nutrients delivery. *Biomaterials*. 2015;61:203-215. doi: 10.1016/j.biomaterials.2015.05.031

49. Ihalainen P, Määttänen A, Sandler N. Printing technologies for biomolecule and cell-based applications. *Int J Pharm*. 2015;494:585-592. doi: 10.1016/j.ijpharm.2015.02.033

50. Kim BS, Das S, Jang J, Cho DW. Decellularized extracellular matrix-based bioinks for engineering tissue- and organ-specific microenvironments. *Chem Rev*. 2020;120:10608-10661. doi: 10.1021/acs.chemrev.9b00808

51. Wang Y, Yuan X, Yao B, Zhu S, Zhu P, Huang S. Tailoring bioinks of extrusion-based bioprinting for cutaneous wound healing. *Bioact Mater*. 2022;17:178-194. doi: 10.1016/j.bioactmat.2022.01.024.

52. Mironov V. Printing technology to produce living tissue. *Expert Opin Biol Ther*. 2003;3:701-704. doi: 10.1517/14712598.3.5.701

53. Chrisey DB. Materials processing: the power of direct writing. *Science*. 2000;289:879-881. doi: 10.1126/science.289.5481.879

54. Bohandy J, Kim BF, Adrian FJ. Metal deposition from a supported metal film using an excimer laser. *J Appl Phys*. 1986;60:1538-1539. doi: 10.1063/1.337287

55. Catros S, Fricain JC, Guillotin B, et al. Laser-assisted bioprinting for creating on-demand patterns of human osteoprogenitor cells and nano-hydroxyapatite. *Biofabrication*. 2011;3(2):025001. doi: 10.1088/1758-5082/3/2/025001

56. Colina M, Serra P, Fernández-Pradas JM, Sevilla L, Morenza JL. DNA deposition through laser induced forward transfer. *Biosens Bioelectron*. 2005;20:1638-1642. doi: 10.1016/j.bios.2004.08.047

57. Dinca V, Kasotakis E, Catherine J, et al.. Directed three-dimensional patterning of self-assembled peptide fibrils. *Nano Lett*. 2008;8(2):538-543. doi: 10.1021/nl072798r

58. Mandrycky C, Wang Z, Kim K, Kim DH. 3D bioprinting for engineering complex tissues. *Biotechnol Adv*. 2016;34: 422-434. doi: 10.1016/j.biotechadv.2015.12.011

59. Paruli EI, Montagna V, García-Soto M, Haupt K, Gonzato C. A general photoiniferter approach to the surface functionalization of acrylic and methacrylic structures written by two-photon stereolithography. *Nanoscale*. 2023;15:2860-2870. doi: 10.1039/d2nr06627k

60. Li W, Wang M, Ma H, et al. Stereolithography apparatus and digital light processing-based 3D bioprinting for tissue fabrication. *iScience*. 2023;26:106039. doi: 10.1016/j.mser.2017.07.001

61. Gauvin R, Chen YC, Lee JW, et al. Microfabrication of complex porous tissue engineering scaffolds using 3D projection stereolithography. *Biomaterials*. 2012;33(15):3824-3834. doi: 10.1016/j.biomaterials.2012.01.048

62. Melchels FP, Feijen J, Grijpma DW. A review on stereolithography and its applications in biomedical engineering. *Biomaterials* 2010;31:6121-6130. doi: 10.1016/j.biomaterials.2010.04.050

63. Peng W, Unutmaz D, Ozbolat IT. Bioprinting towards physiologically relevant tissue models for pharmaceutics. *Trends Biotechnol*. 2016;34:722-732. doi: 10.1016/j.tibtech.2016.05.013

64. Kara A, Distler T, Polley C. et al. 3D printed gelatin/decellularized bone composite scaffolds for bone tissue engineering: fabrication, characterization and cytocompatibility study. *Mater Today Bio*. 2022;15:100309. doi: 10.1016/j.mtbio.2022.100309

65. Isaeva EV, Beketov EE, Demyashkin GA, et al. Cartilage formation in vivo using high concentration collagen-based bioink with MSC and decellularized ECM granules. *Int J Mol Sci*. 2022;23(5):2703. doi: 10.3390/ijms23052703

66. Sorkio A, Koch L, Koivusalo L, et al. Human stem cell based corneal tissue mimicking structures using laser-assisted 3D bioprinting and functional bioinks. *Biomaterials*. 2018;171:57-71. doi: 10.1016/j.biomaterials.2018.04.034

67. Koch L, Deiwick A, Chichkov B. Capillary-like formations of endothelial cells in defined patterns generated by laser bioprinting. *Micromachines (Basel)*. 2021;12(12):1538. doi: 10.3390/mi12121538

68. Yu C, Ma X, Zhu W, et al. Scanningless and continuous 3D bioprinting of human tissues with decellularized extracellular matrix. *Biomaterials*. 2019;194:1-13. doi: 10.1016/j.biomaterials.2018.12.009

69. Chen P, Zheng L, Wang Y, et al. Desktop-stereolithography 3D printing of a radially oriented extracellular matrix/mesenchymal stem cell exosome bioink for osteochondral defect regeneration. *Theranostics*. 2019;9(9):2439-2459. doi: 10.7150/thno.31017

70. Choudhury D, Tun HW, Wang T, Naing MW. Organ-derived decellularized extracellular matrix: a game changer

for bioink manufacturing? *Trends Biotechnol.* 2018;36(8): 787-805.
doi: 10.1016/j.tibtech.2018.03.003

71. Aamodt JM, Grainger DW. Extracellular matrix-based biomaterial scaffolds and the host response. *Biomaterials.* 2016;86:68-82.
doi: 10.1016/j.biomaterials.2016.02.003

72. Huang K, Li Q, Li Y, et al. Cartilage tissue regeneration: the roles of cells, stimulating factors and scaffolds. *Curr Stem Cell Res Ther*. 2018;13(7):547-567.
doi: 10.2174/1574888X12666170608080722

73. Katebifar S, Jaiswal D, Arul MR, et al. Natural polymer-based micronanostructured scaffolds for bone tissue engineering. *Methods Mol Biol*. 2022;2394:669-691.
doi: 10.1007/978-1-0716-1811-0_35

74. Miszuk J, Liang Z, Hu J, et al. An elastic mineralized 3D electrospun PCL nanofibrous scaffold for drug release and bone tissue engineering. *ACS Appl Bio Mater*. 2021;4(4):3639-3648.
doi: 10.1021/acsabm.1c00134

75. Miszuk JM, Hu J, Sun H. Biomimetic nanofibrous 3D materials for craniofacial bone tissue engineering. *ACS Appl Bio Mater.* 2020;3:6538-6545.
doi: 10.1021/acsabm.0c00946

76. Wu YA, Chiu YC, Lin YH, Ho CC, Shie MY, Chen YW. 3D-printed bioactive calcium silicate/poly-ε-caprolactone bioscaffolds modified with biomimetic extracellular matrices for bone regeneration. *Int J Mol Sci*. 2019;20(4):942.
doi: 10.3390/ijms20040942

77. Wei W, Li J, Chen S, et al. In vitro osteogenic induction of bone marrow mesenchymal stem cells with a decellularized matrix derived from human adipose stem cells and in vivo implantation for bone regeneration. *J Mater Chem B.* 2017;5:2468-2482.
doi: 10.1039/c6tb03150a

78. Yi S, Ding F, Gong L, Gu X. Extracellular matrix scaffolds for tissue engineering and regenerative medicine. *Curr Stem Cell Res Ther.* 2017;12:233-246.
doi: 10.2174/1574888x11666160905092513

79. Mahdy MAA. Skeletal muscle fibrosis: an overview. *Cell Tissue Res.* 2019;375:575-588.
doi: 10.1007/s00441-018-2955-2

80. Satyam A, Tsokos MG, Tresback JS, Zeugolis DI, Tsokos GC. Cell derived extracellular matrix-rich biomimetic substrate supports podocyte proliferation, differentiation and maintenance of native phenotype. *Adv Funct Mater.* 2020;30(44):1908752.
doi: 10.1002/adfm.201908752

81. Chan TM, Lin HP, Lin SZ. In situ altering of the extracellular matrix to direct the programming of endogenous stem cells. *Stem Cells.* 2014;32:1989-1990.
doi: 10.1002/stem.1693

82. Navaee F, Renaud P, Kleger A, Braschler T. Highly efficient cardiac differentiation and maintenance by thrombin-coagulated fibrin hydrogels enriched with decellularized porcine heart extracellular matrix. *Int J Mol Sci.* 2023;24(3):2842.
doi: 10.3390/ijms24032842

83. Lu P, Takai K, Weaver VM, Werb Z. Extracellular matrix degradation and remodeling in development and disease. *Cold Spring Harb Perspect Biol*. 2011;3(12): a005058.
doi: 10.1101/cshperspect.a005058

84. Brizzi MF, Tarone G, Defilippi P. Extracellular matrix, integrins, and growth factors as tailors of the stem cell niche. *Curr Opin Cell Biol.* 2012;24:645-651.
doi: 10.1016/j.ceb.2012.07.001

85. Velleman SG. Recent developments in breast muscle myopathies associated with growth in poultry. *Annu Rev Anim Biosci.* 2019;7:289-308.
doi: 10.1146/annurev-animal-020518-115311

86. Yu H, Mouw JK, Weaver VM. Forcing form and function: biomechanical regulation of tumor evolution. *Trends Cell Biol* 2011;21:47-56.
doi: 10.1016/j.tcb.2010.08.015

87. Shih YR, Tseng KF, Lai HY, Lin CH, Lee OK. Matrix stiffness regulation of integrin-mediated mechanotransduction during osteogenic differentiation of human mesenchymal stem cells. *J Bone Miner Res.* 2011;26:730-738.
doi: 10.1002/jbmr.278

88. Gobaa S, Hoehnel S, Roccio M, Negro A, Kobel S, Lutolf MP. Artificial niche microarrays for probing single stem cell fate in high throughput. *Nat Methods*. 2011;8(11):949-955.
doi: 10.1038/nmeth.1732

89. Sart S, Jeske R, Chen X, Ma T, Li Y. Engineering stem cell-derived extracellular matrices: decellularization, characterization, and biological function. *Tissue Eng Part B Rev.* 2020;26:402-422.
doi: 10.1089/ten.TEB.2019.0349

90. Wanjare M, Agarwal N, Gerecht, S. Biomechanical strain induces elastin and collagen production in human pluripotent stem cell-derived vascular smooth muscle cells. *Am J Physiol Cell Physiol.* 2015;309:C271-C281.
doi: 10.1152/ajpcell.00366.2014

91. Crapo PM, Gilbert TW, Badylak SF. An overview of tissue and whole organ decellularization processes. *Biomaterials.* 2011;32(12):3233-3243.
doi: 10.1016/j.biomaterials.2011.01.057

92. Nagata S, Hanayama R, Kawane K. Autoimmunity and the clearance of dead cells. *Cell.* 2010;140(5):619-630.
doi: 10.1016/j.cell.2010.02.014

93. Zheng MH, Chen J, Kirilak Y, Willers C, Xu J, Wood D. Porcine small intestine submucosa (SIS) is not an acellular collagenous matrix and contains porcine DNA: possible

implications in human implantation. *J Biomed Mater Res B Appl Biomater*. 2005;73(1):61-67.
doi: 10.1002/jbm.b.30170

94. Badylak SF, Taylor D, Uygun K. Whole-organ tissue engineering: decellularization and recellularization of three-dimensional matrix scaffolds. *Annu Rev Biomed Eng*. 2011;13:27-53.
doi: 10.1146/annurev-bioeng-071910-124743

95. Buckenmeyer MJ, Meder TJ, Prest TA, Brown BN. Decellularization techniques and their applications for the repair and regeneration of the nervous system. *Methods*. 2020;171:41-61.
doi: 10.1016/j.ymeth.2019.07.023

96. Gilbert TW, Sellaro TL, Badylak SF. Decellularization of tissues and organs. *Biomaterials*. 2006;27:3675-3683.
doi: 10.1016/j.biomaterials.2006.02.014

97. Mendibil U, Ruiz-Hernandez R, Retegi-Carrion S, Garcia-Urquia N, Olalde-Graells B, Abarrategi A. Tissue-specific decellularization methods: rationale and strategies to achieve regenerative compounds. *Int J Mol Sci*. 2020;21(15):5447.
doi: 10.3390/ijms21155447

98. Hung SH, Su CH, Lee FP, Tseng H. Larynx decellularization: combining freeze-drying and sonication as an effective method. *J Voice*. 2013;27:289-294.
doi: 10.1016/j.jvoice.2013.01.018

99. Kim BS, Das S, Jang J, Cho D.-W. Decellularized extracellular matrix-based bioinks for engineering tissue-and organ-specific microenvironments. *Chem Rev*. 2020;120:10608-10661.

100. Nonaka PN, Campillo N, Uriarte JJ, et al. Effects of freezing/thawing on the mechanical properties of decellularized lungs. *J Biomed Mater Res A*. 2014;102(2):413-419.
doi: 10.1002/jbm.a.34708

101. Funamoto S, Nam K, Kimura T, et al. The use of high-hydrostatic pressure treatment to decellularize blood vessels. *Biomaterials*. 2010;31(13):3590-3595.
doi: 10.1016/j.biomaterials.2010.01.073

102. Hashimoto Y, Funamoto S, Sasaki S, et al. Preparation and characterization of decellularized cornea using high-hydrostatic pressurization for corneal tissue engineering. *Biomaterials*. 2010;31(14):3941-3948.
doi: 10.1016/j.biomaterials.2010.01.122

103. Naso F, Gandaglia A. Can heart valve decellularization be standardized? A review of the parameters used for the quality control of decellularization processes. *Front Bioeng Biotechnol*. 2022;10:830899.
doi: 10.3389/fbioe.2022.830899

104. Zubarevich A, Osswald A, Amanov L, et al. Development and evaluation of a novel combined perfusion decellularization heart-lung model for tissue engineering of bioartificial heart-lung scaffolds. *Artif Organs*. 2023;47(3):481-489.
doi: 10.1111/aor.14419

105. Kim YS, Majid M, Melchiorri AJ, Mikos AG. Applications of decellularized extracellular matrix in bone and cartilage tissue engineering. *Bioeng Transl Med*. 2019;4:83-95.
doi: 10.1002/btm2.10110

106. Zhang CY, Fu CP, Li XY, et al. Three-dimensional bioprinting of decellularized extracellular matrix-based bioinks for tissue engineering. *Molecules*. 2022;27(11):3442.
doi: 10.3390/molecules27113442

107. Procházková A, Poláchová M, Dítě J, Netuková M, Studený P. Chemical, physical, and biological corneal decellularization methods: a review of literature. *J Ophthalmol*. 2024;2024:1191462.
doi: 10.1155/2024/1191462

108. Wang B, Qinglai T, Yang Q, et al. Functional acellular matrix for tissue repair. *Mater Today Bio*. 2022;18:100530.
doi: 10.1016/j.mtbio.2022.100530

109. Reing JE, Brown BN, Daly KA, et al. The effects of processing methods upon mechanical and biologic properties of porcine dermal extracellular matrix scaffolds. *Biomaterials*. 2010;31(33):8626-8633.
doi: 10.1016/j.biomaterials.2010.07.083

110. Belviso I, Sacco AM, Cozzolino D, et al. Cardiac-derived extracellular matrix: A decellularization protocol for heart regeneration. *PLoS One*. 2022;17(10):e0276224.
doi: 10.1371/journal.pone.0276224

111. Willemse J, Verstegen MMA, Vermeulen A, et al. Fast, robust and effective decellularization of whole human livers using mild detergents and pressure controlled perfusion. *Mater Sci Eng C Mater Biol Appl*. 2020;108:110200.
doi: 10.1016/j.msec.2019.110200

112. Bongolan T, Whiteley J, Castillo-Prado J, et al. Decellularization of porcine kidney with submicellar concentrations of SDS results in the retention of ECM proteins required for the adhesion and maintenance of human adult renal epithelial cells. *Biomater Sci*. 2022;10(11):2972-2990

113. Alshaikh AB, Padma AM, Dehlin M, et al. Decellularization and recellularization of the ovary for bioengineering applications; studies in the mouse. *Reprod Biol Endocrinol*. 2020;18:75.
doi: 10.1186/s12958-020-00630-y

114. Naik A, Griffin M, Szarko M, Butler PE. Optimizing the decellularization process of an upper limb skeletal muscle; implications for muscle tissue engineering. *Artif Organs*. 2020;44:178-183.
doi: 10.1111/aor.13575

115. Kasravi M, Ahmadi A, Babajani A, et al. Immunogenicity of decellularized extracellular matrix scaffolds: a bottleneck in tissue engineering and regenerative medicine. *Biomater Res*. 2023;27:10.
doi: 10.1186/s40824-023-00348-z

116. Abaci A, Guvendiren M. Designing decellularized extracellular matrix-based bioinks for 3D bioprinting. *Adv Healthc Mater.* 2020;9:e2000734.
doi: 10.1002/adhm.202000734

117. Giraldo-Gomez DM, Leon-Mancilla B, Del Prado-Audelo ML, et al. Trypsin as enhancement in cyclical tracheal decellularization: morphological and biophysical characterization. *Mater Sci Eng C Mater Biol Appl.* 2016;59:930-937.
doi: 10.1016/j.msec.2015.10.094

118. Yang Y, Lin H, Shen H, Wang B, Lei G, Tuan RS. Mesenchymal stem cell-derived extracellular matrix enhances chondrogenic phenotype of and cartilage formation by encapsulated chondrocytes in vitro and in vivo. *Acta Biomater*. 2018;69:71-82.
doi: 10.1016/j.actbio.2017.12.043

119. Liguori GR, Liguori TTA, de Moraes SR, et al. Molecular and biomechanical clues from cardiac tissue decellularized extracellular matrix drive stromal cell plasticity. *Front Bioeng Biotechnol*. 2020;8:520.
doi: 10.3389/fbioe.2020.00520

120. Jang J, Park HJ, Kim SW, et al. 3D printed complex tissue construct using stem cell-laden decellularized extracellular matrix bioinks for cardiac repair. *Biomaterials*. 2017;112: 264-274.
doi: 10.1016/j.biomaterials.2016.10.026

121. Wang X, Pierre V, Liu C, Senapati S, Park PS, Senyo SE. Exogenous extracellular matrix proteins decrease cardiac fibroblast activation in stiffening microenvironment through CAPG. *J Mol Cell Cardiol*. 2021;159:105-119.
doi: 10.1016/j.yjmcc.2021.06.001

122. Mesquita FCP, Morrissey J, Lee P-F, et al. Cues from human atrial extracellular matrix enrich the atrial differentiation of human induced pluripotent stem cell-derived cardiomyocytes. *Biomater Sci.* 2021;9:3737-3749.
doi: 10.1039/d0bm01686a

123. Choi YJ, Park SJ, Yi H-G, et al. Muscle-derived extracellular matrix on sinusoidal wavy surfaces synergistically promotes myogenic differentiation and maturation. *J Mater Chem B.* 2018;6:5530-5539.
doi: 10.1039/c8tb01475b

124. Choi YJ, Jun YJ, Kim DY, et al. A 3D cell printed muscle construct with tissue-derived bioink for the treatment of volumetric muscle loss. *Biomaterials.* 2019;206: 160-169.
doi: 10.1016/j.biomaterials.2019.03.036

125. Kim W, Lee H, Lee J, et al. Efficient myotube formation in 3D bioprinted tissue construct by biochemical and topographical cues. *Biomaterials.* 2020;230:119632.
doi: 10.1016/j.biomaterials.2019.119632

126. Zhao F, Cheng J, Sun M, et al. Digestion degree is a key factor to regulate the printability of pure tendon decellularized extracellular matrix bio-ink in extrusion-based 3D cell printing. *Biofabrication.* 2020;12:045011.
doi: 10.1088/1758-5090/aba411

127. Zhao F, Cheng J, Zhang J, et al. Comparison of three different acidic solutions in tendon decellularized extracellular matrix bio-ink fabrication for 3D cell printing. *Acta Biomater.* 2021;131:262-275.
doi: 10.1016/j.actbio.2021.06.026

128. Zhang X, Song W, Han K, et al. Three-dimensional bioprinting of a structure-, composition-, and mechanics-graded biomimetic scaffold coated with specific decellularized extracellular matrix to improve the tendon-to-bone healing. *ACS Appl Mater Interfaces.* 2023;15:28964-28980.
doi: 10.1021/acsami.3c03793

129. Lee J, Hong J, Kim W, Kim GH. Bone-derived dECM/alginate bioink for fabricating a 3D cell-laden mesh structure for bone tissue engineering. *Carbohydr Polym.* 2020;250:116914.
doi: 10.1016/j.carbpol.2020.116914

130. Parthiban SP, Athirasala A, Tahayeri A, et al. BoneMA-synthesis and characterization of a methacrylated bone-derived hydrogel for bioprinting ofin-vitrovascularized tissue constructs. *Biofabrication.* 2021;13(3):10.1088/1758-5090/abb11f..
doi: 10.1088/1758-5090/abb11f

131. Zhang X, Liu Y, Zuo Q, et al. 3D bioprinting of biomimetic bilayered scaffold consisting of decellularized extracellular matrix and silk fibroin for osteochondral repair. *Int J Bioprint.* 2021;7(4):401.
doi: 10.18063/ijb.v7i4.401

132. Hwangbo H, Lee J, Kim G. Mechanically and biologically enhanced 3D-printed HA/PLLA/dECM biocomposites for bone tissue engineering. *Int J Biol Macromol*. 2022; 218:9-21.
doi: 10.1016/j.ijbiomac.2022.07.040

133. Zhu S, Chen P, Chen Y, Li M, Chen C, Lu H. 3D-printed extracellular matrix/polyethylene glycol diacrylate hydrogel incorporating the anti-inflammatory phytomolecule honokiol for regeneration of osteochondral defects. *Am J Sports Med*. 2020;48(11):2808-2818.
doi: 10.1177/0363546520941842

134. Chae S, Lee SS, Choi YJ, et al. 3D cell-printing of biocompatible and functional meniscus constructs using meniscus-derived bioink. *Biomaterials*. 2021;267:120466.
doi: 10.1016/j.biomaterials.2020.120466

135. Setayeshmehr M, Hafeez S, van Blitterswijk C, Moroni L, Mota C, Baker MB. Bioprinting via a dual-gel bioink based on poly(vinyl alcohol) and solubilized extracellular matrix towards cartilage engineering. *Int J Mol Sci*. 2021;22(8):3901.
doi: 10.3390/ijms22083901

136. Visscher DO, Lee H, van Zuijlen PPM, et al. A photo-crosslinkable cartilage-derived extracellular matrix bioink

for auricular cartilage tissue engineering. *Acta Biomater*. 2021;121:193-203.
doi: 10.1016/j.actbio.2020.11.029

137. Lu J, Huang J, Jin J, et al. The design and characterization of a strong bio-ink for meniscus regeneration. *Int J Bioprint*. 2022;8(4):600.
doi: 10.18063/ijb.v8i4.600

138. Nouri Barkestani M, Naserian S, Uzan G, Shamdani S. Post-decellularization techniques ameliorate cartilage decellularization process for tissue engineering applications. *J Tissue Eng*. 2021;12:2041731420983562.
doi: 10.1177/2041731420983562

139. McInnes AD, Moser MAJ, Chen X. Preparation and use of decellularized extracellular matrix for tissue engineering. *J Funct Biomater*. 2022;13(4):240.
doi: 10.3390/jfb13040240

140. Al-Hakim Khalak F, García-Villén F, Ruiz-Alonso S, Pedraz JL, Saenz-Del-Burgo L. Decellularized extracellular matrix-based bioinks for tendon regeneration in three-dimensional bioprinting. *Int J Mol Sci*. 2022;23(21):12930.
doi: 10.3390/ijms232112930

141. Li S, Liu Z, Gao X, et al. Preparation and properties of a 3D printed nHA/PLA bone tissue engineering scaffold loaded with a β-CD-CHX combined dECM hydrogel. *RSC Adv*. 2024;14:9848-9859.
doi: 10.1039/d4ra00261j

142. Hussain Z, Ding P, Zhang L, Zhang Y. Multifaceted tannin crosslinked bioinspired dECM decorated nanofibers modulating cell-scaffold biointerface for tympanic membrane perforation bioengineering. *Biomed Mater* 2022;17(3):1.
doi: 10.1088/1748-605X/ac6125

143. Wu J, Han Y, Fu Q, et al. Application of tissue-derived bioink for articular cartilage lesion repair. *Chem Eng J*. 2022;450:8-9.
doi: 10.1016/j.cej.2022.138292

144. Yoo SJ, Hussein N, Peel B, et al. 3D modeling and printing in congenital heart surgery: entering the stage of maturation. *Front Pediatr*. 2021;9:621672.
doi: 10.3389/fped.2021.621672

145. Zhe M, Wu X, Yu P, et al. Recent advances in decellularized extracellular matrix-based bioinks for 3D bioprinting in tissue engineering. *Materials (Basel)*. 2023;16(8):3197.
doi: 10.3390/ma16083197

146. Xiang Y, Miller K, Guan J, Kiratitanaporn W, Tang M, Chen S. 3D bioprinting of complex tissues in vitro: state-of-the-art and future perspectives. *Arch Toxicol*. 2022;96(3):691-710.
doi: 10.1007/s00204-021-03212-y

147. Jang J, Kim TG, Kim BS, Kim SW, Kwon SM, Cho DW. Tailoring mechanical properties of decellularized extracellular matrix bioink by vitamin B2-induced photo-crosslinking. *Acta Biomater*. 2016;33:88-95.
doi: 10.1016/j.actbio.2016.01.013

148. Sung K, Patel NR, Ashammakhi N, Nguyen KL. 3-Dimensional bioprinting of cardiovascular tissues: emerging technology. *JACC Basic Transl Sci*. 2021;6: 467-482.
doi: 10.1016/j.jacbts.2020.12.006

149. Sanz-Fraile H, Herranz-Diez C, Ulldemolins A, et al. Characterization of bioinks prepared via gelifying extracellular matrix from decellularized porcine myocardia. *Gels*. 2023;9(9):745.
doi: 10.3390/gels9090745

150. Ostrovidov S, Hosseini V, Ahadian S, et al. Skeletal muscle tissue engineering: methods to form skeletal myotubes and their applications. *Tissue Eng Part B Rev*. 2014;20(5): 403-436.
doi: 10.1089/ten.TEB.2013.0534

151. Behre A, Tashman JW, Dikyol C, et al. 3D bioprinted patient-specific extracellular matrix scaffolds for soft tissue defects. *Adv Healthc Mater*. 2022;11(24):e2200866.
doi: 10.1002/adhm.202200866

152. Wang D, Zhang X, Huang S, et al. Engineering multi-tissue units for regenerative medicine: bone-tendon-muscle units of the rotator cuff. *Biomaterials*. 2021;272:120789.
doi: 10.1016/j.biomaterials.2021.120789

153. Yoshimoto Y, Oishi Y. Mechanisms of skeletal muscle-tendon development and regeneration/healing as potential therapeutic targets. *Pharmacol Ther*. 2023;243:108357.
doi: 10.1016/j.pharmthera.2023.108357

154. Xu Y, Murrell GA. The basic science of tendinopathy. *Clin Orthop Relat Res*. 2008;466:1528-1538.
doi: 10.1007/s11999-008-0286-4

155. Andres BM, Murrell GA. Treatment of tendinopathy: what works, what does not, and what is on the horizon. *Clin Orthop Relat Res*. 2008;466:1539-1554.
doi: 10.1007/s11999-008-0260-1

156. Lui PP. Stem cell technology for tendon regeneration: current status, challenges, and future research directions. *Stem Cells Cloning*. 2015;8:163-174.
doi: 10.2147/sccaa.S60832

157. Migliorini F, Tingart M, Maffulli N. Progress with stem cell therapies for tendon tissue regeneration. *Expert Opin Biol Ther*. 2020;20:1373-1379.
doi: 10.1080/14712598.2020.1786532

158. No YJ, Castilho M, Ramaswamy Y, Zreiqat, H. Role of biomaterials and controlled architecture on tendon/ligament repair and regeneration. *Adv Mater*. 2020;32:e1904511.
doi: 10.1002/adma.201904511

159. Liu Y., Ramanath HS, Wang DA. Tendon tissue engineering using scaffold enhancing strategies. *Trends Biotechnol*. 2008;26:201-209.
doi: 10.1016/j.tibtech.2008.01.003

160. Anjum S, Li T, Saeed M, Ao Q. Exploring polysaccharide and protein-enriched decellularized matrix scaffolds for

tendon and ligament repair: a review. *Int J Biol Macromol*. 2024;254:127891.
doi: 10.1016/j.ijbiomac.2023.127891

161. Toprakhisar B, Nadernezhad A, Bakirci E, Khani N, Skvortsov GA, Koc B. Development of bioink from decellularized tendon extracellular matrix for 3d bioprinting. *Macromol Biosci*. 2018;18(10):e1800024.
doi: 10.1002/mabi.201800024

162. Chae S, Choi YJ, Cho DW. Mechanically and biologically promoted cell-laden constructs generated using tissue-specific bioinks for tendon/ligament tissue engineering applications. *Biofabrication.* 2022;14(2):025013.
doi: 10.1088/1758-5090/ac4fb6

163. Kim D, Kim GH. Bioprinted hASC-laden cell constructs with mechanically stable and cell alignment cue for tenogenic differentiation. *Biofabrication.* 2023;15(4):1.
doi: 10.1088/1758-5090/ace740

164. Balestri W, Morris RH, Hunt JA, Reinwald Y. Current advances on the regeneration of musculoskeletal interfaces. *Tissue Eng Part B Rev.* 2021;27:548-571.
doi: 10.1089/ten.TEB.2020.0112

165. Bonnevie ED, Mauck RL. Physiology and engineering of the graded interfaces of musculoskeletal junctions. *Annu Rev Biomed Eng.* 2018;20:403-429.
doi: 10.1146/annurev-bioeng-062117-121113

166. Chae S, Sun Y, Choi YJ, Ha DH, Jeon I, Cho DW. 3D cell-printing of tendon-bone interface using tissue-derived extracellular matrix bioinks for chronic rotator cuff repair. *Biofabrication*. 2021;13(3):1-2,27.
doi: 10.1088/1758-5090/abd159

167. Chae S, Yong U, Park W, et al. 3D cell-printing of gradient multi-tissue interfaces for rotator cuff regeneration. *Bioact Mater*. 2022;19:611-625.
doi: 10.1016/j.bioactmat.2022.05.004

168. Liu H, Yang L, Zhang E, et al. Biomimetic tendon extracellular matrix composite gradient scaffold enhances ligament-to-bone junction reconstruction. *Acta Biomater*. 2017;56:129-140.
doi: 10.1016/j.actbio.2017.05.027

169. Shengnan Q, Bennett S, Wen W, Aiguo L, Jiake X. The role of tendon derived stem/progenitor cells and extracellular matrix components in the bone tendon junction repair. *Bone*. 2021;153:116172.
doi: 10.1016/j.bone.2021.116172

170. Tong S, Sun Y, Kuang B, et al. A comprehensive review of muscle-tendon junction: structure, function, injury and repair. *Biomedicines*. 2024;12(2):423.
doi: 10.3390/biomedicines12020423

171. Kim WJ, Kim GH. A bioprinted complex tissue model for myotendinous junction with biochemical and biophysical cues. *Bioeng Transl Med*. 2022;7(3):e10321.
doi: 10.1002/btm2.10321

172. Badar W, Ali H, Brooker ON, et al. Collagen pre-strain discontinuity at the bone-Cartilage interface. *PLoS One*. 2022;17(9):e0273832.
doi: 10.1371/journal.pone.0273832

173. Xu J, Ji J, Jiao J, et al. 3D printing for bone-cartilage interface regeneration. *Front Bioeng Biotechnol*. 2022;10:828921.
doi: 10.3389/fbioe.2022.828921

174. Terpstra ML, Li J, Mensinga A, et al. Bioink with cartilage-derived extracellular matrix microfibers enables spatial control of vascular capillary formation in bioprinted constructs. *Biofabrication*. 2022;14(3).
doi: 10.1088/1758-5090/ac6282

175. Zhang Y, Wu D, Zhao X, et al. Stem cell-friendly scaffold biomaterials: applications for bone tissue engineering and regenerative medicine. *Front Bioeng Biotechnol*. 2020;8:598607.
doi: 10.3389/fbioe.2020.598607

176. Kim D, Lee H, Lee GH, Hoang TH, Kim HR, Kim GH. Fabrication of bone-derived decellularized extracellular matrix/ceramic-based biocomposites and their osteo/odontogenic differentiation ability for dentin regeneration. *Bioeng Transl Med*. 2022;7(3):e10317.
doi: 10.1002/btm2.10317

177. Hung BP, Naved BA, Nyberg EL, et al. Three-dimensional printing of bone extracellular matrix for craniofacial regeneration. *ACS Biomater Sci Eng*. 2016;2(10):1806-1816.
doi: 10.1021/acsbiomaterials.6b00101

178. Kang Y, Xu J, Meng L, et al. 3D bioprinting of dECM/Gel/QCS/nHAp hybrid scaffolds laden with mesenchymal stem cell-derived exosomes to improve angiogenesis and osteogenesis. *Biofabrication*. 2023;15(2).
doi: 10.1088/1758-5090/acb6b8.

179. Lammi MJ, Piltti J, Prittinen J, Qu C. Challenges in fabrication of tissue-engineered cartilage with correct cellular colonization and extracellular matrix assembly. *Int J Mol Sci*. 2018;19(9):2700.
doi: 10.3390/ijms19092700

180. Ahmed TA, Hincke MT. Strategies for articular cartilage lesion repair and functional restoration. *Tissue Eng Part B Rev.* 2010;16:305-329.
doi: 10.1089/ten.TEB.2009.0590

181. Hogan KJ, Öztatlı H, Perez MR, et al. Development of photoreactive demineralized bone matrix 3D printing colloidal inks for bone tissue engineering. *Regen Biomater*. 2023;10:rbad090.
doi: 10.1093/rb/rbad090

182. Yuan Z, Lyu Z, Liu X, Zhang J, Wang Y. Mg-BGNs/DCECM composite scaffold for cartilage regeneration: a preliminary in vitro study. *Pharmaceutics*. 2021;13(10):1550.
doi: 10.3390/pharmaceutics13101550

183. Behan K, Dufour A, Garcia O, Kelly D. Methacrylated cartilage ECM-based hydrogels as injectables and bioinks

for cartilage tissue engineering. *Biomolecules*. 2022; 12(2):216.
doi: 10.3390/biom12020216

184. Yang Z, Zhao T, Gao C, et al. 3D-bioprinted difunctional scaffold for in situ cartilage regeneration based on aptamer-directed cell recruitment and growth factor-enhanced cell chondrogenesis. *ACS Appl Mater Interfaces*. 2021;13(20):23369-23383

185. Meng X, Zhou Z, Chen X, et al. A sturgeon cartilage extracellular matrix-derived bioactive bioink for tissue engineering applications. *Int J Bioprint*. 2023;9(5):768.
doi: 10.18063/ijb.768

186. Yang Z, Cao F, Li H, et al. Microenvironmentally optimized 3D-printed TGFβ-functionalized scaffolds facilitate endogenous cartilage regeneration in sheep. *Acta Biomater.* 2022;150:181-198.
doi: 10.1016/j.actbio.2022.07.029

187. Zhang H, Wang Y, Zheng Z, et al. Strategies for improving the 3D printability of decellularized extracellular matrix bioink. *Theranostics*. 2023;13(8):2562-2587.
doi: 10.7150/thno.81785

188. Seok JM, Ahn M, Kim D, Lee JS. Decellularized matrix bioink with gelatin methacrylate for simultaneous improvements in printability and biofunctionality. *Int J Biol Macromol.* 2024;262:130194.
doi: 10.1016/j.ijbiomac.2024.130194

189. Won JY, Lee MH, Kim MJ, et al. A potential dermal substitute using decellularized dermis extracellular matrix derived bio-ink. *Artif Cells Nanomed Biotechnol*. 2019;47(1): 644-649.
doi: 10.1080/21691401.2019.1575842

190. Tan YH, Helms HR, Nakayama KH. Decellularization strategies for regenerating cardiac and skeletal muscle tissues. *Front Bioeng Biotechnol*. 2022;10:831300.
doi: 10.3389/fbioe.2022.831300

191. Saldin LT, Cramer MC, Velankar SS, White LJ, Badylak SF. Extracellular matrix hydrogels from decellularized tissues: structure and function. *Acta Biomater*. 2017;49:1-15.
doi: 10.1016/j.actbio.2016.11.068

192. Yuan Z, Liu S, Hao C, et al. AMECM/DCB scaffold prompts successful total meniscus reconstruction in a rabbit total meniscectomy model. *Biomaterials*. 2016;111:13-26.
doi: 10.1016/j.biomaterials.2016.09.017

193. Silva AC, Rodrigues SC, Caldeira J, et al. Three-dimensional scaffolds of fetal decellularized hearts exhibit enhanced potential to support cardiac cells in comparison to the adult. *Biomaterials*. 2016;104:52-64.
doi: 10.1016/j.biomaterials.2016.06.062

194. Robertson MJ, Dries-Devlin JL, Kren SM, Burchfield JS, Taylor DA. Optimizing recellularization of whole decellularized heart extracellular matrix. *PLoS One*. 2014;9(2):e90406.
doi: 10.1371/journal.pone.0090406

195. Kobayashi M, Kadota J, Hashimoto Y, et al. Elastic modulus of ECM hydrogels derived from decellularized tissue affects capillary network formation in endothelial cells. *Int J Mol Sci*. 2020;21(17):6304.
doi: 10.3390/ijms21176304

196. Radeke C, Pons R, Mihajlovic M, et al. Transparent and cell-guiding cellulose nanofiber 3d printing bioinks. *ACS Appl Mater Interfaces*. 2023;15(2): 2564-2577.
doi: 10.1021/acsami.2c16126

197. Arezoo N, Mohammad H, Malihezaman M. Tissue engineering of mouse uterus using menstrual blood stem cells (MenSCs) and decellularized uterine scaffold. *Stem Cell Res Ther*. 2021;12(1):475.
doi: 10.1186/s13287-021-02543-y.

198. Brown M, Li J, Moraes C, Tabrizian M, Li-Jessen NYK. Decellularized extracellular matrix: new promising and challenging biomaterials for regenerative medicine. *Biomaterials*. 2022;289:121786.
doi: 10.1016/j.biomaterials.2022.12178

199. Han H, Kim M, Yong U, et al. Tissue-specific gelatin bioink as a rheology modifier for high printability and adjustable tissue properties. *Biomater Sci.* 2024;12: 2599-2613.
doi: 10.1039/d3bm02111d

200. Lian L, Xie M, Luo Z, et al. Rapid volumetric bioprinting of decellularized extracellular matrix bioinks. *Adv Mater*. 2024;e2304846.
doi: 10.1002/adma.202304846

201. Lee H, Ju YM, Kim I, et al. A novel decellularized skeletal muscle-derived ECM scaffolding system for in situ muscle regeneration. *Methods*. 2020;171:77-85.
doi: 10.1016/j.ymeth.2019.06.027

202. Witt R, Weigand A, Boos AM, et al. Mesenchymal stem cells and myoblast differentiation under HGF and IGF-1 stimulation for 3D skeletal muscle tissue engineering. *BMC Cell Biol*. 2017;18(1):15.
doi: 10.1186/s12860-017-0131-2

203. Sani M, Hosseinie R, Latifi M, et al. Engineered artificial articular cartilage made of decellularized extracellular matrix by mechanical and IGF-1 stimulation. *Biomater Adv*. 2022;139:213019.
doi: 10.1016/j.bioadv.2022.213019

204. Su X, Wang T, Guo S. Applications of 3D printed bone tissue engineering scaffolds in the stem cell field. *Regen Ther.* 2021;16:63-72.
doi: 10.1016/j.reth.2021.01.007

205. Iwasaki N, Roldo M, Karali A, Blunn G. In vitro development of a muscle-tendon junction construct using decellularised extracellular matrix: effect of cyclic tensile loading. *Biomater Adv*. 2024;161:213873.
doi: 10.1016/j.bioadv.2024.213873

206. Li J, Zhang J, Ye H, et al. Pulmonary decellularized extracellular matrix (dECM) modified polyethylene terephthalate three-dimensional cell carriers regulate the proliferation and paracrine activity of mesenchymal stem cells. *Front Bioeng Biotechnol*. 2024;11:1324424.
doi: 10.3389/fbioe.2023.1324424

207. Potere F, Belgio B, Croci GA, et al. 3D bioprinting of multi-layered segments of a vessel-like structure with ECM and novel derived bioink. *Front Bioeng Biotechnol*. 2022;10:918690.
doi: 10.3389/fbioe.2022.918690

208. Ong CS, Nam L, Ong K, et al. 3D and 4D bioprinting of the myocardium: current approaches, challenges, and future prospects. *Biomed Res Int*. 2018;2018:6497242.
doi: 10.1155/2018/6497242

ACCSCIENCE PUBLISHING

International Journal of Bioprinting

REVIEW ARTICLE

Advancements in 3D bioprinting for precision medicine: Enhancing patient-derived organoids and extracellular vesicle applications in inflammatory diseases

Hyun Sung Park[†], Jae Han Park[†], Mi-Kyung Oh*, and Kyung-Rok Yu*

Department of Agricultural Biotechnology and Research Institute of Agriculture and Life Science, Seoul National University, Seoul, Republic of Korea

(This article belongs to the Special Issue: *The latest advancements in bioprinting technology*)

Abstract

The integration of three-dimensional (3D) bioprinting with cultures of patient-derived organoids represents a transformative advancement in precision medicine, enabling the creation of anatomically accurate and physiologically relevant tissue models. These models are pivotal for personalized disease modeling, therapeutic development, and regenerative medicine. 3D bioprinting enhances the structural and functional fidelity of organoids, thereby improving their application in drug screening and disease intervention strategies. Additionally, this technology facilitates the study of extracellular vesicles (EVs) released from patient-derived organoids, which are rich in bioactive molecules and play crucial roles in modulating immune responses. Particularly in chronic inflammatory conditions, these organoid-derived EVs are instrumental in cellular communication and improve our understanding of disease mechanisms beyond traditional biopsies. This review focuses on the latest developments in 3D bioprinting techniques for organoids and EVs, highlighting their potential to revolutionize the treatment of inflammatory diseases through precision medicine.

Keywords: 3D bioprinting; Patient-derived organoids; Extracellular vesicles; Immune-mediated chronic diseases; Personalized medicine

[†]These authors contributed equally to this work.

***Corresponding authors:**
Mi-Kyung Oh (ipomk@snu.ac.kr)

Kyung-Rok Yu (cellyu@snu.ac.kr)

Citation: Park HS, Park JH, Oh M-K, Yu K-R. Advancements in 3D bioprinting for precision medicine: enhancing patient-derived organoids and extracellular vesicle applications in inflammatory diseases. *Int J Bioprint*. 2024;10(5):4054. doi: 10.36922/ijb.4054

Received: June 27, 2024
Revised: July 23, 2024
Accepted: July 25, 2024
Published Online: July 30, 2024

Copyright: © 2024 Author(s). This is an Open Access article distributed under the terms of the Creative Commons Attribution License, permitting distribution, and reproduction in any medium, provided the original work is properly cited.

Publisher's Note: AccScience Publishing remains neutral with regard to jurisdictional claims in published maps and institutional affiliations.

1. Introduction

Chronic inflammatory diseases, such as rheumatoid arthritis (RA), inflammatory bowel disease (IBD), and neuroinflammation, are complex medical conditions characterized by persistent inflammation and tissue damage.[1,2] The pathophysiology of these diseases involves a combination of genetic, environmental, and immunological factors that result in varying patient responses to standard treatments, necessitating a more personalized treatment approach.

In recent years, the integration of three-dimensional (3D) bioprinting technologies with patient-derived organoids (PDOs) has transformed precision medicine by enabling the development of personalized disease models and advancing therapeutic research. Organoids, miniaturized versions of organs grown *in vitro*, have shown immense

potential in modeling human diseases due to their high culture success rate, close resemblance to primary tissue, and short culture cycle.[3–5] However, traditional organoid culture methods rely on the self-organization of cells in a 3D environment, which can result in a variety of morphologies, genetic drift, and the lack of endogenous tumor-associated stromal components.[6] These limitations hinder the reproducibility, scalability, and clinical applicability of organoid models.

3D bioprinting technology addresses these challenges by enabling precise layer-by-layer positioning of biological materials, living cells, and biochemical factors to create complex tissue structures that closely resemble *in vivo* environments.[7] This technology allows for the construction of organoids with defined structures and spatial arrangements, enhancing consistency across experimental models and improving their utility in research and clinical applications.[8,9] By incorporating vascular structures, immune cells, achieving precise spatial architecture, and scaling up to tissue sizes, 3D bioprinting plays a pivotal role in overcoming limitations in organoid construction.[10] The fabrication of 3D biological structures with multiple functional, structural, and mechanical components through 3D bioprinting has facilitated drug development, toxicity studies, and the study of tissue and disease formation and progression.[11] Moreover, 3D bioprinting technology offers novel opportunities for studying inflammatory diseases by incorporating immune cells, stromal cells, and other relevant cell types into organoid models.[12,13]

A significant advancement resulting from the integration of 3D bioprinting and organoid cultures is the study of extracellular vesicles (EVs) released from these organoids. EVs, including exosomes and microvesicles, are nano-sized particles that play a crucial role in intercellular communication by transporting bioactive molecules such as proteins, lipids, and RNA.[14] They emerge as important mediators of immune regulation and are implicated in the pathogenesis of various chronic inflammatory diseases. Analysis of EVs facilitated by 3D bioprinting technology provides new insights into disease mechanisms at the molecular level, surpassing traditional biopsy methods.[15] Moreover, EVs from organoids have the potential to identify essential biomarkers and therapeutic targets for chronic inflammatory diseases like RA, IBD, and neuroinflammation.[16–18] Chronic inflammatory conditions are particularly challenging to treat due to their complex pathophysiology and the variability in patient responses to treatments. Organoid-derived EVs (OEVs) offer a novel perspective on cellular communication networks and immune modulation mechanisms specific to these conditions, which may serve as potential biomarkers and therapeutic targets.[19–22] Investigating EVs released from cultured organoids through 3D bioprinting may reveal the complex mechanisms underlying chronic inflammatory diseases, leading to more effective and personalized intervention strategies.

Here, we review recent advancements in 3D bioprinting technologies for PDOs and the emerging field of 3D-bioprinted OEVs, focusing on their potential applications in tackling immune-mediated chronic diseases. By analyzing current advancements, challenges, and future prospects, this review underscores the potential of 3D-bioprinted PDOs and EVs in advancing precision medicine strategies for inflammation-related conditions.

2. 3D-bioprinted organoids: State-of-the-art in 3D bioprinting of organoids

2.1. Organoids for novel model systems

Developing effective *in vitro* models to reflect the complexity of immune interactions in chronic inflammation is crucial for deeply understanding inflammatory response. Studying tissue biology in mammals presents challenges due to sample accessibility and ethical concerns. One innovative approach to overcome these challenges is organoid technology, which utilizes the intrinsic ability of stem cells to self-organize into 3D structures that resemble *in vivo* organs (Figure 1).

Compared to *in vitro* cell line models or *in vivo* animal models, organoids offer several distinct advantages. Organoids have high culture success rates, which ensures reproducibility and reliability in experimental outcomes.[3] Additionally, their close resemblance to primary tissue in three dimensions makes them more physiologically relevant for studying disease mechanisms and drug responses.[5] The short culture cycle of organoids also facilitates rapid experimentation and reduces the time and costs associated with traditional models.[4] Moreover, organoids enable the establishment of low-malignancy models, offering a safer and more ethical alternative for studying disease progression.[23,24]

Importantly, organoids can be derived from stem cells or tissue progenitors of the body, which in turn allows them to be used to establish patient-specific disease models for personalized precision medicine. Since the discovery in 2009 that adult tissue-resident stem cells can proliferate and self-organize into organoids *in vitro*, this methodology has been adapted to generate organoids from various epithelial tissues of major organs such as the skin, kidney, liver, and intestines.[5] These organoids have been used in physiological and disease-related studies on topics, including complex inflammation-related disorders such as IBD.[25] The utilization of PDOs has paved the way for the development of personalized therapy, enabling

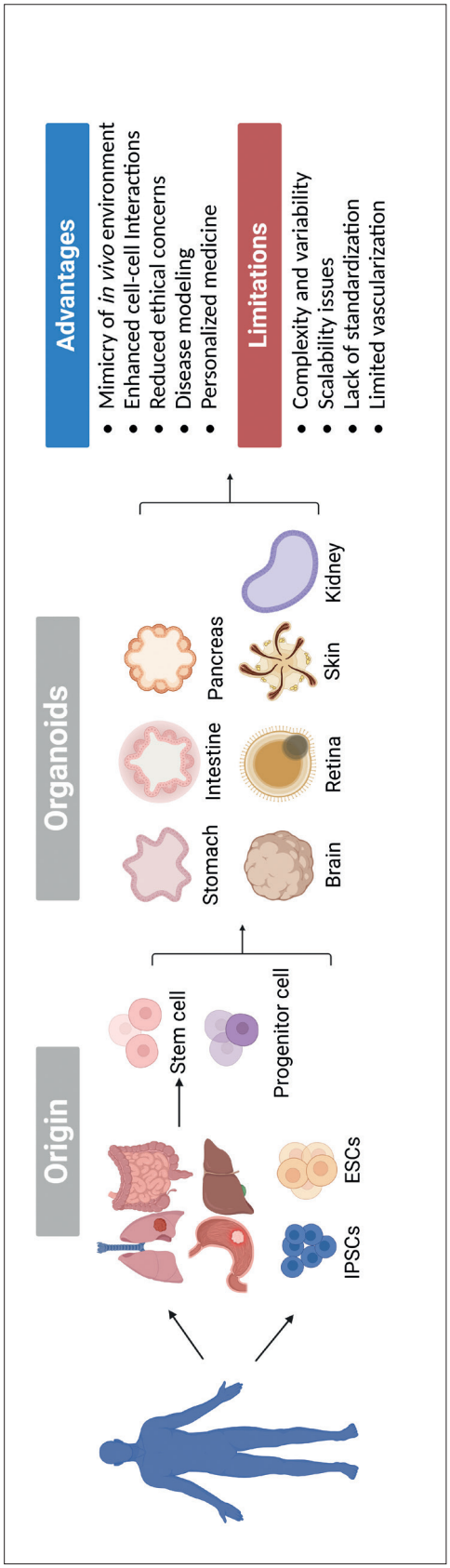


Figure 1. Organoids for novel model systems. Organoids derived from primary tissue, embryonic stem cells (ESCs), or induced pluripotent stem cells (iPSCs) can model organ development through self-renewal and self-organization *in vitro*. While organoids have advantages of mimicking the specific *in vivo* environment of individuals, they also suffer technical limitations such as scalability issues and a lack of vascular systems. Schematic created with BioRender.

the personalization of treatment strategies based on the characteristics of the patient's own cells.[26]

Additionally, organoids have been instrumental in establishing a model susceptible to T cell-mediated tissue damage and have provided insight into the role of autophagy in preventing inflammation-induced apoptosis and preserving barrier integrity in chronic colitis.[12,13] These 3D structures can provide experimental manipulability while maintaining biological complexity, bridging the gap between traditional 2D cell cultures and animal models. However, traditional organoid culture methods, which rely on self-organization, may result in creating diverse morphologies and cell arrangements, which are different from that of real organs. Integration of 3D bioprinting technology and organoid culture systems is needed as a potential solution to address the limitations of traditional organoid culture systems.

2.2. Principles of 3D bioprinting and organoid formation

3D bioprinting technology enables the precise layering of cells, biopolymers, and biomaterials to create complex and accurate tissue structures. This technology significantly enhances the structural and functional fidelity of organoids, making them more anatomically precise and physiologically relevant. By incorporating 3D bioprinting with PDOs, researchers can overcome the limitations of self-organization, achieving consistent morphologies and cell arrangements closer to their native tissues.[27]

The principles of 3D bioprinting include the selection of suitable bioinks, the design of printing protocols, and the optimization of printing parameters to ensure cell viability and functionality. Organoid formation through 3D bioprinting involves the encapsulation of stem cells within a supportive matrix, followed by controlled differentiation and self-organization to form tissue-specific structures.[10] Here, we present common bioinks and various bioprinting strategies.

2.2.1. Cell sources and bioinks

The success of 3D bioprinting organoids depends on the development of appropriate bioinks that can support cell growth and differentiation. Bioinks, which are composed of biomaterials, live cells, and biomolecules, represent a crucial component in 3D bioprinting processes (Figure 2A).

Various materials such as alginate, agarose, gelatin, fibrin, and Matrigel are commonly used as bioinks, each offering unique properties such as biocompatibility, mechanical strength, and bioactivity.[28–31] Both natural polymers such as collagen, gelatin, and alginate and synthetic polymers like polycaprolactone (PCL) and polyethylene glycol (PEG) are commonly used for

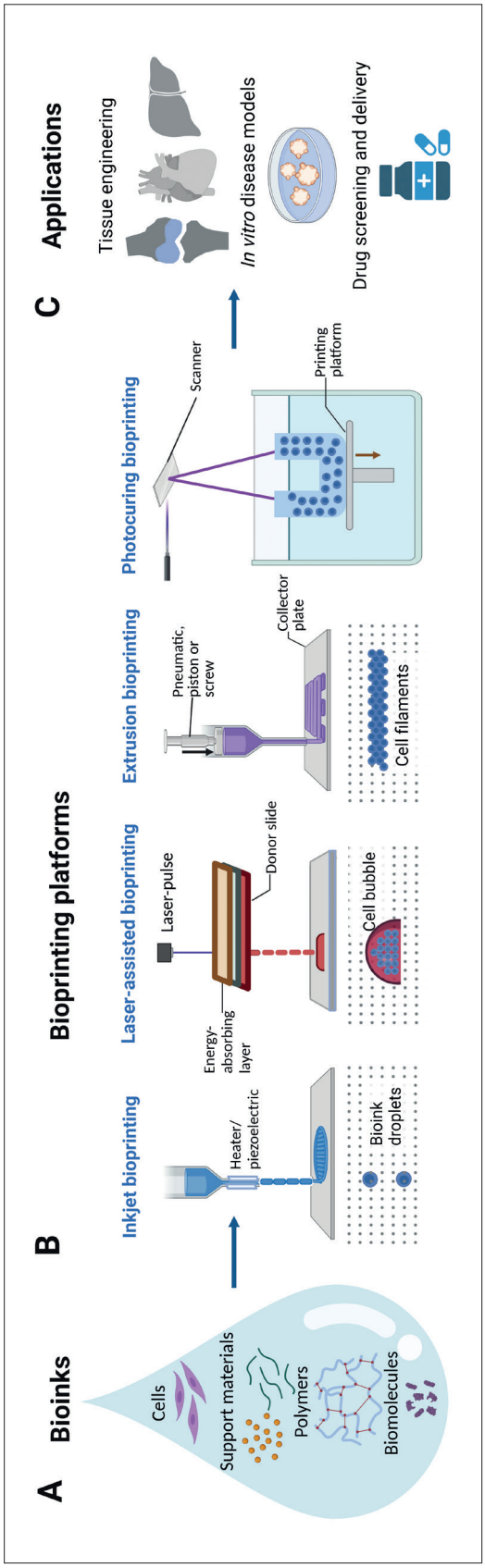


Figure 2. Overview of bioink composition, common bioprinting methods, and their applications. (A) The main elements of bioinks are cells, support materials like hydrogel, polymers like decellularized extracellular matrix (dECM), and biomolecules including signaling molecules. (B) Four main 3D printing methods are inkjet bioprinting, laser-assisted bioprinting, extrusion bioprinting, and photocuring bioprinting. (C) The applications of 3D bioprinting range from tissue construct printing and disease model establishment to drug testing and delivery. Schematic created with BioRender.

bioprinting applications due to their biocompatibility and customizable characteristics.

Current methodologies focus on optimizing bioink formulations to enhance printability, structural integrity, and cell-matrix interactions. Additionally, incorporating bioactive molecules like growth factors (e.g., transforming growth factor beta [TGF-β], bone morphogenetic protein [BMP], vascular endothelial growth factor [VEGF]) and extracellular matrix (ECM) proteins or peptides (e.g., RGD) into bioinks significantly improves cell behavior, tissue regeneration, and functionality. These multifunctional bioinks represent a significant breakthrough, enabling the fabrication of complex functional tissues and organs.[32]

The selection of appropriate cell types, particularly stem cells, is crucial in bioprinting organoids to ensure the functionality and relevance of the resulting tissue model. Stem cells, known for their self-renewal and pluripotency, offer significant therapeutic potential.[33] Patient-derived cells, including stem cells, primary cells, and induced pluripotent stem cells (iPSCs), are commonly used in bioprinting to create organoids that mimic the characteristics of the target tissue.[34] Additionally, the incorporation of multiple cell types, such as epithelial cells, stromal cells, and immune cells, in bioprinted organoids enables the replication of the complexity of native tissues, facilitating the study of cell-cell interactions and disease processes.

Researchers have explored diverse bioink formulations to enhance the functionality of bioprinted organoids. For example, the use of decellularized extracellular matrix (dECM) bioinks has gained interest due to their ability to create a more natural microenvironment that enhances cellular function. These dECM hydrogels, derived from various tissues, have been instrumental in reconstructing organs and structures such as tumors, hearts, muscles, arteries, nerves, corneas, and bones.[35]

Therefore, the development of appropriate bioinks, the selection of suitable cell types, and the optimization of bioink formulations are essential considerations in the 3D bioprinting of organoids to ensure the functionality and relevance of the resulting tissue model.[36] When choosing an appropriate bioink, the printer type and bioprinting approach should also be considered.

2.2.2. Current methodologies used in 3D bioprinting organoids

3D bioprinting technologies have revolutionized tissue engineering and precision medicine by enabling the precise fabrication of complex multicellular structures both *in vitro* and *in vivo*. Among the widely used 3D bioprinting

technologies are inkjet bioprinting, laser-assisted bioprinting, photocuring bioprinting, and extrusion-based bioprinting (Figure 2B). Each of these technologies offers distinct advantages and challenges for organoid fabrication. A comparison of different bioprinting technologies for printing organoids is provided in Table 1.

Inkjet bioprinting is widely used for high-throughput applications that require detailed structures, such as small, intricate organoids and high-throughput drug screening models.[43,44] This process utilizes a thermal or piezoelectric actuator to generate droplets of the bioink consistently.[45,46] The technique allows for the deposition of droplets smaller than 50 μm in a non-contact manner with high resolution, maintaining high cell viability due to low shear stress during droplet ejection.[47,48] Inkjet bioprinting is used to create detailed tissue models for drug testing and studies involving sensitive cells, such as embryonic stem cells.[38] However, challenges such as bioink viscosity control and susceptibility to clogging exist, limiting its application with certain tissue types.[49]

Laser-assisted bioprinting is an innovative technology that utilizes laser beams to precisely deposit biomaterials onto substrates, eliminating the need for nozzles commonly used in traditional bioprinting methods.[50] This approach enhances printing resolution and cell viability, making it suitable for applications requiring high precision and intricate cellular arrangements, such as the creation of detailed tissue constructs and organoids. Laser-assisted bioprinting was used to successfully fabricate liver and intestinal organoids, demonstrating its potential for generating complex tissue structures while maintaining high cell viability.[32,51,52] The technique involves a three-part process consisting of a donor-slide (or ribbon), a laser pulse, and a receiver-slide, enabling the gentle deposition of biomaterials to preserve cell viability.[53] One of the key advantages of laser-assisted bioprinting is its ability to accommodate various cell types and bioinks, which enhances its applicability in tissue engineering and regenerative medicine.[54] Despite its advantages, laser-assisted bioprinting faces several limitations that may hinder its widespread adoption. One significant challenge is the restricted range of compatible biomaterials, which limits the diversity of constructs that can be produced using this technique.[50] Moreover, the high equipment costs associated with laser-assisted bioprinting setup make it not only a complex but also a potentially expensive technology to implement, posing a barrier to its accessibility for researchers and institutions looking to adopt bioprinting technologies.

Extrusion-based bioprinting is versatile and scalable, making it suitable for producing large and robust tissue constructs, including various organoid models.[55,56] This technique extrudes bioinks as discontinuous filaments using a pneumatic piston or screw mechanism, enabling the construction of complex 3D structures layer by layer.[57] The versatility of extrusion-based bioprinting lies in the ability to use a variety of bioinks with different viscosities. This makes it suitable for producing large, complex

Table 1. Advantages and disadvantages of bioprinting techniques for organoid printing.

Printing method	Key aspects	Advantages	Disadvantages	Ref.
Inkjet-based bioprinting	High-throughput; drug screening; creating detailed tissue models; sensitive cell printing	• High throughput • Low shear stress • Low cost • High resolution • Multiple materials	• Nozzle clogging • Viscosity limitations • Shear force stress • Limited to certain tissue types	[37–39]
Laser-assisted bioprinting	High-precision; suitable for applications requiring high cell viability	• High cell densities • High cell viability • Versatility • Nozzle-free	• High cost • Complex setup • Material limitations • UV-induced DNA damage	[39–41]
Extrusion-based bioprinting	Creating large and robust tissue constructs; fabricating liver, kidney, and intestinal organoids	• Scalability • Mechanical strength • Versatility • Multiple biomaterials form separate nozzles	• High shear stress • Low resolution • Viscosity management	[41]
Photocuring bioprinting	Creating complex, high-resolution structures; creating organoid scaffolds and detailed tissue models	• High speed • High resolution • Nozzle-free • Supports complex structures	• Material constraints • Costly equipment • Layer limitations • UV-induced DNA damage	[42]

Abbreviation: UV, ultraviolet.

tissue constructs with strong mechanical properties and is ideal for fabricating organoids such as liver, kidney, and intestinal models. For instance, the Dokmeci group successfully bioprinted organoids comprising hepatocytes and fibroblasts within methacrylated gelatin hydrogels, showcasing the potential of extrusion-based printing in generating functional tissue models.[58] Despite its advantages, extrusion-based bioprinting does have limitations. The technique exposes bioinks to high pressure and shear stress, which can potentially damage cells and impact their viability. Moreover, the resolution of extrusion-based bioprinting is typically lower compared to those of other methods such as inkjet or photocuring bioprinting. To address these challenges, careful optimization of bioink properties is essential to balance viscosity and mechanical characteristics for successful printing and to maintain cell viability.[59,60]

Photocuring bioprinting, also known as light-projection bioprinting, is a technique that utilizes light to solidify light-sensitive crosslinkers into 3D shapes without the need for nozzles. This method is advantageous as it reduces shear forces on cells, thereby ensuring high cell viability.[42] There are two main photocuring bioprinting methods used to construct organoids: volumetric bioprinting and digital light processing (DLP) bioprinting. Volumetric bioprinting employs optical tomography to rapidly create intricate 3D structures, such as supportive scaffolds for organoids, which can enhance their functionality. For example, Bernal *et al.* utilized volumetric bioprinting to create 3D structures with biocompatible resins that support liver organoids, providing a robust platform for biomedical research.[61] On the other hand, DLP bioprinting uses visible or ultraviolet light to solidify photosensitive resins layer-by-layer onto the print head, allowing for high-speed printing of detailed 3D structures. Grix *et al.* demonstrated the use of DLP bioprinting to create liver organoids with perfusable channels, which possessed increased viability and improved biofunctionality compared to traditional monolayer cultures.[62] Photocuring bioprinting offers high speed and resolution, making it ideal for creating intricate and complex structures. However, it is limited to photosensitive resins and crosslinkers, and the equipment required is costly.

Understanding the trade-offs associated with these different bioprinting techniques is crucial for selecting the most suitable method based on the specific requirements of the organoid model and its intended application in disease modeling, drug screening, or regenerative medicine. Further research and development will improve the application of these technologies in organoid printing.

2.3. 3D-bioprinted patient-derived organoids in precision medicine

2.3.1. Patient-derived organoids in precision medicine

PDOs have significantly impacted cancer research and therapy by enabling the modeling of patient-specific responses to treatments. These 3D cultures accurately replicate the genomic and histological characteristics of the original tumors, proving to be crucial for personalized cancer medicine. The tumor organoids developed from various cancer types, including prostate cancer, gastrointestinal cancer, breast cancer, and ovarian cancer, have shown effectiveness in preclinical drug testing and co-clinical trials.[63–66] PDOs provide several advantages, such as the capacity to generate organoids from small tumor samples like needle biopsies and from different regions within the same tumor, facilitating the exploration of tumor heterogeneity. These models have the potential to screen anti-cancer drugs, optimize immunotherapy, and identifying prognostic biomarkers.[67]

The integration of PDOs in precision medicine has enabled the modeling of various diseases and drug responses, providing a platform for personalized treatment strategies. In the context of genetic diseases, Schene *et al.* demonstrated the utility of prime editing in repairing genetic defects within PDOs, showcasing the precision and therapeutic potential of this gene editing strategy.[68] Additionally, the combination of CRISPR genome editing (knock out, base, or prime editing) with 3D organoid cultures has facilitated the modeling of disease progression and the study of genetic diseases, bridging the gap between patient-derived cells and disease understanding.[69,70]

In specific cases like Leigh syndrome, an incurable mitochondrial disease linked to a *SURF1* mutation, Cas9 genome editing was applied to correct the mutated *SURF1* gene within PDOs, shedding light on the physiological connection between SURF1 and Leigh syndrome.[71] Furthermore, patient-derived iPSCs have been employed to model macrocephaly/autism phenotypes, showcasing the versatility of PDOs in studying complex genetic conditions.[72,73] Moreover, the CRISPR-Cas9 system has been applied in brain organoid models to induce congenital nervous system malformation disease models, aiding the study of these complex disorders.[74]

In the context of cystic fibrosis, forskolin-induced swelling in healthy organoids contrasts with the lack of swelling observed in intestinal organoids derived from cystic fibrosis patients carrying the F508 deletion mutation in the *CFTR* gene.[70] However, the introduction of adenine base editing and the prime editing by the Geurts group facilitated genetic and functional repair in PDOs with *CFTR* mutations, showcasing the potential of

genome editing in correcting disease-associated genetic defects.[75,76] These advances highlight the important role of PDOs in precision medicine and provide a platform to study disease progression, genetic disorders, and personalized treatment strategies.

2.3.2. 3D bioprinting of patient-derived organoids

PDOs have become essential in advancing precision medicine, particularly in tumor immunology studies. These 3D tissue cultures have enabled the successful propagation of human tumor biopsies *in vitro*, enhancing our comprehension of the tumor microenvironment and genetics.[77] However, conventional PDO models face several challenges. While most tumor PDOs replicate the genetic composition of the parental tumor in early passages, the extent of genetic drift or the proportion of genetically stable cells in later passages remains unclear.[6] Additionally, the lack of endogenous tumor-associated stromal components is another significant limitation of current organoid methods.

Recent advances in 3D bioprinting have shown promising advancements to address these challenges. Table 2 summarizes and compares the notable advancements. 3D bioprinting techniques enable precise layering of cells, biomaterials, and biochemical factors, facilitating the creation of complex tissue structures that closely resemble *in vivo* environments.[10] This technology can play pivotal roles in overcoming issues in organoid construction, including incorporating vascular structures, immune cells, achieving precise spatial architecture, and scaling up to tissue sizes.

Researchers have made significant progress in creating artificial vascular networks using bioprinting techniques, enabling the generation of intricate tissue structures.[78] Additionally, innovative bioprinting approaches have been developed to transfer spheroids into self-healing support hydrogels at high resolution, allowing for the precise manipulation of single spheroids and organoids.[79] The development of aspiration-assisted bioprinting and multi-material bioprinters has improved the precision and versatility of bioprinting, enabling the construction of high-cell density and heterogeneous tissue models.[80,81] Moreover, the utilization of bioinks containing nanoparticles has enhanced the mechanical strength and functionality of bioprinted tissues, supporting the long-term expansion and improved drug testing of organoids.[82] Furthermore, the incorporation of organoid-forming stem cells into centimeter-scale tissues through bioprinting has facilitated studies on organ development, disease progression, and potential therapeutic interventions.[83] Temperature-controlled printing platforms have been utilized to enhance cell viability and successfully fabricate complex tissue structures, showcasing the potential of 3D printing technology in tissue engineering.[84] These advancements not only support the long-term expansion and improved drug testing of PDOs but also enable the recapitulation of the real structure and function of organoids, addressing critical challenges faced by conventional PDO models.

The advancements in 3D bioprinting have opened new horizons in disease modeling and precision medicine. Researchers have successfully developed patient-specific

Table 2. Advances and innovations of 3D bioprinting.

Technique	Advancement	Significance	Ref.
Vascular network bioprinting	Creation of intricate tissue structures using bioprinting	Enables generation of complex vascularized tissues, improving tissue engineering outcomes	[78]
Precise spheroid manipulation	Transfer of spheroids into self-healing hydrogels at high resolution	Allows precise manipulation of spheroids and organoids, creating high-cell density, heterogeneous models	[79]
Aspiration-assisted bioprinting	Enhanced precision and versatility in biofabrication	Improves precision and versatility of bioprinting, constructing high-cell density, heterogeneous models	[80]
Multi-material bioprinting	Simultaneous printing of multiple cell types	Creates heterogeneous tissue structures, enhancing the complexity of bioprinted models	[81]
Nanoparticle-enhanced bioink printing	Development of bioinks containing nanoparticles	Increases mechanical strength and functionality of tissues, supporting long-term expansion and improved drug testing	[82]
Large-scale tissue bioprinting	Printing of organoid-forming stem cells to form large tissues	Facilitates studies on organ development, disease progression, and therapeutic interventions	[83]
Temperature-controlled bioprinting	Use of temperature-controlled printing to enhance cell viability	Successfully fabricates complex tissue structures, demonstrating the potential of 3D printing in tissue engineering	[84]

Abbreviation: 3D, three-dimensional.

implants for bone regeneration and joint organoids that mimic natural joint tissues, offering effective treatment options.[52,85,86] Moreover, 3D bioprinting has been instrumental in creating tumor models and brain organoids for personalized drug screening and disease modeling.[10] For example, embedded 3D bioprinting and photo-crosslinkable bioinks were invented to create brain-like co-culture constructs with heterogeneous neuronal populations, demonstrating their potential for neuronal differentiation and modeling neurological diseases.[87] This innovative approach has led to the development of bioprinted brain organoids for individual drug screening in neurological diseases.[88]

In cancer research, acoustically bioprinted patient-derived microtissues have been developed to model cancer invasion and predict treatment responses in colorectal cancer patients, showcasing the personalized and predictive capabilities of 3D bioprinting.[89] Flores-Torres *et al.* established bioprinted tumor models to maintain the PDO of gastric adenocarcinoma using hydrogels composed of alginate and gelatin.[88] Additionally, bioprinted iPSC-derived cancer tissues offer opportunities to study early cancer development and precision oncology, facilitating the discovery of patient-specific drugs.[90]

Despite the challenges associated with conventional PDO models, the application of 3D bioprinting has shown promise in enhancing organoid culture and addressing existing limitations, ultimately paving the way for more accurate and sophisticated models in precision medicine (Figure 3).

2.4. Applications of 3D bioprinting of organoids in studying inflammation

Organoids, particularly those generated through 3D bioprinting, have emerged as valuable tools for studying inflammatory diseases and cancer immunotherapy. By incorporating immune cells, stromal cells, and other relevant cell types into organoid models, the complex cellular interactions and microenvironments observed in autoimmune diseases can be recapitulated. These models enable the exploration of disease mechanisms, such as the impact of specific genes and signaling pathways in inflammation, and facilitate the screening of potential therapeutic interventions. Table 3 summarizes the literature related to 3D bioprinting organoids and inflammatory diseases.

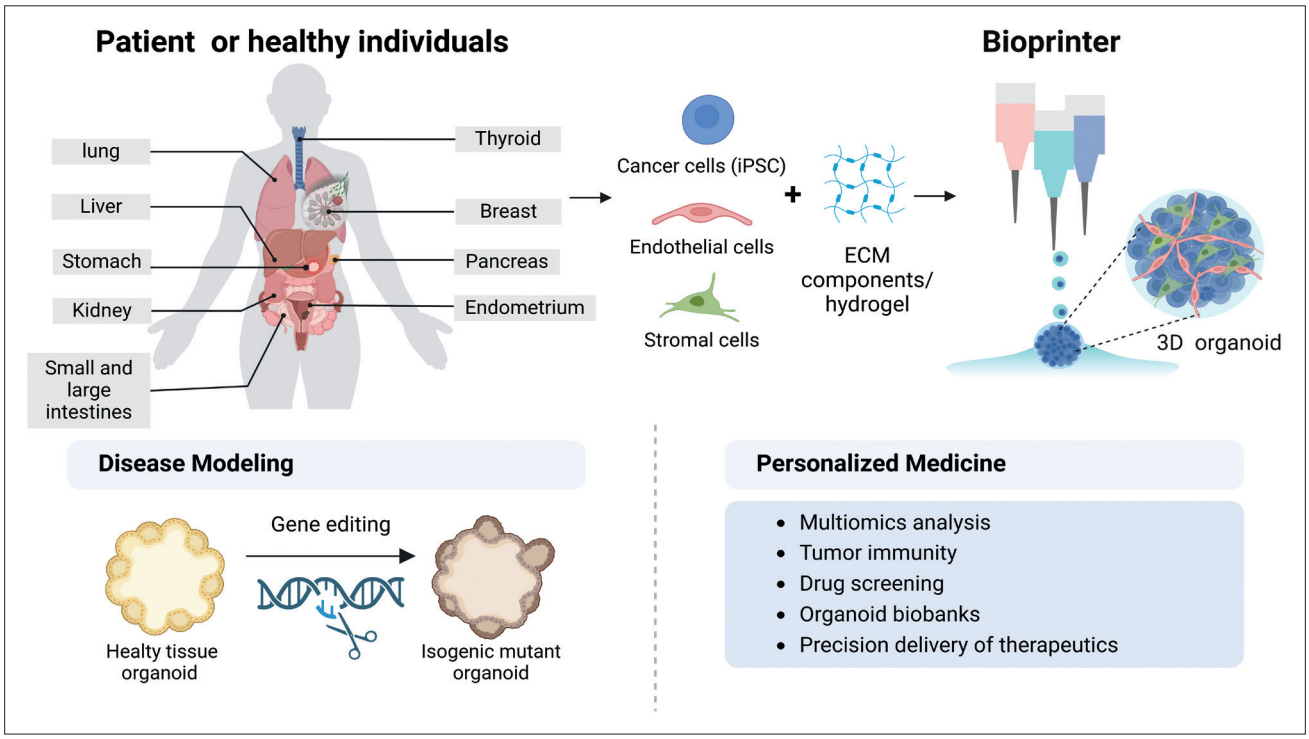


Figure 3. Potential applications of patient-derived organoids (PDOs). PDOs can be derived from surgically resected tumor tissue, tumor biopsies, or normal tissue surrounding the tumor. By incorporating various types of cells into bioinks for 3D bioprinting, multiple consistent PDOs can be produced. These PDOs can be utilized to establish disease models through gene editing or used as platforms for personalized medicine due to their personalized origin. Abbreviations: ECM, extracellular matrix; iPSC, induced pluripotent stem cell.

Table 3. Application of studying inflammation with 3D-bioprinted organoid culture platforms.

Disease model	Cell type used	Key findings	Ref.
Inflammatory bowel disease	Caco-2 and HT29 (colon cancer cells)	Development of 3D-bioprinted colitis-like condition model to evaluate the barrier function of anti-inflammatory drugs	[91]
Rheumatoid arthritis	EA.hy 926 (vascular endothelial cells); MH7A (synovial fibroblasts)	Established 3D co-culture pannus model to screen anti-rheumatoid arthritis drugs.	[92]
Intestine toxicity and inflammation	Adult human intestinal myofibroblasts; human intestinal epithelial cells; Caco-2	Development of 3D-printed human intestinal tissues that mimic physiological barrier function to test compound-induced toxicity	[93]
Type 1 diabetes mellitus	Murine islet β-cells	Development of bioink comprising GelMA, ECM, and PRP to enhance pro-angiogenic and immunoregulatory function for 3D-printed islet organoid	[94]
Type 1 diabetes mellitus	Rat islet	Incorporation of islets into HAMA/pECM hydrogel bioink to study vascularization and inflammatory response of 3D-printed islet organoids	[95]
Immune-driven brain aging	Cortical organoid derived from hESCs	Development of human brain organoid microphysiological analysis platform that perfuses primary monocytes from different age groups into human cortical organoids	[96]
Microglia-mediated neuroinflammation	Neuro-2a neuroblast cells; HMC3 human microglia	3D printing tubular brain organoid platform co-cultured with microglia to test neuroinflammation after opioid exposure	[97]

Abbreviations: 3D, three-dimensional; dECM, cellularized extracellular matrix; GelMA, gelatin methacryloyl; hESCs, human embryonic stem cells; pECM, pancreatic extracellular matrix; and PRP, platelet-rich plasma.

One of the notable applications of 3D bioprinting is the creation of intestinal organoids for studying IBD. These organoids can model the impaired interaction between epithelial cells and the microbiome, which is crucial for understanding IBD pathogenesis. By co-culturing these organoids with immune cells and microbes, it is possible to identify the pathological mechanisms driving IBD, including the contributions of microbial dysbiosis and immune responses to disease progression.[98,99] Deng *et al.* developed an innovative intestinal organ culture system designed to mimic the regenerative process of proliferative crypts following intestinal epithelial injury.[100] Additionally, the researchers isolated crypt cells from patients to produce PDOs and compared the physiological differences between normal and disease states.[101] PDOs derived from disease states have shown reduced mRNA transcript levels of tight junction markers, increased cell death, reduced proliferation, and impaired differentiation abilities.[102] Furthermore, organoids from Crohn's disease patients exhibit unique transcriptomic and secretomic signatures, revealing disease-specific mechanisms and responses.[103] To overcome the limitations of current 3D culture systems, bioprinting techniques have been explored to create 3D intestinal tissues composed of human primary intestinal epithelial cells and myofibroblasts. These bioprinted tissues exhibit physiological barrier function and responses to toxicity and inflammation, offering new opportunities for drug discovery, disease diagnosis, and regenerative medicine research.[93] Recent advancements in 3D bioprinting techniques, such as the development of the BATE technique by Jonathan *et al.*, have enabled the creation of centimeter-sized gastrointestinal tissues with self-organizing features, enhancing the scalability and applicability of bioprinted organoids in various research areas.[83]

Rheumatoid arthritis is characterized by inflammation in joint tissue, particularly by the formation of pannus, which is an inflamed fibroblastic tissue in the joint that leads to increased angiogenesis.[92] Pannus plays a crucial role in RA pathogenesis by contributing to joint destruction through leukocyte infiltration, synovial membrane proliferation, and neovascularization. To better understand the 3D properties of pannus and explore potential treatments, 3D bioprinting technology has been adopted to fabricate 3D pannus tissue using synovial fibroblasts, vascular endothelial cells, and hydrogels, in order to replicate the complex structure of pannus. Such 3D-printed pannus models hold promise for future drug screening research, offering a more accurate representation of the disease environment for testing and developing new therapies.[92]

Inflammatory diseases, such as autoimmune uveitis, involve complex interactions between immune responses and retinal tissues. The development of 3D-bioprinted retinal organoids is particularly significant for studying

inflammatory diseases like autoimmune uveitis because they provide a controlled environment to investigate how inflammation affects retinal cells. Sun *et al.* developed retinal organoids derived from human iPSCs using 3D printing technology on a polydimethylsiloxane (PDMS) microwell platform. This approach allows the creation of uniform organoids with long sustained growth, which exhibit proper differentiation into neural retina, ciliary margin, and retinal pigment epithelium. The use of human platelet lysate as an alternative to fetal bovine serum enhanced the clinical relevance of this model, offering a standardized platform for retinal development research, disease modeling, and drug screening.[104] These organoids can be used to model inflammatory responses by exposing them to pro-inflammatory cytokines or other inflammatory stimuli, thereby mimicking the conditions seen in inflammatory retinal diseases like autoimmune uveitis.

Finally, neuroinflammation plays a crucial role in the pathogenesis of Alzheimer's disease and Parkinson's disease, characterized by an imbalance in the "redox state" and chronic inflammation, leading to cell damage and death. Research emphasizes the significant involvement of microglial and astrocytes in neuroinflammation and neurodegeneration in these conditions.[105,106] Microglia and astrocytes are recognized for inducing and releasing various inflammatory mediators in response to oxidative stress, further amplifying the inflammatory response.[107,108] The use of cerebral organoids has emerged as a valuable tool for studying neuroinflammation, as the transcriptome and responses of microglia in cerebral organoids closely resemble those of adult microglia.[109,110] Thus, cerebral organoids have been pivotal in replicating disease hallmarks and testing potential therapeutic interventions for neurodegenerative diseases. For instance, in Alzheimer's disease, cerebral organoids derived from patient-specific iPSCs with a duplication in the *APP* gene exhibited key disease features like amyloid β aggregation and tau phosphorylation, enabling the screening of inhibitors and reduction in aggregate formation.[111] Similarly, in Parkinson's disease, brain organoids developed from iPSCs containing the *LRRK2* G2019S mutation highlighted synaptic dysfunction as a key altered pathway in PDOs, offering insights into disease mechanisms.[112]

Advancements in bioprinting techniques have further enhanced our capacity to create 3D brain structures for neurodegenerative disease modeling. Novel printing techniques using gellan gum modified with RGD peptides have been developed to encapsulate primary cortical neural cells, which possess good viability and demonstrate differentiated morphology of cortical neurons within the printed constructs.[113] Additionally, the use of nanofibrillated cellulose functionalized with carbon nanotubes has been proposed to support neural cells, enhancing cell attachment and conductivity for improved cell communication and neural network formation.[114] These models offer a valuable platform for investigating the complex interplay between inflammation and neurodegenerative diseases, which is fundamental for understanding the disease mechanisms and exploring potential therapeutic targets.

These studies suggest that 3D bioprinting technology plays a crucial role in the field of disease modeling by enabling the creation of complex organoid models that closely mimic the cellular interactions and microenvironments observed in various inflammatory diseases.

2.5. Challenges and limitations in 3D bioprinting organoids for precision medicine

Although 3D bioprinting has shown significant progress in organoid platforms, it still faces several challenges and limitations.[115,116] One major obstacle lies in the size difference between organoids and real organs, which impacts the replication of organ complexity. Organoids are significantly smaller than actual organs, making it challenging to capture the intricate structural and functional details of human organs. This size discrepancy can also lead to hypoxia-related damage due to inadequate nutrient supply.[117,118]

The long duration of the current manufacturing process can also contribute to hypoxia-related issues by interrupting the continuous nutrient and oxygen supply required for optimal cell growth. Moreover, the absence of a functional vascular network in bioprinted tissues can result in hypoxic conditions and hinder tissue development, necessitating improved vascularization techniques.[119]

Researchers have explored various approaches to address these challenges, For instance, the development of 3D-printed bioreactors has shown promise in enhancing vascularization in kidney organoids.[120] Additionally, integrating vascular networks into organoids using human pluripotent stem cells engineered to express ETV2, a transcription factor essential for endothelial cell development, has demonstrated potential in forming complex blood vessel-like networks within organoids.[121] These strategies aim to replicate the vascularization seen in native tissues, which is crucial for the long-term viability and functionality of organoids.

Controlling the organization of multiple cell types within complex 3D architectures is another significant challenge in 3D bioprinting. Although this technique allows precise cell arrangement, achieving precise configurations remains difficult. Furthermore, the manipulation of cell organization within dynamic 3D

structures remains a limitation in current bioprinting models. While 3D bioprinting has been instrumental in studying biochemical and biophysical cues in various diseases, the challenge lies in precisely controlling the organization of different cell types within these structures.[122,123] This limitation underscores the need for further advancements in bioprinting technology to enable more sophisticated manipulation of cell organization within organoids.

Despite these challenges, 3D bioprinting offers the advantage of engineering complex and controllable 3D tissue models with high resolution.[124] However, challenges such as achieving precise construction, addressing hypoxia-related issues, enhancing vascularization, and controlling cell organization persist. Continued research and innovation in bioink development, vascularization techniques, and cell manipulation strategies are essential for overcoming these challenges and unlocking the full potential of 3D bioprinting in precision medicine applications.

3. Synergistic effects of combining 3D-bioprinted organoids with extracellular vesicles

3.1. Overview of organoid-derived extracellular vesicles

OEVs constitute a specific subset of EVs derived from organoids, which are 3D cell culture models that mimic the structure and function of organs. OEVs, like other EVs, are also involved in the transport of bioactive content and have garnered significant attention for their potential applications in drug delivery.[125] These vesicles, including exosomes, macrovesicles, and apoptotic bodies, are spherical nanoparticles with lipid bilayers that transport bioactive content. Exosomes are the most studied due to their optimal size and robust biological functions.[126] OEVs carry proteins (e.g., ESCRT, Alix, TSG101, CD9, CD63, CD81), nucleic acids (mRNA, microRNA, DNA), and lipids (cholesterol, ceramide, sphingolipids), which collectively reflect the physiological state of the source and transmit the biochemical signals to the target recipient cells.[127,128] OEV biogenesis involves the formation of intraluminal vesicles within multivesicular bodies (MVBs), with exosomes released via the plasma membrane.[129] OEVs are internalized by recipient cells through endocytosis, membrane fusion, and receptor-mediated pathways, subsequently affecting cellular responses.[130] Factors like tetraspanins and lectin receptors aid in targeting and binding.[131] Internalization is influenced by microenvironmental factors such as pH and temperature[132] (Figure 4).

3.2. Therapeutic potential of organoid-derived extracellular vesicles in inflammatory-related disorders.

EVs derived from cells in organoid models exhibit distinct characteristics compared to traditional EVs derived from 2D cultures. Table 4 outlines the advantages and challenges associated with current EVs derived from 3D culture conditions. Research indicates that EVs collected under 3D conditions have a significant advantage in quantity compared to those from 2D cultures, with higher similarity with *in vivo* patient plasma-derived EVs in terms of secretion dynamics and molecular content, including small RNA.[133,134] Specifically, EVs from organoids exhibit 96% RNA similarity to serum-derived EVs, and the yield of EVs is 1.5–4.5 times higher in 3D cultures compared to 2D cultures.[135,136]. This abundance of OEVs enhances their efficacy in modulating inflammatory responses and promoting tissue repair.[137]

Current research has demonstrated the efficacy of OEVs in various inflammatory conditions such as IBD, acute kidney injury, arthritis, and neuroinflammation in preclinical studies (Table 5). Research on human and mouse gut organoids confirms that OEVs can modulate immune responses in various cell types like dendritic cells and macrophages. In murine models, EVs from intestinal organoids reduced systemic inflammation and alleviated colitis symptoms, indicating the potential of OEVs as a targeted therapeutic approach for inflammatory conditions, especially when enriched with specific cargo such as microRNAs.[138]

Recent studies have highlighted the enhanced therapeutic efficacy of mesenchymal stem cell (MSC)-derived exosomes produced in 3D culture systems for treating conditions like acute kidney injury. These 3D-cultured exosomes have shown superior performance in reducing renal injury markers and inflammation, suggesting a promising approach for exosome-based therapies in inflammatory and degenerative diseases.[139] Additionally, exosomes derived from umbilical MSCs in 3D microgravity environments have exhibited potential for cartilage repair by maintaining chondrocyte stability, promoting migration, and regulating matrix synthesis.[140] Cerebral organoid-derived exosomes have been investigated for their role in alleviating oxidative stress in Parkinson's disease models, showcasing the diverse applications of OEVs in complex neurological conditions.[141] Zhou *et al.* demonstrated that EVs released from human retinal organoids derived from iPSCs contain microRNAs that regulate gene expression in target retinal progenitor cells, influencing retinal cell function, differentiation, and regeneration. This finding indicates the importance of EVs

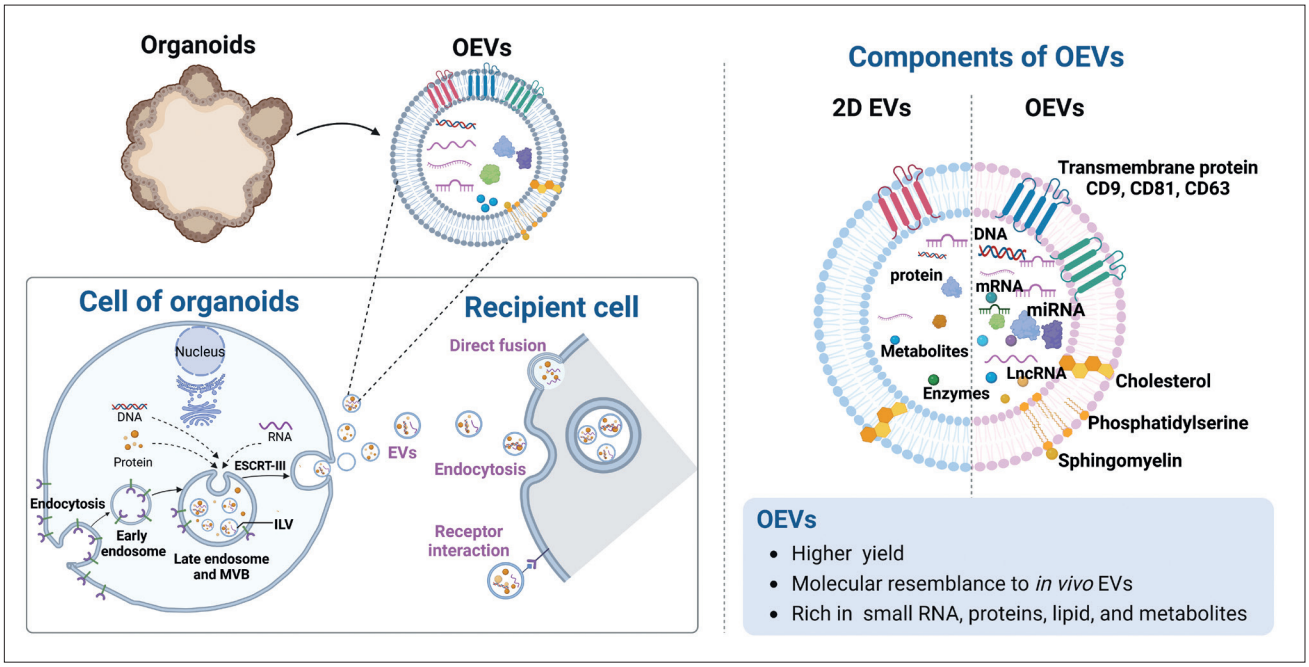


Figure 4. Composition and biogenesis of organoid-derived extracellular vesicles (OEVs). OEV biogenesis occurs through multiple pathways, including through multivesicular bodies (MVBs) within endosomes, which lead to the secretion of extracellular vesicles (EVs), and through fusion with the plasma membrane. Inward budding of MVBs forms intraluminal vesicles (ILVs), and cargos that sorted into the ILVs are regulated by factors such as ESCRT-III. Released OEVs interact with recipient cells through various mechanisms including direct fusion, endocytosis, or receptor interaction. OEVs' diverse constituents include signaling proteins, nucleic acids, lipids, amino acids, enzymes, and metabolites, which reflect their cell of origin.

Table 4. Advantages and challenges of extracellular vesicles derived from 3D culture conditions.

Aspect	Advantages	Challenges
Quantity	EVs from 3D cultures have a significantly higher yield (1.5–4.5 times more) compared to 2D cultures.	Scaling up production while maintaining consistency and quality can be complex and resource intensive.
Similarity to *in vivo* EVs	OEVs show higher similarity to patient plasma EVs, with 96% RNA similarity to serum-derived EVs.	Ensure that these similarities translate to functional equivalence in therapeutic applications.
Secretion dynamics	Enhanced secretion dynamics more closely resemble those of *in vivo* conditions.	Monitoring and controlling secretion dynamics *in vitro* to match those *in vivo* can be technically challenging.
Molecular content	Higher content of small RNA and other bioactive molecules compared to 2D culture-derived EVs.	Variability in molecular content depends on the organoid type and culture conditions.
Efficacy in modulating responses	There is a greater efficacy in modulating inflammatory responses and promoting tissue repair.	Understanding the mechanisms and pathways involved is required for optimizing therapeutic applications.
Scalability for therapeutics	There is potential for larger-scale production for use in clinical applications.	It is challenging to develop cost-effective and reproducible methods for large-scale production.

Abbreviations: OEVs, organoid-derived extracellular vesicles; 3D, three-dimensional; 2D, two-dimensional; and EVs, extracellular vesicles.

in retinal development and disease treatment.[143,144] These studies suggest that the unique properties of OEVs provide a promising avenue for the development of targeted and efficient therapeutic strategies for a wide range of inflammatory and degenerative disorders.

3.3. Integration of 3D bioprinting organoid and extracellular vesicles

The integration of 3D bioprinting organoids and EVs presents a promising avenue for advancing precision medicine applications, particularly in the field of inflammation. While 3D organoid systems offer significant advantages, challenges exist in utilizing 3D culture systems to study EVs. One such challenge is the presence of necrotic cores in spheroids, complicating EV analysis due to the release of apoptotic bodies.[145] Variability in 3D culture methods can also impact EV studies, requiring tailored normalization approaches for analysis.[146] Additionally, standardization of isolation and characterization protocols is crucial for clinical

Table 5. Current research on organoids as promising models for studying extracellular vesicles in various inflammatory diseases.

Disease model	Key findings	Ref.
Inflammatory bowel disease	EVs from human intestinal organoids modulated LPS-induced inflammatory response, with various microRNA contributing to these effects.	[138]
Acute kidney injury	EVs from 3D cultured MSC exhibited yield increase compared to those from 2D culture and have superior anti-inflammatory effects, significantly reducing renal injury.	[139]
Osteochondral defects	EVs derived from 3D cultured umbilical MSC positively affected chondrocyte proliferation, migration, and stability, conferring chondroprotective effects and promoting osteochondral regeneration activity.	[140]
Parkinson's disease	EVs from cerebral organoids reduced oxidative stress and apoptosis in astrocytes while promoting neuronal differentiation.	[141]
Retinal development and disease	EVs derived from retinal organoids regulate the expression of genes related to development, functions, and disease in retinal progenitor cells.	[142]

Abbreviations: EVs, extracellular vesicles; LPS, lipopolysaccharide; 3D, three-dimensional; 2D, two-dimensional; and MSC, mesenchymal stem cell.

translation, as scalability and low yields hinder large-scale therapeutic applications.[147]

The application of 3D bioprinting technologies has shown significant advancements in enhancing the function and properties of OEVs, improving production efficiency, and offering the potential for regenerative medicine and immune-mediated treatment of chronic diseases. By utilizing automated ECM plating processes, 3D bioprinting enhances the speed, accuracy, and performance of matrices, leading to improved organoid production efficiency. The structural integrity, controlled release, and targeted applications provided by 3D bioprinting offer a promising approach to maximize the therapeutic benefits of EVs, making them more effective in precision medicine applications, especially in inflammation.

Overall, the integration of 3D bioprinting in generating tissue structures, organoids, and EVs holds immense potential for personalized cancer treatment, tissue regeneration, and disease treatment. Improving organoid models using 3D bioprinting technologies to better represent the cellular and molecular environment of human tissues is crucial to addressing the limitations of current models and enhancing the efficacy of OEVs in various applications.

Research indicates that bioprinted EVs can significantly impact various medical fields by promoting angiogenesis, osteogenesis, chondrogenesis, myogenesis, and carcinoprevention. The current review includes a total of eight bioprinted EVs studies covering a variety of medical applications (Table 6). The study by Maiullari *et al.* specifically focuses on the use of 3D-bioprinted endothelial-derived EVs for promoting neovascularization, demonstrating the potential of bioprinted EVs in enhancing vascularization and tissue regeneration.[148] Zhang *et al.* demonstrated that 3D-printed polylactic acid (PLA) scaffolds with MSC-derived exosomes possess immunoregulatory potential and promote osteogenic differentiation, showing potential

Table 6. Current studies of 3D-bioprinted extracellular vesicles for various medical applications.

Medical application	Key findings	Ref.
Neovascularization	3D-bioprinted endothelial-derived EVs promoted vascularization and tissue regeneration.	[148]
Bone tissue regeneration	3D-printed PLA scaffolds with MSC-derived exosomes promoted osteogenic differentiation.	[149]
Osteogenesis and angiogenesis	hADSCs-EVs promoted bone formation and angiogenesis *in vitro* and *in vivo*.	[150]
Improved migration and osteogenesis	Bioceramic-induced macrophage-derived EVs enhanced migration, immune response, osteogenesis, and angiogenesis.	[151]
Anti-cancer efficacy	Exo-ssDNA-SA-FasL induced tumor cell apoptosis and modulated immune responses.	[152]
Cartilage and bone regeneration	MSC-derived EVs in ECM/GelMA bioink induced cartilage and bone regeneration.	[153]
Myogenesis	Bioprinted M2-EVs promoted myogenesis and myotube formation *in vitro*.	[154]
Cancer biomarker capture	EVs antibody microarrays captured plasma tumor-specific EVs for early cancer detection.	[155]

Abbreviations: 3D, three-dimensional; ECM, extracellular matrix; EVs, extracellular vesicles; GelMA, gelatin methacryloyl; hADSCs, human adipose-derived stem cells; MSC, mesenchymal stem cell; PLA, Polylactic acid; and M2, M2 type macrophage.

applications in bone tissue regeneration.[149] In one study, Kang *et al*. investigated the use of bioprinted human adipose-derived stem cell-derived EVs (hADSC-sEVs) for bone and angiogenesis *in vitro* and *in vivo*, demonstrating their ability to promote osteogenesis and angiogenesis.[150] A study by Sun *et al*. demonstrated that bioceramic-induced macrophage-derived EVs significantly improved migration, attachment, immune response, and osteogenesis in human bone marrow-derived stem cells (hBMSCs), and angiogenesis in human umbilical vein endothelial cells (HUVECs).[151] Yerneni *et al*. investigated bioprinted oligonucleotide-tethered macrophage-derived small EVs (Exo-ssDNA-SA-FasL) for inducing tumor cell apoptosis and immunomodulation. Their study triggered FasL/Fas-mediated apoptosis in squamous cell carcinoma cells *in vitro* and reduced CD3+ and CD4+ T cells *in vivo*, demonstrating notable anti-cancer efficacy and immunomodulation potential.[152] Another study printed mesenchymal stem cell-derived small extracellular vesicles (MSC-sEVs) in cartilage ECM and GelMA bioink, inducing cartilage and bone regeneration *in vivo*. The 3D-printed ECM/GelMA/exosomes scaffold showed results in addressing chondrocyte mitochondrial dysfunction, enhancing chondrocyte migration, and polarizing synovial macrophages toward an M2 phenotype.[153] Yerneni *et al*. used bioprinted murine macrophage-derived EVs to manufacture an *in vitro* ECM microenvironment consisting of exosomes.[154] EVs were enriched from a murine macrophage cell line (J774A.1) in M0 (non-activated), M1 (pro-inflammatory), and M2 (pro-regenerative) phenotypes and bioprinted in glycerol bioink on collagen type-I-coated slides. Myogenesis in murine myoblasts—C2C12 cells—was assessed, showing that the bioprinted M1-EVs microenvironment inhibited, while M2-EVs promoted, myogenesis by upregulating myosin heavy chain (MF20) expression and myotube formation.[154] These findings show the potential of bioprinted EVs in influencing cell bioactivity and promoting myogenesis *in vitro*. Another study used a bioprinting technique to print EV antibody microarrays to capture plasma tumor-specific stem cell-derived EVs (sEVs) from head and neck squamous cell carcinoma patients.[155] These studies indicate the emerging interest in utilizing 3D-bioprinted sEVs for various applications.

3.4. Applications of precision medicine for inflammation

The integration of 3D-bioprinted organoids with EVs presents a promising approach in the field of precision medicine, particularly for inflammatory conditions. EVs derived from 3D-bioprinted organoids can carry targeted therapeutic agents or genetic material, which can modulate inflammatory responses when delivered to affected tissues. This targeted strategy allows for the development of personalized treatment strategies, which can lead to reduced side effects and increased intervention efficacy tailored to individual patients. For instance, incorporating EVs loaded with anti-inflammatory agents into bioinks for printing organoids enables controlled and sustained release of these agents directly at the site of inflammation. This method offers precise delivery and sustained release, making it an effective strategy for managing chronic inflammatory diseases like RA or IBD.[149,150,153]

The application of OEVs in precision medicine extends to various areas such as biomarker discovery, drug screening, and personalized treatment strategies. EVs have shown promise in identifying disease-specific biomarkers, aiding in early diagnosis, and monitoring disease progression. Proteomic analysis of EVs from cancerous and healthy organoid cultures has improved the specificity and sensitivity of cancer diagnosis, enhancing personalized medicine by providing specific biomarkers reflective of the individual's microenvironment.[156–158] Patient-derived exosomes have demonstrated therapeutic potential in cancer therapy by targeting specific molecular pathways to mitigate aggressive cancer characteristics.[159] Additionally, EVs derived from intestinal organoids have shown the ability to modulate immune responses, suggesting therapeutic applications for inflammatory conditions like colitis.[20]

The use of 3D bioprinting to create patient-specific organoids integrated with EVs represents an advanced approach in regenerative medicine and personalized therapy. This method utilizes patient-specific data obtained through advanced imaging technologies like computed tomography (CT) or X-ray scans to create precise models of tissue defects. By employing personalized computer-aided design (CAD) modeling, 3D-bioprinted constructs can be fabricated to replicate the unique characteristics of the patient's tissues. Compared to traditional methods, incorporating EVs into these bioprinted models enhances their therapeutic potential by more accurately mimicking the complex biological environment.[160,161]

Therefore, the combination of 3D-bioprinted organoids with EVs offers a promising avenue for precision medicine in managing inflammatory conditions and advancing personalized treatment strategies. This approach enables targeted delivery of therapeutic agents and enhances disease monitoring, diagnosis, and treatment efficacy through the use of 3D-bioprinted OEVs (Figure 5).

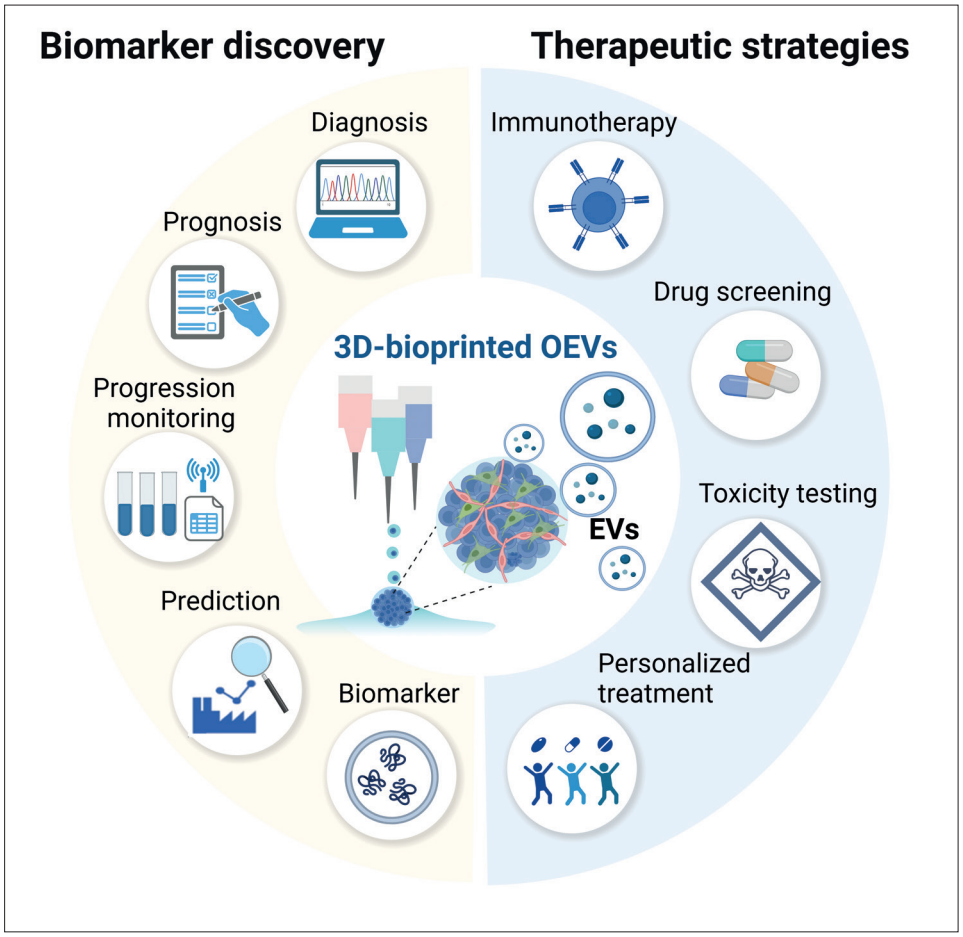


Figure 5. Potential applications of 3D-bioprinted organoid-derived extracellular vesicles (OEVs) for precision medicine. 3D-bioprinted OEVs can be used as biomarkers in cancer diagnosis, prediction, and monitoring disease progression. Additionally, due to their ability to mimic the EVs of individual patients, they can be exploited for personalized drug screening, toxicity testing, and personalized treatments.

4. Future directions and challenges in integrating 3D bioprinting with organoid and extracellular vesicle technology

The integration of 3D bioprinting with organoid and EV technology holds significant promise for advancing precision medicine and personalized therapies. This innovative technique enables the spatial and temporal patterning of cell-derived EVs at high resolution within scaffolds, allowing for the creation of complex tissues composed of various cell types with synchronized development. By utilizing 3D bioprinting techniques such as extrusion, inkjet, or laser-assisted bioprinting, researchers can address challenges associated with maintaining the biological function of bioprinted OEVs. These gentler bioprinting methods ensure the preservation of the bioactivity of encapsulated biotherapeutics, including EVs, during the printing process.[162]

By incorporating EVs into 3D-bioprinted organoids, researchers can create more accurate disease models that mimic pathological conditions, facilitating a deeper understanding of disease mechanisms and accelerating drug screening processes. This innovative approach has shown great potential in regenerative medicine by enhancing tissue regeneration and improving targeting efficacy. However, in translating personalized bioprinted EVs into clinical applications, addressing technical challenges such as standardizing EV production to Good Manufacturing Practice (GMP) grades, optimizing EV enrichment, and refining targeted delivery methods are crucial. These efforts are essential to ensure the safety and efficacy of personalized bioprinted EV constructs.

GMP-grade production involves stringent quality control measures to maintain the consistency, purity, and safety of EVs. Standardized protocols for EV isolation, purification, and characterization that are scalable

and reproducible are essential for clinical applications. Additionally, regulatory guidelines need to be established to govern the production and use of bioprinted EVs in clinical settings.

Optimizing the enrichment of EVs is another critical challenge. Current methods for EV isolation, such as ultracentrifugation, size-exclusion chromatography, and immunoaffinity capture, often result in low yields and purity. Enhancing these techniques or developing new methods to increase the efficiency of EV enrichment is necessary. Additionally, understanding the heterogeneity of EV populations and identifying therapeutically relevant subtypes are crucial for optimizing enrichment processes.

Continued advancements in 3D bioprinting technology, including improvements in printer resolution, speed, and bioink formulations, are essential for the successful integration of EVs with bioprinted organoids. Innovations such as multi-material printing and real-time monitoring of the bioprinting process can enhance the precision and functionality of bioprinted constructs. Furthermore, developing bioinks that can support the encapsulation and controlled release of EVs will be crucial for creating effective therapeutic constructs.

While the bioprinted EVs, particularly OEVs, show promising therapeutic potential in various fields, further research is necessary to validate their efficacy across various therapeutic applications. OEVs may offer advantages over traditional EVs in terms of quantity and physiological effects, making them more suitable for therapeutic applications. By exploring a broader range of 3D-bioprinted OEVs in different therapeutic areas such as chronic inflammatory diseases, researchers can uncover new applications and maximize the utility of bioprinted EVs.

Despite the promising prospects, research on 3D-bioprinted OEVs is still limited and their application as a therapeutic tool remains largely unexplored. The potential of 3D-bioprinted OEVs in revolutionizing biomedical research and providing new therapeutic avenues for complex diseases, particularly inflammatory conditions, is substantial. As 3D bioprinting technology advances and multifunctional integrated organoids are developed, the ability to simulate the human body's physiological environment and functions *in vitro* will improve. These integrated organoids can be used to study complex disease mechanisms, test drug efficacy and toxicity, and develop personalized treatment strategies. The ability to extract more effective OEVs from these advanced models will meet the demands of disease treatment and showcase the significant potential of 3D-bioprinted OEVs in benefiting patients.

5. Conclusion and outlooks

The integration of 3D bioprinting with EVs and organoids represents a cutting-edge approach with tremendous potential in precision medicine. Overcoming technical challenges, standardizing production processes, optimizing EV enrichment, and conducting further research to validate their efficacy are crucial steps in harnessing the full potential of 3D-bioprinted OEVs for personalized medicine and regenerative therapies. Continued research and innovation will pave the way for new therapeutic avenues, improving the treatment of complex diseases and advancing personalized medicine. As this field progresses, the significant potential of 3D-bioprinted OEVs will become increasingly apparent, offering promising solutions for various medical applications and enhancing patient outcomes in the future.

Acknowledgments

All figures were created using BioRender.

Funding

This work was supported by the National Research Foundation of Korea (NRF) funded by the Republic of Korea government (2022R1C1C1009606), and the Basic Science Research Program through the National Research Foundation of Korea (NRF) funded by the Ministry of Education (2022R1I1A1A01071265).

Conflict of interest

The authors declare they have no competing interests

Author contributions

Conceptualization: Mi-Kyung Oh, Kyung-Rok Yu
Writing – original draft: All authors
Writing – review & editing: Mi-Kyung Oh, Kyung-Rok Yu

Ethics approval and consent to participate

Not applicable.

Consent for publication

Not applicable.

Availability of data

Not applicable.

References

1. Karami Fath M, Azami J, Jaafari N, et al. Exosome application in treatment and diagnosis of B-cell disorders: leukemias,

multiple sclerosis, and arthritis rheumatoid. *Cell Mol Biol Lett.* 2022;27(1):74.
doi: 10.1186/s11658-022-00377-x

2. Mozdiak E, O'Malley JW, Arasaradnam RP. Inflammatory bowel disease. *BMJ*. 2015;351:h4416.
doi: 10.1136/bmj.h4416

3. Zhao Z, Chen X, Dowbaj AM, et al. Organoids. *Nat Rev Methods Primers*. 2022;2(1):94.
doi: 10.1038/s43586-022-00174-y

4. Lancaster MA, Knoblich JA. Organogenesis in a dish: modeling development and disease using organoid technologies. *Science*. 2014:345(6194):1247125.
doi: 10.1126/science.1247125

5. Grassi L, Alfonsi R, Francescangeli F, et al. Organoids as a new model for improving regenerative medicine and cancer personalized therapy in renal diseases. *Cell Death Dis.* 2019;10(3):201.
doi: 10.1038/s41419-019-1453-0

6. Pauli C, Hopkins BD, Prandi D, et al. Personalized in vitro and in vivo cancer models to guide precision medicine. *Cancer Discov.* 2017;7(5):462-477.
doi: 10.1158/2159-8290.Cd-16-1154

7. Zhang Y, Li G, Wang J, Zhou F, Ren X, Su J. Small joint organoids 3D bioprinting: construction strategy and application. *Small.* 2024;20(8):e2302506.
doi: 10.1002/smll.202302506

8. Datta P, Dey M, Ataie Z, Unutmaz D, Ozbolat IT. 3D bioprinting for reconstituting the cancer microenvironment. *NPJ Precis Oncol.* 2020; 4:18.
doi: 10.1038/s41698-020-0121-2

9. Augustine R, Kalva SN, Ahmad R, et al. 3D bioprinted cancer models: revolutionizing personalized cancer therapy. *Transl Oncol.* 2021;14(4):101015.
doi: 10.1016/j.tranon.2021.101015

10. Zhang J, Wehrle E, Rubert M, Müller R. 3D bioprinting of human tissues: biofabrication, bioinks, and bioreactors. *Int J Mol Sci.* 2021;22(8):3971.
doi: 10.3390/ijms22083971

11. Dey M, Ozbolat IT. 3D bioprinting of cells, tissues and organs. *Sci Rep.* 2020;10(1):14023.
doi: 10.1038/s41598-020-70086-y

12. Gopalakrishnan S, Bakke I, Hansen MD, et al. Comprehensive protocols for culturing and molecular biological analysis of IBD patient-derived colon epithelial organoids. *Front Immunol.* 2023;14:1097383.
doi: 10.3389/fimmu.2023.1097383

13. Pott J, Kabat AM, Maloy KJ. Intestinal epithelial cell autophagy is required to protect against TNF-induced apoptosis during chronic colitis in mice. *Cell Host Microbe.* 2018;23(2):191-202.e194.
doi: 10.1016/j.chom.2017.12.017.

14. Liu H, Su J. Organoid and organoid extracellular vesicles for osteoporotic fractures therapy: current status and future perspectives. *Interdiscip Med.* 2023;1(3):e20230011.
doi: 10.1002/inmd.20230011

15. Wang H. Modeling neurological diseases with human brain organoids. *Front Synaptic Neurosci.* 2018;10:15.
doi: 10.3389/fnsyn.2018.00015

16. Szvicsek Z, Oszvald Á, Szabó L, et al. Extracellular vesicle release from intestinal organoids is modulated by Apc mutation and other colorectal cancer progression factors. *Cell Mol Life Sci.* 2019;76(12):2463-2476.
doi: 10.1007/s00018-019-03052-1

17. Gabrielli M, Tozzi F, Verderio C, Origlia N. Emerging roles of extracellular vesicles in Alzheimer's disease: focus on synaptic dysfunction and vesicle-neuron interaction. *Cells.* 2022;12(1):63.
doi: 10.3390/cells12010063

18. Bakinowska E, Kiełbowski K, Pawlik A. The role of extracellular vesicles in the pathogenesis and treatment of rheumatoid arthritis and osteoarthritis. *Cells.* 2023;12(23):2716.
doi: 10.3390/cells12232716

19. Arthur P, Kandoi S, Lee S, et al. Biophysical, molecular and proteomic profiling of human retinal organoid-derived exosomes. *Pharm Res.* 2022;40(4):801-816.
doi: 10.1007/s11095-022-03350-7

20. Szvicsek Z, Oszvald Á, Szabó L, et al. Extracellular vesicle release from intestinal organoids is modulated by Apc mutation and other colorectal cancer progression factors. *Cell Mol Life Sci.* 2019;76(12):2463-2476.
doi: 10.1007/s00018-019-03052-1

21. Arthur P, Kandoi S, Lee S, et al. Biophysical, molecular and proteomic profiling of human retinal organoid-derived exosomes. *Pharm Res.* 2022;40(4):801-816.
doi: 10.1007/s11095-022-03350-7

22. Buenafe AC, Dorrell C, Reddy AP, Klimek J, Marks DL. Proteomic analysis distinguishes extracellular vesicles produced by cancerous versus healthy pancreatic organoids. *Sci Rep*. 2022;12(1):3556.

doi: 10.1038/s41598-022-07451-6

23. Liu Y, Li N, Zhu Y. Pancreatic organoids: A frontier method for investigating pancreatic-related diseases. *Int J Mol Sci.* 2023;24(4):4027.
doi: 10.3390/ijms24044027

24. Prasad M, Kumar R, Buragohain L, Kumari A, Ghosh M. Organoid technology: a reliable developmental biology tool for organ-specific nanotoxicity evaluation. *Front Cell Dev Biol.* 2021;9:696668.
doi: 10.3389/fcell.2021.696668

25. Liu H, Sun J, Wang M, Wang S, Su J, Xu C. Intestinal organoids and organoids extracellular vesicles for inflammatory bowel disease treatment. *Chem Eng J.* 2023;465:142842.
doi: 10.1016/j.cej.2023.142842

26. Lucafò M, Muzzo A, Marcuzzi M, Giorio L, Decorti G, Stocco G. Patient-derived organoids for therapy personalization in inflammatory bowel diseases. *World J Gastroenterol.* 2022;28(24):2636-2653. doi: 10.3748/wjg.v28.i24.2636

27. Velasco V, Shariati SA, Esfandyarpour R. Microtechnology-based methods for organoid models. *Microsyst Nanoeng.* 2020;6(1):76. doi: 10.1038/s41378-020-00185-3

28. Teixeira MC, Lameirinhas NS, Carvalho JPF, Silvestre AJD, Vilela C, Freire CSR. A guide to polysaccharide-based hydrogel bioinks for 3D bioprinting applications. *Int J Mol Sci.* 2022;23(12):6564. doi: 10.3390/ijms23126564

29. Hospodiuk M, Dey M, Sosnoski D, Ozbolat IT. The bioink: a comprehensive review on bioprintable materials. *Biotechnol Adv.* 2017;35(2):217-239. doi: 10.1016/j.biotechadv.2016.12.006

30 Sun B, Han Y, Jiang W, Dai K. 3D printing bioink preparation and application in cartilage tissue reconstruction in vitro. *J Shanghai Jiaotong Univ (Sci).* 2021;26(3):267-271. doi: 10.1007/s12204-021-2292-6

31. Liu W, Heinrich MA, Zhou Y, et al. Extrusion bioprinting of shear-thinning gelatin methacryloyl bioinks. *Adv Healthc Mater.* 2017;6(12):1601451. doi: 10.1002/adhm.201601451

32. Wan H, Xiang J, Mao G, Pan S, Li B, Lu Y. Recent advances in the application of 3d-printing bioinks based on decellularized extracellular matrix in tissue engineering. *ACS Omega*. 2024;9(23):24219-24235. doi: 10.1021/acsomega.4c02847

33. Takahashi K, Tanabe K, Ohnuki M, et al. Induction of pluripotent stem cells from adult human fibroblasts by defined factors. *Cell.* 2007;131(5):861-872. doi: 10.1016/j.cell.2007.11.019

34. Benwood C, Walters-Shumka J, Scheck K, Willerth SM. 3D bioprinting patient-derived induced pluripotent stem cell models of Alzheimer's disease using a smart bioink. *Bioelectron Med.* 2023;9(1):10. doi: 10.1186/s42234-023-00112-7

35. Liu H, Gong Y, Zhang K, et al. Recent advances in decellularized matrix-derived materials for bioink and 3d bioprinting. *Gels.* 2023;9(3):195. doi: 10.3390/gels9030195

36. Song SS, Park HJ, Kim YK, Kang SW. Revolutionizing biomedical research: the imperative need for heart–kidney-connected organoids. *Apl Bioeng.* 2024;8(1):010902. doi: 10.1063/5.0190840

37. Xu C, Chai W, Huang Y, Markwald RR. Scaffold-free inkjet printing of three-dimensional zigzag cellular tubes. *Biotechnol Bioeng.* 2012;109(12):3152-3160. doi: 10.1002/bit.24591

38. Serex L, Sharma K, Rizov V, Bertsch A, McKinney JD, Renaud P. Microfluidic-assisted bioprinting of tissues and organoids at high cell concentrations. *Biofabrication.* 2021;13(2):025006. doi: 10.1088/1758-5090/abca80

39. Muenks D, Kyosev Y. Productivity comparison between vat polymerization and fused filament fabrication methods for additive manufacturing of polymers. *3D Print Addit Manuf.* 2021;10(1):40-49. doi: 10.1089/3dp.2021.0009

40. Cendrero AM, Fortunato GM, Munoz-Guijosa JM, De Maria C, Díaz Lantada A. Benefits of non-planar printing strategies towards eco-efficient 3D printing. *Sustainability.* 2021;13(4):1599. doi: 10.3390/su13041599

41. Wan X, Luo L, Liu Y, Leng J. Direct ink writing based 4D printing of materials and their applications. *Adv Sci.* 2020;7(16):2001000. doi: 10.1002/advs.202001000

42. Cui H, Nowicki M, Fisher JP, Zhang LG. 3D bioprinting for organ regeneration. *Adv Healthc Mater.* 2017;6(1):1601118. doi: 10.1002/adhm.201601118

43. Hansen CJ, Saksena R, Kolesky DB, et al. High-throughput printing via microvascular multinozzle arrays. *Adv Mater.* 2013;25(1):96-102. doi: 10.1002/adma.201203321

44. Ravanbakhsh H, Karamzadeh V, Bao G, Mongeau L, Juncker D, Zhang YS. Emerging technologies in multi-material bioprinting. *Adv Mater.* 2021;33(49):2104730. doi: 10.1002/adma.202104730

45. Singh M, Haverinen HM, Dhagat P, Jabbour GE. Inkjet printing—process and its applications. *Adv Mater.* 2010;22(6):673-685. doi: 10.1002/adma.200901141

46. Cui X, Boland T. Human microvasculature fabrication using thermal inkjet printing technology. *Biomaterials.* 2009;30(31):6221-6227. doi: 10.1016/j.biomaterials.2009.07.056

47. Park JA, Yoon S, Kwon J, et al. Freeform micropatterning of living cells into cell culture medium using direct inkjet printing. *Sci Rep.* 2017;7(1):14610. doi: 10.1038/s41598-017-14726-w

48. Matsusaki M, Sakaue K, Kadowaki K, Akashi M. Three-dimensional human tissue chips fabricated by rapid and automatic inkjet cell printing. *Adv Healthc Mater.* 2013;2(4):534-539. doi: 10.1002/adhm.201200299

49. Jamieson C, Keenan P, Kirkwood D, et al. A review of recent advances in 3D bioprinting with an eye on future regenerative therapies in veterinary medicine. *Front Vet Sci.* 2020;7:584193. doi: 10.3389/fvets.2020.584193

50. Li J, Chen M, Fan X, Zhou H. Recent advances in bioprinting techniques: approaches, applications and future prospects. *J Transl Med.* 2016;14(1):271. doi: 10.1186/s12967-016-1028-0

51. Carberry BJ, Hergert JE, Yavitt FM, et al. 3D printing of sacrificial thioester elastomers using digital light processing for templating 3D organoid structures in soft biomatrices. *Biofabrication.* 2021;13(4):044104. doi: 10.1088/1758-5090/ac1c98

52. Zhang Y, Li G, Wang J, Zhou F, Ren X, Su J. Small joint organoids 3D bioprinting: construction strategy and application. *Small.* 2023;20(8):2302506. doi: 10.1002/smll.202302506

53. Kačarević ŽP, Rider PM, Alkildani S, et al. An introduction to 3D bioprinting: possibilities, challenges and future aspects. *Materials (Basel).* 2018;11(11):2199. doi: 10.3390/ma11112199

54. Chang MY, Bogacheva MS, Lou YR. Challenges for the applications of human pluripotent stem cell-derived liver organoids. *Front Cell and Dev Biol.* 2021; 9:748576. doi: 10.3389/fcell.2021.748576

55. Hospodiuk M, Dey M, Sosnoski DM, Özbolat İT. The bioink: a comprehensive review on bioprintable materials. *Biotechnol Adv.* 2017;35(2):217-239. doi: 10.1016/j.biotechadv.2016.12.006

56. Li J, Chen M, Fan X, Zhou H. Recent advances in bioprinting techniques: approaches, applications and future prospects. *J Transl Med.* 2016;14:1-15. doi: 10.1186/s12967-016-1028-0

57. Kryou C, Leva V, Chatzipetrou M, Zergioti I. Bioprinting for liver transplantation. *Bioengineering.* 2019;6(4):95. doi: 10.3390/bioengineering6040095

58. Bertassoni LE, Cardoso JC, Manoharan V, et al. Direct-write bioprinting of cell-laden methacrylated gelatin hydrogels. *Biofabrication.* 2014;6(2):024105. doi: 10.1088/1758-5082/6/2/024105

59. Paxton N, Smolan W, Böck T, Melchels FPW, Groll J. Proposal to assess printability of bioinks for extrusion-based bioprinting and evaluation of rheological properties governing bioprintability. *Biofabrication.* 2017; 9:044107. doi: 10.1088/1758-5090/aa8dd8

60. Liu W, Heinrich MA, Zhou Y, et al. Extrusion bioprinting of shear-thinning gelatin methacryloyl bioinks. *Adv Healthc Mater.* 2017;6(12):1601451. doi: 10.1002/adhm.201601451

61. Bernal PN, Bouwmeester M, Madrid-Wolff J, et al. Volumetric bioprinting of organoids and optically tuned hydrogels to build liver-like metabolic biofactories. *Adv Mater.* 2022;34(15):2110054. doi: 10.1002/adma.202110054

62. Grix T, Ruppelt A, Thomas A, et al. Bioprinting perfusion-enabled liver equivalents for advanced organ-on-a-chip applications. *Genes.* 2018;9(4):176. doi: 10.3390/genes9040176

63. Pamarthy S, Sabaawy HE. Patient derived organoids in prostate cancer: improving therapeutic efficacy in precision medicine. *Mol Cancer.* 2021;20(1):125. doi: 10.1186/s12943-021-01426-3

64. Vlachogiannis G, Hedayat S, Vatsiou A, et al. Patient-derived organoids model treatment response of metastatic gastrointestinal cancers. *Science.* 2018;359(6378):920-926. doi: 10.1126/science.aao2774

65. Sachs N, Ligt JD, Kopper O, et al. A living biobank of breast cancer organoids captures disease heterogeneity. *Cell.* 2018;172(1–2):373-386.e310. doi: 10.1016/j.cell.2017.11.010

66. Maenhoudt N, Defraye C, Boretto M, et al. Developing organoids from ovarian cancer as experimental and preclinical models. *Stem Cell Rep.* 2020;14(4):717-729. doi: 10.1016/j.stemcr.2020.03.004

67. Aboulkheyr Es H, Montazeri L, Aref AR, Vosough M, Baharvand H. Personalized cancer medicine: an organoid approach. *Trends Biotechnol.* 2018;36(4):358-371. doi: 10.1016/j.tibtech.2017.12.005

68. Schene IF, Joore IP, Oka R, et al. Prime editing for functional repair in patient-derived disease models. *Nat Commun.* 2020;11(1):5352. doi: 10.1038/s41467-020-19136-7

69. Gopal S, Rodrigues AL, Dordick JS. Exploiting CRISPR Cas9 in three-dimensional stem cell cultures to model disease. *Front Bioeng Biotechnol.* 2020;8:692. doi: 10.3389/fbioe.2020.00692

70. Dekkers JF, Wiegerinck CL, de Jonge HR, et al. A functional CFTR assay using primary cystic fibrosis intestinal organoids. *Nat Med.* 2013;19(7):939-945. doi: 10.1038/nm.3201

71. Inak G, Rybak-Wolf A, Lisowski P, et al. Defective metabolic programming impairs early neuronal morphogenesis in neural cultures and an organoid model of Leigh syndrome. *Nat Commun.* 2021;12(1):1929. doi: 10.1038/s41467-021-22117-z

72. Zhang W, Ma L, Yang M, et al. Cerebral organoid and mouse models reveal a RAB39b-PI3K-mTOR pathway-dependent dysregulation of cortical development leading to macrocephaly/autism phenotypes. *Genes Dev.* 2020; 34(7–8):580-597. doi: 10.1101/gad.332494.119

73. An HL, Kuo HC, Tang TK. Modeling human primary microcephaly with hiPSC-derived brain organoids carrying CPAP-E1235V disease-associated mutant protein. *Front Cell Dev Biol.* 2022;10:830432. doi: 10.3389/fcell.2022.830432

74. Xiaoshuai L, Qiushi W, Rui W. Advantages of CRISPR-Cas9 combined organoid model in the study of congenital nervous system malformations. *Front Bioeng Biotechnol.* 2022;10:932936.
doi: 10.3389/fbioe.2022.932936

75. Geurts MH, de Poel E, Pleguezuelos-Manzano C, et al. Evaluating CRISPR-based prime editing for cancer modeling and CFTR repair in organoids. *Life Sci Alliance.* 2021;4(10).
doi: 10.26508/lsa.202000940

76. Geurts MH, de Poel E, Amatngalim GD, et al. CRISPR-based adenine editors correct nonsense mutations in a cystic fibrosis organoid biobank. *Cell Stem Cell.* 2020;26(4):503-510.e507.
doi: 10.1016/j.stem.2020.01.019

77. Al-Mansour AHM, Rizk ANGA, Al-Mansour HMS, et al. Updates in the use of 3D bioprinting in biomedical engineering for clinical application: a review. *J Pharm Res Int*. 2022;34:42-53.
doi: 10.9734/jpri/2022/v34i587263

78. Miller JS, Stevens KR, Yang MT, et al. Rapid casting of patterned vascular networks for perfusable engineered three-dimensional tissues. *Nat Mater.* 2012;11(9):768-774.
doi: 10.1038/nmat3357

79. Daly AC, Davidson MD, Burdick JA. 3D bioprinting of high cell-density heterogeneous tissue models through spheroid fusion within self-healing hydrogels. *Nat Commun.* 2021;12(1):753.
doi: 10.1038/s41467-021-21029-2

80. Ayan B, Heo DN, Zhang Z, et al. Aspiration-assisted bioprinting for precise positioning of biologics. *Sci Adv.* 2020;6(10):eaaw5111.
doi: 10.1126/sciadv.aaw5111

81. Kang HW, Lee SJ, Ko IK, Kengla C, Yoo JJ, Atala A. A 3D bioprinting system to produce human-scale tissue constructs with structural integrity. *Nat Biotechnol.* 2016;34(3):312-319.
doi: 10.1038/nbt.3413

82. Zhang YS, Yue K, Aleman J, et al. 3D bioprinting for tissue and organ fabrication. *Ann Biomed Eng.* 2017;45(1):148-163.
doi: 10.1007/s10439-016-1612-8

83. Brassard JA, Nikolaev M, Hübscher T, Hofer M, Lutolf MP. Recapitulating macro-scale tissue self-organization through organoid bioprinting. *Nat Mater.* 2021;20(1):22-29.
doi: 10.1038/s41563-020-00803-5

84. Kolesky DB, Truby RL, Gladman AS, Busbee TA, Homan KA, Lewis JA. 3D bioprinting of vascularized, heterogeneous cell-laden tissue constructs. *Adv Mater.* 2014;26(19):3124-3130.
doi: 10.1002/adma.201305506

85. Freeman FE, Burdis R, Kelly DJ. Printing new bones: from print-and-implant devices to bioprinted bone organ precursors. *Trends Mol Med*. 2021;27(7):700-711.
doi: 10.1016/j.molmed.2021.05.001

86. Qu J, Kalyani FS, Liu L, Cheng T, Chen L. Tumor organoids: synergistic applications, current challenges, and future prospects in cancer therapy. *Cancer Commun.* 2021;41(12):1331-1353.
doi: 10.1002/cac2.12224

87. Li YE, Jodat YA, Samanipour R, et al. Toward a neurospheroid niche model: optimizing embedded 3D bioprinting for fabrication of neurospheroid brain-like co-culture constructs. *Biofabrication.* 2020;13(1):015014.
doi: 10.1088/1758-5090/abc1be

88. Flores-Torres S, Peza-Chavez O, Kuasne H, et al. Alginate-gelatin-matrigel hydrogels enable the development and multigenerational passaging of patient-derived 3D bioprinted cancer spheroid models. *Biofabrication.* 2021;13(2):025001.
doi: 10.1088/1758-5090/abdb87

89. Chen H, Wu Z, Gong Z, et al. Acoustic bioprinting of patient-derived organoids for predicting cancer therapy responses. *Adv Healthc Mater.* 2022;11(13):e2102784.
doi: 10.1002/adhm.202102784

90. Soman SS, Vijayavenkataraman S. Applications of 3D bioprinted-induced pluripotent stem cells in healthcare. *Int J Bioprint*. 2020;6(4):280.
doi: 10.18063/ijb.v6i4.280

91. Almutary AG, Alnuqaydan AM, Almatroodi SA, Bakshi HA, Chellappan DK, Tambuwala MM. Development of 3D-bioprinted colitis-mimicking model to assess epithelial barrier function using albumin nano-encapsulated anti-inflammatory drugs. *Biomimetics (Basel)*. 2023;8(1):41.
doi: 10.3390/biomimetics8010041

92. Lin J, Sun AR, Li J, et al. A three-dimensional co-culture model for rheumatoid arthritis pannus tissue. *Front Bioeng Biotechnol.* 2021;9:764212.
doi: 10.3389/fbioe.2021.764212

93. Madden LR, Nguyen TV, Garcia-Mojica S, et al. Bioprinted 3D primary human intestinal tissues model aspects of native physiology and ADME/tox functions. *iScience.* 2018;2:156-167.
doi: 10.1016/j.isci.2018.03.015

94. Zhu B, Wang D, Pan H, et al. Three-in-one customized bioink for islet organoid: GelMA/ECM/PRP orchestrate pro-angiogenic and immunoregulatory function. *Colloids Surf B: Biointerfaces.* 2023;221:113017.
doi: 10.1016/j.colsurfb.2022.113017

95. Wang D, Guo Y, Zhu J, et al. Hyaluronic acid methacrylate/pancreatic extracellular matrix as a potential 3D printing bioink for constructing islet organoids. *Acta Biomater.* 2023;165:86-101.
doi: 10.1016/j.actbio.2022.06.036

96. Ao Z, Song S, Tian C, et al. Understanding immune-driven brain aging by human brain organoid microphysiological analysis platform. *Adv Sci.* 2022;9(27):2200475.
doi: 10.1002/advs.202200475

97. Ao Z, Cai H, Wu Z, et al. Tubular human brain organoids to model microglia-mediated neuroinflammation. *Lab Chip.* 2021;21(14):2751-2762.
doi: 10.1039/d1lc00030f

98. Jian H, Li X, Dong Q, Tian S, Bai S. In vitro construction of liver organoids with biomimetic lobule structure by a multicellular 3D bioprinting strategy. *Cell Prolif.* 2023;56(5):e13465.
doi: 10.1111/cpr.13465

99. Jelinsky SA, Derksen M, Bauman EB, et al. Molecular and functional characterization of human intestinal organoids and monolayers for modeling epithelial barrier. *Inflamm Bowel Dis*. 2022;29(2):195-206.
doi: 10.1093/ibd/izac212

100. Qu M, Xiong L, Lyu Y, et al. Establishment of intestinal organoid cultures modeling injury-associated epithelial regeneration. *Cell Res.* 2021;31(3):259-271.
doi: 10.1038/s41422-020-00453-x

101. d'Aldebert E, Quaranta M, Sébert M, et al. Characterization of human colon organoids from inflammatory bowel disease patients. *Front Cell Dev Biol*. 2020;8:363.
doi: 10.3389/fcell.2020.00363

102. Meir M, Salm J, Fey C, et al. Enteroids generated from patients with severe inflammation in Crohn's disease maintain alterations of junctional proteins. *J Crohn's Colitis*. 2020;14(10):1473-1487.
doi: 10.1093/ecco-jcc/jjaa085

103. Niklinska-Schirtz BJ, Venkateswaran S, Anbazhagan M, et al. Ileal derived organoids from Crohn's disease patients show unique transcriptomic and secretomic signatures. *Cell Mol Gastroenterol Hepatol.* 2021;12(4):1267-1280.
doi: 10.1016/j.jcmgh.2021.06.018

104. Sun X, Cui Z, Liang Y, et al. One-stop assembly of adherent 3D retinal organoids from hiPSCs based on 3D-printed derived PDMS microwell platform. *Biofabrication.* 2023;15(3):035005.
doi: 10.1088/1758-5090/acc761

105. Fuller S, Steele M, Münch G. Activated astroglia during chronic inflammation in Alzheimer's disease--do they neglect their neurosupportive roles? *Mutat Res.* 2010; 690(1–2):40-49.
doi: 10.1016/j.mrfmmm.2009.08.016

106. Bélarbi K, Cuvelier E, Bonte MA, et al. Glycosphingolipids and neuroinflammation in Parkinson's disease. *Mol Neurodegener.* 2020;15(1):59.
doi: 10.1186/s13024-020-00408-1

107. Chiurchiù V, Maccarrone M. Chronic inflammatory disorders and their redox control: from molecular mechanisms to therapeutic opportunities. *Antioxid Redox Signal.* 2011;15(9):2605-2641.
doi: 10.1089/ars.2010.3547

108. Bélanger M, Magistretti PJ. The role of astroglia in neuroprotection. *Dialogues Clin Neurosci.* 2009;11(3): 281-295.
doi: 10.31887/dcns.2009.11.3/mbelanger

109. Bordoni M, Rey F, Fantini V, et al. From neuronal differentiation of iPSCs to 3D neuro-organoids: modelling and therapy of neurodegenerative diseases. *Int J Mol Sci.* 2018;19(12):3972.
doi: 10.3390/ijms19123972

110. Ormel PR, Sá RVD, Bodegraven EJV, et al. Microglia innately develop within cerebral organoids. *Nat Commun.* 2018;9(1):4167.
doi: 10.1038/s41467-018-06684-2

111. Bi FC, Yang XH, Cheng X, et al. Optimization of cerebral organoids: a more qualified model for Alzheimer's disease research. *Transl Neurodegener.* 2021;10(1):27.
doi: 10.1186/s40035-021-00252-3

112. Kim H, Park HJ, Choi H, et al. Modeling G2019S-LRRK2 sporadic Parkinson's disease in 3D midbrain organoids. *Stem Cell Rep.* 2019;12(3):518-531.
doi: 10.1016/j.stemcr.2019.01.020

113. Lozano R, Stevens L, Thompson BC, et al. 3D printing of layered brain-like structures using peptide modified gellan gum substrates. *Biomaterials.* 2015;67: 264-273.
doi: 10.1016/j.biomaterials.2015.07.022

114. Kuzmenko V, Karabulut E, Pernevik E, Enoksson P, Gatenholm P. Tailor-made conductive inks from cellulose nanofibrils for 3D printing of neural guidelines. *Carbohydr Polym.* 2018;189:22-30.
doi: 10.1016/j.carbpol.2018.01.097

115. Zhou Z, Cong L, Cong X. Patient-derived organoids in precision medicine: drug screening, organoid-on-a-chip and living organoid biobank. *Front Oncol.* 2021;11:762184.
doi: 10.3389/fonc.2021.762184

116. Ayan B, Heo DN, Zhang Z, et al. Aspiration-assisted bioprinting for precise positioning of biologics. *Sci Adv.* 2020;6(10):eaaw5111.
doi: 10.1126/sciadv.aaw5111

117. Lehmann R, Lee CM, Shugart EC, et al. Human organoids: a new dimension in cell biology. *Mol Biol Cell.* 2019;30(10):1129-1137.
doi: 10.1091/mbc.E19-03-0135

118. Cidonio G, Glinka M, Dawson JI, Oreffo ROC. The cell in the ink: improving biofabrication by printing stem cells for skeletal regenerative medicine. *Biomaterials.* 2019;209: 10-24.
doi: 10.1016/j.biomaterials.2019.04.009

119. Dey M, Özbolat İT. 3D bioprinting of cells, tissues and organs. *Sci Rep.* 2020;10(1):14023.
doi: 10.1038/s41598-020-70086-y

120. Rajasekar S, Lin D, Abdul L, et al. IFlowPlate – a customized 384-well plate for the culture of perfusable vascularized colon organoids. *Adv Mater.* 2020;32(46):e2002974. doi: 10.1002/adma.202002974

121. Cakir B, Xiang Y, Tanaka Y, et al. Engineering of human brain organoids with a functional vascular-like system. *Nat Methods.* 2019;16(11):1169-1175. doi: 10.1038/s41592-019-0586-5

122. Zhang YS, Arneri A, Bersini S, et al. Bioprinting 3D microfibrous scaffolds for engineering endothelialized myocardium and heart-on-a-chip. *Biomaterials.* 2016;110:45-59. doi: 10.1016/j.biomaterials.2016.09.003

123. Zhang J, Griesbach J, Ganeyev M, et al. Long-term mechanical loading is required for the formation of 3D bioprinted functional osteocyte bone organoids. *Biofabrication.* 2022;14(3):035018. doi: 10.1088/1758-5090/ac73b9

124. Kronemberger GS, Miranda GSD, Tavares RSN, Kopke ÚDA, Baptista LS. Recapitulating tumorigenesis in vitro: opportunities and challenges of 3D bioprinting. *Front Bioeng Biotechnol.* 2021;9:682498. doi: 10.3389/fbioe.2021.682498

125. Abdollahi S. Extracellular vesicles from organoids and 3D culture systems. *Biotechnol Bioeng.* 2021;118(3):1029-1049. doi: 10.1002/bit.27606

126. Agarwal P, Anees A, Harsiddharay RK, Kumar P, Tripathi PK. A comprehensive review on exosome: recent progress and outlook. *Pharm Nanotechnol.* 2023;12(1):2-13. doi: 10.2174/2211738511666230523114311

127. Zhang Y, Liu Y, Liu H, Tang WH. Exosomes: biogenesis, biologic function and clinical potential. *Cell Biosci.* 2019;9(1):19. doi: 10.1186/s13578-019-0282-2

128. Teng F, Fussenegger M. Shedding light on extracellular vesicle biogenesis and bioengineering. *Adv Sci.* 2020;8(1):2003505. doi: 10.1002/advs.202003505

129. Spiers JG, Vassileff N, Hill AF. Neuroinflammatory modulation of extracellular vesicle biogenesis and cargo loading. *Neuromolecular Med.* 2022;24(4):385-391. doi: 10.1007/s12017-022-08704-3

130. Niel GV, D'Angelo G, Raposo G. Shedding light on the cell biology of extracellular vesicles. *Nat Rev Mol Cell Biol.* 2018;19(4):213-228. doi: 10.1038/nrm.2017.125

131. Krylova SV, Feng D. The machinery of exosomes: biogenesis, release, and uptake. *Int J Mol Sci.* 2023;24(2):1337. doi: 10.3390/ijms24021337

132. Sedgwick AE, D'Souza-Schorey C. The biology of extracellular microvesicles. *Traffic.* 2018;19(5):319-327. doi: 10.1111/tra.12558

133. Thippabhotla S, Zhong C, He M. 3D cell culture stimulates the secretion of in vivo like extracellular vesicles. *Sci Rep.* 2019;9(1):13012. doi: 10.1038/s41598-019-49671-3

134. Bettio V, Mazzucco E, Antona A, et al. Extracellular vesicles from human plasma for biomarkers discovery: impact of anticoagulants and isolation techniques. *PLoS One.* 2023;18(5):e0285440. doi: 10.1371/journal.pone.0285440

135. Clevers, H. Modeling development and disease with organoids. *Cell.* 2016;165(7):1586-1597. doi: 10.1016/j.cell.2016.05.082

136. Rocha S, Carvalho J, Oliveira P, et al. 3D cellular architecture affects MicroRNA and protein cargo of extracellular vesicles. *Adv Sci (Weinh).*2019;6(4):1800948. doi: 10.1002/advs.201800948

137. Zhang Y, Chopp M, Zhang ZG, et al. Systemic administration of cell-free exosomes generated by human bone marrow derived mesenchymal stem cells cultured under 2D and 3D conditions improves functional recovery in rats after traumatic brain injury. *Neurochem Int.* 2017;111:69-81. doi: 10.1016/j.neuint.2016.08.003

138. Zhang Y, Yan Y, Meng J, Girotra M, Ramakrishnan S, Roy S. Immune modulation mediated by extracellular vesicles of intestinal organoids is disrupted by opioids. *Mucosal Immunol.* 2021;14(4):887-898. doi: 10.1038/s41385-021-00392-9

139. Cao J, Wang B, Tang T, et al. Three-dimensional culture of MSCs produces exosomes with improved yield and enhanced therapeutic efficacy for cisplatin-induced acute kidney injury. *Stem Cell Res Ther.* 2020;11(1):206. doi: 10.1186/s13287-020-01719-2

140. Yan L, Wu X. Exosomes produced from 3D cultures of umbilical cord mesenchymal stem cells in a hollow-fiber bioreactor show improved osteochondral regeneration activity. *Cell Biol Toxicol.* 2020;36(2):165-178. doi: 10.1007/s10565-019-09504-5

141. Ji X, Zhou S, Wang N, et al. Cerebral-organoid-derived exosomes alleviate oxidative stress and promote LMX1A-dependent dopaminergic differentiation. *Int J Mol Sci.* 2023;24(13):11048. doi: 10.3390/ijms241311048

142. Zhou J, Flores-Bellver M, Pan J, et al. Human retinal organoids release extracellular vesicles that regulate gene expression in target human retinal progenitor cells. *Sci Rep.* 2021;11(1):21128. doi: 10.1038/s41598-021-00542-w

143. Zhou J, Flores-Bellver M, Pan J, et al. Human retinal organoids release extracellular vesicles that regulate gene expression in target human retinal progenitor cells. *Sci Rep.* 2021;11(1):21128. doi: 10.1038/s41598-021-00542-w

144 Manai F, Smedowski A, Kaarniranta K, Comincini S, Amadio M. Extracellular vesicles in degenerative retinal diseases: a new therapeutic paradigm. *J Control Release.* 2024;365:448-468.
doi: 10.1016/j.jconrel.2023.11.035

145. Rocha S, Carvalho J, Oliveira P, et al. 3D cellular architecture affects MicroRNA and protein cargo of extracellular vesicles. *Adv Sci.* 2018;6(4):1800948.
doi: 10.1002/advs.201800948

146. Abdollahi S. Extracellular vesicles from organoids and 3D culture systems. *Biotechnol Bioeng.* 2020;118(3):1029-1049.
doi: 10.1002/bit.27606

147. Li H, Gao L, Du J, Ma T, Ye Z, Li Z. To better generate organoids, what can we learn from teratomas? *Front Cell Dev Biol.* 2021;9:700482.
doi: 10.3389/fcell.2021.700482

148. Maiullari F, Chirivì M, Costantini M, et al. In vivo organized neovascularization induced by 3D bioprinted endothelial-derived extracellular vesicles. *Biofabrication.* 2021;13(3):035014.
doi: 10.1088/1758-5090/abdacf

149. Zhang Y, Huo M, Wang Y, et al. A tailored bioactive 3D porous poly(lactic-acid)-exosome scaffold with osteo-immunomodulatory and osteogenic differentiation properties. *J Biol Eng.* 2022;16(1):22.
doi: 10.1186/s13036-022-00301-z

150. Kang Y, Xu J, Meng L, et al. 3D bioprinting of dECM/Gel/QCS/nHAp hybrid scaffolds laden with mesenchymal stem cell-derived exosomes to improve angiogenesis and osteogenesis. *Biofabrication.* 2023;15(2):024103.
doi: 10.1088/1758-5090/acb6b8

151. Sun Y, Zhang B, Zhai D, Wu C. Three-dimensional printing of bioceramic-induced macrophage exosomes: immunomodulation and osteogenesis/angiogenesis. *NPG Asia Mater.* 2021;13(1):72.
doi: 10.1038/s41427-021-00340-w

152. Yerneni SS, Lathwal S, Shrestha P, et al. Rapid on-demand extracellular vesicle augmentation with versatile oligonucleotide tethers. *ACS Nano.* 2019;13(9):10555-10565.
doi: 10.1021/acsnano.9b04651

153. Chen P, Zheng L, Wang Y, et al. Desktop-stereolithography 3D printing of a radially oriented extracellular matrix/mesenchymal stem cell exosome bioink for osteochondral defect regeneration. *Theranostics.* 2019;9(9):2439-2459.
doi: 10.7150/thno.31017

154. Yerneni SS, Whiteside TL, Weiss LE, Campbell PG. Bioprinting exosome-like extracellular vesicle microenvironments. *Bioprinting.* 2019;13:e00041.
doi: 10.1016/j.bprint.2019.e00041

155. Theodoraki MN, Yerneni S, Gooding WE, et al. Circulating exosomes measure responses to therapy in head and neck cancer patients treated with cetuximab, ipilimumab, and IMRT. *OncoImmunology.* 2019;8(7):e1593805.
doi: 10.1080/2162402X.2019.1593805

156. Buenafe AC, Dorrell C, Reddy AP, Klimek J, Marks DL. Proteomic analysis distinguishes extracellular vesicles produced by cancerous versus healthy pancreatic organoids. *Sci Rep.* 2022;12(1):3556.
doi: 10.1038/s41598-022-07451-6

157. Huang L, Bockorny B, Paul I, et al. Pancreatic tumor organoids for modeling in vivo drug response and discovering clinically-actionable biomarkers. *bioRxiv.* 2019:513267.
doi: 10.1101/513267

158. Risha Y, Minic Z, Ghobadloo SM, Berezovski MV. The proteomic analysis of breast cell line exosomes reveals disease patterns and potential biomarkers. *Sci Rep.* 2020;10(1):13572.
doi: 10.1038/s41598-020-70393-4

159. Hyung S, Ko J, Heo YJ, et al. Patient-derived exosomes facilitate therapeutic targeting of oncogenic MET in advanced gastric cancer. *Sci Adv.* 2023;9(47):eadk1098.
doi: 10.1126/sciadv.adk1098

160. Han P, Ivanovski S. 3D bioprinted extracellular vesicles for tissue engineering-a perspective. *Biofabrication.* 2022;15(1):013001.
doi: 10.1088/1758-5090/ac9809

161. Bartnikowski M, Vaquette C, Ivanovski S. Workflow for highly porous resorbable custom 3D printed scaffolds using medical grade polymer for large volume alveolar bone regeneration. *Clin Oral Implants Res.* 2020;31(5):431-441.
doi: 10.1111/clr.13579

162. Liu W, Heinrich MA, Zhou Y, et al. Extrusion bioprinting of shear-thinning gelatin methacryloyl bioinks. *Adv Healthc Mater.* 2017;6(12):1601451.
doi: 10.1002/adhm.201601451

ACCSCIENCE PUBLISHING

International Journal of Bioprinting

REVIEW ARTICLE

The application of 3D bioprinting technology in liver manufacturing: Progress, challenges, and prospects

Yifan Hou[1,2,3], Xin Liu[1,2*], Xinhuan Wang[1,2], Shen Ji[1,2], and Qi Gu[1,2,3*]

[1]Key laboratory of Organ Regeneration and Reconstruction, State Key Laboratory of Membrane Biology, Institute of Zoology, Chinese Academy of Sciences, Beijing, P. R. China

[2]Beijing Institute for Stem Cell and Regenerative Medicine, Beijing, P. R. China

[3]University of Chinese Academy of Sciences, Beijing, P. R. China

(This article belongs to the *Special Issue: Made-to-order Organ*)

Abstract

Recreating the complexity of liver structure and the diversity of cells and functions *in vitro* remains a significant focus in liver tissue engineering. 3D bioprinting technology features advantages in personalized manufacturing, replicating complex internal structures, and precise arrangement of multi-materials and cells, thus holding vast potential in tissue engineering, particularly for liver manufacturing. In this review, we discuss the complexity of the liver structure and function, including its composition and both development and regeneration processes. We then analyze the current limitations in liver transplantation, e.g., donor organ shortage, and the shortcomings of various liver transplantation alternatives, highlighting the importance of 3D bioprinting for liver fabrication. Furthermore, the composition and properties of the bioinks used in the liver 3D-printing process and the corresponding research outcomes are discussed. Notably, we summarize the latest advances and challenges in the field of liver fabrication and explore future development directions, namely vascular and bile duct structures. In summation, this review can provide guidance and inspiration for future research and applications related to liver reconstruction and manufacturing.

Keywords: Liver fabrication; Bioprinting; Bioink; Vascularization

***Corresponding authors:**
Xin Liu (liuxin2022@ioz.ac.cn)

Qi Gu (qgu@ioz.ac.cn)

Citation: Hou Y, Liu X, Wang X, Ji S, Gu Q. The application of 3D bioprinting technology in liver manufacturing: Progress, challenges, and prospects. *Int J Bioprint*. 2024;10(5):3819. doi: 10.36922/ijb.3819

Received: June 1, 2024
Accepted: July 12, 2024
Published Online: August 23, 2024

Copyright: © 2024 Author(s). This is an Open Access article distributed under the terms of the Creative Commons Attribution License, permitting distribution, and reproduction in any medium, provided the original work is properly cited.

Publisher's Note: AccScience Publishing remains neutral with regard to jurisdictional claims in published maps and institutional affiliations.

1. Introduction

The liver is the largest internal organ in the human body and is essential for various physiological functions, such as synthesis, metabolism, detoxification, and immunity. During embryonic development, the composition of cells and extracellular matrix (ECM) within the liver undergo significant changes, gradually evolving into a complex organ with a sophisticated structure and vascular system that includes multiple cell types.[1–3] Additionally, the liver possesses a remarkable regenerative capacity, capable of restoring its original size and function even after removal of up to 70% of its mass.[4–6]

Several factors, such as viruses, alcohol, fat accumulation, and drugs, can cause hepatocyte damage or reduce liver function, potentially leading to end-stage liver disease.[7,8] Liver transplantation is the most effective clinical treatment for patients with

liver failure and other end-stage liver diseases, but it faces the challenge of donor organ shortages. Other potential alternatives to liver transplantation, such as bioartificial liver systems or hepatocyte transplantation therapy, can only provide temporary support to extend patient survival and are also constrained by cell availability.[9] *In vitro* models, such as organoids and organ-on-a-chip, have demonstrated potential in basic liver research, disease modeling, drug screening, and personalized medicine. However, further research is warranted before clinical treatment due to the undefined composition of the culture conditions, simplistic structure, and limited size.[10–14] The fabrication of a liver holds significant promise for addressing the numerous challenges associated with traditional organ transplantation and providing new treatment options for patients with liver diseases.[15,16] Three-dimensional (3D) bioprinting has broad application prospects in the field of organ fabrication due to its advantages in personalized manufacturing, replicating complex *in vivo* structures, and the orderly arrangement of various materials and cells.

This review aims to summarize the latest advances and challenges in the field of liver 3D printing, as well as future development directions. Firstly, we introduce the functions, cellular composition, and development and regeneration processes of the liver, highlighting its complex structure and diverse functions. Following this, the history of liver tissue engineering is reviewed, including the limitations of traditional liver transplantation and the emergence and development of *in vitro* liver models. The discussion then focuses on the application of bioprinting technology in liver biofabrication, including cell sources, biomaterial selection, and the optimization of bioprinting techniques. Special attention is focused on the progress and shortcomings of 3D bioprinting for integrating vascular and bile duct structures into *in vitro* liver tissues. Finally, the review concludes by discussing the ongoing challenges in liver biofabrication and exploring future development directions (Figure 1).

2. Liver function, cell types, development, and regeneration

The liver is the largest internal organ in the human body[17–19] and consists of diverse cell types to perform critical functions in metabolism, detoxification, protein synthesis, bile secretion, and immune response.[20–22] The liver is typically located in the right upper quadrant of the abdomen, beneath the diaphragm, and adjacent to the top of the stomach, right kidney, and intestines. It has a cone-shaped, deep reddish-brown appearance.[19,23] The liver receives approximately 13% of the body's blood supply, with blood vessels, such as the hepatic artery and portal vein, delivering oxygen-rich and nutrient-rich blood, respectively, through the hepatic vein.[24–26] The fundamental structural and functional unit of the liver is the hepatic lobule, roughly 1 mm in diameter, with an adult liver comprising approximately 500,000–1,000,000 lobules.[27,28] Each lobule features a hexagonal structure with a portal triad (composed of the portal vein, hepatic artery, and bile duct) at each vertex (Figure 2A). The hepatic lobule is centered around the central vein, with hepatocytes arranged radially outward to form hepatic cords. Adjacent hepatocytes form bile canaliculi structures under the functional seal of tight junctions.[29–32] Between the hepatic cords lie liver sinusoids, where blood flows from the portal vein area towards the central vein area, creating gradients of oxygen, nutrients, and hormones. Hepatocytes are exposed to different microenvironments, leading to the spatial zonation of liver functions. Around the portal vein (zone 1), activities, such as oxidative metabolism, gluconeogenesis, amino acid breakdown, and cholesterol biosynthesis, predominantly occur. In contrast, areas around the central vein (zone 3) are primarily responsible for glycolysis, lipogenesis, and alcohol detoxification.[28] Zone 2 hepatocytes are the main contributors to homeostatic proliferation.[33,34] Within the liver sinusoids, all liver cell types are distributed, including parenchymal cells (hepatocytes, cholangiocytes), non-parenchymal cells (endothelial cells, Kupffer cells, hepatic stellate cells), and infiltrating lymphocytes (such as B cells, T cells, and natural killer [NK] cells) (Table 1; Figure 2B).

The liver develops from the ventral foregut endoderm and also gives rise to the lungs, ventral pancreas, and thyroid. As early as embryonic day 8.5 (E8.5) in mice, the liver-specific gene for albumin (ALB) is actively expressed in the ventral foregut endoderm. By E9.0, the ventral foregut region adjacent to the cardiac mesoderm and septum thickens, forming the hepatic diverticulum. Subsequently, in E9.5, the diverticulum further thickens, transitioning from a single layer of cuboidal endodermal cells to multilayered hepatoblasts, which proliferate and invade the surrounding septum to form hepatic buds. With the continuous proliferation of hepatoblasts, at approximately E11.5, the hepatic buds morphologically transform into distinct liver tissue. From E13.5 to E15.5, bipotential hepatoblasts begin to differentiate into hepatocytes and cholangiocytes, accompanied by the emergence of ductal plates and asymmetric ductal structures.[49–51] Postnatally, the liver volume and cell numbers increase to meet metabolic demands. Over 5 weeks, liver weight increases by fivefold, and a lobular structure is formed[52,53] (Table 2).

The liver possesses remarkable regenerative abilities. Within 15 h after undergoing a two-thirds partial hepatectomy (PHx), rat hepatocytes initiated DNA synthesis and could restore the original liver weight within 10 days[54] (Figure 3A). Generally, liver regeneration is

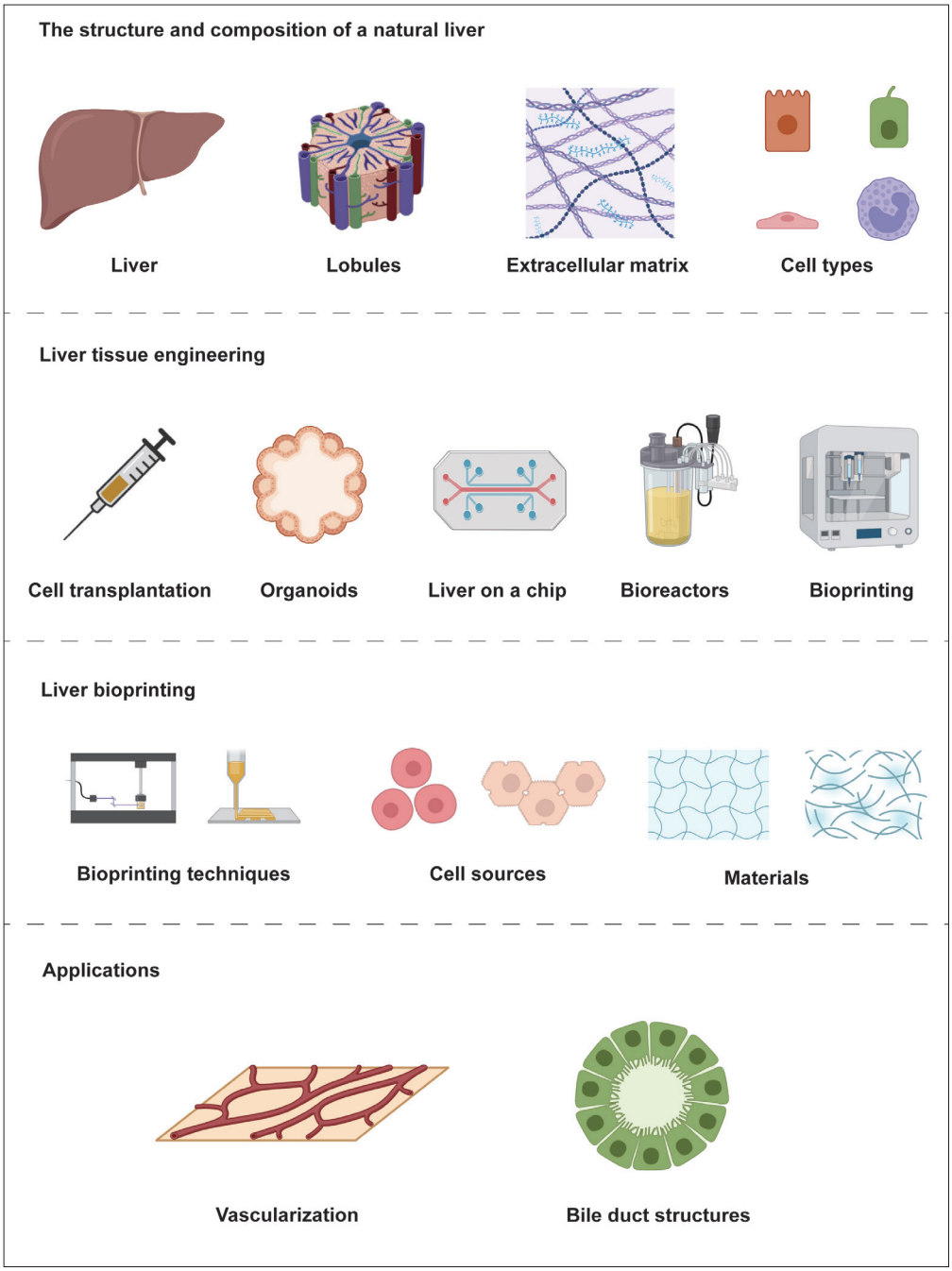


Figure 1. Schematic diagram on liver manufacturing. The figure was created using BioRender (BioRender.com).

triggered by factors, such as partial hepatectomy or liver injury. Enteric factors in the liver, such as lipopolysaccharide (LPS), are upregulated and reach the liver through the portal vein. They activate non-parenchymal liver cells, including Kupffer cells and stellate cells, and upregulate the expression of tumor necrosis factor α (TNF-α) and interleukin-6 (IL-6). These signals prompt hepatocytes to transition from the G_0 phase to the S phase. Other factors, such as hepatocyte growth factor (HGF), amphiregulin, triiodothyronine (T3), bone morphogenetic protein-7 (BMP-7), and Wnt/β-catenin, also mediate the liver's regenerative response, allowing hepatocytes to bypass cell cycle checkpoints to initiate DNA synthesis and hepatocyte proliferation. Additionally, transforming growth factor β

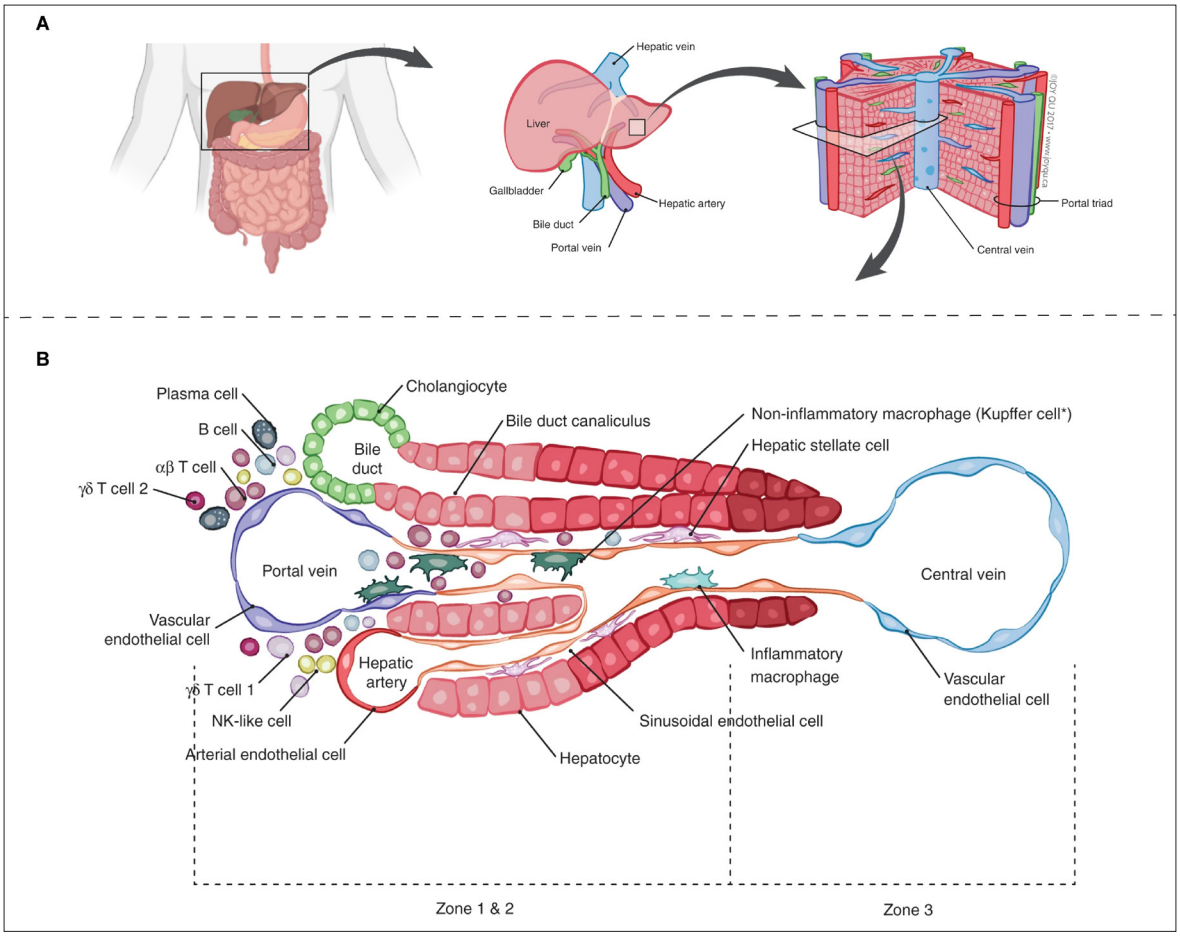


Figure 2. The position and cell types of the liver. (A) The position of the liver in the human body, and the structure of hepatic lobules. (B) Different types of cells in the liver, and their distribution within the hepatic lobules. Adapted with permission from MacParland et al.[35] Abbreviation: NK, natural killer.

(TGF-β) signaling produced by hepatic stellate cells inhibits hepatocyte DNA synthesis, which is blocked during the proliferation phase[54–56] (Figure 3B). Miyaoka et al. also indicated that cellular hypertrophy plays an important role in liver regeneration. In mice, the liver weight started to increase from the first day after a 70% PHx and reached a plateau by day 7. Regeneration after a 30% PHx was achieved solely through hypertrophy without cell division, and hypertrophy preceded proliferation following a 70% PHx. Both proliferation and hypertrophy contributed almost equally to regeneration after a 70% PHx.[57]

3.The development process of liver manufacturing

Every year, over 2 million people lose their lives due to liver-related diseases, which account for 4% of global mortality.[58] Factors contributing to hepatocyte damage and decreased liver function include drug-induced toxicity, alcoholic and non-alcoholic fatty liver diseases, hepatotropic infections, and genetic disorders.[59] Liver transplantation is a life-saving treatment and is considered the gold standard for treating metabolic disorders and end-stage liver failure. In China, the total number of liver disease patients exceeds 300 million, with over 1 million deaths annually from end-stage liver disease. However, due to a severe shortage of donor organs, the number of patients receiving liver transplants in China does not exceed 6000 per year.[60] Therefore, there is an urgent need to develop alternative strategies for liver transplantation.

3.1. Xenotransplantation and hepatocyte transplantation

Xenotransplantation is recognized as a promising method to address the shortage of donor organs. This technique involves transplanting organs from other species into humans. Pig organs, in particular, are similar to human organs in terms of size and function. Pigs also reproduce

Table 1. Types of cells in the liver[35]

Cell types	Amount	Characteristics and functions	Markers
Hepatocytes	Approximately 60% of total liver cells; approximately 80% of liver volume	Highly polarized epithelial cells that form cord-like structures; gluconeogenesis, β-oxidation, drug metabolism, and detoxification	ALB, HNF4α, CK18, CYP3A4
Liver sinusoidal endothelial cells[36–38]	Approximately 15–20% of liver cells; 3% of liver volume	Form a dynamic barrier between blood and the hepatic microenvironment; scavenger endothelial cells, i.e., clear large molecules from the blood via receptor-mediated endocytosis through fenestrations	CD31, LYVE1, CD34, CD105 [39]
Cholangiocytes[40–43] (biliary epithelial cells)	3–5% of total human liver cells	Secrete bile into the duodenum; hormone-mediated regulation of bile flow and alkalinity; absorb bile acids and reabsorb bile components, such as glucose and glutathione; contribute approximately 40% of total bile production via ion transporters and hormone receptors on their polarized membranes; synthesize and secrete various pro-inflammatory factors, cytokines, chemokines, and angiogenic factors; actively participate in inflammatory responses	SOX9, CK7, CK19, CFTR, SLC4A2[44]
Hepatic stellate cells[45,46]	5–8% of total liver cells	Primary reservoir of vitamin A; major contributor to tissue fibrosis; express α-smooth muscle actin (ACTA2) upon activation for extracellular matrix deposition	α-SMA, RBP1
Kupffer cells[47,48]	2% of liver volume	Immune sentinels in the liver; identification and clearance of foreign substances; secretion of cell factors (e.g., TGF and TNF); involvement in the metabolism of bilirubin, iron, lipoproteins, and cholesterol	CD68, MARCO
Lymphocytes (T cells, natural killer [NK]-like cells, B cells)	NK cells: 20–30% of the total lymphocyte population in the liver; B cells: 37.5% of the intrahepatic immune cell population	NK and T cells serve as the first-line immune defense against invading pathogens, modulate liver injury, and recruit circulating lymphocytes; B cells affect immune control directly via neutralizing antibodies, or indirectly via communication with the complement cascade and other effector immune cells	CD4, CD8, KLRC1, NCR1

Table 2. Developmental stages and corresponding characteristics in the liver[52]

Developmental stage	Characteristics
E7.5 (W3)	Separation of the definitive endoderm from the mesoderm, eventually developing into foregut, midgut, and hindgut
E8.0	Establishment of the STM
E8.5 (W3–4)	Emergence of hepatic progenitor cells in the ventral foregut endoderm
E9.0 (W4)	Formation of hepatic diverticulum and hepatic bud
E10.5–12.5 (W4–6)	Development of the portal vein and central vein
E11.5	Onset of extensive hematopoietic cell proliferation
E11.5 (W6)	Morphological transformation of hepatic bud into distinct liver tissue; formation of the bile duct plate
E13.5–15.5	Differentiation of hepatoblasts into hepatocytes
E15.0 (W12)	Formation of asymmetric primitive bile duct structures, subsequently transforming into symmetric bile duct structures
Perinatal period (W8)	Emergence of the hepatic artery
Postnatal	Liver weight increases by at least 500%; establishment of lobular pattern

Abbreviations: E, mouse embryonic day; STM, septum transversum mesenchyme; W, human week.

quickly and pose fewer ethical concerns when used for organ transplantation, making them the primary animal source for xenotransplantation research. With gene editing technology, successful live pig heart and kidney transplants have already been achieved.[61,62]

Recently, Wei and Sun's team pioneered gene-edited pig liver xenotransplantation by transplanting the liver of a pig with 10 genetic modifications into a 71-year-old male patient with a large right lobe liver cancer. This procedure included the knockout of three pig xenogeneic antigen

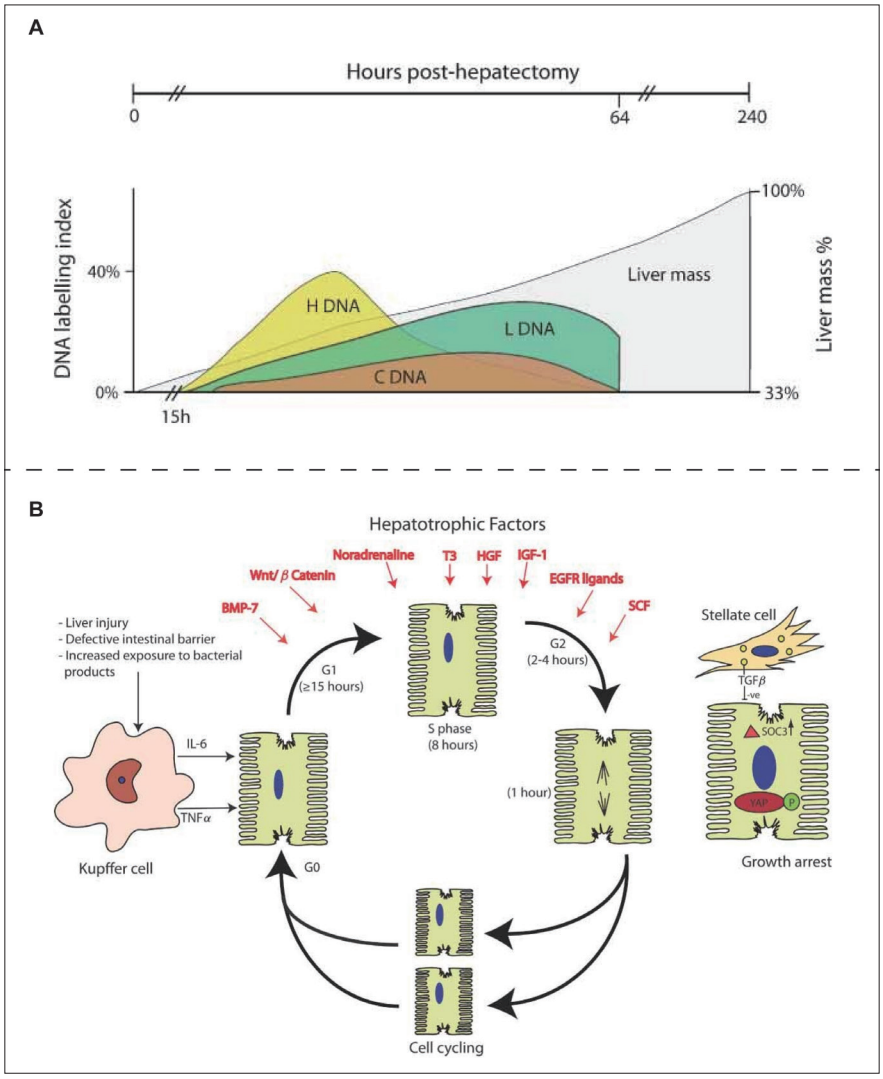


Figure 3. Liver regeneration. (A) The kinetics of liver regeneration in the rat after a two-thirds PHx. The hepatocyte DNA labeling index (H DNA) increases within 15 h and peaks at approximately 40% at 24 h. Liver sinusoidal endothelial cells (L DNA) and cholangiocytes (C DNA) enter DNA synthesis later than hepatocytes. Hepatocyte proliferation is essentially completed within 96 h, and the preoperative liver weight is restored within 10 days. (B) A wide range of cytokines and growth factors have been implicated in mediating the liver's regenerative response. Adapted with permission from Alison et al.[54] Abbreviations: BMP-7, bone morphogenetic protein-7; C DNA, Cholangiocyte DNA; DNA, hepatocyte DNA; EGFR, epidermal growth factor receptor; HGF, hepatocyte growth factor; L DNA, liver sinusoidal endothelial cell DNA; IGF-1, Insulin like growth factor-1; IL-6, Interleukin-6; PHx, partial hepatectomy; SCF, stem cell factor; SOCS3, suppressor of cytokine signaling 3; TNF-α, tumor necrosis factor α; T3, Triiodothyronine; TGF-β, transforming growth factor β; YAP, Yes-associated protein.

synthesis genes (*GGTA1*, *CMAH*, and *β4GalNT2*) to prevent hyperacute rejection. Additionally, the overexpression of complement regulatory proteins (hCD46, hCD55, and hCD59), coagulation inhibition proteins (hTBM, hCD39, hEPCR), and immune cell recognition markers (hCD47) effectively mitigates acute humoral rejection, inhibits thrombosis, and reduces post-transplant inflammatory responses and immune cell activation-related rejection. The patient has not experienced hyperacute or acute rejection, maintains normal blood flow, and secretes approximately 200 mL of bile daily. The primary challenges in xenotransplantation include achieving long-term survival and further reducing immune rejection. Currently, patients receiving xenotransplants typically survive for around 2 months.[61]

Hepatocyte transplantation presents another promising approach, where healthy hepatocytes are transplanted into the patient's liver to treat metabolic liver diseases

and acute liver failure. However, there is currently a lack of robust evidence supporting the long-term therapeutic effects of hepatocyte transplantation in clinical practice. Additionally, many unresolved issues remain, including obtaining quality-assured hepatocytes, improving the efficiency of transplantation and engraftment, and developing effective immunosuppression protocols.[63]

3.2. Bioartificial liver

Artificial liver support systems are extracorporeal devices designed to prolong the survival of patients with liver failure by supporting liver regeneration (bridge to regeneration) or patients until suitable organs are available for orthotopic liver transplantation (bridge to transplantation). Artificial liver support systems include non-biological and biological artificial livers.[64] Non-biological artificial livers primarily rely on chemical and physical methods, such as filtration or adsorption, to remove metabolic toxins. In addition to removing water-soluble substances, non-biological artificial livers can also clear lipophilic substances and ALB-bound substances, such as bilirubin, bile acids, metabolites of aromatic amino acids, medium-chain fatty acids, and cytokines.[65,66] Besides detoxification, the liver is also involved in synthesizing proteins such as ALB and clotting factors, storing vitamins and glycogen, metabolizing fats and hormones, secreting bile, and maintaining the balance of the body's internal environment. The complex mechanisms that uphold internal homeostasis and ensure bodily equilibrium are unlikely to be fully replaced by standalone non-biological detoxification methods. Non-biological artificial livers cannot substitute for the biological functions of the liver. Therefore, research has shifted towards biological artificial liver support systems.

Biological artificial livers contain hepatocytes cultured from artificial sources, which not only possess detoxification functions but also synthetic and metabolic functions.[67] Currently, the hepatocytes used in various biological artificial livers mainly include primary human hepatocytes, porcine hepatocytes, and human hepatoblastoma lines. However, primary human hepatocytes have limited proliferative capacity *in vitro*; porcine hepatocytes are challenged by issues related to xenogenic viruses and immune barriers[68,69]; and human hepatoblastoma lines lack some liver functions, such as normal urea cycle enzymes and limited metabolic functions, making them less than ideal seed cells.[70] Chen et al. used human induced pluripotent stem cell (hiPSC)-derived hepatocytes, which can be expanded, cryopreserved *in vitro*, and further matured into functional liver organoids at a large scale. However, the induction and differentiation process is complex, requiring a differentiation period exceeding 38 days.[71] Li et al. used chemical reprogramming technology to transform mouse and human primary hepatocytes into expandable hepatocyte-derived liver progenitor-like cells (HepLPCs). This cell line exhibits significantly improved protein synthesis, urea generation, ammonia clearance, and hepatocyte growth factor secretion compared to traditional artificial hepatocytes, representing a new, sustainably expandable, functional human hepatocyte line (Figure 4A). Additionally, overexpression of FOXA3 in immortalized human HepLPCs (iHepLPCs) further enhances liver function and results in a more mature hepatocyte morphology (Figure 4B). However, its expansion time is approximately 2 weeks, and it lacks validation in human experiments, with cell functions inferior to primary hepatocytes.[72] Hui et al. achieved the large-scale expansion ($\times 10^9$) of functionally proliferative hepatocytes (human-induced hepatocytes, hiHep) by overexpressing liver transcription factors (FOXA3, HNF1A, and HNF4A) in human fibroblasts and subsequently established a serum-free culture system suitable for differentiating hepatocytes, thereby stably producing GMP-grade hiHep cells, which have entered the preclinical stage.[73,74] Overall, high-quality seed cells are a focal point in the development of biological artificial livers.

3.3. Liver organoids

Organoids are cell-based *in vitro* models that mimic the structure and function of *in vivo* tissues. They can be utilized for studying the fundamental mechanisms of biological development, regeneration, and repair, as well as for applications in diagnostics, disease modeling, drug discovery, and personalized medicine. Typically, organoids are derived from embryonic or adult cells, including progenitor or differentiated cells from healthy or diseased tissues.[75–78] In the field of liver organoids, commonly used hepatocyte types include those derived from induced pluripotent stem cells (iPSCs) or embryonic stem cells (ESCs), as well as liver progenitor cells from tissues. Primary hepatocytes can also be used for the culturing of liver organoids.[79] Huch et al. demonstrated that Lgr5+ cells isolated from damaged mouse liver bile ducts could be expanded and differentiated into liver organoids in a culture medium supplemented with Rspo1.[80] Similarly, in 2015, they obtained similar results using EpCAM+ cholangiocytes from human liver tissue samples. Gene expression profiling demonstrated that liver organoids expressed high levels of hepatocyte markers, such as ALB, cytokeratin, apolipoprotein B (APOB), and complement factor C3, and they were capable of glycogen accumulation and low-density lipoprotein (LDL) uptake.[81] Vyas et al. utilized human fetal liver progenitor cells to self-organize into liver organoids, which demonstrated the process of liver organogenesis and gradually formed differentiated hepatocytes and bile duct structures.[82] Liver organoids derived from human fetal liver progenitor cells

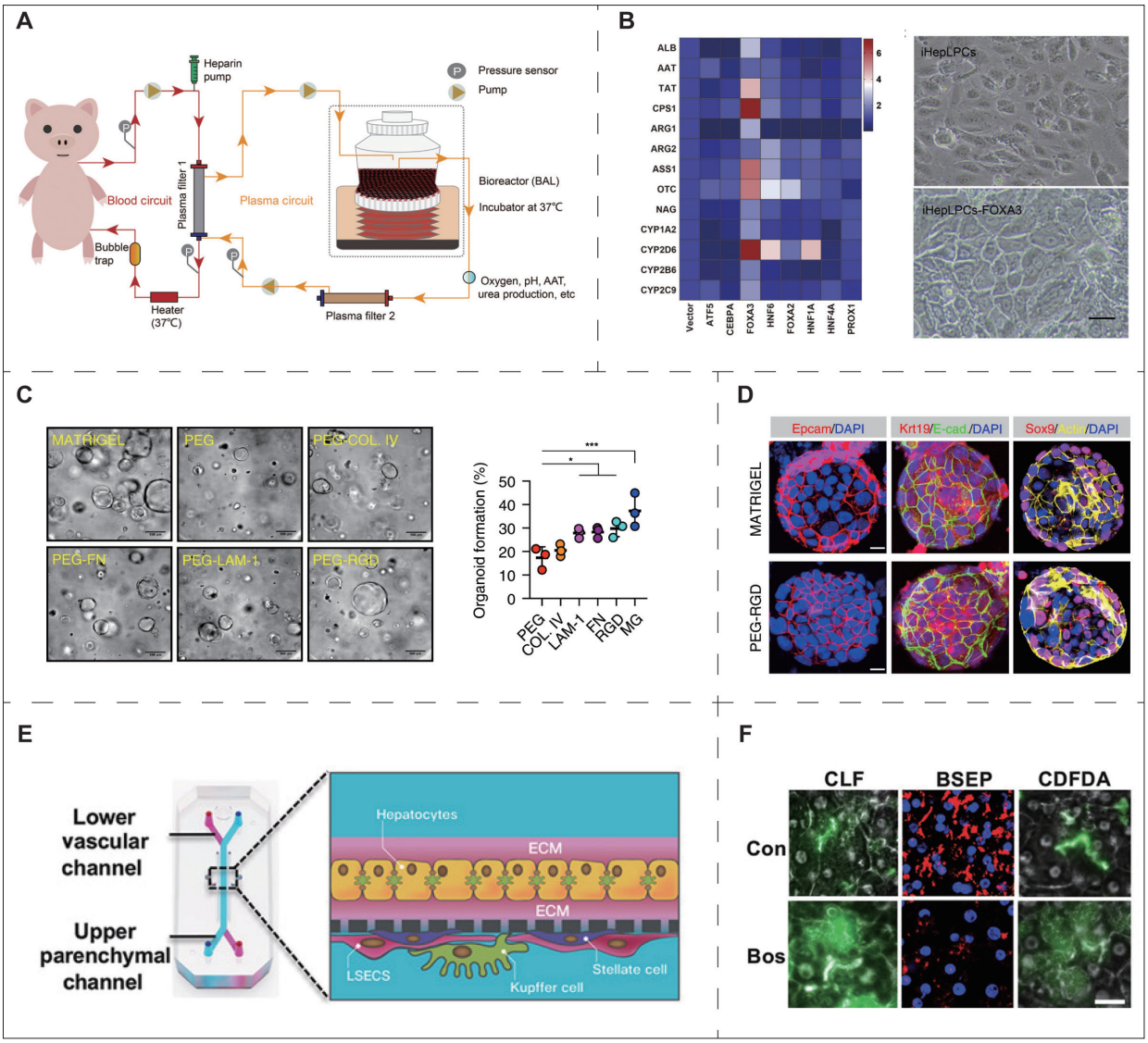


Figure 4. Representation of current *in vitro* liver tissue culture and engineering platforms. (A) Schematic diagram of the bioartificial liver system. Plasma filter 1 was used to separate plasma from blood to the plasma circuit; plasma filter 2 served as an immunoprotective barrier. (B) Heatmap of hepatic functional gene expression after transcription factor transfection (left; $n = 3$); bright-field microscopic images of the morphology of iHepLPCs-FOXA3 observed using an inverted microscope (right); scale bar: 50 μm. Adapted with permission from Li et al.[72] (C) Mouse liver progenitor cells three days after embedment in Matrigel (MG), plain poly(ethylene glycol) (PEG), and functionalized PEG with the indicated extracellular matrix (ECM) components: collagen IV (COL.IV), fibronectin (FN), laminin-1 (LAM-1), and RGD-representing peptide (RGD) (left); quantification of organoid formation efficiency relative to the panel (right). (D) Liver organoid immunostaining of Epcam, Krt19, and Sox9 was performed 6 days after embedment of liver progenitor cells in Matrigel or PEG-RGD. Adapted with permission from Sorrentino et al.[85] (E) Schematic of the liver-on-a-chip. (F) Representative images of CLF, BSEP, and CDFDA after 30 μM bosentan (Bos) treatment versus vehicle control (Con) for 7 days in the chips. Adapted with permission from Jang et al.[95] Abbreviations: BSEP, bile salt export pump; CDFDA, 5(6)-carboxy-2′,7′-dichlorofluorescein diacetate; CLF, cholyl-lysyl-fluorescein; DAPI, 4',6-diamidino-2-phenylindole; E-cad, E-cadherin; Epcam, epithelial cell adhesion molecule; Krt19, Keratin 19; LSEC: Liver sinusoidal endothelial cell; Sox9, SRY (sex-determining region Y)-box 9. Figure 4C: scale bar 100 μm; Figure 4F: scale bar 20 μm.

also exhibited partial metabolic and secretory functions. Moreover, multiple research teams have developed liver organoids consisting of various cell types. Takebe et al. used a combination of iPSC-derived hepatoblasts, mesenchymal stem cells, and endothelial cells to simulate liver bud formation (iPSC-LB).[83] Human iPSC-LB shares similarities with E10.5 mouse liver buds and rapidly establishes connections with the host vasculature within 48 h post-transplantation. Wu et al. induced iPSC co-differentiation into hepatocytes and cholangiocytes to construct liver-

biliary organoids. The hepatocyte-like cells could absorb indocyanine green, accumulate lipids and glycogen, secrete ALB and urea, and possess drug metabolism capabilities. Likewise, cholangiocytes exhibited γ-glutamyl transferase activity and could store bile acids. Additionally, when transplanted into immunodeficient mice, organoids could survive for over 8 weeks.[84] Currently, the main limitation of organoids is the undefined growth environment, which leads to high variability and poor reproducibility, thereby restricting their clinical translation.[75] Sorrentino et al. used poly(ethylene glycol) (PEG) hydrogels incorporated with RGD peptides as a substitute for Matrigel in liver organoid culture. The stiffness of this hydrogel was adjustable and could be designed to match the stiffness of the liver (≈1.3 kPa). Compared to PEG hydrogels incorporating laminin, collagen IV, and fibronectin, the efficiency of organoid formation in PEG-RGD hydrogels was closer to that in Matrigel, displaying similar morphology and gene expression patterns[85] (Figure 4C and D). This study paves the way for the future clinical application of organoids.

3.4. Liver-on-a-chip

Organ-on-a-chip is a microfluidic cell culture device where cells are cultured in continuously perfused chambers. It is designed to mimic tissue- and organ-level physiological functions and replicate multicellular structures, tissue–tissue interfaces, physicochemical microenvironments, and vascular perfusion found in the human body.[86] Organ-on-a-chip technology holds great potential in various fields, such as tissue development, organ physiology, disease modeling, and drug screening.[87–92] Specifically in the liver, organ-on-a-chip technology supports the co-culture of multiple liver cell types while incorporating vascular channels. This enables the establishment of liver disease models and the screening of hepatotoxic drugs.[93,94] Jang et al. designed a liver-on-a-chip composed of rat, dog, or human hepatocytes, human liver sinusoidal endothelial cells (LSECs), Kupffer cells, and hepatic stellate cells. The chip exhibited various hepatotoxicity phenotypes, including hepatocyte injury, lipid accumulation, bile stasis, and fibrosis, enabling the assessment of species-specific differences in drug metabolism and toxicity[95] (Figure 4E). Compared to traditional sandwich monoculture plates, this model is more sensitive in detecting bosentan toxicity. Co-treatment of bosentan (30 μM) with the bile salt export pump (BSEP) substrate cholyl-lysyl-fluorescein (CLF) inhibited CLF efflux, leading to its intracellular accumulation in the liver chip. This was consistent with the known mechanism of bosentan hepatotoxicity in humans (Figure 4F). Building upon this work, Nawroth et al. established a liver organ-on-a-chip with biomimetic hepatic sinusoids and bile duct structures to model alcohol-related liver disease (ALD) by co-culturing primary hepatocytes, hepatic sinusoidal endothelial cells, and stellate cells. Upon exposure to blood alcohol levels, the chip exhibited ALD biomarkers, including lipid accumulation and oxidative stress.[96] Moreover, Ewart et al. conducted tests on 870 liver chips based on the same design using 27 known drugs recommended by the Innovation and Quality (IQ Consortium) with or without hepatotoxicity and compared the results with 3D culture spheroids of primary human hepatocytes. The findings indicated that liver chips exhibited higher accuracy, sensitivity, and economic value.[97] By constructing biomimetic liver lobule chips to simulate the physicochemical microenvironment of the liver, it is possible to more accurately replicate liver disease models, extend cell culture time *in vitro*, and facilitate testing for acute and chronic hepatotoxicity.[98,99] Currently, the limitations of chips lie in their maintenance duration and the challenge of achieving substance and information (signaling molecules) exchange between multiple organs.[100,101]

4. Bioprinting of liver tissue

3D bioprinting technology generally refers to the computer-assisted transfer process of patterning and assembling biological and non-biological materials to create bioengineered structures, according to specified 2D or 3D tissue designs. The advantage of 3D printing technology lies in its ability to simulate the structure and function of natural tissues through precise deposition and assembly of materials and cells, enabling spatiotemporal control of cell–cell and cell–ECM communication for reconstructing tissue-like structures. This technology has broad applications in tissue engineering, organ transplantation, drug screening, and other fields.[102] Furthermore, compared to organ-on-chip and organoid technologies, bioprinting can manufacture larger volumes (up to centimeters) and intricate tissue structures *in vitro*, achieving higher fidelity to physiological tissues. Generally, the entire 3D bioprinting process can be divided into three stages: (i) before printing, the design of the print is determined by obtaining the required anatomical structures and dimensional information through imaging techniques (e.g., computed tomography [CT], magnetic resonance imaging [MRI], X-ray) and defining the structure and dimensions of the print with computer-aided design (CAD) software; (ii) the selection of bioink (cells, materials) and printing method (extrusion-based bioprinting, photopolymerization-based bioprinting, etc.) is made; and (iii) the printed structure is cultured and utilized for subsequent applications.[103] Among these, the most important aspects are determining the printing method and selecting the bioink (Figure 5).

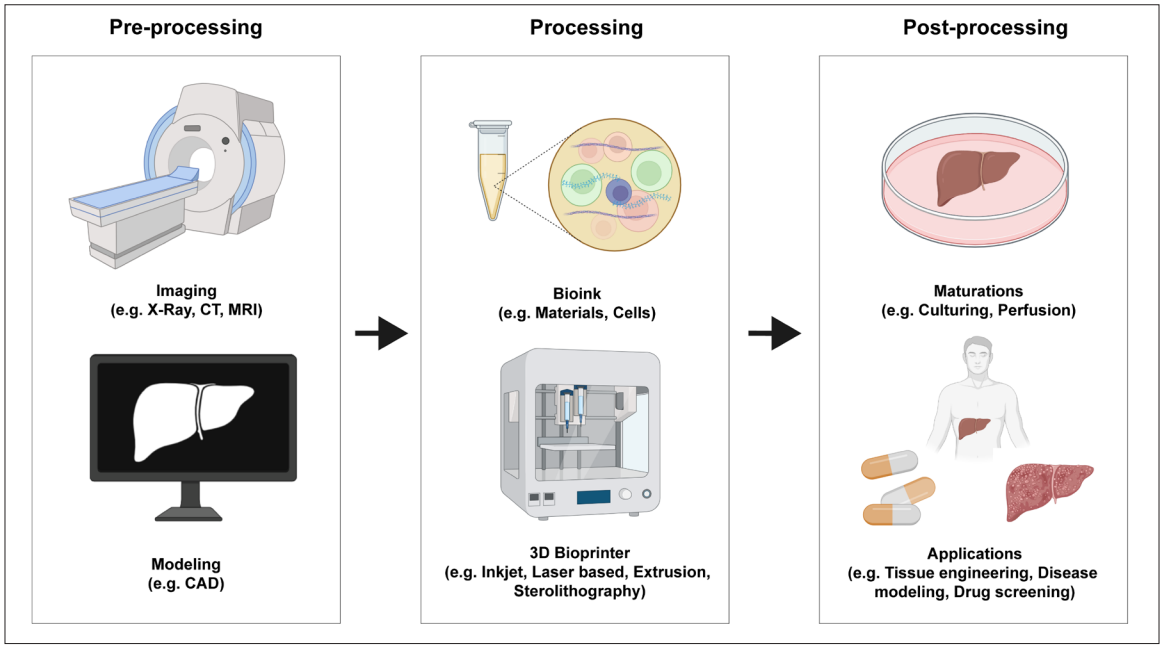


Figure 5. The 3D bioprinting process. The figure was created using BioRender (BioRender.com). Abbreviations: CAD, computer-aided design; CT, computed tomography; MRI, magnetic resonance imaging.

4.1. Bioinks

Bioink is fundamental to 3D bioprinting, ideally requiring three key qualities: printability (mechanical properties), cell viability maintenance, and guidance of cell behavior (biological properties). This necessitates balancing mechanical and biological performance[104,105] (Figure 6A). Mechanical properties refer to the ability of the printing material to form a stable 3D structure with high structural integrity and fidelity after printing, while also ensuring that the viability and performance of cells are not negatively affected by the bioprinting process, such as the high shear forces in extrusion-based printing.[106] In extrusion-based printing, bioink is extruded and deposited onto a collection platform in a controlled manner in filaments, thus emphasizing the viscosity demands of the bioprinting process. Viscosity refers to the degree of stickiness; generally, substances with higher viscosity correspond to less flow, while those with lower viscosity would flow more easily. Lower viscosity is required during printing to facilitate material extrusion from the printhead, while higher viscosity is required post-extrusion to maintain the stability of the printed structure.[107] Hence, materials with shear-thinning characteristics (i.e., non-Newtonian behavior where viscosity decreases with increasing shear rate) are widely used in many 3D bioprinting applications. When subjected to high shear stress, shear-thinning hydrogels exhibit low viscosity and return to their original viscosity after the shear stress is removed. The viscoelasticity of a material is also crucial for protecting cells from the effects of high-shear stress. Viscoelasticity is a time-dependent mechanical property that combines the characteristics of an elastic solid and a viscous liquid, and it is a nearly universal characteristic of the ECM of biological tissues. Viscoelastic materials exhibit an instantaneous elastic response to applied stress, store energy, and have a time-dependent viscous response that dissipates energy. Additionally, these materials can also exhibit distinct features, such as stress relaxation (decay of stress under constant strain) and creep (increased deformation of an object under constant applied stress).[108,109] Rizwan et al. designed a viscoelastic hydrogel using hyaluronan and laminin via an adjustable stress relaxation rate. This hydrogel could mimic the stress relaxation rate of the liver under physiological conditions and support the growth of cholangiocyte organoids.[110]

Biological performance generally requires bioinks to have low cytotoxicity and support cell adhesion, proliferation, and migration, thereby facilitating cell functionality. In particular, they also support cell-mediated matrix remodeling, which is crucial for regulating ECM production and remodeling. The advancement in tissue engineering techniques has redefined the biocompatibility of implanted materials not only to coexist with endogenous tissues without adverse immune reactions but also to actively modulate inflammatory responses, support

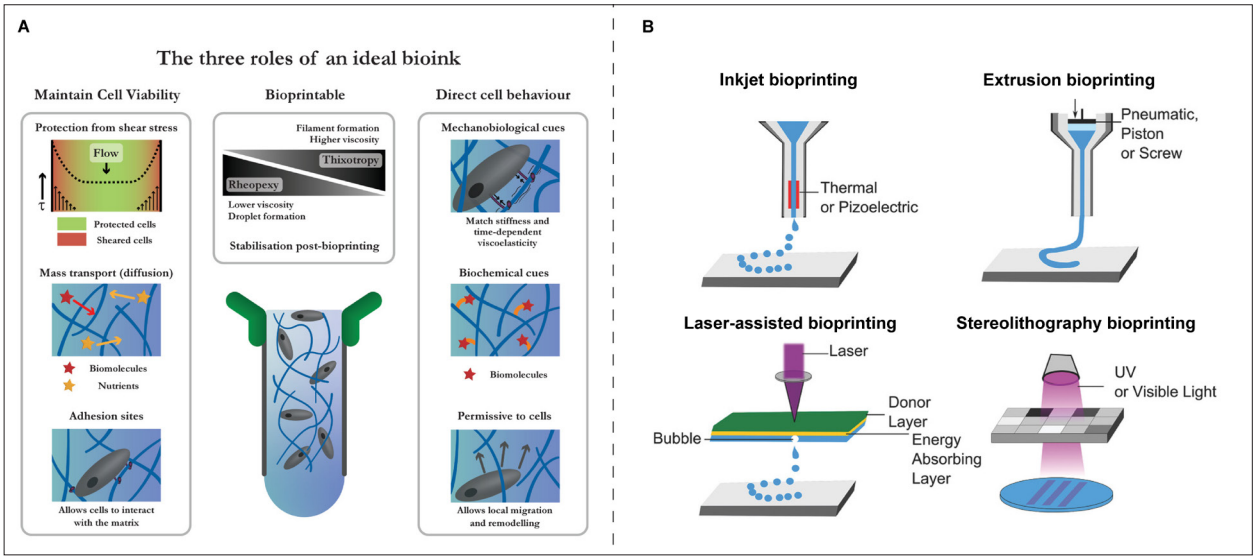


Figure 6. 3D printing strategies and material properties. (A) An ideal bioink fulfills three main roles: maintain cell viability; bioprintability; and direct cell behavior. Adapted with permission from Morgan et al.[104] (B) Different printing strategies: inkjet bioprinting; extrusion bioprinting; laser-assisted bioprinting; and stereolithography bioprinting. Adapted with permission from Foyt et al.[148] Abbreviation: UV, ultraviolet.

implant integration, and enhance wound healing and tissue regeneration. These materials aim to achieve optimal effects within the host, embodying a concept termed "immune interaction" materials.[111,112]

Currently, several natural, naturally derived, and synthetic biopolymer-based materials can be used as bioink. Natural materials include protein-based materials such as gelatin, collagen, fibronectin, and silk fibroin; polysaccharide-based materials such as hyaluronic acid, agarose, and alginate; ECM-based materials such as decellularized ECM (dECM) and Matrigel; as well as mixtures or derivatives of these natural materials. Synthetic materials mainly include Pluronics and PEG.[113] The main components of the liver ECM include collagen, laminin, fibronectin, and proteoglycans.[114] These materials are all ideal candidates for bioink.

4.1.1. Gelatin

Gelatin is a peptide mixture produced by the hydrolysis of collagen, retaining natural cell-binding motifs such as RGD and matrix metalloproteinase (MMP)-sensitive degradation sites. However, gelatin gels often lack thermal stability and mechanical strength, thus necessitating their combination with other materials or chemical crosslinking for use as tissue culture materials. The addition of methacrylate groups to the amine groups of gelatin forms methacrylated gelatin (GelMA), a photocurable hydrogel material that is stable at 37°C. Due to its excellent cell compatibility and mechanical properties, GelMA is widely used in bioprinting.[115] However, a drawback of GelMA is the requirement of a photoinitiator during photocuring, which can be toxic to cells at higher concentrations.[106]

4.1.2. Collagen

Collagen is the most abundant fibrous protein in mammals and a major component of the ECM. Collagen is composed of three left-handed peptide helices coiled together to form a right-handed triple helix, with adjacent helices crosslinked at the end of each helical peptide bond. The resulting long fibrils can form much thicker bundles, with their thickness determining the tensile strength of connective tissue.[116] Collagen contains RGD peptides, supports cell adhesion, and is biodegradable with good biocompatibility.[117] Lee et al. encapsulated hepatocytes, human umbilical vein endothelial cells (HUVECs), and human lung fibroblasts with collagen as a bioink, while simultaneously printing polycaprolactone (PCL) scaffolds to prevent collagen gel collapse and maintain structural integrity. The collagen bioink facilitated the formation of capillary networks, resulting in hepatocytes exhibiting good ALB and urea synthesis capabilities.[118]

4.1.3. Silk fibroin

Silk fibroin is a naturally occurring high-molecular weight fibrous protein extracted from silkworm silk through a process of degumming. Silk fibroin possesses excellent mechanical and physicochemical properties, such as flexibility, tensile strength, breathability, moisture permeability, and controlled-release properties. Additionally, the gelation conditions are mild, making it suitable for cell encapsulation.[119] Fibroin is commonly used

as a hemostatic agent and sealant due to its remarkable biocompatibility, support for cell adhesion, and minimal inflammatory and foreign body responses. Moreover, fibroin monomers can polymerize into a gel via thrombin solution catalysis.

4.1.4. Alginate

Alginate is a linear anionic polysaccharide containing 1,4-linked β-D-mannuronic acid and α-L-guluronic acid residues. Alginate is considered biocompatible and biodegradable. At pH values below 3, it self-assembles into acidic gels through the formation of intermolecular hydrogen bonds. Additionally, alginate can form physical gels through synergistic binding with divalent cations such as Ca^{2+}.[120]

4.1.5. Hyaluronic acid

Hyaluronic acid (HA) is a hydrophilic linear anionic polysaccharide composed of 1,3-β-D-glucuronic acid and 1,4-β-N-acetyl-D-glucosamine residues. It is commonly used as a lubricant to prevent postoperative adhesions. HA is commonly found in natural tissues and is an important component of the liver sinusoidal space. It possesses excellent biocompatibility and can form hydrogels when modified through esterification and crosslinking of its carboxyl or hydroxyl groups. Methacrylate-modified HA can undergo photocrosslinking[121]; glycidyl methacrylate-hyaluronic acid (GMHA) promotes endothelial cell proliferation, supports vascular formation, and has been used to construct vascularized liver tissue.[122,123]

4.1.6. Agarose

Agarose has a gelation principle similar to that of gelatin, forming a gel upon heating and cooling.[124] It is commonly used in 3D bioprinting as sacrificial material or mixed with other materials to adjust ink viscosity.[125] Specifically, agarose can be used to support the culture of hepatocyte spheroids.[126]

4.1.7. Matrigel

Matrigel is derived from mouse tumor ECM and basement membrane, containing 30% collagen IV, 60% adhesive proteins (i.e., laminin), and 10% small molecules (elastin, heparan sulfate proteoglycan, fibronectin, etc.). Matrigel contains growth factors, abundant proteins and peptides, and cell adhesion motifs, thus exhibiting good biocompatibility. It can be used for angiogenesis, organoid culture, 3D cell culture, *in vivo* studies, drug screening, toxicology testing, disease modeling, etc. However, due to the undefined composition of Matrigel, batch-to-batch variations limit its application and clinical potential.[127]

4.1.8. Decellularized extracellular matrix

Decellularized extracellular matrix (dECM) contains proteins and polymers in appropriate proportions to the native ECM, along with other biochemical cues present in the original natural ECM. Currently, dECM from various organs, including the liver, cartilage, heart, fat, skin, vascular tissues, and bladder, has been used in bioprinting. dECM can promote cell survival, differentiation, and long-term functionality. Due to the poor mechanical properties of dECM, it often requires blending with polymers for better structural stability.[128] Deng et al. utilized liver dECM mixed with gelatin and sodium alginate as a bioink for constructing an *in vitro*-expanded primary hepatocyte (eHep cell)-loaded bioartificial liver. The addition of gelatin and sodium alginate improved the mechanical properties of the liver dECM, providing the necessary mechanical support for printing liver structures. The 3D-bioprinted liver cultured *in vitro* exhibited mature hepatic functional phenotypes, such as glycogen storage and drug metabolism. Moreover, upon transplantation, it was able to extend the lifespan of mice with liver failure.[129]

4.1.9. Polyethylene glycol

Polyethylene glycol (PEG) is a linear polymer composed of repeating ethylene glycol units ($HO\text{-}CH_2\text{-}CH_2\text{-}OH$) in its chemical structure. PEG is highly soluble in water, compatible with other organic solvents, and exhibits excellent biocompatibility. Simple PEG-based scaffolds alone cannot promote cell adhesion, and cell apoptosis often occurs due to the absence of cell-matrix binding sites. PEG-based materials can be modified with RGD derivatives to enhance cell adhesion or peptide sensitivity to cell proteases (e.g., from the MMP family), for reshaping and cell traction studies.[130] PEG hydrogels crosslinked by FXIIIa can be adjusted to a stiffness of ≈1.3 kPa, and incorporating key ECM proteins from the natural liver, such as laminin-111, collagen IV, and fibronectin, into the PEG network facilitates the culture of liver organoids.[85]

4.1.10. Pluronics

Pluronics are ABA triblock copolymers of various types, typically named with a letter followed by two or three digits. They are composed of polyethylene oxide (PEO) and polypropylene oxide (PPO). Pluronic F127, widely used in 3D bioprinting, generally undergoes temperature-induced gelation, remaining solid at higher temperatures and transitioning to a liquid state upon cooling. Due to its lack of bioactivity, Pluronic F127 is often used as a sacrificial material to introduce vascular-like structures in hydrogels.[131]

4.2. Cell types

Cells are also a crucial component of bioinks. The cell sources commonly used for 3D bioprinting include stem cells (ESCs, iPSCs) and somatic cells.[132] In liver bioprinting, primary hepatocytes are the most ideal natural cell source, possessing high metabolic activity and relatively similar *in*

vivo functionality. However, primary hepatocytes exhibit reduced proliferation capacity once removed from the *in vivo* microenvironment, and they begin to experience oxidative stress, leading to a rapid decline in function, making them unsuitable for passaging and large-scale expansion. HepG2 liver cancer cell lines have the ability for indefinite passaging, but they still exhibit some functional differences compared to primary cells. HepaRG cells are bipotent liver progenitor cells with high proliferative potential, capable of differentiating into cholangiocyte- and hepatocyte-like cells. HepaRG cells, after dimethyl sulfoxide (DMSO)-induced differentiation, can express most major cytochrome P450 (CYP), such as CYP3A4, 2E1, and 1A2, making them a powerful tool for studying drug metabolism and hepatotoxicity. However, HepaRG cells still exhibit significant gaps in other liver functions, such as ALB production, urea synthesis, and bile secretion, compared to primary hepatocytes. Additionally, their long differentiation period (approximately 28 days) limits their broader use.[133–137]

Stem cells have the potential to differentiate into various cell types and provide a regenerative source of hepatocytes, such as ESCs and iPSCs.[21] Pluripotent stem cells initiate differentiation from the inner cell mass and undergo directed differentiation to become hepatic progenitor cells. These hepatic progenitor cells can subsequently differentiate into both hepatocytes and cholangiocytes.[84,139–142] Additionally, non-parenchymal cells, such as liver sinusoidal endothelial cells, hepatic stellate cells, and Kupffer cells, can also be derived from pluripotent stem cells. Nonetheless, current challenges in stem cell differentiation include low differentiation efficiency, long differentiation time, and the production of heterogeneous cell populations. Subsequent research has found that mimicking the liver microenvironment and co-culturing hepatocytes with other cell types can enhance the maintenance of hepatocyte function. For instance, hepatic stellate cells can mimic the ECM environment of the liver; mesenchymal stem cells can enhance liver function via paracrine secretion of cytokines; endothelial cells can accelerate vascularization and provide oxygen and nutrients required by hepatocytes; and cholangiocytes can promote bile duct system formation and liver-specific gene expression.[142,143] Furthermore, 3D hepatocyte cultures, such as hepatocyte spheroids and liver organoids, can induce polarity in hepatocytes, forming a closely connected spatial structure. This environment supports the formation of bile duct structures, which are crucial for bile production by hepatocytes.[144–147]

4.3. Inkjet bioprinting

The selection of printing method generally depends on the type of bioink used and the desired printing accuracy and structural complexity (Figure 6B). Table 3 compares the different bioprinting technologies. Inkjet-based 3D bioprinting is the earliest form of bioprinting, sharing similarities with traditional inkjet printing. It utilizes piezoelectric or thermal-driven printheads to continuously deposit tiny droplets of bioink onto a substrate, and the layer-by-layer printing approach forms cell-laden 3D structures. Inkjet printing boasts high speed and resolution (up to 50

Table 3. Comparison of different bioprinting techniques

Bioprinting technique	Advantages	Limitations
Inkjet bioprinting	Fast printing speed; high resolution (50 μm); relatively low-cost	Low driving pressure, challenging to print high-viscosity (>10 cP) materials and high-density cells; weak mechanical integrity; uneven droplet size; potential for mechanical or thermal damage to cells
Laser-assisted bioprinting	No nozzle, eliminating nozzle clogging and mechanical damage to cells; high precision (10 μm); supports high cell density	High cost; long printing time; low cell viability
Photocuring-based bioprinting	Fast printing speed; high resolution (<100 μm)	Applicable only to photocrosslinkable bioinks; requires long post-processing time
Volumetric bioprinting	Fast printing speed (<1 min); supports large-volume structure printing (cm scale)	Low printing resolution (30–500 μm); does not support multi-material, multi-cellular printing; low light penetration
Extrusion-based bioprinting	Supports printing of high-viscosity materials and high-density cell solutions	Slow printing speed; low resolution (>100 μm); cell viability may be reduced due to shear forces
Suspension-based bioprinting	Supports extrusion-based printing of low-viscosity materials; high printing accuracy (<50 μm)	Complex post-processing; uneven material deposition; slow printing speed
Coaxial printing	Coaxial multi-material, multi-cell printing	Does not support printing branched structures

μm), along with relatively low costs, as commercial printers can be directly modified into inkjet bioprinters.[149,150] Matsusaki et al. designed a liver microtissue chip integrated with over 400 simplified multilayered structures using inkjet printing, co-cultivating HepG2 cells and HUVECs for high-throughput drug screening[151] (Figure 7A). The 3L (HUVEC/HepG2/HUVEC) structure exhibited higher hepatocyte activity compared to the 2L (HUVEC/HepG2) and 1L (HepG2) structures due to increased cell–cell interactions between the top and bottom layers (Figure 7B). Jian et al. utilized multicellular droplet-based bioprinting technology to construct liver organoids with biomimetic hepatic lobule structures. The printing process utilized two types of bioinks: (i) sodium alginate-HA-RGD containing ``HepaRG cells" and "Fmoc-Tyr-Lys" (Fmoc-YKd)-calcium chloride containing HUVECs/hepatic stellate cells. These bioinks retained the printed structure through *in situ* gelation facilitated by electrostatic interactions. Compared to 2D monolayer cultures, the printed liver organoids exhibited higher cell viability and superior ALB and urea synthesis capabilities.[152]

However, this technology faces significant challenges. Due to the low driving pressure of the printheads, it is challenging to print high-viscosity (>10 cP) materials and high-density cells, resulting in printed structures with weak mechanical integrity. Moreover, during inkjet printing, the low droplet placement accuracy and size uniformity may cause mechanical or thermal damage to cells. These drawbacks limit the widespread application of inkjet printing technology.[19]

4.4. Laser-assisted bioprinting

Laser-assisted bioprinting generally consists of two main techniques: laser-guided direct writing (LGDW) and laser-induced forward transfer (LIFT). It is a nozzle-free printing technology typically composed of three layers from top to bottom: an energy-absorbing layer, a donor layer, and a bioink layer. The bioink layer is suspended at the bottom of the donor layer. When a laser pulse is applied to the energy-absorbing layer (e.g., titanium or gold), the corresponding position of the donor layer below is vaporized, generating high-pressure bubbles that push the bioink onto a collection platform containing biopolymers or cell culture medium. By controlling the *z*-axis of the collection platform, 3D structures can be formed. One inherent advantage of laser-assisted bioprinting is its nozzle-free printing method, eliminating issues related to nozzle-clogging and preventing mechanical damage to cells. Therefore, it is suitable for printing high-viscosity biological materials and bioinks with high cell densities. The printing accuracy can reach the level of single-cell droplets (approximately 10 μm in size). However, it also has drawbacks such as high cost, time-consuming, and low cell viability.[22,153,154]

4.5. Photocuring-based bioprinting

Photocuring-based bioprinting involves continuous crosslinking of hydrogels for constructing 3D-printed bodies. This is achieved by locally solidifying hydrogels within a 2D plane and vertically moving crosslinking layers to build the final 3D structure. Photocuring-based printing was initially used for scaffolds containing cells, and it was later adapted for bioprinting applications. Depending on the modes of light transmission, photocuring-based printing generally falls into two categories: stereolithography (SLA) and digital light processing (DLP). In SLA printing, a scanning laser beam is projected point-by-point onto a liquid photosensitive material to form a solidified layer. After the first layer is solidified, the platform rises to a certain height, followed by crosslinking of the second layer. This process is repeated until a complete 3D structure is printed. In contrast, DLP uses digital mirror devices to directly solidify printing layers, rapidly forming 2D patterns. Ma et al. utilized a DLP-based 3D bioprinting system to embed hepatocyte progenitor cells derived from hiPSCs, along with endothelial and mesenchymal support cells, into a 3D hexagonal hydrogel construct. This setup facilitates the mimicking of liver lobules to simulate the cellular arrangement of the liver under physiological conditions. Compared to traditional 2D and 3D models, the three-cell co-culture model constructed by this strategy reported enhanced expression of liver-specific genes (HNF4α, TTR, and ALB), increased secretion of metabolic products (ALB and urea), and enhanced CYP induction function.[122] Similarly, Zhu et al. employed a DLP-based microscale continuous optical bioprinting technology to construct vascularized liver tissue with complex 3D microstructures, observing an alignment between the printed vascular network and the host vascular system after transplantation.[155] Wang et al. also utilized GelMA mixed with hyaluronic acid methacrylate (HAMA) for DLP-based liver bioprinting. Notably, by using hyaluronidase (Hase) to enzymatically digest HAMA molecules, the mechanical properties of the printed constructs could be adjusted to match those of physiological tissue. A mixture of 5% GelMA and 1.5% HAMA was used for liver tissue construction and subjected to enzymatic digestion (Figure 7C). Hepatocytes in the Hase-treated group exhibited better cell viability and metabolic activity, as well as higher ALB and urea production[156] (Figure 7D and E). Grigoryan and colleagues utilized SLA-based printing equipment to prepare fibronectin hydrogel tissues containing aggregates of hepatocytes. Compared to tissues containing single cells, the activity of the ALB promoter in aggregate-loaded hydrogel tissues was increased by over 60-fold.[146]

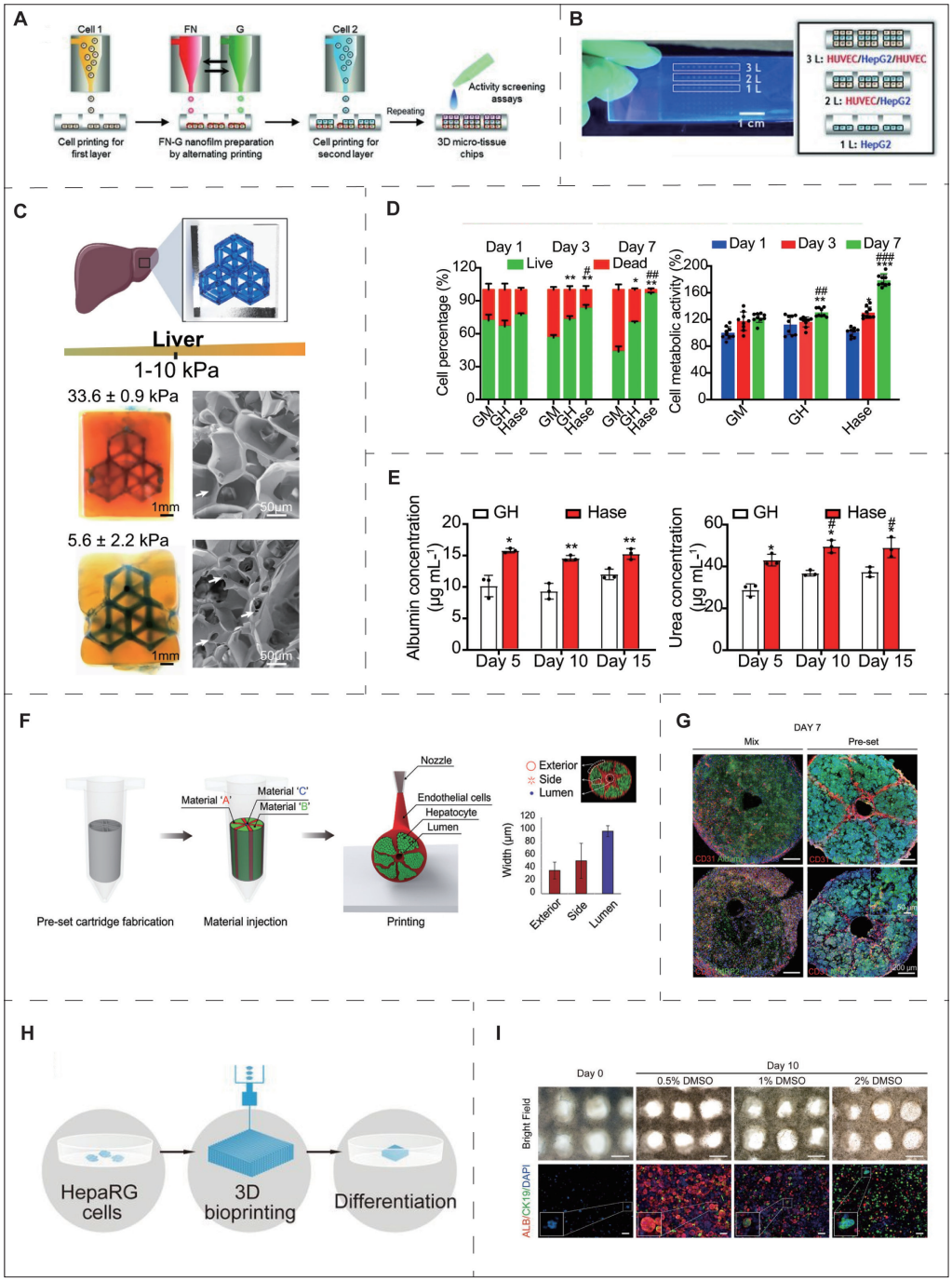


Figure 7. Bioprinting of liver tissue. (A) Schematic illustration of the development of 3D micro-tissue arrays via the layer-by-layer printing of single cells and proteins. (B) Photograph of co-culture arrays under ultraviolet (UV) light. Adapted with permission from Matsusaki et al.[151] (C) 3D tissue mimics printed with 5.0% GelMA containing 1.5% HAMA to emulate the liver. (C, bottom rows) Photographs of the printed constructs before and after hyaluronidase (Hase) digestion and their corresponding scanning electron microscope (SEM) images. (D) Quantitative analyses of the percentages of live/dead cells and metabolic activities of the HepG2/C3A cells. (E) Quantitative results of albumin (ALB)- and urea-secretion levels of the HepG2/C3A cells grown in the bioprinted GelMA/HAMA (5.0%/1.5%) constructs without or with Hase digestion (1000 U/mL; 24 h) after 5, 10, and 15 days. Adapted with permission from Wang et al.[156] (F) Schematic illustration of the preset extrusion-based bioprinting technique for hepatic lobule printing, and the average width of the printed construct. (G) Immunostaining of human umbilical vein endothelial cells (HUVECs) and hepatocytes. Adapted with permission from Kang et al.[27] (H) Schematic illustration of the 3D cell-printing process. (I) Top view of 3D HepaRG/hydrogel constructs on days 0 and 10. Scale bar: 1 mm. Expressions of hepatocyte marker protein, ALB (red), and cholangiocyte marker protein, CK19 (green), were determined by immunofluorescence staining. Scale bar: 100 μm. Adapted with permission from Yang et al.[161] Abbreviations: DMSO, dimethyl sulfoxide; FN, fibronectin; G, gelatin; GM, GelMA; GH, GelMA and Hase. Figure 7C: scale bar: 1 mm, 50 μm; Figure 7G: scale bar: 200 μm, 50 μm.

Generally, photocuring-based printing does not require extrusion through a nozzle, thus offering faster printing speeds and a higher resolution (<100 μm). However, its applicability is limited to light-crosslinkable bioinks and requires longer post-processing times, thereby restricting the range of applications for photocuring-based printing.

Volumetric bioprinting is an innovative photocuring-based 3D printing technology. Unlike SLA and DLP, which build up materials layer-by-layer, volumetric printing rapidly forms 3D objects in a liquid vat by projecting repeated light images from different angles into a transparent photopolymer liquid. This method can complete printing within minutes (or even seconds) without generating harmful mechanical stress on cells.[157] Bernal et al. used volumetric printing technology to construct complex 3D structures containing liver organoids at centimeter-scale within 20 s. They selected 5% GelMA as the bioresin and added LAP as the photoinitiator. By introducing iodixanol, they adjusted the optical properties of the bioresin to address cell-mediated scattering issues. The volumetric bioprinted liver organoids exhibited good cell viability, retaining their structure and polarity.[158] Currently, volumetric bioprinting faces limitations such as low printing resolution (30–500 μm), which makes it more suitable for constructing centimeter-scale structures. Additionally, improving light penetration and achieving multi-material, multi-cellular volumetric printing are urgent challenges that need to be addressed.

4.6. Extrusion-based bioprinting

Extrusion-based bioprinting technology utilizes pneumatic- or mechanically-driven nozzles to extrude bioink in a controlled manner, depositing it onto a platform to form a 2D structure. As the nozzle or platform moves in the *z*-axis direction, layers are stacked to create 3D structures. Extrusion-based bioprinting technology evolved from inkjet printing and is currently the most widely used bioprinting technique due to its ability to handle high-viscosity biological materials and high-density seed cells, utilizing a wide range of available materials. For instance, Miller et al. constructed a rigid filament network using carbohydrate glass via extrusion-based printing. These networks, serving as cell-compatible sacrificial templates, generated hollow cylindrical networks that can be lined with endothelial cells and perfused with blood, making them an ideal strategy for constructing vascularized tissues.[159] Liu et al. designed a multi-material bioprinter with multi-level temperature control based on extrusion-based 3D printing to construct a centimeter-scale 3D liver tissue model containing branched vascular networks. The vascularized liver tissue facilitated the formation of capillary networks and direct surgical anastomosis of the carotid artery and jugular vein.[160] Kang *et al.* employed a preset extrusion-based bioprinting technique to create liver lobule structures containing multiple cells and materials. These biomimetic liver lobules included hepatocytes, endothelial cells, and complex tubular structures (Figure 7F). The preset models exhibited excellent structural integrity and higher levels of ALB and urea synthesis, as well as expression levels of ALB, MRP2, and CD31, compared to co-cultures of hepatocytes and endothelial cells alone[27] (Figure 7G). Similarly, Hong et al. utilized preset extrusion-based bioprinting combined with a microfluidic emulsification technique to produce 3D-vascularized liver tissue spheroids. These liver tissue spheroids featured liver lobule-like cross-sections, complete tissue structures, and high levels of MRP2, ALB, and CD31 expression.[99] Yang et al. used gelatin and alginate-encapsulated HepaRG cells as bioink to construct 3D-bioprinted liver-like organs via extrusion-based printing (Figure 7H). Increasing the concentration of DMSO added during the induction process facilitated cholangiocyte differentiation (Figure 7I). Protein expression of ALB, MRP2, and CYP3A4 in HepaRG cells within 3D-bioprinted hepatorganoids (3DP-HOs) was significantly higher than in 2D cultures. Additionally, levels of ALB, α-1-antitrypsin, and factor VII secreted by 3DP-HOs were comparable to those of primary human hepatocytes.[161] Currently, extrusion-based printing faces challenges with slow printing speeds, low resolution (>100 μm), and reduced cell viability due to shear force.

4.7. Suspension-based bioprinting

High-viscosity bioinks are often selected to ensure high fidelity and stable deposition, which limits the selection range of bioinks. Additionally, high-viscosity materials often require high extrusion pressure for deposition, leading to decreased cell viability. In this regard, suspension-based bioprinting allows for the use of low-viscosity materials, such as collagen, fibronectin, and cells without biomaterials. This technique also utilizes extrusion-based 3D printers, but does not deposit materials downwards onto flat surfaces; instead, it deposits them into a supporting bath of suspension medium, preventing the settling and collapse of printed structures. Suspension media have unique mechanical properties; they exhibit solid-like characteristics under little or no stress, transitioning to liquid-like properties after applying stress greater than the yield stress. When the bioink enters the suspension medium, microstructures spontaneously recover, transforming the medium from liquid to solid state and encapsulating the deposited material.[162] The Feinberg team printed collagen into a suspension bath based on gelatin microspheres to manufacture trileaflet heart valves. This Freeform Reversible Embedding of Suspended Hydrogels (FRESH) technique reported a

printing accuracy of <50 μm, effectively overcoming challenges related to printing collagen.[163,164] Fang et al. developed a dual-phase bioink based on densely packed cell aggregates for embedded printing in a suspension bath, aiming to construct dense liver tissue constructs. This bioink features high cell density (~1.7×10^8 cells/cm) without compromising cell viability (~83%).[165]

4.8. Coaxial printing

Coaxial printing is a specialized form of extrusion-based printing, where an outer layer of bioink and an inner layer of sacrificial material are simultaneously extruded through a coaxial nozzle. After removal of the inner sacrificial material, a hollow tubular structure is formed. This technology enables the printing of concentric multi-material and multi-cellular structures. By adjusting the nozzle diameter, the size of the printed structure can be altered, presenting significant potential for constructing biological tissues with perfusable vascular networks. Taymour et al. utilized seaweed alginate and methylcellulose loaded with HepG2 spheroids dissolved in human fresh frozen plasma as shell material, and coaxially printed collagen-, fibronectin-, and gelatin-encapsulated fibroblast and endothelial cells as core material to construct 3D vascularized liver tissue. This triple-cell co-culture model enhances the secretion of ALB from hepatocytes and serves as a valuable tool for studying cell–cell interactions.[166] However, coaxial printing still faces significant challenges in constructing branched vascular networks. Table 4 summarizes the recent representative studies in liver bioprinting.

5. Typical applications of 3D bioprinting in the liver

5.1. Vascularization

Blood vessels are a critical component in maintaining the vitality and function of various tissues and organs within the body. In addition to transporting oxygen and nutrients and clearing metabolic wastes, the vascular system also regulates blood clotting, the transport of inflammatory cells, and crucial cell signaling interactions in an organ-specific manner. The liver harbors a rich network of blood vessels, including major vessels (e.g., hepatic artery, portal vein, and central vein) and various hepatic sinusoids surrounding the hepatic cords within the liver lobules, thereby facilitating material exchange between hepatocytes and blood. Therefore, the introduction of vascular structures is necessary when constructing liver tissue *in vitro*. Furthermore, in tissue engineering, the diffusion limit for oxygen and nutrients is 200 μm. To construct large-scale engineered tissues, a hierarchical vascular network is indispensable. Small-scale capillary networks can self-organize through endothelial cells. Adding vascular endothelial growth factor (VEGF), basic fibroblast growth factor (bFGF), platelet-derived growth factor (PDGF), and inducing hypoxia in the culture medium promotes angiogenesis. However, constructing large-scale, perfusable blood vessels requires the use of sacrificial materials. The general process of sacrificial bioprinting involves first printing the geometric structure using sacrificial materials. Subsequently, after the entire structure is printed, the sacrificial material is removed by dissolution or temperature induction to induce phase transition, leaving behind a sacrificial template. Finally, endothelial cells are introduced to endothelialize the channels.[167] Hepatic sinusoidal endothelial cells are the ideal source for endothelial cells, as they are highly specialized endothelial cells with fenestrations on their membranes and an absence of an organized basement membrane. These features enhance membrane permeability, facilitating direct substance exchange between hepatocytes and the bloodstream. However, due to the difficulty in isolating hepatic sinusoidal endothelial cells and their low purity, HUVECs are often used as substitutes in printing processes. Commonly used sacrificial template materials include gelatin, Pluronic F127, carbohydrate glass, sodium alginate, and agarose. Additionally, the team led by Miller utilized laser-sintered carbohydrate-based compounds as sacrificial templates, which were then dissolved in water or phosphate-buffered saline (PBS) to construct dendritic vascular networks. These dendritic vascular networks were capable of sustaining cellular metabolic activity within tissue models exceeding 1 cm in thickness.[168]

There has been significant progress in constructing vascularized liver tissues using various extrusion-based printing strategies, including the development of complex vascular structures resembling hepatic lobules.[27,99] As aforementioned, Xiong et al. constructed functional liver tissue with high cell density and perfusable vascular networks by simultaneously printing granular cell aggregate-based biphasic (GCAB) bioink and gelatin bioink loaded with endothelial cells.[165] The GCAB bioink ensures high cell density, while the gelatin bioink serves as a sacrificial material to create vascular channels (Figure 8A). Taymour et al. selected collagen-, fibrin-, and gelatin-encapsulating fibroblasts and endothelial cells as the core materials for coaxial printing.[166] Collagen and fibrin support angiogenesis, while gelatin increases the viscosity of the bioink (Figure 8B). Similarly, Liu et al. used gelatin as a sacrificial material and employed a combination of cell-laden bioink (3% GelMA + 0.25% fibrin), fugitive bioink (10% gelatin), and elastic bioink (10% GelMA) for multi-material bioprinting to create perfusable, surgically anastomotic 3D-vascularized liver tissue (Figure 8C).[160] Miller's team developed a technique

Table 4. Representative studies on liver bioprinting

Printing technique	Printing materials	Crosslinking method	Mechanical strength	Hepatic cells	Other cells	Size	Culture time	Functions	Ref.
Inkjet printing	Fibronectin; gelatin	Spontaneous crosslinking	Not mentioned	HepG2	HUVECs	Thickness: 50–100 μm; diameter: 1 mm	1 week	Increased ALB secretion and CYP450 metabolic activity with the number of layers	[151]
DLP	GelMA; GMHA	UV light	4 kPa	hiPSC-derived	HUVECs; ADSCs	3 × 3 mm; thickness: ≈200 μm	10 days	Increased levels of ALB, urea production, and CYP enzymatic activity in the tri-culture model	[122]
	GelMA; GMHA	UV light	4–6 kPa	HepG2	HUVECs	XY-plane: 4 × 5 mm; *Z*-direction: 600 μm	1 week	Anastomosis of printed lumen-like structures with host blood vessels post-implantation	[155]
SLA	Fibrin/GelMA; PEGDA	UV light	Not mentioned	Rat primary hepatocytes	HUVECs; NHDFs	16 × 10 × 4 mm	10 days	Printed hepatocyte structures exhibited improved ALB activity and anastomosis with host blood vessels post-implantation	[146]
Extrusion-based bioprinting	GelMA; fibrin; gelatin	UV light; temperature; thrombin	Not mentioned	HepG2	HUVECs; HFFs	12 × 8 × 6 mm	1 week	Printed liver tissue exhibited improved ALB expression and could be surgically anastomosed with the host vascular system	[160]
	Gelatin; alginate	$CaCl_2$	Not mentioned	HepaRG	-	10 × 10 × 3 mm; interconnected channel diameter: ≈500 μm	10 days	3DP-HOs acquired liver functions, e.g., ALB secretion, drug metabolism, and glycogen storage, after 7 days of differentiation; transplantation of 3DP-HOs significantly improved the survival of mice	[161]
	Collagen; gelatin; alginate	Temperature; pH	6–14 kPa	HepG2	HUVECs	Diameter: 1 mm; 4 × 5.2 × 2.5 mm	10 days	Compared to hepatic cell/endothelial cell mixtures, the fabricated hepatic lobule exhibited higher ALB secretion, urea production, CYP enzymatic activity, and levels of ALB, MRP2, and CD31 proteins	[27]
	Collagen	Temperature	Not mentioned	HepG2	HUVECs	Diameter: 416 ± 26.14 μm	10 days	Structured spheroids synthesized more functional hepatic proteins than non-structured ones	[99]

doi: 10.36922/ijb.3819

	dECM; gelatin	Temperature	Not mentioned	HepaRG	HUVECs	0.03 × 0.1 × 1 mm	7 days	Bile duct channel chips enhanced bile duct system formation and liver-specific gene expression and function	[142]
	Agarose; GelMA	UV light	<6 kPa	HepG2	HUVECs; RBE cholangiocarcinoma cells	10 × 12 × 5 mm	9 days	>4000 differentially expressed genes in the 3D co-culture model; cholangiocarcinoma cells in the 3D model were more sensitive to anti-tumor drugs	[143]
Suspension-based bioprinting	GelMA	Visible light (405 nm; 20 mW/cm^2)	33.7 ± 6.2 kPa	HepG2	HUVECs	Cubic hepatic tissue construct thickness: ~4 mm	1 week	Printed liver tissue enhanced ALB levels and supported capillary network formation	[165]
Coaxial printing	*Shell:* Alginate; methylcellulose *Core:* Collagen; fibrin; gelatin	Temperature; $CaCl_2$; thrombin	Not mentioned	HepG2	HUVECs; NHDFs	6 × 6 mm	14 days	Enhanced ALB secretion	[166]

Abbreviations: 3DP-Hos, 3D-bioprinted hepatorganoids; ADSCs, adipose-derived stem cells; ALB, albumin; dECM, decellularized extracellular matrix; DLP, digital light processing; GelMA, methacrylated gelatin; GMHA, glycidyl methacrylate-hyaluronic acid; HA, hyaluronic acid; HFFs, human foreskin fibroblasts; hiPSC, human induced pluripotent stem cell; HUVECs, human umbilical vein endothelial cells; NHDFs, normal human dermal fibroblasts; PEGDA, polyethylene glycol diacrylate; SLA, stereolithography; UV, ultraviolet.

doi: 10.36922/ijb.3819

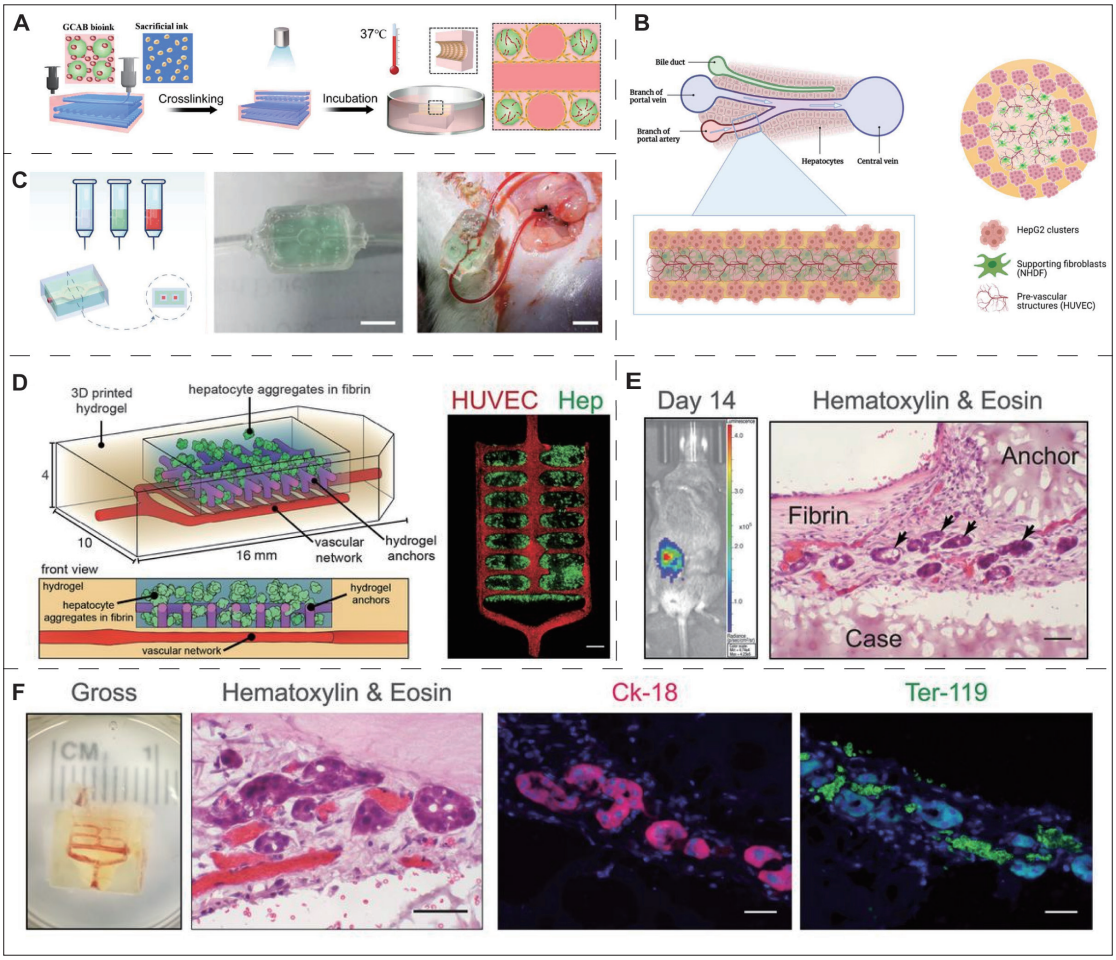


Figure 8. Vascularization of bioprinted liver tissue. (A) 3D printing of functional hepatic tissues via a perfusable vascular network. Adapted with permission from Fang et al.[165] (B) Schematic representation of the core–shell bioprinted triple culture liver model. Adapted with permission from Taymour et al.[166] (C) Schematic representation of multi-material extrusion bioprinting strategies and "one-to-two-" channeled tissues encapsulated in polydimethylsiloxane (PDMS) connected with polyurethane (PU) tubes. Observation of transplanted tissues after establishing anastomosis; the carotid artery and jugular vein display arterial clip slip and establishment of blood perfusion. Scale bar: 1 cm. Adapted with permission from Liu et al.[160] (D) Pre-vascularized hepatic hydrogel carriers. (E) Hepatocytes exhibit albumin (ALB) promoter activity after implantation in mice. (F) Hydrogel carriers infiltrated with host blood. Scale bars: 40μm XX. Adapted with permission from Grigoryan et al.[146] Abbreviations: CK18, Cytokeratin 18; GCAB, granular cell aggregate-based biphasic bioink; HUVECs, human umbilical vein endothelial cells. Figure 8D: scale bar: 1 mm; Figure 8E: scale bar: 50 μm.

by adding edible dyes that absorb blue light into hydrogels, allowing the hydrogels to cure under high-resolution blue light exposure.[146] This method enabled the construction of complex vascular structures within the hydrogels (Figure 8D). After implantation in chronically injured mice for 14 days, functional hepatocytes remained viable and displayed blood infiltration (Figure 8E and F). However, as mentioned earlier, extrusion-based bioprinting methods, including coaxial printing, are limited by resolution and can only print vessels with diameters exceeding 200 μm. Even with the FRESH system, the diameter of the lumens can only be refined to approximately 100 μm, resulting in relatively low resolution (approximately 10 times the diameter of a cell). Photopolymerization-based printing methods can enhance printing precision and speed, but current printing resolutions are still limited to around 300 μm. Hence, further innovation in manufacturing strategies is warranted to overcome these resolution limitations.[169]

5.2. Bile duct formation

The bile duct system comprises a complex network of ducts starting from the Hering duct and ending at the ampulla of Vater in the duodenum, primarily responsible for transporting bile from the liver to the intestinal lumen.[40] Bile contains cholesterol, bile pigments, bile acids, phospholipids, and bicarbonate, and its functions include

emulsifying fats, transporting detoxification products from the liver, and promoting the absorption of fatty acids and fat-soluble vitamins.[41] From a developmental biology perspective, intrahepatic bile ducts originate from the hepatic region of the ventral foregut endoderm, while extrahepatic bile ducts emerge from the pancreatic ductal region.[170,171] Cholangiocytes are highly polarized epithelial cells lining the inner walls of intrahepatic and extrahepatic bile ducts. These cells form a single-layered epithelium within the bile duct lumen, responsible for providing a barrier to prevent the toxic effects of bile on other cells, while also facilitating the transfer of water, electrolytes, and bile acids, and altering the composition of bile.[172] Intrahepatic bile ducts of different diameters are lined with cholangiocytes of varying sizes, each with distinct functions. It is generally believed that small cholangiocytes are undifferentiated and immature, whereas large cholangiocytes are differentiated and mature, i.e., capable of responding to regulatory signals within the bile ducts[173] (Figure 9A).

The bile duct system is of paramount importance for the liver. Dysfunctional bile ducts can lead to bile accumulation in the liver, ultimately resulting in liver damage and potentially progressing to end-stage liver cirrhosis. Biliary diseases account for approximately one-third of adult liver transplants and 70% of pediatric liver transplants.[174] In the United States, primary sclerosing cholangitis (PSC) alone constitutes 5% of liver transplants, and biliary complications are the leading cause of graft failure after deceased donor liver transplantation.

There have been recent developments in bioprinting bile ducts.[174,175–177] Lewis et al. cultured immortalized mouse extrahepatic bile duct epithelial cells in liver dECM hydrogels to form structures resembling bile duct trees.[177] After 7 days of culture, cholangiocytes in the liver dECM formed branching structures, which further developed into a complex 3D network over a longer period (21 days) (Figure 9B). Vallier et al. reconstructed murine extrahepatic bile duct trees using primary extrahepatic cholangiocytes and utilized extrahepatic cholangiocyte organoids (ECOs) to repair human bile duct epithelium.[179,180] In their follow-up work, they demonstrated that cholangiocytes from different regions, including intrahepatic ducts (IHD), common bile duct (CBD), and gallbladder (GB), formed organoids *in vitro* that exhibited distinct gene expression characteristics[179] (Figure 9C). They also constructed branching cholangiocyte organoids (BRCOs) by modulating the JAG1/NOTCH2 signaling pathway.[181] Wells et al. designed a bile duct chip to study the barrier function of monolayer cholangiocytes and introduced vascular structures in subsequent studies to investigate inflammatory and fibrotic biliary diseases.[182,183] However, there is still limited work combining liver tissue with bile duct structures, which holds significant importance. For example, co-culturing hepatocytes and cholangiocytes introduces bile duct structures into liver organoids or hepatocyte spheroids. These cells can be (i) primary hepatocytes and primary cholangiocytes; or (ii) hepatocytes and cholangiocytes differentiated from pluripotent stem cells.[82,84,138,139,144,183] Tanimizu et al. generated a hepatobiliary tubular organoid (HBTO) by co-culturing mouse liver progenitor cells and cholangiocytes using a sandwich culture method (Figure 9D). Among them, hepatocytes and cholangiocytes established functional hepatobiliary connecting structures. Hepatocytes formed a bile duct network and secreted metabolites into them for transport. Hepatocytes in HBTO could maintain metabolic function long-term, including ALB secretion and CYP activity.[183] Nevertheless, current hepatobiliary organoids lack ductal structures for bile excretion, preventing directional bile excretion and collection.

Bioprinting technology, with its ability to precisely distribute cells and materials and create ductal structures using sacrificial materials, represents an ideal strategy for constructing bile duct-containing liver tissue. Lee et al. used gelatin as a sacrificial material and encapsulated HepaRG cells in liver dECM as bioink for bioprinting, where HepaRG cells differentiated into hepatocytes and cholangiocytes. They validated the formation of the bile duct system using cholesterol-fluorescein (CLF; a fluorescent bile acid derivative widely used to assess hepatobiliary transport function) and indocyanine green (ICG; a non-toxic organic anion used clinically to assess liver function and capable of hepatocyte transport) to validate bile duct system formation[142] (Figure 9E–G). Liu et al. used gelatin microfibers as sacrificial templates and GelMA as bioink to construct a 3D cholangiocarcinoma model containing HepG2, RBE cholangiocarcinoma cells, and endothelial cells. RBE cholangiocarcinoma cells and endothelial cells were seeded in channels created after removing the sacrificial material, subsequently forming tight cell–cell connections between cholangiocytes.[143] The primary challenge in constructing bile duct-containing liver tissue is the inability to direct bile produced by hepatocytes into the bile ducts. In particular, there is a lack of hepatocytes capable of producing bile in large quantities *in vitro*, and also a lack of hepatobiliary connection structures capable of directing bile transport.

6. Challenges and future outlook

Liver tissue engineering has advanced in recent years, offering various liver transplant alternatives poised to treat liver diseases and alleviate the shortage of organ transplants. 3D bioprinting technology, with its ability

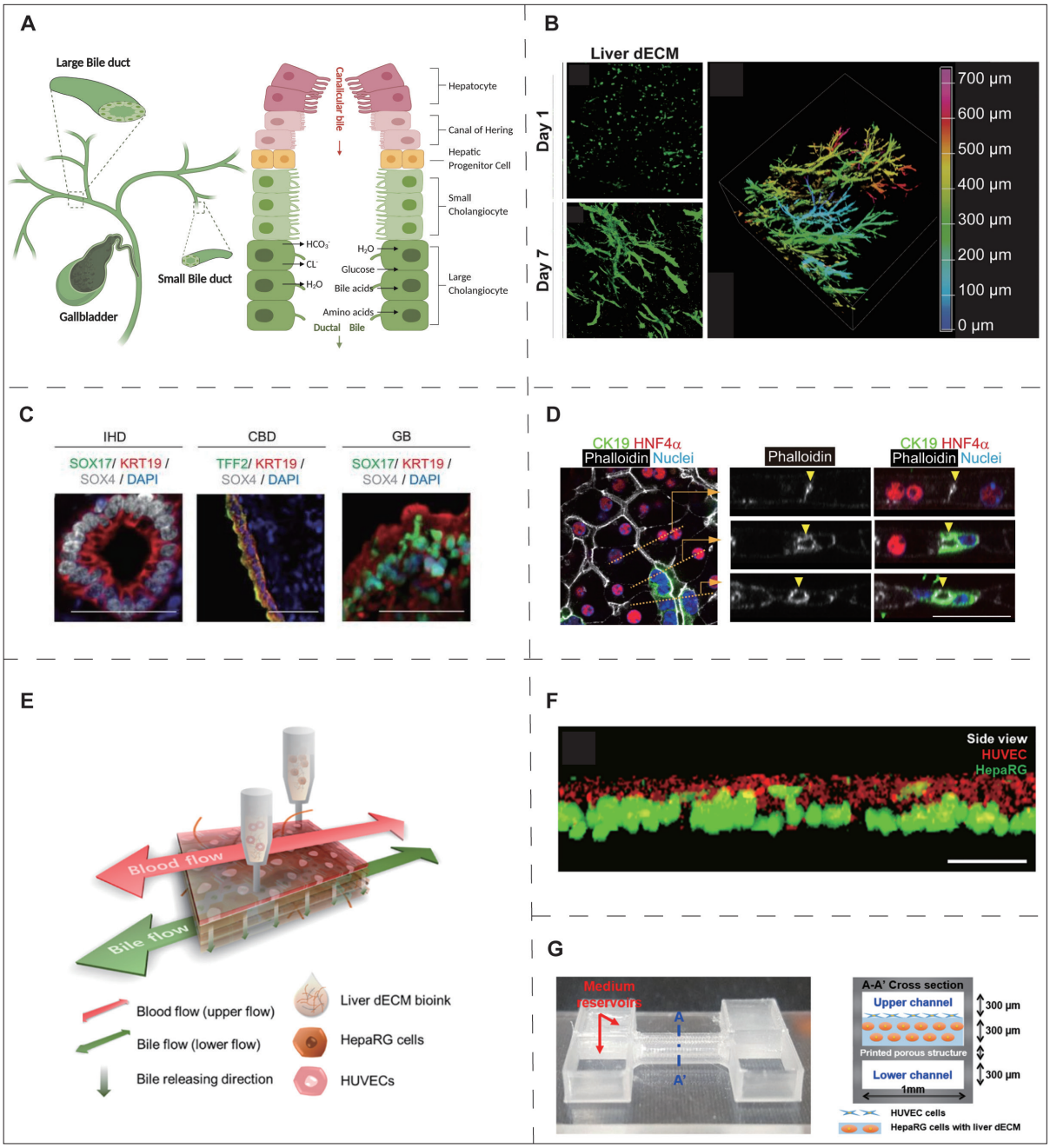


Figure 9. Biomanufacturing of bile ducts. (A) Biliary tree, bile duct, cholangiocytes, and ductal bile formation. Adapted with permission from Wang et al.[173] (B) Cholangiocytes encapsulated in the liver decellularized extracellular matrix (dECM) spontaneously form duct-like structures. Adapted with permission from Lewis et al.[177] (C) Immunofluorescence images of primary cholangiocytes illustrate the differential expression of representative region markers. Scale bars: 50 μm. Adapted with permission from Sampaziotis et al.[178] (D) Hepatobiliary connections in co-culture optical cross-sections along broken lines in the left panel are displayed in the right panels. The BC within the HNF4α+ hepatocyte clusters (arrowheads in upper right panels) connect to the lumen, which consists of CK19+ cholangiocytes and HNF4α+ hepatocytes (arrowheads in middle right panels), and then eventually reach the duct of CK19+ cholangiocytes (arrowheads in lower right panels). At 4 weeks after MG overlay, the immunostaining with phalloidin (white), anti-HNF4α antibody (red), anti-CK19 antibody (green), and Hoechst 33342 (blue) was repeated five times independently. Three fields were examined in each sample. Three out of 15 areas were further used to collect serial optical sections for 3D reconstruction. The representative images are displayed in this figure. Scale bars: 50 μm. Adapted with permission from Tanimizu et al.[183] (E) Cell-printing of the 3D liver-on-a-chip with vascular/biliary systems. (F) The evaluation of cell positioning after bioprinting 3D liver-on-a-chip. Scale bar: 100 μm. (G) Cell-printed 3D liver-on-a-chip with dual fluidic condition. Adapted with permission from Lee et al.[143] Abbreviations: BC, bile canaliculi; CBD, common bile duct; CK19: Cytokeratin 19; DAPI, 4',6-diamidino-2-phenylindole; GB, gallbladder; HNF4α: Hepatocyte Nuclear Factor 4 alpha; HUVECs, human umbilical vein endothelial cells; IHD, intrahepatic ducts; Krt19, Keratin 19; MG: Matrigel; Sox17, SRY (sex-determining region Y)-box 17; Sox4, SRY (sex-determining region Y)-box 4; TFF2, Trefoil Factor 2.

to precisely assemble cells and materials, has become a highly promising approach for liver manufacturing. Currently, bioprinted liver tissues have demonstrated a certain level of liver functions, such as the synthesis of ALB and urea, glycogen accumulation, and drug metabolism. Furthermore, with the introduction of cholangiocytes, endothelial cells, and stromal cells, the composition of bioprinted liver tissues is becoming more similar to that of natural liver tissue. Additionally, the establishment of perfusable multi-scale vascular networks has enabled the creation of larger vascularized liver tissues (>1 cm), overcoming the limitations of nutrient and oxygen diffusion.

Despite the enormous potential of 3D bioprinting technology, many challenges remain in the field of liver manufacturing. Firstly, the number and density of cells currently used to construct liver tissues *in vitro* remain significantly different from those of natural livers, and the size is limited to the centimeter scale, far from the size of a natural liver. Secondly, although other cell types (e.g., cholangiocytes, endothelial cells, and stromal cells) have been incorporated, they often exhibit simple co-culture rather than functional interactions. Furthermore, the bioinks and subsequent *in vitro* cultures mainly use natural biomaterials. While these materials may support cell viability, they often have batch variations, and components such as Matrigel and dECM are even unclear, severely limiting their clinical applications. Hence, developing bioinks with defined components and adjustable properties is a promising research direction. Additionally, present bile duct structures can only transport exogenous bile acids, and achieving the transport of bile produced by hepatocytes themselves remains challenging. Finally, achieving immunization *in vitro* for the liver, a vital immune organ in the human body, has not been successful.

Nonetheless, bioprinting technology has made significant progress in recent years. Volumetric bioprinting technology can create entire cell-laden structures of any size and shape within seconds.[184–186] Acoustic-assisted 3D printing uses non-contact liquid handling methods to avoid cross-contamination. This printing method also overcomes nozzle limitations, avoiding issues such as nozzle-clogging. Additionally, ultrasonic standing waves and acoustics-based bioprinting can be applied to microfluidic technology, enabling the manipulation of particles and cells.[187–195] 4D bioprinting technology is also gradually emerging. By combining the fourth dimension "time" with 3D printing, it is possible to simulate the complex dynamics of natural tissues, thereby improving the functional response of constructed tissues. Although current 4D bioprinting lacks biocompatibility and the printability of multi-component materials, and is only used in theoretical and *in vitro* research without established application scenarios for 4D bioprinted products, it remains a promising research direction.[196] Robotic arm-based bioprinting, with its enhanced dimensional freedom, can increase the complexity and flexibility of bioprinting. This technology allows for the printing of various patterns on curved or dynamic surfaces.[197] Machine learning is also a current research hotspot, as its algorithms can automatically construct mathematical models and make predictions or decisions based on new data. Utilizing machine learning for the functional evaluation of bioartificial organs holds promise for optimizing the cultivation conditions of 3D-printed structures and extending the cultivation time.[198] In the future, bioprinting technology is expected to achieve a significant leap from mimicking the form to replicating the function, thereby alleviating the organ shortage crisis and ushering in a new era of regenerative medicine.

7. Conclusion

This review delves into the field of liver tissue engineering, particularly the cutting-edge applications and potential of 3D bioprinting technology in liver manufacturing. As a crucial internal organ, the liver's complex structure and diverse functions play a central role in maintaining vital activities. The article first details the physiological functions, cellular composition, and unique development and regeneration mechanisms of the liver, emphasizing its importance in biomedical research. Facing the shortage of liver transplant donors and the limitations of existing alternatives, the article highlights 3D bioprinting technology as an innovative solution for liver organ fabrication. This technology, with its capabilities for personalized customization, replication of complex structures, and precise arrangement of multi-material cells, shows tremendous potential in tissue engineering. By reviewing the latest research advances in liver bioprinting, the article thoroughly introduces the composition and properties of bioinks and their specific applications and outcomes in liver bioprinting. Moreover, the article deeply analyzes the current challenges in liver fabrication, such as constructing vascular and bile duct structures, and explores future development directions. It emphasizes the critical role of ongoing efforts to optimize biomaterials, cell sources, and printing technologies in advancing liver biofabrication toward clinical application. In summary, this article aims to provide a comprehensive and in-depth perspective for researchers in the field of liver tissue engineering, and to offer insights into future directions for innovation and development in liver disease treatment strategies.

Acknowledgments

None.

Funding

This research was supported by the National Natural Science Foundation of China (62127811, U23A20453, U21A20396, T2222029), the National Key Research and Development Program of China (2022YFA1104701), Initiative Scientific Research Program of Institute of Zoology (2023IOZ0101), and the CAS Engineering Laboratory for Intelligent Organ Manufacturing (KFJ-PTXM-039).

Conflict of interest

The authors declare no conflicts of interest.

Author contributions

Conceptualization: Yifan Hou, Xin Liu, Shen Ji, Xinhuan Wang
Investigation: Yifan Hou
Supervision: Qi Gu
Visualization: Yifan Hou
Writing – original draft: Yifan Hou, Xin Liu
Writing – review & editing: Yifan Hou, Xin Liu, Shen Ji, Xinhuan Wang, Qi Gu

Ethics approval and consent to participate

Not applicable.

Consent for publication

Not applicable.

Availability of data

Not applicable.

References

1. Lemaigre FP. Mechanisms of liver development: concepts for understanding liver disorders and design of novel therapies. *Gastroenterology*. 2009;137(1):62-79.
doi: 10.1053/j.gastro.2009.03.035

2. Ober EA, Lemaigre FP. Development of the liver: Insights into organ and tissue morphogenesis. *J Hepatol*. 2018;68(5):1049-1062.
doi: 10.1016/j.jhep.2018.01.005

3. Wang X, Yang L, Wang Y-C, et al. Comparative analysis of cell lineage differentiation during hepatogenesis in humans and mice at the single-cell transcriptome level. *Cell Res*. 2020;30(12):1109-1126.
doi: 10.1038/s41422-020-0378-6

4. Macchi F, Sadler KC. Unraveling the epigenetic basis of liver development, regeneration and disease. *Trends Genet*. 2020;36(8):587-597.
doi: 10.1016/j.tig.2020.05.002

5. Matchett KP, Wilson-Kanamori JR, Portman JR, et al. Multimodal decoding of human liver regeneration. *Nature*. 2024;630(8015):158-165.
doi: 10.1038/s41586-024-07376-2

6. Sun T, Pikiolek M, Orsini V, et al. AXIN2⁺ Pericentral hepatocytes have limited contributions to liver homeostasis and regeneration. *Cell Stem Cell*. 2020;26(1):97-107.e6.
doi: 10.1016/j.stem.2019.10.011

7. Raasch M, Fritsche E, Kurtz A, Bauer M, Mosig AS. Microphysiological systems meet hiPSC technology - new tools for disease modeling of liver infections in basic research and drug development. *Adv Drug Deliv Rev*. 2019;140:51-67.
doi: 10.1016/j.addr.2018.06.008

8. Heymann F, Tacke F. Immunology in the liver — from homeostasis to disease. *Nat Rev Gastroenterol Hepatol*. 2016;13(2):88-110.
doi: 10.1038/nrgastro.2015.200

9. Palakkan AA, Hay DC, PR Anil Kumar, TV Kumary, Ross JA. Liver tissue engineering and cell sources: issues and challenges. *Liver Int*. 2013;33(5):666-676.
doi: 10.1111/liv.12134

10. Prior N, Inacio P, Huch M. Liver organoids: from basic research to therapeutic applications. *Gut*. 2019;68(12):2228-2237.
doi: 10.1136/gutjnl-2019-319256

11. Osonoi S, Takebe T. Organoid-guided precision hepatology for metabolic liver disease. *J Hepatol*. 2024;80(5):805-821.
doi: 10.1016/j.jhep.2024.01.002

12. Panwar A, Das P, Tan LP. 3D hepatic organoid-based advancements in LIVER tissue engineering. *Bioengineering (Basel)*. 2021;8(11):185.
doi: 10.3390/bioengineering8110185

13. Yang Z, Liu X, Cribbin EM, Kim AM, Li JJ, Yong KT. Liver-on-a-chip: considerations, advances, and beyond. *Biomicrofluidics*. 2022;16(6):061502.
doi: 10.1063/5.0106855

14. Dalsbecker P, Beck Adiels C, Goksör M. Liver-on-a-chip devices: the pros and cons of complexity. *Am J Physiol Gastrointest Liver Physiol*. 2022;323(3):G188-G204.
doi: 10.1152/ajpgi.00346.2021

15. Mirdamadi ES, Kalhori D, Zakeri N, Azarpira N, Solati-Hashjin M. Liver tissue engineering as an emerging alternative for liver disease treatment. *Tissue Eng Part B Rev*. 2020;26(2):145-163.
doi: 10.1089/ten.TEB.2019.0233

16. Zhang L, Guan Z, Ye JS, Yin YF, Stoltz JF, de Isla N. Research progress in liver tissue engineering. *Biomed Mater Eng*. 2017;28(s1):S113-s119.
doi: 10.3233/bme-171632

17. Agarwal T, Banerjee D, Konwarh R, et al. Recent advances in bioprinting technologies for engineering hepatic tissue. *Mater Sci Eng C Mater Biol Appl*. 2021;123:112013.
doi: 10.1016/j.msec.2021.112013

18. Zahra H, Paria P, Polina B, et al. Mimicking the liver function in micro-patterned units: challenges and perspectives in 3D bioprinting. *Bioprinting*. 2022;27:e00208.
doi: 10.1016/j.bprint.2022.e00208

19. Arka S, Sourabh G. 3D bioprinting strategies for recapitulation of hepatic structure and function in bioengineered liver: a State-of-the-art review. *Curr Opin Biomed Eng*. 2024;30:100526.
doi: 10.1016/j.cobme.2024.100526

20. Agarwal T, Subramanian B, Maiti TK. Liver tissue engineering: challenges and opportunities. *ACS Biomater Sci Eng*. 2019;5(9):4167-4182.
doi: 10.1021/acsbiomaterials.9b00745

21. Ordovás L, Park Y, Verfaillie CM. Stem cells and liver engineering. *Biotechnol Adv*. 2013;31(7):1094-1107.
doi: 10.1016/j.biotechadv.2013.07.002

22. Ali ASM, Wu D, Bannach-Brown A, et al. 3D bioprinting of liver models: a systematic scoping review of methods, bioinks, and reporting quality. *Materials Today Bio*. 2024;26:100991.
doi: 10.1016/j.mtbio.2024.100991

23. Thompson WL, Takebe T. Human liver model systems in a dish. *Dev Growth Differ*. 2021;63(1):47-58.
doi: 10.1111/dgd.12708

24. Collardeau-Frachon S, Scoazec J-Y. Vascular development and differentiation during human liver organogenesis. *Anat Rec. (Hoboken)*. 2008;291(6):614-627.
doi: 10.1002/ar.20679

25. Swartley OM, Foley JF, Livingston DP, 3rd, Cullen JM, Elmore SA. Histology atlas of the developing mouse hepatobiliary hemolymphatic vascular system with emphasis on embryonic days 11.5-18.5 and early postnatal development. *Toxicol Pathol*. 2016;44(5):705-725.
doi: 10.1177/0192623316630836

26. Zhang H, Pu W, Tian X, et al. Genetic lineage tracing identifies endocardial origin of liver vasculature. *Nat Genet*. 2016;48(5):537-543.
doi: 10.1038/ng.3536

27. Kang D, Hong G, An S, et al. Bioprinting of multiscaled hepatic lobules within a highly vascularized construct. *Small*. 2020;16(13):1905505.
doi: 10.1002/smll.201905505

28. Ben-Moshe S, Itzkovitz S. Spatial heterogeneity in the mammalian liver. *Nat Rev Gastroenterol Hepatol*. 2019;16(7):395-410.
doi: 10.1038/s41575-019-0134-x

29. Gissen P, Arias IM. Structural and functional hepatocyte polarity and liver disease. *J Hepatol*. 2015;63(4):1023-1037.
doi: 10.1016/j.jhep.2015.06.015

30. Fu D, Wakabayashi Y, Ido Y, Lippincott-Schwartz J, Arias IM. Regulation of bile canalicular network formation and maintenance by AMP-activated protein kinase and LKB1. *J Cell Sci*. 2010;123(Pt 19):3294-3302.
doi: 10.1242/jcs.068098

31. Wang T, Yanger K, Stanger BZ, Cassio D, Bi E. Cytokinesis defines a spatial landmark for hepatocyte polarization and apical lumen formation. *J Cell Sci*. 2014;127(Pt 11):2483-2492.
doi: 10.1242/jcs.139923

32. Zhang Y, De Mets R, Monzel C, et al. Biomimetic niches reveal the minimal cues to trigger apical lumen formation in single hepatocytes. *Nat Mater*. 2020;19(9):1026-1035.
doi: 10.1038/s41563-020-0662-3

33. He L, Pu W, Liu X, et al. Proliferation tracing reveals regional hepatocyte generation in liver homeostasis and repair. *Science*. 2021;371(6532):eabc4346.
doi: 10.1126/science.abc4346

34. Wei Y, Wang YG, Jia Y, et al. Liver homeostasis is maintained by midlobular zone 2 hepatocytes. *Science*. 2021;371(6532):eabb1625.
doi: 10.1126/science.abb1625

35. MacParland SA, Liu JC, Ma X-Z, et al. Single cell RNA sequencing of human liver reveals distinct intrahepatic macrophage populations. *Nat Commun*. 2018;"9(1):4383.
doi: 10.1038/s41467-018-06318-7

36. He S, Luo Y, Ma W, et al. Endothelial POFUT1 controls injury-induced liver fibrosis by repressing fibrinogen synthesis. *J Hepatol*. 2024;81(1):135-148.
doi: 10.1016/j.jhep.2024.02.032

37. Shetty S, Lalor PF, Adams DH. Liver sinusoidal endothelial cells — gatekeepers of hepatic immunity. *Nat Rev Gastroenterol Hepatol*. 2018;15(9):555-567.
doi: 10.1038/s41575-018-0020-y

38. Gracia-Sancho J, Caparrós E, Fernández-Iglesias A, Francés R. Role of liver sinusoidal endothelial cells in liver diseases. *Nat Rev Gastroenterol Hepatol*. 2021;18(6):411-431.
doi: 10.1038/s41575-020-00411-3

39. Formes H, Bernardes JP, Mann A, et al. The gut microbiota instructs the hepatic endothelial cell transcriptome. *iScience*. 2021;24(10):103092.
doi: 10.1016/j.isci.2021.103092

40. Banales JM, Huebert RC, Karlsen T, Strazzabosco M, LaRusso NF, Gores GJ. Cholangiocyte pathobiology. *Nat Rev Gastroenterol Hepatol*. 2019;16(5):269-281. doi: 10.1038/s41575-019-0125-y

41. Tabibian JH, Masyuk AI, Masyuk TV, O'Hara SP, LaRusso NF. Physiology of cholangiocytes. *Compr Physiol*. 2013;3(1): 541-565. doi: 10.1002/cphy.c120019

42. Cervantes-Alvarez E, Wang Y, Collin de l'Hortet A, Guzman-Lepe J, Zhu J, Takeishi K. Current strategies to generate mature human induced pluripotent stem cells derived cholangiocytes and future applications. *Organogenesis*. 2017;13(1):1-15. doi: 10.1080/15476278.2016.1278133

43. Sampaziotis F, Cardoso de Brito M, Madrigal P, et al. Cholangiocytes derived from human induced pluripotent stem cells for disease modeling and drug validation. *Nat Biotechnol*. 2015;33(8):845-852. doi: 10.1038/nbt.3275

44. Ogawa M, Jiang J-X, Xia S, et al. Generation of functional ciliated cholangiocytes from human pluripotent stem cells. *Nat Commun*. 2021;12(1):6504. doi: 10.1038/s41467-021-26764-0

45. Kamm DR, McCommis KS. Hepatic stellate cells in physiology and pathology. *J Physiol*. 2022;600(8): 1825-1837. doi: 10.1113/jp281061

46. Tsuchida T, Friedman SL. Mechanisms of hepatic stellate cell activation. *Nat Rev Gastroenterol Hepatol*. 2017;14(7): 397-411. doi: 10.1038/nrgastro.2017.38

47. Krenkel O, Tacke F. Liver macrophages in tissue homeostasis and disease. *Nat Rev Immunol*. 2017;17(5):306-321. doi: 10.1038/nri.2017.11

48. Pollard JW. Trophic macrophages in development and disease. *Nat Rev Immunol*. 2009;9(4):259-270. doi: 10.1038/nri2528

49. Zong Y, Stanger BZ. Molecular mechanisms of liver and bile duct development. *Wiley Interdiscip Rev Dev Biol*. 2012;1(5):643-655. doi: 10.1002/wdev.47

50. Si-Tayeb K, Lemaigre FP, Duncan SA. Organogenesis and development of the liver. *Dev Cell*. 2010;18(2):175-189. doi: 10.1016/j.devcel.2010.01.011

51. Gordillo M, Evans T, Gouon-Evans V. Orchestrating liver development. *Development*. 2015;142(12):2094-2108. doi: 10.1242/dev.114215

52. Yang L, Li L-C, Lamaoqiezhong, et al. The contributions of mesoderm-derived cells in liver development. *Semin Cell Dev Biol*. 2019;92:63-76. doi: 10.1016/j.semcdb.2018.09.003

53. Liang Y, Kaneko K, Xin B, et al. Temporal analyses of postnatal liver development and maturation by single-cell transcriptomics. *Dev Cell*. 2022;57(3):398-414.e5. doi: 10.1016/j.devcel.2022.01.004

54. Alison M, Islam S, Lim S. Stem cells in liver regeneration, fibrosis and cancer: the good, the bad and the ugly. *J Pathol*. 2009;217(2):282-298. doi: 10.1002/path.2453

55. Miyajima A, Tanaka M, Itoh T. Stem/Progenitor cells in liver development, homeostasis, regeneration, and reprogramming. *Cell Stem Cell*. 2014;14(5):561-574. doi: 10.1016/j.stem.2014.04.010

56. Michalopoulos GK. Liver regeneration. *J Cell Physiol*. 2007;213(2):286-300. doi: 10.1002/jcp.21172

57. Miyaoka Y, Ebato K, Kato H, Arakawa S, Shimizu S, Miyajima A. Hypertrophy and unconventional cell division of hepatocytes underlie liver regeneration. *Curr Biol*. 2012;22(13):1166-1175. doi: 10.1016/j.cub.2012.05.016

58. Devarbhavi H, Asrani SK, Arab JP, Nartey YA, Pose E, Kamath PS. Global burden of liver disease: 2023 update. *J Hepatol*. 2023;79(2):516-537. doi: 10.1016/j.jhep.2023.03.017

59. Bhatia SN, Underhill GH, Zaret KS, Fox IJ. Cell and tissue engineering for liver disease. *Sci Transl Med*. 2014;6(245):245sr2. doi: 10.1126/scitranslmed.3005975

60. Sun Y, Chang J, Liu X, Liu C. Mortality trends of liver diseases in mainland China over three decades: an age-period-cohort analysis. *BMJ Open*. 2019;9(11):e029793. doi: 10.1136/bmjopen-2019-029793

61. Mohiuddin MM, Singh AK, Scobie L, et al. Graft dysfunction in compassionate use of genetically engineered pig-to-human cardiac xenotransplantation: a case report. *Lancet*. 2023;402(10399):397-410. doi: 10.1016/S0140-6736(23)00775-4

62. Mallapaty S, Kozlov M. First pig kidney transplant in a person: what it means for the future. *Nature*. 2024;628(8006):13-14. doi: 10.1038/d41586-024-00879-y

63. Sun Z, Yuan X, Wu J, et al. Hepatocyte transplantation: the progress and the challenges. *Hepatol Commun*. 2023;7(10):e0266. doi: 10.1097/hc9.0000000000000266

64. Struecker B, Raschzok N, Sauer IM. Liver support strategies: cutting-edge technologies. *Nat Rev Gastroenterol Hepatol*. 2014;11(3):166-176. doi: 10.1038/nrgastro.2013.204

65. Millis JM, Losanoff JE. Technology Insight: liver support systems. *Nat Clin Pract Gastroenterol Hepatol*. 2005;2(9): 398-405.

doi: 10.1038/ncpgasthep0254

66. Krisper P, Stauber RE. Technology insight: artificial extracorporeal liver support—how does Prometheus® compare with MARS®? *Nat Clin Pract Nephrol*. 2007;3(5):267-276.
doi: 10.1038/ncpneph0466

67. Strain AJ, Neuberger JM. A bioartificial liver--state of the art. *Science*. 2002;295(5557):1005-1009.
doi: 10.1126/science.1068660

68. Glorioso JM, Mao SA, Rodysill B, et al. Pivotal preclinical trial of the spheroid reservoir bioartificial liver. *J Hepatol*. 2015;63(2):388-398.
doi: 10.1016/j.jhep.2015.03.021

69. Li Y, Wu Q, Wang Y, et al. Novel spheroid reservoir bioartificial liver improves survival of nonhuman primates in a toxin-induced model of acute liver failure. *Theranostics*. 2018;8(20):5562-5574.
doi: 10.7150/thno.26540

70. Thompson J, Jones N, Al-Khafaji A, et al. Extracorporeal cellular therapy (ELAD) in severe alcoholic hepatitis: a multinational, prospective, controlled, randomized trial. *Liver Transpl*. 2018;24(3):380-393.
doi: 10.1002/lt.24986

71. Chen S, Wang J, Ren H, et al. Hepatic spheroids derived from human induced pluripotent stem cells in bio-artificial liver rescue porcine acute liver failure. *Cell Res*. 2020;30(1):95-97.
doi: 10.1038/s41422-019-0261-5

72. Li W-J, Zhu X-J, Yuan T-J, et al. An extracorporeal bioartificial liver embedded with 3D-layered human liver progenitor-like cells relieves acute liver failure in pigs. *Sci Transl Med*. 2020;12(551):eaba5146.
doi: 10.1126/scitranslmed.aba5146

73. Wang Y, Zheng Q, Sun Z, et al. Reversal of liver failure using a bioartificial liver device implanted with clinical-grade human-induced hepatocytes. *Cell Stem Cell*. 2023;30(5):617-631.e8.
doi: 10.1016/j.stem.2023.03.013

74. Shi X-L, Gao Y, Yan Y, et al. Improved survival of porcine acute liver failure by a bioartificial liver device implanted with induced human functional hepatocytes. *Cell Res*. 2016;26(2):206-216.
doi: 10.1038/cr.2016.6

75. Hofer M, Lutolf MP. Engineering organoids. *Nat Rev Mater*. 2021;6(5):402-420.
doi: 10.1038/s41578-021-00279-y

76. Zhao Z, Chen X, Dowbaj AM, et al. Organoids. *Nat Rev Methods Primers*. 2022;2(1):94.
doi: 10.1038/s43586-022-00174-y

77. Rossi G, Manfrin A, Lutolf MP. Progress and potential in organoid research. *Nat Rev Genet*. 2018;19(11):671-687.
doi: 10.1038/s41576-018-0051-9

78. Harrison SP, Baumgarten SF, Verma R, Lunov O, Dejneka A, Sullivan GJ. Liver organoids: recent developments, limitations and potential. *Front Med (Lausanne)*. 2021;8:574047.
doi: 10.3389/fmed.2021.574047

79. Hu H, Gehart H, Artegiani B, et al. Long-term expansion of functional mouse and human hepatocytes as 3D organoids. *Cell*. 2018;175(6):1591-1606.e19.
doi: 10.1016/j.cell.2018.11.013

80. Huch M, Dorrell C, Boj SF, et al. In vitro expansion of single Lgr5+ liver stem cells induced by Wnt-driven regeneration. *Nature*. 2013;494(7436):247-250.
doi: 10.1038/nature11826

81. Huch M, Gehart H, van Boxtel R, et al. Long-term culture of genome-stable bipotent stem cells from adult human liver. *Cell*. 2015;160(1):299-312.
doi: 10.1016/j.cell.2014.11.050

82. Vyas D, Baptista PM, Brovold M, et al. Self-assembled liver organoids recapitulate hepatobiliary organogenesis in vitro. *Hepatology*. 2018;67(2):750-761.
doi: 10.1002/hep.29483

83. Takebe T, Sekine K, Enomura M, et al. Vascularized and functional human liver from an iPSC-derived organ bud transplant. *Nature*. 2013;499(7459):481-484.
doi: 10.1038/nature12271

84. Wu F, Wu D, Ren Y, et al. Generation of hepatobiliary organoids from human induced pluripotent stem cells. *J Hepatol*. 2019;70(6):1145-1158.
doi: 10.1016/j.jhep.2018.12.028

85. Sorrentino G, Rezakhani S, Yildiz E, et al. Mechano-modulatory synthetic niches for liver organoid derivation. *Nat Commun*. 2020;11(1):3416.
doi: 10.1038/s41467-020-17161-0

86. Zhang S, Xu G, Wu J, et al. Microphysiological constructs and systems: biofabrication tactics, biomimetic evaluation approaches, and biomedical applications. *Small Methods*. 2024;8(1):2300685.
doi: 10.1002/smtd.202300685

87. Zhang B, Korolj A, Lai BFL, Radisic M. Advances in organ-on-a-chip engineering. *Nat Rev Mater*. 2018;3(8):257-278.
doi: 10.1038/s41578-018-0034-7

88. Leung CM, de Haan P, Ronaldson-Bouchard K, et al. A guide to the organ-on-a-chip. *Nat Rev Methods Primers*. 2022;2(1):33.
doi: 10.1038/s43586-022-00118-6

89. Ingber DE. Human organs-on-chips for disease modelling, drug development and personalized medicine. *Nat Rev Genet*. 2022;23(8):467-491.
doi: 10.1038/s41576-022-00466-9

90. Low LA, Mummery C, Berridge BR, Austin CP, Tagle DA. Organs-on-chips: into the next decade. *Nat Rev Drug Discov*. 2021;20(5):345-361.
doi: 10.1038/s41573-020-0079-3

91. Bhatia SN, Ingber DE. Microfluidic organs-on-chips. *Nat Biotechnol*. 2014;32(8):760-772. doi: 10.1038/nbt.2989

92. Moradi E, Jalili-Firoozinezhad S, Solati-Hashjin M. Microfluidic organ-on-a-chip models of human liver tissue. *Acta Biomater*. 2020;116:67-83. doi: 10.1016/j.actbio.2020.08.041

93. Rennert K, Steinborn S, Gröger M, et al. A microfluidically perfused three dimensional human liver model. *Biomaterials*. 2015;71:119-131. doi: 10.1016/j.biomaterials.2015.08.043

94. Siwczak F, Cseresnyes Z, Hassan MIA, et al. Human macrophage polarization determines bacterial persistence of Staphylococcus aureus in a liver-on-chip-based infection model. *Biomaterials*. 2022;287:121632. doi: 10.1016/j.biomaterials.2022.121632

95. Jang K-J, Otieno MA, Ronxhi J, et al. Reproducing human and cross-species drug toxicities using a Liver-Chip. *Sci Transl Med*. 2019;11(517):eaax5516. doi: 10.1126/scitranslmed.aax5516

96. Nawroth JC, Petropolis DB, Manatakis DV, et al. Modeling alcohol-associated liver disease in a human Liver-Chip. *Cell Rep*. 2021;36(3):109393. doi: 10.1016/j.celrep.2021.109393

97. Ewart L, Apostolou A, Briggs SA, et al. Performance assessment and economic analysis of a human Liver-Chip for predictive toxicology. *Commun Med*. 2022;2(1):154. doi: 10.1038/s43856-022-00209-1

98. Du K, Li S, Li C, et al. Modeling nonalcoholic fatty liver disease on a liver lobule chip with dual blood supply. *Acta Biomater*. 2021;134:228-239. doi: 10.1016/j.actbio.2021.07.013

99. Hong G, Kim J, Oh H, et al. Production of multiple cell-laden microtissue spheroids with a biomimetic hepatic-lobule-like structure. *Adv Mater*. 2021;33(36):2102624. doi: 10.1002/adma.202102624

100. Vunjak-Novakovic G, Ronaldson-Bouchard K, Radisic M. Organs-on-a-chip models for biological research. *Cell*. 2021;184(18):4597-4611. doi: 10.1016/j.cell.2021.08.005

101. Ehrlich A, Duche D, Ouedraogo G, Nahmias Y. Challenges and opportunities in the design of liver-on-chip microdevices. *Annu Rev Biomed Eng*. 2019;21:219-239. doi: 10.1146/annurev-bioeng-060418-052305

102. Moroni L, Burdick JA, Highley C, et al. Biofabrication strategies for 3D in vitro models and regenerative medicine. *Nat Rev Mater*. 2018;3(5):21-37. doi: 10.1038/s41578-018-0006-y

103. Daly AC, Prendergast ME, Hughes AJ, Burdick JA. Bioprinting for the biologist. *Cell*. 2021;184(1):18-32. doi: 10.1016/j.cell.2020.12.002

104. Morgan FLC, Moroni L, Baker MB. Dynamic bioinks to advance bioprinting. *Adv Healthcare Mater*. 2020;9(15):1901798. doi: 10.1002/adhm.201901798

105. Chimene D, Lennox KK, Kaunas RR, Gaharwar AK. Advanced bioinks for 3D printing: a materials science perspective. *Ann Biomed Eng*. 2016;44(6):2090-2102. doi: 10.1007/s10439-016-1638-y

106. Heinrich MA, Liu W, Jimenez A, et al. 3D bioprinting: from benches to translational applications. *Small*. 2019;15(23):1805510. doi: 10.1002/smll.201805510

107. Malda J, Visser J, Melchels FP, et al. 25th anniversary article: engineering hydrogels for biofabrication. *Adv Mater*. 2013;25(36):5011-5028. doi: 10.1002/adma.201302042

108. Lou J, Mooney DJ. Chemical strategies to engineer hydrogels for cell culture. *Nat Rev Chem*. 2022;6(10):726-744. doi: 10.1038/s41570-022-00420-7

109. Chaudhuri O, Cooper-White J, Janmey PA, Mooney DJ, Shenoy VB. Effects of extracellular matrix viscoelasticity on cellular behaviour. *Nature*. 2020;584(7822):535-546. doi: 10.1038/s41586-020-2612-2

110. Rizwan M, Ling C, Guo C, et al. Viscoelastic notch signaling hydrogel induces liver bile duct organoid growth and morphogenesis. *Adv Healthc Mater*. 2022;11(23):2200880. doi: 10.1002/adhm.202200880

111. Murphy SV, Atala A. 3D bioprinting of tissues and organs. *Nat Biotechnol*. 2014;32(8):773-785. doi: 10.1038/nbt.2958

112. Vasconcelos DP, Águas AP, Barbosa MA, Pelegrín P, Barbosa JN. The inflammasome in host response to biomaterials: bridging inflammation and tissue regeneration. *Acta Biomater*. 2019;83:1-12. doi: 10.1016/j.actbio.2018.09.056

113. Levato R, Jungst T, Scheuring RG, Blunk T, Groll J, Malda J. From shape to function: the next step in bioprinting. *Adv Mater*. 2020;32(12):1906423. doi: 10.1002/adma.201906423

114. Wang Y, Cui C-B, Yamauchi M, et al. Lineage restriction of human hepatic stem cells to mature fates is made efficient by tissue-specific biomatrix scaffolds. *Hepatology*. 2011;53(1):293-305. doi: 10.1002/hep.24012

115. Nichol JW, Koshy ST, Bae H, Hwang CM, Yamanlar S, Khademhosseini A. Cell-laden microengineered gelatin methacrylate hydrogels. *Biomaterials*. 2010;31(21):5536-5544. doi: 10.1016/j.biomaterials.2010.03.064

116. Mouw JK, Ou G, Weaver VM. Extracellular matrix assembly: a multiscale deconstruction. *Nat Rev Mol Cell Biol*. 2014;15(12):771-785.
doi: 10.1038/nrm3902

117. Donderwinkel I, van Hest JCM, Cameron NR. Bio-inks for 3D bioprinting: recent advances and future prospects. *Polymer Chem*. 2017;8(31):4451-4471.
doi: 10.1039/C7PY00826K

118. Lee JW, Choi Y-J, Yong W-J, et al. Development of a 3D cell printed construct considering angiogenesis for liver tissue engineering. *Biofabrication*. 2016;8(1):015007.
doi: 10.1088/1758-5090/8/1/015007

119. Reizabal A, Costa CM, Pérez-Álvarez L, Vilas-Vilela JL, Lanceros-Méndez S. Silk fibroin as sustainable advanced material: material properties and characteristics, processing, and applications. *Adv Funct Mater*. 2023;33(3):2210764.
doi: 10.1002/adfm.202210764

120. Maity C, Das N. Alginate-based smart materials and their application: recent advances and perspectives. *Top Curr Chem (Cham)*. 2021;380(1):3.
doi: 10.1007/s41061-021-00360-8

121. Spearman BS, Agrawal NK, Rubiano A, Simmons CS, Mobini S, Schmidt CE. Tunable methacrylated hyaluronic acid-based hydrogels as scaffolds for soft tissue engineering applications. *J Biomed Mater Res A*. 2020;108(2):279-291.
doi: 10.1002/jbm.a.36814

122. Ma X, Qu X, Zhu W, et al. Deterministically patterned biomimetic human iPSC-derived hepatic model via rapid 3D bioprinting. *Proc Natl Acad Sci U S A*. 2016;113(8):2206-2211.
doi: 10.1073/pnas.1524510113

123. Baier Leach J, Bivens KA, Patrick CW, Jr., Schmidt CE. Photocrosslinked hyaluronic acid hydrogels: natural, biodegradable tissue engineering scaffolds. *Biotechnol Bioeng*. 2003;82(5):578-589.
doi: 10.1002/bit.10605

124. Zarrintaj P, Manouchehri S, Ahmadi Z, et al. Agarose-based biomaterials for tissue engineering. *Carbohydr Polym*. 2018;187:66-84.
doi: 10.1016/j.carbpol.2018.01.060

125. López-Marcial GR, Zeng AY, Osuna C, Dennis J, García JM, O'Connell GD. Agarose-based hydrogels as suitable bioprinting materials for tissue engineering. *ACS Biomater Sci Eng*. 2018;4(10):3610-3616.
doi: 10.1021/acsbiomaterials.8b00903

126. Hasebe Y, Okumura N, Koh T, et al. Formation of rat hepatocyte spheroids on agarose. *Hepatol Res*. 2005;32(2):89-95.
doi: 10.1016/j.hepres.2005.03.012

127. Passaniti A, Kleinman HK, Martin GR. Matrigel: history/background, uses, and future applications. *J Cell Commun Signal*. 2022;16(4):621-626.
doi: 10.1007/s12079-021-00643-1

128. Jiang S, Zhuang Y, Cai M, Wang X, Lin K. Decellularized extracellular matrix: a promising strategy for skin repair and regeneration. *Eng Regenerat*. 2023;4(4):357-374.
doi: 10.1016/j.engreg.2023.05.001

129. Deng B, Ma Y, Huang J, et al. Revitalizing liver function in mice with liver failure through transplantation of 3D-bioprinted liver with expanded primary hepatocytes. *Sci Adv*. 2024;10(23):eado1550.
doi: 10.1126/sciadv.ado1550

130. Lutolf MP, Lauer-Fields JL, Schmoekel HG, et al. Synthetic matrix metalloproteinase-sensitive hydrogels for the conduction of tissue regeneration: engineering cell-invasion characteristics. *Proc Natl Acad Sci U S A*. 2003;100(9):5413-5418.
doi: 10.1073/pnas.0737381100

131. Kolesky DB, Homan KA, Skylar-Scott MA, Lewis JA. Three-dimensional bioprinting of thick vascularized tissues. *Proc Natl Acad Sci U S A*. 2016;113(12):3179-3184.
doi: 10.1073/pnas.1521342113

132. Gu Q, Tomaskovic-Crook E, Wallace GG, Crook JM. 3D bioprinting human induced pluripotent stem cell constructs for in situ cell proliferation and successive multilineage differentiation. *Adv Healthc Mater*. 2017;6(17):1700175.
doi: 10.1002/adhm.201700175

133. Andersson TB, Kanebratt KP, Kenna JG. The HepaRG cell line: a unique in vitro tool for understanding drug metabolism and toxicology in human. *Expert Opin Drug Metab Toxicol*. 2012;8(7):909-920.
doi: 10.1517/17425255.2012.685159

134. Cerec V, Glaise D, Garnier D, et al. Transdifferentiation of hepatocyte-like cells from the human hepatoma HepaRG cell line through bipotent progenitor. *Hepatology*. 2007;45(4):957-967.
doi: 10.1002/hep.21536

135. Gripon P, Rumin S, Urban S, et al. Infection of a human hepatoma cell line by hepatitis B virus. *Proc Natl Acad Sci U S A*. 2002;99(24):15655-15660.
doi: 10.1073/pnas.232137699

136. Higuchi Y, Kawai K, Yamazaki H, et al. The human hepatic cell line HepaRG as a possible cell source for the generation of humanized liver TK-NOG mice. *Xenobiotica*. 2014;44(2):146-153.
doi: 10.3109/00498254.2013.836257

137. Laurent V, Glaise D, Nübel T, Gilot D, Corlu A, Loyer P. Highly efficient SiRNA and gene transfer into hepatocyte-like HepaRG cells and primary human hepatocytes: new means for drug metabolism and toxicity studies. *Methods Mol Biol*. 2013;987:295-314.
doi: 10.1007/978-1-62703-321-3_25

138. Koike H, Iwasawa K, Ouchi R, et al. Engineering human hepato-biliary-pancreatic organoids from pluripotent stem cells. *Nat Protoc*. 2021;16(2):919-936.
doi: 10.1038/s41596-020-00441-w

139. Koike H, Iwasawa K, Ouchi R, et al. Modelling human hepato-biliary-pancreatic organogenesis from the foregut-midgut boundary. *Nature*. 2019;574(7776):112-116. doi: 10.1038/s41586-019-1598-0

140. Hannan NR, Segeritz CP, Touboul T, Vallier L. Production of hepatocyte-like cells from human pluripotent stem cells. *Nat Protoc*. 2013;8(2):430-437. doi: 10.1038/nprot.2012.153

141. Dao Thi VL, Wu X, Belote RL, et al. Stem cell-derived polarized hepatocytes. *Nat Commun*. 2020;11(1):1677. doi: 10.1038/s41467-020-15337-2

142. Lee H, Chae S, Kim JY, et al. Cell-printed 3D liver-on-a-chip possessing a liver microenvironment and biliary system. *Biofabrication*. 2019;11(2):025001. doi: 10.1088/1758-5090/aaf9fa

143. Liu Q, Mille LS, Villalobos C, et al. 3D-bioprinted cholangiocarcinoma-on-a-chip model for evaluating drug responses. *Bio-Design Manuf*. 2023;6(4):373-389. doi: 10.1007/s42242-022-00229-9

144. Hafiz EOA, Bulutoglu B, Mansy SS, et al. Development of liver microtissues with functional biliary ductular network. *Biotechnol Bioeng*. 2021;118(1):17-29. doi: 10.1002/bit.27546

145. Stevens KR, Scull MA, Ramanan V, et al. In situ expansion of engineered human liver tissue in a mouse model of chronic liver disease. *Sci Transl Med*. 2017;9(399):eaah5505. doi: 10.1126/scitranslmed.aah5505

146. Grigoryan B, Paulsen SJ, Corbett DC, et al. Multivascular networks and functional intravascular topologies within biocompatible hydrogels. *Science*. 2019;364(6439): 458-464. doi: 10.1126/science.aav9750

147. Peng X, Janićijević Ž, Lemm S, et al. Impact of viscosity on human hepatoma spheroids in soft core–shell microcapsules. *Adv Healthc Mater*. 2024;13(11):2302609. doi: 10.1002/adhm.202302609

148. Foyt DA, Norman MDA, Yu TTL, Gentleman E. Exploiting advanced hydrogel technologies to address key challenges in regenerative medicine. *Adv Healthc Mater*. 2018;7(8):1700939. doi: 10.1002/adhm.201700939

149. Bishop ES, Mostafa S, Pakvasa M, et al. 3-D bioprinting technologies in tissue engineering and regenerative medicine: current and future trends. *Genes Dis*. 2017;4(4):185-195. doi: 10.1016/j.gendis.2017.10.002

150. Xu C, Zhang M, Huang Y, Ogale A, Fu J, Markwald RR. Study of droplet formation process during drop-on-demand inkjetting of living cell-Laden Bioink. *Langmuir*. 2014;30(30):9130-9138. doi: 10.1021/la501430x

151. Matsusaki M, Sakaue K, Kadowaki K, Akashi M. Three-dimensional human tissue chips fabricated by rapid and automatic inkjet cell printing. *Adv Healthc Mater*. 2013;2(4):534-539. doi: 10.1002/adhm.201200299

152. Jian H, Li X, Dong Q, Tian S, Bai S. In vitro construction of liver organoids with biomimetic lobule structure by a multicellular 3D bioprinting strategy. *Cell Prolif*. 2023;56(5):e13465. doi: 10.1111/cpr.13465

153. Gu Z, Fu J, Lin H, He Y. Development of 3D bioprinting: from printing methods to biomedical applications. *Asian J Pharm Sci*. 2020;15(5):529-557. doi: 10.1016/j.ajps.2019.11.003

154. Dou C, Perez V, Qu J, Tsin A, Xu B, Li J. A State-of-the-Art review of laser-assisted bioprinting and its future research trends. *ChemBioEng Rev*. 2021;8(5):517-534. doi: 10.1002/cben.202000037

155. Zhu W, Qu X, Zhu J, et al. Direct 3D bioprinting of prevascularized tissue constructs with complex microarchitecture. *Biomaterials*. 2017;124:106-115. doi: 10.1016/j.biomaterials.2017.01.042

156. Wang M, Li W, Hao J, et al. Molecularly cleavable bioinks facilitate high-performance digital light processing-based bioprinting of functional volumetric soft tissues. *Nat Commun*. 2022;13(1):3317. doi: 10.1038/s41467-022-31002-2

157. Jing S, Lian L, Hou Y, et al. Advances in volumetric bioprinting. *Biofabrication*. 2024;16(1):012004. doi: 10.1088/1758-5090/ad0978

158. Bernal PN, Bouwmeester M, Madrid-Wolff J, et al. Volumetric bioprinting of organoids and optically tuned hydrogels to build liver-like metabolic biofactories. *Adv Mater*. 2022;34(15):2110054. doi: 10.1002/adma.202110054

159. Miller JS, Stevens KR, Yang MT, et al. Rapid casting of patterned vascular networks for perfusable engineered three-dimensional tissues. *Nat Mater*. 2012;11(9):768-774. doi: 10.1038/nmat3357

160. Liu X, Wang X, Zhang L, et al. 3D liver tissue model with branched vascular networks by multimaterial bioprinting. *Adv Healthc Mater*. 2021;10(23):2101405. doi: 10.1002/adhm.202101405

161. Yang H, Sun L, Pang Y, et al. Three-dimensional bioprinted hepatorganoids prolong survival of mice with liver failure. *Gut*. 2021;70(3):567-574. doi: 10.1136/gutjnl-2019-319960

162. McCormack A, Highley CB, Leslie NR, Melchels FPW. 3D printing in suspension baths: keeping the promises of bioprinting afloat. *Trends Biotechnol*. 2020;38(6):584-593. doi: 10.1016/j.tibtech.2019.12.020

163. Lee A, Hudson AR, Shiwarski DJ, et al. 3D bioprinting of collagen to rebuild components of the human heart. *Science*. 2019;365(6452):482-487. doi: 10.1126/science.aav9051

164. Hinton TJ, Jallerat Q, Palchesko RN, et al. Three-dimensional printing of complex biological structures by freeform reversible embedding of suspended hydrogels. *Sci Adv*. 2015;1(9):e1500758.
doi: 10.1126/sciadv.1500758

165. Fang Y, Ji M, Yang Y, et al. 3D printing of vascularized hepatic tissues with a high cell density and heterogeneous microenvironment. *Biofabrication*. 2023;15(4):045004.
doi: 10.1088/1758-5090/ace5e0

166. Taymour R, Chicaiza-Cabezas NA, Gelinsky M, Lode A. Core–shell bioprinting of vascularized in vitro liver sinusoid models. *Biofabrication*. 2022;14(4):045019.
doi: 10.1088/1758-5090/ac9019

167. Wang H, Liu X, Gu Q, Zheng X. Vascularized organ bioprinting: from strategy to paradigm. *Cell Prolif*. 2023;56(5):e13453.
doi: 10.1111/cpr.13453

168. Kinstlinger IS, Saxton SH, Calderon GA, et al. Generation of model tissues with dendritic vascular networks via sacrificial laser-sintered carbohydrate templates. *Nat Biomed Eng*. 2020;4(9):916-932.
doi: 10.1038/s41551-020-0566-1

169. O'Connor C, Brady E, Zheng Y, Moore E, Stevens KR. Engineering the multiscale complexity of vascular networks. *Nat Rev Mater*. 2022;7(9):702-716.
doi: 10.1038/s41578-022-00447-8

170. Zong Y, Stanger BZ. Molecular mechanisms of bile duct development. *Int J Biochem Cell Biol*. 2011;43(2):257-264.
doi: 10.1016/j.biocel.2010.06.020

171. Raynaud P, Carpentier R, Antoniou A, Lemaigre FP. Biliary differentiation and bile duct morphogenesis in development and disease. *Int J Biochem Cell Biol*. 2011;43(2):245-256.
doi: 10.1016/j.biocel.2009.07.020

172. Justin AW, Saeb-Parsy K, Markaki AE, Vallier L, Sampaziotis F. Advances in the generation of bioengineered bile ducts. *Biochim Biophys Acta Mol Basis Dis*. 2018;1864(4PtB):1532-1538.
doi: 10.1016/j.bbadis.2017.10.034

173. Wang Z, Faria J, Penning LC, Masereeuw R, Spee B. Tissue-engineered bile ducts for disease modeling and therapy. *Tissue Eng Part C Methods*. 2021;27(2):59-76.
doi: 10.1089/ten.TEC.2020.0283

174. Squires RH, Ng V, Romero R, et al. Evaluation of the pediatric patient for liver transplantation. *J Pediatr Gastroenterol Nutr*. 2014;59(1):112-131.
doi: 10.1097/MPG.0000000000000431

175. Brevini T, Tysoe OC, Sampaziotis F. Tissue engineering of the biliary tract and modelling of cholestatic disorders. *J Hepatol*. 2020;73(4):918-932.
doi: 10.1016/j.jhep.2020.05.049

176. Sun Q, Shen Z, Liang X, et al. Progress and current limitations of materials for artificial bile duct engineering. *Materials*. 2021;14(23):7468.
doi: 10.3390/ma14237468

177. Lewis PL, Su J, Yan M, et al. Complex bile duct network formation within liver decellularized extracellular matrix hydrogels. *Sci Rep*. 2018;8(1):12220.
doi: 10.1038/s41598-018-30433-6

178. Sampaziotis F, Muraro D, Tysoe OC, et al. Cholangiocyte organoids can repair bile ducts after transplantation in the human liver. *Science*. 2021;371(6531):839-846.
doi: 10.1126/science.aaz6964

179. Sampaziotis F, Justin AW, Tysoe OC, et al. Reconstruction of the mouse extrahepatic biliary tree using primary human extrahepatic cholangiocyte organoids. *Nat Med*. 2017;23(8):954-963.
doi: 10.1038/nm.4360

180. Roos FJM, van Tienderen GS, Wu H, et al. Human branching cholangiocyte organoids recapitulate functional bile duct formation. *Cell Stem Cell*. 2022;29(5):776-794.e13.
doi: 10.1016/j.stem.2022.04.011

181. Du Y, de Jong IEM, Gupta K, et al. Human vascularized bile duct-on-a chip: a multi-cellular micro-physiological system for studying cholestatic liver disease. *Biofabrication*. 2023;16(1):015004.
doi: 10.1088/1758-5090/ad0261

182. Du Y, Khandekar G, Llewellyn J, Polacheck W, Chen CS, Wells RG. A bile duct-on-a-chip with organ-level functions. *Hepatology*. 2020;71(4):1350-1363.
doi: 10.1002/hep.30918

183. Tanimizu N, Ichinohe N, Sasaki Y, et al. Generation of functional liver organoids on combining hepatocytes and cholangiocytes with hepatobiliary connections ex vivo. *Nature Commun*. 2021;12(1):3390.
doi: 10.1038/s41467-021-23575-1

184. Loterie D, Delrot P, Moser C. High-resolution tomographic volumetric additive manufacturing. *Nat Commun*. 2020;11(1):852.
doi: 10.1038/s41467-020-14630-4

185. Kelly BE, Bhattacharya I, Heidari H, Shusteff M, Spadaccini CM, Taylor HK. Volumetric additive manufacturing via tomographic reconstruction. *Science*. 2019;363(6431):1075-1079.
doi: 10.1126/science.aau7114

186. Bernal PN, Delrot P, Loterie D, et al. Volumetric bioprinting of complex living-tissue constructs within seconds. *Adv Mater*. 2019;31(42):e1904209.
doi: 10.1002/adma.201904209

187. Cai H, Wu Z, Ao Z, et al. Trapping cell spheroids and organoids using digital acoustofluidics. *Biofabrication*. 2020;12(3):035025.
doi: 10.1088/1758-5090/ab9582

188. Johnson K, Melchert D, Gianola DS, Begley M, Ray TR. Recent progress in acoustic field-assisted 3D-printing of functional composite materials. *MRS Adv*. 2021;6(25): 636-643.
doi: 10.1557/s43580-021-00090-5

189. Foresti D, Kroll KT, Amissah R, et al. Acoustophoretic printing. *Sci Adv*. 2018;4(8):eaat1659.
doi: 10.1126/sciadv.aat1659

190. Jentsch S, Nasehi R, Kuckelkorn C, Gundert B, Aveic S, Fischer H. Multiscale 3D bioprinting by nozzle-free acoustic droplet ejection. *Small Methods*. 2021;5(6):2000971.
doi: 10.1002/smtd.202000971

191. Guo Q, Su X, Zhang X, Shao M, Yu H, Li D. A review on acoustic droplet ejection technology and system. *Soft Matter*. 2021;17(11):3010-3021.
doi: 10.1039/D0SM02193H

192. Liu C, Pandit PP, Parsons C, Khan F, Hu Y. Acoustic field-assisted inkjet-based additive manufacturing of carbon fiber-reinforced polydimethylsiloxane composites. *J Manuf Process*. 2022;80:87-94.
doi: 10.1016/j.jmapro.2022.05.059

193. Wadsworth P, Nelson I, Porter DL, Raeymaekers B, Naleway SE. Manufacturing bioinspired flexible materials using ultrasound directed self-assembly and 3D printing. *Mater Design*. 2020;185:108243.
doi: 10.1016/j.matdes.2019.108243

194. Chen K, Jiang E, Wei X, et al. The acoustic droplet printing of functional tumor microenvironments. *Lab Chip*. 2021;21(8):1604-1612.
doi: 10.1039/D1LC00003A

195. Lei Y, Hu H. SAW-driven droplet jetting technology in microfluidic: a review. *Biomicrofluidics*. 2020;14(6): 061505.
doi: 10.1063/5.0014768

196. Kim SH, Seo YB, Yeon YK, et al. 4D-bioprinted silk hydrogels for tissue engineering. *Biomaterials*. 2020;260: 120281.
doi: 10.1016/j.biomaterials.2020.120281

197. Li K, Huang W, Guo H, et al. Advancements in robotic arm-based 3D bioprinting for biomedical applications. *Life Med*. 2023;2(6):lnad046
doi: 10.1093/lifemedi/lnad046

198. An J, Zhang S, Wu J, et al. Assessing bioartificial organ function: the 3P model framework and its validation. *Lab Chip*. 2024;24(6):1586-1601.
doi: 10.1039/D3LC01020A

ACCSCIENCE PUBLISHING

International Journal of Bioprinting

RESEARCH ARTICLE

Experimental and numerical approaches for optimizing conjunction area design to enhance switching efficiency in single-nozzle multi-ink bioprinting systems

Mitsuyuki Hidaka, Masaru Kojima, Colin Zhang, Yasunori Okano, and Shinji Sakai*

Department of Materials Engineering Science, Osaka University, Osaka, Japan

Abstract

Three-dimensional (3D) bioprinting has emerged as a promising technology in the field of tissue engineering. Notably, the advancement of multi-ink printing technology is crucial for further progress in 3D bioprinting. In this study, we developed a single-nozzle system with multiple inlets for multi-ink bioprinting that achieves high switching efficiency through a combination of numerical and experimental approaches. This single-nozzle system demonstrates the potential for higher-resolution printing and quicker ink switching compared with multi-nozzle printing systems. In general, inks used in bioprinting have low viscosity (<10 Pa·s); however, their behaviors inside a single nozzle have not been thoroughly investigated. Initially, we conducted numerical simulations to analyze fluid behavior within single nozzles, focusing on the junction of multiple ink inlets, to propose an advanced nozzle design. We proposed a novel index called switching efficiency (*Se*) for evaluating the switching behavior of the bioink inside the single nozzle. Numerical simulation results showed that the nozzle design and combinations of inks affected *Se*. In addition, subsequent experimental analysis confirmed the consistency of the simulation results. The proposed design, developed using simulations, featured a single nozzle with enhanced switching efficiency, demonstrating a smaller transition length compared with that of conventional single nozzles or T-junction nozzles in printing line structures of different viscous inks. This is the first study to employ numerical simulation in designing a single nozzle with multiple inlets to switch ink in multi-ink bioprinting. This methodology will broaden the potential of single nozzles for high-resolution printing in bioprinting applications.

Keywords: 3D bioprinting; Multi-ink printing; Single-nozzle printing; Numerical simulation

***Corresponding authors:**
Shinji Sakai
(sakai@cheng.es.osaka-u.ac.jp)

Citation: Hidaka M, Kojima M, Zhang C, Okano Y, Sakai S. Experimental and numerical approaches for optimizing conjunction area design to enhance switching efficiency in single-nozzle multi-ink bioprinting systems. *Int J Bioprint*. 2024;10(5):4091. doi: 10.36922/ijb.4091

Received: June 30, 2024
Revised: July 26, 2024
Accepted: August 6, 2024
Published Online: August 8, 2024

Copyright: © 2024 Author(s). This is an Open Access article distributed under the terms of the Creative Commons Attribution License, permitting distribution, and reproduction in any medium, provided the original work is properly cited.

Publisher's Note: AccScience Publishing remains neutral with regard to jurisdictional claims in published maps and institutional affiliations.

1. Introduction

Three-dimensional (3D) printing is a manufacturing technology that automatically assembles materials in 3D patterns. This technology builds materials layer by layer, enabling the construction of complex structures at reduced costs and time.[1,2] The recent trend sees the adoption of 3D printing in tissue engineering, where inks containing cells

and biomaterials (bioinks) are printed using a 3D printer,[3–6] a process known as 3D bioprinting. This method provides 3D structures of cells and biomaterials in specific patterns, presenting a promising approach for constructing artificial tissues or organs.[7,8]

The main bioprinting methods are extrusion-based, vat polymerization-based, and material jetting-based bioprinting.[6,9,10] In particular, extrusion-based bioprinting is widely investigated for its simplicity and ability to accommodate various bioinks that maintain high cell viability.[4] However, despite its advances, challenges remain in building large, complex structures with high fidelity due to limited resolution and printing speed.[8,11,12] For instance, printing an organ-scale structure might take 2–10 h, potentially decreasing cell viability in the bioink.[13] Additionally, current 3D bioprinting technology produces simple structures using a single bioink with limited functionality.[14] Therefore, a multi-ink printing technique capable of constructing large-scale structures using multiple bioinks with high resolution and rapid printing speed is essential. Considerable research has been directed toward these challenges[11,15]; nonetheless, further exploration is necessary.

Generally, a multi-nozzle printing system, where multiple inks are extruded from separate nozzles, is employed for multi-ink printing.[16,17] While this system allows for the fabrication of complex 3D structures composed of multiple inks by increasing the number of nozzles, switching inks can be time-consuming due to the need to calibrate each nozzle separately. For example, Brunel et al. reported 3D printing a structure that mimicked the human heart with cardiomyocytes and endothelial cells using a multi-nozzle printing system and a support bath.[18] This 3D-printed structure had a high resemblance to the actual human heart, but it had a volume of less than 1 cm^3. To scale up this construct, the process of changing materials should be improved. Moreover, the complexity of the 3D printer increases with the number of nozzles in multi-nozzle systems.[19] Thus, multi-ink printing technology is required, which can rapidly switch inks with high resolution and speed in extrusion-based bioprinting.

In contrast to multi-nozzle systems, single-nozzle systems, which extrude multiple inks from a single nozzle, offer rapid switching capabilities.[20] Skylar-Scott et al. achieved high-resolution printing of silicon ink using a single nozzle that can switch materials within 1 s at a resolution of 0.5 mm,[21] enabling the printing of complex and large (>50 cm^3) structures. Similarly, Cameron et al. reported the use of a single nozzle for printing with starch ink at a resolution of 5 mm.[22] These systems would be desirable for achieving high speed and resolution in multi-material bioprinting. However, the reported single-nozzle systems used only high-viscosity inks (100–10,000 Pa·s).[20,23]

Most bioinks are of low viscosity (<10 Pa·s)[24–26] because high viscosity can damage the cells in the bioink due to the shear stress during extrusion.[27] The viscosity is crucial at the interface of multiple liquids, and the sharpness of the switching phenomenon within a single nozzle is likely to decrease as ink viscosity decreases.[28] The behavior of low-viscosity bioink inside a single nozzle has not been thoroughly investigated. Therefore, understanding this behavior is necessary for developing a single-nozzle printing system that can efficiently handle multiple types of bioinks.

In this study, we utilized numerical simulations to understand the behavior of bioink inside a single nozzle and propose a design capable of switching multiple inks with high resolution. Numerical simulation, a tool for analyzing fluid behaviors in the bioengineering field,[29–31] is employed to facilitate the development of a novel single nozzle that can efficiently switch between bioinks of different viscosities, at lower cost and in shorter time than that of experimental approaches. A dual-inlet system, which is a single-nozzle printing system, was considered for the analysis as a simple example. We introduced a new physical quantity called switching efficiency (*Se*) to analyze bioink behavior and examined the effects of the nozzle's conjunction area design and bioink viscosity on the efficiency of bioink switching. Sodium alginate (SA) aqueous solutions, known for their biocompatibility, shear-thinning properties, and mechanical properties, were utilized as model bioinks.[24,32,33] Our findings suggest that switching efficiency depends on both the design of the conjunction area and the viscosity of the bioink. In particular, viscosity greatly affected *Se*, indicating the need for a single design to switch different viscous bioinks. Based on these results, we proposed nozzles capable of switching between bioinks of different viscosities with high efficiency, and line structures of different viscous SA inks were printed using the nozzles to evaluate their performance. To the best of our knowledge, this is the first reported study using both numerical and experimental approaches to enhance the single nozzle in multi-ink bioprinting.[34–36]

2. Materials and methods

2.1. Materials

Tyramine hydrochloride and water-soluble carbodiimide (WSCD) were sourced from Combi-Blocks (CA, USA) and Peptide Institute (Osaka, Japan), respectively. N-Hydroxysuccinimide (NHS) and sodium persulfate (SPS) were purchased from Fujifilm Wako Pure Chemical Industries (Osaka, Japan). $Ru(bpy)_3 \cdot Cl_2 \cdot 6H_2O$ was procured from Sigma-Aldrich (St. Louis, MO, USA).

SA (I-3, molecular weight: 24 kDa) was obtained from KIMIKA (Tokyo, Japan). The phenol derivative of SA (SA-Ph) was synthesized according to the methods described in previous studies,[37,38] with the phenol groups introduced to SA at a concentration of 1.8×10^{-4} mol/g-SA.

2.2. Definition of switching efficiency

Switching efficiency (*Se*) is the metric used to evaluate the liquid behavior inside a single nozzle. Considering a liquid flowing at v (cm^3/s) into the conjunction area where two inlets join with a volume of V (cm^3) (Figure 1A), the ideal switching time (t_i) is defined as follows:

$$t_i = \frac{V}{v}. \tag{I}$$

Se is defined as

$$Se = \frac{t_i}{t_m}, \tag{II}$$

where t_m is the switching time measured through numerical simulation and experimentation. *Se* is the ratio between t_m and t_i. Ideally, efficient switching occurs at *Se* = 1, while inefficient switching occurs at almost zero (Figure 1B).

2.3. Numerical simulations

2.3.1. Governing equations for the flow inside the single nozzles

The fluid behavior inside a single nozzle was analyzed using the numerical simulation software OpenFOAM (ver 8). This analysis involved solving the continuity equations and Navier–Stokes equations, which describe the motion and interaction of incompressible fluids within the nozzle. The flow was assumed to be laminar and incompressible. These equations are expressed as follows:

$$\nabla \cdot \boldsymbol{v}_{\mathrm{f}} = 0, \tag{III}$$

$$\frac{\partial}{\partial t}\rho_{\mathrm{f}}\boldsymbol{v}_{\mathrm{f}} + \nabla \cdot \left(\rho_{\mathrm{f}}\boldsymbol{v}_{\mathrm{f}}\boldsymbol{v}_{\mathrm{f}}\right) = -\nabla p + \nabla^2 \mu_{\mathrm{f}}\boldsymbol{v}_{\mathrm{f}} + \rho_{\mathrm{f}}\boldsymbol{g} + \sigma k \boldsymbol{n}_s \delta, \tag{IV}$$

where $\boldsymbol{v}_{\mathrm{f}}$, $\boldsymbol{\rho}_{\mathrm{f}}$, and μ_{f} are the velocity, density, and viscosity of the fluid, $\boldsymbol{p}$ is the static pressure, $\boldsymbol{g}$ is acceleration gravity, σ is the surface tension, κ is the curvature of the fluid interface, $\boldsymbol{n}_{\mathrm{s}}$ is the normal vector of the interface, and δ is the delta function.

The volume of fluid (VOF) method was employed to analyze the liquid–liquid interface, while the continuum surface force (CSF) model was used to examine the surface tension between the liquids. The governing equations are as follows:

$$\frac{\partial \alpha}{\partial t} + \nabla \cdot \left(\alpha \boldsymbol{v}\right) + \nabla \cdot \left(\left(1-\alpha\right)\alpha \boldsymbol{v}_{\mathrm{r}}\right) = 0, \tag{V}$$

$$\boldsymbol{v} = \alpha \boldsymbol{v}_{in1} + \left(1-\alpha\right)\boldsymbol{v}_{in2}, \tag{VI}$$

$$\boldsymbol{v}_{\mathrm{r}} = \boldsymbol{v}_{\mathrm{in1}} - \boldsymbol{v}_{\mathrm{in2}}, \tag{VII}$$

where ∇ is the directional derivative; α is the ratio of one fluid in a single nozzle; v_{in1} and v_{in2} are the inlet velocity from Inlets 1 and 2, respectively; and v_r is the relative velocity.

The physical property of the interface is calculated from α as follows:

$$\rho = \alpha\rho_{\mathrm{in1}} + \left(1-\alpha\right)\rho_{\mathrm{in2}}, \tag{VIII}$$

$$\mu = \alpha\mu_{\mathrm{in1}} + \left(1-\alpha\right)\mu_{\mathrm{in2}}, \tag{IX}$$

where α is the ratio of one fluid filled in a single nozzle.

ρ_{in1} and ρ_{in2} are the densities of the fluids from Inlets 1 and 2, respectively; and μ_{in1} and μ_{in1} are the viscosities of the fluid from Inlets 1 and 2, respectively. The analysis utilized the viscosity data of the SA solution, which behaves as a shear-thinning fluid.[39,40] The behavior is described by the power law model as follows:

$$\mu = K\dot{\gamma}^{n-1} \tag{X}$$

where μ is the viscosity of the fluid, K is the consistency index, $\dot{\gamma}$ is the shear rate, and n is the flow index. K and n were determined by experimentally measuring the viscosities of the inks as follows: the viscosities of SA solutions at concentrations of 0.5, 1.0, and 2.0 wt% were measured over a shear rate range of 0.01–10/s using a rheometer (HAAKE MARS III, Thermo Fisher Scientific, MA, USA) equipped with a parallel plate geometry at a temperature of 25°C (Figure S1, Supporting Information).

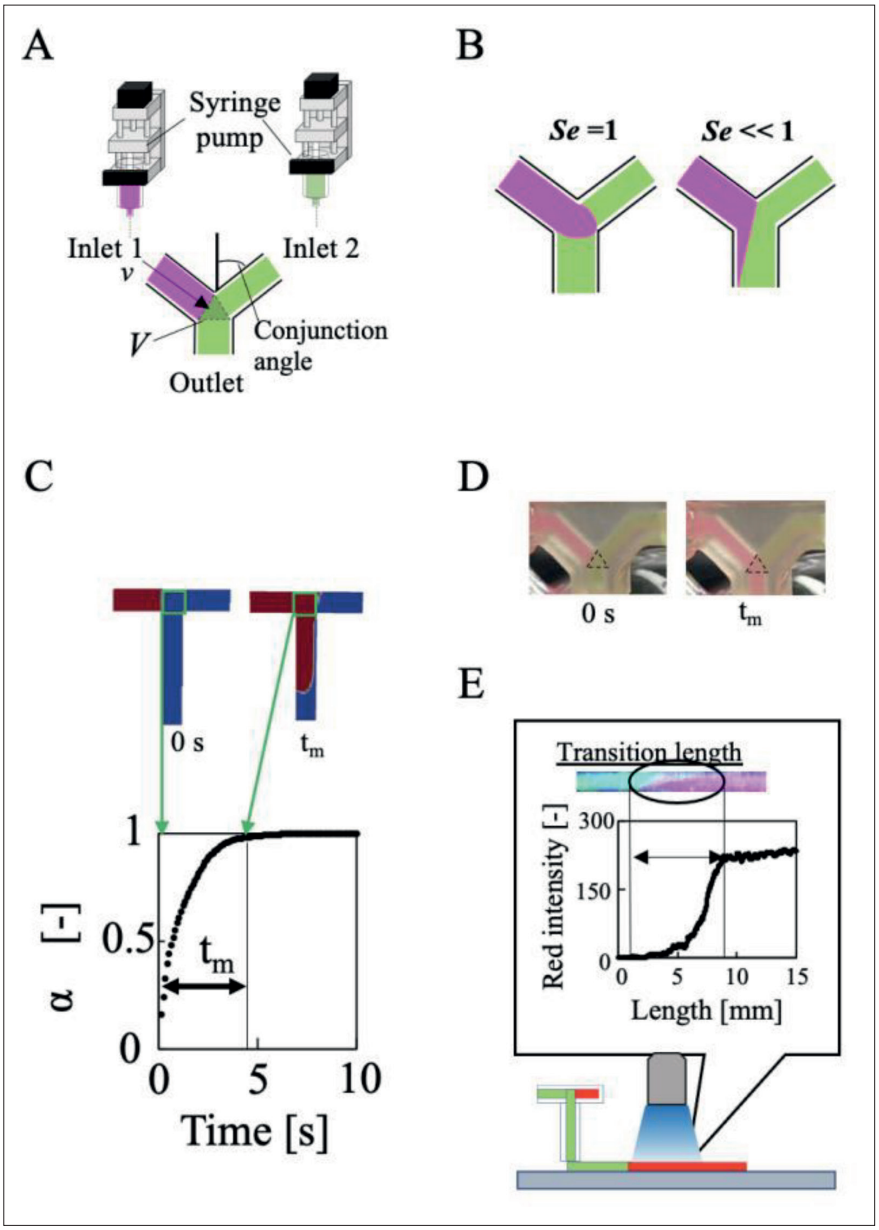


Figure 1. Experimental setup and evaluation method. (A) Schematic of syringe pumps and a single nozzle setup. v is the flow rate (cm³/s) and V (cm³) is the volume of the connection area. (B) Diagram of switching efficiency (*Se*). High switching efficiency is represented as *Se* = 1, while low switching efficiency is denoted as *Se* << 1. (C) Numerical determination of transition time (t_m). (D) Experimental determination of t_m. (E) Determination of the transition length using multi-material printing.

The gap size for the measurements was set at 1.0 mm. Non-linear regression was employed to derive the values of K and n using Excel (ver 16.79, Microsoft, Redmond, WA, USA). Table 1 lists the viscosity data for the SA solutions.

2.3.2. Mesh preparation

The models of the single nozzles employed in the experiment were prepared for numerical simulation as follows: Each model, with a diameter of 1.5 mm, inlet lengths of 4.0 mm, and an outlet length of 8.0 mm, was designed using CAD software (Fusion360, Autodesk, *San Francisco,* USA) and imported into the mesh software Xsim (Ver. 0.15.20220403.0000). The number of elements was established at 30,000 based on the results of a mesh convergence test (Figure S2, Supporting Information). The boundary and initial conditions were set as follows: the channel walls were designated as non-slip, Inlet 1 maintained a constant flow rate, Inlet 2 was set to constant

Table 1. Viscosity characterization of sodium alginate solutions.

Concentration (wt%)	K (Pa·s^n)	n (-)
0.5	2.54×10^{-2}	0.25
1.0	0.169	0.64
2.0	0.589	0.76

pressure, and the outlet pressure was atmospheric. After configuring these settings, a case file was generated for OpenFOAM. InterFoam, a solver for multi-phase flow within OpenFOAM, was employed for the subsequent calculations.

2.3.3. Evaluation method in numerical simulation

In the numerical simulation, the ink (with viscosity shown in **Table 1**) flowed from Inlet 1 at a rate of 2.71×10^{-2} cm^3/s. The parameter α, as outlined in **Equation (IX)**, was analyzed in the conjunction area of the nozzle using the numerical simulation. The t_m in the numerical simulation was defined as the moment when α reached 99%, as illustrated in Figure 1C.

2.3.4. Effect of conjunction angle on switching efficiency in numerical simulation

The effect of the conjunction angle on *Se* was assessed through numerical simulations. 3D models of single nozzles with conjunction angles of 15°, 45°, 75°, and 90° were prepared. The conjunction angle was defined as the angle presented in Figure 1A. A 1.0 wt% SA solution flowed into the conjunction area of each nozzle, and t_m was measured. Subsequently, *Se* was calculated using **Equation (II)**.

2.3.5. Effect of viscosity on switching efficiency in numerical simulation

The effect of viscosity on *Se* and the influence of conjunction angles were evaluated via numerical simulations using single nozzles with angles of 15°, 45°, 75°, and 90°. Four combinations of different viscous SA solutions were tested as follows:

1. A 0.5 wt% SA solution flowed against a 1.0 wt% SA solution already present in the conjunction area.
2. A 1.0 wt% SA solution flowed against a 0.5 wt% SA solution filled in the conjunction area.
3. A 0.5 wt% SA solution flowed against a 2.0 wt% SA solution filled in the conjunction area.
4. A 2.0 wt% SA solution flowed against a 0.5 wt% SA solution filled in the conjunction area.

2.3.6. Novel design proposal of a single nozzle in numerical simulation

A single nozzle with high switching efficiency was proposed based on numerical simulations. Initially, models of single nozzles with asymmetric shapes were prepared. A 1.0 wt% SA solution was used on both sides of the conjunction area to investigate which flow direction exhibited enhanced switching efficiency. Based on these results, novel nozzle designs were developed. Subsequently, 0.5 and 1.0 wt% SA solutions flowed through these new nozzle designs to evaluate *Se*.

2.4. Experimental procedures

2.4.1. Single nozzle preparation

The nozzles, each with a diameter of 1.5 mm, were fabricated using a vat polymerization-based 3D printer (NOVA 3D Elfin 2, Shenzhen Nova Intelligent Technology Co., Shenzhen, China). These nozzles were constructed from photocurable clear plastic resin (NOVA3D High Transparency UV Resin, Shenzhen Nova Intelligent Technology Co., Shenzhen, China).

2.4.2. Setup of printing system

A 3D printing system (FLSUN-QQ-S, Zhengzhou Chaokuo Electronic Technology Co., Henan, China) equipped with a light source (λ = 450 nm) was used to print 3D hydrogel structures.[41] A single nozzle, fabricated as previously described, was attached to this 3D printing system. In this setup, SA-Ph ink containing 2.0 mM SPS and 1.0 mM $Ru(bpy)_3$ was gelated through exposure to visible light (λ = 450 nm). 3D structures consisting of several types of bioinks, including SA-Ph, the phenol derivative of hyaluronic acid and chitosan (hyaluronic acid-Ph and chitosan-Ph, respectively), can be printed using the system (Figure S3, Supporting Information).

2.4.3. Effect of conjunction angle on switching efficiency in experiment

The effect of the conjunction angle on *Se* was experimentally analyzed to compare the experimental findings with results from numerical simulations. Four types of nozzles with angles of 15°, 45°, 75°, and 90° were prepared. Each bioink was sequentially extruded at a rate of 2.71×10^{-2} cm^3/s using a syringe pump, and the switching behavior was monitored using a video camera. t_m was measured by analyzing the video data, where t_m is the time taken for one ink to completely fill the conjunction area, as shown in Figure 1D. *Se* was calculated for each nozzle using **Equation (II)**.

2.4.4. Effect of viscosity on switching efficiency in experiment

For the analysis, 0.5, 1.0, and 2.0 wt% SA solutions, each dyed either green or pink, were utilized. SA solutions

ranging from 0.5 to 2.0 wt% concentration flowed from Inlet 1 into the conjunction area, which was already filled with SA solution within the same concentration range. The *Se* was evaluated using the method previously described.

2.4.5. Evaluation of the Se of the nozzle developed via numerical simulation

Based on the results from **Section 2.2.6.**, the same nozzle designs were replicated, and their *Se* was measured using the method previously described to verify the consistency of the numerical simulations. SA solutions with different viscosities (0.5 and 1.0 wt%) flowed into the conjunction area of these nozzles, and the *Se* for each was calculated. These results were compared with the *Se* obtained from the T-junction nozzle to assess performance differences.

2.4.6. Multi-ink printing of hydrogel structure with different viscous inks

Line structures utilizing two types of SA-Ph inks were printed using the nozzle designed through numerical simulation. The two inlets of the nozzle were connected to syringe cartridges containing SA-Ph inks dyed pink and green. SA-Ph ink with pink dye was first extruded from Inlet 1 at a rate of 2.71×10^{-2} cm^3/s, forming a line structure through the nozzle. After stopping the flow from Inlet 1, SA-Ph ink with green dye from Inlet 2 was similarly extruded at 2.71×10^{-2} cm^3/s. The extruded inks underwent gelation upon exposure to visible light ($\lambda = 450$ nm).

Subsequently, line structures featuring alternating colors were printed, and images of the transition zone between the green and pink inks were captured. These images were analyzed using the image processing software ImageJ (version 1.53a). The red color intensity along the printed line was plotted against its length.[22] The transition length is the segment where the red intensity rapidly changes, as illustrated in Figure 1E.

2.5. Statistical analysis

Data is presented as the mean ± standard deviation. Statistical analysis was performed using analysis of variance (ANOVA) followed by Tukey's post-hoc comparison to assess differences between groups. Statistical significance was set at $p < 0.05$. All analyses were conducted using Excel (ver16.79, Microsoft, WA, USA).

3. Results and discussion

3.1. Effect of conjunction angle on switching efficiency

First, we hypothesized that the conjunction angle of the single nozzle would be a crucial factor in the switching behavior of bioink. The effect of the conjunction angle on *Se* was investigated through numerical simulations (Figure 2A). The conjunction angle significantly impacted the switching phenomenon. The *Se* for the acute-angle nozzles (15°, 45°) was higher than that for the obtuse-angle nozzle (75°) (Figure 2C, depicted in white bars). Furthermore, the *Se* of the T-junction nozzle (90°) was higher than that of the obtuse-angle nozzle. The highest switching efficiency recorded was 0.28 at a 15° conjunction angle, while the lowest was 0.02 at 75°. In obtuse-angle nozzles, the fluid was proposed to flow along the outlet wall, taking a longer time to fill the conjunction area, thereby resulting in a lower *Se*.

The same analysis was conducted experimentally with nozzles of different conjunction angles (Figure 2B). The experimental results corresponded well with the simulation results (Figure 2C, shown by black bars). The *Se* of the obtuse-angle nozzle (75°) was 0.03 ± 0.00, while the *Se* of acute-angle nozzles (15°, 45°) and the T-junction nozzle (90°) were 0.25 ± 0.02, 0.10 ± 0.02, and 0.21 ± 0.04, respectively, all higher than that of the obtuse-angle nozzle. The discrepancies between the simulation and experimental results were likely arise from the fluid model used. In the simulation, the power law model was employed to describe fluid behavior due to its simplicity. This model has been widely used for modeling SA solutions.[42,43] Although the model is sufficient for SA solutions, the Herschel–Bulkley model can provide higher accuracy in reproducing liquid behaviors when applied to various types of liquids, including Bingham and Newtonian fluids.[44,45] This study demonstrated that numerical simulation can effectively reveal the effect of the shape of the conjunction area in a single nozzle on switching behavior using *Se*.

3.2. Effect of viscosity on switching efficiency

We also hypothesized that viscosity would affect the switching behavior. The effect of the viscosity of the SA solution on switching efficiency within the nozzle was investigated. The combinations of inks are depicted in Figure 3A. The results showed that viscosity is an important factor in switching. In numerical simulations (Figure 3B, shown by white bars), the *Se* was lower when a low-viscosity ink (0.5 wt%) flowed against a high-viscosity ink (1.0 wt%) compared with when a high-viscosity ink flowed against a low-viscosity ink (Figure 3C, shown in I and II). Notably, the ink did not switch even after 20 s when a 0.5 wt% SA solution flowed against a 2.0 wt% SA solution in the conjunction area (Figure 3B, labeled as N).

The same analysis was conducted experimentally (Figure 3B, shown by black bars). The *Se* was higher when a high-viscosity ink (1.0 wt%) flowed against a low-viscosity ink (0.5 wt%) than when a low-viscosity ink flowed against a high-viscosity ink. Furthermore, the 0.5 wt% SA solution did not switch against the 2.0 wt% ink within 20 s. The experimental results closely matched

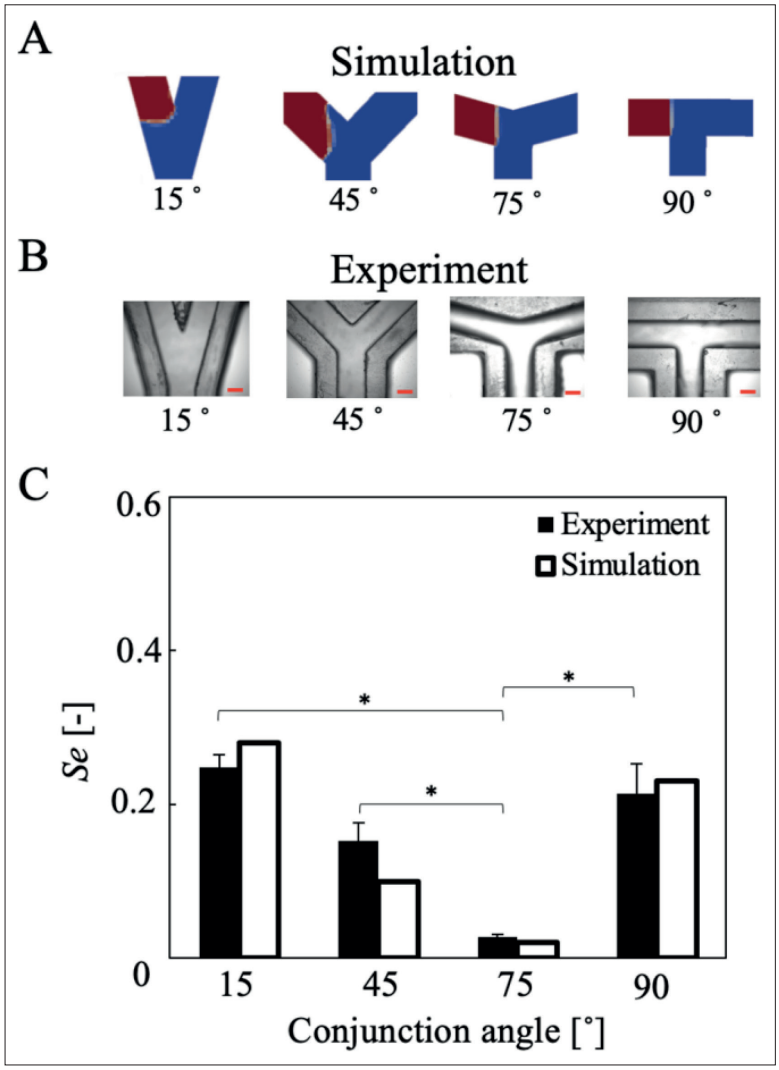


Figure 2. Consistency test of numerical simulation against experiment by testing the switching behavior in different shape of nozzle. (A, B) Single nozzle shapes prepared for simulation (A) and experiment (B); scale bar = 1 mm. (C) Effects of single nozzle's conjunction angle on switching efficiency (*Se*) at 1.0 wt% SA solution in the experiment (black bars) and simulation (white bars). Experimental data were obtained five times for each sample. Data are expressed as mean ± S.D.; * $p < 0.05$.

the simulation results, demonstrating that the effects of viscosity on switching could be effectively analyzed through numerical simulations.

Furthermore, the effect of viscosity was also analyzed in nozzles with different conjunction angles (Figure 2A) using numerical simulations (Figure 3D). The nozzle with a 15° conjunction angle exhibited the highest *Se* for any ink combination, while the nozzle with a 75° conjunction angle had the lowest efficiency for any combination. These results demonstrated that viscosity significantly affects switching efficiency in any nozzle configuration used in this study. Therefore, developing a nozzle that can efficiently switch between different viscous bioinks is necessary for achieving high-resolution multi-ink printing.

3.3. Effect of asymmetrical nozzle shape on switching efficiency

We previously demonstrated that the shape of the conjunction area in a single nozzle influences *Se*. Considering this impact, we hypothesized that flow direction is a critical factor for efficiently switching between different viscous inks. To test this hypothesis, the impact of ink flow direction on *Se* was investigated using five types of asymmetrical nozzles (Figure 4A; labeled I–V). In numerical simulations, 1.0 wt% SA solution was

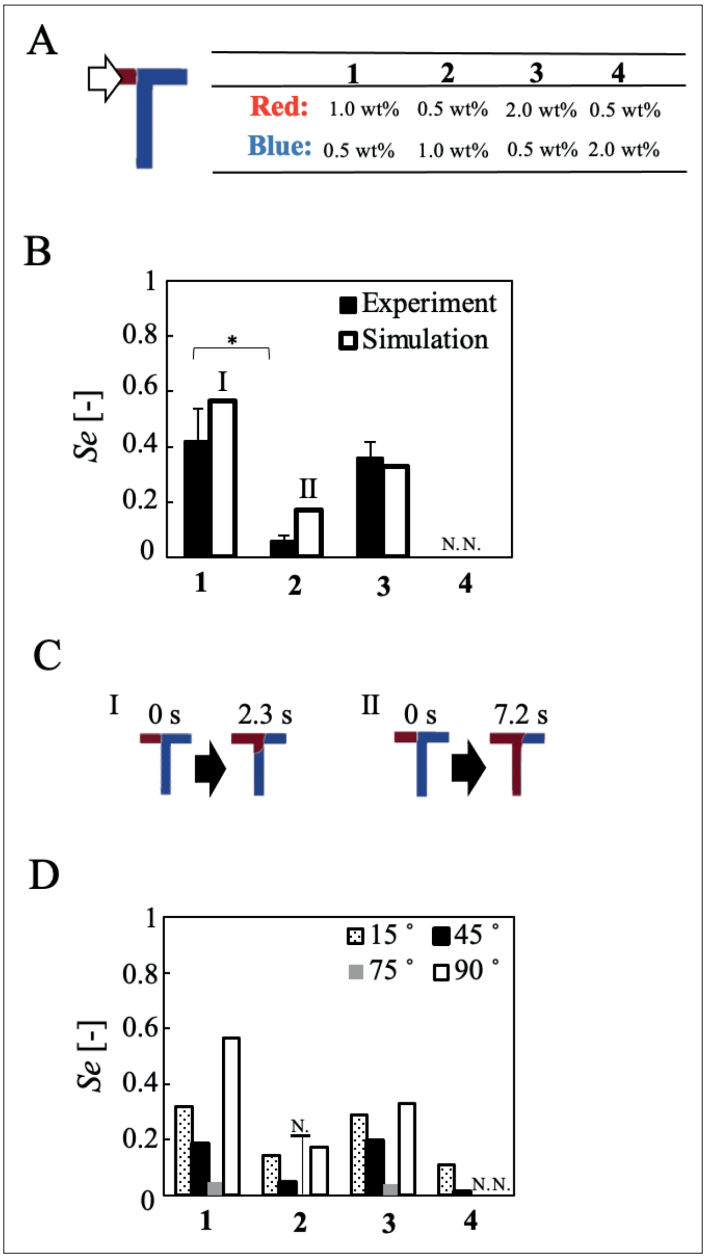


Figure 3. Consistency test of numerical simulation against experiment by testing the switching behavior of different viscous inks. (A) Schematic of the T-junction nozzle showing ink flow and the combination of ink concentrations. Conditions A, B, C, and D, as outlined in the table, are applied to the red and blue areas shown in the schematic, followed by analysis. (B) Effects of viscosity on switching efficiency (*Se*) in the T-junction nozzle (conjunction angle = 90°), depicted in experiments (black bars) and numerical simulations (white bars) under conditions A, B, C, and D. Experimental data were collected five times for each sample. Data are presented as mean ± S.D.; * $p < 0.05$. "N" indicates that switching did not occur within 20 s. (C) Switching behavior observed when a 1.0 wt% SA solution was switched against a 0.5 wt% solution (I) and when a 0.5 wt% SA solution was switched against a 1.0 wt% solution (II). (D) Effects of viscosity on *Se* in numerical simulations conducted on single nozzles with different conjunction angles under conditions A, B, C, and D. "N" denotes that switching did not occur within 20 s.

directed into the conjunction area either horizontally (indicated by a white arrow) or vertically (indicated by a gray arrow). Results indicated that the vertical flow toward the conjunction area achieved higher *Se* than that of the horizontal flow (Figure 4B).

From these findings, we proposed a novel design strategy for single nozzles to optimize switching between inks of different viscosities: lower-viscosity ink should flow vertically toward the conjunction area, while higher-viscosity ink should flow horizontally. This strategy is based

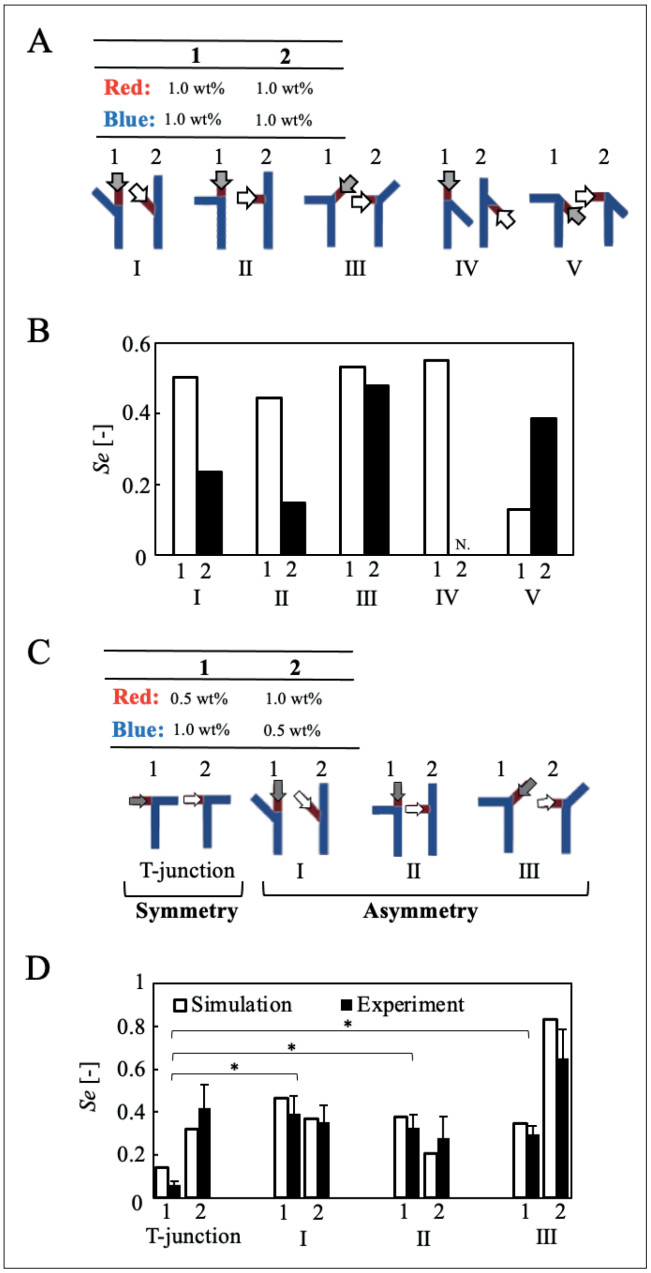


Figure 4. Nozzle design proposal using numerical simulation and its performance test. (A) Schematics of five asymmetrical nozzles prepared for simulation with ink flow and combinations of ink concentrations. Gray and white arrows indicate input flow directions. Conditions 1 and 2 (detailed in the table) are applied to the red and blue areas of the schematic for analysis. (B) Effects of flow direction on *Se* in five asymmetrical single nozzles in numerical simulations under conditions 1 and 2. (C) Schematics of the T-junction and asymmetry nozzles (I–III) prepared for simulation and experiment. Gray and white arrows indicate input flow directions. Conditions A and B (detailed in the table) are applied to the red and blue areas shown in the schematic, followed by analysis. (D) Comparison of switching efficiency (*Se*) between the T-junction nozzle and asymmetrical nozzles (I–III) in numerical simulation (represented by white bars) and experiment (represented by black bars). Experimental data were collected five times for each sample. Data are presented as mean ± S.D.; * $p < 0.05$. "N" indicates that switching did not occur within 20 s.

on the observation of the effects of the conjunction angle and viscosity on switching. We also anticipate that this strategy can counterbalance the influence of flow direction, enabling efficient switching of different viscous inks.

To validate this strategy, three types of asymmetrical nozzles were proposed and fabricated, and their *Se* values were analyzed both numerically and experimentally. In simulations, different viscous inks (0.5 and 1.0 wt%) were

directed through each of the three types of asymmetrical nozzles (Figure 4C; labeled I–III). The *Se* values were compared with those of a symmetrical or T-junction nozzle. The results showed that the asymmetrical nozzles exhibited better *Se* than the T-junction nozzle. Asymmetrical nozzles I, II, and III achieved *Se* values of 0.46, 0.37, and 0.34, respectively, (Figure 4D; labeled I–III, category 1, white bars) when low-viscosity ink flowed against high-viscosity ink, outperforming the T-junction nozzle. Conversely, the *Se* values for the three asymmetrical nozzles were 0.34, 0.20, and 0.83, respectively, when high-viscosity ink flowed against low-viscosity ink (Figure 4D; labeled I–III, category 2, white bars), which were comparable to or higher than those of the T-junction nozzle. These simulation results demonstrated that asymmetrical nozzles could switch inks with higher efficiency than T-junction nozzles.

Experimentally, the *Se* values of asymmetrical nozzles I, II, and III were 0.39 ± 0.08, 0.33 ± 0.06, and 0.30 ± 0.04, respectively (Figure 4D; labeled I–III, category 1, black bars) when low-viscosity ink flowed against high-viscosity ink, again surpassing the performance of the T-junction nozzle. However, when high-viscosity ink flowed against low-viscosity ink, the *Se* values were 0.35 ± 0.081 (nozzle I, statistically comparable to the T-junction nozzle), 0.28 ± 0.10 (nozzle II, no significant difference from the T-junction nozzle), and 0.65 ± 0.14 (nozzle III), showing that performance was comparable to or better than that of the T-junction nozzle (Figure 4D; labeled I–III, category 2, black bars). These experimental results aligned well with the simulation findings, confirming that our strategy to balance the effects of viscosity and flow direction is effective in achieving high-efficiency ink switching.

3.4. Multi-ink printing

Multi-ink printing was tested using the proposed asymmetrical nozzles to switch between inks of different viscosities. High-viscosity ink (1.0 wt% SA) flowed horizontally toward the conjunction area, while low-viscosity ink (0.5 wt% SA) flowed vertically (Figure 5A). The asymmetrical nozzle designed through simulation was fabricated (Figure 5B), and line structures were printed using two different viscous inks. Transition lengths were measured to evaluate the effectiveness of ink switching. For comparison, a standard T-junction channel was used for multi-ink bioprinting. The widths of the transition areas of printed line structures were 1.8–2.1 mm, showing no significant difference (Figure S4A, Supporting Information). Figure S4B, Supporting Information, presents the transition areas of printed line structures. In the T-junction setup, the transition length was 23.2 ± 4.2 mm when 0.5 wt% SA ink flowed against 1.0 wt% SA ink (Figure 5C; T-junction, category 1, black bar), and it was 7.5 ± 1.3 mm when 1.0 wt% SA ink flowed against 0.5 wt% SA ink (Figure 5C; T-junction nozzle, category 1, white bar). Conversely, all proposed asymmetrical nozzles (I–III) demonstrated shorter transition lengths compared with the T-junction nozzle under the same conditions ($p < 0.05$). Specifically, the transition lengths for nozzles I, II, and III were 8.5 ± 2.5, 9.2 ± 2.3, and 6.9 ± 2.6 mm, respectively, when 0.5 wt% SA ink flowed against 1.0 wt% SA ink (Figure 5C; nozzles "I–III, category 1, black bars). When 1.0 wt% SA ink flowed against 0.5 wt% SA ink, the transition lengths were 6.9 ± 2.6, 10.9 ± 4.3, and 7.5 ± 1.3 mm, respectively (no significant difference, Figure 5C; nozzles I–III, category 2, white bars), which were comparable to those observed with the T-junction nozzle. These results indicate that the asymmetrical nozzles facilitated more efficient switching of lower-viscosity ink against higher-viscosity ink with shorter transition lengths. Skylar–Scott et al.[21] created a single-nozzle printing system with high fidelity by utilizing a pressure-controlling system that required experimental adjustments for each ink, which features a complex control system. Considering that most bioinks have low viscosity and their behavior is significantly influenced by pressure, a complex system is necessary to manage such inks in microfluidic channels, such as bioprinting nozzles. Thus, our proposed nozzle, which effectively leverages the offset of effects on viscosity and flow direction, offers a simpler and more efficient solution for controlling the switching of different viscous bioinks.

3.5. Investigation and proposal of nozzle design for further improvement in single-nozzle printing

In this study, we primarily focused on the effects of the nozzle shape and ink viscosities on *Se*. It is worthy to note that switching behavior could also be influenced by a repertoire of factors, which should be considered in further numerical simulation-based investigations with the aim to enhance the resolution of single-nozzle multi-ink bioprinting. For example, when switching 0.5 wt% SA ink against 2.0 wt% SA ink in various nozzles (Figure 6A), the 0.5 wt% ink did not effectively switch against the 2.0 wt% ink in the T-junction, asymmetrical, and cross nozzles, resulting in low *Se* (Figure 6B). The simulations revealed that the liquid remained on one side of the nozzle (Figure 6A, indicated by a red circle), contributing to a low *Se* in both T-junction and asymmetrical nozzles. To address this, a cross nozzle design was proposed, allowing lower-viscosity ink to be extruded from the top of the conjunction area, with a higher-viscosity ink arriving from both sides of the nozzle.

Compared to the T-junction and asymmetrical nozzles, the cross nozzle demonstrated improved switching between 2.0 and 0.5 wt% SA inks (Figure 6B). Moreover, transition lengths were measured in the cross nozzle (Figure 6C) setup, where the transition length was 31.7 ±

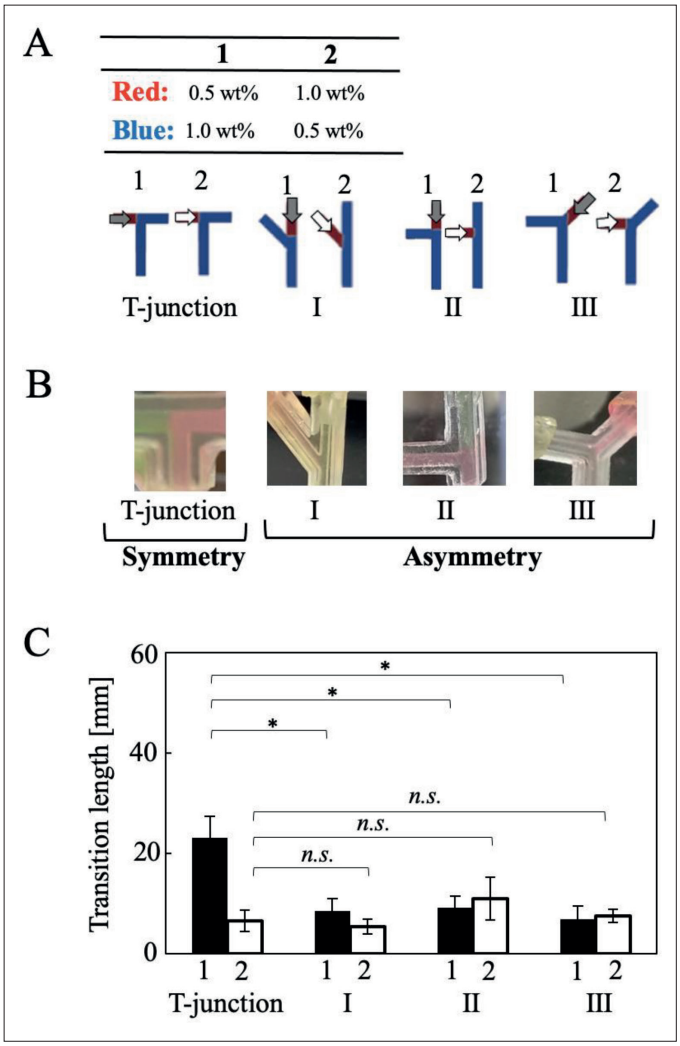


Figure 5. Line structure printing test using the proposed nozzles and their comparisons against T-junction nozzle. (A) Schematics of the T-junction nozzle and asymmetry nozzles (I–III) prepared for both simulation and experiment. (B) T-junction and three asymmetrical nozzles fabricated using vat polymerization printing. (C) Comparison of transition lengths between the T-junction nozzle and asymmetrical nozzles based on printing experiments. Experimental data were collected five times for each sample. Data are presented as mean ± S.D.; * $p < 0.05$.

6.5 mm when 0.5 wt% SA ink switched against 2.0 wt% SA ink, significantly longer than the 6.3 ± 1.8 mm when 2.0 wt% SA ink switched against 0.5 wt% SA ink in the T-junction nozzle (Figure 6D; T-junction, cross, category 2 in each nozzle type). A significant difference was observed between the transition lengths. In addition, the widths of the transition area of the printed line structures were 1.6–2.2 mm, which showed no significant difference (Figure S5A, Supporting Information). The transition areas of the printed line structures are shown in Figure S5B, Supporting Information. Switching low-viscosity ink with high fidelity in the T-junction nozzle proved challenging. Conversely, the transition length was 9.8 ± 4.5 mm when 2.0 wt% SA ink was switched with 0.5 wt% SA ink in the cross nozzle, compared to 15.3 ± 1.7 mm when 2.0 wt% SA ink switched against 0.5 wt% SA ink (Figure 6D; T-junction, cross, category 1 in each nozzle type). Although the transition length using the cross nozzle was longer than that of the T-junction nozzle for the same ink combination, the length was approximately five times shorter when 0.5 wt% SA ink was switched with 2.0 wt% SA ink, accounting for the effects of viscosity and nozzle shape on the switching process. This setup allows for the testing of various ink combinations in numerical simulations for single-nozzle printing.

Further exploration was conducted with 1.0 wt% SA ink against itself in a T-junction nozzle. The simulation showed that switching occurred when the liquid reached the corner of the conjunction area (Figure 7A). We

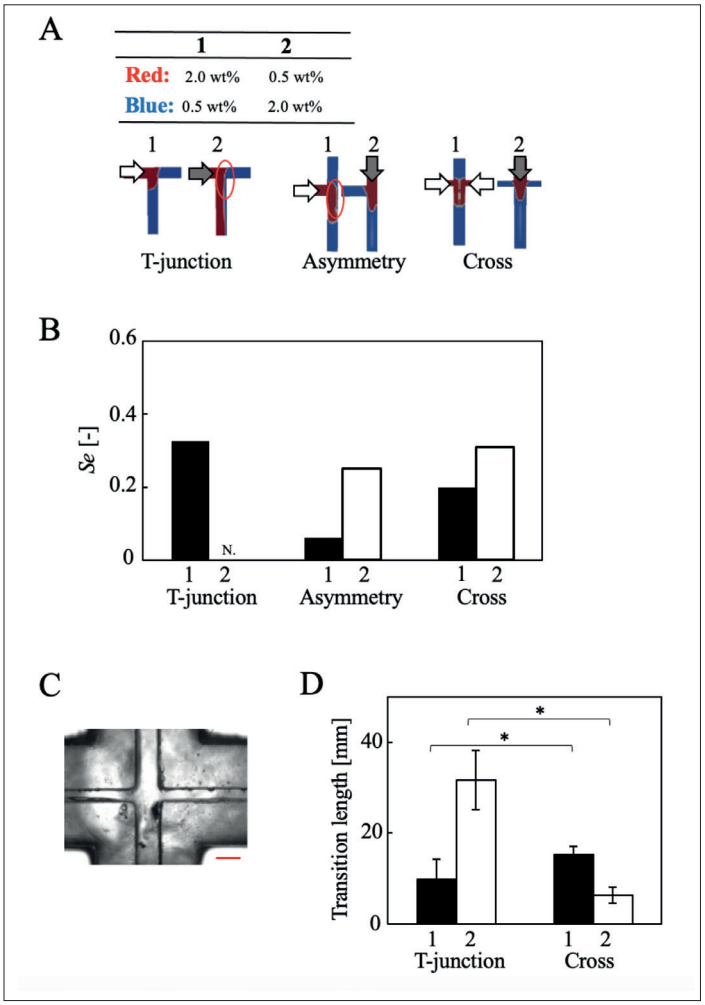


Figure 6. Nozzle proposal for switching 2 and 0.5 wt% SA inks with high efficiency. (A) Schematics of the T-junction nozzle, asymmetrical nozzle, and cross nozzle prepared for simulation and experiment. (B) Switching efficiency (*Se*) of the T-junction, asymmetrical, and cross nozzles. "N" indicates that switching did not occur within 20 s. (C) Cross nozzle fabricated using a vat polymerization-based printer; scale bar = 1 mm. (D) Comparison of the transition length between cross and T-junction nozzles based on printing experiments. Experimental data were obtained five times for each sample. Data are expressed as mean ± S.D.; * $p < 0.05$.

anticipated that the ink switching would occur more rapidly in a nozzle with modified corners. Consequently, the corners of the T-junction nozzle were trimmed, as shown in Figure 7B. This modification facilitated smoother ink switching compared with the standard T-junction nozzle. Furthermore, the transition length in the corner-shaved nozzle was measured and illustrated in Figure 7C. In this configuration, the SA ink transitioned more smoothly than that in a conventional T-junction nozzle, as depicted in Figure 7D. The widths of the transition area of printed line structures were 1.7–2.2 mm, which showed no significant difference, as shown in Figure S6A, Supporting Information. Figure S6B, Supporting Information, shows the transition areas of printed line structures. This methodology allowed us to experiment with various nozzle shapes and ink combinations through numerical simulation, enhancing our understanding and capabilities in nozzle design for bioprinting. Future modifications could include incorporating additional parameters such as diffusion coefficients and other fluid models into the simulations to further refine nozzle designs for multi-ink printing.

4. Limitations and future perspective

We explored proposals for constructing 3D structures with a higher resolution. Our findings demonstrate that utilizing both numerical and experimental approaches is effective for designing a single nozzle for multi-ink printing. However, transition lengths exceeding 5 mm are inadequate for achieving the micro-scale structures

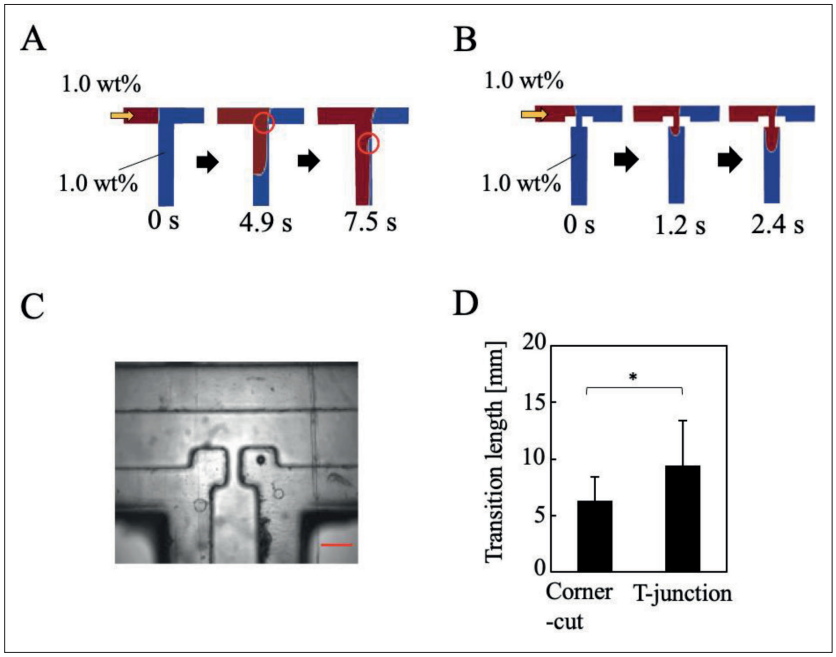


Figure 7. Nozzle proposal for switching SA inks with higher switching efficiency. (A) Typical switching behavior inside a T-junction nozzle in the simulation. (B) Switching behavior of the T-junction nozzle with corners cut in the simulation. (C) Corner-cut nozzle fabricated using a vat polymerization-based printer; scale bar = 1 mm. (D) Comparison of transition length between coner-shaved and T-junction nozzles. Experimental data were obtained five times for each sample. Data are expressed as mean ± S.D.; * $p < 0.05$.

necessary for tissue engineering applications.[11] Therefore, the development of multi-ink printing techniques with a micro-order resolution is essential for further advancement of 3D bioprinting. In addition, it is expected that the surface tension of the liquids considerably affects the switching behavior inside small single nozzles.[46] Thus, we believe that the single nozzle should be designed based on this effect for multi-ink printing with micro-order resolution.

In this study, a commercially available vat-polymerization-based 3D printer was employed to fabricate single nozzles. While this method is economical and rapid, the resolution is restricted to a few hundred micrometers. Alternately, the milling process has been widely utilized to fabricate nozzles[19,20]; however, this method is unsuitable for creating micro-scale structures. Advanced fine processing technologies, such as stereolithography, facilitate the construction of microchannels with dimensions on the order of several dozen micrometers. This advancement can facilitate the creation of nozzles capable of printing multi-ink structures at the micro-scale.[29,47]

Furthermore, precise control over small volumes of bioink is critical in nozzles designed for micro-scale operation. In such systems, minor pressure variations in the nozzle, syringe pumps, and connecting tubes can significantly influence the bioink flow rate, potentially reducing resolution. For instance, silicon tubing may expand under pressure when liquid flows through it, resulting in a decreased flow rate and delay.[20] In our experiments, we utilized plastic syringes, silicon tubes, and acrylic-based single nozzles. Implementing a more rigid structure could enhance the resolution of the single-nozzle printing system.

Moreover, the printing speed is crucial for building large structures. Cells contained in a bioink do not survive without a suitable environment for culturing. Therefore, the 3D printing process should be fast such that the 3D-printed structure can be immediately kept in a cell culture environment after printing. We experimentally investigated the effect of flow rate on switching efficiency, and the result showed that *Se* decreased as the flow rate increased when flowing 0.5 wt% SA solution against 0.5 wt% SA solution in a T-junction nozzle (Figure S7, Supporting Information). In future work, we aim to investigate further design optimization when we consider the fast printing process in single-nozzle bioprinting.

Additionally, incorporating feedback technology could further improve printing resolution. Typical bioprinting systems lack a real-time feedback mechanism during the printing process, solely relying on initial printer settings.[1,14] This reliance can lead to failures or the production of low-resolution structures if any issues arise during printing. Therefore, a feedback system that monitors

printing progress and automatically adjusts parameters could be invaluable for achieving higher resolution in 3D bioprinting. This integrated approach, combining advanced nozzle design, precise bioink control, and feedback systems, represents a significant step forward in producing complex, high-resolution 3D structures suitable for tissue engineering and other advanced applications.[48]

5. Conclusion

Switching efficiency (*Se*) was used to evaluate the influence of the nozzle shape and ink viscosity on liquid behavior within a nozzle, aiming to achieve high switching efficiency in multi-ink printing with a single nozzle. Numerical simulations were conducted to analyze the fluid dynamics inside the nozzle, and these results were then validated against experimental findings. The correlation between the simulation and experimental outcomes highlighted the use of *Se* in assessing the ink behavior within a single nozzle. Our study confirmed that both the nozzle design and ink viscosity are critical factors in efficiently switching between different viscous inks. Based on these findings, innovative single nozzle designs were developed through numerical simulation. Then, these newly designed nozzles were utilized to print line structures with bioinks of varying viscosities. The nozzles designed through this process demonstrated a reduced transition length compared with traditional symmetrical and T-junction nozzles, highlighting their improved performance. To the best of our knowledge, this study is the first to employ numerical simulation to enhance the design of a single nozzle for bioprinting applications. The successful application of *Se* as a metric and the subsequent redesign of the nozzle have potential implications for advancing the field of bioprinting, offering more precise and efficient methods for creating complex tissue structures.

Acknowledgments

None.

Funding

This work was supported by the following sources: JST SPRING (Grant Number JPMJSP2138) and JSPS KAKENHI (Grant Number 24KJ1594).

Conflict of interest

Shinji Sakai serves as the Editorial Board Member of the journal, but did not in any way involve in the editorial and peer-review process conducted for this paper, directly or indirectly. Other authors declare no conflicts of interest.

Author contributions

Conceptualization: Mitsuyuki Hidaka, Shinji Sakai
Formal analysis: Mitsuyuki Hidaka
Investigation: Mitsuyuki Hidaka
Methodology: Mitsuyuki Hidaka
Project administration: Shinji Sakai
Supervision: Shinji Sakai
Visualization: Mitsuyuki Hidaka, Masaru Kojima
Writing–original draft: Mitsuyuki Hidaka
Writing–review & editing: All authors

Ethics approval and consent to participate

Not applicable.

Consent for publication

Not applicable.

Availability of data

Data is available from the corresponding author upon reasonable request.

References

1. Oropallo W, Piegl LA. Ten challenges in 3D printing. *Eng Comput*. 2016;32(1):135-148. doi: 10.1007/s00366-015-0407-0.
2. Sun J, Zhou W, Huang D, Fuh JYH, Hong GS. An overview of 3D printing technologies for food fabrication. *Food Bioproc Tech.* 2015;8(8):1605-1615. doi: 10.1007/s11947-015-1528-6.
3. Duan B. State-of-the-art review of 3D bioprinting for cardiovascular tissue engineering. *Ann Biomed Eng.* 2017;45(1): 195-209. doi: 10.1007/s10439-016-1607-5
4. Ng WL, Chua CK, Shen YF. Print me an organ! Why we are not there yet. *Prog Polym Sci.* 2019;97:101145. doi: 10.1016/j.progpolymsci.2019.101145
5. Singh S, Choudhury D, Yu F, Mironov V, Naing MW. In situ bioprinting – bioprinting from benchside to bedside? *Acta Biomater*. 2020;101:14-25. doi: 10.1016/j.actbio.2019.08.045
6. Vithani K, Goyanes A, Jannin V, Basit AW, Gaisford S, Boyd BJ. An overview of 3D printing technologies for soft materials and potential opportunities for lipid-based drug delivery systems. *Pharm Res*. 2019;36(1):4. doi: 10.1007/s11095-018-2531-1
7. Ramesh S, Harrysson OLA, Rao PK, et al. Extrusion bioprinting: recent progress, challenges, and future opportunities. *Bioprinting.* 2021;21:e00116. doi: 10.1016/j.bprint.2020.e00116

8. Heinrich MA, Liu W, Jimenez A, et al. 3D bioprinting: from benches to translational applications. *Small*. 2019; 15(23):1–47.
doi: 10.1002/smll.201805510

9. Derakhshanfar S, Mbeleck R, Xu K, Zhang X, Zhong W, Xing M. 3D bioprinting for biomedical devices and tissue engineering: a review of recent trends and advances. *Bioact Mater*. 2018;3(2):144-156.
doi: 10.1016/j.bioactmat.2017.11.008

10. Ng WL, Lee JM, Zhou M, et al. Vat polymerization-based bioprinting - process, materials, applications and regulatory challenges. *Biofabrication*. 2020;12(2):022001.
doi: 10.1088/1758-5090/ab6034

11. Miri AK, Mirzaee I, Hassan S, et al. Effective bioprinting resolution in tissue model fabrication. *Lab Chip*. 2019;19(11):2019-2037.
doi: 10.1039/c8lc01037d

12. Hernandez-Quintanar L, Rodriguez-Salvador M. Discovering new 3D bioprinting applications: analyzing the case of optical tissue phantoms. *Int J Bioprint*. 2019; 5(1):1-11.
doi: 10.18063/IJB.v5i1.178

13. Hinton TJ, Lee A, Feinberg AW. 3D bioprinting from the micrometer to millimeter length scales: size does matter. *Curr Opin Biomed Eng*. 2017;1:31-37.
doi: 10.1016/j.cobme.2017.02.004

14. Murphy SV, De Coppi P, Atala A. Opportunities and challenges of translational 3D bioprinting. *Nat Biomed Eng*. 2020;4(4):370-380.
doi: 10.1038/s41551-019-0471-7

15. Santoni S, Gugliandolo SG, Sponchioni M, Moscatelli D, Colosimo BM. 3D bioprinting: current status and trends—a guide to the literature and industrial practice. *Biodes Manuf*. 2021;5:14-42.
doi: 10.1007/s42242-021-00165-0

16. Gu Z, Fu J, Lin H, He Y. Development of 3D bioprinting: from printing methods to biomedical applications. *Asian J Pharm Sci*. 2020;15(5):529-557.
doi: 10.1016/j.ajps.2019.11.003

17. Liu Z, Zhang M, Bhandari B, Wang Y. 3D printing: printing precision and application in food sector. *Trends Food Sci Technol*. 2017;69:83-94.
doi: 10.1016/j.tifs.2017.08.018

18. Brunel LG, Hull SM, Heilshorn SC. Engineered assistive materials for 3D bioprinting: support bath and sacrificial inks. *Biofabrication*. 2022;14:032001.
doi: 10.1088/1758-5900/ac6bbe

19. Sodupe-Ortega E, Sanz-Garcia A, Pernia-Espinoza A, Escobedo-Lucea C. Accurate calibration in multi-material 3D bioprinting for tissue engineering. *Materials*. 2018;11(8):1-19.
doi: 10.3390/ma11081402

20. Hardin JO, Ober TJ, Valentine AD, Lewis JA. Microfluidic printheads for multimaterial 3D printing of viscoelastic inks. *Adv Mater*. 2015;27(21):3279-3284.
doi: 10.1002/adma.201500222

21. Skylar-Scott MA, Mueller J, Visser CW, Lewis JA. Voxelated soft matter via multimaterial multinozzle 3D printing. *Nature*. 2019;575(7782):330-335.
doi: 10.1038/s41586-019-1736-8

22. Cameron T, Naseri E, Maccallum B, Ahmadi A. Development of a disposable single-nozzle printhead for 3D bioprinting of continuous multi-material constructs. *Micromachines (Basel)*. 2020;11(5):459.
doi: 10.3390/mi11050459

23. Zhou LY, Gao Q, Fu JZ, et al. Multimaterial 3D printing of highly stretchable silicone elastomers. *ACS Appl Mater Interfaces*. 2019;11(26):23573-23583.
doi: 10.1021/acsami.9b04873

24. Tai C, Bouissil S, Gantumur E, et al. Use of anionic polysaccharides in the development of 3D bioprinting technology. *Appl Sci*. 2019;9(13):2596.
doi: 10.3390/app9132596

25. Kolesky DB, Homan KA, Skylar-Scott MA, Lewis JA. Three-dimensional bioprinting of thick vascularized tissues. *Proc Natl Acad Sci U S A*. 2016;113(12):3179-3184.
doi: 10.1073/pnas.1521342113

26. Jessop ZM, Al-Sabah A, Gao N, et al. Printability of pulp derived crystal, fibril and blend nanocellulose-alginate bioinks for extrusion 3D bioprinting. *Biofabrication*. 2019;11(4):045006.
doi: 10.1088/1758-5090/ab0631

27. Nair K, Gandhi M, Khalil S, et al. Characterization of cell viability during bioprinting processes. *Biotechnol J*. 2009;4(8):1168-1177.
doi: 10.1002/biot.200900004

28. Nadernezhad A, Khani N, Skvortsov GA, et al. Multifunctional 3D printing of heterogeneous hydrogel structures. *Sci Rep*. 2016;6:33178.
doi: 10.1038/srep33178

29. Yang L, Li S, Liu J, Cheng J. Fluid mixing in droplet-based microfluidics with T junction and convergent–divergent sinusoidal microchannels. *Electrophoresis*. 2018;39(3): 512-520.
doi: 10.1002/elps.201700374

30. Juraeva M, Kang DJ. Mixing performance of a cross-channel split-and-recombine micro-mixer combined with mixing cell. *Micromachines (Basel)*. 2020;11(7):685.
doi: 10.3390/mi11070685

31. Shamloo A, Mirzakhanloo M, Dabirzadeh MR. Numerical simulation for efficient mixing of Newtonian and non-Newtonian fluids in an electro-osmotic micro-mixer. *Chem Eng Process: Process Intensif*. 2016;107:11-20.
doi: 10.1016/j.cep.2016.06.003

32. Xu K, Ganapathy K, Andl T, et al. 3D porous chitosan-alginate scaffold stiffness promotes differential responses in prostate cancer cell lines. *Biomaterials*. 2019;217:119311. doi: 10.1016/j.biomaterials.2019.119311

33. de Melo BAG, Jodat YA, Mehrotra S, et al. 3D printed cartilage-like tissue constructs with spatially controlled mechanical properties. *Adv Funct Mater*. 2019;29(51):1-13. doi: 10.1002/adfm.201906330

34. Trucco D, Sharma A, Manferdini C, et al. Modeling and fabrication of silk fibroin-gelatin-based constructs using extrusion-based three-dimensional bioprinting. *ACS Biomater Sci Eng*. 2021;7(7):3306-3320. doi: 10.1021/acsbiomaterials.1c00410

35. Köpf M, Nasehi R, Kreimendahl F, Jockenhoevel S, Fischer H. Bioprinting-associated shear stress and hydrostatic pressure affect the angiogenic potential of human umbilical vein endothelial cells. *Int J Bioprint*. 2022;8(4):96-107. doi: 10.18063/ijb.v8i4.606

36. Zaeri A, Zgeib R, Cao K, Zhang F, Chang RC. Numerical analysis on the effects of microfluidic-based bioprinting parameters on the microfiber geometrical outcomes. *Sci Rep*. 2022;12(1):3364. doi: 10.1038/s41598-022-07392-0

37. Sakai S, Mochizuki K, Qu Y, Mail M, Nakahata M, Taya M. Peroxidase-catalyzed microextrusion bioprinting of cell-laden hydrogel constructs in vaporized ppm-level hydrogen peroxide. *Biofabrication*. 2018;10(4):045007. doi: 10.1088/1758-5090/aadc9e

38. Sakai S, Ohi H, Taya M. Gelatin/hyaluronic acid content in hydrogels obtained through blue light-induced gelation affects hydrogel properties and adipose stem cell behaviors. *Biomolecules*. 2019;9(8):342. doi: 10.3390/biom9080342

39. Pössl A, Hartzke D, Schmidts TM, Runkel FE, Schlupp P. A targeted rheological bioink development guideline and its systematic correlation with printing behavior. *Biofabrication*. 2021;13(3):035021. doi: 10.1088/1758-5090/abde1e

40. Zheng J, Zeng R, Zhang F, Kan J. Effects of sodium carboxymethyl cellulose on rheological properties and gelation behaviors of sodium alginate induced by calcium ions. *LWT*. 2019;103:131-138. doi: 10.1016/j.lwt.2018.12.081

41. Hidaka M, Kojima M, Nakahata M, Sakai S. Visible light-curable chitosan ink for extrusion-based and vat polymerization-based 3D bioprintings. *Polymers (Basel)*. 2021;13(9):1382. doi: 10.3390/polym13091382

42. Jiong Z, Ruiqi Z, Fusheng Z, Jianquan K. Effects of sodium carboxymethyl cellulose on rheological properties and gelation behaviors of sodium alginate induced by calcium ions. *LWT*. 2019;103:131-138. doi: 10.1016/j.lwt.2018.12.081

43. Minerva AHG, Javier SF, Maribel CM, et al. Protective effect of alginate microcapsules with different rheological behavior on Lactiplantibacillus plantarum 299v. *Gels*. 2023; 9(9):682. doi: 10.3390/gels9090682

44. Emebu S, Ogunleye RO, Achbergerová E, Vítková L, Ponížil P, Martinez CM. Review and proposition for model-based multivariable-multiobjective optimisation of extrusion-based bioprinting. *Appl Mater Today*. 2023;34:101914. doi: 10.1016/j.apmt.2023.101914

45. Elie M, Eric C. Precise method to estimate the Hershel-Bulkley parameters from pipe rheometer measurements. *Fluids*. 2021;6(4):157. doi: 10.3390/fluids6040157

46. Huber T, Pierre G. Extension of the natural element method to surface tension and wettability for the simulation of polymer flows at the micro and nano scales. *J Nonnewton Fluid Mech*. 2013;300:9-16. doi: 10.1016/j.jnnfm.2012.10.003

47. Jalal J, Leong TSH. Microstreaming and its role in applications: a mini-review. *Fluids*. 2018;3(4):93. doi: 10.3390/fluids3040093

48. Wang L, Xu ME, Luo L, Zhou Y, Si P. Iterative feedback bio-printing-derived cell-laden hydrogel scaffolds with optimal geometrical fidelity and cellular controllability. *Sci Rep*. 2018;8(1):2802. doi: 10.1038/s41598-018-21274-4

ACCSCIENCE PUBLISHING

International Journal of Bioprinting

RESEARCH ARTICLE

Manipulating fungal growth in engineered living materials through precise deposition of nutrients

Jia Heng Teoh[1], Eugene Soh[1], and Hortense Le Ferrand[1,2,3,4,*]

[1]School of Mechanical and Aerospace Engineering, Nanyang Technological University, Singapore

[2]School of Materials Science and Engineering, Nanyang Technological University, Singapore

[3]Singapore Center for 3D Printing, Nanyang Technological University, Singapore

[4]Future Cities Laboratory, Singapore ETH Centre, Singapore

Abstract

One main challenge of emerging fungal-based engineered living materials (ELMs) lies in achieving localized multi-material properties in these structures. Although three-dimensional (3D) printing can efficiently vary local composition and properties, it has not yet been demonstrated in fungal-based ELMs. This work thus explores the concept of using nutrients to manipulate fungal foraging behavior in 3D structures fabricated using direct ink writing (DIW) for the next generation of fungal-based ELMs. Using two fungal strains (*Pleurotus ostreatus* and *Ganoderma lucidum*), this study showed that the ink formulation used is suitable for both DIW and mycelium growth. Varying the nutrient content allows for either the inhibition or promotion of exploration and bridging of mycelium in different sections, the control of mycelium density in three dimensions and the fabrication of patterned surfaces. There is potential in fabricating patterned fungal-based ELMs and lab-on-a-chip systems to investigate the effects of other substances and microorganisms on the foraging behavior of mycelium.

Keywords: 3D printing; Direct ink writing; Engineered living material; Mycelium; Hydrogel; Foraging behavior

***Corresponding author:**
Hortense Le Ferrand
(hortense@ntu.edu.sg)

Citation: Teoh JH, Soh E, Le Ferrand H. Manipulating fungal growth in engineered living materials through precise deposition of nutrients. *Int J Bioprint*. 2024;10(5):3939. doi: 10.36922/ijb.3939

Received: June 14, 2024
Revised: July 18, 2024
Accepted: July 27, 2024
Published Online: July 30, 2024

Copyright: © 2024 Author(s). This is an Open Access article distributed under the terms of the Creative Commons Attribution License, permitting distribution, and reproduction in any medium, provided the original work is properly cited.

Publisher's Note: AccScience Publishing remains neutral with regard to jurisdictional claims in published maps and institutional affiliations.

1. Introduction

Engineered living materials (ELMs) are an emerging type of biomaterials that utilizes living cells to give functionalities to an otherwise inanimate material.[1–3] Among other cells, fungal-based ELMs—which incorporate filamentous fungus that form a three-dimensional (3D) net of fungal cells called mycelium—have demonstrated interesting properties leading to potential applications such as self-healing textiles,[4–6] living structures,[7] or robotics.[8] In designing fungal-based ELMs, it is important to ensure that the fungus is growing effectively throughout the structure with the desired mycelium density. Mycelium is known to grow a uniform fungal skin on the exterior of the structure at the material–air interface, whereas the center of the structure is usually devoid of mycelium due to positive aerotropism.[9,10] Being able to control the growth of mycelium in materials is instrumental for tailoring the mechanical properties of the structure, in particular its stiffness.[10] Furthermore, for ELMs to function as living

machines, they may need to also be compartmentalized with various properties and functions within one ELM, calling for material heterogeneity and localized growth of cells. There is therefore a need to be able to control the growth and location of mycelium on materials to enable production of new types of ELMs.

A common method to create localized properties in a material is to use multi-material 3D printing. By using methods including fused deposition modeling (FDM) and direct ink writing (DIW), materials such as plastics and hydrogels can be precisely positioned in a 3D space, allowing for the fabrication of complex structures.[11,12] With multiple nozzles, additional materials and compositions can be incorporated into the same process, allowing for the fabrication of a multi-material structure.[13–15] The utilization of 3D printing in fungal-based ELMs with variations in material, mycelium inoculation techniques, and scale has been gaining traction. For example, direct inoculation involves the addition of mycelium into the ink prior to the fabrication of the structure.[8,16–18] As for indirect inoculation, the structure is first printed before it is placed in direct contact with separately cultured fungi. The fungi then grow toward the structure, eventually enveloping it in the process.[19,20] However, the use of multiple nozzles in fabricating complex, multi-material fungal-based ELMs has yet to be explored. On the contrary, it is generally found that mycelium materials grow a homogeneous fungal skin on their surface that prevents local tailoring of their properties. Exploring ways to create multi-material types of fungal-based ELMs are thus needed.

In nature, organisms have developed various growth, foraging, or translocation strategies to survive in ecosystems that may not provide continuous supply of nutrients.[21] When faced with an environment that is either abundant or lacking in nutrients, filamentous fungi tend to exhibit two main foraging behaviors: phalanx and guerrilla.[22,23] Phalanx, also known as exploitative growth, is characterized by a slow extension rate of hyphae and high mycelium density. Guerrilla, also known as explorative growth, is characterized by a fast extension rate of hyphae, which are the single filaments in the mycelium network, but a low mycelium density. In a low-nutrient environment, guerrilla is the dominant growth pattern whereas guerrilla is usually observed when the fungus is in a high-nutrient environment.[8,22,24,25] Fungi are able to switch between these foraging behaviors depending on the environment they encounter.[26,27] While available nutrients do dictate the type of growth behavior, the degree to which fungi explore or exploit their environment also depends on the species.[22,28,29] In a similar environment, species such as *Coprinus angulatus* and *Psilocybe* cf. *subviscida* may exhibit guerrilla-type behavior in terms of being fast growers and long-range foragers while others such as *Tricholomella constricta* and *Leucopaxillus genetianeus* exhibit phalanx-type behavior as they have the tendency to grow slowly and branch profusely.[22] These species and nutrient-dependent variations in mycelium morphology could therefore be used to tailor the local distribution and morphology of mycelium for future fungal-based ELMs.

In this work, we investigated the growth of mycelium from two fungal species *Ganoderma lucidum* (*G. lucidum*, Lingzhi mushroom) and *Pleurotus ostreatus* (*P. ostreatus*, oyster mushroom) in 3D-printed structures containing local variations of nutrient content. More specifically, mycelium-containing inks were developed with varying concentrations of malt and peptone as growth media. These inks were then precisely locally deposited using DIW. The control and tailoring of the mycelium density, growth behavior over acellular gaps containing different levels of nutrients, and mycelium growth in various directions were demonstrated. Finally, intentionally patterned structures were fabricated as proof-of-concept examples of what this approach can achieve. While fundamental, this work can be leveraged to create more complex types of fungal-based ELMs to manipulate properties such as self-healing capabilities and to explore new applications.

2. Materials and methods

2.1. Materials

The following items were purchased from Sigma Aldrich (USA): malt, peptone, agar, carboxymethyl cellulose (CMC), sodium alginate, calcium chloride, and gentamicin sulfate. *P. ostreatus* spawn bags were obtained from Bewilder (Singapore), whereas *G. lucidum* was acquired from Malaysian Feedmills Farms (Malaysia).

2.2. Mycelium culture

In this study, mycelium was cultured on both solid agar substrates and in liquid cultures. For solid agar substrates, malt agar plates were made by dissolving agar (2.5% w/v), malt (2.0% w/v), and peptone (0.1% w/v) in deionized water. The mixture was then autoclaved (Hiclave HG 80, Hirayama, Japan) at 121°C for 20 min and poured into 90 mm Petri dishes. The mixture was allowed to cool and set before they were inoculated with a solid agar plug of 9 mm diameter containing mycelium from a previously inoculated plate. For liquid mycelium cultures, malt broth was made by dissolving malt (1.7% w/v) and peptone (0.3% w/v) in deionized water and was autoclaved at 121°C for 20 min. After cooling, the broth was supplemented with gentamicin sulfate (50 μg/mL), followed by the addition of a solid agar plug containing mycelium. Liquid mycelium cultures were then left to grow under constant magnetic

stirring for 7–10 days before they were used for subsequent experiments.

2.3. Effect of malt and peptone on mycelium growth

A two-level full factorial design of experiment was adopted to study the effect of malt and peptone on mycelium growth. Malt agar plates were made as described above, except that the malt and peptone concentrations were varied at two different levels, as shown in **Table 1**. The growth of mycelium on each set was monitored over 14 days. Digital images of the agar plates were taken and processed using ImageJ,[30] and the growth rate was quantified by measuring the area of mycelium on each set over 14 days. To determine the dry weight of biomass produced, the mycelium films were peeled from each agar plate after 14 days of culture. They were then dried in an oven at 50°C for 3 days before they were subsequently weighed. Triplicates were analyzed to ensure reproducibility of results.

2.4. Inks preparation for 3D printing

The inks for DIW were made by dissolving alginate (1.2% w/v) and CMC (3.6% w/v) in a solution of malt and peptone at 45°C. The concentration of malt and peptone was adjusted according to Table 1. In addition, another set of inks that would be mixed with liquid mycelium was made using malt (2% w/v) and peptone (0.1% w/v) and were denoted as the medium level of both malt and peptone, respectively. The inks were stirred using a magnetic stirrer until all the alginate and CMC had completely dissolved. Agar (3% w/v) was then added, and the temperature was increased to facilitate the dissolution of agar. The mixture was then autoclaved at 121°C for 20 min, and once removed from the autoclave, it was stirred until it had set. Liquid mycelium was then mixed into the ink at a ratio of 1:5 (v/v) and was stirred until a fine paste was formed. For acellular inks, malt and peptone broths of the corresponding malt and peptone concentrations, respectively, that were devoid of mycelium were added instead at the same volumetric ratio.

2.5. Rheology

The rheological properties of the inks were evaluated using a Bohlin Gemini HR Nano rheometer (Malvern, UK). A 15 mm serrated plate and a measuring gap of 0.5 mm were used. Samples were pre-sheared using a shear rate of 10 s^{-1} for 30 s before being allowed to equilibrate for 60 s. For steady-state viscosity tests, a shear rate range of 0.01–1000 s^{-1} was used. The viscosity as a function of shear rate was then recorded. For amplitude sweep tests, using a frequency of 0.5 Hz, the shear stress was increased from 0.1 to 500 Pa. The storage and loss moduli were recorded. All samples were tested at 25°C. Triplicates of each sample were analyzed.

Table 1. Concentrations of malt and peptone associated with high and low levels, respectively, as used in the two-level full factorial design of experiment

Nutrient component	Concentration (% [w/v])	
	Low level (−1)	High level (+1)
Malt	0.1	5
Peptone	0.01	1

2.6. 3D printing of multi-material constructs

3D-printed constructs were fabricated using DIW with an Allevi 2 bioprinter (3D Systems, USA). The structures were designed using FreeCAD and the gcode files were generated using PrusaSlicer. The inks were loaded into a 10 mL syringe (BD, USA). 22G tapered nozzles (Nordson, USA) were used. Pneumatic pressure ranging from 20 to 30 psi was applied along with a print speed of 20 mm/s. After printing, constructs were sprayed with a solution of deionized water containing calcium chloride (3% w/v) supplemented with gentamicin sulfate (50 μg/mL) to crosslink the alginate. The growth of mycelium on the multi-material constructs was recorded over a period of 10 days. Triplicates of each design were printed and observed.

2.7. Scanning electron microscopy

The microstructure of pure mycelium sheets and fabricated fungal-based ELMs were imaged by means of scanning electron microscopy (SEM; JEOL-5600LV, Japan) on square samples each with a length of roughly 5 mm. Prior to imaging via SEM, all samples were placed in a −20°C fridge overnight and subsequently lyophilized for 24 h. Samples were cut into small pieces and mounted onto the SEM stage using carbon tape. All samples were coated with gold for 75 s at 15 mA, which is equivalent to about 11 nm coating thickness. For the SEM, an acceleration voltage of 10 kV was used. SEM images were processed using ImageJ to measure the surface porosity and hyphae diameter. The surface porosity was calculated by obtaining the average of the percentage of areas occupied by pores in the electron micrograph at three random points of each sample. The hyphae diameter was obtained by measuring the projected width of hyphae at 15 different points in an electron micrograph of the sample.

2.8. Statistical analysis

Statistical analysis was conducted using Microsoft Excel. A two-way analysis of variance (ANOVA) with a significance level of 0.05, followed by a post hoc Tukey's HSD test, was performed for data comparison. Data are presented as mean ± standard deviation.

3. Results and discussion

3.1. Ink formulation and 3D printing strategies for fungal-based ELMs

To enable the 3D printing via DIW of aqueous inks containing fungal cells to create ELMs, it is important to first design an ink system that simultaneously allows the safe growth of the fungi and satisfies the 3D printing requirements. The ink should therefore contain the nutrients necessary for the fungus to grow and develop its mycelium while the ink should also exhibit the rheological properties necessary for their extrusion through the nozzle and their shape retention after 3D printing (Figure 1). *G. lucidum* and *P. ostreatus* were two fungal species selected for this investigation, owing to their extensive use in the fabrication of mycelium-bound composites and fungal-based ELMs,[31] and their availability. Indeed, *G. lucidum* is known for its medicinal properties in traditional Chinese medicine and *P. ostreatus* is a popular mushroom used in various cuisines.

The ink for producing the fungal-based ELMs was formulated to contain agar, alginate, and CMC (Figure 1A). Agar is a polysaccharide known to be suitable for fungal growth.[32] For this ink, it provides necessary stiffness and strength for achieving the desired rheological properties of the ink. As the ink cannot be printed at elevated temperatures owing to the presence of mycelium in the ink during printing,[33,34] the agar was present as solid gel particulates, which tend to form discontinuous filaments when extruded.[17] To remedy this, CMC was added to act as a rheological modifier, allowing for a smooth extrusion of the ink at room temperature (see Supplementary File, Figure S1). Alginate was also supplemented to act as a crosslinking agent that undergoes gelation in the presence of calcium chloride.[35,36] After printing, calcium chloride solution was sprayed onto the construct to fix the printed shape to prevent sagging or deformation until the mycelium fully colonized the structure. Conveniently, the calcium ions from calcium chloride have also been reported in the literature to stimulate mycelium growth,[37] which provides an additional benefit to the process. The moisture from the calcium chloride spray also helped provide a moist environment for mycelium growth and gentamicin was incorporated into the spray to prevent contamination before the mycelium was fully grown. This is especially beneficial when the structure is printed in a non-sterile environment, away from biosafety cabinets, as conducted in this work. The ratio of each component was tailored based on each component's contribution to the rheology of the overall ink. Agar had the greatest contribution to the viscosity and rigidity of the ink, followed by CMC. While alginate was essential as the crosslinking agent, it had the least contribution to the rheology of the ink and its addition also decreased the rigidity of the overall ink (see Figures S2–S4, Supporting Information). Thus, high concentrations of agar and CMC were incorporated to provide the bulk of the viscosity and rigidity of the ink while sufficient alginate was added to enable the structure to be rigid after printing and crosslinking using calcium chloride.

The composite inks exhibited a shear-thinning behavior, which made them suitable for 3D printing via DIW (Figure 1B). The viscosity profile of the ink was also independent of the concentration of malt and peptone incorporated. As such, the printing parameters did not need to be adjusted when modifying the concentration of malt and peptone, which made it convenient for multi-material 3D printing. Furthermore, the inks had solid-like properties as the storage modulus was greater than the loss modulus ($G' > G''$) in the linear viscoelastic region for all inks (Figure 1C). Therefore, the inks did not spontaneously flow under the influence of gravity after the printing process, allowing for buildability and high shape fidelity. Indeed, various well-defined shapes could be printed using the finalized ink compositions (see Figure S5, Supporting Information).

The 3D-printed structures can be inoculated with mycelium either before the printing process (i.e., mycelium spawn or liquid culture is incorporated into the ink before printing)[8,16–18,38] or after printing (i.e., mycelium spawn is embedded into the 3D-printed structure or the structure is placed in direct contact with mycelium that was cultured separately).[19,39] In this study, the ink was inoculated directly with the liquid mycelium culture being incorporated into the ink. Compared to direct inoculation using solid spawns, the risk of clogging was lower when using the liquid culture (due to the heterogeneity of the ink caused by the added spawns), and the homogeneity of the ink was maintained. This is especially important in this study as a 22G nozzle (0.41 mm internal diameter) was used. Based on Figure 1D, the ink containing medium levels of malt and peptone can effectively support the growth of both *P. ostreatus* and *G. lucidum*. After 4 days, white, fluffy spots were seen at various parts of the surface of the structure as the mycelium began to grow. The mycelium then eventually enveloped the entire surface of the structure. These preliminary experiments that were meant to demonstrate the 3D printing of the inks have already revealed the different growth or foraging behaviors from the two fungi.

Indeed, *P. ostreatus* had a greater tendency to form hyphae that spread away from the structure and extend into the air once the surface was fully covered by the mycelium. The lack of any specific direction in the tip extension of the hyphae resulted in the underlying structure being less pronounced after the mycelium had completely enveloped

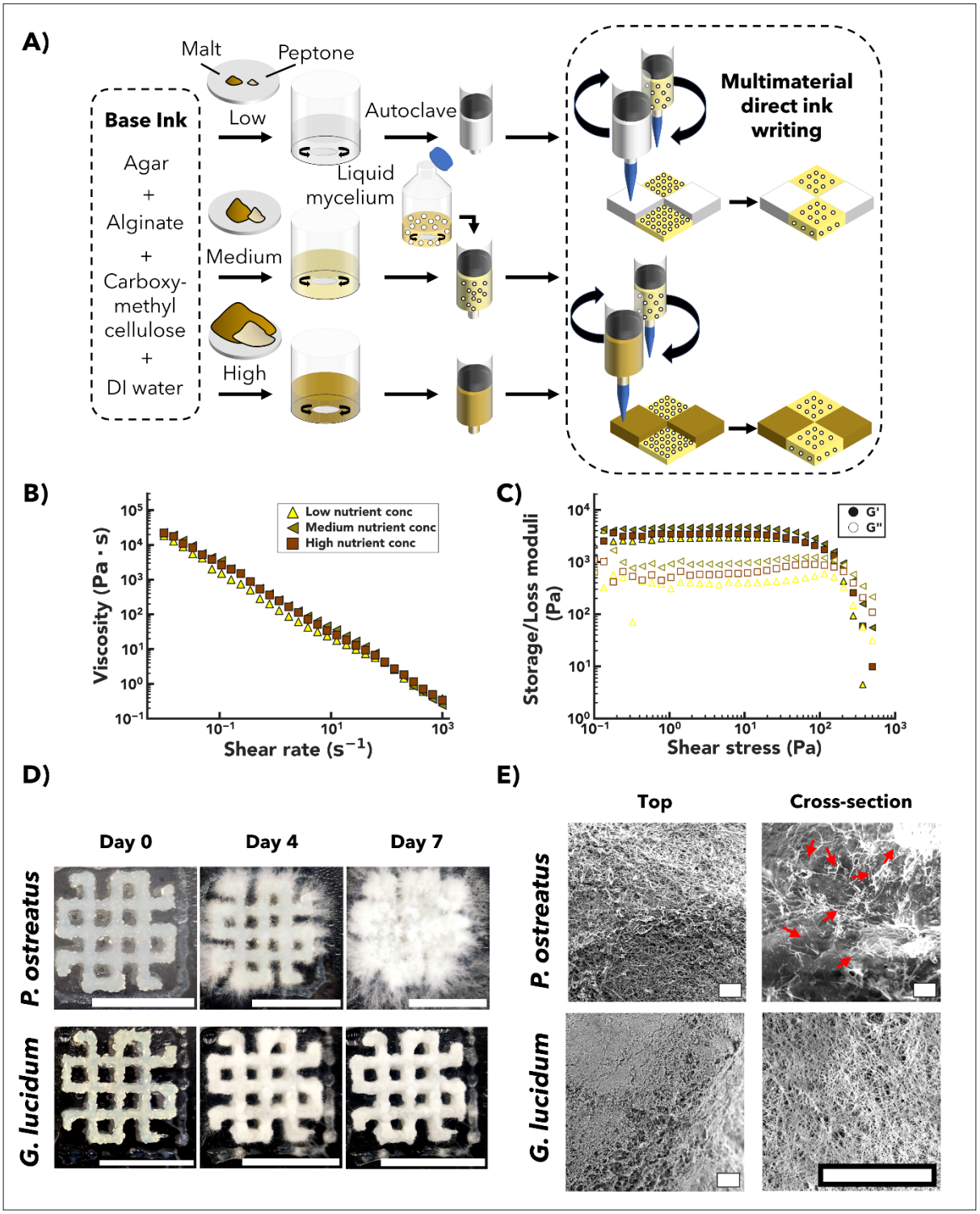


Figure 1. Ink formulation and 3D printing strategies for fungal-based ELMs. (A) Schematics showing the ink preparation with three levels of malt and peptone content (low, medium, high) and the addition of liquid mycelium in the medium-content ink. These inks were then used in the multi-nozzle 3D printer to create materials with local variations in nutrient content and mycelium. (B) Viscosity as a function of shear rate for the inks prepared with the three nutrient levels. (C) Storage (*G*') and loss (*G*") moduli as a function of shear stress for the inks prepared with the three nutrient levels. (D) Digital images of the growth of *G. lucidum* and *P. ostreatus* in 3D-printed constructs over 7 days. Image contrast of all images was slightly enhanced for better clarity. Scale bars: 20 mm. (E) Electron micrographs of the mycelium network of *P. ostreatus* and *G. lucidum* on the top and inside the macropores of 3D-printed constructs after 14 days of growth. Scale bars: 100 μm. For micrographs depicting sparse mycelium networks, red arrows are included to indicate mycelium present.

the structure. Meanwhile, *G. lucidum* was observed to better conform to the 3D-printed structure. Thus, the curves and contours of the 3D structure remained visible even after complete coverage by the mycelium of *G. lucidum*. This observation demonstrates the different foraging strategies that each fungus employs in a similar environment. Furthermore, while *P. ostreatus* readily colonized the air-material surfaces, it had a lower tendency to colonize the cramp spaces within the macropores of the structure. This is shown by the sparse mycelium found in the cross-section of the macropores (Figure 1E). In contrast, the mycelium of *G. lucidum* was equally dense on both the top and inside the macropores of the underlying structure (Figure 1E). However, growth of the mycelium of *P. ostreatus* in the macropores was possible, provided that they are sufficiently large (see Figure S6, Supporting Information).

Having demonstrated the possibility of preparing inks for 3D printing and growing mycelium effectively for two fungal species with different growth behaviors, the effect of the nutrient composition present in the inks on their growth was then studied.

3.2. Nutrient concentration controls the foraging behavior of *P. ostreatus* and *G. lucidum*

Various media and substrates are suitable for fungal cultures. Availability and assay types are among the factors considered when determining the choice of media. Among the plethora of media used for fungal culture, a mixture of malt and peptone are commonly used in the literature and is also chosen here to vary the nutritional content of the inks. Malt serves as a source of polysaccharides to provide energy for the fungi while peptone acts as a nitrogen source for the synthesis of proteins and other components inside the fungal cell. To study the growth of the two fungi *P. ostreatus* and *G. lucidum* when these nutrients are varied, solid-state mycelium growth on agar plates containing low and high levels of malt and peptone were studied (Figure 2, see Figure S7 and time-lapse videos in Videos S1 and S2, Supporting Information).

Agar plates with four levels of nutrient concentrations were prepared following a two-level full factorial design where malt and peptones were varied in low and high concentrations only. The agar plates were inoculated at their center by adding an agar plug containing mycelium. Differences in the mycelium formed from these four nutrient levels could be readily observed for both species (Figure 2A). At low levels of malt and peptone, both *G. lucidum* and *P. ostreatus* formed thin and sparse mycelium. From the naked eye, the mycelium was translucent, with the underlying agar still visible, suggesting it to be very thin and fragile. Increasing the concentration of peptone helped *P. ostreatus* form thicker mycelium, but the mycelium sheet formed was only dense near the inoculating agar plug. The increase growth resulting from the increase in peptone was less pronounced for *G. lucidum*. However, for both strains, malt had a significant effect on the mycelium growth regardless of the concentration of peptone with the mycelium layer becoming opaque at high levels of malt.

To quantify these growth behaviors, the growth rate (the area of mycelium present on the agar plate) was recorded during the 14 days of growth (Figure 2B). Most growth profiles display a sigmoid curve that is typical across different organisms,[40] which was also observed for both fungi in this study. There was an initial lag phase, during which the mycelium from the agar plugs probably initially adjusted to the new environment, followed by an exponential growth phase, and a stationary phase that was reached when the mycelium had covered the entire area of the Petri dish. The growth rate of *P. ostreatus* was faster at low concentrations of malt and peptone as its growth curve was higher than for the other concentrations and was the quickest to plateau (Figure 2B, top). As a fast growth rate is a known attribute of guerrilla-type behavior, this suggests that the fungus adopted an explorative foraging behavior in this environment.[8,22] When the concentration of malt was high, the growth rate became slower but appeared to be independent of the concentration of peptone. The growth rate was the slowest when the concentration of malt was low, and the concentration of peptone was high. Surprisingly, for *G. lucidum*, mycelium grown on agar with high concentrations of malt has a faster rate than those grown on agar with low concentrations of malt (Figure 2B, bottom). This may seem to contradict the theory that low-nutrient environments lead to a faster growth rate due to the fungus exhibiting guerrilla foraging. However, other studies in the literature also suggest that this theory still holds for ranges of malt concentration that are higher than the one used in this study.[8] This suggests that at low malt concentrations, nutrient deficiency may have hindered the growth rate of mycelium. Nevertheless, the mycelium density remained sparser at low-nutrient conditions, which is another attribute indicating guerrilla-type foraging behavior besides high growth rate. Like *P. ostreatus*, the growth rate was the slowest when the concentration of peptone was high while the concentration of malt was low.

To further quantify the exploitative foraging behavior of the fungi, the dry biomass of the mycelium sheet formed in each condition was obtained after 14 days of culture (Figure 2C). At low malt concentrations, an increase in peptone caused a non-significant increase in the thickness of the mycelium formed. Malt had a greater influence on the dry biomass harvested for both strains of fungi investigated

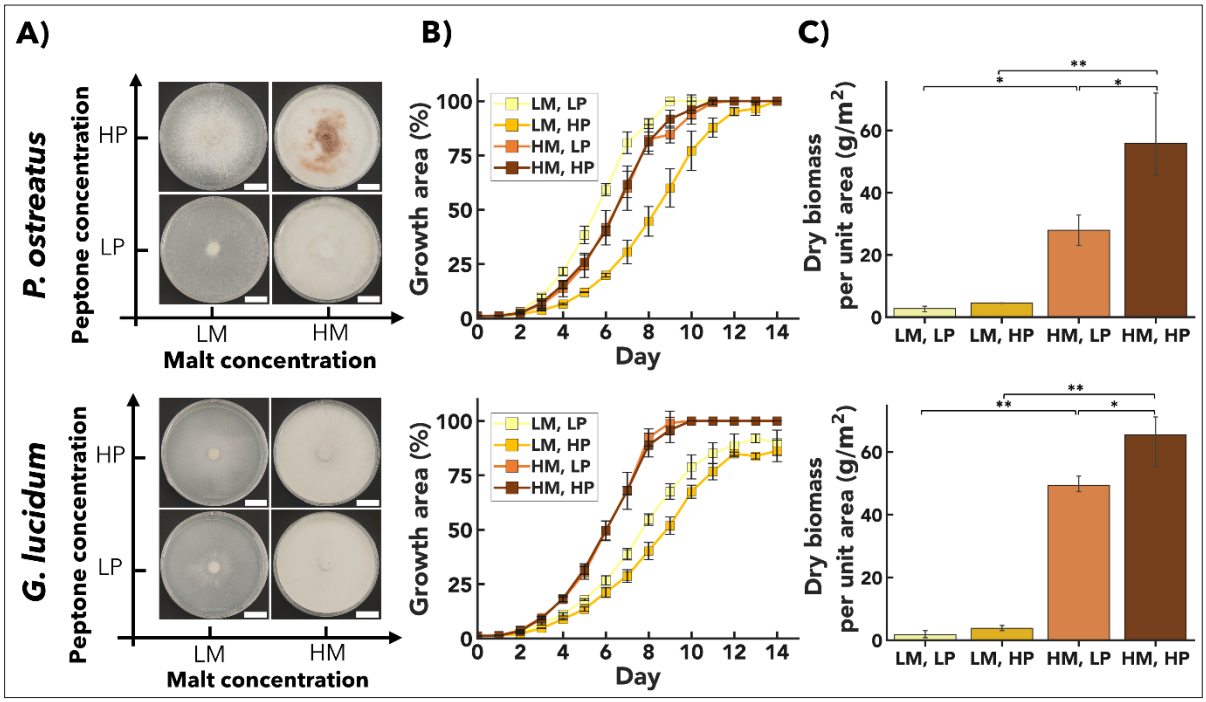


Figure 2. Nutrient concentration controls the foraging behavior of *P. ostreatus* (top panels) and *G. lucidum* (bottom panels). (A) Digital images of mycelium grown on agar plates containing varying concentrations of malt and peptone after 14 days of culture following the two-level full factorial design (see **Materials and methods** section for details). Scale bars: 20 mm. (B) Growth area of the mycelium during 14 days of culture for the four different nutrient compositions. (C) Dry biomass per unit area of the mycelium sheets harvested after 14 days of culture for the four nutrient compositions. Data are presented as mean ± standard deviation. *p <0.05, **p <0.01. Abbreviations: H, high; L, low; M, malt; P, peptone.

but both malt and peptone complemented each other. This synergy resulted in a statistically significant increase in absolute dry biomass obtained when the concentration of peptone was increased at high levels of malt concentration. While malt promoted a greater increase in dry biomass obtained, this quantity increased further in the presence of high levels of peptone.

The variation in malt and peptone concentrations demonstrated various foraging behaviors for the two fungi studied here. This difference in growth led to mycelium formation with differing macroscopic appearances, which could readily influence their properties. A microscopic characterization of the mycelium was therefore conducted to better understand the implications of the varying growth rates.

3.3. Tuning nutrient concentration allows for various morphology of the mycelium of *P. ostreatus* and *G. lucidum*

To determine the effect of the nutrients and the growth rates on the morphology of the mycelium of the two fungi, the mycelium sheets grown in the four nutrient conditions as described in the previous sections were analyzed using electron microscopy (Figure 3).

The microstructures of the mycelium sheets grown after 14 days (Figure 3A) are consistent with the macroscopic observations made from mycelium grown on agar plates (Figure 2A). The density of the mycelium of both *P. ostreatus* and *G. lucidum* increased when the concentration of malt was increased. At low malt and peptone concentrations, there were visible gaps in the network for both strains but as the concentration of nutrients increased, there was tighter packing of the hyphae, owing to the increased mycelium density due to the higher occurrence of branching.

The surface porosity and projected hyphae diameter were also evaluated from these electron micrographs. The surface porosity was significantly reduced when the concentration of malt available to the mycelium increased (Figure 3B). This holds true for both strains regardless of the concentration of peptone. Meanwhile, peptone had a significant influence on the reduction of the surface porosity of the mycelium of *P. ostreatus*, but its effect on the microstructure was negligible for *G. lucidum*. In turn, both malt and peptone had a positive effect on the

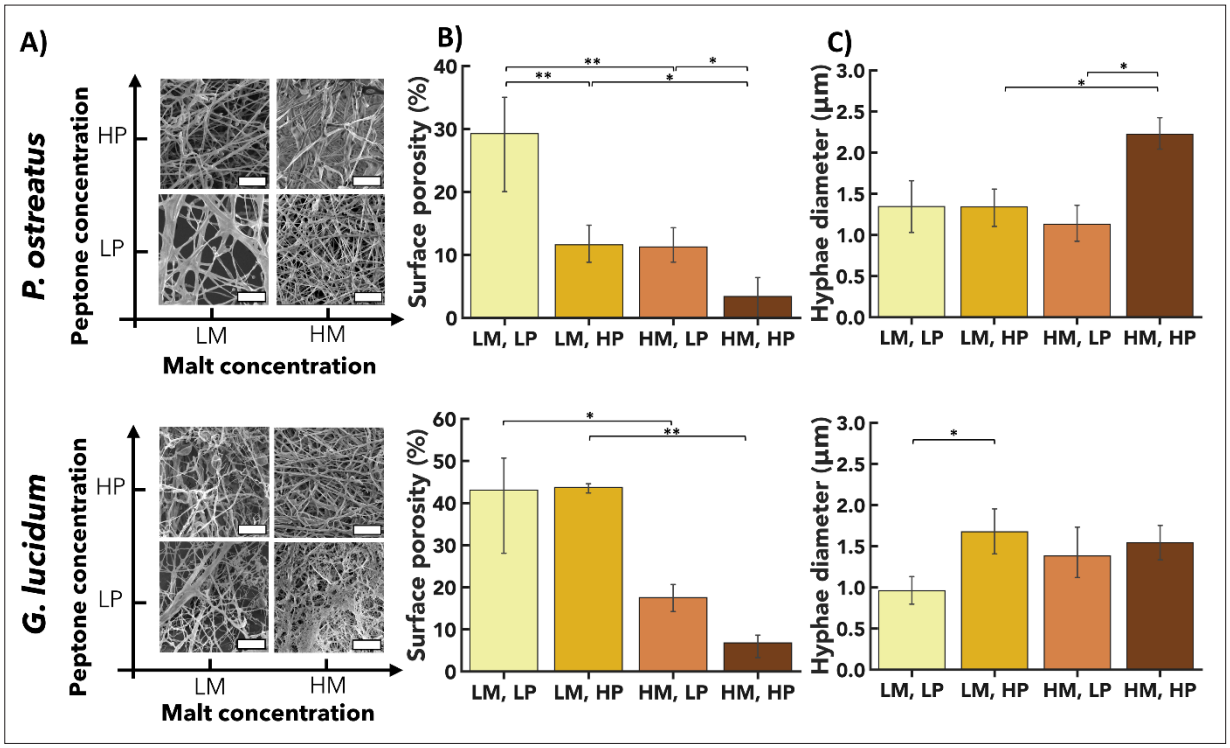


Figure 3. Tuning nutrient concentration allows for various morphology of the mycelium of *P. ostreatus* (top panels) and *G. lucidum* (bottom panels). (A) Electron micrographs of the mycelium grown after 14 days of culture on agar plates containing different concentrations of malt and peptone. Scale bars: 20 µm. (B) Surface porosity of the mycelium after 14 days of culture in the four nutrient conditions. (C) Hyphae diameter of the mycelium after 14 days of culture in the four nutrient conditions. Data are presented as mean ± standard deviation. *$p < 0.05$, **$p < 0.01$. Abbreviations: H, high; L, low; M, malt; P, peptone.

diameter of the hyphae formed that increased when the nutrient concentration increased (Figure 2C). However, the extent of the increase in diameter was different for both strains. For *P. ostreatus*, an increase in malt caused a significant increase in hyphae diameter, but only when the concentration of peptone was high. The same is true for peptone, whereby peptone significantly increased the hyphae diameter when the concentration of malt was high. Meanwhile, for *G. lucidum*, a significant increase in hyphae diameter was observed only when increasing the concentration of peptone when the concentration of malt was low. This observation provides another evidence of the inherent difference between the growth and metabolic activity of both species.

These results establish that malt is more dominant than peptone in affecting the morphology and density of the mycelium of both fungi, resulting in visible macroscopic and microscopic differences. However, peptone by itself still has a significant influence and it cannot be omitted from the formulation of the ink. These macroscopic and microscopic differences may also lead to different surface properties such as hydrophobicity (see Figure S8, Supporting Information). For subsequent experiments on creating structures with localized nutrient variations, low-nutrient zones contained low concentrations of malt and peptone, and high-nutrient zones contained high concentrations of malt and peptone.

3.4. Local variations in nutrients on a two-dimensional surface guide the growth and foraging behavior of mycelium

Considering the difference in growth behaviors of the two fungi on substrates containing different concentrations of nutrients, their behavior on substrates containing local variations in nutrient content was then investigated. To achieve this, multi-material DIW was used to print porous two-dimensional (2D) lattices using the three inks indicated in Figure 1A. The inks were inoculated with liquid mycelium from either *P. ostreatus* or *G. lucidum*, and the fungus was allowed to grow in the structure after printing for about 2 weeks to understand the effects of varying the position of nutrients on the direction of growth and other aspects of the mycelium (Figure 4).

Four sample designs, which could be readily fabricated using our multi-material DIW approach, were tested (Figure 4A). The objective of using these designs was to observe the foraging behavior of mycelium in structures with local variations in nutrient content and to determine if these variations can either promote or inhibit extension (Design I and Design II) or bridging (Design III and Design IV) between different inoculated regions in the structure. Each design contained zones of origin (yellow with white circles), which were printed using the ink containing liquid mycelium and medium levels of malt and peptone. After incubation, the mycelium grew from the zones of origin and extended into the other zones. The prints were intentionally designed to be porous, in order to allow air to flow homogeneously throughout the samples and avoid additional effects of various oxygen contents.

The foraging behavior of the mycelium of *P. ostreatus* on the four structures showed significant variations and effects of the designs (Figure 4B). These results are consistent with the growth of mycelium on various agar formulations (Figure 2), where a clear contrast in mycelium density can be observed between zones of different nutrient levels. When approaching a low-nutrient zone (Design I and Design III), the mycelium formed is sparse. As such, both the extension (Design I) and bridging (Design III) of mycelium are inhibited. This results in a clear contrast between mycelium at the zones of origin and the low-nutrient zones. This contrast

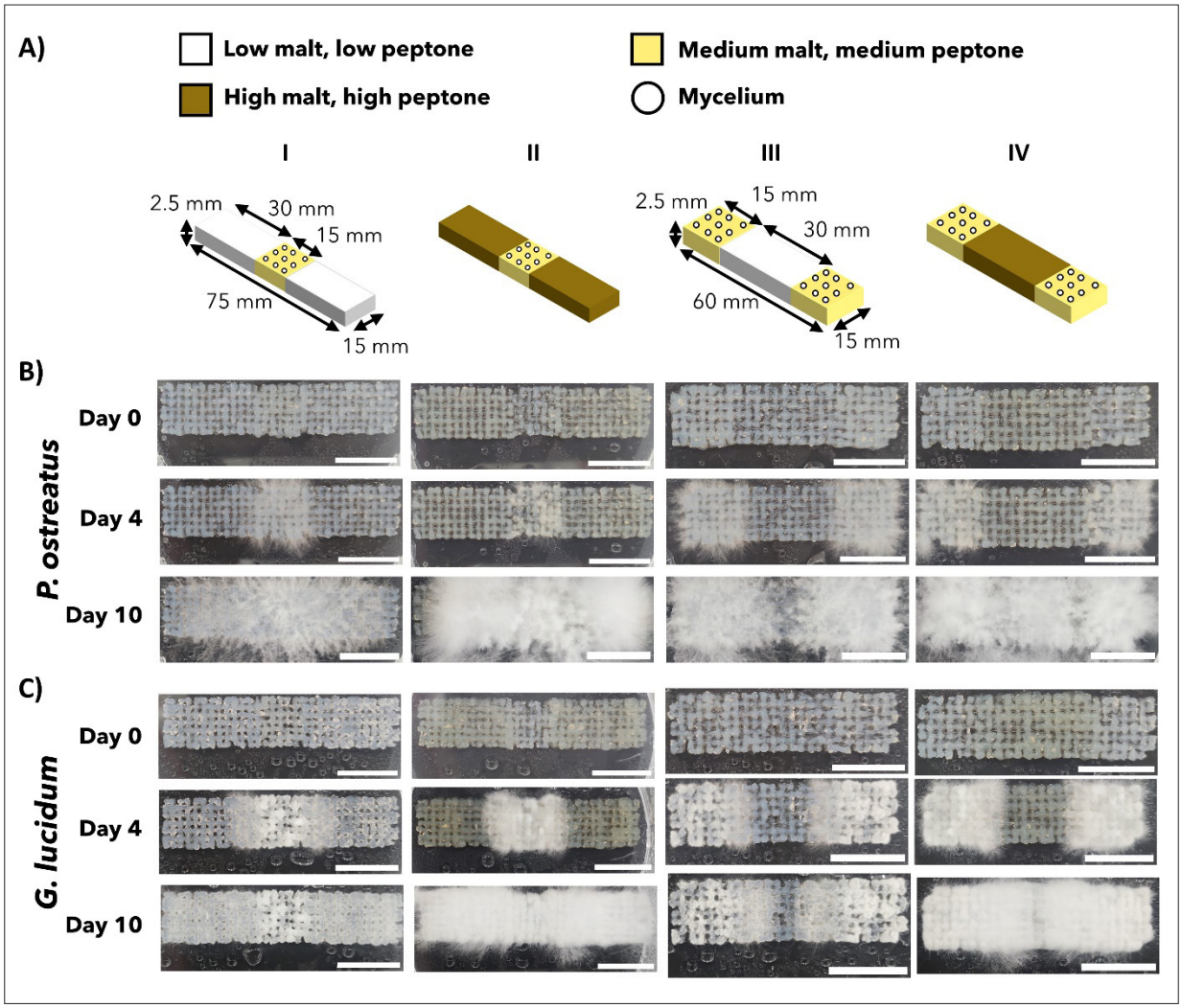


Figure 4. Local variations in nutrients on a 2D surface guides the growth and foraging behavior of mycelium of *P. ostreatus* and *G. lucidum*. (A) Schematics of design of 3D-printed fungal-based engineered living materials (ELMs) detailing the different constituent materials. Growth of mycelium of (B) *P. ostreatus* and (C) *G. lucidum* on the 3D-printed substrates with zones containing varying concentrations of malt, peptone, and liquid mycelium, respectively. Scale bars: 20 mm.

was particularly visible after 4 days of growth and was still apparent after 10 days, albeit less strongly. On the contrary, when the zone had a high nutrient level (Design II and Design IV), both extension and bridging were promoted and the density of mycelium over this zone became indistinguishable from the rest of the network on the ELM. It should be noted, nevertheless, that the extension and bridging are mostly occurring after 10 days. When comparing designs containing high-nutrient zones (Design II and Design IV) to designs containing low-nutrient zones (Design I and Design III), the mycelia emerging from zones of origin were denser for designs containing high-nutrient zones, presumably due to the diffusion of malt and peptone from high-nutrient zones to the zones of origin. For designs with low-nutrient zones, the opposite may also be true, where the initial mycelium formed was sparser due to the diffusion of malt and peptone from the zones of origin to the low-nutrient zones.

Similar observations were made for the same designs containing *G. lucidum* for their extension and bridging in the four multi-material structures (Figure 4C). While the behavior resembled that of *P. ostreatus*, the mycelium of *G. lucidum* had the tendency to conform to the underlying structure with less likelihood to spread its hyphae in all directions, resulting in the shape profile of the underlying structure being more pronounced (compared with Figure 1D). Meanwhile, for *P. ostreatus*, there was also a greater tendency for the mycelium to extend beyond the 3D-printed structure and onto the Petri dish housing the ELM. Otherwise, the growth behavior of both *G. lucidum* and *P. ostreatus* were consistent with the phalanx/guerrilla theory on foraging behavior.

Both Designs I and II also showed the potential of varying local nutrient contents to either promote or inhibit the self-healing capabilities of fungal mycelium. It has been established that live mycelium materials can regenerate,[6,17] allowing holes on mycelium sheets to be filled or two separate structures to combine when placed together. By placing a material of low-nutrient content between two regions containing fungal mycelium, the bridging of mycelium between the two region was inhibited and the self-healing property of the fungal mycelium could be suppressed to a certain extent. Meanwhile, the self-healing capability of mycelium could be promoted if the material in between contained high nutrient levels, promoting the growth of mycelium over the gap. As such, this study also showed the possibility of controlling this phenomenon in fungal-based ELMs.

Therefore, the growth behavior of the two fungi on a flat 2D plane was observed and their behavior in a 3D space was then studied.

3.5. Local variations in nutrients in a 3D complex structure guides the growth and foraging behavior of mycelium

Since ELMs exist in various shapes and complexities, the effects of varying nutrients on all three axes should also be investigated. Furthermore, 3D printing via DIW conveniently allows for 3D shapes to be built and the inks were formulated to allow both extrudability and buildability. The extension and growth of the mycelium from the two species could therefore be observed in three dimensions and in complex patterns (Figure 5).

To test the growth of mycelium in the vertical direction, cuboid structures were designed where the base of the cube is the zone of origin (**Figure 5A**). The structures were again 3D-printed with pores to allow air to flow through the structure and homogeneous growth at the core of the sample. After the base was printed, the subsequent layers were then printed using inks with either a low- or high-nutrient content. For both strains of fungi, the mycelium first emerged from the base of the structure 4 days after printing. However, at this point, the network was barely visible, containing only a few strands of hyphae. By day 7, the mycelium became more visible as the subsequent layers above were gradually covered until complete coverage observed by day 10. If the nutrient content of the higher layers is low, the mycelium formed in the upper layers is sparse, and vice versa. The designs also demonstrated that not all inks used in the fabrication process need to include liquid mycelium. Indeed, only a section needs to be inoculated and the mycelium will eventually envelop the entire structure. This is interesting as it potentially reduces the amount of liquid mycelium required, which should be easier for the fabrication of large-volume structures. It also facilitates the ink preparation and storage as the ink without mycelium can be stored in the fridge until use, whereas inks containing mycelium need to be prepared fresh before use. If an ink containing mycelium is kept for too long, mycelium may develop inside any air bubbles present within the ink, ultimately compromising the homogeneity of the ink leading to 3D printing difficulties later.

From the preceding observations, it has been established that mycelium growth can be controlled through the precise deposition of nutrients in the substrate, allowing for structures with various surface patterns to be fabricated (see also Figures S9 and S10, Supporting Information). As such, a potential application of this technology is the creation of distinct and detailed patterns on the surface of structures. Positioning zones of high- and low-nutrient contents in the ELM should guide the growth of mycelium in specific directions, allowing for the fabrication of structures with esthetical value. Figure 5B highlights an example of this application. Using a low-nutrient zone, the growth of a

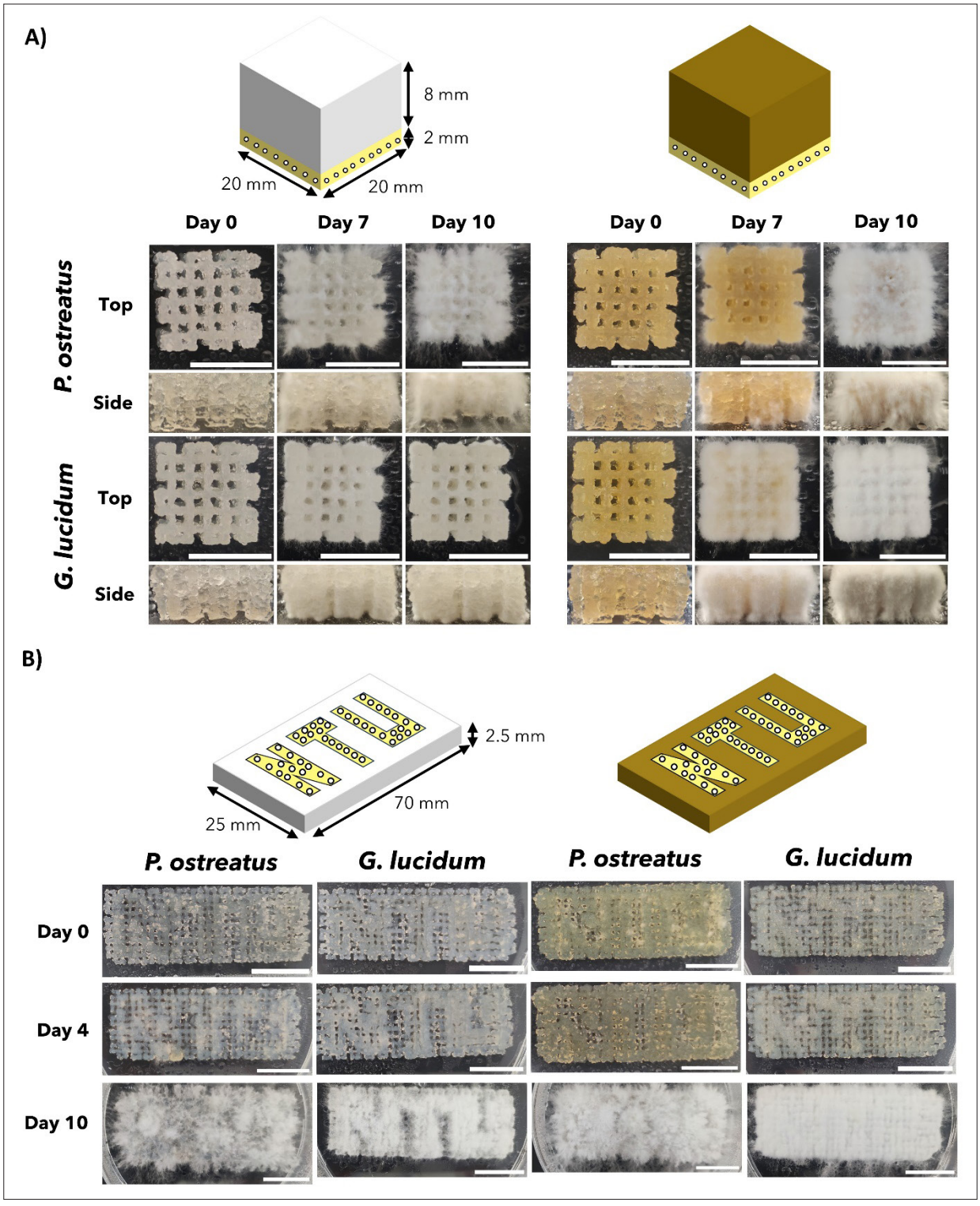


Figure 5. Local variations in nutrients in a 3D complex structure guides the growth and foraging behavior of mycelium from *P. ostreatus* and *G. lucidum*. (A) 3D-printed substrates inoculated with *P. ostreatus* and *G. lucidum*, respectively, with stacked zones containing varying concentrations of malt and peptone. Different fungal strains (*G. lucidum* and *P. ostreatus*) and nutrient contents were used. Scale bars: 20 mm. (B) Fabrication of textured mycelium surfaces by using multi-material 3D printing. Different fungal strains (*G. lucidum* and *P. ostreatus*) and nutrient contents were used. Scale bars: 20 mm.

dense mycelium network was limited to the zones of origin. When the mycelium began to extend into the surrounding low-nutrient level zones, the network became sparser. This creates a contrast in the mycelium network between the two zones, allowing for underlying patterns to be discernible. In contrast, for designs with the surrounding zones containing a high nutrient level, the density of the network was higher, eliminating the underlying pattern of the zone of origin. Owing to the inherent exploitative behavior of *G. lucidum*, pattern generation was more successful when this species was used, with the letterings being distinguishable after attaining complete mycelium growth on day 10. Meanwhile, since it is established that the mycelium of *P. ostreatus* tends to extend in all directions, pattern generation on the surface of the substrate is less successful, despite the visible difference in mycelium density between the high- and low-nutrient zones.

While the effect of nutrient heterogeneity on fungal growth was previously demonstrated in the literature,[21,27,41] this study significantly expands these prior discoveries. Firstly, preceding studies sought to understand fungal growth behavior in soil, and thus, the substrates used were at most 2D. This study does not have such a limitation and therefore also investigates growth in all three spatial dimensions. There is also potential to utilize this knowledge to create fungal-based ELMs and mycelium-bound composites of greater complexity. Regarding the creation of a heterogeneous nutrient environment, previous studies achieved this by manually arranging various cubes of agar to form a tessellation. This study utilizes modern fabrication methods in the form of DIW to fabricate shapes with greater complexity and dimensions, in contrast to those with simple patterns and arrangements. This study also investigates how both factors of the carbon (malt) and nitrogen (peptone) sources interact with each other to affect the growth of fungi on such substrates. On the contrary, previous studies either focused on comparing between different media formulations[21,33,42] or only investigated a single component at a time.[25] Finally, the application of fabricating patterned structures leveraging the ability to manipulate the foraging behavior of fungi was demonstrated in this work, underscoring the potential utility of this phenomenon.

While the use of 3D printing to fabricate fungal-based engineered living materials has been established, notably by the study conducted by Gantenbein et al.,[8] this work seeks to expand on their findings. In this study, instead of a homogenous structure, multi-material samples with heterogeneous distribution of nutrients were fabricated using a multi-nozzle 3D printing system. A second strain of fungi, *P. ostreatus* was explored and the difference in its growth behavior with *G. lucidum* on 3D-printed ELMs in the same environment and with the same nutrient levels was observed as well. This expands on the possibility of different fungi exhibiting different growth patterns on ELMs when generalizing this technology to other strains of fungi. While the difference between explorative and exploitative growth was previously investigated in literature, this was conducted only to optimize the concentration of malt to be included in their final ink composition. In contrast, the nutrient content in the ink used in this study was purposely adjusted to elicit the changes in growth behavior of the mycelium at various locations of the structure. Also, the peptone was included as a second source of nutrients besides malt to determine its main effect on fungal growth and its interaction with malt content.

4. Conclusion

In this study, the effect of different nutrient content on the foraging behavior of mycelium was explored. With two fungal strains used as case studies, their behaviors on multi-material constructs with localized variations in nutrient content fabricated using DIW were investigated. In regions with low-nutrient content, both fungi exhibited guerrilla behavior with mycelium of low density formed, while phalanx behavior was observed in regions of high-nutrient content, resulting in the formation of dense mycelium. *G. lucidum* is more exploitative, with less tendency to extend its hyphae in all directions, as compared to *P. ostreatus*, resulting in greater conformation to the underlying ELM. In the development of existing fungal-based ELMs, this fundamental study provides a possibility of controlling the growth of mycelium on the structure using nutrients to create more complex structures with expanded functionalities. While there was no particular application explored in this study, it is expected that the findings here will provide reference for future developments towards the following applications. Improving the esthetics of apparels made using mycelium is possible by creating patterns containing either high- or low-nutrient content on the surface of such textiles. There is also the potential of using such ELMs as a miniature model of a particular environment to model the behavior of fungi in said environment. This can subsequently be used to better understand the capabilities and effectiveness of using fungi to mycoremediate and remove contaminants from the environment, or to evaluate the efficacy of anti-fungal products. The 3D printing system is also capable of modeling 3D ecosystems with complex shapes and is not limited to just creating a 2D ecosystem.

Beyond the investigation of malt and peptone, other nutrient sources can also be explored as well. The effect of other materials on the growth and foraging behavior of mycelium such as metal ions and other microorganisms

including bacteria and plant cells can also be incorporated and investigated, provided that the printability of the ink is not affected by the incorporation of such materials. Fungal behavior in complex architectures manufactured via 3D printing can also be another potential area inspired by this study, opening the way for the exploration of 3D-printed biodegradable and living products.

Acknowledgements

None.

Funding

The authors acknowledge funding from the National Research Foundation of Singapore and ETH Zurich, Switzerland, with the grant Future Cities Laboratory Global, Module A4: Mycelium digitalization.

Conflict of interest

The authors declare they have no competing interests.

Author contributions

Conceptualization: Jia Heng Teoh, Hortense Le Ferrand
Formal analysis: Jia Heng Teoh
Funding acquisition: Hortense Le Ferrand
Investigation: Jia Heng Teoh
Methodology: Jia Heng Teoh, Eugene Soh
Supervision: Hortense Le Ferrand
Visualization: Jia Heng Teoh, Hortense Le Ferrand
Writing – original draft: Jia Heng Teoh
Writing – review & editing: All authors

Ethics approval and consent to participate

Not applicable.

Consent for publication

Not applicable.

Availability of data

Additional data are available in the Supplementary File. Data are available from the corresponding author upon reasonable request.

References

1. Rodrigo-Navarro A, Sankaran S, Dalby MJ, del Campo A, Salmeron-Sanchez M. Engineered living biomaterials. *Nat Rev Mater*. 2021;6(12):1175-1190.
doi: 10.1038/s41578-021-00350-8

2. Wang Y, Liu Y, Li J, Chen Y, Liu S, Zhong C. Engineered living materials (ELMs) design: from function allocation to dynamic behavior modulation. *Curr Opin Chem Biol*. 2022;70:102188.
doi: 10.1016/j.cbpa.2022.102188

3. Lantada AD, Korvink JG, Islam M. Taxonomy for engineered living materials. *Cell Rep Phys Sci*. 2022;3(4):100807.
doi: 10.1016/j.xcrp.2022.100807

4. Vandelook S, Elsacker E, Van Wylick A, De Laet L, Peeters E. Current state and future prospects of pure mycelium materials. *Fungal Biol Biotechnol*. 2021;8(1):20.
doi: 10.1186/s40694-021-00128-1

5. Jones M, Gandia A, John S, Bismarck A. Leather-like material biofabrication using fungi. *Nat Sustain*. 2021;4(1):9-16.
doi: 10.1038/s41893-020-00606-1

6. Elsacker E, Zhang M, Dade-Robertson M. Fungal engineered living materials: the viability of pure mycelium materials with self-healing functionalities. *Adv Funct Mater*. 2023;33(29):2301875.
doi: 10.1002/adfm.202301875

7. McBee RM, Lucht M, Mukhitov N, et al. Engineering living and regenerative fungal–bacterial biocomposite structures. *Nat Mater*. 2022;21(4):471-478.
doi: 10.1038/s41563-021-01123-y

8. Gantenbein S, Colucci E, Käch J, et al. Three-dimensional printing of mycelium hydrogels into living complex materials. *Nat Mater*. 2023;22(1):128-134.
doi: 10.1038/s41563-022-01429-5

9. Brand A, Gow NA. Mechanisms of hypha orientation of fungi. *Curr Opin Microbiol*. 2009;12(4):350-357.
doi: 10.1016/j.mib.2009.05.007

10. Soh E, Le Ferrand H. Woodpile structural designs to increase the stiffness of mycelium-bound composites. *Mater Design*. 2023;225:111530.
doi: 10.1016/j.matdes.2022.111530

11. Murphy SV, Atala A. 3D bioprinting of tissues and organs. *Nat Biotechnol*. 2014;32(8):773-785.
doi: 10.1038/nbt.2958

12. Schaffner M, Rühs PA, Coulter F, Kilcher S, Studart AR. 3D printing of bacteria into functional complex materials. *Sci Adv*. 2017;3(12):eaao6804.
doi: 10.1126/sciadv.aao6804

13. Teoh JH, Mozhi A, Sunil V, Tay SM, Fuh J, Wang CH. 3D printing personalized, photocrosslinkable hydrogel wound dressings for the treatment of thermal burns. *Adv Funct Mater*. 2021;31(48):2105932.
doi: 10.1002/adfm.202105932

14. Skylar-Scott MA, Mueller J, Visser CW, Lewis JA. Voxelated soft matter via multimaterial multinozzle 3D printing. *Nature*. 2019;575(7782):330-335.
doi: 10.1038/s41586-019-1736-8

15. Cheng J, Wang R, Sun Z, et al. Centrifugal multimaterial 3D printing of multifunctional heterogeneous objects. *Nat Commun*. 2022;13(1):1-10.

doi: 10.1038/s41467-022-35622-6

16. Soh E, Chew ZY, Saeidi N, Javadian A, Hebel D, Le Ferrand H. Development of an extrudable paste to build mycelium-bound composites. *Mater Design*. 2020;195:109058. doi: 10.1016/j.matdes.2020.109058
17. Soh E, Teoh JH, Leong B, Xing T, Le Ferrand H. 3D printing of mycelium engineered living materials using a waste-based ink and non-sterile conditions. *Mater Design*. 2023;236:112481. doi: 10.1016/j.matdes.2023.112481
18. Elsacker E, Peeters E, De Laet L. Large-scale robotic extrusion-based additive manufacturing with living mycelium materials. *Sustain Fut*. 2022;4:100085. doi: 10.1016/j.sftr.2022.100085
19. Jauk J, Gosch L, Vašatko H, Christian I, Klaus A, Stavric M. MyCera. Application of mycelial growth within digitally manufactured clay structures. *Int J Arch Comput*. 2022;20(1):147807712210822. doi: 10.1177/14780771221082248
20. Shen SC, Lee NA, Lockett WJ, et al. Robust myco-composites: a biocomposite platform for versatile hybrid-living materials. *Mater Horiz*. 2024;11(7):1689-1703. doi: 10.1039/D3MH01277H
21. Boswell GP, Jacobs H, Davidson FA, Gadd GM, Ritz K. Functional consequences of nutrient translocation in mycelial fungi. *J Theor Biol*. 2002;217(4):459-477. doi: 10.1006/jtbi.2002.3048
22. Aleklett K, Ohlsson P, Bengtsson M, Hammer EC. Fungal foraging behaviour and hyphal space exploration in micro-structured Soil Chips. *ISME J*. 2021;15(6):1782-1793. doi: 10.1038/s41396-020-00886-7
23. Ye XH, Yu FH, Dong M. A trade-off between guerrilla and phalanx growth forms in *Leymus secalinus* under different nutrient supplies. *Ann Bot*. 2006;98(1):187-191. doi: 10.1093/aob/mcl086
24. Fomina M, Ritz K, Gadd GM. Nutritional influence on the ability of fungal mycelia to penetrate toxic metal-containing domains. *Mycol Res*. 2003;107(7):861-871. doi: 10.1017/S095375620300786X
25. Nussbaum N, von Wyl T, Gandia A, Romanens E, Rühs PA, Fischer P. Impact of malt concentration in solid substrate on mycelial growth and network connectivity in Ganoderma species. *Sci Rep*. 2023;13(1):21051. doi: 10.1038/s41598-023-48203-4
26. Fukasawa Y, Ishii K. Foraging strategies of fungal mycelial networks: responses to quantity and distance of new resources. *Front Cell Dev Biol*. 2023;11:1244673. doi: 10.3389/fcell.2023.1244673
27. Davidson FA, Park AW. A mathematical model for fungal development in heterogeneous environments. *Appl Math Lett*. 1998;11(6):51-56. doi: 10.1016/S0893-9659(98)00102-5
28. Aguilar-Trigueros CA, Boddy L, Rillig MC, Fricker MD. Network traits predict ecological strategies in fungi. *ISME Commun*. 2022;2(1):1-11. doi: 10.1038/s43705-021-00085-1
29. Veresoglou SD, Wang D, Andrade-Linares DR, Hempel S, Rillig MC. Fungal decision to exploit or explore depends on growth rate. *Microb Ecol*. 2018;75(2):289-292. doi: 10.1007/s00248-017-1053-4
30. Schneider CA, Rasband WS, Eliceiri KW. NIH image to ImageJ: 25 years of image analysis. *Nat Methods*. 2012;9(7):671-675. doi: 10.1038/nmeth.2089
31. Yang L, Park D, Qin Z. Material function of mycelium-based bio-composite: a review. *Front Mater*. 2021;8:737377. doi: 10.3389/fmats.2021.737377
32. Hotz EC, Bradshaw AJ, Elliott C, Carlson K, Dentinger BTM, Naleway SE. Effect of agar concentration on structure and physiology of fungal hyphal systems. *J Mater Res Technol*. 2023;24:7614-7623. doi: 10.1016/j.jmrt.2023.05.013
33. Hoa HT, Wang CL. The effects of temperature and nutritional conditions on mycelium growth of two oyster mushrooms (*Pleurotus ostreatus* and *Pleurotus cystidiosus*). *Mycobiology*. 2015;43(1):14-23. doi: 10.5941/MYCO.2015.43.1.14
34. Qiu Z, Wu X, Gao W, Zhang J, Huang C. High temperature induced disruption of the cell wall integrity and structure in Pleurotus ostreatus mycelia. *Appl Microbiol Biotechnol*. 2018;102(15):6627-6636. doi: 10.1007/s00253-018-9090-6
35. Wang J, Liu Y, Zhang X, et al. 3D printed agar/ calcium alginate hydrogels with high shape fidelity and tailorable mechanical properties. *Polymer*. 2021;214:123238. doi: 10.1016/j.polymer.2020.123238
36. Mallakpour S, Azadi E, Hussain CM. State-of-the-art of 3D printing technology of alginate-based hydrogels—an emerging technique for industrial applications. *Adv Colloid Interface Sci*. 2021;293:102436. doi: 10.1016/j.cis.2021.102436
37. Jones EBG, Jennings DH. The effect of cations on the growth of fungi. *New Phytol*. 1965;64(1):86-100. doi: 10.1111/j.1469-8137.1965.tb05378.x
38. Lin N, Taghizadehmakoei A, Polovina L, et al. 3D bioprinting of food grade hydrogel infused with living *Pleurotus ostreatus* Mycelium in non-sterile conditions. *ACS Appl Bio Mater*. 2024;7(5):2982-2992. doi: 10.1021/acsabm.4c00048
39. Abdallah YK, Estévez AT. Biowelding 3D-Printed biodigital brick of seashell-based biocomposite by pleurotus ostreatus mycelium. *Biomimetics*. 2023;8(6):504. doi: 10.3390/biomimetics8060504

40. Kaufmann KW. Fitting and using growth curves. *Oecologia*. 1981;49(3):293-299. doi: 10.1007/BF00347588

41. Ritz K. Growth responses of some soil fungi to spatially heterogeneous nutrients. *FEMS Microbiol Ecol*. 1995;16(4):269-279. doi: 10.1111/j.1574-6941.1995.tb00291.x

42. Haneef M, Ceseracciu L, Canale C, Bayer IS, Heredia-Guerrero JA, Athanassiou A. Advanced materials from fungal mycelium: fabrication and tuning of physical properties. *Sci Rep*. 2017;7(1):41292. doi: 10.1038/srep41292

ACCSCIENCE PUBLISHING

International Journal of Bioprinting

RESEARCH ARTICLE

Biomimetic structural design and performance study of 3D-printed graded minimal surface bone scaffolds with enhanced bioactivity

Tang Liu[1†], Yuxin Lin[1†], Lin Sang[2], Fei Wang[1], Jiawei Hu[1], Kun Guo[3], Shanglian Ju[4*], Yiping Zhao[1*], and Xiaohong Shu[5]

[1]Department of Radiology, The Second Affiliated Hospital of Dalian Medical University, Dalian, Liaoning, China

[2]School of Materials Science and Engineering, Dalian University of Technology, Dalian, Liaoning, China

[3]Department of Pathology, The Second Affiliated Hospital of Dalian Medical University, Dalian, Liaoning, China

[4]Department of Orthopedics, The Second Affiliated Hospital of Dalian Medical University, Dalian, Liaoning, China

[5]College of Pharmacy, Dalian Medical University, Dalian, Liaoning, China

Abstract

Bone bionics and structural engineering have played a vital role in bone regeneration, with artificial scaffolds generating widespread interest. However, the mechanical properties and bone regeneration potential of biomimetic structures remain unclear. Herein, biodegradable polymer composites based on poly(butylene adipate-co-terephthalate)/poly(lactic acid) (PBAT/PLA) were 3D-printed into lattice structures as tissue engineering scaffolds. For structural design, graded diamond (D) minimal surfaces were proposed and designed to mimic the natural bone structure. The graded topologies were realized by designing gradient thickness either radially from center to edge or vertically from top to bottom. The mechanical performance of these graded samples displayed better load-carrying and energy absorption capacity than the uniform counterparts. No obvious damage was detected in the internal microstructure of the compressed samples using computed tomography. Subsequently, platelet-rich plasma (PRP), containing diverse cytokines, was loaded on the graded scaffolds. The PRP-loaded D-scaffold reported improved *in vitro* cell proliferation and osteoblast differentiation. Finally, femoral condyle defect repair results indicated that the PRP-loaded D-scaffold effectively promoted early-stage bone regeneration. Overall, this work provides insights into fabricating artificial scaffolds with bioactive factors and biomimetic lattice structures.

Keywords: Biomimetic structural design; Mechanical properties; Computed tomography; Bone scaffolds; Platelet-rich plasma

†These authors contributed equally to this work.

***Corresponding authors:**
Shanglian Ju
(jushanglian@163.com)

Yiping Zhao
(yipizhao1975@dmu.edu.cn)

Citation: Liu T, Lin Y, Sang L, et al. Biomimetic structural design and performance study of 3D-printed graded minimal surface bone scaffolds with enhanced bioactivity. *Int J Bioprint.* 2024;10(5):3416. doi: 10.36922/ijb.3416

Received: April 12, 2024
Accepted: May 21, 2024
Published Online: July 1, 2024

Copyright: © 2024 Author(s). This is an Open Access article distributed under the terms of the Creative Commons Attribution License, permitting distribution, and reproduction in any medium, provided the original work is properly cited.

Publisher's Note: AccScience Publishing remains neutral with regard to jurisdictional claims in published maps and institutional affiliations.

1. Introduction

Lattice structures, possessing continuous and interconnected open pores, have garnered great interest in artificial materials and biological systems.[1–3] Periodic

minimal surface structures are of particular interest due to their favorable advantages, including good strength and stiffness, interconnected cellular structure, and designed topography.[4–6] These structures could efficiently load external stress and provide the implants with sufficient supporting capacity, making them excellent scaffold candidates in tissue engineering.[7,8]

Geometry engineering is an effective strategy to improve the performance of the scaffold. The structural design of the triply periodic minimal surface (TPMS) model could be established using mathematical expressions supported by additive manufacturing techniques.[9–11] Among the diverse periodic geometric parameters, cellular morphology, porosity, and wall thickness greatly influence the mechanical properties of the model. For instance, gyroid and diamond (D) surfaces possess good bearing capacity.[12–14] Previous work has demonstrated the remarkable load-carrying and energy absorption capacity of graded lattices, thereby enabling resistance to impact and bone stress.[15–17] Liu et al. proposed a 3D controllable TPMS structure based on Schwarz P and gyroid surfaces for application as a hip implant. Zou et al. developed three types of TPMS structures to mimic the properties of bone scaffolds.[15] The TPMS additively manufactured by Ti-6Al-4V achieved enhanced elastic modulus and compressive strength within the range of human bones. Since natural bone consists of dense cortical and cancellous bone, the construction of graded periodic minimal surface structures would be more beneficial as artificial scaffolds.[17]

In contrast, the mechanical and biological performances of these structures are greatly dependent on the material type. Recently, biodegradable materials have been broadly used in biomedical applications.[18] Meanwhile, three-dimensionl (3D) printing technology is an efficient tool to realize scaffold preparation in association with high efficacy, convenience, and precision. Biodegradable polyesters, including poly(lactic acid) (PLA), poly(caprolactone) (PCL), poly(glycolic acid) (PGA), and their blends, have been used for fused filament fabrication (FFF) in biomedical applications due to their biocompatibility, biodegradability, and adjustable properties.[19–23] Poly(butylene adipate-co-terephthalate) (PBAT) is a biodegradable polyester, which exhibits good elasticity and flexibility.[19] Several studies have revealed that PBAT-based composites have the potential for biomedical applications. Ulbrich et al.[20] proposed 3D-printed composite scaffolds of PBAT/niobium-containing bioactive glasses for new bone formation. Qiu et al.[21] proposed a PBAT/sodium alginate blend with better mechanical and biological properties as a candidate for vascular stent. In our previous work, the PBAT/PLA filaments were 3D-printed into complex lattice structures and had balanced stiffness-toughness performance, making them an ideal candidate for scaffold development.

In terms of bioactivity, the combination of lattice scaffolds with bioactive factors could better promote new bone ingrowth and regeneration.[24,25] Platelet-rich plasma (PRP) has been recently applied as a therapeutic agent to heal damaged tissues, especially in wound dressings.[26–28] It is derived from autologous blood with a certain platelet concentration with several immunoregulatory factors.[26] The rich growth factors found in PRP include platelet-derived growth factor (PDGF-AA, BB, and AB), transforming growth factor (TGF-$\beta 1$ and $\beta 2$), insulin-like growth factor (IGF), vascular endothelial growth factor (VEGF), and epithelial growth factor (EGF). It has been demonstrated that PRP significantly contributes to wound dressing. However, the influence of PRP-loaded scaffolds on bone regeneration warrants further research.

Herein, we investigate the mechanical behavior and biological performance of PRP-loaded bone scaffolds with gradient minimal surface structures. Biodegradable PBAT/PLA blends were selected as scaffolding materials. The typical minimal D-surface was first utilized to design gradient structures to mimic natural bone and subsequently fabricated by FFF. In particular, two patterns of the graded geometries, i.e., radially from center to edge or vertically from top to bottom, were successfully realized by controlling the thickness of the cellular wall. The influence of gradient thickness on the internal microstructure and mechanical performance was determined. After achieving the optimized gradient D-scaffold structure, bioactive PRPs were loaded onto the D-scaffolds, and the biological performance was assessed by *in vitro* cell viability and *in vivo* animal femoral condyle defect. The biological results demonstrated good biocompatibility and bioactivity for bone implantation. The current study provides new prospects for scaffold structural design in view of bone bionics and bioactive factors on osteogenesis.

2. Materials and methods

2.1. Materials

PBAT with a melting temperature (T_m) of 125°C was provided by Kanghui New Materials Hi-Tech Co., Ltd. (China). PLA (4032D) was purchased from Nature Works (America).

2.2. Fabrication and 3D printing of poly(butylene adipate-co-terephthalate)/poly(lactic acid) composites

PBAT/PLA blends with a weight ratio of 70:30 were prepared using a twin-screw extruder according to previous literature.[19] Before compounding, the raw pellets were

dried at 60°C for 4 h. The composite pellets were collected through a water bath and subsequently granulated. The blends were dried in an oven at 60°C for 8 h. The PBAT/PLA were then fabricated into filaments using a filament extruder. The extruder barrel heating zone was set at a range of 190–210°C. The PBAT/PLA specimens were 3D printed using a near-end FFF 3D printer.

2.3. Design of homogeneous and graded bone scaffold structures

The bone scaffold structures were designed based on minimal D-surface structures. Homogeneous and graded minimal D-surface structures were mathematically approximated using the implicit method. The equation for D-surface structures is presented as **Equation 1.**[29]

$$\begin{aligned}\phi D\,(x, y, z) = {} & \sin(\omega x)\sin(\omega y)\sin(\omega z) + \\ & \sin(\omega x)\cos(\omega y)\cos(\omega z) + \cos(\omega x) \\ & \sin(\omega y)\cos(\omega z) + \cos(\omega x)\cos(\omega y) \\ & \sin(\omega z) = C\end{aligned} \tag{1}$$

where x, y, and z represent spatial coordinates. The structure was generated as the solution of the level-set function $\phi = C$. The solid model of the surface was created by extracting the zero-level set surface $C = 0$ for **Equation 1**.

The homogeneous D-surfaces were creased by Rhino 7.4 software and presented in Figure 1. For the homogeneous D-surfaces, samples with the wall thickness of 1.0 mm and sample with the wall thickness of 1.2 mm were fabricated. Each group had three parallel specimens. Specifically, an extension field was generated using the implicit function, and a sheet surface model was generated.

For the graded D-surfaces, two kinds of models were established. Firstly, a cylindrical model with gradient thickness in a radial pattern was established. The gradient thickness was in the range of 0.8–1.2 and 0.9–1.6 mm, respectively. The diameter of the cylinder was 15 mm, and the height was 18 mm. The other graded model had a set gradient thickness along the z-axis. The cube size had a dimension of 20 × 20 × 20 mm. The gradient thickness was set in the range of 0.6–1.8, 0.8–1.6, and 1.0–1.4 mm, respectively. After designing using Rhino software, the generated models were exported as STL files and then imported into CURA 5.4 software for slicing and FFF printing. To compare the load-bearing and energy absorption capacity, the relative density of the homogeneous and graded models was kept the same.

2.4. Platelet-rich plasma preparation and loading in scaffolds

Blood was extracted from adult rabbits through cardiac puncture under aseptic conditions. Approximately 4 mL of extracted blood was centrifuged at room temperature to obtain three distinct phases, including the platelet-poor layer, buffy-coat PRP, and erythrocytes (from the top to bottom layer). The two upper layers were transferred to a fresh tube and centrifuged according to the following program: acceleration for 30 s, 2700 rpm for 2 min, 2400 rpm for 4 min, 2700 rpm for 4 min, and 3000 rpm for 3 min. The superficial plasma was discarded, and the remaining precipitated platelets were collected as PRP.

To keep the factor bioactivity, PRP was fabricated just before use and loaded on the 3D-printed scaffolds. Before *in vitro* and *in vivo* biological tests, 1 mL of PRP was extracted using a syringe and dropped on the sterilized scaffolds. The scaffolds were placed in a sterilized vacuum drying oven for 2 h to facilitate PRP infiltration into the scaffolds.

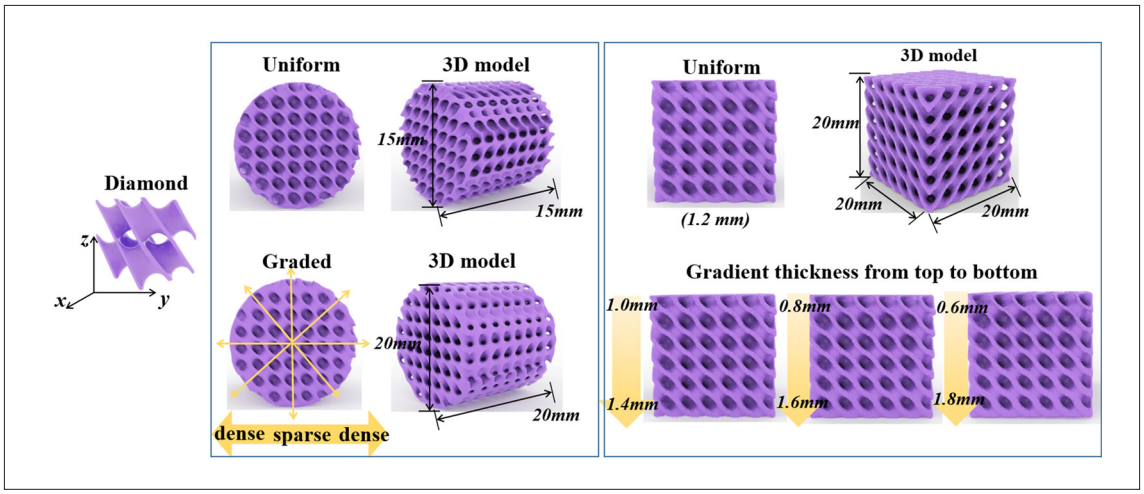


Figure 1. The model of uniform and graded diamond minimal surfaces. The graded cylindrical model is radially distributed across the wall thickness, and the graded cube has a gradient thickness vertically distributed from top to bottom.

2.5. Scaffold characterization

The surface microstructure of the scaffold structure was observed by scanning electron microscope (SEM) (QUANTA 450, FEI; Thermo Fisher Scientific, USA) after pretreatment with a thin gold layer. The internal microstructure was scanned using computed tomography (CT) (SIEMENS SOMATOM Drive; SIEMENS Healthineers, Germany). The scanning parameters were: a voltage of 70 kV, a current of 100 mA, and a slice thickness of 500 μm. The 3D models were reconstructed using SIEMENS software analysis system, Syngo Via VB40 (SIEMENS Healthineers, Germany).

The compressive property of D-surface scaffolds was tested using a universal testing machine (TSE 105D; Wance, China). According to ASTM D-695, the D-surface samples were evaluated at a constant rate of 1 mm/min. The force and displacement curves were recorded, and the compression process was pictured per 1 s by an advanced contactless charge-coupled device. Each group of samples had three parallel samples, and the average value with standard error bars was presented.

A micro-CT scanner (Xradia 610 Versa; Zeiss, Germany) was used to scan the internal structure of bone-implanted scaffolds. The scanning power and voltage were 8.5 W and 70 kV, respectively. The sliced image was collected at every 30 μm and subsequently reconstructed into 3D models using Dragonfly software (Zeiss, Germany).

2.6. *In vitro* studies

2.6.1. Cell culture

Cell culture was performed using mouse fibrosis L929 (Cell Bank of Typical Culture Preservation Committee of Chinese Academy of Sciences, China) and mouse osteoblast MC3T3-E1 subclone 14 (Shanghai Zhongqiao Xinzhou Biotech Co., Ltd., China). Roswell Park Memorial Institute (RPMI 1640; Gibco, USA) and Minimum Essential Medium (α-MEM; Gibco, USA), supplemented with 10% fetal bovine serum (FBS) and penicillin/streptomycin, were selected for cell culture. Trypsin-EDTA solution (0.25%; Gibco, USA) was used for subculture, and L929 cells were cultured at 95% humidity and 5% CO_2 at 37°C.

2.6.2. Proliferation on 3D-printed D-scaffolds

Two scaffold groups were selected, i.e., bare scaffolds and PRP-loaded D-scaffolds. Prior to cell culture, the scaffolds were washed three times with phosphate-buffered saline (PBS) (Hyclone, USA) and sterilized using 70% ethanol solution accompanied by ultraviolet (UV) irradiation. L929 cells with a density of 3×10^3 cells/mL were pre-seeded into the graded D-surface scaffolds and incubated in a 96-well plate at 37°C with 5% CO_2 and 95% humidity for 4 h. Later, the medium culture was discarded to remove the non-adherent cells, and fresh medium was supplied. After 24, 48, and 96 h, the medium was removed from the 96-well plate and washed with sterilized PBS. Thereafter, 100 μL of 10% Cell Counting Kit-8 (CCK8) working solution (XCM BIOTECH, China) was added and incubated for 2 h. The optical density (OD) value of the reaction solution was measured at 450 nm using a microplate reader.

2.6.3. Calcein AM and nuclear propidium iodide staining

The scaffolds cultured after 24, 48, and 96 h were stained, and the cell morphology was analyzed accordingly. Calcein AM and PI dye (Beyotime, China) were added and incubated for 30 min. The scaffolds were then washed with PBS and observed under an inverted phase contrast fluorescence microscope (LEICA, Germany).

2.6.4. Alkaline phosphatase assay

A density of 4×10^4 cells/mL of MC3T3-E1 subclone 14 was seeded on cell plates, sterilized scaffolds, and PRP-loaded scaffolds, and their alkaline phosphatase (ALP) activity was detected by using a kit (XCM BIOTECH, China) after 7 and 14 days of incubation. When the cells reached 70–80% confluence, the osteogenic media supplemented with 10 mM β-glycerophosphate (Macklin, China) and 0.05 mg/mL L-ascorbic acid (Xilong Scientific, China) was added to each cell-seeded well. On days 7 and 14, the BCA protein concentration assay kit (XCM BIOTECH, China) was used to detect the total protein concentration for each group. The relative ALP activity was measured by normalizing the ALP activity (obtained at λ = 405 nm) with total protein concentration (obtained at λ =562 nm). Each sample group was evaluated in triplicates.

2.7. *In vivo* studies

A total of six New Zealand white rabbits (2.5 ± 0.1 kg) were purchased from Kangda Boai Biotechnology Co., Ltd., China. The rabbits were anesthetized using 1 mL/kg of 3% pentobarbital sodium via auricular vein infusion and 0.1 mL/kg for adequate anesthesia. The distal lateral leg was then shaved and disinfected. The skin was incised at the target surgical sites and disinfected using iodophor. A 1-cm-long incision was made in the distal lateral leg. A low-speed electric drill was used to induce 4 × 8 mm bone defects. The sterilized PRP-loaded graded scaffolds (8 mm in height with a diameter of 4 mm) were then implanted in the bone defect. The bare PBAT/PLA scaffold and the unfilled defect were set as controls.

One week after surgery, the rabbits were examined by CT. Then the rabbits were euthanized, and the implanted

scaffold with surrounding tissues was examined by micro-CT and histological analysis. The implanted scaffold with tissues was fixed overnight with 4% paraformaldehyde and scanned using micro-CT (Xradia 610, 70 kV, 8.5 W; Zeiss, Germany). The fixed scaffolds were then embedded in paraffin, sliced in 4-μm thickness, and stained by hematoxylin-eosin (H&E). All protocols were approved by the Institutional Animal Ethical Committee (IAEC) of The Second Affiliated Hospital of Dalian Medical University (approval no: AEE22048). All methods were performed in accordance with relevant guidelines and regulations.

2.8. Statistical analysis

Quantitative data are presented as the mean ± standard deviation (SD). One-way Analysis of Variance (ANOVA) and subsequent comparisons between each group of scaffolds were analyzed using SPSS 25.0 statistics software.

3. Results and discussion

3.1. 3D printing of uniform and graded diamond surface structures

To better mimic natural bone, graded structures were additively manufactured with two modes of gradient thickness, i.e., radially from center to edge and vertically from top to bottom (Figure 2). For the cylindrical sample, the central part of the porous structure was sparser than the outer edge, suggesting an increasing thickness from center to edge. In contrast, the wall thickness of the cube sample became thicker closer to the bottom. As the thickness increased, the porous size became smaller. The successful FFF-printed D-surfaces suggested the printability of PBAT/PLA into fine lattice structures. Good ductility of PBAT/PLA has been demonstrated with an ultimate fracture strength and elongation at break of 19 MPa and 350%, respectively.[19]

Since FFF is a layer-by-layer deposition technique, the printing quality is important for the structures' mechanical performance. The internal 3D structure of D-surfaces was observed by CT. Figure 3 features the reconstruction and slicing images of uniform and graded D-surfaces (0.8–1.6 mm) in the x–z plane. In Figure 3a, the D-surface sample has a thickness of 1.2 mm. The homogeneous D-surface displayed uniform thickness, and the cellular topology was confirmed via sliced images. From the sliced images, the D-surface exhibited a continuous 3D lattice structure with no obvious manufacturing defects, making it beneficial for load-carrying and stress transfer. Besides, the interconnected porous structure would be favored for nutrient exchange and waste metabolism as tissue engineering scaffolds.[30] In Figure 3b, the graded D-surfaces also displayed high printing quality. Notably, the gradient thickness along the z-axis is distinctive from top to bottom. In the graded samples, the porous structure became smaller due to the increase in thickness. Accordingly, the FFF technique is suitable for manufacturing complex lattice structures.

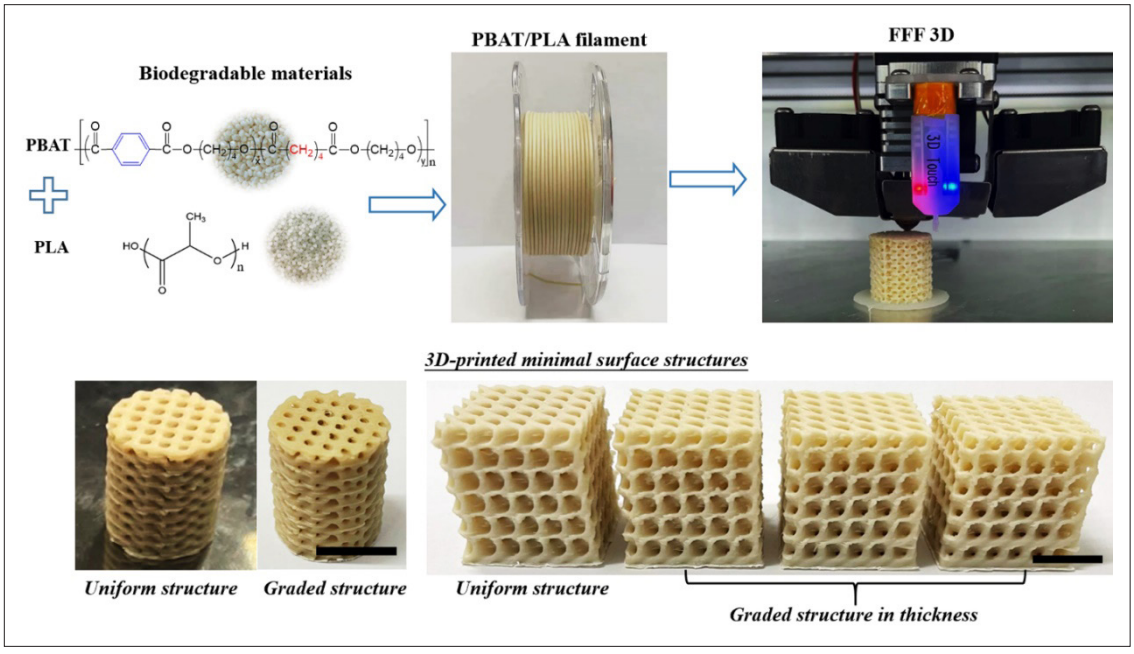


Figure 2. 3D-printed uniform and graded cylindrical and cubic diamond (D)-surface samples. Scale bar: 10 mm. Abbreviations: FFF: fused filament fabrication; PBAT/PLA: poly(butylene adipate-co-terephthalate)/poly(lactic acid).

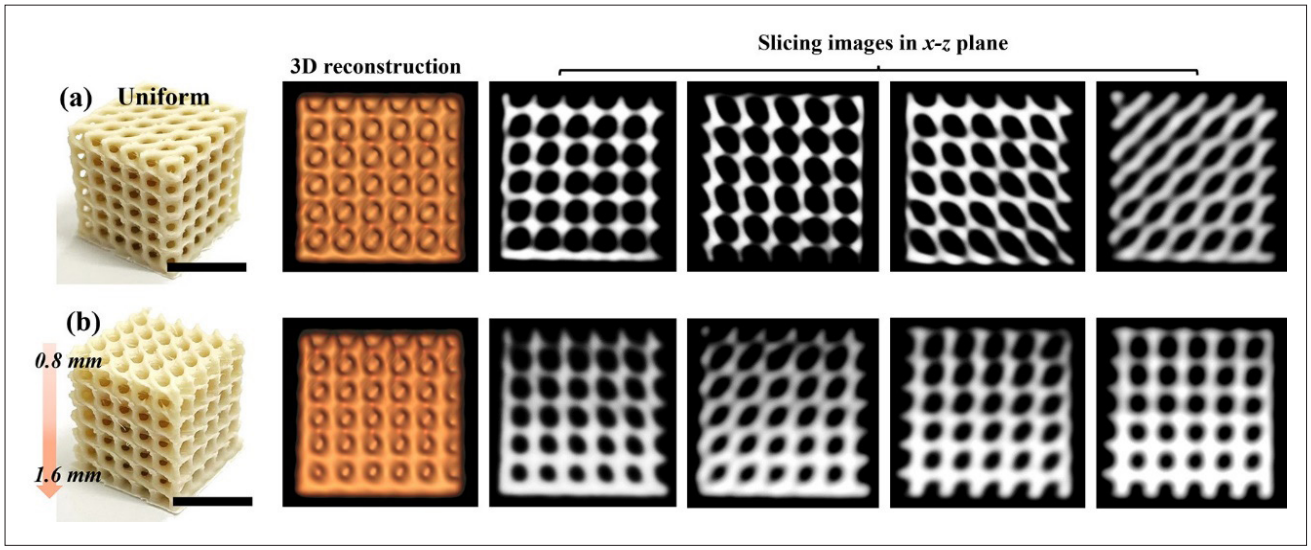


Figure 3. Computed tomography (CT) reconstruction and sliced images of uniform (1.2 mm) and graded (0.8–1.6 mm) diamond (D)-surfaces using poly(butylene adipate-co-terephthalate)/poly(lactic acid) (PBAT/PLA) filaments. Scale bars: 10 mm.

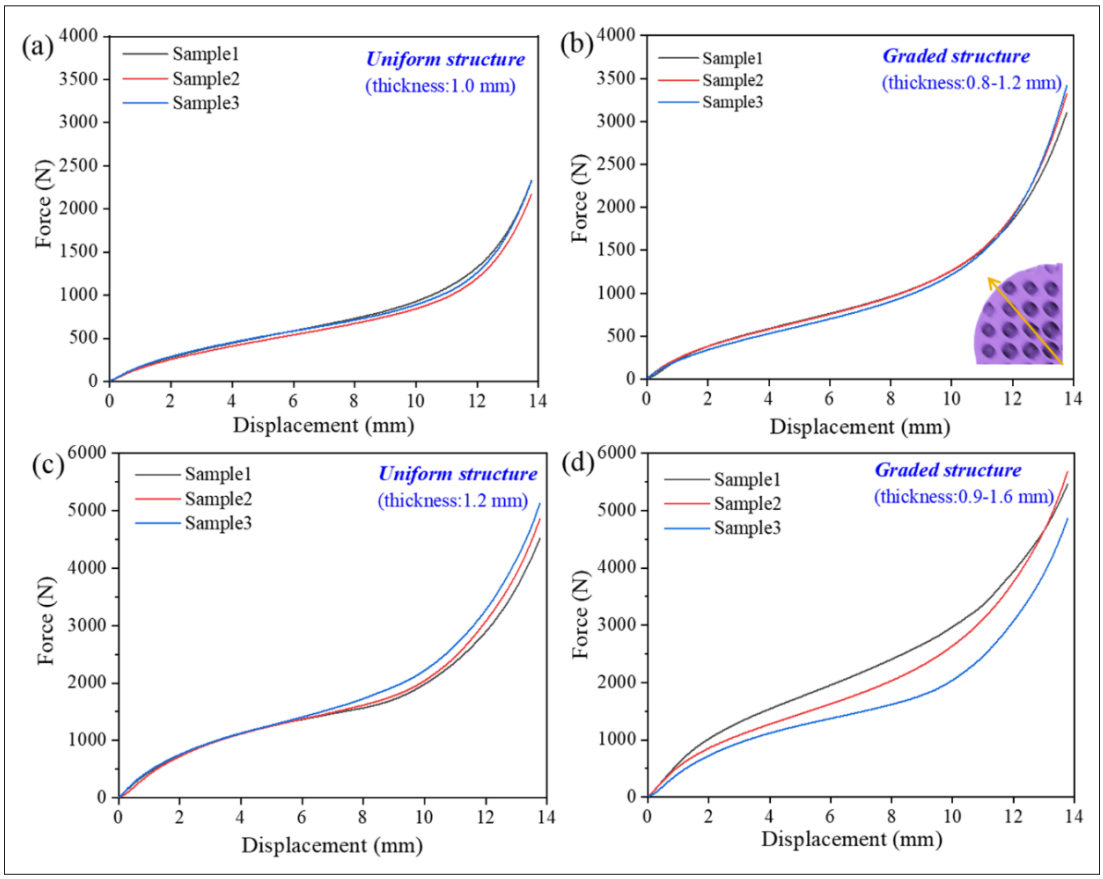


Figure 4. Force–displacement curves of 3D-printed graded diamond (D)-surface structures with (a) uniform thickness of 1.0 mm, (b) graded thickness (0.8–1.2 mm) from center to outer edge, (c) uniform thickness of 1.2 mm, and (d) graded thickness (0.9–1.6 mm) using poly(butylene adipate-co-terephthalate)/poly(lactic acid) (PBAT/PLA) filaments. The relative densities are similar for (a) and (b) and (c) and (d), respectively.

3.2. Load-carrying capacity of graded D-surface structures

3.2.1. Compressive behavior of uniform and graded D-surface structures from center to outer edge

The load-carrying and energy absorption capacity are important factors when applied as tissue engineering scaffolds to ensure sufficient support at bone defect sites. Therefore, the compression performance of uniform and graded D-surface structures was assessed accordingly. Two gradient design patterns were considered, including a radial and a vertical pattern (Figure 1). The former is similar to the natural bone, with outer cortical and inner cancellous bone structures. Figure 4 indicates the compression force–displacement curves of uniform and graded D-surface cylindrical samples. Since PBAT/PLA possesses excellent ductility, the compression tests were terminated at a compression displacement strain of 70%. For all samples, each group was prepared with three parallel specimens, and the corresponding curves indicated high reproducibility. All the curves exhibited a similar response, consisting of an elastic stage, a plateau, and a densification stage. The curves increased steadily with increasing displacement, suggesting a plastic deformation of the D-surface samples.

Uniform D-surface samples with 1.2 mm thickness could withstand an enhanced compressive force during the whole compressive process (Figure 4a and c). The load-bearing capacity also increased with increasing wall thickness. Furthermore, the designed samples could withstand a higher compressive force in contrast with the uniform samples of the same relative density (Figure 4b and d). This is mainly attributed to the larger thickness in the outer edge providing support under external force, similar to the pressure of natural bone. Accordingly, the biomimetic D-surface structure provides good deformation resistance and possesses superior mechanical performance, making these structures ideal candidates as tissue scaffolds.[31]

The buckling process of PBAT/PLA D-surface scaffolds with uniform and gradient wall thickness at different compression strains is presented in Figure 5. The deformation behavior displayed no notable variation between the uniform and graded samples. When the

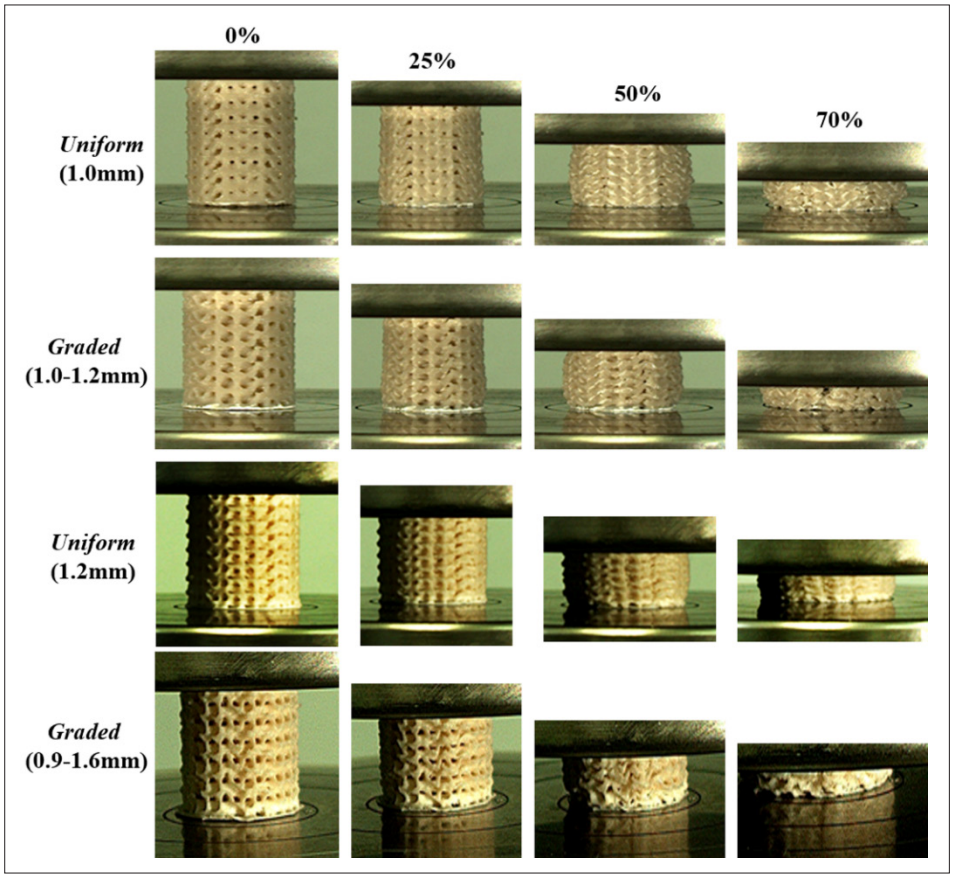


Figure 5. Compression deformation process of diamond (D)-surface cylindrical samples.

compression force is loaded, the D-surface samples demonstrated an overall bulky deformation mechanism, revealing good stress transfer throughout the sample. No obvious cracking or brittle breaking was observed, suggesting the good toughness of the PBAT/PLA material.

Based on the compression force–displacement curves, the total energy absorption (EA) represents the total energy absorbed during the entire compression process, and the specific energy absorption (SEA) per unit mass of lattice structures is calculated using the following equations:

$$EA = \int_0^d F \, d\delta \tag{2}$$

$$SEA = \frac{EA}{m} \tag{3}$$

where F is the compression force, δ is the displacement, d is the final displacement, and m is the mass of the lattice structures.

The comparison of energy absorption between the uniform and graded samples is presented in Figure 6. As the compression strain increases, SEA exhibits a linear upward trend for all the D-surface samples. The energy absorption displayed a steady increase. For the uniform structure, the absorbed energy increased with increasing wall thickness. The SEA value for the uniform D-surface structure with 1.0 mm thickness was 2702.12 J/g, whereas that of the uniform D-surface structure with 1.2 mm thickness was as high as 6752.50 J/g, corresponding to nearly 150% enhancement. In contrast, the graded samples displayed superior energy absorption capacity over the uniform samples at the same relative density. For example, the SEA value of graded D-surface samples was 8313.30 J/g, which was 23% higher than that of the uniform control with 1.2 mm. This was mainly due to thicker-edged samples providing stronger support against the external compression force.

3.2.2. Compressive behavior of uniform and graded D-surface structures from top to bottom

The second gradient pattern for the graded D-surfaces is a cubic structure with gradient thickness from top to bottom. The sparse structure at one end would be more suitable to be applied as the cancellous femur head structure. To explore the gradient thickness on the compression performance, three thickness gradients, including 0.6–1.8, 0.8–1.6, and 1.0–1.4 mm, were adopted in contrast with the control having a thickness of 1.2 mm. The force–displacement curves and histograms of SEA values are displayed in Figure 7. All graded samples exhibited better compression performance than the uniform sample. In general, the plateau stage corresponded to the main compression load and the most energy absorbed. In Figure 7a, the plateau region of graded samples was higher than the uniform sample, suggesting a superior carrying and energy absorption capacity. Both graded D-surface samples in the thickness range of 0.6–1.8 and 0.8–1.6 mm reached an SEA of approximately 7700 J/g, while the uniform sample had an SEA of 5738.3 J/g. The excellent compression performance of the second gradient model is mainly attributed to the thicker wall at the bottom, contributing to a robust support and stress-transfer process throughout the bulky samples.

To further explore the influence of cubic D-surfaces with gradient thickness on deformation behavior, the compression process was evaluated and the uniform and

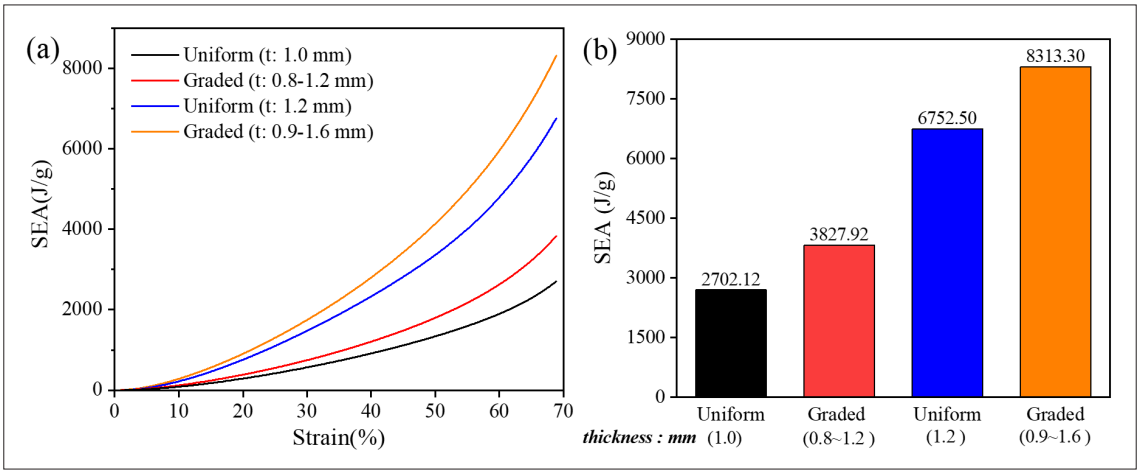


Figure 6. The energy absorption capacity for uniform and gradient D-surface scaffolds. (a) The specific absorbed energy versus compression strain, and the (b) histogram representation for uniform and graded cylindrical samples. Abbreviations: SEA: specific energy absorption; *t*: thickness.

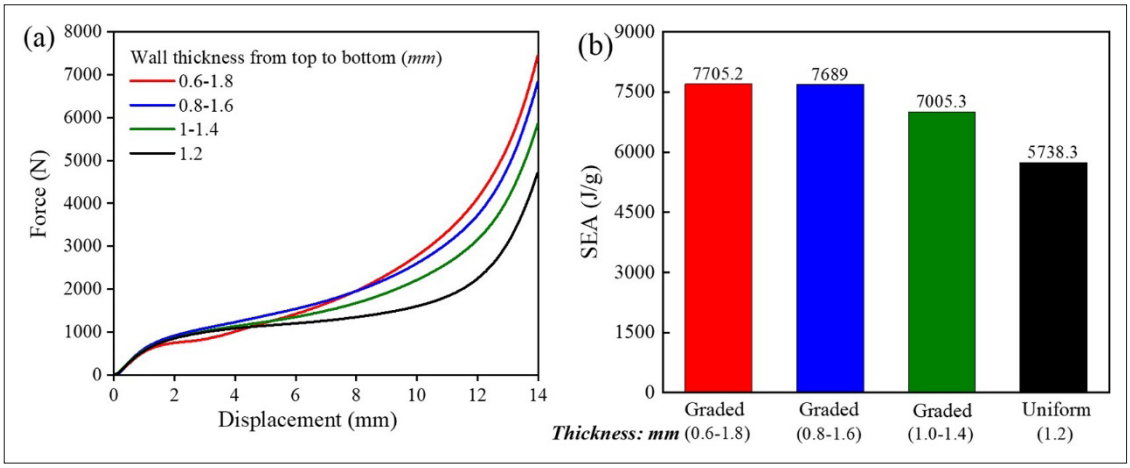


Figure 7. XXX (a) The compression force–displacement curve of cubic diamond (D)-surface samples with varying thickness, and the corresponding (b) histogram of specific energy absorption (SEA) values.

graded compressed samples were analyzed by CT scanning. Figure 8 displays the uniform D-surfaces with a thickness of 1.2 mm and representative graded samples with a thickness range of 0.8–1.6 mm. As presented in Figure 8a, the 3D-printed D-surface sample exhibited plastic deformation under large compression displacement, and the whole sample kept an overall deformation without cracks or disintegration in the internal microstructure. For the compressive performance of gradient D-scaffolds, large deformation at the compressive strain of 70% was sufficient to exhibit the entire buckling process, including the initial yielding, plateau, and densification stages. After compression at the strain of 70%, the sample height rebounded to some extent, suggesting the resilience of PBAT/PLA materials. The sliced images displayed the material imaging along the *x*–*z* plane. It could be observed that the interconnected and porous structures were well preserved after compression. Deformed and distorted walls were observed in the entire sample, suggesting a uniform deformation. In contrast, the graded D-surface sample exhibited a similar failure mechanism. An overall outward expansion was observed, and the deformation was slightly

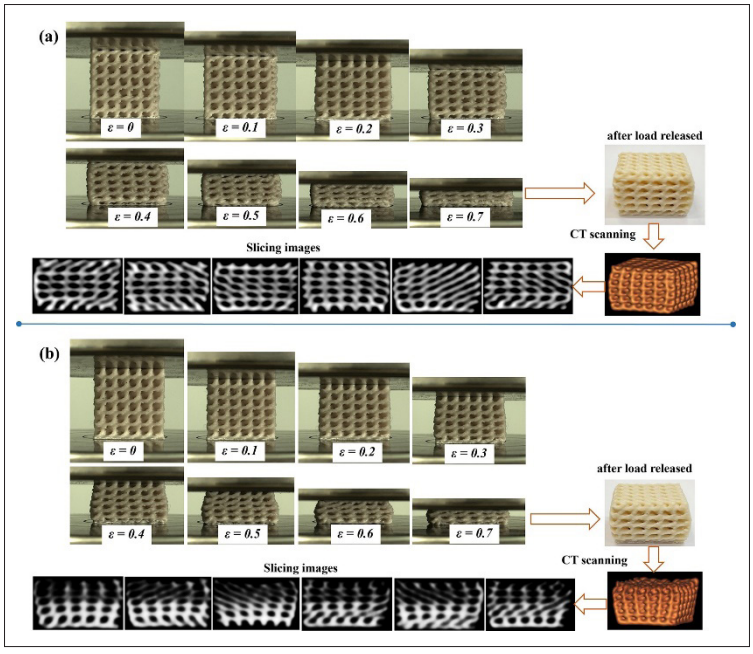


Figure 8. The compressive process of (a) uniform diamond (D)-surface samples with a thickness of 1.2 mm and the compressed sample obtained via computed tomography (CT) scanning and (b) graded D-surface sample with a thickness range of 0.8–1.6 mm and the compressed sample obtained via CT scanning. Abbreviation: *ε*: compressive strain.

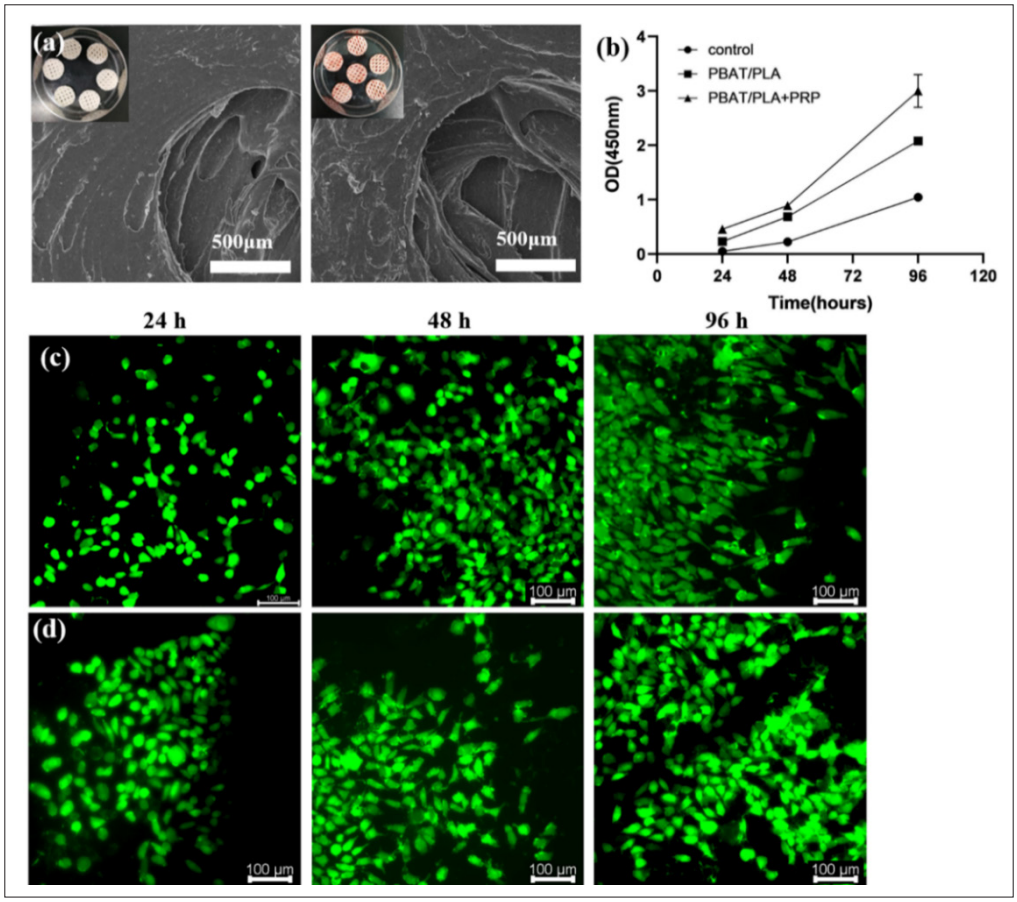


Figure 9. The *in vitro* biological performance of D-surface scaffolds. (a) Microstructure of the samples obtained with scanning electron microscopy (SEM). (b) Cell Counting Kit-8 (CCK-8) assay results of the L929 culture. (c and d) Fluorescence imaging of (c) the poly(butylene adipate-co-terephthalate)/poly(lactic acid) (PBAT/PLA) scaffolds and (d) PBAT/PLA with platelet-rich plasma (PBAT/PLA+PRP) scaffolds proliferated for 24, 48, and 96 h. Scale bars: (a) 500 μm; (c and d) 100 μm. Magnification: 200×. Abbreviation: OD: optical density.

different from the uniform sample. The large deformation tended to concentrate on the region with thinner thickness, and the thicker bottom part well supported the external load, correlating to the enhanced compression performance of the graded samples. Therefore, the graded D-surface structures have a good load-carrying and energy absorption capacity, making them suitable as bone implants and tissue engineering scaffolds.

3.3. *In vitro* biocompatibility of scaffolds

3.3.1. Cell viability

The surface of the bare and the PRP-loaded (PBAT/PLA+PRP) scaffolds was observed by SEM. It could be observed that the PBAT/PLA+PRP scaffold was coated with a thin PRP layer (Figure 9a). The viability of L929 fibroblasts was assayed by comparing between the PRP-loaded scaffold, the bare scaffold, and the cell plate (control). The CCK-8 assay results demonstrated that the PBAT/PLA+PRP scaffold exhibited an enhanced OD value, suggesting enhanced cell proliferation with prolonged culture time (Figure 9b). Cell proliferation on the PBAT/PLA and PBAT/PLA+PRP scaffolds was then observed through fluorescence staining. After 24 h of cell culture, the live cells were attached to the scaffolds, exhibiting a clear porous structure. As the cell culture continued, the amount of live cells sharply increased, and no PI-stained dead cells were detected. The cell viability assay demonstrated that both the PBAT/PLA and PBAT/PLA+PRP scaffolds possess good biocompatibility, and the PRP layer promoted cell proliferation.[32]

3.3.2. Mineralization activity

The ALP activity of the 3D-printed scaffold groups was further evaluated, and the results are displayed in Figure 10. ALP is an early-stage indicator to assess osteoblast differentiation. As displayed, ALP activity increased with longer culture time. The stimulation of osteoblast differentiation was evident in the PRP-loaded scaffold group (PBAT/PLA+PRP), indicating that PRP loading

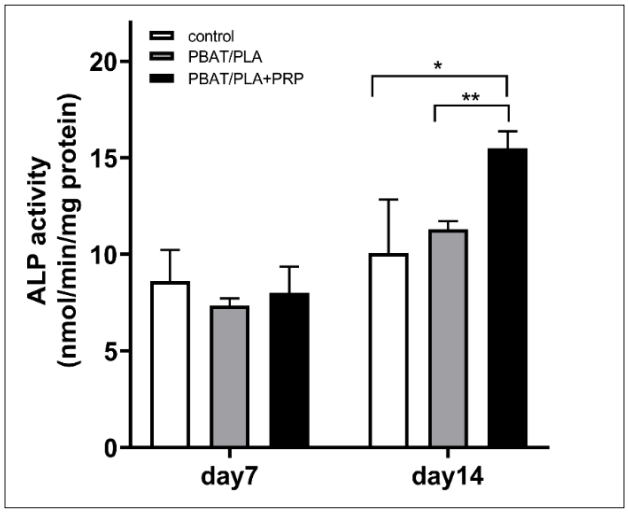


Figure 10. The alkaline phosphatase (ALP) activity in the bare (PBAT/PLA) and PRP-loaded (PBAT/PLA+PRP) scaffolds after MC3T3-E1 subclone 14 culturing for 7 and 14 days. The cell plate was set as the control. Data were analyzed by *t*-test ($n = 3$). *$p < 0.05$; **$p < 0.01$.

could accelerate mineralization via released cytokines in the osteogenic maturation process.[33]

3.4. *In vivo* biocompatibility of scaffolds

Based on the *in vitro* biocompatibility, it is critical to investigate the bone repair effect of PRP-loaded D-surface scaffolds in a pre-clinical setting. A rabbit femur defect model was created using New Zealand white rabbits. The PRP-loaded scaffolds and the operation process are displayed in Figure 11a. PBAT/PLA and PRP-loaded PBAT/PLA graded scaffolds were selected for the animal tests, and the unfilled defect was set as the control. Four weeks after implantation, the experimental rabbits recovered well, and no postoperative infection or other complications were observed. Local femur defects with the control, PBAT/PLA, and PBAT/PLA+PRP scaffolds are presented in Figure 11b. Histological analysis of the bone repair induced by different scaffolds for the rabbit defect models is presented in Figure 11c–e. Four weeks after implantation, fibrous tissue (F) proliferation, new bone

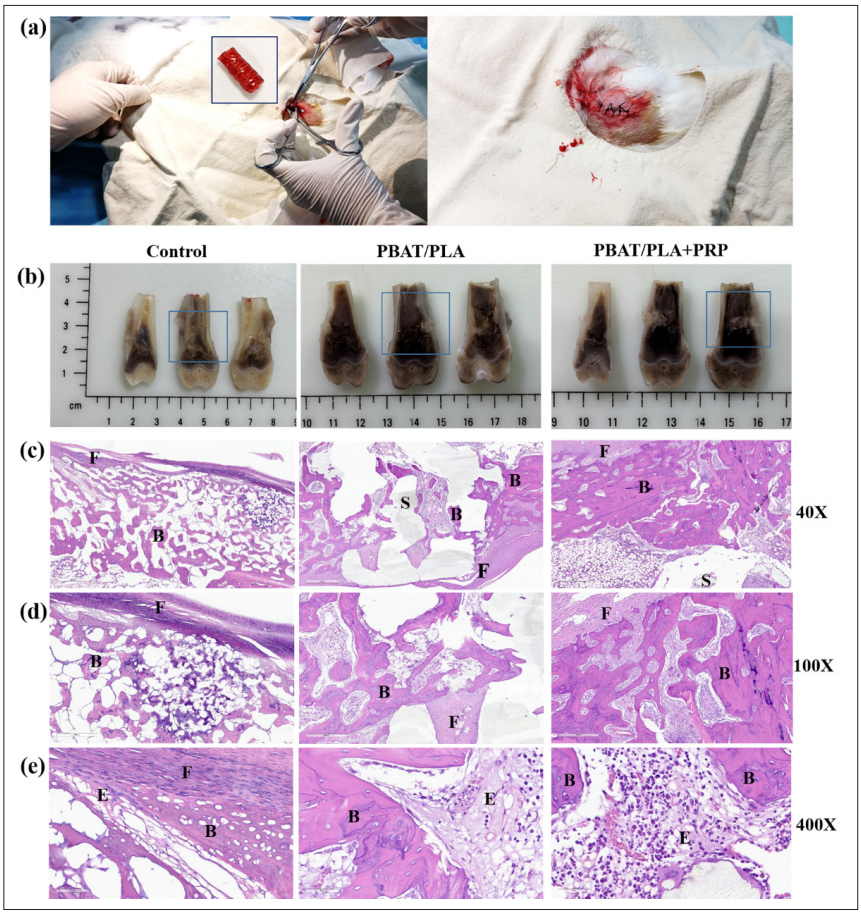


Figure 11. The *in vivo* biological performance of implanted D-surface scaffolds. (a) Platelet-rich plasma (PRP)-loaded scaffolds implanted in the rabbit defect. (b) Femurs with implanted scaffolds. (c–e) Hematoxylin-eosin (H&E) staining images of the control, poly(butylene adipate-co-terephthalate)/poly(lactic acid) (PBAT/PLA) scaffold, and PBAT/PLA+PRP scaffold. Magnification: (c) 40×, (d) 100×, and (e) 400×. Abbreviations: B: new bone tissue; S: scaffolds; E: edema; F: fibrous tissue.

(B) formation, and mild edema (E) were observed among the three groups of bone cortex.[34] It was noticeable that the PBAT/PLA+PRP scaffold has a much higher degree of bone generation than those in the PBAT/PLA and control scaffolds. Overall, the *in vitro* study results indicated that the D-surface scaffold groups have sufficient surface area for cell attachment, migration, and proliferation. The PRP-loaded scaffolds have demonstrated the release of bioactivity factors to foster an early-stage conducive 3D microenvironment for osteoblasts.

Rabbit femurs with the PBAT/PLA+PRP scaffold were monitored and scanned by a clinical CT at 1, 2, and 4 weeks after implantation. The scanned sliced images were collected and reconstituted. By using the volume rendering technique and multi-planner reformation technique, the bone parameter

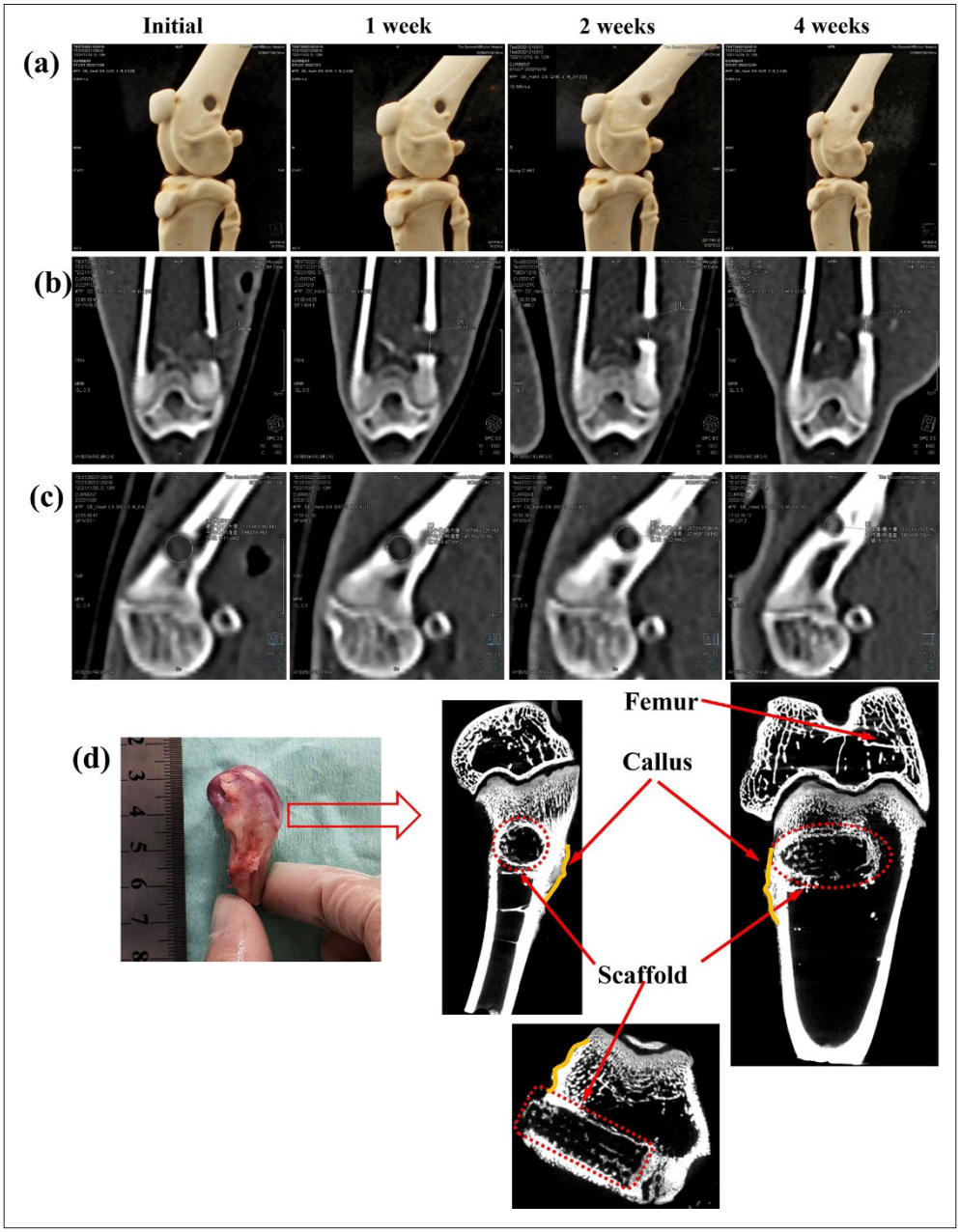


Figure 12. Clinical computed tomography (CT) scanning of the experimental rabbit, and the reconstituted images based on (a) volume rendering technique (VRT) and (b and c) multi-planner reformation (MPR) from different views. (d) The poly(butylene adipate-co-terephthalate)/poly(lactic acid) with platelet-rich plasma (PBAT/PLA+PRP) scaffold implanted in the rabbit femur, and the reconstituted images scanned by micro-CT 4 weeks after implantation.

analysis was measured from the testing data (Figure 12a–c). The results demonstrated that the implantation of PRP-loaded scaffolds effectively promoted the generation of new bone with decreased defect size (Figure 12a). From the side view, the defect length was decreased from 0.39 to 0.37, 0.35, and 0.28 cm at 1, 2, and 4 weeks after implantation, respectively. From the top view, the defect area was 11, 9.47, 8.32, and 6.99 mm^2 at 0, 1, 2, and 4 weeks after implantation, indicating enhanced bone repair. Moreover, 4 weeks after implantation, the femur containing the PBAT/PLA+PRP scaffolds was collected. It was observed that PRP-loaded scaffolds stimulated the formation of evident calluses surrounding the defect sites. The scaffolds were not detected since the polymeric materials were radiolucent in contrast with the femur bone. Specifically, some new-generated bone tissues were observed in the porous scaffolds, suggesting effective new bone formation. Both clinical CT and micro-CT demonstrated that PRP exhibited a positive effect on the formation of new bones.[35,36]

4. Conclusion

In this paper, biodegradable PBAT/PLA tissue engineering scaffolds with biomimetic structures and bioactive PRP-loading were successfully fabricated by FFF 3D printing technology. The key properties including the mechanical and biological performance were explored.

For the structural design, the graded D-surface structure was proposed and generated by Rhino software, including a gradient thickness from top to bottom and from center to outer edge. The mechanical performance of the 3D-printed scaffolds demonstrated that both the two kinds of graded samples exhibit better load-carrying and energy absorption capacity than the uniform structures with the same relative density. The interconnected and continuous surface structures endowed the D-surface scaffolds with robust and stable support, making them a good candidate as artificial scaffolds. The internal microstructure examined by CT confirmed the variation in thickness for the D-surface scaffolds. Meanwhile, after compression loading, no obvious damage was detected in the deformed scaffold samples, highlighting the toughness of the biodegradable composite materials.

Subsequently, PRP with diverse cytokines was loaded on the graded scaffolds, and the *in vitro* cell biological activity suggests an enhancement in cell proliferation and osteoblast differentiation. Furthermore, the PRP-loaded D-surface scaffold displayed enhanced early-stage bone regeneration for femoral condyle defect repair. More new bone tissues were formed in PBAT/PLA+PRP scaffolds when implanted in the rabbit femur defects compared to the other samples, and the defect size was greatly reduced four weeks after implantation.

Therefore, the current work offers insights into the structural design of minimal surface and material bioactivity for bone scaffolds, fostering the development of bone implants through a bionics perspective.

Acknowledgments

None.

Funding

This work was financially supported by the National Natural Science Foundation of China (No. 52175216), the Fundamental Research Funds for the Central Universities (DUT23YG220), the "1+X" program for Clinical Competency Enhancement–Interdisciplinary Innovation Project, the Second Hospital of Dalian Medical University (No. 2022JCXKYB21), and the Dalian Medical University Interdisciplinary Research Cooperation Project Team Funding (JCHZ2023011).

Conflict of interest

The authors declare no conflicts of interest.

Author contributions

Conceptualization: Yiping Zhao, Shanglian Ju
Formal analysis: Fei Wang, Jiawei Hu
Investigation: Yiping Zhao, Shanglian Ju, Jiawei Hu, Kun Guo, Lin Sang, Tang Liu, Yuxin Lin
Methodology: Tang Liu, Yuxin Liu
Writing – original draft: Tang Liu, Lin Sang
Writing – review & editing: Yiping Zhao, Kun Guo, Xiaohong Shu

Ethics approval and consent to participate

Experimental animal research was approved by the Animal Ethics Committee (IAEC) of the Dalian Medical University (approval number: AEE22048).

Consent for publication

Not applicable.

Availability of data

Data that support the findings of this study are available from the corresponding authors upon reasonable request.

References

1. Zhang YT, Aiyiti W, Du S, Jia R, Jiang HF. Design and mechanical behaviors of a novel tantalum lattice structure fabricated by SLM. *Virtual Phys Prototy*. 2023;18(1):2192702. doi: 10.1080/17452759.2023.2192702
2. Chang CM, Wong PC, Ou SL, Ko CE, Wang YT. Optimizing implant lattice design for large distal femur defects: stimulating interface bone growth to enhance osseointegration. *Int J Bioprint.* 2024;10:544-562. doi: 10.36922/ijb.2590
3. Cuan-Urquizo E, Silva RG. Fused filament fabrication of cellular, lattice and porous mechanical metamaterials: a review. *Virtual Phys Prototy*. 2023;18:2224300. doi: 10.1080/17452759.2023.2224300
4. Maskery I, Ashcroft IA. The deformation and elastic anisotropy of a new gyroid-based honeycomb made by laser sintering. *Addi Manuf*. 2020;36:101548. doi: 10.1016/j.addma.2020.101548
5. Xi HF, Zhou ZC, Zhang HH, Huang SQ, Xiao H. Multi-morphology TPMS structures with multi-stage yield stress platform and multi-level energy absorption: design, manufacturing, and mechanical properties. *Eng Struct*. 2023;294:116733. doi: 10.1016/j.engstruct.2023.116733
6. Yin HF, Tan DW, Wen GL, Tian WY, Wu QK. Crashworthiness analysis and optimization design of TPMS-filled structure. *Int J Crashworthiness*. 2022;27:1481-1498. doi: 10.1080/13588265.2021.1959171
7. Wang HW, Chen CH, Chen KH, Zeng YH, Lin CL. Designing a 3D-printed medical implant with mechanically macrostructural topology and microbionic lattices: a novel wedge-shaped spacer for high tibial osteotomy and biomechanical study. *Int J Bioprint*. 2024;10:1584. doi: 10.36922/ijb.1584
8. Wang XB, Zhang L, Song B, et al. Anisotropic mechanical and mass-transport performance of Ti6Al4V plate-lattice scaffolds prepared by laser powder bed fusion. *Acta Biomater.* 2022;148:374-388. doi: 10.1016/j.actbio.2022.06.016
9. Fu H, Huang X, Kaewunruen S. Experimental investigations into nonlinear dynamic behaviours of triply periodical minimal surface structures. *Compos Struct*. 2023;323:117510. doi: 10.1016/j.compstruct.2023.117510
10. Cai JX, Ma YB, Deng ZC. On the effective elastic modulus of the ribbed structure based on Schwarz Primitive triply periodic minimal surface. *Thin Wall Struct*. 2022;170:108642. doi: 10.1016/j.tws.2021.108642
11. Oh SH, An CH, Seo B, Kim J, Park CY, Park K. Functional morphology change of TPMS structures for design and additive manufacturing of compact heat exchangers. *Addi Manuf*. 2023;76:103778. doi: 10.1016/j.addma.2023.103778
12. Reynolds BW, Fee CJ, Morison KR, Holland DJ. Characterisation of heat transfer within 3D printed TPMS heat exchangers. *Int J Heat Mass Transfer*. 2023;212:124264. doi: 10.1016/j.ijheatmasstransfer.2023.124264
13. Sang L, Wu WY, Sun ZQ, et al. Reusability and energy absorption behavior of 4D-printed heterogeneous lattice structures based on biomass shape memory polyester. *J Mater Res Technol.* 2023;27:1563-1578. doi: 10.1016/j.jmrt.2023.09.323
14. Laskowska D, Szatkiewicz T, Balasz B, Mitura K. Mechanical properties and energy absorption abilities of diamond TPMS cylindrical structures fabricated by selective laser melting with 316L stainless steel. *Materials*. 2023;16:3196. doi: 10.3390/ma16083196
15. Bo L, Jiawei F, Zhiwei L, Yong H, Jianzhong F. Controllable three-dimension auxetic structure design strategies based on triply periodic minimal surfaces and the application in hip implant. *Virtual Phys Prototy*. 2023;18:e2170890. doi: 10.1080/17452759.2023.2170890
16. Zou SJ, Mu YR, Pan BC, et al. Mechanical and biological properties of enhanced porous scaffolds based on triply periodic minimal surfaces. *Mater Des.* 2022;219:110803. doi: 10.1016/j.matdes.2022.110803
17. Zhang Q, Ma LM, Ji XF, et al. High-strength hydroxyapatite scaffolds with minimal surface macrostructures for load-bearing bone regeneration. *Adv Funct Mater*. 2022;32:2204182. doi: 10.1002/adfm.202204182
18. Zhang ZH, He FT, Wang B, et al. Biodegradable PGA/PBAT blends for 3D printing: material performance and periodic minimal surface structures. *Polymers.* 2021;13(1):3757. doi: 10.3390/polym13213757
19. Cao YX, Lai SY, Wu WY, et al. Design and mechanical evaluation of additively-manufactured graded TPMS lattices with biodegradable polymer composites. *J Mater Res Technol*. 2023;23:2868-2880. doi: 10.1016/j.jmrt.2023.01.221
20. Ulbrich LM, Balbinot GD, Brotto GL, et al. 3D printing of poly(butylene adipate-co-terephthalate) (PBAT)/ niobium containing bioactive glasses (BAGNb) scaffolds: characterization of composites, in vitro bioactivity, and in vivo bone repair. *J Tissue Eng Regen Med*. 2022;16:267-278. doi: 10.1002/term.3276
21. Qiu SW, Xia YH, Sun JD, Wang SS, Xing QS. Poly (butylene adipate-co-terephthalate)/Sodium alginate blends have superior characteristics and can be used to fabricate vascular stents. *Mater Res Express*. 2022;9:055401. doi: 10.1088/2053-1591/ac6a4c
22. Zeng C, Zhang MM. 3D-printed PCL/β-TCP/CS composite artificial bone and histocompatibility study. *J Orthop Surg Res*. 2024;18:981.

doi: 10.1186/s13018-023-04489-8

23. Yeo T, Ko YG, Kim EJ, Kwon OK, Chuang HY, Kwon OH. Promoting bone regeneration by 3D-printed poly(glycolic acid)/hydroxyapatite composite scaffolds. *J Ind Eng Chem*. 2021;94:343-351.
doi: 10.1016/j.jiec.2020.11.004

24. Mushtaq RT, Wang YE, Bao CW, et al. Maximizing performance and efficiency in 3D printing of polylactic acid biomaterials: Unveiling of microstructural morphology, and implications of process parameters and modeling of the mechanical strength, surface roughness, print time, and print energy for fused filament fabricated (FFF) bioparts. *Int J Biol Macromol*. 2024;259:12920.
doi: 10.1016/j.ijbiomac.2024.129201

25. Natarajan A, Sivadas VP, Nair PD. 3D-printed biphasic scaffolds for the simultaneous regeneration of osteochondral tissues. *Biomed Mater*. 2021;16:054102.
doi: 10.1088/1748-605X/ac14cb

26. Kechagias J, Chaidas D, Vidakis N, Salonitis K, Vaxevanidis NM. Key parameters controlling surface quality and dimensional accuracy: a critical review of FFF process. *Mater Manuf Process*. 2022;37(9):963-984.
doi: 10.1080/10426914.2022.2032144

27. Bahraminasab M, Doostmohammadi N, Talebi A, et al. 3D printed polylactic acid/gelatin-nano-hydroxyapatite/platelet-rich plasma scaffold for critical-sized skull defect regeneration. *Biomed Eng Online*. 2022;21:86.
doi: 10.1186/s12938-022-01056-w

28. Wei L, Wu SH, Kuss M, et al. 3D printing of silk fibroin-based hybrid scaffold treated with platelet rich plasma for bone tissue engineering. *Bioact Mater*. 2019;4:256-260.
doi: 10.1016/j.bioactmat.2019.09.001

29. Liu W, Sang L, Zhang ZH, Ju SL, Wang F, Zhao YP. Compression and resilient behavior of graded triply periodic minimal surface structures with soft materials fabricated by fused filament fabrication. *J Manuf Process*. 2023;105:1-13.
doi: 10.1016/j.jmapro.2023.09.034

30. Huang SF, Chang CM, Lian CY, Chan YT, Liu ZY, Lin CL. Biomechanical evaluation of an osteoporotic anatomical 3D printed posterior lumbar interbody fusion cage with internal lattice design based on weighted topology optimization. *Int J Bioprinting*. 2023,9:697.
doi: 10.18063/ijb.697

31. Liu QY, Wei F, Coathup M, Shen W, Wu DZ. Effect of porosity and pore shape on the mechanical and biological properties of additively manufactured bone scaffolds. *Adv Healthc Mater*. 2023;12:2301111.
doi: 10.1002/adhm.202301111

32. Seker S, Aral D, Elcin AE, Murat EY. Biomimetic mineralization of platelet lysate/oxidized dextran cryogel as a macroporous 3D composite scaffold for bone repair. *Biomed Mater*. 2024;19:025006.
doi: 10.1088/1748-605X/ad1c9a

33. Li ZL, Wang YX, Zhao CK, et al. Polysaccharide hybrid scaffold encapsulated endogenous factors for microfracture enhancement by sustainable release and cell recruitment. *Compos Part B Eng*. 2024;273:111235.
doi: 10.1016/j.compositesb.2024.111235

34. Xue P, Tan XX, Xi HZ, et al. Low-temperature deposition 3D printing biotin-doped PLGA/β-TCP scaffold for repair of bone defects in osteonecrosis of femoral head. *Int J Bioprint*. 2024;10:1152.
doi: 10.36922/ijb.1152

35. Gao X, Wang H, Luan S, Zhou G. Low-temperature printed hierarchically porous induced-biomineralization polyaryletherketone scaffold for bone tissue engineering. *Adv Healthc Mater*. 2022;11:e2200977.
doi: 10.1002/adhm.202200977

36. Zhu H, Lin ZH, Luan QF, et al. Angiogenesis-promoting composite TPMS bone tissue engineering scaffold for mandibular defect regeneration. *Int J Bioprint*. 2024;10(1);0153.
doi: 10.36922/ijb.0153

ACCSCIENCE PUBLISHING

International Journal of Bioprinting

RESEARCH ARTICLE

Spatiotemporal delivery of BMP-2 and FGF-18 in 3D-bioprinted tri-phasic osteochondral scaffolds enhanced compartmentalized osteogenic and chondrogenic differentiation of mesenchymal stem cells isolated from rats with varied organizational morphologies

Weiwei Su[1,2†], Shiyu Li[1,3†], Panjing Yin[1,3†], Weihan Zheng[1,3], Ling Wang[4], Zhuosheng Lin[1], Ziyue Li[1,3], Zi Yan[1,3], Yaobin Wu[1*], Chong Wang[5*], and Wenhua Huang[1,2,3*]

[1]Guangdong Engineering Research Center for Translation of Medical 3D Printing Application, Guangdong Provincial Key Laboratory of Digital Medicine and Biomechanics, National Key Discipline of Human Anatomy, School of Basic Medical Sciences, Southern Medical University, Guangzhou, Guangdong, China

[2]Department of Orthopedics, Affiliated Hospital of Putian University, Putian University, Putian, Fujian, China

[3]The Third Affiliated Hospital of Southern Medical University, Guangdong Medical Innovation Platform for Translation of 3D Printing Application, Southern Medical University, Guangzhou, Guangdong, China

[4]Biomaterials Research Center, School of Biomedical Engineering, Southern Medical University, Guangzhou, Guangdong, China

[5]Department of Intelligent Manufacturing Engineering, School of Mechanical Engineering, Dongguan University of Technology, Songshan Lake, Dongguan, Guangdong, China

[†]These authors contributed equally to this work.

***Corresponding authors:**
Yaobin Wu
(wuyaobin2018@smu.edu.cn)

Chong Wang
(wangchong@dgut.edu.cn)

Wenhua Huang
(hwh@smu.edu.cn)

Citation: Su W, Li S, Yin P, et al. Spatiotemporal delivery of BMP-2 and FGF-18 in 3D-bioprinted tri-phasic osteochondral scaffolds enhanced compartmentalized osteogenic and chondrogenic differentiation of mesenchymal stem cells isolated from rats with varied organizational morphologies. *Int J Bioprint*. 2024;10(5):3229. doi: 10.36922/ijb.3229

Received: March 21, 2024
Accepted: May 13, 2024
Published Online: July 2, 2024

Copyright: © 2024 Author(s). This is an Open Access article distributed under the terms of the Creative Commons Attribution License, permitting distribution, and reproduction in any medium, provided the original work is properly cited.

Publisher's Note: AccScience Publishing remains neutral with regard to jurisdictional claims in published maps and institutional affiliations.

Abstract

Replicating the heterogeneous structure and promoting compartmentalized osteogenesis/chondrogenesis are critical considerations in designing scaffolds for osteochondral tissue regeneration. However, desirable osteochondral regeneration cannot be achieved mainly due to the absence of effective delivery strategies for growth factors (GFs) and the insufficiency of desirable organizational morphologies for seed cells. Herein, we developed a tri-phasic osteochondral scaffold consisting of bone morphogenetic protein-2 (BMP-2)-loaded subchondral layer, fibroblast growth factor-18 (FGF-18)-loaded cartilage layer, and an interface layer that acted as a barrier to reduce the mutual interference of GFs, via cryogenic 3D bioprinting. BMP-2 could exert osteogenic effects for 14 days, and FGF-18 could exert chondrogenic effects for 21 days, demonstrating the time-controlled release function of BMP-2 and FGF-18. By further seeding discrete rat bone marrow mesenchymal stem cells (rBMSCs) and rBMSC microspheres, respectively, onto the subchondral layer and cartilage layer, the engineered cell-laden osteochondral tissue was constructed. The spatiotemporal release of BMP-2 and FGF-18 in the subchondral layer and cartilage layer promoted the osteogenic differentiation of discrete rBMSCs and chondrogenic differentiation of rBMSC microspheres in the subchondral layer and cartilage layer, respectively. In summary, by seeding rBMSCs with varied organizational morphologies in

3D-printed osteochondral scaffolds with a spatiotemporally controlled strategy, engineered osteochondral tissue with compartmentalized osteogenic/chondrogenic differentiation potent can be formed, displaying a facile and promising way to achieve desirable osteochondral tissue regeneration.

Keywords: 3D printing; Growth factor; Controlled release; Cell microspheres; Osteochondral regeneration; Osteogenic/chondrogenic differentiation

1. Introduction

Injury of osteochondral tissue with heterogeneous features is a common clinical problem often caused by degenerative and traumatic factors, such as age, obesity, and mechanical trauma.[1–3] Existing treatments, such as arthroscopic debridement, marrow stimulation, autologous transplantation, and allogeneic transplantation, have diverse limitations and often yield suboptimal outcomes.[4,5] In recent years, tissue engineering technology, which is composed of three key factors including seed cells, scaffolds, and growth factors (GFs), has become a desirable alternative to induce osteochondral tissue regeneration.[6,7] However, the appropriate delivery of GFs in osteochondral scaffolds, which is vital for the spatiotemporal regulation of osteogenic/chondrogenic differentiation of mesenchymal stem cells (MSCs), remains a great challenge.[8,9] Spatiotemporal control has emerged as a burgeoning research area in recent years, emphasizing the divergent impacts of drugs on tissue across both time and space.[10–12] On one hand, different GFs exert their effects at different time points, necessitating sustained GF release instead of burst GF release for regenerative therapies, highlighting the importance of time-controlled release.[8,13] On the other hand, successful repair of subchondral tissue and cartilage tissue requires distinct microenvironments and different GFs. Minimizing or excluding crosstalk between these GFs is crucial, underscoring the need for spatially controlled release.[14,15] Therefore, a spatiotemporally controlled GF release should be designed to align with the timing and location of osteogenic/chondrogenic differentiation of MSCs. This approach can facilitate the maturation of engineered cell-laden osteochondral tissue.[16,17]

It is known that bone morphogenetic protein-2 (BMP-2) released at the early phase can promote subchondral bone regeneration,[18] while fibroblast growth factor-18 (FGF-18) can facilitate cartilage regeneration at both early and mid-late phases of tissue regeneration.[19] Therefore, proposing a solution to match the different release rates of BMP-2 and FGF-18 in the subchondral layer and the cartilage layer, respectively, is of great importance. Given that the dense calcified interface layer of the native osteochondral tissue can act as a barrier to effectively prevent the mutual diffusion of GFs between the subchondral and cartilage layers,[20,21] constructing an engineered biomimetic osteochondral scaffold that can replicate the physiological structure of native osteochondral tissue. This design can reduce the diffusion of BMP-2 to the cartilage layer and FGF-18 to the subchondral layer, thereby enhancing the regional osteogenic/chondrogenic differentiation of MSCs.

Desirable cell growth and appropriate differentiation also play a key role in successful tissue engineering.[22] Previous studies suggested that the initial shape and morphologies of stem cells can also influence chondrogenic differentiation efficacy.[23,24] Although hyaline chondrocytes exhibit a rounded morphology and are distributed in hyaline cartilage lacunae as cell aggregates,[25] in most tissue engineering approaches, discrete stem cells suspended in the culture medium are directly seeded in scaffolds, and fibrochondrocytes were often obtained after chondrogenic differentiation.[26,27] Fibrocartilage is primarily found in intervertebral discs and joint discs, where it can withstand significant pressure and provide protection.[28] Conversely, hyaline cartilage is predominantly located on joint surfaces, offering a smooth surface for joint movement and dispersing impact from motion.[29] In previous studies on osteochondral tissue engineering, fibrocartilage has been identified as a marker of failure in cartilage repair.[30,31] The structure and morphology of the cytoskeleton, particularly the stability of microtubule proteins, play a critical role in determining various cellular phenotypes, which is vital for the conversion between fibrocartilage and hyaline cartilage.[32] Previous studies have demonstrated that microtubule-stabilizing drugs (e.g., docetaxel) can promote the conversion of fibrochondrocytes to hyaline chondrocytes.[33,34] However, compared to microtubule-stabilizing drugs, controlling the formation of chondrocyte cytoskeleton by adjusting the initial organizational morphology of stem cells offers a more direct approach to regulating the formation of hyaline cartilage.[35] Recently, some researchers found that MSCs with an altered initial organizational morphology (e.g., MSC aggregates) are advantageous in obtaining hyaline chondrocytes after chondrogenic differentiation.[23] Furthermore, these cell

aggregates can mimic the microstructure of cartilage lacunae and are probably more suitable for cartilage regeneration than discrete cells.

In this study, we developed a tri-phasic scaffold with a biomimetic structure and a spatiotemporally controlled delivery capability of BMP-2 and FGF-18 via cryogenic 3D bioprinting, followed by the infusion of gelatin methacrylate (GelMA) hydrogel in the cartilage layer. A poly(lactic-co-glycolic acid)/tricalcium phosphate (PLGA/TCP) interface layer was printed between the subchondral layer and cartilage layer to prevent the mutual diffusion of BMP-2 and FGF-18. Thereafter, discrete MSCs were seeded in the subchondral layer while MSC microspheres were seeded in the cartilage layer. The spatiotemporal delivery of BMP-2 and FGF-18 in the respective layers facilitated the osteogenic differentiation of discrete MSCs in the subchondral layer and the chondrogenic differentiation of MSC microspheres in the cartilage layer, respectively. This study provided an innovative strategy for constructing engineered biomimetic cell-laden osteochondral tissue with desirable MSC differentiation endpoints and displayed great potential for osteochondral regeneration.

2. Materials and methods

2.1. Materials

Poly(lactic-co-glycolic acid) (PLGA) (lactic acid [LA]:glycolic acid [GA] = 50:50) and shape-memory poly (D,L-lactic acid-co-trimethylene carbonate) (P[DLLA-TMC]) (DLLA:TMC = 80:20) were obtained from Jinan Daigang Biotechnology Ltd. (China). β-tricalcium phosphate particles (β-TCP) were purchased from Aladdin (China). BMP-2 and FGF-18 were Beyotime products (China). Dulbecco's Modified Eagle Medium (DMEM), Dulbecco's Phosphate Buffered Saline (DPBS), fetal bovine serum (FBS), penicillin (100 U/mL), streptomycin (100 U/mL), and bovine serum albumin (BSA) were purchased from Gibco (United States of America [USA]). Dichloromethane (DCM) was obtained from Macklin (China). Gelatin (derived from porcine skin; analytical grade; 99% pure), methacrylic anhydride (MA) (94%), and lithium phenyl-2, 4, 6-trimethyl benzoyl phosphinate (LAP) were purchased from Sigma-Aldrich (USA).

2.2. Preparation of bioinks for osteochondral scaffolds

Three different bioinks were prepared for the biofabrication of biomimetic osteochondral scaffolds. Firstly, 3 g PLGA was dissolved completely into 9 mL DCM, and 3 g TCP particles were then added into the solution above to obtain uniform a β-TCP/PLGA/DCM emulsion after 20 min of ultra-sonication. Approximately 1 mL of deionized (DI) water containing BMP-2 (final concentration of 1, 2, 3, and 4 μg BMP-2 per g scaffold, respectively) was subsequently added into the emulsion and stirred for 20 min, resulting in the water-in-oil bioink for the subchondral layer. Secondly, the bioink for the interface layer was prepared the same as the subchondral layer except without BMP-2. Thirdly, 6 g P(DLLA-TMC) was fully dissolved into 9 mL DCM under 20 min of ultra-sonication. Approximately 1 mL DI water containing FGF-18 (final concentration of 1, 2, 3, and 4 μg FGF-18 per g scaffold, respectively) was then added into the P(DLLA-TMC)/DCM emulsion and stirred for 20 min, resulting in the bioink for the cartilage layer. Finally, 5% GelMA hydrogel precursor with 0.2% LAP photoinitiator was added to fill the macropores of the cartilage layer with hydrogels.

2.3. Cryogenic 3D bioprinting of osteochondral scaffolds

A digital stereolithography (STL) file was imported into a cryogenic 3D bioprinter, and scaffolds with a grid pattern and gradient structure were subsequently printed. Typically, four layers of subchondral struts were printed first, followed by two layers of interface struts and four layers of cartilage struts. The subchondral and cartilage layers contained parallel rods with a length of 10 mm and a diameter of 0.4 mm; the distance between the two parallel rods was 0.8 mm. In contrast, the interface layer contained parallel rods with a length of 10 mm and a diameter of 0.2 mm; the distance between the two parallel rods was 0.2 mm. All the above rods in adjacent layers had a cross angle of 90°. Furthermore, the above biofabricated scaffolds were lyophilized for 24 h to remove DCM. After the production of the osteochondral frame, GelMA hydrogel was dispensed into the macropores of the cartilage frame, followed by photopolymerizing at 365 nm ultraviolet (UV) light with light intensity 12 mW/cm^2 for 15 s.

2.4. Characterization of osteochondral scaffolds

Scanning electron microscopy (SEM, S-3000N, Hitachi, Japan) was employed to observe the microscopic morphology of these scaffolds at a voltage of 5 kV after lyophilization and gold plating (thickness: 10 nm). Compression testing was used to measure the mechanical properties of osteochondral scaffolds under wet conditions at 37°C. Specifically, three samples for each type of scaffold ($5 \times 5 \times 5$ mm^3) were tested, and the strain speed of 1 mm/min was adopted. The *in vitro* degradation of scaffolds was investigated by measuring the remaining weight (%) within an 8-week test period. Typically, 100 mg of each sample was immersed in simulated body fluid (SBF) in tubes under a shaking water bath at 37°C and 80 rpm. At each time point (2, 4, 6, and 8 weeks), the test samples were taken out and lyophilized for 48 h, after which the remaining weight was calculated.

2.5. Isolation and cultivation of rat bone marrow mesenchymal stem cells

Rat bone marrow mesenchymal stem cells (rBMSCs) were derived from the femoral cavity of 10 2-week-old Sprague–Dawley rats following the previous study.[36] rBMSCs were cultured in DMEM with 10% FBS and antibiotics (100 U/mL streptomycin and 100 U/mL penicillin) in an incubator at 37°C with 5% CO_2. The medium was changed every 2 days, and cells at three to five passages (P3–P5) were used in all experiments.

2.6. Alkaline phosphatase staining and collagen II immunofluorescence analysis

Rat bone marrow mesenchymal stem cells (rBMSCs) seeded on tissue culture plates and cultured with osteogenic medium (DMEM with 10% FBS, 100 U/mL streptomycin, 100 U/mL penicillin, 100 nM dexamethasone, 10 mM β-glycerophosphate disodium salt hydrate, and 50 μM 2-phospho-L-ascorbic acid trisodium salt) for 14 days were set as the osteogenesis positive control group (OM-group). After induction using different concentrations (0, 50, 100, 150, and 200 ng/mL) of BMP-2, samples were washed twice with DPBS and then fixed with 4% paraformaldehyde (PFA) for 20 min. The BCIP/NBT ALP kit (Sigma, USA) was used for ALP staining and staining results were captured using a macro camera (Canon, Japan). Furthermore, rBMSCs seeded on tissue culture plates and cultured with chondrogenic medium (DMEM with 5% FBS, 100 U/mL streptomycin, 100 U/mL penicillin, 10 nM dexamethasone, 50 μg/mL 2-phospho-L-ascorbic acid trisodium salt, 10 ng/mL TGF-β1, and 1% insulin-transferrin-selenium) for 21 days were set as the chondrogenesis positive control group (CM-group). After induction using different concentrations (0, 10, 50, 100, and 150 ng/mL) of FGF-18, samples were rinsed with DPBS twice, fixed with 4% PFA for 20 min, and permeabilized with 0.2% Triton X-100 for 20 min. After incubating in 1% BSA for 1 h, samples were treated with collagen II (COL II) monoclonal antibody (Boster Biological Technology, China) diluted at 1:500 and incubated at 4°C overnight. After rinsing with DPBS, samples were incubated in a solution of Alexa Fluor 488-conjugated secondary antibodies diluted at 1:800 for 1 h at 37°C. The samples were then subjected to a confocal laser scanning microscopy (LSM 880, Carl Zeiss, Germany) for fluorescence staining image observation. rBMSCs cultured in the chondrogenic medium served as the positive control group. The quantitative analysis of the relative percentage area coverage of ALP and fluorescence intensity of COL II were measured and analyzed by ImageJ software.

2.7. *In vitro* release behavior of scaffolds with different concentrations of growth factors

The *in vitro* release of the subchondral layer with BMP-2 in different amounts (1, 2, 3, and 4 μg BMP-2 per g scaffold) and cartilage layer with FGF-18 in different amounts (1, 2, 3, and 4 μg BMP-2 per g scaffold) was studied over a 30-day period. The BMP-2 ELISA kit (Westang, China) and FGF-18 ELISA kit (Westang, China) were used to determine the concentration of BMP-2 and FGF-18, respectively. The GF-loading amount in each group was defined as C_1. The cumulative release concentration at each time point can be obtained and recorded as C_{day0}, C_{day3}, C_{day6}, ..., C_{day27}, C_{day30}. Furthermore, the percentage release was calculated based on the percentage of GF content to GF loading at a certain time point. For example, the percentage of BMP-2 released on day 3:

$$\%\ release_{BMP-2}(day\,3) = \frac{C_{day3}}{C_1} \times 100\% \quad \text{(I)}$$

The released dose for every 3 days is calculated by subtracting the release concentration at two adjacent time points. For example, the released dose of FGF-18 from day 3 to day 6:

$$Release\ dose_{FGF-18}\ (day\ 3\ \text{to}\ 6) = C_{day6} - C_{day3} \quad \text{(II)}$$

2.8. Release behavior of osteochondral scaffolds in gelatin methacrylate gels

The integrated osteochondral scaffolds (3 μg/g BMP-2 of the subchondral layer and 2 μg/g FGF-18 of the cartilage layer) were fabricated via cryogenic 3D bioprinting (described in Section 2.3). The osteochondral scaffolds were then encapsulated into 5% GelMA gel to simulate the *in vivo* matrix environment. The released content of BMP-2 and FGF-18 were measured using ELISA kits (described in Section 2.7).

2.9. Preparation and characterization of rat bone marrow mesenchymal stem cell microspheres

To prepare the rBMSC microspheres, rBMSCs suspension was dropped into a microwell culture plate (Stemcell Technologies, Canada) by 6×10^5 cells per well. After a 24-h cultivation, the rBMSC microspheres were formed. The microsphere size was measured using ImageJ software. SEM was employed to observe the microscopic morphology of rBMSC microspheres after lyophilization. The rBMSC microspheres were subjected to staining of the nucleus and F-actin. Briefly, the rBMSC microspheres were fixed with 4% PFA for 20 min, permeabilized with 0.2% Triton X-100 for 20 min, and then incubated in 1% BSA for 1 h. Subsequently, samples were treated with a solution of Alexa Fluor 594 phalloidin for the F-actin staining for 1 h at 37°C and with a solution of DAPI for nucleus staining for 10 min at room temperature. Samples were subjected

to a confocal laser scanning microscopy for fluorescence staining image observation.

2.10. Cell viability and proliferation on osteochondral scaffolds

The rBMSCs suspension (0.2 mL, 5×10^5 cells/mL) was dropped onto the subchondral and interface layers, and rBMSC microspheres/GelMA solution (0.2 mL, 10^3 microspheres/mL) was dropped onto the cartilage and interface layers. Cell viability was detected by Live/Dead staining. Briefly, after 1 and 3 days of cultivation, cell-laden scaffolds were rinsed with DPBS and incubated in ethidium homodimer-1 (4 μM) and calcein AM (2 μM) for 20 min at 37°C, where living cells and dead cells were presented with green and red colors, respectively. ImageJ software was used to analyze cell viability. The cell proliferation properties were examined using Cell Counting Kit-8 (CCK-8, GlpBio, USA) after 1, 4, and 7 days of cultivation. Briefly, samples were incubated in CCK-8 solution at 37°C for 4 h, and the absorbance was measured using a microplate reader (Synergy HT, Bio-Tek Instruments, USA) at 450 nm.

2.11. Osteogenic differentiation of rat bone marrow mesenchymal stem cells in osteochondral scaffolds

Rat bone marrow mesenchymal stem cells (rBMSCs) seeded on tissue culture plates and cultured with ordinary culture medium (DMEM with 10% FBS and antibiotics) were set as the negative control group. After 14 days of cultivation, osteochondral scaffolds were subjected to staining of the nucleus, F-actin, and osteogenic markers (Runt-related transcription factor-2 [RUNX2], collagen I [COL I], or osteocalcin [OCN]). Briefly, after fixation with 4% PFA, permeabilization in 0.2% Triton X-100, and incubation in 1% BSA, samples were treated with monoclonal antibodies for RUNX2, COL I, or OCN (Boster Biological Technology, China) diluted at 1:500 and incubated at 4°C overnight. After rinsing with DPBS, samples were incubated in a solution of Alexa Fluor 488-conjugated secondary antibodies diluted at 1:800 for 1 h at 37°C. The samples were then treated with a solution of Alexa Fluor 594 phalloidin and DAPI for F-actin and nucleus staining. The fluorescence of each sample was observed using a confocal laser scanning microscope. To investigate ALP production, after fixing with 4% PFA for 20 min, samples were treated with ALP staining (described in Section 2.6). Furthermore, for real-time quantitative polymerase chain reaction (RT-qPCR) analysis, Trizol (Thermo Fisher Scientific, USA) was used to extract total RNA. Thereafter, reverse transcription was performed using a reverse transcription reagent kit (ABM, Canada). MagicSYBR mixture, ROX, cDNA, and mixed primers were loaded onto a 96-well plate, and RT-qPCR was performed in an Applied Biosystems QuantStudio™ 3 Real-Time PCR Instrument (Singapore). The primer sequences are displayed in Table 1.

2.12. Chondrogenic differentiation of osteochondral scaffolds

After 21 days of cultivation, osteochondral scaffolds were subjected to staining of the nucleus, F-actin, and chondrogenic markers (sry-related HMG box protein-9 [SOX9], COL II, and aggrecan [ACAN]). Briefly, after fixation with 4% PFA, permeabilization in 0.2% Triton X-100, and incubation in 1% BSA, samples were treated with SOX9, COL II, and ACAN monoclonal antibodies

Table 1. Primers used in real-time quantitative polymerase chain reaction (RT-qPCR) analysis

Gene	Primer (5' to 3')	Sequence (5' to 3')
GAPDH	Forward	ACCACAGTCCATGCCATCAC
	Reverse	TCCACCACCCTGTTGCTGTA
RUNX2	Forward	GAACCAAGAAGGCACAGAC
	Reverse	AATGCGCCCTAAATCACTG
COL I	Forward	CAAGAAGACATCCCTGAAGTC
	Reverse	GCATACATCAGGTTTCCACG
OCN	Forward	CTTTGTGTCCAAGCAGGAG
	Reverse	CTCCCAGCCATTGATACAG
SOX9	Forward	CTCTGGAGACTTCTGAACGA
	Reverse	ACTTGTAATCCGGGTGGTC
COL II	Forward	AGGAGACAGAGGAGAAGCT
	Reverse	CTTGAGGACCCTGGATTCC
ACAN	Forward	CTGACCAGACTGTCAGATACC
	Reverse	TCCTCACACCAGGAAACTC

(Boster Biological Technology, China) diluted at 1:500 and incubated at 4°C overnight. The subsequent steps were performed as described in Section 2.11. To investigate the production of glycosaminoglycan (GAG), after 21 days of cultivation, toluidine blue and alcian blue were used to stain the fixed cell-laden osteochondral scaffolds. Briefly, after washing with DPBS, samples were fixed with 4% PFA for 30 min. The samples were then treated with 1% toluidine blue and 1% alcian blue working solutions, respectively. Furthermore, RT-qPCR was performed as described in Section 2.11. The primer sequences are displayed in Table 1.

2.13. Statistical analysis

All experiments included at least three replicates for each sample, and numerical data are expressed as mean ± standard deviation. For statistical comparisons, the Student's *t*-test was used for two groups, and one-way analysis of variance (ANOVA) was used for multiple groups. Additionally, $p < 0.05$ was considered statistically significant. Three replicates were performed for each analysis.

3. Results

3.1. Design of osteochondral scaffolds with spatiotemporally-controlled growth factor release

In this study, an engineered osteochondral tissue was designed to facilitate osteochondral tissue regeneration (Figure 1). The tissue consists of a subchondral layer, an interface layer, and a cartilage layer, and the tissue was further seeded with MSCs with varied organizational morphologies. Cryogenic 3D-printed BMP-2/TCP/PLGA

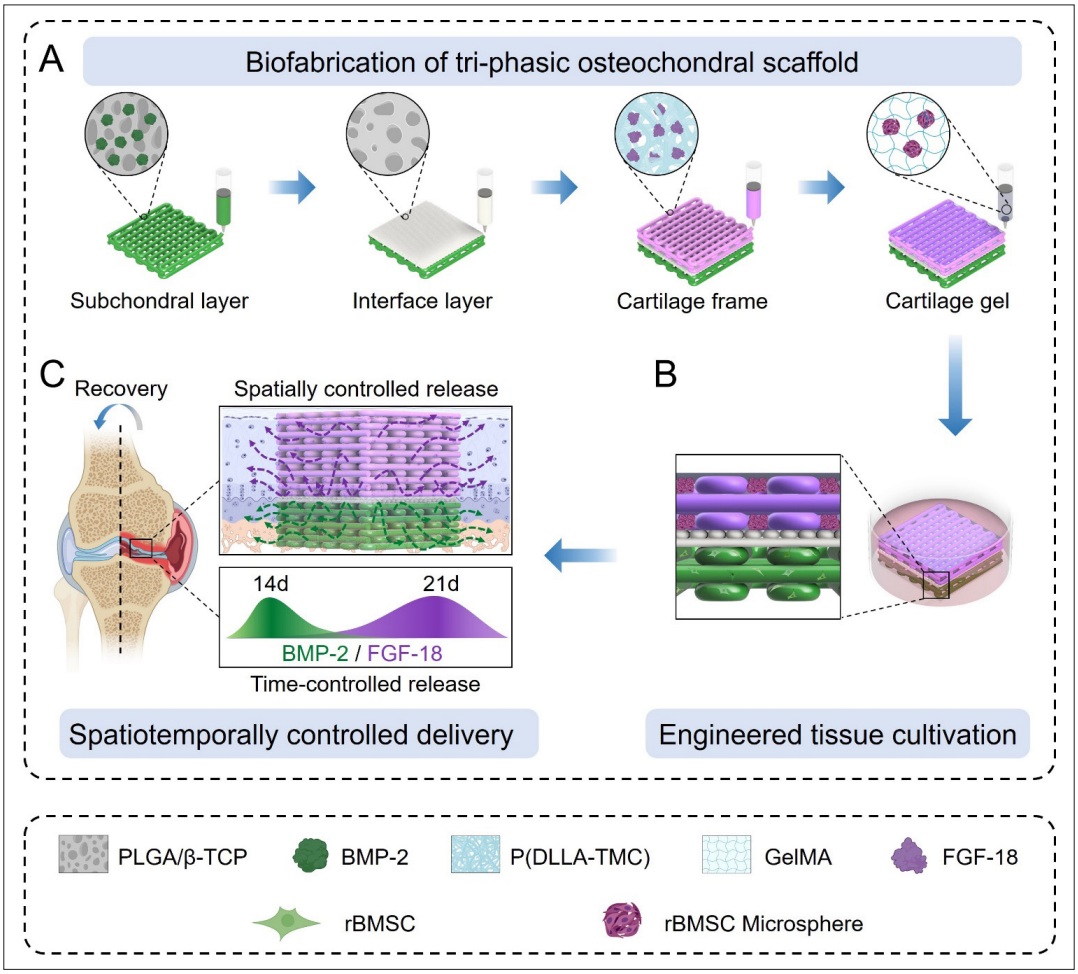


Figure 1. Schematic illustration of the development of engineered osteochondral tissue with the spatiotemporally controlled delivery strategy for osteochondral regeneration. (A) The schematic biofabrication process of the tri-phasic osteochondral scaffold. (B) The cultivation of engineered osteochondral tissue. (C) The spatiotemporally controlled delivery strategy for osteochondral regeneration. Abbreviations: BMP-2, bone morphogenetic protein-2; FGF-18, fibroblast growth factor-18; GelMA, gelatin methacrylate; P(DLLA-TMC), poly(D,L-lactic acid-co-trimethylene carbonate); PLGA/β-TCP, poly(lactic-co-glycolic acid)/β-tricalcium phosphate; rBMSC, rat bone marrow mesenchymal stem cell.

composite struts were used to build the subchondral layer to facilitate osteogenic differentiation of rBMSCs, while the cryogenic 3D-printed FGF-18/P(DLLA-TMC) framework, which was further filled with GelMA hydrogel, was used as the cartilage layer to promote chondrogenic differentiation of rBMSC microspheres. The sustained delivery of BMP-2 and FGF-18 at the subchondral and cartilage layers, respectively, was designed to match the requirements of regionally effective osteogenesis and chondrogenesis. The designed interface layer mimics the dense non-porous calcified anatomy of native osteochondral interface tissue and prevents the mutual interference of BMP-2 and FGF-18, thereby achieving the spatially controlled release of GFs. Through cryogenic 3D printing and subsequent lyophilization, the three different layers were tightly bonded together, which could spatiotemporally direct osteogenic/chondrogenic differentiation of rBMSCs.

3.2. Characterization of integrated osteochondral scaffolds

The macroscopic and microscopic morphology of the osteochondral scaffold without cell seeding is displayed in Figure 2A and B. The subchondral layer exhibited a regular grid-like pattern, and each strut had a microporous structure, in which secondary micropores with a diameter of 8.10 ± 1.87 μm and β-TCP particles were uniformly dispersed on the strut surface. The micromorphology of the interface layer was similar to the subchondral layer and had no macroporous grid structure, as a compact structure can be used as a barrier. The cartilage layer consisted of a P(DLLA-TMC) frame, with a latticed structure comprising numerous secondary micropores, and GelMA hydrogel blocks, which exhibited a loose and porous structure. The digital and SEM images of the osteochondral scaffold revealed that the three layers (subchondral, interface, and

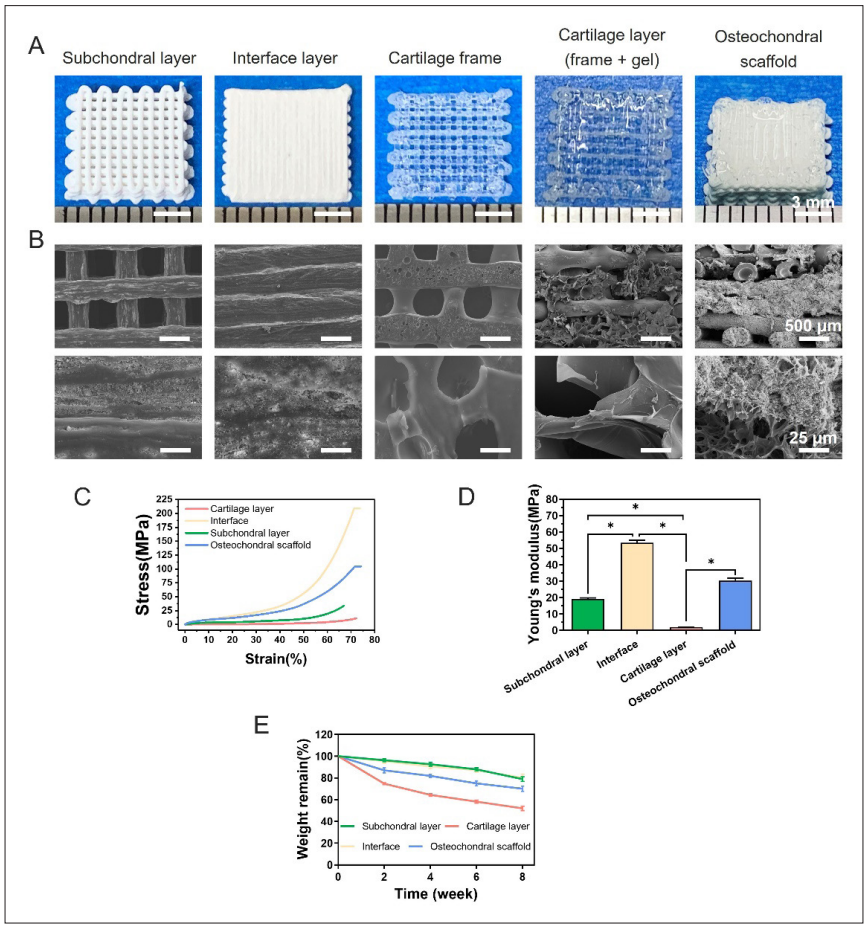


Figure 2. Characterization of integrated osteochondral scaffolds. (A) Digital images and (B) scanning electron microscope (SEM) images displaying the macro- and micromorphology of different layers within osteochondral scaffolds, respectively. (C) Stress–strain curves and (D) Young's modulus of osteochondral scaffolds under wet conditions at 37°C. (E) Degradation of osteochondral scaffolds in a shaking water bath at 37°C and 80 rpm. *$p < 0.05$. Scale bars: (A) XXX. Magnification: (B, top) ×50; (B, bottom) ×1000.

cartilage layers) were tightly bonded together and exhibited their original morphology.

To investigate the mechanical compatibility between the scaffold and native osteochondral tissues, we conducted compression tests on the 3D-printed osteochondral scaffolds. The stress–strain curve demonstrated that the compressive strengths of different layers of the osteochondral scaffold were of a considerable difference (cartilage layer < subchondral layer < interface layer), and the overall compressive strength of the osteochondral scaffold was between the subchondral and interface layers (Figure 2C). The Young's modulus of the cartilage layer (2.01 ± 0.22 MPa), the interface layer (53.43 ± 2.75 MPa), the subchondral layer (19.20 ± 1.13 MPa), and the integrated osteochondral scaffold (30.33 ± 2.80 MPa) were comparable to that of human osteochondral tissues (cartilage tissue: approximately 1.0 MPa; subchondral tissue: 20–500 MPa) (Figure 2D).[37–40] Next, the degradation behavior of scaffolds was investigated over an 8-week period. As displayed in Figure 2E, both the subchondral and interface layers demonstrated a slow degradation rate (<12% at 8 weeks), and no significant difference was observed. The slow but continuous degradation was due to the hydrolysis of PLGA and the decomposition of β-TCP. The cartilage layer reported a much faster degradation rate (>47% at 8 weeks), mainly owing to the relatively fast degradation of GelMA hydrogel and slow hydrolysis of the P(DLLA-TMC) matrix. Conversely, the osteochondral scaffold exhibited a moderate degradation rate between the other layers. These data indicated that a tri-phasic osteochondral scaffold that structurally and mechanically matched the native osteochondral tissues was successfully constructed via cryogenic 3D printing.

3.3. The spatiotemporally controlled release of BMP-2 and FGF-18

To investigate the optimal concentration of BMP-2 and FGF-18 for rBMSCs differentiation, ALP staining and immunofluorescence staining of COL II were conducted, respectively. ALP staining revealed that the addition of BMP-2 could significantly enhance the osteogenic differentiation of rBMSCs (Figure 3A). Specifically, after 14 days of culture, the ALP staining area in the group treated with 150 ng/mL BMP-2 was significantly larger than that treated with 0, 50, and 100 ng/mL BMP-2. In contrast, no significant difference was observed among the groups treated with 150 and 200 ng/mL BMP-2 and the positive control group (Figure 3B). Furthermore, the immunofluorescence staining of COL II demonstrated that the addition of FGF-18 could significantly enhance the chondrogenic differentiation of rBMSCs (Figure 3C). Specifically, after 21 days of cultivation, the fluorescence intensity of COL II in the group treated with 50 ng/mL FGF-18 was significantly higher than that in groups treated with 0 and 10 ng/mL FGF-18. In contrast, no significant difference was observed among the groups treated with 50, 100, and 150 ng/mL BMP-2, as well as the positive control group (Figure 3D). The optimal concentrations for osteogenic and chondrogenic differentiation of rBMSCs were determined to be 150 ng/mL of BMP-2 and 50 ng/mL of FGF-18, respectively.

Next, we fabricated subchondral scaffolds containing different amounts of BMP-2 (1, 2, 3, and 4 μg BMP-2 per g scaffold) and cartilage scaffolds containing different amounts of FGF-18 (1, 2, 3, and 4 μg BMP-2 per g scaffold) to determine the precise GF loading amount required to maintain the optimal concentration mentioned above. Figure 3E–G features the release behavior of BMP-2 from subchondral scaffolds in SBF over a 30-day period (measured using ELISA). The subchondral scaffolds loaded with BMP-2 exhibited decreased release rates when the initial loading amount was decreased (Figure 3E). The percentage of BMP-2 release increased and reached 84.81–86.50% within 30 days (Figure 3F). The BMP-2 released every 3 days revealed that subchondral scaffolds loaded with 3 and 4 μg/g BMP-2 could maintain a concentration of 150 ng/mL for up to 14 days, whereas subchondral scaffolds loaded with 1 and 2 μg/g BMP-2 could not achieve this concentration retention (Figure 3G). Figure 3H–J presents the release behavior of FGF-18 from cartilage scaffolds in SBF measured using ELISA for 30 days. For cartilage scaffolds loaded with different amounts of FGF-18, the total FGF-18 release was also positively correlated with the loading amount (Figure 3H). The percentage release of FGF-18 reached 64.11–66.87% in 30 days (Figure 3I). The FGF-18 released every 3 days demonstrated that cartilage scaffolds loaded with 2, 3, and 4 μg/g of FGF-18 could maintain a concentration of 50 ng/mL for up to 21 days, whereas cartilage scaffolds loaded with 1 μg/g of FGF-18 could not achieve this concentration retention (Figure 3J). These results demonstrated that BMP-2 could sustain osteogenic effects for 14 days, while FGF-18 could sustain chondrogenic effects for 21 days, thus validating the time-controlled release function of BMP-2 and FGF-18. Therefore, the optimal loading amount of BMP-2 and FGF-18 in subchondral scaffolds and cartilage scaffolds for improved osteochondral regeneration was set as 3 and 2 μg/g, respectively.

Furthermore, to investigate the spatially controlled release of BMP-2 and FGF-18 in integrated osteochondral scaffolds, the osteochondral scaffolds were encapsulated with 5% GelMA gel to mimic the *in vivo* matrix environment, which would contribute to the restricted diffusion of GFs (Figure 4A). In the cartilage layer of the osteochondral scaffold, the percentage release of FGF-18

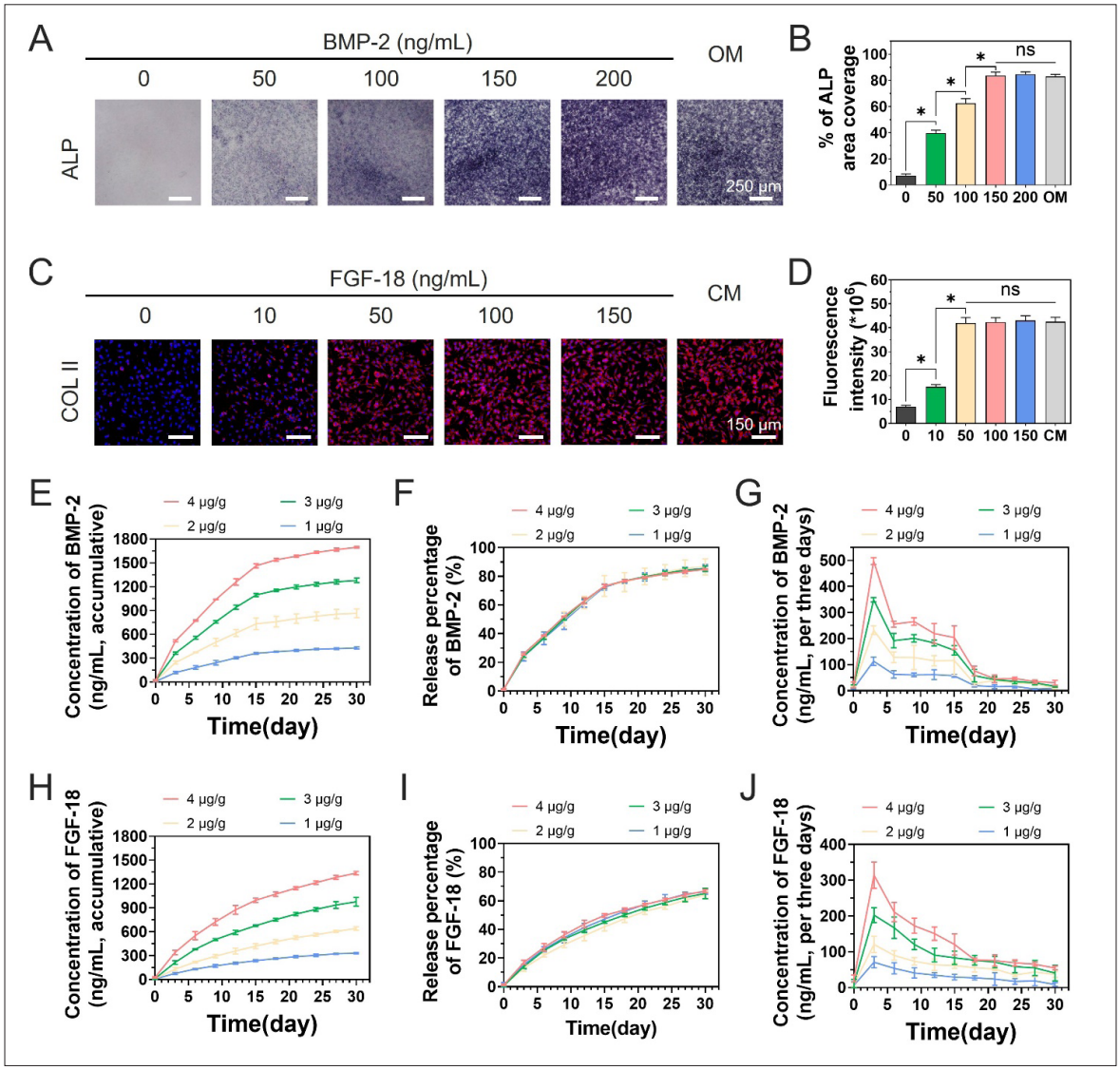


Figure 3. Optimal concentrations screening for osteogenic/chondrogenic differentiation and characterization of time-controlled release behavior of osteochondral scaffolds. (A) Alkaline phosphatase (ALP) staining and (B) relative percentage area coverage of ALP for bone marrow mesenchymal stem cells (BMSCs) at 14 days after cultivation with culture medium (concentration of bone morphogenetic protein-2 [BMP-2]: 0, 50, 100, 150, and 200 ng/mL) or osteogenic medium (OM). (C) Collagen II (COL II) immunofluorescence staining and (D) fluorescence intensity of BMSCs at 21 days after cultivation with culture medium (concentration of fibroblast growth factor-18 [FGF-18]: 0, 10, 50, 100, and 150 ng/mL) or chondrogenic medium (CM). (E) The total concentration of released BMP-2, (F) percentage of released BMP-2, and (G) concentration of BMP-2 released every 3 days at the subchondral layer (amount of BMP-2: 1, 2, 3, and 4 μg/g). (H) Total concentration of released FGF-18, (I) percentage of released FGF-18, and (J) concentration of FGF-18 released every 3 days at the cartilage layer (amount of FGF-18: 1, 2, 3, and 4 μg/g). *$p < 0.05$; *ns* denotes $p > 0.05$.

reached 61.97 ± 0.76% on day 30, and the FGF-18 released every 3 days could maintain a concentration of 50 ng/mL for up to 21 days. Meanwhile, the percentage release of BMP-2 was below 5.7% on day 30, and the BMP-2 released every 3 days was consistently below 20 ng/mL at each time point (Figure 4B and C). Conversely, in the subchondral layer of the osteochondral scaffold, the percentage release of BMP-2 reached 81.14 ± 2.30% on day 30, and the BMP-2 released every 3 days could maintain a concentration of 150 ng/mL for up to 14 days. Meanwhile, the percentage release of FGF-18 was below 5.4% on day 30, and the FGF-18 released every 3 days was consistently below 10 ng/mL at each time point (Figure 4D and E). These results suggested that the interface can obstruct the mutual diffusion of BMP-2 and FGF-18 to the opposite layer, and the osteochondral scaffold could maintain a suitable microenvironment for compartmentalized osteogenic and chondrogenic differentiation.

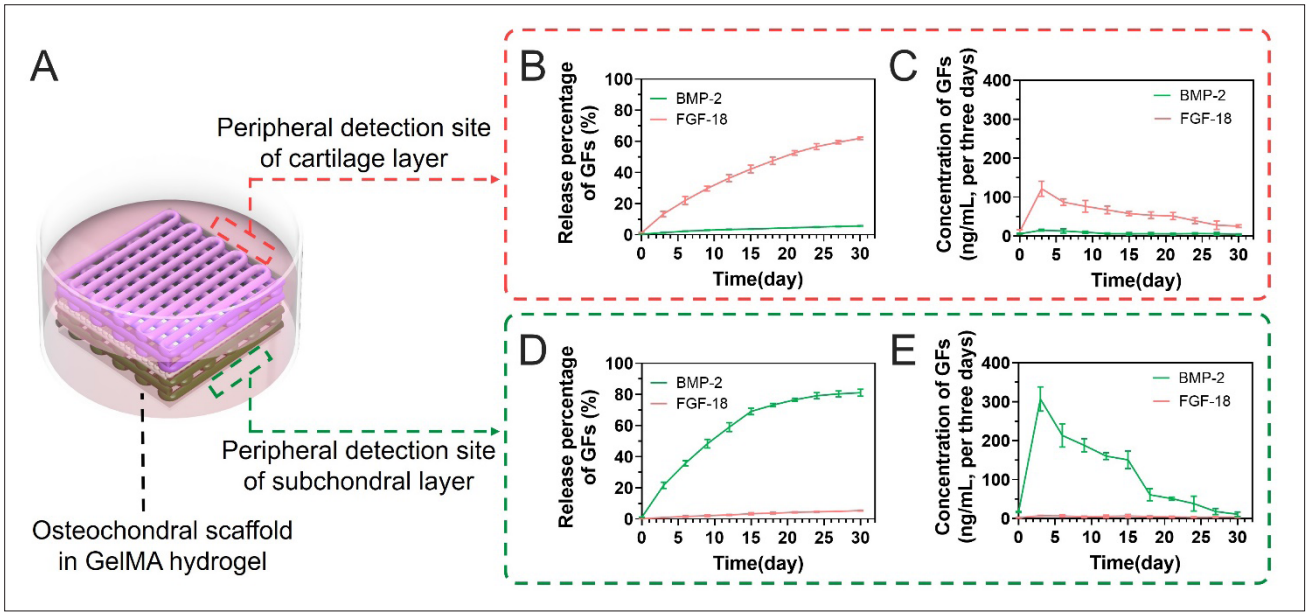


Figure 4. Characterization of spatially controlled release behavior of osteochondral scaffolds. (A) Schematic illustration of osteochondral scaffolds encapsulated in gelatin methacrylate (GelMA) gels. (B) Percentage release of bone morphogenetic protein-2 (BMP-2) and fibroblast growth factor-18 (FGF-18) and (C) concentration of released BMP-2/FGF-18 every 3 days in the cartilage layer of the scaffolds. (D) Percentage release of BMP-2/FGF-18 and (E) concentration of released BMP-2/FGF-18 every 3 days in the subchondral layer of the scaffolds. Abbreviation: GF, growth factor.

3.4. Characterization of rat bone marrow mesenchymal stem cell microspheres

After 24 h of cultivation in the microwell culture plate, the rBMSCs spontaneously aggregated into rBMSC microspheres (Figure 5A). The size distribution of microspheres was concentrated in the range of 110–120 μm, with an average diameter of 116.84 ± 11.39 μm (Figure 5B). The SEM images revealed that rBMSCs aggregated into rBMSC microspheres, and most rBMSCs in the microspheres exhibit a rounded morphology with short or even no tentacles (Figure 5C). The fluorescence images further revealed that the rBMSCs aggregated into rBMSC microspheres with a relatively uniform size (Figure 5D). Furthermore, taking inspiration from the aggregation of hyaline chondrocytes into spherical cartilage lacunae distributed within the extracellular matrix (ECM), rBMSC microspheres were encapsulated by GelMA hydrogel to mimic the structural characteristics of native cartilage lacunae (Figure 5E). These data indicated the successful formation of rBMSC microspheres, which are structurally similar to cartilage lacunae.

3.5. Viability and proliferation of rat bone marrow mesenchymal stem cells on osteochondral scaffolds

To assess the viability of rBMSCs with different organizational morphologies in the osteochondral scaffolds, rBMSCs or rBMSC microspheres were individually seeded in the subchondral, interface, or cartilage layer. The Live/Dead staining images revealed that, in the subchondral and interface layers, most rBMSCs that were stained with green fluorescence (alive) after 1 and 3 days of cultivation had a fusiform shape, and only a few rBMSCs were stained with red fluorescence (dead). Likewise, in the cartilage and interface layers, most rBMSCs in microspheres were alive (green), and only a few rBMSCs were dead (red) (Figure 6A). Quantitative analysis demonstrated that more than 90% of the rBMSCs remained alive during the 3-day cultivation in each layer (Figure 6B), indicating that the osteochondral scaffolds had excellent biocompatibility. The proliferation of rBMSCs was assessed using the CCK-8 assay. The absorbance increased in each group with increasing culture time, indicating that the osteochondral tissue scaffold provided a conducive environment for rBMSC proliferation (Figure 6C).

3.6. Osteogenic/chondrogenic differentiation of rat bone marrow mesenchymal stem cells in osteochondral scaffolds

To investigate the osteogenic or chondrogenic differentiation of rBMSCs with different organizational morphologies in the whole osteochondral scaffolds, rBMSCs were seeded in the subchondral layer and rBMSC microspheres were seeded in the cartilage layer. The osteogenic potential of rBMSCs in osteochondral scaffolds was investigated by visualizing the expression of RUNX2, COL I, and OCN through immunofluorescence staining

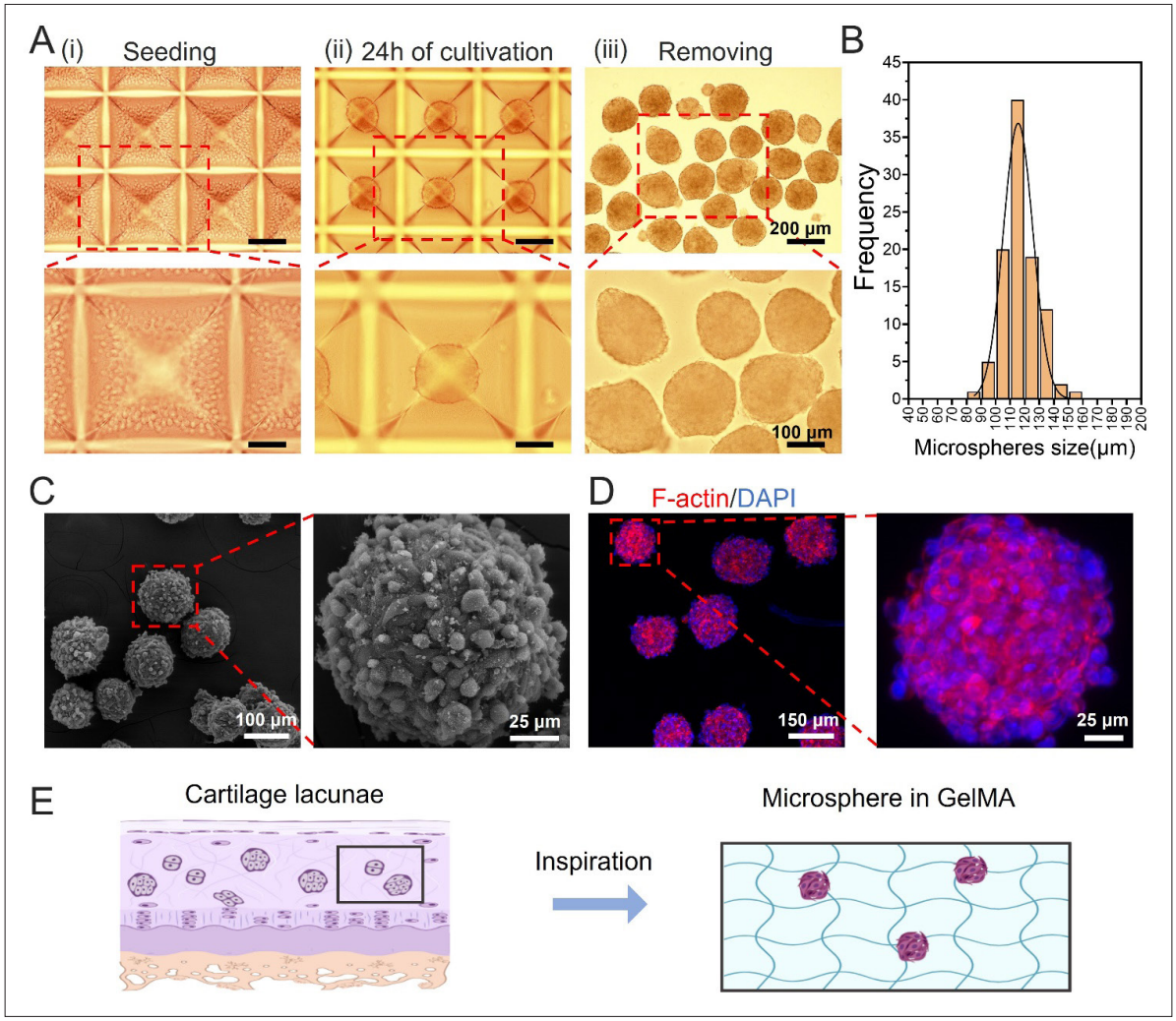


Figure 5. Fabrication of rat bone marrow mesenchymal stem cell (rBMSC) microspheres. (A) rBMSCs and rBMSC microspheres that are (i) seeded, (ii) cultivated for 24 h, and (iii) removed in/from the microwell culture plate. (B) Histograms of diameter distribution of rBMSC microspheres. (C) Scanning electron microscope (SEM) images of rBMSC microspheres after lyophilization. (D) Immunofluorescence staining of F-actin (red) and DAPI (blue) in rBMSC microspheres. (E) The inspiration and structural similarity between cartilage lacunae and rBMSC microspheres. Magnification: ×100 (left) and ×400 (right) . Abbreviation: GelMA, gelatin methacrylate.

after 14 days of culture. The subchondral layer with or without BMP-2 was designated as BMP-2$^+$ or BMP-2$^-$, respectively. The cartilage layer with or without FGF-18 was designated as FGF-18$^+$ or FGF-18$^-$, respectively. Compared to the subchondral layer (BMP-2$^-$) and cartilage layer (FGF-18$^+$), the expression levels of RUNX2, COL I, and OCN were more pronounced in the subchondral layer (BMP-2$^+$) (Figure 7A–C). ALP staining was also conducted to reflect the osteogenic differentiation of rBMSCs. After 14 days of culture, there was minimal expression of ALP (stained in purple) in the subchondral layer (BMP-2$^-$) and cartilage layer (FGF-18$^+$), while ALP expression was significantly upregulated in the subchondral layer (BMP-2$^+$) (Figure S1, Supporting Information). Additionally, there was scarcely any ALP expression in the cartilage layer (FGF-18$^+$). Furthermore, gene expression analysis revealed that the expression levels of RUNX2, COL I, and OCN in the subchondral layer (BMP-2$^-$) were significantly higher compared to the tissue culture plate group but significantly lower compared to the subchondral layer (BMP-2$^+$). In addition, there was no significant difference in RUNX2, COL I, and OCN expression levels in the subchondral layer (BMP-2$^+$) and OM group (Figure 7D).

The chondrogenic potential of rBMSC microspheres in osteochondral scaffolds was assessed by visualizing the expression of SOX9, COL II, and ACAN via immunofluorescence staining after 21 days of culture.

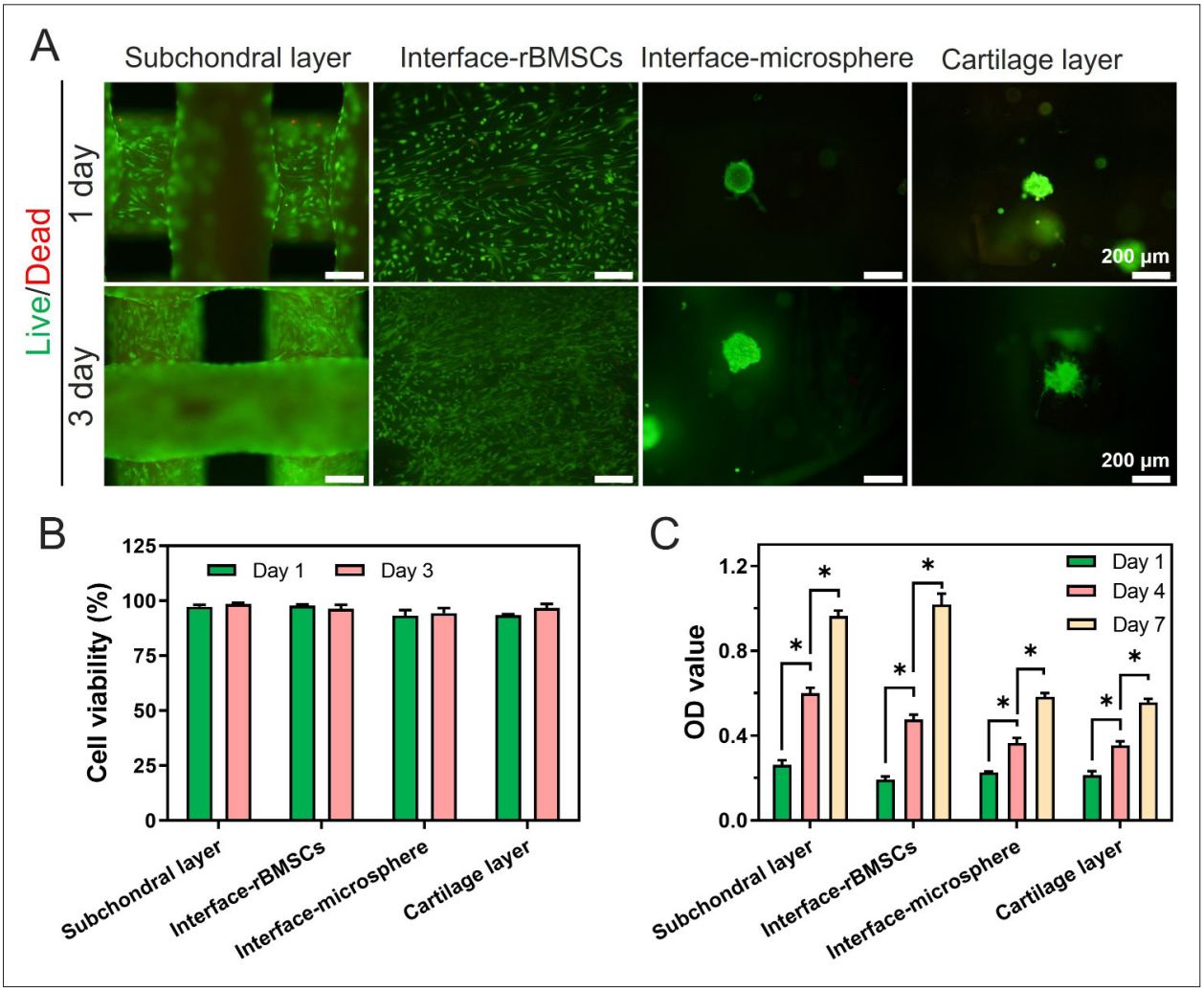


Figure 6. Biocompatibility of rat bone marrow mesenchymal stem cells (rBMSCs) or rBMSC microspheres in the subchondral, interface, or cartilage layer, respectively. (A) Live (green) and dead (red) staining of rBMSCs and rBMSC microspheres in integrated osteochondral scaffolds after 1 and 3 days of culture. (B) Cell viability (%) of rBMSCs and rBMSC microspheres based on Live/Dead staining analysis. (C) CCK8 absorbance of rBMSCs and rBMSC microspheres in osteochondral scaffolds on days 1, 4, and 7 after culture. *$p < 0.05$. Abbreviation: OD, optical density.

Compared to the cartilage layer (FGF-18$^-$) and subchondral layer (BMP-2$^+$), the expression levels of SOX9, COL II, and ACAN were more pronounced in the cartilage layer (FGF-18$^+$). In addition, the rBMSC microspheres displayed an expanded shape with long tentacles in the cartilage layer (FGF-18$^-$), whereas a rounded shape with short tentacles was observed in the cartilage layer (FGF-18$^+$) (Figure 8A–C). Furthermore, toluidine blue and alcian blue staining were conducted to study the expression of GAG. Dark blue and indigo blue colors were observed in the cartilage layer (FGF-18$^+$), while much lighter dark blue and indigo blue colors were observed in the cartilage layer (FGF-18$^-$) and subchondral layer (BMP-2$^+$) (Figure S2, Supporting Information). Moreover, there was scarcely any GAG expression in the subchondral layer (BMP-2$^+$). Furthermore, gene expression analysis revealed that the expression levels of SOX9, COL II, and ACAN in the cartilage layer (FGF-18$^-$) were significantly higher than that in the tissue culture plate group but significantly lower than that in the cartilage layer (FGF-18$^+$). In addition, the gene expression levels of SOX9, COL II, and ACAN in the cartilage layer (FGF-18$^+$) were not significantly different from the CM group (Figure 8D). These data suggested that the spatiotemporally controlled release of BMP-2 and FGF-18 could promote the compartmentalized osteogenic and chondrogenic differentiation of integrated osteochondral scaffolds, respectively.

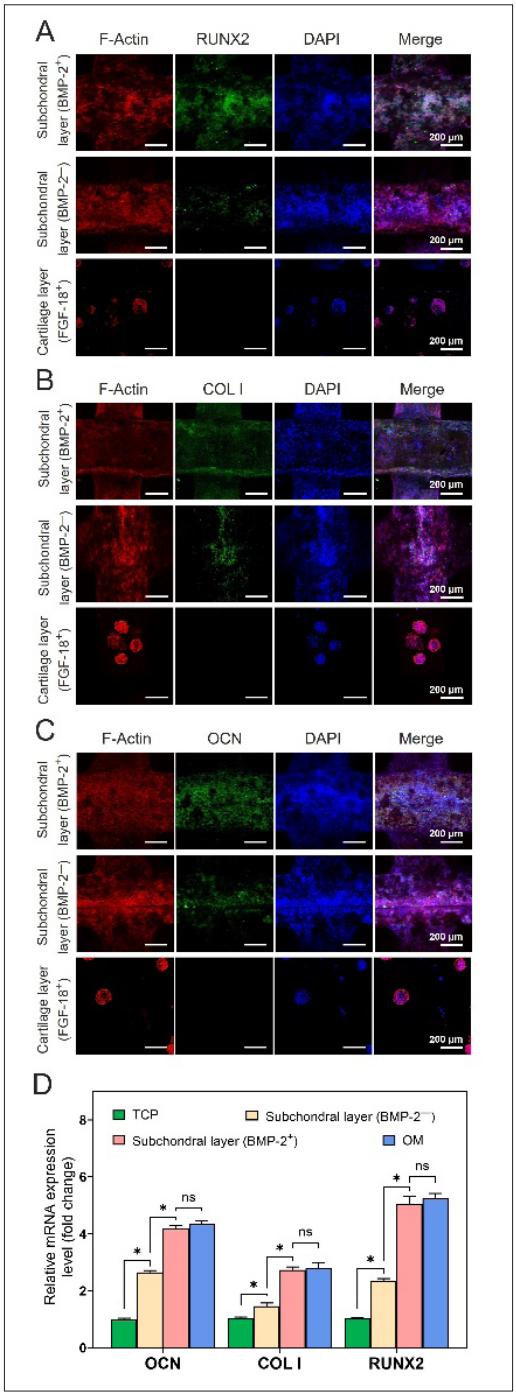


Figure 7. Osteogenic differentiation of rat bone marrow mesenchymal stem cells (rBMSCs) in the integrated osteochondral scaffolds. (A–C) Immunofluorescence staining of F-actin (red), osteogenic biomarkers (RUNX2, COL I, and OCN) (green), and DAPI (blue) at the subchondral or cartilage layer of the integrated osteochondral scaffolds. (D) Expression of osteogenic genes, including OCN, COL I, and RUNX2, at the subchondral layer of the integrated osteochondral scaffolds. *$p <$ 0.05; ns denotes $p > 0.05$. Abbreviations: BMP-2, bone morphogenetic protein-2; COL I, collagen I; FGF-18, fibroblast growth factor-18; OCN, osteocalcin; OM, osteogenic medium; RUNX2, runt-related transcription factor factor-2; TCP, tissue culture plate group.

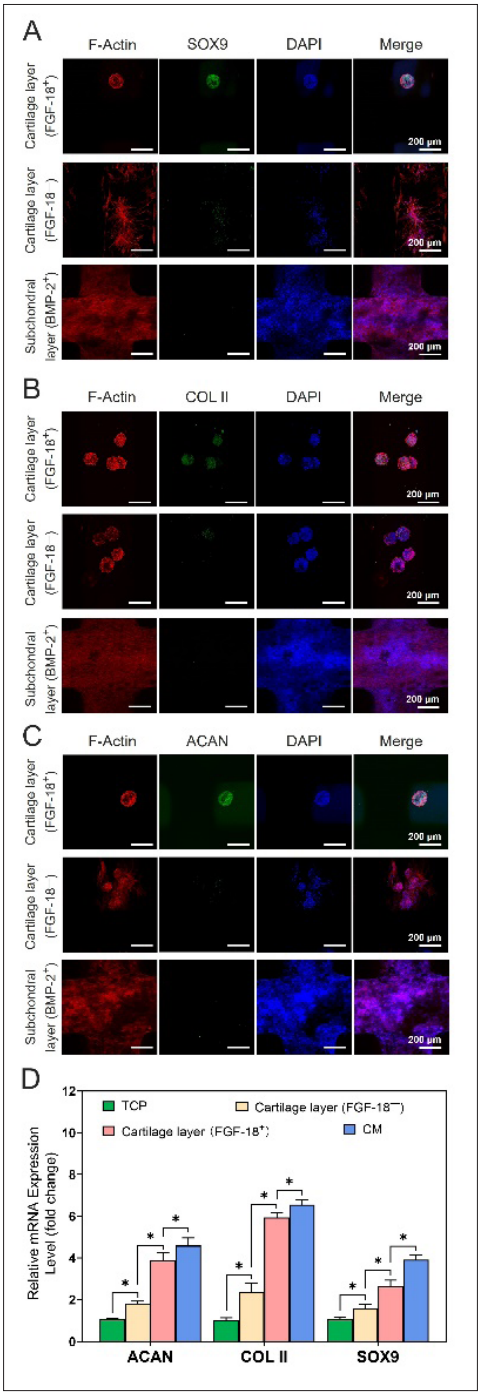


Figure 8. Chondrogenic differentiation of rat bone marrow mesenchymal stem cell (rBMSC) microspheres in the integrated osteochondral tissue engineering scaffolds. (A–C) Immunofluorescence staining of F-actin (red), chondrogenic biomarkers (SOX9, COL II, and ACAN) (green), and DAPI (blue) at the cartilage or subchondral layer of the integrated osteochondral scaffolds. (D) Expression of chondrogenic genes, including SOX9, COL II, and ACAN, at the cartilage layer of the integrated osteochondral scaffolds. *$p < 0.05$. Abbreviations: ACAN, aggrecan; BMP-2, bone morphogenetic protein-2; COL II, collagen II; CM, chondrogenic medium; FGF-18, fibroblast growth factor-18; SOX9, sry-related HMG box protein-9; TCP, tissue culture plate group.

4. Discussion

The regeneration of osteochondral tissue is an intricately complex process, where the physiological microenvironments vary significantly at different regions and repair phases.[20,41] Hyaline cartilage, a hydrogel-like elastic osteochondral tissue, consists of rounded hyaline chondrocytes and cartilage ECM rich in hyaluronic acid, COL II, and chondroitin sulfate. Meanwhile, the subchondral tissue is loose but mechanically strong, consisting of trabecula made of COL I and bone apatite, blood vessels, fusiform osteoblasts, osteoclasts, and osteocytes.[20] This study aims to develop an engineered osteochondral scaffold with biomimetic structures, a spatiotemporally controlled delivery of osteogenic/chondrogenic GFs, and an efficient loading of rBMSCs with varied organizational morphologies. This approach ensures a match of the release timing and location of osteogenic/chondrogenic GFs during the natural osteochondral tissue regeneration process and stimulates the formation of osteochondral tissues with a heterogeneous structure containing differentiated cells with appropriate phenotypes.[42,43]

Biomanufacturing techniques are increasingly employed to fabricate biomimetic scaffolds, as they can endow scaffolds with controlled structural, biological, and even cellular features that affect cell behavior and achieve desirable outcomes.[44,45] In this study, given the spatiotemporal presence of GFs and regional loading of rBMSCs with varied organizational morphologies in the osteochondral scaffolds, an engineered osteochondral tissue having regionally distributed osteoblasts and hyaline chondrocytes was developed. Compared to traditional fabrication techniques (e.g., molding, electrospinning, and salt leaching), 3D printing is advantageous in fabricating porous scaffolds with controlled and tailored pore sizes, thereby facilitating the efficient exchange of oxygen, nutrients, and cellular metabolic wastes to support cell/tissue growth.[46,47] However, traditional 3D printing technologies face challenges in generating scaffolds with desirable microenvironments, which are critical for inducing favorable cellular responses. For instance, in fused deposition modeling (FDM)-based 3D printing, the high temperatures during the printing process can lead to the deactivation of biologically active biomolecules, such as GFs loaded in bioinks.[46] In contrast, digital light processing (DLP)-based 3D printing with either toxic photocrosslinkable resins or biocompatible hydrogels being used as the printing inks, the inherent cytotoxicity or insufficient mechanical strength further restricts its use in making biocompatible scaffolds with desirable mechanical properties.[48] Recently, cryogenic 3D printing has been widely employed to fabricate bone tissue engineering scaffolds as it can fabricate scaffolds with hierarchically porous structures, the desired mechanical strength, and the sustained biological activity of GFs and even living cells.[49] In this study, we used water-in-DCM emulsions, containing BMP-2 (or FGF-18), P(DLLA-TMC) (or PLGA), or β-TCP powders, as printing inks with subsequent lyophilization via cryogenic 3D printing to develop osteochondral scaffolds with heterogeneous mechanical features and desirable microporous structures for *in situ* spatial delivery of BMP-2/FGF-18. DCM served as a solvent for polyester dissolution and a temporary bonding adhesive between layers. Upon freeze-drying, DCM removal enabled the convenient fabrication of integrated scaffolds with closely bonded subchondral, interface, and cartilage layers. Notably, our osteochondral scaffolds could maintain high levels of GF biological activity, efficiently inducing osteogenic and chondrogenic differentiation of rBMSCs.

There are currently numerous studies focusing on either bone repair or cartilage regeneration.[50,51] However, the construction of multi-layer scaffolds for subchondral and cartilage integration to promote osteochondral repair remains challenging.[6,42] In our previous study, to achieve osteochondral regeneration, we utilized a double-layer scaffold, which exhibited osteogenic and chondrogenic properties in the subchondral and cartilage layers, respectively.[52] However, the absence of an interface layer resulted in the spreading of GFs from the subchondral layer to the cartilage layer and vice versa, thereby disrupting their respective differentiation processes. Therefore, in this study, we fabricated a tri-phasic osteochondral scaffold, comprising the subchondral, interface, and cartilage layers, to facilitate osteochondral repair. Given that subchondral tissue is a mechanically strong calcified tissue with a porous structure, BMP-2/β-TCP/PLGA composites were selected as the matrix to print the subchondral layer due to their excellent biocompatibility, mechanical property, osteoconductivity, and osteoinductivity.[53,54] To segregate the subchondral layer from the cartilage layer, densely arranged β-TCP/PLGA struts were utilized as the calcified non-porous interface layer. Meanwhile, P(DLLA-TMC), a thermo-responsive shape-memory polyester that could become soft and elastic at 37°C, was used as the matrix to print the grid-like frame in the cartilage layer, providing the cartilage layer with suitable elastic modulus, which was comparable to the native cartilage tissue.[55] Besides, the P(DLLA-TMC) frame was filled with GelMA hydrogel to provide the 3D-printed cartilage layer with a non-porous hydrogel-like feature and further serve as a barrier to slow down the release rate of FGF-18.[56] BMP-2 and FGF-18 are osteogenic and chondrogenic growth factors, respectively, commonly employed in osteochondral tissue engineering. Compared to the control medium (DMEM with 10% FBS

and antibiotics) in the TCP group, the addition of BMP-2 can induce osteogenic differentiation via the activation of Smad, Wnt/β-catenin, and RhoA/ROCK2 signaling pathways.[57–59] In contrast, the addition of FGF-18 can induce chondrogenic differentiation via the activation of MEK/ERK and FGFR3-mediated pathways.[60,61] Therefore, the sustained release of BMP-2 and FGF-18 from the osteochondral scaffold can enhance the osteogenic and chondrogenic differentiation of rBMSCs.

The repair process of both the subchondral tissue and the hyaline cartilage involves inflammation infiltration, angiogenesis, tissue regeneration, and tissue remodeling.[62,63] BMP-2 can induce osteogenic differentiation of MSCs and regulate bone regeneration signaling pathways at the early phase of tissue regeneration.[18] Likewise, FGF-18 plays a pivotal role in both the early and mid-late phases of tissue regeneration by promoting the proliferation and chondrogenic differentiation of MSCs, inhibiting the apoptosis of chondrocytes, and regulating the synthesis of cartilage ECM.[19] To maximize the effect of BMP-2 and FGF-18 in inducing osteogenic/chondrogenic differentiation of MSCs at different layers during the osteochondral tissue regeneration process, the release rates of BMP-2 and FGF-18 were tuned according to their respective action time points. In this study, we verified that the effective concentration of BMP-2 was 150 ng/mL and the subchondral layer could maintain the effective concentration of BMP-2 for up to 14 days. Likewise, the effective concentration of FGF-18 was 50 ng/mL, and the cartilage layer could maintain the effective concentration of FGF-18 for up to 21 days. These data indicated that the osteochondral scaffolds exhibited temporally controlled release of BMP-2 and FGF-18, probably attributed to the different release rates of BMP-2 and FGF-18 in their respective matrix. The dense interface layer between the subchondral and cartilage layers further reduced the crosstalk between BMP-2 and FGF-18. This could be due to the significantly lower concentration of BMP-2 in the cartilage layer (<20 ng/mL, per 3 days) than the effective concentration of 150 ng/mL, and the considerably lower concentration of FGF-18 in the subchondral layer (<10 ng/mL, per 3 days) than the effective concentration of 50 ng/mL. These data indicated that the integrated osteochondral scaffold exhibited spatially controlled release of BMP-2 and FGF-18 mainly due to the presence of a dense non-porous interface layer.

The compartmentalized osteogenic/chondrogenic differentiation of MSCs is crucial for the development of engineered osteochondral tissue to improve osteochondral regeneration.[64] Previous studies developed engineered osteochondral tissue by fabricating scaffolds loaded with various biomolecules that are conducive to osteogenic/chondrogenic differentiation.[43,45] However, these strategies solely utilized discrete MSCs as seed cells, overlooking the distinct organizational morphologies of cells in the subchondral and cartilage layers, leading to suboptimal compartmentalized osteogenic/chondrogenic differentiation. In this study, we seeded discrete rBMSCs and rBMSC microspheres in the subchondral and cartilage layers, respectively. The discrete rBMSCs in the subchondral layer displayed significantly enhanced osteogenic differentiation and exhibited a fusiform cell shape, which is similar to the morphology of osteocytes. Previous studies suggested that the initial organizational morphology of MSCs could significantly affect chondrogenic differentiation. Discrete MSCs often differentiate into fibrochondrocytes, while MSCs from MSC aggregates tend to differentiate into hyaline chondrocytes.[23,30] Furthermore, cell microspheres are structurally similar to chondrocytes in cartilage lacuna,[65] and such an environment is favorable for obtaining a hyaline chondrocyte phenotype. Specifically, the native cartilage lacunae comprise rounded hyaline chondrocytes and exhibit a spherical morphology encapsulated by the ECM.[66] In this study, to mimic anatomical features, rBMSC microspheres, consisting of rounded stem cells aggregated into a spherical morphology, are encapsulated within GelMA hydrogel, closely resembling the ECM.[67,68] In our study, we seeded rBMSC microspheres instead of discrete rBMSCs in the cartilage layer to improve rBMSC chondrogenic differentiation and replicated the physiological structure of native cartilage. The chondrocytes derived from rBMSCs had a round shape, which was similar to the morphology of native hyaline chondrocytes. In summary, we developed an engineered cell-laden osteochondral scaffold that was capable of spatiotemporally controlling the release of BMP-2/FGF-18 and promoting the compartmentalized osteogenic/chondrogenic differentiation of rBMSCs with varied organizational morphologies in the osteochondral engineered tissue, thereby facilitating the integrated regeneration of osteochondral tissue.

5. Conclusion

In this study, we developed a tri-phasic osteochondral scaffold with a biomimetic structure and spatiotemporally controlled delivery of BMP-2/FGF-18 via multi-nozzle cryogenic 3D printing, followed by the seeding of MSCs with varied organizational morphologies. Through the spatially and temporally controlled release of BMP-2 and FGF-18, enhanced osteogenic and chondrogenic differentiation of MSCs in the subchondral layer and the cartilage layer was achieved, respectively, and the desirable cell phenotype could be obtained. Our findings provide

an innovative strategy for constructing 3D biomimetic-engineered osteochondral tissue with great potential for osteochondral regeneration.

Acknowledgments

None.

Funding

This work was supported by the National Key R&D Program of China (2022YFB4600600), the National Natural Science Foundation of China (32271181 and 82300018), the Guangdong Basic and Applied Basic Research Foundation (2021A1515111074), the Department of Education of Guangdong Province, China (2021ZDZX2014), the Dongguan Science and Technology of Social Development Program, Guangdong, China (20211800904542).

Conflict of interest

The authors declare no conflicts of interest.

Author contributions

Conceptualization: Yaobin Wu, Chong Wang, Wenhua Huang,
Formal analysis: Zhuosheng Lin, Ziyue Li, Zi Yan
Investigation: Weiwei Su, Shiyu Li, Panjing Yin
Methodology: Weihan Zheng, Ling Wang
Writing – original draft: Weiwei Su
Writing – review & editing: Shiyu Li, Chong Wang, Wenhua Huang

Ethics approval and consent to participate

Not applicable.

Consent for publication

Not applicable.

Availability of data

Data is available from the corresponding author upon reasonable request.

References

1. Olstad K, Ekman S, Carlson CS. An update on the pathogenesis of osteochondrosis. *Vet Pathol*. 2015;52(5):785-802.
doi: 10.1177/0300985815588778

2. He Y, Li Z, Alexander PG, et al. Pathogenesis of osteoarthritis: risk factors, regulatory pathways in chondrocytes, and experimental models. *Biology*. 2020;9(8):194.
doi: 10.3390/biology9080194

3. Abramoff B, Caldera FE. Osteoarthritis pathology, diagnosis, and treatment options. *Méd Clin North Am*. 2020;104(2):293-311.
doi: 10.1016/j.mcna.2019.10.007

4. Hermann W, Lambova S, Muller-Ladner U. Current treatment options for osteoarthritis. *Curr Rheumatol Rev*. 2017;14(2):108-116.
doi: 10.2174/1573397113666170829155149

5. Madry H. Surgical therapy in osteoarthritis. *Osteoarthr Cartil*. 2022;30(8):1019-1034.
doi: 10.1016/j.joca.2022.01.012

6. Wei W, Dai H. Articular cartilage and osteochondral tissue engineering techniques: recent advances and challenges. *Bioact Mater*. 2021;6(12):4830-4855.
doi: 10.1016/j.bioactmat.2021.05.011

7. Zhou L, Gjvm VO, Malda J, et al. Innovative tissue-engineered strategies for osteochondral defect repair and regeneration: current progress and challenges. *Adv Healthc Mater*. 2020;9(23):e2001008.
doi: 10.1002/adhm.202001008

8. Colella F, Garcia JP, Sorbona M, et al. Drug delivery in intervertebral disc degeneration and osteoarthritis: selecting the optimal platform for the delivery of disease-modifying agents. *J Control Release*. 2020;328:985-999.
doi: 10.1016/j.jconrel.2020.08.041

9. Rahimi M, Charmi G, Matyjaszewski K, Banquy X, Pietrasik J. Recent developments in natural and synthetic polymeric drug delivery systems used for the treatment of osteoarthritis. *Acta Biomater*. 2021;123:31-50.
doi: 10.1016/j.actbio.2021.01.003

10. Zhan A, Chen L, Sun W, et al. Enhancement of diabetic wound healing using a core-shell nanofiber platform with sequential antibacterial, angiogenic, and collagen deposition activities. *Mater Des*. 2022;218:110660.
doi: 10.1016/j.matdes.2022.110660

11. He W, Li C, Zhao S, et al. Integrating coaxial electrospinning and 3D printing technologies for the development of biphasic porous scaffolds enabling spatiotemporal control in tumor ablation and osteochondral regeneration. *Bioact Mater*. 2024;34:338-353.
doi: 10.1016/j.bioactmat.2023.12.020

12. Li S, Zheng W, Deng W, et al. Logic-based strategy for spatiotemporal release of dual extracellular vesicles in osteoarthritis treatment. *Adv Sci*. (Weinh). 2024:e2403227.
doi: 10.1002/advs.202403227

13. Bhat BB, Mehta CH, Suresh A, Velagacherla V, Nayak UY. Controlled release technologies for chronotherapy: current status and future perspectives. *Curr Pharm Des*. 2023;29(14):1069-1091.

doi: 10.2174/1381612829666230423144232

14. Santo VE, Gomes ME, Mano JF, Reis RL. From nano- to macro-scale: nanotechnology approaches for spatially controlled delivery of bioactive factors for bone and cartilage engineering. *Nanomedicine*. 2012;7(7):1045-1066. doi: 10.2217/nnm.12.78

15. Lu S, Lam J, Trachtenberg JE, et al. Dual growth factor delivery from bilayered, biodegradable hydrogel composites for spatially-guided osteochondral tissue repair. *Biomaterials*. 2014;35(31):8829-8839. doi: 10.1016/j.biomaterials.2014.07.006

16. Fortier LA, Barker JU, Strauss EJ, McCarrel TM, Cole BJ. The role of growth factors in cartilage repair. *Clin Orthop Relat Res*. 2011;469(10):2706-2715. doi: 10.1007/s11999-011-1857-3

17. Devescovi V, Leonardi E, Ciapetti G, Cenni E. Growth factors in bone repair. *Chir Organi Mov*. 2008;92(3):161-168. doi: 10.1007/s12306-008-0064-1

18. Kim S, Lee S, Kim K. Cutting-edge enabling technologies for regenerative medicine. *Adv Exp Med Biol*. 2018;1078: 233-244. doi: 10.1007/978-981-13-0950-2_12

19. Augustyniak E, Trzeciak T, Richter M, Kaczmarczyk J, Suchorska W. The role of growth factors in stem cell-directed chondrogenesis: a real hope for damaged cartilage regeneration. *Int Orthop*. 2015;39(5):995-1003. doi: 10.1007/s00264-014-2619-0

20. Ansari S, Khorshidi S, Karkhaneh A. Engineering of gradient osteochondral tissue: from nature to lab. *Acta Biomater*. 2019;87:41-54. doi: 10.1016/j.actbio.2019.01.071

21. Hoemann C, Lafantaisie-Favreau CH, Lascau-Coman V, Chen G, Guzmán-Morales J. The cartilage-bone interface. *J Knee Surg*. 2012;25(2):85-98. doi: 10.1055/s-0032-1319782

22. Seong JM, Kim BC, Park JH, Kwon IK, Mantalaris A, Hwang YS. Stem cells in bone tissue engineering. *Biomed Mater*. 2010;5(6):062001. doi: 10.1088/1748-6041/5/6/062001

23. Li Q, Xu S, Feng Q, et al. 3D printed silk-gelatin hydrogel scaffold with different porous structure and cell seeding strategy for cartilage regeneration. *Bioact Mater*. 2021;6(10):3396-3410. doi: 10.1016/j.bioactmat.2021.03.013

24. Sarem M, Otto O, Tanaka S, Shastri VP. Cell number in mesenchymal stem cell aggregates dictates cell stiffness and chondrogenesis. *Stem Cell Res Ther*. 2019;10(1):10. doi: 10.1186/s13287-018-1103-y

25. Karim A, Amin AK, Hall AC. The clustering and morphology of chondrocytes in normal and mildly degenerate human femoral head cartilage studied by confocal laser scanning microscopy. *J Anat*. 2018;232(4):686-698. doi: 10.1111/joa.12768

26. Xiang XN, Zhu SY, He HC, Yu X, Xu Y, He CQ. Mesenchymal stromal cell-based therapy for cartilage regeneration in knee osteoarthritis. *Stem Cell Res Ther*. 2022; 13(1):14. doi: 10.1186/s13287-021-02689-9

27. Liu Y, Zhou G, Cao Y. Recent progress in cartilage tissue engineering—our experience and future directions. *Engineering*. 2017;3(1):28-35. doi: 10.1016/j.eng.2017.01.010

28. Buchanan JL. Types of fibrocartilage. *Clin Podiatr Med Surg*. 2022;39(3):357-361. doi: 10.1016/j.cpm.2022.02.001

29. Kheir E, Shaw D. Hyaline articular cartilage. *Orthop Trauma*. 2009;23(6):450-455. doi: 10.1016/j.mporth.2009.01.003

30. Armiento AR, Alini M, Stoddart MJ. Articular fibrocartilage - why does hyaline cartilage fail to repair? *Adv Drug Deliv Rev*. 2019;146:289-305. doi: 10.1016/j.addr.2018.12.015

31. Osch GJVMV, Brittberg M, Dennis JE, et al. Cartilage repair: past and future – lessons for regenerative medicine. *J Cell Mol Med*. 2009;13(5):792-810. doi: 10.1111/j.1582-4934.2009.00789.x

32. Goodson HV, Jonasson EM. Microtubules and microtubule-associated proteins. *Cold Spring Harb Perspect Biol*. 2018;10(6):a022608. doi: 10.1101/cshperspect.a022608

33. Li J, Jiang H, Lv Z, et al. Articular fibrocartilage-targeted therapy by microtubule stabilization. *Sci Adv*. 2022;8(46):eabn8420. doi: 10.1126/sciadv.abn8420

34. Li J, Fan C, Lv Z, et al. Microtubule stabilization targeting regenerative chondrocyte cluster for cartilage regeneration. *Theranostics*. 2023;13(10):3480-3496. doi: 10.7150/thno.85077

35. Hall AC. The role of chondrocyte morphology and volume in controlling phenotype—implications for osteoarthritis, cartilage repair, and cartilage engineering. *Curr Rheumatol Rep*. 2019;21(8):38. doi: 10.1007/s11926-019-0837-6

36. Yang Y, Zheng W, Tan W, et al. Injectable MMP1-sensitive microspheres with spatiotemporally controlled exosome release promote neovascularized bone healing. *Acta Biomater*. 2023;157:321-336. doi: 10.1016/j.actbio.2022.11.065

37. Beck EC, Barragan M, Tadros MH, Gehrke SH, Detamore MS. Approaching the compressive modulus of articular cartilage with a decellularized cartilage-based hydrogel. *Acta Biomater*. 2016;38: 94-105. doi: 10.1016/j.actbio.2016.04.019

38. Little CJ, Bawolin NK, Chen X. Mechanical properties of natural cartilage and tissue-engineered constructs. *Tissue Eng Part B: Rev*. 2011;17(4):213-227.
doi: 10.1089/ten.teb.2010.0572

39. Keaveny TM, Hayes WC. A 20-year perspective on the mechanical properties of trabecular bone. *J Biomech Eng*. 1993;115(4B):534-542.
doi: 10.1115/1.2895536

40. Rezwan K, Chen QZ, Blaker JJ, Boccaccini AR. Biodegradable and bioactive porous polymer/inorganic composite scaffolds for bone tissue engineering. *Biomaterials*. 2006;27(18): 3413-3431.
doi: 10.1016/j.biomaterials.2006.01.039

41. Zhang N, Wang Y, Zhang J, Guo J, He J. Controlled domain gels with a biomimetic gradient environment for osteochondral tissue regeneration. *Acta Biomater*. 2021;135:304-317.
doi: 10.1016/j.actbio.2021.08.029

42. Yildirim N, Amanzhanova A, Kulzhanova G, Mukasheva F, Erisken C. Osteochondral interface: regenerative engineering and challenges. *ACS Biomater Sci Eng*. 2023;9(3):1205-1223.
doi: 10.1021/acsbiomaterials.2c01321

43. Niu X, Li N, Du Z, Li X. Integrated gradient tissue-engineered osteochondral scaffolds: Challenges, current efforts and future perspectives. *Bioact Mater*. 2023;20: 574-597.
doi: 10.1016/j.bioactmat.2022.06.011

44. Santos-Beato P, Midha S, Pitsillides AA, Miller A, Torii R, Kalaskar DM. Biofabrication of the osteochondral unit and its applications: current and future directions for 3D bioprinting. *J Tissue Eng*. 2022;13:20417314221133480.
doi: 10.1177/20417314221133480

45. Vyas C, Mishbak H, Cooper G, Peach C, Pereira RF, Bartolo P. Biological perspectives and current biofabrication strategies in osteochondral tissue engineering. *Biomanufacturing Rev*. 2020;5(1):2.
doi: 10.1007/s40898-020-00008-y

46. Wang C, Huang W, Zhou Y, et al. 3D printing of bone tissue engineering scaffolds. *Bioact Mater*. 2020;5(1):82-91.
doi: 10.1016/j.bioactmat.2020.01.004

47. Zaszczyńska A, Moczulska-Heljak M, Gradys A, Sajkiewicz P. Advances in 3D printing for tissue engineering. *Materials (Basel)*. 2021;14(12):3149.
doi: 10.3390/ma14123149

48. Quan H, Zhang T, Xu H, Luo S, Nie J, Zhu X. Photo-curing 3D printing technique and its challenges. *Bioact Mater*. 2020;5(1):110-115.
doi: 10.1016/j.bioactmat.2019.12.003

49. Li Z, Xu M, Wang J, Zhang F. Recent advances in cryogenic 3D printing technologies. *Adv Eng Mater*. 2022;24(10):2200245.
doi: 10.1002/adem.202200245

50. Maia FR, Bastos AR, Oliveira JM, Correlo VM, Reis RL. Recent approaches towards bone tissue engineering. *Bone*. 2022;154:116256.
doi: 10.1016/j.bone.2021.116256

51. Wasyłeczko M, Sikorska W, Chwojnowski A. Review of synthetic and hybrid scaffolds in cartilage tissue engineering. *Membranes (Basel)*. 2020;10(11):348.
doi: 10.3390/membranes10110348

52. Wang C, Yue H, Huang W, et al. Cryogenic 3D printing of heterogeneous scaffolds with gradient mechanical strengths and spatial delivery of osteogenic peptide/TGF-1 for osteochondral tissue regeneration. *Biofabrication*. 2020;12(2):025030.
doi: 10.1088/1758-5090/ab7ab5

53. Li D, Guo Y, Lu H, et al. The effect of local delivery of adiponectin from biodegradable microsphere–scaffold composites on new bone formation in adiponectin knockout mice. *J Mater Chem B*. 2016;4(27):4771-4779.
doi: 10.1039/c6tb00704j

54. Yu X, Tang X, Gohil SV, Laurencin CT. Biomaterials for bone regenerative engineering. *Adv Healthc Mater*. 2015;4(9):1268-1285.
doi: 10.1002/adhm.201400760

55. Salaris V, Leonés A, Lopez D, Kenny JM, Peponi L. Shape-memory materials via electrospinning: a review. *Polymers (Basel)*. 2022;14(5):995.
doi: 10.3390/polym14050995

56. Pérez-Luna VH, González-Reynoso O. Encapsulation of biological agents in hydrogels for therapeutic applications. *Gels*. 2018;4(3):61.
doi: 10.3390/gels4030061

57. Ryoo HM, Lee MH, Kim YJ. Critical molecular switches involved in BMP-2-induced osteogenic differentiation of mesenchymal cells. *Gene*. 2006;366(1):51-57.
doi: 10.1016/j.gene.2005.10.011

58. Wu M, Chen F, Liu H, et al. Bioinspired sandwich-like hybrid surface functionalized scaffold capable of regulating osteogenesis, angiogenesis, and osteoclastogenesis for robust bone regeneration. *Mater Today Bio*. 2022; 17:100458.
doi: 10.1016/j.mtbio.2022.100458

59. Lu Q, Diao J, Wang Y, et al. 3D printed pore morphology mediates bone marrow stem cell behaviors via RhoA/ROCK2 signaling pathway for accelerating bone regeneration. *Bioact Mater*. 2023;26:413-424.
doi: 10.1016/j.bioactmat.2023.02.025

60. Bradley EW, Carpio LR, Newton AC, Westendorf JJ. Deletion of the PH-domain and Leucine-rich repeat protein phosphatase 1 (Phlpp1) increases fibroblast growth factor (Fgf) 18 expression and promotes chondrocyte proliferation*. *J Biol Chem*. 2015;290(26):16272-16280.
doi: 10.1074/jbc.m114.612937

61. Davidson D, Blanc A, Filion D, et al. Fibroblast growth factor (FGF) 18 signals through FGF receptor 3 to promote chondrogenesis*. *J Biol Chem*. 2005;280(21): 20509-20515.
doi: 10.1074/jbc.m410148200

62. Einhorn TA, Gerstenfeld LC. Fracture healing: mechanisms and interventions. *Nat Rev Rheumatol*. 2015;11(1):45-54.
doi: 10.1038/nrrheum.2014.164

63. Li M, Yin H, Yan Z, et al. The immune microenvironment in cartilage injury and repair. *Acta Biomater*. 2022;140: 23-42.
doi: 10.1016/j.actbio.2021.12.006

64. Taskin MB, Klausen LH, Dong M, Chen M. Emerging wet electrohydrodynamic approaches for versatile bioactive 3D interfaces. *Nano Res*. 2020;13(2):315-327.
doi: 10.1007/s12274-020-2635-x

65. Lee S, Lee K, Kim SH, Jung Y. Enhanced cartilaginous tissue formation with a cell aggregate-fibrin-polymer scaffold complex. *Polymers (Basel)*. 2017;9(8):348.
doi: 10.3390/polym9080348

66. Ghadially FN. Structure and function of articular cartilage. *Clin Rheum Dis*. 1981;7(1):3-28.
doi: 10.1016/s0307-742x(21)00330-1

67. Xiao S, Zhao T, Wang J, et al. Gelatin methacrylate (GelMA)-based hydrogels for cell transplantation: an effective strategy for tissue engineering. *Stem Cell Rev Rep*. 2019;15(5): 664-679.
doi: 10.1007/s12015-019-09893-4

68. Tibbitt MW, Anseth KS. Hydrogels as extracellular matrix mimics for 3D cell culture. *Biotechnol Bioeng*. 2009;103(4):655-663.
doi: 10.1002/bit.22361

ACCSCIENCE PUBLISHING

International Journal of Bioprinting

RESEARCH ARTICLE

A preliminary investigation on the effect of ingredient flow speed in extrusion-based printing through experimental and theoretical approaches

Phoebe Xin Ni Leam[1]*, Aakanksha Pant[1], Jia An[2], Chen Huei Leo[2,3], U-Xuan Tan[1,2], and Chee Kai Chua[1,2]

[1]Pillar of Engineering Product Development, Singapore University of Technology and Design, Singapore, Singapore

[2]Centre for Healthcare Education, Entrepreneurship and Research @ SUTD (CHEERS), Singapore University of Technology and Design, Singapore, Singapore

[3]Cluster of Science, Mathematics and Technology, Singapore University of Technology and Design, Singapore, Singapore

(This article belongs to the *Special Issue: Special Issue of International Journal of Bioprinting in the BDMC 2023 Conference*)

Abstract

Despite the widespread use of Foodini three-dimensional (3D) printers for 3D food printing, there is a lack of analysis regarding the effect of the ingredient flow speed in current food printing research. In this study, we utilized experimental and theoretical approaches to investigate the effect of printing parameters in the 3D extrusion process. In particular, the dot extrusion (no slicing required) and model extrusion (inclusive of text, shapes, 3D models, and clip art that require slicing) modes of operation were studied. In dot extrusion, the experimental results suggest that the amount of food material extruded over a fixed time is constant and independent of the internal nozzle geometry. However, this only applies to food materials ≥20 mL, and there is a lack of control over the extrusion rate for the dot extrusion mode. Moreover, varying the ingredient flow speed did not change the extrusion time. In model extrusion, the resolution of the print was only affected by the ingredient flow speed, and varying the printing speed did not affect the print resolution. A mathematical model was introduced to understand the complex relationship between the printing process parameters and the extrusion resolution. The model is unique as it accounts for the material properties of the food ink and the printer-specific controls (i.e., ingredient flow speed). In this research, the experimental and theoretical approaches were considered independent investigations and provided complementary insights, unlike the conventional prediction–validation relationship. Therefore, the findings of this study can be used as an alternative framework to understand future food printers. Overall, the preliminary findings underscore the complexity introduced by a novel printer process parameter, namely ingredient flow speed. The study offers valuable insights into Foodini-based extrusion printing and serves as a foundational guide for further exploration in this evolving field.

***Keywords*:** 3D food printing; Mathematical model; Extrusion-based printers; Shear-thinning materials

***Corresponding author:**
Phoebe Xin Ni Leam
(phoebe_leam@mymail.sutd.edu.sg)

Citation: Leam PXN, Pant A, An J, Leo CH, Tan UX, Chua CK. A preliminary investigation on the effect of ingredient flow speed in extrusion-based printing through experimental and theoretical approaches. *Int J Bioprint*. 2024;10(5):2787. doi: 10.36922/ijb.2787

Received: January 19, 2024
Accepted: April 18, 2024
Published Online: August 6, 2024

Copyright: © 2024 Author(s). This is an Open Access article distributed under the terms of the Creative Commons Attribution License, permitting distribution, and reproduction in any medium, provided the original work is properly cited.

Publisher's Note: AccScience Publishing remains neutral with regard to jurisdictional claims in published maps and institutional affiliations.

1. Introduction

The rapid technological advancement in additive manufacturing (AM) with computer-assisted tools has broadened its application in different fields, such as aerospace,[1] medical,[2] and manufacturing,[3,4] among others.[5] One of these innovations is three-dimensional (3D) food printing (3DFP), which combines the aspects of AM and gastronomy to generate edible 3D constructs. The capability to precisely deposit different edible materials has the potential to revolutionize the food industry by enabling the creation of personalized and nutritionally tailored meals for individuals with special dietary needs.[6,7] Researchers in this field have attempted to customize 3D-printed edibles in terms of their geometry,[8] texture,[9,10] and nutrients.[11,12] 3DFP enables precise portion control, thereby reducing the amount of food waste generated, which is a major concern as countries work towards sustainability and food security.[13] With efficient use of ingredients, such as alternative proteins and upcycled food waste, 3DFP has the potential to address food scarcity.[14,15]

Among the 3DFP techniques, extrusion-based 3DFP is the predominant approach,[16] where food inks are ejected through a tiny nozzle and deposited layerwise. These food inks are classified into two main categories: natively extrudable and non-natively extrudable food inks.[17] Natively extrudable inks refer to intrinsically printable food inks, such as milk, chocolate, and hydrogels. Conversely, non-natively extrudable food inks require additives to adjust their rheological properties, such that these inks become shear-thinning for extrusion, such as vegetable inks[14,18] and meat.[19] Extensive research has been conducted to develop novel food inks,[20] which would typically require laborious and time-consuming experiments to acquire a printable ink.[21]

Besides extensive experiments, it is also essential to establish a theoretical understanding of the relationship between the printing material and process. A thorough understanding of the 3D food extrusion process and the printing parameters can decrease the number of experiments required to attain a unique, printable food ink. The theoretical aspect of 3DFP can be realized through a mathematical model that connects the extrusion process parameters to the printing quality, such as print resolution. There are existing mathematical models studying the extrusion process, but these models are specific to hydrogels[22] and are adapted for flow within needle-like nozzles.[23–25] The difference in properties between hydrogels and food materials (e.g., the fiber strands in food) would imply that existing models cannot be directly applied to the latter.[14]

In recent years, several studies have reported the use of a commercially available 3D food printer, Foodini, as a research tool in 3DFP.[6,14,26–33] Foodini facilitates food printing experiments and enables a better understanding of the mathematical principles behind extrusion-based 3D food printers. Nonetheless, it is necessary to optimize the Foodini process parameters to 3D print new varieties of food inks, and this process requires a mathematical model that examines the flow of food materials in the capsule. Unlike conventional 3D extrusion-based food printers with direct control of the printing parameters (e.g., extrusion pressure and flow rate), Foodini operates on volume extrusion and adjusts ingredient flow speed to accommodate different food inks.[34] Therefore, the present study aimed to investigate the control parameters of Foodini and introduce a theoretical model for its operation.

This study consists of two parts: (i) an experimental investigation of Foodini process parameters and (ii) a theoretical model for Foodini-based extrusion. In the experimental part, the effects of nozzle size, print speed, and ingredient flow speed were investigated by using mashed potatoes (MPs). Due to the lack of conventional process controls, such as pressure or extrusion rate, in Foodini printers, direct validation of the models could not be conducted experimentally. Both experimental and theoretical aspects in this study provide complementary insights, especially when investigating the effect of ingredient flow speed. Taken together, the combination of experimental and theoretical approaches could be utilized as an alternative framework for future experiments and mathematical modeling in 3DFP.

2. Materials and methods

2.1. Preparation of mashed potato food ink

Potatoes are a nutrient-dense source of food that provide essential carbohydrates and key nutrients, such as dietary fiber, vitamins, and minerals, which are required for a balanced diet.[35] Moreover, potatoes are easily extrudable (e.g., via food processing). These traits have led to the use of potatoes in various forms for different experiments.[9,36–40] The starch in potatoes is expanded and broken down upon heating and boiling, respectively, and can improve the printability of potatoes as the starch particles solidify.[41] A gel network, similar to hydrogels, is formed when the starch particles swell upon absorbing water molecules.[42] Furthermore, potatoes that are boiled and mashed become a shear-thinning fluid, which is crucial in 3DFP. The viscoelastic properties of the MPs allow the food ink to behave as a fluid at high shear rates and return to its original state when the shear force is removed.

MP powder was sourced from a local bakery supplier (Redman by Phoon Huat, Singapore). According to the food packaging label, the dry potato powder consists of potato, mono and diglycerides, sodium acid pyrophosphate, and

citric acid. Approximately, 60 g of potato powder was mixed with water at 100°C at three different mass ratios: 0.15, 0.2, and 0.25 wt/wt. The mixture was blended manually for 5 min until a puree-like consistency was attained and all the lumps in the mixture had dissolved. Pre-printability tests were conducted to determine if the MP ink is suitable for 3D printing. Through this qualitative analysis, the ratio of dry potato powder to boiling water was determined to be 0.2 wt/wt. The MP inks were subsequently loaded into the Foodini capsule before 3D printing.

2.2. Rheological characterization

An oscillatory rheometer (Modular Compact Rheometer, Anton Paar, Austria) was utilized to examine the rheological properties of MP food ink with an aluminum parallel plate with a diameter of 25 mm and truncation gap of 1000 μm. To prevent edge effects from affecting the characterization profile of the inks, the rotating shaft was descended to remove any overflowing food inks off the disc. To understand the rheology profile of the MP food ink at room temperature, viscosity tests were performed by exerting a stepwise shear rate increase from 1 to 1000 s^{-1}. Triplicate measurements of the MP inks were recorded.

2.3. Measurement of nozzle geometry

A digital microscope (VHX-7000, Keyence, Japan) was deployed at ×20 magnification to analyze the nozzles from different perspectives (interior, external, and side) and identify any contrast between the different nozzles.

2.4. 3D printing experiments

An extrusion-based 3D food printer, Foodini (Natural Machines, Spain), was utilized to print 3D models using the print settings listed in Table 1. Three nozzles (0.8, 1.5, and 4 mm) were used in this study. The control parameters that would be studied were printing speed (V_{PS}) and ingredient flow speed (V_{IFS}). According to the knowledge database of Natural Machines, printing speed (mm/min) is defined as the speed of the nozzle head moving in the horizontal axis. Ingredient flow speed is defined as the material extrusion flow on the vertical axis and is a dimensionless parameter. Unlike the typical food printers which control the flow using a volumetric flow rate, Foodini printers regulate the flow via ingredient flow speed. A higher ingredient flow speed would lead to a larger volume being extruded, resulting in a larger printed width. This indicates that the ingredient flow speed is related to the volumetric flow rate by an arbitrary value.

The extrusion process parameters were studied using two printing modes available in the Foodini Creator hub, namely dot and model extrusions. The two printing modes differ in terms of whether the slicer software is applied to the model. For model extrusion, the uploaded files would go through the Foodini in-built slicer software, which will generate a set of printing instructions for the printer for dot extrusion. Unlike model extrusion, there is no conversion of models into codes for the 3D food printer since the only input needed from the user is the extrusion volume.

Table 1. Foodini printer settings optimized for 4.0 mm nozzle diameter

Printer settings	Values
Nozzle size (mm)	4
Print speed (mm/min)	14000
Ingredient flow speed	1.65
Fill factor (%)	1
First ingredient hold (mm)	4.2
First ingredient flow (mm)	6.25
First layer nozzle height (mm)	3.4
First layer speed (%)	100
Ingredient hold (mm)	3
Line thickness (mm)	3.4
Distance between layers (mm)	3.5

2.4.1. 3D printing using dot extrusion

The dot function in the Foodini Creator hub allows different amounts of MP food inks to be extruded at once. By allowing a set volume of food inks to be extruded freely, the time taken for each extrusion and the mass of food ink extruded can be studied. By setting the dot extrusion at different volumes from 1 to 50 mL, three dots of MP food inks were extruded on a glass slide and subsequently weighed. By altering the amount of food ink extruded from 1 to 10 mL, the time taken for each dot extrusion was measured thrice by finding the two frames of the video where extrusion occurred. The average time taken was then recorded (Table S1, Supporting Information).

2.4.2. 3D printing using model extrusion

Three straight lines were 3D printed on a ceramic plate, where the line width served as a measure of the printing resolution, i.e., the standard of measurement.[23,43] The model had a length of 100 mm and a width of 4 mm and was created using the "line drawing" function in Foodini Creator. The straight line was subsequently printed for different printing parameters, such as printing speed and ingredient flow speed of 200–50,000 mm/min and 0.1–50, respectively. Resolution refers to the width of the 3D-printed straight line. Comparisons of the straight line were made at three different printing speeds (3500, 14,000, and 25,000 mm/min) and three ingredient flow speeds (1.65, 3.3, and 5.0).

2.5. Measurement of filament width and actual printing speed

Measurements of the length and line width of the printed straight line were performed thrice using ImageJ software (National Institutes of Health, USA). Premium Rush (Adobe Inc., USA) was used to locate the two frames when extrusion occurred, and the time taken for each print was measured. The actual printing speed was acquired by dividing the average length of the printed straight line by the average time taken for each print.

3. Results

3.1. Rheological characterization of MP food ink

To understand the rheological behavior of the MP food inks, viscosity experiments were conducted. The rheology results are depicted in Figure 1A, where it can be observed that the viscosity of the MP food inks decreased at a high shear rate and increased at a low shear rate. The ability to exhibit shear thinning behavior meant that MP inks are pseudoplastic materials, which is essential for food extrusion printing[44,45] as the food has to behave like a liquid to be extruded and a solid to form stable self-supporting structures.[46]

The data from the rheological study were then fitted to a viscosity model. According to researchers in the 3DFP field,[40,47] the power law model is a better fit for MP food inks as compared to other models.[48] Furthermore, the power law model is best suited for shear-thinning fluids[49] and chosen due to the best fit of $R^2 = 0.9991$. The relationship between kinematic viscosity (v) and shear rate ($\dot{\gamma}$) was analyzed using Equation (I):

$$v = K\dot{\gamma}^{n-1} \quad \text{I}$$

where the power law index (n) and flow consistency index (K) are displayed as the function of non-Newtonian viscosity (v). The power law index (n) indicates the flow behavior. A shear-thinning fluid would have $n < 1$. A smaller n indicates stronger shear thinning capability of the fluid. Fluids with small n and K form ideal food inks as these fluids can be ejected out of the extruder with ease.[50,51] Equation (I) was subsequently linearized into log form to determine the value of the power law and flow consistency index (Figure 1B and Equation [II]).

$$\log v = \log K + (n - 1) \log \dot{\gamma} \quad \text{II}$$

Through curve fitting, the power law index and flow consistency index are determined to be 0.347 and 131.5, respectively. These values could be useful for designing any mathematical model.

3.2. 3D printing using dot extrusion

3.2.1. Effect of nozzle geometry on food extrusion

The nozzle is a crucial part of 3D printing as the materials would be extruded through this small orifice. In 3DFP, the nozzle diameter is essential to get a robust model. According to existing 3DFP experiments,[45] a high-resolution 3D model would require a small-sized nozzle diameter. However, utilizing a smaller-sized nozzle would increase the printing time of the 3D models as compared to using a larger-sized nozzle. Therefore, the nozzle size was examined to understand its effect on food extrusion. With a digital microscope, it was observed that the exterior design of the different-sized nozzles was tapered. Even though the nozzles were tapered internally, the nozzles differed in terms of the geometry at the orifice. From Figure 2A, the digital microscope revealed a flat, thin wall

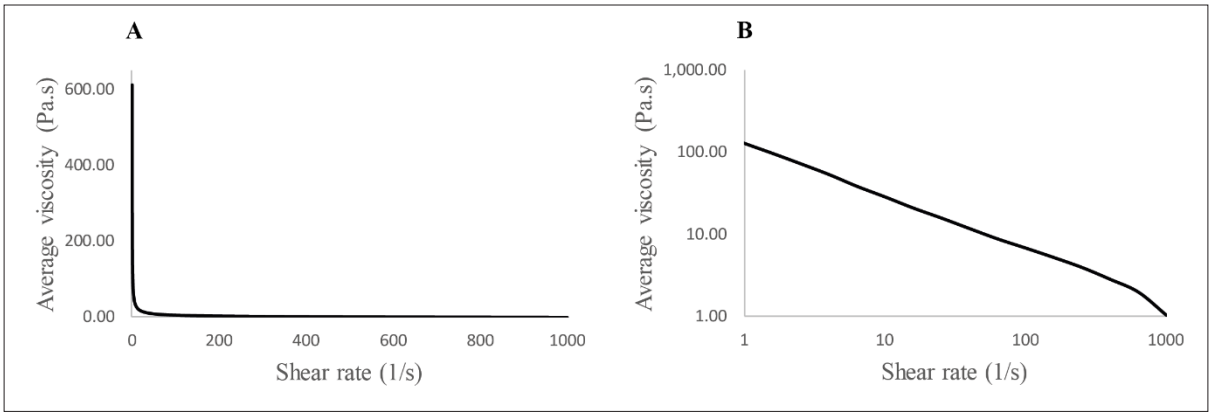


Figure 1. Rheological characterization of mashed potato (MP) food ink: (A) viscosity of the MP ink versus shear rate curve, and (B) linearized viscosity versus shear rate curve in logarithm form for curve fitting.

for the 0.8-mm nozzle, whereas the other nozzles (1.5 and 4.0 mm) were tapered throughout. The presence of the thin wall, indicated by the red circle in Figure 2B, suggests that lesser material would be extruded due to the restriction at the orifice. To prove this theory, dot extrusion at different volumes of 1–50 mL was extruded on a glass slide and weighed. Experimental results for the different nozzles reported that the time taken to extrude the set amount of MP food ink is identical (Figure 3A). Although Figure 3B displays the comparable mass of extruded MP food inks, the amount of extruded MP food ink decreased slightly for the smaller nozzle (0.8 mm) at low-volume extrusion. This deviation is much more pronounced in Figure 3C, whereby the mass flow rate of the MP food ink varied significantly for the different nozzles at low-volume extrusion. One possible reason for this occurrence could be the high noise factor which intensified the variations caused by the low control parameters. Nonetheless, the mass flow rate of

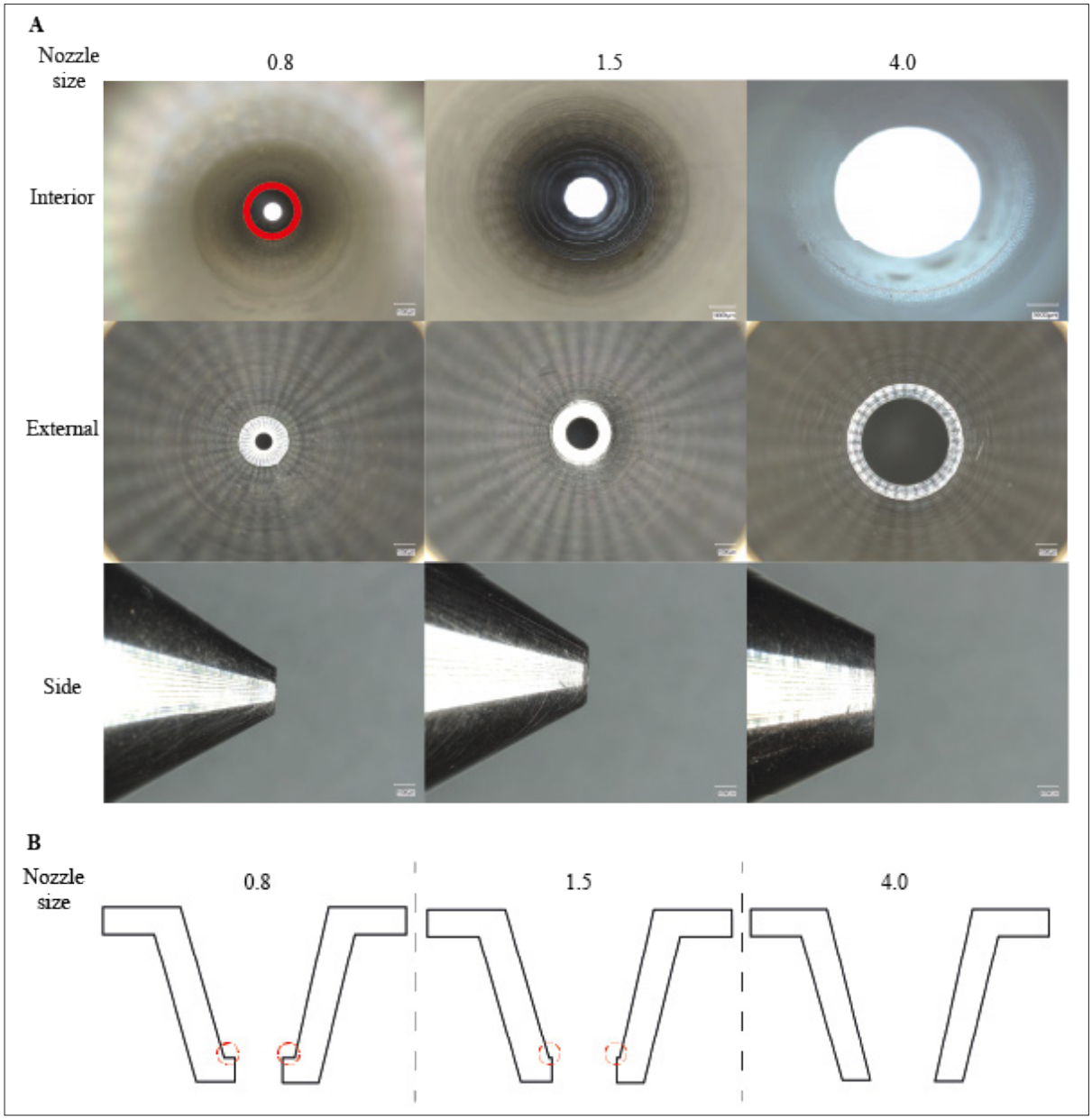


Figure 2. Effect of nozzle geometry on food extrusion. (A) Comparison of different nozzle diameters (0.8, 1.5, and 4.0 mm) at different perspectives using a digital microscope. Flat thin walls at the exit are indicated by the red circles. Scale bar: 1 mm. (B) Cross-sectional view of the internal geometry for different nozzle diameters (0.8, 1.5, and 4.0 mm) where the flat thin walls at the exit are indicated by the red circle.

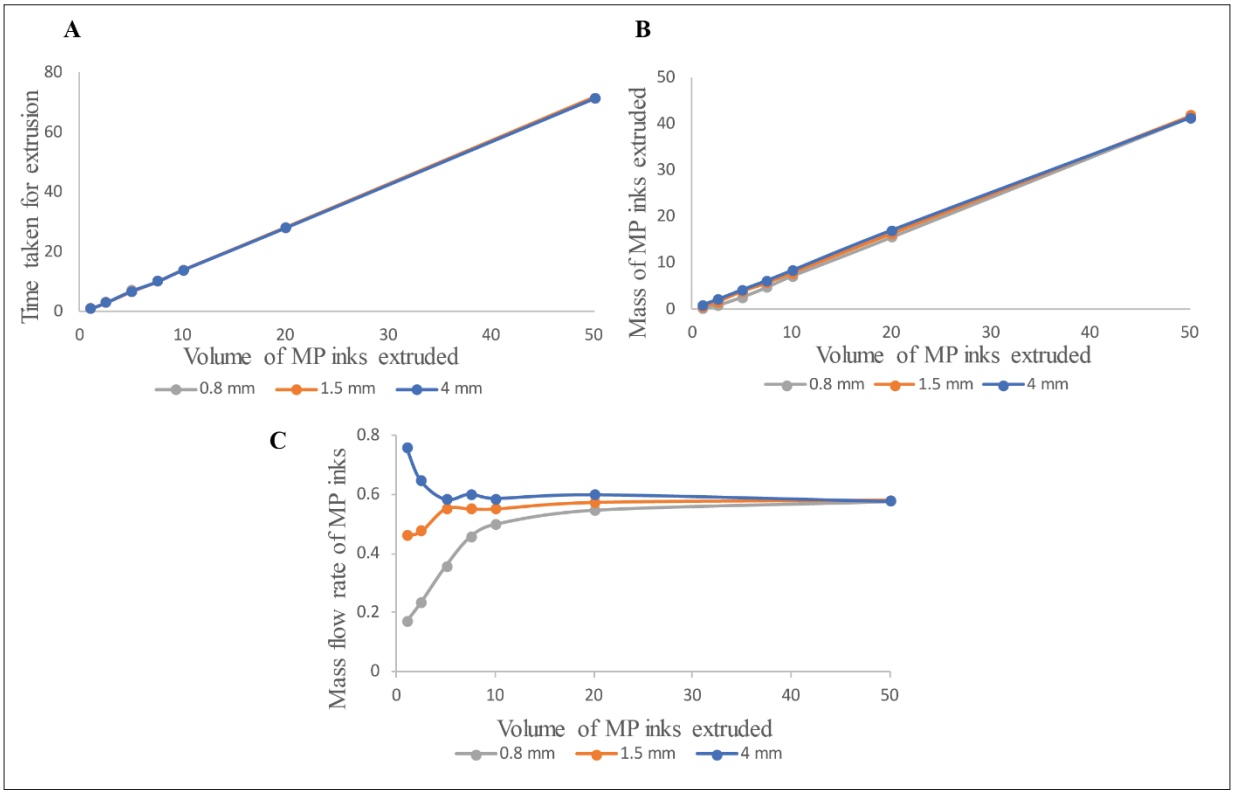


Figure 3. Effect of nozzle geometry on (A) time taken for extrusion, (B) mass of mashed potato (MP) food ink extruded, and (C) mass flow rate of food inks.

the MP food inks was relatively constant at 0.57 when the extruded volume was greater than 20 mL. Therefore, the geometry of the nozzle affects the food extrusion process but only at low-volume extrusion. The 4.0-mm nozzle was subsequently used throughout this research unless specified otherwise.

3.2.2. Effect of ingredient flow speed on extrusion time

To determine if there was any effect of the printing process parameters on the extrusion time, dot extrusion experiments were conducted with different printing process parameters. When dot extrusion occurs at a fixed point (i.e., the center of the dish without translational movement in the *x*- and *y*-axes), the printing speed is considered zero. However, it was discovered that ingredient flow speed does not affect the printing time, albeit printing speed is a variable in Equation (IX) (discussed later). This is evident from the experimental results (Figure 4), where the time taken for each material extrusion at each dot volume (1–50 mL) was the same at different ingredient flow speeds (Table S2, Supporting Information). One possible reason for this occurrence is that dot extrusion does not require slicing, thereby suggesting that the printing process parameters do not affect the extrusion process. Thus, ingredient flow speed does not affect the extrusion rate in dot volume extrusion.

3.3. 3D printing using model extrusion

3.3.1. Effect of printing speed on the width of the printed line

One of the main objectives of this paper is to study the effects of the control parameter on the print resolution. One of the said parameters is the printing speed, which refers to the speed of the nozzle head on the horizontal axis. Results revealed that at constant ingredient flow speed, there were some variations between the printing speed in the Foodini advanced user settings and the actual printing speed (Table 2). The printing speed displayed in Foodini was significantly higher compared to the actual printing speed. One possible reason is that the slicer in the Foodini Creator hub uses the speed acquired directly from the electric motor, which considers other functions of the printer, thereby resulting in a higher printing speed. Despite the differences in printing speed, the effect of printing speed on the resolution was still studied as the actual printing speed would increase when the printing speed in Foodini increases. In Figure 5A and B, the average width of the 3D-printed line remained relatively constant at 4.4

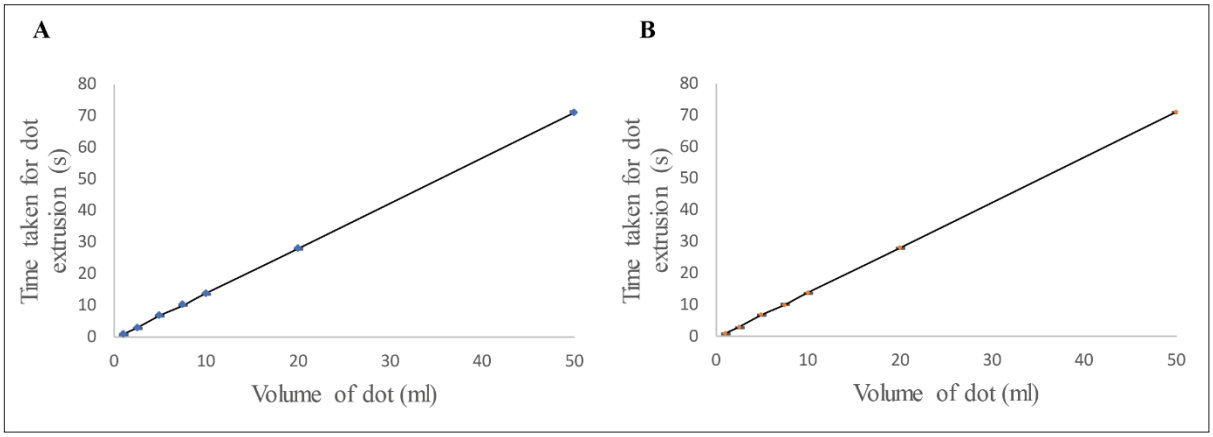


Figure 4. Effect of ingredient flow speed on extrusion time: (A) ingredient flow speed (V_{IFS}) = 1.65, and (B) V_{IFS} = 3.3.

mm despite the modifications in the printing speed while all other printing process parameters were kept constant (Table S3, Supporting Information). This is unexpected as it deviates from the conventional extrusion-based 3D printing knowledge, whereby an increase in printing speed will normally result in a decrease in width when printing a single-layered straight line.[23] In another experiment, where the Foodini print speed and the diameter of the nozzles were varied, the width of the printed line was consistent with each other. This suggested that the printed width is independent of the nozzle geometry, but this was not the case for the printed width at a higher printing speed and smaller nozzle. This could be attributed to the thin, flat wall that exists at the orifice, thereby limiting the amount of food ink extruded. Therefore, the printed width is much smaller at higher printing speeds and smaller nozzles (Table S4, Supporting Information).

3.3.2. Effect of ingredient flow speed on the width of the printed line

Ingredient flow speed is a dimensionless parameter that affects food material extrusion. Depending on the rheological property of the food material, the ingredient flow speed can be adjusted to extrude more or lesser materials. Unlike other 3D food printers that control material extrusion via pneumatic pressure, Foodini uses displacement extrusion to regulate the extrusion rate. Ingredient flow speed was altered to control the extruder on the vertical axis. Results reported an increase in the width of the printed line following an increase in the ingredient flow speed (Figure 6A and B; Table S3, Supporting Information). This indicates that ingredient flow speed functions similarly to the volumetric flow rate in a typical 3D food printer (Figure 6B). Subsequently, additional experiments were performed to determine if the correlation between ingredient flow speed and volumetric flow rate can be quantified (Table S5, Supporting Information). Altering the ingredient flow speed at constant printing speed, the arbitrary number (represented by M) changed at different ingredient flow speeds. This suggests that a scale factor exists between ingredient flow speed and volumetric flow rate. However, varying the printing speed at constant ingredient flow speed would also change the arbitrary value M, indicating that the arbitrary scale is affected not only by ingredient flow speed but also by printing speed. This establishes a relationship between ingredient flow speed, printing speed, and the arbitrary number M. Thus, it is challenging to correlate the ingredient flow speed directly with the volumetric flow rate due to this complex and interconnected relationship.

Table 2. Comparison between the printing speed in Foodini and the actual printing speed at an ingredient flow speed of 1.65

Parameter	Printing speed (mm/min)		
Foodini settings	3500	14,000	25,000
Actual	532 ± 1.7	1914 ± 52.2	3082 ± 86.9

Note: All values of actual printing speed are expressed as mean ± standard deviation.

3.3.3. Relationship between printing speed and ingredient flow speed

We also evaluated the effects of varying both the printing speed and ingredient flow speed. Notably, the actual printing speed decreased with an increase in ingredient flow speed (Figure 7A). Increasing the ingredient flow speed would be equivalent to pushing the materials harder, resulting in more materials exiting the nozzle. In this regard, it was expected that the printing speed would increase simultaneously with the extruded material volume and ingredient flow speed to ensure consistent line width

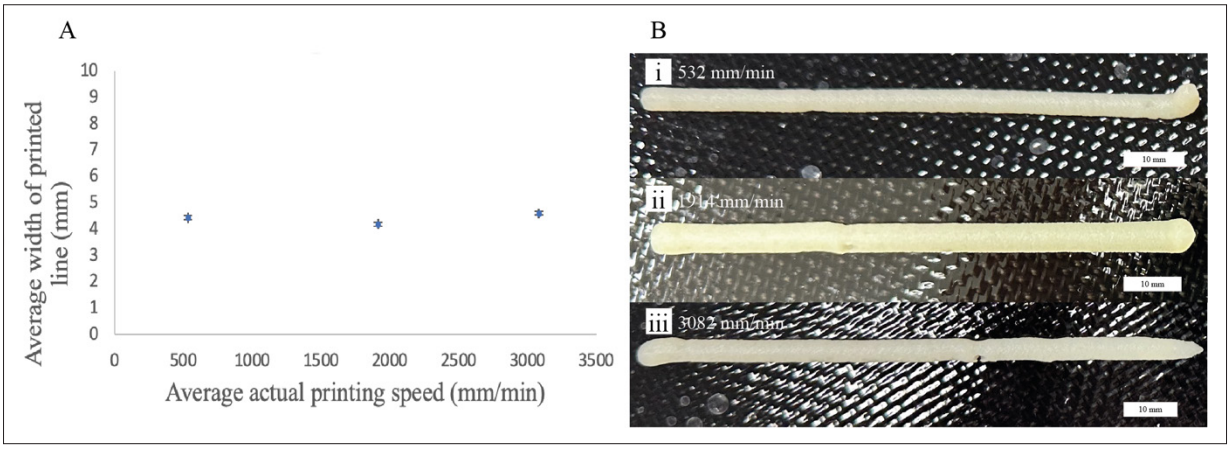


Figure 5. Effect of printing speed on the width of the printed line. (A) Average width of the 3D-printed line of mashed potatoes (MP) against the average actual printing speed, and (B) comparison of the printed width of the 3D-printed line at set Foodini printing speeds, i.e., (i) 3500 mm/min, (ii) 14,000 mm/min, and (iii) 25,000 mm/min, which correspond to average actual printing speeds of (i) 532 mm/min, (ii) 1914 mm/min, and (iii) 3082 mm/min. Scale bars: 10 mm.

without thickening, but the experimental results reported that the actual printing speed was decreased (Figure 7A and B). This observation could be attributed to the complicated relationship displayed in Equation (IX), where the decrease in printing speed could be the net result of interactions of all parameters.

4. Discussion

This section proposes a theoretical model for the 3D food extrusion process in Foodini 3D printers and is segmented into three parts: (i) to discuss the flow of the fluid in a pipe, (ii) to understand the food extrusion system, and (iii) connect the fluid flow model to the food extrusion process.

4.1. Governing equations for modeling fluid flow

The 3D food extrusion process is modeled based on non-Newtonian fluid flow in a pipe (Figure 8A), which is unlike most models that are designed for needle-like nozzles and capillary flow. The rationale for this basis is due to the difference in nozzle geometry (Figure 2A) for the Foodini 3D printers. Under the assumption that the fluid flow in the capsule is steady, unidirectional, and uniform in the *z*-axis, the MP food inks are driven into the capsule at a constant volumetric flow rate. In this study, the MP food inks are assumed to be incompressible and follow laminar flow. Under the condition that there is no slip and that the pressure at the nozzle is equal to the atmospheric pressure

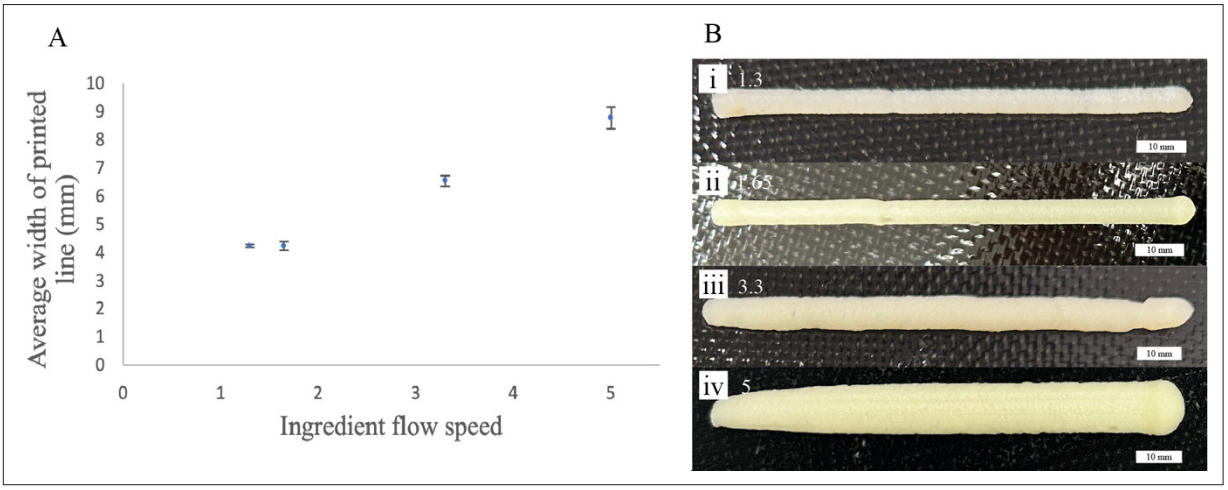


Figure 6. Effect of ingredient flow speed on the width of the printed line. (A) Average width of the 3D-printed line of mashed potatoes (MP) against the ingredient flow speed, and (B) comparison of printed width of the 3D-printed line at set Foodini ingredient flow speeds, i.e., 1.3, 1.65, 3.3, and 5. Scale bars: 10 mm.

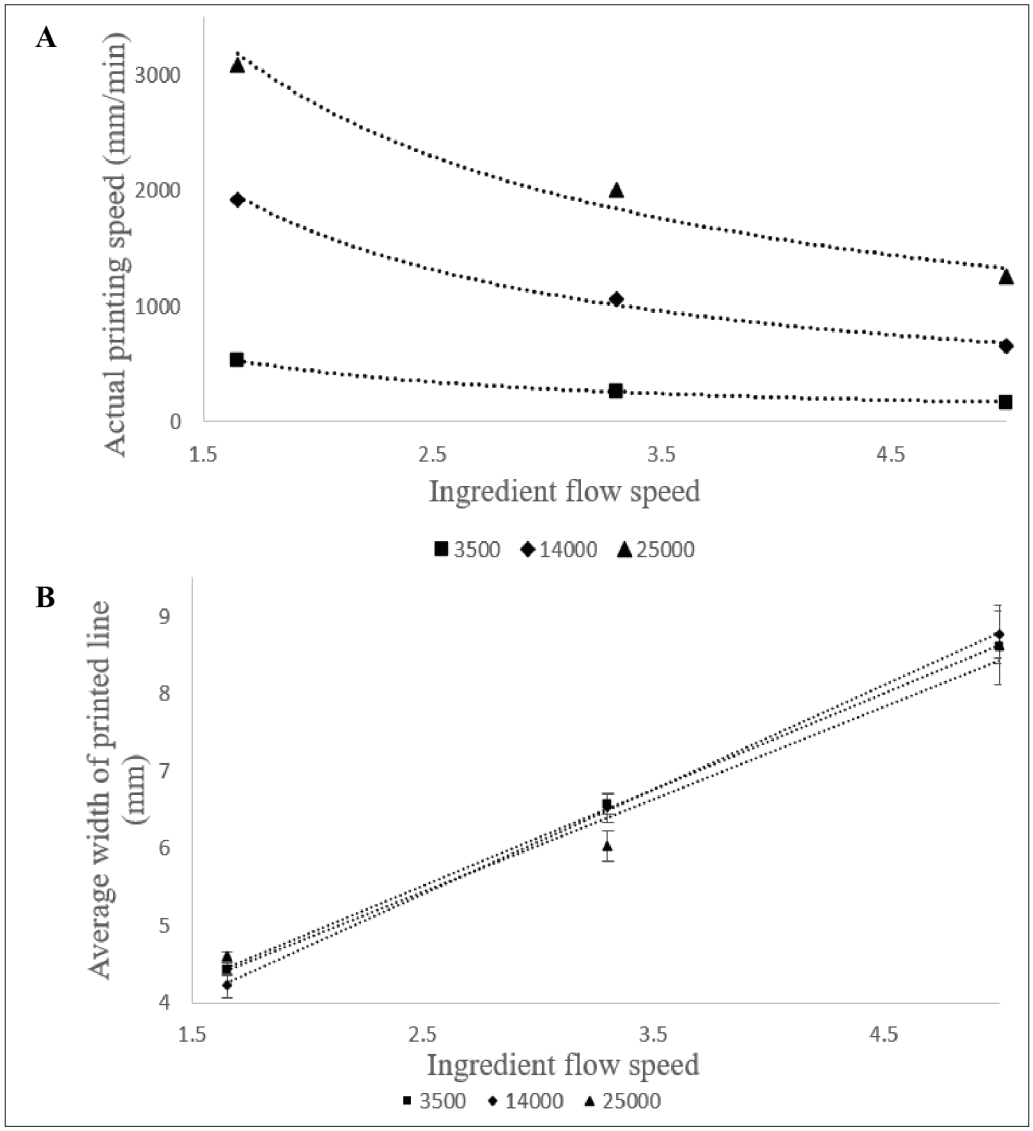


Figure 7. Effect of ingredient flow speed on (A) the actual printing speed and (B) the average width of the printed line for different printing speeds set in Foodini.

(0 Pa for gauge pressure), the mathematical model is established over two general equations, which govern the conservation of momentum and volumetric flow rate. After many derivations from previous literature, the flow rate through the pipe Q is represented by Equation (III).[44,49,52]

$$Q = \frac{\pi R^3}{\frac{1}{n}+3}\left(\frac{\Delta P R}{2LK}\right)^{\frac{1}{n}} \quad \text{III}$$

where R (m) denotes the inner radius of the Foodini capsule, ΔP (Pa) is the pressure drop through the capsule and nozzle, and L (m) is the extrusion length. Equation (IV) can be derived from Equation (III) after making pressure drop the subject, resulting in an equation that models fluid flow.

$$\Delta P = \frac{2LK}{R}\left[\frac{Q\left(\frac{1}{n}+3\right)}{\pi R^3}\right]^n \quad \text{IV}$$

4.2. Constitutive equations specific to Foodini 3D printers

To optimize the distinct control parameters of the Foodini 3D printer, a thorough analysis and modeling of its dispensing system are required (Figure 8B). The ingredient

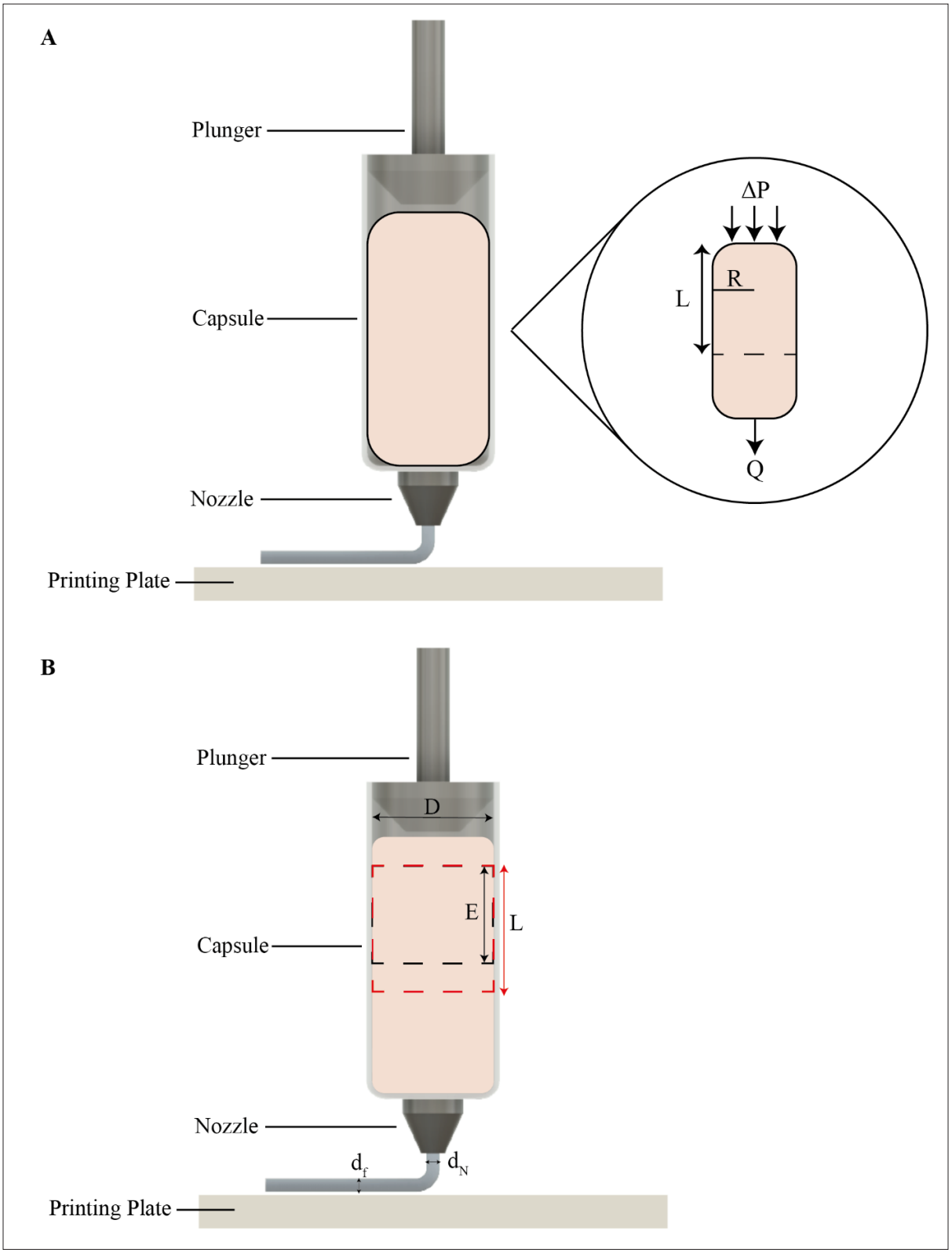


Figure 8. Schematic diagram of (A) the plunger-based extrusion for fluid flow modeling and (B) the graphical representation of ingredient flow speed in Foodini 3D food printers. Abbreviations: *Q*: flow rate; *R*: inner radius; *D*: diameter; Δ*P*: pressure drop; *L*: extrusion length based on material properties; *E*: extrusion length based on design model; d_N: diameter of nozzle; d_f: width of printed line.

flow speed V_{IFS} is defined as a ratio between the total length required based on the material's rheological properties L and the length required based on the design of the model E (Equation [V]). An increase or decrease in L would lead to a linear change in the ingredient flow speed, which affects the amount of material extruded subsequently. Based on this understanding, the ingredient flow speed is also equal to the ratio of the total required volume V_{Req} and the volume of the design model V_E.

$$V_{IFS} = \frac{L}{E} = \frac{V_{Req}}{V_E} \quad \text{V}$$

Equation (V) can be rearranged to Equation (VI), where V_{Req} is the subject:

$$V_{Req} = V_{IFS} \cdot V_E \quad \text{VI}$$

Following conservation of mass, the volume extruded by the plunger is equivalent to the amount of food ink exiting the nozzle. The total volume required (Equation [VII]) is tantamount to the volume of the printed straight line, which was modeled using the general equation $V_{Req} = \frac{\pi}{4} d^2 h$, where d represents the diameter and h represents the height. Equation (VII) is derived by replacing d with the diameter of the printed line d_f and h with the length of printed line l_{line}, which is equal to the printing speed V_{PS} multiplied by the time taken to extrude.

$$V_{Req} = \frac{\pi}{4} \cdot {d_f}^2 \cdot V_{PS} \cdot t \quad \text{VII}$$

Equation (VIII) is derived by replacing V_{Req} with Equation (VI).

$$V_{IFS} \cdot V_E = \frac{\pi}{4} \cdot {d_f}^2 \cdot V_{PS} \cdot t \quad \text{VIII}$$

$$d_f = \sqrt{\frac{4 \cdot V_{IFS} \cdot V_E}{\pi \cdot V_{PS} \cdot t}} \quad \text{IX}$$

From Equation (IX), it can be observed that there is a complex relationship between the independent (d_f) and dependent parameters (V_{IFS} and V_{PS}). In addition, the equation states that an increase in ingredient flow speed and a decrease in printing speed will result in a reduction in the width of the straight line. This is under the assumption that the printing process parameters are truly independent variables and work similarly to typical 3D food printers. However, this is not the case as the printing process parameter does not operate in a way that conforms to this logic. Thus, the factorial design to find out the interaction between the controllable variables (V_{IFS} and V_{PS}) is not suitable, as the two variables might not be truly independent of each other. In addition, the actual printing speed is largely different from the set printing speed (Table 2), and the control over printing speed is not precise and limited.

4.3. Integration of constitutive equations into the fluid flow model

Based on our understanding of the Foodini process parameters and fluid flow model, the constitutive Foodini Equation (VI) is integrated into the governing Equation (IV) of the fluid flow model to derive a novel equation that models the food extrusion process using Foodini control parameters, as well as the rheological properties of the food ink.

$$Q = V_{Req} = V_{IFS} \cdot V_E \quad \text{X}$$

$$\Delta P = \frac{2LK}{R} \left[\frac{V_{IFS} \cdot V_E \left(\frac{1}{n} + 3 \right)}{\pi R^3} \right]^n \quad \text{XI}$$

Subsequently, replacing L with the following $L = \frac{V_{Req}}{\pi R^2}$ gives Equation (XII).

$$\Delta P = \frac{2K}{R} \cdot \frac{V_{IFS} \cdot V_E}{\pi R^2} \left[\frac{V_{IFS} \cdot V_E \left(\frac{1}{n} + 3 \right)}{\pi R^3} \right]^n \quad \text{XII}$$

To understand the relationship between ΔP and the ingredient flow speed V_{IFS}, the ingredient flow speed is taken out and combined, which is expressed in the equation below.

$$\Delta P = \frac{2K}{R} \cdot \frac{V_E}{\pi R^2} \left[\frac{V_E \left(\frac{1}{n} + 3 \right)}{\pi R^3} \right]^n \cdot {V_{IFS}}^{n+1} \quad \text{XIII}$$

Since the radius of the capsule R, design volume V_E, flow behavior n, and consistency index k are constants, Equation (XIII) can be reduced to the following Equation (XIV).

$$\Delta P = A \cdot V_{IFS}{}^{n+1} \text{ where } A = \frac{2K}{R} \cdot \frac{V_E}{\pi R^2} \left[\frac{V_E \left(\frac{1}{n} + 3 \right)}{\pi R^2} \right]^n \quad \text{XIV}$$

Thus, the proposed theoretical relationship between ΔP and ingredient flow speed V_{IFS} can be described as follows:

$$\Delta P \propto V_{IFS}{}^{n+1}$$

It is predicted that there is a power law relationship between pressure drop and ingredient flow speed. However, the measurement of pressure drop inside the Foodini capsule proves to be extremely challenging. It is not practical, within current means, to validate the power law relationship via experimentation. Nevertheless, this proposed theoretical relationship aligns with the current logic that higher pressure would result in larger material extrusion.

5. Conclusion

In this research, both experimental and theoretical approaches were used to understand the extrusion-based printing process of Foodini, particularly the effect of ingredient flow speed. Despite the increasing use of Foodini in research, this is the first work that attempts to analyze the food extrusion process in Foodini. Through this study, a novel Foodini-specific model is introduced, which elucidates the correlation between the process parameters and the extrusion resolution. The proposed model also serves as a framework for future food printers and a modeling approach superior to a math model. Furthermore, this model is unique as it considers the rheological properties of the materials and printer-specific process controls, i.e., V_{IFS}. However, one limitation of this model is that there is no existing method to validate the model, as Foodini is not equipped with the capability to measure pressure. Experimental results have reported a constant extrusion rate that is independent of the nozzle geometry and ingredient flow speed in the dot extrusion mode. However, in other printing modes where slicing is required, the ingredient flow speed affects the extrusion rate. Another finding about the Foodini printer is the difference between the printing speed of Foodini and the actual printing speed, which could be due to the direct conversion of the speed of the electric motor. In addition, experimental data unveiled that the amount of material extruded is independent of the nozzle geometry when the volume extruded is greater than 20 mL. Other findings included the effects of the process parameters on the resolution, which revealed two interesting observations: (i) the printing speed in Foodini does not affect the diameter of the 3D-printed straight line, and (ii) the ingredient flow speed V_{IFS} affects the actual printing speed, even when the printing speed in Foodini is kept constant. Nonetheless, the findings of this investigation validated the complex relationship between the parameters due to the introduction of V_{IFS}. A direct validation method should be developed in the future to verify the model. Although MPs are used as the ink of study, more food materials can be researched and analyzed to improve the applicability of the model. Overall, this study offers valuable insights into Foodini-based extrusion printing and may serve as a foundational guide for further exploration in this evolving field.

Acknowledgments

P.X.N.L acknowledged the financial support from the SUTD PhD Fellowship presented by the Ministry of Education (MOE), Singapore.

Funding

The authors would like to thank SUTD Kickstarter Initiative SKI_2021_02_05 for the funding support.

Conflict of interest

The authors declare no conflicts of interest.

Author contributions

Conceptualization: Phoebe Xin Ni Leam, Jia An, Chen Huei Leo, U-Xuan Tan, Chee Kai Chua

Formal analysis: Phoebe Xin Ni Leam, Aakanksha Pant, Jia An, U-Xuan Tan, Chee Kai Chua

Investigation: Phoebe Xin Ni Leam, Aakanksha Pant, Jia An, U-Xuan Tan, Chee Kai Chua

Methodology: Phoebe Xin Ni Leam, Aakanksha Pant, Jia An, Chen Huei Leo, U-Xuan Tan, Chee Kai Chua

Writing – original draft: Phoebe Xin Ni Leam, Aakanksha Pant, Jia An, U-Xuan Tan, Chee Kai Chua

Writing – review & editing: Phoebe Xin Ni Leam, Aakanksha Pant, Jia An, Chen Huei Leo, U-Xuan Tan, Chee Kai Chua

Ethics approval and consent to participate

Not applicable.

Consent for publication

Not applicable.

Availability of data

Data are available from the corresponding author upon reasonable request.

References

1. Joshi SC, Sheikh AA. 3D printing in aerospace and its long-term sustainability. *Virtual Phys Prototyp*. 2015;10(4):175-185. doi: 10.1080/17452759.2015.1111519
2. Gu Z, Fu J, Lin H, et al. Development of 3D bioprinting: from printing methods to biomedical applications. *Asian J Pharm Sci*. 2020;15(5):529-557. doi: 10.1016/j.ajps.2019.11.003
3. Lee J-Y, An J, Chua CK. Fundamentals and applications of 3D printing for novel materials. *Appl Mater Today*. 2017;7:120-133. doi: 10.1016/j.apmt.2017.02.004
4. Lee AY, An J, Chua CK. Two-way 4D printing: a review on the reversibility of 3D-printed shape memory materials. *Engineering* 2017;3(5):663-674. doi: 10.1016/j.Eng.2017.05.014
5. Thangalakshmi S, Arora VK. Three-dimensional (3D) food printing and its process parameters. In: Sandhu K, Singh S, (eds) *Food Printing: 3D Printing in Food Industry*. Singapore: Springer; 2022:35-45. doi: 10.1007/978-981-16-8121-9_3
6. Pant A, Lee AY, Karyappa R, et al. 3D food printing of fresh vegetables using food hydrocolloids for dysphagic patients. *Food Hydrocoll*. 2021;114:106546-106546. doi: 10.1016/J.FOODHYD.2020.106546
7. Tejada-Ortigoza V, Cuan-Urquizo E. Towards the development of 3D-printed food: a rheological and mechanical approach. *Foods*. 2022;11(9):1191.
8. Severini C, Azzollini D, Albenzio M, et al. On printability, quality and nutritional properties of 3D printed cereal based snacks enriched with edible insects. *Food Res Int*. 2018;106:666-676. doi: 10.1016/j.foodres.2018.01.034
9. Liu Z, Bhandari B, Prakash S, et al. Creation of internal structure of mashed potato construct by 3D printing and its textural properties. *Food Res Int*. 2018;111:534-543. doi: 10.1016/j.foodres.2018.05.075
10. Guénard-Lampron V, Masson M, Leichtnam O, et al. Impact of 3D printing and post-processing parameters on shape, texture and microstructure of carrot appetizer cake. *Innovative Food Sci Emerg Technol*. 2021;72:102738. doi: 10.1016/j.ifset.2021.102738
11. Lee CP, Karyappa R, Hashimoto M. 3D printing of milk-based product. *RSC Adv*. 2020;10(50):29821-29828. doi: 10.1039/d0ra05035k
12. Zhang L, Lou Y, Schutyser MAI. 3D printing of cereal-based food structures containing probiotics. *Food Struct*. 2018;18:14-22. doi: 10.1016/j.foostr.2018.10.002
13. Leroy JL, Ruel M, Frongillo EA, et al. Measuring the food access dimension of food security: a critical review and mapping of indicators. *Food Nutr Bull*. 2015;36(2):167-195. doi: 10.1177/0379572115587274
14. Pant A, Leam PXN, Chua CK, et al. Valorisation of vegetable food waste utilising three-dimensional food printing. *Virtual Phys Prototyp*. 2022;18(1). doi: 10.1080/17452759.2022.2146593
15. Lee CP, Takahashi M, Arai S, et al. 3D printing of Okara Ink: the effect of particle size on the printability. *ACS Food Sci Technol*. 2021;1(11):2053-2061. doi: 10.1021/acsfoodscitech.1c00236
16. Hussain S, Malakar S, Arora VK. Extrusion-based 3D food printing: technological approaches, material characteristics, printing stability, and post-processing. *Food Eng Rev*. 2022;14(1):100-119. doi: 10.1007/s12393-021-09293-w
17. Voon SL, An J, Wong G, et al. 3D food printing: a categorised review of inks and their development. *Virtual Phys Prototyp*. 2019;14(3):203-218. doi: 10.1080/17452759.2019.1603508
18. Chen X, Zhang M, Tang T. Microwave-induced rapid shape change of 4D printed vegetable-based food. *Foods*. 2023;12(11):2158. doi: 10.3390/foods12112158
19. Dick A, Bhandari B, Dong X, et al. Feasibility study of hydrocolloid incorporated 3D printed pork as dysphagia food. *Food Hydrocoll*. 2020;107:105940. doi: 10.1016/j.foodhyd.2020.105940
20. Lipton J, Arnold D, Nigl F, et al. Multi-material Food Printing with Complex Internal Structure Suitable for Conventional Post-processing. Austin, TX: University of Texas at Austin; 2010.
21. Zhang Y, Lee AY, Pojchanun K, et al. Systematic engineering approach for optimization of multi-component alternative protein-fortified 3D printing food Ink. *Food Hydrocoll*. 2022;131:107803. doi: 10.1016/j.foodhyd.2022.107803
22. Liang Y, Chitrakar B, Liu Z, et al. Preparation and characterization of 3D-printed antibacterial hydrogel with benzyl isothiocyanate. *Int J Bioprint*. 2023;9(2):671. doi: 10.18063/ijb.v9i2.671
23. Suntornnond R, Tan EYS, An J, et al. A mathematical model on the resolution of extrusion bioprinting for the development of new bioinks. *Materials*. 2016;9(9):756. doi: 10.3390/ma9090756

24. Lee JM, Yeong WY. A preliminary model of time-pressure dispensing system for bioprinting based on printing and material parameters. *Virtual Phys Prototyp*. 2014; 10(1):3-8.
doi: 10.1080/17452759.2014.979557

25. Patel P, Mujmer K, Aswal VK, et al. Structure, rheology, and 3D printing of salt-induced κ-carrageenan gels. *Mater Today Commun*. 2023;35: 105807.
doi: 10.1016/j.mtcomm.2023.105807

26. Maldonado-Rosas R, Pérez-Castillo JL, Cuan-Urquizo E, et al. The role of controlled voids shape on the flexural properties of 3D printed food: an approach for tailoring their mechanical properties. *Virtual Phys Prototyp*. 2024; 19(1).
doi: 10.1080/17452759.2023.2284816

27. Lee AY, Pant A, Hashimoto M, et al. 3D food printing – Asian snacks and desserts. Mater Today Proc. 2022; 70:611-615.

28. Ahmadzadeh S, Clary T, Rosales A, et al. Upcycling imperfect broccoli and carrots into healthy snacks using an innovative 3D food printing approach. *Food Sci Nutr*. 2023;12(1):84-93.
doi: 10.1002/fsn3.3820

29. Chow CY, Thybo CD, Sager VF, et al. Printability, stability and sensory properties of protein-enriched 3D-printed lemon mousse for personalised in-between meals. *Food Hydrocoll*. 2021;120:106943.
doi: 10.1016/j.foodhyd.2021.106943

30. Gudjónsdóttir M, Napitupulu RJ, Petty Kristinsson HT. Low field NMR for quality monitoring of 3D printed surimi from cod by-products: effects of the pH shift method compared with conventional washing. *Magn Reson Chem*. 2019;57(9):638-648.
doi: 10.1002/mrc.4855

31. Hamilton AN, Gibson KE. Transfer rates of Salmonella Typhimurium, Listeria monocytogenes, and a human norovirus surrogate impacted by macronutrient composition of food inks in 3D food printing systems. *Food Microbiol*. 2023;113:104268.
doi: 10.1016/j.fm.2023.104268

32. Mirazimi F, Saldo J, Sepulcre F, et al. Enriched puree potato with soy protein for dysphagia patients by using 3D printing. *Food Front*. 2022;3(4):706-715.
doi: 10.1002/fft2.149

33. Tay JU, Zhou C, Lee HW, et al. 3D printing of salmon fillet mimic: imparting printability via high-pressure homogenization and post-printing texturization via transglutaminase. *Food Hydrocoll*. 2023;140: 108564.
doi: 10.1016/j.foodhyd.2023.108564

34. Tan JD, Lee CP, Foo SY, et al. 3D printability and biochemical analysis of revalorized orange peel waste. *Int J Bioprint*. 2023;9(5):776.
doi: 10.18063/ijb.776

35. Tian J, Chen J, Ye X, et al. Health benefits of the potato affected by domestic cooking: a review. *Food Chem*. 2016;202:165-175.
doi: 10.1016/j.foodchem.2016.01.120

36. Beals KA. Potatoes, nutrition and health. *Am J Potato Res*. 2019;96(2):102-110.
doi: 10.1007/s12230-018-09705-4

37. Zhang Z, Zheng B, Tang Y, et al. Starch concentration is an important factor for controlling its digestibility during hot-extrusion 3D printing. *Food Chem*. 2022; 379:132180.
doi: 10.1016/j.foodchem.2022.132180

38. Liu Z, Zhang M, Yang C-h. Dual extrusion 3D printing of mashed potatoes/strawberry juice gel. *Lwt*. 2018;96:589-596.
doi: 10.1016/j.lwt.2018.06.014

39. Liu Z, Zhang M, Bhandari B, et al. Impact of rheological properties of mashed potatoes on 3D printing. *J Food Eng*. 2018;220:76-82.
doi: 10.1016/j.jfoodeng.2017.04.017

40. Cui Y, Li C, Guo Y, et al. Rheological & 3D printing properties of potato starch composite gels. *J Food Eng*. 2022;313(1):110756.
doi: 10.1016/j.jfoodeng.2021.110756

41. Wu H, Sang S, Weng P, et al. Structural, rheological, and gelling characteristics of starch-based materials in context to 3D food printing applications in precision nutrition. *Compr Rev Food Sci Food Saf*. 2023;22(6):4217-4241.
doi: 10.1111/1541-4337.13217

42. Liu Y, Dong L, Li Y, et al. Soy protein isolate-citrus pectin composite hydrogels induced by TGase and ultrasonic treatment: potential targeted delivery system for probiotics. *Food Hydrocoll*. 2023;143(11): 108901.
doi: 10.1016/j.foodhyd.2023.108901

43. Ma Y, Schutyser MAI, Boom RM, et al. Predicting the extrudability of complex food materials during 3D printing based on image analysis and gray-box data-driven modelling. *Innovative Food Sci Emerg Technol*. 2021;73:102764.
doi: 10.1016/j.ifset.2021.102764

44. Liu Z, Bhandari B, Prakash S, et al. Linking rheology and printability of a multicomponent gel system of carrageenan-xanthan-starch in extrusion based additive manufacturing. *Food Hydrocoll*. 2019;87:413-424.
doi: 10.1016/j.foodhyd.2018.08.026

45. Liu Z, Zhang M, Bhandari B. Effect of gums on the rheological, microstructural and extrusion printing characteristics of mashed potatoes. *Int J Biol Macromol*. 2018;117:1179-1187.
doi: 10.1016/j.ijbiomac.2018.06.048

46. Liu Z, Zhang M, Bhandari B, et al. 3D printing: printing precision and application in food sector. *Trends Food Sci Technol*. 2017;69:83-94.
doi: 10.1016/j.tifs.2017.08.018

47. Sun Y, Zhang M, Chen H. LF-NMR intelligent evaluation of rheology and printability for 3D printing of cookie dough pretreated by microwave. *Lwt*. 2020;132: 109752. doi: 10.1016/j.lwt.2020.109752

48. Tagliavini G, Solari F, Montanari R. CFD simulation of a co-rotating twin-screw extruder: validation of a rheological model for a starch-based dough for snack food. *Int J Food Eng*. 2017;14(2):20170116.

49. Liu Z, Zhang M, Ye Y. Indirect prediction of 3D printability of mashed potatoes based on LF-NMR measurements. *J Food Eng*. 2020;287: 110137. doi: 10.1016/j.jfoodeng.2020.110137

50. Huang M-s, Zhang M, Guo C-f. 3D printability of brown rice gel modified by some food hydrocolloids. *J Food Process Preserv*. 2020;44(7):e14502. doi: 10.1111/jfpp.14502

51. Teng X, Zhang M, Bhandri B. 3D printing of Cordyceps flower powder. *J Food Process Eng*. 2019;42(6):e13179. doi: 10.1111/jfpe.13179

52. Liu Y, Liang X, Saeed A, et al. Properties of 3D printed dough and optimization of printing parameters. *Innovative Food Sci Emerg Technol*. 2019;54:9-18. doi: 10.1016/j.ifset.2019.03.008

ACCSCIENCE PUBLISHING

International Journal of Bioprinting

RESEARCH ARTICLE

3D-printed Mg-substituted hydroxyapatite/gelatin methacryloyl hydrogels encapsulated with PDA@DOX particles for bone tumor therapy and bone tissue regeneration

Shangsi Chen[1†], Yue Wang[1,2†], Junzhi Li[3†], Haoran Sun[4*], Ming-Fung Francis Siu[2*], and Shenglong Tan[5*]

[1]Department of Mechanical Engineering, Faculty of Engineering, The University of Hong Kong, Pokfulam Road, Hong Kong, China

[2]Department of Building and Real Estate, Faculty of Construction and Environment, The Hong Kong Polytechnic University, Hung Hom, Kowloon, Hong Kong, China

[3]Department of Surgery, School of Clinical Medicine, The University of Hong Kong, Pokfulam Road, Hong Kong, China

[4]Koln 3D Technology (Medical) Limited, Hong Kong Science Park, Shatin, Hong Kong, China

[5]Department of Endodontics, Stomatological Hospital, Southern Medical University, Guangzhou, China

(This article belongs to the *Special Issue: Advanced Biomaterials for 3D Printing and Healthcare Application*)

Abstract

The development of bifunctional scaffolds for clinical applications, aimed at preventing tumor recurrence and promoting bone tissue regeneration simultaneously at the surgical site, is imperative in repairing bone tumor-related defects. In the current study, Mg-substituted hydroxyapatite (MgHAp) nanocomposites were synthesized via a biomineralization process. Doxorubicin hydrochloride (DOX), an anticancer drug, was incorporated in polydopamine (PDA) particles to synthesize PDA@DOX particles. MgHAp/gelatin methacryloyl (GelMA) hydrogels encapsulated with PDA@DOX particles were designed and fabricated to construct MgHAp/GelMA-PDA@DOX hydrogels via 3D printing. The 3D-printed MgHAp/GelMA-PDA@DOX hydrogels exhibited antitumor synergy by providing combined chemotherapy and phototherapy for bone tumor cell ablation. The hydrogels showed a good photothermal effect and could induce hyperthermia upon irradiation with an 808 nm near-infrared (NIR) laser. Moreover, MgHAp/GelMA-PDA@DOX hydrogels could release DOX sustainably and controllably. *In vitro* experiments demonstrated that 3D-printed MgHAp/GelMA-PDA@DOX hydrogels could effectively eradicate MG63 cells through the synergy of induced hyperthermia and DOX release. Furthermore, due to the sustained release of Mg^{2+}, 3D-printed MgHAp/GelMA-PDA@DOX hydrogels could promote the proliferation of rat bone marrow-derived mesenchymal stem cells and facilitate alkaline phosphatase activity and the expression of osteogenic genes, such as osteocalcin (*Ocn*), type I collagen (*Col1*), runt-related transcription factor-2 (*Runx2*), and bone morphogenetic protein-2 (*Bmp2*), indicating their excellent osteogenic effect. As a result, 3D-printed MgHAp/GelMA-PDA@DOX hydrogels showed great potential in the treatment of bone tumor-related defects by effectively killing tumor cells and simultaneously promoting bone tissue regeneration.

[†]These authors contributed equally to this work.

***Corresponding authors:**
Haoran Sun
(haoran@koln3d-tech.com)

Ming-Fung Francis Siu
(francis.siu@polyu.edu.hk)

Shenglong Tan
(tansl1989@outlook.com)

Citation: Chen S, Wang Y, Li J, Sun H, Siu MF, Tan S. 3D-printed Mg-substituted hydroxyapatite/gelatin methacryloyl hydrogels encapsulated with PDA@DOX particles for bone tumor therapy and bone tissue regeneration. *Int J Bioprint*. 2024;10(5):3526. doi: 10.36922/ijb.3526

Received: April 29, 2024
Accepted: May 14, 2024
Published Online: July 17, 2024

Copyright: © 2024 Author(s). This is an Open Access article distributed under the terms of the Creative Commons Attribution License, permitting distribution, and reproduction in any medium, provided the original work is properly cited.

Publisher's Note: AccScience Publishing remains neutral with regard to jurisdictional claims in published maps and institutional affiliations.

***Keywords*:** 3D printing; Magnesium; Anti-tumor effect; Bone tissue regeneration; Controlled release

1. Introduction

Osteosarcoma, a malignant bone tumor, is typically managed through surgical resection in clinical practice.[1] However, incomplete removal of tumor cells often leads to tumor recurrence. Consequently, chemotherapy and radiotherapy are commonly employed post-surgery to eradicate residual tumor cells.[2,3] Nevertheless, previous studies have indicated that these non-targeted approaches may result in side effects such as damage to normal cells and drug resistance development. To overcome these limitations, the development of an on-site controlled drug release system mediated and assisted by photothermal therapy (PTT) is crucial for minimizing drug dosage and avoiding cytotoxicity while enhancing therapeutic efficacy in tumor treatment.[4,5] Photothermal agents play an essential role in achieving effective PTT by inducing hyperthermia at cancerous site and simultaneously modulating drug release upon near-infrared (NIR) laser irradiation, thereby effectively eradicating residual tumor cells and enhancing antitumor efficacy.[6,7] Among various photothermal agents, such as gold nanoparticles, copper nanoparticles, magnetic iron-oxide nanoparticles, and carbon-based nanomaterials, polydopamine (PDA) nanoparticles have attracted significant interest in tissue engineering and controlled drug release due to their remarkable biocompatibility, biodegradability, and excellent photothermal property.[8,9] Furthermore, the abundant catechol and amine groups of PDA nanoparticles confer excellent adhesive capability that facilitates high drug loading efficiency. In this context, many studies have employed PDA nanoparticles for encapsulating diverse drugs and biomolecules in tissue engineering and cancer therapy applications.[10,11]

Resection of a bone tumor inevitably results in bone defects post-surgery. Despite the inherent self-regeneration ability of native bone tissue, three-dimensional (3D) tissue engineering scaffolds are preferred to be used to significantly accelerate the healing process of bone defects.[12,13] Tissue engineering scaffolds possess 3D structures that mimic the anatomical characteristics and provide essential functions of targeted tissues through the combination of suitable biomaterials and cells, along with the incorporation of appropriate biomolecules, and therefore have been widely used for treating bone defects.[14–16] Compared to conventional 3D scaffold manufacturing technologies, i.e., solvent casting/particle leaching, freeze-drying, gas forming, thermal-induced phasing separation, and electrospinning, 3D printing technology significantly enhances the potential in regenerating tissues due to its remarkable ability in constructing customized and patient-specific scaffolds that closely mimic the intricate and complex anatomical structures of native tissues.[17–19] Numerous 3D-printed scaffolds have been extensively designed and employed to repair bone tissues in preclinical and clinical trials. For example, some 3D-printed metallic scaffolds (e.g., stainless steel, titanium) have been used in clinical practice for bone tissue engineering.[20] Among various 3D-printed scaffolds, gelatin methacryloyl (GelMA)-based hydrogels and hydroxyapatite (HAp)-based scaffolds have shown great potential in bone tissue engineering.[21–23]

GelMA is a popular biomaterial for 3D printing.[24,25] It is an engineered gelatin-based biomaterial synthesized through the methacrylation of the lysine groups in the gelatin backbones.[26] As a result, GelMA exhibits great similarity to gelatin in terms of excellent biocompatibility, biodegradability, and temperature-responsive behavior, as well as the presence of Arg-Gly-Asp (RGD) sequences, which facilitate cell adhesion. Additionally, GelMA possesses good photo-crosslinking ability and can be covalently crosslinked with water-soluble photoinitiators when exposed to visible or ultraviolet (UV) light, thereby forming stable hydrogel networks. Therefore, 3D-printed GelMA hydrogels have gained significant attention in bone tissue engineering.[27,28] For example, Zhang et al. demonstrated that 3D-printed reduced graphene oxide (rGO)/GelMA hydrogels could enhance osteogenic and neurogenic dual differentiation simultaneously for potential neutralized bone regeneration.[29] However, it should be noted that GelMA inks often exhibit poor printability and the resulting GelMA hydrogels possess inadequate mechanical strength, posing challenges for 3D printing and bone tissue regeneration.

Many efforts have been devoted to improving the printability of GelMA inks and enhancing the mechanical performance of 3D-printed GelMA hydrogels.[25,30] Generally, incorporating ceramic nanoparticles in GelMA hydrogels has proven effective in addressing these challenges.[31,32] HAp—a bioceramic known for its exceptional biocompatibility, bioactivity, and osteoconductivity—is widely used as a bone substitute biomaterial, and HAp-based scaffolds have demonstrated significant potential in bone tissue regeneration. Previous studies have indicated that 3D-printed HAp/GelMA hydrogels could improve the printability of inks, enhance mechanical strength, and promote bone tissue regeneration.[33] For example, Song et al. demonstrated

that HAp/GelMA hydrogels showed excellent mechanical strength and could facilitate osteogenic differentiation *in vitro* and accelerate the formation of new bone in rabbit skull defects *in vivo*.[34] Furthermore, previous studies have revealed that magnesium (Mg)-doped HAp (MgHAp) displayed a superior osteogenic effect in comparison to HAp, owing to the sustained release of Mg^{2+} ions. The release of Mg^{2+} enabled to modulate bone metabolism, regulate osteoblast and osteoclast activity, and stimulate new bone formation.[35,36] Consequently, compared to HAp/GelMA hydrogels, 3D-printed MgHAp/GelMA hydrogels may potentially provide an enhanced therapeutic efficacy for the treatment of bone defects.

In the current study, to build an on-site controlled drug release system that can induce hyperthermia and modulate drug release for eradicating tumor cells and simultaneously promote bone tissue regeneration, MgHAp/GelMA hydrogels encapsulated with PDA@DOX particles (MgHAp/GelMA-PDA@DOX) were fabricated via 3D printing (Figure 1). PDA particles encapsulated with an anticancer drug, doxorubicin hydrochloride (DOX), were synthesized and then incorporated in MgHAp/GelMA hydrogels. The incorporation of MgHAp significantly improved the printability of inks and enhanced the mechanical strength of resulting hydrogels. Moreover, 3D-printed MgHAp/GelMA-PDA@DOX hydrogels exhibited a good photothermal effect and enabled sustainable and controllable release of DOX. *In vitro* experiments demonstrated that 3D-printed MgHAp/GelMA-PDA@DOX hydrogels could be combined with chemotherapy and PTT and hence effectively eradicate MG63 osteosarcoma cells. Compared to HAp/GelMA-PDA hydrogels, MgHAp/GelMA-PDA hydrogels promoted proliferation and osteogenic differentiation of rat bone marrow-derived mesenchymal stem cells (rBMSCs) *in vitro* owing to the sustained release of Mg^{2+}. Therefore, 3D-printed MgHAp/GelMA-PDA@DOX hydrogels hold great potential for both cancer therapy and bone tissue regeneration, which is desirable for the treatment of bone tumor-related defects.

2. Materials and methods

2.1. Materials

Type I collagen (COL1), citric acid, gelatin (Gel; type A from porcine skin, powder, gel strength ~300 g Bloom), methacrylic anhydride (MA; 94%), 2-hydroxy-

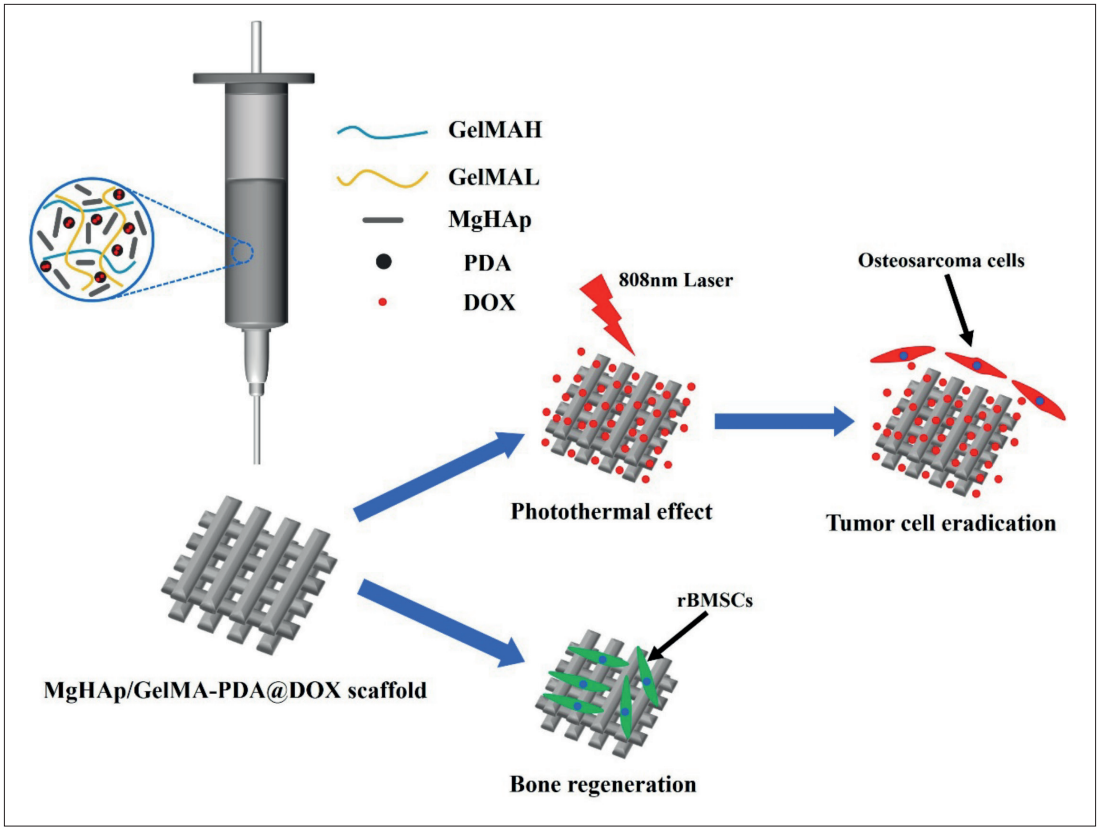


Figure 1. Schematic illustration of the fabrication of MgHAp/GelMA-PDA@DOX hydrogels using 3D printing and their dual functionality in eradicating tumor cells and promoting bone tissue regeneration.

2-methylpropiophenone, and ammonium hydroxide solution (NH_4OH; 28%) were purchased from Sigma-Aldrich (St. Louis, MO, USA). Dopamine hydrochloride (98%) and doxorubicin hydrochloride (DOX) were bought from Aladdin Co., Ltd., China. Sodium chloride (NaCl), sodium hydroxide (NaOH), anhydrous chloride ($CaCl_2$), magnesium chloride hexahydrate ($MgCl_2{\cdot}6H_2O$), disodium hydrogen phosphate dodecahydrate ($Na_2HPO_4{\cdot}12H_2O$), and ethanol were supplied by Sinopharm Chemical Reagent Co., Ltd., China. Dialysis tubing cellulose membrane (MWCO: 10 kDa) was bought from Thermo Fisher Scientific. All reagents were used as-received without further purification.

2.2. Synthesis of MgHAp nanocomposites, GelMA, and PDA@DOX particles

HAp and MgHAp nanocomposites were synthesized via a biomimetic mineralization process following the procedure as described in the previous study.[35] Briefly, 0.5 g COL1 was dissolved in 100 mL deionized (DI) water under constant magnetic at a 37°C water bath. Then, 500 mL 0.1 M $CaCl_2$, 300 mL 0.1 M Na_2HPO_4, 40 mL 1 M citric acid, and 3.6 g NaCl were added in a sequence order. Subsequently, a 4 M NaOH solution was added dropwise to adjust the pH to 9–10. The reaction system was then incubated in an incubator at 37°C for 7 days. Afterward, the white precipitate was suspended in 75% ethanol. The precipitate was centrifuged at 12,000 rpm/min for 10 min and washed with DI water three times and then freeze-dried. Finally, HAp nanocomposites were obtained and stored at 4°C for further use. For the synthesis of MgHAp nanocomposites, 500 mL 0.1 M $CaCl_2$ was replaced by 450 mL 0.1 M $CaCl_2$ and 50 mL 0.1 M $MgCl_2$, while the other procedures remained the same. The morphology and microstructure of HAp and MgHAp nanocomposites were characterized using a field emission scanning electron microscope (SEM; Hitachi S4800, Japan) and transmission electron microscope (TEM; Themis, Thermo Scientific, USA). The crystallographic phase of HAp and MgHAp nanocomposites was investigated using an X-ray diffractometer (XRD; 7000S, Shimadzu, Japan) over a range of 2θ from 10° to 70°. The characteristic groups in HAp and MgHAp nanocomposites were examined using an FT-IR spectrometer (PerkinElmer, USA) under the attenuated total reflection (ATR) mode.

Two sets of GelMA with a high degree of methacrylation (~80%) and a low degree of methacrylation (~20%) were synthesized according to the previous reported method.[26] Accordingly, GelMA with a high degree of methacrylation was designated as GelMAH, while GelMA with a low degree of methacrylation was designated as GelMAL. Briefly, 10 g gelatin was dissolved in 100 mL phosphate-buffered saline (PBS; pH 7.4, Gibco) at 50°C under constant magnetic stirring for 1 h. Subsequently, 0.8 mL (for GelMAL) or 8.0 mL (for GelMAH) methacrylic anhydride (MA) was added dropwise to the gelatin solution. The reaction continued for 3 h and was then stopped by adding five times the volume of PBS to the system. Afterward, the solution was transferred into a dialysis tubing cellulose membrane and dialyzed against DI water at 40°C for 1 week. The DI water was refreshed daily. Finally, GelMA was freeze-dried and stored at 4°C for further use. The degree of methacrylation of GelMA was characterized using ^{1}H NMR spectroscopy (Bruker Avance III 400, Germany). The secondary structure of GelMA was studied using a circular dichroism (CD) spectrometer (JASCO J-815, Japan) at 4 and 37°C, respectively. The characteristic groups of GelMA were investigated using an FT-IR spectrometer under ATR mode. Moreover, the phase transition temperatures of GelMAH and GelMAL solutions were determined using a Rheometer (MCR 302, Anton Paar, Austria).

PDA and PDA@DOX particles were synthesized following the procedure described in our previous study with slight modifications.[37] Briefly, 350 mL absolute ethanol, 12 mL NH_4OH, and 288 mL DI water were mixed homogenously under constant magnetic stirring for 30 min. Dopamine hydrochloride (2.5 g) was dissolved in 50 mL DI water. The dopamine solution was then added to the mixture for reaction at room temperature in an open-air environment for 24 h. PDA particles were obtained followed the centrifugation at 12,000 rpm/min for 10 min and subsequently dried in an oven at 80°C. PDA@DOX particles were synthesized using the same procedure but with the addition of 0.5 g DOX dissolved in the dopamine solution. The morphology and microstructure of PDA and PDA@DOX particles were examined using SEM and TEM. Moreover, the diameter of the PDA and PDA@DOX particles was calculated using the ImageJ software.

2.3. Rheological properties of printing inks

The compositions of the printing inks are listed in Table 1. Briefly, taking MgHAp/GelMA-PDA as a typical example, a 20% w/v GelMA solution was prepared by dissolving 10% w/v GelMAL and 10% w/v GelMAH in PBS at 40°C in a water bath under constant magnetic stirring. Subsequently, 2% w/v MgHAp and 0.5% w/v PDA were added to the GelMA solution. Photoinitiator was added to the printing ink with a final concentration of 0.2% w/v.

The phase transition temperatures of the printing inks were characterized from 10 to 40°C using a rotational rheometer equipped with a parallel plate unit with a 20 mm diameter and 1.0 mm measurement gap (1% strain and 1 Hz). The shear-thinning behavior of the printing inks was studied at shear rate ranging from 0.1 to 100 s^{-1} at 25°C.

Table 1. Concentrations of HAp, MgHAp, GelMA, and PDA in different printing inks.

	GelMAL (% w/v)	GelMAH (% w/v)	HAp (% w/v)	MgHAp (% w/v)	PDA (% w/v)	Photoinitiator (% w/v)
GelMA	10	10	0	0	0	0.2
HAp/GelMA	10	10	2	0	0	0.2
MgHAp/GelMA	10	10	0	2	0	0.2
MgHAp/GelMA-PDA	10	10	0	2	0.5	0.2

Abbreviations: GelMA, gelatin methacryloyl; GelMAH, GelMA with a high degree of methacrylation; GelMAL, GelMA with a low degree of methacrylation; HAp, hydroxyapatite; MgHAp, magnesium-substituted hydroxyapatite; PDA, polydopamine.

The storage moduli (G') and loss moduli (G'') of the inks subjected to a maximum strain (γ) of 1.0% were measured at a frequency range of 0.1–100 rad/s at 25°C. The G' and G'' of the inks crosslinked by UV exposure for 5 min were also measured. Moreover, the thixotropic behavior of the inks was studied by repetitive application of shear rates of 0.1 s^{-1} for 120 s and 100 s^{-1} for 60 s at 25°C.

2.4. 3D printing of MgHAp/GelMA-PDA hydrogels

3D printing of GelMA, HAp/GelMA, MgHAp/GelMA, and MgHAp/GelMA-PDA hydrogels was performed using a 3D bioprinter (3D Discovery™ Evolution, regenHU Ltd., Switzerland). The printing inks were transferred into a syringe and installed on the 3D bioprinter. The printing temperature was set to 25°C, and the printing platform was kept at room temperature. The inner diameter of printing nozzle was 0.26 mm. The printing speed was set to 8 mm/s to match the ink extrusion rate. After 3D printing, the hydrogels were exposed to 5-min UV light irradiation for covalently crosslinking GelMA polymer chains. Subsequently, the 3D-printed GelMA, HAp/GelMA, MgHAp/GelMA, and MgHAp/GelMA-PDA hydrogels were freeze-dried and stored at 4°C for further use.

2.5. Characterization of 3D-printed MgHAp/GelMA-PDA hydrogels

2.5.1. Printability of inks and structural fidelity of printed hydrogels

The printability (Pr) values of GelMA, HAp/GelMA, MgHAp/GelMA, and MgHAp/GelMA-PDA inks were calculated using the ImageJ software to measure the area and perimeter of interconnected pores of hydrogels immediately after 3D printing. Pr values were calculated using the following formula:[38]

$$Pr = \frac{L^2}{16A} \quad \text{(I)}$$

where Pr is the printability value of printing inks, L is the perimeter of the printed pore, and A is the area of the pore in the printed hydrogels.

The structural fidelity of printed GelMA, HAp/GelMA, MgHAp/GelMA, and MgHAp/GelMA-PDA hydrogels was determined using the ImageJ software by calculating the expansion percentage of printed strut. It was calculated according to the following formula:

$$Strut\ diameter\ expansion\ percentage(\%) = \frac{(D_1 - D_0)}{D_0} \times 100 \quad \text{(II)}$$

where D_1 is the diameter of printed strut of hydrogels, and D_0 is the diameter of designed strut of hydrogels.

2.5.2. Morphology and microstructure

The morphology and microstructure of printed GelMA, HAp/GelMA, MgHAp/GelMA, and MgHAp/GelMA-PDA hydrogels were determined using an SEM. Dry GelMA, HAp/GelMA, MgHAp/GelMA, and MgHAp/GelMA-PDA hydrogel samples were sputter-coated with a thin layer of gold. Then, the morphology and microstructure of the gold-coated samples were observed under SEM in a high vacuum mode at 10 kV. Additionally, to visualize the presence of MgHAp nanocomposites in hydrogel samples, the energy dispersive X-ray spectrometer (EDS) mapping was performed.

2.5.3. Mechanical properties

The mechanical properties of 3D-printed GelMA, HAp/GelMA, MgHAp/GelMA, and MgHAp/GelMA-PDA hydrogels crosslinked by UV light were determined through compression tests. Dry and wet hydrogel samples (10 mm in diameter and 5 mm in height) were compressed at a testing speed of 0.5 mm/min using a universal mechanical testing machine (Model 5848, Instron Ltd., USA), respectively. The ultimate compression strength of printed hydrogels was the highest load at the break divided by the original cross-sectional area of the hydrogel samples. Young's modulus of printed hydrogels was calculated using the slope of the initial linear section of stress–strain curves.

2.5.4. Swelling behavior and in vitro degradation

To investigate the dynamic swelling behavior, dry hydrogel samples were weighed and measured as W_0. Then, hydrogel samples were immersed in PBS at 37°C water baths. At each predetermined time point, hydrogel samples were

taken out, and the excess PBS on sample surface was gently removed. The weight of swollen hydrogel samples was measured as W_1. The swelling ratios of printed GelMA, HAp/GelMA, MgHAp/GelMA, and MgHAp/GelMA-PDA hydrogels were calculated according to the following formula:

$$Swelling\ ratio(\%) = \frac{(W_1 - W_0)}{W_0} \times 100 \quad \text{(III)}$$

where W_0 represents the weight of dry hydrogel samples, and W_1 represents the weight of swollen hydrogel samples.

To determine *in vitro* degradation behavior of 3D-printed GelMA, HAp/GelMA, MgHAp/GelMA, and MgHAp/GelMA-PDA hydrogels, the weight of each dry hydrogel sample was weighed as M_0. Afterward, hydrogel samples were immersed in 5 mL PBS supplemented with 0.02% sodium azide (NaN_3) and placed in a shaking water bath at 37°C. PBS was refreshed every 2 days. At each predetermined time point, hydrogel samples were taken out and freeze-dried. The weight of each degraded hydrogel sample was weighed as M_1. The *in vitro* degradation rate of printed hydrogels was calculated according to the following formula:

$$Degradation\ rate(\%) = \frac{(M_0 - M_1)}{M_0} \times 100 \quad \text{(IV)}$$

where M_0 represents the weight of each dry hydrogel sample, and M_1 represents the weight of each degraded hydrogel sample.

2.5.5. pH change and ion release

To study the pH changes of 3D-printed GelMA, HAp/GelMA, MgHAp/GelMA, and MgHAp/GelMA-PDA hydrogels, 0.5 g hydrogel samples were immersed in 5 mL PBS in a shaking water bath at 37°C. At each predetermined time point, pH value of the immersion liquid was detected using a pH meter. Additionally, to investigate ion release behavior of printed hydrogels, 0.5 g hydrogel samples were immersed in 5 mL PBS in a shaking water bath at 37°C. At each predetermined time point, 0.5 mL PBS was removed and another fresh 0.5 mL PBS was added. The concentration of Mg^{2+} and Ca^{2+} in PBS was determined using an inductively coupled plasma mass spectrometer (ICP-MS, ELAN DRC-e, PerkinElmer, USA).

2.6. Photothermal effect and in vitro DOX release behavior

To investigate the photothermal effect of 3D-printed GelMA, HAp/GelMA, MgHAp/GelMA, and MgHAp/GelMA-PDA hydrogels, hydrogel samples were irradiated by an NIR laser (wavelength: 808 nm) at different power densities (0.5 and 1.0 W/cm^2), respectively. At each predetermined time point, the temperatures of hydrogel samples were recorded using an infrared camera (GUIDE EasIR-9, AutoNavi, China).

To study the effect of NIR laser irradiation on DOX release, 3D-printed MgHAp/GelMA-PDA@DOX hydrogel samples were immersed in PBS and exposed to different power densities of NIR laser (0, 0.5, and 1.0 W/cm^2) for 30 min every 1 h at 37°C. At each predetermined time point, the released medium was collected, and an equal amount of PBS was replenished. The amount of DOX in the released medium was measured using a UV–vis spectrometer (UV-2600, Shimadzu, Japan) at the wavelength of 480 nm. The cumulative release curves of DOX were then established. Furthermore, to determine the pH-responsive DOX release behavior of MgHAp/GelMA-PDA@DOX hydrogels, hydrogel samples were immersed in pH 4.5 and pH 7.4 buffer solutions at 37°C, respectively. At each predetermined time point, the release medium was collected, and an equal amount of fresh buffer solution was added. The amount of DOX released was measured using a UV–vis spectrometer at the wavelength of 480 nm. The cumulative release curves of DOX were then established.

2.7. *In vitro* antitumor efficiency

In the current study, MG63 osteosarcoma cells were used to evaluate the antitumor efficiency of 3D-printed MgHAp/GelMA-PDA@DOX hydrogels. MG63 cells at a density of 1×10^4 cells per well were seeded on the hydrogel samples in a 24-well cell culture plate. Hydrogel samples were cultured in the Dulbecco's modified eagle medium (DMEM; Gibco) supplemented with 10% v/v fetal bovine serum (FBS; Gibco) and 1% v/v penicillin/streptomycin (Gibco) in a CO_2 incubator at 37°C. Hydrogel samples were irradiated with an 808 nm NIR laser for 5 min every day. After culturing for 4 and 24 h, a live/dead assay (Invitrogen, Thermo Fisher Scientific) was employed to determine the survival rate of MG63 cells cultured on the hydrogel samples. Moreover, the cell viability of MG63 cells on the hydrogel samples was assessed using 3-(4,5-dimethylthiazol-2-yl)-2,5 diphenyl tetrazolium bromide (MTT; Invitrogen, Thermo Fisher Scientific) tests at each predetermined time point (1, 3, and 5 days).

2.8. Proliferation and osteogenic differentiation of rBMSCs on 3D-printed scaffolds

The proliferation behavior of rBMSCs on 3D-printed MgHAp/GelMA-PDA hydrogels was studied through MTT tests. Briefly, rBMSCs at a density of 1×10^4 cells per well were seeded on hydrogel samples in a 24-well cell culture plate and cultured in medium in a CO_2 incubator at

37°C. After culturing for 1, 3, and 7 days, cell proliferation was evaluated using the MTT assay.

To investigate the effect of Mg^{2+} release on rBMSCs osteogenic differentiation, 1×10^5 cells per well were seeded on hydrogel samples in a 24-well cell culture plate. Following a culture period of 3 days, the culture medium was replaced by an osteogenic differentiation medium (which was prepared by adding 0.1 mM dexamethasone, 50 mM ascorbic acid, and 10 mM β-sodium glycerophosphate in culture medium). After culturing for 7 and 14 days, the activity of alkaline phosphatase (ALP) of rBMSCs on the hydrogel samples was measured using an ALP assay (Wako, Japan) according to the manufacturer's protocol. Additionally, the total protein concentration was measured using the BCA kit (Thermo Fisher Scientific). Moreover, the expression of ALP was assessed by means of ALP staining. Briefly, after being cultured in osteogenic differentiation medium for 14 days, rBMSCs were fixed with 4% paraformaldehyde (Sigma-Aldrich, St Louis, MO, USA) for 15 min, washed with PBS, and incubated with ALP staining solution for 30 min in the dark. The images were recorded using a microscope (Leica DMi8, Germany).

Furthermore, the expression of osteogenesis-related genes, such as osteocalcin (*Ocn*), *Col1*, runt-related transcription factor-2 (*Runx2*), and bone morphogenetic protein-2 (*Bmp2*) was studied using quantitative real-time polymerase chain reaction (qRT-PCR) analysis. Briefly, after culturing rBMSCs on hydrogel samples in osteogenic medium for 14 days, the total RNA was extracted using Trizol reagent (Servicebio, China). The obtained RNA was reverse-transcribed to complementary DNA (cDNA) using the Revert-Aid First Strand cDNA Synthesis Kit (Thermo Fisher Scientific). Then, qRT-PCR analysis was performed. Housekeeping gene glyceraldehyde 3-phosphate dehydrogenase (*Gapdh*) was used as the control to normalize the expression of osteogenesis-related genes. The $2^{-\Delta\Delta Ct}$ method was used to calculate the mRNA expression levels. The sequences of the primers ae listed in Table S1, Supporting Information.

In addition, after being cultured in osteogenic medium for 14 days, rBMSCs on hydrogel samples were fixed with 4% paraformaldehyde for 15 min and then incubated with anti-COLI rabbit primary antibody (Abcam) for 1 h and then FITC-conjugated goat anti-rabbit secondary antibody (Santa Cruz Biotechnology Inc., USA) for 1 h. Cell nuclei were stained with DAPI solution. The morphology of rBMSCs was examined using a confocal laser scanning microscope (Leica DMi8, Germany).

2.9. Statistical analysis

The results presented in the current study were obtained from at least three separate samples or tests and are expressed as the mean ± standard deviation (SD). One-way analysis of variance (ANOVA) was performed to carry out statistical analysis. Data analyses in the current study were conducted using Excel and SPSS.

Differences were considered statistically significant when $p < 0.05$, $p < 0.01$, and $p < 0.001$.

3. Results and discussion

3.1. Synthesis and characterization of MgHAp, GelMA, and PDA@DOX

Previous studies have employed biomimetic self-assembly mineralization method to fabricate HAp to mimic the structure and composition of natural bone.[39] As a result, HAp synthesized through biomineralization process exhibited a positive effect on cell activities (e.g., cell attachment, proliferation, and differentiation) and could promote new bone formation. Moreover, considering the inherent components of natural bone, i.e., inorganic HAp, organic COL1 and citric acid, research employing COL1 and citric acid as bitemplate for HAp nanocomposites synthesis emerged as COL1 enabled to modulate nucleation sites and crystal growth of HAp due to its well-organized fiber orientation, while citric acid could regulate HAp formation owing to its abundant carboxyl groups.[35,40] Therefore, in the current study, HAp nanocomposites with a great similarity in structure and composition of apatite in natural bone were synthesized using COL1 and citric acid as bitemplate through a biomineralization process. Magnesium is an important metal element in human body, with 60% present in the human bone. Studies have indicated that Mg^{2+} played an essential role in bone metabolism by regulating osteoblast and osteoclast activities.[36,41] Moreover, compared to HAp, MgHAp could promote cell proliferation and osteogenic differentiation through activating integrin on the cell surface.[42] Thus, MgHAp was synthesized in the current work for investigation. As shown in Figure 2A, the morphology of both HAp and MgHAp nanocomposites exhibited a plate-like structure, and the size of HAp and MgHAp nanocomposites was around 40–70 nm, showing great similarity to the shape of apatite in natural bone. Figure 2B and C show the element compositions of HAp and MgHAp nanocomposites. Notably, there was a small amount of Mg element in the EDS spectrum, as shown in Figure 2C, indicating the presence of Mg^{2+} in MgHAp nanocomposites. As shown in Figure 2D, XRD patterns showed that HAp and MgHAp nanocomposites were mainly hydroxyapatite phase. However, due to the incorporation of COL1 and citric acid in the nanocomposites, HAp and MgHAp showed a low crystallinity in comparison to pure hydroxyapatite mineral. Furthermore, compared to HAp nanocomposites, MgHAp nanocomposites exhibited an even lower crystallinity due

to the substitution of Mg^{2+} in hydroxyapatite phase. The FT-IR spectra in Figure 2E confirmed the compositions of HAp and MgHAp nanocomposites. The characteristic peaks at 1032.8 and 1037.6 cm^{-1} were attributed to the antisymmetric P–O stretching, while the peaks at 563.1 and 565.1 cm^{-1} were due to O–P–O bending of hydroxyapatite. Additionally, the characteristic peaks at 3444.4 and 3438.6 cm^{-1} might be attributed to the vibrations of O–H of water and N–H of COL1. The amide I band in COL1 and carboxyl groups in citric acid appeared at 1596.8 and 1608.44 cm^{-1} respectively.

GelMA is a popular biomaterial for 3D printing due to its remarkable temperature-responsive behavior, forming triple-helix structure in the gel state at low temperatures while exhibiting random coil structure in the sol state upon heating.[26] Additionally, GelMA exhibits good photocurable properties and can be covalently crosslinked upon visible or UV light irradiation to form stable hydrogel networks.[43] Previous studies have indicated that the temperature-responsive behavior and photocurable properties of GelMA were significantly affected by the degree of methacrylation.[44,45] GelMA with a high degree of methacrylation has a low sol–gel transition temperature, which is not beneficial for extrusion-based 3D printing. When crosslinked by UV light, GelMA with a high degree of methacrylation can exhibit high mechanical strength, making it more suitable for bone tissue engineering. On the contrary, GelMA with a low degree of methacrylation has a high sol–gel transition temperature, which makes it more suitable for extrusion-based 3D printing. However, GelMA with a low degree of methacrylation can have low mechanical strength. A high sol–gel transition temperature can provide convenience for 3D printing, while a high mechanical strength is beneficial for bone tissue regeneration. Therefore, in the current study, GelMAH (high degree of methacrylation) and GelMAL (low degree of methacrylation) were synthesized in PBS. As shown in Figure 3A, the ^1H NMR spectra showed that new peaks around 6.00–5.86 ppm (m, -O-CH_2-CH=CH_2) and 5.38–5.22 ppm (t, -O-CH_2-CH=CH_2) appeared in GelMAH and GelMAL polymer chains. Additionally, the increased intensity of the methyl peak at ~1.8 ppm and the reduced intensity of the lysine methylene peak at 2.8–3.0 ppm further showed the successful substitution of methacrylate groups in GelMAH and GelMAL. Degrees of methacrylation of GelMAH and GelMAL calculated using the 2,4,6-trinitrobenzenesulfonic acid (TNBS) method were ~80% and ~20%, respectively (Figure 3B). The CD spectra presented in Figure 3C suggested that the methacryloylation of GelMA had an impact on the secondary structure. The intensity at 198 nm is ascribed to the random coil structure formation, and the intensity at 222 nm results from the formation of triple helix structure. As shown in Figure 3C, Gel exhibited a higher intensity at 222 nm at 4°C than GelMAH and GelMAL, suggesting that the formation of methacrylate groups in GelMA chains influences the interactions between GelMA polymer chains and therefore slightly interfered with the secondary structure. The FT-IR spectra in Figure 3D indicated that GelMAH and GelMAL preserved the characteristic peaks (amide I, amide II, amide III) of gelatin. Furthermore, Figure 3E indicates that the sol–gel temperatures of Gel, GelMAH, and GelMAL are 32.9, 27.7, and 30.8°C, respectively. GelMAH had a high degree of methacrylation and therefore imparted a high interference to the secondary structure, thereby resulting in a low sol–gel temperature.

Due to the excellent adhesive property, biocompatibility and good photothermal effect, PDA particles have been widely used as drug carriers and can provide controlled and sustained *in situ* drug delivery.[46] In the current study, DOX was encapsulated in PDA particles to fabricate PDA@DOX particles via *in situ* polymerization in a weakly alkaline solution.[37] As shown in Figures 4 and S1, Supporting Information, the PDA and PDA@DOX particles were spherical in shape, with an average diameter of 227.5 ± 3.1 and 161.8 ± 9.1 nm, respectively. The encapsulation of DOX in PDA particles did not significantly affect the morphology and diameter of the PDA@DOX particles.

3.2. Rheological properties of printing inks

As mentioned, GelMA with a low degree of methacrylation exhibits a high sol–gel transition temperature and thus is beneficial for 3D printing. However, GelMA with a low degree of methacrylation usually possesses low mechanical strength, which is not suitable for bone tissue regeneration.[47] On the contrary, GelMA with a high degree of methacrylation usually has a low transition temperature and possesses high mechanical strength when crosslinked by UV light. In the current study, to develop an optimal printing ink for 3D printing and bone tissue regeneration, GelMA inks consisting of 10% GelMAH and 10% GelMAL were prepared. As shown in Figures 5A and S2, Supporting Information, the sol–gel transition temperatures of GelMA, HAp/GelMA, MgHAp/GelMA, and MgHAp/GelMA-PDA inks were 31.5, 33.6, 29.4, and 31.8°C, respectively. The gel–sol transition temperatures of GelMA, HAp/GelMA, MgHAp/GelMA, and MgHAp/GelMA-PDA inks were 30.8, 30.9, 29.8, 35.7°C, respectively (Figure 5B). All printing inks exhibited high transition temperatures above 29°C, providing great convenience for extrusion-based 3D printing.

For extrusion-based 3D printing, the viscosity of inks is essential for achieving good extrudability.[48] If the viscosity is too low, inks can easily leak from the nozzle

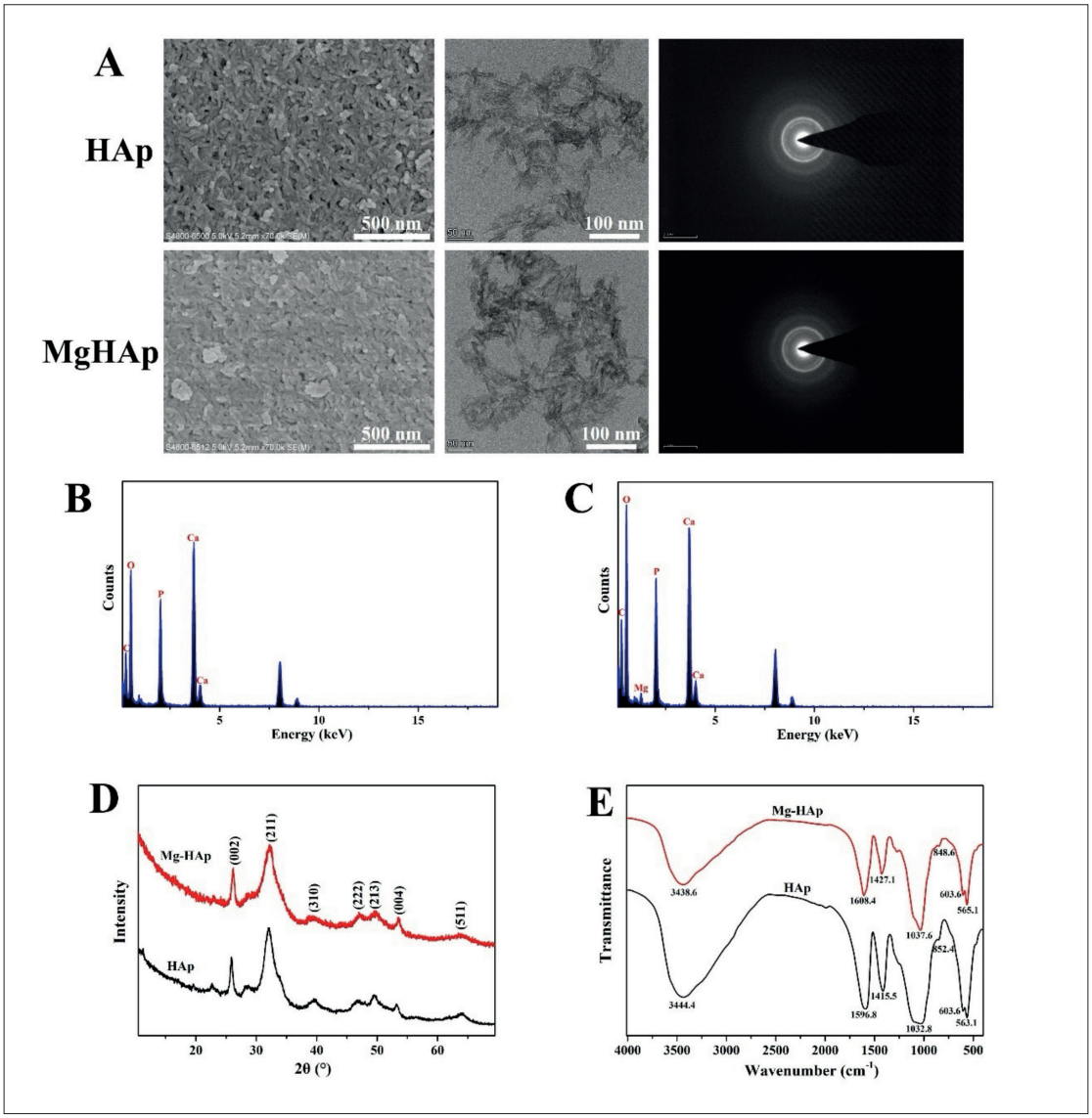


Figure 2. Characterization of HAp and MgHAp nanocomposites. (A) SEM and TEM images showing the morphology and structure of HAp and MgHAp nanocomposites. (B, C) EDS spectra of HAp (B) and MgHAp (C) nanocomposites. (D, E) XRD patterns (D) and FT-IR spectra (E) of HAp and MgHAp nanocomposites.

of the printing head, resulting in difficulty in maintaining the structural stability of printed hydrogels. On the other hand, if the viscosity is too high, the inks are semi-solid and hence high pressures are required for extrusion; otherwise, the inks may not be extruded from the nozzle. Therefore, a good or desirable printing ink should exhibit a shear-thinning behavior, like non-Newtonian fluids, characterized by decreasing viscosity with an increase in shear rate.[49] As shown in Figure 5C, GelMA, HAp/GelMA, MgHAp/GelMA, and MgHAp/GelMA-PDA inks exhibited excellent shear-thinning behavior over an increase in shear rate from 0.1 to 1000 s^{-1}, indicating that all inks were suitable for 3D printing. The rheological properties of GelMA, HAp/GelMA, MgHAp/GelMA, and MgHAp/GelMA-PDA inks, with or without UV crosslinking, were determined through frequency sweep tests. Figure 5D indicates that the G' values of all inks without UV crosslinking were higher than G'' at 25 °C, suggesting the elastic state of inks. It might be attributed to the 20% GelMA in the inks. Additionally, UV crosslinking led to the dramatic increase of G' and G'' values of all inks (Figure 5E), as a result of the crosslinking of GelMA chains, which contributed to the formation of robust hydrogel networks. Furthermore, the thixotropic behavior of the inks was investigated under the repeated application of a low shear rate (0.1 s^{-1}) for 120 s and a high shear rate (100 s^{-1}) for 60

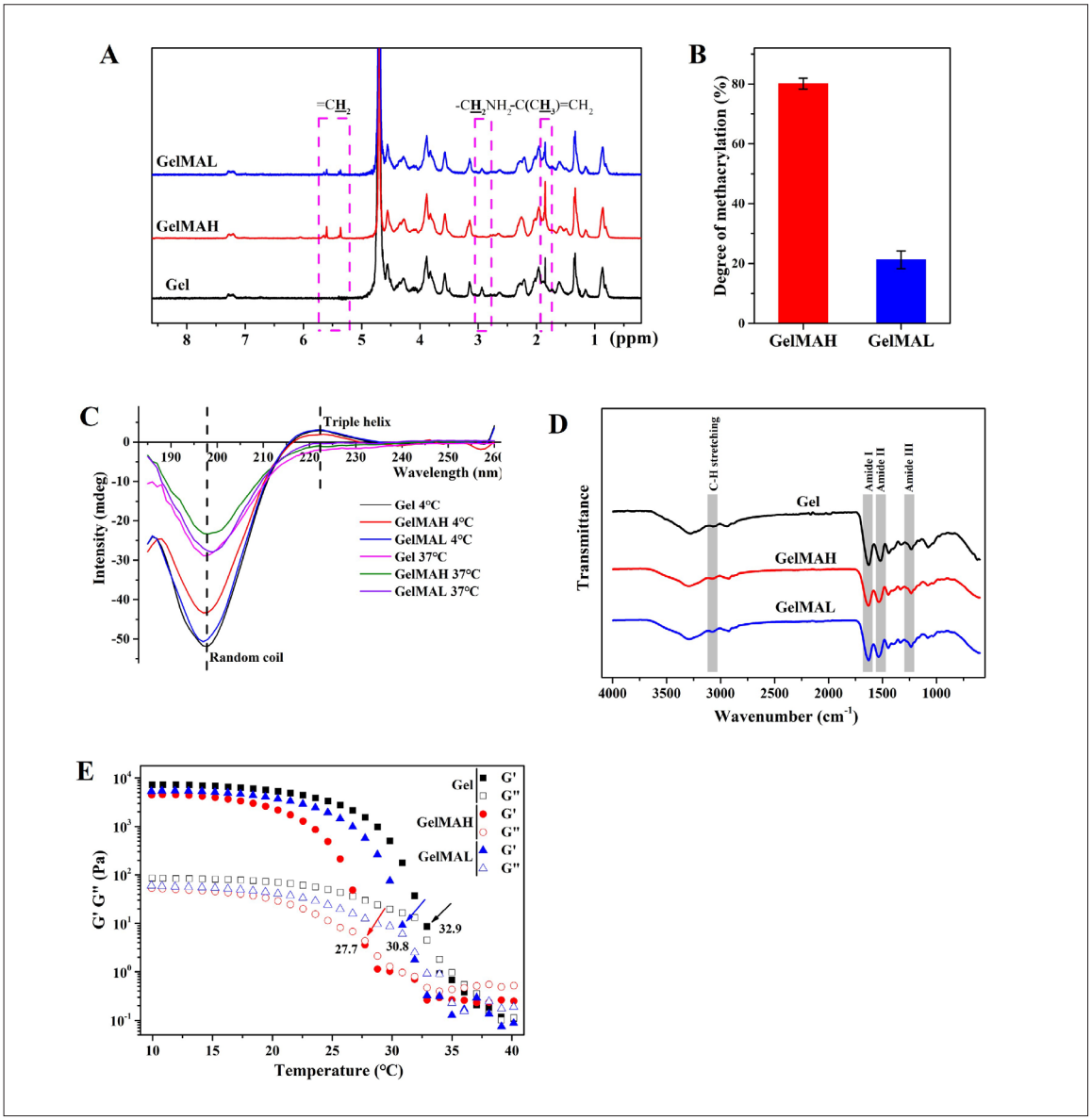


Figure 3. Characterization of GelMAH and GelMAL. (A) ^{1}H NMR spectra of Gel, GelMAH, and GelMAL. (B) Degree of methacrylation of GelMAH and GelMAL calculated using the 2,4,6-trinitrobenzenesulfonic acid (TNBS) method. (C) Circular dichroism (CD) spectra of Gel, GelMAH, and GelMAL at 4 and 37°C, respectively. (D) FT-IR spectra of Gel, GelMAH, and GelMAL. (E) Variation of *G′* and *G″* in terms of temperature for Gel, GelMAH, and GelMAL. Abbreviations: Gel, gelatin; GelMAH, GelMA with a high degree of methacrylation; GelMAL, GelMA with a low degree of methacrylation.

s. As shown in Figure 5F, GelMA, HAp/GelMA, MgHAp/GelMA, and MgHAp/GelMA-PDA inks all possessed excellent thixotropic behavior. The viscosity of the inks dramatically decreased when subjected to a high shear rate and immediately recovered to the original state after the removal of shear rate. These results confirmed that GelMA, HAp/GelMA, MgHAp/GelMA, and MgHAp/GelMA-PDA inks could be easily extruded from the printing nozzle and would be suitable for extrusion-based 3D printing.

3.3. Properties and characterization of 3D printed scaffolds

The printability of inks plays a crucial role in assessing their suitability for 3D printing.[50,51] Printability refers to the ability of a printing ink to be continuously and consistently printed, while forming stable 3D structures in accordance with the design during and after printing process. Printability has an impact on the physical properties (e.g., pore shape, pore size, and porosity) of printed structures, thereby determining their mechanical properties and

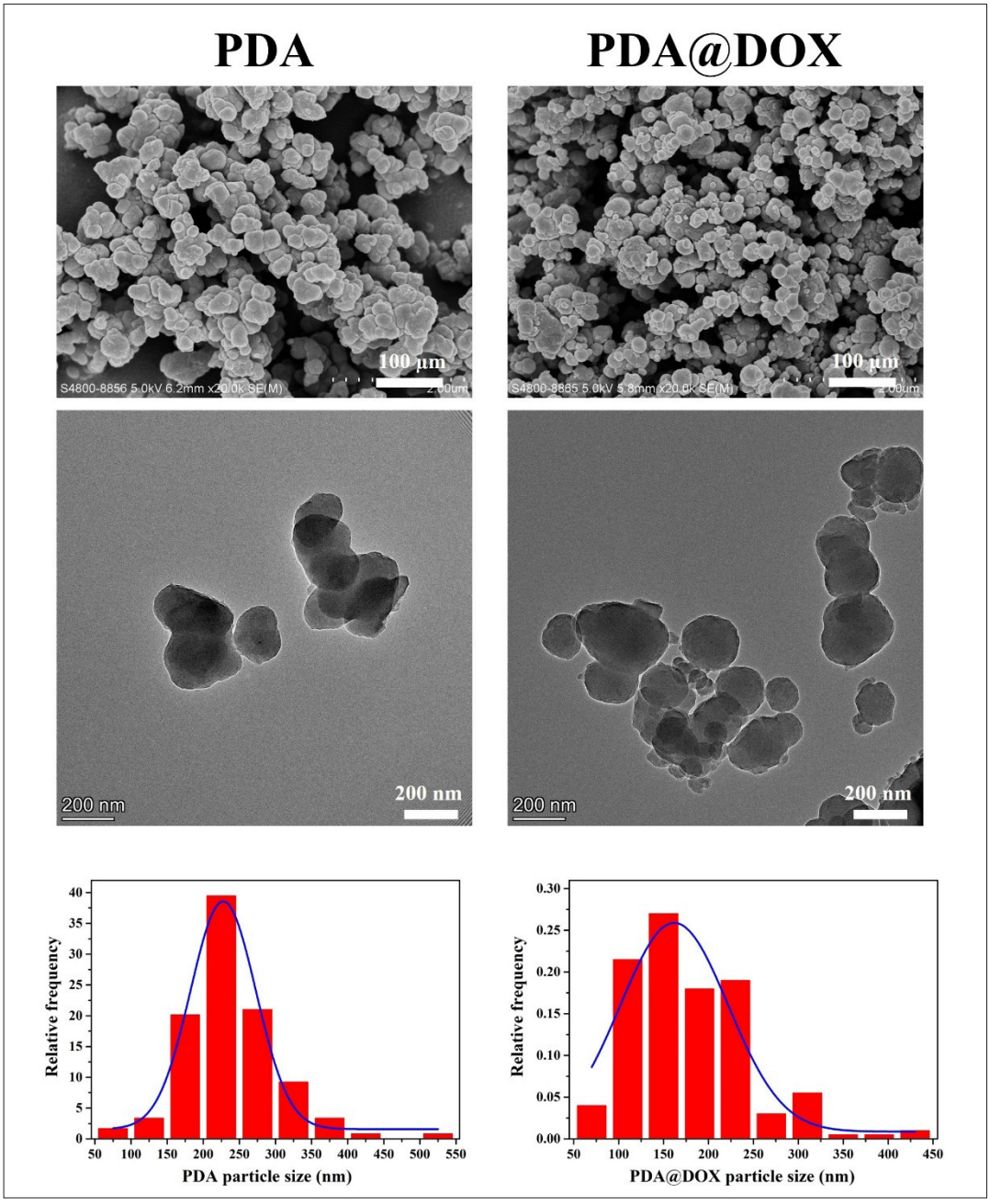


Figure 4. SEM and TEM images showing the morphology and particle size of PDA and PDA@DOX particles, and the size distribution of PDA and PDA@DOX particles.

biological performance. In the current study, a 20% GelMA inks composed of 10% GelMAH and 10% GelMAL were used to improve the printability. As calculated from the optical images showing the morphology of printed hydrogels (Figure 6A), the printability value of GelMA inks was approximately 0.875 ± 0.007, which was much better than those described in previous studies (Figure 6B).[24,52] The printability values of 3D-printed HAp/GelMA, MgHAp/GelMA, and MgHAp/GelMA-PDA inks were 0.962 ± 0.087, 1.090 ± 0.128, and 0.905 ± 0.015, respectively. The addition of HAp and MgHAp nanocomposites improved the printability. On the other hand, fidelity is an important factor in determining the ability to maintain the structure of printed objects.[53,54] It is an index that is commonly used to evaluate the similarity between the structure of printed objects and their design. Printed

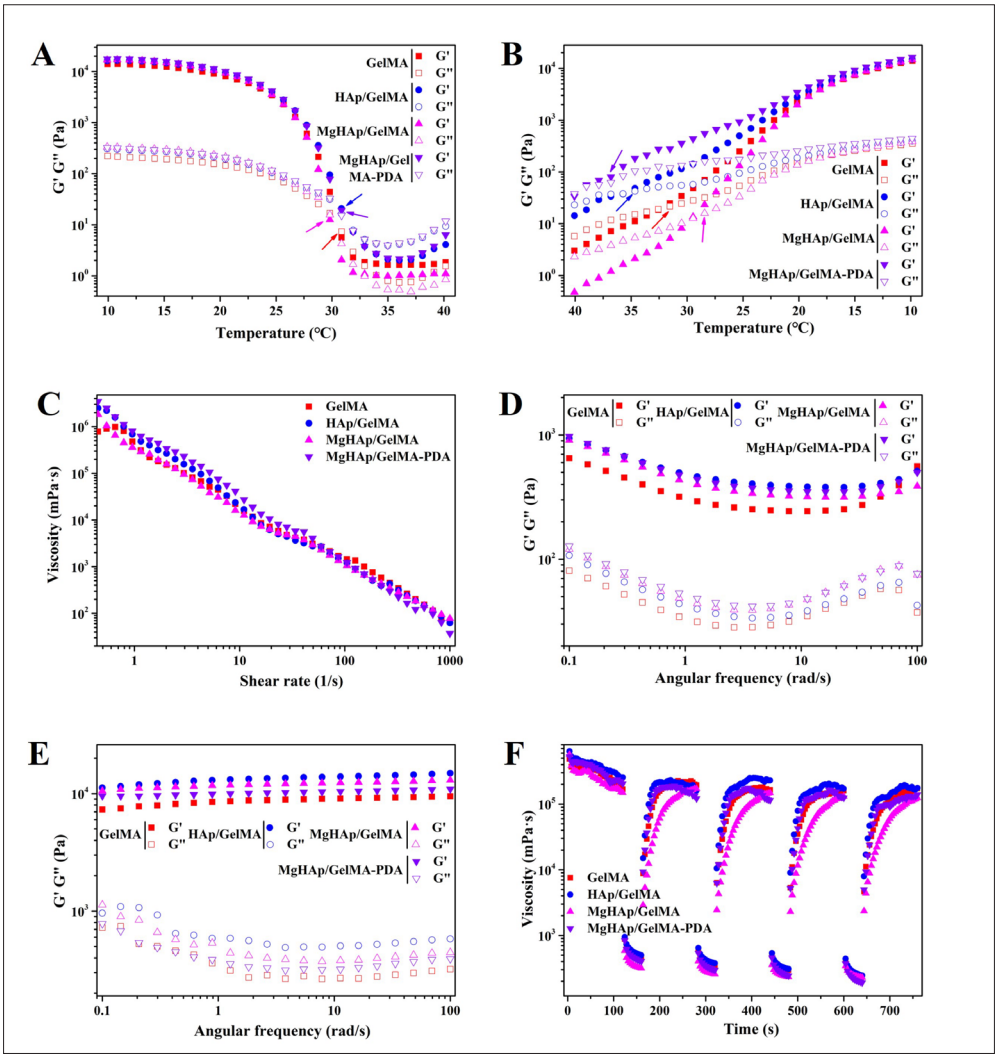


Figure 5. Rheological properties of the printing inks. (A, B) Inks from gel state to sol state (A), and inks from sol state to gel state (B). (C) Shear thinning behavior of GelMA, HAp/GelMA, MgHAp/GelMA, and MgHAp/GelMA-PDA inks. (D) Variation of *G′* and *G″* in terms of angular frequency of GelMA, HAp/GelMA, MgHAp/GelMA, and MgHAp/GelMA-PDA inks. (E) Variation of *G′* and *G″* in terms of angular frequency of GelMA, HAp/GelMA, MgHAp/GelMA, and MgHAp/GelMA-PDA inks crosslinked by UV light. (F) Thixotropic behavior of GelMA, HAp/GelMA, MgHAp/GelMA, and MgHAp/GelMA-PDA inks.

structures with poor fidelity can lead to the deformation of printed struts, which increases the width and decreases the thickness of struts. In the current study, the struct diameter expansion rate was employed to assess the fidelity of printed hydrogels. As shown in Figure 6C, the struct diameter expansion rates of 3D-printed GelMA, HAp/GelMA, MgHAp/GelMA, and MgHAp/GelMA-PDA hydrogels were 38.51 ± 7.56%, 53.60 ± 5.73%, 39.52 ± 5.37%, and 93.54 ± 11.33%, respectively. GelMA, HAp/GelMA, and MgHAp/GelMA hydrogels exhibited similar fidelity, whereas the addition of PDA particles caused the decrease in fidelity in the MgHAp/GelMA-PDA hydrogel, which might be attributed to PDA particles interfering with the interactions between GelMA chains.

Figure 6D shows the surface and cross-sectional morphology and microstructure of dried 3D-printed GelMA, HAp/GelMA, MgHAp/GelMA, and MgHAp/GelMA-PDA hydrogels crosslinked by UV light. Hydrogels all exhibited interconnected macro-pores, which facilitated oxygen and nutrients transportation and the removal of waste, thereby promoting vascularization and tissue regeneration.[55] Moreover, 3D-printed GelMA, HAp/GelMA, MgHAp/GelMA, and MgHAp/GelMA-PDA hydrogels possessed micro-pores, which were beneficial for cell infiltration, ingrowth, and micro-blood vessels

formation.[56] The EDS mapping images shown in Figure 6D indicate the element distribution in the cross-sectional area of the printed MgHAp/GelMA hydrogel. It clearly showed the distribution of MgHAp nanocomposites in MgHAp/GelMA hydrogel. Also, EDS pattern in Figure S3, Supporting Information reveals the presence of Mg in the printed MgHAp/GelMA-PDA hydrogel. Furthermore, the thermogravimetric analysis (TGA) results in Figure S4, Supporting Information shows the thermal degradation behavior of 3D-printed GelMA, HAp/GelMA, MgHAp/GelMA, and MgHAp/GelMA-PDA hydrogels. This indicates that due to the addition of HAp and MgHAp nanocomposites, the remained weight percentages of HAp/GelMA, MgHAp/GelMA, and MgHAp/GelMA-PDA scaffolds increased after sintering at 800°C in comparison to that of GelMA hydrogel. However, the fastest thermal degradation temperature stayed nearly the same for GelMA (333.6°C), HAp/GelMA (324.1°C), MgHAp/GelMA (333.5°C), and MgHAp/GelMA-PDA (337.8°C) hydrogels. Overall, HAp and MgHAp nanocomposites were well-dispersed in the printed hydrogels.

Generally, GelMA hydrogels have poor mechanical properties. For example, Rizwan et al. found that the compression modulus of 15% GelMA hydrogels was below 50 kPa.[57] O'connell et al. showed that the peak storage modulus of 10% GelMA hydrogels could not exceed 10 kPa, even with a high photoinitiator concentration and light intensity and a long exposure time of UV light.[58] Consequently, ceramic particles were encapsulated in GelMA hydrogels to reinforce their mechanical strength.[25] In the current study, the mechanical properties of 3D-printed GelMA, HAp/GelMA, MgHAp/GelMA, and MgHAp/GelMA-PDA hydrogels were investigated through compression tests. As shown in Figures 7 and S5, Supporting Information the compression strength of 3D-printed GelMA hydrogels in the wet and dry states was 0.124 ± 0.014 and 2.590 ± 0.475 MPa, respectively. The combination of GelMAH and GelMAL significantly increased the mechanical strength because GelMAH could be efficiently crosslinked by UV light and GelMAL had a high sol–gel transition temperature and thus could be efficiently thermally crosslinked. On the other hand, the addition of 10% HAp or MgHAp in GelMA hydrogels significantly increased mechanical strength. The compression strength of 3D-printed HAp/GelMA and MgHAp/GelMA hydrogels in the wet state was 0.171 ± 0.011 and 0.182 ± 0.023 MPa, respectively. However, the compression strength of MgHAp/GelMA-PDA hydrogels in the wet state decreased to 0.099 ± 0.012 MPa, which could be attributed to the addition of PDA particles decreasing the UV crosslinking efficiency. As a result, the Young's modulus of GelMA, HAp/GelMA, MgHAp/GelMA, and MgHAp/GelMA-PDA hydrogels in the wet state were 0.114 ± 0.005, 0.195 ± 0.033, 0.211 ± 0.019, and 0.111 ± 0.059 MPa, respectively. While in the dry state, the Young's modulus of GelMA, HAp/GelMA, MgHAp/GelMA, and MgHAp/GelMA-PDA hydrogels were 10.020 ± 3.343, 28.750 ± 9.248, 36.190 ± 11.186, and 31.913 ± 10.770 MPa, respectively. Notably, the mechanical strength of 3D-printed MgHAp/GelMA-PDA hydrogels was still far behind that of the native bone. Hydrogel scaffolds usually possess insufficient mechanical strength for bone tissue regeneration. To reinforce the mechanical properties of hydrogels, ceramic particles have been widely used. In the current study, the addition of 10% of MgHAp significantly increased the modulus of hydrogels in both dry and wet state. To further improve the mechanical properties, more MgHAp nanocomposites could be incorporated into hydrogels. However, a higher percentage of MgHAp can lead to the formation of a compact network within hydrogels, thereby impacting the swelling and degradation behavior of MgHAp/GelMA-PDA hydrogels as well as influencing DOX release and cellular metabolism. Hence, striking a balance among the mechanical properties of hydrogels is critical.

The swelling behavior of hydrogels is related to their structural and dimensional stability as hydrogels tend to swell upon interaction with biological fluids, leading to changes in weight and size. Therefore, the swelling behavior of hydrogels is essential for diffusion/migration of encapsulated small biomolecules, drugs, and cells.[59] As shown in Figure 8A, printed hydrogels reached their swelling equilibrium after being immersed in PBS for 12 h. The swelling ratios of GelMA, HAp/GelMA, MgHAp/GelMA, and MgHAp/GelMA-PDA hydrogels were 328.05 ± 9.01%, 326.64 ± 3.97%, 322.01 ± 3.77%, and 307.59 ± 7.41%, respectively. The degradation of a hydrogel could facilitate the formation of extracellular matrix (ECM), thereby creating an optimal microenvironment for cell growth.[60] Moreover, the biodegradation rate of hydrogels should be compatible with the rate at which new tissue is formed. Figure 8B displays the *in vitro* degradation behavior of the printed hydrogels. Printed GelMA, HAp/GelMA, and MgHAp/GelMA hydrogels manifested similar degradation behavior. Following an immersion in PBS for 4 weeks, the degradation rates of GelMA, HAp/GelMA, and MgHAp/GelMA hydrogels were 50.41 ± 1.27%, 54.40 ± 0.85%, and 60.87 ± 0.99%, respectively. However, MgHAp/GelMA-PDA hydrogels exhibited a higher degradation rate. After 4 weeks of degradation, the degradation rate of MgHAp/GelMA-PDA hydrogels was 84.32 ± 0.79%. The relatively high degradation rate was attributed to the addition of PDA particles, which reduced the UV crosslinking efficiency.

Figure 8C–E graphically represents the changes of pH value, Ca^{2+}, and Mg^{2+} in PBS after soaking GelMA, HAp/GelMA, MgHAp/GelMA, and MgHAp/GelMA-PDA hydrogels in PBS for 2 weeks. As shown in Figure 8C, the change of pH of hydrogels appeared to be similar. The pH of GelMA, HAp/GelMA, MgHAp/GelMA, and MgHAp/GelMA-PDA hydrogels reduced on the first day, followed by an increase in the next 13 days. The Ca^{2+} release profiles in Figure 8D indicated that printed HAp/GelMA, MgHAp/GelMA, and MgHAp/

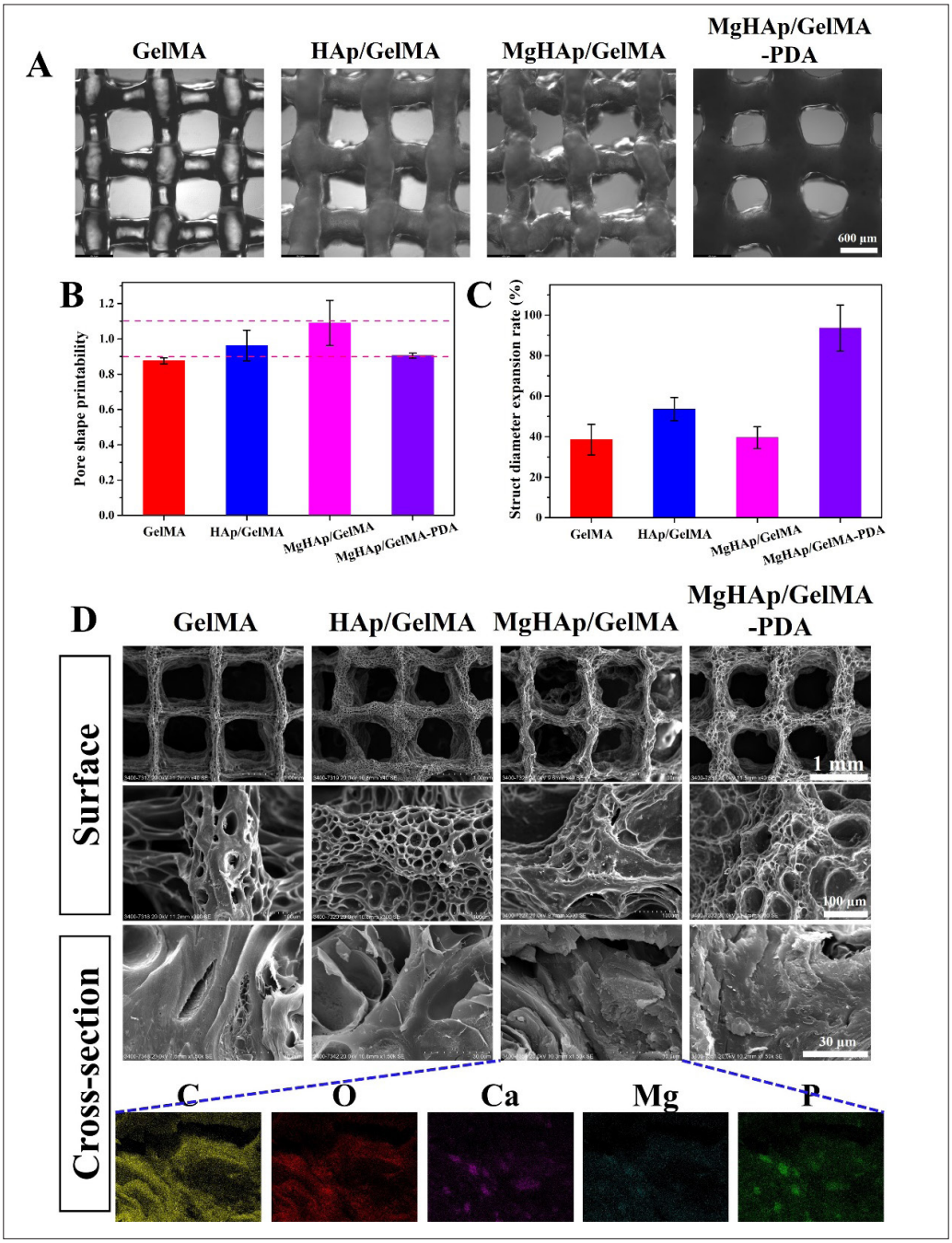


Figure 6. Morphology and structure of 3D-printed hydrogels. (A) Optical images showing the morphology and structure of GelMA, HAp/GelMA, MgHAp/GelMA, and MgHAp/GelMA-PDA hydrogels after 3D printing. (B) Printability values of GelMA, HAp/GelMA, MgHAp/GelMA, and MgHAp/GelMA-PDA inks. (C) Struct diameter expansion rates of GelMA, HAp/GelMA, MgHAp/GelMA, and MgHAp/GelMA-PDA hydrogels. (D) Surface and cross-sectional morphology of 3D-printed GelMA, HAp/GelMA, MgHAp/GelMA, and MgHAp/GelMA-PDA hydrogels and EDS mapping images showing the element distribution in the MgHAp/GelMA hydrogel.

GelMA-PDA hydrogels exhibited almost the same release trend. Furthermore, the MgHAp/GelMA and MgHAp/GelMA-PDA hydrogels shared the similar Mg^{2+} release profile. The concentrations of Ca^{2+} and Mg^{2+} gradually increased with the immersion time, suggesting the sustained release of Ca^{2+} and Mg^{2+} from MgHAp/GelMA and MgHAp/GelMA-PDA hydrogels.

3.4. Photothermal effect and *in vitro* release of DOX

As aforementioned, constructing an on-site controlled anti-tumor drug delivery system assisted by PTT enables to greatly advance tumor treatment due to the synergy of chemotherapy and induced hyperthermia.[5,61] PDA particles are highly biocompatible and have been widely used as photothermal agent for controlled drug release due to their relatively high photothermal conversion efficiency. In addition, the abundant catechol and amine groups on PDA nanoparticles confer substantial adhesive capabilities that enable high drug loading efficiency.[62] Therefore, in the current study, anti-tumor drug, DOX, was loaded in PDA particles to form PDA@DOX particles. Moreover, PDA@DOX particles were loaded in 3D-printed hydrogels for providing combined therapy and synergistic effect. Firstly, the photothermal behavior of 3D-printed GelMA, HAp/GelMA, MgHAp/GelMA, and MgHAp/GelMA-PDA hydrogels was investigated. Figure 9A–C shows the temperature changes of hydrogels when they were irradiated by an 808 nm NIR laser at different power densities (0.5 and 1.0 W/cm^2). After being irradiated by NIR laser at 0.5 and 1.0 W/cm^2 for 3 min, MgHAp/GelMA-PDA hydrogels were heated to 42.7 and 48.4°C, respectively. Previous studies have indicated that tumor cells were efficiently killed when the local temperature had gone up to 42–50°C.[63] In this context, MgHAp/GelMA-PDA@DOX hydrogels could provide effective hyperthermic ablation of tumor cells when implanted at the tumor resection site of the body. Furthermore, to determine the effect of NIR laser irradiation on DOX release, 3D-printed MgHAp/GelMA-PDA@DOX hydrogels were used. As a result, more

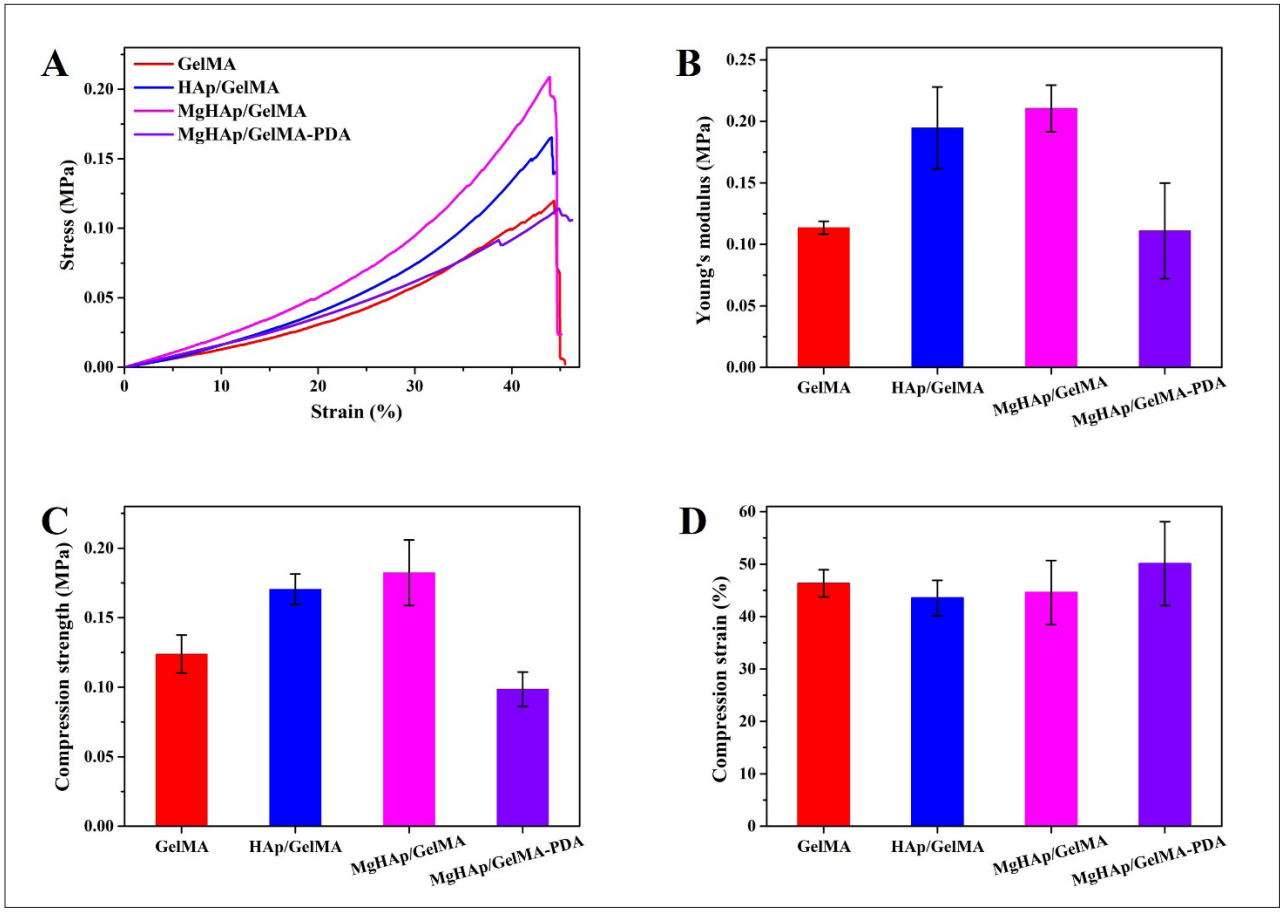


Figure 7. Mechanical properties of printed hydrogels in wet state. (A–D) Typical compression stress–strain curves (A), Young's modulus (B), compression strength (C), and compression strain (D) of 3D-printed GelMA, HAp/GelMA, MgHAp/GelMA, and MgHAp/GelMA-PDA hydrogels.

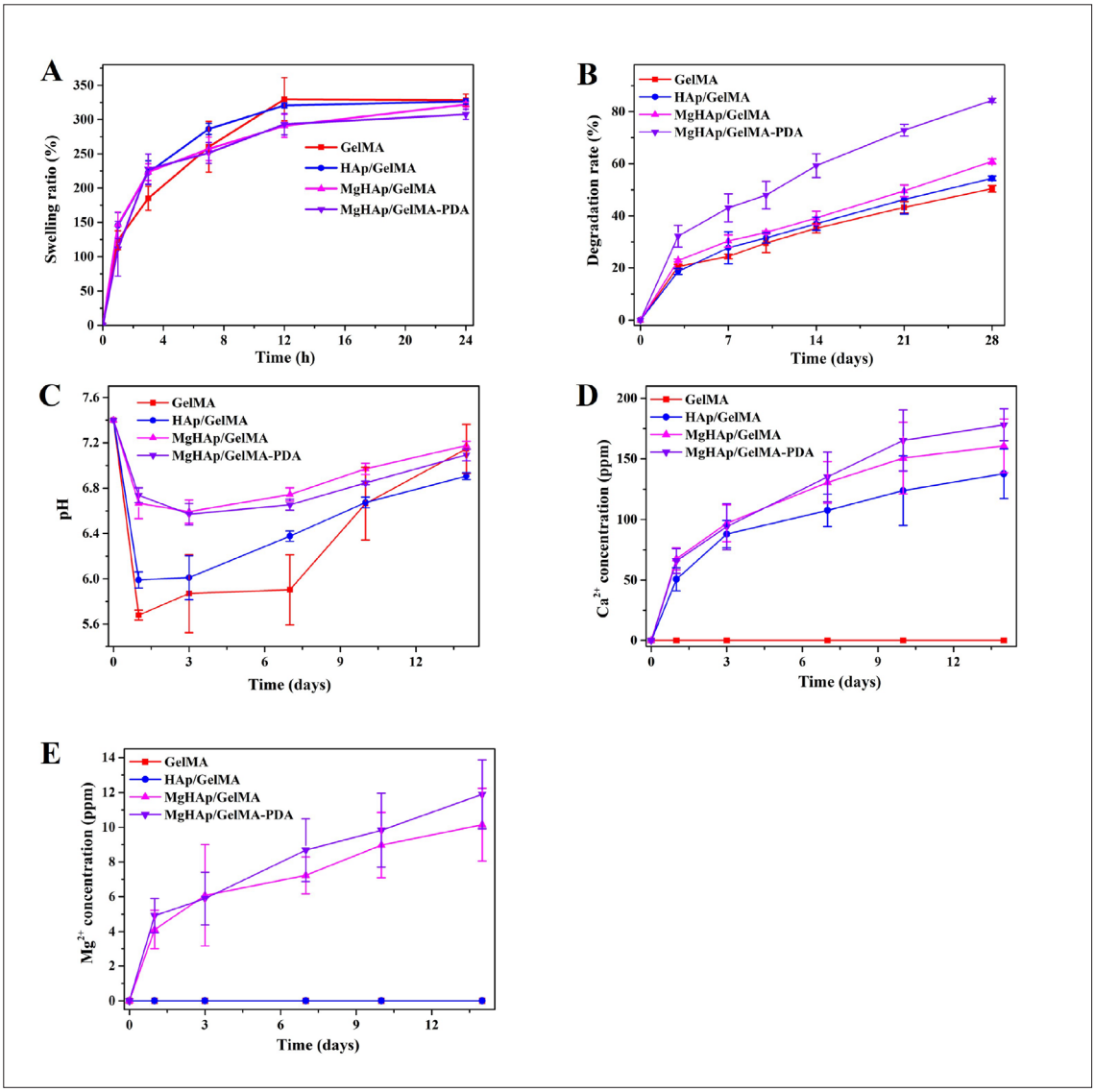


Figure 8. Swelling behavior (A), *in vitro* degradation behavior (B), pH change (C), Ca^{2+} release (D), and Mg^{2+} release (E) of 3D-printed GelMA, HAp/GelMA, MgHAp/GelMA, and MgHAp/GelMA-PDA hydrogels.

DOX was released from the hydrogels under NIR laser irradiation (Figure 9D). Additionally, a higher power density of NIR laser elicited a larger release of DOX. The NIR laser irradiation greatly promoted DOX release from MgHAp/GelMA-PDA@DOX hydrogels, which was possibly due to the Brownian movements of molecules. The entropy and temperature of MgHAp/GelMA-PDA@DOX hydrogels was enhanced when heated by NIR laser irradiation, thereby accelerating the movements of DOX molecules and the disintegration of hydrogels.

Since the tumor microenvironment is often acidic and hypoxic, studying DOX release in buffer solutions with different pH values (pH 4.5 and 7.4) is essential. As shown in Figures 9E and S6, Supporting Information, compared to PDA@DOX particles in which DOX could be quickly released in 12 h in either PBS or acidic solution, DOX could be sustainably released from MgHAp/GelMA-PDA@DOX hydrogels for more than 7 days in an acidic environment while the release of DOX reached a plateau after 3 days being immersed in PBS at pH 7.4. The sustained DOX release in acidic environment would achieve a prolonged therapeutic effect and hence could facilitate cell membrane permeability and effectively kill tumor cells.[64]

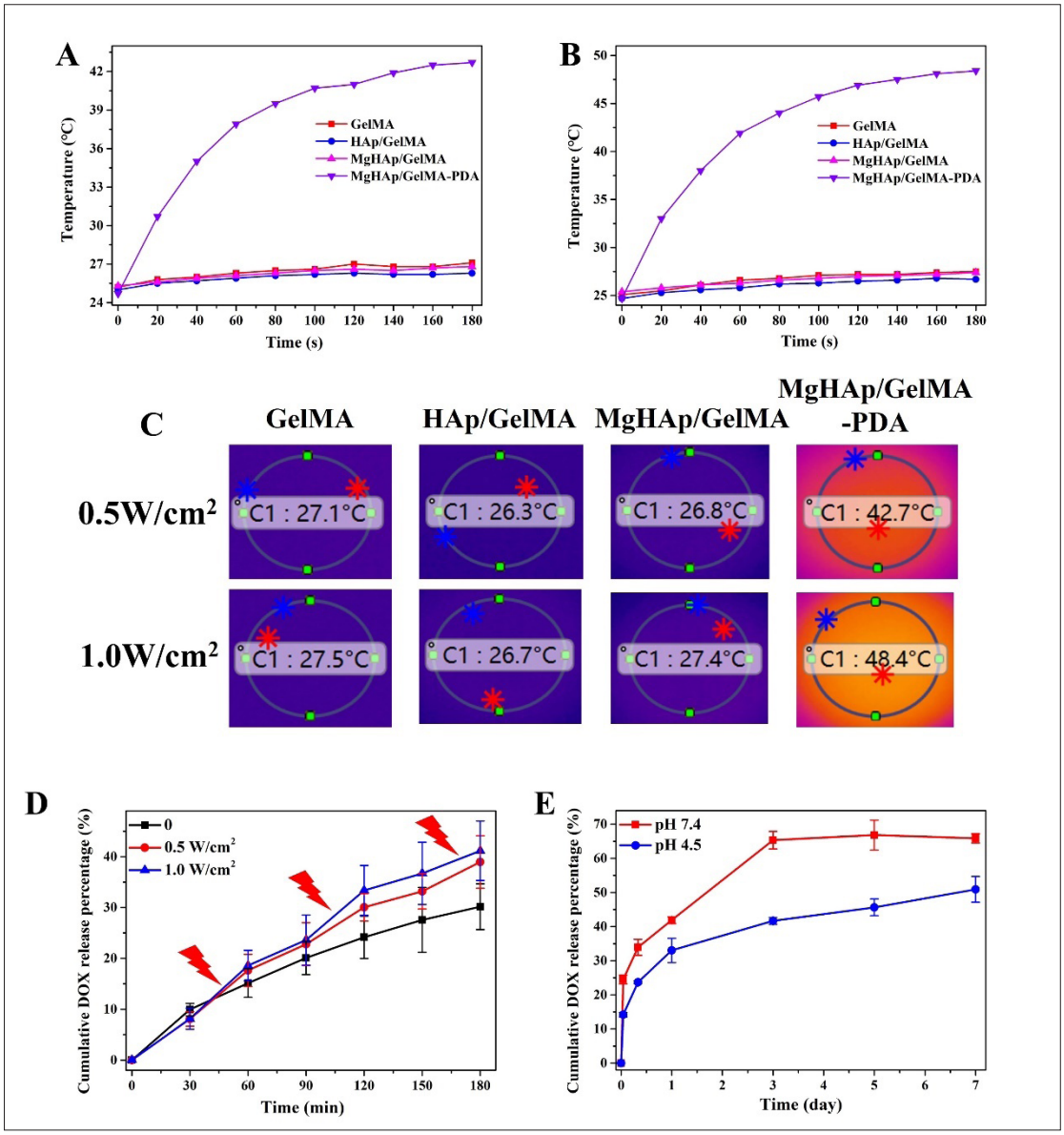


Figure 9. Photothermal effect and controlled DOX release behavior of printed hydrogels. (A, B) Temperature changes of 3D-printed GelMA, HAp/GelMA, MgHAp/GelMA, and MgHAp/GelMA-PDA hydrogels under the irradiation of 808 nm NIR laser at power densities of 0.5 W/cm^2 (A) and 1.0 W/cm^2 (B). (C) Infrared thermal images of 3D-printed GelMA, HAp/GelMA, MgHAp/GelMA, and MgHAp/GelMA-PDA hydrogels after being irradiated by NIR laser for 3 min. (D) *In vitro* DOX release curves of MgHAp/GelMA-PDA@DOX hydrogels with (0.5 and 1.0 W/cm^2) and without NIR laser irradiation (pH 7.4, PBS). (E) *In vitro* DOX release curves of MgHAp/GelMA-PDA@DOX hydrogels in pH 4.5 and 7.4 buffer solutions.

3.5. *In vitro* antitumor efficiency

Chemotherapy assisted by PTT enables the controlled release of DOX on demand while simultaneously providing hyperthermia, showing great synergy for tumor treatment. Many studies have revealed that NIR laser irradiation could cause the local temperature within the range of 42–50°C and thus provide hyperthermia and synergistically stimulate DOX release to improve anticancer therapy.[4,9,65] Therefore, in the current study, 3D-printed MgHAp/GelMA-PDA@DOX hydrogels combined with NIR laser irradiation were employed to investigate the *in vitro* antitumor efficiency. As shown in Figure 10A, after being cultured for 4 and 24 h, many bone tumor cells were found dead in the MgHAp/GelMA-PDA+NIR, MgHAp/GelMA-PDA@DOX, and MgHAp/GelMA-PDA@DOX+NIR groups. Moreover, Figure 10B indicates that the cell survival rates of MG63 cells in the MgHAp/GelMA-PDA, MgHAp/GelMA-PDA+NIR, MgHAp/GelMA-PDA@DOX, and

MgHAp/GelMA-PDA@DOX+NIR groups, after being cultured for 24 h, were 96.66 ± 0.11%, 47.01 ± 0.93%, 42.57 ± 3.11%, and 8.53 ± 1.12 %, respectively. Compared to the MgHAp/GelMA-PDA group, the MgHAp/GelMA-PDA+NIR and MgHAp/GelMA-PDA@DOX groups exhibited dramatically lower cell survival rates, which could be attributed to the hyperthermia triggered by NIR laser irradiation or the sustained release of DOX. Additionally, almost all MG63 cells were eradicated in the MgHAp/GelMA-PDA@DOX+NIR group after 24 h of culture, as a result of the synergistic effect of chemotherapy and hyperthermia induced by NIR laser. The significant decrease in cell viability of MG63 cells in the MgHAp/GelMA-PDA@DOX+NIR group further confirmed the synergistic effect of chemotherapy and PTT for tumor cell eradication (Figure 10C). Consequently, 3D-printed MgHAp/GelMA-PDA@DOX hydrogels that had been irradiated by NIR laser possessed excellent antitumor efficiency and could decimate tumor cells through the synergy of chemotherapy and PTT.

3.6. Proliferation and osteogenic differentiation of 3D-printed hydrogels

To investigate the *in vitro* biological properties of printed hydrogels, rBMSCs were cultured on the hydrogels. It is well-known that GelMA contains RGD sequences that can promote cell attachment and growth. As shown in Figure 11, all 3D-printed hydrogels were conducive to cell growth. In the current study, HAp/GelMA hydrogels exhibited a higher proliferation rate of rBMSCs than GelMA hydrogels. This could be attributed to the enhanced mechanical strength of hydrogels due to the incorporation of HAp nanocomposites. Meanwhile, compared to HAp/GelMA hydrogels, MgHAp/GelMA hydrogels exhibited a higher proliferation rate of rBMSCs, which could result from the release of Mg^{2+}. Previous studies showed that Mg^{2+} could enhance cell attachment and proliferation.[35,66] Notably, because of the encapsulation of PDA particles, MgHAp/GelMA-PDA hydrogels exhibited the highest cell proliferation rate. Many studies have reported that PDA particles could facilitate cell adhesion and proliferation.[67]

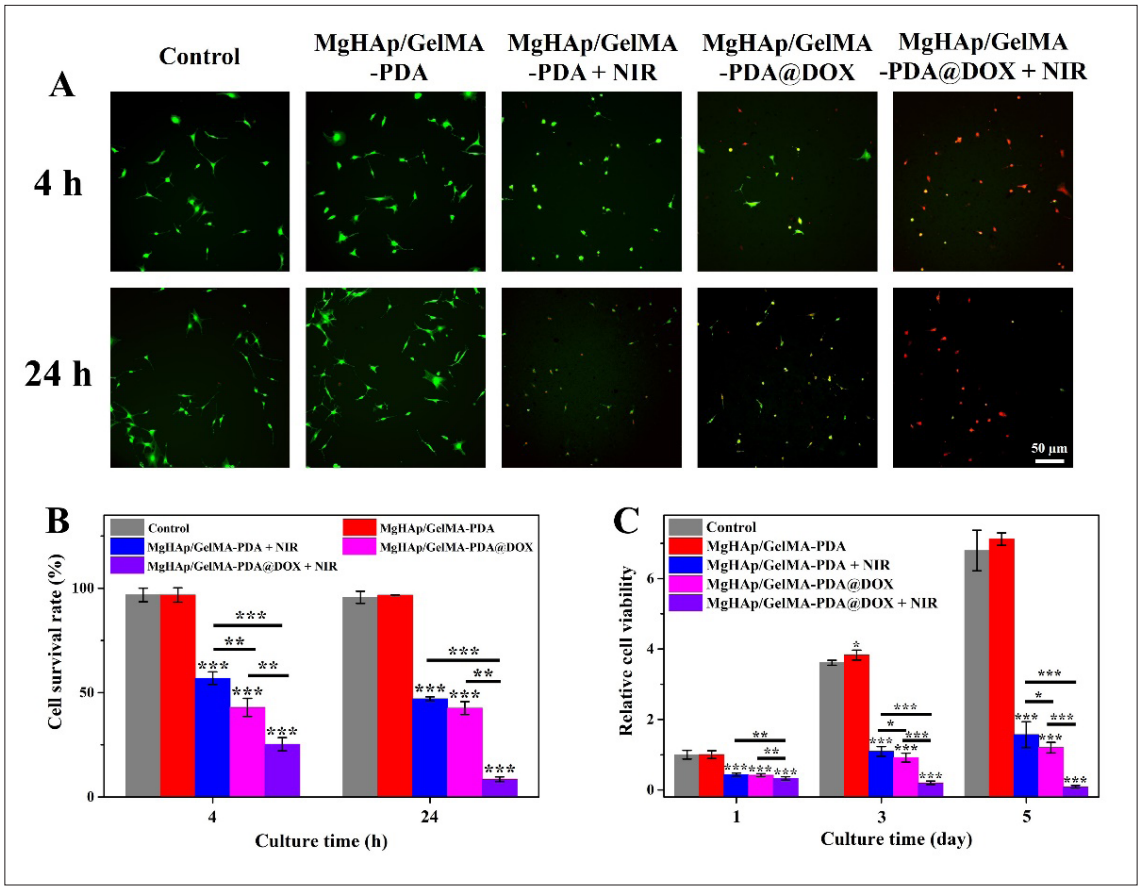


Figure 10. *In vitro* antitumor efficiency of MgHAp/GelMA-PDA@DOX hydrogels irradiated by NIR laser. (A) Fluorescence images showing the morphology of living and dead MG63 cells incubated on hydrogels for 4 and 24 h. (B) Cell survival rates of MG63 cells on hydrogels after incubation for 4 and 24 h. (C) Relative cell viability of MG63 cells cultured on hydrogels for 1, 3, and 5 days.

For example, Yang et al. suggested that PDA particles possessed a large amount of amine and hydroxyl groups and thus benefited cell adhesion, spread, and growth.[68]

To investigate the osteogenic effect of printed hydrogels, the ALP activity expression was studied. As shown in Figure 12A and B, the ALP activity of rBMSCs on HAp/GelMA hydrogels was higher than that on GelMA hydrogels. Previous studies have demonstrated that HAp nanocomposites could promote the osteogenic differentiation of rBMSCs.[69,70] Moreover, MgHAp/GelMA and MgHAp/GelMA-PDA hydrogels exhibited the highest ALP activity expression after 7 and 14 days of culture, showing good osteogenic effect. Furthermore, the qRT-PCR results, as shown in Figure 12C–F, indicated that the expression of osteogenic genes, *i.e.*, *Ocn*, *Col1*, *Runx2*, and *Bmp2*, in MgHAp/GelMA and MgHAp/GelMA-PDA hydrogels was upregulated in comparison to GelMA and HAp/GelMA hydrogels. The confocal images in Figure 12G further demonstrates that MgHAp/GelMA and MgHAp/GelMA-PDA hydrogels had the highest expression of COL1. As a result, the sustained release of Mg^{2+} from MgHAp/GelMA and MgHAp/GelMA-PDA hydrogels significantly promoted osteogenic differentiation of rBMSCs, which was consistent with previous studies.[36,71,72] Mg^{2+} could regulate osteoblast activity by binding to the specific sites on the integrin α chains of cell surface and thus promote the expression of osteogenic genes. For example, Sun et al. showed that Mg^{2+} released from Wollastonite ceramic could promote the ALP activity, the expression of osteogenic genes, such as *Ocn*, *Runx2*, *Col1*, and *Osx* of MC3T3-E1 cells, and the repair of rabbit skull defects.[73] As a result, 3D-printed MgHAp/GelMA-PDA@DOX hydrogels showed great potential for treating bone tumor-related defects by providing synergy for effectively eradicating tumor cells and promoting osteogenesis.

4. Conclusion

In the current study, MgHAp nanocomposites were synthesized via a biomineralization process. GelMA and PDA@DOX particles were fabricated. MgHAp/GelMA-PDA@DOX hydrogels were constructed via 3D printing. MgHAp nanocomposites and PDA particles

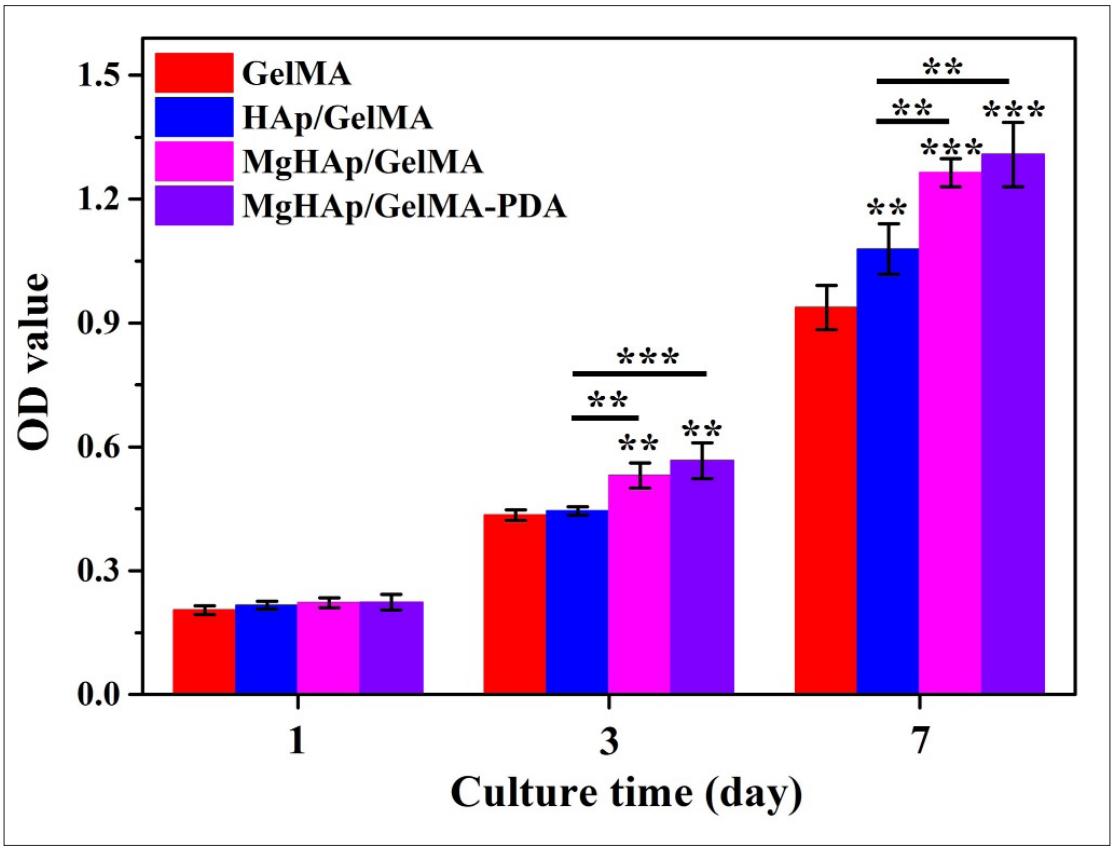


Figure 11. Proliferation profiles of rBMSCs cultured on 3D-printed GelMA, HAp/GelMA, MgHAp/GelMA, and MgHAp/GelMA-PDA hydrogels. ** $p < 0.01$, *** $p < 0.001$ versus GelMA.

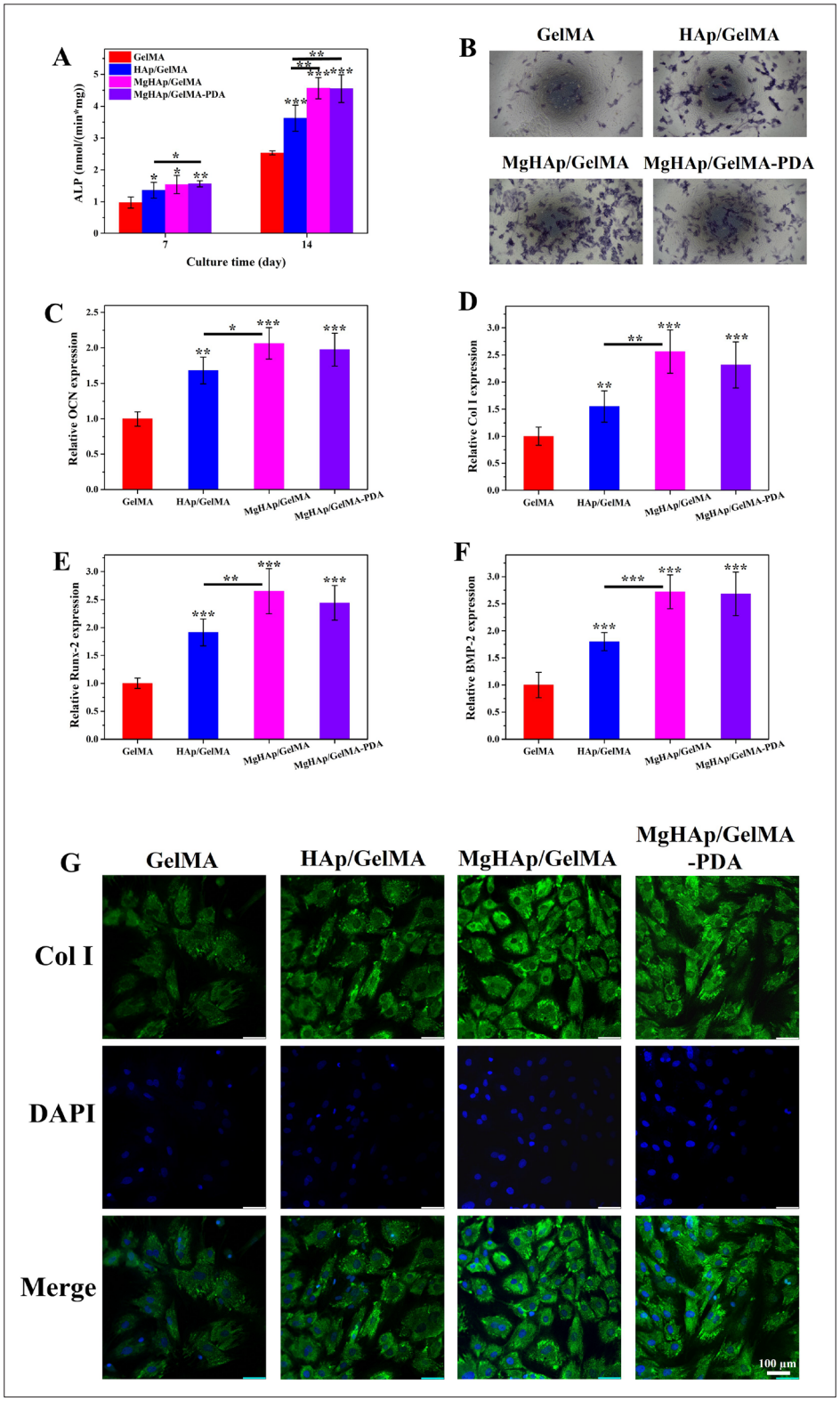


Figure 12. Osteogenic differentiation of rBMSCs on hydrogels. (A) Alkaline phosphatase (ALP) activity of rBMSCs on hydrogels after being cultured for 7 and 14 days. (B) Optical images showing the ALP staining results of rBMSCs cultured for 14 days. (C–F) The relative expression of osteogenic genes, namely *Ocn* (C), *Col1* (D), *Runx2* (E), and *Bmp2* (F), in rBMSCs cultured on hydrogels for 14 days. (G) Confocal images showing the expression of COL1 in rBMSCs cultured on hydrogels for 14 days.

were homogenously dispersed within the hydrogels. The incorporation of MgHAp nanocomposites improved the printability of inks and promoted structural fidelity of printed structures. Additionally, MgHAp nanocomposites enhanced the mechanical strength of hydrogels. Moreover, MgHAp/GelMA-PDA@DOX hydrogels enabled the sustained and controlled release of Mg^{2+}. MgHAp/GelMA-PDA@DOX hydrogels exhibited an excellent photothermal effect and could generate hyperthermia upon irradiation with NIR laser. The release of DOX from hydrogels could be controlled by NIR laser irradiation and was also pH-responsive. *In vitro* antitumor experiments indicated that MgHAp/GelMA-PDA@DOX hydrogels could effectively kill the MG63 osteosarcoma cells through the synergistic effect of induced hyperthermia and DOX release. Moreover, compared to HAp/GelMA hydrogels, MgHAp/GelMA-PDA hydrogels could promote proliferation and osteogenic differentiation of rBMSCs due to the sustained release of Mg^{2+}. Consequently, 3D-printed MgHAp/GelMA-PDA@DOX hydrogels hold great promise in treating bone tumor-related defects by providing effective anti-tumor efficiency and the promotion of osteogenic effect.

Acknowledgments

None

Funding

This work was financially supported by the National Nature Science Foundation of China (Grant No. 82201133) and Fong On Construction Ltd. in Hong Kong (Grant No. ZDBM, ZDCA). The research sponsored from Fong On Construction Ltd. (HK) has potential interest in exploring the potential application of extrusion-based 3D printing technology in automation within the construction industry.

Conflict of interest

The authors declare no conflicts of interest.

Author contributions

Conceptualization: Shangsi Chen, Shenglong Tan
Investigation: Shangsi Chen, Yue Wang, Junzhi Li
Methodology: Shangsi Chen, Yue Wang, Junzhi Li
Supervision: Haoran Sun, Ming-Fung Francis Siu, Shenglong Tan
Writing – original draft: All authors
Writing – review & editing: Haoran Sun, Ming-Fung Francis Siu, Shenglong Tan

Ethics approval and consent to participate

Not applicable.

Consent for publication

Not applicable.

Availability of data

Data are available from the corresponding author upon reasonable request.

References

1. Isakoff MS, Bielack SS, Meltzer P, Gorlick R. Osteosarcoma: current treatment and a collaborative pathway to success. *J Clin Oncol*. 2015;33(27):3029-3035. doi: 10.1200/JCO.2014.59.4895
2. Chen HHW, Kuo MT. Improving radiotherapy in cancer treatment: promises and challenges. *Oncotarget*. 2017;8(37):62742-62758. doi: 10.18632/oncotarget.18409
3. Behranvand N, Nasri F, Zolfaghari Emameh R, et al. Chemotherapy: a double-edged sword in cancer treatment. *Cancer Immunol Immunother*. 2022;71(3):507-526. doi: 10.1007/s00262-021-03013-3
4. Su J, Sun H, Meng Q, et al. Bioinspired nanoparticles with NIR-controlled drug release for synergetic chemophotothermal therapy of metastatic breast cancer. *Adv Funct Mater*. 2016;26(41):7495-7506. doi: 10.1002/adfm.201603381
5. Fan R, Chen C, Hou H, et al. Tumor acidity and near-infrared light responsive dual drug delivery polydopamine-based nanoparticles for chemo-photothermal therapy. *Adv Funct Mater*. 2021;31(18):2009733. doi: 10.1002/adfm.202009733
6. An D, Fu J, Zhang B, et al. NIR-II responsive inorganic 2D nanomaterials for cancer photothermal therapy: recent advances and future challenges. *Adv Funct Mater*. 2021;31(32):2101625. doi: 10.1002/adfm.202101625
7. Ren Y, Yan Y, Qi H. Photothermal conversion and transfer in photothermal therapy: from macroscale to nanoscale. *Adv Colloid Interface Sci*. 2022;308:102753. doi: 10.1016/j.cis.2022.102753
8. Batul R, Tamanna T, Khaliq A, Yu A. Recent progress in the biomedical applications of polydopamine nanostructures. *Biomater Sci*. 2017;5(7):1204-1229. doi: 10.1039/c7bm00187h
9. Qiu J, Shi Y, Xia Y. Polydopamine nanobottles with photothermal capability for controlled release and related applications. *Adv Mater*. 2021;33(45):e2104729. doi: 10.1002/adma.202104729
10. Bedhiafi T, Idoudi S, Alhams AA, et al. Applications of polydopaminic nanomaterials in mucosal drug delivery. *J Control Release*. 2023;353:842-849.

doi: 10.1016/j.jconrel.2022.12.037

11. Chen S, Tan S, Zheng L, Wang M. Multilayered shape-morphing scaffolds with a hierarchical structure for uterine tissue regeneration. *ACS Appl Mater Interfaces*. 2024;16(6):6772-6788.
doi: 10.1021/acsami.3c14983

12. Abbasi N, Hamlet S, Love RM, Nguyen NT. Porous scaffolds for bone regeneration. *J Sci: Adv Mater Devices*. 2020; 5(1):1-9.
doi: 10.1016/j.jsamd.2020.01.007

13. Chen S, Shi Y, Zhang X, Ma J. Evaluation of BMP-2 and VEGF loaded 3D printed hydroxyapatite composite scaffolds with enhanced osteogenic capacity in vitro and in vivo. *Mater Sci Eng C Mater Biol Appl*. 2020;112:110893.
doi: 10.1016/j.msec.2020.110893

14. Bose S, Roy M, Bandyopadhyay A. Recent advances in bone tissue engineering scaffolds. *Trends Biotechnol*. 2012;30(10):546-554.
doi: 10.1016/j.tibtech.2012.07.005

15. Roseti L, Parisi V, Petretta M, et al. Scaffolds for bone tissue engineering: state of the art and new perspectives. *Mater Sci Eng C Mater Biol Appl*. 2017;78:1246-1262.
doi: 10.1016/j.msec.2017.05.017

16. Lai J, Wang C, Liu J, et al. Low temperature hybrid 3D printing of hierarchically porous bone tissue engineering scaffolds within situdelivery of osteogenic peptide and mesenchymal stem cells. *Biofabrication*. 2022;14(4):045006.
doi: 10.1088/1758-5090/ac84b0

17. Do AV, Khorsand B, Geary SM, Salem AK. 3D printing of scaffolds for tissue regeneration applications. *Adv Healthc Mater*. 2015;4(12):1742-1762.
doi: 10.1002/adhm.201500168

18. Wang S, Zhao S, Yu J, Gu Z, Zhang Y. Advances in translational 3D printing for cartilage, bone, and osteochondral tissue engineering. *Small*. 2022;18(36):e2201869.
doi: 10.1002/smll.202201869

19. MacDonald E, Wicker R. Multiprocess 3D printing for increasing component functionality. *Science*. 2016;353(6307):aaf2093.
doi: 10.1126/science.aaf2093

20. Velasquez-Garcia LF, Kornbluth Y. Biomedical applications of metal 3D printing. *Annu Rev Biomed Eng*. 2021;23: 307-338.
doi: 10.1146/annurev-bioeng-082020-032402

21. Ratheesh G, Vaquette C, Xiao Y. Patient-specific bone particles bioprinting for bone tissue engineering. *Adv Healthc Mater*. 2020;9(23):e2001323.
doi: 10.1002/adhm.202001323

22. Van hede D, Liang B, Anania S, et al. 3D-printed synthetic hydroxyapatite scaffold with in silico optimized macrostructure enhances bone formation in vivo. *Adv Funct Mater*. 2021;32(6):2105002.
doi: 10.1002/adfm.202105002

23. Wang Y, Chen SS, Liang HW, Liu Y, Bai JM, Wang M. Digital light processing (DLP) of nano biphasic calcium phosphate bioceramic for making bone tissue engineering scaffolds. *Ceram Int*. 2022;48(19):27681-27692.
doi: 10.1016/j.ceramint.2022.06.067

24. Yin J, Yan M, Wang Y, Fu J, Suo H. 3D bioprinting of low-concentration cell-laden gelatin methacrylate (GelMA) bioinks with a two-step cross-linking strategy. *ACS Appl Mater Interfaces*. 2018;10(8):6849-6857.
doi: 10.1021/acsami.7b16059

25. Guo A, Zhang S, Yang R, Sui C. Enhancing the mechanical strength of 3D printed GelMA for soft tissue engineering applications. *Mater Today Bio*. 2024; 24:100939.
doi: 10.1016/j.mtbio.2023.100939

26. Chen S, Wang Y, Lai J, Tan S, Wang M. Structure and properties of gelatin methacryloyl (GelMA) synthesized in different reaction systems. *Biomacromolecules*. 2023;24(6):2928-2941.
doi: 10.1021/acs.biomac.3c00302

27. Jiang G, Li S, Yu K, et al. A 3D-printed PRP-GelMA hydrogel promotes osteochondral regeneration through M2 macrophage polarization in a rabbit model. *Acta Biomater*. 2021;128:150-162.
doi: 10.1016/j.actbio.2021.04.010

28. Xu C, Chang Y, Xu Y, et al. Silicon-phosphorus-nanosheets-integrated 3D-printable hydrogel as a bioactive and biodegradable scaffold for vascularized bone regeneration. *Adv Healthc Mater*. 2022;11(6):e2101911.
doi: 10.1002/adhm.202101911

29. Zhang X, Zhang H, Zhang Y, et al. 3D printed reduced graphene oxide-GelMA hybrid hydrogel scaffolds for potential neuralized bone regeneration. *J Mater Chem B*. 2023;11(6):1288-1301.
doi: 10.1039/d2tb01979e

30. Xavier Mendes A, Moraes Silva S, O'Connell CD, et al. Enhanced electroactivity, mechanical properties, and printability through the addition of graphene oxide to photo-cross-linkable gelatin methacryloyl hydrogel. *ACS Biomater Sci Eng*. 2021;7(6):2279-2295.
doi: 10.1021/acsbiomaterials.0c01734

31. Choi E, Kim D, Kang D, et al. 3D-printed gelatin methacrylate (GelMA)/silanated silica scaffold assisted by two-stage cooling system for hard tissue regeneration. *Regen Biomater*. 2021;8(2):rbab001.
doi: 10.1093/rb/rbab001

32. Gui XY, Zhang BQ, Song P, et al. 3D printing of biomimetic hierarchical porous architecture scaffold with dual osteoinduction and osteoconduction biofunctions for large size bone defect repair. *Appl Mater Today*. 2024; 37:102085.
doi: 10.1016/j.apmt.2024.102085

33. Pu X, Tong L, Wang X, et al. Bioinspired hydrogel anchoring 3DP GelMA/HAp scaffolds accelerates bone reconstruction. *ACS Appl Mater Interfaces*. 2022;14(18):20591-20602. doi: 10.1021/acsami.1c25015

34. Song P, Li MX, Zhang BQ, et al. DLP fabricating of precision GelMA/HAp porous composite scaffold for bone tissue engineering application. *Compos B Eng*. 2022;244:110163. doi: 10.1016/j.compositesb.2022.110163

35. Chen S, Shi Y, Zhang X, Ma J. Biomimetic synthesis of Mg-substituted hydroxyapatite nanocomposites and three-dimensional printing of composite scaffolds for bone regeneration. *J Biomed Mater Res A*. 2019;107(11): 2512-2521. doi: 10.1002/jbm.a.36757

36. Zhou H, Liang B, Jiang HT, Deng ZL, Yu KX. Magnesium-based biomaterials as emerging agents for bone repair and regeneration: from mechanism to application. *J Magnes Alloy*. 2021;9(3):779-804. doi: 10.1016/j.jma.2021.03.004

37. Chen S, Wang Y, Zhang X, Ma J, Wang M. Double-crosslinked bifunctional hydrogels with encapsulated anti-cancer drug for bone tumor cell ablation and bone tissue regeneration. *Colloids Surf B Biointerfaces*. 2022;213:112364. doi: 10.1016/j.colsurfb.2022.112364

38. Ouyang L, Yao R, Zhao Y, Sun W. Effect of bioink properties on printability and cell viability for 3D bioplotting of embryonic stem cells. *Biofabrication*. 2016;8(3):035020. doi: 10.1088/1758-5090/8/3/035020

39. Ma J, Wang J, Ai X, Zhang S. Biomimetic self-assembly of apatite hybrid materials: from a single molecular template to bi-/multi-molecular templates. *Biotechnol Adv*. 2014;32(4):744-60. doi: 10.1016/j.biotechadv.2013.10.014

40. Luo Y, Chen S, Shi Y, Ma J. 3D printing of strontium-doped hydroxyapatite based composite scaffolds for repairing critical-sized rabbit calvarial defects. *Biomed Mater*. 2018;13(6):065004. doi: 10.1088/1748-605X/aad923

41. Kang Y, Xu C, Meng L, Dong X, Qi M, Jiang D. Exosome-functionalized magnesium-organic framework-based scaffolds with osteogenic, angiogenic and anti-inflammatory properties for accelerated bone regeneration. *Bioact Mater*. 2022;18:26-41. doi: 10.1016/j.bioactmat.2022.02.012

42. Antoniac IV, Antoniac A, Vasile E, et al. In vitro characterization of novel nanostructured collagen-hydroxyapatite composite scaffolds doped with magnesium with improved biodegradation rate for hard tissue regeneration. *Bioact Mater*. 2021;6(10):3383-3395. doi: 10.1016/j.bioactmat.2021.02.030

43. Chen SS, Li JZ, Zheng LW, Huang J, Wang M. Biomimicking trilayer scaffolds with controlled estradiol release for uterine tissue regeneration. *Exploration*. 2024:20230141. doi: 10.1002/Exp.20230141

44. Kumar H, Sakthivel K, Mohamed MGA, Boras E, Shin SR, Kim K. Designing gelatin methacryloyl (GelMA)-based bioinks for visible light stereolithographic 3D biofabrication. *Macromol Biosci*. 2021;21(1):e2000317. doi: 10.1002/mabi.202000317

45. Lee BH, Lum N, Seow LY, Lim PQ, Tan LP. Synthesis and characterization of types A and B gelatin methacryloyl for bioink applications. *Materials (Basel)*. 2016;9(10):797. doi: 10.3390/ma9100797

46. Wang Z, Duan Y, Duan Y. Application of polydopamine in tumor targeted drug delivery system and its drug release behavior. *J Control Release*. 2018;290:56-74. doi: 10.1016/j.jconrel.2018.10.009

47. Yue K, Trujillo-de Santiago G, Alvarez MM, Tamayol A, Annabi N, Khademhosseini A. Synthesis, properties, and biomedical applications of gelatin methacryloyl (GelMA) hydrogels. *Biomaterials*. 2015;73:254-271. doi: 10.1016/j.biomaterials.2015.08.045

48. Outrequin TCR, Gamonpilas C, Siriwatwechakul W, Sreearunothai P. Extrusion-based 3D printing of food biopolymers: a highlight on the important rheological parameters to reach printability. *J Food Eng*. 2023; 342:111371. doi: 10.1016/j.jfoodeng.2022.111371

49. Sanchez-Sanchez R, Rodriguez-Rego JM, Macias-Garcia A, Mendoza-Cerezo L, Diaz-Parralejo A. Relationship between shear-thinning rheological properties of bioinks and bioprinting parameters. *Int J Bioprint*. 2023; 9(2):687. doi: 10.18063/ijb.687

50. Kyle S, Jessop ZM, Al-Sabah A, Whitaker IS. 'Printability' of candidate biomaterials for extrusion based 3D printing: state-of-the-art. *Adv Healthc Mater*. 2017;6(16):1700264. doi: 10.1002/adhm.201700264

51. Schwab A, Levato R, D'Este M, Piluso S, Eglin D, Malda J. Printability and shape fidelity of bioinks in 3D bioprinting. *Chem Rev*. 2020;120(19):11028-11055. doi: 10.1021/acs.chemrev.0c00084

52. Ning L, Mehta R, Cao C, et al. Embedded 3D bioprinting of gelatin methacryloyl-based constructs with highly tunable structural fidelity. *ACS Appl Mater Interfaces*. 2020;12(40):44563-44577. doi: 10.1021/acsami.0c15078

53. Mora-Boza A, Wlodarczyk-Biegun MK, Del Campo A, Vazquez-Lasa B, Roman JS. Glycerylphytate as an ionic crosslinker for 3D printing of multi-layered scaffolds with improved shape fidelity and biological features. *Biomater Sci*. 2019;8(1):506-516. doi: 10.1039/c9bm01271k

54. Latif M, Jiang Y, Kumar B, Song JM, Cho HC, Kim J. High content nanocellulose 3D-printed and esterified structures with strong interfacial adhesion, high mechanical

properties, and shape fidelity. *Adv Mater Interfaces*. 2022;9(16):202200280.
doi: 10.1002/admi.202200280

55. Bose S, Vahabzadeh S, Bandyopadhyay A. Bone tissue engineering using 3D printing. *Mater Today*. 2013;16(12):496-504.
doi: 10.1016/j.mattod.2013.11.017

56. Wang ZC, Huang CZ, Han X, et al. Fabrication of aerogel scaffolds with adjustable macro/micro-pore structure through 3D printing and sacrificial template method for tissue engineering. *Mater Design*. 2022;217(1):110662.
doi: 10.1016/j.matdes.2022.110662

57. Rizwan M, Chan SW, Comeau PA, Willett TL, Yim EKF. Effect of sterilization treatment on mechanical properties, biodegradation, bioactivity and printability of GelMA hydrogels. *Biomed Mater*. 2020;15(6):065017.
doi: 10.1088/1748-605X/aba40c

58. O'Connell CD, Zhang B, Onofrillo C, et al. Tailoring the mechanical properties of gelatin methacryloyl hydrogels through manipulation of the photocrosslinking conditions. *Soft Matter*. 2018;14(11):2142-2151.
doi: 10.1039/c7sm02187a

59. Bashir S, Hina M, Iqbal J, et al. Fundamental concepts of hydrogels: synthesis, properties, and their applications. *Polymers (Basel)*. 2020;12(11):2702.
doi: 10.3390/polym12112702

60. Piao Y, You H, Xu T, et al. Biomedical applications of gelatin methacryloyl hydrogels. *Eng Regen*. 2021;2:47-56.
doi: 10.1016/j.engreg.2021.03.002

61. Zhang XA, Wei H, Dong C, et al. 3D printed hydrogel/bioceramics core/shell scaffold with NIR-II triggered drug release for chemo-photothermal therapy of bone tumors and enhanced bone repair. *Chem Eng J*. 2023; 461:141855.
doi: 10.1016/j.cej.2023.141855

62. Jin A, Wang Y, Lin K, Jiang L. Nanoparticles modified by polydopamine: working as "drug" carriers. *Bioact Mater*. 2020;5(3):522-541.
doi: 10.1016/j.bioactmat.2020.04.003

63. Cheng W, Nie JP, Gao NS, et al. A multifunctional nanoplatform against multidrug resistant cancer: merging the best of targeted chemo/gene/photothermal therapy. *Adv Funct Mater*. 2017;27(45):1704135.
doi: 10.1002/adfm.201704135

64. Shahzadi I, Islam M, Saeed H, et al. Formation of biocompatible MgO/cellulose grafted hydrogel for efficient bactericidal and controlled release of doxorubicin. *Int J Biol Macromol*. 2022;220:1277-1286.
doi: 10.1016/j.ijbiomac.2022.08.142

65. Chu X, Zhang L, Li Y, He Y, Zhang Y, Du C. NIR responsive doxorubicin-loaded hollow copper ferrite @ polydopamine for dynergistic chemodynamic/photothermal/chemo-therapy. *Small*. 2023;19(7):e2205414.
doi: 10.1002/smll.202205414

66. Gao P, Fan B, Yu X, et al. Biofunctional magnesium coated Ti6Al4V scaffold enhances osteogenesis and angiogenesis in vitro and in vivo for orthopedic application. *Bioact Mater*. 2020;5(3):680-693.
doi: 10.1016/j.bioactmat.2020.04.019

67. Qian Y, Zhao X, Han Q, Chen W, Li H, Yuan W. An integrated multi-layer 3D-fabrication of PDA/RGD coated graphene loaded PCL nanoscaffold for peripheral nerve restoration. *Nat Commun*. 2018;9(1):323.
doi: 10.1038/s41467-017-02598-7

68. Yang Z, Si J, Cui Z, et al. Biomimetic composite scaffolds based on surface modification of polydopamine on electrospun poly(lactic acid)/cellulose nanofibrils. *Carbohydr Polym*. 2017;174:750-759.
doi: 10.1016/j.carbpol.2017.07.010

69. Cheng H, Chabok R, Guan X, et al. Synergistic interplay between the two major bone minerals, hydroxyapatite and whitlockite nanoparticles, for osteogenic differentiation of mesenchymal stem cells. *Acta Biomater*. 2018;69:342-351.
doi: 10.1016/j.actbio.2018.01.016

70. Liu X, Wei Y, Xuan C, et al. A biomimetic biphasic osteochondral scaffold with layer-specific release of stem cell differentiation inducers for the reconstruction of osteochondral defects. *Adv Healthc Mater*. 2020;9(23):e2000076.
doi: 10.1002/adhm.202000076

71. Li D, Zhang D, Yuan Q, et al. In vitro and in vivo assessment of the effect of biodegradable magnesium alloys on osteogenesis. *Acta Biomater*. 2022;141:454-465.
doi: 10.1016/j.actbio.2021.12.032

72. Wang L, Pang Y, Tang Y, et al. A biomimetic piezoelectric scaffold with sustained Mg(2+) release promotes neurogenic and angiogenic differentiation for enhanced bone regeneration. *Bioact Mater*. 2023;25:399-414.
doi: 10.1016/j.bioactmat.2022.11.004

73. Sun M, Liu A, Shao H, et al. Systematical evaluation of mechanically strong 3D printed diluted magnesium doping wollastonite scaffolds on osteogenic capacity in rabbit calvarial defects. *Sci Rep*. 2016;6:34029.
doi: 10.1038/srep34029

ACCSCIENCE PUBLISHING

International Journal of Bioprinting

RESEARCH ARTICLE

A functionally graded gyroid-type three-periodic minimal surface framework applied to implant-supported fixed complete dentures

Jiwei Ren[1], Renkai Huang[1,2*], Linqing Huang[3], Shaoying Yang[1], Chunrong Pan[1], Yuchun Sun[2,4,5], Sukun Tian[2,4,5*], Xuehua Wu[1], Dongsheng Wang[6,7,8], and Youwen Yang[1,8*]

[1]Department of Intelligent Manufacturing, School of Mechanical and Electrical Engineering, Jiangxi University of Science and Technology, Ganzhou, Jiangxi, China

[2]NHC Key Laboratory of Digital Stomatology, Faculty of Prosthodontics, Peking University School and Hospital of Stomatology, Beijing, China

[3]Institute of Green Metallurgy and Process Intensification, School of Metallurgical Engineering, Jiangxi University of Science and Technology, Ganzhou, Jiangxi, China

[4]Center of Digital Dentistry, Faculty of Prosthodontics, Peking University School and Hospital of Stomatology, Beijing, China

[5]National Engineering Research Center of Oral Biomaterials and Digital Medical Devices, Faculty of Prosthodontics, Peking University School and Hospital of Stomatology, Beijing, China

[6]Advanced Copper-based Material Industry Generic Technology Research Center of Anhui Province, Scool of Mechanical Engineering, Tongling University, Tongling, Anhui, China

[7]Key Laboratory of Construction Hydraulic Robots of Anhui Higher Education Institutes, Scool of Mechanical Engineering, Tongling University, Tongling, Anhui, China

[8]Key Laboratory of Additive Manufacturing of Tongling City, Scool of Mechanical Engineering, Tongling University, Tongling, Anhui, China

***Corresponding authors:**
Renkai Huang
(huang_renkai@jxust.edu.cn)

Sukun Tian
(sukhum169@hotmail.com)

Youwen Yang
(yangyouwen@jxust.edu.cn)

Citation: Ren J, Huang R, Huang L, et al. A functionally graded gyroid-type three-periodic minimal surface framework applied to implant-supported fixed complete dentures. *Int J Bioprint*. 2024;10(5):3453. doi: 10.36922/ijb.3453

Received: April 19, 2024
Accepted: May 30, 2024
Published Online: July 19, 2024

Copyright: © 2024 Author(s). This is an Open Access article distributed under the terms of the Creative Commons Attribution License, permitting distribution, and reproduction in any medium, provided the original work is properly cited.

Publisher's Note: AccScience Publishing remains neutral with regard to jurisdictional claims in published maps and institutional affiliations.

Abstract

Titanium alloy, particularly Ti6Al4V, is commonly used for constructing the framework of implant-supported fixed complete dentures (IFCDs) but exhibits poor specific strength and impact toughness. Three-periodic minimal surface (TPMS) porous structures have the advantages of high specific strength, lightweight, and shock and energy absorption. Therefore, the functionally graded TPMS porous structure was adopted to design the framework for IFCDs in this study. Nine types of TPMS-based lattice structures with radial gradient variations were designed. Finite element analysis and experimental results indicate that the relative density increases outward and the cell size decreases outward from the center. The B-I porous structure has the highest strength and impact toughness compared to other gradient porous structure types. Moreover, the IFCD framework, utilizing the B-I porous structure, exhibited a 50% reduction in weight compared to the solid framework. When compared to the hollow framework with the same weight, the B-I framework demonstrated a 42.81% lower maximum equivalent stress under normal chewing conditions without undergoing plastic deformation. Therefore, the B-I framework meets the mechanical performance requirements for daily chewing and exhibits superior mechanical properties over conventional structures.

Keywords: Implant-supported fixed complete dentures; Porous frameworks; Three-periodic minimal surfaces; Functional gradient; Mechanical properties

1. Introduction

With the aging of the population worldwide, a large number of patients suffer from complete edentulism due to conditions such as caries or periodontal disease, necessitating prosthetic rehabilitation.[1,2] Implant-supported complete dentures (IFCDs) have become increasingly popular among dental clinicians for rehabilitating edentulous patients due to their high survival rates and strong occlusal force.[2–5] IFCDs consist of a framework portion and veneering materials. The framework primarily provides mechanical performance, while the veneering materials primarily serve to enhance esthetics and partially bear occlusal functions. As the supporting part of IFCDs, the framework should have good stiffness, specific strength, impact toughness, and biocompatibility. Its commonly used materials include pure titanium and titanium alloys, Co-Cr alloys, and zirconia.[6,7]

Among them, titanium and its alloys are known for their excellent corrosion resistance and biocompatibility. Additionally, they offer moderate price points and exhibit robust bonding strength with decorative materials like resin and zirconia.[8–10] Selective laser melting (SLM) can process titanium alloys to yield specific properties. As noted by Kanazawa et al.,[11] SLM-processed titanium alloy-based complete dentures for the maxilla usually exhibit higher hardness values and fewer pores compared to those obtained by conventional casting. However, most existing IFCDs' metal frameworks assume solid structures, which results in more strain being generated around the implants due to their weight.[12] Moreover, metal frameworks with solid structures have a poor energy absorption effect,[13] resulting in the inability to effectively reduce the impact of the framework on the jaw during chewing.[14] For example, Edelhoff et al.[15] found that solid frameworks exhibited limited capacity to absorb and disperse energy effectively, making them susceptible to fractures and failures under sudden impacts or intense chewing conditions. From the description above, IFCDs with solid metal frameworks are characterized by relatively high rates of prosthesis-related complications and failure, commonly including excessive occlusal wear, screw loosening or fracture, and framework fracture or failure.[16–18]

Thus, this article attempts to replace the traditional metal framework with the three-periodic minimal surface (TPMS)-based porous framework. Owing to its zero mean curvature, high surface area-to-volume ratio, lightweight, high specific strength, shock absorption, and energy absorption properties,[19–23] the TPMS porous structure is widely used as a crucial type of structure for biological replacements.[24–28] Previously, a novel bone tissue composite scaffold based on TPMS structures and cell-laden alginate hydrogel was developed.[29] It was demonstrated that combining alginate and TPMS structures can achieve high mechanical properties. Novak et al.[30] investigated the mechanical properties of two samples of a gyroid and a diamond unit cell hybridized linearly and radially. They found that the hybrid lattices can achieve the plateau region with progressive (longitudinal hybrid) and constant characteristics (radial hybrid). Zhang et al.[31] used a diamond structure as the unit structure and prepared radial gradient (outer dense and inner sparse) porous framework structures using SLM. The framework structure mimics the structural characteristics of loose and porous cancellous bone inside human bone tissue and dense cortical bone outside, indicating their good comprehensive mechanical properties. Jiulu et al.[32] investigated the impact of the interlacing-cell number on the processability, uniaxial compression mechanical performance, and hyperelastic response of Ni-Ti gyroid TPMS lattice structures in the design of TPMS. They found that increasing the interlacing cell number led to a more uniform stress distribution in the structure, thereby enhancing the recoverable strain in Ni-Ti gyroid TPMS lattice structures. Al-Ketan et al.[33] fabricated porous gradient structures based on layered gyroid and diamond structures to investigate the effects of relative density gradient, linear gradient of cell size, and the mixed lattice method on the performance of gradient porous structures. The results indicated that the deformation mechanism of layered gradient TPMS structures differed from that of mesh gradient TPMS structures, and the former mechanism had better mechanical properties than the latter.

Our work aims to develop a lightweight and high-performance IFCD framework using functionally graded TPMS structures. We developed nine gyroid models with gradient variations, considering the natural tooth structure and the forces experienced during chewing. Finite element analysis (FEA) is conducted to predict the mechanical behavior of these models. Thereafter, corresponding Ti6Al4V samples were fabricated through SLM, and a comprehensive study regarding their mechanical properties, particularly the deformation patterns, was performed by compression tests. Our findings revealed that the functionally graded IFCD framework exhibited a significantly superior load-bearing capacity in chewing simulations compared to hollow frameworks of the same weight.

2. Methods

2.1. Functionally graded TPMS framework design for implant-supported fixed complete dentures

2.1.1. Sheet-network gyroid structure designs

The four most common TPMS structures are illustrated in Figure 1A. According to the study by Castro et al.,[34] sheet-network gyroid structures, compared to other TPMS porous structures, exhibit higher surface area, better manufacturability, superior energy absorption, and load-bearing capabilities. These structures have smooth surfaces with an average curvature of 0 to effectively reduce local stress concentration. Consequently, we employed the sheet-network gyroid lattice as the research object (Figure 1B).

The level-set approximation equation is the most commonly used method to describe TPMS. The equation for gyroid is

$$\varphi_G = \cos(X)\sin(Y) + \cos(Y)\sin(Z) + \cos(Z)\sin(X) = c \quad \text{(I)}$$

where $X = 2\pi x/t$, $Y = 2\pi y/t$, and $Z = 2\pi z/t$ refer to the periodic changes in the x, y, and z directions, respectively, t is a parameter that determines the size of the unit cell, and c indicates the value of the surface offset that governs the internal void morphology of the lattice structures. In the level-set approximation equations, a hyperboloid can be formed by solving $-c \le \varphi(x,y,z) \le c$. The space surrounded by two surfaces is the solid part of the TPMS porous structure as depicted in Figure 1C.

2.1.2. Gradient porous gyroid structure designs

The internal structure of a tooth exhibits a hierarchical organization, comprising three primary components: enamel, dentin, and pulp.[35] This hierarchical organization results in a gradient variation in the mechanical properties of teeth, from the interior to the exterior regions. Additionally, density and unit cell size are crucial parameters affecting the mechanical properties of TPMS porous structures. They jointly control the wall thickness, thereby influencing the structures' elastic modulus and compressive performance.[36] Therefore, this study adopted a radial gradient variation method based on the gyroid structure (including variations in porosity and cell size gradients) to design a biomimetic framework for IFCDs. This study combines two design types: (i) relative density gradient variation and (ii) cell size gradient variation. The former is controlled by parameter c, and the latter is influenced by parameter t.

The relative density is a crucial parameter in TPMS-based porous structures, as it not only determines pore

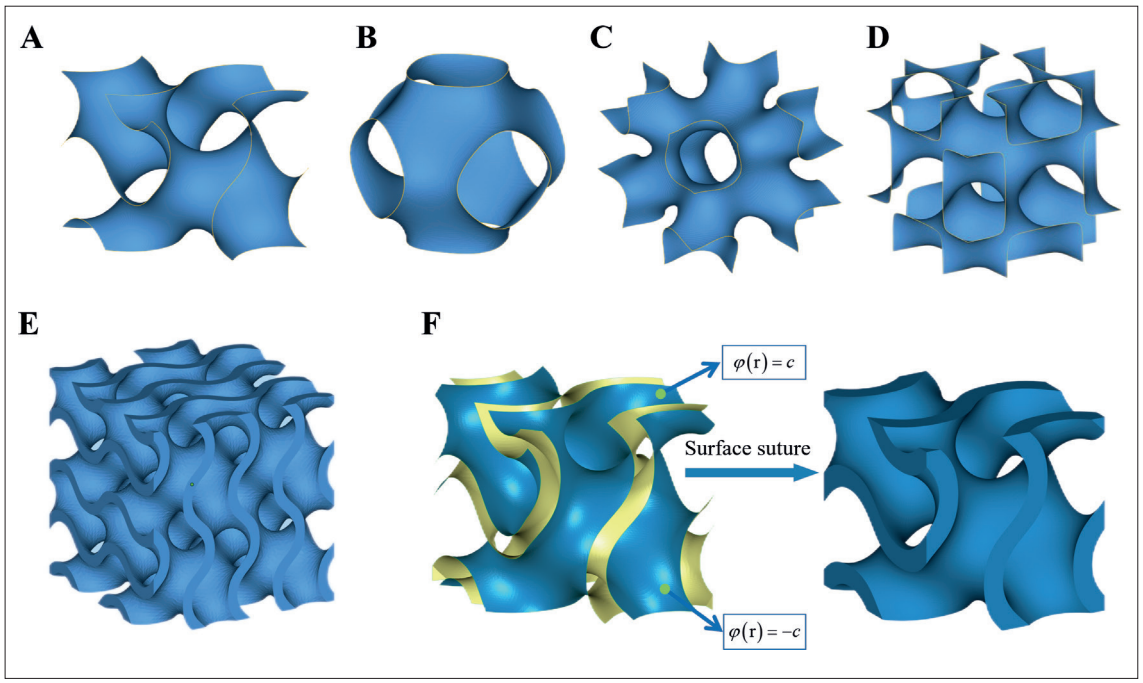


Figure 1. Four kinds of three-periodic minimal surface (TPMS) and the formation principle of the sheet-networks gyroid structures. (A) Four types of three-periodic minimal surface (TPMS) structures. (B) The sheet-network gyroid structure. (C) Construction of sheet-network gyroid structures. Abbreviation: I-WP, Schoen's I-graph-wrapped package.

size but also directly affects various mechanical properties, including yield strength and flexural strength.[37] By adjusting parameter c (i.e., controlling wall thickness), the relative density can be precisely adjusted. The approximate linear relationship between the parameter c and the relative density ρ is as follows:

$$\rho = 66.1c \quad \text{(II)}$$

Under fixed cell size conditions, higher relative density corresponds to smaller pores. When the relative density is equal to 60%, the gyroid structure becomes locally self-intersecting, and the internal pores become discontinuous (Figure 2A). According to **Equation II**, it can be deduced that the coefficient c_{max} attains a value of 0.9 at a relative density of 60%. Furthermore, there is an approximate relationship between wall thickness, relative density, and monocyte size:[38]

$$\omega_{min} \approx 0.183 \cdot t \cdot c \quad \text{(III)}$$

where ω_{min} is the minimum wall thickness, and t is the parameter that determines the size of the unit cell. Therefore c should be restricted to $[\omega_{min} / 0.183 \cdot t, 0.9]$, where ω_{min} generally refers to the minimum printable thickness. Taking into account the practical conditions of the manufacturing equipment, assuming $\omega_{min} \geq 0.15mm$, the relationship between c and t can be expressed as:

$$t_{min} \cdot c_{min} \geq 0.82 \quad \text{(IV)}$$

For ease of subsequent calculations and to demonstrate gradient variation, we set $c_{min} = 0.45$ and $t_{min} = 2$. Within a specific overall model size, excessive cell sizes will lead to significant deviations in the outer shape of the filled structure compared to the original model (Figure 2B). Therefore, this study sets $c \in [0.45,0.9]$ (the corresponding range of relative density values at 30–60%) and $t \in [2,3]$.

The design types of relative density gradient variation include first-increasing-then-decreasing (A), first-decreasing-then-increasing (B), and constant (C) from the radial direction, as depicted in Figure 3A. Likewise, we also implemented radial gradient changes for the design types of cell size gradient variation, including first-increasing-then-decreasing (I), first-decreasing-then-increasing (II), and constant (III), as displayed in Figure 3B.

Nine radial gradient design types were obtained and named according to their respective gradient variation. For example, A-I represents an initially increasing central

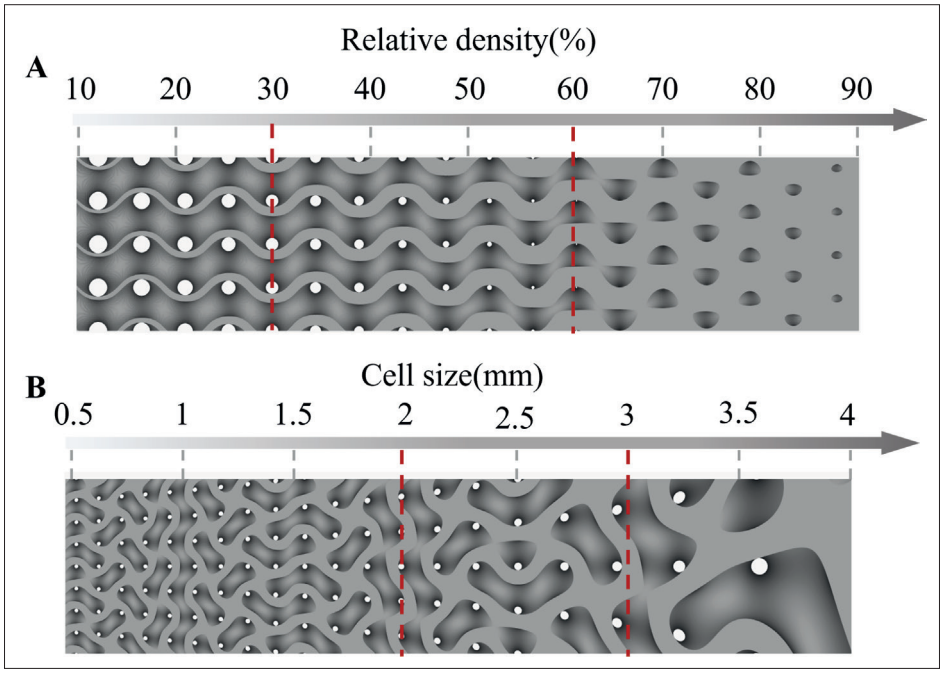


Figure 2. Schematic diagram of changes in relative density and unit cell size of porous structures. (A) Fixed unit cell size with a relative density of 10–90%. (B) Fixed relative density, with the unit cell size at 0.5–4 mm.

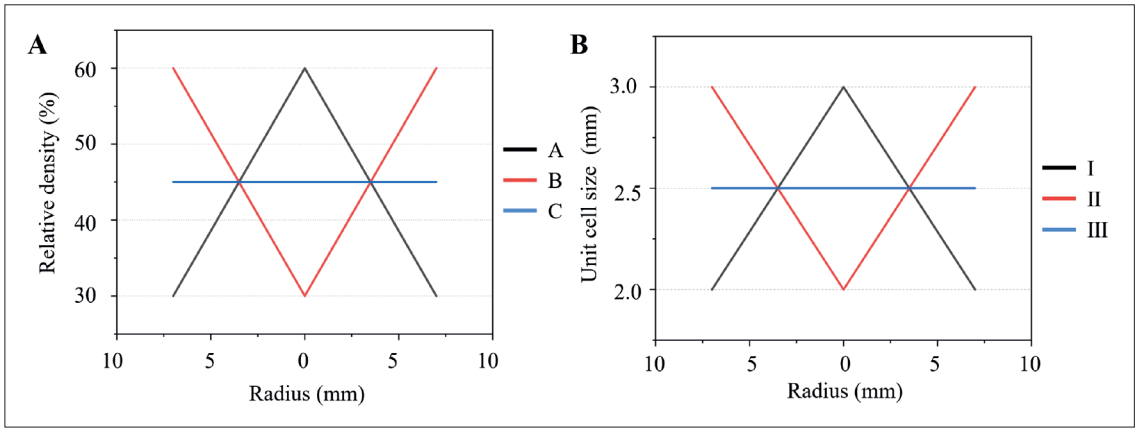


Figure 3. Gradient designs for three-periodic minimal surface (TPMS)-based porous structures: (A) relative density and (B) unit cell size. Figure legends: A, B, and C denote first-increasing-then-decreasing, first-decreasing-then-increasing, and constant, respectively; I, II, and III denote first-increasing-then-decreasing, first-decreasing-then-increasing, and constant, respectively.

relative density to 60%, followed by a subsequent outward decrease to 30%, and an initially increasing central unit cell size to 3 mm, followed by a subsequent outward decrease to 2 mm. All obtained structures are listed in Table 1.

The bias function c and the cell size function t in **Equation I**, which defines the gyroid structure, can be expressed as follows:

$$c = c(x,y,z) = a \cdot \sqrt{x^2 + y^2 + b} \quad \text{(V)}$$

$$t = t(x,y,z) = \alpha \cdot \sqrt{x^2 + y^2 + \beta} \quad \text{(VI)}$$

Table 1. Radial gradient design

Relative density (%)	Unit cell size (mm)		
	First increasing then decreasing	First decreasing then increasing	Constant
First increasing then decreasing	A-I	A-II	A-III
First decreasing then increasing	B-I	B-II	B-III
Constant	C-I	C-II	C-III

Relative density (%)	Unit cell size (mm)		
	2.0-3.0-2.0	3.0-2.0-3.0	2.5
30-60-30	A-I	A-II	A-III
60-30-60	B-I	B-II	B-III
45	C-I	C-II	C-III

where x and y represent two directions in space; $\sqrt{x^2 + y^2}$ represents the distance from a spatial point to the origin; a and b represent two parameters controlling the gradient change of porosity; α and β represent two parameters controlling the gradient change of unit cell size. The general expression of the gradient porous gyroid structure can be obtained by combining **Equations I, V, and VI**:

$$\begin{cases} \varphi_G = \cos\left(\frac{2\cdot\pi\cdot x}{t(x,y,z)}\right)\sin\left(\frac{2\cdot\pi\cdot y}{t(x,y,z)}\right) + \cos\left(\frac{2\cdot\pi\cdot y}{t(x,y,z)}\right)\sin\left(\frac{2\cdot\pi\cdot z}{2.5}\right) \\ \quad + \cos\left(\frac{2\cdot\pi\cdot z}{2.5}\right)\sin\left(\frac{2\cdot\pi\cdot y}{t(x,y,z)}\right), \left(0 < \sqrt{x^2+y^2} < 7\right) \\ -c(x,y,z) \le \varphi_G \le c(x,y,z), \left(0 < \sqrt{x^2+y^2} < 7\right) \end{cases} \quad \text{(VII)}$$

The expressions $c(x,y,z)$ and $t(x,y,z)$ can be obtained using **Equation II** to solve bivariate linear functions. For instance, a cylindrical model with a radius of 7 mm and the radial gradient variation A-I would yield the following equations derived from combining **Equations V, VI, and VII**:

$$\begin{cases} a \cdot 0 + b = 0.9 \\ a \cdot 7 + b = 0.45 \end{cases} \quad \text{(VIII)}$$

$$\begin{cases} \alpha \cdot 0 + \beta = 3 \\ \alpha \cdot 7 + \beta = 2 \end{cases} \quad \text{(IX)}$$

Utilizing **Equations VIII and IX**, we determined the values of a = —0.064, b = 0.9, α = —0.143, and β = 3. Therefore, $c(x,y,z)$ and $t(x,y,z)$ of A-I can be obtained as:

$$\begin{cases} c(x,y,z) = -0.064 \cdot \sqrt{x^2 + y^2} + 0.9 \\ t(x,y,z) = 3 - 0.143 \cdot \sqrt{x^2 + y^2} \end{cases} \quad (X)$$

The derivation methods for $c(x,y,z)$ and $t(x,y,z)$ of the other eight structures are analogous, and their corresponding outcomes are presented in Table 2. Substituting the expressions $c(x,y,z)$ and $t(x,y,z)$ for each structure into **Equation VII** yields the model expression.

Nine gradient porous models were modeled in MSLattice (Oraib Al-Ketan, UAE).[39] This software offers flexibility, enabling users to design their own TPMS lattice based on level-set approximations. The modeling principle involves offsetting the level-set approximation equation used to define the isosurface, followed by constructing a solid domain at spatial nodes enclosed between two surfaces to obtain the lattice structure. The schematic diagrams of the resulting nine gradient change models are illustrated in Figure 4. Additionally, it can be observed from the figure that the transitions between gradients are uniform and consistent with the design.

Table 2. Expression of gradient porous-structure function

Type	Function	
	$c(x,y,z)$	$t(x,y,z)$
A-I	$-0.064 \cdot \sqrt{x^2 + y^2} + 0.9$	$3 - 0.143 \cdot \sqrt{x^2 + y^2}$
A-II	$-0.064 \cdot \sqrt{x^2 + y^2} + 0.9$	$2 + 0.143 \cdot \sqrt{x^2 + y^2}$
A-III	$-0.064 \cdot \sqrt{x^2 + y^2} + 0.9$	2.5
B-I	$0.064 \cdot \sqrt{x^2 + y^2} + 0.45$	$3 - 0.143 \cdot \sqrt{x^2 + y^2}$
B-II	$0.064 \cdot \sqrt{x^2 + y^2} + 0.45$	$2 + 0.143 \cdot \sqrt{x^2 + y^2}$
B-III	$0.064 \cdot \sqrt{x^2 + y^2} + 0.45$	2.5
C-I	0.68	$3 - 0.143 \cdot \sqrt{x^2 + y^2}$
C-II	0.68	$2 + 0.143 \cdot \sqrt{x^2 + y^2}$
C-III	0.68	2.5

2.1.3. Framework design of implant-supported fixed complete dentures based on the optimal gradient TPMS structure

The mechanical properties of TPMS structures change with a radial gradient, unlike uniform structures. Firstly, the gradient TPMS structure with the best mechanical properties was identified through experiments and FEA. Subsequently, based on the dimensions of each tooth in IFCDs and the TPMS gradient structure design method outlined in **Section 2.1.2.**, optimal gradient structures suitable for the required sizes were generated. The structural type remained consistent, with the same gradient variations in unit size and relative density. Using the center point of each tooth as the gradient center, these structures were then filled into IFCDs to create functional gradient TPMS frameworks. Figure 5A illustrates the filling process for molars, with the remaining teeth filled sequentially using the same approach.

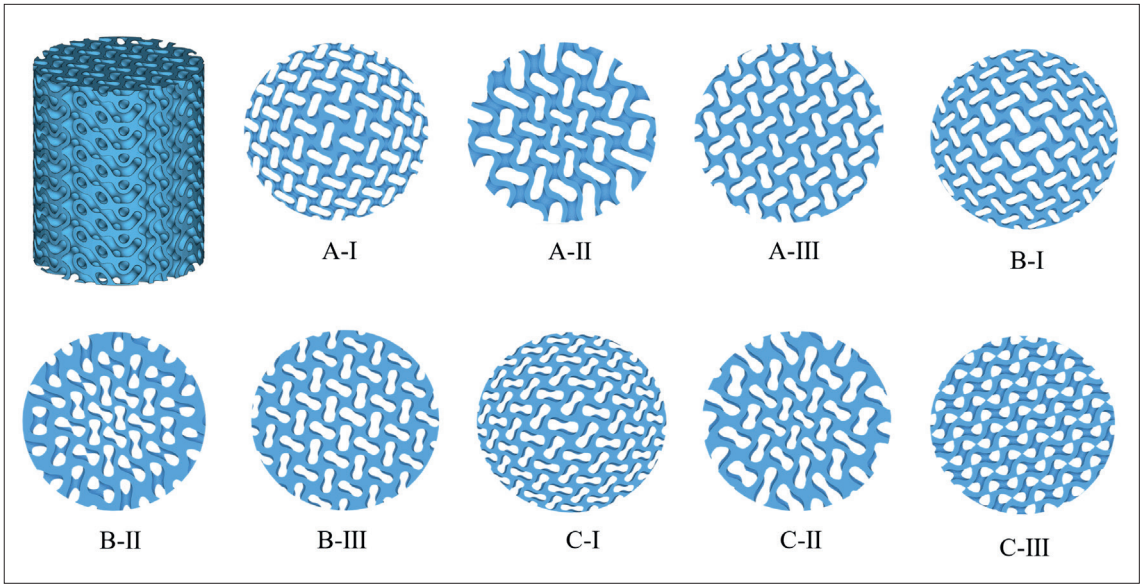


Figure 4. The overall schematic and top views of the three-periodic minimal surface (TPMS)-based gradient porous models.

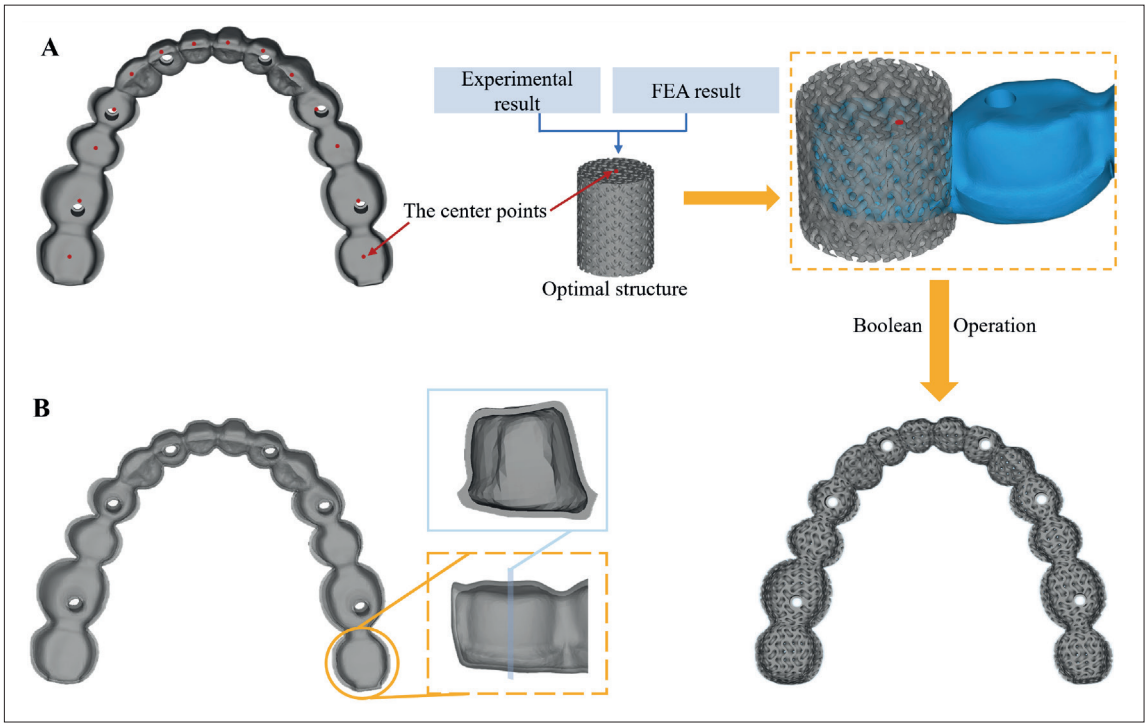


Figure 5. The design process of porous implant-supported fixed complete dentures (IFCDs) and hollow IFCDs. (A) Schematic diagram of the filled IFCDs framework. (B) Schematic diagram of the hollow-processed IFCD. Abbreviation: FEA, finite element analysis.

Moreover, we also designed a hollow framework with the same mass as the functionally graded TPMS framework for comparative analysis. A hollow framework with the same volume as the functionally graded TPMS framework can be obtained using the void function in modeling software. The two structures, made from the same material, have the same mass, and the final result is displayed in Figure 5B.

2.2. Finite element analysis

To predict and compare the mechanical performance of nine TPMS-based gradient porous models, FEA was conducted on the models using commercial software (ANSYS, United States of America [USA]). Models were assigned the material properties of Ti6Al4V, considering both elastic and plastic deformation stages in real experimental processes. In the linear stage, the elastic modulus of the titanium alloy varies under different conditions, fluctuating between 108 and 117 GPa.[40] Due to this small fluctuation range, this study sets the material's elastic modulus to 110 GPa and defines the Poisson's ratio as 0.3. In the nonlinear phase, the true stress–strain values of the material are taken into account,[41] as presented in Table 3.

2.2.1. TPMS-based gradient porous structures

Prior to the analysis, the bottom of the model was fully fixed, and a displacement load was applied to the top, resulting in a 10% strain on the structure. The compression boundary conditions are illustrated in Figure 6A. The material model adopted an elastoplastic model, with titanium alloy Ti6Al4V as the defined material. The environmental temperature was set to 20°C, and the mesh size was set to 0.2 mm. This mesh size produced reliable results and enhanced computational efficiency.[42] With

Table 3. True stress–strain values of the Ti6Al4V material

True stress (MPa)	944	973	996	1015	1029	1040	1047	1054
Plastic strain	0	0.002	0.007	0.011	0.016	0.02	0.025	0.03

True stress (MPa)	Plastic strain
944	0
973	0.002
996	0.007
1015	0.011
1029	0.016
1040	0.02
1047	0.025
1054	0.03

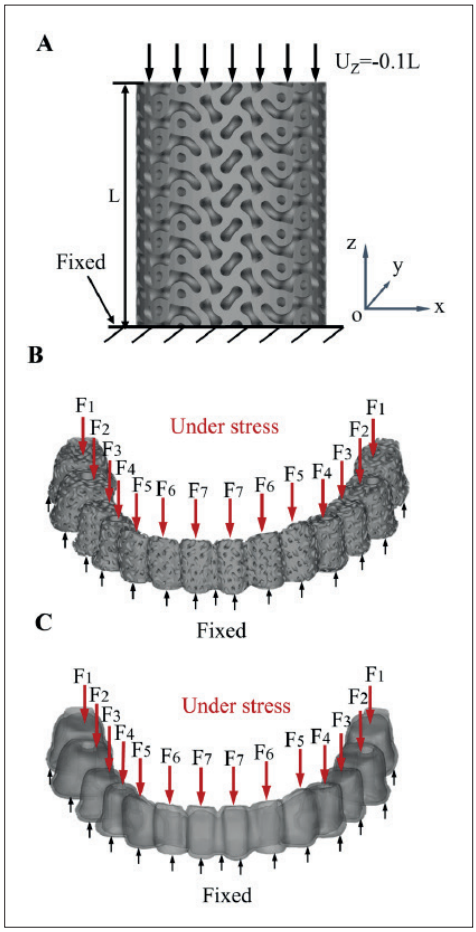


Figure 6. Configuration of boundary conditions for the (A) compression test model, (B) functionally graded porous three-periodic minimal surface (TPMS) framework, and (C) hollow implant-supported fixed complete dentures (IFCDs). Abbreviation: U_z, displacement in the negative direction of the *Z*-axis.

these parameter settings, the deformation and stress distribution are calculated.

2.2.2. Functionally graded TPMS framework

According to pertinent literature,[43] teeth are primarily subjected to axial occlusal forces during mastication, with variations among different teeth, as detailed in Table 4. Finite element methods were employed to simulate the stress distribution of functionally graded porous IFCDs under actual chewing conditions, compared with hollow IFCDs of equivalent mass (Figure 5B), with boundary conditions as depicted in Figure 6B and C.

2.3. Sample fabrication and experimental testing

2.3.1. TPMS-based gradient porous structures

Owing to the extensive number of samples, we selected five specific architectures for further analysis, comprising the mechanically superior construct B-I as indicated by FEA, a homogeneous control (C-III), and three additional samples with varying gradients: constant relative density with cell size gradient (C-II), constant cell size with relative density gradient (A-III), and a gradient opposite to the mechanically optimal sample (A-II). These structures were manufactured using an SLM printer (SLM 280; Nikon SLM Solutions AG, Germany). For each structure type, three samples were printed. The titanium alloy Ti6Al4V, with spherical morphology and particle size range of 15–45 μm, was used to build the samples. To ensure the quality of the manufactured samples, we employed the default parameters provided by the printer manufacturer for printing Ti6Al4V. The SLM processing parameters were optimized and are summarized in Table 5.

Table 4. Amount of force exerted on different teeth during the chewing process

Teeth	Second molars ($F_{1)}$	Frist molars (F_2)	Second premolars (F_3)	Frist premolars (F_4)	Canines (F_5)	Lateral incisor (F_6)	Central incisor (F_7)
Power (N)	483	483	367	280	215	137	130

Teeth	Power (N)
Second molars (F1)	483
First Molars (F2)	483
Second premolars (F3)	367
First premolars (F4)	280
Canines (F5)	215
Lateral incisors (F6)	137
Central incisors (F7)	130

Table 5. Selective laser melting (SLM) processing parameters for Ti6Al4V alloy powder

Laser power (W)	Scanning speed (mm/s)	Spot size (μm)	Layer thickness (μm)	Hatch spacing (μm)
150	650	100	60	60

Parameter	Specification
Laser power (W)	150
Scanning speed (mm/s)	650
Spot size (μm)	100
Layer thickness (μm)	60
Hatch spacing (μm)	60

An electronic analytical balance and a vernier caliper were used to measure the weight and size of the static compression test samples, respectively. Based on the measurements, the relative density of the samples was then calculated using the weighing method to evaluate printing accuracy.

The surface morphology of the samples was obtained using scanning electron microscopy (SEM; Zeiss Sigma 300; Zeiss, Germany). Subsequently, the samples were subjected to grinding and polishing to observe micro-pores and microstructures. The grinding process was conducted using an automatic polishing machine, followed by multiple polishing steps using different sandpapers (#2000, #2500, and #3000) to achieve a mirror-like finish. The samples were etched for ~60 s using a Kroll etchant to expose the microstructure, then observed using an ultra-depth 3D microscope (Keyence VHX-7000; Keyence, Japan).

Teeth experience a wide range of complex forces during daily occlusal activities, including axial occlusal and lateral forces. Therefore, porous frameworks must possess adequate yield and flexural strength. In this regard, static compression, three-point bending, and impact experiments were conducted to assess the mechanical performance of samples, ensuring that the IFCD framework meets the usage requirements.

At room temperature, the static compression tests were performed using an electromechanical universal testing machine (Empyrean; Malvern Panalytical, United Kingdom [UK]). The experimental sample models and dimensions are illustrated in Figure 7A. The indenter's descent speed was set at 1 mm/min, and the porous stent was subjected to compression until failure. This test aims to assess samples' compressive behavior and yield strength.

The Charpy impact test was employed to evaluate the impact toughness of the porous samples. The experimental

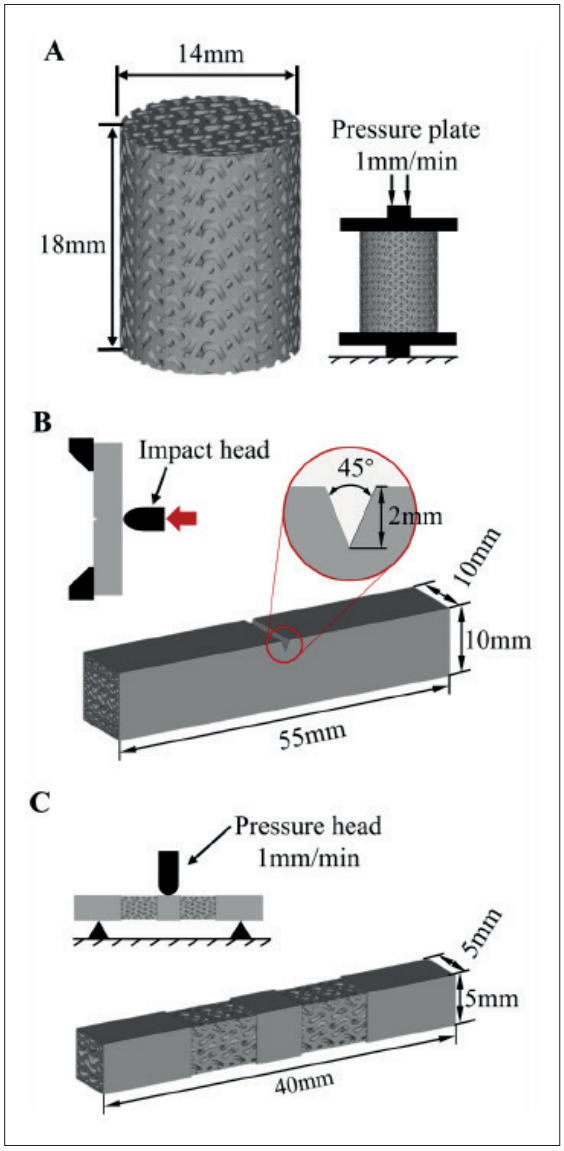


Figure 7. Models and dimensions of samples for mechanical experiments: (A) quasi-static compression tests, (B) impact tests, and (C) three-point bending experiments.

sample models were prepared according to the dimensions specified in the GB/T229-2007 standard (55 × 10 × 10 mm), as depicted in Figure 7B. A V-shaped notch was introduced into the sample, and the impact toughness and absorbed energy were measured.

For the three-point bending test, the porous samples with dimensions of 5 × 5 × 40 mm (Figure 7C) were subjected to a bending force using the electromechanical universal testing machine (Empyrean; Malvern Panalytical, UK). The loading speed was set at 1 mm/min to determine the flexural strength and deformation behavior of samples under bending conditions.

2.3.2. Functionally graded TPMS framework

After obtaining the porous denture framework models, samples were fabricated using the parameters outlined in **Section 2.3.1.**, and the weights were measured to compare the reduction effects with solid frames.

3. Results and discussion

3.1. Finite element analysis

3.1.1. TPMS-based gradient porous structures

The total deformation cloud, von Mises cloud, and equivalent plastic strain cloud distributions from compression finite element (FE) simulations are selectively depicted in Figure 8 for structures with superior mechanical characteristics (B-I), inferior performance (A-II), and the homogeneous reference (C-III), representing a subset of the extensive data set. It is observed from the cloud diagram that inconspicuous stress concentration occurs during the compression process. The location of the stress

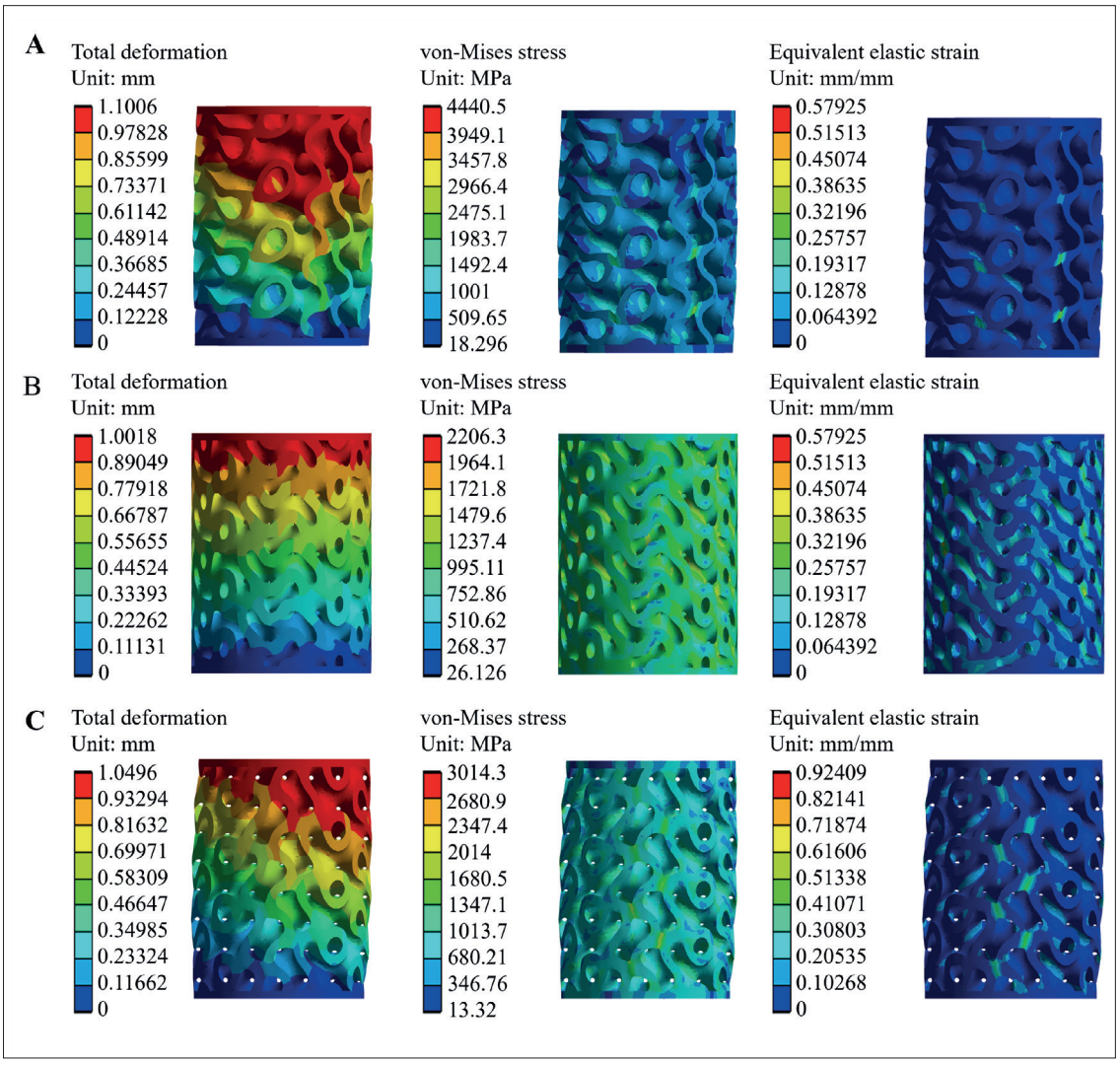


Figure 8. Total deformation cloud, von Mises cloud, and equivalent plastic strain cloud of (A) A-II, (B) B-I, and (C) C-III structures.

concentration area is roughly the same as the equivalent plastic strain area, indicating that plastic deformation will occur first in these areas. The stress concentration areas of these porous models mainly concentrate on the junctions between unit cells. These regions have smaller cross-sectional areas and are prone to deformation when subjected to external forces. In terms of stress distribution, B-I exhibits a more uniform stress distribution and the smallest maximum equivalent stress.

Based on the stress and strain data for each structure, the stress–strain curves are illustrated in Figure 9A. The curves are roughly divided into three stages: elastic distortion stage (I), yield stage (II), and strengthening stage (III). The elastic modulus can be obtained from the slope of the elastic deformation stage. Elastic moduli and yield strengths for various structures can be obtained from the curve data, and specific values are listed in Table 6. The elastic modulus of B-I is the highest (30.42 GPa), which is 27.3% greater than that of C-III (~22.14 GPa). This comparison demonstrates the superior mechanical performance of B-I in terms of its ability to withstand elastic deformation.

The yield strength represents the stress at which a porous model undergoes plastic deformation and reaches its yield point, indicating its capacity to withstand external loads. In this study, the yield strength is determined based on the stress corresponding to a plastic strain of 0.2%.[44] Among the tested structures, B-I exhibits the highest yield strength (281 MPa), while C-II demonstrates the lowest yield strength (178 MPa). Notably, B-I (281 MPa) displays a significant increase in yield strength (by 67MPa) compared to C-III (214 MPa). These findings underscore the heightened load-bearing capacity of B-I, particularly in its resistance to plastic deformation.

Building upon the stress–strain curves, the variation in energy absorption during the deformation of porous structures under loading can be obtained (Figure 9B). The energy absorption of the porous structure increases progressively with deformation. Notably, the B-I structure exhibits the highest energy absorption (34.31 MJ/m^3) among the tested structures. In comparison with C-III (26.58 MJ/m^3), the energy absorption value of B-I is 29.1% higher. This implies that B-I is capable of effectively dissipating energy during deformation, making it a favorable choice for applications requiring impact resistance and energy absorption.

3.1.2. Functionally graded TPMS framework

Quasi-static compression tests were conducted on the functionally graded and hollow IFCD frameworks of the same weight using FEA, yielding the total deformation and

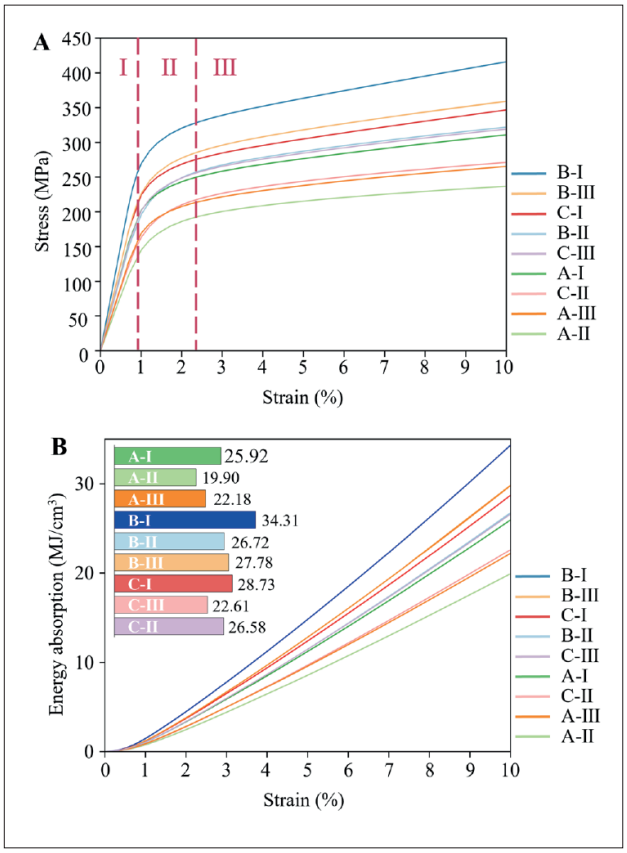


Figure 9. Finite element simulation results. (A) Stress–strain curves and (B) energy absorption curves of nine structures. (A) I, II, and III refer to elastic distortion stage (I), yield stage (II), and strengthening stage (III).

von Mises cloud illustrated in Figure 10. Upon comparison, it can be observed that multi-porous IFCDs exhibit lower maximum equivalent stress and maximum strain than hollow IFCDs. From the von Mises cloud of the IFCD frameworks, the stress in most areas of the stent during normal chewing movement is <27.57 MPa, and there is no obvious stress concentration area. From Figure 10A and B, it can be seen that the deformation is mainly concentrated in the incisors. The molar teeth that bear the primary chewing function, exhibited minimal deformation, and all teeth remained free from plastic strain, meeting the required criteria for usage.

3.2. Experimental samples

The experimental samples prepared for compression, impact, and three-point bending tests are presented in Figure 11. The macroscopic appearance of the prepared samples aligns with the intended design, as depicted in Figure 11B. Compression test samples were used to evaluate the actual relative density and micro-morphology.

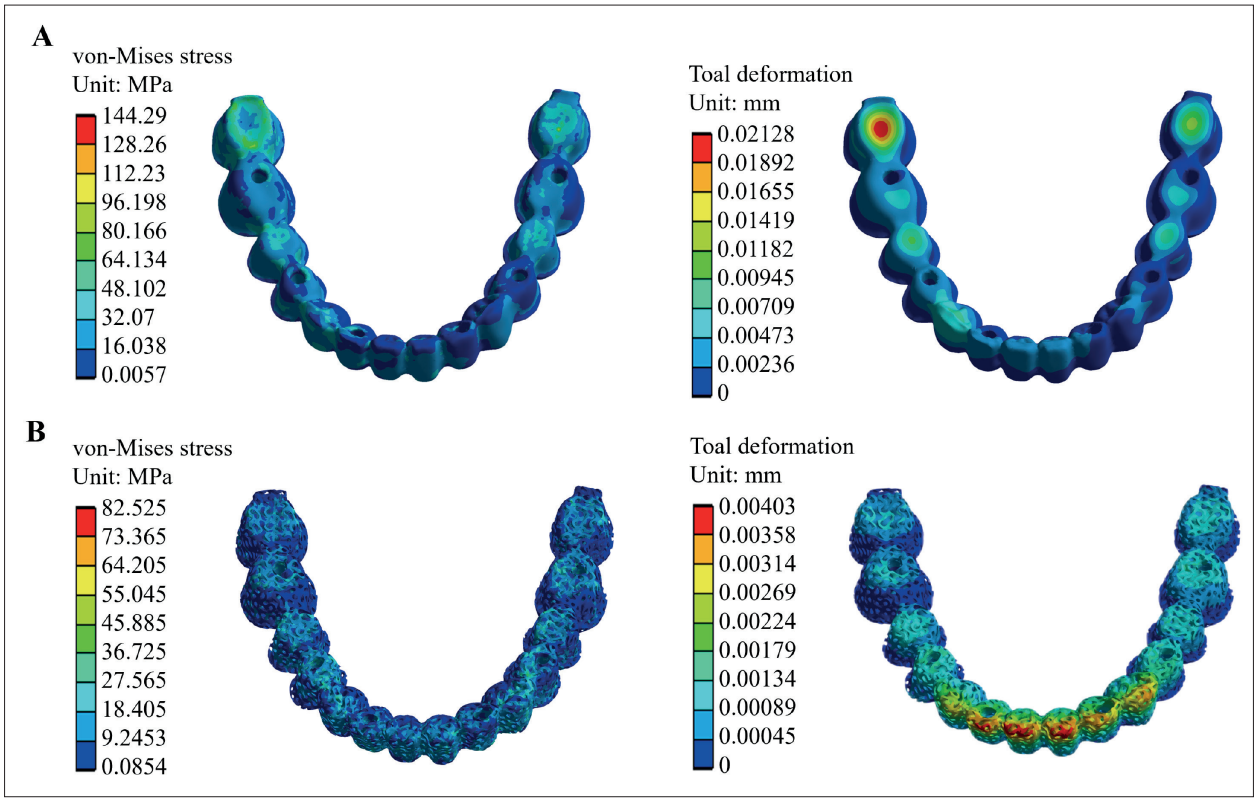


Figure 10. Implant-supported fixed complete denture (IFCD) frameworks based on functionally graded three-periodic minimal surface (TPMS) structures. (A) The von Mises and total deformation clouds of the IFCD framework. (B) The von Mises and total deformation clouds of the hollow framework.

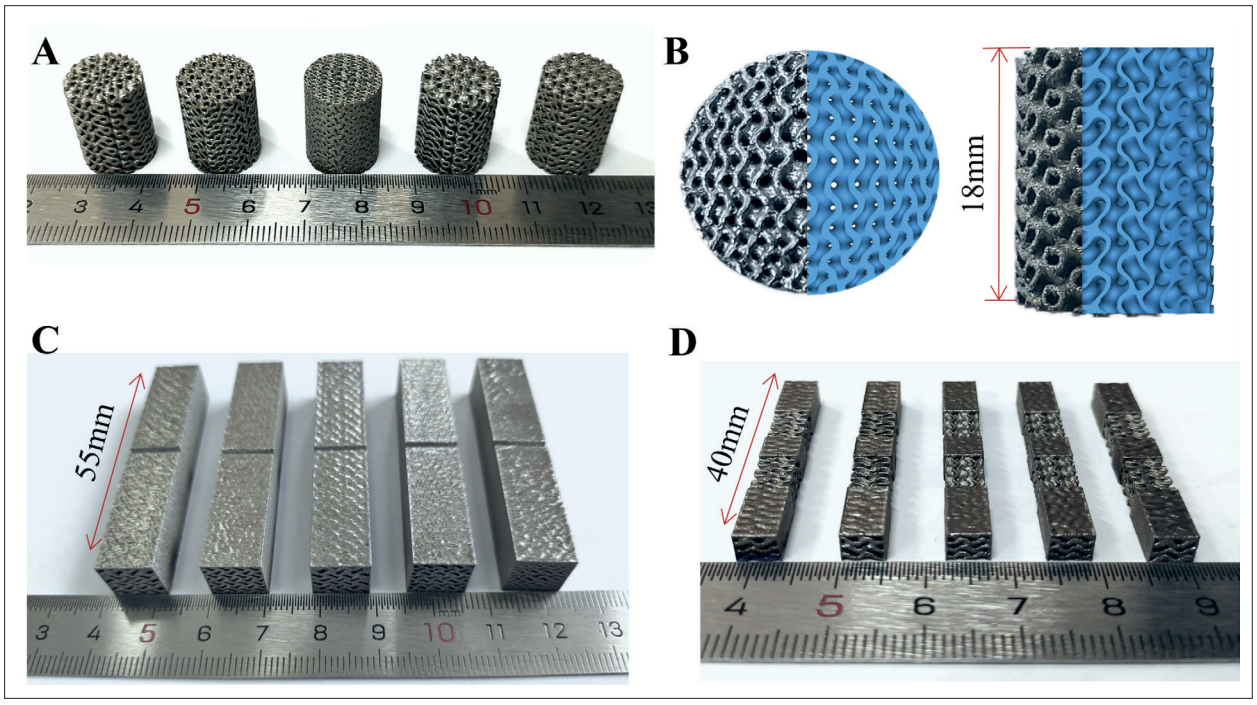


Figure 11. Images of SLM manufactured test samples. (A) Compression test samples. (B) Comparison between experimental samples and designed models. (C) Impact test samples. (D) Three-point bending test samples.

The comparison between the actual and theoretical porosity and height was conducted by measuring the size and weight of each sample, and the results are summarized in Table 6. The results indicate that under the same printing process conditions, the actual height of the test sample is lower than the theoretical height, and this discrepancy can be attributed to the loss of some height during sample detachment from the substrate. Additionally, the actual relative density of all samples is higher than the theoretical relative density due to the thermal gradient between the layers during the SLM preparation process, thereby inducing powder adherence to the surface of the sample. This observation is further supported by Figure 12, which is in line with pertinent literature findings.[45] Among the samples, the actual relative density of A-II is closest to the theoretical relative density, with a difference of only 2.24%. The relative density error of B-I is the largest, with a difference of 9.51%.

SEM was used to characterize the surface morphology and local features of the samples. Figure 12A, B, and C displays the top, middle, and bottom portions of the sample, respectively. It can be observed that a multitude of spherical particles adhere to the surface, including incomplete metal and welding particles (Figure 12D). In addition, a small amount of step effect and pores are also observed, causing the sample surface to be rough. Additionally, the sample was bisected and polished to a mirror finish. The microstructure obtained via SEM is displayed in Figure 12E, revealing a minimal presence of pores. These characteristic round defects are attributed to gases trapped within the powder during the melting process, with no visible cracks detected. The microstructure of the etched sample (Figure 12F) exhibits a typical basketweave pattern, permeated by the acicular α-phase. In summary, the sample exhibits good manufacturing quality, with no cracks or significant defects that would compromise its mechanical properties.

3.3. Mechanical properties

3.3.1. Compressive characteristics

Three sets of experimental data were acquired, and the average values were computed to generate a fitted stress–strain curve (Figure 13B). Based on the curve, the elastic modulus and yield strength of the samples were determined and summarized in Table 7. From the FE results, it is observed that the mechanical properties of the porous samples obtained through experimentation are lower than the simulated values. This difference may arise due to various factors, such as the uneven distribution of powder particle size, powder oxidation, and residual stress during the manufacturing process, as well as the geometric discrepancies between the modeled and manufactured structures. The ratio of experimental mechanical property values of porous structures to FE simulation values reported in the literature ranges from 23.41% to 92.37%.[46,47] The comparative results of experimental and FE simulation values presented

Table 6. Comparison between the computer-aided design (CAD) and experimental characteristics of samples

Sample	Height (mm)			Relative density (%)		
	CAD	Reality	Difference	CAD	Reality	Difference
A-II	18	17.32 (±0.52)	−0.68	45	47.24 (±0.86)	+2.24
A-III	18	17.28 (±0.23)	−0.72	45	47.83 (±0.44)	+2.83
B-I	18	17.35 (±0.11)	−0.65	45	54.51 (±0.35)	+9.51
C-II	18	17.25 (±0.59)	−0.75	45	53.07 (±0.36)	+8.07
C-III	18	17.30 (±0.25)	−0.70	45	52.59 (±0.41)	+7.59

Characteristic	Sample				
	A-II	A-III	B-I	C-II	C-III
Height (mm)					
CAD	18	18	18	18	18
Experimental	17.32 ± 0.52	17.28 ± 0.23	17.35 ± 0.11	17.25 ± 0.59	17.30 ± 0.25
Difference	−0.68	−0.72	−0.65	−0.75	-0.70
Relative density (%)					
CAD	45	45	45	45	45
Experimental	47.24 ± 0.86	47.83 ± 0.44	54.51 ± 0.35	53.07 ± 0.36	52.59 ± 0.41
Difference	+2.24	+2.83	+9.51	+8.07	+7.59

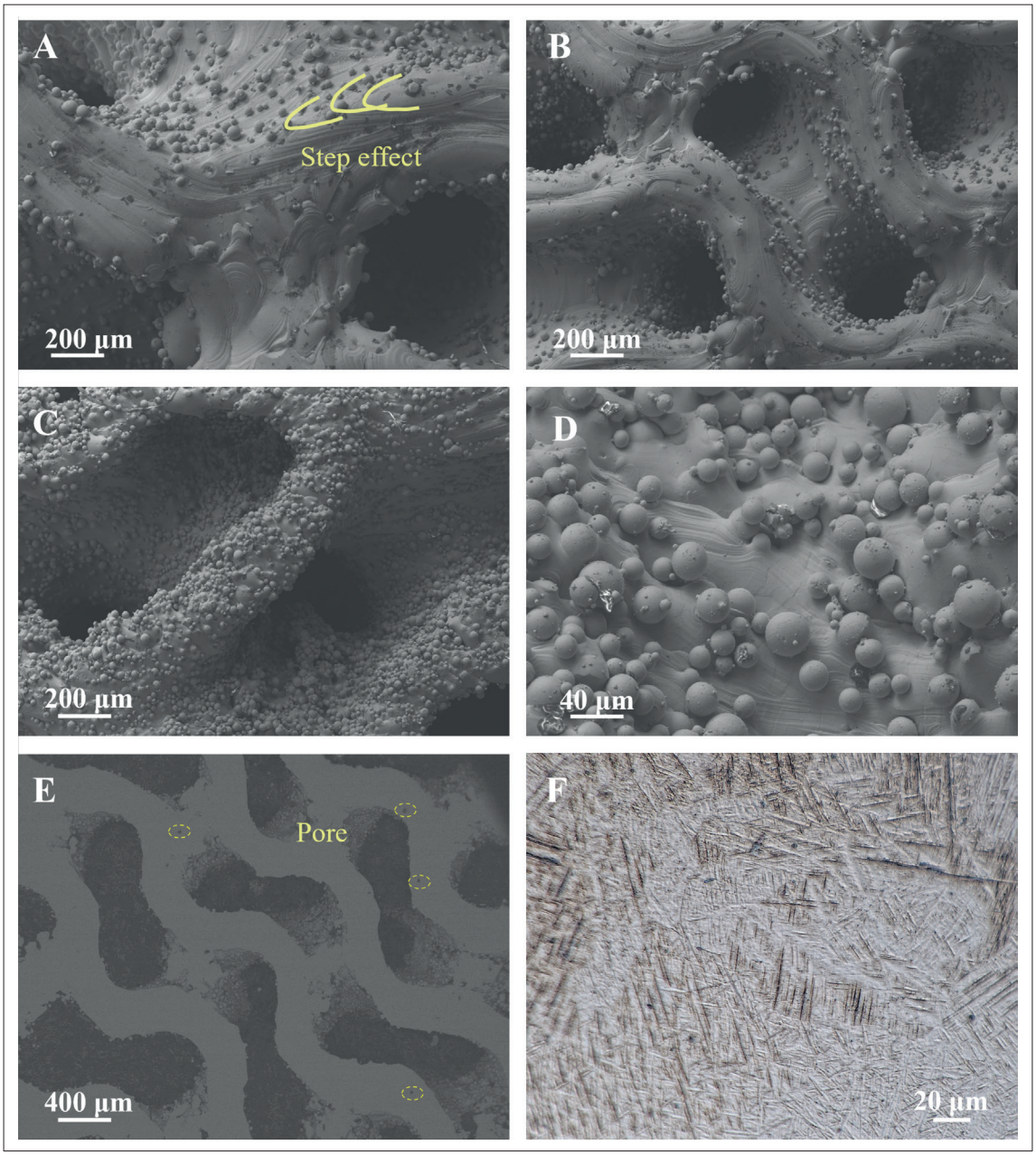


Figure 12. The microstructural features of the sample surface were characterized using scanning electron microscopy (SEM), revealing the (A) top, (B) middle, and (C) bottom views of the sample. (D) Magnified images of surface particles. (E) Microstructural morphology of the sample's cross-section. (F) Microstructure of the sample following etching treatment.

in Table 7 indicate that the ratios fall within the range. Consistent with the findings from FEA, the B-I sample demonstrated superior mechanical properties, exhibiting a 39.38% higher elastic modulus and a 24.53% increase in yield strength compared to C-III. In addition, compared to conventional body-centered cubic and cubic lattice structures, the B-I sample exhibits a significantly higher elastic modulus (by ~86%) and stronger compressive strength (by ~27%).[48]

The deformation modes of the five samples under compression loading are depicted in Figure 13A. During the compression process, all the samples exhibit similar deformation modes, characterized by the formation of shear bands at a 45° angle to the direction of compression

during the failure stage. From Figure 13E, it can be observed that the shear bands generated by B-I are the most obvious, while the shear bands generated by A-II, A-III, and C-II are not obvious. Under compressive loading, stress is transmitted to various parts of the porous model from external forces. When the pressure reaches a certain level, the stress is transferred through the weakest connecting points, leading to the formation of shear bands. As displayed in the FE results of Figure 9, the stress concentration occurs at the connections of the model units, exhibiting a consistent 45° distribution. This concentration of stress and its transmission occur predominantly along this plane, resulting in the formation of 45° shear bands.

3.3.2. Impact characteristics

The Charpy impact test was conducted using a pendulum impact testing machine, and the absorbed energy and impact toughness were obtained as displayed in Figure 13C. The highest impact toughness of C-II is 8.75 J/cm^2, while that of B-I is slightly lower at 7.95 J/cm^2, both of which are higher than that of C-III (6.96 J/cm^2).

3.3.3. Bending characteristics

The load–displacement curve is obtained after averaging the experimental data (Figure 13D). From the curve, the bending elastic modulus and flexural strength of five samples are calculated (Table 8). Among them, B-I has the best bending elastic modulus and flexural strength, which are 17.14% and 28.87% higher than those of C-III, respectively. A-II has the lowest bending elastic modulus and flexural strength.

3.4. Comparison of functionally graded implant-supported fixed complete dentures

Based on the results of the experiments above, it is evident that B-I exhibits superior mechanical properties compared to the other types, making it well-suited for use as the IFCD framework. As displayed in Figure 14A and B, each tooth in the IFCD was filled with B-I to obtain functionally graded TPMS frameworks. It can be observed from the details and cross-section of the model that the teeth conform to the characteristics of B-I. Its relative density increases outwards from 30% (in the center) to 60% (at the edge), and the size of the unit cell decreases outwards from 3 mm (in the center) to 2 mm (at the edge). The samples manufactured by SLM are displayed in Figure 14C and D. The dimensions of the measured samples are consistent with the design models and exhibit the same gradient variation types, as depicted in Figure 14C. The measured weight of the sample was 9.07 g, while the weight of the solid should be 19.27 g, representing a reduction of 52.93%.

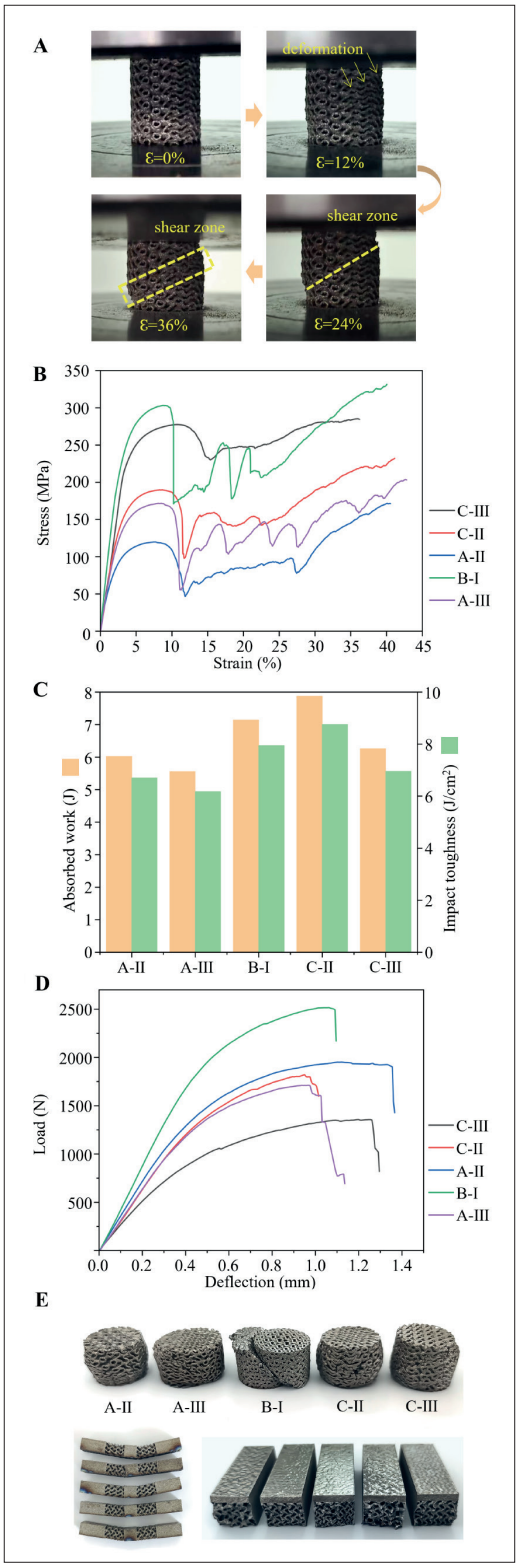


Figure 13. Results of mechanical testing of samples. (A) Deformation patterns, (B) stress–strain responses, (C) impact toughness and absorbed energy, (D) load–displacement curve, and (E) samples' structure after the tests.

Table 7. Comparison between finite element (FE) simulation and experimental results

	Elastic modulus (GPa)			Yield strength (MPa)		
	EV	SV	EV/SV	EV	SV	EV/SV
A-II	8.46	14.66 (±0.7)	57.71	81.21	159 (±6.8)	51.08
A-III	10.54	18.43 (±1.1)	57.19	126.56	180 (±12.2)	70.31
B-I	20.81	30.42 (±2.2)	68.41	205.32	281 (±27.3)	73.08
C-II	9.31	17.38 (±1.4)	53.57	105.27	178 (±9.7)	59.14
C-III	14.93	22.14 (±3.1)	67.43	164.88	214 (±12.5)	77.05

Characteristic	Sample				
	A-II	A-III	B-I	C-II	C-III
Elastic modulus (GPa)					
EV	8.46	10.54	20.81	9.31	14.93
SV	14.66 ± 0.7	18.43 ± 1.1	30.42 ± 2.2	17.38 ± 1.4	22.14 ± 3.1
EV/SV	57.71	57.19	68.41	53.57	67.43
Yield strength (MPa)					
EV	81.21	126.56	205.32	105.27	164.88
SV	159 ± 6.8	180 ± 12.2	281 ± 27.3	178 ± 9.7	214 ± 12.5
EV/SV	51.08	70.31	73.08	59.14	77.05

Abbreviations: EV, experimental value; SV, simulation value.

Table 8. Three-point bending experimental results

Characteristic	Sample				
	A-II	A-III	B-I	C-II	C-III
Flexural modulus (GPa)	8.36 ± 0.7	10.26 ± 0.5	13.67 ± 1.5	9.71 ± 0.9	11.67 ± 1.1
Bending strength (MPa)	325.71 ± 18.9	410.97 ± 23.5	603.76 ± 22.6	436.92 ± 19.3	468.52 ± 20.9

4. Conclusion

In this study, we investigated the mechanical properties of functionally graded TPMS structures manufactured using SLM with Ti6Al4V powder. These structures were then applied to the framework design of IFCDs. The main findings of this study can be summarized as follows:

(i) Finite element analysis (FEA) revealed that the B-I exhibited a more uniform stress distribution during the compression process and demonstrated significant mechanical performance and energy absorption advantages compared to other models. In comparison to the homogeneous model, B-I displayed a 23.8% increase in yield strength, a 27.3% increase in elastic modulus, and a 29.1% increase in energy absorption capacity.

(ii) In comparison to the uniform C-III with a relative density of 45%, B-I exhibited significant improvements in mechanical performance, encompassing a 39.38% increase in elastic modulus (reaching 30.42 GPa), a 24.53% increase in yield strength (reaching 205.32 MPa), a 28.87% increase in flexural strength (reaching 603.76 MPa), and an impact toughness of 7.95 J/cm^2 (higher than that of the homogeneous sample, i.e., 6.96 J/cm^2). All samples exhibited a similar failure mode during compression, forming 45° shear bands.

(iii) In comparison to a hollow IFCD framework of the same weight, the functionally graded IFCD framework not only met the requirements for masticatory function but also exhibited superior mechanical performance, particularly in the molar

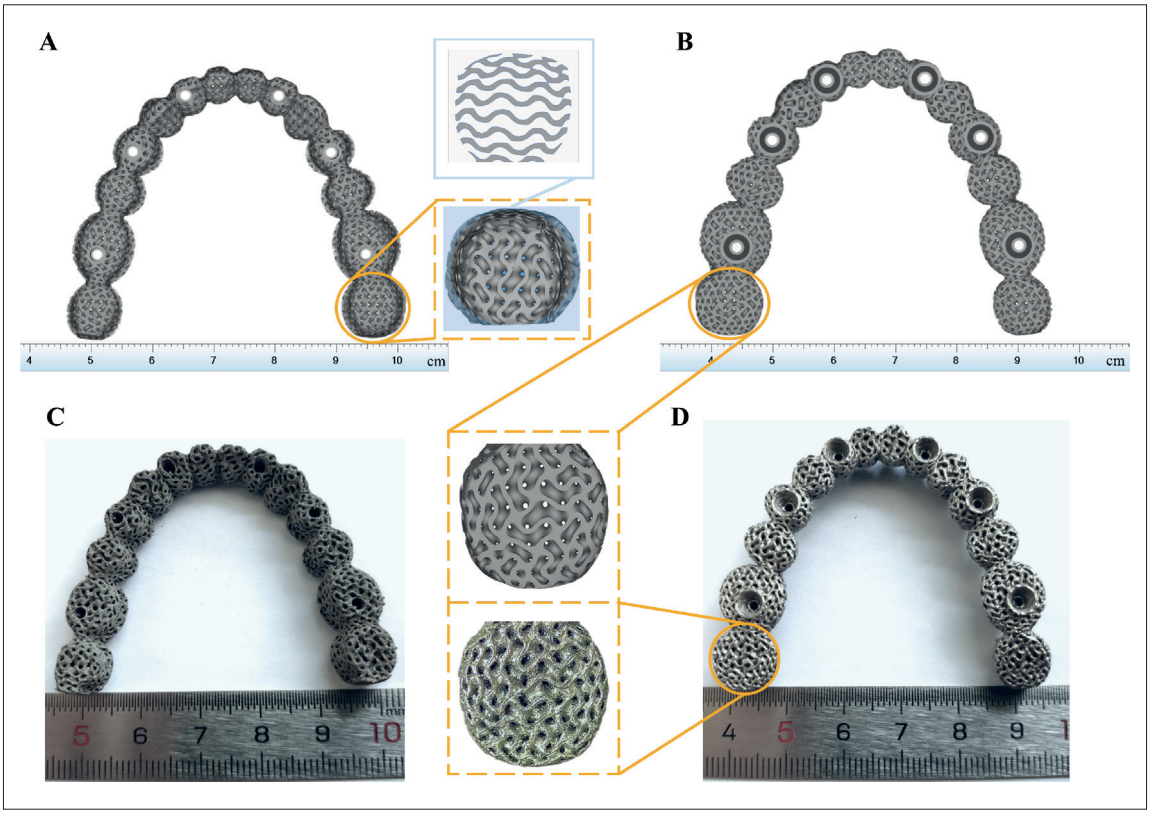


Figure 14. The implant-supported fixed complete denture (IFCD) framework based on functionally graded TPMS. (A and B) View of the model: top (A) and bottom (B). (C and D) View of the sample: top (C) and bottom (D).

region with enhanced load-bearing capacity. Additionally, the weight of the functionally graded framework was reduced by 52.93% compared to a solid framework.

In our work, the functionally graded IFCD framework displays its potential for dental applications, providing theoretical support for further practical implementations. Moreover, the strength of the bond between the framework and the zirconia veneer also determines the overall performance of the final IFCDs. Our subsequent work will focus on investigating the adhesive strength between the framework and the zirconia veneer.

Acknowledgments

None

Funding

This work was supported by the Project Supported by the (i) National Natural Science Foundation of China (No. 52165043), (ii) Beijing Natural Science Foundation and Haidian Original Innovation Joint Fund (No. L232145), (iii) Open Project of NHC Key Laboratory of Digital Stomatology of Peking University School of Stomatology (PKUSS20230501), (iv) Science and Technology Research Project of Department of Education of Jiangxi Provincial, China (No. GJJ210877), (v) High-level Talents Scientific Research Start-up Program of Jiangxi University of Science and Technology (No. 205200100556, No. 205200100350), (vi) Jiangxi Provincial Natural Science Foundation of China (20224ACB214008), (vii) Anhui Natural Science Foundation (2308085ME171), (viii) The University Synergy Innovation Program of Anhui Province (GXXT-2023-025; GXXT-2023-026), and (ix) Jiangxi Provincial Cultivation Program for Academic and Technical Leaders of Major Subjects (20225BCJ23008).

Conflict of interest

The authors declare no conflicts of interest.

Author contributions

Conceptualization: Yuchun Sun, Sukun Tian, Xuehua Wu, Youwen Yang

Data curation: Jiwei Ren, Renkai Huang, Shaoying Yang, Yuchun Sun, Sukun Tian, Xuehua Wu
Investigation: Jiwei Ren, Renkai Huang, Linqing Huang, Shaoying Yang
Methodology: Jiwei Ren, Chunrong Pan, Dongsheng Wang, Youwen Yang
Resources: Youwen Yang
Supervision: Chunrong Pan, Dongsheng Wang, Youwen Yang
Writing – original draft: Jiwei Ren
Writing – review & editing: Jiwei Ren, Renkai Huang

Ethics approval and consent to participate

Not applicable.

Consent for publication

Not applicable.

Availability of data

Data is available from the corresponding author upon reasonable request.

References

1. Guo Y-q, Ma Y, Cai S-n, Yu H. Optimal impression materials for implant-supported fixed complete dentures: a systematic review and meta-analysis. *J Prosthet Dent.* 2023;Inpress. doi: 10.1016/j.prosdent.2023.06.024
2. Cinquini C, Alfonsi F, Marchio V, et al. The use of zirconia for implant-supported fixed complete dental prostheses: a narrative review. *Dent J (Basel).* 2023;11(6):144. doi: 10.3390/dj11060144
3. Vahnström M, Johansson PH, Svanborg P, Stenport VF. Comparison of porcelain veneer fracture in implant-supported fixed full-arch prostheses with a framework of either titanium, cobalt–chromium, or zirconia: an in vitro study. *Clin Exp Dent Res.* 2022;8(2):544-551. doi: 10.1002/cre2.558
4. Alberto LHJ, Kalluri L, Esquivel-Upshaw JF, Duan Y. Three-dimensional finite element analysis of different connector designs for all-ceramic implant-supported fixed dental prostheses. *Ceramics.* 2022; 5(1):34-43. doi: 10.3390/ceramics5010004
5. Thompson J, Schoenbaum TR, Pannu D, Knoernschild K. Survival analysis of zirconia implant-supported, fixed complete dentures: a 5-year retrospective cohort study. *J Prosthet Dent.* 2023;Inpress. doi: 10.1016/j.prosdent.2023.04.031
6. Messias A, Nicolau P, Guerra F. Different interventions for rehabilitation of the edentulous maxilla with implant-supported prostheses: an overview of systematic reviews. *Int J Prosthodont.* 2021;34(Suppl):s63-s84. doi: 10.11607/ijp.7162
7. Zhang L, Liu H, Yao H, Zeng Y, Chen J. Preparation, microstructure, and properties of ZrO2(3Y)/Al2O3 bioceramics for 3D printing of all-ceramic dental implants by vat photopolymerization. *Chin J Mech Eng: Addit Manuf Front.* 2022;1(2):100023. doi: 10.1016/j.cjmeam.2022.100023
8. Baltatu MS, Țugui CA, Perju MC, et al. Biocompatible titanium alloys used in medical applications. *Rev Chim.* 2019;70(4):1302-1306. doi: 10.37358/RC.19.4.7114
9. Nouri A, Hodgson PD, Wen C. Biomimetic porous titanium scaffolds for orthopedic and dental applications. *Biomimetics Learn Nat.* 2010;21:415-450. doi: 10.5772/8787
10. Al-Meraikhi H, Yilmaz B, McGlumphy E, Brantley W, Johnston WM. In vitro fit of CAD-CAM complete arch screw-retained titanium and zirconia implant prostheses fabricated on 4 implants. *J Prosthet Dent.* 2018;119(3):409-416. doi: 10.1016/j.prosdent.2017.04.023
11. Kanazawa M, Iwaki M, Minakuchi S, Nomura N. Fabrication of titanium alloy frameworks for complete dentures by selective laser melting. *J Prosthet Dent.* 2014;112(6): 1441-1447. doi: 10.1016/j.prosdent.2014.06.017
12. Tribst JPM, Dal Piva AMO, Borges ALS, Rodrigues VA, Bottino MA, Kleverlaan CJ. Does the prosthesis weight matter? 3D finite element analysis of a fixed implant-supported prosthesis at different weights and implant numbers. *J Adv Prosthodont.* 2020;12(2):67-74. doi: 10.4047/jap.2020.12.2.67
13. Zhang L, Feih S, Daynes S, et al. Energy absorption characteristics of metallic triply periodic minimal surface sheet structures under compressive loading. *Addit Manuf.* 2018;23:505-515. doi: 10.1016/j.addma.2018.08.007
14. Tribst J, Rodrigues V, Dal Piva A, Borges A, Nishioka R. The importance of correct implants positioning and masticatory load direction on a fixed prosthesis. *J Clin Exp Dent.* 2018;10(1):e81-e87. doi: 10.4317/jced.54489
15. Edelhoff D, Schubert O, Stimmelmayr M, Schweiger J. CAD/CAM full-mouth rehabilitation of an elderly patient: one-piece digital complete denture meets multilayered zirconia with gradient technology. *J Esthet Restor Dent.* 2024;36(1):174-185. doi: 10.1111/jerd.13031
16. Ventura J, Jiménez-Castellanos E, Romero J, Enrile F. Tooth fractures in fixed full-arch implant-supported acrylic resin prostheses: a retrospective clinical study. *Int J Prosthodont.* 2016;29(2):161-165. doi: 10.11607/ijp.4400

17. Mackert J, El-Shewy M, Pannu DS, Schoenbaum TR. Prosthetic complications and survival rates of metal-acrylic implant fixed complete dental prostheses: a retrospective study up to 10 years. *J Prosthet Dent.* 2022;Inpress. doi: 10.1016/j.prosdent.2022.06.019

18. Fischer K, Stenberg T. Prospective 10-year cohort study based on a randomized, controlled trial (RCT) on implant-supported full-arch maxillary prostheses. part II: prosthetic outcomes and maintenance. *Clin Implant Dent Relat Res.* 2013;15(4):498-508. doi: 10.1111/j.1708-8208.2011.00383.x

19. Melchels FPW, Bertoldi K, Gabbrielli R, Velders AH, Feijen J, Grijpma DW. Mathematically defined tissue engineering scaffold architectures prepared by stereolithography. *Biomaterials.* 2010;31(27):6909-6916. doi: 10.1016/j.biomaterials.2010.05.068

20. Toosi S, Javid-Naderi MJ, Tamayol A, Ebrahimzadeh MH, Yaghoubian S, Mousavi Shaegh SA. Additively manufactured porous scaffolds by design for treatment of bone defects. *Front Bioeng Biotechnol.* 2024;11:1252636. doi: 10.3389/fbioe.2023.1252636

21. Catchpole-Smith S, Sélo RRJ, Davis A, Ashcroft I, Tuck CJ, Clare AT. Thermal conductivity of TPMS lattice structures manufactured via laser powder bed fusion. *Addit Manuf.* 2019;30(4):100846. doi: 10.1016/j.addma.2019.100846

22. Wei SS, Zhang JL, Zhang L, et al. Laser powder bed fusion additive manufacturing of NiTi shape memory alloys: a review. *Int J Extreme Manuf.* 2023;5(3):032001. doi: 10.1088/2631-7990/acc7d9

23. Dong Z, Han CJ, Zhao YZ, et al. Role of heterogenous microstructure and deformation behavior in achieving superior strength-ductility synergy in zinc fabricated via laser powder bed fusion. *Int J Extrem Manuf.* 2024;6(4):045003. doi: 10.1088/2631-7990/ad3929

24. Kapfer SC, Hyde ST, Mecke K, Arns CH, Schröder-Turk GE. Minimal surface scaffold designs for tissue engineering. *Biomaterials.* 2011;32(29):6875-6882. doi: 10.1016/j.biomaterials.2011.06.012

25. Dwivedi A, Khurana MK, Bala YG. Heat-treated nickel alloys produced using laser powder bed fusion-based additive manufacturing methods: a review. *Chinese J Mech Eng Additive Manuf Front.* 2023;2(3):100087. doi: 10.1016/j.cjmeam.2023.100087

26. Wu LY, Xue J, Tian X, Liu T, Li D. 3D-printed metamaterials with versatile functionalities. *Chin J Mech Eng Additive Manuf Front.* 2023;2(3):100091. doi: 10.1016/j.cjmeam.2023.100091

27. Jin Y, Zou S, Pan B, Li G, Shao L, Du J. Biomechanical properties of cylindrical and twisted triply periodic minimal surface scaffolds fabricated by laser powder bed fusion. *Addit Manuf.* 2022;56:102899. doi: 10.1016/j.addma.2022.102899

28. Xue L, Atli KC, Picak S, et al. Controlling martensitic transformation characteristics in defect-free NiTi shape memory alloys fabricated using laser powder bed fusion and a process optimization framework. *Acta Mater.* 2021; 215:117017. doi: 10.1016/j.actamat.2021.117017

29. Zhang X-Y, Yan X-C, Fang G, Liu M. Biomechanical influence of structural variation strategies on functionally graded scaffolds constructed with triply periodic minimal surface. *Addit Manuf.* 2020;32:101015. doi: 10.1016/j.addma.2019.101015

30. Novak N, Al-Ketan O, Borovinšek M, et al. Development of novel hybrid TPMS cellular lattices and their mechanical characterisation. *J Mater Res Technol.* 2021; 15:1318-1329. doi: 10.1016/j.jmrt.2021.08.092

31. Zhang X-Y, Fang G, Leeflang S, Zadpoor AA, Zhou J. Topological design, permeability and mechanical behavior of additively manufactured functionally graded porous metallic biomaterials. *Acta Biomater.* 2019; 84:437-452. doi: 10.1016/j.actbio.2018.12.013

32. Jiulu J, Siqi W, Lei Y, et al. Ni–Ti multicell interlacing gyroid lattice structures with ultra-high hyperelastic response fabricated by laser powder bed fusion. *Int J Mach Tools Manuf.* 2024;195:0890-6955. doi: 10.1016/j.ijmachtools.2023.104099

33. Al-Ketan O, Lee D-W, Rowshan R, Abu Al-Rub RK. Functionally graded and multi-morphology sheet TPMS lattices: design, manufacturing, and mechanical properties. *J Mech Behav Biomed Mater.* 2019;102:103520. doi: 10.1016/j.jmbbm.2019.103520

34. Castro APG, Ruben RB, Gonçalves SB, Pinheiro J, Guedes JM, Fernandes PR. Numerical and experimental evaluation of TPMS Gyroid scaffolds for bone tissue engineering. *Comput Methods Biomech Biomed Engin.* 2019;22(6): 567-573. doi: 10.1080/10255842.2019.1569638

35. Zhang Y-R, Du W-P, Zhou X, Yu H-y. Review of research on the mechanical properties of the human tooth. *Int J Oral Sci.* 2014;6(2):61-69. doi: 10.1038/ijos.2014.21

36. Gabrieli R, Wenger R, Mazza M, Verné E, Baino F. Design, stereolithographic 3D printing, and characterization of TPMS scaffolds. *Materials (Basel).* 2024;17(3):654. doi: 10.3390/ma17030654

37. Wang X, Xu S, Zhou S, et al. Topological design and additive manufacturing of porous metals for bone scaffolds and orthopaedic implants: a review. *Biomaterials.* 2016;83: 127-141. doi: 10.1016/j.biomaterials.2016.01.012

38. Hu J, Wang S, Li B, Li F, Luo Z, Liu L. Efficient representation and optimization for TPMS-based porous structures. *IEEE Trans Vis Comput Graph.* 2022;28(7):2615-2627.

doi: 10.1109/TVCG.2020.3037697

39. Al-Ketan O, Abu Al-Rub RK. MSLattice: a free software for generating uniform and graded lattices based on triply periodic minimal surfaces. *Mater Des Process Commun.* 2021;3(6):e205.
doi: 10.1002/mdp2.205

40. Fan Z. On the young's moduli of Ti6Al4V alloys. *Scrip Metall Material.* 1993;29(11):1427-1432.
doi: 10.1016/0956-716X(93)90331-L

41. Bai L. Multi-objective structural optimization design of Ti6Al4V lattice structure formed by SLM. *J Mech Eng.* 2018;54(5):156-165.
doi: 10.3901/JME.2018.05.156

42. Yang L, Yan C, Han C, Chen P, Yang S, Shi Y. Mechanical response of a triply periodic minimal surface cellular structures manufactured by selective laser melting. *Int J Mech Sci.* 2018;148:149-157.
doi: 10.1016/j.ijmecsci.2018.08.039

43. Rene JS, Smita S, Satish S, Buvaneshwari A, Velmurugan N. Impact of Contracted Endodontic Access Cavities on the Fracture Resistance of Endodontically Treated Teeth After Mechanical Aging by Simulated Chewing Forces. *J Endodont*. 2023;49(9):1176-1182.
doi: 10.1016/j.joen.2023.06.018

44. Guo W, Yang Y, Liu C, et al. 3D printed TPMS structural PLA/GO scaffold: process parameter optimization, porous structure, mechanical and biological properties. *J Mech Behav Biomed Mater.* 2023;142:105848.
doi: 10.1016/j.jmbbm.2023.105848

45. Sun Q, Sun J, Guo K, Wang L. Compressive mechanical properties and energy absorption characteristics of SLM fabricated Ti6Al4V triply periodic minimal surface cellular structures. *Mech Mater.* 2022;166:104241.
doi: 10.1016/j.mechmat.2022.104241

46. Dumas M, Terriault P, Brailovski VJM. Modeling and characterization of a porosity graded lattice structure for additively manufactured biomaterials. *Mater Design*. 2017;121:383-392.
doi: 10.1016/j.matdes.2017.02.021

47. Na Q, Yuheng W, Yijun S, Jianguang F. Experimental and numerical studies on mechanical properties of TPMS structures. *Int J Mech Sci*. 2024;261:108657.
doi: 10.1016/j.ijmecsci.2023.108657

48. Papazoglou DP, Neidhard-Doll AT, Pinnell MF, Erdahl DS, Osborn TH. Compression and tensile testing of L-PBF Ti-6Al-4V lattice structures with biomimetic porosities and strut geometries for orthopedic implants. *Metals.* 2024;2:232.
doi: 10.3390/met14020232

ACCSCIENCE PUBLISHING

International Journal of Bioprinting

RESEARCH ARTICLE

A study on the synergistic chondro-inductive effects of collagen II and its high-resolution 3D-printed scaffolds

Kaixuan Li[1,2†], Hanxiao Huang[1,2,3†], and Cailiang Shen[1,2*]

[1]Department of Orthopedics, The First Affiliated Hospital of Anhui Medical University, Hefei, Anhui, China

[2]Laboratory of Spinal and Spinal Cord Injury Regeneration and Repair, Department of Spine Surgery, The First Affiliated Hospital of Anhui Medical University, Hefei, Anhui, China

[3]Department of Stomatology, The First Affiliated Hospital of Anhui Medical University, Hefei, Anhui, China

Abstract

Collagen II is the most essential component of the cartilage-specific extracellular matrix (ECM). However, research on collagen II-based scaffold fabrication, structural optimization, and correlation to the chondrogenic activities of stem cells is currently limited, presumably due to challenges related to its hydrogel processability. Existing collagen II-containing scaffolds are mainly produced by freeze-drying and exhibit limited properties, such as pore interconnectivity and tortuosity. Additionally, the chondro-inductive capability of collagen II composition and its underlying mechanism remains unclear, warranting further research. In this study, we addressed the aforementioned issues by investigating and enhancing the rheological properties of collagen II-based hydrogel, resulting in a high printing resolution exceeding 150 μm. The collagen II composition reportedly facilitated the condensation and chondrogenic activities of mesenchymal stem cells (MSCs) compared to gelatin. Moreover, high-resolution collagen II-based scaffolds promoted cell proliferation and chondrogenic differentiation to a higher degree. Therefore, we optimized the compositional and structural characteristics of collagen II-based scaffolds for enhancing chondrogenic activities. We anticipate that this study will broaden our understanding of collagen II-based scaffold designs and condition optimizations for cartilage tissue engineering.

***Keywords*:** Collagen II; 3D printing; Scaffold structure; Printing resolution; Chondrogenic differentiation

†These authors contributed equally to the work.

***Corresponding author:**
Cailiang Shen
(shencailiang@ahmu.edu.cn)

Citation: Li K, Huang H, Shen C. A study on the synergistic chondro-inductive effects of collagen II and its high-resolution 3D-printed scaffolds. *Int J Bioprint*. 2024;10(5):3371. doi: 10.36922/ijb.3371

Received: April 6, 2024
Accepted: June 10, 2024
Published Online: July 25, 2024

Copyright: © 2024 Author(s). This is an Open Access article distributed under the terms of the Creative Commons Attribution License, permitting distribution, and reproduction in any medium, provided the original work is properly cited.

Publisher's Note: AccScience Publishing remains neutral with regard to jurisdictional claims in published maps and institutional affiliations.

1. Introduction

Cartilage is a hydrated and densely fibrillated tissue that provides connecting, load-bearing, and vibration-absorbing functions in the human body.[1-3] Due to a lack of vasculature and resultant supply of nutrition, self-regeneration is limited in the cartilage. Therefore, tissue engineering may be particularly useful for cartilage regeneration.[4,5] The key outcome in cartilage tissue engineering is the sufficient production of cartilage-specific extracellular matrix (ECM) compounds, including collagen II,[6,7] glycosaminoglycan

(GAG),[8] and chondroitin.[7] In cartilage tissue engineering, ECM production should be sufficient to maintain the overall mechanical strength of the regenerated tissue.[9–11] Likewise, more cartilage-specific compounds are required to achieve mechanical properties and loading responses similar to natural cartilage.[12,13] Accordingly, promoting the proliferation of stem cells is crucial to increase the overall production of ECM compounds,[14] while enhancing chondrogenic differentiation of stem cells is essential to increase the proportion of cartilage-specific compounds.[15] Collagen II is a naturally derived protein with excellent biocompatibility and surface arginine-glycine-glutamic acid (RGE) sequence that favors cell adhesion, rendering it one of the most ideal biopolymers for tissue engineering. As the key cartilage-specific compound, collagen II has reportedly promoted chondrogenic differentiation of stem cells in several studies.[16,17] Additionally, collagen II imparts cartilage-specific mechanical properties and behaviors that are essential to mimic the load-bearing properties and mechanical responses of native cartilage tissues. These functions are distinct from those of collagen I, gelatin, and other natural biopolymers.[18,19] According to recent animal studies, implantation of collagen II-based scaffolds promoted cartilage repair better than their collagen I counterparts, reflected by the higher amount of regenerated cartilage tissue and its connectivity,[6,13,20] further demonstrating its prospects in cartilage tissue engineering. However, collagen II-containing scaffolds are mainly in a foam form produced by freeze-drying. In other studies, collagen II was injected as a bulk hydrogel or used as a film, lacking porosity, and diverging from the concept of a conventional scaffold.[16,20–23] In freeze-dried foam scaffolds, the lack of symmetry and uniformity in the position, shape, and size of pores limits pore interconnectivity and increases the tortuosity of the pore channels.[24] These structural defects are not favorable for cell migration, penetration, and transportation of oxygen, water, nutrition, and metabolic waste necessary for cell proliferation.

To our knowledge, collagen II-based mesh scaffolds have been scarcely reported, despite their potential to address the aforementioned issues. The rheological properties (e.g., viscoelastic, shear-thinning behavior, and solidification kinetics) of collagen II-based hydrogel inks remain unclear. In particular, when collagen I and gelatin-based hydrogels were excessively used and printed with a good shape fidelity under a cryogenic condition,[25–28] the temperature effects on the rheological properties of collagen II-based hydrogels require further evaluation for printing optimization. Besides that, scaffold resolution has been reported to significantly influence cell proliferation and chondrogenic differentiation. However, the direct correlation of printing optimization and resolution enhancement towards cell activities has yet to be studied for collagen II-based scaffolds, especially compared to scaffolds of similar structures composed of other biomaterials.

In this study, we investigated the rheological properties of collagen II-based hydrogels at cryogenic conditions, and we obtained a high resolution exceeding 150 μm. On this basis, we investigated how collagen II composition enhances chondrogenic differentiation of mesenchymal stem cells (MSCs) compared to gelatin-based scaffolds, in terms of level of condensation and hypoxic conditions, to elucidate the underlying mechanisms. The study further evaluates scaffolds with different pore sizes for optimization and explores underlying mechanisms. Finally, an ideal cartilage-specific scaffold was designed based on the optimized composition and structural characteristics. We anticipate that this study will broaden our understanding of the role of collagen II, corresponding scaffold designs, and optimized conditions for cartilage tissue engineering.

2. Materials and methods

2.1. Materials

Gelatin (gel strength: ~250 bloom; biotechnology grade), alginate (mannuronic acid [M]/guluronic acid [G] = 1:1; biochemical grade; low-viscosity type), anhydrous $CaCl_2$, collagen I (from cow calcaneal tendon), collagen II (from bovine cartilage), and genipin were supplied by Macklin (China). Cellulose nanofiber (CNF) was supplied by Jinjiahao Co. Ltd. (China). Male Sprague-Dawley (SD) rats (2–3 weeks old) were purchased from the Animal Research Center of Anhui Medical University (China).

2.2. Fabrication of 3D scaffolds by extrusion printing

2.2.1. Ink preparation

Ink solutions of CNF/gelatin/alginate, CNF/collagen I/alginate, and CNF/collagen II/alginate were prepared by dissolving 3% (w/v) gelatin, collagen I, and collagen II in the readily-purchased 2 wt% CNF solution at 37°C, respectively; after dissolution, 15% (w/v) alginate was added to the solutions. The collagen II/alginate solution was prepared by dissolving 3% (w/v) collagen II and 15% (w/v) alginate in deionized water.

All four solutions were continuously stirred with a magnetic bar at 37°C for 1 h. The mixtures were then stirred by a motor-driven propeller under 25°C and at 150 RPM for 15 min.

2.2.2. Preparation of the crosslinking solution

The crosslinking solution was prepared by dissolving 30% (w/v) $CaCl_2$ in distilled water in a 100 mL flask placed

in a 4°C-water bath. Thereafter, 0.02% (w/v) genipin was added to the solution. The water bath was removed and the solution was stirred with a magnetic bar for 1 h.

2.2.3. 3D printing

3D printing was performed using an extrusion-based 3D printer (Regenovo, China). A 3D cryogenic well was connected to both the printer and a chiller, which provides water circulation to induce a cooling effect. The room temperature was fixed at 25°C. Tapered plastic needles (27G; inner diameter: 200 μm; outer diameter: 400 μm) were used for printing. The scaffold was printed layer-by-layer for a total of seven layers in a mesh pattern where rods in adjacent layers were perpendicular to each other. The degree of orientation of the first, third, fifth, and seventh layers was set to 90°, while that of the second, fourth, and sixth layers was set to 0°. To prevent ink overflow and deficiency when printing the starting and ending points of each rod, respectively, the rod was printed in a continuous zig-zag pattern for every layer. The printing head kept extruding ink materials when printing each single layer. The height of each layer was set to 0.14 mm. An extrusion pressure of 0.08 MPa was used for printing the CNF/collagen I/alginate hydrogel ink, while 0.22 MPa was used for printing all the other hydrogel inks. The temperature of the cryogenic well was set to −1°C for printing all samples. The distance between the centerline of the adjacent rod, denoted as rod distance, was set to 450 μm when printing the CNF/gelatin/alginate scaffold (sample a) and CNF/collagen I/alginate scaffold (sample b). The rod distance was set to 320, 450, and 550 μm when printing the CNF/collagen II/alginate scaffold (samples d–f, respectively). The printing speed was set to 7 mm/s when printing samples a, b, e, and f; the printing speed was set to 10 mm/s when printing sample d.

2.2.4. Post-treatment procedure

The crosslinking solution was stored in the refrigerator at 4°C before use. After printing, the cryogenic well was kept at −8°C for 20 min. The crosslinking solution was added to the frozen scaffold dropwise until it was immersed. The cryogenic well was then kept at 7°C for 20 min, and the thawed scaffolds were peeled off, collected, and immediately stored in the refrigerator at −20°C.

2.2.5. Preparation of the non-porous bulk scaffolds

The same CNF/collagen II/alginate hydrogel ink used for 3D printing was heated to 37°C and held isothermally for 1 h. The ink was then injected into a six-well culture plate with a 20-mL syringe. The as-prepared crosslinking solution was added to the ink for 20 min, and the solution (sample c) was stored immediately thereafter in the refrigerator at −20°C.

2.3. Morphological study

2.3.1. Scanning electron microscopy

To prepare for scanning electron microscopy (SEM), scaffolds of samples a–f were immersed in liquid nitrogen for 30 s and fractured. The samples were gently touched with filter paper to remove excess surface water, placed into a sputter coater, and vacuumed immediately for 20 min. The samples were loaded into the vacuum chamber of the SEM instrument (Zeiss, Germany) and vacuumed again. SEM observation was performed under the secondary electron (SE) mode, and the accelerating voltage was set to 3 kV. ImageJ was used to analyze the average rod diameter and pore size in the SEM images.

2.3.2. Transmission electron microscopy

To prepare for transmission electron microscopy (TEM), the as-purchased CNF solution (2 wt%) was diluted by 100×. A TEM instrument (Talos L120C G2; Thermal Scientific, United States of America [USA]) with an accelerating voltage of 120 kV was used to study the nanoscale morphology of CNF.

2.4. Rheological study

All rheological studies were conducted on the collagen II and gelatin-containing hydrogel inks using an MCR302e rheometer (Anton Paar, Austria). A movable and isothermal sample cover and a 25-mm parallel plate were used for all rheological tests. Before the sample was loaded or removed, the temperature of the chamber was fixed at 25°C for 10 min before adjusting to other temperatures.

2.4.1. Oscillation temperature ramp test

Temperature ramp test was conducted at a range of −3 to 37°C. The strain was held constant at 1%, and the oscillation frequency was set to 1 rad/s.

2.4.2. Steady-shear flow test

Steady-shear flow tests were conducted at a shear rate range of 0.1–100 s^{-1}, and the test temperature was set to −1°C.

2.4.3. Creep test

A creep test was conducted under constant stress of 100 Pa for the first 300 s. Thereafter, the shear stress was immediately reduced to 0 Pa, and the test was conducted for an additional 500 s.

2.4.4. Oscillation frequency sweep test

A frequency sweep test was conducted at −1°C and at a frequency range of 0.1–100 rad/s.

2.5. Cell culture and characterizations

2.5.1. Cell extraction and seeding

Mesenchymal stem cells (MSCs) were isolated from the bone marrow aspirate, i.e., from the tibia and femur

marrow, of SD mice. Before cell seeding, all scaffolds were immersed in 75 wt% ethanol for 10 min, washed once with phosphate-buffered saline (PBS; Beyotime, China), exposed to ultraviolet (UV) radiation for 30 min, and immersed in Minimum Essential Medium α (α-MEM; Vivacell, China), supplemented with 10 wt% fetal bovine serum (Gibco, Australia), 10 kU/mL penicillin (Beyotime, China), and 10 mg/mL streptomycin (Beyotime, China) (henceforth denoted as complete medium) for 24 h. MSCs passage 2 (P2) were seeded onto scaffolds at a density of 10^5 cells/mL for CCK-8 testing and 10^6 cells/mL for all other tests. Cell culture was conducted in an incubator (Thermo Fisher Scientific, USA) at 37°C and 5% CO_2. After 24 h with observable cell attachment, the complete medium was replaced by a chondrogenic differentiation medium to induce the chondrogenic differentiation. The chondrogenic differentiation medium is composed of the as-prepared α-MEM culture medium, supplemented with 10 μg/mL transforming growth factor-β3 (Abbkine, China), 10 mM β-glycerol phosphate (Sigma-Aldrich, USA), and 100 nM dexamethasone (Sigma-Aldrich, USA).

2.5.2. CCK-8 test

CCK-8 test was conducted on days 1, 3, and 5 of culture. Before the test, the existing culture medium was replaced with α-MEM medium, supplemented with 10 wt% CCK-8 cell-counting agent (Beyotime, China), and incubated for 1 h. During the test, 100 μL of cell supernatant was extracted and its optical density (OD) value was measured at a wavelength of 450 nm using a spectrophotometer (Multiskan GO; Thermo Fisher Scientific, USA). Each sample type was assessed in triplicates, and data are presented as mean ± standard deviation. One-way analysis of variance (ANOVA) was performed for comparison between sample types using GraphPad Prism 7. Statistical significance is considered for $p < 0.05$.

2.5.3. Reverse transcription-quantitative polymerase chain reaction

On day 7 of culture, the E.Z.N.A.® Total RNA Kit (Solarbio, China) was used to extract total RNA from bone MSCs (BMSCs). NovoStart® SYBR qPCR SuperMix plus (Novoprotein, China) was used to measure the gene expression levels of collagen I (*COL1*), collagen II (*COL2*), hypoxia-inducible factor-1α (*HIF1A*), SRY-box transcription factor 9 (*SOX9*), runt-related transcription factor-2 (*RUNX2*), Aggrecan core protein (*ACAN*), focal adhesion kinase (*FAK*), and N-cadherin (*NCAD*). Relative gene expression was normalized to the reference gene of glyceraldehyde-3-phosphate dehydrogenase (*GAPDH*).

Quantitative reverse transcription polymerase chain reaction (RT-qPCR) was conducted as follows:

(i) RNA extraction: Cells were digested using a TRK Lysis Buffer (Omega Bio-tek, USA), and impurities were removed by centrifugation in an RNA homogenizer spin column (Omega Bio-tek, USA). The filtrate was collected and transferred to a HiBind RNA mini-column (XXX, YYY). Nuclease-free water was then used to collect RNAs attached to the column. The total RNA concentration was measured using a NanoDrop spectrophotometer (Thermo Fisher Scientific, USA) and the 260/280 nm absorbance ratio was recorded.

(ii) Reverse transcription: Following the kit's instructions, gDNA Purge and 2× NovoScript® Plus 1st Strand cDNA Synthesis SuperMix were added to the extracted RNA for reverse transcription into cDNA. The mixture was incubated at 50°C for 15 min and subsequently at 75°C for 5 min. The resultant cDNA was then directly used for qPCR.

(iii) qPCR: According to the manufacturer's instructions, 2× NovoStart® SYBR qPCR SuperMix Plus, forward and reverse primers, template, and RNase-free water were sequentially added to the cDNA sample with a final volume of 20 μL. qPCR amplification was performed and the reaction program was set to 95°C for 1 min for initiation, followed by 35–45 cycles of incubation at 95°C for 20 s and 60°C for 1 min.

The results were subsequently analyzed using the ΔΔCt method.[29] The cycle threshold (Ct) value is the cycle number at which the fluorescence signal exceeds the background noise. The Ct values of the reference and target genes of the experimental and control groups were measured using qPCR. The ΔCt value was then calculated for each sample as the difference between the Ct values of the experimental and control groups:

$$\Delta\Delta Ct = \Delta Ct\ (\text{experimental group}) - \Delta Ct\ (\text{control group}) \quad (I)$$

Next, the relative expression of the target gene in the experimental group compared to the control group was determined as follows:

$$\text{Relative expression} = 2^{-\Delta\Delta Ct} \quad (II)$$

2.5.4. Cell morphology staining

Cell morphology staining was performed using Actin-Tracker Red (Beyotime, China) and 4′,6-diamidino-2-phenylindole (DAPI; Beyotime, China) staining to visualize the cell cytoskeleton and nucleus, respectively. The stained cells were fixed with a mounting medium (Biosharp, China) and examined under an upright microscope (Leica,

Germany). The staining results were visualized using excitation wavelengths of 496 and 480 nm, and emission wavelengths of 340 and 516 nm, respectively.

2.5.5. Western blotting

At day 7 of cell culture, total protein was extracted from BMSCs. Specifically, BMSCs were lysed in RIPA buffer (Beyotime, China). The resulting lysate was collected, and the protein concentration was determined by using the Bradford assay (Sangon Biotech, China). Subsequently, equal amounts of protein were separated on a 12% SDS-PAGE gel and transferred onto 0.22 μm polyvinylidene difluoride (PVDF) membranes (Sigma-Aldrich, USA). In this process, a constant current of 252 mA was applied. The membranes were then blocked with 5% skim milk and incubated overnight at 4°C with primary antibodies specific to focal adhesion kinase (FAK), N-cadherin, Collagen II, Aggrecan, and GAPDH. After three washes with Tris-buffered saline with Tween-20 (TBST; Beyotime, China), the membranes were incubated with horseradish peroxidase-conjugated secondary antibodies at 25°C for 1.5 h. Finally, the membranes were washed again with TBST, and the immunoreactive bands were visualized using an enhanced chemiluminescence detection kit (Beyotime, China).

2.5.6. Immunofluorescence staining

Bone MSCs (BMSCs) cultured on the scaffold were treated with 4% paraformaldehyde solution for 15 min, permeabilized with 0.1% Triton X-100 solution in PBS for 10 min, and blocked with 5% bovine serum albumin (BSA) for 30 min. The BMSCs were incubated with the primary antibody of collagen II (Abcam, USA) at 4°C and subsequently with the secondary antibody of collagen II (Abcam, USA) at room temperature for 1 h. Finally, the scaffolds were stained with DAPI, and images were obtained via a fluorescence microscope (Leica, Germany).

3. Results

3.1. Characterization of biopolymers

Cellulose nanofiber (CNF) was used as a filler to modify the rheological properties of the collagen II-based hydrogel, and its morphology was studied using TEM. The fiber diameter was within the nanoscale range (1–100 nm), and the fiber length was mostly longer than 500 nm. Despite 100× dilution of the as-purchased CNF (2 wt%) solution, entanglement was still observed (Figure 1). Furthermore, GPC was conducted to determine the molecular weight and distribution of collagen II and alginate (Table 1).

3.2. Rheological properties of collagen II-containing hydrogel inks

In our preparation of the hydrogel ink, it was determined that 3% (w/v) collagen II is the highest feasible concentration, potentially reaching its solubility limit. According to Figure 2, all the hydrogel inks exhibited a shear-thinning property, and the addition of CNF increased the viscosity and shear stress of the inks.

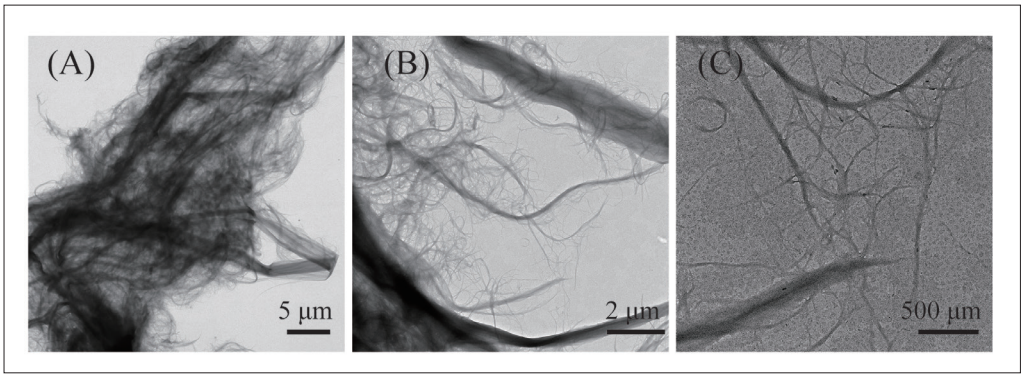


Figure 1. Transmission electron microscope (TEM) images of cellulose nanofiber at a magnification of (A) ×2700, (B) ×5300, and (C) ×13,500.

Table 1. Molecular weight of collagen II and alginate determined from gel permeation chromatography (GPC)

Substance	M_n (Da)	M_w (Da)	M_z (Da)	Polydispersity
Collagen II	25,774	533,724	1,685,898	20.71
Alginate	26,281	527,004	1,632,056	20.05

Abbreviations: M_n, number average; M_w, weight average; M_z, Z-average.

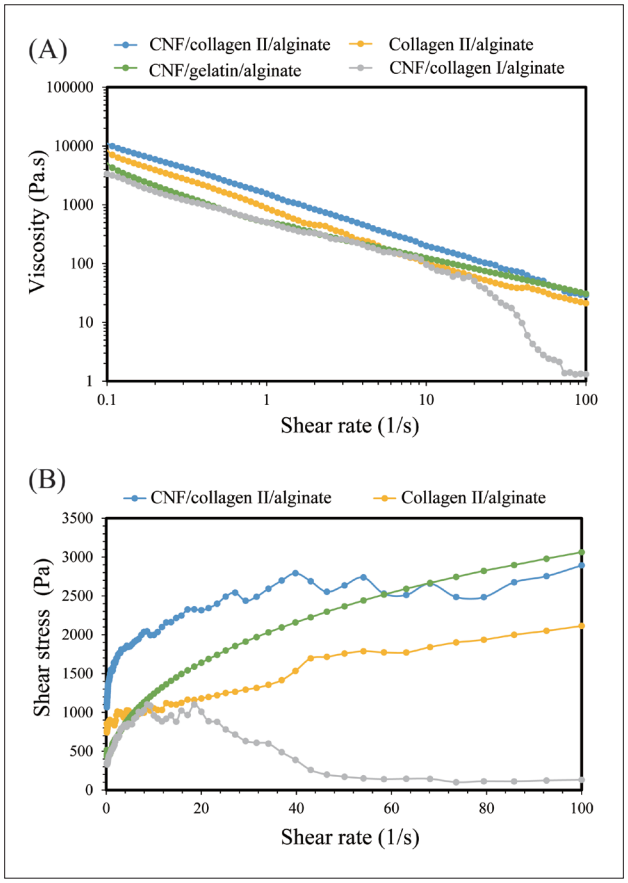


Figure 2. Steady-shear flow test of the hydrogel inks: (A) viscosity versus shear rate; (B) shear stress versus shear rate. Abbreviation: CNF, cellulose nanofiber.

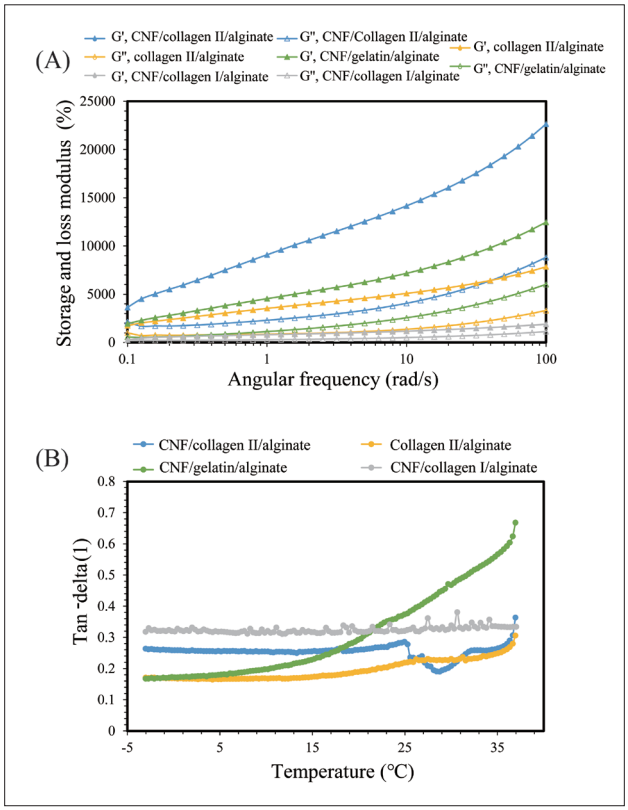


Figure 3. Measurements of the viscoelasticity of the hydrogel inks. (A) Oscillation frequency sweep test of the hydrogel inks: *G'* and *G"* versus frequency. (B) Oscillation temperature sweep test of the hydrogel inks: Tan-delta versus temperature. Abbreviation: CNF, cellulose nanofiber; *G'*, storage modulus; *G"*, loss modulus.

Similarly, the storage modulus of the collagen II-based hydrogel was significantly increased after the addition of CNF, corresponding to an increase in ink rigidity (Figure 3A). The effects of temperature were observed as the gelatin-based ink exhibited apparent gelation during the cooling process, while the change in the collagen II-based hydrogel was less apparent. Interestingly, the addition of CNF resulted in higher viscoelasticity (Figure 3B), possibly due to disruption in the entanglement of collagen macromolecules by CNF. A creep test was conducted to evaluate ink shape fidelity (Figure 4). The gelatin-based hydrogel exhibited a quick strain recovery at 1 s, presumably due to the formation of rigid and elastic triple helix microstructures during gelation. In contrast, all collagen II-based hydrogels did undergo gelation during cooling, resulting in loose intermolecular bonding and little resistance to shear deformation. Within the collagen II-based hydrogels, CNF addition significantly reduced creep strain over time, thereby enhancing ink shape fidelity. The rigid nanoscale network structure of CNF limited the movement of collagen II macromolecules and reduced their flow and elasticity.

3.3. Morphology of 3D-printed collagen II-containing scaffolds

Based on our results in Figure 4, the collagen II/alginate ink had a larger creep strain over time, reflecting limited shape fidelity. Consistently, CNF addition greatly reduced the rod diameter of the printed structure (Figure 5A and B), resulting in resolution enhancement.

The planar and cross-sectional views of the 3D-printed scaffolds are displayed in Figures 6 and 7, respectively. The printed rods had a self-supporting overhang structure and a relatively round shape instead of a flattened shape. This suggests good shape fidelity during the printing process, successful post-treatment, and SEM sample preparation in maintaining the sample geometry and dimensions. The combined use of the CNF and cryogenic printing techniques led to high printing resolution (Table 2). Furthermore, to evaluate the dimensional change after swelling, the pore size and rod diameter of the printed scaffolds were measured

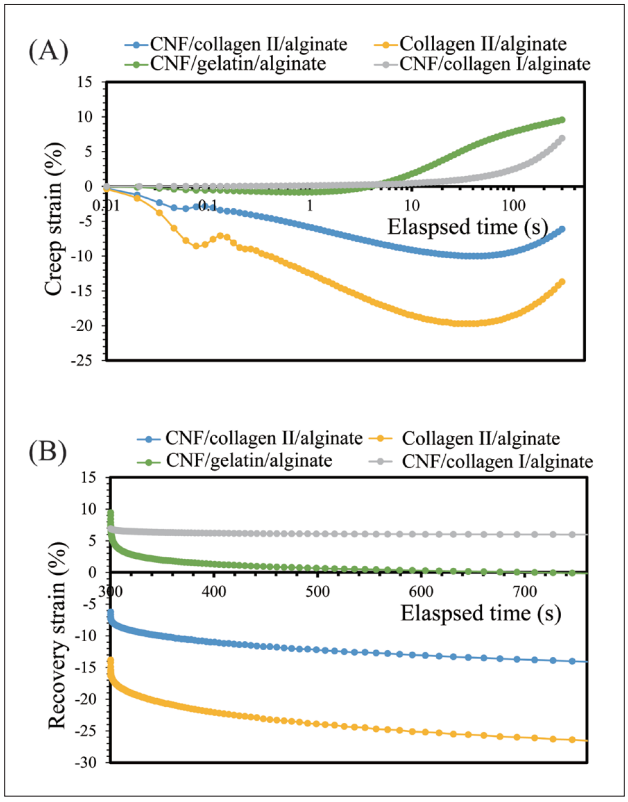


Figure 4. Creep strain of hydrogel inks (A) under a constant pressure of 100 Pa and (B) with pressure removed. Abbreviation: CNF, cellulose nanofiber.

after cell culture (Figure 8; Table 2). Sample c, being a bulk nonporous sample, was not relevant to the discussion on rod diameter and pore size changes. According to our results, the swelling was minimal, with observed shrinkage. The minimal dimensional change after rehydration could be contributed by the rigid nanoscale network of CNF and the high concentration of the crosslinking solution.

3.4. Biological study

At 12 h of culture, cell distribution was relatively uniform, and only small cell aggregates were observed (Figure 7). In contrast, on day 4 of culture (96 h), large cell aggregates formed on all collagen II-based porous mesh scaffolds (Figure 8D and E) rather than on their gelatin and collagen I counterparts (Figure 8A and B), suggesting that collagen II facilitates cell condensation. Cell distribution on each material-based scaffold (on day 4) was further observed under higher magnification. At high cell densities, cell aggregates were absent in gelatin- and collagen I-based scaffolds, highlighting that collagen II and the mesh scaffold structure were crucial factors inducing aggregation (Figure 9).

Furthermore, the OD value increased over time in all scaffolds (Figure 9A). Within collagen II scaffolds, the level of proliferation was significantly higher in sample d, evidenced by the greater scaffold resolution (Figure 9B). The proliferation rate of sample c (nonporous bulk scaffolds) was significantly lower than that of samples d and e (3D-printed porous mesh scaffolds) (Figure 9B).

For the expression of related genes, the level of chondrogenic differentiation of MSCs corresponds to the upregulation of chondrogenic markers. Chondrogenic differentiation was higher in 3D-printed collagen II-based mesh porous scaffolds than in their collagen I and gelatin counterparts. The expression of chondrogenic markers was lower in the bulk nonporous collagen II-based scaffold (sample c) than in mesh porous scaffolds (Figure 10). Collagen II-based mesh porous scaffolds with smaller pores and thinner rods further enhanced chondrogenic differentiation, while osteogenic genes (*COL1* and *RUNX2*) were upregulated in collagen I-based scaffolds. Therefore, the compositional and structural characteristics of the scaffolds were optimized simultaneously for sample d to enhance chondrogenic differentiation. The expression of the hypoxic factor HIF-1α displayed a similar trend for cell proliferation and was the highest in samples b and d. Lastly, high scaffold resolution significantly facilitated cell condensation, observed from the significantly upregulated expression of *NCAD* and *FAK* (Figures 10 and 11), suggesting structure-mediated cell condensation

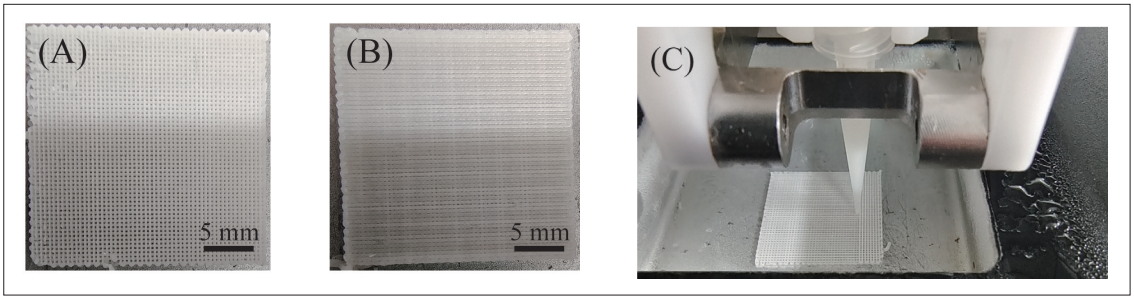


Figure 5. Improved printing resolution by adding CNF. (A and B) Macroscale images of the readily printed (A) collagen II/alginate and (B) CNF/collagen II/alginate scaffolds. (C) Printing of the CNF/collagen/alginate ink in a cryogenic well.

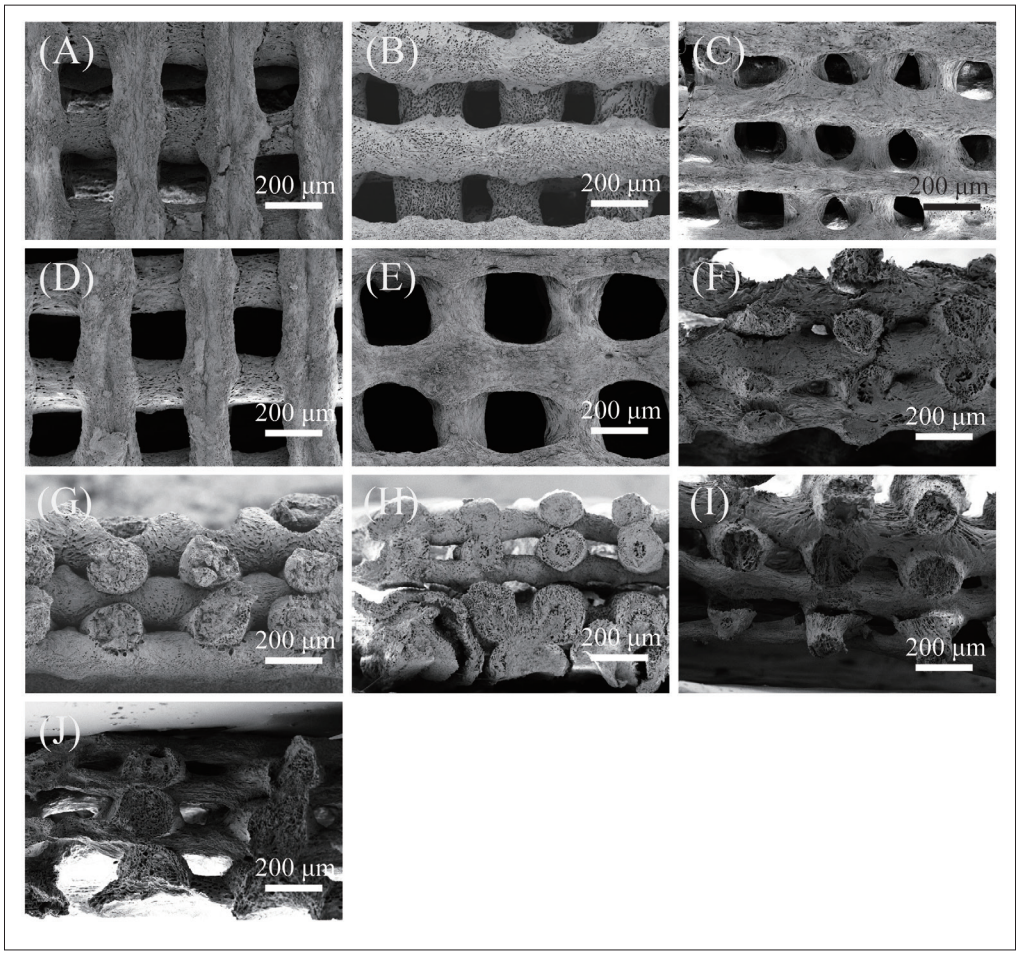


Figure 6. Microscale morphology of 3D-printed scaffolds with varying resolutions. (A and B) Microscale planar-view images of (A) CNF/gelatin/alginate and (B) CNF/collagen I/alginate scaffolds at a rod distance of 450 μm. (C–E) Microscale planar-view images of CNF/collagen II/alginate scaffolds at a rod distance of 320 (C), 450 (D), and 550 μm (E). (F and G) Cross-sectional view images of (F) CNF/gelatin/alginate and (G) CNF/collagen I/alginate scaffolds at a rod distance of 450 μm. (H–J) Cross-sectional view images of CNF/collagen II/alginate scaffolds at a rod distance of 320 (H), 450 (I), and 550 μm (J). Magnification: 50×. Scale bars: 200 μm.

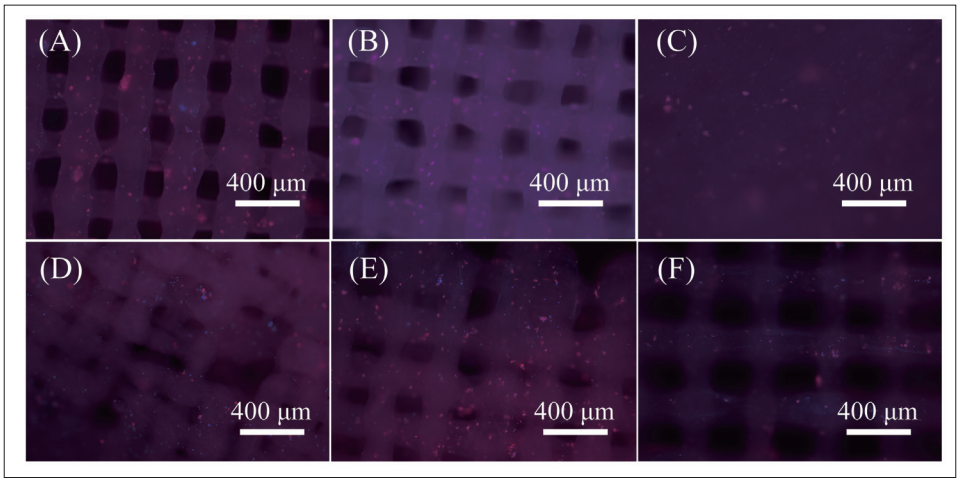


Figure 7. Microscopic images of mesenchymal stem cells (MSCs) stained with DAPI (blue) and F-actin (red) at 12 h of culture: (A and B) CNF/gelatin/alginate (A) and CNF/collagen I/alginate (B) scaffolds with a rod distance of 450 μm; (C) CNF/collagen II/alginate scaffold in bulk nonporous form; (D–F) CNF/collagen II/alginate scaffolds with a rod distance of 320 (D), 450 (E), and 550 μm (F), respectively. Abbreviations: CNF, cellulose nanofiber; DAPI, 4′,6-diamidino-2-phenylindole. Scale bars: 400 μm.

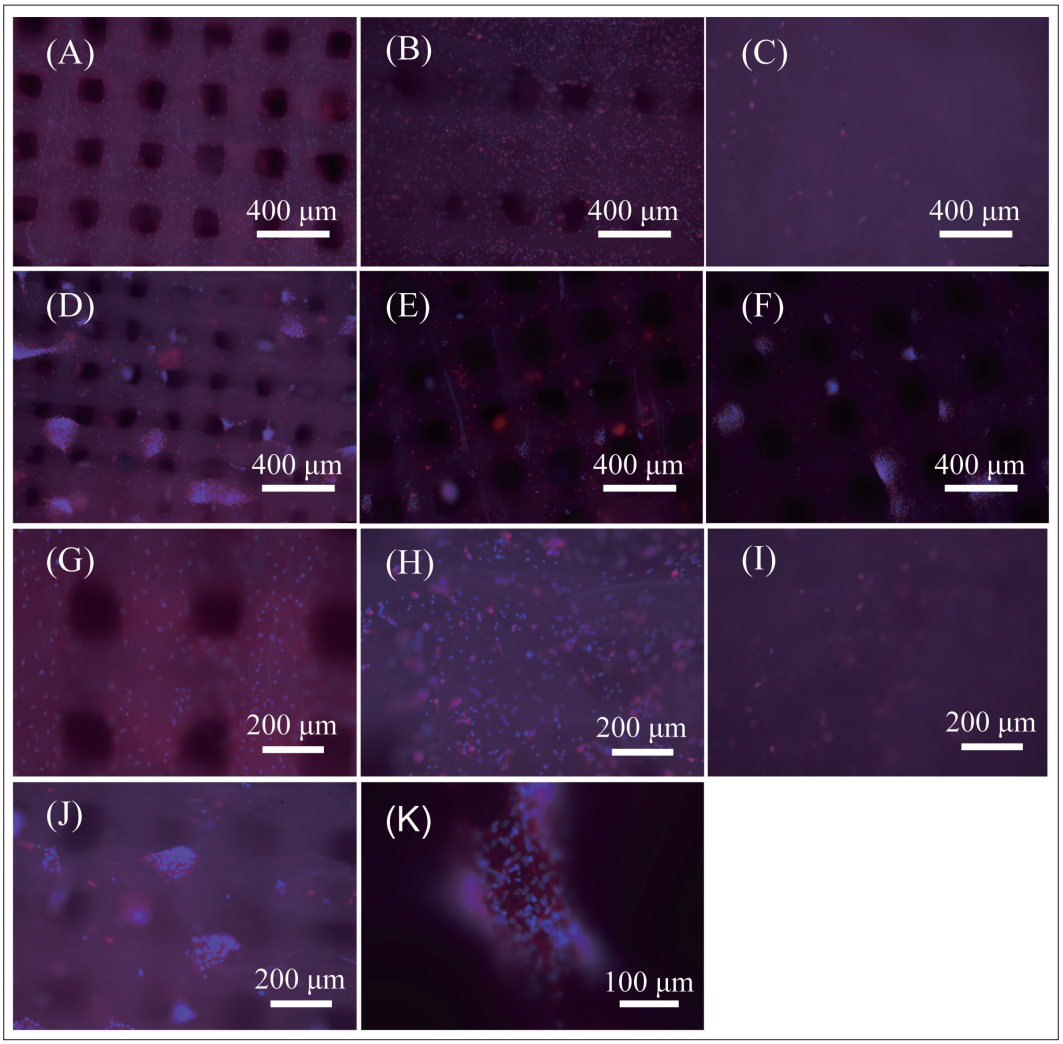


Figure 8. Microscopic images of mesenchymal stem cells (MSCs) stained with DAPI (blue) and F-actin (red) at 96 h of culture: (A and B) CNF/gelatin/alginate (A) and CNF/collagen I/alginate (B) scaffolds with a rod distance of 450 μm; (C) CNF/collagen II/alginate scaffold in bulk nonporous form; (D–F) CNF/collagen II/alginate scaffolds with a rod distance of 320 (D), 450 (E), and 550 μm (F), respectively; (G–H) CNF/gelatin/alginate (G) and CNF/collagen I/alginate (H) scaffolds with a rod distance of 450 μm; (I) collagen II-based bulk nonporous scaffolds; and (J and K) morphology of cell aggregates in CNF/collagen II/alginate mesh porous scaffold with a rod distance of 320 μm. Scale bars: 400 μm (A–F); 200 μm (G–J); 100 μm (K). Abbreviation: DAPI, 4',6-diamidino-2-phenylindole. Magnifications: J (100×), K (200×).

Table 2. Average pore size and rod diameter of scaffolds in samples a–f

Sample no.	Material and composition	Methods of fabrication	Scaffold structure
a	2% (w/v) CNF/ 3% (w/v) gelatin/ 15% (w/v) alginate	3D printing	Mesh scaffold, rod- distance at 450 μm
b	2% (w/v) CNF/ 3% (w/v) collagen I/ 15% (w/v) alginate		
c	2% (w/v) CNF/ 3% (w/v) collagen II/ 15% (w/v) alginate	Syringe injection (into the culture-plate)	Nonporous and solid scaffold; the concept of rod-distance was not applicable
d		3D printing	Mesh scaffold, rod-distance at 320 μm
e			Mesh scaffold, rod-distance at 450 μm
f			Mesh scaffold, rod-distance at 550 μm

Abbreviations: CNF, cellulose nanofiber; N/A, not applicable.

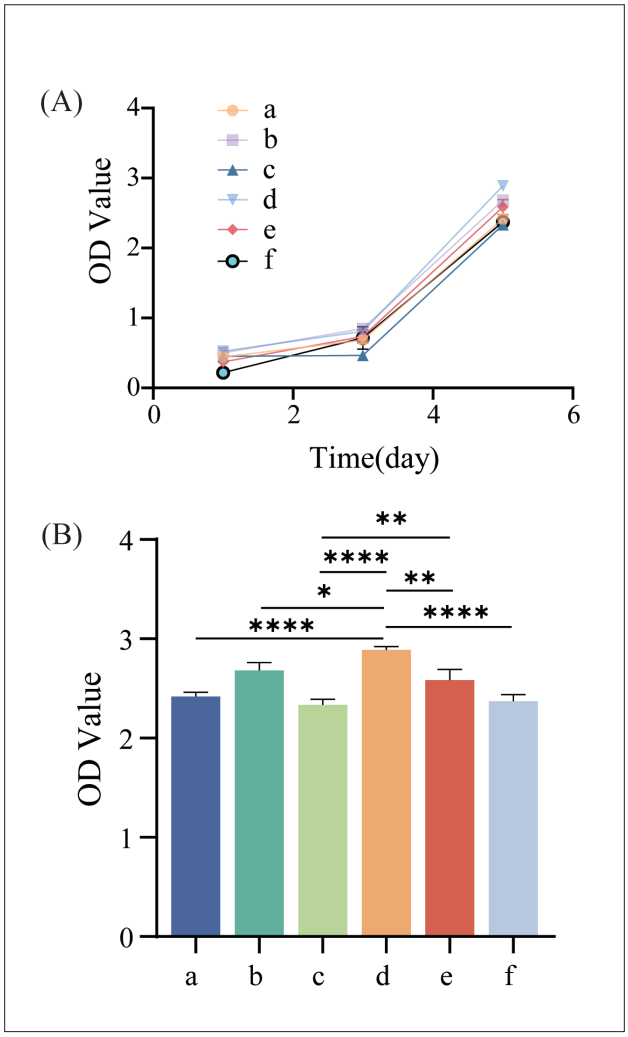


Figure 9. CCK-8 results based on scaffolds from samples a–f: (A) from day 1 to 5; and (B) on day 5. ****$p < 0.0001$; **$p < 0.01$; *$p < 0.05$. Abbreviation: OD, optical density.

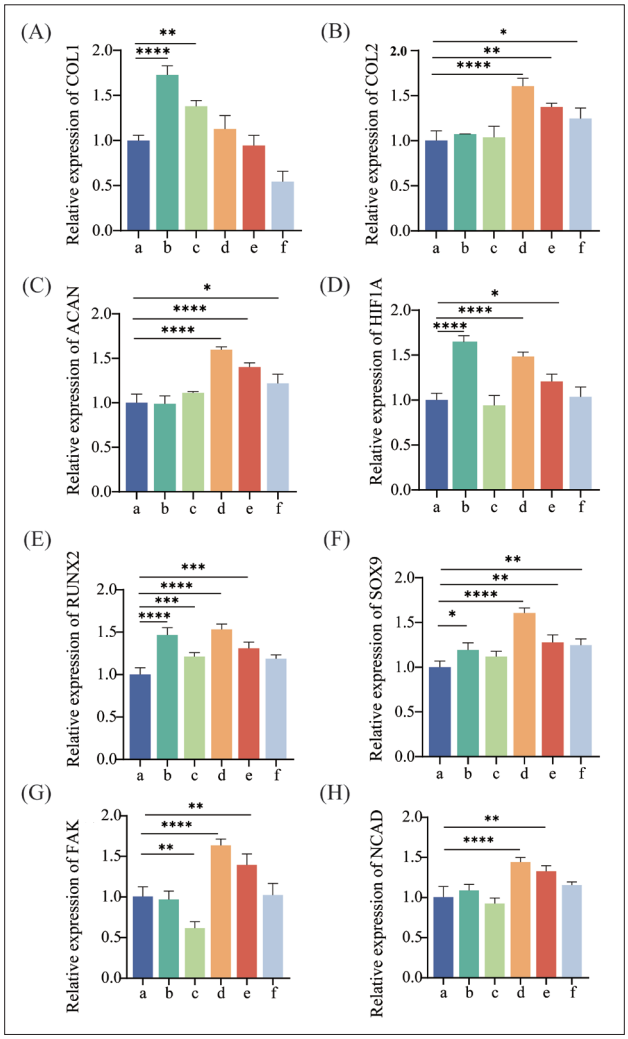


Figure 10. The mRNA expressions of key chondrogenic and osteogenic markers: (A) collagen I (Col-I), (B) collagen II (Col-II), (C) Aggrecan core protein (ACAN), (D) hypoxia-inducible factor-1α (HIF-1α), (E) runt-related transcription factor-2 (Runx-2), (F) SRY-box transcription factor 9 (SOX-9), (G) focal adhesion kinase (FAK), and (H) N-Cadherin. The scaffold samples evaluated were: CNF/gelatin/alginate (a) and CNF/collagen I/alginate (b) scaffolds with a rod distance of 450 μm, CNF/collagen II/alginate scaffolds in bulk nonporous form (c), and 3D-printed mesh form with a rod distance of 320 (d), 450 (e), and 550 μm (f), respectively. ****$p < 0.0001$; ***$p < 0.001$; **$p < 0.001$; *$p < 0.05$. Abbreviation: CNF, cellulose nanofiber.

in the 3D-printed scaffolds. To further understand the effects of scaffold composition and structures on the synthesis of cartilage-specific ECMs, western blotting was conducted on all scaffolds to study the level of expression of Aggrecan and collagen II. The expression of Aggrecan was the highest in collagen II-based mesh porous scaffolds (samples d–f) than in the non-porous bulk scaffold (sample c) and gelatin- and collagen I-based mesh porous scaffolds (samples a and b) (Figure 11B). The expression of collagen II exhibited the same trend. To summarize, collagen II-based scaffolds with the highest resolution (sample d), exhibited the highest cartilage-specific ECM production.

Based on our immunostaining results (Figure 12), 3D-printed collagen II-based mesh porous scaffolds produced more collagen II than the bulk nonporous collagen II-, 3D-printed collagen I-, and gelatin-based mesh porous scaffolds. This finding is consistent with the western blot results (Figure 11).

4. Discussion

4.1. Rheological properties and printing outcomes of collagen II-based hydrogel inks

In this study, we have successfully constructed high-resolution collagen II-based scaffolds (sample d) with an

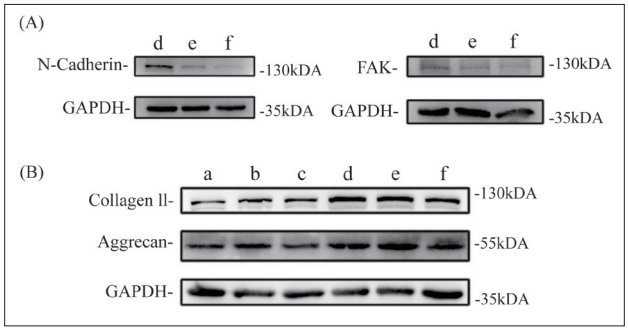


Figure 11. Western blot results. (A) N-cadherin and focal adhesion kinase (FAK) expression in collagen II-based scaffolds with a rod distance of 320 (d), 450 (e), and 550 μm (f). (B) Aggrecan and collagen II expression on gelatin- (a) and collagen I-based (b) scaffolds with a rod distance of 450 μm, collagen II-based bulk scaffolds without pores (c), and collagen II-based scaffolds with a rod distance of 320 (d), 450 (e), and 550 μm (f), respectively. Abbreviation: GADPH, glyceraldehyde 3-phosphate dehydrogenase.

average rod diameter of 122 ± 17 μm via 3D printing. The scaffold features one of the highest resolutions among reported hydrogel-based 3D printing thus far. Generally, it is challenging to print a rod thinner than the needle size,[30] and most reported printing resolutions range between 250 and 500 μm.[25,31–33] The scaffold resolution in our work greatly exceeded this range and the limit imposed by the needle size, without much difference after printing completion or swelling. Therefore, we not only succeeded in printing collagen II-based mesh scaffolds, but also enhanced the printing resolution of general hydrogel inks to a greater extent than most existing studies.

Our results also elucidated the rheological properties and behaviors of collagen II-based hydrogels, correlating them with printing performance. Although collagen II remained in a constant gel state over a wide temperature range (−5 to 37°C), its gelation strength was quite limited compared to gelatin at cryogenic conditions. Therefore, it was insufficient to simultaneously maintain high ink shape fidelity and printing resolution (e.g., exceeding 150 μm). Fortunately, we addressed the lack of shape fidelity by using a rigid nano-network filler, CNF.

4.2. Effects of collagen II on chondrogenic differentiation and its underlying mechanism

Several studies have utilized the collagen II composition but did not investigate its underlying mechanism in chondrogenic differentiation.[22] Some researchers hypothesized that collagen II could promote chondrogenic differentiation by promoting the condensation of MSCs, as the process is essential for chondrogenic differentiation.[16,21,34] Nonetheless, the assumption lacks both qualitative and quantitative evidence and corroboration.

At the beginning of cell culture (12 h), cell distribution was relatively uniform in all scaffolds. However, apparent cell aggregates (~100 μm) were observed in all collagen II-based scaffolds on day 4 (96 h), and they were distributed over the majority of the scaffold area. In contrast, the aggregates were not observable in gelatin- and collagen I-based scaffolds. To our knowledge, this work is among the earliest to successfully visualize the enhancement of MSC condensation with collagen II.

Quantitatively, the expression of N-cadherin was upregulated in collagen II-containing scaffolds than their gelatin and collagen I counterparts (Figure 10). N-cadherin was identified as a major regulator of MSC condensation in early chondrogenic differentiation,[35–37] and a higher concentration of N-cadherin correlated to more apparent cell aggregates.[38] The qualitative and quantitative evidence of cell condensation from the study went beyond existing studies of collagen II-containing scaffolds by exploring the mechanisms underlying the chondro-inductive capability of collagen II.

4.3. Synergistic effects of collagen II and printing resolution on chondrogenic differentiation

While existing studies have utilized collagen II in cell culture, their corresponding scaffold structures did not exhibit significant improvements. In particular, some studies utilized bulk scaffolds without pores.[39–41] Herein, the difference between collagen II-based nonporous bulk scaffolds (sample c) and 3D-printed mesh porous scaffolds (sample d–f) was studied and compared, in terms of their ability to enhance cell proliferation and chondrogenic differentiation. Our results revealed that the proliferation rate in sample c was not significantly different from the other samples, and the sample reported the lowest proliferation rate on days 3–5 (Figure 9B). Cell migration and substance transportation could be compromised by the lack of pores and interconnected pore networks, resulting in poor cell proliferation.[42–44] Similarly, sample c also exhibited downregulated expressions of chondrogenic markers, Aggrecan, and ECM compared to the other 3D-printed mesh scaffolds, emphasizing the importance of 3D-printed interconnected pore networks (Figure 11).

Furthermore, 3D-printed mesh porous scaffolds with higher resolution are more favorable for cell proliferation and chondrogenic differentiation. According to our results, all chondrogenic markers were upregulated in scaffolds with smaller pores, and the underlying mechanisms could be explained as follows:

(i) The level of cell condensation was higher in scaffolds with smaller pores, as observed from the upregulated FAK and N-cadherin expression (Figure 11). This

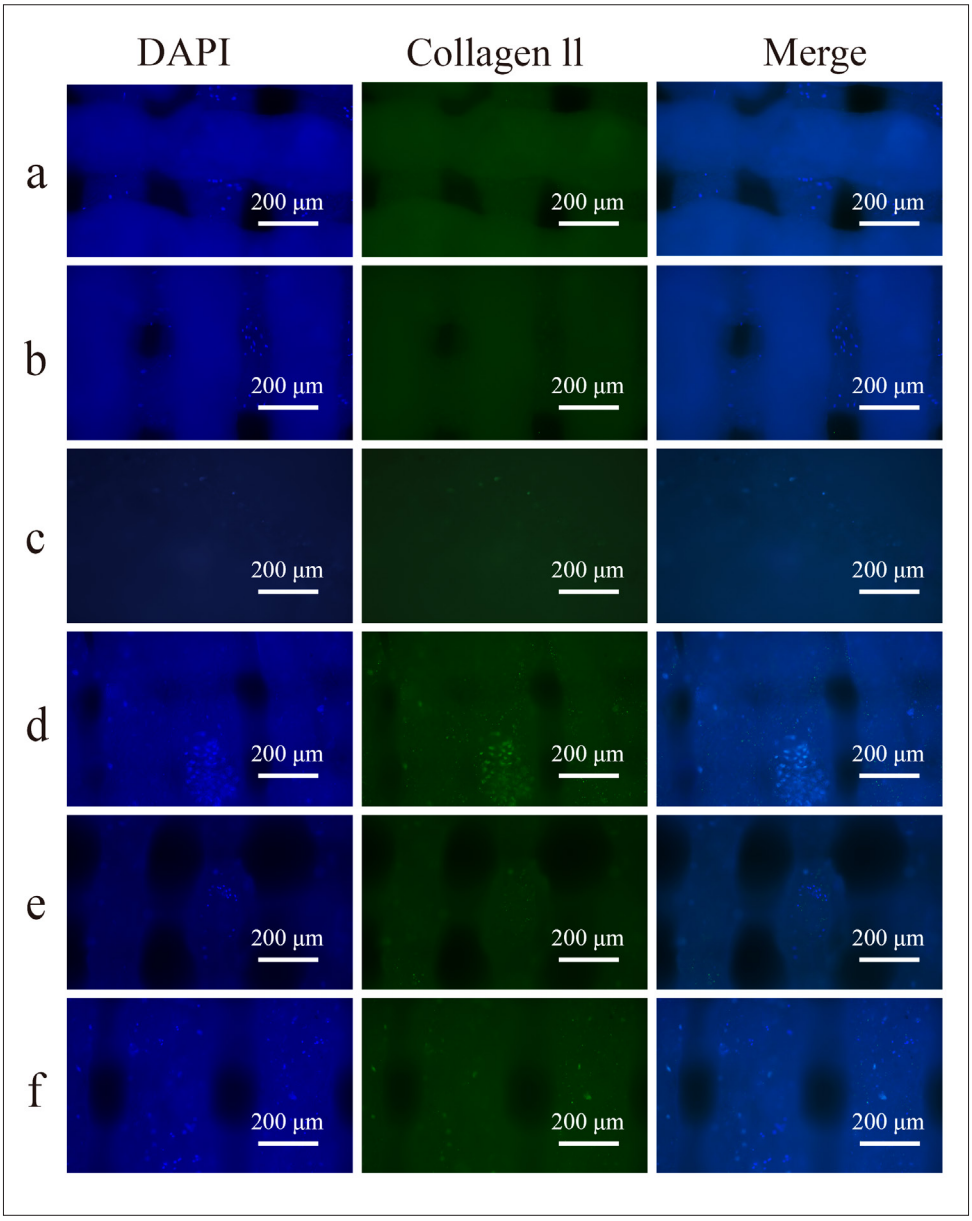


Figure 12. Immunostaining images of gelatin- (A) and collagen I-based (B) scaffolds with a rod distance of 450 μm, (C) collagen II-based nonporous bulk scaffolds, and (D–F) collagen II-based scaffolds with a rod distance of 320 (D), 450 (E), and 550 μm (F), respectively. DAPI staining: blue; collagen II staining: green. Abbreviation: DAPI, 4',6-diamidino-2-phenylindole.

could be attributed to a higher number of cells (based on CCK-8 results, Figure 9) in scaffolds with smaller pores. According to the random walk model,[45] a higher number of junctions in mesh scaffolds favors cell migration, and scaffolds with smaller pores also have more junctions, making them more favorable for cell migration and subsequent cell condensation.

(ii) The upregulated expression of HIF-1α in scaffolds with smaller pores suggests favorable chondrogenic differentiation in these scaffolds.[46] In this regard, the hypoxic condition in scaffolds with smaller pores may be attributed to a higher number of cells and enhanced cell condensation. Moreover, smaller pores may also reduce oxygen transportation to cells.

Several studies using 3D-printed mesh scaffolds have investigated the effects of pore size on the proliferation and chondrogenic differentiation of MSCs. Smaller pore sizes generally favor chondrogenic differentiation but hinder cell proliferation. For example, Di Luca et al.[47] reported upregulated expression of ACAN, collagen II, and SOX-9

in scaffolds with 500 μm pores compared to scaffolds with 700 and 900 μm pores, but the level of proliferation was lower in the former scaffolds. Similarly, Sun et al.[48] reported upregulation of chondrogenic markers and reduced level of proliferation in scaffolds with 150 μm pores compared to scaffolds with larger pores.

Most studies correlating smaller pores to reduced cell proliferation often utilize mesh scaffolds composed of thermoplastic polymers or metals. In contrast, collagen II in hydrogel form was used in our study, achieving greater cell proliferation in scaffolds with smaller pores (i.e., <150 μm). Hence, we infer that pore size effects could be material-dependent. Small pores are usually unfavorable for solvent diffusion, which would subsequently hinder cell metabolism and proliferation.[49] Nonetheless, the collagen II composition used in this study could have addressed the aforementioned issues based on three critical aspects:

(i) the surface RGE groups could bind to cells and organic compounds[50];

(ii) the hydrogel form could have facilitated the adsorption of nutrition substances; and

(iii) the higher number of cells and aggregation results in enhanced cell–cell communication.[51]

Collectively, we demonstrated that collagen II enhances the proliferation and chondrogenic differentiation of MSCs via its biochemical properties and the presence of small pores on the scaffolds.

4.4. Prospective applications in cartilage tissue engineering

Growth factors are essential for cartilage tissue engineering, but their inclusion is costly and requires significant efforts in preservation, handling, blending, release control, and optimization.[52,53] Conversely, the use of collagen II to induce chondrogenic differentiation could reduce the overall cost and effort required for growth factors. Additionally, collagen II can be used synergistically with growth factors to promote chondrogenic differentiation.

Improving both the compositional and structural properties of a cartilage scaffold used to be challenging primarily due to difficulties in hydrogel processing. Some studies have used cartilage-specific biomaterials or other natural protein-based hydrogels with excellent biocompatibility (collagen I, gelatin, etc.), but the developed scaffolds often exhibit undesirable structural characteristics, such as foam scaffolds produced by freeze-drying[21–23,54,55] and nanoscale porous film scaffolds produced by electrospinning.[56] These scaffolds lack uniform, symmetrical, and interconnected macro-micro pores to sufficiently support cell migration, growth, and substance transportation.[7,57] Recent works have addressed the structural issues above with 3D-printed mesh scaffolds, but these scaffolds have poor resolution (250–500 μm), resulting in low porosity and surface area for essential cell activities.[24,30,58–61] Likewise, there are well-designed 3D-printed mesh scaffolds with high resolution (~150 μm), interconnectivity, and symmetry, but utilize poorly bioactive materials[48,49,62] These biomaterials, including metals, ceramics, and thermoplastic polymers (e.g., polycaprolactone), are stiff and hydrophobic, unlike hydrogel scaffolds that provide a favorable viscoelastic[63–65] and hydrophilic environment[66,67] for cell adhesion and proliferation. From the biochemical perspective, the use of natural proteins, such as collagen and gelatin, introduces surface RGD/RGE sequences that could enhance chondrogenic differentiation and cell adhesion.[68–70]

In comparison to previously reported studies, our collagen II-containing scaffolds are superior in both compositional and structural properties (with a high resolution near 120 μm), and the scaffolds could synergistically induce chondrogenic differentiation and cartilage-specific ECM synthesis, highlighting their potential for further applications in cartilage tissue engineering.

4.5. Clinical relevance of printing high-resolution natural protein-based hydrogel

In this study, we developed collagen II-based scaffolds with a high resolution, i.e., sample d with an average pore size of 133 ± 17 μm and a rod diameter of 122 ± 18 μm. As aforementioned, collagen II enhances cell proliferation, chondrogenic differentiation, and cartilage-specific ECM production, and the effects are augmented by the small pores on the scaffold. Herein, we discuss the future clinical relevance of producing small-sized pores in tissue scaffolds.

Tissue engineering facilitates tissue defect repairs but has yet to become widely used in clinical routines. One of the key hurdles is the inadequate production of ECMs, resulting in diminished mechanical properties of the regenerated tissue.[71–73] As a consequence, the tissue often fails to match the load-bearing capacity of the host tissue and fulfill its function.[74] Inadequate ECM production may also limit the total volume of regenerated tissue, resulting in voids and a greater probability of tissue fracture.[75] Therefore, it is crucial for scaffolds to enhance tissue-specific ECM production.[24,62]

In this study, the collagen II-based scaffolds with a high resolution (sample d) significantly improved the level of proliferation, chondrogenic differentiation, and cartilage-specific ECM production. Additionally, pore size is essential for increasing total ECM production, and this could be

applied to regenerated tissues to increase their volume and enhance their mechanical properties. This approach could reduce the gap between the regenerated tissue and native host tissue, facilitating the clinical translation of collagen II-based scaffolds for tissue repair applications.

5. Conclusion

In this work, collagen II-containing mesh scaffolds were successfully fabricated by 3D printing, and the scaffolds feature a much higher resolution than most reported hydrogel-based scaffolds. Collagen II enhances the level of MSC condensation based on the cell distribution pattern and quantitative upregulation of FAK and N-cadherin. Therefore, collagen II-containing scaffolds exhibit greater chondrogenic differentiation compared to gelatin-based scaffolds. Additionally, smaller pores and rod diameters were found to promote the proliferation and chondrogenic differentiation of MSCs, synergistic to the enhancement of collagen II. Therefore, we demonstrated the effect and underlying mechanism of collagen II in enhancing chondrogenic differentiation and constructed a scaffold with optimized compositional and structural characteristics. These findings will broaden our understanding of scaffold design for cartilage tissue engineering.

Acknowledgments

The authors would like to thank the Center for Scientific Research of Anhui Medical University for their valuable assistance with our experiments.

Funding

This work was supported by the National Natural Science Foundation of China (81772408) and the Key Research and Development Program of the Anhui Province (2022e07020046).

Conflict of interest

The authors declare no conflicts of interest.

Author contributions

Conceptualization: Kaixuan Li, Hanxiao Huang
Formal analysis: Kaixuan Li
Funding acquisition: Cailiang Shen
Investigation: Kaixuan Li, Hanxiao Huang
Methodology: Kaixuan Li, Hanxiao Huang
Writing - original draft: Hanxiao Huang
Writing- review & editing: Kaixuan Li

Ethics approval and consent to participate

In this study, animal-related procedures were conducted in accordance with the ethical standards approved by the Experimental Animal Ethics Committee of Anhui Medical University (approval number: LLSC 20221081).

Consent for publication

Not applicable.

Availability of data

Research data are available in the **Supplementary File**.

References

1. Petitjean N, Canadas P, Royer P, Noël D, Le Floc'h S. Cartilage biomechanics: from the basic facts to the challenges of tissue engineering. *J Biomed Mater Res A*. 2023;111(7):1067-1089. doi: 10.1002/jbm.a.37478
2. Xu X, Xu L, Xia J, Wen C, Liang Y, Zhang Y. Harnessing knee joint resident mesenchymal stem cells in cartilage tissue engineering. *Acta Biomater*. 2023;168:372-387. doi: 10.1016/j.actbio.2023.07.024
3. Stampoultzis T, Karami P, Pioletti DP. Thoughts on cartilage tissue engineering: a 21st century perspective. *Curr Res Transl Med*. 2021;69(3):103299. doi: 10.1016/j.retram.2021.103299
4. Nguyen TPT, Li F, Shrestha S, et al. Cell-laden injectable microgels: current status and future prospects for cartilage regeneration. *Biomaterials*. 2021;279:121214. doi: 10.1016/j.biomaterials.2021.121214
5. Yang Z, Li H, Yuan Z, et al. Endogenous cell recruitment strategy for articular cartilage regeneration. *Acta Biomater*. 2020;114:31-52. doi: 10.1016/j.actbio.2020.07.008
6. Wu Z, Korntner SH, Mullen AM, Zeugolis DI. Collagen type II: from biosynthesis to advanced biomaterials for cartilage engineering. *Biomater Biosyst*. 2021;4:100030. doi: 10.1016/j.bbiosy.2021.100030
7. Huang H, Ayariga J, Ning H, Nyairo E, Dean D. Freeze-printing of pectin/alginate scaffolds with high resolution, overhang structures and interconnected porous network. *Addit Manuf*. 2021;46:102120. doi: 10.1016/j.addma.2021.102120
8. Statham P, Jones E, Jennings LM, Fermor HL. Reproducing the biomechanical environment of the chondrocyte for cartilage tissue engineering. *Tissue Eng Part B Rev*. 2021;28(2):405-420. doi: 10.1089/ten.teb.2020.0373
9. Bielajew BJ, Donahue RP, Lamkin EK, Hu JC, Hascall VC, Athanasiou KA. Proteomic, mechanical, and biochemical characterization of cartilage development. *Acta Biomater*. 2022;143:52-62. doi: 10.1016/j.actbio.2022.02.037
10. Sani M, Hosseinie R, Latifi M, et al. Engineered artificial articular cartilage made of decellularized extracellular

matrix by mechanical and IGF-1 stimulation. *Biomater Adv*. 2022;139:213019.
doi: 10.1016/j.bioadv.2022.213019

11. Peng Z, Sun H, Bunpetch V, et al. The regulation of cartilage extracellular matrix homeostasis in joint cartilage degeneration and regeneration. *Biomaterials*. 2021;268:120555.
doi: 10.1016/j.biomaterials.2020.120555

12. Sarrigiannidis SO, Rey JM, Dobre O, González-García C, Dalby MJ, Salmeron-Sanchez M. A tough act to follow: collagen hydrogel modifications to improve mechanical and growth factor loading capabilities. *Mater Today Bio*. 2021;10:100098.
doi: 10.1016/j.mtbio.2021.100098

13. Kilmer CE, Battistoni CM, Cox A, Breur GJ, Panitch A, Liu JC. Collagen Type I and II blend hydrogel with autologous mesenchymal stem cells as a scaffold for articular cartilage defect repair. *ACS Biomater Sci Eng*. 2020;6(6):3464-3476.
doi: 10.1021/acsbiomaterials.9b01939

14. Cámara-Torres M, Sinha R, Mota C, Moroni L. Improving cell distribution on 3D additive manufactured scaffolds through engineered seeding media density and viscosity. *Acta Biomater*. 2020;101(1):183-195.
doi: 10.1016/j.actbio.2019.11.020

15. Pfeiffer E, Vickers SM, Frank E, Grodzinsky AJ, Spector M. The effects of glycosaminoglycan content on the compressive modulus of cartilage engineered in type II collagen scaffolds. *Osteoarthritis Cartilage*. 2008;16(10):1237-1244.
doi: 10.1016/j.joca.2008.02.014

16. Yang K, Sun J, Dan W, et al. Photo-crosslinked mono-component type II collagen hydrogel as matrix to induce chondrogenic diffrentiation of bone marrow mesenchymal stem cells. *J Mater Chem B*. 2017;5:8707-8718.
doi: 10.1039/C7TB02348K

17. Piperigkou Z, Bainantzou D, Makri N, et al. Enhancement of mesenchymal stem cells' chondrogenic potential by type II collagen-based bioscaffolds. *Mol Biol Rep*. 2023;50(6):5125-5135.
doi: 10.1007/s11033-023-08461-x

18. Kato YP, Christiansen DL, Hahn RA, Shieh S-J, Goldstein JD, Silver FH. Mechanical properties of collagen fibres: a comparison of reconstituted and rat tail tendon fibres. *Biomaterials*. 1989;10(1):38-42.
doi: 10.1016/0142-9612(89)90007-0

19. Sun Y-L, Luo Z-P, Fertala A, An K-N. Stretching type II collagen with optical tweezers. *J Biomech*. 2004;37(11):1665-1669.
doi: 10.1016/j.jbiomech.2004.02.028

20. Hu X, Jin M, Sun K, et al. Type II collagen scaffolds repair critical-sized osteochondral defects under induced conditions of osteoarthritis in rat knee joints via inhibiting TGF-β-Smad1/5/8 signaling pathway. *Bioactive Mater*. 2024;35:416-428.
doi: 10.1016/j.bioactmat.2024.02.008

21. Tamaddon M, Burrows M, Ferreira S, et al. Monomeric, porous type II collagen scaffolds promote chondrogenic differentiation of human bone marrow mesenchymal stem cells in vitro. *Sci Rep*. 2017;7:43519.
doi: 10.1038/srep43519

22. Intini C, Lemoine M, Hodgkinson T, Casey S, Gleeson J, O'Brien F. A highly porous type II collagen containing scaffold for the treatment of cartilage defects enhances MSC chondrogenesis and early cartilaginous matrix deposition. *Biomater Sci*. 2022;10:970-983.
doi: 10.1039/D1BM01417J

23. Ko CS, Huang J-P, Huang C-W, Chu IM. Type II collagen-chondroitin sulfate-hyaluronan scaffold cross-linked by genipin for cartilage tissue engineering. *J Biosci Bioeng*. 2009;107(2):177-182.
doi: 10.1016/j.jbiosc.2008.09.020

24. Rustom LE, Poellmann MJ, Johnson AJW. Mineralization in micropores of calcium phosphate scaffolds. *Acta Biomater*. 2019;83:435-455.
doi: 10.1016/j.actbio.2018.11.003

25. Suo H, Zhang J, Xu M, Wang L. Low-temperature 3D printing of collagen and chitosan composite for tissue engineering. *Mater Sci Eng C*. 2021;123:111963.
doi: 10.1016/j.msec.2021.111963

26. Bhardwaj D, Singhmar R, Garg M, et al. Designing advanced hydrogel inks with direct ink writing based 3D printability for engineered biostructures. *Eur Polym J*. 2024;205:112736.
doi: 10.1016/j.eurpolymj.2023.112736

27. Gupta D, Singh AK, Dravid A, Bellare J. Multiscale porosity in compressible cryogenically 3D printed gels for bone tissue engineering. *ACS Appl Mater Interfaces*. 2019;11(22):20437-20452.
doi: 10.1021/acsami.9b05460

28. Gupta D, Vashisth P, Bellare J. Multiscale porosity in a 3D printed gellan–gelatin composite for bone tissue engineering. *Biomed Mater*. 2021;16(3):034103.
doi: 10.1088/1748-605x/abf1a7

29. Livak KJ, Schmittgen TD. Analysis of relative gene expression data using real-time quantitative PCR and the 2−ΔΔCT method. *Methods*. 2001;25(4):402-408.
doi: 10.1006/meth.2001.1262

30. Townsend JM, Beck EC, Gehrke SH, Berkland CJ, Detamore MS. Flow behavior prior to crosslinking: the need for precursor rheology for placement of hydrogels in medical applications and for 3D bioprinting. *Prog Polymer Sci*. 2019;91:126-140.
doi: 10.1016/j.progpolymsci.2019.01.003

31. Shi L, Hu Y, Ullah MW, et al. Cryogenic free-form extrusion bioprinting of decellularized small intestinal submucosa for potential applications in skin tissue engineering. *Biofabrication*. 2019;11(3):035023.

doi: 10.1088/1758-5090/ab15a9

32. Hu Y, Wu B, Xiong Y, et al. Cryogenic 3D printed hydrogel scaffolds loading exosomes accelerate diabetic wound healing. *Chem Eng J*. 2021;426:130634. doi: 10.1016/j.cej.2021.130634

33. Yang L, Jin S, Shi L, et al. Cryogenically 3D printed biomimetic scaffolds containing decellularized small intestinal submucosa and Sr2+/Fe3+ co-substituted hydroxyapatite for bone tissue engineering. *Chem Eng J*. 2022;431:133459. doi: 10.1016/j.cej.2021.133459

34. Lu Z, Zandieh Doulabi B, Huang C, Bank R, Helder M. Collagen type II enhances chondrogenesis in adipose tissue–derived stem cells by affecting cell shape. *Tissue Eng Part A*. 2010;16(1):81-90. doi: 10.1089/ten.TEA.2009.0222

35. Li R, Xu J, Wong DSH, Li J, Zhao P, Bian L. Self-assembled N-cadherin mimetic peptide hydrogels promote the chondrogenesis of mesenchymal stem cells through inhibition of canonical Wnt/β-catenin signaling. *Biomaterials*. 2017;145:33-43. doi: 10.1016/j.biomaterials.2017.08.031

36. Ke W, Ma L, Wang B, et al. N-cadherin mimetic hydrogel enhances MSC chondrogenesis through cell metabolism. *Acta Biomater*. 2022;150:83-95. doi: 10.1016/j.actbio.2022.07.050

37. Wang Y, Xiao Y, Long S, Fan Y, Zhang X. Role of N-Cadherin in a niche-mimicking microenvironment for chondrogenesis of mesenchymal stem cells in vitro. *ACS Biomater Sci Eng*. 2020;6(6):3491-3501. doi: 10.1021/acsbiomaterials.0c00149

38. Eren Cimenci C, Kurtulus GU, Caliskan OS, Guler MO, Tekinay AB. N-cadherin mimetic peptide nanofiber system induces chondrogenic differentiation of mesenchymal stem cells. *Bioconjugate Chem*. 2019;30(9):2417-2426. doi: 10.1021/acs.bioconjchem.9b00514

39. Choi B, Kim S, Lin B, Wu BM, Lee M. Cartilaginous extracellular matrix-modified chitosan hydrogels for cartilage tissue engineering. *ACS Appl Mater Interfaces*. 2014;6(22):20110-20121. doi: 10.1021/am505723k

40. Ren X, Wang F, Chen C, Gong X, Yin L, Yang L. Engineering zonal cartilage through bioprinting collagen type II hydrogel constructs with biomimetic chondrocyte density gradient. *BMC Musculoskeletal Disord*. 2016;17(1):301. doi: 10.1186/s12891-016-1130-8

41. Gibney R, Ferraris E. Bioprinting of collagen Type I and II via aerosol jet printing for the replication of dense collagenous tissues. original research. *Front Bioeng Biotechnol*. 2021;9: 786945. doi: 10.3389/fbioe.2021.786945

42. Eviana Putri NR, Wang X, Chen Y, Li X, Kawazoe N, Chen G. Preparation of PLGA-collagen hybrid scaffolds with controlled pore structures for cartilage tissue engineering. *Prog Nat Sci Mater Int*. 2020;30(5):642-650. doi: 10.1016/j.pnsc.2020.07.003

43. Cheng A, Schwartz Z, Kahn A, et al. Advances in porous scaffold design for bone and cartilage tissue engineering and regeneration. *Tissue Eng Part B Rev*. 2019;25(1):14-29. doi: 10.1089/ten.teb.2018.0119

44. Zhang Q, Lu H, Kawazoe N, Chen G. Preparation of collagen scaffolds with controlled pore structures and improved mechanical property for cartilage tissue engineering. *J Bioactive Compat Polym*. 2013;28(5):426-438. doi: 10.1177/0883911513494620

45. Harley BAC, Kim H-D, Zaman MH, Yannas IV, Lauffenburger DA, Gibson LJ. Microarchitecture of three-dimensional scaffolds influences cell migration behavior via junction interactions. *Biophys J*. 2008;95(8):4013-4024. doi: 10.1529/biophysj.107.122598

46. Bai Y, Gong X, Dou C, Cao Z, Dong S. Redox control of chondrocyte differentiation and chondrogenesis. *Free Radic Biol Med*. 2019;132:83-89. doi: 10.1016/j.freeradbiomed.2018.10.443

47. Di Luca A, Szlazak K, Lorenzo-Moldero I, et al. Influencing chondrogenic differentiation of human mesenchymal stromal cells in scaffolds displaying a structural gradient in pore size. *Acta Biomater*. 2016;36:210-219. doi: 10.1016/j.actbio.2016.03.014

48. Sun Y, Wu Q, Zhang Y, Dai K, Wei Y. 3D-bioprinted gradient-structured scaffold generates anisotropic cartilage with vascularization by pore-size-dependent activation of HIF1α/FAK signaling axis. *Nanomedicine*. 2021;37:102426. doi: 10.1016/j.nano.2021.102426

49. Luo C, Wang C, Wu X, et al. Influence of porous tantalum scaffold pore size on osteogenesis and osteointegration: a comprehensive study based on 3D-printing technology. *Mater Sci Eng C Mater Biol Appl*. 2021;129:112382. doi: 10.1016/j.msec.2021.112382

50. Mahzoon S, Detamore MS. Chondroinductive peptides: drawing inspirations from cell–matrix interactions. *Tissue Eng Part B Rev*. 2019;25(3):249-257. doi: 10.1089/ten.teb.2018.0003

51. Asgarpour K, Shojaei Z, Amiri F, et al. Exosomal microRNAs derived from mesenchymal stem cells: cell-to-cell messages. *Cell Commun Signal*. 2020;18(1):149. doi: 10.1186/s12964-020-00650-6

52. Kwon H, Paschos NK, Hu JC, Athanasiou K. Articular cartilage tissue engineering: the role of signaling molecules. *Cell Mol Life Sci*. 2016;73(6):1173-1194. doi: 10.1007/s00018-015-2115-8

53. Chen L, Liu J, Guan M, Zhou T, Duan X, Xiang Z. Growth factor and its polymer scaffold-based delivery system for cartilage tissue engineering. *Int J Nanomed*. 2020;15: 6097-6111. doi: 10.2147/IJN.S249829

54. Lee C-R, Grodzinsky A, Spector M. Biosynthetic response of passaged chondrocytes in a type II collagen scaffold to mechanical compression. *J Biomed Mater Res A*. 2003;64(3):560-569.
doi: 10.1002/jbm.a.10443

55. Li Y, Liu Y, Li R, et al. Collagen-based biomaterials for bone tissue engineering. *Mater Design*. 2021;210:110049.
doi: 10.1016/j.matdes.2021.110049

56. Shields KJ, Beckman MJ, Bowlin GL, Wayne JS. Mechanical properties and cellular proliferation of electrospun collagen type II. *Tissue Eng*. 2004;10(9-10):1510-1517.
doi: 10.1089/ten.2004.10.1510

57. Jang J-W, Min K-E, Kim C, Shin J, Lee J, Yi S. Review: scaffold characteristics, fabrication methods, and biomaterials for the bone tissue engineering. *Int J Precision Eng Manuf*. 2023;24(3):511-529.
doi: 10.1007/s12541-022-00755-7

58. Koo E, Choi E-J, Lee J, Kim H, Kim G, Do S-H. 3D printed cell-laden collagen and hybrid scaffolds for in vivo articular cartilage tissue regeneration. *J Ind Eng Chem*. 2018;66: 343-355.
doi: 10.1016/j.jiec.2018.05.049

59. Maihemuti A, Zhang H, Lin X, et al. 3D-printed fish gelatin scaffolds for cartilage tissue engineering. *Bioact Mater*. 2023;26:77-87.
doi: 10.1016/j.bioactmat.2023.02.007

60. Nocera AD, Comín R, Salvatierra NA, Cid MP. Development of 3D printed fibrillar collagen scaffold for tissue engineering. *Biomed Microdevices*. 2018;20(2):26.
doi: 10.1007/s10544-018-0270-z

61. Marques CF, Diogo GS, Pina S, Oliveira JM, Silva TH, Reis RL. Collagen-based bioinks for hard tissue engineering applications: a comprehensive review. *J Mater Sci Mater Med*. 2019;30(3):32.
doi: 10.1007/s10856-019-6234-x

62. Diao J, OuYang J, Deng T, et al. 3D-plotted beta-tricalcium phosphate scaffolds with smaller pore sizes improve in vivo bone regeneration and biomechanical properties in a critical-sized calvarial defect rat model. *Adv Healthc Mater*. 2018;7(17):e1800441.
doi: 10.1002/adhm.201800441

63. Cacopardo L, Guazzelli N, Nossa R, Mattei G, Ahluwalia A. Engineering hydrogel viscoelasticity. *J Mech Behav Biomed Mater*. 2019;89:162-167.
doi: 10.1016/j.jmbbm.2018.09.031

64. Vining KH, Stafford A, Mooney DJ. Sequential modes of crosslinking tune viscoelasticity of cell-instructive hydrogels. *Biomaterials*. 2019;188:187-197.
doi: 10.1016/j.biomaterials.2018.10.013

65. Ma Y, Han T, Yang Q, et al. Viscoelastic cell microenvironment: hydrogel-based strategy for recapitulating dynamic ECM mechanics. *Adv Funct Mater*. 2021;31(24):2100848.
doi: 10.1002/adfm.202100848

66. Oh SH, Lee JH. Hydrophilization of synthetic biodegradable polymer scaffolds for improved cell/tissue compatibility. *Biomed Mater*. 2013;8(1):014101.
doi: 10.1088/1748-6041/8/1/014101

67. Wang W, Caetano G, Ambler WS, et al. Enhancing the hydrophilicity and cell attachment of 3D printed PCL/ Graphene scaffolds for bone tissue engineering. *Materials (Basel)*. 2016;9(12):992.
doi: 10.3390/ma9120992

68. Chollet C, Lazare S, Guillemot F, Durrieu MC. Impact of RGD micro-patterns on cell adhesion. *Colloids Surf B Biointerfaces*. 2010;75(1):107-114.
doi: 10.1016/j.colsurfb.2009.08.024

69. Wu S-C, Chang W-H, Dong G-C, Chen K-Y, Chen Y-S, Yao C-H. Cell adhesion and proliferation enhancement by gelatin nanofiber scaffolds. *J Bioactive Compatible Polyms*. 2011;26(6):565-577.
doi: 10.1177/0883911511423563

70. Steward AJ, Liu Y, Wagner DR. Engineering cell attachments to scaffolds in cartilage tissue engineering. *JOM*. 2011;63(4):74-82.
doi: 10.1007/s11837-011-0062-x

71. Padhi A, Nain AS. ECM in Differentiation: a review of matrix structure, composition and mechanical properties. *Ann Biomed Eng*. 2020;48(3):1071-1089.
doi: 10.1007/s10439-019-02337-7

72. Ross JJ, Tranquillo RT. ECM gene expression correlates with in vitro tissue growth and development in fibrin gel remodeled by neonatal smooth muscle cells. *Matrix Biol*. 2003;22(6):477-490.
doi: 10.1016/S0945-053X(03)00078-7

73. Kjaer M. Role of extracellular matrix in adaptation of tendon and skeletal muscle to mechanical loading. *Physiol Rev*. 2004;84(2):649-698.
doi: 10.1152/physrev.00031.2003

74. Ho-Shui-Ling A, Bolander J, Rustom LE, Johnson AW, Luyten FP, Picart C. Bone regeneration strategies: engineered scaffolds, bioactive molecules and stem cells current stage and future perspectives. *Biomaterials*. 2018;180:143-162.
doi: 10.1016/j.biomaterials.2018.07.017

75. Andreaus U, Giorgio I, Madeo A. Modeling of the interaction between bone tissue and resorbable biomaterial as linear elastic materials with voids. *Z Angew Math Phys*. 2015;66(1):209-237.
doi: 10.1007/s00033-014-0403-z

ACCSCIENCE PUBLISHING

International Journal of Bioprinting

RESEARCH ARTICLE

Double-protein-loaded 3D-printed polyetheretherketone cage for promoting interbody fusion via osteogenic differentiation

Feng Zheng[1,2†], Xiaoqiang Gao[1†], Sheng Chai[2†], Haibin Lin[1*], and Huan Liu[3*]

[1]Department of Orthopedics, Affiliated Hospital of Putian University, Putian, Fujian, China

[2]The School of Clinical Medicine, Fujian Medical University, Fuzhou, Fujian, China

[3]Department of Orthopedics, The Affiliated Traditional Chinese Medicine Hospital, Southwest Medical University, Luzhou, Sichuan, China

Abstract

Intervertebral disc degeneration (IDD) is a common condition characterized by age-related wear and tear of the spine. In advanced stages or severe cases of IDD, surgical treatment involving the implantation of an interbody cage is often the primary treatment approach. Polyetheretherketone (PEEK) has been widely used in orthopedic and spinal implants due to its remarkable mechanical properties, biocompatibility, and corrosion resistance. However, when used in interbody cages, PEEK exhibits poor processability and biological inertness, which are significant disadvantages that need to be addressed. In this work, we first fabricated the PEEK cage via the fused deposition modeling (FDM) method. To improve its fusion effect, bone morphogenetic protein 2 (BMP2) was loaded onto sulfonated PEEK and sealed with gelatin/chitosan (Gel/Chi) multilayer films. Substance P was then grafted on the surface with a Schiff base. When the cage is implanted, substance P is released first, recruiting bone marrow-mesenchymal stem cells (MSCs) to the implant surface. Subsequently, upon degradation of the Gel/Chi multilayer films, BMP2 is slowly released and promotes osteogenic differentiation of MSCs. *In vivo* results revealed that the double-protein-loaded PEEK cage exhibited remarkable fusion effects. This work provides a novel approach for the design and fabrication of a PEEK intervertebral fusion device with an excellent fusion effect.

Keywords: Polyetheretherketone; 3D printing; Interbody cage; Mesenchymal stem cell recruitment

†These authors contributed equally to this work.

***Corresponding authors:**
Haibin Lin (fsyy@ptu.edu.cn)

Huan Liu (huanliu@swmu.edu.cn)

Citation: Zheng F, Gao X, Chai S, Lin H, Liu H. Double-protein-loaded 3D-printed polyetheretherketone cage for promoting interbody fusion via osteogenic differentiation. *Int J Bioprint*. 2024;10(5):3574. doi: 10.36922/ijb.3574

Received: May 5, 2024
Accepted: June 14, 2024
Published Online: July 29, 2024

Copyright: © 2024 Author(s). This is an Open Access article distributed under the terms of the Creative Commons Attribution License, permitting distribution, and reproduction in any medium, provided the original work is properly cited.

Publisher's Note: AccScience Publishing remains neutral with regard to jurisdictional claims in published maps and institutional affiliations.

1. Introduction

Intervertebral disc degeneration (IDD) is an age-related disease of the spine. Its clinical manifestations involve the gradual breakdown or deterioration of structures in the lumbar spine.[1,2] The early stages of IDD can be treated with conservative management, including physical therapy, physical interventions, and pain management.[3–5] However, in advanced stages or severe cases of IDD, surgical treatments, including discectomy, laminectomy, and artificial disc replacement, are often preferred.[6,7] Interbody cages, one of the most commonly used artificial disc devices, are placed between two adjacent

vertebrae, typically in the disc space, to restore disc height and facilitate fusion. Currently, most interbody fusion devices used in clinical practice are made of titanium alloy (Ti) or polyetheretherketone (PEEK).[8,9]

Polyetheretherketone (PEEK) is a high-performance polymer that has found various applications in the medical field, including bone repair. Unlike other bone repair materials, PEEK has mechanical properties similar to the human bone, which helps minimize stress shielding and bone resorption caused by a high modulus of elasticity.[10] Moreover, PEEK features good biocompatibility, radiolucency, and corrosion resistance, making it highly suitable for widespread use in orthopedic and spinal implants.[11,12] PEEK has several advantageous properties for bone repair applications, but it also has some inadequacies and challenges that need to be considered. These challenges include processing difficulties, its bioinert nature, and weak osteointegration capabilities.[13,14] Due to its thermoplastic nature, it is difficult to process PEEK into complex shapes. Therefore, 3D printing technology is an appropriate method for achieving precise and consistent manufacturing, especially for the production of intricate implants. Although the bioinert property of PEEK is advantageous for reducing inflammatory responses, it may restrict its capacity to actively regulate immune response and promote bone regeneration.[15] It has been observed that using pure PEEK for interbody fusion without autograft increases the occurrence of lumbar isthmic spondylolisthesis.[16]

Fused deposition modeling (FDM) is a material extrusion-based 3D printing process that is widely adopted for fabricating high-performance polymer components with complex geometries, particularly for clinical applications.[17] PEEK filament is heated to its melting point within the nozzle of the 3D printer and subsequently extruded layer-by-layer (LBL) to fabricate the desired structure. The mechanical properties of 3D-printed PEEK can be influenced by various parameters, including heating temperature (extrusion temperature and ambient temperature), filling rate, and construction direction.[18,19]

Bone morphogenetic protein 2 (BMP2) is a protein that belongs to the transforming growth factor-β (TGF-β) superfamily. It plays a crucial role in bone development, regeneration, and repair by inducing bone formation. BMP2 promotes the differentiation of mesenchymal stem cells (MSCs) into osteoblasts, which are responsible for producing bone matrix and initiating the mineralization process.[20,21] This process is crucial for the development of new bone tissue. BMP2 has been highly effective in promoting spinal fusion by enhancing bone growth between vertebrae, thereby stabilizing the spine and accelerating the fusion process.[22] Maintaining the biological activity and long-term release of BMP2 is a key issue when used in spinal fusion.

Substance P (SP) is a neuropeptide belonging to the tachykinin family, originally isolated from extracts of intestinal tissues.[23] It has a sequence composed of a chain of 11 amino acid residues: Arg-Pro-Lys-Pro-Gln-Gln-Phe-Phe-Gly-Leu-Met-NH_2.[24] SP was first discovered in 1931 and is widely distributed throughout the peripheral and central nervous systems, where it functions mainly as a pain signaling transmitter.[25] Meanwhile, SP acts as a chemoattractant and activator for macrophages, lymphocytes, neutrophils, and eosinophils.[26] The role of SP in inflammation and skeletal system diseases has been extensively debated. Some research has indicated that SP produces a variety of proinflammatory effects by binding and activating the NK-1 receptor (NK-1R) on target cells.[27] Conversely, some researchers suggest that supplementing MSCs with SP increases the secretion of paracrine/angiogenic factors, such as VEGF, SDF-1a, and PDGF-BB, *in vitro*.[28] It is believed that SP can restore the cellular potential of senescent stem cells by modulating the generation of paracrine factors from MSCs, potentially enhancing MSC-mediated tissue repair. Additionally, studies have demonstrated that SP can recruit endogenous MSCs to facilitate bone healing.[29,30]

To prepare a novel intervertebral fusion device, we initially scanned and performed a 3D reconstruction of rabbit intervertebral discs. Thereafter, we fabricated the device via FDM. As displayed in Figure 1, sulfonation treatment was applied to create a network of porous structures on the surface, enhancing its fusion effect. This increases surface roughness and creates a reservoir for BMP2. The resulting structure has the potential for improved bone repair. To achieve long-term release of BMP2, gelatin (Gel) and chitosan (Chi) multilayer films were coated via LBL self-assembly. SP was grafted onto the outermost Chi layer through a Schiff base reaction. Upon implantation of the modified PEEK, SP is released first, attracting more MSCs to the implant. Subsequently, BMP2 is slowly released to promote osteogenic differentiation of MSCs and enhance bone repair. *In vitro* and *in vivo* experiments were conducted to evaluate the fusion effect.

2. Materials and methods

2.1. Materials

Medical grade PEEK powder was provided by Beijing YUNS Technology Co., Ltd. (China). BMP2 was purchased from Zhong Ke Wu Yuan Biotechnology Co., Ltd. (China). SP was purchased from Aladdin Industrial Co. (China). Chi (with aldehyde groups) and Gel were purchased from ZiKER Biotechnology Co., Ltd. (China). Alkaline phosphatase

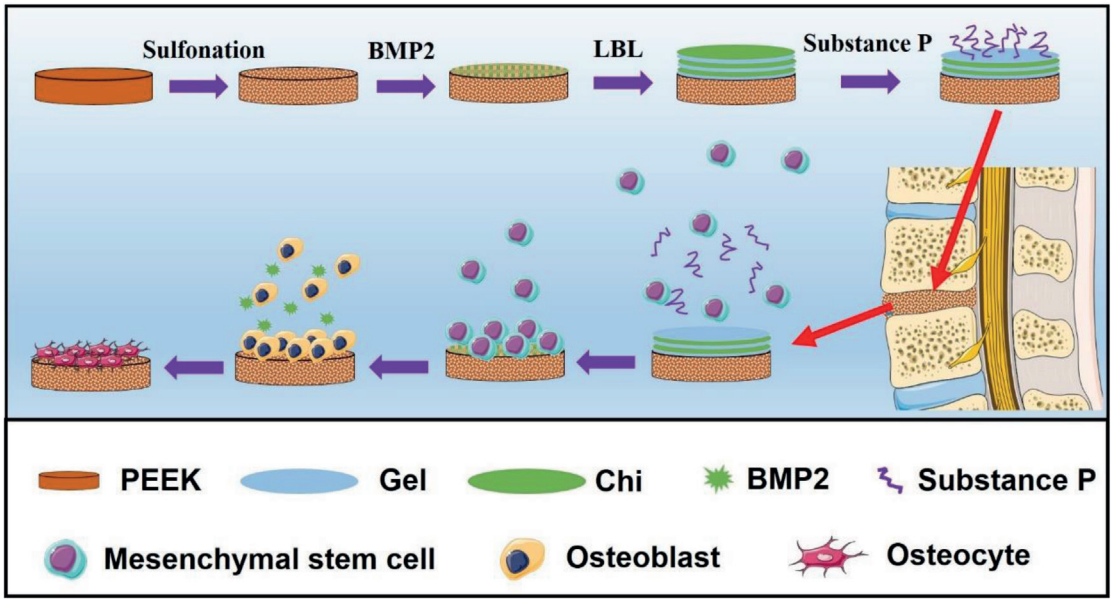


Figure 1. Design and preparation of modified polyetheretherketone (PEEK) via layer-by-layer (LBL) self-assembly, and its functions after implantation. Abbreviations: BMP2, bone morphogenetic protein 2; Chi, chitosan; Gel, gelatin.

(ALP) activity detection kit, ALP color development kit, Cycein red dye, and Triton X-100 were obtained from Sigma-Aldrich (United States of America [USA]). Cell counting kit-8 (CCK-8) was obtained from Beyotime (China). Sirius Red staining solution was purchased from Sollebo (China). An RNA extraction kit was purchased from Bioteck (USA). An RNA reverse transcription kit was purchased from Takara-Bio Corporation (Japan).

2.2. Sample preparation

The PEEK sample was fabricated by Beijing YUNS Technology Co., Ltd. using a fused filament fabrication (FFF) 3D printer (miniFactory Ultra). The print parameters are listed in Table S1, Supporting information. Figure S1, Supporting Information displays the samples designed based on the vertebral structure (P). The head of the sample was designed as a triangle, making implantation more convenient than traditional interbody fusion devices.

To achieve a porous structure on the surface of the PEEK sample, we treated the samples with concentrated sulfuric acid at room temperature, followed by immersion in deionized water. The resulting samples were then hydrothermally treated at 120°C for 4 h to remove any remaining residues. The samples were labeled as S-P. BMP2 was then dissolved in double-distilled water and spin-coated onto the S-P sample. The resulting samples were labeled as S-P-BMP2.

The Gel/Chi multilayer films were prepared using the LBL method on a clean bench. Firstly, 10 mL of Gel solution (5 mg/mL in distilled water) was added to the surface of the S-P-BMP2 sample and rotated for 20 s using a spin-coater. Thereafter, 10 μL of Chi solution (5 mg/mL in distilled water, pH 5.5) was added and rotated for 20 s. This process was repeated five times to obtain S-P-BMP2/LBL. Finally, SP was deposited onto the S-P-BMP2/LBL surface. To reduce the burst release of SP, a gel solution was added to the surface and rotated for 20 s. The resulting sample was named S-P-BMP2/LBL-SP.

2.3. Sample characterization

The morphology and roughness of the samples were characterized by observing their surfaces using field emission scanning electron microscopy (SEM; FEI Nova 400 Nano SEM; Phillips Co, Holland) and atomic force microscopy (AFM; Dimension; Bruker, Germany). The hydrophilicity and hydrophobicity of the samples were analyzed by measuring their water contact angles.

2.4. Release behavior of BMP2 and substance P

To examine the release profile of the embedded peptide, fluorescein isothiocyanate (FITC; Solarbio, China) was used to label SP (FITC@SP) following the protocol outlined in a previous study.[31] The supernatant was extracted at different time intervals after immersing the samples in phosphate-buffered saline (PBS; Solarbio, China). The release behavior of SP was monitored based on FITC fluorescence measurements using a fluorescence spectrophotometer (RF-6000; Shimadzu, Japan). BMP2 was labeled with a red fluorescent protein (RFP; Bioss, China), and its release behavior was detected using the same method described above.

2.5. Mobility assessment of mesenchymal stem cells

The migration capacity of MSCs was assessed using the transwell assay. A 24-well transwell chamber (pore size: 8 mm; Corning, China) was used to evaluate the effect of different samples on the migration of MSCs. Approximately 1×10^4 cells were seeded in the upper chamber, and samples with different coatings were placed in the bottle chamber and immersed in 600 mL of medium supplemented with 1% fetal bovine serum (FBS; ExCell, China). After 12 and 24 h of incubation, non-migrated MSCs in the upper chamber were gently removed with a cotton swab. The remaining MSCs were treated with 4% paraformaldehyde (Sigma, USA) and stained with 0.1% crystal violet solution (Glpbio, USA). Each group (n = 4) was imaged using an Olympus inverted microscope (Olympus, Japan), and cell migration capacity is determined from the mean number of stained cells.

2.6. Cell viability assay

MSCs were seeded on the surface of each sample and processed for fluorescein diacetate/propyl iodide (FDA/PI) staining and CCK-8 experiments after 4 and 7 days of incubation. The media of different samples were washed with PBS, and the working solution was added to the different samples. When the FDA/PI solution was used, the samples had to be incubated for 10 min and subsequently photographed using a fluorescence microscope (Olympus, Japan). For the CCK-8 experiment, we had to determine the absorbance value (optical density [OD]) at 450 nm using a spectrophotometric microplate reader (Thermo Fisher, USA). The OD value is directly proportional to the cell activity.

2.7. Osteogenic response of mesenchymal stem cells

In this study, MSCs were cultured by conditional culture. The chromogenic and activity detection of ALP, collagen secretion detection, and mineralization detection were performed. MSCs were co-cultured for 4 and 7 days, respectively. The BCIP/NBT ALP kit was used for qualitative observation. The MicroBCA Protein Assay Kit (Abcam, UK) and the p-nitrophenyl phosphate assay kit (Millipore, USA) were employed for quantitative analysis.

2.8. Collagen secretion assay

MSCs were co-cultured for 14 days. Sirius Red was used to stain the various samples for qualitative observation of collagen secretion. Thereafter, 1 mM NaOH was used to treat stained samples for quantitative analysis. Finally, collagen secretion was measured at an OD value of 540 nm using a spectrophotometric microplate reader (Thermo Fisher, USA).

2.9. Mineralization assay

MSCs were co-cultured for 14 days. Alizarin Red (Glpbio, USA) working solution (pH 4.1) was applied to stain the samples for 20 min for qualitative observation. Acetic acid solution (10% [v/v]) (Southwest, China) and ammonia solution (10% [v/v]) (Southwest, China) were then used to treat the stained samples. Finally, the mineralization of MSCs was measured at an OD value of 405 nm using a spectrophotometric microplate reader (Thermo Fisher, USA).

2.10. Osteogenesis-related gene expression

The osteogenesis-related gene expression of MSCs was evaluated by quantitative reverse-transcription polymerase chain reaction (qRT-PCR). MSCs were seeded on the surface of different samples and after 3 days of incubation, qRT-PCR experiments were performed. The cells were lysed with TRK lysate and then centrifuged for RNA extraction. The mRNA concentration of each sample was then determined using a NanoDrop 2000 Spectrophotometer (Thermo Fisher, USA). The reagent was then removed from the frozen Takara PrimeScript RT Reagent Kit with gDNA Eraser (Takara, Japan) and thawed on the ice box. The RNA obtained was reverse transcribed into cDNA using the kit. The expression of genes (*ALP*, *COLI*, *OCN*, *OPN*, *OPG*, and *RUNX2*) was quantified using a qPCR instrument (Bio-Rad, USA), and the primers of osteogenesis-related genes are listed in Table 1.

2.11. *In vivo* animal evaluation

New Zealand white rabbits (6 months old; n = 16) were randomly divided into four groups, and the nucleus pulposus in the L4/5 intervertebral disc was removed from the rabbits in all groups. Subsequently, different PEEK cages were implanted into the L4/5 intervertebral disc for 2 months. All animal experiments were approved by the Experimental Animal Ethics Committee of Southwest Medical University (approval number: 20230228-013). After 2 months, the L4 and L5 vertebral bodies were sectioned to assess the interbody fusion effect using micro-computed tomography (CT) (PerkinElmer, USA) and the push-out test using an electronic static material testing system (Instron, UK).

2.12. Statistical analysis

Data are presented as mean ± standard deviation. One-way analysis of variance (ANOVA) and student's t-test were performed to determine the statistical significance of the data, i.e., $^*p < 0.05$; $^{**}p < 0.01$; and $^{***}p < 0.001$.

3. Results

3.1. Sample characterization

Substance P (SP) is a peptide composed of a chain of 11 amino acid residues in its sequence. To graft SP onto Gel/Chi multilayer films and maintain its bioactivity, a Schiff base reaction utilizing chitosan with an aldehyde group

Table 1. Primers for osteogenesis-related genes

Target gene	Primers	
	Forward (5'–3')	Reverse (5'–3')
ACTB	ATTTCTGAATGGCCCAGGT	CTGCCTCAACACCTCAACC
GAPDH	GCTCTCCAGAACATCATCC	TGCTTCACCACCTTCTTG
RUNX2	GCCGTAGAGAGCAGGGAAGAC	CTGGCTTGGATTAGGGAGTCAC
ALP	AGCGACACGGACAAGAAGC	GGCAAAGACCGCCACATC
COLI	CCTGAGCCAGCAGATTGA	TCCGCTCTTCCAGTCAG
OCN	GAGGGCAGTAAGGTGGTGAA	COTCCTGGAAGCCAATGTG
OPN	GACAGCAACGGGAAGACC	CAGGCTGGCTTTGGAACT
OPG	GCCCAGACGAGATTGAGAG	CAGACTGTGGGTGACGGTT

Abbreviations: *ACTB*, Actin-β; *ALP*, Alkaline phosphatase; *COLI*, Collagen type I; *GAPDH*, Glyceraldehyde 3-phosphate dehydrogenase; *OCN*, Osteocalcin; *OPN*, Osteopontin; *OPG*, Osteoprotegerin; *RUNX2*, Runt-related transcription factor 2.

was employed (Figure 2A). The surface topographies of PEEK after each treatment were notably altered (Figure 2B). Before treatment, PEEK displayed a smooth surface, with minor lines due to FDM. However, a porous network structure appeared on the PEEK surface after sulfonation that can be used as a storage pool for BMP2. No obvious change was observed in the surface network structure of PEEK after loading with BMP2. However, after LBL coating with Gel/Chi multilayer films, the porous network structure became less distinct, and the surface was further smoothed after grafting with SP. The surface roughness of different samples was evaluated with AFM. The results (Figure 2D and E) displayed a similar trend with SEM. S-P and S-P-BMP2 have the highest surface roughness due to sulfonation. However, after coating with Gel/Chi multilayer films, the surface roughness decreased significantly.

The water contact angle was used to evaluate the hydrophilicity of PEEK after each treatment process. The results indicated that 3D-printed PEEK exhibited poorer hydrophilicity even after treatment with sulfonation and loading with BMP2. However, its hydrophilicity could be improved by coating with Gel/Chi multilayer films due to the good hydrophilicity of gelatin. Previous studies have demonstrated that good hydrophilicity and appropriate roughness of the material surface could enhance its bioactivity. Furthermore, changes in the water contact angle confirmed that the modified BMP2/SP-loaded PEEK was successfully prepared (Figure 2C).

3.2. Cytocompatibility assay *in vitro*

To determine the cytocompatibility of different samples, we evaluated the cell viability and morphology of MSCs. Figure 3A and C indicates that pure 3D-printed PEEK has good cytoactivity, with the absence of dead cells on its surface. However, after sulfonation, the S-P group reported the poorest cytoactivity after days 4 and 7 of culture, possibly due to the residual sulfuric acid. Furthermore, after BMP2-loading and sealing with Gel/Chi multilayer films, cell viability in S-P-BMP2/LBL was greatly enhanced. Additionally, the cytocompatibility of S-P-BMP2/LBL-SP was further improved after being grafted with recruiting protein P. Notably, cell distribution on the surface of S-P appeared stripy, which may be attributed to the line path of extruding and stacking PEEK during the FDM 3D printing process. Sulfonation treatment accentuated these line paths (Figure 3B), as MSCs tend to grow along them. However, after coating Gel/Chi films, cell distributions on S-P-BMP2/LBL and S-P-BMP2/LBL-SP became less pronounced. These results are highly consistent with the surface roughness observations.

3.3. *In vitro* release of bioactive molecules and recruitment of mesenchymal stem cells

Figure 4A illustrates the cumulative release of BMP2 and the recruiting protein P. The recruiting protein P was released rapidly within the first 72 h, reaching its peak after 120 h. The rapid release of the recruiting protein P facilitates the recruitment of MSCs upon implantation. The transwell assay was used to evaluate the recruitment effects of BMP2, with 1×10^4 MSCs seeded in the upper chamber (Figure 4B). After 12 and 24 h, the migrated MSCs were evaluated using a crystal violet solution. Figure 4C displays the migration of MSCs from the upper chamber onto the surface of PEEK. After 12 h, more MSCs were found on the surfaces of S-P-BMP2/LBL and S-P-BMP2/LBL-SP, particularly evident in the S-P-BMP2/LBL-SP group (Figure 4C). This tendency became more pronounced after 24 h, with a remarkable interconnected network of purple MSCs and an increase in cell numbers (Figure 4D). The results in Figure 3 indicate that the sulfonation treatment group has the

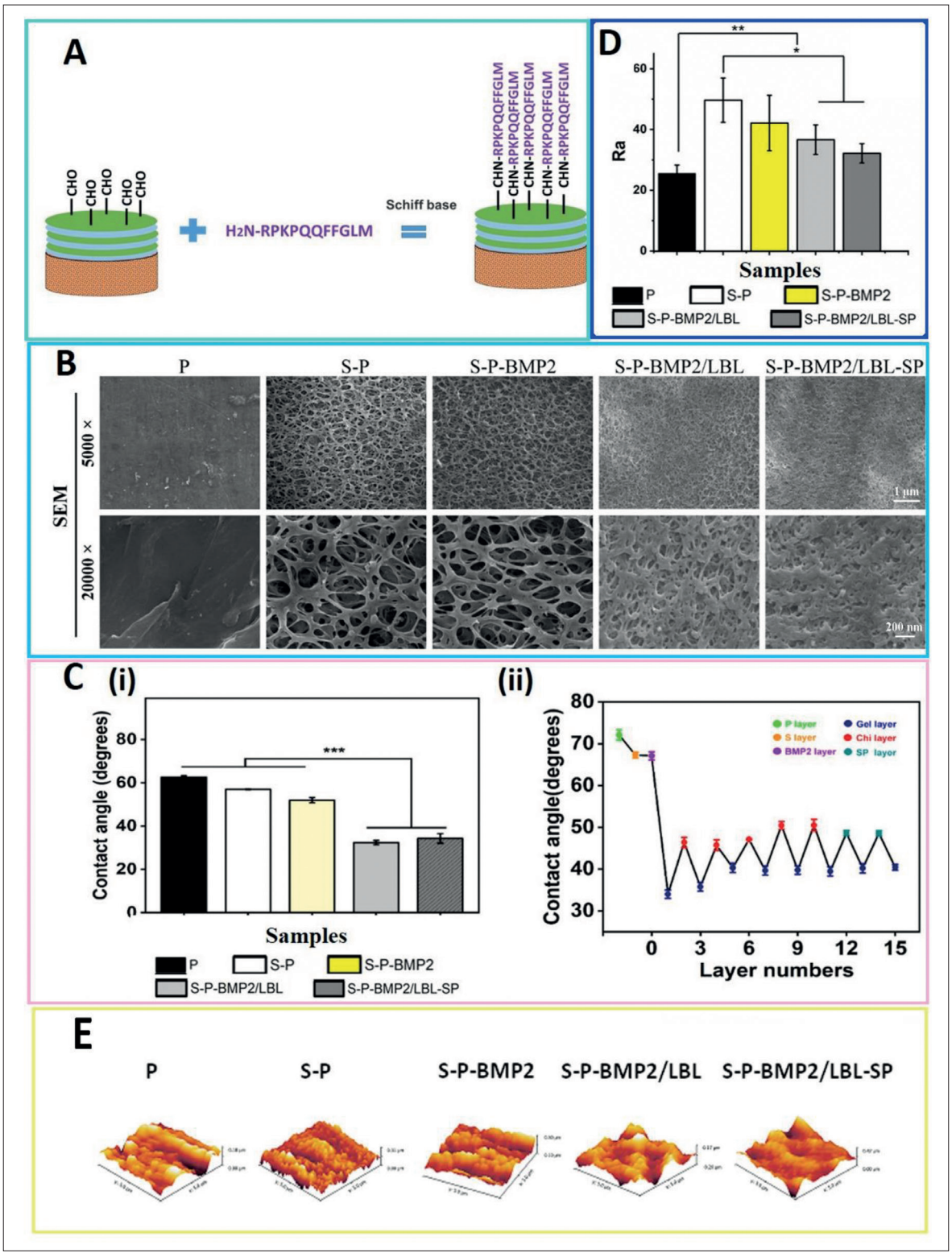


Figure 2. Preparation methods and material characterization. (A) Illustration of substance P grafted to aldehyde-containing chitosan via Schiff base reaction. (B) Scanning electron microscopy (SEM) images of different samples. (C) Water contact angle of (C, i) different samples and (C, ii) different layers. Abbreviation: BMP2, bone morphogenetic protein 2; Chi, Chitosan; Gel, Gelatin; P, Polyetheretherketone; S, Sulfonation; SP, Substance P. (D) Surface roughness (Ra) of different samples. (E) Atomic force microscopy (AFM) images of different samples. Magnification: ×5000 (B, top); ×20000 (B, bottom). Scale bars: 1 μm (B, top); 200 nm (B, bottom). *$p < 0.05$; **$p < 0.01$; ***$p < 0.001$.

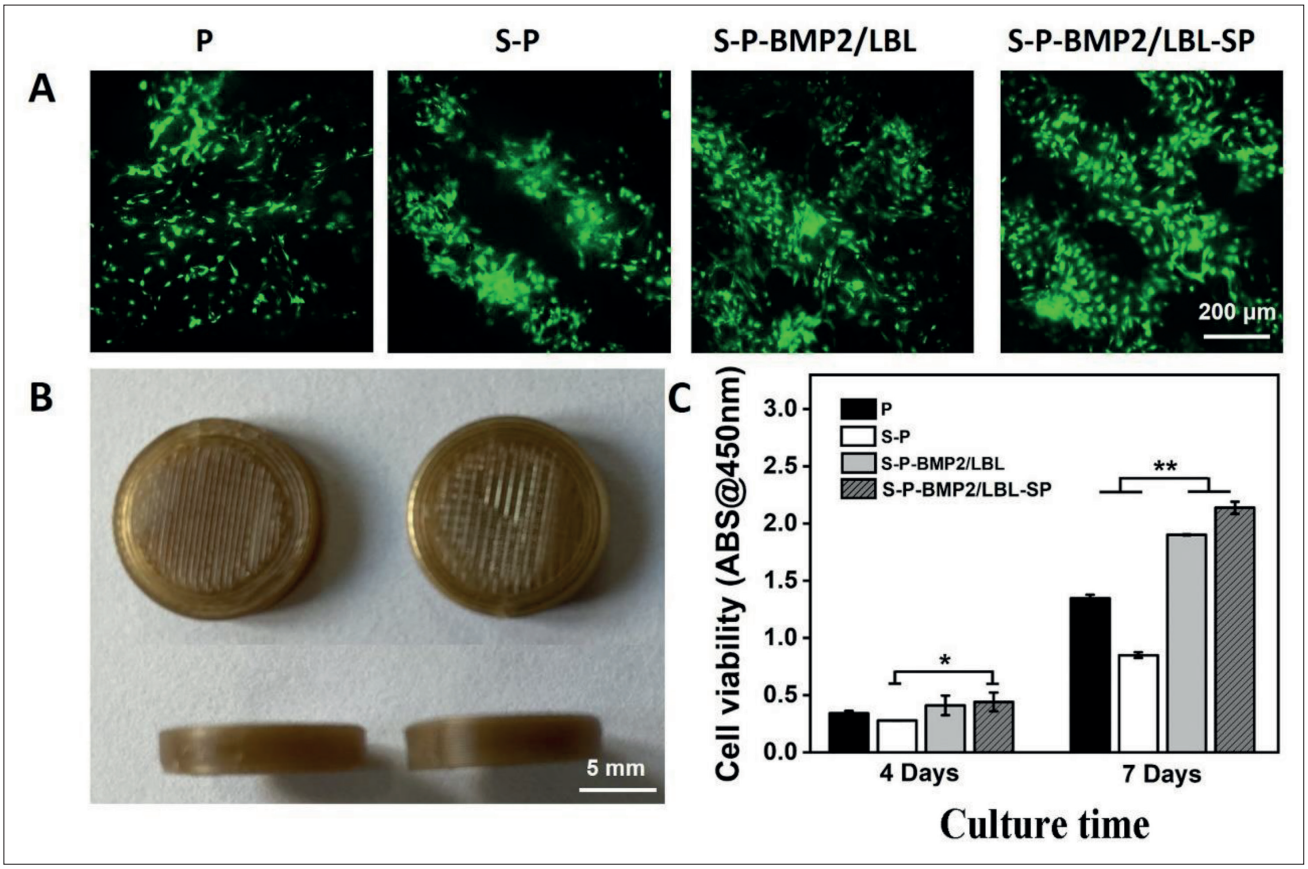


Figure 3. Cell viability evaluation. (A) Live/dead staining of mesenchymal stem cells (MSCs) on different surfaces. Scale bars: 200 μm. (B) Image of the 3D-printed polyetheretherketone (PEEK) cages. Scale bars: 5 mm. (C) Viability of MSCs after co-culturing with different samples. *$p < 0.05$; **$p < 0.01$. Abbreviation: ABS, absorbance.

poorest cell recruitment ability. The release of BMP2 was slower but reached the highest amount after 240 h. The order of release of the recruiting protein P and BMP2 could meet the repair needs of PEEK implantation.

3.4. Evaluation of osteogenic differentiation of mesenchymal stem cells

The osteogenic differentiation potential of MSCs was evaluated based on ALP activity, collagen secretion, and ECM mineralization. Figure 5 indicates that there were more ALP staining nodules on the S-P-BMP2/LBL and S-P-BMP2/LBL-SP surfaces, suggesting enhanced early osteogenic differentiation. Additionally, the effect on mid- and late-stage osteogenic differentiation of MSCs was evaluated using Sirius Red and Alizarin Red staining. The staining results indicate that the S-P-BMP2/LBL and S-P-BMP2/LBL-SP exhibit higher levels of collagen secretion and ECM mineralization in MSCs. The osteogenic differentiation results suggest that S-P-BMP2/LBL-SP has the greatest potential for osteogenic differentiation after BMP2-loading and protein P recruitment.

To further investigate osteoblast differentiation at the genetic level, the mRNA expressions of osteoblast-related genes, including *ALP*, *COLI*, *OCN*, *OPN*, *OPG*, and *RUNX2*, were measured after 7 days of culture (Figure 6). It was revealed that the expressions of *ALP*, *COLI*, *OCN*, and *OPN* on S-P-BMP2/LBL and S-P-BMP2/LBL-SP substrates were significantly upregulated.

3.5. *In vivo* results of interbody fusion effect

The interbody fusion effect was evaluated using micro-computed tomography (CT) (Figure 7) and the push-out test (Figure 8). The results of micro-CT indicate that there was almost no new bone formation between the two adjacent cones in the P and S-P groups. However, the interbody fusion effect was more pronounced in the S-P-BMP2/LBL group, characterized by the presence of newly formed bone in the gap between the two adjacent cones. Similar observations were noted for the S-P-BMP2/LBL-SP group.

Figure 8 displays the force–displacement curve for the push-out test. The maximum pushing force was approximately 40 and 70 N for the PEEK and sulfonation

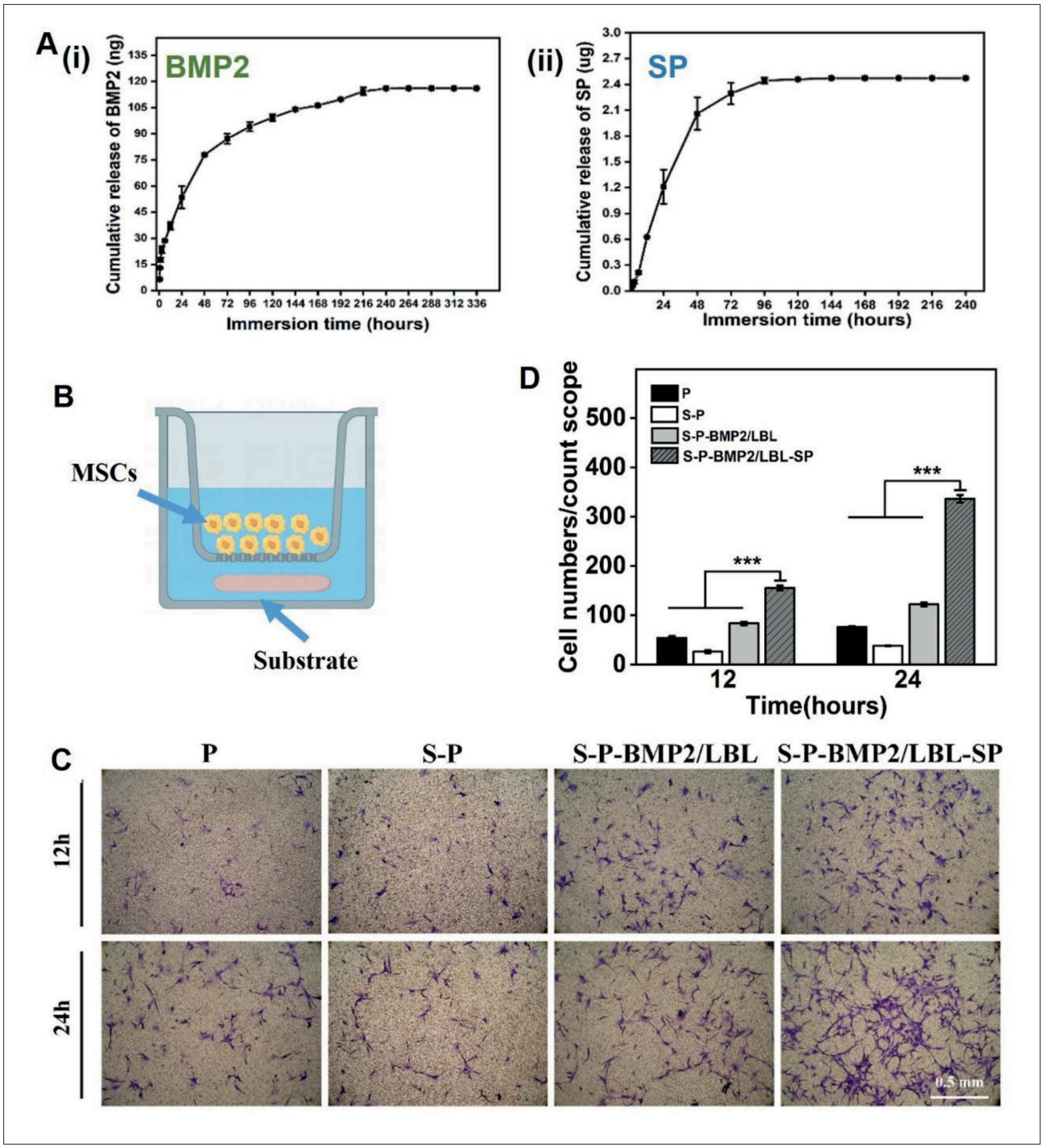


Figure 4. Protein release and cell migration. (A) Cumulative release curves of (i) BMP2 and (ii) Substance P (SP). (B) Illustration of the transwell assay. (C) Crystal violet staining of different samples. (D) Number of migrated mesenchymal stem cells (MSCs) on the surface of different samples. Scale bar: 0.5 mm. ***$p < 0.001$.

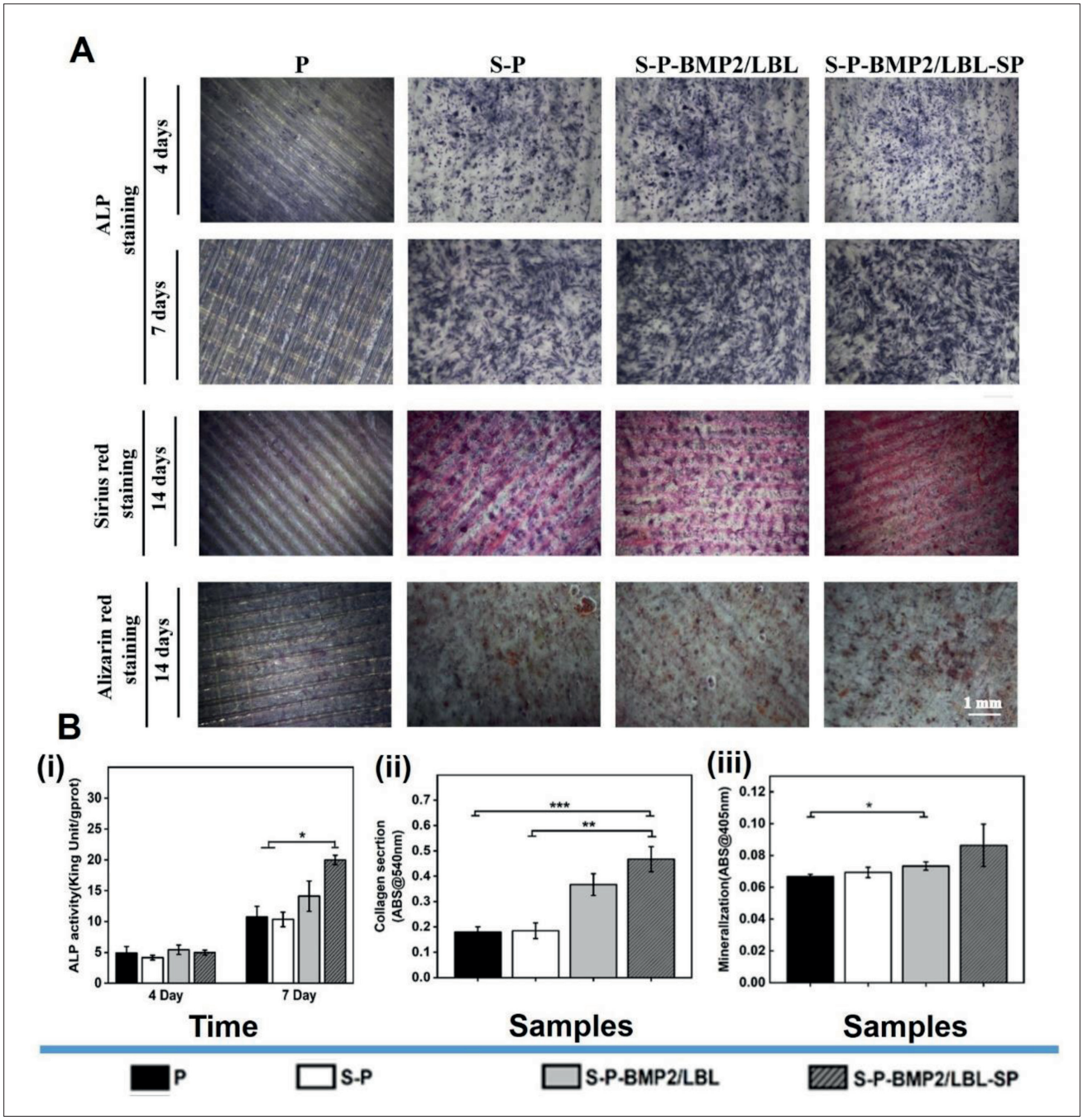


Figure 5. Evaluation of osteogenic differentiation. (A) Alkaline phosphatase (ALP), Sirius Red, and Alizarin Red staining images of mesenchymal stem cells (MSCs). (B) Quantitative analysis of (i) ALP, (ii) collagen, and (iii) mineralization levels of MSCs (n = 4). Scale bar: 1 mm. Abbreviation: ABS, absorbance. $^{*}p < 0.05$; $^{**}p < 0.01$; $^{***}p < 0.001$.

PEEK groups, respectively. However, the maximum pushing force for S-P-BMP2/LBL increased to 160 N, which was further enhanced to 190 N after being grafted with recruiting protein P (S-P-BMP2/LBL-SP). Based on these results, it can be concluded that BMP2-loaded PEEK exhibits a better interbody fusion effect, with the strongest effect observed in the S-P-BMP2/LBL-SP group.

Figure S2 depicts the sclerous tissue section with successful PEEK implantation in the middle of the vertebrae.

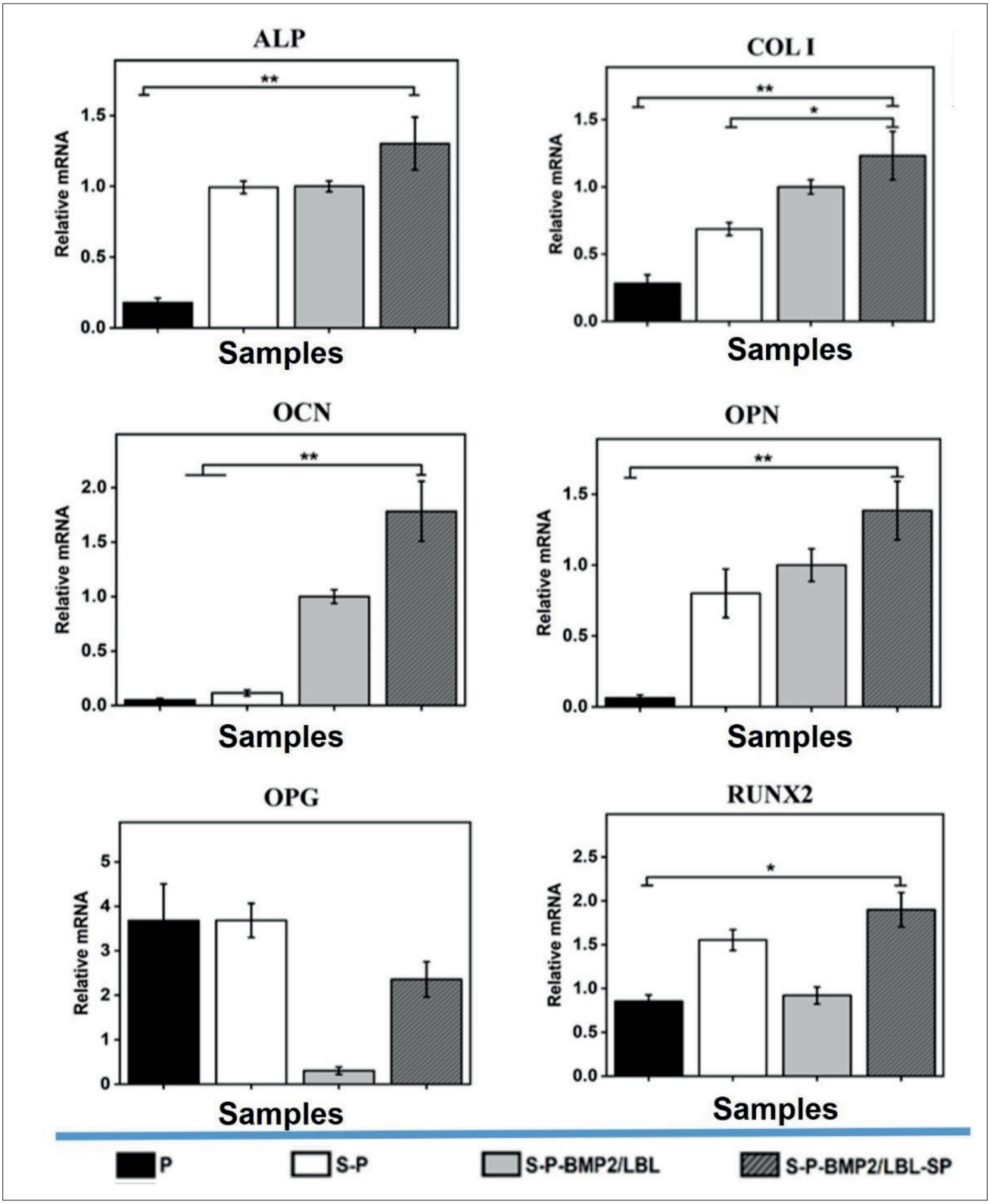


Figure 6. Quantitative reverse transcription polymerase chain reaction (qRT-PCR) results on the gene expressions of alkaline phosphatase (*ALP*), collagen type I (*COLI*), osteocalcin (*OCN*), osteopontin (*OPN*), osteoprotegerin (*OPG*), and runt-related transcription factor 2 (*RUNX2*) ($n = 5$). *$p < 0.05$; **$p < 0.01$.

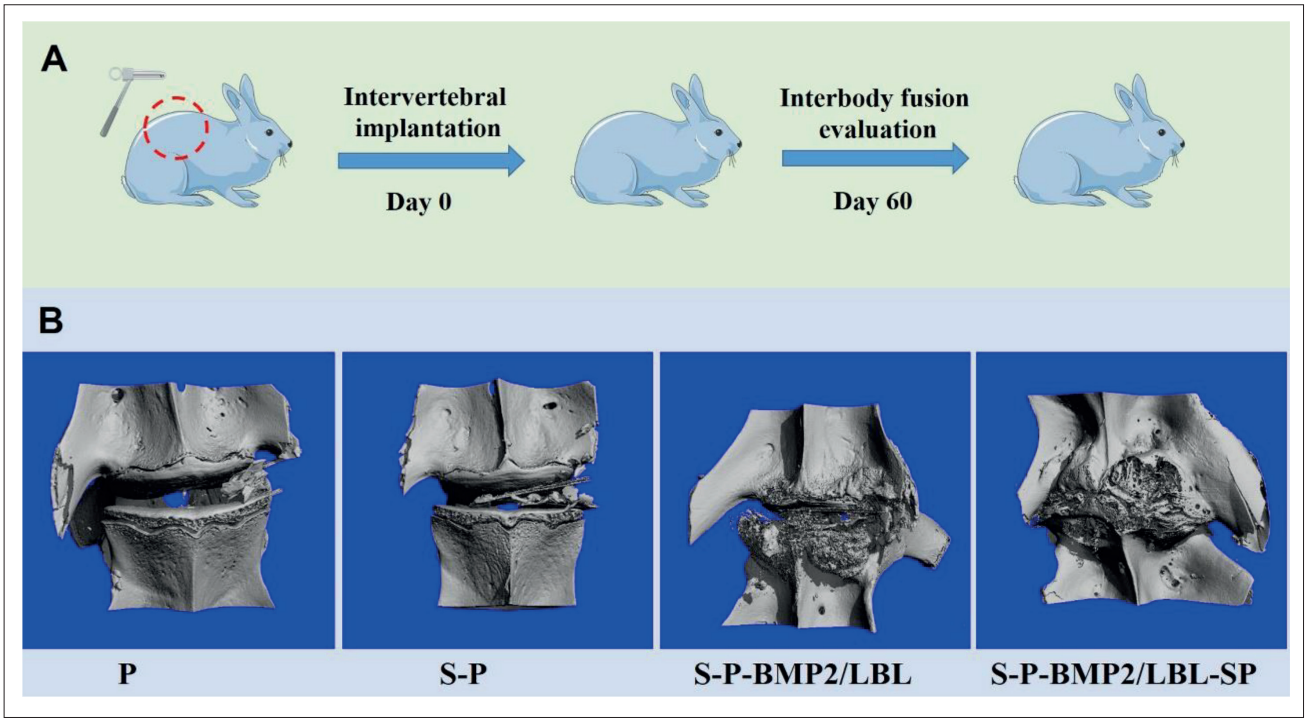


Figure 7. Schematic illustration of *in vivo* implantation and interbody fusion evaluation. (A) The surgical procedure of intervertebral implantation. (B) Micro-computed tomography (CT) results of different polyetheretherketone (PEEK) samples.

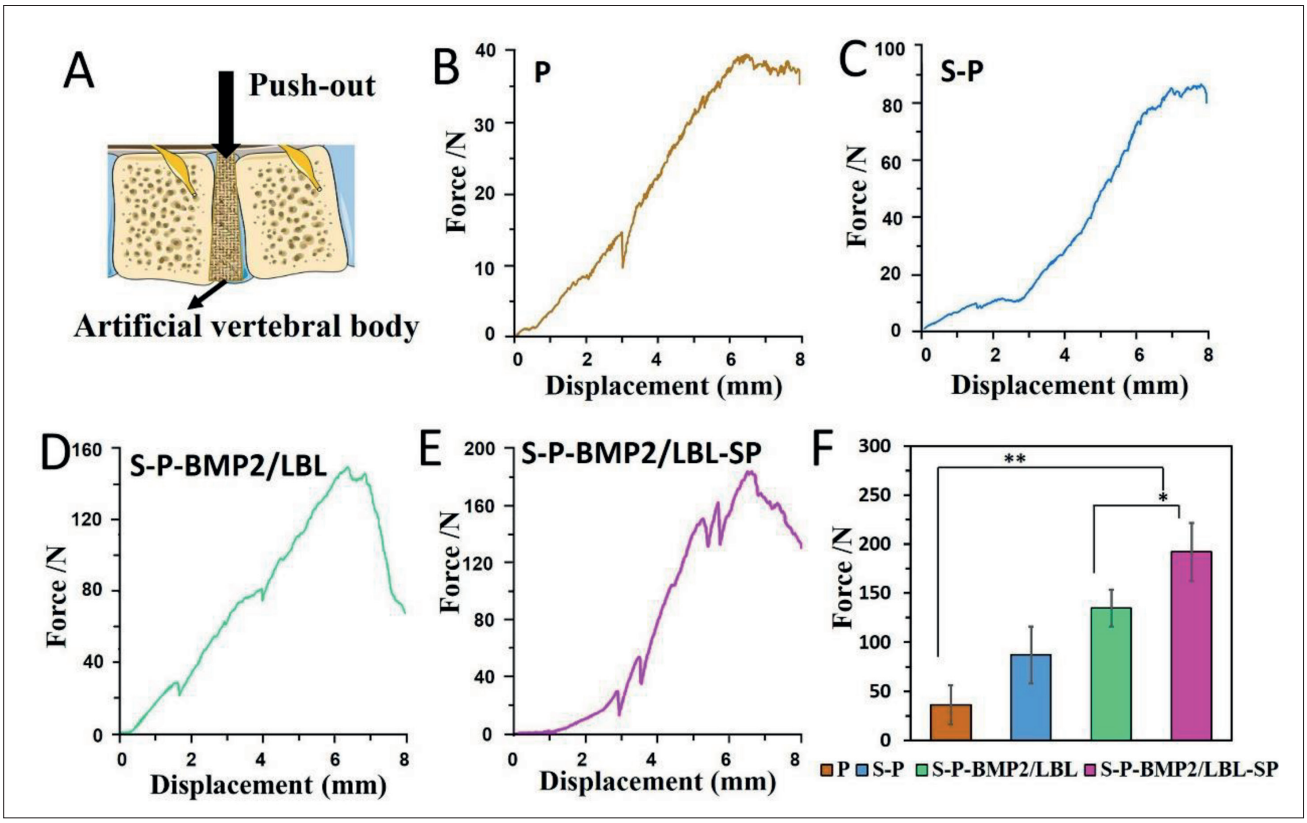


Figure 8. Push-out test results of different polyetheretherketone (PEEK) samples after 6 weeks of implantation. (A) Illustration of the push-out test. (B–E) Force–displacement curves for P (B), S-P (C), S-P-BMP2/LBL (D), and S-P-BMP2/LBL-SP (E). (F) Maximum pushing force of different samples. *$p < 0.05$; **$p < 0.01$.

However, some of the PEEK substrates were damaged due to surgical forces applied during the procedure.

4. Discussion

Intervertebral disc degeneration (IDD) refers to a group of conditions that involve the gradual breakdown or deterioration of structures in the lumbar spine.[32] It is often associated with aging and wear and tear on the spine.[1,2,33] IDD can affect various components of the spine, leading to symptoms such as pain, stiffness, and limited mobility.[34] In severe cases, surgical interventions, such as discectomy, spinal fusion, and artificial disc replacement, may be considered.[6,35] Spinal fusion with an interbody cage is a commonly adopted clinical procedure. Currently, most interbody cages are made of Ti alloy or PEEK.

Polyetheretherketone (PEEK) is known for its excellent mechanical, thermal, and chemical properties, making it suitable for various applications across medical and other industries.[36,37] However, PEEK interbody cages face limitations in processability, bioinertness, and radiolucency.[38] Hence, FDM 3D printing is a feasible method for fabricating PEEK interbody cages with complex geometries.[39]

As displayed in Figure 3B, 3D-printed PEEK cages exhibit a prominent rough striped surface structure attributed to the melting and cooling time. The rough surface of PEEK is beneficial for the stability of implanted cages. To accelerate the fusion of PEEK cages, BMP2 and SP were incorporated into the structure. BMP2 was loaded into the porous network structures formed from sulfonation, and the structure was then sealed with Gel/Chi multilayer films. SP is a peptide with a chain of 11 amino acid residues, serving as a chemoattractant and activator for macrophages, lymphocytes, and stem cells.[26,40] SP is capable of restoring the cellular potential of senescent stem cells by possibly modulating the expression of paracrine factors from MSCs, which could accelerate MSC-mediated tissue repair.[41,42]

To retain the bioactivity of SP, we grafted SP on the outermost Chi layer via Schiff base reaction. All groups reported good cytoactivity, except for the sulfonation group. When the modified PEEK cage is implanted into the body, SP would be released first to recruit MSCs to the implant (Figure 4). Subsequently, BMP2 is released slowly (Figure 4A) to promote osteogenic differentiation of MSCs (Figures 5 and 6). Results from micro-CT and the push-out test validated the fusion effects of BMP2-loaded PEEK cages, particularly in the S-P-BMP2/LBL-SP group.

5. Conclusion

In this study, we designed and fabricated a 3D-printed PEEK intervertebral fusion device via FDM. To improve its fusion effect, we sequentially sulfonated the structure, loaded it with BMP2, and grafted SP on the structure. After the fusion device is implanted, SP is initially released, recruiting MSCs to the implant surface from surrounding tissues. As the Gel/Chi multilayer films degrade, BMP2 is gradually released, further promoting osteogenic differentiation of MSCs. The *in vivo* results revealed that S-P-BMP2/LBL and S-P-BMP2/LBL-SP exhibited superior fusion effects, particularly attributable to the strategy of recruiting MSCs before osteogenic differentiation. This work presents a novel approach for designing and preparing PEEK intervertebral fusion devices with excellent fusion effects.

Acknowledgments

None.

Funding

This work was supported by the Sichuan Provincial Department of Science and Technology (grant number: 2023ZYD0072).

Conflict of interest

The authors declare no conflicts of interest.

Author contributions

Conceptualization: Feng Zheng, Haibin Lin
Methodology: Feng Zheng, Haibin Lin
Formal analysis: Xiaoqiang Gao, Sheng Chai
Investigation: Xiaoqiang Gao, Sheng Chai
Project administration: Feng Zheng, Haibin Lin
Supervision: Huan Liu
Visualization: Feng Zheng, Huan Liu
Writing - Original Draft: Feng Zheng, Xiaoqiang Gao, Sheng Chai
Writing - Review & Editing: Huan Liu
All authors read and approved the final manuscript.

Ethics approval and consent to participate

All animal experiments were approved by the Experimental Animal Ethics Committee of Southwest Medical University (20230228-013).

Consent for publication

Not applicable.

Availability of data

Data is available from the corresponding author upon reasonable request.

References

1. Song C, Hu P, Peng R, Li F, Fang Z, Xu Y. Bioenergetic dysfunction in the pathogenesis of intervertebral disc degeneration. *Pharmacol Res*. 2024;26:107119. doi: 10.1016/j.phrs.2024.107119
2. Novais EJ, Narayanan R, Canseco JA, et al. A new perspective on intervertebral disc calcification-from bench to bedside. *Bone Res*. 2024;12(1):3. doi: 10.1038/s41413-023-00307-3
3. Samanta A, Lufkin T, Kraus P. Intervertebral disc degeneration-current therapeutic options and challenges. *Front Public Health*. 2023;11:1156749. doi: 10.3389/fpubh.2023.1156749
4. Tong W, Lu Z, Qin L, et al. Cell therapy for the degenerating intervertebral disc. *Transl Res*. 2017,181:49-58. doi: 10.1016/j.trsl.2016.11.008
5. Kirnaz S, Capadona C, Wong T, et al. Fundamentals of intervertebral disc degeneration. *World Neurosurg*. 2022;157:264-273. doi: 10.1016/j.wneu.2021.09.066
6. Xin J, Wang Y, Zheng Z, Wang S, Na S, Zhang S. Treatment of intervertebral disc degeneration. *Orthop Surg*. 2022;14(7):1271-1280. doi: 10.1111/os.13254
7. Kos N, Gradisnik L, Velnar T. A brief review of the degenerative intervertebral disc disease. *Med Arch*. 2019;73(6):421-424. doi: 10.5455/medarh.2019.73.421-424
8. Zhu C, He M, Mao L, et al. Titanium-interlayer mediated hydroxyapatite coating on polyetheretherketone: a prospective study in patients with single-level cervical degenerative disc disease. *J Transl Med*. 2021;19(1):14. doi: 10.1186/s12967-020-02688-z
9. Kersten RF, van Gaalen SM, de Gast A, Öner FC. Polyetheretherketone (PEEK) cages in cervical applications: a systematic review. *Spine J*. 2015;15(6):1446-1460. doi: 10.1016/j.spinee.2013.08.030
10. de Ruiter L, Rankin K, Browne M, Briscoe A, Janssen D, Verdonschot N. Decreased stress shielding with a PEEK femoral total knee prosthesis measured in validated computational models. *J Biomech*. 2021;118:110270. doi: 10.1016/j.jbiomech.2021.110270
11. Zheng Z, Liu P, Zhang X, et al. Strategies to improve bioactive and antibacterial properties of polyetheretherketone (PEEK) for use as orthopedic implants. *Mater Today Bio*. 2022;16:100402. doi: 10.1016/j.mtbio.2022.100402
12. Kurtz SM, Devine JN. PEEK biomaterials in trauma, orthopedic, and spinal implants. *Biomaterials*. 2007;28(32):4845-4869. doi: 10.1016/j.biomaterials.2007.07.013
13. Li T, Song Z, Yang X, Du J. Influence of processing parameters on the mechanical properties of peek plates by hot compression molding. *Materials (Basel)*. 2022;16(1):36. doi: 10.3390/ma16010036
14. Yu D, Lei X, Zhu H. Modification of polyetheretherketone (PEEK) physical features to improve osteointegration. *J Zhejiang Univ Sci B*. 2022;23(3):189-203. doi: 10.1631/jzus.B2100622
15. Zhang Z, Zhang X, Zheng Z, et al. Latest advances: improving the anti-inflammatory and immunomodulatory properties of PEEK materials. *Mater Today Bio*. 2023;22:100748. doi: 10.1016/j.mtbio.2023.100748
16. Wang G, Han D, Cao Z, Guan H, Xuan T. Outcomes of autograft alone versus PEEK+ autograft interbody fusion in the treatment of adult lumbar isthmic spondylolisthesis. *Clin Neurol Neurosurg*. 2017;155:1-6. doi: 10.1016/j.clineuro.2017.01.020
17. Wang L, Yang C, Sun C, et al. Fused deposition modeling PEEK implants for personalized surgical application: from clinical need to biofabrication. *Int J Bioprint*. 2022;8(4):615. doi: 10.18063/ijb.v8i4.615
18. Wang Y, Müller WD, Rumjahn A, Schwitalla A. Parameters influencing the outcome of additive manufacturing of tiny medical devices based on PEEK. *Materials (Basel)*. 2020;13(2):466. doi: 10.3390/ma13020466
19. Rendas P, Figueiredo L, Machado C, Mourão A, Vidal C, Soares B. Mechanical performance and bioactivation of 3D-printed PEEK for high-performance implant manufacture: a review. *Prog Biomater*. 2023;12(2):89-111. doi: 10.1007/s40204-022-00214-6
20. Florian B, Michel K, Steffi G, et al. MSC differentiation on two-photon polymerized, stiffness and BMP2 modified biological copolymers. *Biomed Mater*. 2019;14(3):035001. doi: 10.1088/1748-605X/ab0362
21. Zhou N, Hu N, Liao JY, et al. HIF-1α as a regulator of BMP2-induced chondrogenic differentiation, osteogenic differentiation, and endochondral ossification in stem cells. *Cell Physiol Biochem*. 2015;36(1):44-60. doi: 10.1159/000374052
22. Bedair TM, Lee CK, Kim DS, et al. Magnesium hydroxide-incorporated PLGA composite attenuates inflammation and promotes BMP2-induced bone formation in spinal fusion. *J Tissue Eng*. 2020;11:2041731420967591. doi: 10.1177/2041731420967591
23. Mashaghi A, Marmalidou A, Tehrani M, Grace PM, Pothoulakis C, Dana R. Neuropeptide substance P and the immune response. *Cell Mol Life Sci*. 2016;73(22):4249-4264.

doi: 10.1007/s00018-016-2293-z

24. Sun T, Jiang X, Wang Q, et al. Substance P mediated DGLs complexing with DACHPt for targeting therapy of Glioma. *ACS Appl Mater Interfaces*. 2017;9(40):34603-34617. doi: 10.1021/acsami.7b05997

25. Zieglgänsberger W. Substance P and pain chronicity. *Cell Tissue Res*. 2019;375(1):227-241. doi: 10.1007/s00441-018-2922-y

26. Kim S, Piao J, Son Y, Hong HS. Substance P enhances proliferation and paracrine potential of adipose-derived stem cells in vitro. *Biochem Biophys Res Commun*. 2017;485(1):131-137. doi: 10.1016/j.bbrc.2017.02.036

27. Bhatia M. H_2S and substance P in inflammation. *Methods Enzymol*. 2015;555:195-205. doi: 10.1016/bs.mie.2014.11.024

28. Hong HS, Kim S, Jin Y, Son Y. Substance P enhances the therapeutic effect of MSCs by modulating their angiogenic potential. *J Cell Mol Med*. 2020;24(21):12560-12571. doi: 10.1111/jcmm.15804

29. Kim SJ, Kim JE, Choe G, et al. Self-assembled peptide-substance P hydrogels alleviate inflammation and ameliorate the cartilage regeneration in knee osteoarthritis. *Biomater Res*. 2023;27(1):40. doi: 10.1186/s40824-023-00387-6

30. Mu C, Hu Y, Hou Y, et al. Substance P-embedded multilayer on titanium substrates promotes local osseointegration via MSC recruitment. *J Mater Chem B*. 2020;8(6):1212-1222. doi: 10.1039/c9tb01124b

31. Huang L, Luo Z, Hu Y, et al. Enhancement of local bone remodeling in osteoporotic rabbits by biomimic multilayered structures on Ti6Al4V implants. *J Biomed Mater Res A*. 2016;104(6):1437-1451. doi: 10.1002/jbm.a.35667

32. Beierfuß A, Dietrich H, Kremser C, et al. Knockout of Apolipoprotein E in rabbit promotes premature intervertebral disc degeneration: a new in vivo model for therapeutic approaches of spinal disc disorders. *PLoS One*. 2017;12(11):e0187564. doi: 10.1371/journal.pone.0187564

33. Pan M, Li Q, Li S, et al. Percutaneous endoscopic lumbar discectomy: indications and complications. *Pain Physician*. 2020; 23(1):49-56. doi: 10.36076/ppj.2020/23/49

34. Perera K, Ivone R, Natekin E, Wilga CA, Shen J, Menon JU. 3D bioprinted implants for cartilage repair in intervertebral discs and knee menisci. *Front Bioeng Biotechnol*. 2022;9:754113. doi: 10.3389/fbioe.2021.754113

35. Thavaneswaran P, Vandepeer M. Lumbar artificial intervertebral disc replacement: a systematic review. *ANZ J Surg*. 2014;84(3):121-127. doi: 10.1111/ans.12315

36. Han X, Gao W, Zhou Z, et al. Application of biomolecules modification strategies on PEEK and its composites for osteogenesis and antibacterial properties. *Colloids Surf B Biointerfaces*. 2022;215:112492. doi: 10.1016/j.colsurfb.2022.112492

37. Dua R, Rashad Z, Spears J, Dunn G, Maxwell M. Applications of 3D-printed PEEK via fused filament fabrication: a systematic review. *Polymers (Basel)*. 2021;13(22):4046. doi: 10.3390/polym13224046

38. Schönhoff LM, Mayinger F, Eichberger M, Reznikova E, Stawarczyk B. 3D printing of dental restorations: mechanical properties of thermoplastic polymer materials. *J Mech Behav Biomed Mater*. 2021;119:104544. doi: 10.1016/j.jmbbm.2021

39. Zhang H, Duan M, Qin S, Zhang Z. Preparation and modification of porous polyetheretherketone (PEEK) cage material based on fused deposition modeling (FDM). *Polymers (Basel)*. 2022;14(24):5403. doi: 10.3390/polym14245403

40. Jung J, Jeong J, Hong HS. Substance P improves MSC-mediated RPE regeneration by modulating PDGF-BB. *Biochem Biophys Res Commun*. 2019;515(4):524-530. doi: 10.1016/j.bbrc.2019.05.186

41. Kim JE, Lee JH, Kim SH, Jung Y. Skin regeneration with self-assembled peptide hydrogels conjugated with substance P in a diabetic rat model. *Tissue Eng Part A*. 2018; 24(1-2):21-33. doi: 10.1089/ten.TEA.2016.0517

42. Zhang Y, An S, Hao J, Tian F, Fang X, Wang J. Systemic injection of substance P promotes murine calvarial repair through mobilizing endogenous mesenchymal stem cells. *Sci Rep*. 2018;8(1):12996. doi: 10.1038/s41598-018-31414-5

ACCSCIENCE PUBLISHING

International Journal of Bioprinting

RESEARCH ARTICLE

Amphiphobic encapsulation for biodegradable electronics

Daeun Sung[1], Yerim Lee[1,2], Seunghun Han[1,2], Sumin Kim[1,2], Bon Jekal[1,2], Minki Hong[1,2], Keunhong Jeong[3], and Jahyun Koo[1,2]*

[1] Department of Physics and Chemistry, School of Biomedical Engineering, Korea University, Seoul, South Korea

[2] Interdisciplinary Program in Precision Public Health, Korea University, Seoul, South Korea

[3] Department of Chemistry, Korea Military Academy, Seoul, South Korea

Abstract

Biodegradable electronics, capable of degradation and resorption in biological environments, require an encapsulation layer for precise lifetime control to perform versatile sensing and actuation in various clinical scenarios. Recent advances in biodegradable polymer chemistry have enabled the development of photocurable encapsulation of biodegradable electronics. However, challenges, such as nonuniform irradiation and incomplete crosslinking due to the limited penetration depth of the light source, restrict their long-term implantable operation. In this study, a 50-μm layer-by-layer three-dimensional (3D) printing approach was adopted for a photocurable encapsulation layer to enhance the lifetime of biodegradable electronics through predictable and homogeneous crosslinking of the encapsulation material. The waterproof and mechanical properties of the 3D-printed polybutanedithiol 1,3,5-triallyl-1,3,5-triazine-2,4,6(1H,3H,5H)-trione pentenoic anhydride (PBTPA) polymer are analyzed and compared with at-once UV-cured PBTPAs. Our study also investigates the enhanced waterproofing properties of the binary hydrophobic polyanhydride, known for its amphiphobic structure. This structure combines both water-trapping and repulsion mechanisms, supported by a high-density network of hydrogen bonding, that create a barrier against water penetration. The 50-μm layer-by-layer 3D printing approach enables controlled irradiation, thereby improving the lifetime of biodegradable electronics and enhancing their mechanical properties. These advancements broaden the scope of biodegradable electronic applications in various fields.

Keywords: 3D printing; Additive manufacturing; Biodegradable electronics; Amphiphobic; Encapsulation

***Corresponding author:**
Jahyun Koo
(jahyunkoo@korea.ac.kr)

Citation: Sung D, Lee Y, Han S, et al. Amphiphobic encapsulation for biodegradable electronics. *Int J Bioprint*. 2024;10(5):3871. doi: 10.36922/ijb.3871

Received: June 5, 2024
Accepted: July 4, 2024
Published Online: August 14, 2024

Copyright: © 2024 Author(s). This is an Open Access article distributed under the terms of the Creative Commons Attribution License, permitting distribution, and reproduction in any medium, provided the original work is properly cited.

Publisher's Note: AccScience Publishing remains neutral with regard to jurisdictional claims in published maps and institutional affiliations.

1. Introduction

Transient electronics can degrade and dissolve in the body or environment after operation without leaving any residue. These types of devices are actively researched due to their potential contribution to hardware security, reduced environmental burden, and temporary implantable devices.[1-9] In biomedical engineering, transient electronics can

eliminate the risks associated with the secondary surgical extraction process of implant devices,[10–12] leading to the development of bioresorbable drug-delivery systems,[13–15] electrophysiological sensors,[16–18] mechanical sensors,[19–21] nerve stimulators,[22–26] and pacemakers.[27] Researchers are also studying the fundamental chemistry of dissolution and strategies to trigger transience.[6,28,29] For clinical use in real-world environments, transient devices should be designed to bioresorb only after operating for a specified duration. Therefore, the main challenge in transient electronics is controlling and extending their operational lifetime.

A controllable encapsulation layer for transient electronics could provide a feasible solution to this challenge. In the body's environment, the hydrolysis of constituent materials can act as a primary trigger for transient device degradation. Therefore, the waterproof encapsulation layer is essential to enhance the lifetime of electronics. These encapsulation materials should be soft and biocompatible to function effectively *in vivo*, ideally offering a long operational lifespan. The requirement of these properties has driven extensive research in the development of new materials for encapsulation layers. Polymers (e.g., polybutanedithiol 1,3,5-triallyl-1,3,5-triazine-2,4,6[1H,3H,5H]-trione pentenoic anhydride [PBTPA],[30] polyurethane [PU],[24,31] poly[lactic-co-glycolic acid] [PLGA][15,24]), natural waxes,[28,32] and inorganic materials (e.g., SiO_2 and Si_3N_4[33]) could serve as encapsulation materials. The common processes for fabricating the encapsulation layer mainly include drop-casting (e.g., for PU and PLGA), mold-based techniques (e.g., for PBTPA), and screen-printing (e.g., for PBTPA). However, conventional methods have many limitations when it comes to micro-processing and precise thickness control. For example, PBTPA, a type of polyanhydride, is a photocurable and biodegradable polymer suitable for use as an encapsulation layer in transient electronics due to its hydrophobic chemistry and surface erosion characteristics. The molding process and screen-printing followed by ultraviolet (UV) irradiation are frequently used to fabricate the PBTPA encapsulation layers.[15,24] These simple fabrication methods have gained considerable attention due to their convenience and rapidity. However, they fail at precisely controlling the properties because of the nonuniform irradiation on PBTPA with different thicknesses, leading to incomplete crosslinking.

Three-dimensional (3D) printing has been applied in various engineering fields, owing to its cost-effectiveness, capability for personalization, and tunable mechanical properties. The principles of 3D printing can vary according to the specific requirements of each engineering field, such as digital light processing (DLP), fused filament fabrication (FFF),[34,35] and selective laser sintering (SLS).[36] This diversity of principles offers novel solutions to address issues, such as incomplete crosslinking in transient electronics. In this study, we utilized the DLP method, known for its high output speed and capability to produce sophisticated designs, to photo-cure PBTPA. In the DLP process of PBTPA, achieving the desired final polymer membrane thickness involves dividing it into multiple layers and stacking them sequentially. This process relies on a fixed UV light source within a customized DLP device, with the substrate containing the PBTPA precursor solution moving vertically downward after each unit layer is photo-synthesized and stacked. Implementing a 50-μm layer-by-layer 3D printing method could improve the polymeric lifetime and mechanical properties by ensuring complete crosslinking throughout the entire encapsulation layer. The waterproofing characteristic, Young's modulus, and toughness were selected as the criteria for evaluating PBTPA as the encapsulation layer. Based on these criteria, we found that the physical properties of the polymer can be enhanced by changing the crosslinking degree via fine thickness-controlled 3D printing and minimizing the light attenuation effect. In addition, introducing a unique amphiphobic structure using binary hydrophobic polyanhydride layers enhanced the application of 3D-printed polymer membranes, in terms of waterproofing and mechanical properties. This amphiphobic encapsulation maximized the lifetime of transient devices through the unique interaction between layer-by-layer hydrophobic polymer layers. We believe that our 3D-printed multi-unit layers can provide alternatives for versatile selections of encapsulation materials in transient electronics.

2. Materials and methods

2.1. Materials

The chemicals 4-pentenoic anhydride (4PA), 1,3,5-triallyl-1,3,5-triazine-2,4,6(1H,3H,5H)-trione (TTT), 1,4-butanedithiol (BDT), and 2,2-dimethoxy-2-phenylacetophenone were used to synthesize bioresorbable polyanhydride (Sigma-Aldrich, United States of America [USA]). Agarose and phosphate-buffered saline (PBS) were obtained from Sigma-Aldrich (USA) for device-level demonstration.

2.2. Preparation and 3D printing of PBTPA solution

The 3D printer was fabricated by ourselves by installing a light-emitting diode (LED; PRO4710; Wintech, USA) as an ultraviolet (UV) source into customized hardware. The customized hardware consisted of an Arduino board and a 200-angle motor to repeatedly move the substrate in the vertical direction as the unit polymer layer is synthesized.

The final polyanhydride film can be produced by repeatedly moving the 3D printer's substrate in the *z*-axis direction (50 μm) after the unit layer of the dispensed precursor solution is cured.

The chemicals 4PA, TTT, and BDT were mixed at a molar ratio of 1:4:7 in a 10 mL vial, with 2,2-dimethoxy-2-phenylacetophenone as the photoinitiator (a total mass of 0.5%), which was added to prepare a 1:4:7 PBTPA solution. The 1:1:2.5 PBTPA solution that was needed to create an amphiphobic structure was prepared similarly except for a change in the composition. The solution was pre-cured under UV light at 365 nm to prevent the PBTPA solution from flowing down on the substrate of the 3D printer. After conducting the pre-curing process for approximately 2 min, the 3D printing condition was optimized to expose the 50-μm-thick PBTPA layers to UV light (365 nm) for 5000 ms to form one unit layer. The entire 500-μm-thick PBTPA layer could be printed by repeating this procedure—dispensing 50 μm of the PBTPA solution and curing it for 5000 ms.

2.3. Preparation of screen-printed PBTPA

The PBTPA solution for screen-printing was also produced in the same manner as above, and it was pre-cured in a hood for more than a day to obtain a viscosity suitable for screen-printing. As a spacer on a glass substrate, 50-μm-thick single-sided tape was deposited at intervals of approximately 3 mm and stacked at two positions. The pre-cured PBTPA solution was dropped using a disposable pipette and spread thinly using a razor as a applicator . The thin PBTPA solution membrane was cured under 365 nm UV light for approximately 20 min and then removed using a razor.

2.4. 3D printing of the amphiphobic encapsulation layer

The 1:4:7 and 1:1:2.5 PBTPA solutions were produced as aforementioned, and both the solutions were pre-cured for approximately 2 min. Under the specified thickness requirements, 1:1:2.5 PBTPA and 1:4:7 PBTPA were stacked alternately in layers of 50 μm each. For example, in the case of 3P/150h1-100h2, 1:1:2.5, 1:4:7, and 1:1:2.5 PBTPA were dispersed and cured three, four, and three times, respectively.

2.5. Characterization of the polyanhydride encapsulation layer

To quantify the attenuation effect of conventional screen-printed PBTPA layers, light transmittance (*T*) was measured using an ultraviolet-visible-near-infrared (UV–vis-NIR) spectrometer (Agilent Technologies, USA).

To investigate the waterproofing performance of 3D-printed PBTPA, resistance monitoring of Mg, a representative transient metal, was conducted. Cr with a thickness of 20 nm was used as an adhesion layer on a glass substrate using electron-beam (e-beam) deposition. Subsequently, 300 nm of Mg was deposited on top of the Cr layer using a similar process. Mg was patterned to have a serpentine resistor pattern using laser cutting and a PBTPA layer was placed thereon to investigate the waterproofing performance. Thereafter, the polydimethylsiloxane (PDMS) well was fixed using epoxy to expose the PBTPA area covering the serpentine Mg to deionized (DI) water. DI water was used to degrade the Mg pattern. The hole in the PDMS well was covered with another PDMS layer to prevent the evaporation of DI water. The resistance was measured at the end of the Mg resistor connected to a Cu wire. The prepared test device was stored in an oven at 37°C and its resistance was measured once every few hours.

A tensile test was conducted to obtain the stress–strain curve of each sample group using a universal testing machine (UTM; UNITEST M1; Test One, Korea), and the strain, Young's modulus, and toughness were calculated accordingly. All 3D-printed samples for the tensile test were fabricated in accordance with the ASTM-D1708 standard (Figure S6, Supporting Information). The screen-printed PBTPA was physically cut into the same standard using CAMEO 4 (Silhouette, USA).

2.6. Simulation

For the molecular dynamics (MD) simulations in this study, we utilized the NAMD 2.13 software, which is integrated within Discovery Studio. The simulations incorporated the CHARMM force field for an accurate representation of the molecular interactions. The simulations were executed on a multicore system using Charm++ for parallel computation, enhancing its efficiency. Our model systems, representing amphiphobic and hydrophobic PBTPA structures, were simulated over a period of 1000 ps to observe their dynamic behavior and stability. The setup parameters for the simulations were selected to reflect realistic physical conditions, with the CHARMM force field providing the necessary potential functions for the interactions between atoms. The simulation environment included explicit solvent models, and electrostatic interactions were calculated using the Ewald summation method. Bond lengths within the molecules were constrained using the SHAKE algorithm, ensuring structural integrity throughout the simulation period.

Data from the simulations, specifically focusing on electrostatic energy stabilization and hydrogen bonding, were analyzed to evaluate the stability and interaction patterns within the PBTPA structures. This analysis was used to understand the molecular basis of the effectiveness of amphiphobic encapsulation.

2.7. Device-level demonstration

Schematic diagrams for the flexible printed circuit board (fPCB) and the board layout were designed using AUTODESK EAGLE (version 9.6.2). The components included a red LED (IN-S63ASR; Inolux, USA), 0402-in. footprint capacitors, and six-turn double-layered coils for wireless power transferring (resonant frequency: 13.56 MHz). All components were mounted onto the fPCB manufactured by an ISO-9001-compliant vendor, using solder paste (SMDLTLFP; Chip Quik, USA). The device measured 11 mm in width and 9 mm in length. The fPCB device, including the LED, was embedded in 1% agarose, containing PBS, and stored in a 37°C oven.

3. Results and discussion

3.1. 3D printing of the polyanhydride encapsulation layer

Our 3D printing technique utilizes the DLP principle, which involves dispersing the PBTPA solution and applying UV irradiation to create an optimized unit layer with 50 μm thickness. We achieved the desired thickness of PBTPA by dividing it into thin unit layers, resulting in superior waterproofing properties through both physical and chemical means (Figure 1). The layer-by-layer 3D printing process isolates polymer defects in each layer. The decoupled defects in the unit layer increase the effective

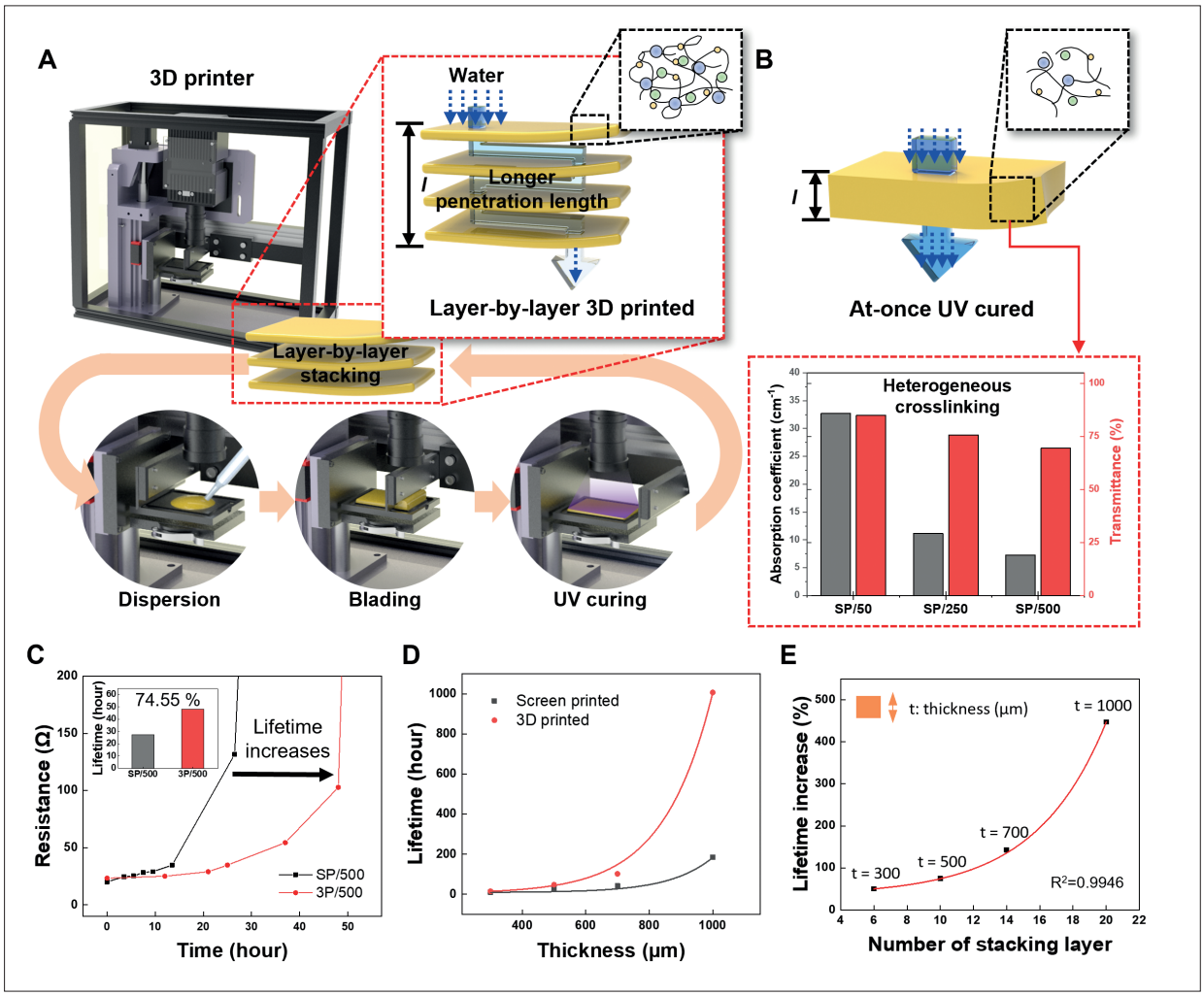


Figure 1. 3D printing strategy of polyanhydride encapsulation for transient electronics. (A) Graphical scheme for 3D-printed polyanhydride encapsulation to provide a longer penetration path through layer-by-layer printing. (B) The attenuation effect increases with the thickness of the screen-printed PBTPA, evidenced by the decreased absorption coefficient (α) and transmittance (T) at 365 nm. (C) Increased lifetime of Mg resistor (300 nm of Mg pattern on 20 nm of Cr) when using 3D-printed PBTPA layer. (D) The lifetime exponentially increases with the thickness of the total encapsulation layer; lifetime was evaluated as the time taken for the Mg resistor to reach a resistance of 200 Ω. (E) Measured lifetime increase (%) of the 3D-printed encapsulation layer according to its number of stacking layer, relative to a screen-printed encapsulation layer. Abbreviations: PBTPA, polybutanedithiol 1,3,5-triallyl-1,3,5-triazine-2,4,6(1H,3H,5H)-trione pentenoic anhydride; SP/500, screen-printed 500-μm-thick film; 3P/500, 3D-printed 500-μm-thick film.

diffusion length of water.[37] Uniform UV is simultaneously irradiated within thin unit layers in our 3D printing process, leading to predictable and sufficient chemical crosslinking. This uniform UV exposure is distinguished from the one-time screen-printing method, which may cause non-uniform polymerization and decreased crosslinking density. During one-time polymerization processes, residual uncrosslinked polymer chains may remain in the fluid, increasing the wettability of the polymer itself due to the reduced surface tension of water.[38]

In addition, in non-uniform photocuring processes within thick layers, microstructural inhomogenity can occur due to differences in light transmittance depending on the thickness, a phenomenon known as the attenuation effect. The relationship between UV attenuation and thickness can be confirmed using the Beer–Lambert law, through which UV light transmittance follows:

$$I = I_0 e^{-\alpha x} \quad \text{(I)}$$

where I and I_0 are the intensity of the transmitted light and incident light, respectively, α is the absorption coefficient, and x is the optical path length in the medium. To verify the attenuation of the at-once UV-cured (screen-printed) PBTPAs, the Beer–Lambert law was utilized to calculate the decrease in absorption coefficient and transmittance with increasing thickness. The modified Beer–Lamber law and the definition of absorbance (A) and transmittance (T) were applied:

$$\alpha = \frac{-ln\frac{I}{I_0}}{x}[cm^{-1}] \quad \text{(II)}$$

$$A \equiv \frac{I}{I_0} \quad \text{(III)}$$

$$T \equiv \frac{I}{I_0} \times 100\,[\%] \quad \text{(IV)}$$

Figure 1B presents a summary of the absorption coefficient and transmittance of the screen-printed PBTPAs, which were calculated based on the absorbance at 365 nm (Figure S1, Supporting Information). This wavelength corresponds to the UV light used for curing the PBTPAs during the experiment. As the thickness of PBTPA increases from 50 to 500 μm, there is a gradual decrease in absorption coefficient and transmittance, suggesting a corresponding increase in the attenuation effect. In this regard, the attenuation effect becomes more pronounced further away from the surface directly exposed to the UV light. Figure 1B illustrates this trend, providing mathematical confirmation that the increasing thickness leads to less precise polymerization.

Insufficient polymerization in thick films results in poor waterproofing and mechanical properties. To confirm this, the electrical dissolution rate (EDR)[39] of the Mg resistor was measured to compare the waterproofing performance of the 3D-printed PBTPA with that of screen-printed PBTPA (Figures 1C and S2, S3, Supporting Information). For the EDR test, Mg/Cr with a thickness of 300/20 nm was used. The unit layer-by-layer 3D-printed encapsulation PBTPA layer significantly enhanced waterproofing performance compared to the screen-printed layer. The lifetime evaluated as the time, until the resistance reaches 200 Ω, was increased from 27.5 to 48 h (i.e., 74.55%), highlighting the crucial role of fabrication methods for the encapsulation layer. It was demonstrated that our multi-unit printed PBTPA layer exhibits significantly enhanced exponential waterproofing characteristics with increasing total thickness, surpassing findings from prior studies (Figure 1D and E).[30] Various thicknesses of screen- and 3D-printed PBTPAs were examined to verify this trend (Figure S4, Supporting Information). The 3D-printed PBTPA with a thickness of 300 μm displayed an increased lifetime from 10 to 15 h compared to the screen-printed PBTPA of the same thickness. Additionally, the 3D-printed PBTPA with a thickness of 1 mm exhibited an even greater lifetime increase from 184 to 1007 h. The number of stacking layers and lifetime increase was also plotted according to this observance, as the enhanced waterproofing characteristic comes from the layer-by-layer deposited structure. The number of stacking layers denotes the number of unit layers printed as 50 μm. The lifetime improved by 50%, 74.55%, 142.86%, and 447.28% as the number of stacking layers increased, following an exponential function (R^2 = 0.9946). The layer-by-layer 3D printing technique allows the formation of homogeneous UV-light-controlled PBTPA films without altering the polymer's chemical bonds (Figure S5, Supporting Information). Our finding validates that the multi-unit layered printing process does not cause over-curing and chemical cleavage of polymers, making it an effective alternative to conventional methods as a water diffusion barrier.

It is also important to consider the mechanical characteristics for the long-term operation of transient devices with soft body tissues, including Young's modulus (E), toughness, and stain/elongation (ε) at the break. Soft tissues are known to have a Young's modulus ranging from 100 Pa to 10 MPa.[40] There are also repeated displacements in the kidney[41] and heart[42]; volumetric changes in the heart

(up to 8%)[43] and stomach (up to 40%)[44]; and large angular displacement or flexion in the spinal cord or skin.[45] Figure 2 presents the stress–strain curve and summarizes the differences between SP/500 and 3P/500, in terms of strain, Young's modulus, and toughness. The tensile test of PBTPA layers was conducted according to the ASTM-D1708 standard (Figure S6, Supporting Information). The strain/elongation of the 3D-printed PBTPA was approximately 186.01% higher compared to the screen-printed PBTPA (45.39% vs. 15.87%); Young's modulus of the 3D-printed PBTPA was approximately 50.16% lower compared to the screen-printed PBTPA (30.75 kPa vs. 61.69 kPa) (Figure S7, Supporting Information). These improvements are comparable to or even exceed the impact of changing the molar composition ratio of the PBTPA layer to obtain softer PBTPA.[30] The different molar composition ratio of 4PA, TTT, and BDT (1:4:7–1:1:2.5) resulted in a slight increase in elongation (15.14%) and a decrease in Young's modulus (79.28%), based on previous research.[30] Therefore, the 3D printing method, yielding 186.01% increased strain and 50.12% reduced Young's modulus, could be used to adjust the mechanical and waterproofing properties in at-once UV curing processes. Soft materials typically allow more frequent water diffusion through the film, but the homogenous polymerization by 3D printing enhances both waterproofing and mechanical characteristics. Hence, the 3D-printed polymer membrane can better stabilize implanted devices and enable robust and longer operation, particularly in dynamic tissues.[24] Specifically, 3D-printed membranes further extend the application of transient devices to more diverse physiological environments, such as the human intestine (20–40 kPa Young's modulus),[46] supraspinatus tendon (10–20 kPa Young's modulus), and gland muscles (30–45 kPa Young's modulus)[47] or stomach (≈40% strain). Moreover, the increased toughness of 3D-printed PBTPA (≈290.59 %) supports this possibility.

3.2. 3D-printed amphiphobic encapsulation

The 3D printing process enables the formation of amphiphobic encapsulation structures using binary hydrophobic polyanhydride. This unique membrane structure has been fabricated utilizing two types of PBTPA solutions, i.e., with 1:1:2.5 and 1:4:7 of 4PA, TTT, and BDT. The 1:1:2.5 and 1:4:7 PBTPA solutions were alternatively dispensed onto the 3D printer substrate to ensure alternate stacking between the two unit layers (Figure S8, Supporting Information). A similar strategy for stacking materials of different properties to establish a water barrier has been studied in the development of organic LEDs (OLEDs). Encapsulation films made of a single material cannot maintain the desired water-barrier effect if they exceed the critical thickness. This has led to the development of multi-material water barriers.[48,49] This effect is also applicable in the 3D-printed amphiphobic encapsulation of transient electronics (Figure 3A). The binary hydrophobic polyanhydrides, i.e., less hydrophobic 1:1:2.5 PBTPA and more hydrophobic 1:4:7 PBTPA, form a thick bulk membrane via layer-by-layer 3D printing, which increases the diffusion length of water from decoupled defects in the unit layer. In addition, amphiphobic PBTPAs interact with water molecules in two distinctive ways: water trapping and water repulsion. These distinctive interactions are attributed to the small size of defects (pore or pinhole) on PBTPA

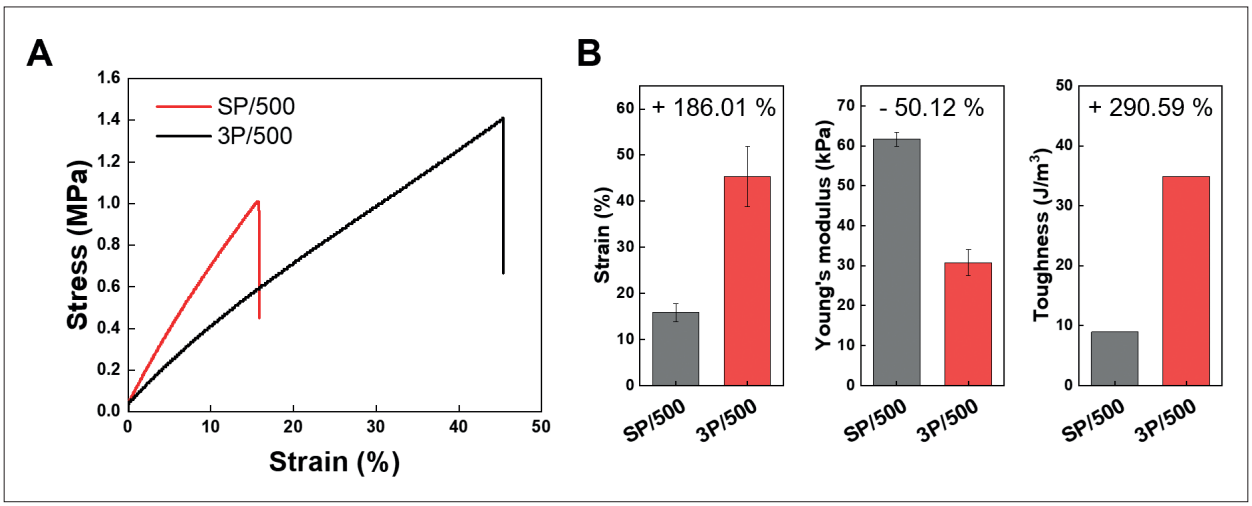
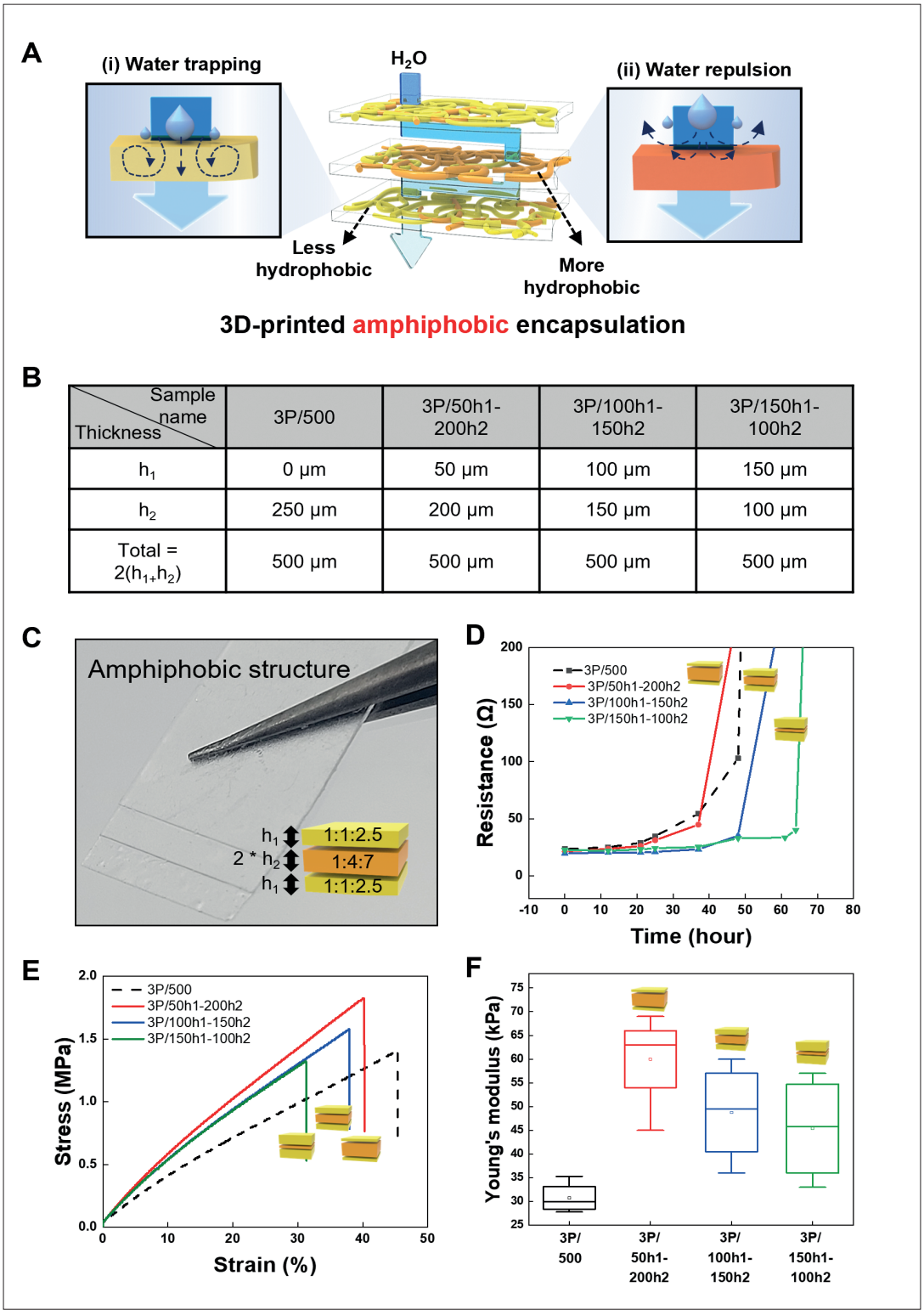


Figure 2. Enhanced mechanical properties of the 3D-printed polyanhydride encapsulation layer. (A) Stress–strain curve comparison between SP/500 and 3P/500. (B) Comparison between SP/500 and 3P/500, in terms of strain, Young's modulus, and toughness. Abbreviations: 3P/500, 3D-printed 500-μm-thick film; SP/500, screen-printed 500-μm-thick film.



Sample name / Thickness	3P/500	3P/50h1-200h2	3P/100h1-150h2	3P/150h1-100h2
h_1	0 μm	50 μm	100 μm	150 μm
h_2	250 μm	200 μm	150 μm	100 μm
Total = $2(h_1+h_2)$	500 μm	500 μm	500 μm	500 μm

Figure 3. 3D-printed amphiphobic encapsulation employing binary hydrophobic polyanhydride. (A) Benefits of 3D-printed amphiphobic encapsulation include longer penetration length and water trapping/repulsion effects. (B) Thicknesses of the 3D-printed amphiphobic layers' unit components including 1:4:7 PBTPA and 1:1:2.5 PBTPA; the samples were named based on the heights, h1 and h2. (C) Photograph of 3P/150h1–100h2. (D) Measured resistance of Mg resistors (i.e., 300 nm Mg on top of 20 nm Cr) based on the heights, h1 and h2; dotted line denotes measurement for 3P/500. 300 nm of Mg pattern on 20 nm of Cr was used to test lifetime. (E) Stress–strain curves of 3D-printed amphiphobic PBTPAs. (F) Young's modulus of 3D-printed amphiphobic PBTPAs (n = 4). Abbreviation: PBTPA, polybutanedithiol 1,3,5-triallyl-1,3,5-triazine-2,4,6(1H,3H,5H)-trione pentenoic anhydride.

formed from crosslinking during 3D printing. These tiny defects facilitate the close interaction between the water droplets and pinholes, favoring water trapping to the less hydrophobic 1:1:2.5 PBTPA and water repulsion to the more hydrophobic 1:4:7 PBTPA. This affinity is due to the high probability of hydrogen-bond network formation in the confined environment, and both interactions can be conducive to maximizing waterproofing properties.[50]

In addition, MD simulations were conducted using model compounds. One sample structure consisted of three layers of 1:4:7 PBTPA (hydrophobic PBTPA); another sample structure was designed by modifying the 1:1:2.5 PBTPA structure to adopt a 1:1:3 ratio and inserting it between the layers of 1:4:7 PBTPA (amphiphobic PBTPA) to analyze the inter-atomic forces between PBTPA layers (Figure S9, Supporting Information). The energy analysis revealed that after the structures stabilized, the electrostatic energy stabilization was 24.2 and 23.4 kcal/mol, respectively. Notably, the amphiphobic structure had 17 hydrogen bonds compared to the hydrophobic structure with 13 hydrogen bonds. In comparison to the 1:4:7 PBTPA structure, the 1:1:3 PBTPA structure has a smaller size, contributes less to energy stabilization, and has fewer atoms available for hydrogen bonding. The amphiphobic structure essentially has more hydrogen bonds due to fewer defects in 3D printing, thereby facilitating more efficient interactions with water. The conjunction of the two effects further inhibits water penetration.

The amphiphobic PBTPA was fabricated by sandwiching 1:4:7 PBTPA between 1:1:2.5 PBTPAs. In Figure 3B, the thickness of the 1:1:2.5 and 1:4:7 PBTPA layers are denoted as h1 and h2, respectively. The total thickness of the amphiphobic PBTPA was maintained at 500 μm. The as-prepared amphiphobic PBTPA was photographed with an exaggeration of the width of each PBTPA layer (Figure 3C). The layers of amphiphobic PBTPA (i.e., 1:1:2.5 PBTPA and 1:4:7 PBTPA) were carefully integrated without any air gap or weak adhesion between the samples. Notably, the less hydrophobic 1:1:2.5 PBTPA is more sensitive to water absorption due to the higher content of hydrophilic constituent, 4PA.[30] Nonetheless, 3D printing has enhanced the durability of the amphiphobic PBTPA despite the strong presence of 4PA, and the amphiphobic PBTPA displayed relative stability for more than 3 months in a 37°C aqueous environment.

The EDR tests compared the waterproofing performance of amphiphobic PBTPAs (Figures 3D and S2, Supporting Information). The measured lifetimes were 46 h for 3P/50h1-200h2, 57.5 h for 3P/100h1-150h2, and 66 h for 3P/150h1-100h2. For 3P/100h1-150h2 and 3P/150h1-100h2, the lifetimes were approximately 19.79% and 37.5% longer than 3P/500. The shortest lifetime similar to that of 3P/500 was observed when the thickest 1:4:7 PBTPA was stacked in the amphiphobic structure among the samples. The addition of the less hydrophobic 1:1:2.5 PBTPA layers to the more hydrophobic 1:4:7 PBTPA layers significantly improves waterproofing. This finding indicates that the less hydrophobic 1:1:2.5 PBTPA) is not favorable for inhibiting water penetration, suggesting that the less hydrophobic layer imparts a water-trapping effect (Figure 3A). The less hydrophobic 1:1:2.5 PBTPA comes into direct contact with bulk water on the top and traps the water within the small pores. Conversely, the more hydrophobic 1:4:7 PBTPA demonstrates water blocking. In summation, the combination of 3D printing and amphiphobic encapsulation strategies enhances the performance and characteristics of the membranes.

The mechanical properties of amphiphobic PBTPA were analyzed using a stress–strain curve. 3P/500, 3P/50h1-200h2, 3P/100h1-150h2, and 3P/150h1-100h2 samples displayed an elongation of 45.25%, 40.20%, 37.78%, and 30.78%, respectively (Figure 3E and F; n = 4). Notably, an increase in the ratio of 1:1:2.5 PBTPA makes it softer and more stretchable than 1:4:7 PBTPA, resulting in decreased elongation and Young's modulus. Contrary to Young's modulus in Figure 3E, Figure 3F displays a 1:4:7-PBTPA-thickness-proportional elongation at break. The amphiphobic PBTPA structure features a higher overall Young's modulus, particularly for 3P/50h1-200h2 (containing lesser 1:1:2.5 PBTPA). The slightly decreased elongation and increased Young's modulus are still desirable compared to the screen-printed layer (SP/500). Nonetheless, the amphiphobic multilayered PBTPA structure can significantly enhance the lifetime of electronics with slight reductions in the elongation and Young's modulus.

The effect of the number of amphiphobic stacks was also investigated in Figure 4. The selected number of stacks to be compared was 1, 3, 5, and 10. 3P/500 and 3P/150h1-100h2 were selected as representative amphiphobic samples for stacking numbers 1 and 3, respectively. Alternating layers of 1:1:2.5 PBTPA and 1:4:7 PBTPA, totaling 5 or 10 layers, were stacked at 100 and 50 μm, respectively. They were named $3P/(100*5)_{amphiphobic}$ and $3P/(50*10)_{amphiphobic}$, respectively (Figure 4A). Our findings revealed that the number of amphiphobic stacks significantly affects the waterproofing properties of the amphiphobic layer (Figure 4B and C). The lifetime of the amphiphobic layers increased with the number of stacks, i.e., from 48 h (3P/500) to 66 h (3P/150h1/100h2), 105 h ($3P/[100*5]_{amphiphobic}$), and 125 h ($3P/[50*10]_{amphiphobic}$),

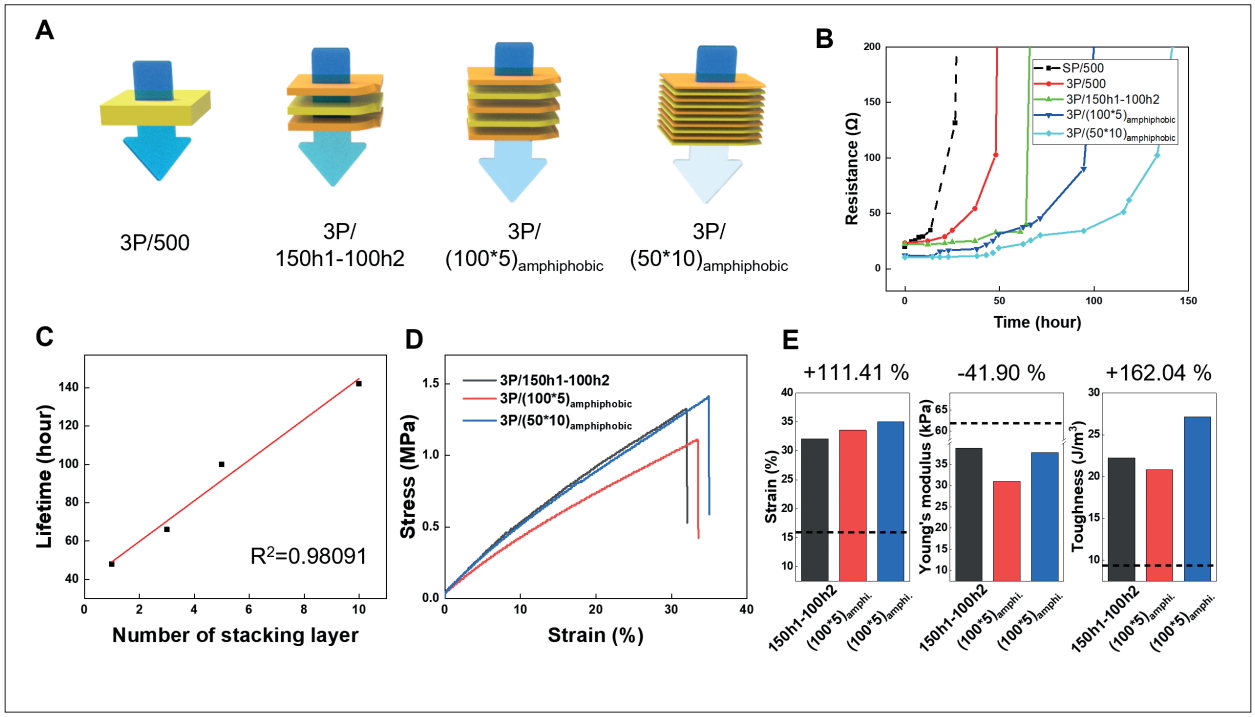


Figure 4. Effect of the number of amphiphobic stacks on encapsulation characteristics. (A) Varying encapsulation layers are distinguished by the number of stacking, ranging from 1 (3P/500) to 10 (3P/$[50*10]_{amphiphobic}$). (B) Measured resistance of Mg resistors (i.e., 300 nm Mg on top of 20 nm Cr) based on the number of stacking layers. (C) Linear regression results of measured resistance based on the number of stacking layers. (D and E) Mechanical properties of amphiphobic layers: stress–strain curves (D) and comparison of samples, in terms of strain, Young's modulus, and toughness, against SP/500 (dashed line) (E).

exhibiting a linear relationship ($y = 10.61x + 38.58$; $R^2 = 0.98091$). Regarding the mechanical characteristics of the amphiphobic layer, there were minimal differences in strain, modulus, and toughness among samples, despite their disparate waterproofing properties (Figure 4D and E). All amphiphobic samples displayed enhanced mechanical properties compared to SP/500 (dashed line in Figure 4E) with minimal standard deviations. Average strain and toughness increased by 111.41% and 162.04%, while modulus decreased by 41.90%. The improved properties of amphiphobic PBTPA, including both waterproofing and mechanical characteristics, would make it suitable for real-world, clinical applications.

To verify the practical application of our proposed 3D-printed polyanhydride membrane, additional device-level demonstration was performed. Figure 5A features the device, which includes an LED and a bioresorbable Mg tracer. The completed device includes an antenna, enabling the LED to be powered on from an external wireless power source (Figure 5B). Additionally, the device is embedded in agarose (containing PBS), and the LED turns off as the resistance increases due to the dissolution of Mg (Figure 5C). The time when the LED turns off is defined as the functional lifetime, and this parameter validates the waterproofing functionality of the device. The samples (SP/500, 3P/500, and 3P/$[50*10]_{amphiphobic}$) reported functional lifetimes of 6, 12, and 30 h, respectively (Figure 5D). This trend is similar to that observed in the EDR test. In the actual implant device, metals (Mo, Fe, and W) with slower melting rates and thicker than 300 nm may be used to extend the operational lifetime.[30]

4. Conclusion

In this study, we evaluated and compared the properties of PBTPA, a photocurable and biodegradable encapsulation polymer, in screen-printed and 3D-printed encapsulation layers, in terms of their waterproofing, lifetime, elongation, Young's modulus, and toughness. The results indicated that 3D printing can maintain consistent crosslinking while reducing the attenuation effects that may occur during screen-printing. A comparison of the elongation, Young's modulus, and toughness from the stress–strain curve demonstrated the successful fabrication of 3D-printed encapsulation layers that are relatively soft and stretchable, with remarkable waterproofing properties. The newly introduced concept of amphiphobic

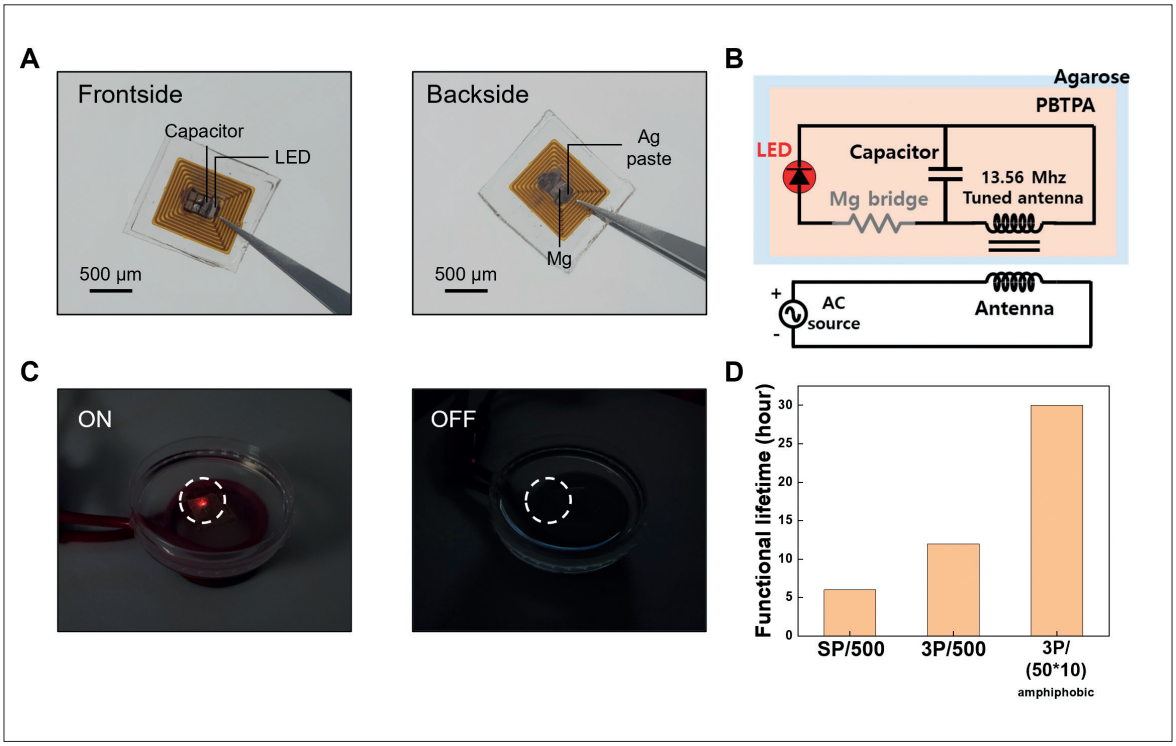


Figure 5. Device-level demonstrations for SP/500, 3P/500, and 3P/(50*10)$_{amphiphobic}$. (A) Photographs of the device designed to turn off the light-emitting diode (LED) lights following the dissolution of Mg. (B) Schematic illustration of the wireless power transfer system and test setup. (C) Photographs of the test device embedded in agarose, with the LED turned on and off. (D) Functional lifetimes in SP/500, 3P/500, and 3P/(50*10)$_{amphiphobic}$ determined from the device. Abbreviation: PBTPA, polybutanedithiol 1,3,5-triallyl-1,3,5-triazine-2,4,6(1H,3H,5H)-trione pentenoic anhydride.

multilayering via 3D printing provides a unique strategy by combining binary layers to induce both water trapping and repulsion. Specifically, it has been confirmed that implementing amphiphobic stacking can result in a significant enhancement of 416.36% in waterproof effects. Additionally, there were significant improvements of 111.41%, 41.9 %, and 162.04 % in strain, modulus, and toughness, respectively. Therefore, 3D printing allows for precisely controlled encapsulation properties, offering flexibility in imparting the desired properties to medical devices. These advantages can be further investigated in the development of transient electronics.

Acknowledgments

None.

Funding

This work was supported by the National Research Foundation of Korea (NRF) grant (RS-2024-00345402), Korea Health Industry Development Institute (KHIDI) (Grant No. RS-2022-KH125686, RS-2023-KH136924), and Korea University grants (K2323201, K2109981). Following are results of a study on the "Leaders in INdustry-university Cooperation 3.0" Project, supported by the Ministry of Education and National Research Foundation of Korea.

Conflict of interest

The authors declare that they have no known competing financial interests or personal relationships that could have appeared to influence the work reported in this paper.

Author contributions

Conceptualization: Daeun Sung, Yerim Lee, Jahyun Koo
Formal analysis: Daeun Sung, Keunhong Jeong
Investigation: Daeun Sung, Yerim Lee, Seunghun Han, Sumin Kim
Methodology: Daeun Sung, Yerim Lee, Minki Hong
Software: Keunhong Jeong
Supervision: Jahyun Koo
Writing – original draft: Daeun Sung, Keunhong Jeong
Writing – review & editing: Daeun Sung, Yerim Lee, Bon Jekal, Minki Hong, Jahyun Koo

Ethics approval and consent to participate

Not applicable.

Consent for publication

Not applicable.

Availability of data

Data will be made available on request.

References

1. Shim JS, Rogers JA, Kang SK. Physically transient electronic materials and devices. *Mater Sci Eng R Rep*. 2021; 145:100624.
doi: 10.1016/j.mser.2021.100624

2. Bae H, Lee BH, Lee D, et al. Physically transient memory on a rapidly dissoluble paper for security application. *Sci Rep*. 2016;6(1):38324.
doi: 10.1038/srep38324

3. Tran H, Feig VR, Liu K, et al. Stretchable and fully degradable semiconductors for transient electronics. *ACS Cent Sci*. 2019;5(11):1884-1891.
doi: 10.1021/acscentsci.9b00850

4. Hu W, Jiang J, Xie D, et al. Transient security transistors self-supported on biodegradable natural-polymer membranes for brain-inspired neuromorphic applications. *Nanoscale*. 2018;10:14893-14901.
doi: 10.1039/c8nr04136a

5. Lee G, Choi YS, Yoon HJ, Rogers JA. Advances in physicochemically stimuli-responsive materials for on-demand transient electronic systems. *Matter*. 2020;3(4):1031-1052.
doi: 10.1016/j.matt.2020.08.021

6. Kang SK, Yin L, Bettinger C. The emergence of transient electronic devices. *MRS Bull*. 2020;45(2):87-95.
doi: 10.1557/mrs.2020.19

7. Jamshidi R, Taghavimehr M, Chen Y, Hashemi N, Montazami R. Transient electronics as sustainable systems: from fundamentals to applications. *Adv Sustain Syst*. 2022;6(2):2100057.
doi: 10.1002/adsu.202100057

8. Kim KS, Yoo J, Shim JS, et al. Biodegradable molybdenum/polybutylene adipate terephthalate conductive paste for flexible and stretchable transient electronics. *Adv Mater Technol*. 2022;7(2):2001297.
doi: 10.1002/admt.202001297

9. Kim KS, Maeng WY, Kim S, et al. Isotropic conductive paste for bioresorbable electronics. *Mater Today Bio*. 2023;18:100541.
doi: 10.1016/j.mtbio.2023.100541

10. Choi Y, Koo J, Rogers JA. Inorganic materials for transient electronics in biomedical applications. *MRS Bull*. 2020;45(2):103-112.
doi: 10.1557/mrs.2020.25

11. Li R, Wang L, Kong D, Yin L. Recent progress on biodegradable materials and transient electronics. *Bioact Mater*. 2018;3(3):322-333.
doi: 10.1016/j.bioactmat.2017.12.001

12. Fanelli A, Ghezzi D. Transient electronics: new opportunities for implantable neurotechnology. *Curr Opin Biotechnol*. 2021;72:22-28.
doi: 10.1016/j.copbio.2021.08.011

13. Lee J, Cho HR, Cha GD, et al. Flexible, sticky, and biodegradable wireless device for drug delivery to brain tumors. *Nat Commun*. 2019;10(1):5205.
doi: 10.1038/s41467-019-13198-y

14. Benhabbour SR, Kovarova M, Jones C, et al. Ultra-long-acting tunable biodegradable and removable controlled release implants for drug delivery. *Nat Commun*. 2019;10(1):4324.
doi: 10.1038/s41467-019-12141-5

15. Koo J, Kim SB, Choi YS, et al. Wirelessly controlled, bioresorbable drug delivery device with active valves that exploit electrochemically triggered crevice corrosion. *Sci Adv*. 2020;6(35):eabb1093.
doi: 10.1126/sciadv.abb1093

16. Pal RK, Farghaly AA, Wang C, Collinson MM, Kundu SC, Yadavalli VK. Conducting polymer-silk biocomposites for flexible and biodegradable electrochemical sensors. *Biosens Bioelectron*. 2016;81:294-302.
doi: 10.1016/j.bios.2016.03.010

17. Li R, Qi H, Ma Y, et al. A flexible and physically transient electrochemical sensor for real-time wireless nitric oxide monitoring. *Nat Commun*. 2020;11(1):3207.
doi: 10.1038/s41467-020-17008-8

18. Kim HS, Yang SM, Jang TM, Oh N, Kim HS, Hwang SW. Bioresorbable silicon nanomembranes and iron catalyst nanoparticles for flexible, transient electrochemical dopamine monitors. *Adv Healthc Mater*. 2018;7(24):e1801071.
doi: 10.1002/adhm.201801071

19. Lu D, Yan Y, Deng Y, et al. Bioresorbable wireless sensors as temporary implants for in vivo measurements of pressure. *Adv Funct Mater*. 2020;30(40):2003754.
doi: 10.1002/adfm.202003754

20. Shin J, Yan Y, Bai W, et al. Bioresorbable pressure sensors protected with thermally grown silicon dioxide for the monitoring of chronic diseases and healing processes. *Nat Biomed Eng*. 2019;3(1):37-46.
doi: 10.1038/s41551-018-0300-4

21. Shin J, Liu Z, Bai W, et al. Bioresorbable optical sensor systems for monitoring of intracranial pressure and temperature. *Sci Adv*. 2019;5(7):eaaw1899.
doi: 10.1126/sciadv.aaw1899

22. Lee G, Ray E, Yoon HJ, et al. A bioresorbable peripheral nerve stimulator for electronic pain block. *Sci Adv*. 2022;8(40):eabp9169.
doi: 10.1126/sciadv.abp9169

23. Koo J, MacEwan MR, Kang SK, et al. Wireless bioresorbable electronic system enables sustained nonpharmacological neuroregenerative therapy. *Nat Med*. 2018;24(12):1830-1836.
doi: 10.1038/s41591-018-0196-2

24. Choi YS, Hsueh YY, Koo J, et al. Stretchable, dynamic covalent polymers for soft, long-lived bioresorbable electronic stimulators designed to facilitate neuromuscular regeneration. *Nat Commun*. 2020;11(1):5990.
doi: 10.1038/s41467-020-19660-6

25. Maeng WY, Tseng WL, Li S, Koo J, Hsueh YY. Electroceuticals for peripheral nerve regeneration. *Biofabrication*. 2022;14(4):042002.
doi: 10.1088/1758-5090/ac8baa

26. Kim G, Hong M, Lee Y, Koo J. Biodegradable materials and devices for neuroelectronics. *MRS Bull*. 2023;48(5):518-530.
doi: 10.1557/s43577-023-00529-0

27. Choi YS, Yin RT, Pfenniger A, et al. Fully implantable and bioresorbable cardiac pacemakers without leads or batteries. *Nat Biotechnol*. 2021;39(10):1228-1238.
doi: 10.1038/s41587-021-00948-x

28. Park CW, Kang SK, Hernandez HL, et al. Thermally triggered degradation of transient electronic devices. *Adv Mater*. 2015;27(25):3783-3788.
doi: 10.1002/adma.201501180

29. Gao Y, Zhang Y, Wang X, et al. Moisture-triggered physically transient electronics. *Sci Adv*. 2017;3(9):e1701222.
doi: 10.1126/sciadv.1701222

30. Choi YS, Koo J, Lee YJ, et al. Biodegradable polyanhydrides as encapsulation layers for transient electronics. *Adv Funct Mater*. 2020;30(31):2000941.
doi: 10.1002/adfm.202000941

31. Kim SY, Han G, Hwang DB, et al. Design and usability evaluations of a 3D-printed implantable drug delivery device for acute liver failure in preclinical settings. *Adv Healthc Mater*. 2021;10(14):e2100497.
doi: 10.1002/adhm.202100497

32. Won SM, Koo J, Crawford KE, et al. Natural wax for transient electronics. *Adv Funct Mater*. 2018;28(32):1801819.
doi: 10.1002/adfm.201801819

33. Kang SK, Hwang SW, Cheng H, et al. Dissolution behaviors and applications of silicon oxides and nitrides in transient electronics. *Adv Funct Mater*. 2014;24(28):4427-4434.
doi: 10.1002/adfm.201304293

34. Han G, Lee H, Kang JM, et al. 3D-printed NIR-responsive bullets as multifunctional nanodrug platforms for image-guided local chemo-photothermal therapy. *Chem Eng J*. 2023;477:147083.
doi: 10.1016/j.cej.2023.147083

35. Jang TS, Park SJ, Lee JE, et al. Topography-supported nanoarchitectonics of hybrid scaffold for systematically modulated bone regeneration and remodeling. *Adv Funct Mater*. 2022;32(51):2206863.
doi: 10.1002/adfm.202206863

36. Quan H, Zhang T, Xu H, Luo S, Nie J, Zhu X. Photo-curing 3D printing technique and its challenges. *Bioact Mater*. 2020;5(1):110-115.
doi: 10.1016/j.bioactmat.2019.12.003

37. Wu J, Fei F, Wei C, et al. Efficient multi-barrier thin film encapsulation of OLED using alternating Al2O3 and polymer layers. *RSC Adv*. 2018;8(11):5721-5727.
doi: 10.1039/c8ra00023a

38. Zhao W, Zhou J, Hu H, Xu C, Xu Q. The role of crosslinking density in surface stress and surface energy of soft solids. *Soft Matter*. 2022;18(3):507-513.
doi: 10.1039/d1sm01600h

39. Cheng H, Vepachedu V. Recent development of transient electronics. *Theor Appl Mech Lett*. 2016;6(1):21-31.
doi: 10.1016/j.taml.2015.11.012

40. Yin L, Cheng H, Mao S, et al. Dissolvable metals for transient electronics. *Adv Funct Mater*. 2014;24(5):645-658.
doi: 10.1002/adfm.201301847

41. Fallegger F, Schiavone G, Lacour SP. Conformable hybrid systems for implantable bioelectronic interfaces. *Adv Mater*. 2020;32(15):e1903904.
doi: 10.1002/adma.201903904

42. Enzmann DR, Pelc NJ. Brain motion: measurement with phase-contrast MR imaging. *Radiology*. 1992;185(3):653-660.
doi: 10.1148/radiology.185.3.1438741

43. Carlsson M, Cain P, Holmqvist C, Stahlberg F, Lundback S, Arheden H. Total heart volume variation throughout the cardiac cycle in humans. *Am J Physiol Heart Circ Physiol*. 2004;287(1):H243-50.
doi: 10.1152/ajpheart.01125.2003

44. Banerjee S, Pal A, Fox M. Volume and position change of the stomach during gastric accommodation and emptying: a detailed three-dimensional morphological analysis based on MRI. *Neurogastroenterol Motil*. 2020;32(8):e13865.
doi: 10.1111/nmo.13865

45. Harrison DE, Cailliet R, Harrison DD, Troyanovich SJ, Harrison SO. A review of biomechanics of the central nervous system--part I: spinal canal deformations resulting from changes in posture. *J Manipulative Physiol Ther*. 1999;22(4):227-234.
doi: 10.1016/s0161-4754(99)70049-7

46. Handorf AM, Zhou Y, Halanski MA, Li WJ. Tissue stiffness dictates development, homeostasis, and disease progression. *Organogenesis*. 2015;11(1):1-15.
doi: 10.1080/15476278.2015.1019687

47. Liu J, Zheng H, Poh PSP, Machens HG, Schilling AF. Hydrogels for engineering of perfusable vascular networks. *Int J Mol Sci*. 2015;16(7):15997-16016. doi: 10.3390/ijms160715997

48. Lu KW, Chen HL, Chen HP, Kuo CC. Design of organic/inorganic multilayer water vapor barrier thin films deposited via plasma polymerization for encapsulation. *Thin Solid Films*. 2023;767:139672. doi: 10.1016/j.tsf.2023.139672

49. Grover R, Srivastava R, Kamalasanan MN, Mehta DS. Multilayer thin film encapsulation for organic light emitting diodes. *RSC Adv*. 2014;4(21):10808-10814. doi: 10.1039/c3ra46077k

50. Xu F, Song Y, Wei M, Wang Y. Water flow through interlayer channels of two-dimensional materials with various hydrophilicities. *J Phys Chem C*. 2018;122(27):15772-15779. doi: 10.1021/acs.jpcc.8b04719

ACCSCIENCE PUBLISHING

International Journal of Bioprinting

RESEARCH ARTICLE

3D-Printed mesoporous bioglass/polycaprolactone scaffolds induce macrophage polarization toward M2 phenotype and immunomodulates osteogenic differentiation of BMSCs

Weihua Huang[1,2,3,4†], Shuai Huang[1†], Xitao Linghu[3], Wei-Chih Chen[1], Yang Wang[1], Jingjie Li[1], Huinan Yin[1], Hang Zhang[1], Weikang Xu[2,5,6*], and Qingde Wa[3*]

[1]Department of Orthopaedic Surgery, the Second Affiliated Hospital of Guangzhou Medical University, Haizhu District, Guangzhou, Guangdong, China

[2]Institute of Biological and Medical Engineering, Guangdong Academy of Sciences, Jianghai Avenue Central, Haizhu District, Guangzhou ,Guangdong, China

[3]Department of Orthopaedic Surgery, the Second Affiliated Hospital of Zunyi Medical University, Zunyi, Guizhou, China

[4]Department of Orthopaedic Surgery, The Affiliated Qingyuan Hospital (Qingyuan People's Hospital), Guangzhou Medical University, Qingcheng District, Qingyuan, Guangdong, China

[5]National Engineering Research Center for Healthcare Devices, Guangdong Provincial Key Laboratory of Medical Electronic Instruments and Materials, Guangdong Institute of Medical Instruments, Tianhe District, Guangzhou, Guangdong, China

[6]Guangdong Chinese Medicine Intelligent Diagnosis and Treatment Engineering Technology Research center, Jianghai Avenue Central, Haizhu District, Guangzhou ,Guangdong, China

[†]These authors contributed equally to this work.

***Corresponding authors:**
Weikang Xu
(759200816@qq.com)

Qingde Wa
(wqd887zsy@126.com)

Citation: Huang W, Huang S, Linghu X, et al. 3D-Printed mesoporous bioglass/polycaprolactone scaffolds induce macrophage polarization toward M2 phenotype and immunomodulates osteogenic differentiation of BMSCs. *Int J Bioprint*. 2024;10(5):3551. doi: 10.36922/ijb.3551

Received: April 30, 2024
Accepted: June 19, 2024
Published Online: July 31, 2024

Copyright: © 2024 Author(s). This is an Open Access article distributed under the terms of the Creative Commons Attribution License, permitting distribution, and reproduction in any medium, provided the original work is properly cited.

Publisher's Note: AccScience Publishing remains neutral with regard to jurisdictional claims in published maps and institutional affiliations.

Abstract

Bioceramic composite polycaprolactone (PCL) scaffolds are widely used in bone defect repair studies. Among them, bioactive glass (BG) is considered an excellent bone-based repair material due to its unique inorganic amorphous structure, bioactivity, and osseointegration properties. However, the dense pores and low specific surface area of ordinary BGs and mesoporous BGs limit the mechanical properties and bioactivity of the overall scaffolds, and it is often necessary to increase the proportion of BGs to offset these shortcomings. Here, we prepared highly active dendritic mesoporous structured bioactive glass (MBG) with a high specific surface area (457.14 m^2/g) and pore volume (1.38 cm^3/g) by sol-gel method. PCL scaffolds containing different percentages of MBG were prepared by three-dimensional printing technology, and the physicochemical and immunomodulatory osteogenic properties were investigated. The results showed that the low-concentration MBG/PCL scaffolds with 10% content (10MBG/PCL) possessed the highest compressive strength (about two times that of pure PCL scaffolds) and excellent *in vitro* immunomodulatory osteogenic properties. Finally, 10MBG/PCL was selected for further exploration to investigate the effects of different fiber diameters (F300, F500, F800) and pore sizes (P200, P500, P800) on the scaffolds performance. Ultimately, we found that the 10MBG/PCL scaffolds with fiber diameter and pore size of 500 μm had high osteogenic potential, significantly induced macrophage polarization toward the M2 phenotype, and downregulated the expression of inflammatory genes

and that this group was the most capable of mediating macrophage polarization and thus inducing the osteogenic differentiation of rat bone marrow mesenchymal stem cells (BMSCs) to form an immune microenvironment conducive to osteogenesis. This study is a step forward in the exploration of the performance of BG composite PCL scaffolds and provides a new idea for the development of bone graft materials.

Keywords: 3D printing; Dendritic mesoporous structured bioactive glass; Macrophages; Bone marrow mesenchymal stem cells; Immunoregulation; Osteogenic differentiation

1. Introduction

Currently, bone defects due to factors such as trauma or surgery are becoming more and more common. According to statistics, millions of patients with bone defects worldwide require autologous bone grafting every year, but the inadequate sources and donor sites of autologous bone limit its application.[1-3] The development of bone tissue engineering has promoted the emergence of engineered scaffolds on the market. Good mechanical properties, biocompatibility, and osteogenic activity are the basic requirements for engineered scaffolds used in bone graft substitution.[4] Polycaprolactone (PCL) is one of the commonly used materials for bone tissue engineering because of its high biocompatibility. However, PCL is hydrophobic and lacks osteogenic potential, and is often used as a matrix component of composite scaffolds in bone tissue engineering.[5,6]

Since the invention of bioglass 45S5 by Prof. Larry Hench in the 1970s, the field of medical materials has opened up to the study of coordinated osteointegration of bioglasses.[7] Bioglass 45S5 accelerates bone formation by releasing Na^+ and rapidly exchanging it with H^+ and HO_3^+ to form a silica layer on the silica-based surface, and then by recruiting ions such as Ca^{2+} and P^{5+} to form a hydroxycarbonate apatite layer (HCA).[7-9] Nevertheless, high-temperature sintered bioglass is prone to agglomeration and has low specific surface area, which affects its biological activity. In addition, the Na^+ and Ca^{2+} ions released from the degradation of bioglass may cause cytotoxicity due to the change of local pH and delay the formation of HCA.[10] These drawbacks limit the application of bioglass 45S5. Fortunately, due to the use of templating agents (CTAC, P123, F127), bioactive glasses (BGs) with mesoporous structures have emerged in the research landscape. Mesoporous BGs have better histocompatibility, their ordered mesoporous structure increases their bioactivity, and ions such as Si^{2+}, Ca^{2+}, and P^{5+} released during *in vivo* degradation contribute to the formation of the bone matrix such as hydroxyapatite.[11,12] Studies have shown that the incorporation of mesoporous BGs can enhance the mechanical properties and bioactivity of the matrix material, resulting in composites with excellent bone and vascular regeneration properties.[13,14] For example, Zhao et al. used mesoporous BGs composite fiber protein hydrogel for maxillofacial bone defects.[15] The results showed the enhancement effect of mesoporous BGs on the mechanical strength, bioactivity, and osteogenesis of the material. As mentioned above, BGs improve the hydrophilic properties of PCL and enhance its osteogenic activity, while PCL as an engineered scaffold matrix can provide a stable support medium for bone defect repair. However, the dense pores and low specific surface area of ordinary BGs and mesoporous BGs limit the mechanical properties and bioactivity of the overall scaffold. Therefore, the current composite scaffolds show a continuous increase in compressive strength and osteogenic activity with increasing glass content. For instance, Wang et al.'s study on the osteogenic properties of BGs/PCL scaffolds showed that scaffolds with the highest BGs percentage (20%) possessed the highest mechanical strength and osteogenic activity.[16] But this seems to be detrimental to the degradation and resorption of BGs *in vivo*.

More importantly, bone regeneration and repair are closely related to the immune microenvironment.[17] "Osteoimmunology," first proposed by Joseph R. Arron and Yongwon Choi, focuses on revealing the interplay between bone cell remodeling and immune cells.[18] Studies have shown that the immune microenvironment influences bone regeneration, with macrophages (MPs) playing a central role in osteogenesis.[19] However, MPs exhibit plasticity and can polarize toward either M1 or M2 phenotypes. The pro-inflammatory phenotype M1 induces tissue inflammatory responses, while the M2 phenotype is involved in tissue repair.[20] As a result, the ability of biomaterials to immunomodulate MPs polarization from M1 to M2 is one of the keys to bone regeneration.[17] It has been demonstrated that BGs can modulate the host immune response to the implant and promote MPs polarization to the M2 phenotype, creating an immune microenvironment favorable for stem cell differentiation.[21-23] This may be because the ionic products such as Si^{2+} and Ca^{2+} degraded by BGs modified the original ionic microenvironment.[24,25]

Indeed, PCL possesses excellent *in vivo* compatibility, but the acidic products of degradation likewise induce aseptic inflammation and promote MPs modulation and tumor necrosis factor alpha (TNFα) expression.[26,27] However, whether BGs can improve the immunomodulatory effects of PCL has rarely been reported. In addition, fiber thickness and pore size have a profound effect on the immunomodulatory properties of the scaffolds. Upon the expression of inflammatory genes, thicker fibers and larger pore sizes seem to be more favorable for extracellular matrix secretion and deposition, tending to expression of M2 phenotype genes (CD206, ARG).[28] For example, Abebayehu et al.'s study on electrospun polydioxanone scaffolds reported that larger pore size or thicker fibers tend to promote the M2 phenotype of MPs.[29] Zhu et al.'s study on PCL electrospun fibers similarly found that scaffolds with coarse fibers and large pore sizes exhibited better immune properties.[30] However, these are basically based on studies at the nano- or tens of microns level. Currently, studies on immunomodulation using three-dimensional (3D)-printed BGs/PCL scaffolds are relatively scarce, and there is an even greater lack of systematic studies on MPs polarization modulation and immune-coordinated osteogenesis in large fiber diameters (300–800 μm) and pore sizes (200–800 μm).

In this study, we prepared a SiO_2-CaO_2-P_2O_5 ternary dendritic mesoporous structured bioactive glass (MBG) with high specific surface area and pore size by sol-gel method. MBG/PCL scaffolds were prepared by mixing different ratios of BMG powder with PCL using a fused deposition molding (FDM) 3D printer. The composite scaffolds were investigated for their physicochemical properties and immune-coordinated osteogenic properties, to select the optimal MBG ratio scaffolds with the best compressive strength and osteogenic activity. Finally, MBG/PCL scaffolds with different fiber diameters and pore sizes were prepared based on the optimal MBG ratio to explore the effects of fiber thickness and pore size on the physicochemical properties of the scaffolds, the regulation of MPs polarization to the M2 phenotype, and the promotion of osteogenic potential.

2. Materials and methods

2.1. Materials

Cetyltrimethylammonium chloride (CTAC), tetraethylorthosilicate (TEOS), cyclohexane, triethyl phosphate, calcium nitrate tetrahydrate, sodium hydroxide, anhydrous ethanol, and dichloromethane were purchased from Guangzhou Chemical Reagent Factory (China). PCL (molecular weight: 54,000) was obtained from Jinan Daigang Biotech Co. (China). Vitamin C and β-glycerophosphoric acid sodium were purchased from Macklin (Shanghai China). Dexamethasone was obtained from J&K Scientific (Beijing China). Ultrapure RNA Kit, HiFiScript cDNA Synthesis Kit, and Ultra SYBR Mixture (Low ROX) were purchased from CWBIO (Beijing China). Alkaline phosphatase (ALP) kit, BCA protein assay kit, and RIPA lysate were supplied by Biyun Tian Biotechnology Co. (China). Dulbecco's modified Eagle medium (DMEM), fetal bovine serum, penicillin–streptomycin solution, phosphate buffer, trypsin, and CCK8 kit were obtained from Gibco (USA). Rat bone marrow mesenchymal stem cells (BMSCs) and macrophage cells (RAW264.7) were supplied by Gibco. Rat bone marrow mesenchymal stem cells (BMSCs) and macrophage cells (RAW264.7) were supplied by ATCC (USA).

2.2. Preparation of dendritic mesoporous bioactive glass (MBG) and MBG/PCL scaffolds

2.2.1 Preparation of dendritic mesoporous bioactive glass (MBG)

SiO_2-CaO_2-P_2O_5 ternary MBG were synthesized with reference to the previous methods.[31] Briefly, 1.8 g of CTAC was added to an appropriate amount of aqueous ethanol to form the aqueous phase, 5.2 mL of TEOS was dissolved in 5 mL of cyclohexane solution to form the oil phase, and the oil and aqueous phases were mixed and stirred for 30 min. Aqueous sodium hydroxide (1 M) was added to catalyze the reaction, followed by the sequential addition of triethyl phosphate and tetrahydrate calcium nitrate, and stirring was performed overnight. The sample was subjected to centrifugation (4000 rpm, room temperature, 8 min) after stirring, and left to stand for 24 h to yield a white precipitate, which was washed alternately with anhydrous ethanol and deionized water, and MBG powder was obtained after drying and calcination.

2.2.2. Preparation of MBG/PCL scaffolds

MBG powders (0 mg, 50 mg, 100 mg, 200 mg, and 300 mg) were weighed and dissolved in 10 mL of dichloromethane solution containing 1 g PCL. After stirring well, the solution was poured into the corresponding glass dishes respectively, and the dichloromethane was fully evaporated to obtain 0% MBG/PCL (0MBG/PCL), 5% MBG/PCL (5MBG/PCL), 10% MBG/PCL (10MBG/PCL), 20% MBG/PCL (20MBG/PCL), and 30% MBG/PCL (30MBG/ PCL) of the scaffold feedstock. The raw materials were put into the cylinder of a 3D printer (EFL-BP-6603, Suzhou Institute of Intelligent Manufacturing, Suzhou, China), heated, and melted, and subsequently, the cylindrical 3D scaffolds were printed out (the diameter of the scaffolds for the mechanical strength test was 10 mm and the height was 5 mm, and the specifications of the rest of the scaffolds for

the performance and cellular experiments were 7 mm in diameter and 1 mm in height).

2.3. Characterization materials

2.3.1 Surface morphology of MBG

The microscopic mesopore morphology and structure of MBG were tested and characterized by a high-resolution field emission scanning electron microscope (Merlin) from Carl Zeiss, Germany, and a transmission electron microscope (JEM-2100HR) from JEOL, Japan, respectively. The mesopore structure was tested and characterized by an instrument that analyzes specific surface area and pore size (NOVA4200e, Kantar Instruments, USA). The structure was tested at 250°C for 4 h. The N_2 adsorption–desorption curves of the bioactive glasses were analyzed, and the parameters such as specific surface area, pore volume, average pore size, and distribution were calculated.

2.3.2. Surface morphology of the scaffolds

The surface of the scaffolds was sprayed with gold. The microscopic morphology and structure of the scaffolds were observed by a scanning electron microscope operated at an accelerating voltage of 10 kV. Quantitative analysis of the scaffolds with different filament diameters and fiber spacing was performed using Image J software.

2.3.3. Compositional analysis of the scaffolds

The scaffolds were characterized and analyzed by Fourier transform infrared spectroscopy (FTIR) in the wavenumber range of 4000–400 cm^{-1} for the infrared characteristic absorption peaks of the scaffolds. Thermal weight loss data of the scaffolds were determined using a thermogravimetric analyzer, in which the samples were heated from room temperature to 800°C under a nitrogen atmosphere at a rate of 10°C/min.

2.3.4. Determination of porosity of the scaffolds

The mass of the dried scaffolds sample was measured as M_0. The total mass of the specific gravity flask filled with anhydrous ethanol at room temperature was recorded as M_1, the total mass of the sample placed in the flask and ultrasonicated for 10 min to exhaust the air bubbles was measured as M_2, and the residual mass of the sample removed and weighed was recorded as M_3. The scaffolds obtained the porosity was calculated by the following formula:

$$P = (M_2 - M_3 - M_0)/(M_1 - M_3) \quad (I)$$

2.3.5. Mechanical strength test of the scaffolds

The mechanical properties of the scaffolds were analyzed by placing them on an INSTON testing machine (34 sc-5) with a compression rate of 1 mm/min after drying.

2.3.6. Hydrophilicity test of the scaffolds

The scaffolds were placed on a Contact Angle Tester (DSA25, KRUSS, Germany), and drops were placed on the surface of the scaffolds, with a volume of 2 μL of liquid per drop, adjusting the position of the sample in contact with the drop to coincide with the baseline of the measurement, taking photographs to obtain a static image of the drop at this point in time, and calculating the magnitude of contact angle (θ) of the scaffolds for each group of scaffolds using the contact angle measurement software.

2.4. Cellular experiments

2.4.1. Sterilization of cell culture and materials

BMSCs and RAW264.7 cells were cultured after resuscitation in a thermostatic cell culture incubator (MCO-18AIC, PHCbi, Japan) at 37°C with a CO_2 concentration of 5%. The complete medium used constituted a high-sugar medium (DMEM) as the basal medium supplemented with 10% FBS, 100 μg/mL of penicillin, and 100 μg/mL of streptomycin. The medium was changed once a day or once in 2 days during the culture process depending on the cell condition. Cells were passaged upon reaching 70–80% confluence. Only cells at passages 3–5 were used in this experiment.

The scaffolds in each group were soaked in 75% ethanol solution for 2 h before the experiment, and the scaffolds were lubricated with PBS three times and overnight in an ultraviolet (UV) sterilizer (30 L–800 L, Shengzhiyuanhe Scientific and Educational Equipment Co., Ltd., Jiangsu, China).

2.4.2. Histocompatibility evaluation of the scaffolds

BMSCs were utilized to evaluate the histocompatibility of biological cells with the scaffolds. Briefly, sterilized scaffold samples were placed in 48-well plates, and 5×10^4 BMSCs were seeded in the samples. The medium was removed after 1, 3, and 7 days of incubation, and cell proliferation rate on the different scaffolds was assessed using the CCK-8 kit assay, with OD values measured using an enzyme labeling instrument (Tecan Spark, Austria).

Cell viability assay of BMSCs was performed by staining the cells on the sample surface with live-dead cell dye. Afterward, the morphology status and distribution of cells on the sample surface were observed using an inverted fluorescence microscope. Selected cells were tested after 72 h of adhesion and proliferation on the sample surface.

2.4.3. Detection of MPs polarization gene expression levels

RAW264.7 cells were inoculated onto the scaffold samples placed in 48-well plates at a density of 5×10^4 cells per well. The complete culture medium was changed every 2–3 days

(the medium removed from each group of samples was collected and mixed with osteogenic induction solution at a ratio of 1:5 to prepare MP-conditioned medium for spare use). On days 1 and 3, real-time fluorescence quantitative polymerase chain reaction (PCR) was used to detect the expression of the M1 immunomarker genes *Tnfa*, recombinant human interleukin-1 beta (*Il1b*), and the M2 immunomarker genes *CD206* and arginase (*Arg*). Glyceraldehyde phosphate dehydrogenase (*Gapdh*) was used as an internal reference gene.

2.4.4. Evaluation of the osteogenic performance of each group of scaffolds.

BMSCs (1×10^5) were added into 48-well plates containing scaffold samples. After 24 h of incubation, the supernatant was aspirated and discarded, and complete culture medium or osteogenic induction medium (100 mL complete culture medium + 0.39 mg dexamethasone + 1.76 mg vitamin C + 306.11 mg sodium β-glycerophosphate) or MP-conditioned medium was added, respectively. The medium was changed periodically. After 7 and 14 days of osteogenic induction, the induction was terminated, and real-time fluorescence quantitative PCR was used to detect the osteogenic marker genes alkaline phosphatase (*Alp*), Runt-related transcription factor 2 (*Runx2*), osteopontin (*Opn*), type I collagen (*Col1*), and bone morphogenetic protein-2 (*Bmp2*) in the cells, and *Gapdh* was used as the internal reference gene. ALP enzyme activity was assayed on days 7 and 14 using the BCA method.

2.5. Statistical analysis

The experiments were repeated six times, and the results are expressed as the mean ± standard deviation. All statistical analyses were processed using GraphPad Prism software. One-way analysis of variance (ANOVA) followed by Dunnett's multiple comparison test was used to determine significant differences between the experimental groups. Results with *p*-value less than 0.05 were considered statistically significant.

3. Results

3.1. Characterization of MBG

The MBG micromorphology was characterized by SEM and TEM. It can be seen from Figure 1A that our prepared MBG is a microsphere formed by the stacked combination of many small nanoscale particles, and the glass microspheres are well dispersed with a loose and porous surface. From the transmission electron micrographs (Figure 1B), it can be found that the pore channels of the glass microspheres are dendritically distributed. The N_2 adsorption–desorption curves in Figure 1C indicate that the MBGs are mesoporous materials exhibiting type IV isotherms, which were adopted by the BJH (Barrett, Joyner, Halenda) pore size distribution calculation model. The pore size distribution graph of MBGs can is displayed in Figure 1D. The mesopore size distribution of the glass microspheres was between 3 nm and 54 nm, and the specific surface area of the bioactive glass microspheres was calculated to be 457.14 m^2/g, the pore volume was 1.38 cm^3/g, and the average pore size was 11.83 nm.

3.2. Characterization and physicochemical properties of MBG/PCL scaffolds

PCL scaffolds containing different concentrations of MBG were printed using a 3D printer. Observed by SEM, as shown in Figure 2A, the filament diameters of the scaffold group researched were of uniform thickness, and the fiber directions differed by 90° from each other. Scattered pores existed on the surface of the scaffolds, and MBG particles were visibly attached to the surface of 5MBG/PCL, 10MBG/PCL, 20MBG/PCL, and 30MBG/PCL scaffolds. Under high magnification, we found that the scaffold surface became rougher with the increase of MBG content, with 30MBG/PCL demonstrating the most significant result. These rough surfaces can provide sites for cell adhesion, which is more conducive to guiding cell proliferation, differentiation, and other behaviors.[32,33] As shown in Figures 2B and 3E, the contact angles of 0MBG/PCL, 5MBG/PCL, 10MBG/PCL, 20MBG/PCL, and 30MBG/PCL scaffolds were 108.78 ± 1.45°, 107.93 ± 1.42°, 107.35 ± 1.65°, 99.12 ± 3.69°, and 96.15 ± 0.97°. The smaller contact angle indicates that the material is more hydrophilic. Overall, the addition of MBG improves the hydrophilicity of PCL materials, and the degree of improvement is related to the concentration of MBG. As shown by FTIR analysis (Figure 3A), the characteristic peaks of PCL appeared in all groups of scaffolds, of which -$(CH_2)_4$- at 2850–3000 cm^{-1} was CH stretching vibration, 1750 cm^{-1} was C=O stretching vibration peak, and 1150–1250 cm^{-1} represented -C-O-. The original characteristic peaks of PCL gradually decreased with the increase of MBG content. By thermogravimetric analysis of each group of scaffolds (Figure 3B), the mass loss of scaffolds with low to high MBG content was 100%, 95.896%, 91.43%, 86.005%, and 78.807% in order, and the mass of the remaining inorganic particles in each group of scaffolds was the same as the proportion of the mixed MBG. In the compression resistance test of the scaffolds (Figure 3C), we can see that the maximum compressive strength of pure PCL scaffolds was 8.39 ± 0.47 MPa, and with the increase of MBG content, the PCL's compression resistance experienced a gradual increased. The compressive strength of 5MBG/PCL scaffold was 9.70 ± 0.62 MPa, and it was most significant at 17.81 ± 0.35 MPa for 210MBG/PCL scaffold. However, on this basis, the compressive strength of the scaffolds gradually decreased with the increase in MBG content. 20MBG/PCL (11.21 ± 0.70 MPa) and

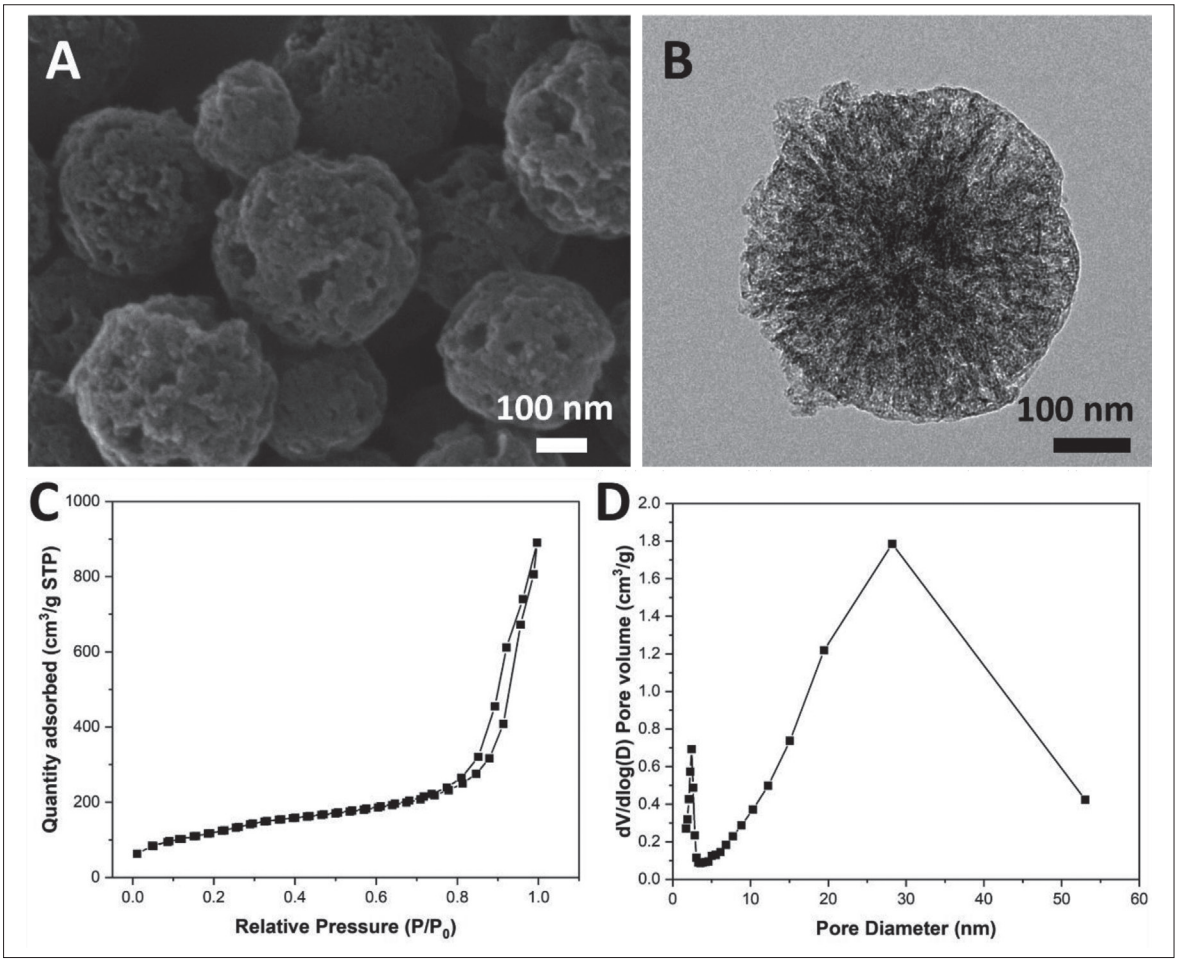


Figure 1. Characterization of MBG. (A, B) SEM and TEM images of MBG, respectively. (C) Isothermal graph of N_2 adsorption-desorption of MBG. (D) Pore size distribution graph of MBG.

30MBG/PCL (9.70 ± 4.07 MPa) scaffolds rapidly collapsed after reaching the peak compressive strength. As shown in Figure 3D, the porosity of each group of scaffolds was 76.06 ± 2.58%, 73.96 ± 2.83%, 71.32 ± 4.83%, 76.16 ± 3.25%, and 71.96 ± 2.47% in descending order of MBG content, with no significant difference between groups.

3.3. Evaluation of compatibility and osteogenic properties of the scaffold

As shown in Figure 4C, the OD values of BMSCs proliferating on the scaffolds in each scaffold group increased with the incubation time. On day 1 of co-culture, the OD value of the 10MBG/PCL group was significantly higher than that of the 0MBG/PCL group, whereas the difference between the remaining groups was insignificant. However, the proliferative activity of the 10MBG/PCL group was significantly better than those of the other groups on days 3 and 7. This result was consistent with the live/dead staining fluorescence intensity on day 3 (Figure 4A).

To assess the difference in performance of scaffolds in promoting ALP secretion from BMSCs in the presence (+OIM) and absence (-OIM) of osteoinductive fluid (OIM), we co-cultured scaffolds containing different MBG contents with BMSCs in +OIM and -OIM conditions for 7 days, and examined their ALP staining and quantification. The results, as shown in Figure S1 (Supplementary File), OIM significantly upregulated the scaffold-promoted ALP expression, as compared to the -OIM condition, a finding which we hypothesized to be related to the directional differentiation of BMSCs. BMSCs have multiple trajectories for differentiation, and OIM can induce the directional differentiation of BMSCs into osteoblasts.

The expression results of osteogenic differentiation-related genes (*Alp*, *Opn*, *Runx2*, *Bmp2*, *Col1*) in MBG/PCL scaffold-promoted BMSCs are shown in Figure 4E. In the early stage of osteogenic differentiation, the expression of osteogenic genes (*Alp*, *Opn*, and *Bmp2*) in 5MBG/PCL, 10MBG/PCL, and 20MBG/PCL scaffolds was

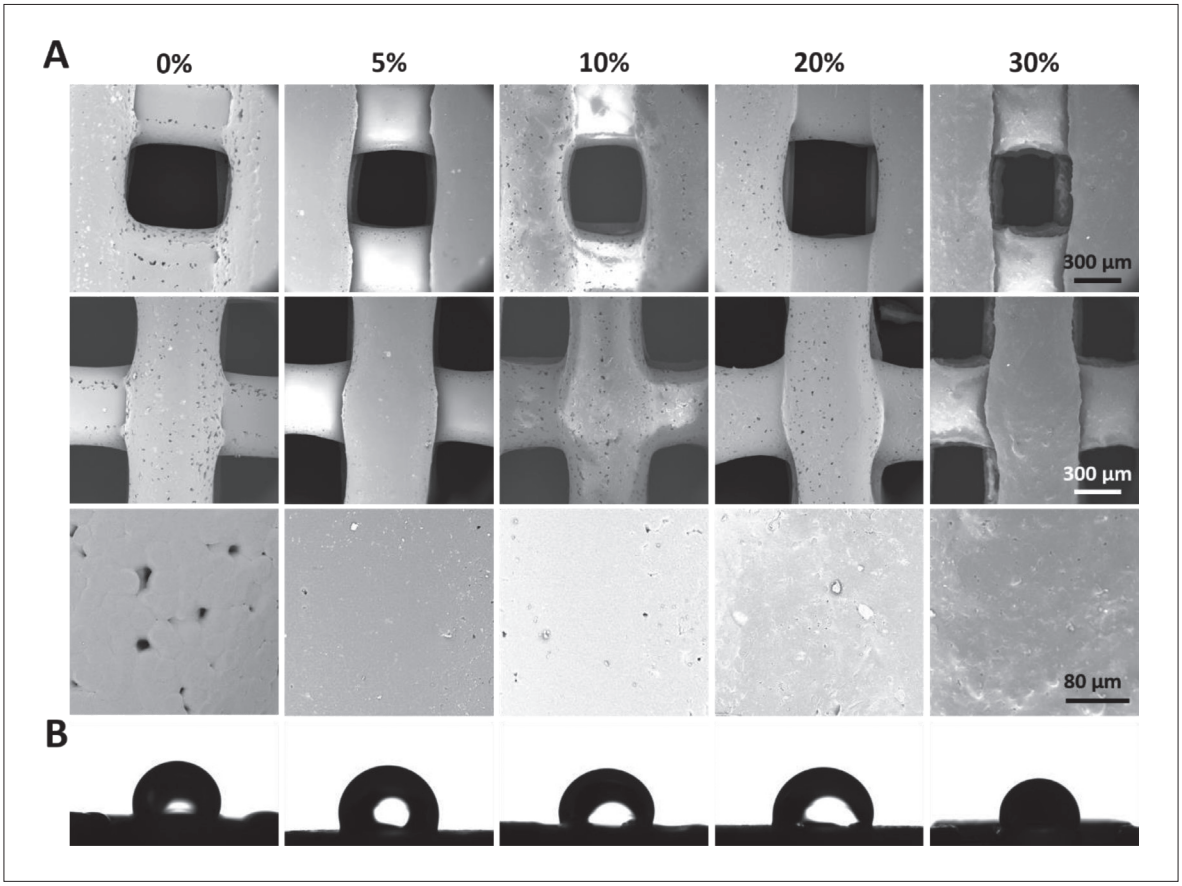


Figure 2. Surface morphology and contact angle images of MBG/PCL scaffolds. (A) SEM images of 0MBG/PCL, 5MBG/PCL, 10MBG/PCL, 20MBG/PCL, and 30MBG/PCL scaffolds. (B) Contact angle pictures of 0MBG/PCL, 5MBG/PCL, 10MBG/PCL, 20MBG/PCL, and 30MBG/PCL scaffolds.

significantly higher than that in the 0MBG/PCL group, while the difference between the 30MBG/PCL and 0MBG/PCL groups was not significant. On the other hand, the expression of *Col1* in the MBG-containing scaffolds was significantly higher than that in *the pure PCL group*. Notably, the 10MBG/PCL group scaffolds were the most significant in the upregulation of the expression of the above-mentioned genes compared to the other groups. Regarding the expression of *Runx2*, the 10MBG/PCL group likewise exhibited significantly higher expression than the 0MBG/PCL and 5MBG/PCL groups, whereas it was not significantly different than 20MBG/PCL and 30MBG/PCL in terms of *Runx2* expression. Even after 14 days of osteogenic induction, the 10MBG/PCL group still held the most potent ability in upregulating the expression of *Opn*, *Runx2*, *Bmp2*, and *Col1* compared to the other groups. The *Alp* expression of 10MBG/PCL and 20MBG/PCL scaffolds significantly surpassed that of 0MBG/PCL group, with 10MBG/PCL exhibiting higher gene expression compared with 30MBG/PCL, whereas there was no significant difference between the remaining groups. BMSCs were co-cultured with scaffolds, and ALP activity was quantified at 7 days of osteogenic induction (Figure 4D), and scaffolds in the 10MBG/PCL group had the highest ALP expression, while the difference between the remaining groups was not significant, which was also in agreement with the results of ALP staining (Figure 4B). In summary, the doping of MBG in PCL materials can enhance their *in vitro* osteogenic properties, with 10MBG/PCL scaffolds having the best pro-osteogenic differentiation properties for BMSCs.

3.4. Evaluation of scaffolds for MPs polarization and immunomodulation of osteogenic differentiation properties of BMSCs

MPs polarization status affects the process of bone regeneration. Based on Figure 5A, we found that among the various scaffolds inducing the polarization of RAW264.7 cells, the 10MBG/PCL scaffold had the most significant performance in upregulating the expression of M2-type genes (*CD206*, *Arg*) as well as inhibiting the expression of M1-type genes (*Tnfa*, *Il1b*). Compared with pure PCL scaffolds, MBG endowed PCL with an ability to promote MPs polarization to the M2 phenotype. The expression of

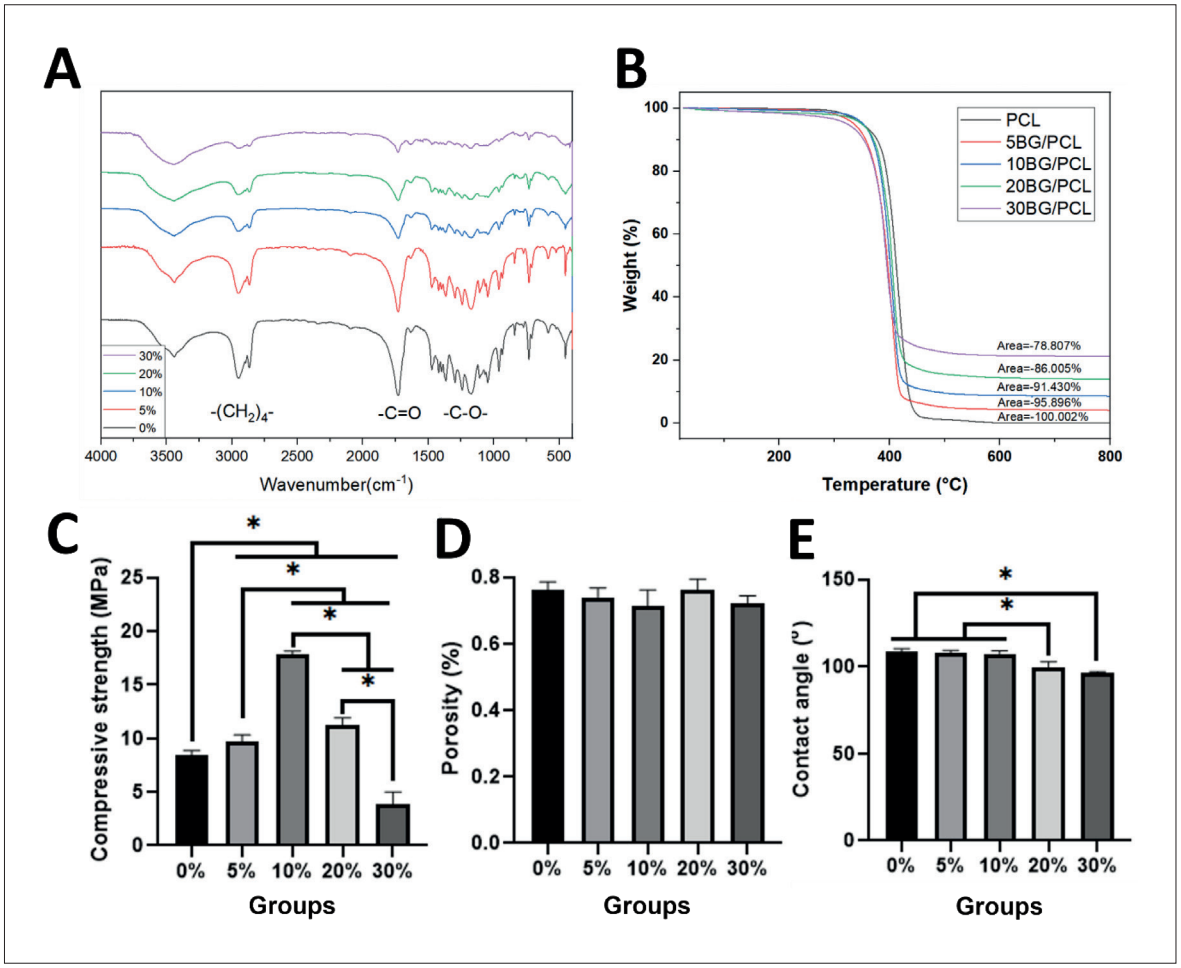


Figure 3. Physicochemical characterization of MBG/PCL scaffolds. (A) FTIR spectra. (B) Thermogravimetric analysis graph. (C) Comparison of compressive strength between scaffolds. (D) Comparison of porosity between scaffolds. (E) Comparison of hydrophilicity between scaffolds, measured by contact angle.

CD206 in MBG scaffolds was extremely low in all groups except for the 10MBG/PCL group, but better than that of the 0MBG/PCL group. The expression of *Arg* gene was upregulated the most significantly in the 10MBG/PCL group, and the expression was the lowest in the 0MBG/PCL group, while there was no significant difference in the MBG scaffolds of the other three groups. Regarding the M1-type genes, the 10MBG/PCL group significantly inhibited the expression of *Tnfa* and *Il1b*, whereas the 0MBG/PCL group upregulated them most significantly. The 30MBG/PCL showed stronger inhibition on *Tnfa* expression compared with than the 5MBG/PCL and 20MBG/PCL groups. However, the inhibition of *Il1b* was more evident in the 20MBG/PCL and 5MBG/PCL groups than in the 30MBG/PCL group.

To evaluate the *potential of scaffold-mediated M2 polarization of MPs to promote osteogenic differentiation of BMSCs, the* scaffolds in each group were added with corresponding MP-conditioned medium for pro-BMSCs osteogenic differentiation. Basically, the expression of osteogenic genes in MBG-containing scaffolds was significantly higher than that in *the pure PCL group*, except for the 0MBG/PCL and 30MBG/PCL groups, which showed no significant difference in the expression of *Col1* (Figure 5C). Compared with other groups, the expression of osteogenesis-related genes (*Alp*, *Runx2*, *Opn*, *Col1*, *Bmp2*) was most significantly upregulated in the 10MBG/PCL group. ALP staining and quantification, as displayed in Figure 5B-1 and B-2, showed that the ALP activity of the composite scaffolds was significantly higher than that of *the pure PCL group*, with the 10MBG/PCL group demonstrating the most pronounced ALP activity. The ALP activity of the 20MBG/PCL group was higher than that of the 30MBG/PCL group, but none of them was significantly different from that of 5MBG/PCL group.

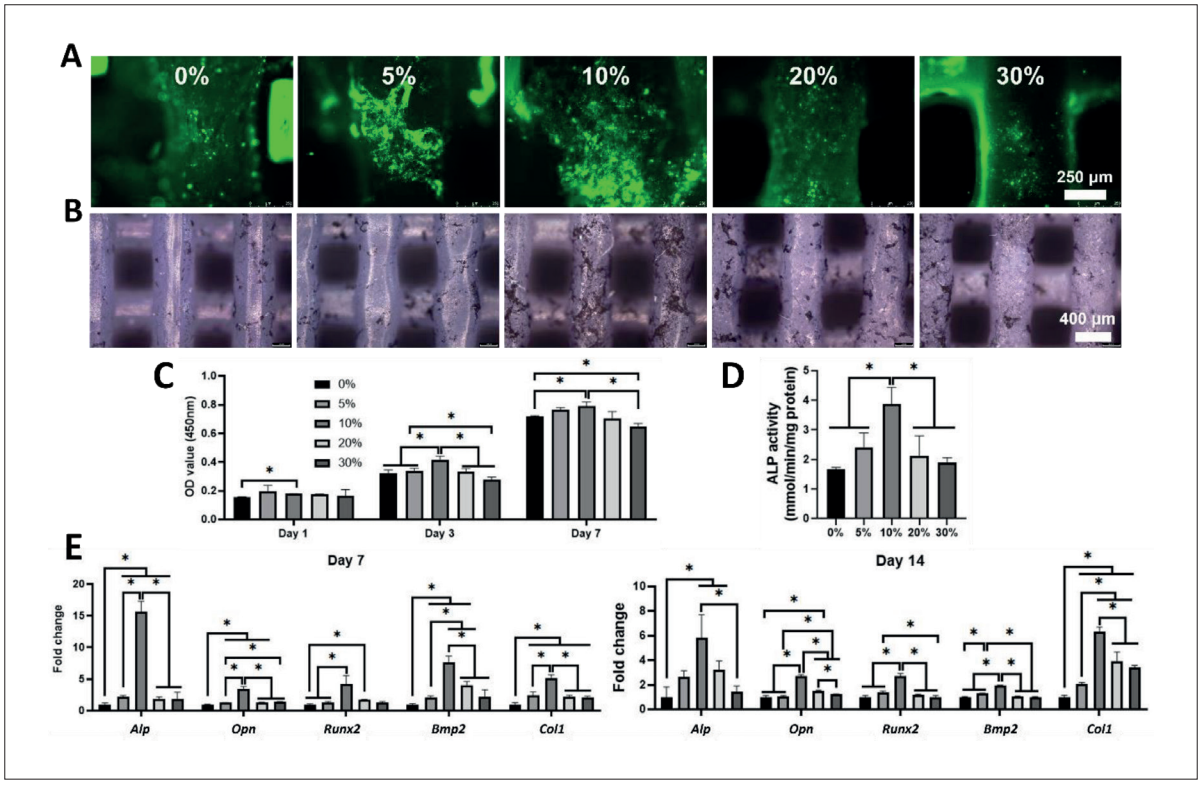


Figure 4. Cytocompatibility and osteogenic properties of MBG/PCL scaffolds. (A) Live/dead staining results of BMSCs co-cultured with scaffolds for 3 days. (B) ALP staining of MBG/PCL scaffold on day 7. (C) Proliferative activity of BMSCs on scaffolds on days 1, 3, and 7. (D) Quantitative analysis of ALP activity in MBG/PCL scaffolds on day 7. (E) Expression of osteogenesis-related genes (*Alp*, *Opn*, *Runx2*, *Bmp2*, *Col1*) in BMSCs co-cultured with scaffolds on days 7 and 14.

According to the results of the cellular experiments, the 10MBG/PCL scaffolds had a stronger immunomodulatory ability to induce MPs polarization toward M2 and inhibit the process of polarization toward the M1 phenotype compared with other groups. This is fully reflected in the potential of MP-conditioned medium to promote osteogenic differentiation of BMSCs.

3.5. Effect of fiber diameter and pore size on the characterization and physicochemical properties of MBG/PCL scaffolds

The 10MBG/PCL group materials were selected for further experiments, and 3D printing parameters were set using 10MBG/PCL scaffolds as templates. The three groups of scaffolds with uniform pore diameters of 500 μm and different fiber diameters (300 μm, 500 μm, 800 μm) were printed and labeled as F300, F500, and F800, respectively, while the scaffolds with uniform fiber diameter of 500 μm and different pore diameters (200 μm, 500 μm, 800 μm) were labeled as P200, P500, and P800, respectively.

As can be seen via SEM (Figure 6A), the pore diameters of the three groups of scaffolds, F300, F500, and F800, were the same, and the fiber thicknesses were 314.80 ± 1.30 μm, 516.67 ± 6.43 μm, and 811.33 ± 5.51 μm, respectively, which was in accordance with the initial design parameter gradient. The fiber directions differed by 90° interlacing each other, and there were scattered pores and MBG adherence on the surface of the scaffold. There was no significant difference in the surface roughness of the scaffolds in the three groups as seen under high magnification. The pictures and quantitation of these scaffolds' hydrophilicity are shown in Figure 6B and E. The best result was 91.30 ± 7.93° for F500, followed by 98.08 ± 5.69° for F800. The compressive strength results were still the most significant for F500 (Figure 6D). On this basis, when the fiber scaffolds decreased by 200 μm, the compressive performance of the scaffolds decreased by 15.72 MPa. An increase in fiber diameter by 300 μm increased the compressive performance of the scaffolds by 4.28 MPa. The porosity of the three scaffolds was inversely related to compressive performance, with an increase in the porosity of the F300 by 1.73% compared to that of the F500, and a downward adjustment of the F800 by 6.06% (Figure 6C).

In the comparison of scaffolds with different pore diameters, the fiber diameters of scaffolds in the P200,

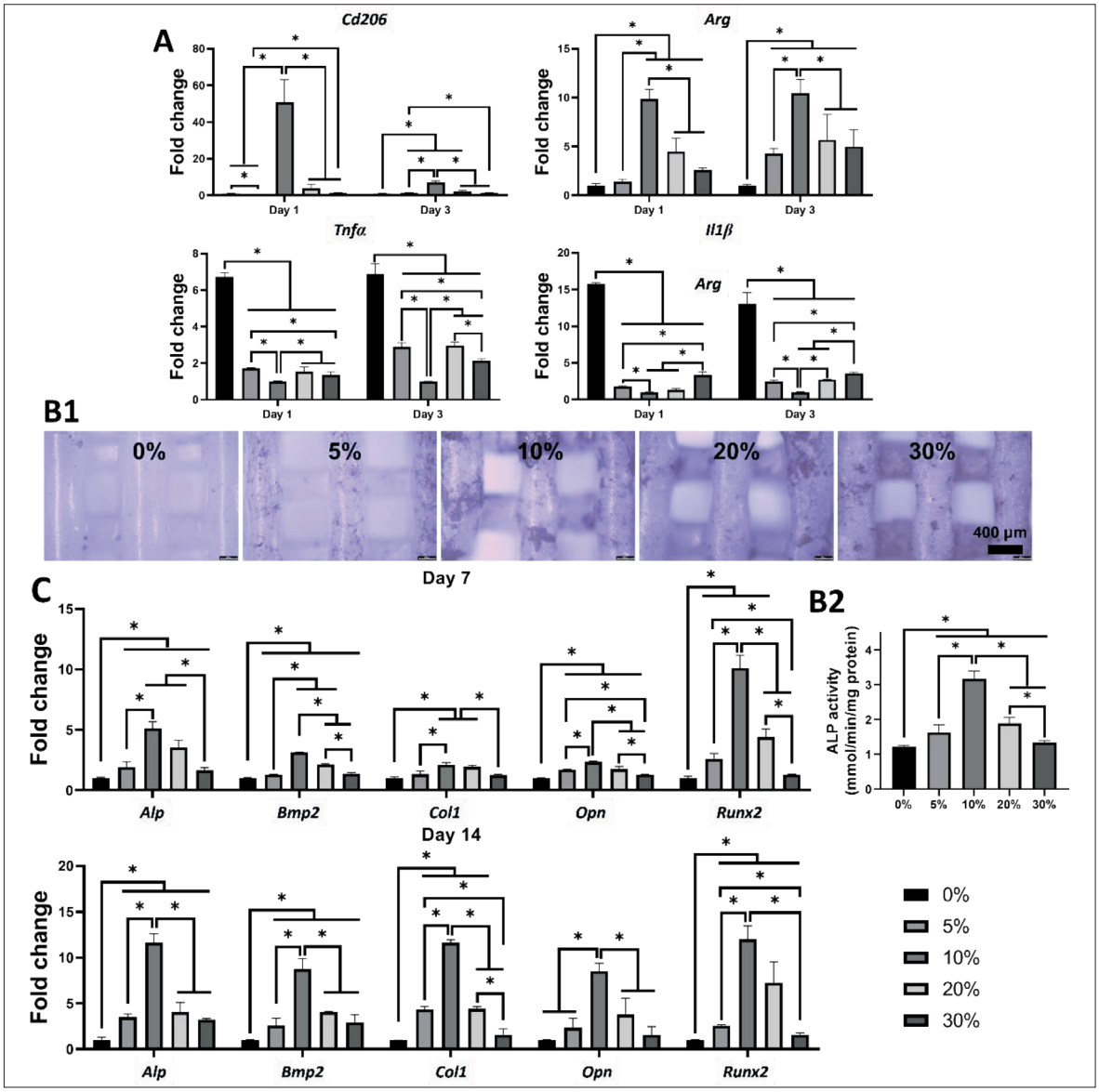


Figure 5. Differential immunomodulatory properties of MBG/PCL scaffolds. (A) Levels of RAW264.7 cell polarization gene expression promoted by the scaffolds. (B1, B2) ALP staining of MBG/PCL scaffolds with BMSCs cultured in an MP-conditioned medium (B1) and the corresponding quantification plot (B2). (C) Expression levels of osteogenesis-related genes (*Alp*, *Opn*, *Runx2*, *Bmp2*, *Col1*) in BMSCs cultured in MBG/PCL scaffolds with MP-conditioned medium.

P500, and P800 groups were basically the same, and the pore diameters experienced gradual increase with the gradient of the initial design parameters, which were 241.33 ± 29.79 μm, 535.17 ± 21.57 μm, and 794.80 ± 22.70 μm, respectively (Figure 7A). The fibers were crisscrossed with each other, and the surface of the scaffold was brimming with pores and MBG consistent with the previous scaffold. According to Figure 7B and E, P500 has the largest contact angle, while P200 and P800 have almost similar contact angles of 86.53 ± 1.86° and 85.45 ± 0.47°, respectively. Through Figure 7C, we can see that the larger the pore size of the scaffolds, the higher the porosity (porosities of P200, P500, and P800: 70.01 ± 2.12%, 71.32 ± 4.83%, and 80.37 ± 1.91%, respectively). Meanwhile, the compressive strength of the scaffold decreases with increasing pore size. P200 has the best mechanical properties, while P500 decreases by about 4.90 MPa, and P800 shows the lowest compressive strength, which is 3.13 ± 1.09 MPa (Figure 7D).

3.6 Effect of fiber thickness on the immunomodulatory osteogenic properties of MBG/PCL scaffolds

As can be seen from the fluorescence staining results of Figure 8A, BMSCs were able to colonize scaffolds with

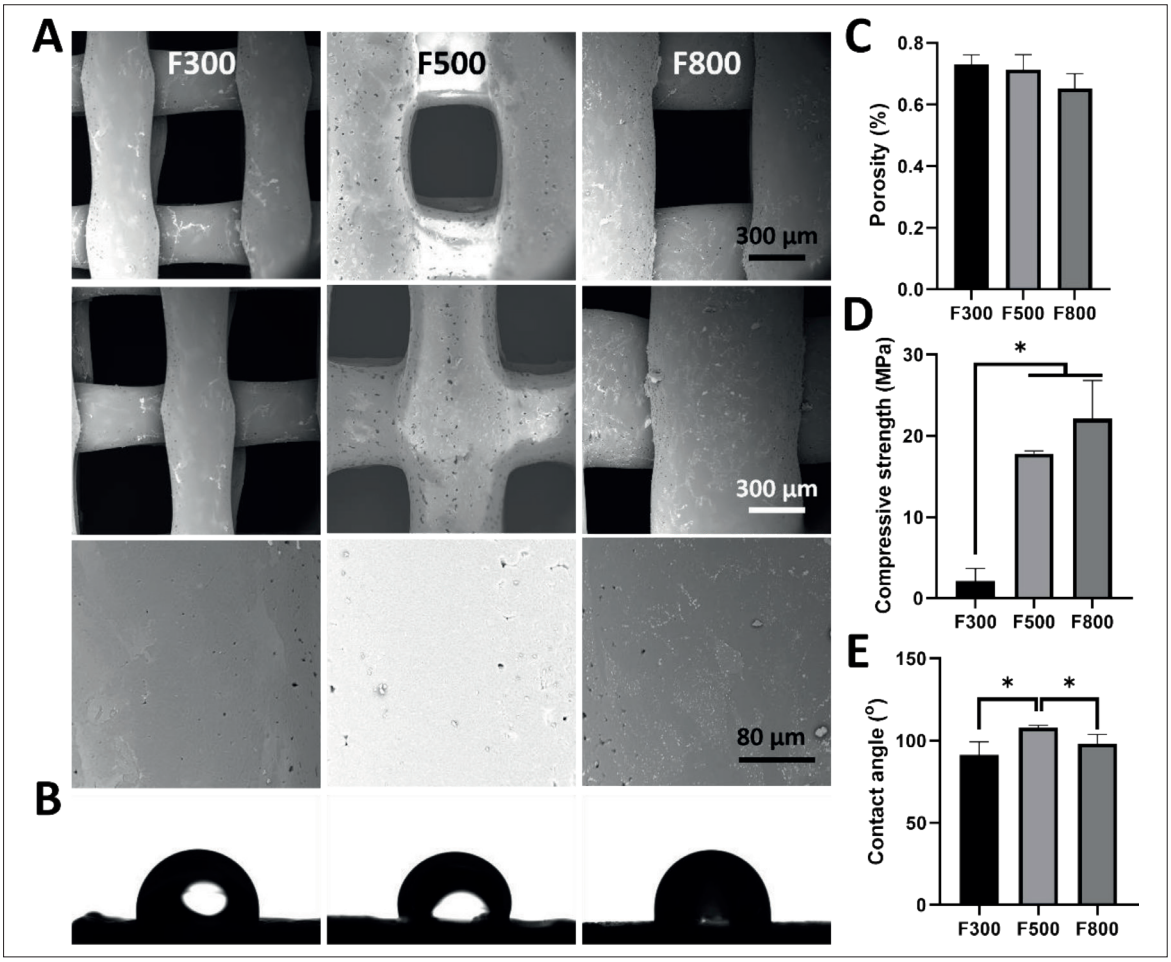


Figure 6. Surface morphology and physicochemical properties of F300, F500, and F800. (A) SEM images of F300, F500, and F800. (B, E) Contact angle pictures and comparison of hydrophilicity between F300, F500, and F800. (C, D) Comparison of porosity and mechanical property between F300, F500, and F800.

different fiber diameters. Among them, F500 had the highest intensity of fluorescence, followed by F800, which was consistent with the OD gradient of cell proliferation. In 1-, 3-, and 7-day cultures (Figure 8C), the proliferative activity of the cells generally showed a decreasing order of F500, F800, and F300. In terms of osteogenic properties, F500 upregulated the expression of osteogenic genes (*Alp*, *Runx2*, *Opn*, *Col1*, *Bmp2*) most significantly, followed by F300, and the lowest was F800 (Figure 8E). There was no significant difference between F800 and F300 in ALP staining and quantification, and F500 excelled in these aspects (Figure 8B and D).

The effect of fiber thickness on the scaffold's performance in promoting MPs polarization is shown in Figure 9A. F500 significantly upregulated the expression of *CD206*, and F300 had slightly higher *CD206* expression than on day 1, but the difference was not significant on day 3. On day 1, F300 significantly upregulated the expression of *Arg*, and F500 had the lowest expression. However, on day 3, F500 exhibited the most significant upregulation of *Arg* expression, while F300 and F800 again did not show a difference. F500 significantly suppressed the expression of M1-type genes (*Tnfa*, *Il1b*), which were upregulated by F300; however, F800 surpassed F300 in terms of *Tnfa* expression on day 3. Under the mediation of MP-conditioned medium, F500 promoted the upregulation of the expression of osteogenic genes (*Alp*, *Opn*, *Bmp2*, *Col1*) at all time points most significantly. The *Runx2* expression of F500 was significantly higher than that of F800 on day 7 and not significantly different from that of F300. On day 14, F300 was superior to F800, but F500 did not show differences with the remaining two groups (Figure 9C). F300 and F800 did not show significant differences in staining and quantification of ALP, and F500 significantly promoted

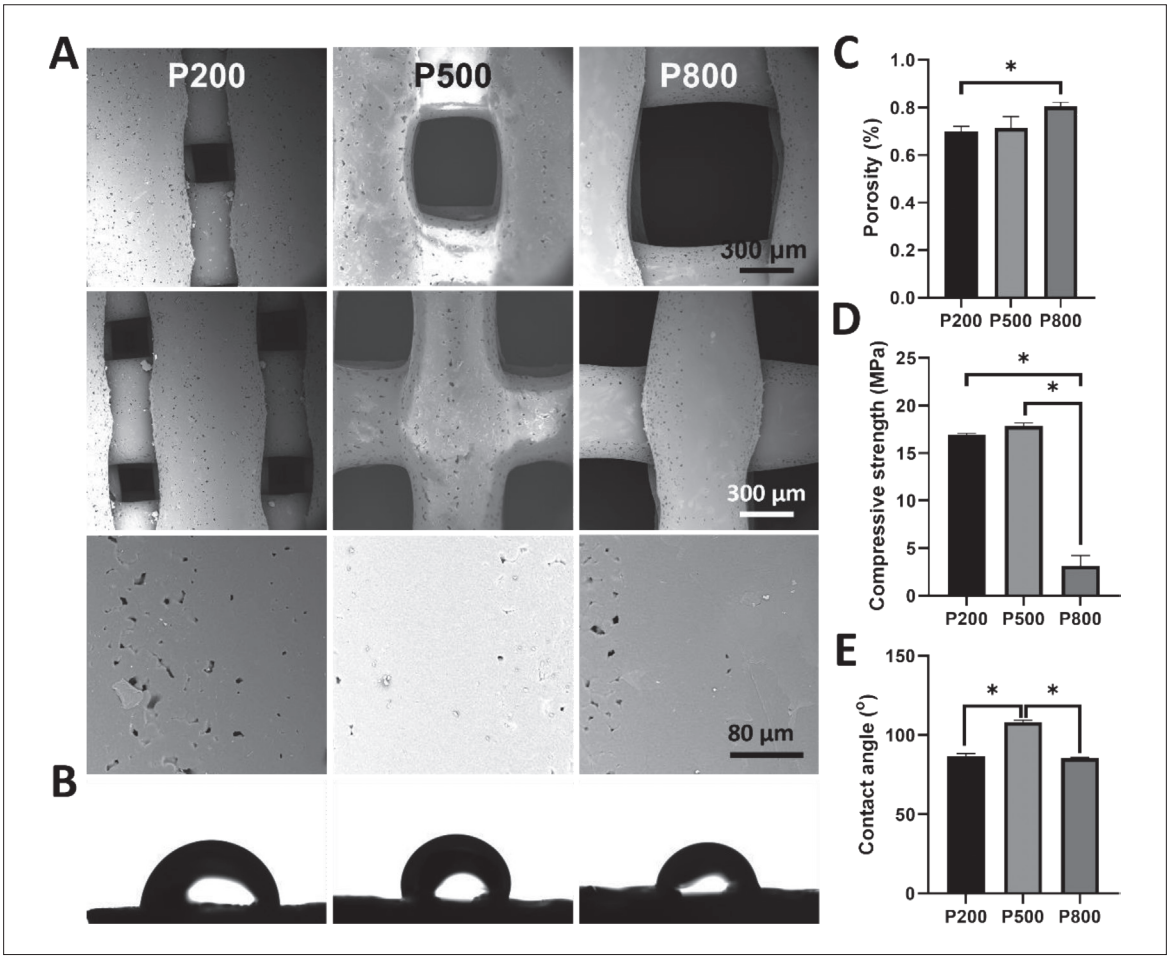


Figure 7. Surface morphology and physicochemical properties of P200, P500, and P800. (A) SEM images of P200, P500, and P800. (B, E) Contact angle pictures and comparison of hydrophilicity between P200, P500, and P800. (C, D) Comparison of porosity and mechanical property between P200, P500, and P800.

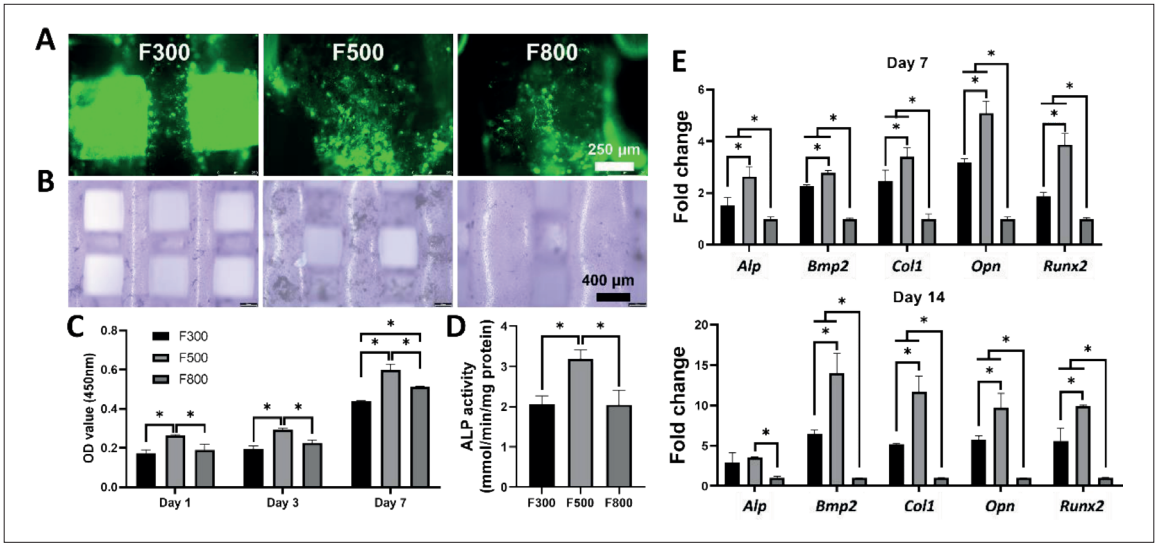


Figure 8. Differential plots of proliferative activity and osteogenic properties of F300, F500, and F800 cells. (A, C) Live/dead staining and proliferative activity of BMSCs of F300, F500, and F800. (B, D) Staining and quantification plots of ALP of F300, F500, and F800 co-cultured with BMSCs on day 7. (E) Expression levels of osteogenic genes (*Alp*, *Runx2*, *Opn*, *Col1*, *Bmp2*) in F300, F500, and F800 co-cultured with BMSCs on days 7 and 14 of co-culture.

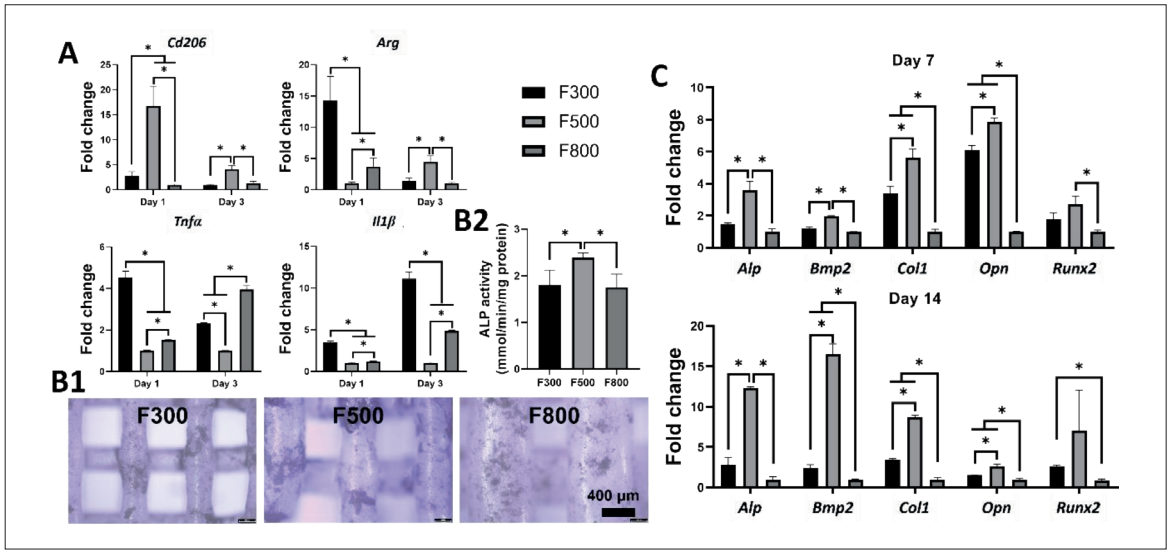


Figure 9. RAW264.7 cell polarization and immunomodulation of osteogenic properties promoted by F300, F500, and F800 scaffolds. (A) Levels of RAW264.7 cell polarization gene expression induced by the scaffolds. (B1, B2) Staining and quantification plots of F300, F500, and F800 in MP-conditioned medium, which mediated the expression of ALP in BMSCs. (C) Expression levels of osteogenic genes (*Alp*, *Opn*, *Runx2*, *Bmp2*, *Col1*) in F300, F500, and F800 scaffolds in MP-conditioned medium.

ALP secretion (Figure 9B-1 and B-2). Overall, the levels of immunomodulatory osteogenic properties of these three scaffolds were in this order: F500 > F300 > F800.

3.7. Effect of pore size on the immunomodulatory osteogenic properties of MBG/PCL scaffolds

In this subsection, we continued to evaluate the effect of pore size on the performance of the scaffolds. The scaffolds were co-cultured with BMSCs, and on the first day of proliferation, P800 had the highest OD, and there was no significant difference between P200 and P500. On days 3 and 7, the cell proliferative activity of P500 was significantly enhanced. Overall, the BMSCs proliferative activity for these scaffolds is in this order: P500 > P800 > P200, and the results are demonstrated in Figure 10C. In the fluorescence staining after 3 days of co-culture, we observed the similar trend. The fluorescence intensity of P500 was the strongest, followed by that of P800, and P200 had the weakest fluorescence intensity (Figure 10A). According to the ALP staining and quantification on day 7, we could see that P500 had the most significant ALP expression effect, and the ALP expression was higher in P200 than in P800 (Figure 10B and D). However, in the expression of *Alp*, *Opn*, *Runx2*, *Bmp2*, and *Col1*, P800 was superior to P200, with the most significant upregulation performance noted in P500 (Figure 10E).

The effect of pore size on the scaffold's performance in promoting MP polarization is shown in Figure 11A. Large pore size seems to promote MPs polarization toward the M2 phenotype at a greater extent. Compared with P200, P500 and P800 significantly upregulated the expression of *CD206* and *Arg*. Meanwhile, the expression of *Arg* on the first day was higher in P500 than in P800, while there was no significant difference in *Arg* expression between P500 and P800. P200 induced the expression of inflammatory genes (*Tnfa*, *Il1b*) the most significantly, followed by P800, while P500 exhibited a significant inhibitory effect on the expression of these inflammatory genes. Mediated by MP-conditioned medium, P500 significantly upregulated the expression of osteogenic genes at all time points, and the *in vitro* immuno-osteogenic properties of P800 were superior to those of P200 (Figure 11C). Similarly, P500 had the highest staining and levels of ALP, followed by P800, while P200 had the lowest levels in these parameters (Figure 11B-1 and B-2). Overall, the levels of immunomodulatory osteogenic properties of these scaffolds are in this order: P500 > P800 > P200.

4. Discussion

Three-dimensional printing allows for the direct layer-by-layer fabrication of highly accurate 3D solids based on the structure of the bone as well as the type of bone defect, with the assistance of imaging data and computer-aided design models, which are widely used in bone tissue engineering.[34-36] The performance requirements of bone tissue-engineered scaffolds can be easily met by 3D-printed composite materials (e.g., polymers and bioceramics), and thus, 3D printing of these materials is currently a hot research

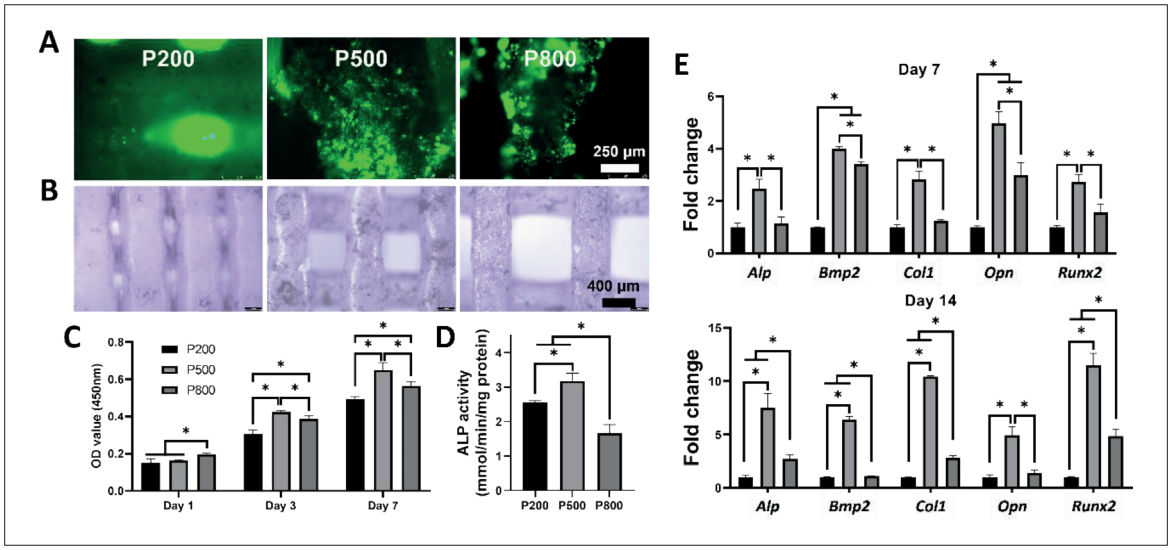


Figure 10. Differential plots of proliferative activity and osteogenic properties of P200, P500, and P800 cells. (A, C) Live/dead staining and proliferative activity of BMSCs of P200, P500, and P800. (B, D) Staining and quantification of ALP in P200, P500, and P800 co-cultured with BMSCs on day 7. (E) Expression levels of osteogenic genes (*Alp*, *Runx2*, *Opn*, *Col1*, *Bmp2*) of P200, P500, and P800 co-cultured with BMSCs on days 7 and 14.

topic.[37] Particularly, bioceramics such as BGs are regarded as excellent bone-based restorative materials owing to their unique inorganic amorphous structure, bioactivity, and osseointegration properties. However, the dense pores and low specific surface area of common BGs and mesoporous BGs limit the mechanical properties and bioactivity of the most scaffolds, and it is often necessary to increase the proportion of glass to offset these shortcomings.[16,38] But, this is a detrimental move since the glass could degrade *in vivo* and taken up by the body.[16,38] Therefore, in this study, we synthesized SiO_2-CaO_2-P_2O_5 ternary MBG by sol-gel method, and the dendritic nano-mesoporous structure endowed the BGs with higher specific surface area (457.14 m^2/g) and pore volume (1.38 cm^3/g) (Figure 1). 3D printing

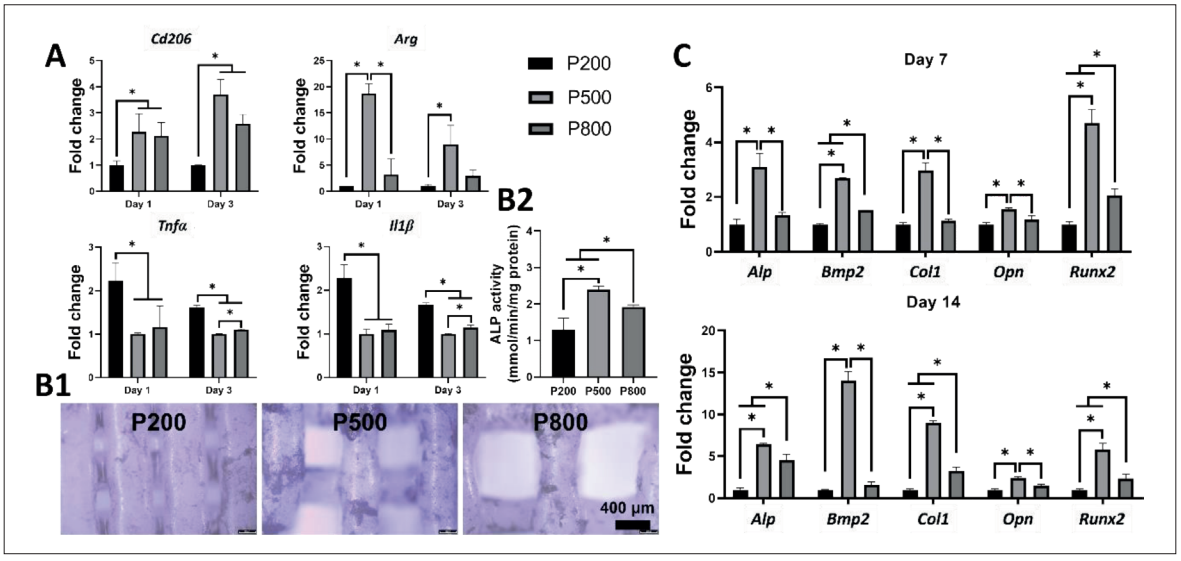


Figure 11. RAW264.7 cell polarization and immunomodulation of osteogenic properties promoted by P200, P500, and P800. (A) Levels of RAW264.7 cell polarization gene expression induced by the scaffolds. (B1, B2) Staining and quantification plots of P200, P500, and P800 in MP-conditioned medium, which mediated the expression of ALP in BMSCs. (C) Expression levels of osteogenic genes (Alp, Opn, Runx2, Bmp2, Col1) in P200, P500, and P800 scaffolds in MP-conditioned medium.

was employed to prepare MBG/PCL scaffolds. Based on the SEM observation and contact angle measurement, the addition of MBG increased the roughness of the PCL scaffold surface and enhanced the hydrophilicity of the PCL material (Figure 2). It was shown that cells can change the curvature of the cell membrane by contacting with the rough surface morphology of the material and cause a change in protein conformation, directing the expansion of membrane proteins toward the material surface, which is favorable for cell adhesion and osseointegration.[39] For example, Wang et al. found that significantly higher ALP activity and cell mineralization were detected in human bone marrow mesenchymal stem cells (hMSCs) cultured on rough-surface composites compared to smooth-surface PEEK/nano-fluorinated hydroxyapatite composites.[40] The hydrophilic nature of the material surface synergizes the above changes at the cellular molecular level.[41] Meanwhile, the compressive capacity of PCL scaffolds was enhanced with the incorporation of MBG, which was the most pronounced with 10% MBG/PCL. The compressive capacity of 20% and 30% scaffolds even started to decline after reaching the peak. This is because the way PCL encapsulates MBG particles resembles a "sea-island" structure. We hypothesize that when the content of MBG ("island" component) increases further, it adversely affects the overall connectivity of PCL ("sea" component), which in turn reduces the maximum compressive strength of the scaffolds. At the same time, a larger proportion of MBG agglomerates in the PCL,[42] which leads to uneven force during compressive deformation, resulting in the overall collapse of the scaffolds. It was shown that bioceramic particles could increase the mechanical properties by mutual bonding with polymer matrix macromolecules, and mesoporous glass particles with higher specific surface area and pore space could enhance this bonding.[43] This may be the reason why the mechanical properties can be significantly enhanced by using low concentration in this study. It is well known that cancellous bone is an interconnected porous structure with porosity varying from 30% to 95%, and the pores of the bionic scaffolds provide material exchange channels similar to those of cancellous bone, which are more conducive to the inward growth of blood vessels and new bone.[44-47] In a study by Mastrogiacomo et al., it was noted that pore size and interconnected pores are key to osteoconduction, providing space for cell adhesion and bone ingrowth and allowing for efficient *in vivo* vascularization suitable for the maintenance of bone tissue regeneration and possible remodeling.[48] Similarly, in their study on the effect of scaffold shape on bone regeneration, Hayashi et al. reported that the presence of internal pores in the scaffold is more favorable for new bone deposition than a dense structure.[49] Therefore, an ideal bone tissue-engineered scaffold should have a porous structure. In this study, all MBG/PCL scaffolds with different concentrations have a porosity exceeding 70%, with little difference between groups. This further demonstrated that MBG did not significantly block the original pores of the scaffolds while modifying PCL, fulfilling the requirements of tissue engineering.

Overall, the MBG/PCL scaffolds significantly upregulated the expression of osteogenesis-related genes (*Alp*, *Opn*, *Runx2*, *Bmp2*, *Col1*), as compared to the pure PCL scaffolds, and similar trend was also observed in ALP staining and quantification, which is consistent with previous studies.[50,51] Specially, the 10MBG/PCL group of scaffolds had the best performance in this respect. It was shown that Si^{2+}, Ca^{2+}, and P^{5+} ions released from BGs regulate the cell cycle and upregulate or activate the expression of osteogenic genes during contact with cells such as BMSCs, and that nano-sized BGs possessed stronger bioactivity, with smaller-sized BGs contributing to a greater ability to move cells from the G0/G1 to the S/G2 phases, whereas larger-sized BGs allowed a greater proportion of cells to remain in the G0/G1 phase.[52] This may be the reason why the proliferative activity of scaffolds containing 20% and 30% MBG showed lower proliferative activity (MBG agglomerates on the PCL surface). More importantly, since the BGs used for composite with PCL in this study were of dendritic pore structure, the specific surface area and pore volume were significantly larger than that of conventional mesoporous BGs, and the active ions were solubilized at a faster rate, resulting in stronger bioactivity.[53,54] Consequently, by adding a smaller amount of BGs with a dendritic pore structure, we could significantly enhance both the compressive strength and induce osteogenic activity of the composite scaffold *in vitro*.

Inflammation is an important part of implantation of bone tissue-engineered scaffolds, and MPs play a key role in promoting the post-implantation inflammation. The polarization status of the MPs phenotype is one of the key factors for the success or failure of implantation. In the present study, we found that MPs polarization was strongly influenced by MBG content. MBG significantly reduced the expression of low M1 phenotype genes and promoted MPs polarization toward the M2 phenotype, which is consistent with previous studies.[21,22] In particular, compared to the high-concentration groups such as 20MBG/PCL and 30MBG/PCL, the 10MBG/PCL group of scaffolds induced the most significant performance of MPs conversion from M1 to M2 phenotype. We speculate that this is related to the dose of MBG and that higher concentrations of MBG may prolong the process of MPs polarization to M1, expressing more M1 phenotype genes such as *Tnfa* and *Il1b*, posing a challenge to the resolution of inflammation.[55] The above reasoning is equally applicable

to the immunomodulation of osteogenesis. In the presence of an MP-conditioned medium, the 10MBG/PCL group scaffolds upregulated M2 phenotypic genes, such as *CD206* and *Arg*, and formed an immune microenvironment conducive to osteogenesis, stimulating the upregulation of osteogenic gene expression in BMSCs, and demonstrating excellent immune-coordinated osteogenic properties.

Fiber diameter and pore size have a critical impact on the performance of the scaffolds. In terms of compressive strength, coarser fibers increased the force area of the scaffolds, and thus the overall performance of the scaffolds showed that the compressive capacity of the scaffolds increased with the coarsening of the fibers.[56] The overall compressive capacity of the scaffolds increased with the coarsening of the fibers. Similarly, the widening of the pore size reduces the force area of the scaffolds, which in turn leads to the weakening of the compressive capacity. In terms of the porosity of the scaffolds, the amount of the same material filled in the unit volume determines the porosity of the scaffolds, specifically reflecting the associations among several parameters: (i) the coarser the fiber of the scaffolds, the lower the porosity; and (ii) the larger the pore diameter, the higher the porosity. However, the difference in the hydrophilicity of the scaffolds could be due to the slight gap in MBG deposition during 3D printing. In terms of promoting the proliferation of BMSCs, the finer the fiber, the higher the number of filament diameters per unit area, which can provide more adhesion sites for cells. However, due to the relatively larger arc of F300, it is instead most unfavorable for early cell adhesion. Differences in cell proliferation were also reflected in osteogenic properties. In a comparison of pore sizes, the more filling material per unit area, the larger the area to which cells could adhere. Nonetheless, the relatively small pore size of P200 has a much lower porosity than that of P800, which is unfavorable for material exchange, and therefore, BMSCs showed the lowest proliferative activity.[57,58] In addition, in a study comparing the effects of scaffold pore size on osteogenesis, Swanson et al. found that smaller pore sizes were detrimental to the functional differentiation of osteogenic tissue phenotypes, and sufficiently large (>250 μm) pore sizes favored bone mineralization.[59] In contrast, we found that F500 and P500 possessed the most significant osteogenic potential. A plausible reason for this disparity is that scaffolds with a fiber diameter of 500 μm and a pore size of 500 μm are in the optimal balance between physicochemical properties, cell adhesion, and nutrient exchange.[60]

Upon the expression of inflammatory genes, thicker fibers and larger pore sizes appear to be more favorable for extracellular matrix secretion and deposition, tending to expression of M2 phenotype genes (*CD206*, *ARG*).[28] However, MPs polarization to M2 phenotype was more pronounced in F300 than in F800, possibly due to the fact that with the same area, F300 has more fiber crossings, which facilitate MPs stretching and promote M2 polarization. P200 and P800 were comparatively weaker in promoting MPs polarization than P500, possibly because the scaffold performance and cell permeation were not optimally balanced.[60] This may also be due to the lack of optimal balance between scaffold performance and cell permeation. Meanwhile, the pore size of the scaffolds had a greater effect on MPs polarization compared to fiber thickness, which is consistent with previous studies on micro-sized scaffolds.[61,62] The present study verified that MPs polarization regulates osteogenesis and that the microenvironment enriched with M2-type cytokines promotes bone regeneration. In the presence of an MP-conditioned medium, F500 and P500 still possessed optimal immune-coordinated osteogenic properties. In particular, the scaffold's pore size that contributed to optimal osteogenic and immunomodulatory potential in this study was similar to that described in previous studies.[63,64]

In summary, highly active MBG conferred higher compressive strength and more potent osteogenic activity to the scaffolds. MBG significantly inhibited the expression of pro-inflammatory genes (*Tnfa* and *Il1b*) and promoted the polarization of MPs to the M2 phenotype, creating an optimal microenvironment for immune-coordinated osteogenesis. Meanwhile, fiber diameter and pore size had a significant effect on the performance of the scaffolds, and the scaffolds with both fiber diameter and pore size of 500 μm had the best performance in regulating MPs and osteogenesis. These findings offer an insight on the size of the scaffolds when conducting subsequent studies. In addition, the high specific surface area and pore size of MBG prepared in this study as drug delivery systems are also aspects worthy of future research.

5. Conclusion

In this study, we synthesized highly active MBG to enhance the overall compressive properties and bioactivity of PCL scaffolds. Among them, 10MBG/PCL possessed the highest compressive strength (about twofold of pure PCL scaffolds) and the most excellent *in vitro* induced osteogenic activity. 10MBG/PCL scaffolds significantly inhibited the MPs M1 phenotypic polarization process and upregulated the M2 anti-inflammatory phenotypic genes. Further exploration revealed that the physicochemical properties and osteogenic activity of the scaffolds were affected by both

fiber thickness and pore size. However, the pore size of the scaffolds had a more pronounced impact than the fiber thickness on MPs polarization. In conclusion, 10MBG/PCL scaffolds with fiber diameter of 500 μm and pore size of 500 μm possessed the best osteogenic potential, which significantly induced MPs polarization toward the M2 phenotype, and this group was the most capable of mediating macrophage polarization and thus inducing osteogenic differentiation of BMSCs, forming an immune microenvironment conducive to bone regeneration. This study is a step forward in exploring the performance of BG composite PCL scaffolds and provides a new direction for the development of bone graft materials.

Acknowledgments

None.

Funding

This research was supported by the National Natural Science Foundation of China (32000964, 82160577), the Guangdong Province Science and Technology Plan Project (2024A1515012265, 2020B1111560001, and 2022A1515140193), the Program for Science and Technology Project of Guizhou Province, Qiankehe Platform Talents (No. [2021] 5613), the Key Program for Science and Technology Project of Guizhou Province (No. ZK [2021] 007), and the GDAS' Project of Science and Technology Development (2022GDASZH-2022020402-01,2022GDASZH-2022010110, and 2020GDASZH-2022030604-01).

Conflict of interest

The authors declare no conflict of interest.

Author contributions

Conceptualization: Weihua Huang, Shuai Huang, Weikang Xu, Qingde Wa
Data curation: Weihua Huang, Shuai Huang, Weikang Xu, Qingde Wa
Formal analysis: Weihua Huang, Shuai Huang
Funding acquisition: Weikang Xu, Qingde Wa
Investigation: Weihua Huang, Shuai Huang
Methodology: Weihua Huang, Shuai Huang
Project administration: Weihua Huang, Shuai Huang, Xitao Linghu, Wei-Chih Chen, Yang Wang, Jingjie Li, Huinan Yin, Hang Zhang
Resources: Weihua Huang, Shuai Huang
Validation: Weikang Xu, Qingde Wa
Visualization: Weikang Xu, Qingde Wa
Software: Weihua Huang, Shuai Huang
Writing – original draft: Weihua Huang, Shuai Huang
Writing – review & editing: Weikang Xu, Qingde Wa

Ethics approval and consent to participate

Not applicable.

Consent for publication

Not applicable.

Availability of data

Data are available from the corresponding author upon reasonable request.

References

1. Ye S, Seo K-B, Park B-H, et al. Comparison of the osteogenic potential of bone dust and iliac bone chip. *Spine J.* 2013;13(11):1659-1666.
doi: 10.1016/j.spinee.2013.06.012

2. Zhang J, Jiang Y, Shang, et al. Biodegradable metals for bone defect repair: A systematic review and meta-analysis based on animal studies. *Bioact Mater.* 2021;6(11):4027-4052.
doi: 10.1016/j.bioactmat.2021.03.035

3. Khodakaram-Tafti A, Mehrabani D, Shaterzadeh-Yazdi H, Zamiri B, Omidi, M. Tissue engineering in maxillary bone defects. *World J Plast Surg.* 2018;7(1):3-11.

4. Turnbull G, Clarke J, Picard F, et al. 3D bioactive composite scaffolds for bone tissue engineering. *Bioact Mater.* 2018;3(3):278-314.
doi: 10.1016/j.bioactmat.2017.10.001

5. Siddiqui N, Asawa S, Birru B, Baadhe R, Rao S. PCL-based composite scaffold matrices for tissue engineering applications. *Mol Biotechnol.* 2018;60(7):506-532.
doi: 10.1007/s12033-018-0084-5

6. Gharibshahian M, Salehi M, Beheshtizadeh N, et al. Recent advances on 3D-printed PCL-based composite scaffolds for bone tissue engineering. *Front Bioeng Biotechnol.* 2023;11:1168504.
doi: 10.3389/fbioe.2023.1168504

7. Jones JR. Reprint of: review of bioactive glass: from Hench to hybrids. *Acta Biomater.* 2015;23(Suppl 1):S53-S82.
doi: 10.1016/j.actbio.2015.07.019

8. Hench LL, Polak JM. Third-generation biomedical materials. *Science.* 2002;295(5557):1014.
doi: 10.1126/science.1067404

9. Kokubo T, Kim HM, Kawashita M. Novel bioactive materials with different mechanical properties. *Biomaterials.* 2003;24(13):2161-2175.
doi: 10.1016/s0142-9612(03)00044-9

10. Skallevold HE, Rokaya D, Khurshid Z, Zafar MS. Bioactive glass applications in dentistry. *Int J Mol Sci.* 2019;20(23).
doi: 10.3390/ijms20235960

11. Schumacher M, Habibovic P, van Rijt S. Mesoporous bioactive glass composition effects on degradation and bioactivity. *Bioact Mater.* 2021;6(7):1921-1931. doi: 10.1016/j.bioactmat.2020.12.007

12. Zheng K, Boccaccini AR. Sol-gel processing of bioactive glass nanoparticles: a review. *Adv Colloid Interface Sci.* 2017;249:363-373. doi: 10.1016/j.cis.2017.03.008

13. El-Fiqi A, Mandakhbayar N, Jo SB, et al. Nanotherapeutics for regeneration of degenerated tissue infected by bacteria through the multiple delivery of bioactive ions and growth factor with antibacterial/angiogenic and osteogenic/odontogenic capacity. *Bioact Mater.* 2021;6(1):123-136. doi: 10.1016/j.bioactmat.2020.07.010

14. Xin T, Gu Y, Cheng R, et al. Inorganic strengthened hydrogel membrane as regenerative periosteum. *Acs Appl Mater Interfaces.* 2017;9(47):41168-41180. doi: 10.1021/acsami.7b13167

15. Zhao H, Wang X, Jin A, et al. Reducing relapse and accelerating osteogenesis in rapid maxillary expansion using an injectable mesoporous bioactive glass/fibrin glue composite hydrogel. *Bioact Mater.* 2022;18:507-525. doi: 10.1016/j.bioactmat.2022.03.001

16. Wang C, Meng C, Zhang Z, Zhu Q. 3D printing of polycaprolactone/bioactive glass composite scaffolds for in situ bone repair. *Ceram Int.* 2022;48(6):7491-7499. doi: 10.1016/j.ceramint.2021.11.293

17. Huang W, Cai X, Xiao C, Song W, Yin H, Xu W. Surface micropatterning of 3D printed PCL scaffolds promotes osteogenic differentiation of BMSCs and regulates macrophage M2 polarization. *Heliyon* 2024;10(5):e26621-e26621. doi: 10.1016/j.heliyon.2024.e26621

18. Arron JR, Choi Y. Osteoimmunology - bone versus immune system. *Nature.* 2000;408(6812):535-536. doi: 10.1038/35046196

19. Yang N, Liu Y. The role of the immune microenvironment in bone regeneration. *Int J Med Sci.* 2021;18(16):3697-3707. doi: 10.7150/ijms.61080

20. Wu Z, Bai J, Ge G, et al. Regulating macrophage polarization in high glucose microenvironment using lithium-modified bioglass-hydrogel for diabetic bone regeneration. *Adv Healthc Mater.* 2022;11(13). doi: 10.1002/adhm.202200298

21. Feito MJ, Casarrubios L, Onaderra M, et al. Response of RAW 264.7 and J774A.1 macrophages to particles and nanoparticles of a mesoporous bioactive glass: a comparative study. *Colloids Surf B.* 2021;208. doi: 10.1016/j.colsurfb.2021.112110

22. Xu H, Zhu Y, Hsiao AW-T, et al. Bioactive glass-elicited stem cell-derived extracellular vesicles regulate M2 macrophage polarization and angiogenesis to improve tendon regeneration and functional recovery. *Biomaterials.* 2023;294. doi: 10.1016/j.biomaterials.2023.121998

23. Zheng K, Niu W, Lei B, Boccaccini AR. Immunomodulatory bioactive glasses for tissue regeneration. *Acta Biomater.* 2021;133:168-186. doi: 10.1016/j.actbio.2021.08.023

24. Gomez-Cerezo N, Casarrubios L, Morales I, et al. Effects of a mesoporous bioactive glass on osteoblasts, osteoclasts and macrophages. *J Colloid Interface Sci.* 2018;528:309-320. doi: 10.1016/j.jcis.2018.05.099

25. Huang Y, Wu C, Zhang X, Chang J, Dai K. Regulation of immune response by bioactive ions released from silicate bioceramics for bone regeneration. *Acta Biomater.* 2018;66:81-92. doi: 10.1016/j.actbio.2017.08.044

26. Singh RP, Ramarao P. Accumulated polymer degradation products as effector molecules in cytotoxicity of polymeric nanoparticles. *Toxicol Sci.* 2013;136(1):131-143. doi: 10.1093/toxsci/kft179

27. Wang X, Zachman AL, Chun YW, Shen F-W, Hwang Y-S, Sung H-J. Polymeric stent materials dysregulate macrophage and endothelial cell functions: implications for coronary artery stent. *Int J Cardiol.* 2014;174(3):688-695. doi: 10.1016/j.ijcard.2014.04.228

28. Wang Z, Cui Y, Wang J, et al. The effect of thick fibers and large pores of electrospun poly(ε-caprolactone) vascular grafts on macrophage polarization and arterial regeneration. *Biomaterials.* 2014;35(22):5700-5710. doi: 10.1016/j.biomaterials.2014.03.078

29. Abebayehu D, Spence A, Boyan BD, Schwartz Z, Ryan JJ, McClure MJ. Galectin-1 promotes an M2 macrophage response to polydioxanone scaffolds. *J Biomed Mater Res Part A.* 2017;105(9):2562-2571. doi: 10.1002/jbm.a.36113

30. Zhu G, Zhang R, Xie Q, et al. Shish-kebab structure fiber with nano and micro diameter regulate macrophage polarization for anti-inflammatory and bone differentiation. *Mater Today Bio.* 2023;23. doi: 10.1016/j.mtbio.2023.100880

31. Wang Y, Liao T, Shi M, Liu C, Chen X. Facile synthesis and in vitro bioactivity of radial mesoporous bioactive glasses. *Mater Lett.* 2017;206:205-209. doi: 10.1016/j.matlet.2017.07.021

32. Chaudhary S, Ghosal D, Tripathi P, Kumar S. Cellular metabolism: a link connecting cellular behaviour with the physiochemical properties of biomaterials for bone tissue engineering. *Biomater Sci.* 2023;11(7):2277-2291. doi: 10.1039/d2bm01410f

33. Lewallen EA, Trousdale WH, Thaler R, et al. Surface roughness of titanium orthopedic implants alters the

biological phenotype of human mesenchymal stromal cells. *Tissue Eng Part A.* 2021;27(23-24):1503-1516.
doi: 10.1089/ten.tea.2020.0369

34. Yuan B, Zhou S-y, Chen X-s. Rapid prototyping technology and its application in bone tissue engineering. *J Zhejiang Univ Sci B.* 2017;18(4):303-315.
doi: 10.1631/jzus.B1600118

35. van der Heide D, Cidonio G, Stoddart MJ, D'Este M. 3D printing of inorganic-biopolymer composites for bone regeneration. *Biofabrication.* 2022;14(4).
doi: 10.1088/1758-5090/ac8cb2

36. Garot C, Bettega G, Picart C. Additive manufacturing of material scaffolds for bone regeneration: toward application in the clinics. *Adv Funct Mater.* 2021;31(5).
doi: 10.1002/adfm.202006967

37. Feng Y, Zhu S, Mei D, et al. Application of 3D printing technology in bone tissue engineering: a review. *Curr Drug Delivery.* 2021;18(7):847-861.
doi: 10.2174/1567201817999201113100322

38. Ebrahimi S, Sipaut CS. The effect of liquid phase concentration on the setting time and compressive strength of hydroxyapatite/bioglass composite cement. *Nanomaterials.* 2021;11(10).
doi: 10.3390/nano11102576

39. Rupp F, Liang L, Geis-Gerstorfer J, Scheideler L, Huettig F. Surface characteristics of dental implants: a review. *Dent Mater.* 2018;34(1):40-57.
doi: 10.1016/j.dental.2017.09.007

40. Wang L, He S, Wu X, et al. Polyetheretherketone/nano-fluorohydroxyapatite composite with antimicrobial activity and osseointegration properties. *Biomaterials.* 2014;35(25):6758-6775.
doi: 10.1016/j.biomaterials.2014.04.085

41. Muecksch C, Urbassek HM. Accelerated molecular dynamics study of the effects of surface hydrophilicity on protein adsorption. *Langmuir.* 2016;32(36): 9156-9162.
doi: 10.1021/acs.langmuir.6b02229

42. Wang X, Molino BZ, Pitkanen S, et al. 3D scaffolds of polycaprolactone/copper-doped bioactive glass: architecture engineering with additive manufacturing and cellular assessments in a coculture of bone marrow stem cells and endothelial cells. *Acs Biomater Sci Eng.* 2019;5(9): 4496-4510.
doi: 10.1021/acsbiomaterials.9b00105

43. Zhou L, Fan L, Zhang F-M, et al. Hybrid gelatin/oxidized chondroitin sulfate hydrogels incorporating bioactive glass nanoparticles with enhanced mechanical properties, mineralization, and osteogenic differentiation. *Bioact Mater.* 2021;6(3):890-904.
doi: 10.1016/j.bioactmat.2020.09.012

44. Yazdimamaghani M, Razavi M, Vashaee D, Moharamzadeh K, Boccaccini AR, Tayebi L. Porous magnesium-based scaffolds for tissue engineering. *Mater Sci Eng C Mater Biol Appl.* 2017;71:1253-1266.
doi: 10.1016/j.msec.2016.11.027

45. Marrella A, Lee TY, Lee DH, et al. Engineering vascularized and innervated bone biomaterials for improved skeletal tissue regeneration. *Mater Today.* 2018;21(4):362-376.
doi: 10.1016/j.mattod.2017.10.005

46. Axpe E, Oyen ML. Applications of alginate-based bioinks in 3D bioprinting. *Int J Mol Sci.* 2016;17(12).
doi: 10.3390/ijms17121976

47. Fiocco L, Elsayed H, Badocco D, et al. Direct ink writing of silica-bonded calcite scaffolds from preceramic polymers and fillers. *Biofabrication.* 2017;9(2).
doi: 10.1088/1758-5090/aa6c37

48. Mastrogiacomo M, Scaglione S, Martinetti R, et al. Role of scaffold internal structure on in vivo bone formation in macroporous calcium phosphate bioceramics. *Biomaterials.* 2006;27(17):3230-3237.
doi: 10.1016/j.biomaterials.2006.01.031

49. Hayashi K, Yanagisawa T, Kishida R, Ishikawa K. Effects of scaffold shape on bone regeneration: tiny shape differences affect the entire system. *Acs Nano.* 2022;16(8):11755-11768.
doi: 10.1021/acsnano.2c03776

50. Gorustovich AA, Roether JA, Boccaccini AR. Effect of bioactive glasses on angiogenesis: a review of in vitro and in vivo evidences. *Tissue Eng Part B Rev.* 2010;16(2):199-207.
doi: 10.1089/ten.teb.2009.0416

51. Hench LL. Genetic design of bioactive glass. *J Eur Ceram Soc.* 2009;29(7):1257-1265.
doi: 10.1016/j.jeurceramsoc.2008.08.002

52. Ajita J, Saravanan S, Selvamurugan N. Effect of size of bioactive glass nanoparticles on mesenchymal stem cell proliferation for dental and orthopedic applications. *Mater Sci Eng C Mater Biol Appl.* 2015;53:142-149.
doi: 10.1016/j.msec.2015.04.041

53. El-Rashidy AA, Roether JA, Harhaus L, Kneser U, Boccaccini AR. Regenerating bone with bioactive glass scaffolds: a review of in vivo studies in bone defect models. *Acta Biomater.* 2017;62:1-28.
doi: 10.1016/j.actbio.2017.08.030

54. Sepulveda P, Jones JR, Hench LL. Characterization of melt-derived 45S5 and sol-gel-derived 58S bioactive glasses. *J Biomed Mater Res.* 2001;58(6):734-740.
doi: 10.1002/jbm.10026

55. Xie W, Fu X, Tang F, et al. Dose-dependent modulation effects of bioactive glass particles on macrophages and diabetic wound healing. *J Mater Chem B.* 2019;7(6):940-952.
doi: 10.1039/c8tb02938e

56. Gao Q, Xie C, Wang P, et al. 3D printed multi-scale scaffolds with ultrafine fibers for providing excellent biocompatibility. *Mater Sci Eng C Mater Biol Appl.* 2020;107.
doi: 10.1016/j.msec.2019.110269

57. Sanz M, Dahlin C, Apatzidou D, et al. Biomaterials and regenerative technologies used in bone regeneration in the craniomaxillofacial region: consensus report of group 2 of the 15th European Workshop on Periodontology on Bone Regeneration. *J Clin Periodontol.* 2019;46:82-91. doi: 10.1111/jcpe.13123

58. Yedekci B, Tezcaner A, Yilmaz B, Demir T, Evis Z. 3D porous PCL-PEG-PCL/strontium, magnesium and boron multi-doped hydroxyapatite composite scaffolds for bone tissue engineering. *J Mech Behav Biomed Mater.* 2022;125. doi: 10.1016/j.jmbbm.2021.104941

59. Swanson WB, Omi M, Zhang Z, et al. Macropore design of tissue engineering scaffolds regulates mesenchymal stem cell differentiation fate. *Biomaterials.* 2021;272. doi: 10.1016/j.biomaterials.2021.120769

60. Wang C, Wu J, Liu L, et al. Improving osteoinduction and osteogenesis of Ti6Al4V alloy porous scaffold by regulating the pore structure. *Front Chem.* 2023;11. doi: 10.3389/fchem.2023.1190630

61. Garg K, Pullen NA, Oskeritzian CA, Ryan JJ, Bowlin GL. Macrophage functional polarization (M1/M2) in response to varying fiber and pore dimensions of electrospun scaffolds. *Biomaterials.* 2013;34(18):4439-4451. doi: 10.1016/j.biomaterials.2013.02.065

62. Horii T, Tsujimoto H, Hagiwara A, et al. Effects of fiber diameter and spacing size of an artificial scaffold on the in vivo cellular response and tissue remodeling. *ACS Appl Biomater.* 2021;4(9):6924-6936. doi: 10.1021/acsabm.1c00572

63. Li W, Dai F, Zhang S, et al. Pore size of 3D-printed polycaprolactone/polyethylene glycol/hydroxyapatite scaffolds affects bone regeneration by modulating macrophage polarization and the foreign body response. *Acs Appl Mater Interfaces.* 2022;14(18):20693-20707. doi: 10.1021/acsami.2c02001

64. Yang X, Gao J, Yang S, et al. Pore size-mediated macrophage M1 to M2 transition affects osseointegration of 3D-printed PEEK scaffolds. *Int J Bioprint.* 2023;9(5):128-144. doi: 10.18063/ijb.755

ACCSCIENCE PUBLISHING

International Journal of Bioprinting

RESEARCH ARTICLE

3D bioprinting of colon organoids in ultrashort self-assembling and decorated peptide matrices

Jiayi Xu[1,2†], Rosario Pérez-Pedroza[1,2†], Manola Moretti[1,2,3], Dana Alhattab[1,2], Alexander Valle-Pérez[1,2], Jezabel García-Parra[1,2], Antonio Cárdenas-Calvario[1,2], Diana Eveline Sanchez-Amador[1,2], and Charlotte A. E. Hauser[1,2,3*]

[1]Laboratory for Nanomedicine, Biological and Environmental Science and Engineering (BESE) Division, King Abdullah University of Science and Technology (KAUST), Thuwal, Saudi Arabia.

[2]Computational Bioscience Research Center, BESE, KAUST, Thuwal, Saudi Arabia

[3]Red Sea Research Center, BESE, KAUST, Thuwal, Saudi Arabia

Abstract

Research into bioinks for organoid culture has the potential to revolutionize our understanding of organ development, function, and disease. Organoids are three-dimensional (3D) cultures of source tissue grown in a support matrix and specialized media. However, the use of animal-derived matrices has limited the potential of organoids in research and therapy. To overcome this limitation, researchers have turned to biofunctional synthetic hydrogel networks to reproduce parameters that govern organoid formation. This study aims to investigate RGD- and YIGSR-decorated ultrashort self-assembling peptides as a modular synthetic hydrogel for organoid culture and 3D bioprinting. Using these motifs, we derived fibronectin (FIB)- and laminin (LAM)-decorated peptides, which self-assemble into nanofibrous hydrogels. We assessed the physicochemical properties of various peptide mixtures. Our findings confirmed the biocompatibility of these formulations and their organoid-forming potential. Subsequently, we identified the most effective scaffolds for organoid formation. We assessed the polarity, differentiation, and functionality of organoids cultured within these scaffolds. We also characterized the properties of a bioprinted construct. This study identifies two formulations, FIB (low) and LAM (high), that favor cell polarization within the cultured organoids as early as day 4. Moreover, these scaffolds were able to induce a gene expression profile resembling the organoids cultured in Matrigel. These peptides were also demonstrated to be suitable for bioprinting at various concentrations without compromising cell viability. Overall, this study demonstrates the promise of modular RGD- and YIGSR-decorated ultrashort self-assembling peptides as effective synthetic hydrogels for organoid culture and 3D bioprinting. These biofunctional peptides provide scaffold effectiveness for advanced organoid manipulation.

***Keywords*:** 3D bioprinting; Colorectal organoid; Scaffold; Biofunctional self-assembling peptides; Laminin; Fibronectin

†These authors contributed equally to this work.

***Corresponding author:**
Charlotte A. E. Hauser
(charlotte.hauser@age.mpg.de)

Citation: Xu J, Pérez-Pedroza R, Moretti M, et al. 3D bioprinting of colon organoids in ultrashort self-assembling and decorated peptide matrices. *Int J Bioprint*. 2024;10(5):3033. doi: 10.36922/ijb.3033

Received: February 27, 2024
Accepted: May 11, 2024
Published Online: August 16, 2024

Copyright: © 2024 Author(s). This is an Open Access article distributed under the terms of the Creative Commons Attribution License, permitting distribution, and reproduction in any medium, provided the original work is properly cited.

Publisher's Note: AccScience Publishing remains neutral with regard to jurisdictional claims in published maps and institutional affiliations.

1. Introduction

Colorectal cancer (CRC) is a prevalent type of cancer that affects either the colon or rectum. CRC is the third most commonly diagnosed cancer worldwide and ranks as the most diagnosed cancer among males and the second most common among females in Saudi Arabia.[1,2] In 2012, CRC was reportedly the third leading cause of cancer death for females and the fourth for males.[3] In 2020, CRC became the second leading cause of cancer death (9.4%) after lung cancer (18%),[4] with over a million newly diagnosed CRC cases and over 576,000 global mortalities. Its prevalence is exceptionally high and keeps increasing in developing countries. Recently, CRC has become a more common disease among the younger population.[5] Notably, the risk of CRC disease is related to gender and age, with men and older people at greater risk.[6] Consequently, as the population grows and ages, CRC may become a more pressing concern.

Hereditary and epigenetic abnormalities in colon epithelial cells contribute to CRC.[5,7] Both environmental and genetic variables influence CRC development, complicating its diagnosis and treatment.[8,9] Various factors, including dietary (red meat, processed meat, alcohol consumption, and obesity), non-dietary (smoking, chronic use of non-steroidal anti-inflammatory drugs, and other diseases), and genetic factors (polyposis or nonpolyposis syndromes), can increase the risk of CRC.[9,10]

Addressing this major public health burden necessitates the urgent development of efficient medical tools and better therapies for CRC. Several methods have been developed for drug screening and therapy development, such as cell lines, animal models, and patient xenografts on animals.[11,12] However, these models have a limited predictive capacity. For instance, cell lines with controlled 2D morphologies respond differently to chemotherapy.[11] Animal models and patient xenografts also have limited value in predicting therapeutic results. Besides being labor-intensive and unsuited for high-throughput drug screening applications, these models pose significant physiological, genetic, and environmental differences between humans and other animals.[13] In addition, there are ethical concerns about using animals for research.[14]

Alternatively, 3D-cultured organoids are a promising substitute for cell lines, animal models, and patient xenografts to mimic human cells' biological properties *in vivo* while avoiding ethical dilemmas. The most commonly used 3D matrix for developing CRC organoids is Matrigel. Nonetheless, batch-to-batch variation and non-human tissue origin limit its use, especially in developing organoids for assessing the efficiency of immunotherapy. The development of a CRC model *in vitro* is challenged by the involvement of multiple cell types and their organized 3D architecture. Like normal tissue, CRC organoids comprise different cell types, such as epithelial stem cells, enteroendocrine cells, and goblet cells.[15] Epithelial stem cells in lower gut crypts (or buds) will proliferate and differentiate into specialized cells in higher locations outside the crypts.[16] Overall, organoids can emulate key tissue features *in vivo*, from genetic to functional aspects, making them a potential and efficient CRC *in vitro* model.[17]

A standardized platform is urgently required to facilitate the scalability and manipulation of organoids. Bioprinting organoids represent an emerging field, characterized by two approaches, either bioprinting undifferentiated pluripotent stem cells or printing differentiated stem cells or fully formed organoids.[18] Current bioprinting methods predominantly rely on permissive extracellular matrices (ECMs), such as Matrigel and collagen I.[19] However, synthetic bioinks offer promising alternatives, characterized by chemical precision, tunability, and reproducibility. Synthetic bioinks allow for the integration of functional chemical groups, including bioactive molecules, owing to the abundance of available groups in the polymer.[20] Nonetheless, synthesizing polymeric synthetic bioinks is often challenging and substantially costly. Additionally, crosslinking methods employed with polymeric bioinks, such as ultraviolet (UV) light exposure, may adversely impact cell viability.[21] Furthermore, polymeric bioinks tend to form covalent bonds, hindering self-healing capabilities, and complicating remodeling unless cleavage systems are integrated.

Ultrashort self-assembling peptide (USAP) scaffolds are supramolecular structures governed by hydrophobic effects, electrostatic interactions, and stacking forces. The weak interactions between residues facilitate the self-assembly of peptides into stable 3D nanofibers.[22–24] Peptide-based nanofibers are relatively similar to fibers found in tissue ECMs, and they are non-immunogenic with a tunable sequence, which can be utilized in several applications.[25–31] These fiber-forming USAPs have also demonstrated potential for stem cell cultures and have been used to generate a multicellular disease model for hematological malignancies.[32] These materials have been proven to recapitulate the cellular microenvironment, maintaining the pluripotency of encapsulated stem cells in long-term cultures for over 30 passages without major chromosomal mutations.[33–36] We have previously developed a USAP-derived peptide containing the IKVAV sequence, a motif that contains cell-adhesive and self-assembling properties.[37]

In this study, we demonstrate the versatility of USAPs as a chemical scaffold for the biofunctionalization of various ligands, while concurrently assessing the tunability of mechanical and biochemical properties in the resultant biofunctional formulations. Our investigation delves into characterizing the gelation properties of these bioinks, and investigating their impact on CRC organoids and assesses the corresponding biological responses across various bioink formulations. Our study aims to develop a biofunctional and chemically well-defined alternative bioink that solidifies under physiological conditions. Hence, we propose the utilization of biofunctional self-assembling peptides as a modular and tunable scaffold for bioprinting organoids, with CRC organoids serving as our primary model system for this study.

The YIGSR motif is a cell-binding motif found in laminin-derived peptides that can modulate cell adhesion and spreading. It has been reported to co-localize laminin-binding proteins with two focal adhesion binding sites (actin and vinculin) and promote vinculin expression, which can direct cell migration.[38] YIGSR-mediated cell adhesion occurs via the 67-kDa laminin receptor, which differs from the RGD-mediated cell adhesion mechanism through multiple integrins.[39] The YIGSR motif can also induce the phosphorylation of cytoplasmic focal adhesion kinase, which is vital in regulating cell motility.

The RGD motif is also a cell-binding motif found in ECM proteins, such as fibronectin, vitronectin, fibrinogen, osteopontin, and bone sialoprotein.[40] The RGD sequence is the attachment site of many adhesive ECM proteins and cell surface proteins, and nearly half of the known integrins recognize this sequence in their adhesion protein ligands.[41] The integrin-binding activity of the RGD motif plays a crucial role in cell adhesion and migration. Synthetic peptides containing the RGDS motif have been used extensively as inhibitors of integrin–ligand interactions in cell adhesion, migration, growth, and differentiation studies. Several studies have proven that the presence of the RGD ligand in artificial matrices facilitates gastrointestinal organoid self-organization.[42–44]

This study presents the design of two biofunctional peptides decorated with the YIGSR and RGD ligands. The nanofiber-forming properties of these peptides were characterized in various combinations with the parent peptide and evaluated as matrices for CRC organoid culture. Additionally, we demonstrate the printability of these bioactive peptides for the high-throughput fabrication of CRC organoids for drug screening applications. These peptides enable the generation of reductive matrices that can stimulate particular cell behaviors in a well-defined 3D environment.

2. Materials and methods

2.1. Peptide synthesis

The peptides, IIFK (Ac-Ile-Ile-Phe-Lys-NH_2), LAM (Ac-Ile-Ile-Phe-Lys-Gly-Gly-Gly-Tyr-Ile-Gly-Ser-Arg-NH_2), and FIB (Ac-Ac-Ile-Ile-Phe-Lys-Gly-Gly-Gly-Arg-Gly-Asp-Ser-NH_2), were synthesized by 9-fluorenylmethoxycarbonyl (Fmoc)-based solid phase peptide synthesis. The Rink amide-methylbenzhydrylamine (MBHA) resin (GL Biochem, China) was pre-swelled with dichloromethane (DCM) (SRL, India) for 30 min, followed by deprotection of the Fmoc group with 20% v/v piperidine/dimethylformamide (DMF) (Merck, Germany) before the first amino acid was introduced. An N-methyl-2-pyrrolidone (NMP) solution (SRL, India), containing 2-(1H-benzotriazol-1-yl)-1,1,3,3-tetramethyluronium tetrafluoroborate (TBTU), 1-hydroxy benzotriazole (HOBt), N,N-diisopropylethylamine (DIPEA), and Fmoc-protected amino acid, was added to the reaction vessel and agitated for 3 h. The resin was then washed, and a capping process was conducted using a mixture of DIPEA and dimethylformamide (Sigma Aldrich, USA). The resin was then cleaved using trifluoroacetic acid (TFA) (Thermo Fisher Scientific, USA), triisopropylsilane (Sigma Aldrich, USA), and water. The pure peptide was obtained through reverse phase-liquid chromatography purification. Purity and peptide mass and structure were confirmed by mass spectra analysis.

2.2. Peptide hydrogel preparation

The lyophilized peptide was sterilized under UV light for 30 min and dissolved in MilliQ water to produce a 2× final concentration. Gelation was initiated by adding 2× phosphate-buffered saline (PBS) (Gibco, USA) to the peptide solution; the hydrogels were incubated at room temperature for 10–30 min. The peptide concentrations used in this manuscript are depicted in Table 1.

2.3. Rheology

Rheology measurements were obtained using an Ares-G2 rheometer (TA Instruments, USA) and a standard 8-mm parallel plate (TA Instruments, USA). Samples for rheology were prepared as described in **Section 2.2** and left at room temperature overnight for gelation. Peptide samples (300 μL) were prepared by casting in a 9 mm glass ring coated with Sigmacote® (Sigma Aldrich, USA). Three dynamic tests were performed in each sample: a standard oscillatory time sweep (time = 300 s, A (amplitude) = 0.1%, f (frequency) = 1 rad/s), a frequency sweep (t = 400 s, A = 0.1%, f = 0.1–100 rad/s), and a standard oscillatory amplitude sweep (t = 300 s, A = 0.001–100%, f = 1 rad/s). Stiffness was calculated based on the average storage modulus from the time sweep. Storage and loss moduli

Table 1. List of peptide combinations

Peptide name	Peptide(s)	Weight ratio	Total concentration (mg/mL)
Parent (low)	IIFK	-	1.5
Parent (high)	IIFK	-	2
FIB (low)	IIFK : IIFKGGGRDS	2:1	1.5
FIB (high)	IIFK : IIFKGGGYIGSR	1:1	2
FIB-LAM	IIFK : IIFKGGGRGDS : IIFKGGGYIGSR	2:1:1	2
LAM (low)	IIFK : IIFKGGGYIGSR	2:1	1.5
LAM (high)	IIFK : IIFKGGGYIGSR	1:1	2

Abbreviations: FIB, fibrinogen-derived peptide containing the RGD motif; LAM, laminin-derived peptide containing YIGSR.

were obtained from an average between the last five points from the time sweep ($n = 30$).

2.4. Inverted vial test

Inverted vial tests were performed using 1 mL of peptide hydrogel at varying concentrations that were gelled with 100 µL of 10× PBS. The vials were kept at room temperature until complete gelation, i.e., when the hydrogel remained intact at the bottom of the glass vial upon inversion ($n = 9$).

2.5. Raman spectroscopy

Raman spectroscopy measurements were performed in a backscattered configuration in a WiTec Alpha 300-R Raman spectrometer equipped with an Andor CCD camera (DU970N; thermoelectrically cooled to −75 °C) (Raman: Oxford Instruments, UK). The measurements were performed on hydrogels with different combinations of peptides at a total concentration of 5 mg/mL in 1× PBS. The spectra were acquired by illuminating the sample using a laser with a wavelength of 532 nm and a power of 12 mW at the source. Data acquisition and analysis were performed as previously reported.[36] Briefly, five single spectra were acquired for each sample by setting the measurement at 20 s integration time and each spectrum was acquired 10 times. Afterward, the spectra were baseline subtracted with a polynomial of grade 5 in the range 950–1900 cm^{-1}, normalized to the 1450 cm^{-1} peak intensity, and averaged. To depict the contribution in the secondary structure of each peptide combination, amide I peak decomposition was performed. Briefly, a Voigt function was fitted to several peaks identified in the region 1500–1800 cm^{-1}, which include 1550 and 1610 cm^{-1} for aromatic amino acids; 1635 cm^{-1} for water; 1650–1658 cm^{-1} for α-helix; 1661–1666 cm^{-1} for β-turns; and 1680–1690 cm^{-1} for unordered secondary structures.

2.6. Scanning electron microscopy

Scanning electron microscopy (SEM) was performed on the hydrogel formulations to elucidate their respective 3D morphology. SEM images were taken using a Teneo VS scanning electron microscope (Thermo Fisher Scientific, United States of America [USA]), with an accelerating voltage of 3 kV, a probe current of 25 pA, and a secondary electron detector (ETD) (Thermo Fisher Scientific, USA). Samples were prepared by diluting the peptides in MilliQ water at 90% of its final concentration. A 20 µL aliquot was added on top of a silicon chip and gelled with 10× PBS. All samples were left to gel overnight before being dehydrated in an ethanol gradient (20%, 40%, 60%, 80%, and 100%; 20 min for each ethanol concentration). The sample was dried using CO_2 in a critical point dryer. After the samples were fully dehydrated ($n = 6$), they were coated twice with 5 nm iridium.

2.7. Atomic force microscopy

Atomic force microscopy (AFM) was performed on the nanofibers (containing the hydrogels) to depict their supramolecular arrangements that are dependent on the type and combination of peptides. The peptide combinations at different ratios were prepared to a final concentration of 3 mg/mL in MilliQ water. The solutions were then let to rest at room temperature overnight. Thereafter, 10 µL drops of each sample were spotted on a freshly cleaved mica sheet, rinsed immediately with 1 mL of MilliQ water, and dried under a nitrogen stream. The samples were immediately imaged under a JPK Nanowizard III AFM microscope (Bruker, USA), mounted on an inverted Olympus IX-81 optical microscope (Olympus, Japan). The cantilevers (AC-240TS-R3, Oxford Instruments, UK) with a nominal oscillation frequency of 7 kHz and spring constant of 2 N/m were calibrated by the contact-free thermal noise method. The images were acquired in tapping mode by damping the free oscillation amplitude (30 nm) of about 10% of its value. Several 2 × 2 µm images were acquired to retrieve a statistically significant number of fibers. The height distribution of the sample was retrieved after subtracting a polynomial surface of grade 5 from the image. The periodicity of the

fibers was retrieved by extracting longitudinal profiles of at least 10 fibers per fiber type.

2.8. SW1222 culture and organoid formation

Commercial CRC-derived cell line SW1222 (ECACC, UK) was used to fabricate organoids. Cells were maintained in fresh medium, comprising Isocove's Modified Dulbecco's Medium (IMDM) (Gibco, USA), supplemented with 1% penicillin/streptomycin (Gibco, USA\ and 10% fetal bovine serum [FBS]) (Gibco, USA), in an incubator at 37°C and with 5% CO_2. The culture media was changed every 2–3 days. Cells in passages 4–26 were used. Cells were split using 0.125% trypsin (Gibco, USA) in a 1:5 split, and cell clusters were removed by running the cells through a 30 µm strainer.

To induce organoid formation, cells were seeded in peptide and Matrigel domes. Single 50 µL domes were prepared in each well of a 24-well plate. Organoids were obtained by seeding 1500 cells in the domes. The Matrigel was left to incubate at 37°C for 20 min before adding the supplemented media to the culture from the walls. The 24-well plates were placed in an incubator at 37°C and with 5% CO_2. The medium was changed every 2–3 days.

2.9. Live/dead assay

A LIVE/DEAD™ Viability/Cytotoxicity Kit (Thermo Fisher Scientific, USA) was used to stain live and dead cells, following the manufacturer's recommendations. Samples were washed with PBS and stained using calcein-AM and ethidium homodimer solutions. Images were taken after a 30-min incubation (37°C) with an EVOS M7000 microscope (Thermo Fisher Scientific, USA) (n = 12).

2.10. Proliferation assay

Proliferation was assessed using a resazurin-based assay. Approximately, 10 µL of Alamar Blue (Thermo Fisher Scientific, USA) was added to each sample in 96-well plates after the culture medium was removed. Samples were incubated for 2.5 h at 37°C. Fluorescence intensity was measured using a PHERAstar FS Microplate Reader (BMG LABTECH, Germany) using the module 485/520 (excitation/emission wavelength) (n = 20).

2.11. Organoid-forming capacity

Images obtained from the cytoskeleton staining were analyzed with Cellpose 2.0 to determine the quality and quantity of organoids obtained in each hydrogel. Cellpose is a neural network-based package for the segmentation of biological images.[45,46] that can be fine-tuned for personalized regions of interest. We developed two sample datasets from one set of original images for the lumen and organoid segmentation from unrelated experiments. The sample datasets were divided into training and evaluation sets using random dataset splitting to ensure 85 images in the re-training set and 15 images in the evaluation set. Pre-trained "Model 02" was re-trained for lumen segmentation for the green and blue channels with 300 epochs having a batch size of eight, a weight decay of 0.0001, and a learning rate of 0.1, as per the default settings by the developers. Pre-trained "Model 03" was re-trained for organoid segmentation for the green and blue channels with 300 epochs having a batch size of eight, a weight decay of 0.0001, and a learning rate of 0.1, as per the default settings by the developers. Once the models were trained, we segmented 370 images obtained through epifluorescence microscopy from the organoids cultured in the peptide formulations. The resulting regions of interest from the lumen and organoid segmentations were converted into masks, paired, and analyzed using ImageJ (National Institutes of Health and the Laboratory for Optical and Computational Instrumentation, USA), (n = 370).

2.12. Immunofluorescence staining

After incubation with 4% paraformaldehyde (PFA) (Pierce, USA) for 15 min to fix the sample, 25 µL peptide solution with 1500 cells cultured on glass coverslips in 24-well plates was incubated with cytoskeleton buffer (0.5% Triton X-100 [Thermo Fisher Scientific, USA], 300 mM sucrose [Sigma Aldrich, USA], and 3 mM $MgCl_2$ [Sigma Aldrich, USA] in 1× PBS) for 5 min and with blocking buffer (0.1% tween-20 [Thermo Fisher Scientific, USA], 1% bovine serum albumin [BSA] [Sigma Aldrich, USA], and 0.3 M glycine [Sigma Aldrich, USA] in 1× PBS) for 30 min at room temperature.

The cells were incubated with primary antibodies overnight at 4°C; i.e., anti-ezrin antibody (Abcam, USA); anti-pan-cadherin (Abcam, USA) antibody; anti-ZO-1 (Abcam, USA) antibody. The samples were then incubated at room temperature for 2 h with rhodamine/phalloidin (1:200 diluted in blocking buffer) and secondary antibodies, i.e., goat anti-rabbit IgG (H+L) secondary antibody DyLight™ 633 (Invitrogen, USA); goat anti-mouse IgG (H+L) cross-adsorbed secondary antibody, Alexa Fluor™ 488 (Invitrogen, USA); and goat anti-rabbit IgG (H+L) secondary antibody DyLight™ 488 (Invitrogen, USA). After incubation, samples were washed once with blocking buffer. DAPI (1 micro g/mL in blocking buffer) was added to the samples and incubated at dark for 5 min before a final wash with blocking buffer.

Images are captured using a confocal microscope, ZEISS LSM 880 (ZEISS, Germany) (n = 6).

2.13. Gene expression analysis

2.13.1. RNA extraction

Approximately 24,000 cells were grown in 200 µL peptide hydrogels and Matrigel in a 6-well plate. After washing with

1× PBS, an RNA purification kit (Thermo Fisher Scientific, USA) was used to lyse the cells and extract RNAs, according to the manufacturer's instructions (n = 5).

2.13.2. Quantitative reverse transcription polymerase chain reaction

Complementary DNA was transcribed from extracted RNA with a High Capacity cDNA Reverse Transcription Kit (Thermo Fisher Scientific, USA) using a Mastercycler proS (Eppendorf, Germany). Thereafter, polymerase chain reaction (PCR) was conducted using a QuantStudio 7 Flex Real-Time PCR System with TaqMan Gene Expression Assay (*GAPDH*, *CHGA*, *EPCAM*, *LGR5*, and *MUC2*) and TaqMan Fast Advanced Master Mix from Thermo Fisher Scientific (USA). *GAPDH* was used as a housekeeping gene for normalization. Matrigel is used as the control to calculate Cycle threshold (CT). A t-test was conducted to determine statistically significant differences at p = 0.01, 0.001, and 0.0001 (n = 15).

2.14. Evaluation of printability and bioprinted organoids

Printing and bioprinting processes were conducted with an in-house-developed robotic 3D bioprinter composed of a five-degrees-of-freedom robotic arm, a custom-designed dual-coaxial nozzle, microfluidic pumps, and a stirring hot plate. The robotic arm was interfaced with Repetier-Host. The printing files were designed in SolidWorks® (Dassault Systemes, France) and sliced into G-codes using Slic3r and Repetier software (Hot-World GmbH, Germany). The dual-coaxial nozzle was fabricated according to literature.[25] The commercial microfluidic pumps were controlled simultaneously using the automated pulse mode. The selected flow rates were 40–45 µL/min (peptide), 20–25 µL/min (5× or 7× PBS, depending on the peptide sequence), and 15 µL/min (1× PBS with the extracted cells) for each of the pumps, respectively.

Gelation tests of different peptide concentrations after printing were conducted using 2, 4, and 6 mg/mL FIB (low) peptide mixture and 1.5, 3, and 6 mg/mL LAM (high) peptide mixture (Table 1). Bioprinting was conducted using 4.5 mg/mL LAM and 6 mg/mL FIB. The cells were mixed with 600 µL of 1× PBS and loaded into the printer. The bioprinted constructs were cultured for 7 days and subsequently analyzed with phase contrast (EVOS M7000; Invitrogen, Invitrogen, USA) and laser scanning confocal microscopes (ZEISS LSM 880 with Airyscan) (ZEISS, Germany), as described above.

The viability of 3D-bioprinted cells was assessed using the LIVE/DEAD Viability/Cytotoxicity Kit (Thermo Fisher Scientific, USA) as described above. Stained printed cell-laden constructs were imaged using an immunofluorescent microscope (EVOS; Thermo Fisher Scientific, USA). The proliferation of cells after 3D printing was performed using an adenosine triphosphate (ATP) cell proliferation assay (CellTiter-Glo 3D; Promega, USA), following the manufacturer's recommendations. Briefly, 100 µL of proliferation reagent was added to each printed structure in the 96-well plate, mixed vigorously, and left for incubation in the dark for 30 min. Luminescence was measured using the PHERAstar FS Microplate Reader (BMG LABTECH, Germany). GraphPad prism (Dotmatics, USA) was used for data analysis, and results are represented as mean ± standard deviation. Statistical analysis was performed using two-way analysis of variance (ANOVA), and values with $p < 0.05$ were considered statistically significant.

3. Results

3.1. Physicochemical characterization of peptide combinations

Previous studies have analyzed the fiber-forming capacity of the parent tetrapeptide IIFK.[36] This peptide comprises a hydrophobic tail of nonpolar amino acids (Ile [I] and Phe [F]) and a positively charged amino acid (Lys [K]) at the C-terminal, making it an amphiphilic sequence. This parent peptide self-assembles into well-ordered supramolecular nanofibers.[34,36] Peptides FIB and LAM were obtained after the parent peptide was decorated with sequences RGDS and YIGSR, respectively. Based on previous studies,[37] we determined that mixtures of decorated peptides and the parent peptide enabled the formation of fibrous structures. Therefore, we generated specific combinations utilizing the parent peptide and biofunctional peptides (Table 1) to be evaluated. We defined mixtures based on low (0.5 mg/mL) and high (1.0 mg/mL) concentrations of biofunctional peptides FIB and LAM. These were mixed with a fixed concentration (1.0 mg/mL) of parent peptide.

The physicochemical characterization of peptides and peptide combinations matrices was performed to elucidate the properties of the hydrogels formed. SEM and AFM were used to characterize the morphology of the hydrogels; Raman spectroscopy was used to characterize the secondary structure of the hydrogel nanofibers; rheology assessment was performed to get an insight into the mechanical properties of the different peptide combinations. Images obtained by SEM and AFM demonstrated that all conditions can form supramolecular assemblies in the form of long nanofibers (Figure 1a and b). SEM imaging further suggests that fibers intertwine in multiple dimensions. AFM topography derived the characteristic nanofiber lengths from combined solutions (Table 2). For instance, FIB-containing nanofibers have a larger diameter than LAM-containing nanofibers. Interestingly, the highest variability in helical periodicity

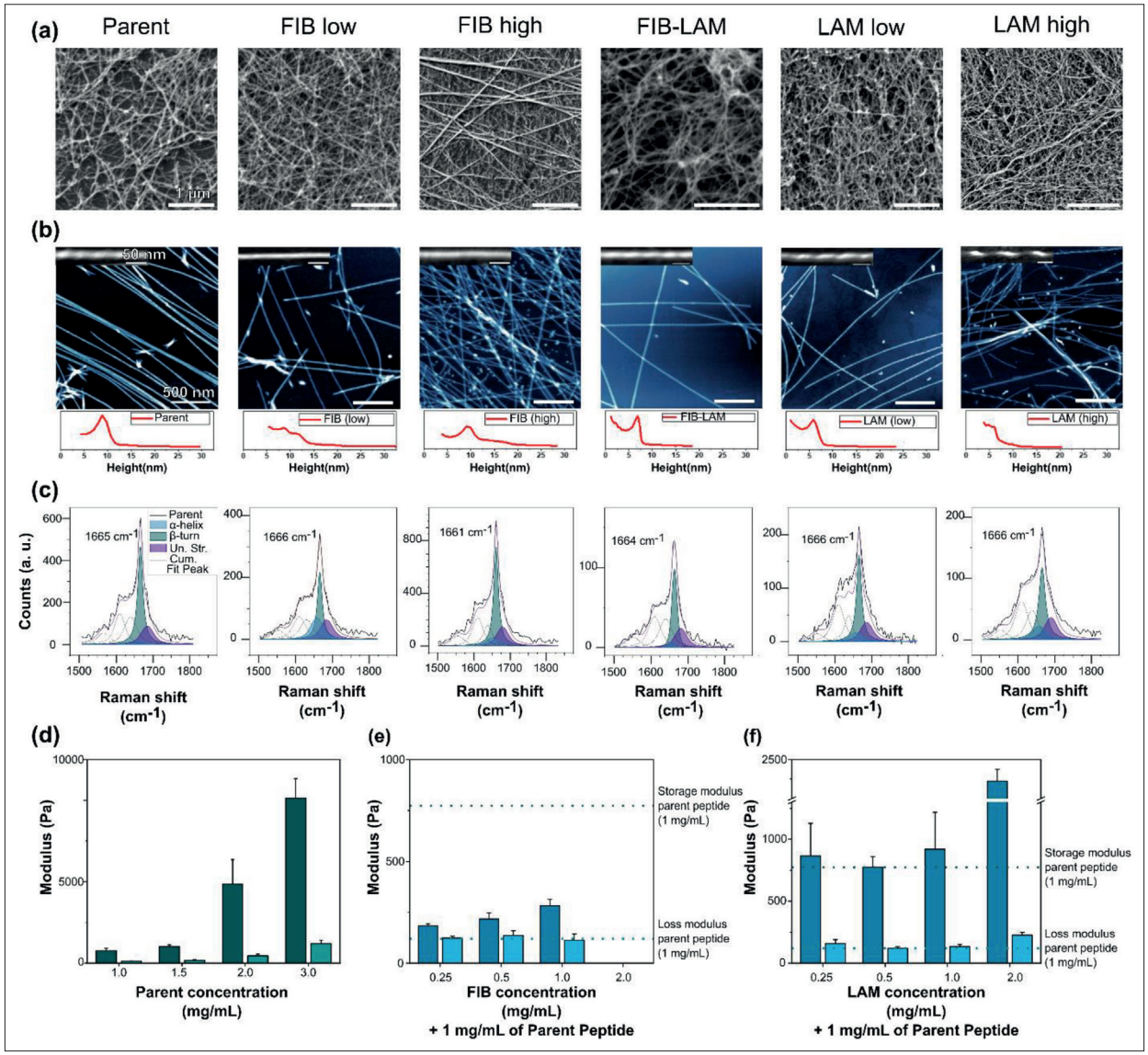


Figure 1. Physicochemical characterizations. (a) Scanning electron microscope (SEM) images of nanofibers generated in different peptide hydrogels. Scale bars: 1 µm. (b) Nanofiber topography images of peptide hydrogels captured by atomic force microscopy (AFM). The bottom graphs indicate the height distribution for each image. Scale bars: 500 nm. (c) Raman analysis of peptide secondary structures with amide I peak deconvolution. The Raman shift of the most represented secondary structure is indicated. (d) Modulus change at different parent peptide concentrations, i.e., 1, 1.5, 2, and 3 mg/mL. (e) Modulus of different concentrations of FIB (0.25, 0.5, and 1 mg/mL) mixed with 1 mg/mL of parent peptide. (f) Modulus of different concentrations of LAM (0.25, 0.5, 1, and 2 mg/mL) mixed with 1 mg/mL IIFK. The dotted lines in (e) and (f) correspond to the storage modulus (731 Pa) and loss modulus (119 Pa) of the parent peptide at 1 mg/mL for comparison. Abbreviations: FIB, fibrinogen-derived peptide containing the RGD motif; LAM, laminin-derived peptide containing YIGSR.

and handedness was obtained from LAM (high) peptides, while the least variable supramolecular structures were obtained from FIB (high) peptides. Moreover, LAM (high) peptides result in both left- and right-handed helices (Figure 1). Most peptides only portrayed a left-handed configuration which resembles that of collagen helices.[47]

Raman spectra also support the observations regarding the structure of the peptide hydrogels. In Figure 1c, we observed the secondary structure components for each peptide as α-helix, β-turn, and unordered structures. We noticed that all combinations presented a substantial component of β-turn, whereas the peaks pertaining to α-helix were non-substantial in all conditions, except in FIB (high) and LAM (low). Unordered structures were detected in all combinations. Moreover, the large full width at half maximum (FWHM) of the β-turn signature for each

Table 2. Diameter, periodicity, and helicity of peptide fibers measured by atomic force microscopy (AFM)

Peptide	Diameter (nm)	Periodicity (nm)	Helicity
Parent	8.9 ± 1.1	53.1 ± 1.9; 82.5 ± 3.1; 24.4 ± 1.4; 65.9 ± 2.9	LH
FIB (low)	8.4 ± 1.6; 11.6 ± 2.3	32.6 ± 2.5; 55.5 ± 2.4; 64.2 ± 2.3	LH
FIB (high)	9.5 ± 1.7	22.6 ± 1.7	LH
LAM (low)	5.8 ± 1.1	37.5 ± 1.2; 58.7 ± 0.1	LH
LAM (high)	4.7 ± 0.2; 5.8 ± 0.1	41.0 ± 0.8; 94.1 ± 0.2; 108.4 ± 1.1; 147.5 ± 2.2	LH; RH
FIB-LAM	6.8 ± 1.1	52.3 ± 0.6; 41.3 ± 0.8; 47.6 ± 0.9	LH

Abbreviations: FIB, fibrinogen-derived peptide containing the RGD motif; LAM, laminin-derived peptide containing YIGSR; LH, left-handed; RH, right-handed.

spectrum is detailed in Table 3. FWHM indicates a less ordered packing of the β-turn secondary structure, which points to multiple arrangements of the nanofibers.[48–50] On the contrary, the FIB (high) peptide in the Raman spectrum displayed a prominent left-shifted β-turn at 1661 cm^{-1}, which indicates a high curvature of the sheet, accompanied by a low FWHM, which supports the AFM periodicity data where we only observed one main periodicity. When the ratio of this combination is increased in favor of the parent peptide, we again observed several periodicity types, similar to the case of having only the parent peptide fibers. Notably, there is no exact matching of any period length for any of the conditions, suggesting various assembling structures that depend on the peptides' ratio and concentration. In an earlier publication, we reported that the parent peptide IIFK single fibers (via AFM) had a diameter of 3.2 nm and were composed primarily of β-turns[36] at the minimal gelation concentration. However, the diameter and periodicity of mixed ultrashort peptides have not been reported until now.

We also evaluated the hydrogel-forming properties of these materials by rheology and inverted vial test (Figure S1, Suporting Information). Storage and loss modulus obtained for LAM and FIB at various concentrations were

Table 3. Raman shift, full width at half maximum (FWHM), and area of each peak for α-helix, β-turn, and unordered structures for each peptide condition

Peptide	Secondary structure	Raman shift (cm^{-1})	FWHM (cm^{-1})	Area (%)
Parent (low)	α-helix	1658	-	4.5
	β-turn	1665	17	68.5
	Unstructured	1684	-	27.0
FIB (low)	α-helix	1658	-	30.0
	β-turn	1666	16	42.4
	Unstructured	1684	-	27.6
FIB (high)	α-helix	1652	-	11.6
	β-turn	1661	16	62.4
	Unstructured	1679	-	26.0
LAM (low)	α-helix	1658	-	13.5
	β-turn	1666	16	58.5
	Unstructured	1686	-	28.0
LAM (high)	α-helix	1658	-	17.4
	β-turn	1666	21	54.7
	Unstructured	1690	-	27.3
FIB-LAM	α-helix	1656	-	4.2
	β-turn	1664	17	59.7
	Unstructured	1681	-	36.1

Abbreviations: FIB, fibrinogen-derived peptide containing the RGD motif; LAM, laminin-derived peptide containing YIGSR.

obtained by a standard rheological time sweep using at least six replicates in five repetitions (Figures S2 and S3, Supporting Information). With these measurements, we aimed to investigate the stiffness of the hydrogels. We observed a tenfold change in the hydrogel's moduli when the concentration of IIFK increased from 1 to 3 mg/mL (Figure 1d). Yet, the storage modulus is roughly maintained at 1 kPa using IIFK at 1.0 and 1.5 mg/mL. It has been reported that organoid growth is enhanced at stiffness values within the range of 0.2–1.3 kPa.[42,51,52] Therefore, IIFK concentration was kept at 1.0 mg/mL for subsequent studies. Additionally, these results suggest that incorporating the FIB peptide (0.25–1.0 mg/mL) could reduce the storage modulus values of the parent peptide (1.0 mg/mL).

In comparison, mixing the LAM peptide with the parent peptide resulted in a hydrogel with similar mechanical properties to IIFK when the content of LAM is less than the concentration of the parent peptide (1.0 mg/mL) while exceeding the concentration of parent peptide with LAM peptide still formed a hydrogel and resulted in a hydrogel with approximately three times the stiffness, i.e., 2224 kPa for LAM (high) (Figure 1f). We also noticed a shift in the loss modulus after reaching the apparent critical concentration of the mixture. We observed that the loss modulus values remained constant for both FIB and LAM mixtures before reaching the 1 mg/mL concentration. We presumed the change in assembly dynamics may drive this phenomenon. Based on copolymerization models, one can also infer that the kinetic constant of dimer formation will define the coaggregation of different peptides in a mixture. Thus, the relative concentration of the parent and biofunctional peptides will result in fibers with different compositions. This may also explain such counterintuitive behavior.

We evaluated the gelation time using an inverted vial test (Figure S1, Supporting Information). The parent peptide gelated at 1.5 and 2.0 mg/mL after 3 and 1 h of initiating gelation, respectively. We had to increase the total concentration of the mixture peptides up to 3 mg/mL for FIB (low) and LAM (low) mixtures to form a hydrogel and up to 4 mg/mL for FIB (high) and LAM (high) to form a hydrogel (Figure S1, Supporting Information). Given the slight differences between loss and storage modulus, we presumed that the resultant gel was not stable enough to hold itself within the inverted glass vial.[53] Notably, the conditions in which these hydrogels exist are very close to the critical concentration,[36] whereby the parent peptide can form a gel after several hours (Figure S1, Supporting Information).

3.2. Culture of colorectal cancer organoids in peptide combinations

Organoids were obtained from the culture of SW1222 cells in the peptide combinations, and Matrigel and 2D control cultures were used as controls. Round cell colonies can be observed in parent (low) and all biofunctionalized peptides, either with FIB, LAM, or both (Figure 2a). These colonies were located in a different layer from the well plate bottom, where cells grew in a 2D fashion. This was evident by the co-presence of the peptide background autofluorescence on the same focal plane as the organoids and surrounding them in all directions (not displayed). In addition, the presence of round colonies with a blurred outline corroborated their location being in a different focal plane than the well bottom. Furthermore, we observed colonies with either round (e.g., colonies found in FIB [high] on day 7) or ellipsoidal shapes (e.g., colonies found in FIB-LAM on day 7), as well as shapes that do not fit under these two categories (e.g., colonies found in parent [high] on day 7) in all the layers.

We presume this change was due to the stiffness of the material (5 kPa; a fivefold increase compared to the parent [low]).[54] At day 7 of organoid culture, higher organoid density was observed in Matrigel compared to peptide culture (Figure 2a). However, round organoids were still observed in the peptide culture, indicating the potential use of these peptide hydrogels for CRC organoid formation. We also observed the growth of cells in a 2D control conformation in peptide hydrogels, indicating that cells can precipitate into the bottom of the wells and grow in the interphase between the bottom and the peptide hydrogel.

Consequently, a viability assay was performed on all peptide concentrations to determine whether the biofunctionalized peptide hydrogels were cytotoxic. We noticed that SW1222 cells seeded in all of the peptide matrices have a large viable population on all days of culturing (Figure 2b). Moreover, these viable populations seem to have a comparable density to those cultured in Matrigel and the 2D control. No cytotoxic effect was detected throughout the culture time. These results demonstrate that all peptide hydrogels supported CRC organoid viability up to 7 days of culture. Besides viability, we also monitored the proliferation of SW1222 cells over time (Figures 2c and S4, Supporting Information). The proliferation assay displayed a significantly increased signal on day 7 compared to day 1 for all peptide combinations and controls (Matrigel and 2D control). On day 1, FIB (high), FIB-LAM, and LAM (low) had significantly higher proliferation rates than Matrigel. On day 4, only the peptide matrices with LAM had the same level of proliferation rate as Matrigel. A higher proliferation rate was observed in cells cultured in LAM (high) compared with Matrigel on day 7. Although the other peptides did not have a higher fluorescence intensity than Matrigel, all the CRC cells encapsulated in different peptides exhibited higher proliferation on day 7 than on day 1. Among all culture conditions, parent peptide (low

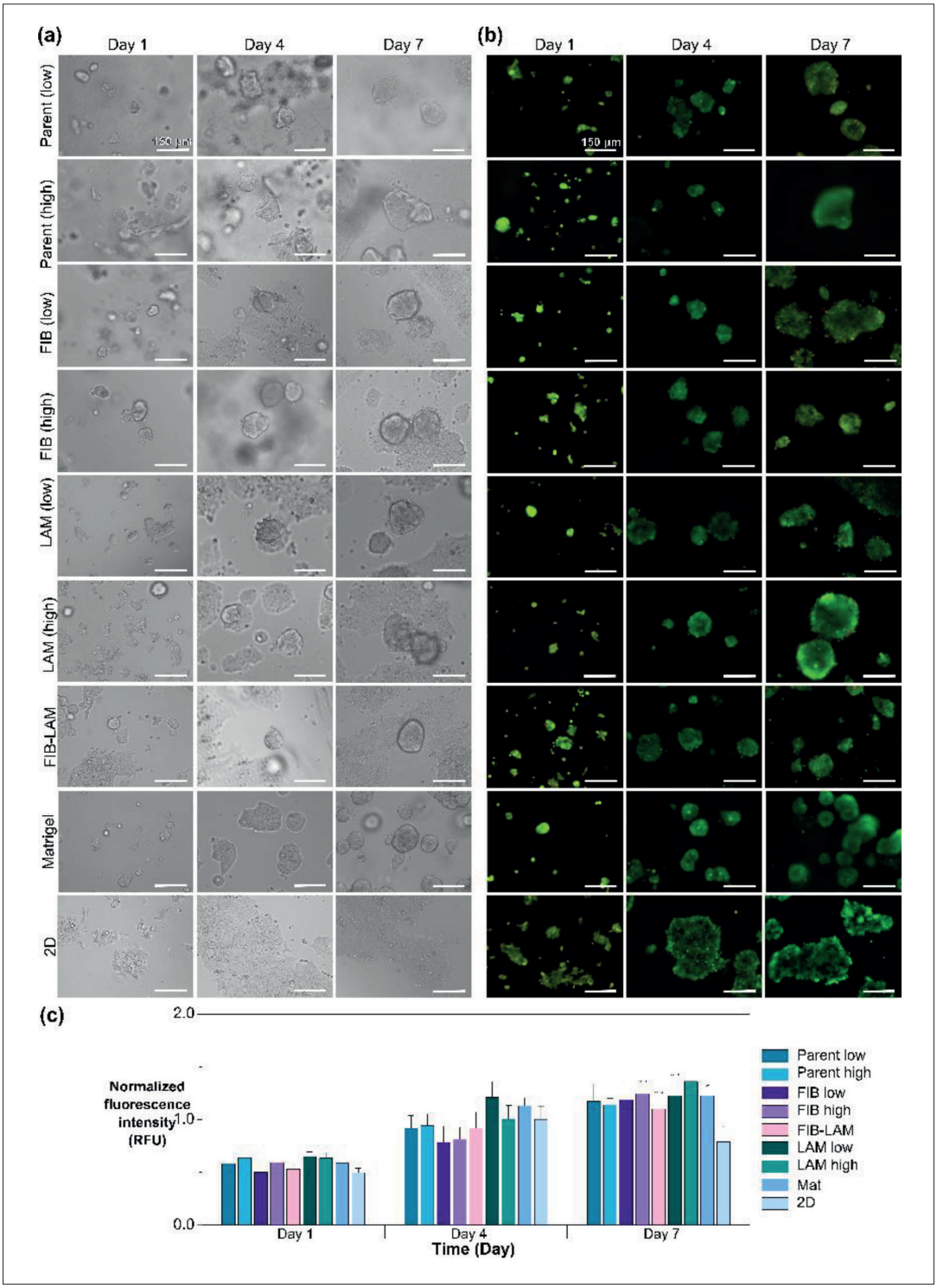


Figure 2. Culture, viability and proliferation evaluation of SW1222 cells in decorated self-assembling peptide scaffolds. (a) Brightfield images of colorectal cancer (CRC) organoids generated in different matrices and 2D control. Scale bars: 150 m. (b) Cell viability in different matrices and 2D control. Live cells were stained with calcein-AM (green), and dead cells were stained with ethidium homodimer-1 (red). Scale bars: 150 µm. (c) Influence of different matrices on CRC cell proliferation assay at days 1, 4, and 7 of culture (n = 20). Matrigel (Mat) is considered a positive control, and the 2D control (2D) is considered a negative control. A t-test was conducted between days 1 and 7 for each single condition. *$p < 0.05$; **$p < 0.01$; ***$p < 0.001$; ****$p < 0.0001$. Abbreviations: FIB, fibrinogen-derived peptide containing the RGD motif; LAM, laminin-derived peptide containing YIGSR.

and high), FIB (low), LAM (low and high), Matrigel, and 2D control reported increasing CRC cell proliferation rate each day. In contrast, FIB (high) and FIB-LAM demonstrated a decrease in proliferation rate from day 1 to 4 that was recovered on day 7.

These results corroborate that our peptide matrices are biocompatible and do not induce dysregulation of the proliferative potential of the cells to be fabricated into organoids. Moreover, we presume that the change in organoid morphology may be a result of the changes in stiffness between parent peptides, FIB-containing peptides, LAM-containing peptides, and Matrigel; it is known that cell morphology will vary according to the stiffness of the 3D scaffold in which they are embedded.[55] Moreover, matrix relaxation and changes in the ECM force facilitate crypt formation,[56] epithelial-mesenchymal transition,[57] and differentiation.[42] Further studies could develop a correlation between the morphological state of the SW1222-derived organoids and their gene expression profile,[58,59] and elucidate dysregulated pathways when cells are cultured in hydrogels with various mechanical properties. However, given the positive results of the viability assay, we postulate that the presented peptide hydrogels must be within a suitable range of stiffness for cell growth. Various studies pointed towards using matrices within the ranges of 300–1000 Pa for the culture of human adult colorectal organoids[42–44] and up to 5.5 kPa for patient-derived xenografts (PDX) of CRC organoids.[60]

After determining that the presence of biofunctional sites in the matrix may play a role in the organoid formation process, we tested the organoid-forming capacity of all peptide combinations. In this regard, we developed a personalized segmentation model based on Cellpose 2.0 and performed morphology analysis. Initially, we analyzed the percentage of colonies that have a lumen and the circularity of the lumen (Figures 3, S5, and S6, Supporting Information). Matrigel reported the highest colony circularity index and percentage of colonies with a lumen. Therefore, it is considered a positive control for this analysis.

After the efficiency analysis of organoid formation, FI (low) and LAM (high) were selected as potential peptide matrices for CRC organoid formation. These two peptides and the mixture FIB-LAM were further evaluated to elucidate the effect of each biofunctionalization and their combination. Cytoskeleton and nuclei staining were used as fluorescent markers to better visualize the internal cell organization and lumen development (Figure 4). CRC cells embedded in Matrigel are considered the positive biological control, where a large, single lumen in the center, and cells aligned at the periphery around the center were observed. Cells grown in 2D control, parent (high), LAM (high), and FIB-LAM have more lumens in one colony. Single-lumen organoids are found primarily on the peptide hydrogels of parent (low) and FIB (low). These two peptide matrices better mimic the morphology of the lumen as those in Matrigel compared to other peptide matrices. Notably, cells grown in peptide hydrogels present cells that are misaligned and sometimes stacked in two or more layers but still pertain to a single lumen. This is contrary to the uniform, single-stacked morphology observed in Matrigel. We observed that colonies cultured in parent (low) and FIB (low) peptides resulted in fewer colonies that presented a multi-layer shape, whereas LAM-containing hydrogels presented a higher degree of multilayering and misalignment.

Since the architecture and polarity of the lumen is a significant part of CRC organoid, cell–cell junctions and apical proteins were labeled by immunofluorescence staining on days 4 and 7. Cell–cell junctions were distributed primarily on the lateral side of all cells within each colony, as observed in the Matrigel control (Figure 4). Expression of pan-cadherin cell–cell junction protein in apical and basolateral membranes points toward disorientation of the cell polarization, as seen in the parent (low) peptide at day 7. Interestingly, colonies cultured in parent (high) peptide do not exhibit such expressions even on day 7, suggesting the inhibition of self-organization of cells into an organoid. Decorated peptides can induce pan-cadherin expression starting at day 4. However, the radial cell arrangement in the LAM-containing hydrogels is less prominent by day 7. Polarization of the colonies was also characterized by the observation of apical markers ZO-1 and ezrin (Figures 5 and 6). On day 4, all biofunctionalized peptides, FIB (low), LAM (high), and FIB-LAM, have ezrin and ZO-1 expressed at the lumen apical epithelium, consistent with Matrigel's organoids. However, not until day 7 did cells in parent (low) express the apical protein biomarkers. Neither cells in the 2D control nor parent (high) have a fluorescent signal, displaying the clear edge of the lumen for ezrin or ZO-1. The results indicate that only CRC cells in matrices with biofunctionalized peptide synchronously express apical protein biomarkers with the cells in Matrigel.

Next, we characterized the gene expression levels of organoids cultured in the selected matrices to elucidate some cell differentiation patterns. We evaluated the expression of genes *LGR5* (stemness), *EpCAM* (epithelial cells), *CHGA* (enteroendocrine cells), and *MUC2* (goblet cells) and normalized its expression to the expression in Matrigel. As observed in Figure 7a, significant overexpression of the *LGR5* gene is observed in all peptide hydrogels except in

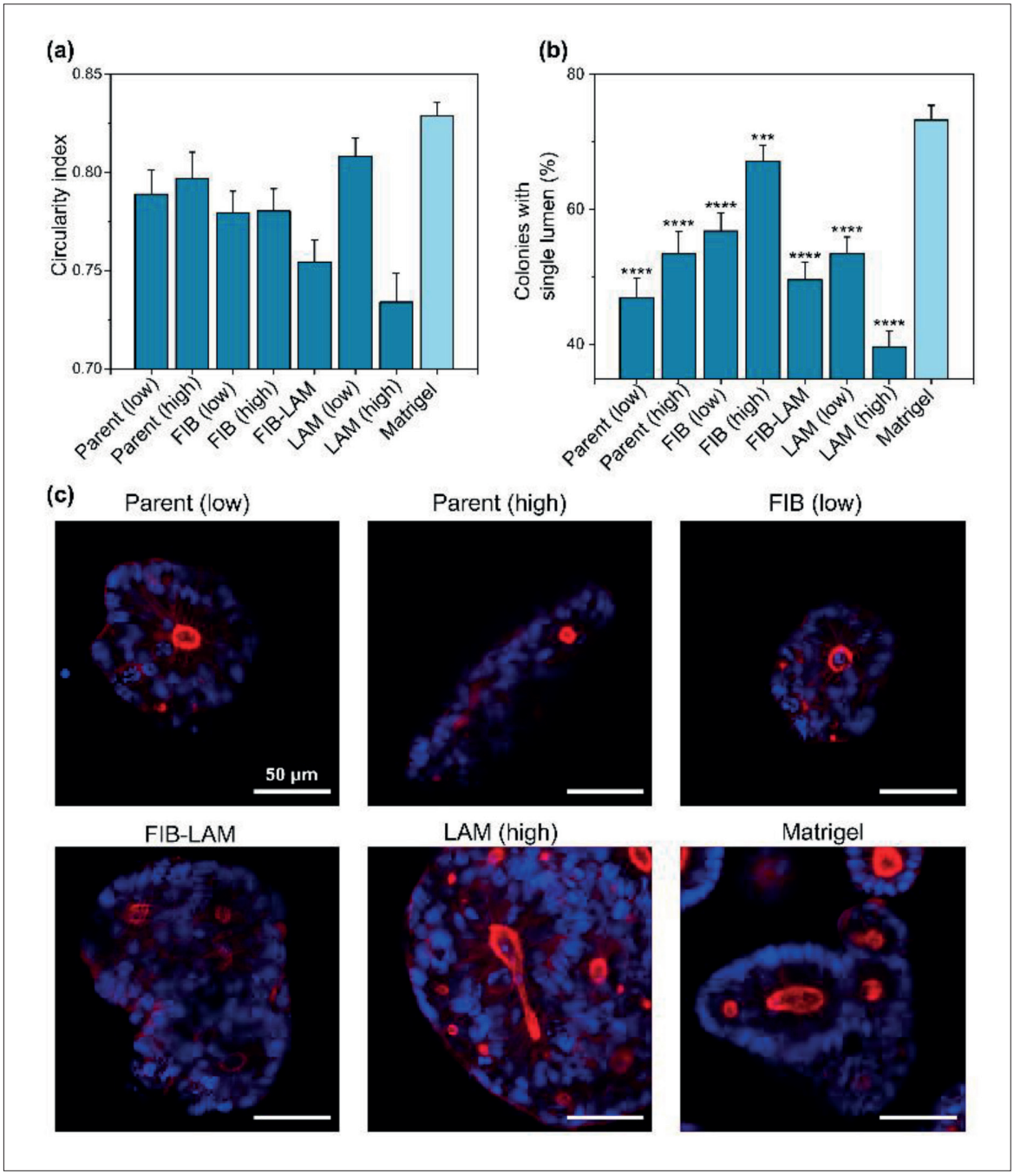


Figure 3. Evaluation of organoid morphology by image analysis. (a) Lumen circularity of colorectal cancer (CRC) colonies in different matrices at day 4 of culture. (b) Percentage of colonies displaying lumen in the different experimental conditions. *$p < 0.05$ relative to the Matrigel control; **$p < 0.01$ relative to the Matrigel control; ***$p < 0.001$ relative to the Matrigel control, ****$p < 0.0001$ relative to the Matrigel control. (c) CRC organoids in different matrices with stained cytoskeleton (red) and cell nucleus (blue). Scale bars: 50 µm. Abbreviations: FIB, fibrinogen-derived peptide containing the RGD motif; LAM, laminin-derived peptide containing YIGSR.

FIB (low), which exhibited an expression level comparable to that of Matrigel. We have demonstrated in earlier studies that tetrapeptide matrices can maintain encapsulated human pluripotent stem cells without a significant loss of pluripotent nuclear transcription factors and surface biomarkers.[34] Hence, we conclude that peptide hydrogels do not intrinsically induce the differentiation of SW1222 cells regardless of the stiffness of the matrix within the ranges

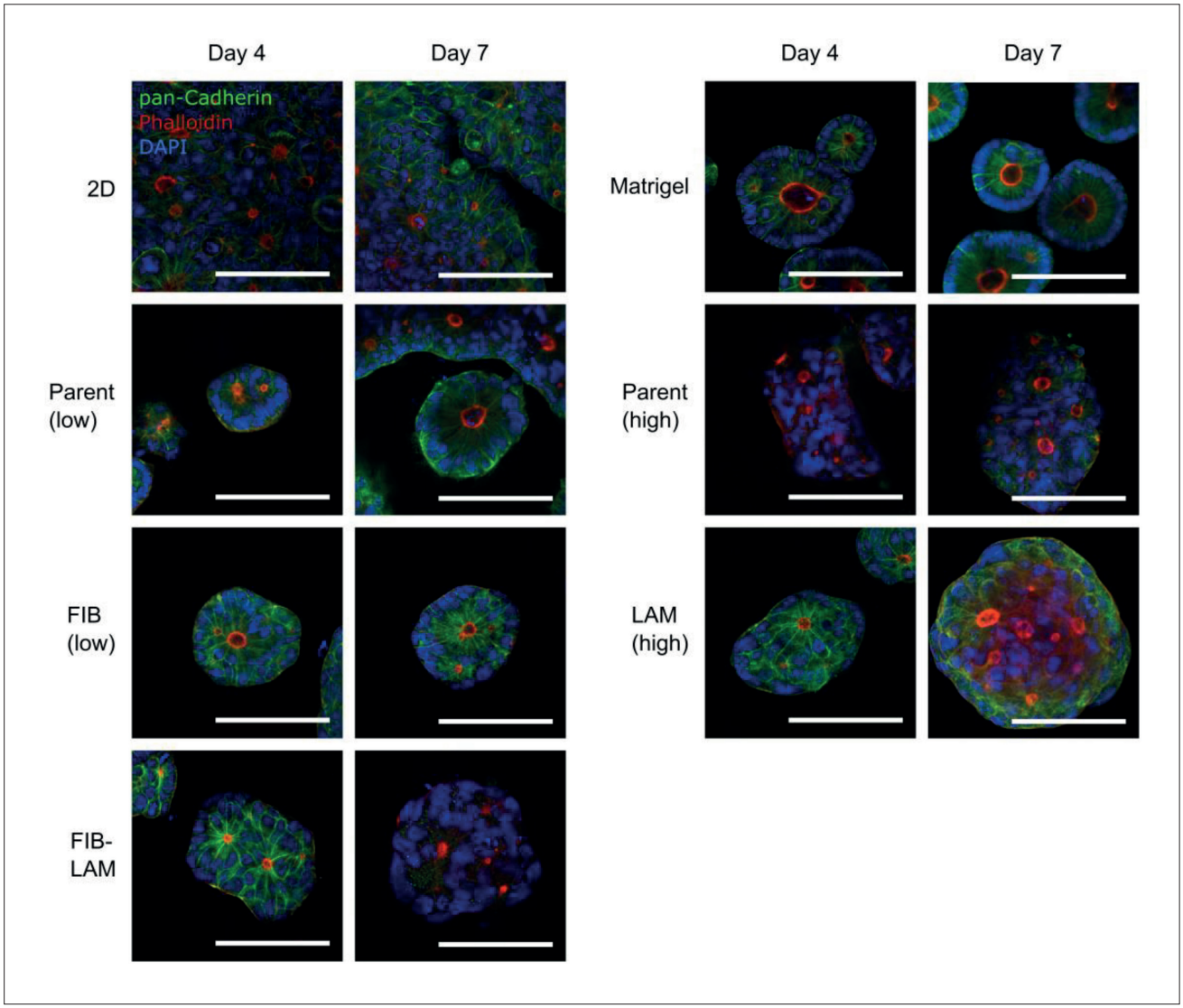


Figure 4. Confocal micrographs depicting immunostained organoids cultured within peptide hydrogels, indicating the presence of pan-cadherin-mediated cell–cell junctions (green). Supplementary counterstaining highlights the cytoskeletal elements (red) and nuclei (blue). Comparative assessment of cell–cell junction expression in biofunctional hydrogels containing FIB and LAM peptides reveals an absence of junctional complexes along both basolateral and apical membranes. Organoids cultured under the parent (low) condition exhibit robust junctional protein expression. Abbreviations: FIB, fibrinogen-derived peptide containing the RGD motif; LAM, laminin-derived peptide containing YIGSR. Scale bar = 100 μm.

explored in this study. In contrast, the FIB (low) peptide reduces the level of LGR5 expression, pointing towards a correlation between LGR5 expression and stiffness.

We also characterized the expression of the CHGA marker corresponding to enteroendocrine cells. As seen in Figure 7b, CHGA is overexpressed in LAM (high) and 2D control, while other conditions have a similar expression level to that of Matrigel. These data indicate that SW1222 cells in 2D cultures have a skewed differentiation to enteroendocrine cells. Hence, the use of 3D matrices within the stiffness ranges of this study may induce LGR5+ cells to disrupt the differentiation process. Interestingly, we identified an overexpression of EpCAM in all peptide hydrogel cultures compared to Matrigel (Figure 7c), including the cells in the 2D culture. The overexpression of the EpCAM molecule could indicate a stronger interaction between cells and the environment. One possible explanation would be that the cell–matrix interactions between the peptide hydrogels and the cells come from a possibly synergetic relationship between the motif interaction and adhesive properties of the fibers. However, further research is warranted to characterize the adhesive properties of the tetrapeptide hydrogels

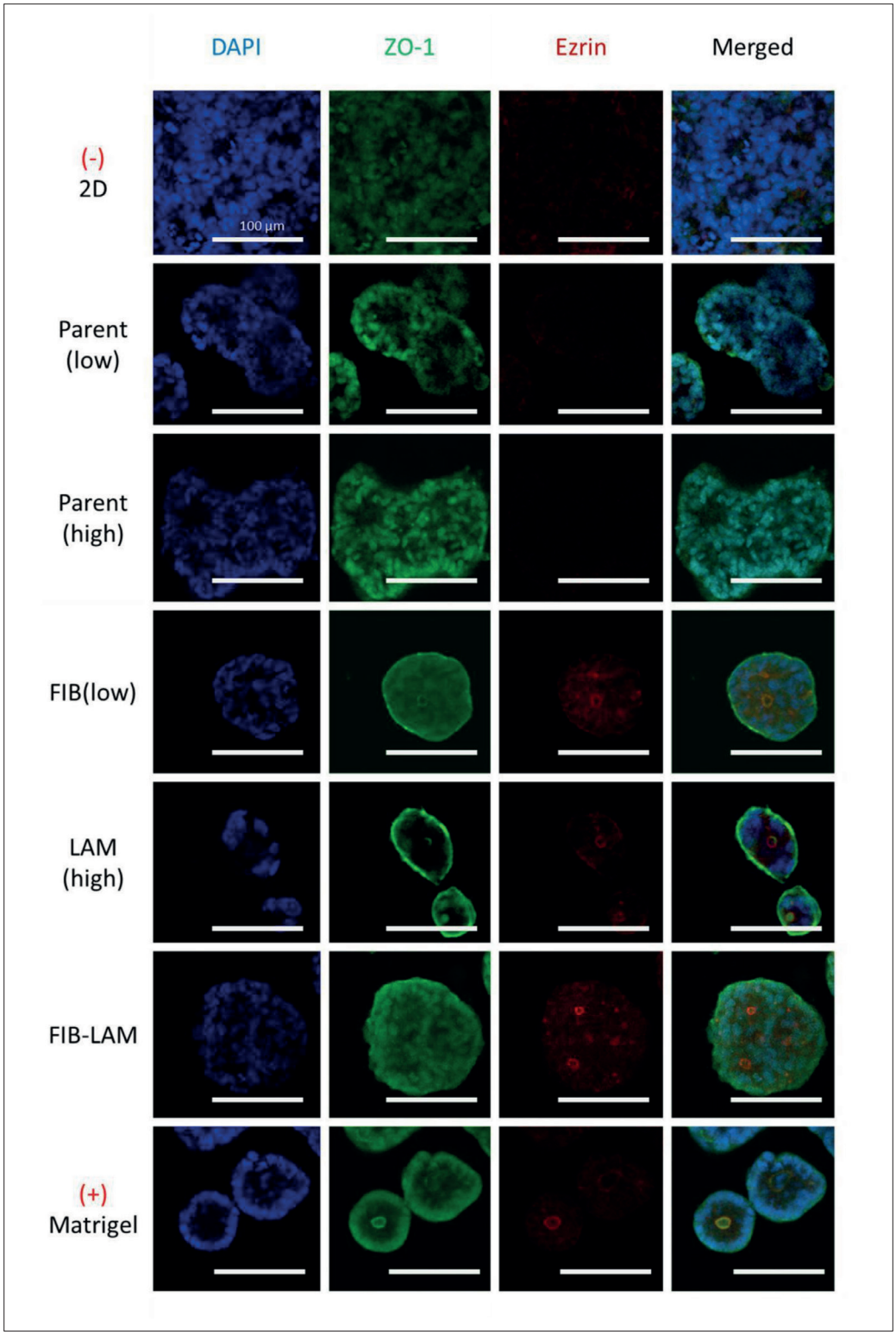


Figure 5. Colorectal cancer (CRC) organoids in different matrices with stained apical polarity markers (ZO1 and ezrin) on day 4. Ezrin marker expression becomes evident by day 4 across all experimental conditions, except the two parent peptides. Notably, ZO-1 expression in the Matrigel, LAM (high), and FIB (low) samples display prominent localization to both the apical and basal epithelial surfaces of the organoid. Positive (Matrigel) and negative (2D) controls are denoted with (+) and (−) signs, respectively. Scale bars: 100 µm. Abbreviations: FIB, fibrinogen-derived peptide containing the RGD motif; LAM, laminin-derived peptide containing YIGSR.

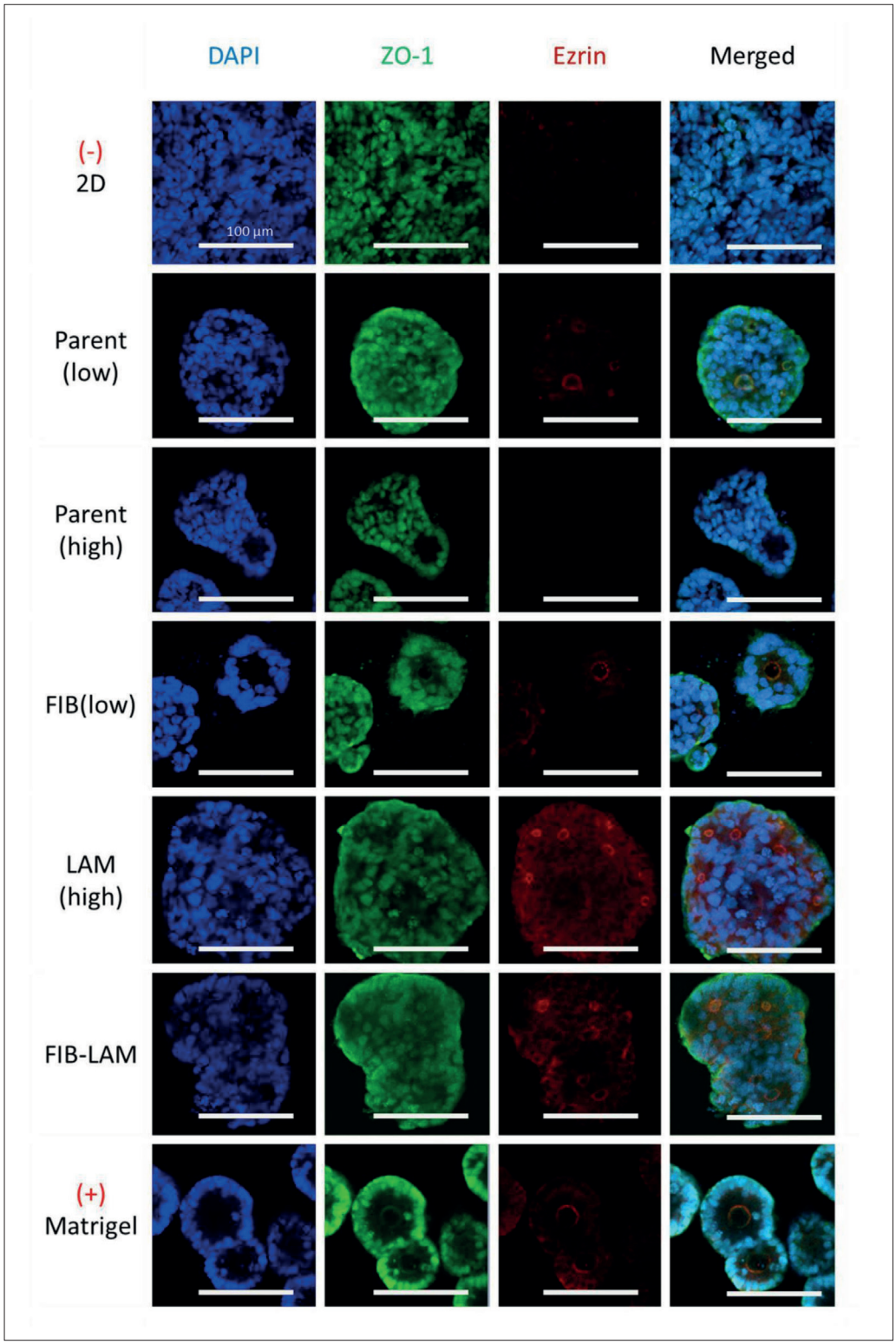


Figure 6. Colorectal cancer (CRC) organoids in different matrices with stained apical polarity markers (ZO1 and ezrin) on day 7. Ezrin expression is present in parent (low) organoid cultures by day 7 and absent in parent (high) cultures. FIB (low) and Matrigel conditions display consistent apical and basal ezrin localization, while LAM (high) exhibits a diffused organoid-wide distribution, diverging from its usual membrane localization. Results are based on three technical replicates and two biological replicates. Positive (Matrigel) and negative (2D) controls are denoted with (+) and (−) signs, respectively. Scale bars: 100 µm. Abbreviations: FIB, fibrinogen-derived peptide containing the RGD motif; LAM, laminin-derived peptide containing YIGSR.

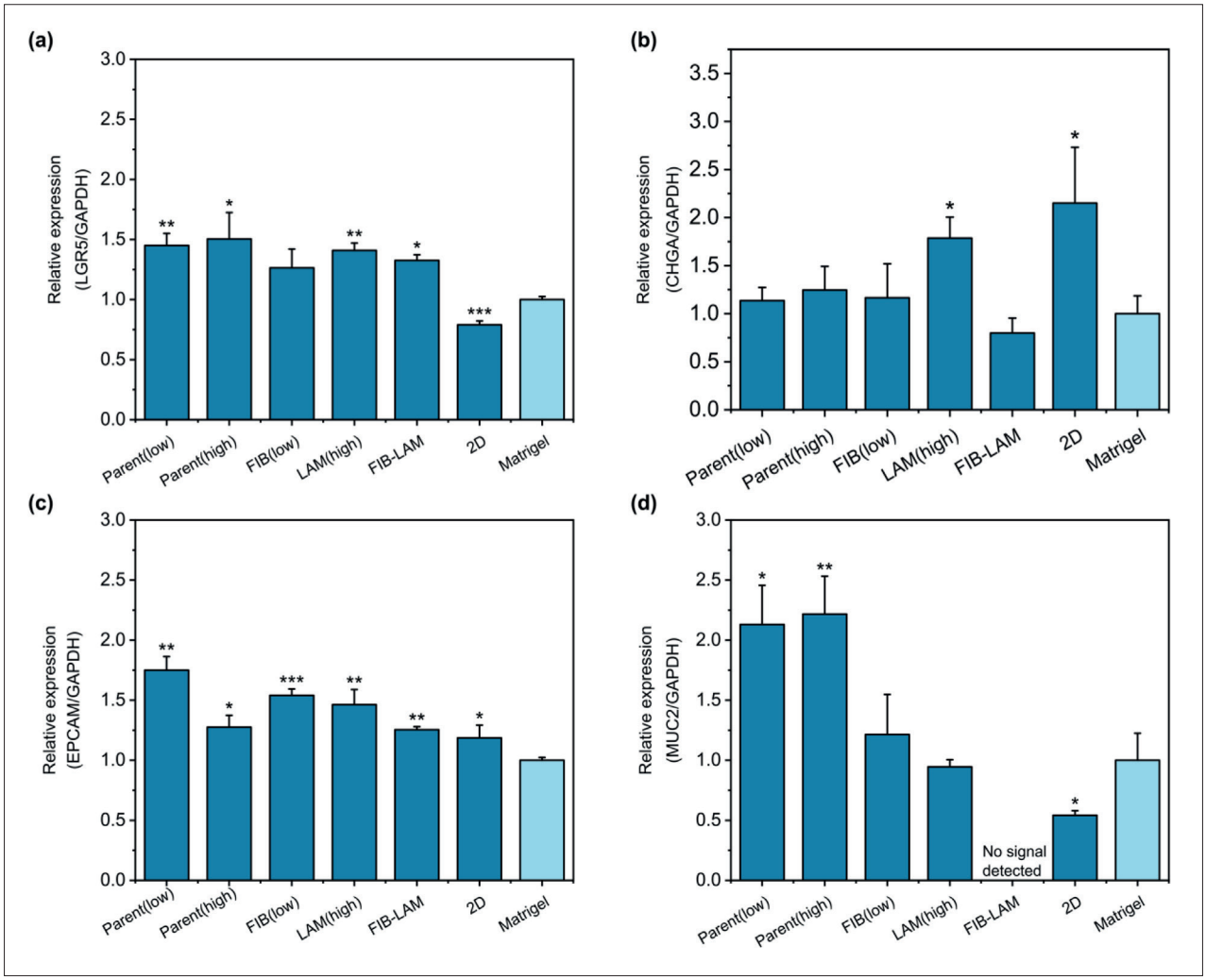


Figure 7. Comparative gene expression levels of distinct cell types, (a) *LGR5*, (b) *CHGA*, (c) *EpCAM*, and (d) *MUC2*, as observed within organoids encapsulated in diverse matrices. *GAPDH* serves as the reference housekeeping gene; Matrigel is employed as the baseline control matrix; error bars are the standard error of the mean; *$p < 0.05$; **$p < 0.01$; ***$p < 0.001$. Abbreviations: FIB, fibrinogen-derived peptide containing the RGD motif; LAM, laminin-derived peptide containing YIGSR.

and their propensity to cell interaction. Alternatively, the overexpression of the EpCAM marker in an organoid culture could be due to a skewed differentiation to epithelial cells. Although the ranges of stiffness for our peptide hydrogels fall within the reported stiffness values of Matrigel, other mechanical properties, such as elasticity and thixotropy, may be driving the expression of CHGA and EpCAM markers in the peptide hydrogels.

Finally, we characterized the expression of MUC2, commonly ascribed to goblet cells. As observed in Figure 7d, the non-biofunctional parent peptides presented an overexpression of MUC2, whereas the FIB (low) and LAM (high) hydrogels reduced mucin-2 expression to the levels found in Matrigel. Interestingly, the FIB-LAM peptide did not express the mucin-2 marker, suggesting either a reduced availability of the motifs from the FIB-LAM fibers or an antagonistic effect between the FIB and LAM peptides. Given that the FIB-LAM fibers have a unique diameter and a periodicity range that barely overlaps with the values from the other peptide fibers, we assume that the fibers assemble in a manner that hinders cell interaction with the motifs. We also presume that fiber assembly affects the intrinsic cell-adhesive properties of the parent peptide, thereby inhibiting the expression of the MUC-2 marker. Interestingly, this effect is only observed in the expression of the MUC-2 marker and not on other markers, such as the intramembrane cell-adhesive marker EpCAM.

As such, these data support the idea that FIB (low) hydrogel permits phenotype expression that is comparable

to that of the cells cultured in Matrigel. Moreover, the FIB peptide also allows cell polarization and self-organization of colonies into an organoid. We also presume that the decorated peptides may interact with cells, as the stiffness change between the low and high conditions for FIB and LAM peptides is negligible. Additionally, circularity and lumen presence in each colony results were significantly different among concentrations. As previously mentioned, it is also widely accepted that the matrix RGD (contained in FIB) ligand is vital for organoid development. However, YIGSR (contained in LAM) is a ligand known for inducing proliferation. In this case, we were able to detect a slight increase in proliferation rate until day 7 at FIB (high). Interestingly, we can observe that the percentage of colonies presenting a lumen was highly affected by the concentration of FIB peptide, while the LAM motif affected both circularity and percentage of colonies per lumen. Given the differences in proliferation between the LAM peptides, we presumed that high LAM concentration would induce cell proliferation. Based on quantitative PCR (qPCR), we can assume that the LAM peptide induces skewed differentiation into enteroendocrine cells. We can observe that the differentiation into goblet cells is similar to that in Matrigel. Remarkably, stemness is higher in LAM-containing peptides but reduced in RGD-containing peptides. This may be a product of our fiber system and/or the result of adding RGD. Increased epithelial integrity and stemness are also noted in all concentrations, but are significantly higher in FIB (low), pointing further to a skewed differentiation.

3.3. Printability and bioprinting of FIB (high) and LAM (low)

We investigated the bioprinting capabilities of the biofunctionalized peptides FIB (low) and LAM (high). This systematic evaluation focused on their gelation properties and suitability for generating stable 3D structures. First, we evaluated the gelation of a droplet of peptide extruded through our in-house bioprinting system.[36] For this test, we used the concentration of FIB (low) and LAM (high) as a starting point and subsequently tested increasing concentrations. We evaluated combinations of FIB (low) and LAM (high) at different total concentrations, 1.5, 3.0, and 4.5 mg/mL in the first case and 2.0, 4.0, and 6.0 mg/mL in the second case.

The retention of the gel is observed in FIB (low) starting at 1.5 mg/mL, while LAM (high) peptide forms a less stable hydrogel at low concentrations. For bioprinting applications, a concentration of at least 4.0 mg/mL of LAM (high) is recommended. Increased gel stability is obtained at 6.0 mg/mL. Previous projects have extensively explored the use of USAPs as bioinks,[22–25] with reported concentrations higher than 6.0 mg/mL. To satisfy the mechanical conditions commonly attributed to colorectal organoid culture, we had to explore the lower limit of these bioink concentrations. Hence, we proceeded to evaluate the printability of the bioinks at 4.5 and 6.0 mg/mL. To this end, we used a crescent moon shape and a criss-cross grid design, as depicted in Figure 8a. As can be observed, both shapes have a better definition using 6.0 mg/mL FIB (low) as video 1 and video 2 demonstrate the printing of the grid with FIB (low) at 6 mg/mL and LAM (high) at 4.5 mg/mL, respectively.

Next, we bioprinted CRC cells and compared the colonies' morphology to determine organoid characteristics. The culture was maintained for up to 8 days and was initially analyzed in terms of cell proliferation and viability (Figure 8b and c). In both peptide mixtures, a high percentage of cell viability was maintained for up to 8 days of culture. Single cells were observed on day 1 post-printing, which started to form the organoid colonies observed on days 4 and 8 post-printing. This indicates that the printing process did not affect cell viability or their potential to form organoid clusters. Similarly, a significant increase in cell proliferation was observed in both peptide bioinks, indicating the biocompatibility of the peptide mixture for 3D bioprinting and its potential use for high-throughput organoid formation for drug screening applications.

We noticed that a higher number of colonies were present in the FIB bioprinted structure, while the LAM peptide exhibited excess debris inside the structure. We examined these further by observing the cytoskeleton using confocal microscopy (Figure 8c). Interestingly, most of the colonies in the LAM peptide displayed a 2D morphology, with various small-sized lumens and no degree of polarization. The colonies found in the FIB peptide presented a reduced number of lumens within the colony and some degree of polarization. The colonies are also smaller in size than the 2D-like colonies observed in the LAM peptide. These morphological characteristics suggest that organoid fabrication in these conditions is also feasible, proposing bioprinting as an alternative method to manipulate and fabricate organoids *in vitro*.

4. Discussion

In this study, we designed and characterized two new biofunctional peptides that can form nanofibers in the presence of the parent self-assembling peptide. In addition, we established various mixtures of peptides and characterized them. We found that the physicochemical properties of the peptides vary according to their sequence, concentration, and ratio. For instance, the gelation of FIB peptide mixtures is limited by the

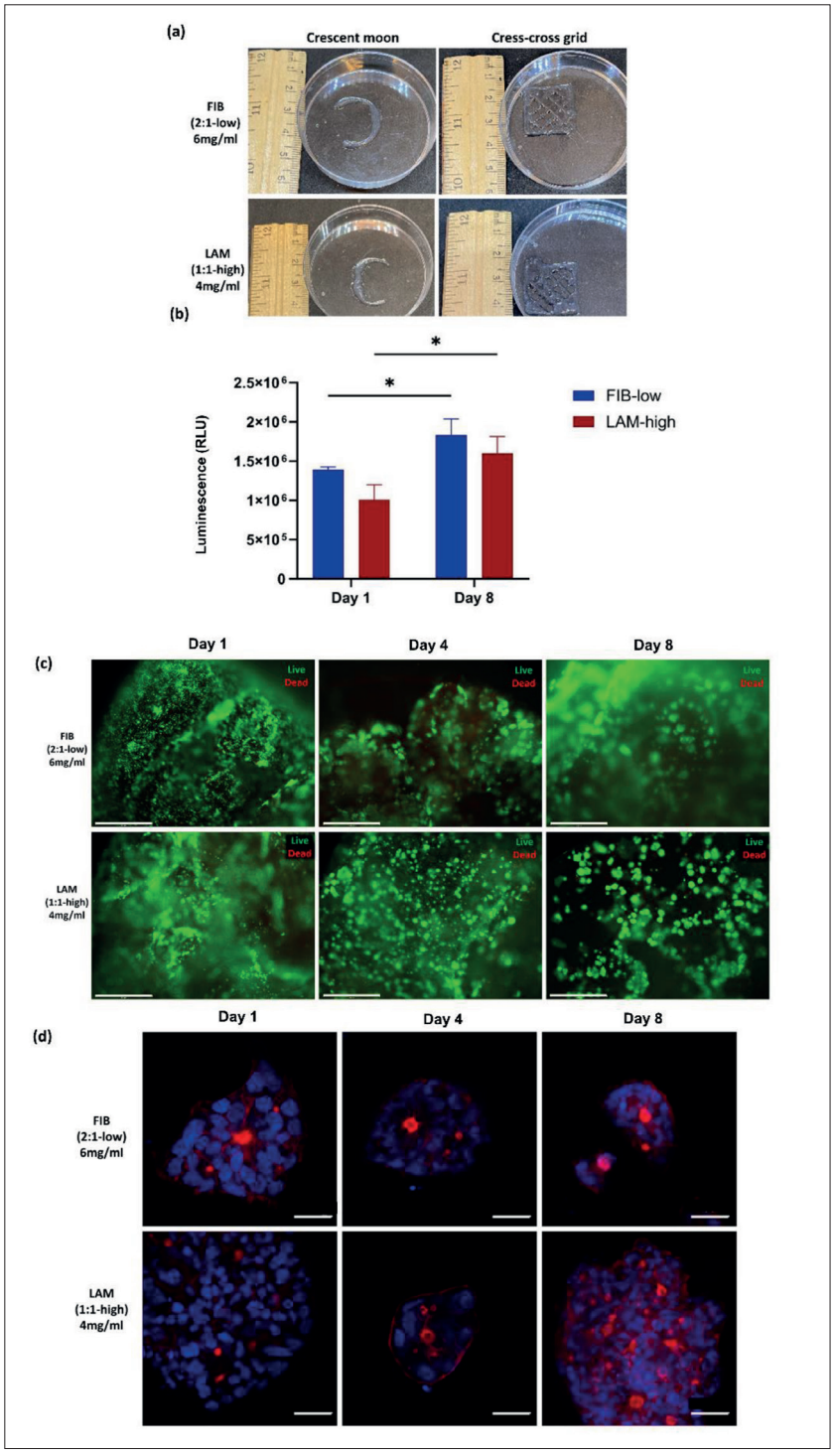


Figure 8. Assessment of bioprintability of FIB-low and LAM-high peptide bioinks. (a) Evaluation of 3D printability based on printed structures using a total concentration of 6 mg/mL (FIB at 2:1 ratio) and 4.0 mg/mL (LAM at 1:1 ratio). (b and c) Biocompatibility assessment after 3D bioprinting using FIB-low and LAM-high peptide bioinks. (b) Assessment of cell proliferation at days 1 and 8 post-printing. A significant difference in cell proliferation was observed between days 1 and 8 for both peptide bioinks (*$p < 0.05$). (c) Live/dead assay for assessing cell viability at days 1, 4, and 8 post-printing. Cells were stained with calcein-AM (green, live cells) and ethidium homodimer-1 (red, dead cells). Scale bars: 650 μm. (d) Confocal imaging of cytoskeleton staining of cells in the bioprinted construct. F-actin was stained with phalloidin (red) and the nucleus with DAPI (blue). Scale bars: 40 μm. Abbreviations: FIB, fibrinogen-derived peptide containing the RGD motif; LAM, laminin-derived peptide containing YIGSR.

Video 1. Criss-cross grid printing of FIB (low) at total concentration of 6 mg/mL.

Video 2. Criss-cross grid printing of LAM (high) at total concentration of 4.5 mg/mL.

concentration of the parent peptide, while the gelation of FIB mixtures is kept constant when the concentration of the decorated peptide is higher or equal to the decorated LAM peptide. We determined the nanofibers' characteristics in each mixture, such as LAM (high) fibers presenting right-handedness. Likewise, we evaluated the biocompatibility of these hydrogels and the effect each had on colorectal organoid fabrication. We concluded that these hydrogels are cytocompatible and facilitate cell proliferation in a magnitude similar to that of Matrigel. By colony morphology evaluation, we obtained two promising peptide formulations (FIB [high] and LAM [low]) to be used as organoid matrices. Accordingly, we characterized the organoids cultured in these promising peptide formulations and the FIB-LAM mixture. For this, we assessed lumen formation on these three formulations. We concluded that organoids cultured in peptide FIB (low) exhibit a polar arrangement and a gene expression profile closer to those cultured in Matrigel. However, the effect between the peptide fibers and cells warrants further investigation to understand the impact of peptide hydrogels on cell adhesion and differentiation.

Moreover, our investigation into the bioprinting capabilities of the biofunctionalized peptides FIB (low) and LAM (high) has provided valuable insights into their performance and suitability for generating stable 3D structures. Through a systematic evaluation of their gelation properties, we observed that FIB (low) exhibited superior gel retention even at lower concentrations than LAM (high), forming a less stable hydrogel at similar concentrations. For optimal bioprinting applications, a concentration of at least 4.0 mg/mL of LAM (high) is recommended, with increased gel stability achieved at 6.0 mg/mL. To meet the mechanical requirements typical of colorectal organoid culture, we explored the lower concentration limits of these bioinks, highlighting the need for precise concentration control in bioprinting applications. Evaluation of the printability of the bioinks at varying concentrations revealed improved shape definition using FIB (low) at 6.0 mg/mL. Additionally, the bioprinting of CRC cells demonstrated morphological differences between colonies printed with FIB and LAM peptides. While FIB bioprinted structures exhibited more colonies with reduced lumen size and increased polarization, LAM peptide structures have a predominance of 2D-like colonies with smaller lumens and minimal polarization.

Our findings indicate the successful fabrication and characterization of various hydrogel formulations derived from biofunctional peptides and their use in bioprinting. We systematically evaluated the effects of these matrices on viability, proliferation, organoid formation, and gene expression. We demonstrated the potential of these matrices to influence organoid morphology and gene expression. Moreover, the bioprinting evaluation suggests the feasibility of organoid fabrication using bioprinting techniques, offering a promising alternative for *in vitro* organoid manipulation and fabrication.

We demonstrated the potential enhancement of USAPs by using biofunctional peptides to obtain the most suitable combination of characteristics for CRC organoid development and their use in a bioprinting setup. We believe that our findings have important implications for advancing the field of organoid culture, bioprinting, and its applications in CRC research. The detailed characterization and optimization of the novel biofunctional peptide bioink provide insights into its potential as a valuable tool in regenerative medicine, disease modeling, and drug testing.

5. Conclusion

In this study, we introduced and characterized two novel biofunctional peptides designed to enhance the capabilities of USAPs for bioprinting colon organoids. These peptides demonstrated the ability to form nanofibers when mixed with the parent self-assembling peptide, and their physicochemical properties were systematically evaluated based on sequence, concentration, and ratio. We found that the gelation behavior of these peptide mixtures varied significantly; for instance, FIB peptides required a higher concentration of the parent peptide to achieve gelation compared to LAM peptides. Biocompatibility assessments revealed that these peptide hydrogels support cell proliferation similarly to Matrigel, with promising formulations identified for organoid culture. Specifically, FIB (low) and LAM (high) formulations were highlighted for their favorable effects on organoid morphology and gene expression, resembling characteristics seen with Matrigel. Notably, organoids cultured in FIB (low) exhibited polar arrangements and gene expression profiles closer to natural colon tissue.

In exploring their bioprinting capabilities, we determined optimal concentrations for achieving stable 3D structures, emphasizing the importance of precise concentration control. FIB (low) demonstrated enhanced shape fidelity at higher concentrations, whereas LAM (high) favored stable gelation at lower concentrations suitable for bioprinting. Bioprinted structures of CRC cells using these peptides revealed distinct morphological differences, suggesting their potential for modeling disease-specific phenotypes.

Overall, our study underscores the potential of biofunctional peptides in enhancing USAPs for organoid

culture and bioprinting applications. These findings contribute valuable insights into advancing organoid research, bioprinting technology, and their implications for CRC modeling and therapeutic development in regenerative medicine.

Acknowledgments

The authors would like to acknowledge KAUST's Bioscience and Imaging Core Labs for supporting the biological characterization and microscopy analyses.

Funding

This work was financially supported by KAUST: Seed Fund Grant and Innovation Fund by KAUST's Innovation and Economic Development; and funding from the Computational Bioscience Research Center, KAUST.

Conflict of interest

The authors declare no conflicts of interest.

Author contribution

Conceptualization: Rosario Pérez-Pedroza, Charlotte A. E. Hauser

Data curation: Rosario Pérez-Pedroza, Jiayi Xu, Diana Eveline Sanchez-Amador, Manola Moretti, Alexander Valle-Perez, Antonio Cárdenas-Calvario, Dana Alhattab, Jezabel Parra-Garcia, Charlotte A. E. Hauser

Formal analysis: Jiayi Xu

Investigation: Rosario Pérez-Pedroza, Jiayi Xu, Diana Eveline Sanchez-Amador, Manola Moretti, Alexander Valle-Perez, Antonio Cárdenas-Calvario, Dana Alhattab, Jezabel Parra-Garcia

Methodology: Rosario Pérez-Pedroza, Manola Moretti

Resources: Charlotte A. E. Hauser

Supervision: Rosario Pérez-Pedroza, Manola Moretti, Charlotte A. E. Hauser

Validation: Rosario Pérez-Pedroza, Jiayi Xu, Diana Eveline Sanchez-Amador, Manola Moretti, Alexander Valle-Perez, Antonio Cárdenas-Calvario, Dana Alhattab, Jezabel Parra-Garcia, Charlotte A. E. Hauser

Writing – original draft: Jiayi Xu, Rosario Pérez Pedroza

Writing – review & editing: Rosario Pérez-Pedroza, Manola Moretti, Charlotte A. E. Hauser

Ethics approval and consent to participate

Not applicable.

Consent for publication

Not applicable.

Data availability

The original data are available from the authors upon request.

References

1. Alsanea N, Abduljabbar AS, Alhomoud S, et al. Colorectal cancer in Saudi Arabia: incidence, survival, demographics and implications for national policies. *Ann Saudi Med*. 2015;35(3):196-202. doi: 10.5144/0256-4947.2015.196
2. Alsanea N, Almadi MA, Abduljabbar AS, et al. National Guidelines for Colorectal Cancer Screening in Saudi Arabia with strength of recommendations and quality of evidence. *Ann Saudi Med*. 2015;35(3):189-195. doi: 10.5144/0256-4947.2015.189
3. Favoriti P, Carbone G, Greco M, Pirozzi F, Pirozzi RE, Corcione F. Worldwide burden of colorectal cancer: a review. *Updates Surg*. 2016;68(1):7-11. doi: 10.1007/s13304-016-0359-y
4. Bray F, Ferlay J, Soerjomataram I, Siegel RL, Torre LA, Jemal A. Global cancer statistics 2018: GLOBOCAN estimates of incidence and mortality worldwide for 36 cancers in 185 countries. *CA Cancer J Clin*. 2018;68(6):394-424. doi: 10.3322/caac.21492
5. Vu JV, Sommovilla J. The molecular genetics of colorectal cancer, hereditary colorectal cancer syndromes, and early-onset colorectal cancer. *Digest Dis Interv*. 2023;07(01): 058-070. doi: 10.1055/s-0042-1757325
6. Kim SE, Paik HY, Yoon H, Lee JE, Kim N, Sung MK. Sex- and gender-specific disparities in colorectal cancer risk. *World J Gastroenterol*. 2015;21(17):5167-5175. doi: 10.3748/wjg.v21.i17.5167
7. Guinney J, Dienstmann R, Wang X, et al. The consensus molecular subtypes of colorectal cancer. *Nat Med*. 2015;21(11):1350-1356. doi: 10.1038/nm.3967
8. Sepulveda AR, Hamilton SR, Allegra CJ, et al. Molecular biomarkers for the evaluation of colorectal cancer: guideline from the American Society for Clinical Pathology, College of American Pathologists, Association for Molecular Pathology, and the American Society of Clinical Oncology. *J Clin Oncol*. 2017;35(13):1453-1486. doi: 10.1200/JCO.2016.71.9807
9. Lipkin M, Reddy B, Newmark H, Lamprecht SA. Dietary factors in human colorectal cancer. *Annu Rev Nutr*. 1999;19:545-586. doi: 10.1146/annurev.nutr.19.1.545
10. Labianca R, Beretta GD, Kildani B, et al. Colon cancer. *Crit Rev Oncol Hematol*. 2010;74(2):106-133. doi: 10.1016/j.critrevonc.2010.01.010

11. Linnekamp JF, Hooff SRV, Prasetyanti PR, et al. Consensus molecular subtypes of colorectal cancer are recapitulated in in vitro and in vivo models. *Cell Death Differ*. 2018;25(3):616-633.
doi: 10.1038/s41418-017-0011-5

12. Sveen A, Bruun J, Eide PW, et al. Colorectal cancer consensus molecular subtypes translated to preclinical models uncover potentially targetable cancer cell dependencies. *Clin Cancer Res*. 2018;24(4):794-806.
doi: 10.1158/1078-0432.CCR-17-1234

13. Idris M, Alves MM, Hofstra RMW, Mahe MM, Melotte V. Intestinal multicellular organoids to study colorectal cancer. *Biochim Biophys Acta Rev Cancer*. 2021;1876(2):188586.
doi: 10.1016/j.bbcan.2021.188586

14. Varga OE, Hansen AK, Sandøe P, Olsson IA. Validating animal models for preclinical research: a scientific and ethical discussion. *Altern Lab Anim*. 2010;38(3):245-248.
doi: 10.1177/026119291003800309

15. Date S, Sato T. Mini-gut organoids: reconstitution of the stem cell niche. *Annu Rev Cell Dev Biol*. 2015;31:269-289.
doi: 10.1146/annurev-cellbio-100814-125218

16. Sato T, Stange DE, Ferrante M, et al. Long-term expansion of epithelial organoids from human colon, adenoma, adenocarcinoma, and Barrett's epithelium. *Gastroenterology*. 2011;141(5):1762-1772.
doi: 10.1053/j.gastro.2011.07.050

17. Drost J, Clevers H. Organoids in cancer research. *Nat Rev Cancer*. 2018;18:407-418.
doi: 10.1038/s41568-018-0007-6

18. Maharjan S, Ma C, Singh B, et al. Advanced 3D imaging and organoid bioprinting for biomedical research and therapeutic applications. *Adv Drug Deliv Rev*. 2024;208:115237.
doi: 10.1016/j.addr.2024.115237

19. De Stefano P, Briatico-Vangosa F, Bianchi E, et al. Bioprinting of matrigel scaffolds for cancer research. *Polymers (Basel)*. 2021;13(12):2026.
doi: 10.3390/polym13122026

20. Lotz O, McKenzie DR, Bilek MM, Akhavan B. Biofunctionalized 3D printed structures for biomedical applications: a critical review of recent advances and future prospects. *Prog Mater Sci*. 2023;137:101124.
doi: 10.1016/j.pmatsci.2023.101124

21. GhavamiNejad A, Ashammakhi N, Wu XY, Khademhosseini A. Crosslinking strategies for 3D bioprinting of polymeric hydrogels. *Small*. 2020;16(35):2002931.
doi: 10.1002/smll.202002931

22. Hauser CA, Deng R, Mishra A, et al. Natural tri- to hexapeptides self-assemble in water to amyloid beta-type fiber aggregates by unexpected alpha-helical intermediate structures. *Proc Natl Acad Sci U S A*. 2011;108(4):1361-1366.
doi: 10.1073/pnas.1014796108

23. Loo Y, Zhang S, Hauser CAE. From short peptides to nanofibers to macromolecular assemblies in biomedicine. *Biotechnol Adv*. 2012;30:593-603.
doi: 10.1016/j.biotechadv.2011.10.004

24. Liu Y, Zhang L, Wei W. Effect of noncovalent interaction on the self-assembly of a designed peptide and its potential use as a carrier for controlled bFGF release. *Int J Nanomedicine*. 2017;12:659-670.
doi: 10.2147/IJN.S124523

25. Abdelrahman S, Alsanie WF, Khan ZN, et al. A Parkinson's disease model composed of 3D bioprinted dopaminergic neurons within a biomimetic peptide scaffold. *Biofabrication*. 2022;14(4):044103.
doi: 10.1088/1758-5090/ac7eec

26. Abdelrahman S, Ge R, Susapto HH, et al. The impact of mechanical cues on the metabolomic and transcriptomic profiles of human dermal fibroblasts cultured in ultrashort self-assembling peptide 3D scaffolds. *ACS Nano*. 2023;17(15):14508-14531.
doi: 10.1021/acsnano.3c01176

27. Alzanbaki H, Moretti M, Hauser CAE. Engineered microgels-their manufacturing and biomedical applications. *Micromachines (Basel)*. 2021;12(1):45.
doi: 10.3390/mi12010045

28. Pérez-Pedroza R, Ávila-Ramirez A, Khan Z, Moreti M, Hauser CAE. Supramolecular biopolymers for tissue engineering. *Adv Polym Technol*. 2021;2021:1-23.
doi: 10.1155/2021/8815006

29. Wang Y, Liu X, Ge R, et al. Peptide gel electrolytes for stabilized zn metal anodes. *ACS Nano*. 2024;18(1):164-177.
doi: 10.1021/acsnano.3c04414

30. Bilalis P, Alrashoudi AA, Susapto HH, et al. Dipeptide-based photoreactive instant glue for environmental and biomedical applications. *ACS Appl Mater Interfaces*. 2023;15(40):46710-46720.
doi: 10.1021/acsami.3c10726

31. Moretti M, Hountondji M, Ge R, et al. Selectively positioned catechol moiety supports ultrashort self-assembling peptide hydrogel adhesion for coral restoration. *Langmuir*. 2023;39(49):17903-17920.
doi: 10.1021/acs.langmuir.3c02553

32. Alhattab DM, Isaioglou I, Alshehri S, Khan ZN. Fabrication of a three-dimensional bone marrow niche-like acute myeloid Leukemia disease model by an automated and controlled process using a robotic multicellular bioprinting system. *Biomater Res*. 2023;27(1):111.
doi: 10.1186/s40824-023-00457-9

33. Loo Y, Chan YS, Szczerbinska I, et al. A chemically well-defined, self-assembling 3D substrate for long-term culture of human pluripotent stem cells. *ACS Appl Bio Mater*. 2019;2(4):1406-1412.
doi: 10.1021/acsabm.8b00686

34. Loo Y, Lakshmanan A, Ni M, Toh LL, Wang S, Hauser CA. Peptide bioink: self-assembling nanofibrous scaffolds for three-dimensional organotypic cultures. *Nano Lett*. 2015;15(10):6919-6925. doi: 10.1021/acs.nanolett.5b02859

35. Alshehri S, Susapto HH, Hauser CAE. Scaffolds from self-assembling tetrapeptides support 3D spreading, osteogenic differentiation, and angiogenesis of mesenchymal stem cells. *Biomacromolecules*. 2021;22(5):2094-2106. doi: 10.1021/acs.biomac.1c00205

36. Susapto HH, Alhattab D, Abdelrahman S, et al. Ultrashort peptide bioinks support automated printing of large-scale constructs assuring long-term survival of printed tissue constructs. *Nano Lett*. 2021;21(7):2719-2729. doi: 10.1021/acs.nanolett.0c04426

37. Pérez-Pedroza R, Al-Jalih F, Xu J, Moretti M, Briola GR, Hauser CAE. Fabrication of lumen-forming colorectal cancer organoids using a newly designed laminin-derived bioink. *Int J Bioprint*. 2022;9(1):633. doi: 10.18063/ijb.v9i1.633

38. Peng G, Yao D, Niu Y, Liu H, Fan Y. Surface modification of multiple bioactive peptides to improve endothelialization of vascular grafts. *Macromol Biosci*. 2019;19(5):e1800368. doi: 10.1002/mabi.201800368

39. Ali S, Saik JE, Gould DJ, Dickinson ME, West JL. Immobilization of cell-adhesive laminin peptides in degradable PEGDA hydrogels influences endothelial cell tubulogenesis. *Biores Open Access*. 2013;2(4):241-249. doi: 10.1089/biores.2013.0021

40. Bellis SL. Advantages of RGD peptides for directing cell association with biomaterials. *Biomaterials*. 2011;32(18):4205-4210. doi: 10.1016/j.biomaterials.2011.02.029

41. Yamada Y, Onda T, Hagiuda A, et al. $RGDX_1$ X_2 motif regulates integrin αvβ5 binding for pluripotent stem cell adhesion. *FASEB J*. 2022;36(7):e22389. doi: 10.1096/fj.202200317R

42. Gjorevski N, Sachs N, Manfrin A, et al. Designer matrices for intestinal stem cell and organoid culture. *Nature*. 2016;539(7630):560-564. doi: 10.1038/nature20168

43. Rezakhani S, Gjorevski N, Lutolf MP. Extracellular matrix requirements for gastrointestinal organoid cultures. *Biomaterials*. 2021;276:121020. doi: 10.1016/j.biomaterials.2021.121020

44. Kim S, Min S, Choi YS, et al. Tissue extracellular matrix hydrogels as alternatives to matrigel for culturing gastrointestinal organoids. *Nat Commun*. 2022;13(1):1692. doi: 10.1038/s41467-022-29279-4

45. Stringer C, Wang T, Michaelos M, Pachitariu M. Cellpose: a generalist algorithm for cellular segmentation. *Nat Methods*. 2021;18(1):100-106. doi: 10.1038/s41592-020-01018-x.

46. Pachitariu M, Stringer C. Cellpose 2.0: how to train your own model. *Nat Methods*. 2022;19(12):1634-1641. doi: 10.1038/s41592-022-01663-4

47. Shoulders MD, Raines RT. Collagen structure and stability. *Annu Rev Biochem*. 2009;78:929-958. doi: 10.1146/annurev.biochem.77.032207.120833

48. Zhang P, Moretti M, Allione M, et al. A droplet reactor on a super-hydrophobic surface allows control and characterization of amyloid fibril growth. *Commun Biol*. 2020;3:457. doi: 10.1038/s42003-020-01187-7

49. Moretti M, Allione M, Marini M, et al. Confined laminar flow on a super-hydrophobic surface drives the initial stages of tau protein aggregation. *Microelectron Eng*. 2018;191:54-59. doi: 10.1016/j.mee.2018.01.025

50. Moretti M, Allione M, Marini M, et al. Raman study of lysozyme amyloid fibrils suspended on super-hydrophobic surfaces by shear flow. *Microelectron Eng*. 2017;178:194-198. doi: 10.1016/ j.mee.2017.05.045

51. Xu ZY, Huang JJ, Liu Y, et al. Extracellular matrix bioink boosts stemness and facilitates transplantation of intestinal organoids as a biosafe Matrigel alternative. *Bioeng Transl Med*. 2022;8(1):e10327. doi: 10.1002/btm2.10327

52. DiMarco RL, Dewi RE, Bernal G, Kuo C, Heilshorn SC. Protein-engineered scaffolds for in vitro 3D culture of primary adult intestinal organoids. *Biomater Sci*. 2015;3(10):1376-1385. doi: 10.1039/c5bm00108k

53. Almdal K, Hvidt DS, Kramer O. Towards a phenomenological definition of the term 'gel'. *Polymer Gels Netw*. 1993;1(1):5-17. doi: 10.1016/0966-7822(93)90020-I

54. Yeung T, Georges PC, Flanagan LA, et al. Effects of substrate stiffness on cell morphology, cytoskeletal structure, and adhesion. *Cell Motil Cytoskeleton*. 2005;60(1):24-34. doi: 10.1002/cm.20041

55. Maldonado M, Wong LY, Echeverria C, et al. The effects of electrospun substrate-mediated cell colony morphology on the self-renewal of human induced pluripotent stem cells. *Biomaterials*. 2015;50:10-19. doi: 10.1016/j.biomaterials.2015.01.037

56. Hushka EA, Yavitt FM, Brown TE, Dempsey PJ, Anseth KS. Relaxation of extracellular matrix forces directs crypt formation and architecture in intestinal organoids. *Adv Healthc Mater*. 2020;9(8):e1901214. doi: 10.1002/adhm.201901214

57. Ruiter FAA, Morgan FLC, Roumans N, et al. Soft, dynamic hydrogel confinement improves kidney organoid

lumen morphology and reduces epithelial-mesenchymal transition in culture. *Adv Sci (Weinh)*. 2022;9(20): e2200543.
doi: 10.1002/advs.202200543.

58. Luca AC, Mersch S, Deenen R, et al. Impact of the 3D microenvironment on phenotype, gene expression, and EGFR inhibition of colorectal cancer cell lines. *PLoS One*. 2013;8(3):e59689.
doi: 10.1371/journal.pone.0059689.

59. Kenny PA, Lee GY, Myers CA, et al. The morphologies of breast cancer cell lines in three-dimensional assays correlate with their profiles of gene expression. *Mol Oncol*. 2007;1(1):84-96.
doi: 10.1016/j.molonc.2007.02.004

60. Ng S, Tan WJ, Pek MMX, Tan MH, Kurisawa M. Mechanically and chemically defined hydrogel matrices for patient-derived colorectal tumor organoid culture. *Biomaterials*. 2019;219:119400.
doi: 10.1016/j.biomaterials.2019.119400

ACCSCIENCE PUBLISHING

International Journal of Bioprinting

RESEARCH ARTICLE

Design and fabrication of anisotropic SiO_2 gyroid bioscaffolds with tunable properties

Ka-Wai Yeung[1], Chi-Yeung Mang[1], Quan-Jing Mei[2], Chi Ho Wong[3], Chak-Yin Tang[1,4]*, Xin Zhao[2], Wing-Cheung Law[1], Gary Chi-Pong Tsui[1], and Zhenjia Huang[1]

[1]Department of Industrial and Systems Engineering, Faculty of Engineering, The Hong Kong Polytechnic University, Hong Kong, China

[2]Department of Applied Biology and Chemical Technology, Faculty of Science, The Hong Kong Polytechnic University, Hong Kong, China

[3]Department of Physics, School of Science, The Hong Kong University of Science and Technology, Hong Kong, China

[4]State Key Laboratory of Ultra-precision Machining Technology, Department of Industrial and Systems Engineering, Faculty of Engineering, The Hong Kong Polytechnic University, Hong Kong, China

Abstract

This paper introduces a mathematical approach and additive manufacturing process to customize the mechanical properties of sheet gyroid bioscaffolds and mimicking the intricate architecture of natural bone. By defining the parameters of the level-set equation, scaffolds with spatially controlled porosity and anisotropic properties can be fabricated though digital light processing and microwave heating. A new susceptor-assisted hybrid pyrolysis-sintering process was developed, resulting in a significant enhancement in quality and mechanical properties of the three-dimensional (3D)-printed ceramic compared to conventional methods. The enhancements are originated from the improved densification, accelerated sintering kinetics, promotion of cristobalite phase transformation, and reduced defect volume under microwave heating. Sheet gyroid scaffolds with radially graded porosity and anisotropic properties were fabricated. Despite the porosity distribution, an increase in the unit cell's aspect ratio amplified the anisotropic mechanical properties. This was also accompanied by a slight decrease in cell proliferation efficiency possibly due to variations in Gaussian curvatures.

Keywords: Biomimetic structure; Triply periodic minimal surface; Microwave technology; 3D Printing; Ceramic bioscaffold

***Corresponding authors:**
Chak-Yin Tang
(cy.tang@polyu.edu.hk)

Citation: Yeung K-W, Mang C-Y, Mei Q-J, et al. Design and fabrication of anisotropic SiO_2 gyroid bioscaffolds with tunable properties. *Int J Bioprint*. 2024;10(5):3609. doi: 10.36922/ijb.3609

Received: May 8, 2024
Accepted: June 11, 2024
Published Online: August 8, 2024

Copyright: © 2024 Author(s). This is an Open Access article distributed under the terms of the Creative Commons Attribution License, permitting distribution, and reproduction in any medium, provided the original work is properly cited.

Publisher's Note: AccScience Publishing remains neutral with regard to jurisdictional claims in published maps and institutional affiliations.

1. Introduction

Ceramic bioscaffolds that mimic the physical and mechanical properties of natural human bone are crucial to achieve optimal bone regeneration. Achieving this involves precise manipulation of factors like volume fraction, pore size, and surface topography. Triply periodic minimal surfaces (TPMS), particularly the gyroid structure, offer promising scaffold design for bone regeneration.[1–4] Their geometries can be meticulously controlled through

mathematical algorithms.[5] The equation-driven architecture enables customization of lattice type, unit cell dimensions, strut sizes, volume fraction, and curvature distribution,[6] which is conducive to regulating cellular behaviors.[7] Recent studies have demonstrated that mimicking the anisotropy of natural bone, along with spatially controllable porosity, can achieve tunable mechanical properties and reduce the *in vivo* stress shielding effect, potentially improving scaffold integration.[8] This allows for the optimization of mechanical properties, enabling the creation of scaffolds that are strong and stiff where needed, yet lightweight and porous in other regions. This tunability in mechanical properties is crucial for matching the mechanical behavior of the scaffold to the surrounding bone tissue, and consequently enhances the integration with the host bone, promoting more effective bone repair and regeneration. Leveraging advanced additive manufacturing techniques and innovative 3D-printable biomaterials are expected to contribute to the development of functional biodevices.[7,9–11] However, optimal TPMS design for enhanced bone regeneration remains a topic of ongoing research.

Three dimensional (3D) printing is a promising technology for producing bone implants and constructs due to the capability of fabricating complex, precise, and customized structures with controlled architectures and properties.[12] The major advantages of 3D cell culture are the ability to create a realistic microenvironment for cells, facilitate cell–cell and cell–matrix interactions, thus enhancing the cell growth and proliferation.[13,14] Currently, 3D printing of ceramic can be achieved by developing photocurable ceramic/polymer composites followed by lithography-based process such as stereolithography and digital light processing (DLP).[15–18] However, generation of dense 3D ceramic generally required lengthy debinding and sintering processes to achieve highly densified products, which reduce the throughput of the manufacturing process and limit their potential applications. To mitigate this limitation, susceptor-assisted microwave heating (SMWH) offers a promising and time-saving alternative for sintering ceramic specimens, due to its intrinsic heating mechanism that lowers sintering activation energy and processing temperature.[19–21] Despite offering a more reliable and controllable sintering process,[22,23] challenges such as crack formation associated with the rapid heating have limited its utilization in additive manufacturing processes.[24] Further research is needed to improve the process and fully exploit the advantages of microwave (MW) technology to enhance the throughput of the 3D scaffolds manufacturing.

In this proof-of-concept study, we introduced a design methodology for creating sheet gyroid structures with tailored geometrical properties, employing bioinert silica as the model materials due to its superior mechanical properties and stability compared to other bioceramics. By controlling the parameters of the level-set equations of the gyroid structure, we achieved spatially controlled porosity and anisotropic properties, generating structures with radially graded porosity (40–60%) to mimic trabecular bone. The scaffolds were fabricated through DLP, followed by a susceptor-assisted hybrid pyrolysis-sintering (SHPS) process utilizing MW heating. This innovative method effectively reduces defects and mitigates crack formation during rapid MW sintering, leading to reduced defect volume by 16.81% and improved compressive strength by 336% compared to conventional furnace heating. Additionally, our study revealed that an increase in aspect ratio of the unit cell amplified the anisotropic mechanical properties of the gyroid structure. However, while the scaffolds exhibit minimal cytotoxicity, this adjustment slightly decreases cell proliferation efficiency compared to the uniform gyroid structure due to variations in Gaussian curvatures. This paper presents a design approach for fabricating equation-driven TPMS structures, including but not limited to gyroid structures, with controlled mechanical properties, and elucidates the correlation between geometric characteristics and both mechanical properties and *in vitro* cell responses. In addition to the potential of mitigating the stress shielding effect through computer-aided scaffold design, our findings also have wider implications for advanced biodevice development. This encompasses the integration of piezoelectric materials,[25] enabling advanced functionalities such as directional biosensing capabilities.

2. Methodology

This study presents a mathematical approach and additive manufacturing process for fabricating different gyroid scaffolds with precisely controlled geometrical properties. Gyroid scaffolds with controlled porosity and tunable anisotropic characteristics were achieved by manipulating the double iso-surface value and the geometric parameters of the level-set equation. DLP technology was utilized to realize the gyroid design, and an innovative pyrolysis-sintering hybridization method based on SMWH was implemented with the goal of improving the quality of the final product. Through this integrated approach, we aimed to demonstrate an advanced design and fabrication strategy of scaffolds for bone regenerative engineering, facilitating their broader application across various fields.

2.1. Design of graded gyroid structure with controlled properties

Different criteria need to be considered when designing a scaffold for bone tissue engineering to achieve optimal physical, mechanical, and morphological properties. Sheet gyroid-type TPMS structure was adopted due to its excellent interconnectivity, fluid permeability, and

mechanical properties.[26] The geometrical properties of the structure can be manipulated by controlling the parameters of the level-set equations of the structure, which are a combination of trigonometric functions that satisfy the equation $\varphi(x, y, z) = c$. The sheet gyroids can be described by the following level-set equation:

$$\sin(2\alpha\pi x)\cos(2\beta\pi y) + \sin(2\beta\pi y)\cos(2\gamma\pi z) + \sin(2\gamma\pi z)\cos(2\alpha\pi x) = c \quad \text{(I)}$$

where the geometric parameters α, β, and γ control the unit cell dimensions in the x, y, and z directions, respectively; c is a function that defines the iso-surface of the sheet gyroid structure which controls the thickness of the sheet and therefore affects the solid volume fraction (ϕ) of the structure. To create a solid domain, a double iso-surface can be defined by solving $-c \leq \varphi_{gy} \geq c$. Scaffold with interconnected pores is desirable to mimic the biological bone tissue, as it promotes nutrient diffusion, and facilitates cell attachment, differentiation, and colonization.[3] Studies have shown that TPMS scaffolds with 30–60% porosity exhibit reduced stress shielding effect.[27] Therefore, the parameters α, β, and γ were fixed at 0.50, and the value of c ranging from 0.62 to 0.91 was identified to achieve desired ϕ (40–60%) of the gyroid structure. Figure 1 illustrates the 8 × 8 × 8 mm^3 sheet gyroid structures with different value of ϕ, including 40% (40VF-gy), 50% (50VF-gy), 60% (60VF-gy), and their corresponding c values.

Graded gyroid scaffold that mimics the anisotropic structure of natural bone can be beneficial for mitigating stress shielding effect and promoting cell growth. Graded porosity and structural anisotropy were achieved by adjusting the parameters of the level-set equation (**Equation (I)**), specifically by defining the parameters for the unit cell dimension and a function for the iso-value $c = C(x, y, z)$. Gyroid structures with varying aspect ratios of the unit cell were constructed by controlling the parameter γ (Figure 2a). It is noteworthy that the value of ϕ in the sheet gyroid structure remained independent of the γ value but showed a positive correlation with the c value (Figure 2b). A radially graded porosity within the gyroid scaffold was achieved by assigning a control function to $C(x, y, z)$ as follows:

$$C(x, y, z) = a(x^2 + y^2 + z^2) + b \quad \text{(II)}$$

To mimic the pore distribution of natural bone, which has a denser outer part (cortical bone) and a more porous inner part (cancellous bone), the center porosity of the gyroid structure is set to 60% (($C_{\phi=60\%} = 0.91$) and the outer porosity to 40% ($C_{\phi=40\%} = 0.62$), the coefficients value can be obtained as follows:

$$\left\{ \begin{array}{l} C_{x=\,y=\,z=\,0} = C_{\phi=\,60\%} = 0.91 \\ C_{x=\,y\,=\,z=\,d/2} = C_{\phi=\,40\%} = 0.62 \end{array} \right\} \quad \text{(III)}$$

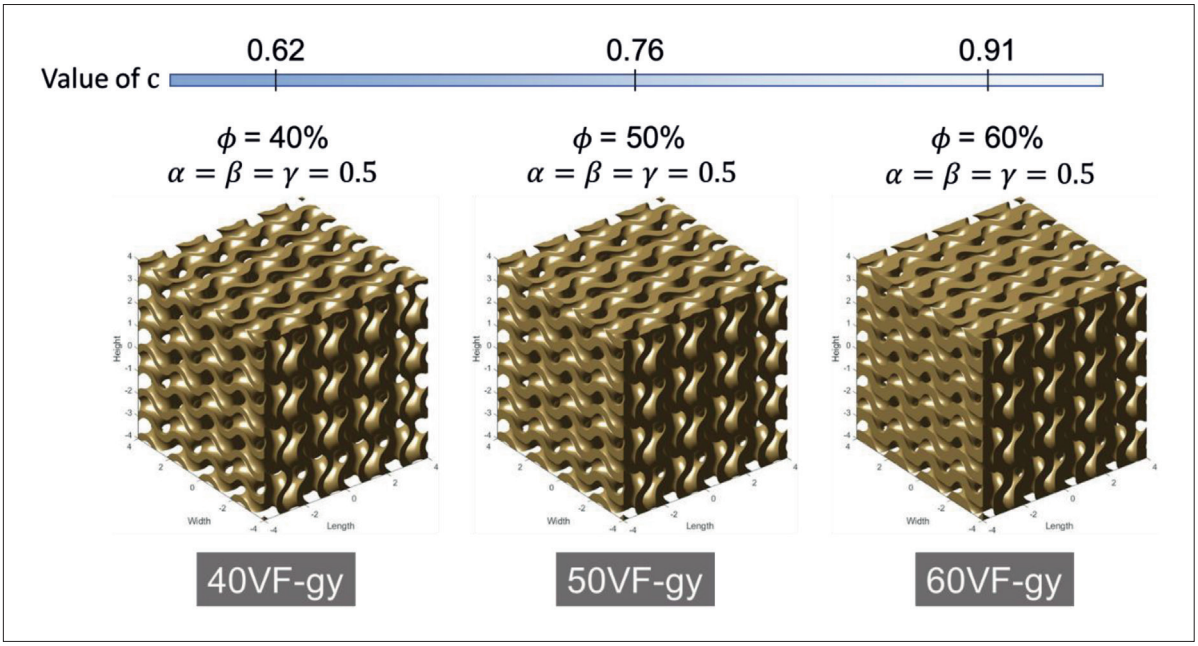


Figure 1. 3D models for the gyroid structure with different volume fractions ϕ: 40VF-gy (ϕ = 40%, c = 0.62), 50VF-gy (ϕ = 50%, c = 0.76), and 60VF-gy (ϕ = 60%, c = 0.91).

From **Equations (II)** and **(III)**, the following equation can be obtained:

$$C(x, y, z) = 0.02(x^2 + y^2 + z^2) + 0.62 \quad \text{(IV)}$$

where d represents the width or diameter of the structure. Figure 2c illustrates the graded sheet gyroid scaffolds with different γ value (γ.25-FGgy, γ.33-FGgy, and γ.50-FGgy) and the corresponding porosity distribution within the scaffold. Computer-aided design (CAD) models for the gyroid structures, including 40VF-gy, 50VF-gy, 60VF-gy, 57.55VF-gy, γ.25-FGgy, γ.33-FGgy, and γ.50-FGgy (Figure 2c), were generated using MSLattice.[5] Table 1 summarizes the total surface area, ϕ, and porosity of all gyroid structure. Besides ϕ, the total surface area of the structure is also affected by the γ and $C(x, y, z)$ values. For the graded gyroid structures, although the values of ϕ are identical due to the same $C(x, y, z)$ control function, the change in γ value can effectively tune the total surface area. This feature enables precise adjustment of the geometric properties of the cellular structure, offering a wide range of potential configurations.

2.2. Preparation of 3D-printed green specimens

The 3D printing was performed on a DLP printer (Admaflex 130, the Netherlands). The 3D printing process employed a commercial photosensitive silicon dioxide (SiO_2) slurry (AdmaPrint S130, the Netherlands), which had a high ceramic loading exceeding 75 wt.% as confirmed by the thermogravimetric analysis (TGA) (Figure 3a). CAD models of the sheet gyroid structures in STL format were imported into the built-in software and sliced for the printing process. The layer thickness of 60 μm was set with an exposure intensity and time of 60 mW/cm^2 and 2000 ms, respectively. After printing, the structures underwent

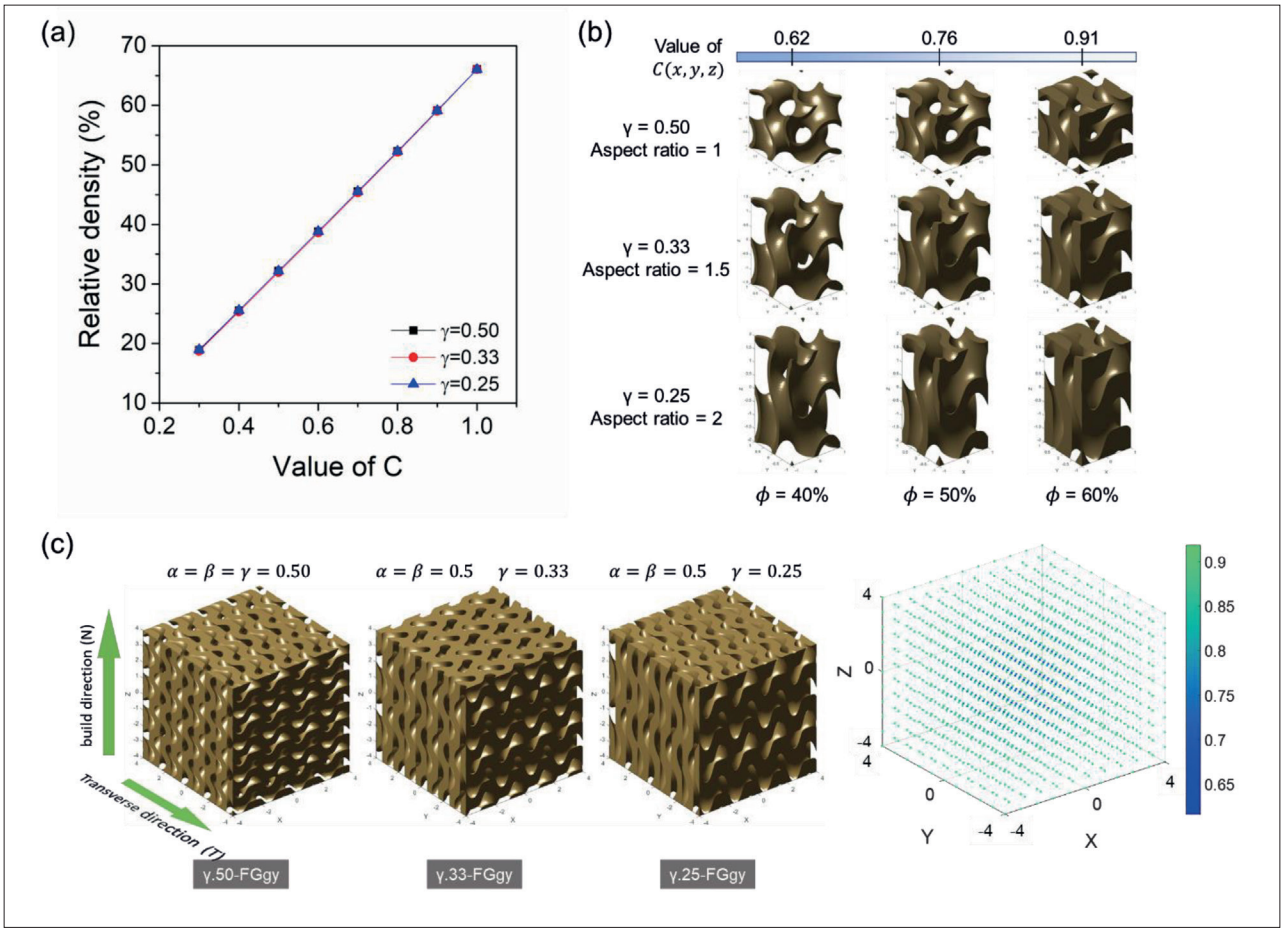


Figure 2. Parametric influence on SiO_2 gyroid scaffolds. (a) The effect of parameters on the volume fraction ϕ. (b) 3D unit cell model at different parameters. (c) Illustration of different radial graded gyroid structures (the building direction [B] of the DLP technology and the transverse direction [T] are also shown) and $C(x, y, z)$ value distribution within the structure (right figure).

Table 1. Summary of the geometric properties of the different sheet gyroid structures.

Model	α	β	γ	Value of $C(x, y, z)$	Total surface area (mm^2)	ϕ (%)	Designed porosity (%)
40VF-gy	0.50	0.50	0.50	0.62	1602.8	40	60
50VF-gy				0.76	1567.3	50	50
60VF-gy				0.91	1512.5	60	40
57.55VF-gy	0.50	0.50	0.50	0.88	1525.2	57.55	42.45
γ.50-FGgy	0.50	0.50	0.50	$C(x, y, z)$	1551.9	57.55	42.45
γ.33-FGgy			0.33		1424.5	57.55	42.45
γ.25-FGgy			0.25		1363.8	57.55	42.45

development using isopropyl alcohol under ultrasonication for 30 min to remove excess slurry, followed by overnight drying in a vacuum chamber at 60°C.

2.3. Post-processing of the DLP-printed structures

This study first employed a conventional furnace (Nabertherm HT29/17, Germany) and a commercial single-mode 2.45 GHz MW furnace (HAMiLab-HV3000, Synotherm, China) for the debinding and sintering process of DLP 3D-printed specimens. A comparative study was performed to assess the effectiveness of the SMWH process for the post-processing of 3D-printed cube specimens. For SMWH process, a kiln with 2-mm-thick inner layer of silicon carbide (SiC) was used as the susceptor for assisting the MW heating. The temperature profile of the debinding was defined by the TGA of the photo-cured SiO_2 slurry, as shown in Figure 3a and b. From the TGA and derivative thermogravimetric (DTG) curves within the temperature range of 50–800°C, weight loss started to occur at above 325°C and a maximum weight loss was recorded at 425.82°C. The weight loss rate reduced at around 525°C, signifying the decomposition of most organic matter. Within the test temperature, a maximum weight loss of 21.56% was recorded.

According to the TGA result, the debinding and sintering profile for the 3D-printed specimens was established. A fast-heating rate of 20°C/min was applied throughout the study to exploit the merits of MW heating, unless otherwise specified. The same heating profile, involving a two-step heating as depicted in Figure 3b, was used for both SMWH and conventional furnace heating process under air atmosphere. In brief, the specimens underwent a 30-min dwell time at 600°C for debinding, followed by sintering at 1150°C for a desired dwell time. Subsequently, the specimens were allowed to cool down at a rate of 1.5°C/min to room temperature. Different dwell times of 10, 20, 40, 80, 120, and 180 min were selected to compare the efficacy of the SMWH process (specimens denoted as MW10m, MW20m, MW40m, MW80m, MW120m, MW180m) and conventional furnace heating (specimens denoted as CS40m, CS80m, CS120m, CS180m). The density, mechanical properties, and the structural properties of the sintered specimens were studied and compared.

Subsequently, an innovative SHPS process was employed using the MW furnace aimed at enhancing the properties of the sintered specimens (Figure 3c). This involves the following stages:

1. In the first stage, the 3D-printed green specimens were heated to 600°C with a dwell time of 30 min under nitrogen (N_2) atmosphere. Then, the specimens were cooled at a rate of 1.5°C/min to room temperature. During this stage, pyrolysis instead of debinding of the green specimens occurred, leaving residual carbon after the first heating stage and retaining the geometrical features of the 3D-printed specimens.[28]
2. In the second stage, a two-step sintering process under air atmosphere was employed, where the specimens were dwell at 800°C for 10 min to completely remove the residual carbon, followed by a dwell at 1150°C for 120 min. The specimens were allowed to cool down at a rate of 1.5°C/min to room temperature.

The quality of the specimens produced using the SHPS process (specimens denoted as SHPS120m) was compared with those fabricated using conventional furnace, which followed the manufacturer recommended heating profile with the same sintering dwell time of 120 min (specimens denoted as RCS120m), as shown in Figure 3d.

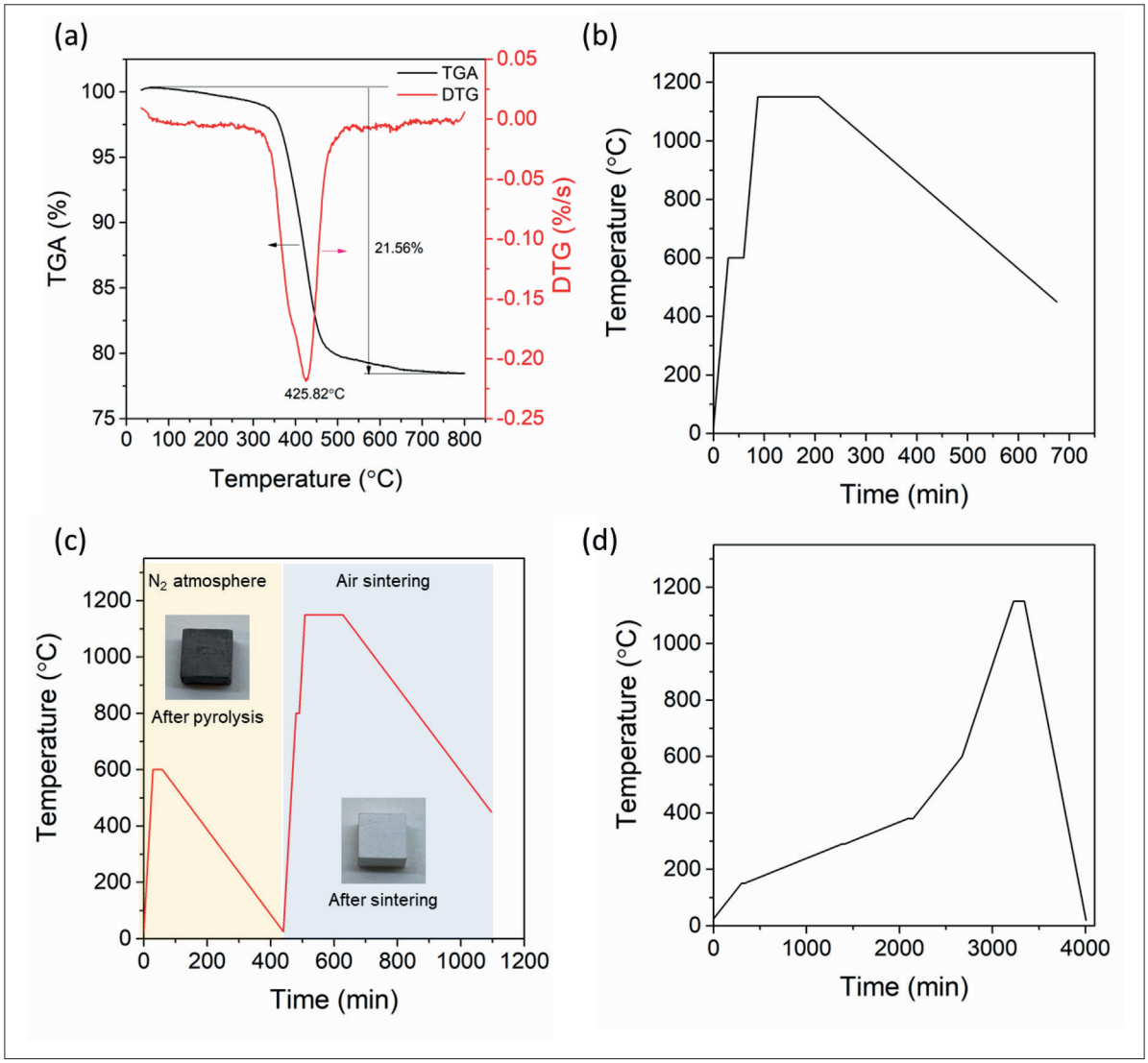


Figure 3. Thermal analysis and heating profiles of 3D printed specimens. (a) Thermogravimetric analysis (TGA) and derivative thermogravimetric (DTG) curves of cured S130 photoresin. (b) The heating profile for the susceptor-assisted microwave heating (SMWH) process under air atmosphere. (c) The susceptor-assisted hybrid pyrolysis-sintering (SHPS) heating profile for debinding and sintering. (d) The heating profile as recommended by the manufacturer using conventional furnace (copyright permission from Admatec).

2.4. Characterization methods

The morphology of the 3D-printed green specimens and sintered specimens were observed using a scanning electron microscope (SEM; TESCAN VEGA3) to assess the presence of defects or cracks after DLP 3D printing and the post-thermal processing. The lateral face corresponding to the printing direction was observed. The bulk density measurement of the sintered cube specimens was conducted using Archimedes' principle by means of a custom-made setup on a balance (Kern ADJ 200-4, Germany) using the theoretical density of 2.2 g/cm^3 of amorphous SiO_2.[29] The porosity of the 3D-printed green specimens and sintered specimens was analyzed by micro-computed tomography (μ-CT; YXLON FF35 CT, Germany), and the defects were captured. All specimens were subjected to a source voltage and current within the ranges of 70–80 kV and 100–110 μA, respectively. The Y.FXT 190.61 transmission tube, which has a 2D detail detectability of 150 nm, was used. X-ray radiographs of the specimens were recorded at various angles, and the projection images were then reconstructed and analyzed using the VGStudio Max 3.5 software. The phase composition of the specimens sintered under varying conditions was characterized using an X-ray

diffractometer (XRD; SmartLab 9 kW). The specimens were subjected to CuKα radiation (λ = 1.54059 Å) in the 2-theta range of 10°–80°, with a scanning rate of 10°/min, and operated at 45 kV and 200 mA.

The compressive properties of the sintered ceramic specimens were evaluated by uniaxial compression tests using (INSTRON 68TM-50, USA). For each set of 3D-printed ceramic specimens, including both cube and gyroid structures, three samples were tested, and the average results were recorded. For the cube samples, the load was applied along the build direction during 3D printing to evaluate the mechanical properties enhanced by the SHPS process. To evaluate the anisotropic properties of the graded gyroid structures, compression tests were performed along both the build (N) and transverse (T) directions (Figure 2c). The peak compressive strength before failure and the stress–strain behavior were recorded. The tests were carried out at a crosshead speed of 0.5 mm/min until the specimen failed, following the ASTM C1424 standard.

2.5. *In vitro* cell culture experiment

Bone marrow-derived mesenchymal stem cells (BMSCs; Cyagen, Hong Kong) were used to examine the cytocompatibility of the graded gyroid scaffolds, including γ.50-FGgy, γ.33-FGgy, and γ.25-FGgy, with ϕ = 57.55%. The cell culture medium was prepared by α-MEM supplemented with 10% fetal bovine serum and 1% penicillin/streptomycin. The scaffolds were disinfected using an autoclave and then washed with phosphate-buffered saline (PBS). The cytocompatibility of the scaffolds was evaluated by seeding BMSCs onto the scaffolds. After putting different scaffolds in the bottom of a 24 well-plate, 1 mL BMSC suspension (2 × 10 cells/mL) was added onto the scaffolds and pipetted for three times to ensure the cell suspension can permeate into the scaffolds. All samples were cultured at 37°C in an incubator with 5% CO_2. After 6 h of cell seeding, the well-plates were changed to remove the unattached cells on the scaffolds. After 1, 3, and 7 days of incubation, the cell viability was assessed by Live/Dead kit according to the manufacturer's protocol. The quantification of cell viability was determined by the ratio of the viable cells to all cells in eight randomly selected images. In addition, the cell number on scaffolds at different time points was evaluated by dissociating the cells with trypsin-EDTA solution and counted by the hemocytometer. The cell density was calculated through normalizing the cell number by the surface area of the scaffolds. To investigate the effects of the graded structure on cell proliferation, a uniform gyroid structure with the same value of ϕ, i.e., 57.55% (57.55VF-gy), was also used for comparison.

3. Result

3.1. Comparative study of the SMWH and conventional post-thermal processing

3.1.1. Effect of processing conditions on physical properties of the sintered ceramic

The efficacy of SMWH process was studied through studying the properties of 3D-printed and sintered ceramic cube. The effects of sintering dwell times under the SMWH process and conventional debinding and sintering were investigated. Figure 4a presents the XRD spectra of the ceramic cube specimens fabricated under different processing conditions. For all specimens prepared through the conventional sintering (CS), a broad peak at 21.3° was detected, corresponding to the amorphous structure of the SiO_2. A low peak intensity was observed at 21.8° for CS120m, indicating the formation of cristobalite phase under a prolonged dwell time. In contrast, almost all specimens fabricated through the SMWH process show predominate peaks for cristobalite at 21.8° and 36.1°. For MW120m, the intensity of the peaks increased significantly. More amorphous SiO_2 transformed into crystal structure when the dwell time increased. In comparison with the CS process, the SMWH process facilitates rapid and efficient energy transfer due to the intrinsic features of MW heating, which also result in reduced activation energy for nucleation and enhanced crystallization during the sintering process.[20]

The physical properties of the sintered ceramic cube under different processing conditions were characterized in terms of their percentage shrinkage, relative density, and the major crystalline structure. Figure 4b depicts shrinkage in the length (L), width (W), and height (H) of the specimens. As the dwell time increased, all specimens exhibited an increase in shrinkage across all dimensions (L, W, and H). For the SMWH process, the shrinkage percentage of the specimens sharply increased from dwell time of 10 to 80 min, while the increase become less obvious when the dwell time further extended to 180 min. The highest shrinkage percentages were recorded as 7.58%, 7.67%, and 8.25% in the L, W, and H dimensions, respectively. Similarly, the specimens prepared through the CS process demonstrated similar trend of the shrinkage percentage as the dwell time increases, but with considerably lower shrinkage percentage compared to the SMWH process. While all specimens fabricated through CS process shrank almost isotropically, a higher percentage of shrinkage in H compared to W and L was recorded for the specimens prepared through the SMWH process. This is because during the layer-by-layer printing process, the sedimentation of ceramic powder creates a resin-rich region on top of each printing layer, forming a lamellar

structure in the 3D-printed specimens after curing.[30] The lamellar structure generally disappears after the post-thermal treatment and formed dense ceramic parts. As a result, after the debinding and sintering process, the 3D-printed structures experience larger shrinkage in the *H* dimension. However, this phenomenon was not observed in the specimens prepared through the CS process. This is likely due to the incomplete debinding due to the high heating rate, which adversely affects the densification of the specimens.

The relative density of the specimens was also compared, as shown in Figure 4c. When subjected to the same heating profile, the specimens fabricated through the SMWH process exhibited higher relative densities compared to those from the CS process. The relative density of the MW specimens ranged from 95.38% to 97.4%, while the CS specimens showed values ranging from 91.89% to 93.49%. These findings suggest that the SMWH process plays a significant role in promoting densification and the formation of a crystal structure in the ceramic cube specimens. The SMWH process promotes formation of cristobalite crystal structure in the ceramic cube specimen and facilitates densification, reducing the energy barrier for sintering compared to conventional furnace heating.[22] As a result, density of the specimens closely approximates to the theoretical density value of 2.2 g/cm^3 for amorphous SiO_2 due to the higher theoretical density value of the cristobalite structure in SiO_2 than the amorphous form. On the other hand, specimens prepared through conventional heating exhibit lower relative density, primarily due to the fast heating rate and short sintering time employed. These conditions may lead to the incomplete removal of the organic binders before reaching the sintering temperature. As a result, the SiO_2 particles are loosely in contact with each other, impeding the diffusion process during sintering. The SMWH process shows a promising result in achieving higher relative density compared to the conventional furnace heating, indicating

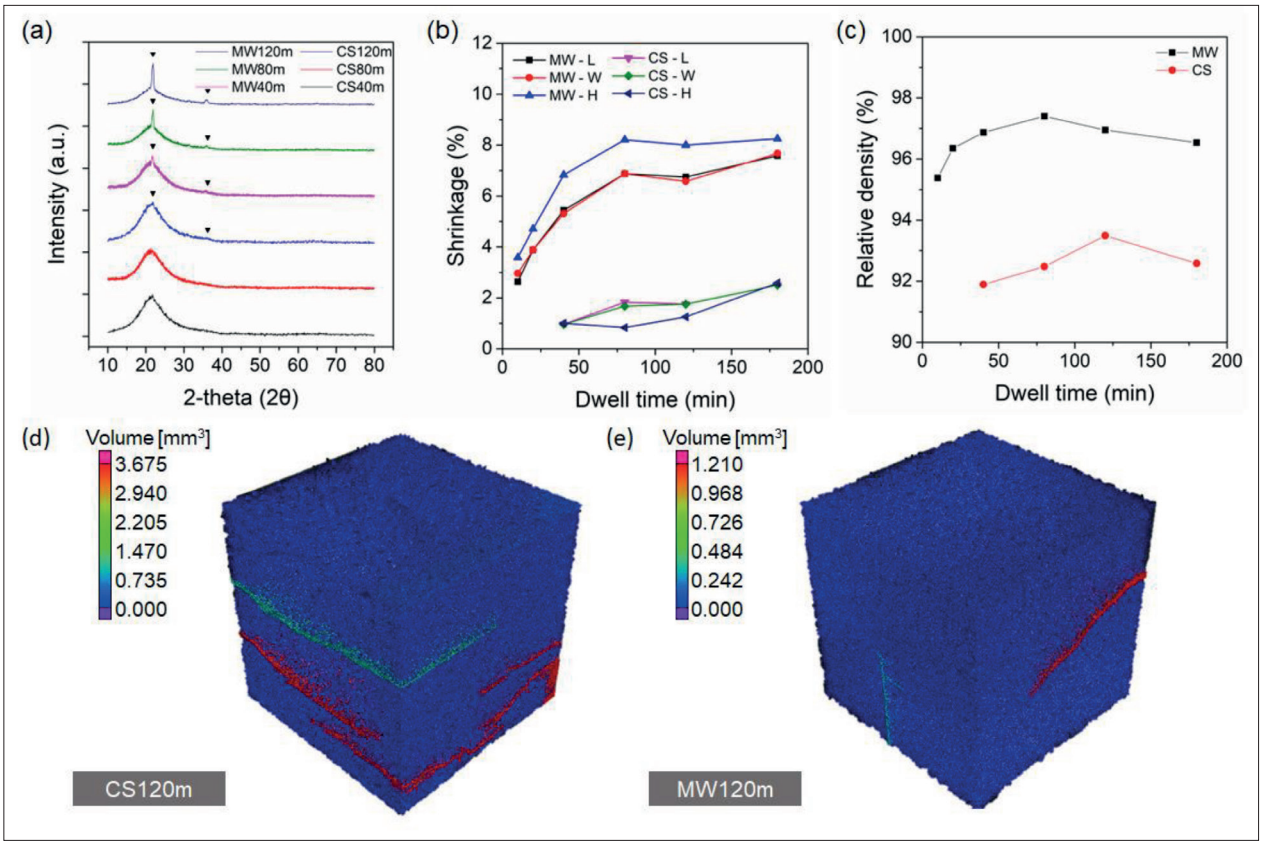


Figure 4. Comparative analysis of 3D-printed ceramic cubes. (a) X-ray diffraction (XRD) pattern for the 3D-printed ceramic cube specimens. (b) Dimensional shrinkage for the ceramic cube specimens processed through susceptor-assisted microwave heating (SMWH) and conventional furnace heating. *L*, *W*, and *H* correspond to the length, width, and height of the specimens, respectively. (c) The effect of the dwell time of sintering on the relative density of the specimens with respect to the theoretical density of amorphous SiO_2. The 3D reconstructed image obtained through micro-computed tomography (μ-CT) showing the defect distribution in the (d) CS120m and (e) MW120m specimens.

its potential as a post-processing technique for 3D-printed green parts to produce denser and more structurally robust ceramic materials.

Figure 4d and e presents the 3D reconstructed image obtained through μ-CT showing the defect distribution in the CS120m and MW120m specimens, respectively. Abundant cracks were formed, and larger defect volumes were observed in the CS120m specimens after sintering compared to MW120m. Under conventional heating, the fast heating rate leads to uneven heating, creating thermal stress, and thus promote crack formation during the heating process.[31] Cracks were also observed for the MW120m specimens, despite their smaller defect volume. This can be attributed to the rapid generation of gas from the decomposition of the binder during the debinding stage, leading to the formation of larger voids within the specimens and making them prone to crack formation. Besides, the cracks were found on the lamellar facets. Owing to the layer-by-layer formation mechanism inherent to the DLP technology, weak points were created that are susceptible to crack initiation and propagation.[30] Despite the advantages offered by the SMWH process, the formation of cracks may have a detrimental effect on the mechanical properties of the sintered specimens. Therefore, it becomes imperative to develop an appropriate heating process utilizing the MW technology in order to minimize defects.

3.1.2. Effect of processing conditions on mechanical properties

The effect of dwell time on the mechanical properties of the sintered ceramic cube specimens was evaluated. The stress–strain relations of the specimens under uniaxial compression are presented in Figure 5a, while the compressive strength and the Young's modulus of the specimens are summarized in Figure 5b and c, respectively. The mechanical properties of the sintered specimens showed an increasing trend with longer dwell times. Specimens fabricated through the SMWH process exhibited better mechanical properties compared to those prepared through conventional furnace heating. At a dwell time of 10 min, the compressive strength of MW10m was measured to be 34.92 ± 3.49 MPa, which is 80% higher than that of the CS180m. The compressive strength sharply increased to 86.62 ± 8.2 MPa for MW120m. As the dwell time was further increased, the enhancement in compressive strength became less pronounced, reaching a peak of 101.35 ± 19.62 MPa for the MW180m specimens. In comparison, the specimens prepared using a conventional furnace exhibited much lower compressive strength values at each dwell time, indicating significant enhancement of mechanical properties through the SMWH process.

The Young's modulus of the specimens prepared through the SMWH process shows a similar trend with compressive strength with longer dwell times, which were also notably higher compared to the specimens prepared through the conventional furnace heating. At a dwell time of 10 min, the MW10m exhibited a modulus of 1.94 ± 0.02 GPa, which gradually increased to 2.79 ± 0.17 GPa for MW180. In contrast, the modulus values of the specimens prepared through the conventional heating process were over 50% lower at each dwell time, ranging from 0.87 ± 0.07 to 1.07 ± 0.14 GPa. The significant improvement in mechanical properties observed in the ceramic cube specimens is primarily attributed to the accelerated densification process facilitated by the SMWH process. In addition, the increased formation of cristobalite phase further contributes to the enhancement of mechanical strength.[26] The specimens prepared through conventional heating exhibit lower relative density, and therefore lower mechanical strength was recorded. The SMWH process offers several advantages including rapid and more homogenous heating. This is achieved through a unique two-way heating mechanism that combines the conventional mode of heating transfer from the MW susceptor with the direct interaction between the MW field and the target materials.[32] While prolonged sintering time can improve the mechanical properties of the specimens, it was found when the dwell time further increased from 120 to 180 min, the improvement in the mechanical properties is limited. Consequently, a 120-min dwell time for the sintering stage of the ceramic specimens was chosen for the remaining of the study.

3.2. Susceptor-assisted hybrid pyrolysis-sintering process

To address defects caused by debinding and sintering and improve the quality of the sintered ceramic specimens, we developed an innovative SHPS process. Figure 6a illustrates the SHPS process for the DLP-printed specimens. During the first heating stage, instead of directly removing the binder in the 3D-printed structures in conventional process, a pyrolysis step at 600°C under N_2 atmosphere was introduced. Based on the TGA analysis, the majority of heteroatoms, including oxygen and hydrogen, were eliminated at this temperature. Consequently, the organic constituents underwent a transformation into pyrolytic carbon, resulting in substantial structural shrinkage. After pyrolysis, the SiO_2 particles were brought closely together before the complete removal of the residual pyrolytic carbon. This particle motion can improve the densification during sintering. After the pyrolysis step, the specimens were then subjected to a sintering step under air atmosphere. An intermediate heating step was introduced at 800°C for complete removal of the pyrolytic

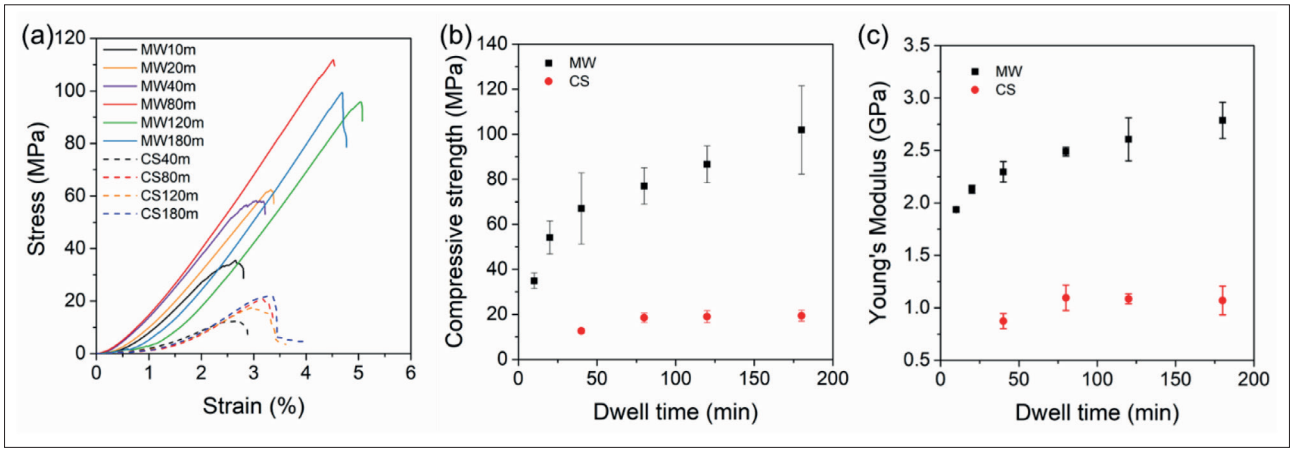


Figure 5. Stress–strain curves (a), compressive strength (b), and Young's modulus (c) of the 3D-printed ceramic cube specimens prepared through SMWH and conventional furnace heating.

carbon, followed by sintering at 1150°C. Throughout the sintering phase, the pyrolytic carbon potentially functions as a microwave susceptor, aiding in the heating process and enhancing heating uniformity.[33] Due to the reduced gas generation and closer particle packing during the sintering stage, fewer defect voids were formed. This suppression of void formation significantly reduces crack formation and improves densification. This is evidenced by the SEM observation of the SHPS120m specimens as shown in Figure 6b (the red arrow indicates the location of cracks). In order to compare the efficacy of SMWH process and the SHPS process, the 3D-printed cube structures were also subjected to the conventional heating following the manufacturer's recommendations (RCS120m). As shown in Figure 6c, abundant cracks can be observed for the sintered RCS120m specimens, regardless of the slow heating rate and cooling rate employed. Although the number of cracks was reduced compared to the MW120m specimens, it was still significantly higher compared to the SHPS120m specimens. The formation of cracks in RCS120m was attributed to the uneven heating resulting from the conventional heating mode. Moreover, the slow heating rate prolonged the generation and release of gases during the debinding process. These may lead to the generation of internal stress which promote the formation of defects including voids and cracks.[34] To support this claim, the 3D μ-CT images of the specimens were compared, as shown in Figure 6e. Although cracks still present in the SHPS120m specimen, the volume was significantly reduced compared to the RCS120m and MW120m specimens. Table 2 summarizes the defect volume ratio and the relative density of the SHPS120m, RCS120m, and MW120m specimens. The total defect volume ratio for SHPS120m specimen is reduced to 3.86%, a 16.81% reduction compared to the RCS120m specimen with a defect volume ratio 4.64%. Moreover, SHPS120m specimen also exhibits the highest relative density of 98.36 ± 0.54% among the three specimens. These findings provide evidence for higher quality of the sintered specimens achieved through the SHPS process.

The crystalline phases of the specimens were also investigated through XRD analysis, as presented in Figure 7a. Both SHPS120m and MW120m show similar XRD patterns, with predominate peaks corresponding to the cristobalite phase at 21.8° and 36.1°. This suggests that the influence of the different heating profile of under MW heating process is minimal compared to dwell time. In contrast, RCS120m exhibits a weak peak intensity only at 21.8°, accompanied by a broad peak at 21.3°. This indicates that the transformation of SiO_2 from amorphous phase to the cristobalite phase is limited, regardless of the long processing time under the manufacturer's recommended heating profile.

Figure 7b depicts the comparison between compressive stress–strain curves of the SHPS120m, RCS120m, MW120m, and CS120m specimens. Compared to CS120m specimen, with a higher heating rate, the relative density and compressive strength of RCS120m improved by 1.64% and 91.72%, respectively. Furthermore, the defect volume of RCS120m reduced significantly from 16.13% to 4.64%. This is mainly attributed to the gradual heating rate at temperatures below 600°C. This slower heating facilitates the slower generation and release of pyrolysis gases, allowing for complete binder decomposition during the debinding process. On the other hand, the SHPS120m specimens show significant improvements in mechanical properties. Specifically, they exhibited a compressive strength of 158.35 ± 19.76 MPa and a modulus of 3.14 ± 0.04 GPa. These values represent roughly 83% and 20%

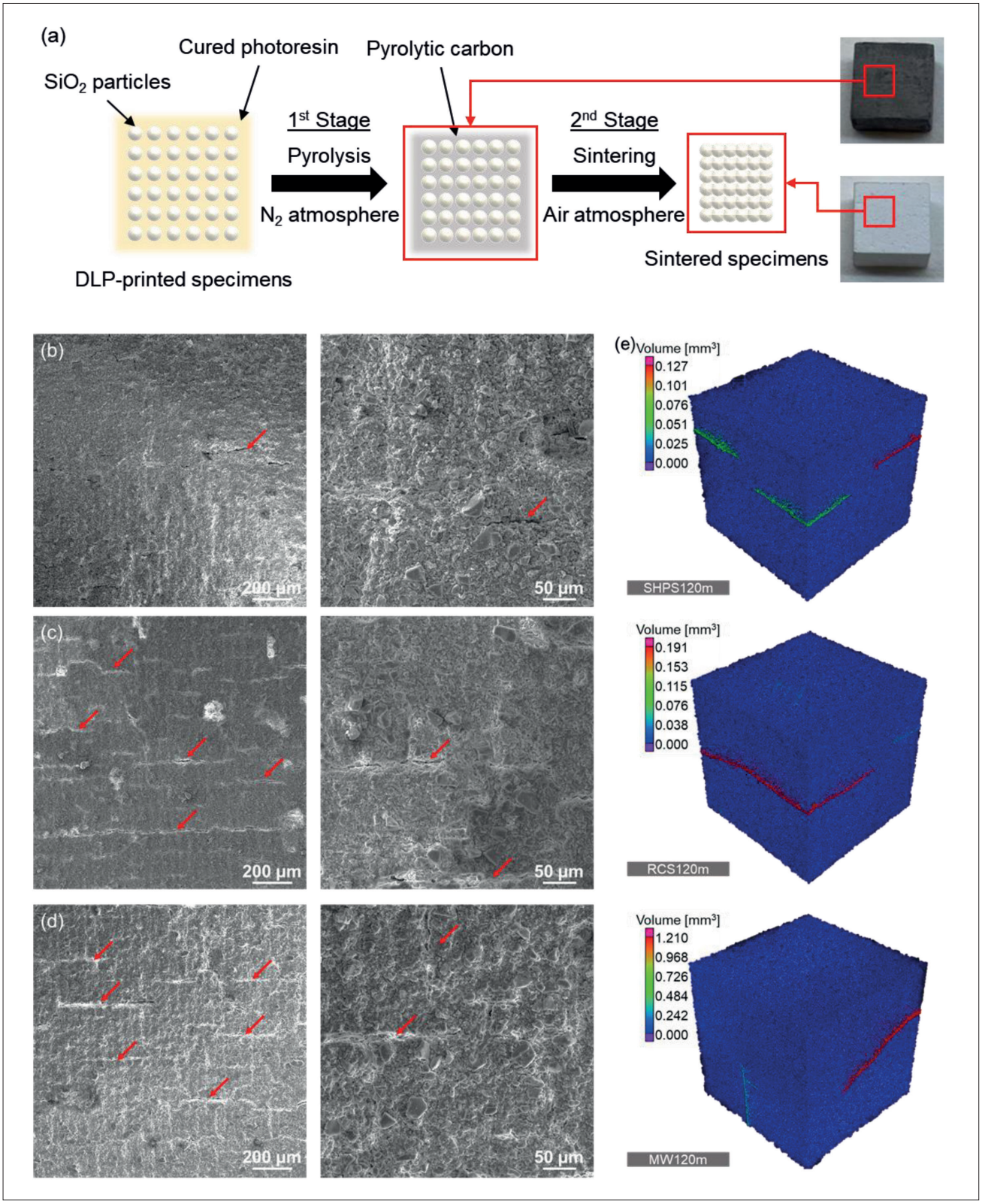


Figure 6. Morphological analysis of specimens fabricated through different processes. (a) Illustration of the pyrolysis and sintering of 3D-printed specimen using susceptor-assisted hybrid pyrolysis-sintering (SHPS) process. The scanning electron microscopic (SEM) images for sintered (b) SHPS120m, (c) RCS120m, (d) MW120m specimens, and (e) the corresponding reconstructed micro-computed tomography (μ-CT) 3D image for defect identification.

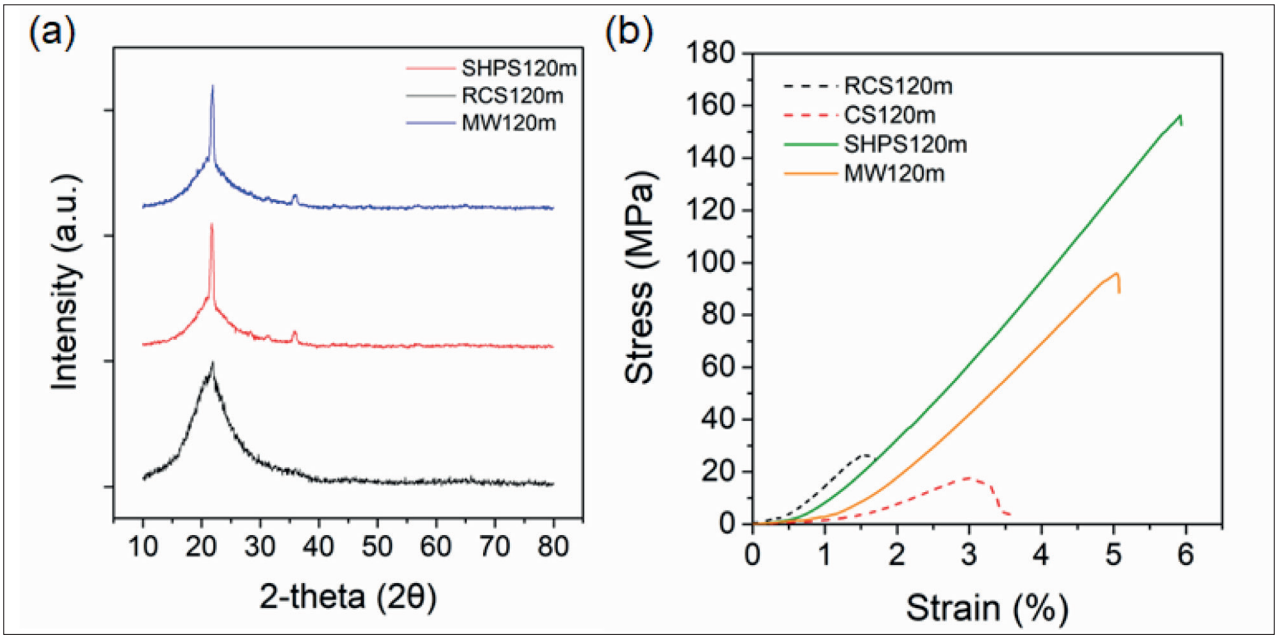


Figure 7. Comparative analysis of specimens fabricated using different processes. (a) X-ray diffraction (XRD) pattern for SHPS120m, RCS120m, and MW120m. (b) The stress–strain curve of the ceramic cube specimens prepared through different heating profiles.

increase, respectively, compared to MW120m. Additionally, compared to RCS120m, SHPS120m specimens showed a remarkable 336% increase in compressive strength and a 28% increase in Young's modulus. The SHPS process leads to a much denser specimen with minimized defects, thereby significantly enhancing the mechanical properties. Therefore, this process was employed for the post-thermal treatment of DLP-printed sheet gyroid structures to ensure the quality of the 3D ceramic scaffold. The compressive strength and Young's modulus of the specimens are summarized in **Table 2**.

3.3. Characterization of DLP-printed gyroid scaffold

Figure 8a shows the SEM images of the sheet gyroid structures before and after the SHPS process, with different value of ϕ. The lamellar facets were examined to identify any structure defects. The DLP-printed sample displayed a rough surface morphology, which is primarily due to the staircase artefacts formed from pixelated light and layer-by-layer forming mechanism of the DLP technology.[35] As observed, the pixelated morphology became more pronounced after sintering, but no signs of cracks, voids, and delamination of layers were observed. This suggests that the gyroid structures were successfully sintered, resulting in a dense specimen through the proposed SHPS method. The wall thickness and the pore diameter of the sheet gyroid structures were also investigated using ImageJ, and the results are summarized in Table 3. As ϕ increased, the wall thickness increases, measuring at 274.1 ± 15.5, 374.6 ± 15.1, and 475.7 ± 25.5 μm for 40VF-gy, 50VF-gy, and 60VF-gy, respectively. Conversely, the pore diameters decreased as the ϕ increased, with values of 674.3 ± 24.9, 576.8 ± 15.0, and 528.4 ± 28.6 μm for 40VF-gy, 50VF-gy, and 60VF-gy, respectively.

Table 2. Summary of the physical properties, including the defect volume ratio, relative density, compressive strength, elastic modulus, and hardness of the sintered SHPS120m, RCS120m specimens, and MW120m.

Sintered sample	Defect volume ratio (%)	Relative density (%)	Compressive strength (MPa)	Young's modulus (GPa)
SHPS120m	3.86	98.36 ± 0.54	158.35 ± 19.76	3.14 ± 0.04
MW120m	7.22	96.95 ± 0.48	86.62 ± 8.2	2.61 ± 0.21
RCS120m	4.64	95.02 ± 0.61	36.35 ± 0.26	2.45 ± 0.07
CS120m	16.13	93.49 ± 0.35	18.96 ± 2.66	1.08 ± 0.05

Figure 8b presents the surface deviation maps of the DLP-printed gyroid structures (before sintering) compared with the CAD models from the 3D μ-CT analysis. As observed, the surface deviation of all specimens laid within −250 to 250 μm. The major reason for the deviation is attributed to the accuracy of the DLP printer, which is defined by the pixel size (i.e., resolution) of the machine. The porosity of the DLP-printed structures was also evaluated through μ-CT analysis and compared with the designed model. The porosity of 40VF-gy, 50VF-gy, and 60VF-gy after SHPS process were recorded as 57.30%, 46.36%, and 41.64%, respectively. A maximum deviation of 7.28% was obtained, suggesting a close matching with the designed model.

3.4. Mechanical properties of the gyroid with and without structural isotropy

In Figure 9a and b, the compressive properties of the sheet gyroid with different value of ϕ are compared. The compressive strength and the Young's modulus of the gyroid structure follow the trend of ϕ. The 60VF-gy exhibited better mechanical properties with a compressive strength of 15.62 ± 1.94 MPa and a modulus of 2.09 ± 0.29 GPa, which was reduced by 90.1% and 33.4%, respectively, compared to the SHPS120m specimens. In contrast, the mechanical strength of the 40VF-gy reduced, with a compressive strength of 6.51 ± 0.40 MPa and a modulus of 1.07 ± 0.05 GPa. This is primarily due to the higher porosity of the specimens.

To investigate the effect of the lattice structure designs of the gyroid structure on the mechanical properties, compressive tests were conducted in both normal (N) and transverse (T) directions. Cubic gyroid structures having radial graded porosity and approximately the same porosity (i.e., ϕ = 57.55%) were generated using unit cells with aspect ratios of 1 (γ.50-FGgy), 1.5 (γ.33-FGgy), and 2 (γ.25-FGgy). Figure 9c depicts the compressive strength of 57.55VF-gy, γ.25-FGgy, γ.33-FGgy, and γ.50-FGgy, respectively. The compressive strength of the 57.55VF-gy was recorded as 13.97 ± 2.20 MPa. It was observed that, despite having similar porosity, the anisotropic mechanical properties were achieved for γ.25-FGgy, γ.33-FGgy, and γ.50-FGgy specimens. In the transverse direction, γ.25-FGgy showed over a threefold increase in compressive strength compared to 57.55VF-gy, with a value of 44.51 ± 3.32 MPa. The aspect

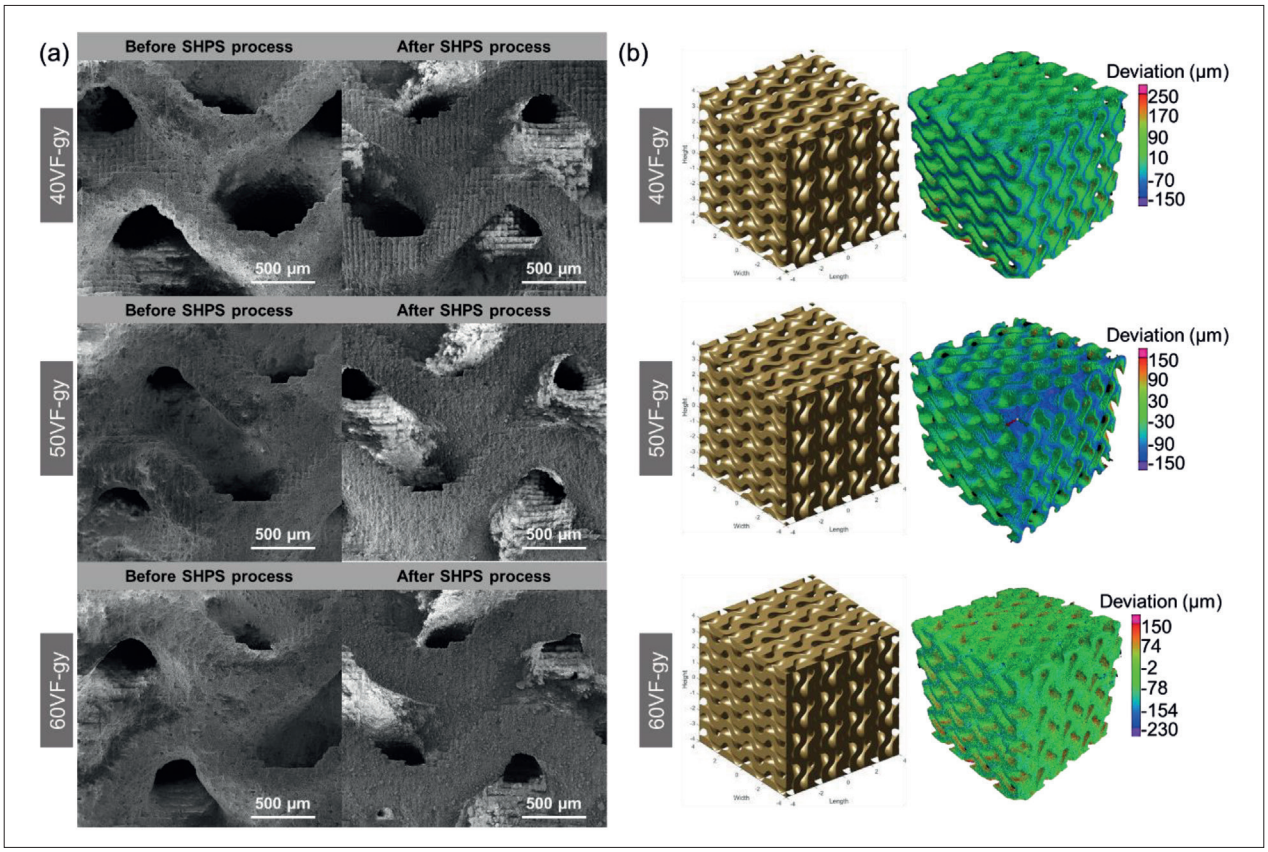


Figure 8. Characterization of SiO_2 gyroid scaffolds. (a) The corresponding scanning electron microscopic (SEM) images before and after the SHPS process. (b) 3D Surface deviation map of the digital light processing (DLP)-printed gyroid structures with different volume fractions ($\neq\phi$).

Table 3. Summary of the physical properties of the DLP-printed structures and the sintered specimens.

Sample	DLP-printed structures			Sintered specimens	
	Designed porosity (%)	Porosity after sintering (%)	Deviation (%)	Wall thickness (μm)	Pore diameter (μm)
40VF-gy	60	57.30	4.50%	274.1 ± 15.5	674.3 ± 24.9
50VF-gy	50	46.36	7.28%	374.6 ± 15.1	576.8 ± 15.0
60VF-gy	40	41.64	4.10%	475.7 ± 25.5	528.4 ± 28.6

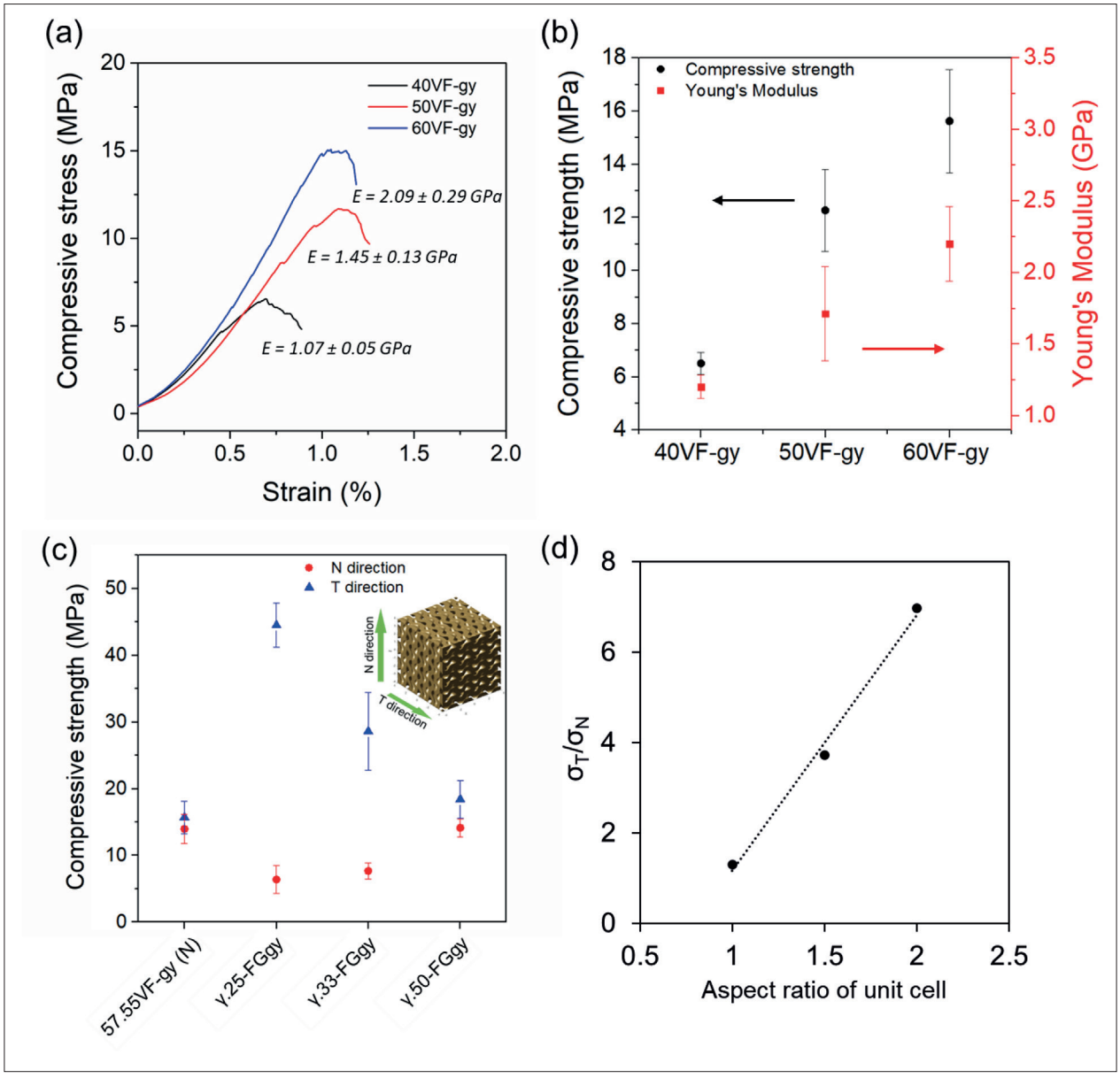


Figure 9. Mechanical properties of SiO_2 gyroid scaffolds with anisotropic properties. (a) The stress–strain curve, (b) compressive strength and Young's modulus of 40VF-gy, 50VF-gy, and 60VF-gy. (c) Compressive strength of 57.55VF-gy, γ.25-FGgy, γ.33-FGgy, and γ.50-FGgy (the compression tests of graded gyroid structures were performed in normal [N] direction and the transverse [T] direction), and (d) the relation between the ratios of the compressive strength in the T direction and the N direction (i.e., σ_T / σ_N) and the aspect ratio of the unit cell.

ratio of the unit cell and the compressive strength of the graded gyroid structure demonstrated a proportional relationship in the transverse direction. The compressive strengths of γ.33-FGgy and γ.50-FGgy were recorded as 28.59 ± 5.83 and 18.40 ± 2.78 MPa, respectively. In contrast, as the aspect ratio decreased from 2 to 1, the compressive strength in the normal direction showed an increasing trend, rising from 6.38 ± 2.08 to 14.14 ± 1.38 MPa. The anisotropic properties of the specimens can be compared using the ratios of the compressive strength in the transverse direction and the normal direction (i.e., σ_T / σ_N). The ratio σ_T / σ_N for γ.25-FGgy, γ.33-FGgy, and γ.50-FGgy are 6.97, 3.72, and 1.3, respectively. The results indicate that despites the pore distribution, the gyroid structure with a higher aspect ratio of the unit cell can result in higher degree of anisotropy (Figure 9d). These findings are particularly useful for bioscaffold design, strategy to mimic the anisotropic properties of native bone. This approach helps mitigate the stress shielding effect, thereby enhancing scaffold integration *in vivo*.

3.5. *In vitro* study

The cytocompatibility of the gyroid scaffolds was evaluated by seeding BMSCs directly onto various scaffold designs, including 57.55VF-gy, γ.50-FGgy, γ.33-FGgy, and γ.25-FGgy. To investigate the effect of the scaffolds' anisotropic properties, a fixed porosity of 57.55% and overall dimensions of 8 × 8 × 8 mm³ were selected. Cell viability and proliferation were assessed at 1, 3, and 7 days of culture. Confocal microscope images, as shown in Figure 10a, revealed an even distribution of cells on the scaffolds after 3 days. According to the live/dead cell viability assay (Figure 10b), all scaffold groups exhibited over 98% cell viability, indicating excellent cytocompatibility. The effects of the scaffold structures of the scaffolds were further evaluated by investigating cell seeding efficiency over different time points. The surface area of each scaffold model, presented in Figure 10b, shows that all scaffolds supported cell proliferation over the culture period, albeit with varying efficiencies (Figure 10c). Among the different specimens, the γ.50-FGgy scaffold demonstrated better cell

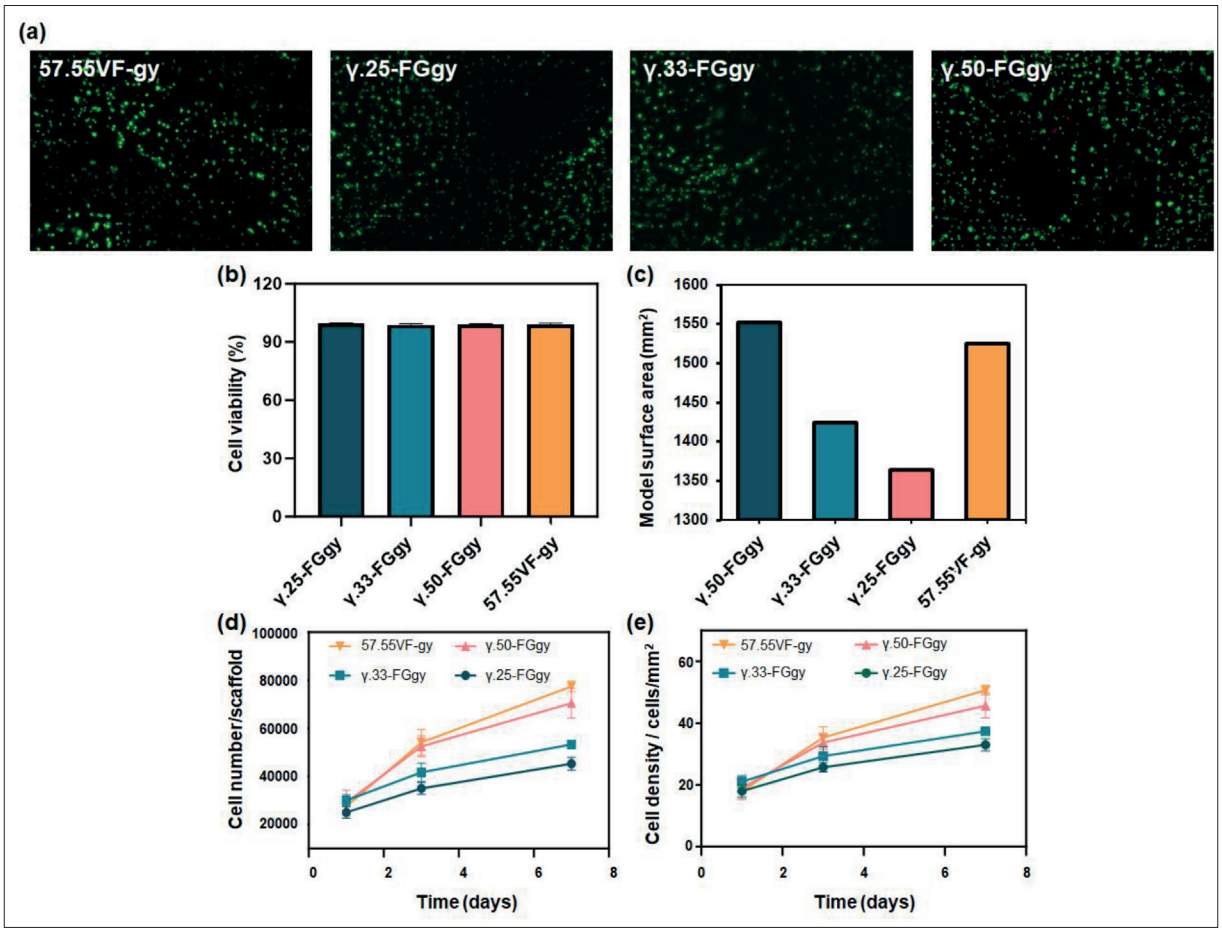


Figure 10. Live/dead staining (a), cell viability (b), models surface area (c) of the scaffolds, as well as cell number (d) and cell density (e) of the gyroid scaffolds.

proliferation efficiency, with a higher cell count observed at day 7. Conversely, the γ.25-FGgy scaffold exhibited the slowest cell proliferation rate. This decrease in proliferation rate correlates with the reduction in total surface area, which decreases from 1551.9 mm² for γ.50-FGgy to 1363.8 mm² for γ.25-FGgy. Additionally, as the aspect ratio of the unit cell of the gyroid structures increases with lower γ values, the average Gaussian curvatures of the scaffolds are affected. This alteration in curvature can significantly impact the proliferation behavior of mesenchymal stem cells, as supported by previous studies.[7,36] To further evaluate the cell seeding efficiency, the cell density on the scaffold over the 7-day culture period was calculated by normalizing the cell number to the surface area (Figure 10d). As the γ value decreased (indicating a higher aspect ratio), the cell counts per square millimeter of scaffold surface area decreased significantly, from 46 cells/mm² for γ.50-FGgy to 33 cells/mm² for γ.25-FGgy. This finding suggests that while anisotropic properties of the scaffold can be achieved by tuning the γ value, there is a trade-off in cell proliferation rates. In comparison, the 57.55VF-gy specimens, which lacked porosity gradients, exhibited the highest cell density after 7 days of culture. This indicates that the presence of structural gradients, while beneficial for mimicking natural bone anisotropy, may reduce the overall cell proliferation rate due to the decreased effective surface area and altered curvature. Overall, these results indicate that gyroid scaffolds with anisotropic properties offer notable benefits in mimicking natural bone structures and could potentially mitigate *in vivo* stress shielding. In addition, designing them requires careful consideration to strike a balance between mechanical properties and optimal cell proliferation rates.

4. Discussion

This study introduces a mathematical design approach for customizing 3D bioscaffolds. By setting appropriate geometric parameters (α, β, and γ) and the iso-surface function $C(x, y, z)$ in the level-set equations, sheet gyroid scaffolds with spatially controlled porosity and anisotropic properties were generated. Given that other types of TPMS share similar mathematical descriptions, this design approach does not limit to sheet gyroid structures but can also be applied to other TPMS variations. Moreover, we established an innovative SHPS processing method, utilizing MW heating technology, to effectively debind and sinter the 3D-printed ceramic green specimens. The comparison between SMWH process and conventional furnace heating highlights the advantages of MW technology in ceramic processing. Additionally, the SHPS process addresses the critical challenge associated with MW technology in sintering 3D-printed ceramic structures, such as crack formation, thus offering a promising solution to enhance the quality of 3D-printed ceramic scaffold. By integrating advanced functional materials like piezoelectric ceramics, this processing method will accelerate the development of 3D-printed ceramic structures for cutting-edge biodevices.

The comparative study between SMWH process and conventional furnace heating revealed advantages of MW technology in enhancing the physical and mechanical properties of the ceramic specimens. The compressive strength of the MW120m was measured at 86.62 ± 8.2 MPa, over 1.8 times higher than the compressive strength of RCS120m. The SMWH process resulted in higher relative densities and different crystalline structures compared to conventional furnace heating, which contributed to the mechanical enhancement of the 3D-printed specimens. The SMWH process facilitates rapid and efficient energy transfer to 3D-printed ceramic specimens through a two-way heating mechanism.[23,32] This rapid energy transfer of MW heating decreases sintering activation energy and processing temperature,[19,20] promoting densification,[37] which result in an improvement in relative density from 95.02% to 96.95%. Additionally, the intrinsic heating mechanism of MW technology reduces activation energy for nucleation and enhances crystallization during the sintering process.[20] Despite the significant enhancements in the mechanical properties, severe crack formation was observed, indicating the need for further improvement of the SMWH process.

An innovative SHPS process was established to reduce the defects caused by debinding and sintering. From the morphological and physical characterizations, the process led to denser ceramic specimens after sintering with minimized defects compared to both SMWH and conventional furnace heating. SEM and μ-CT analyses (Figure 6) confirmed the reduction in crack formation and defect volume in SHPS specimens. Compared with RCS120m which had a defect volume of 4.64%, the defect volume of SHPS120m was reduced by 16.80–3.86%. Consequently, a significant improvement in mechanical properties for SHPS120m specimens was recorded, with about 335% increase in compressive strength (158.35 ± 19.76 MPa) and a 28.2% in Young's modulus (3.14 ± 0.04 GPa), respectively.

The reduction of defects is primarily attributed to the additional pyrolysis step during the SHPS process. Unlike traditional debinding methods that involve removing the polymer, the polymer is transformed into carbon during pyrolysis. Pyrolysis transforms the polymer into carbon. This transformation potentially reduces gas formation and release during the process,

while particle motion occurs as the structure shrinks during pyrolysis. As a result, the SiO_2 particles become tightly packed, thereby enhancing densification during subsequent sintering steps. This improvement leads to enhanced relative density and mechanical properties. These results highlight the promising potential of SHPS method as a post-processing technique for enhancing the quality of 3D-printed ceramic structures. Additionally, it is anticipated that the formulating photosensitive slurry with advanced functional materials such as piezoelectric ceramics can further enhances the potential of the SHPS method. Piezoelectric ceramics possess unique properties that enable them to convert mechanical energy into electrical energy and vice versa. By integrating piezoelectric ceramics into 3D-printed ceramic structures, it becomes possible to develop biodevices with advanced functionalities, such as sensors and actuators.[38]

To demonstrate the practical application of the SHPS method, gyroid scaffolds with different geometries were fabricated. The morphology and mechanical properties of the specimens were investigated. SEM images revealed the pixelated morphology of specimens after sintering, and no cracks, voids, or delamination were observed. The gyroid structures exhibited varying mechanical strengths and porosities depending on their design parameters, such as volume fraction and lattice structure. Results showed that compressive strength and Young's modulus followed the trend of ϕ. As the volume fraction increases, the mechanical properties also increase, with the highest compressive strength of 15.62 ± 1.94 MPa and a modulus of 2.09 ± 0.29 GPa for 60VF-gy. Additionally, the effects of the aspect ratio of the unit cell on the mechanical properties of gyroid structures were investigated. Gyroid scaffolds with anisotropic mechanical properties were fabricated despite having a radially graded porosity distribution. The aspect ratio of the unit cell structure affects the compressive strength of the scaffolds in the normal (σ_N) and transverse directions (σ_T). As the aspect ratio increased from 1 to 2, the ratio of σ_T to σ_N increases from 1.3 to 6.97, indicating a higher degree of anisotropy. The proposed mathematical design approach offers an effective strategy for manipulating the anisotropic properties of ceramic scaffolds, thus possessing great potential to mitigate the stress shielding effect under *in vivo* conditions and promoting bone regeneration.[8] These findings can contribute to the development of ceramic scaffolds with tailorable mechanical properties, offering promising prospects for advancing bone tissue engineering and regeneration applications.

In vitro cell studies were conducted to evaluate the cytocompatibility of gyroid scaffolds with radially graded structures. Confocal microscope images revealed even cell distribution on all scaffolds, with over 98% cell viability observed across all sample groups, indicating excellent biocompatibility. The gyroid structures demonstrated varying cell proliferation efficiencies, which can be attributed to differences in total surface area and Gaussian curvatures. Specifically, gyroid structures with higher γ values (indicating a lower aspect ratio of the unit cell) exhibited higher surface areas (as shown in Table 1 and Figure 10c), which correlated with higher cell counts. For example, the γ.50-FGgy scaffold showed superior cell proliferation efficiency, with significantly higher cell counts observed on day 7. In contrast, the γ.25-FGgy scaffold exhibited a slight decrease in cell proliferation rate. This variation in cell proliferation rates provides valuable insight into how the geometric features of graded gyroid structures affect regenerative performance. The findings suggest that increasing the surface area by adjusting the γ value can enhance cell attachment and proliferation, likely due to the increased hyperboloidal surfaces for cell adhesion and retention. Overall, this work presents a promising strategy for efficiently producing high-quality ceramic scaffolds with customizable geometries that can be tailored to specific biological needs. The ability to fine-tune the geometric parameters of gyroid structures offers significant potential for optimizing scaffold design for various bone regeneration scenarios. However, additional investigation is suggested to further refine these designs and to optimize the gyroid structures for specific *in vivo* bone regeneration applications. Future studies should focus on understanding the long-term effects of these geometric variations on bone healing and integration, as well as exploring the potential for combining these scaffolds with bioactive coatings or growth factors to enhance their regenerative capabilities.

5. Conclusion

This study has successfully demonstrated a computer-aided design approach for generating gyroid structures with tailored properties. By manipulating the geometrical parameters within the level-set equation of the gyroid structure, we are able to adjust the aspect ratio of the unit cell and fabricate structures with radially graded porosity that can mimic the architecture of trabecular bone. A rapid SMWH method was developed, hybridizing the pyrolysis and sintering process, which resulted in significant improvements in the structure quality. This process notably reduced the defect volume in the sintered ceramic structures by 16.81% and remarkably enhanced the compressive strength by 336% compared to conventional furnace heating methods. Furthermore, the relations between geometric features and both mechanical performance

and *in vitro* cellular responses were investigated. It was observed that an increase in the aspect ratio of the unit cell significantly amplified the anisotropic mechanical properties of the gyroid structure. However, this modification slightly reduced cell proliferation efficiency in comparison to the uniform gyroid structure, which can be attributed to variations in Gaussian curvatures. This study presented an effective design methodology for TPMS, including but not limited to gyroid structures, with tailored properties. Our methodology can be extended to the design of smart scaffolds incorporating piezoelectric materials for bone implants beyond traditional materials.

Acknowledgments

The authors gratefully acknowledge the support from U3DP of The Hong Kong Polytechnic University, and extend special thanks to Tab Cheng and Sidney Wong for their valuable assistance.

Funding

The work described in this paper was mainly supported by the funding support to the State Key Laboratories in Hong Kong from the Innovation and Technology Commission (ITC of the Government of the Hong Kong Special Administrative Region [HKSAR] of China), and The Hong Kong Polytechnic University (Project Code: BBX2 and PolyU Project Code: 1-BBTN) and a grant from the Research Committee of The Hong Kong Polytechnic University under project account code G-UAMY.

Conflict of interest

The authors declare they have no competing interests.

Author contributions

Conceptualization: Ka-Wai Yeung, Chak-Yin Tang
Data curation: Ka-Wai Yeung, Chi-Yeung Mang, Quan-Jing Mei
Funding acquisition: Chak-Yin Tang
Investigation: Ka-Wai Yeung, Quan-Jing Mei
Methodology: Ka-Wai Yeung, Chi-Yeung Mang
Supervision: Chak-Yin Tang
Visualization: Ka-Wai Yeung
Writing – original draft: Ka-Wai Yeung
Writing – review & editing: Chi Ho Wong, Chak-Yin Tang, Xin Zhao, Wing-Cheung Law, Gary Chi-Pong Tsui, Zhenjia Huang

Ethics approval and consent to participate

Not applicable.

Consent for publication

Not applicable.

Availability of data

Data is available from the corresponding author upon reasonable request.

References

1. Vijayavenkataraman S, Kuan LY, Lu WF. 3D-printed ceramic triply periodic minimal surface structures for design of functionally graded bone implants. *Mater Design*. 2020;191:108602.
doi: 10.1016/j.matdes.2020.108602

2. Yan C, Hao L, Hussein A, Young P. Ti–6Al–4V triply periodic minimal surface structures for bone implants fabricated via selective laser melting. *J Mech Behav Biomed Mater*. 2015;51:61-73.
doi: 10.1016/j.jmbbm.2015.06.024

3. Dong Z, Zhao X. Application of TPMS structure in bone regeneration. *Eng Regen*. 2021;2(8):154-162.
doi: 10.1016/j.engreg.2021.09.004

4. Shan Y, Bai Y, Yang S, et al. 3D-printed strontium-incorporated β-TCP bioceramic triply periodic minimal surface scaffolds with simultaneous high porosity, enhanced strength, and excellent bioactivity. *J Adv Ceram*. 2023;12(9):1671-1684.
doi: 10.26599/JAC.2023.9220787

5. Al-Ketan O, Abu Al-Rub RK. MSLattice: a free software for generating uniform and graded lattices based on triply periodic minimal surfaces. *Mater Des Process Commun*. 2021;3(6):e205.
doi: 10.1002/mdp2.205

6. Ma S, Song K, Lan J, Ma L. Biological and mechanical property analysis for designed heterogeneous porous scaffolds based on the refined TPMS. *J Mech Behav Biomed Mater*. 2020;107:103727.
doi: 10.1016/j.jmbbm.2020.103727

7. Yang Y, Xu T, Bei H-P, et al. Gaussian curvature–driven direction of cell fate toward osteogenesis with triply periodic minimal surface scaffolds. *Proc Natl Acad Sci U S A*. 2022;119(41):e2206684119.
doi: 10.1073/pnas.2206684119

8. Deering J, Dowling KI, DiCecco L-A, McLean GD, Yu B, Grandfield K. Selective Voronoi tessellation as a method to design anisotropic and biomimetic implants. *J Mech Behav Biomed Mater*. 2021;116:104361.
doi: 10.1016/j.jmbbm.2021.104361

9. Yao Y, Qin W, Xing B, Sha N, Jiao T, Zhao Z. High performance hydroxyapatite ceramics and a triply periodic minimum surface structure fabricated by digital light processing 3D printing. *J Adv Ceram*. 2021;10(1):39-48. doi: 10.1007/s40145-020-0415-4

10. Li G, Li Z, Min Y, Chen S, Han R, Zhao Z. 3D-printed piezoelectric scaffolds with shape memory polymer for bone regeneration. *Small*. 2023;19(40):e2302927. doi: 10.1002/smll.202302927

11. Chen A, Su J, Li Y, et al. 3D/4D printed bio-piezoelectric smart scaffolds for next-generation bone tissue engineering. *Int J Extrem Manuf*. 2023;5(3):032007. doi: 10.1088/2631-7990/acd88f

12. Zhou Q, Su X, Wu J, et al. Additive manufacturing of bioceramic implants for restoration bone engineering: technologies, advances, and future perspectives. *ACS Biomater Sci Eng*. 2023;9(3):1164-1189. doi: 10.1021/acsbiomaterials.2c01164

13. Ravi M, Paramesh V, Kaviya S, Anuradha E, Solomon FP. 3D cell culture systems: advantages and applications. *J Cell Physiol*. 2015;230(1):16-26. doi: 10.1002/jcp.24683

14. Ma J, Qin C, Wu J, et al. 3D printing of strontium silicate microcylinder-containing multicellular biomaterial inks for vascularized skin regeneration. *Adv Healthc Mater*. 2021;10(16):e2100523. doi: 10.1002/adhm.202100523

15. Feng C, Zhang K, He R, et al. Additive manufacturing of hydroxyapatite bioceramic scaffolds: dispersion, digital light processing, sintering, mechanical properties, and biocompatibility. *J Adv Ceram*. 2020;9:360-373. doi: 10.1007/s40145-020-0375-8

16. Chen Z, Li Z, Li J, et al. 3D printing of ceramics: a review. *J Eur Ceram Soc*. 2019;39(4):661-687. doi: 10.1016/j.jeurceramsoc.2018.11.013

17. Ren X, Wang J, Wu Y, et al. One-pot synthesis of hydroxyapatite hybrid bioinks for digital light processing 3D printing in bone regeneration. *J Mater Sci Technol*. 2024;188:84-97. doi: 10.1016/j.jmst.2024.01.001

18. Li Y, Su J, Chen A, et al. Strontium-doped calcium silicate scaffolds with enhanced mechanical properties and tunable biodegradability fabricated by vat photopolymerization. *Int J Bioprint*. 2023;9(6):1233. doi: 10.36922/ijb.1233

19. Akinwekomi AD, Yeung K-W, Tang C-Y, Law W-C, Tsui GC-P. Finite element simulation of hybrid microwave sintering based on power approach. *Int J Adv Manuf Technol*. 2020;110:2503-2515. doi: 10.1007/s00170-020-05952-0

20. Zuo F, Badev A, Saunier S, Goeuriot D, Heuguet R, Marinel S. Microwave versus conventional sintering: estimate of the apparent activation energy for densification of α-alumina and zinc oxide. *J Eur Ceram Soc*. 2014;34(12):3103-3110. doi: 10.1016/j.jeurceramsoc.2014.04.006

21. Tang J, Xu J, Ye Z, Li X, Luo J. Microwave sintered porous CoCrFeNiMo high entropy alloy as an efficient electrocatalyst for alkaline oxygen evolution reaction. *J Mater Sci Technol*. 2021;79:171-177. doi: 10.1016/j.jmst.2020.10.079

22. Yeung K-W, Tang C-Y, Hu R, et al. Fabrication of ceramic bioscaffolds from fly ash cenosphere by susceptor-assisted microwave sintering. *J Eur Ceram Soc*. 2022;42(2):4410-4419. doi: 10.1016/j.jeurceramsoc.2022.03.046

23. Garnault T, Bouvard D, Chaix J-M, Marinel S, Harnois C. Is direct microwave heating well suited for sintering ceramics? *Ceram Int*. 2021;47(12):16716-16729. doi: 10.1016/j.ceramint.2021.02.242

24. Zhou M, Liu W, Wu H, et al. Preparation of a defect-free alumina cutting tool via additive manufacturing based on stereolithography–Optimization of the drying and debinding processes. *Ceram Int*. 2016;42(10):11598-11602. doi: 10.1016/j.ceramint.2016.04.050

25. Cui H, Hensleigh R, Yao D, et al. Three-dimensional printing of piezoelectric materials with designed anisotropy and directional response. *Nature Mater*. 2019;18(3):234-241. doi: 10.1038/s41563-018-0268-1

26. Zhianmanesh M, Varmazyar M, Montazerian H. Fluid permeability of graded porosity scaffolds architectured with minimal surfaces. *ACS Biomater Sci Eng*. 2019;5(3):1228-1237. doi: 10.1021/acsbiomaterials.8b01400

27. Song K, Wang Z, Lan J, Ma S. Porous structure design and mechanical behavior analysis based on TPMS for customized root analogue implant. *J Mech Behav Biomed Mater*. 2021;115:104222. doi: 10.1016/j.jmbbm.2020.104222

28. Yeung K-W, Huang Z, Mang C-Y, et al. Fabrication of predesigned 3D carbon based microstructures via two-photon vat photopolymerization and susceptor-assisted microwave post-processing. *Addit Manuf*. 2023;79(16):103934. doi: 10.1016/j.addma.2023.103934

29. Arita R, Iijima M, Fujishiro Y, et al. Rapid three-dimensional structuring of transparent SiO2 glass using interparticle photo-cross-linkable suspensions. *Commun Mater*. 2020;1(1):30. doi: 10.1038/s43246-020-0029-y

30. Zhao D, Su H, Hu K, et al. Formation mechanism and controlling strategy of lamellar structure in 3D printed alumina ceramics by digital light processing. *Addit Manuf*. 2022;52:102650. doi: 10.1016/j.addma.2022.102650

31. Wan W, Huang C-e, Yang J, Zeng J, Qiu T. Effect of sintering temperature on the properties of fused silica ceramics prepared by gelcasting. *J Electron Mater*. 2014;43(7):2566-2572. doi: 10.1007/s11664-014-3112-7

32. Yeung K-W, Chen L, Tang C-Y, et al. Rapid hybrid microwave cladding of SiO 2/TiO 2 sol–gel derived composite coatings. *J Sol-Gel Sci Technol*. 2021;98(1):35-44. doi: 10.1007/s10971-021-05498-x

33. Bhattacharya M, Basak T. A review on the susceptor assisted microwave processing of materials. *Energy*. 2016;97:306-338. doi: 10.1016/j.energy.2015.11.034

34. Liu Z, Ma C, Chang Z, Yan P, Li F. Advances in crack formation mechanism and inhibition strategy for ceramic additive manufacturing. *J Eur Ceram Soc*. 2023;43(12): 5078-5098. doi: 10.1016/j.jeurceramsoc.2023.05.008

35. Luongo A, Falster V, Doest MB, et al. Microstructure control in 3D printing with digital light processing. Comp Graph Forum. 2020;39(1):347-359. doi: 10.1111/cgf.13807

36. Schamberger B, Ziege R, Anselme K, et al. Curvature in biological systems: its quantification, emergence, and implications across the scales. *Adv Mater*. 2023;35(13):2206110. doi: 10.1002/adma.202206110

37. Karayannis VG. Microwave sintering of ceramic materials. IOP Conf Ser Mater Sci Eng. 2016;161(1):012068. doi: 10.1088/1757-899X/161/1/012068

38. Chorsi MT, Curry EJ, Chorsi HT, et al. Piezoelectric biomaterials for sensors and actuators. *Adv Mater*. 2019;31(1):e1802084. doi: 10.1002/adma.201802084

ACCSCIENCE PUBLISHING

International Journal of Bioprinting

RESEARCH ARTICLE

Dexamethasone-loaded PLGA porous microspheres used as 3D-bioprinted bioink promote tissue-engineered cartilage regeneration

Zhuoqi Chen[1†], Yanjun Feng[1†], Yuchen Wang[1†], Tianfeng Zheng[1†], Jinshi Zeng[1], Wenshuai Liu[1], Yue Ma[1], Xiaowei Yue[1], Tian Li[1], Luosha Gu[1], Qinghua Yang[1*], Haiyue Jiang[1*], and Xia Liu[1,2*]

[1]Research Center of Plastic Surgery Hospital, Chinese Academy of Medical Sciences and Peking Union Medical College, Beijing, China

[2]Key Laboratory of External Tissue and Organ Regeneration, Chinese Academy of Medical Sciences and Peking Union Medical College, Beijing, China

(This article belongs to the Special Issue: *3D printing for tissue engineering and regenerative medicine*)

Abstract

The current investigation focused on fabricating and thoroughly analyzing porous microspheres (MPs) comprising poly (lactic-co-glycolic acid, PLGA) encapsulating dexamethasone, by utilizing the water-in-oil-in-water (W/O/W) emulsion solvent evaporation technique. The meticulous characterization encompassed various parameters, including particle size distribution, morphology, and polymer integrity, all of which exhibited consistent attributes across the MPs populations. The analysis of drug content and release kinetics revealed a sustained and controlled liberation of dexamethasone, characterized by an initial burst release within the initial 3 days followed by a gradual, protracted release profile. Subsequent *in vivo* assessments further validated the potent anti-inflammatory effects of the dexamethasone-loaded PLGA MPs, as evidenced by notable reductions in CD86 immunohistochemical staining intensity, along with the change in membrane thickness. Additionally, the MPs demonstrated an impressive capability to support the maintenance of cartilage phenotype, as indicated by the augmented secretion of cartilage matrix components and elevated glycosaminoglycan content.

Keywords: Cartilage repair; Porous microspheres; Dexamethasone; PLGA porous microspheres; Targeted drug delivery; 3D bioprinting

†These authors contributed equally to this work.

***Corresponding authors:**
Xia Liu
(liuxia@psh.pumc.edu.cn)

Qinghua Yang
(yqh114502@sina.com)

Haiyue Jiang
(Jianghaiyue@psh.pumc.edu.cn)

Citation: Chen Z, Feng Y, Wang Y, et al. Dexamethasone-loaded PLGA porous microspheres used as 3D-bioprinted bioink promote tissue-engineered cartilage regeneration. *Int J Bioprint*. 2024;10(5):3396. doi: 10.36922/ijb.3396

Received: April 9, 2024
Accepted: June 3, 2024
Published Online: August 27, 2024

Copyright: © 2024 Author(s). This is an Open Access article distributed under the terms of the Creative Commons Attribution License, permitting distribution, and reproduction in any medium, provided the original work is properly cited.

Publisher's Note: AccScience Publishing remains neutral with regard to jurisdictional claims in published maps and institutional affiliations.

1. Introduction

Microtia is a common congenital anomaly affecting outer ear development, typically characterized by abnormal or defective auricular morphology. Despite its prevalence, the exact cause of microtia remains unclear, with an incidence rate ranging from 0.83 to 17.4 per 10,000 births.[1] The primary challenge in microtia reconstruction lies in selecting suitable materials for cartilage scaffold construction. Both the autologous costal cartilage tissues and artificial materials are the currently available materials for cartilage scaffold construction. While artificial material scaffolds are prone to extrusion issues,

rib cartilage scaffolds are associated with postoperative pain, pneumothorax, chest wall deformities, and other complications. In light of these shortcomings, tissue engineering offers a promising and minimally invasive alternative for addressing auricular deformities. Thus, there is an urgent need for the design of tissue-engineered cartilage scaffolds.[2–4]

The fabrication of tissue-engineered ears presents multifaceted challenges, with the restricted formation of cartilage tissue and the inability to maintain tissue shape being the prominent concerns. These hurdles are further compounded by inflammatory reactions, which result in suboptimal tissue integrity and compromised mechanical properties.[5,6] Hence, mitigating inflammatory reactions during tissue formation is vital for enhancing cartilage regeneration and bolstering the overall mechanical robustness of tissue-engineered ears.[7–9] Additionally, the insufficient mechanical properties of the materials utilized in tissue engineering contribute to the challenges encountered in achieving desired tissue formation outcomes. These material constraints highlight the significance of developing strategies to enhance the mechanical performance of tissue-engineered constructs while simultaneously mitigating inflammatory responses to facilitate successful tissue regeneration.[10]

Currently, extrusion-based three-dimensional (3D) bioprinting technology is widely used in tissue engineering to fabricate complex 3D biological structures.[11–13] This technology enables precise control over complex structures and functions through layer-by-layer deposition of biodegradable bioinks, allowing the construction of customized structures.[14]

Dexamethasone (DEX) is a synthetic corticosteroid widely utilized in clinical medicine.[15,16] It exerts various crucial physiological and pharmacological effects, including potent anti-inflammatory, immunosuppressive, and anti-allergic properties. DEX finds application in the management of inflammatory diseases, autoimmune diseases, allergic conditions, and other medical issues. Additionally, it is commonly included as a supplement in chondrocyte culture media. While DEX presents potent anti-inflammatory benefits, it entails a wide range of side effects, such as elevated risk of hypertension, diabetes, and osteoporosis.[17,18] To enhance efficacy and reduce systemic side effects of DEX, local sustained release methods can be adopted to achieve the most optimal trade-off between its advantages and shortcomings.

Porous microspheres represent an optimal drug delivery vehicle due to their substantial pore-to-surface ratios and interconnected pores.[19–21] One of the primary benefits of MP drug delivery is their ability to sustain release over time. Moreover, the quantity of MPs can be tailored to meet the patient's requirements, allowing for personalized drug dosing and individualized treatment strategies. Furthermore, current research indicates that MPs can serve as microcarrier systems for cell suspension culture and for tissue defect repair by injecting individual MPs or constructs containing cells and MPs into the affected area.[22,23] Poly (lactic-co-glycolic acid) (PLGA) holds a prominent position in the medical field, particularly in drug delivery systems, where drugs can be encapsulated within MPs and released through micropores into target tissues for sustained and controlled release.[24,25] Additionally, PLGA MPs can function as integral elements of tissue engineering scaffolds, offering structural support, fostering cell adhesion and proliferation, and leaving behind newly formed tissue after gradual degradation. In various tissue engineering applications such as bone, cartilage, and muscle regeneration, PLGA MPs play pivotal roles in fostering tissue regeneration and repair.[26,27] With their multifunctionality and controlled release characteristics, PLGA MPs offer potent tools for both tissue engineering and drug delivery applications. The multifunctionality and controlled release characteristics make them powerful tools for both tissue engineering and drug delivery applications. Moreover, they address the challenge of simultaneous printing with cells, a hurdle faced by other thermoplastic synthetic polymers. The addition of PLGA MPs successfully resolves the printability issue with seed cells, a common limitation with other thermoplastic synthetic polymers. Unlike polycaprolactone (PCL), which necessitates high-temperature printing, PLGA MPs can be mixed with gelatin methacryloyl (GelMA) hydrogel and seed cells at room temperature after preparation and sterilization. This mixture can be directly used for constructing tissue-engineered cartilage, facilitating effective cell adhesion.[28,29]

In this study, we loaded DEX at various concentrations into PLGA MPs, which were used as a material for cartilage construction. We examined its effectiveness in reducing inflammatory responses and promoting cartilage tissue regeneration. The general flow of the experiments described in this paper is schematically illustrated and presented in Figure 1.

2. Materials and methods

2.1. Materials

The chemical reagents used in the experiments, including PLGA (50:50), DEX lyophilized powder (MW: 392.47), polyvinyl alcohol (PVA; MW: 30,000–70,000), GelMA lyophilized powder, and lithium phenyl-2,4,6-trimethylbenzoylphosphinate (LAP; 2.5% w/v) solution

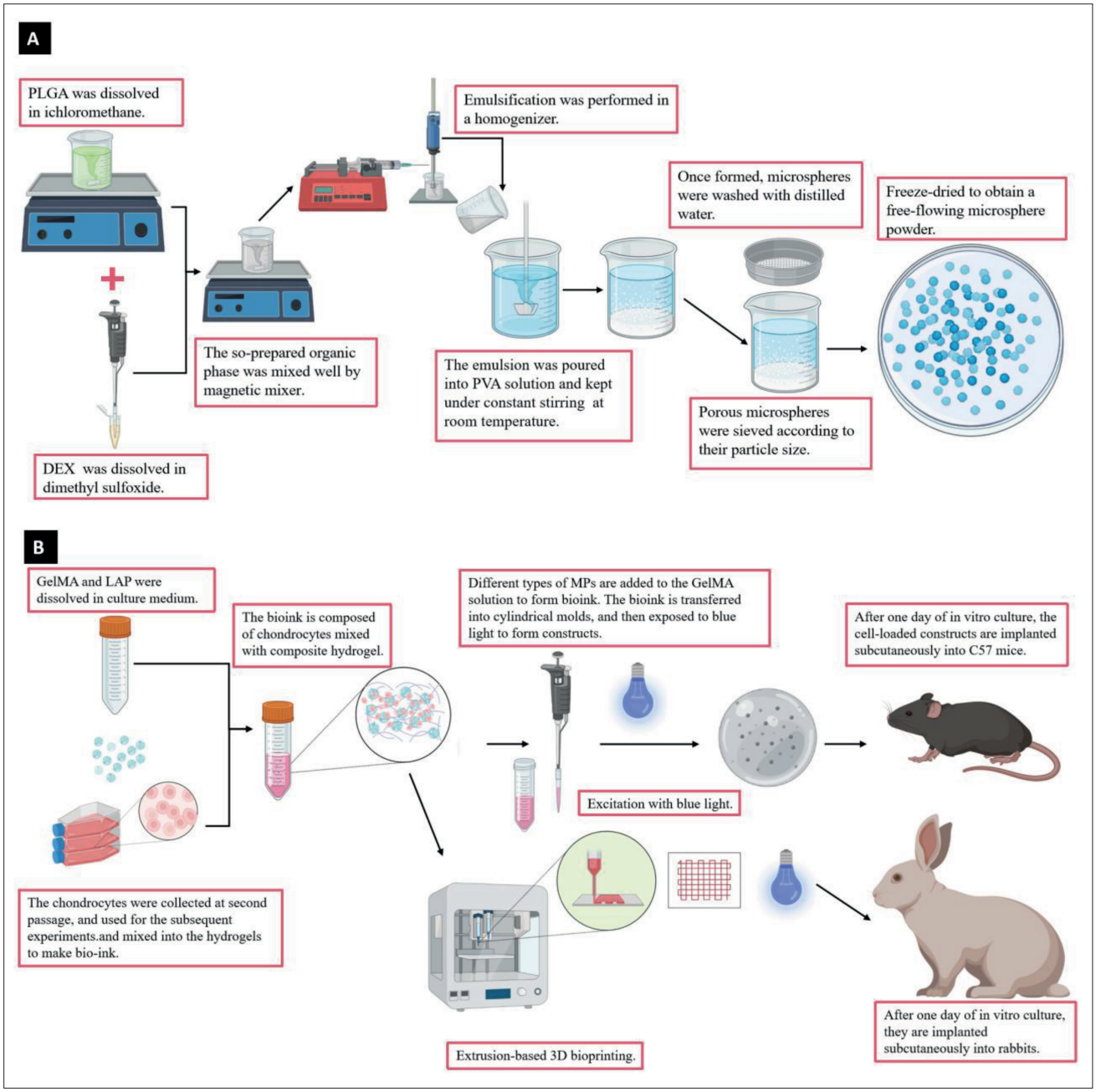


Figure 1. Schematic diagram of experiment flow. (A) Fabrication process of microspheres (MPs). (B) *In vivo* experiment process. Abbreviations: DEX, dexamethasone; GelMA, gelatin methacryloyl; LAP, lithium phenyl-2,4,6-trimethylbenzoylphosphinate; MPs, microspheres; PLGA, poly (lactic-co-glycolic acid).

were purchased from Xienshi Biological Technology Co., Ltd. (Tianjin, China). Dulbecco's Modified Eagle Medium (DMEM), Roswell Park Memorial Institute 1640 medium (RPMI-1640), penicillin-streptomycin-neomycin antibiotics (PSN), fetal bovine serum (FBS), and trypsin were obtained from Gibco (Grand Island, NY, USA). Type II collagenase was purchased from Sigma-Aldrich (Germany). TRIzol Reagent was acquired from Invitrogen (USA).

2.2. Animals

The Japanese White rabbits (7-month-old female) and C57 mice (6-week-old female) were purchased from Long'an Experimental Animal Breeding Center (Beijing,

China). All animal experiments were conducted following approval from the Animal Care and Use Committee of the Plastic Surgery Hospital (Approval No: EAEC 2022-007, EAEC-008).

2.3. Isolation of rabbit articular chondrocytes

Cartilage cells were isolated from the entire ear cartilage of 8-month-old Japanese White rabbits. Cells were obtained from 10 female animals. After removing the skin tissue and most of the cartilage membrane, the tissue was cut into small pieces, with each measuring 1 mm × 1 mm in dimension. These pieces were washed with Dulbecco's phosphate-buffered saline (DPBS) until clear and then digested with trypsin for 30 min to remove the remaining cartilage membrane and connective tissue. Type II collagenase was dissolved in DMEM at a concentration of 0.2% w/v, and then the treated cartilage pieces were processed on a shaker at 37°C for 6–8 h. The digested tissue fluid was filtered through a 70 μm mesh, and the cells were collected after centrifugation, counted, and cultured and expanded in cartilage culture medium containing high-glucose DMEM + 10% FBS + 1% PSN at 37°C in a 5% CO_2 and 95% humid environment. The second-generation cells were collected for subsequent experiments.

2.4. Preparation of DEX-loaded PLGA MPs

In this experiment, MPs were prepared using the W/O/W method. Briefly, 200 mg of PLGA was dissolved in 8 mL of dichloromethane. DEX in different volumes (15, 30, and 60 μL) was separately dissolved in 150 μL of dimethyl sulfoxide (DMSO) until completely dissolved, giving rise to solutions at different concentrations (0.1, 0.2, and 0.4 mg/mL, respectively). The DEX-DMSO solution was then added to the PLGA-DMSO solution to prepare the oil phase.

In this experiment, 2.5 mL of 1% w/v ammonium bicarbonate (NH_4HCO_3) solution was utilized as the inner aqueous phase. The prepared inner aqueous phase solution was gradually added dropwise into the oil phase at a rate of 2.5 mL/min using a syringe pump while stirring with a high-speed disperser, resulting in the formation of the primary emulsion. Subsequently, the primary emulsion was slowly poured into a 0.1% PVA solution (300 mL) while stirring at 800 rpm for 3 h to obtain the secondary emulsion. The MPs were gathered following the completion of stirring. The collected MPs were washed three times with deionized water and subsequently hydrolyzed in a 0.1 mol/L NaOH solution for 20 min. Following hydrolysis, the MPs underwent three additional washes with deionized water under the same conditions. Finally, all MPs were filtered to specifically retain MPs with a diameter of 75–100 μm, freeze-dried, and stored under drying conditions at 4°C for further use.

We conducted a statistical analysis of the pore diameter of porous microspheres. Three representative samples were randomly selected from each group, and 30 pores were measured on each microsphere; therefore, the diameter of a total of 90 pores was measured. Using the measurement tools in ImageJ software, we accurately identified and measured the diameter of each pore. Subsequently, we recorded and calculated the diameter data of all pores in each sample group, and conducted statistical analysis, including calculating the mean and standard deviation. Finally, we compared the differences in pore diameter between different groups using appropriate statistical methods.

2.5. Dexamethasone release and determination of encapsulation efficiency and drug loading efficiency

Four groups of MPs, each consisting of three batches of MPs prepared, totaling 12 samples of 10 mg each, were weighed and transferred into Eppendorf tubes. To each tube, 1 mL of DPBS solution was added, and all the tubes were placed in a 37°C incubator. During each measurement, all DPBS solution was aspirated, and 1 mL of fresh PBS solution was added to replace it. The concentration of DEX in the supernatant was determined by high-performance liquid chromatography (HPLC) analysis.

The encapsulation efficiency (EE) and drug loading efficiency (DL) of the MPs were measured directly from any one of the batches in each group. The EE and DL were calculated using **Equations (I)** and **(II)**.

$$EE\% = \frac{W_{\text{loaded drug}}}{W_{\text{feed drug}}} \times 100\% \quad \text{(I)}$$

$$DL\% = \frac{W_{\text{loaded drug}}}{W_{\text{polymer and loaded drug}}} \times 100\% \quad \text{(II)}$$

where *W* is weight.

2.6. Preparation of bioink and *in vivo* tissue-engineering cartilage culture

Cartilage from the upper 1/3 portion of the right ear of Japanese White rabbits was digested with collagenase to isolate chondrocytes, which were subsequently cultured *in vitro* until passage 2 (P2) cells were obtained. The cells were then digested to obtain a cell suspension. A control group was prepared by mixing 1×10^7 cells/mL, 10% GelMA w/v, and 0.25% LAP w/v.

Four types of MPs (30 mg/mL, w/v), sterilized by ultraviolet (UV) irradiation, were added to the GelMA

solution to create four types of mixed hydrogels. Finally, the seeded cells (1×10^7 cells/mL) were mixed with the hydrogel to form the bioink.

To tissue-engineer cartilage in C57 mice, a silicone rubber base (Sylgard™ 184, Dowsil, USA) was heated at 70°C for 3 h to prepare a circular mold with a diameter of 10 mm and a height of 4 mm. Subsequently, 180 μL of bioink was aspirated and injected into the mold. The bioink was then exposed to blue light with a wavelength of 450 nm and an intensity of 30 mW/cm^2 for 10 s to achieve complete crosslinking. Following crosslinking, the bioink was crosslinked using blue light (450 nm) to form cylindrical structures. These cylindrical structures were cultured *in vitro* for 24 h before being implanted subcutaneously into mice. After 24 h of *in vitro* culture of the cell-loaded constructs, they were implanted subcutaneously into animals to observe cartilage formation. Specimens were collected at 3, 7, and 14 days post-implantation for biomechanical testing, determination of glycosaminoglycan (GAG) content, and histological examination.

Following the 3D bioprinting of the bioink, the constructs were crosslinked and then cultured *in vitro* for 24 h before being implanted subcutaneously in rabbits. After 24 h of *in vitro* culture of the 3D-bioprinted cell-loaded constructs, they were implanted subcutaneously into rabbit and the cartilage formation was observed afterward. Specimens were collected at 7 and 14 days post-implantation for histological examination and determination of GAG content.

2.7. Histological examination

The tissue-engineered cartilage samples were fixed in 4% paraformaldehyde for 48 h, followed by dehydration, embedding in paraffin, and sectioning using a microtome. Subsequently, selected samples were stained using hematoxylin and eosin (H&E), Alcian blue (Solarbio, China), and immunohistochemical staining to assess the deposition of extracellular matrix and histological structure of the regenerated cartilage.[30] Cells and tissues were prepared according to the aforementioned methods. Antibodies against CD86 (ab220188; Abcam, UK) and CD31 (ab9498; Abcam, UK) were used. The images were captured using Motic Images 2.0 (China), and the exported images were analyzed for relative staining intensity around cells by using ImageJ software (Rawak Software, Inc., Germany). Subsequently, the results were subjected to statistical analysis.

2.8. Mechanical compression test

Compression tests were performed utilizing the Instron 5967 biomechanical analyzer (Instron, USA), which was outfitted with a 100 N pressure sensor. A constant compression strain rate of 10 mm/min was maintained until 80% of maximum deformation was reached. The slope of the stress–strain curve was adjusted within the range of 10–20% strain to calculate the Young's modulus of the hydrogel. A humidifier was utilized to maintain ambient air humidity throughout the entire testing process.

2.9. Culture of 3D-bioprinted constructs

The 3D-bioprinted constructs were stained with the Calcein-AM/PI dual staining kit (Dojindo, Japan) to assess cell viability within the hydrogel. Cell viability was evaluated using a confocal microscope (Leica TCS SP8 CARS, USA).

2.10. Scanning electron microscopy

After freeze-drying and gold sputter coating, the samples were analyzed using a Quanta 2000 scanning electron microscope (FEI, the Netherlands), operating at an energy level of 15 kV. The acquired SEM images were analyzed using ImageJ software.

2.11. Fourier transform infrared spectroscopy

Fourier transform infrared spectroscopic (FTIR) analysis was conducted using the iS10 FT-IR spectrometer (Thermo Fisher Scientific, USA) with a wavenumber range of 400–4000 cm^{-1}. The spectrometer featured a resolution of 4 cm^{-1} and a signal-to-noise ratio of 50,000:1, with an average of 32 scans. During the testing process, the Attenuated Total RTimes Perfactory RP slicing software was utilized for slicing. The layer height was set to 320 μm, and the sliced models were imported into the 3D bioprinter's visual machine. The internal structure of the scaffold was defined as a bordered lattice with a line spacing of 400 μm in the printing system. The extrusion pressure for the composite hydrogels ranged from 0.2 to 0.7 bar, with nozzle speeds ranging from 5.5 to 8.5 mm/s. Images were captured using built-in cameras at the 2nd, 4th, and 6th layers during the bioprinting process. After printing six layers, complete crosslinking was achieved under a blue light source with a wavelength of 450 nm and intensity of 30 mW/cm^2 for 10 s.

2.12. Total RNA extraction, cDNA synthesis, and quantitative real-time PCR analysis

For every 100 mg tissue, 1 mL TRIzol (Invitrogen, USA) was added. Tissue specimens were chopped on ice and homogenized with sterile equipment. Following the addition of another 1 mL TRIzol, the mixture was incubated for 15 min at room temperature. Upon being transferred to RNase-free tubes, the lysate was added with 200 μL of chloroform, mixed, and incubated for 15 min. The lysate was then centrifuged at 12,000 × *g* for 15 min at 4°C. Approximately 500 μL of the upper phase, after centrifugation, was transferred to new tubes, followed by addition of 500 μL isopropanol, mixing, incubation for 15

min, and centrifugation at 12,000 × *g* for 15 min at 4°C. The RNA pellet was washed twice with 1 mL of 75% ethanol at 4°C, centrifuged at 12,000 × *g* for 10 min after each washing. The RNA pellet was air-dried and then dissolved in 40 μL DEPC-treated water; the RNA stock solution was stored at −80°C until further use.

The RNA concentration and purity was assessed using Nanodrop (Thermo, USA). Complementary DNA (cDNA) was synthesized using high-capacity cDNA synthesis kit (Takara, Japan), and the resultant products were stored at −20°C.

The cDNA was reverse-transcribed using Prime Script RT reagent kit (Takara, Japan). Real-time RT-PCR was performed with Roche 480II LightCycler and SYBR Green qPCR Master Mix (Takara, Japan). Primer sequences are listed in Table 1. *Gapdh* was used as the reference gene. The thermal cycling conditions for this experiment are as follows: 95°C for 600 s, 30 cycles of 95°C for 10 s each, 60°C for 15 s, and 72°C for 15 s. A melting curve (65–97°C) was generated afterward. The relative gene expression was calculated using $2^{-\Delta\Delta Ct}$ method.

2.13. Molecular weight determination

At 0 and 4 weeks, degradation of PLGA MPs samples in vitro were collected and freeze-dried. Five milligram of each group of samples was measured. One millilitre of tetrahydrofuran (THF) was added to each vial and equilibrated for 24 h for complete dissolution. The solution was filtered through 0.22 μm nylon membrane to remove impurities. The relative molecular weight was determined using LC20 high-performance liquid chromatography pump (Shimadzu, Japan). The conditions for this experiment are as followed: column size = 4.6 mm × 150 mm; particle size = 5 μm; flow rate = 1.0 mL/min; column temperature = 30°C; detection wavelength = 240 nm; mobile phase = acetonitrile-water (35:65); and injection volume = 5 μL. The data were recorded and analyzed.

Table 1. Sequences of primers used in RT-PCR.

Gene name	Primer	Primer sequence (5'–3')
Gapdh	Forward	CGACTTCAACAGTGCCACCCA
	Reverse	CACCCTGTTGCTGTAGCCAAA
Mmp-13	Forward	CCCCTCCTCAACAGTAACGAG
	Reverse	AGTTTGCCTGTCACCTCTAAGC
Il-6	Forward	GAGGCACTGGCGGAAGTCAATC
	Reverse	GAAGTGATTCTCAGCAGGCAGGTC
Tnf-α	Forward	GTCAACCTCCTCTCTGCCAT
	Reverse	ATCCCAAAGTAGACCTGCCC
Col2A1	Forward	GAGCAGCAAGAGCCAGAAGCA
	Reverse	GGAGCCCTCAGTGGACAGCA
Acan	Forward	CAGAACTTTGGTAGAATCCGTAA
	Reverse	CCAGAATGGGCTCCAGACAC
Sox-9	Forward	AATCTCCTGGACCCCTTCAT
	Reverse	GTCCTCTTCGCTCTCCTTCT

2.14. High-performance liquid chromatography

In a 5 mL volumetric flask containing 3 mL of acetonitrile, 25 mg of the sample was added. The mixture was ultrasonicated for 10 min, and then diluted to the mark with acetonitrile and centrifuged at 10,000 rpm for 10 min. One hundred microliter of the supernatant was mixed with 900 μL of the mobile phase in an annotation tube. The mixture was vortex-shaken for 1 min, followed by centrifugation at 10,000 rpm for 5 min. A C18 column was used to hold acetonitrile-phosphate buffer (30 mM, pH 3.5, acetonitrile: buffer = 30:70, v/v) as the mobile phase. The column temperature was set to 25°C and the flow rate to 0.8 mL/min (0–7 min), which increased to 1.6 mL/min (8–12 min) and then reverted back to 0.8 mL/min. Detection should be carried out at 240 nm using a UV detector. The supernatant (20 μL) was injected into the HPLC system using an automatic sampler.

2.15. Statistical analysis

Statistical analyses were conducted using GraphPad Prism 6.0 software. Experimental data were derived from a minimum of three independent experiments and are expressed as mean ± standard deviation. Statistical significance was assessed using either the Student's t-test or one-way ANOVA. A p-value of less than 0.05 was deemed statistically significant. It is essential that the data conform to a normal distribution.

3. Results

3.1. Characterization of MPs

Four groups of PLGA MPs containing different concentrations of DEX were prepared. SEM analysis revealed that MPs across all groups exhibited a porous spherical morphology, with diameters ranging between 75 and 100 μm (Figure 2A). These surfaces displayed small pores with attached filamentous DEX crystals. Notably, as the DEX content increased during fabrication, there was a corresponding rise in the attachment of filamentous DEX on the surface of MPs, confirming the effective loading of DEX into PLGA MPs. The MPs of all groups exhibited circular hollow structures (Figure 2B), indicating that there were no statistically significant differences in pore size among the groups.

To verify the drug loading status of MPs, FT-IR spectroscopy was utilized for characterization. As depicted in Figure 2F, the stretching vibration peak of C=O bonds

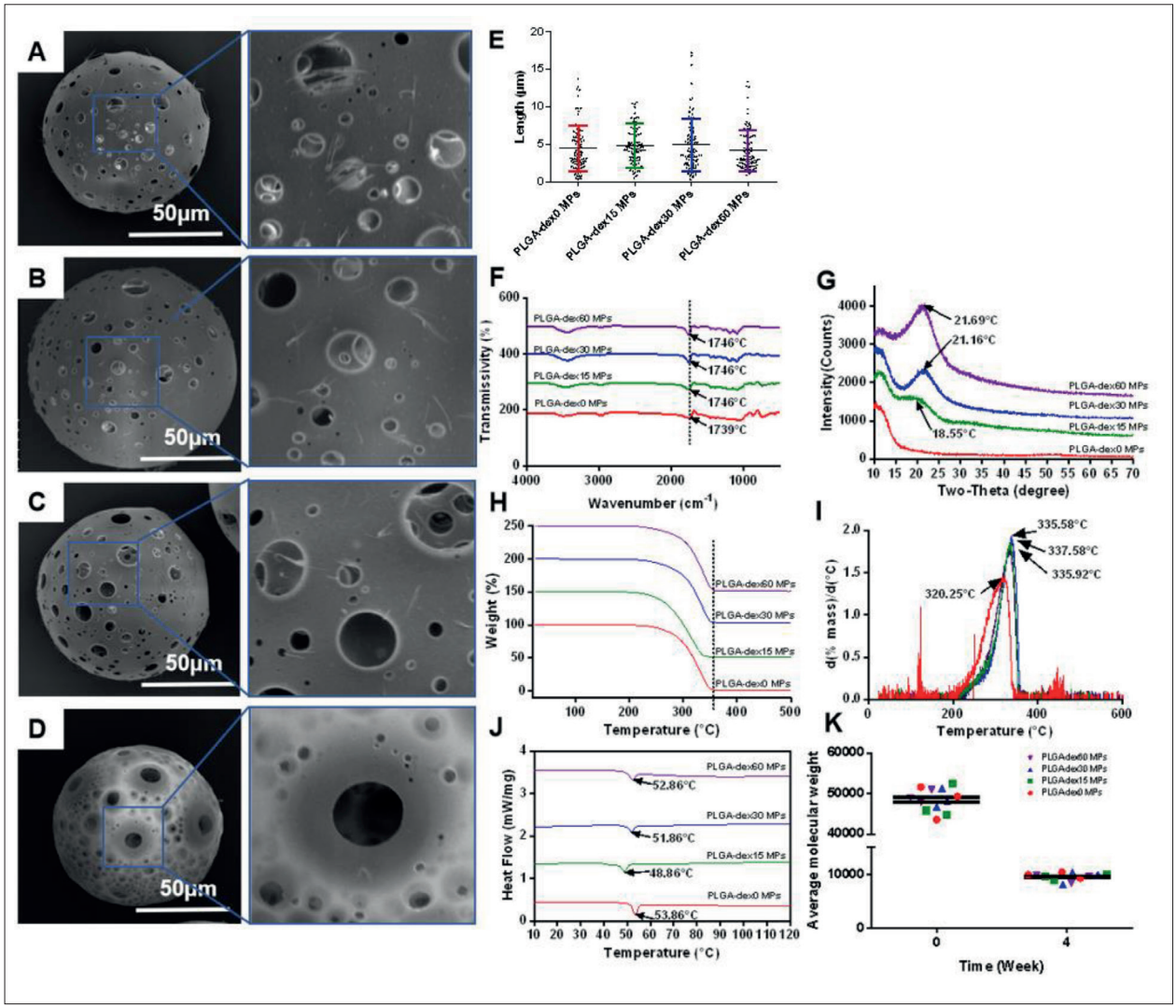


Figure 2. Characterization and analysis of PLGA-dex60, PLGA-dex30, PLGA-dex15, and PLGA-dex0 microspheres: SEM, pore size, FTIR, XRD, TGA, DTG, and DSC results. (A–D) Scanning electron microscopy (SEM) images of the structures of PLGA-dex60 MPs (A), PLGA-dex30 MPs (B), PLGA-dex15 MPs (C), and PLGA-dex0 MPs (D). (E) Distributions of pore sizes and average pore sizes of various groups of PLGA MPs. (F) Fourier transform infrared spectroscopy (FTIR) results of various groups of PLGA MPs. (G) X-ray diffraction (XRD) pattern of various groups of PLGA MPs. (H) Thermogravimetric analysis (TGA) results of various groups of PLGA MPs. (I) Derivative thermogravimetric analysis (DTG) results of various groups of PLGA MPs. (J) Differential scanning calorimeter (DSC) curves and (K) distribution of weight average molecular weight changes.

of PLGA was observed between 1750 and 1755 cm^{-1}, while that of DEX appeared between 1650 and 1660 cm^{-1}. Given the potential overlap of DEX's carbonyl peak with PLGA's C=O peak, the intensity of PLGA's C=O stretching vibration peak may decrease with increasing DEX loading. After physical mixing of PLGA with DEX, the C=O stretching vibration peak of DEX remained discernible, and its intensity increased proportionally with the rise in drug loading. This intensity augmentation correlated with the concentration of DEX in the MPs, almost disappearing relative to blank MPs.

X-ray crystallographic (XRD) analysis was conducted to investigate potential alterations in the crystalline structure of the drug, thereby exploring the crystalline properties of DEX within the MPs. As illustrated in Figure 2G, the XRD spectra of the four groups of PLGA MPs displayed broad and diffuse non-crystalline diffraction peaks, indicating the presence of characteristic peaks of the drug DEX in the XRD spectra of drug-loaded MPs. This suggests that DEX in the MPs adopts an amorphous structure or lacks a long-range periodic arrangement, predominantly existing in an amorphous state. Notably, no significant characteristic

peaks were observed in PLGA-dex0 MPs, whereas peaks for the other groups exhibited escalation with increasing drug concentration during the fabrication of PLGA MPs, which were observed at 18.55, 21.16, and 21.69°C, respectively. These features also reflect differences in the content of DEX among the sample groups.

Figure 2H and I illustrates the thermogravimetric analysis (TGA) results of the MPs in each group. Performed under inert nitrogen conditions, TGA was utilized to assess the thermal stability of the MPs in each group, as indicated by residual mass and the rate of weight change per unit temperature. As depicted in Figure 2H, the main degradation steps of MPs occurred within the range of 190–370°C. The weight change rate per unit temperature, with peak values observed at 322°C for PLGA MPs and 336°C for PLGA MPs loaded with DEX, signifies the maximum rate of weight change at these specific temperature points. The addition of DEX led to an elevation in the temperature at which the MPs exhibited the most rapid weight loss. Examination of the derivative thermogravimetric (DTG) curves depicted in Figure 2I unveils primary peak positions for each group of PLGA MPs at temperatures of 320.25, 335.58, 337.58, and 335.92°C, respectively. The main peak displayed a sharp, symmetrical, single-peak shape, indicating a clear single-peak thermal decomposition process at this temperature, characterized by steep peaks on both sides. From these findings, it can be inferred that the onset temperature of thermal decomposition for PLGA-dex0 MPs was lower, while the onset temperature for the other three groups of PLGA MPs was relatively higher, with peak positions observed in close proximity within the temperature range.

As depicted in Figure 2J, the differential scanning calorimetry (DSC) curves of PLGA MPs with varying concentrations of DEX did not manifest fixed melting points, confirming that the PLGA used in this experiment is an amorphous polymer material. The Tg values were determined to be 53.86, 48.86, 51.86, and 52.86°C, respectively. The endothermic peaks for all concentrations of drug-loaded MPs appeared beyond 50°C, indicating commendable thermal stability under physiological conditions at 37°C.

The alteration in the average molecular weight of PLGA during the *in vitro* degradation process of each group of MPs is depicted in Figure 2K. Initially, there were no notable differences in the molecular weight of PLGA MPs among the groups post-preparation. However, as the degradation time progressed, the molecular weight of all groups of PLGA MPs gradually decreased. A considerable decline in molecular weight was observed for all groups at week 4, indicating the favorable degradability of the PLGA MPs prepared in this experiment. After 4 weeks, the molecular weight had degraded to 20.53%, 19.87%, 19.41%, and 18.92% of the initial molecular weight for each group, respectively. There were no statistically significant differences in molecular weight among the groups, suggesting that drug loading has no significant impact on the molecular weight of the MPs. However, further measurements over an extended duration are warranted to monitor the degradation of PLGA MPs.

The calculated results for the drug encapsulation efficiency of MPs and their pharmacokinetics are summarized in Table 2, showcasing the average DEX content of 0 μg DEX/mg (PLGA-dex0 MPs@GelMA), 25.3 ± 4.9 μg DEX/mg (PLGA-dex15 MPs), 66.5 ± 6.8 μg DEX/mg (PLGA-dex30 MPs), and 152.5 ± 11.7 μg DEX/mg MPs (PLGA-dex60 MPs). The sustained release system employed in this study facilitated a minimum of 45 days of drug control release (Figure 3C), with drug release rates achieving 83.07% (PLGA-dex15@GelMA), 84.62% (PLGA-dex30@GelMA), and 88.89% (PLGA-dex60 MPs), respectively. The drug released within the initial 24 h for PLGA-dex15 MPs, PLGA-dex30 MPs, and PLGA-dex60 MPs groups were approximately 47.17%, 54.75%, and 26.17%, respectively.

To further elucidate the release capacity of each group for DEX (Figure 3A–C), the MPs were subjected to *in vitro* incubation, and the concentration of DEX in the incubation solution was measured to study the release kinetics of DEX from the MPs. Figure 3A demonstrates

Table 2. Drug loading (μg DEX/mg MPs) and encapsulation efficiency of each group (n = 3).

Group	Percentage encapsulation efficiency (%)	Drug loading rate (%)	The content of dexamethasone per milligram of porous microspheres. (μg DEX/mg MPs)
PLGA-dex0 MPs	0	0	0
PLGA-dex15 MPs	0.84	0.059	25.3 ± 4.9
PLGA-dex30 MPs	1.11	0.14	66.5 ± 6.8
PLGA-dex60 MPs	1.27	0.29	152.5 ± 11.7

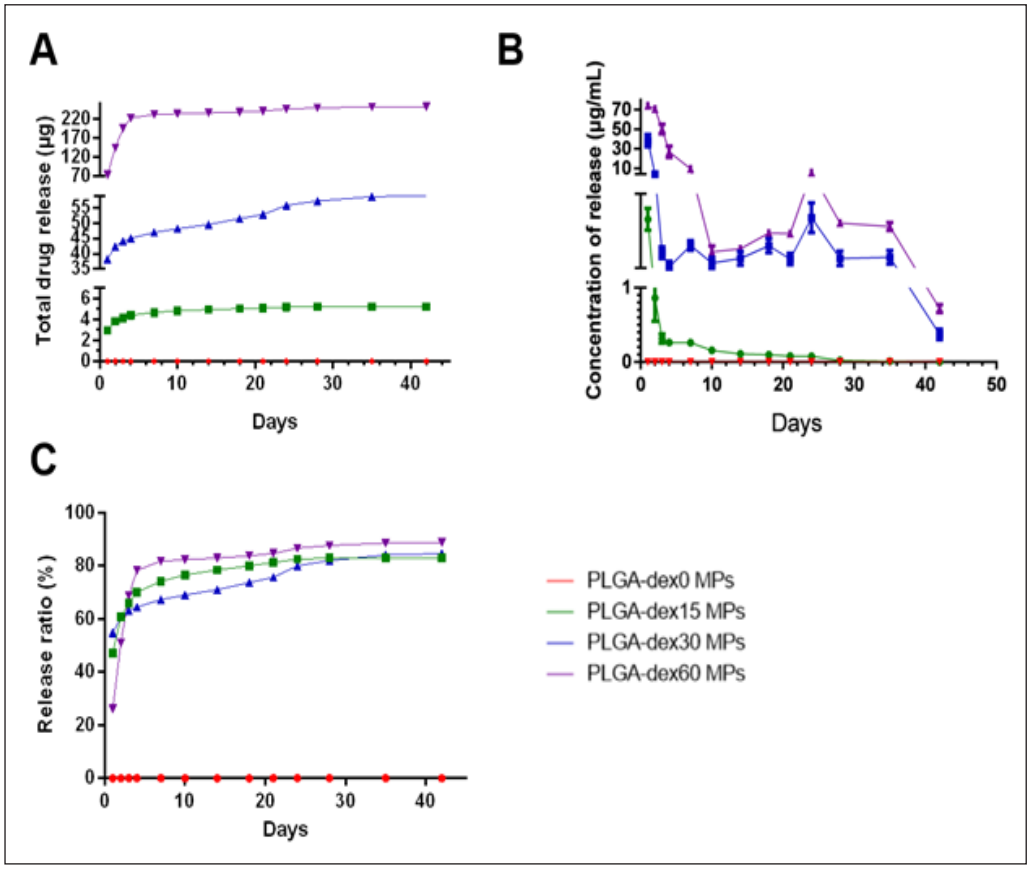


Figure 3. Pharmacokinetics of dexamethasone (DEX) in PLGA MPs ($n = 3$). (A) Cumulative drug release curve. (B) Daily drug release concentration. (C) Cumulative drug release proportion curve.

that the total DEX released over 45 days amounted to 5.23 μg for PLGA-dex15 MPs, 59.07 μg for PLGA-dex30 MPs, and 251.55 μg for PLGA-dex60 MPs. As depicted in Figure 3C, during the initial release period (24 h), a notable burst release phenomenon was observed. Particularly, the PLGA-dex60 MPs exhibited the highest early burst release of DEX, reaching a peak concentration of 74.056 μg, which accounted for 26.17% of the total release.

The PLGA-dex30 MPs demonstrated a maximum burst release of 38.22 μg, constituting 54.75% of the total release, while the PLGA-dex15 MPs exhibited a maximum burst release of 2.97 μg, representing 47.17% of the total release. Following 3 days of release, DEX release from all MPs groups entered a plateau phase, continuing until the end of the detection period. As illustrated in Figure 3B, sustained DEX release was observed across all MPs groups. Ultimately, as depicted in Figure 3C, the total DEX release from PLGA-dex15 MPs, PLGA-dex30 MPs, and PLGA-dex60 MPs amounted to 83.07%, 84.62%, and 88.89%, respectively. Both the release rate and total release of DEX from PLGA-dex60 MPs were higher than those of the other groups.

3.2. Heterotopic transplantation in C57 mice

After implantation of the cartilage tissue engineering constructs for 3, 7, and 14 days, specimens were obtained and photographed for macroscopic observation. As depicted in Figure 4, on the third day, no noticeable capsules were observed on the surfaces of the constructs across all groups. However, starting from the seventh day, thin or thick capsules had begun to form on the surfaces of the constructs in all four groups containing MPs. By the 14th day, connective tissue capsules had developed on the surfaces of all constructs and manifested gradual thickening, with fibrous capsules covering the implants, which is indicative of integration with the host.

3.2.1. Histological performance of cartilage and membrane formation in vivo in C57 mice

Figure 5A and C–E indicates the capsule thickness on day 7, with statistically significant differences between the PLGA-dex30 MPs@GelMA group and the PLGA-dex0 MPs@GelMA group ($p < 0.0001$, $p < 0.05$), while the PLGA-dex15 MPs@GelMA group showed slightly thinner capsules without statistical significance. In comparison to

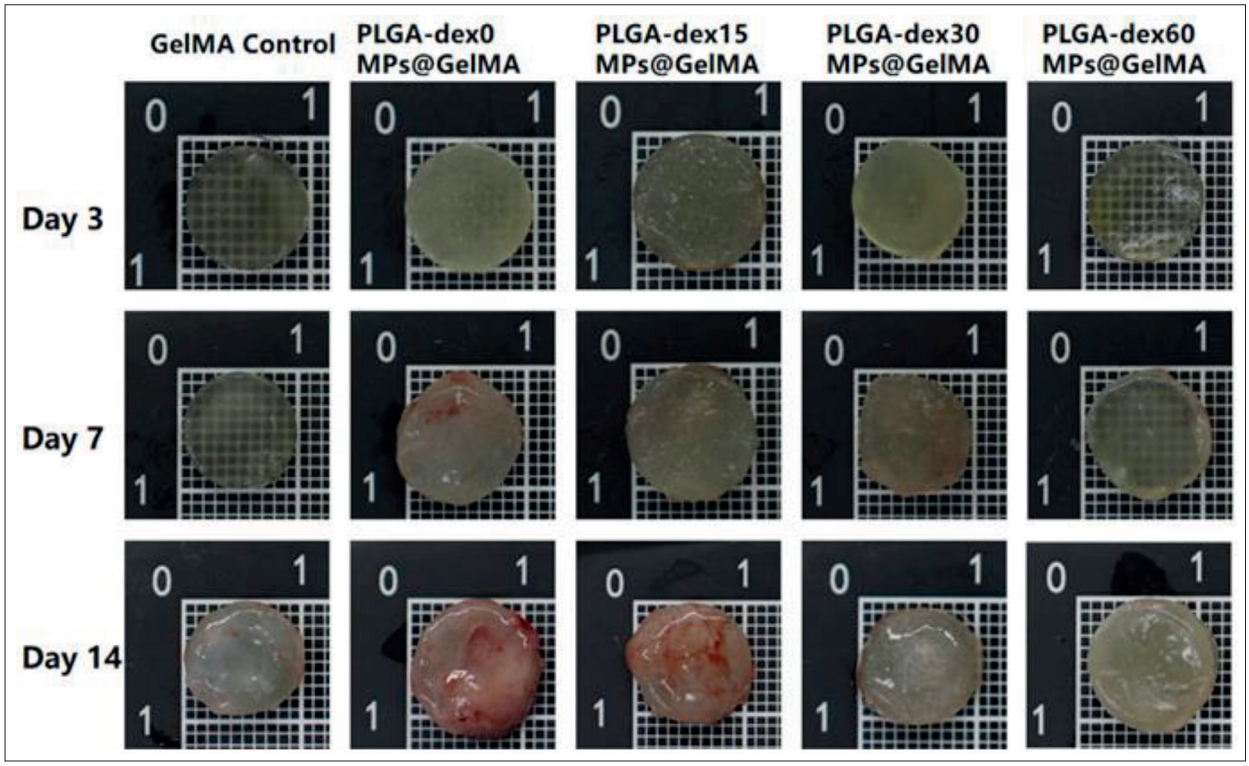


Figure 4. Gross drawings of samples at days 3, 7, and 14 after bioink implantation in C57 mice.

both the GelMA control group and the PLGA-dex60 MPs@GelMA group, the capsules were significantly thicker ($p < 0.0001$). The PLGA-dex60 MPs@GelMA group exhibited the thinnest capsules, with statistical differences compared to all other groups except the GelMA control group.

As illustrated in Figure 5A, the H&E staining results revealed the formation of numerous chondrocyte-like structures within the constructs of the PLGA-dex30 MPs@GelMA group from day 7 onwards. The Alcian blue staining result in Figure 5B showcases the formation of cartilaginous matrix in the regenerated cartilage constructs from day 7 onwards, with matrix secretion increasing with the implantation time. By utilizing ImageJ software, the average optical density (AOD) values of Alcian blue staining were calculated for the respective groups. Remarkably, the PLGA-dex30 MPs@GelMA group exhibited statistically significant differences compared to the other four groups ($p < 0.0001$). By the 14th day, through Alcian blue staining, visibly larger positive areas were observed in the PLGA-dex30 MPs@GelMA group, indicating enhanced cartilaginous matrix secretion. A series of statistical analyses revealed that the positive staining area of PLGA-dex30 MPs@GelMA group was, in general, significantly different compared to the other four groups ($p < 0.0001$).(Figure 5F–H).

3.2.2. Evaluation of anti-inflammatory and cartilage regeneration effects of DEX-loaded PLGA microspheres

In this study, we conducted a fusion approach combining immunohistochemistry and RT-PCR to comprehensively evaluate the anti-inflammatory effects and cartilage regeneration capabilities of DEX-loaded PLGA microspheres in a C57 mouse model.

The immunohistochemical analysis was conducted to investigate the effect of subcutaneous implantation on macrophage polarization toward M1 (CD86+) phenotype at various time points. The PLGA-dex0 MPs@GelMA group had the highest expression of CD86+ and exhibited an increase in both the capsule thickness and CD86+ area as the implantation progressed, as illustrated in Figure 6A. Specific data from day 3 showed significant differences in AOD values between the PLGA-dex30 MPs@GelMA group and both the GelMA control and PLGA-dex15 MPs@GelMA groups ($p < 0.0001$ and $p < 0.05$, respectively), detailed further in Figure 6B–D. By day 7, there were significant differences between the PLGA-dex30 MPs@GelMA group and the PLGA-dex0 MPs@GelMA group ($p < 0.0001$), and no statistical difference was found compared to the PLGA-dex15 MPs@GelMA group ($p > 0.05$). By day 14, capsule thickness analyses revealed

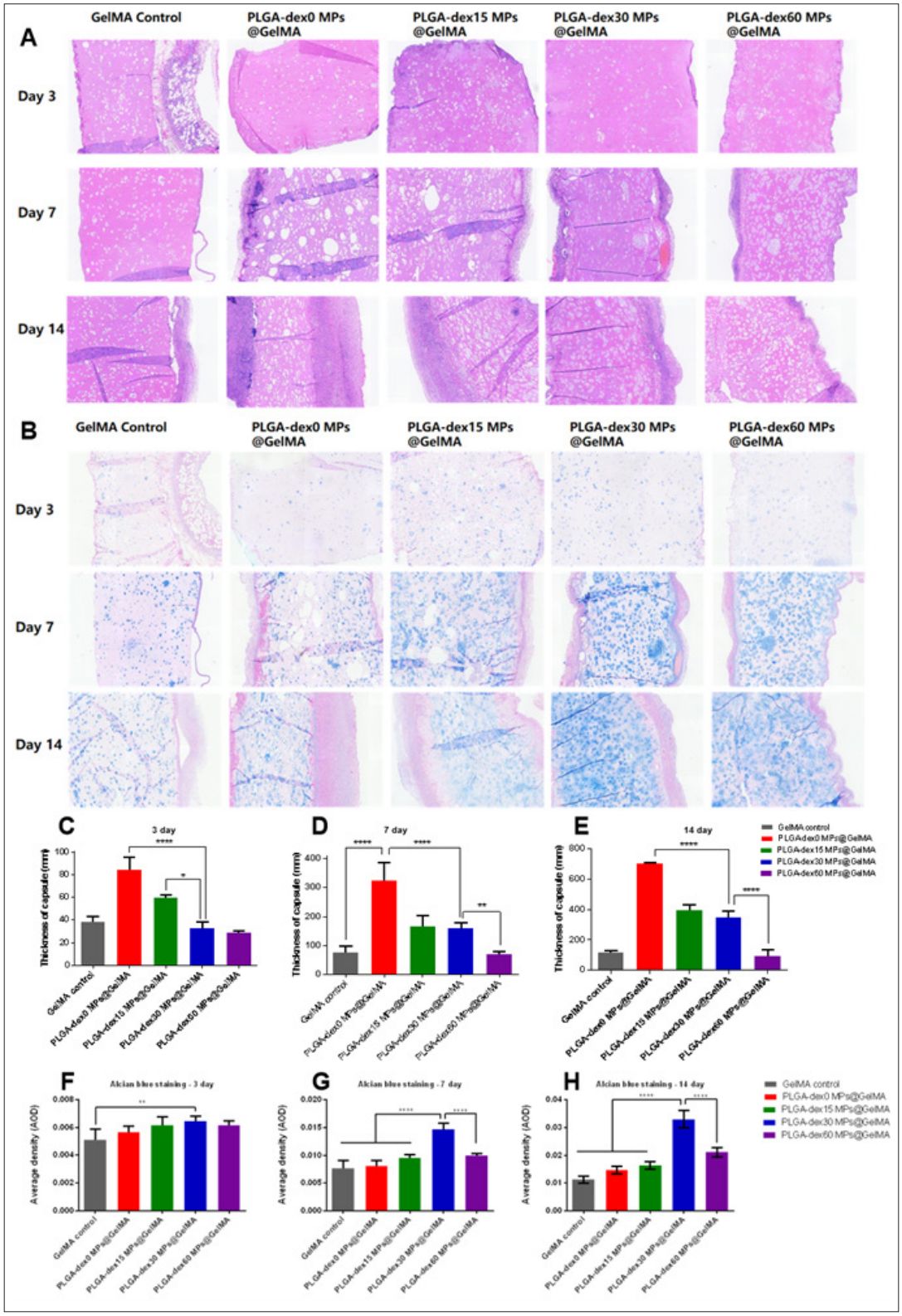


Figure 5. H&E and Alcian blue staining, and statistical analysis of capsule thickness and Alcian blue staining intensity. (A) H&E staining and (B) Alcian blue staining of C57 mouse tissue on days 3, 7, and 14 (n = 5); scale bars: 200 μm. (C–E) Statistics of capsule thickness. (F–H) Statistics of Alcian blue staining intensity.

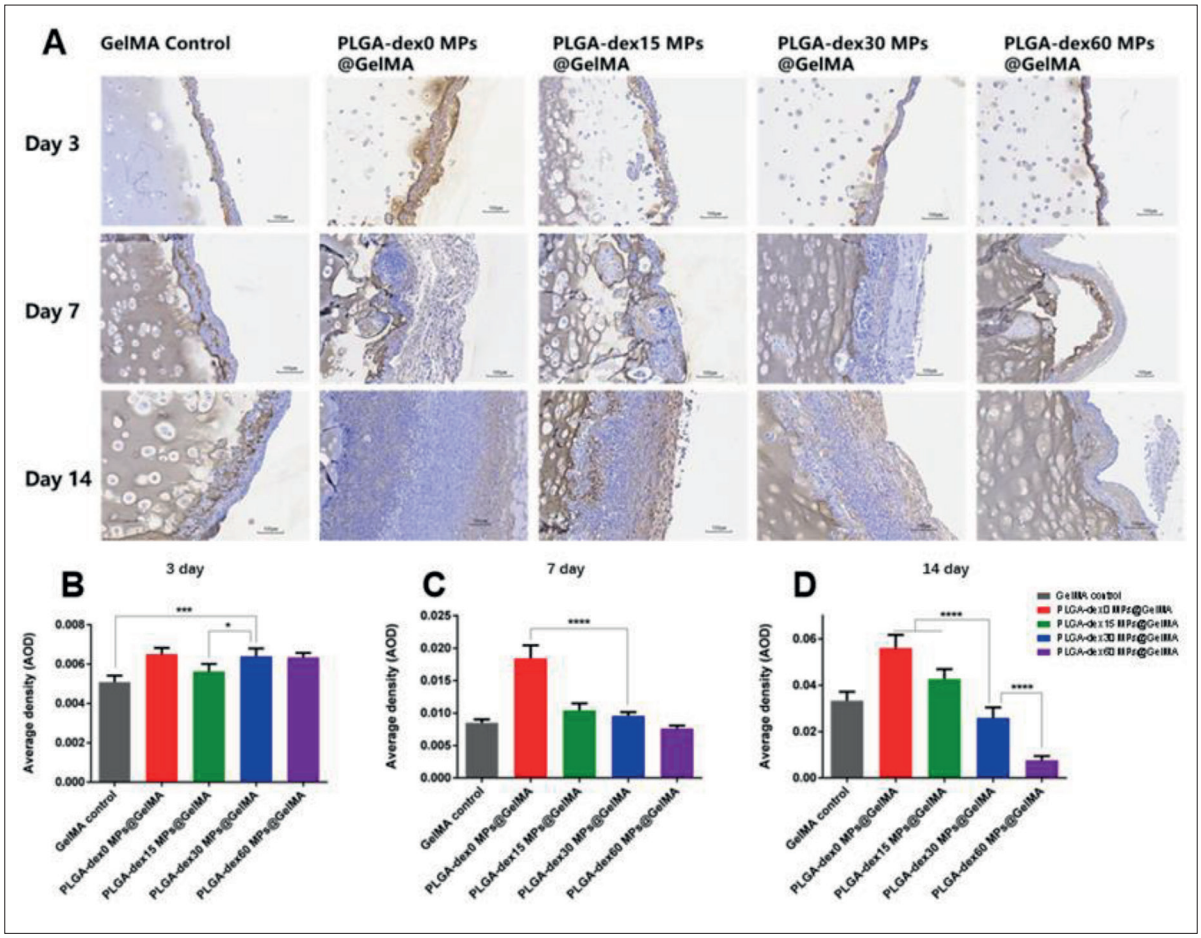


Figure 6. CD86 immunohistochemical analysis reveals time-dependent staining intensity variations across groups. (A) Representative images of CD86 immunohistochemistry in each group at days 3, 7, and 14 (n = 5). (B–D) Statistics of the staining intensity of the positive areas following immunohistochemical staining at days 3, 7, and 14.

significant differences between the PLGA-dex30 MPs@GelMA group and both the PLGA-dex0 MPs@GelMA and PLGA-dex15 MPs@GelMA groups ($p < 0.0001$).

Furthermore, the gene expression analysis, as depicted in Figure 7A–C, highlighted that the PLGA-dex30 MPs@GelMA group exhibited significantly higher expression of cartilage-related genes compared to the other groups, with a correlation observed between increasing DEX concentration and improved cartilage formation capabilities. However, excessively high concentrations may impede chondrocyte regeneration and cartilage matrix accumulation. RT-PCR analysis, as shown in Figure 7D–F, further revealed expression levels of three inflammation-related genes, which decreased as the DEX concentration increased within the DEX-containing groups, with the PLGA-dex60 MPs@GelMA group showing the lowest expression levels. Notably, TNF-α expression displayed a significant difference between the PLGA-dex15 MPs@GelMA group and the PLGA-dex0 MPs@GelMA group ($p < 0.001$), with statistically significant difference from the other two DEX-containing groups.

Through these analyses, the current study not only deepens the understanding of the dual role of DEX-loaded PLGA microspheres in mitigating inflammation and promoting cartilage regeneration but also provides scientific evidence for the application of these materials in 3D-bioprinting tissue-engineered cartilage, attesting to their potential in clinical treatment.

3.2.3. Formation of regenerated cartilage matrix and mechanical testing

The mechanical properties of the regenerated cartilage and their quantitative performance were evaluated using stress–strain curves generated through GraphPad Prism 6.0. A relatively linear region, indicative of the elastic stage of the material, was identified (Figure 8A). To probe the

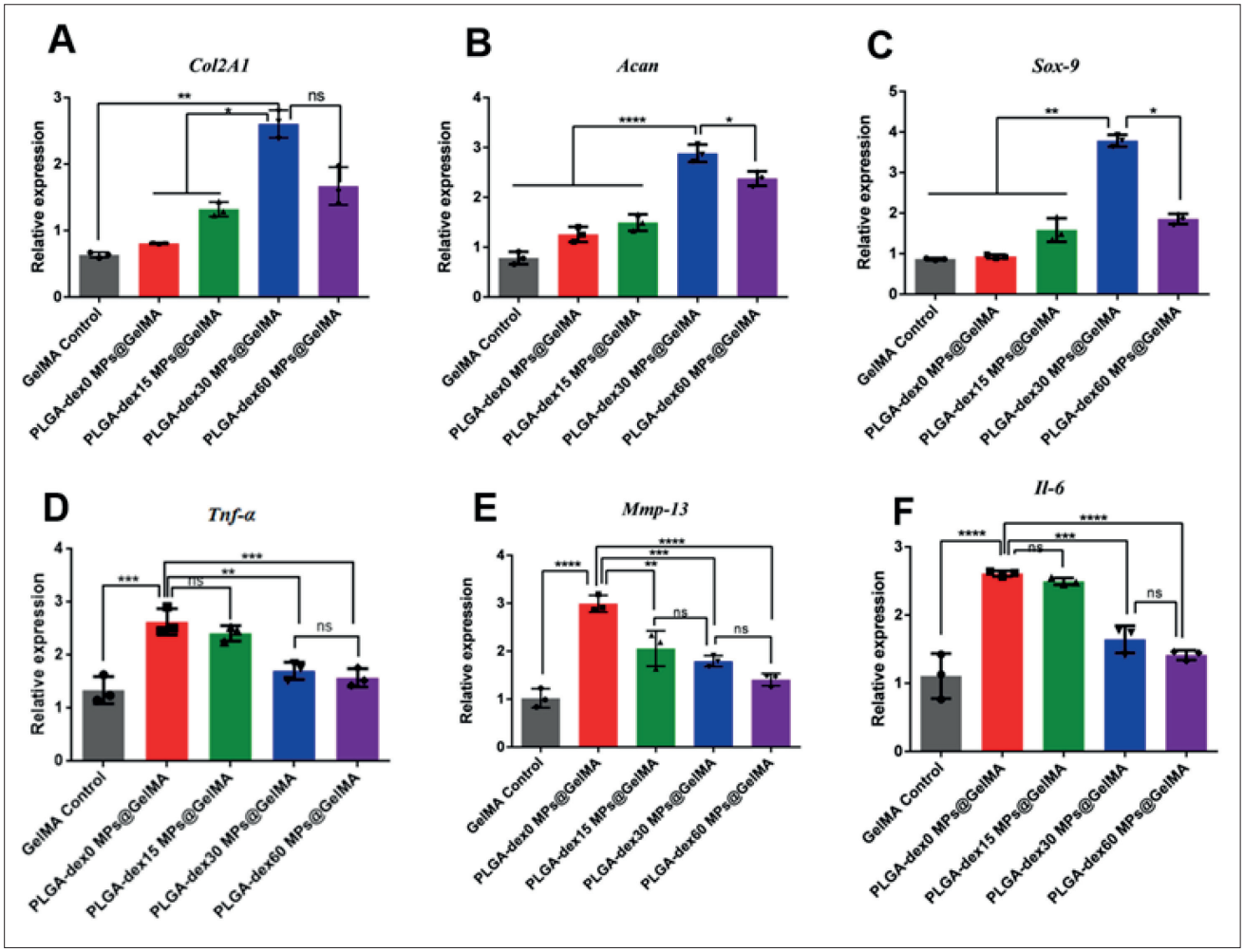


Figure 7. Quantitative gene expression levels of *Col2A1* (A), *Acan* (B), *Sox-9* (C), *Tnf-α* (D), *Mmp-13* (E), and *Il-6* (F) in samples acquired from C57 mice on day 14 after subcutaneous implantation of constructs.

impact of adding MPs on the mechanical properties of the regenerated cartilage, stress–strain curves of various samples were compared on day 14, and the Young's modulus of each group was subjected to statistical analysis. Given the varying degrees of extracellular matrix secretion by chondrocytes, the Young's modulus of the constructs in each group exhibited gradual differences. By day 14, although no statistical difference was observed, the PLGA-dex30 MPs@GelMA group exhibited a trend of higher Young's modulus compared to other groups.

The tissue-engineered cartilage harvested on days 3, 7, and 14 was evaluated for its GAG content (Figure 8B). Statistical analysis of the GAG content on day 3 revealed no significant differences among the groups ($p > 0.05$). However, on day 7, the PLGA-dex30 MPs@GelMA group exhibited a higher GAG content compared to the other four groups, with statistical differences observed only with the PLGA-dex60 MPs@GelMA group ($p < 0.05$). On day 14, statistical analysis indicated that the GAG content of the PLGA-dex30 MPs@GelMA group surpassed that of the other four groups, with statistical differences observed compared to the PLGA-dex0 MPs@GelMA group ($p < 0.05$). These findings suggest that the presence of PLGA MPs can enhance GAG secretion, and significant improvements in GAG content can be achieved by appropriately increasing the DEX concentration on this basis.

3.3. *In vivo* autologous implantation in rabbit

3.3.1. Assessment of printability and selection of bioink

Based on comprehensive *in vivo* evaluations of chondrogenic ability and anti-inflammatory capacity using C57 mice, all groups containing MPs demonstrated enhanced chondrogenic ability compared to the GelMA

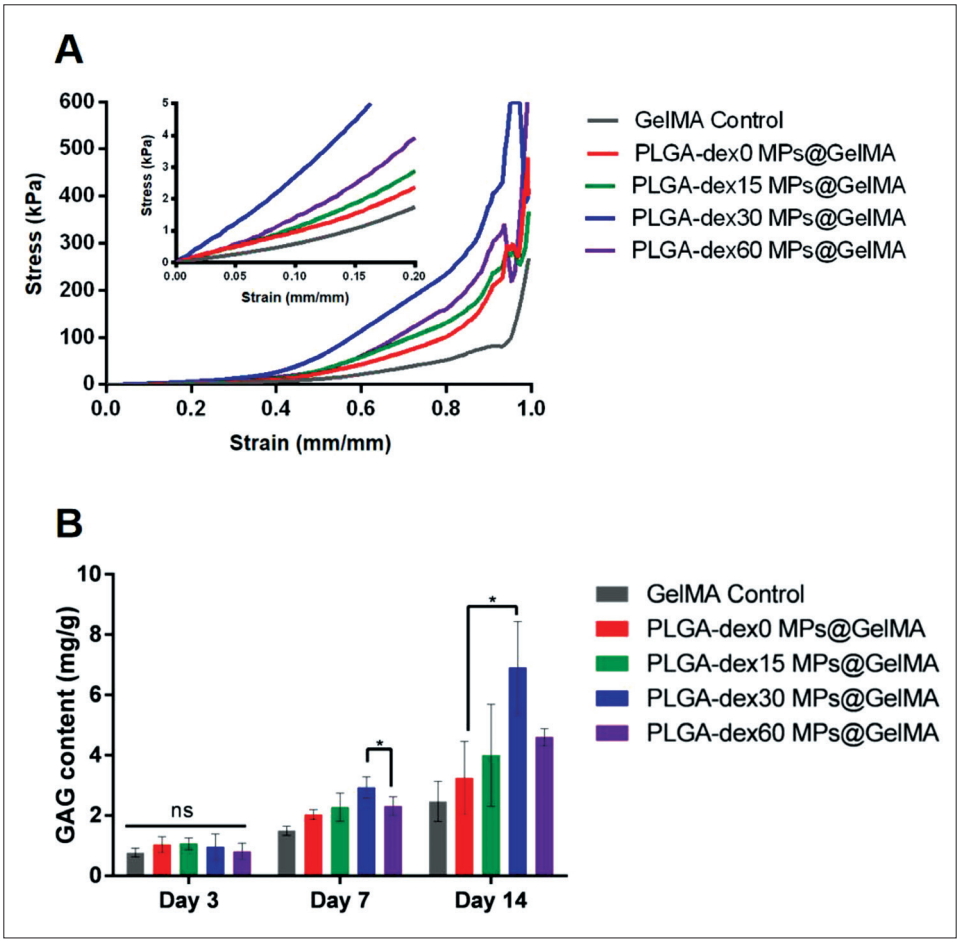


Figure 8. Mechanical and biochemical properties of constructs on day 14, including Young's modulus and glycosaminoglycan (GAG) content. (A) Young's modulus of the five groups of constructs on day 14 (n = 3). (B) Glycosaminoglycan (GAG) content of constructs in each group (n = 3).

control group. Among these four groups, the PLGA-dex30 MPs@GelMA group exhibited the highest chondrogenic ability. Concerning anti-inflammatory capacity, a combined analysis of capsule thickness and inflammation-related RT-PCR results indicated that as the DEX concentration increased, the anti-inflammatory capacity improved. In other words, the PLGA-dex60 MPs@GelMA group demonstrated the strongest anti-inflammatory ability, while the PLGA-dex30 MPs@GelMA group showed a slightly weaker anti-inflammatory ability. Therefore, the PLGA-dex0 MPs@GelMA group was designated as the control, while the PLGA-dex30 MPs@GelMA group served as the experimental group for 3D bioprinting.

To evaluate the printability of each bioink, tests were performed under controlled conditions at a room temperature of 20–22°C. The nozzle temperature was maintained at 19°C, and the platform temperature was set at 23°C. The extrusion pressure was fine-tuned to achieve smooth filament extrusion, by utilizing a 400 μm diameter nozzle. The printability results for the five different bioink groups are depicted and described in Figure S1 (in Supplementary File).

The constructs were evaluated in terms of interlayer adhesion, shape stability, surface smoothness, and structural morphology (Figure 9A). Notably, both groups retained their intended shapes well. After printing six layers, there were no instances of local collapse or deformation within any structure. Interlayer connections remained secure, with no instances of slipping or detachment throughout the printing process.[31–33] Both the PLGA-dex0 MPs@GelMA and PLGA-dex30 MPs@GelMA groups exhibited distinct square cross-sections at the second, fourth, and sixth layers, showcasing more uniform and smoother extrusion lines. The surface of these lines appeared smoother, and the voids within the grid printing structure exhibited more even and regular

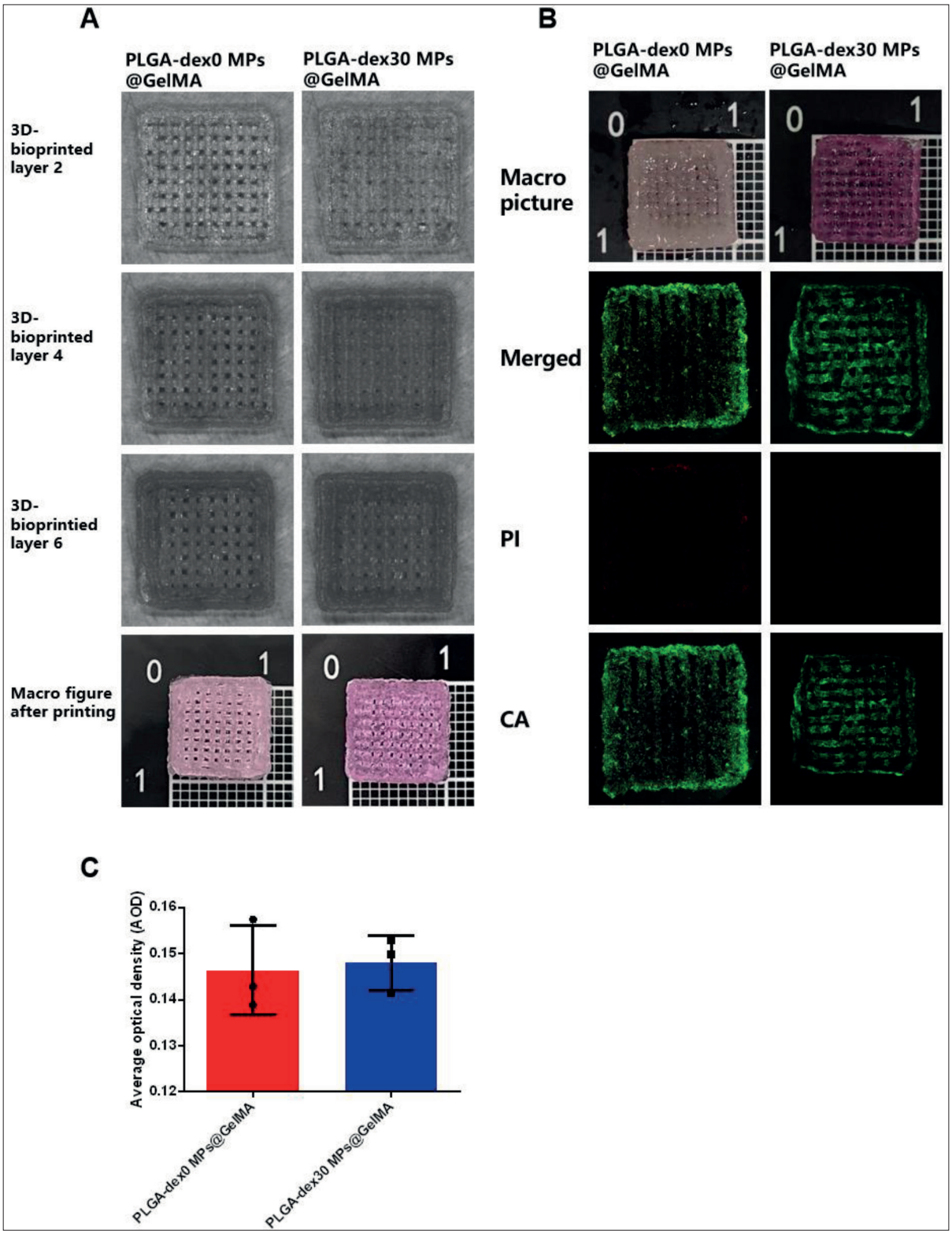


Figure 9. Viability and density analysis of 3D-bioprinted constructs. (A) Images of constructs captured immediately after 3D bioprinting. (B) Calcein AM/PI staining of 3D-printed scaffolds cultured *in vitro* for 24 h (green fluorescence represents live cells; red fluorescence represents dead cells). (C) Statistics of average optical density (AOD) values of live cells (indicated by green fluorescence). Abbreviations: CA, calcein acetoxymethyl (calcein AM); PI, propidium iodide.

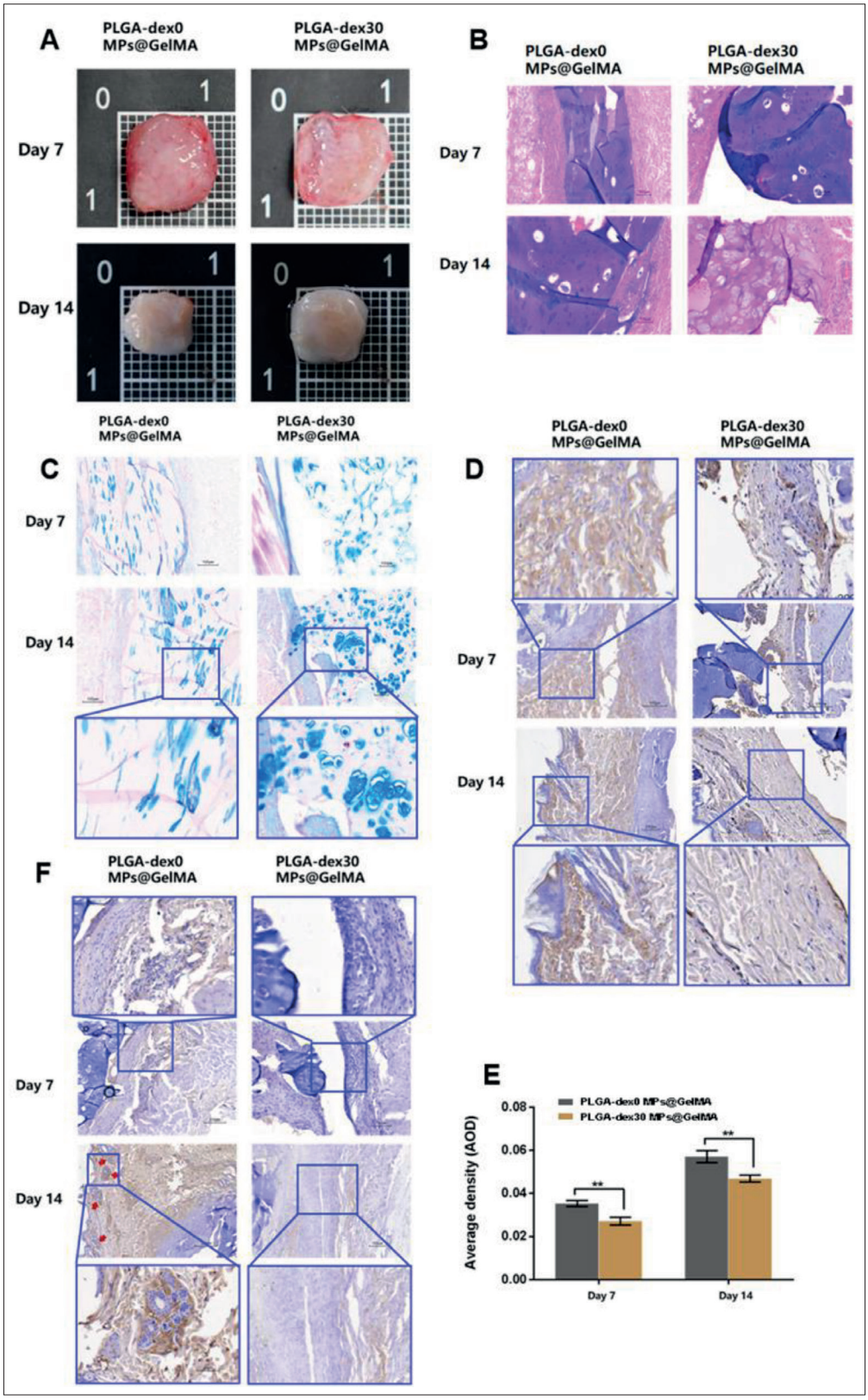


Figure 10. 3D-bioprinted constructs. (A) Gross view of in vivo rabbit samples at days 7 and 14. (B) H&E staining, (C) Alcian blue staining. (D) CD86 immunohistochemical staining. (F) CD31 staining (red arrows indicate CD31-positive areas) of 3D-bioprinted tissue-engineered cartilage. (E) Statistics of intensity of CD86-positive staining area.

distribution, forming more consistent rectangular shapes. Therefore, we conclude that bioinks containing PLGA-dex0 MPs and PLGA-dex30 MPs demonstrate superior printing performance when employed in extrusion-based 3D bioprinting.

3.3.2. Viability staining of 3D-bioprinted constructs

Following an overnight culture of the 3D-bioprinted tissue-engineered constructs, live/dead cell staining was performed. As depicted in Figure 9B, a considerable population of viable cells were evident within the constructs in PLGA-dex0 MPs and PLGA-dex30 MPs groups, with only a minimal presence of dead cells exhibiting red fluorescence. Further details regarding live/dead cell staining following *in vitro* culture for the bioprinting of the two groups of bioinks are provided in Figure S2 (in Supplementary File).

Statistical analysis of the AOD values, which represent the amount of live cells in the two groups (Figure 9C), revealed no significant difference between the groups. No statistically significant differences in fluorescence intensity were observed ($p > 0.05$).

3.3.3. Macroscopic examination of regenerated cartilage

Specimens were examined and photographed at 7 and 14 days post-implantation for macroscopic assessment. As illustrated in Figure 10A, at day 7, both groups displayed evident capsule formation on the surface of the constructs, with minimal volume shrinkage. By day 14, both groups were completely surrounded by capsules, albeit with a noticeable inter-group difference in volume. The PLGA-dex0 MPs@GelMA group exhibited more pronounced shrinkage compared to its initial size, while the PLGA-dex30 MPs@GelMA group maintained a relatively larger volume (Figure 10A).

The macroscopic observation indicates that tissue-engineered cartilage constructs underwent more rapid degradation in the rabbit body compared to in C57 mice. By day 7, significant capsule formation became apparent, and by day 14, the PLGA-dex30 MPs@GelMA constructs exhibited a larger volume compared to the control. This indicates that the sustained release of DEX from PLGA-dex30 MPs slowed down the absorption of capsules by the rabbit body that was in inflammatory condition.

3.3.4. Histological observations

H&E staining consistently revealed pronounced inflammation and necrotic cells surrounding the hydrogel and within the capsule of the PLGA-dex0 MPs@GelMA group starting from day 7. By day 14, there was a noticeable increase in the number of inflammatory cells. In contrast, the PLGA-dex30 MPs@GelMA group showed only a small number of inflammatory cells surrounding the hydrogel and within the capsule on day 7. By day 14, the number of inflammatory cells decreased (Figure 10B). In Figure 10C, Alcian blue dye stained the chondrocytes and the surrounding extracellular matrix in blue. On day 14, the PLGA-dex30 MPs@GelMA group exhibited more chondrocytes, with the largest and most intense staining area surrounding the cartilage matrix, indicating that the PLGA-dex30 MPs@GelMA group possesses higher chondrogenic capacity and drives more rapid chondrocyte maturation compared to the PLGA-dex0 MPs@GelMA group. The presence of medication in the PLGA-dex30 MPs@GelMA bioink resulted in improved chondrocyte activity and the formation of more abundant neo-cartilage, albeit with a weaker vascularization capability. Additionally, **the capsule of group PLGA-dex0 MPs@GelMA** tissue assumed a more orderly arrangement, coupled with a thicker fibrous structure and an apparent inflammatory response. These findings confirm the excellent biocompatibility of PLGA-dex30 MPs@GelMA.

Immunohistochemical staining was conducted to compare the depth of CD86 antibody staining in the capsules of PLGA-dex30 MPs@GelMAand PLGA-dex0 MPs@GelMAgroups (Figure 10D). The results indicated that PLGA-dex30 MPs@GelMA significantly reduced staining depth for M1-type macrophages compared to PLGA-dex0 MPs@GelMA, suggesting that sustained DEX release inhibits M1 cell polarization. In terms of capsule tissue arrangement, PLGA-dex30 MPs@GelMA exhibited a more orderly structure with a dense fibrous matrix, while PLGA-dex0 MPs@GelMA showed thick but disorganized and loose capsules. Quantitative analysis revealed a gradual increase in CD86-positive staining area over time in both groups, with lower intensity observed in PLGA-dex30 MPs@GelMA compared to PLGA-dex0 MPs@GelMA (Figure 10E).

Immunohistochemical staining was conducted to further assess vascularization in the two groups of cartilage tissue engineering constructs (Figure 10F). CD31-positive staining was observed at sites indicated by red arrowheads, exhibiting weaker expression in PLGA-dex30 MPs@GelMA and the strongest expression in the capsule of the PLGA-dex30 MPs@GelMA group. This suggests a significant contribution of DEX to chondrocyte survival and proliferation during tissue regeneration post-implantation of the constructs. To summarize, compared to traditional PLGA MPs carriers, PLGA-dex30 MPs demonstrate superior cellular affinity and confer cell protection, and hold promise for functional tissue

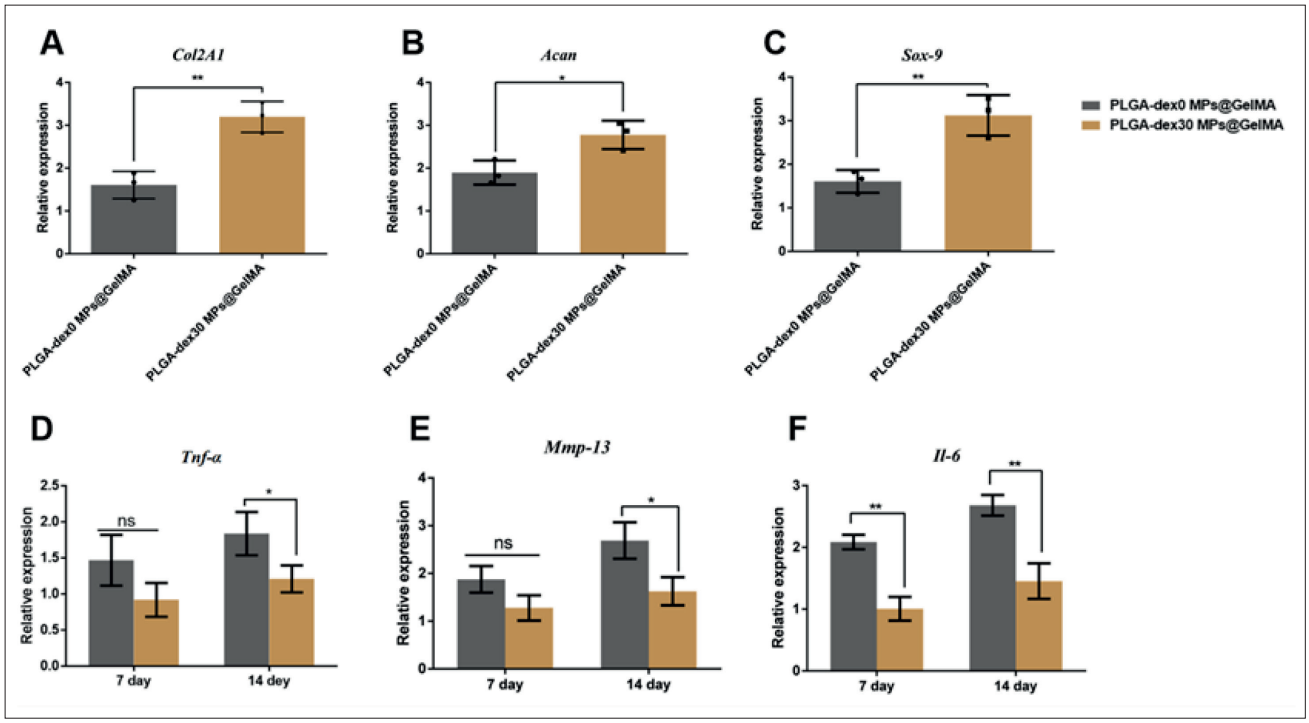


Figure 11. Quantitative gene expression levels of *Sox-9* (A), *Acan* (B), *Col2A1* (C), *Tnf-α* (D), *Il-6* (E), and *Mmp-13* (F) in samples acquired from rabbits on day 14 after subcutaneous implantation of constructs.

regeneration in tissue engineering through drug delivery strategies by PLGA-dex30 MPs.

3.3.5. Expression of cartilage and inflammation-related genes

Samples obtained on day 14 were detected for three chondrogenic genes by means of RT-PCR analysis, as depicted in Figure 11A–C. The relative expression levels of the *Sox-9*, *Acan*, and *Col2a1* were notably higher in the PLGA-dex30 MPs@GelMA group compared to the PLGA-dex0 MPs@GelMA group ($p < 0.01$). Our results also revealed that the scaffolds of the PLGA-dex30 MPs@GelMA group were more capable of maintaining chondrocyte phenotype and promoting cartilage matrix secretion.

Figure 11D–F shows the RT-PCR results for three inflammation-related genes, namely *Il-6*, *Tnf-α*, and *Mmp-13*, in samples collected on both day 7 and day 14. On day 7, the expression of all three inflammatory genes in the PLGA-dex0 MPs@GelMA group surpassed that in the PLGA-dex30 MPs@GelMA group. By day 14, the expression levels of all three inflammatory genes were further elevated compared to day 7, and those in the PLGA-dex0 MPs@GelMA group were notably higher than those in the PLGA-dex30 MPs@GelMA group, indicating statistically significant differences (*Il-6* $P < 0.01$; *Tnf-α* $P < 0.05$; *Mmp-13* $P < 0.05$). The expression of all three inflammation-related genes increased with the implantation time, with the expression levels in the experimental group being lower than those in the control group, aligning with the changes in CD86-positive staining area observed after immunohistochemical staining.

4. Discussion

One of the challenges encountered in tissue engineering of ears is aseptic inflammation triggered by the degradation of high molecular-weight polymers. To tackle this problem, we propose leveraging biodegradable MPs as carriers for sustained drug delivery, given their established utility in tissue engineering.[34–37] In this study, we designed porous PLGA MPs incorporating DEX to enable prolonged release of anti-inflammatory drugs in 3D-bioprinted constructs. The findings of this study underscore the ability of the drug to permeate the constructs, thereby exerting a dual effect of promoting cartilage regeneration and anti-inflammation.

In tissue engineering, synthetic materials such as PCL,[30,38] PLGA,[39] poly-L-lactic acid,[40], etc., are commonly employed to bolster the mechanical integrity of scaffolds. However, the use of synthetic materials often elicits notable

inflammatory responses. In this investigation, GelMA served as the cell-laden material, and it was observed that the addition of PLGA MPs exacerbated the inflammatory response in comparison to the GelMA control group, underscoring the significant contribution of synthetic materials to inflammation. In the study, PLGA was shaped into spherical structures with diameters ranging from 75 to 100 μm to furnish mechanical support. This approach not only reduced the quantity of PLGA employed but also rendered it more suitable for bioink components in 3D bioprinting.

In clinical practice, DEX is typically administered through traditional routes such as intramuscular or intravenous injection. These administration routes have some drawbacks, such as significant fluctuations in drug plasma concentrations. It has been reported that the usual injection frequency of conventional DEX is once daily or every other day to maintain stable pharmacological effects. Dexamethasone exhibits a relatively large pulsatile range in blood plasma concentrations, which often reach peak levels within hours post-injection. According to the literature, peak blood plasma concentrations of DEX can reach up to 2000 ng/mL, which rapidly decline to sub-therapeutic levels within a few hours, leading to patient discomfort and treatment burden.[41–43] In this study, DEX was loaded on PLGA microsphere delivery systems. Considering the principle that a smaller average particle size of MPs leads to a more uniform drug distribution within the MPs and a larger surface area, thereby fostering greater drug dispersion on the MPs surface and increased burst release, and aiming to prevent clogging of the nozzle and achieve better printability in extrusion-based 3D bioprinting, we opted to regulate the particle size of the MPs within the range of 75–100 μm. The results of the *in vitro* release study reveal sustained drug release for a period exceeding 45 days. Superior sustained release capabilities, which enable continuous release of DEX while maintaining therapeutic blood concentrations, can significantly reduce patient discomfort, lower treatment frequency, and enhance treatment convenience and sustainability.[44,45]

The concentration of DEX-loaded MPs is another key factor. The daily release concentrations of the drug-loaded microspheres gradually transitioned from burst release at the beginning of the testing to sustained release over time. Among them, the daily release concentration of PLGA-dex15 MPs ranged from a maximum of 2.9720 μg/mL to a minimum of 0.0087 μg/mL; for the PLGA-dex30 MPs group, the daily release concentration ranged from a maximum of 38.2178 μg/mL to a minimum of 0.3700 μg/mL; and for the PLGA-dex60 MPs group, the daily release concentration ranged from a maximum of 74.0556 μg/mL to a minimum of 0.3700 μg/mL (Figure 3B). Previous studies have indicated that at lower concentrations (0.1–10 nM), DEX can effectively counteract the damage inflicted on cartilage explants by inflammatory cytokines such as TNF-α. At higher concentrations (100 nM to 10μM), it is capable of inhibiting the loss of GAG in chondrocytes and maintaining cellular phenotype stability. This provides a clear biological basis for our selection of different experimental concentration levels.[46,47] Therefore, the gradient concentrations of DEX-loaded porous microspheres were selected based on this rationale. To choose the concentration of DEX, theoretical peak plasma concentration in clinical treatments (7.7 mM) was referenced to ensure that the experimental conditions are relevant to clinical scenarios, thereby enhancing the potential for clinical translation of our findings.[48] The experimental results indicate that all three groups of drug-loaded microspheres possess anti-inflammatory capabilities, and as the concentration of DEX increases, the anti-inflammatory efficacy gradually strengthens. Regarding cartilage formation ability (Figures 4 and 5B), PLGA-dex30 MPs@GelMA group exhibited optimal cartilage formation capability. In this experiment, we set four different DEX concentrations. The results demonstrated that PLGA-dex30 MPs@GelMA group exhibited an optimal balance in terms of drug release efficiency, impact on cell viability, inflammatory response, and cartilage generation capabilities. This concentration of MPs not only ensured effective drug delivery but also optimized the cellular and tissue response to the material, indicating its suitability for 3D printing and tissue engineering applications.

In animal experiments, we subcutaneously implanted rabbit chondrocytes into C57 mice for xenogeneic transplantation and under the rabbit's skin for autologous transplantation. We observed significantly more pronounced inflammatory reactions and evident anti-inflammatory effects of DEX in the xenogeneic transplantation scenario. The initiation of the foreign body inflammatory response typically occurs within a few hours post-contact and may escalate within 24–48 h post-implantation. Studies indicate that the initial 14 days are pivotal for influencing tissue formation outcomes.[49,50] Therefore, our focus was on monitoring the inflammatory response during this critical period. Throughout this time frame, DEX-loaded MPs consistently demonstrated anti-inflammatory effects, characterized by reduced expression of M1 macrophages and lower levels of pro-inflammatory cytokines.[51]

In this study, we chose observation time points at 3, 7, and 14 days primarily to assess early inflammatory responses and anti-inflammatory effects, which are pivotal during the early treatment phase of acute inflammation.[52–54] However, we also acknowledge the significance of long-term effects of tissue-engineered constructs within animal hosts. In subsequent studies, we plan to conduct extended experiments (over 3 months) to comprehensively evaluate the durability and long-term efficacy of the treatment.

As the release of DEX increased within the loaded MPs, we observed a gradual thinning of the capsule, validating the alleviation of inflammatory encapsulation. Simultaneously, the PLGA-dex30 MPs@GelMA group displayed superior capabilities in cartilage regeneration and matrix formation compared to the other two DEX-containing groups. This finding confirmed the maintenance of chondrocyte phenotype and the promotion of chondrocyte proliferation at an optimal DEX concentration. Conversely, excessively high DEX concentrations restricted chondrocyte proliferation, while lower concentrations potentially failed to sufficiently inhibit inflammation, resulting in diminished chondrocyte proliferation capabilities compared to those observed in the PLGA-dex30 MPs@GelMA group.

Several studies have investigated the impact of DEX concentration on tissue formation and anti-inflammatory effects, as well as the application of loaded MPs in various inflammatory conditions. For instance, the PLEL-based MP-gel delivery system (DM/CM/Gel) has been found to effectively suppress joint inflammation while maintaining cartilage integrity.[55] Additionally, a thermosensitive hydrogel (PLEL) containing DEX and resveratrol showed promising therapeutic potential by promoting osteogenesis and alleviating inflammation in osteoporotic bone defects.[56] Digital light processing (DLP)-based bioprinting offers exceptional resolution, speed, and biocompatibility, which make it a promising technique for future applications in cartilage tissue engineering.[57] The combination of human stem cells and synthetic biomaterials in tissue-engineered grafts shows great potential, though it is yet to be widely approved for clinical use.[14] Future experiments can explore the application of DLP bioprinting in cartilage tissue engineering to enhance scaffold precision and biocompatibility.

5. Conclusion

The controlled release of drugs from PLGA MPs in 3D-bioprinted constructs presents a promising strategy for addressing acute inflammation induced by polymer degradation. In this study, we developed MPs composed of PLGA loaded with DEX, with the aim of circumventing the limitations associated with frequent injections or oral administration for *in vivo* drug delivery. This composite hydrogel scaffold, while maintaining mechanical strength, regulated the local inflammatory microenvironment by releasing drug in a sustained manner *in vivo*, thus exhibiting anti-inflammatory effects. The PLGA MPs loaded with DEX exhibited high encapsulation efficiency and sustained release rates over time. Although further validation is needed to assess the long-term anti-inflammatory efficacy and cartilage regeneration potential, the PLGA MPs show promise as a valuable adjunct to cartilage tissue engineering, effectively alleviating inflammation and promoting cartilage regeneration.

Acknowledgments

None

Funding

This work was supported by the Chinese Academy of Medical Sciences Innovation Fund for Medical Sciences (2021-I2M-1-052, 2017-I2M-1-007), and the Natural Science Foundation of China (82371796, 82302832).

Conflict of interest

The authors declare no competing financial interests.

Author contributions

Conceptualization: Zhuoqi Chen, Xia Liu, Qinghua Yang, Haiyue Jiang
Data curation: Zhuoqi Chen, Tian Li, Tianfeng Zheng, Jinshi Zeng
Funding acquisition: Xia Liu, Haiyue Jiang
Investigation: Zhuoqi Chen, Xia Liu, Qinghua Yang
Methodology: Zhuoqi Chen, Jinshi Zeng, Xia Liu
Visualization: Zhuoqi Chen, Xiaowei Yue, Yanjun Feng, Luosha Gu, Yuchen Wang, Yue Ma, Wenshuai Liu
Supervision: Qinghua Yang, Haiyue Jiang
Writing–original draft: Zhuoqi Chen
Writing–review & editing: Xia Liu

Ethics approval and consent to participate

This study was approved by the Ethics Committee of the Plastic Surgery Hospital of the Chinese Academy of Medical Sciences (Approval No: EAEC 2022-007, EAEC-008).

Consent for publication

Not applicable.

Availability of data

The data that used during this study are available from the corresponding author upon reasonable request.

References

1. Wilkes GH, Wong J, Guilfoyle R. Microtia reconstruction. *Plast Reconstr Surg*. 2014;134(3):464e-479e. doi: 10.1097/prs.0000000000000526
2. Griffith LG, Naughton G. Tissue engineering--current challenges and expanding opportunities. *Science*. 2002;295(5557):1009-1014. doi: 10.1126/science.1069210
3. Havla JB, Lotz AS, Richter E, et al. Cartilage tissue engineering for auricular reconstruction: in vitro evaluation of potential genotoxic and cytotoxic effects of scaffold materials. *Toxicol In Vitro*. 2010;24(3):849-853. doi: 10.1016/j.tiv.2009.12.005
4. Di Gesù R, Acharya AP, Jacobs I, Gottardi R. 3D printing for tissue engineering in otolaryngology. *Connect Tissue Res*. 2020;61(2):117-136. doi: 10.1080/03008207.2019.1663837
5. Haudenschild AK, Sherlock BE, Zhou X, et al. Non-destructive detection of matrix stabilization correlates with enhanced mechanical properties of self-assembled articular cartilage. *J Tissue Eng Regen Med*. 2019;13(4):637-648. doi: 10.1002/term.2824
6. Alhattab DM, Khan Z, Alshehri S, Susapto HH, Hauser CAE. 3D bioprinting of ultrashort self-assembling peptides to engineer scaffolds with different matrix stiffness for chondrogenesis. *Int J Bioprint*. 2023;9(4):719. doi: 10.18063/ijb.719
7. Murphy MP, Koepke LS, Lopez MT, et al. Articular cartilage regeneration by activated skeletal stem cells. *Nat Med*. 2020;26(10):1583-1592. doi: 10.1038/s41591-020-1013-2
8. Li M, Yin H, Yan Z, et al. The immune microenvironment in cartilage injury and repair. *Acta Biomater*. 2022;140:23-42. doi: 10.1016/j.actbio.2021.12.006
9. Bonato A, Fisch P, Ponta S, et al. Engineering inflammation-resistant cartilage: bridging gene therapy and tissue engineering. *Adv Healthc Mater*. 2023;12(17):e2202271. doi: 10.1002/adhm.202202271
10. Vahdati A, Zhao Y, Ovaert TC, Wagner DR. Computational investigation of fibrin mechanical and damage properties at the interface between native cartilage and implant. *J Biomech Eng*. 2012;134(11):111004. doi: 10.1115/1.4007748
11. Zhou K, Ding R, Tao X, et al. Peptide-dendrimer-reinforced bioinks for 3D bioprinting of heterogeneous and biomimetic in vitro models. *Acta Biomater*. 2023;169:243-255. doi: 10.1016/j.actbio.2023.08.008
12. Bayindir-Buchhalter I, Göbel U, Stimson L. Biofabrication, biomedical devices, nanomedicine, and tissue engineering – advanced materials in healthcare. *Adv Healthc Mater*. 2018;7(1):1701399. doi: 10.1002/adhm.201701399
13. Liu J, Tagami T, Ozeki T. Fabrication of 3D-printed fish-gelatin-based polymer hydrogel patches for local delivery of PEGylated liposomal doxorubicin. *Mar Drugs*. 2020;18(6):325. doi: 10.3390/md18060325
14. Steijvers E, Ghei A, Xia Z. Manufacturing artificial bone allografts: a perspective. *Biomater Transl*. 2022;3(1):65-80. doi: 10.12336/biomatertransl.2022.01.007
15. Bian L, Stoker AM, Marberry KM, Ateshian GA, Cook JL, Hung CT. Effects of dexamethasone on the functional properties of cartilage explants during long-term culture. *Am J Sports Med*. 2010;38(1):78-85. doi: 10.1177/0363546509354197
16. Stefani RM, Lee AJ, Tan AR, et al. Sustained low-dose dexamethasone delivery via a PLGA microsphere-embedded agarose implant for enhanced osteochondral repair. *Acta Biomater*. 2020;102:326-340. doi: 10.1016/j.actbio.2019.11.052
17. Polderman JA, Farhang-Razi V, Van Dieren S, et al. Adverse side effects of dexamethasone in surgical patients. *Cochrane Database Syst Rev*. 2018;8(8):Cd011940. doi: 10.1002/14651858.CD011940.pub2
18. Polderman JA, Farhang-Razi V, Van Dieren S, et al. Adverse side effects of dexamethasone in surgical patients. *Cochrane Database Syst Rev*. 2018;11(11):CD011940. doi: 10.1002/14651858.CD011940.pub3
19. Salem R, Padia SA, Lam M, et al. Clinical, dosimetric, and reporting considerations for Y-90 glass microspheres in hepatocellular carcinoma: updated 2022 recommendations from an international multidisciplinary working group. *Eur J Nucl Med Mol Imaging*. 2023;50(2):328-343. doi: 10.1007/s00259-022-05956-w
20. Abdel-Rahman O, Elsayed Z. Yttrium-90 microsphere radioembolisation for unresectable hepatocellular carcinoma. *Cochrane Database Syst Rev*. 2020;11(11):Cd011313. doi: 10.1002/14651858.CD011313.pub4
21. Lin X, He J, Li W, et al. Lung-targeting lysostaphin microspheres for methicillin-resistant *Staphylococcus aureus* pneumonia treatment and prevention. *ACS Nano*. 2021;15(10):16625-16641. doi: 10.1021/acsnano.1c06460
22. Kim TK, Yoon JJ, Lee DS, Park TG. Gas foamed open porous biodegradable polymeric microspheres. *Biomaterials*. 2006;27(2):152-159. doi: 10.1016/j.biomaterials.2005.05.081
23. Zhou S, Deng X, Li X. Investigation on a novel core-coated microspheres protein delivery system. *J Control Release*. 2001;75(1-2):27-36.

doi: 10.1016/s0168-3659(01)00379-0

24. Prajapati VD, Jani GK, Kapadia JR. Current knowledge on biodegradable microspheres in drug delivery. *Expert Opin Drug Deliv*. 2015;12(8):1283-1299.
doi: 10.1517/17425247.2015.1015985

25. Wen H, Guo J, Chang B, Yang W. pH-responsive composite microspheres based on magnetic mesoporous silica nanoparticle for drug delivery. *Eur J Pharm Biopharm*. 2013;84(1):91-98.
doi: 10.1016/j.ejpb.2012.11.019

26. Lin TH, Wang HC, Cheng WH, Hsu HC, Yeh ML. Osteochondral tissue regeneration using a tyramine-modified bilayered PLGA scaffold combined with articular chondrocytes in a Porcine model. *Int J Mol Sci*. 2019;20(2):326.
doi: 10.3390/ijms20020326

27. Qian Y, Zhou X, Zhang F, Diekwisch TGH, Luan X, Yang J. Triple PLGA/PCL scaffold modification including silver impregnation, collagen coating, and electrospinning significantly improve biocompatibility, antimicrobial, and osteogenic properties for orofacial tissue regeneration. *ACS Appl Mater Interfaces*. 2019;11(41):37381-37396.
doi: 10.1021/acsami.9b07053

28. Shahverdi M, Seifi S, Akbari A, Mohammadi K, Shamloo A, Movahhedy MR. Melt electrowriting of PLA, PCL, and composite PLA/PCL scaffolds for tissue engineering application. *Sci Rep*. 2022;12(1):19935.
doi: 10.1038/s41598-022-24275-6

29. Hassanajili S, Karami-Pour A, Oryan A, Talaei-Khozani T. Preparation and characterization of PLA/PCL/HA composite scaffolds using indirect 3D printing for bone tissue engineering. *Mater Sci Eng C Mater Biol Appl*. 2019;104:109960.
doi: 10.1016/j.msec.2019.109960

30. Jia L, Hua Y, Zeng J, et al. Bioprinting and regeneration of auricular cartilage using a bioactive bioink based on microporous photocrosslinkable acellular cartilage matrix. *Bioact Mater*. 2022;16:66-81.
doi: 10.1016/j.bioactmat.2022.02.032

31. Lim KS, Galarraga JH, Cui X, Lindberg GCJ, Burdick JA, Woodfield TBF. Fundamentals and applications of photo-cross-linking in bioprinting. *Chem Rev*. 2020;120(19):10662-10694.
doi: 10.1021/acs.chemrev.9b00812

32. Kim SH, Hong H, Ajiteru O, et al. 3D bioprinted silk fibroin hydrogels for tissue engineering. *Nat Protoc*. 2021;16(12):5484-5532.
doi: 10.1038/s41596-021-00622-1

33. Gillispie G, Prim P, Copus J, et al. Assessment methodologies for extrusion-based bioink printability. *Biofabrication*. 2020;12(2):022003.
doi: 10.1088/1758-5090/ab6f0d

34. Jin S, Xia X, Huang J, et al. Recent advances in PLGA-based biomaterials for bone tissue regeneration. *Acta Biomater*. 2021;127:56-79.
doi: 10.1016/j.actbio.2021.03.067

35. Park K. Tolerance levels of PLGA microspheres in the eyes. *J Control Release*. 2017;266:365.
doi: 10.1016/j.jconrel.2017.11.010

36. Jain H, Bairagi A, Srivastava S, Singh SB, Mehra NK. Recent advances in the development of microparticles for pulmonary administration. *Drug Discov Today*. 2020;25(10):1865-1872.
doi: 10.1016/j.drudis.2020.07.018

37. Bian J, Cai F, Chen H, et al. Modulation of local overactive inflammation via injectable hydrogel microspheres. *Nano Lett*. 2021;21(6):2690-2698.
doi: 10.1021/acs.nanolett.0c04713

38. Park JY, Ryu H, Lee B, et al. Development of a functional airway-on-a-chip by 3D cell printing. *Biofabrication*. 2018;11(1):015002.
doi: 10.1088/1758-5090/aae545

39. Long J, Yao Z, Zhang W, et al. Regulation of osteoimmune microenvironment and osteogenesis by 3D-printed PLAG/black phosphorus scaffolds for bone regeneration. *Adv Sci (Weinh)*. 2023;10(28):e2302539.
doi: 10.1002/advs.202302539

40. Yang F, Niu X, Gu X, Xu C, Wang W, Fan Y. Biodegradable magnesium-incorporated poly(l-lactic acid) microspheres for manipulation of drug release and alleviation of inflammatory response. *ACS Appl Mater Interfaces*. 2019;11(26):23546-23557.
doi: 10.1021/acsami.9b03766

41. Aymard G, Warot D, Démolis P, et al. Comparative pharmacokinetics and pharmacodynamics of intravenous and oral Nefopam in healthy volunteers*. *Pharmacol Toxicol*. 2003;92(6):279-286.
doi: 10.1034/j.1600-0773.2003.920605.x

42. Loew D, Schuster O, Graul EH. Dose-dependent pharmacokinetics of dexamethasone. *Eur J Clin Pharmacol*. 1986;30(2):225-230.
doi: 10.1007/bf00614309

43. Yang J, Wu H, Zhang P, Hou DM, Chen J, Zhang SG. The pharmacokinetic profiles of dexamethasone and methylprednisolone concentration in perilymph and plasma following systemic and local administration. *Acta Otolaryngol*. 2008;128(5):496-504.
doi: 10.1080/00016480701558906

44. Wang H, Zhao P, Su W, et al. PLGA/polymeric liposome for targeted drug and gene co-delivery. *Biomaterials*. 2010;31(33):8741-8748.
doi: 10.1016/j.biomaterials.2010.07.082

45. Jin L, Pan Y, Pham AC, Boyd BJ, Norton RS, Nicolazzo JA. Prolonged plasma exposure of the Kv1.3-inhibitory

peptide HsTX1[R14A] by subcutaneous administration of a poly(Lactic-co-Glycolic Acid) (PLGA) microsphere formulation. *J Pharm Sci*. 2021;110(3):1182-1188.
doi: 10.1016/j.xphs.2020.10.014

46. Kato Y, Gospodarowicz D. Stimulation by glucocorticoid of the synthesis of cartilage-matrix proteoglycans produced by rabbit costal chondrocytes in vitro. *J Biol Chem*. 1985;260(4):2364-2373.

47. Lu YC, Evans CH, Grodzinsky AJ. Effects of short-term glucocorticoid treatment on changes in cartilage matrix degradation and chondrocyte gene expression induced by mechanical injury and inflammatory cytokines. *Arthritis Res Ther*. 2011;13(5):R142.
doi: 10.1186/ar3456

48. Cardone DA, Tallia AF. Joint and soft tissue injection. *Am Fam Physician*. 2002;66(2):283-289.

49. Li D, Guo G, Fan R, et al. PLA/F68/dexamethasone implants prepared by hot-melt extrusion for controlled release of anti-inflammatory drug to implantable medical devices: I. Preparation, characterization and hydrolytic degradation study. *Int J Pharm*. 2013;441(1-2): 365-372.
doi: 10.1016/j.ijpharm.2012.11.019

50. Kagaya F, Usui T, Kamiya K, et al. Intraocular dexamethasone delivery system for corneal transplantation in an animal model. *Cornea*. 2002;21(2):200-202.
doi: 10.1097/00003226-200203000-00015

51. Caratti G, Desgeorges T, Juban G, et al. Macrophagic AMPKα1 orchestrates regenerative inflammation induced by glucocorticoids. *EMBO Rep*. 2023;24(2):e55363.
doi: 10.15252/embr.202255363

52. Agarwal R, García AJ. Biomaterial strategies for engineering implants for enhanced osseointegration and bone repair. *Adv Drug Deliv Rev*. 2015;94:53-62.
doi: 10.1016/j.addr.2015.03.013

53. Tsiapla AR, Karagkiozaki V, Bakola V, et al. Biomimetic and biodegradable cellulose acetate scaffolds loaded with dexamethasone for bone implants. *Beilstein J Nanotechnol*. 2018;9:1986-1994.
doi: 10.3762/bjnano.9.189

54. Yoo BW, Kong YT, Chae SW, Kim KN, Song B, Kim J. Comparison of the characteristics of three acellular dermal matrices subjected to distinct processing methods using five types of histochemical staining. *Aesthetic Plast Surg*. 2023;47(4):1315-1323.
doi: 10.1007/s00266-023-03318-x

55. Fang W, Yang F, Li W, et al. Dexamethasone microspheres and celecoxib microcrystals loaded into injectable gels for enhanced knee osteoarthritis therapy. *Int J Pharm*. 2022;622:121802.
doi: 10.1016/j.ijpharm.2022.121802

56. Li J, Li L, Wu T, et al. An injectable thermosensitive hydrogel containing resveratrol and dexamethasone-loaded carbonated hydroxyapatite microspheres for the regeneration of osteoporotic bone defects. *Small Methods*. 2024;8(1):e2300843.
doi: 10.1002/smtd.202300843

57. Ren X, Wang J, Wu Y, et al. One-pot synthesis of hydroxyapatite hybrid bioinks for digital light processing 3D printing in bone regeneration. *J Mater Sci Technol*. 2024;188:84-97.
doi: 10.1016/j.jmst.2024.01.001

ACCSCIENCE PUBLISHING

International Journal of Bioprinting

RESEARCH ARTICLE

The effect of manufacturing method; direct compression, hot-melt extrusion, and 3D printing on polymer stability and drug release from polyethylene oxide tablets

Nour Nashed[1], Barnaby W. Greenland[1], Mridul Majumder[2], Matthew Lam[1,3], Taravat Ghafourian[4], and Ali Nokhodchi[1,5*]

[1] Arundel Building, School of Life Sciences, University of Sussex, Brighton, United Kingdom

[2] M2M Pharmaceuticals Ltd., Reading, United Kingdom

[3] Department of Chemical and Pharmaceutical Sciences, School of Human Sciences, London Metropolitan University, London, United Kingdom

[4] Barry and Judy Silverman College of Pharmacy, Nova Southeastern University, Ft. Lauderdale, Florida, United States of America

[5] Lupin Research Inc., Coral Spring, Florida, United States of America

Abstract

Thermal 3D printing has gained substantial attention in pharmaceutical formulation, especially concerning its potential use in personalized dose delivery. The choice of a printable polymer is crucial in this technique, but it is restricted due to technical issues such as thermal stability and thermal-rheological properties of the polymers. Polyethylene oxide (PEO) is a widely used polymer in drug formulation designs, with potential application in 3D printing due to its favorable rheological properties. However, the thermal stability of PEOs exposed to high temperatures during fused deposition modeling (FDM) needs to be characterized. This research focused on the characterization of two molecular weights (M_w) of PEO (7 and 0.9 M) under various manufacturing methods and formulation compositions. PEO was mixed with other low-viscosity polymers of hydroxypropyl cellulose (HPC) or ethyl cellulose (EC) to achieve printable formulations (PEO/HPC or PEO/EC). Tablets were manufactured by direct compression, compression of hot-melt extrudates (HME) at 150°, or by FDM 3D-printing at 220°. Differential scanning calorimetry (DSC), X-ray powder diffraction (XRPD), gel permeation chromatography (GPC), dissolution tests, and their kinetics studies were carried out. Results demonstrated that thermal processes could reduce the crystallinity of PEO and induce M_w reduction that varies depending on the M_w of PEO. As a result, dissolution efficiency (DE%) varied based on the formulation composition and manufacturing method. For formulations containing PEO and HPC, 3D-printed and HME tablets exhibited higher DE (>60%) compared to directly compressed tablets (DE < 50%), while for those with PEO and EC, 3D printing reduced DE% to <26% compared to direct compression (~30%) and HME tablets (~50%). This was attributed to the hydrophobic nature of EC and the increased hardness of the printed tablets, preventing tablet disintegration during dissolution, which outweighs the M_w reduction in PEO.

Keywords: Manufacturing method; Hot-melt extrusion; Polyethylene oxide; 3D printing; Molecular weight; Thermal stability

***Corresponding author:**
Ali Nokhodchi
(a.nokhodchi@sussex.ac.uk)

Citation: Nashed N, Greenland BW, Majumder M, Lam M, Ghafourian T, Nokhodchi A. The effect of manufacturing method; direct compression, hot-melt extrusion, and 3D printing on polymer stability and drug release from polyethylene oxide tablets. *Int J Bioprint*. 2024;10(5):4055. doi: 10.36922/ijb.4055

Received: June 27, 2024
Revised: July 31, 2024
Accepted: August 2, 2024
Published Online: August 5, 2024

Copyright: © 2024 Author(s). This is an Open Access article distributed under the terms of the Creative Commons Attribution License, permitting distribution, and reproduction in any medium, provided the original work is properly cited.

Publisher's Note: AccScience Publishing remains neutral with regard to jurisdictional claims in published maps and institutional affiliations.

1. Introduction

Polyethylene oxide (PEO) is a synthetic non-ionic hydrophilic polymer considered non-toxic in humans. It is readily available in a wide range of molecular weights (M_w) up to 7 M. The M_w of the polymer used in the formulation can be selected to give a desired release profile with lower M_w typically used for rapid drug release since they dissolve quickly in water.[1,2] Conversely, the higher M_w PEOs (>0.3 M) are used in slow drug release systems.[1,2] In these instances, the PEO is known to swell in water, forming a hydrogel layer with increasing strength and thickness as M_w increases, thereby resulting in a slower drug release profile.[3,4]

Polyethylene oxide (PEO) degradation has been reported to occur at elevated temperatures in the presence of oxygen through a scission of the chemical bond between two carbon atoms, as well as the carbon-oxygen bonds, giving smaller fragments.[5] As a result, the M_w of PEO can decrease, which in turn reduces its viscosity.[1,2] Additionally, the crystallinity of PEO is dependent on its thermal history; specifically cooling rapidly from above its melting point (~70°) can result in a low level of crystallinity in the product, which dramatically affects its solid-state properties.[3,6] This reduction in M_w and crystallinity during high-temperature processing, such as that encountered during hot melt extrusion (HME), is known to increase the drug release rates in formulated tablets.[1,3,7] Thus, it is challenging to maintain the desired extended-release behavior of high M_w PEO (≥0.9 M) formulations when processed at elevated temperatures. Changes in M_w and crystallinity, and the resulting change in gelling behavior, are considered more pronounced when M_w of PEO is increased. For example, under the same storage conditions (40°), there was a more significant drop in the viscosity of PEO 7 M, hence a greater increase in drug release rate, compared to PEO 4 M.[8,9]

Based on thermogravimetric analysis (TGA) studies, Vrandečić et al. found that the degradation of PEO occurs within the temperature range of 330–450°, independent of its M_w. It was also noted that the heating rate had a mixed impact on degradation rates of low and high M_w PEOs; high M_w PEOs (1 and 5 M) degraded faster than low M_w PEOs (100 and 300 k) during rapid heating, while the pattern is inverse during slow heating rate.[10] Conversely, crystalline regions of PEO, which are more prevalent in high M_w PEO samples, appear to have better resistance to degradation than amorphous regions.[10] This may explain the lower stability of low M_w PEOs compared with high M_w PEOs.[6,9] Despite the aforementioned potential liabilities, PEO has been successfully processed by thermal methods (HME and injection molding [IM]) for drug delivery. For example, low M_w PEOs (<300 k) exhibit good stability under temperatures as high as 140° during IM,[3] consistent with an earlier study of PEO for industrial applications where thermoplastic processing was recommended to be carried out at temperatures below 130°.[11]

In contrast, high M_w PEOs (>1 M) displayed a reduction in M_w when processed in a single screw extruder under elevated temperatures (100–170°) and short residence time (2–3 min).[6,12] In HME, PEO is subjected to both mechanical and thermal stresses;[6] thus, extruder configuration can impact the degradation process. In a recent study, formulations containing PEO (7 M) were processed in a twin screw extruder at 130°, which resulted in significant degradation, leading to reduced viscosity and accelerated drug release compared to unstressed formulations.[1] Accordingly, another study indicated that an increase in the M_w of PEO from 100 to 900 k delayed the drug release rate from HME extrudates as expected. Still, no significant extension in drug release time was achieved by further increasing the M_w from 0.9 M up to 7 M.[13] This can be interpreted as a sign of degradation of the high M_w PEO (0.9–7 M) during extrusion.

In practical terms, the high viscosity of molten high M_w PEO (≥0.9 M) can hinder its printability in fused deposition modeling (FDM).[14] Thus, a mixture of high M_w PEOs with other polymers can be used to reduce the melt viscosity and facilitate its printability. In this case, flexible polymers, such as low M_w polyethylene glycol (PEG), can protect PEO during extrusion and printing.[14,15] Given the potential for PEO application in controlled-release drug formulation designs, its complicated behavior under high-temperature processing conditions, and the limited study on the M_w stability of 3D printed formulations containing PEO, the current study aimed to investigate (i) the impact of PEO M_w on its stability when mixed with other polymers; (ii) stability of PEO after dual thermal processing, i.e., HME followed by FDM printing of tablets; and (iii) the impact of PEO stability on physical properties and drug release from the manufactured tablets. Two M_w of PEO (0.9 and 7 M) were investigated under various processing conditions and in combination with hydroxypropyl cellulose (HPC) and ethyl cellulose (EC). Since theophylline is a thermostable drug, it was selected as the model drug for this study to minimize the effect of drug degradation on formulation characterization. Tablets from thermal processes, such as HME and FDM, were compared with milder, non-thermal processes, such as direct compression of a physical mixture of powders.

2. Materials and methods

2.1. Materials

Theophylline anhydrous (purity: >99%) was purchased from Fisher Scientific (United Kingdom, UK) and used as a model drug with a high melting point around 273°.

Low-viscosity HPC (M_w: ~95 k; Kucel™ EF) was provided by Ashland Inc. (Netherlands). Dibutyl sebacate (DBS) was supplied by Sigma-Aldrich (United States of America [USA]). EC (M_w: ~23 k, Ethocel 10 FP) and PEO (M_w: 7 M, POLYOX WSR 303; and M_w: 0.9 M, POLYOX WSR 1105) were obtained from Colorcon Ltd. (UK) as a gift.

2.2. Formulation development

Preliminary observation revealed that formulations solely containing PEO and theophylline were not printable because of the high melt viscosity of PEO (M_w: 0.9 and 7 M). Therefore, a mixture with other polymers was needed to produce printable PEO formulations (Table 1). Since the study focuses on the thermal stability of PEO, thermally stable polymers (HPC and EC)[16] were selected to be mixed with PEO. Theophylline percentage was kept constant (30% [w/w]) in all the developed formulations (see compositions in Table 1). In formulations containing EC (F_3 and F_4), a plasticizer (DBS) was also added to improve printability and reduce the brittleness of EC. DBS was added to EC powder at 13% (w/w) of EC weight (equivalent to 5.2% of the total formulation), mixed thoroughly, and left overnight for better sorption of the liquid plasticizer to the EC chains. Thereafter, the plasticized EC was ready to use in making formulations F_3 and F_4.

All studied formulations (F_1–F_4) were prepared into tablets by three distinct methods: direct compression of the physical mixture (PM), compression of HME extrudates, and 3D printing. All tablets were then studied for dissolution and other physical characteristics.

2.3. Tablet preparation

Tablets were prepared via three different methods: direct compression of PM, compression of powders prepared from HME, and 3D printing of HME filaments (via FDM). The manufactured tablets were stored in enclosed vials in a chamber at room temperature (22 ± 2°) and tested for dissolution within a week.

2.3.1. Physical mixture tablets

Using the formulation compositions mentioned in Table 1, the powders were mixed using mortar and pestle (approximately for 5 min). The powder blend was compressed into a tablet of 333.3 mg with a hydraulic manual tableting press (Model MTCM-I; Globe Pharma, USA), equipped with 10 mm diameter concave punches. The employed pressure was 150 bar, and the dwell time was constant at 10 s.

2.3.2. Hot-melt extrudate tablets

The physical admixture was fed manually at (an average of) 1 g/min into a 10-mm twin-screw extruder L/D 20 (assembled by Point1 Controls/R Controls; Stoke-on-Trent, UK) at a screw speed of 50 rpm. The temperature of the feed zone was set at 130°, and the temperature for the rest of the zones (including the die) was set at 140°. Although this temperature exceeds the melting temperature (T_m) of PEO (73°), it was necessary to exceed the glass transition temperature (T_g) of HPC and EC mixed with PEO. Additionally, PEO was processed at high temperatures above its T_m to investigate (i) the impact of temperature and compare the results with other similar studies[12,15,17] and (ii) the effect of thermal process conditions on PEO stability and drug release. Filaments were collected manually using a winder. After collecting and cooling, the filaments were cut manually into small pieces around 2 mm in length using a pair of scissors. Then, 5 g of the resulting samples were transferred to a ball mill (PM 100; Retsch GmbH, Germany) and ground for 4 min at 400 rpm. The ground powders were collected from the ball mill and kept in tightly closed containers at room temperature. The powders were compressed into tablets using a hydraulic manual tableting press (Model MTCM-I; Globe Pharma, USA) equipped with 10 mm diameter concave punches. Compression was carried out at 150 bar with a 10-s dwell time. The nominal weight of each tablet was 333.3 mg, equivalent to 100 mg of theophylline.

2.3.3. Printed tablets

Filaments were prepared using HME, as mentioned earlier. The diameter of the filaments is crucial as the filaments should fit into the feeding nozzle of the FDM printer, which has a diameter of 1.75 mm. The diameter of the filaments was measured using a vernier caliper, and only filaments with a diameter ranging between 1.7 and 1.8

Table 1. Composition of studied formulations.

Formulation	Composition (%)					
	Theophylline	PEO (7 M)	PEO (0.9 M)	HPC	EC	DBS
F_1	30	30	—	40	—	—
F_2	30	—	30	40	—	—
F_3	30	30	—	—	40	5.2
F_4	30	—	30	—	40	5.2

Abbreviations: PEO: Polyethylene oxide; HPC: Hydroxypropyl cellulose; EC: Ethyl cellulose; DBS: Dibutyl sebacate.

mm were selected for printing tablets. The computer-aided design (CAD) model of a cylindrical tablet was designed online using Tinker CAD and then exported as an STL file, which was imported to the software Makerbot Replicator 2X printer (Makerbot Inc., USA). Printed tablets had a height of 4.5 mm and a diameter of 9.5 mm. Based on the preliminary experiments, those dimensions were selected (i) to get the same tablet weights as those prepared by other methods (333.3 mg) and (ii) to get a similar surface area (SA)/volume (V) ratio as other tablets (0.8 mm^{-1}). This enables a more accurate comparison, as weight and SA/V can have an impact on drug release profiles. Printing settings were as follows: layer height: 0.2 mm; infill density: 100%; number of shells: 2; printing speed: 90 mm/s; bed temperature: 50°; and nozzle temperature: 220°.

2.4. Differential scanning calorimetry

The solid-state and thermal behavior of raw materials and formulations was investigated using differential scanning calorimetry (DSC) 4000 system (Perkin Elmer, USA). It was used to determine the T_m and T_g of EC and HPC, as well as the T_m of PEO, theophylline, and each of the formulations. Approximately 6 mg of each material or formulation was placed into crucible aluminum pans, and samples were scanned from 25 to 300°, encompassing the high temperatures used in HME and printing methods. The samples were scanned at a scanning rate of 10°/min with nitrogen purging at a flow rate of 20 mL/min. The obtained DSC traces were analyzed using Pyris software (Perkin Elmer, USA).

2.5. X-ray powder diffraction

To investigate the effect of extrusion and 3D printing on the crystallinity of the formulations, X-ray powder diffraction (XRPD) patterns of theophylline, PEO, EC, HPC, PM tablets, HME tablets, and FDM tablets were determined using a Siemens D500 X-ray diffractometer (Siemens, Germany) with copper radiofrequency (Rf) radiation at 40 kV voltage and 30 mA. Data were recorded at 2θ of 5–50° at a step width of 0.01° and 1 s time count. XRPD samples are preferably in powder form, which was possible for PM and HME samples. However, 3D-printed tablets were too hard to grind; thus, thin films were printed, followed by manual grinding using a pestle and mortar to achieve finer samples. Peak intensity is an arbitrary factor in this study since tested samples were varied in their weight and particle size; thus, diffractograms were compared for any changes in peak shape, position, and broadening to assess crystallinity.

2.6. Gel permeation chromatography

Gel permeation chromatography (GPC) was run in a 1260 Infinity GPC system (Agilent, UK) equipped with a refractive index detector. Samples for GPC were prepared in 1 mg/mL solutions by dissolving formulation powders in dimethyl formamide (DMF) containing 5 mM NH_4BF_4 and 0.25/100 mL of toluene at 40° for 30 min. In-house experiments revealed that samples were not dissolved by stirring over 24 h at room temperature (25 ± 2°). Thus, heating was essential to achieve complete solubility when preparing the samples. Thereafter, 100 µL of the sample was injected into a PLgel 5 µm guard column (50 × 7.5 mm), followed by two PLgel 5 µm MIXED-D (300 × 7.5 mm) columns at 60°. The mobile phase was DMF containing 5 mM NH_4BF_4 at a flow rate of 1 mL/min. Despite the protocol being developed in-house, it is relatively similar to other protocols where DMF and gentle heating were used with PEO samples.[18,19]

As the aim was to find the impact of different processing conditions on PEO M_w, a comparative study was conducted without using a reference standard. In brief, GPC experiments were conducted with PEO in its pure form and in formulations processed via three distinct methods (PM, HME at 150°, and FDM at 220°). After the GPC test, all obtained chromatographs were compared against each other (a comparative study).

2.7. Particle size analysis of ground filaments

Particle size distribution was measured manually using a nest of five small sieves with different aperture sizes (63, 150, 250, 600, and 2000 µm). Sieving time was 3 min, where sieves were agitated in linear and circular motions with repeated tapping. The sample weight was around 2 g. The starting weight of the sample was recorded and the weight of powder retained on each sieve after the sieving test was also recorded and converted to % of mass retained on each sieve (frequency%). Size distribution was plotted based on the retained mass % against the aperture size of the sieve. The average size (A) was calculated based on the retained mass % (w_i) in each sieve and sieve diameter (d_i), as presented in **Equation I**:[20]

$$A = \frac{\sum w_i \times d_i}{\sum w_i} \quad \text{(I)}$$

2.8. Tablet characteristics

Tablets were characterized in terms of their weight, SA/V ratio, hardness, and porosity. True density was also measured using a helium pycnometer (AccuPyc II 1340; Micromeritics, USA) since the thermal process can alter the true density of the material, as reported in previous work.[16] The density of physical mixture powders, ground filaments, and ground printlets were considered the true

density for PM, HME, and printed tablets, respectively. The hardness of tablets was estimated using a hardness tester (TBH 125 series; Erwaka, Germany). Surface area and volume were calculated based on the dimensions of tablets measured using a vernier caliper. To calculate the approximate porosity of the obtained tablets, the average apparent density of tablets (n = 3) was calculated from their volume and weight. The porosity of all tablets was then calculated by employing **Equation II**:

$$P\% = 1 - \frac{D_a}{D_t} \times 100 \quad \text{(II)}$$

where P is the porosity, D_a is the apparent density, and D_t is the true density.

2.9. *In vitro* dissolution studies and calculations

Dissolution tests were carried out for tablets (n = 3) under sink conditions using a USP type II paddle apparatus (708-DS Dissolution Apparatus; Agilent Technologies, USA) attached to a UV spectrophotometer (Cary 60 UV-Vis; Agilent Technologies, USA). The vessels were filled with 900 mL of deionized water (based on USP); the temperature was set at 37 ± 1°; and the paddle rotation speed was set at 50 rpm. The test duration was 12 h with readings, i.e., the absorbance was measured every 10 min for the first two hours, then every 30 min thereafter. The wavelength used to measure the absorbance of theophylline was 271 nm.[21] Drug release profiles were plotted as the percentage of cumulative drug release versus time (h).

The dissolution data was analyzed using several different measures. First, a quantitative comparison of the dissolution behavior of different tablets was performed using dissolution efficiency (DE%). Next, a qualitative comparison was conducted using similarity (f_2) and difference (f_1) factors to support the quantitative comparison. Here, similar dissolution profiles have a similarity factor (f_2) of ≥50.[22] Finally, the drug release kinetics were analyzed using DDSolver software (an add-in program in Microsoft Excel).[23] In this analysis, several drug release kinetic models were examined to find the best fit, including the zero-order, first-order, Higuchi, and Korsmeyer-Peppas models. As a measure of statistical fit, R^2_{adj} was used, where higher R^2_{adj} values indicate a better fitting model. In the Korsmeyer-Peppas model, the n value can indicate the drug release mechanism if up to 60% of the drug has been released.[24] When n < 0.45, the drug release is governed by diffusion (Fickian model); when n > 0.89, swelling is the main release mechanism and close to zero-order kinetics (non-Fickian model). When 0.45 < n < 0.89, drug release is governed by both diffusion and swelling mechanisms.[24–26]

2.10. Statistical analysis

For dissolution data, as discussed in **Section 2.9**, f_2 and f_1 factors were used as model-independent statistical approaches to compare the dissolution profiles of different tablets,[22] along with parameters from kinetics analysis and DE%. For other experimental data, the significance of differences in porosity, hardness, and density of formulations was analyzed using analysis of variance (ANOVA). The significance level (alpha) was set at 0.05. Two-way ANOVA was used, as the impact of the manufacturing method was studied across different formulations (two independent variables, manufacturing methods, and formulations).

3. Results and discussion

3.1. Selection of polymers and manufacturing methods

High M_w PEOs (≥0.9 M) have the potential to prolong drug release, making it a viable option in formulation design of controlled release formulations. However, their high melt viscosity and M_w instability restrict their application in FDM 3D printing. As a result, formulation scientists who are interested in using PEO in 3D printing formulations would likely mix this polymer with other ingredients to improve printability, since PEO is too viscous to be printed alone. Here, formulations were developed to include PEO mixed with thermally stable and low-viscosity polymers, HPC or EC, with theophylline as the model drug. The developed formulations (F_1–F_4) were made into tablets via three methods with varying thermal and mechanical processing conditions. The methods were direct compression of PMs, direct compression of HMEs, and FDM 3D printing. The resulting tablets of each formulation (F_1–F_4) underwent different physical tests to identify changes in thermal behavior, PEO M_w, crystallinity, and theophylline release profile.

3.2. Differential scanning calorimetry

Differential scanning calorimetry (DSC) was performed at 25–300°, encompassing the high temperatures used in HME (140°) and the printing process (220°). DSC graphs of the processed formulations were compared with those of the starting materials to investigate any changes in their thermal behavior due to the processing conditions (Figures 1 and 2). Since all formulations displayed similar patterns, only the DSC traces of formulation F_2 are presented to avoid repetition.

Ethyl cellulose (EC) is an amorphous polymer that exhibits a flat thermogram, and adding DBS to EC can

induce a plasticizing effect on the EC polymer. HPC is also an amorphous polymer that exhibits a flat line. Its glass transition temperature should be between 100–120°,[27] but this was hardly detectable in the DSC graph as mentioned in other studies.[28] For PEO, the two M_w (0.9 and 7 M) displayed relatively similar melting points at 73.74 and 73.06°, respectively. In agreement with this, it has been reported that high M_w PEOs typically have relatively similar T_m values.[9,11] The T_g value of PEO (−50°[29]) was not the focus of this study. The melting point of the original theophylline was found to be approximately 273°.

The DSC traces of the various processed formulations exhibited the signature PEO and theophylline melting peaks, indicating the presence of their crystalline forms. The T_g of EC in F_3 and F_4 tablets was hardly detectable, which could be attributed to the positioning of the EC T_g immediately after the PEO melting peak. This could have caused the peaks to merge, making it difficult to observe a separate T_g peak. The T_m of theophylline decreased from approximately 273° in its pure form to 243–250° in PM, HME, and 3D-printed samples for all formulations, which can be attributed to its intermolecular interaction with polymers used in the formulations.

The T_m of PEO in PM samples was ~72°, which decreased to ~66° for HME and ~64° for printed samples. This pattern was also noticed in another study where T_m of PEO decreased for HME.[13] Table 2 displays changes in the T_m of PEO in each formulation. The decrease in T_m could result from PEO depolymerization (i.e., reduction of M_w following degradation) or a reduction in its crystallinity. PEO undergoes crystallinity reduction after a thermal process, further reducing its T_m by 7°.[2,30] Additionally, it has been suggested that mixing PEO with amorphous polymers can restrict its recrystallization after cooling, leading to a drop in T_m following thermal processing.[31] To examine these mechanisms, GPC was employed, which reported a reduction in M_w of PEO in HME and 3D-printed samples that may contribute to the reduction in T_m (discussed in **Section 3.4**).

3.3. X-ray powder diffraction

X-ray powder diffraction (XRPD) was employed at 2θ at 5–50° for raw materials and processed samples

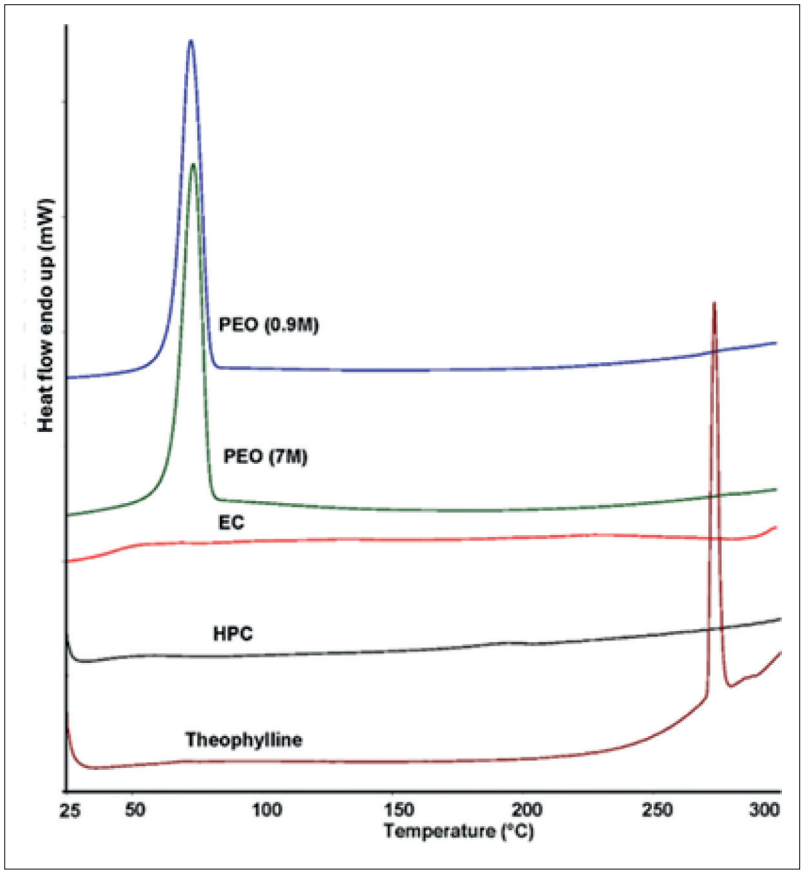


Figure 1. Differential scanning calorimetry (DSC) curves of the starting materials used in this study. Abbreviations: PEO: Polyethylene oxide; HPC: Hydroxypropyl cellulose; EC: Ethyl cellulose.

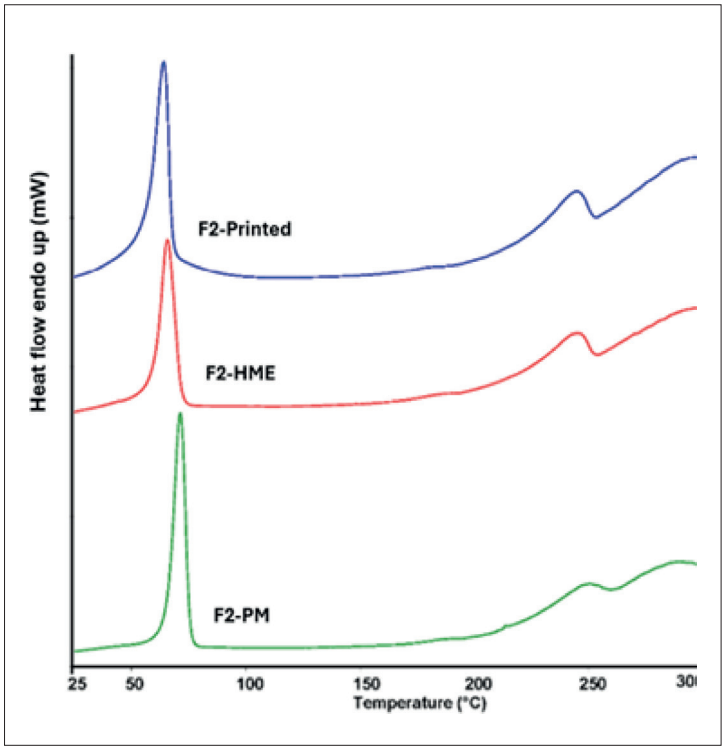


Figure 2. Differential scanning calorimetry (DSC) traces of physical mixture (PM), hot-melt extrudate (HME), and printed samples of formulation F_2. Since all formulations displayed similar patterns, only DSC traces of F_2 are presented to avoid repetition.

Table 2. Melting point (T_m) of polyethylene oxide (PEO) after each process.

Formulation	T_m, mean ± *SD* (°)		
	PM	HME	Printed
F_1	72.11 ± 0.15	67.06 ± 0.82	64.42 ± 0.32
F_2	71.18 ± 0.37	65.61 ± 0.51	65.13 ± 1.22
F_3	71.87 ± 0.25	67.06 ± 1.51	65.41 ± 1.33
F_4	71.24 ± 0.28	66.3 ± 1.43	64.86 ± 2.30

Note: *SD* is calculated from the mean of triplicates. Abbreviations: PM: Physical mixture; HME: Hot-melt extrudates.

(Figures 3 and 4). Theophylline is a crystalline material whose diffractogram displays numerous sharp peaks, with the highest peak at a 2θ of 12.6°. EC and HPC exhibited a halo-shape diffractogram due to their amorphous structures. The diffractogram of PEO, a semi-crystalline polymer, exhibited characteristic crystalline peaks at 2θ of 18.8° and 23°. Since both M_w of PEO have similar characteristics according to previous studies[11] and proved similar in DSC tests, only PEO 7 M was studied for crystallinity in this work.

Meanwhile, in the diffractograms of formulations, the characteristic peaks of theophylline and PEO were detected, indicating the presence of both materials in the crystalline state. However, some noticeable changes can be observed in the peak position, shape, and width in thermally processed samples compared to non-thermally processed samples. Since all formulations displayed similar diffractograms, only the diffractogram for F_2 is presented (Figure 4) to avoid repetition.

Changes in crystal structure and lattice strain can result in peak split,[32] a phenomenon noticed in PEO peaks, especially in formulations F_3 and F_1 containing PEO 7 M (Figure 4). Moreover, there was a broadening in all crystalline peaks of HME and printed samples compared to PM samples, reflecting a change in crystal size or lattice also reported in other studies.[3,6] Overall, based on peak broadening and deformation, as well as the findings of other studies, PEO appears to have exhibited a change in

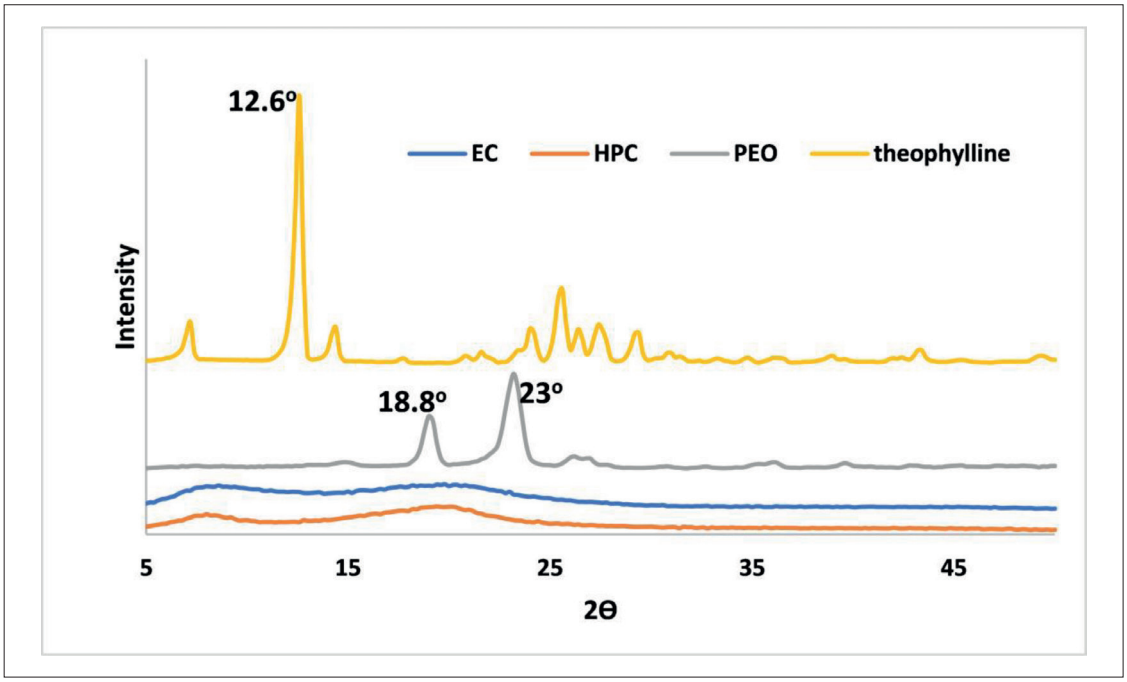


Figure 3. X-ray powder diffraction (XRPD) diffractograms of raw materials. Abbreviations: PEO: Polyethylene oxide; HPC: Hydroxypropyl cellulose; EC: Ethyl cellulose.

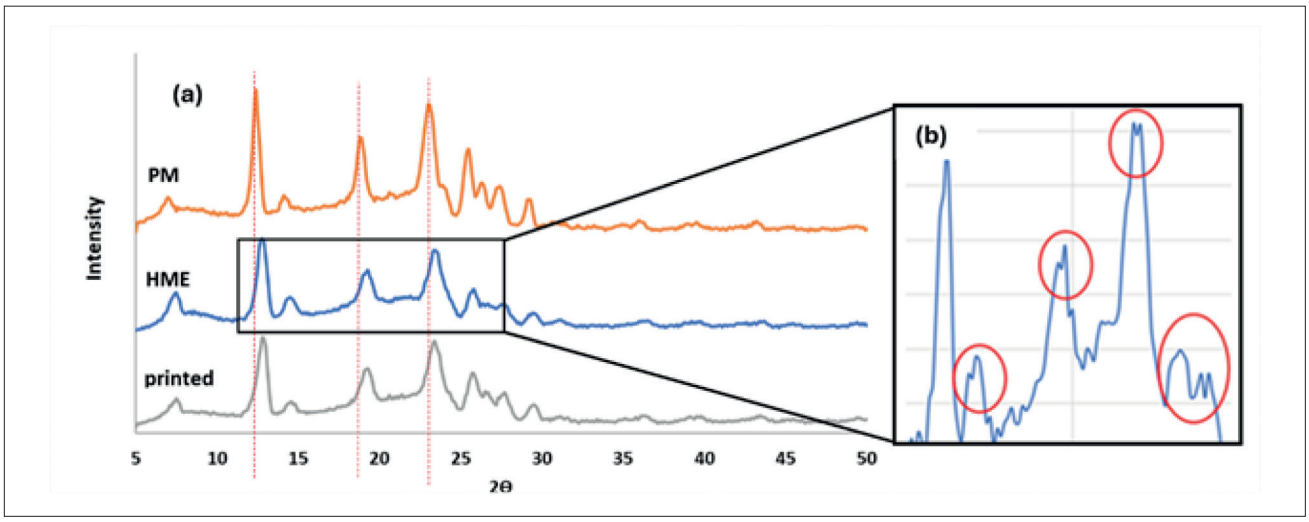


Figure 4. Changes of crystal form after thermal process (a) X-ray powder diffraction (XRPD) diffractograms of physical mixture (PM), hot-melt extrudate (HME), and printed samples of formulation F_2. (b) The 10–30° region of 2θ displays peak splits in thermally processed samples.

crystal size, crystalline lattice, strain, and crystallinity (%) upon heating.[3,6] Such changes can modify the drug release rate, as mentioned in another work.[7]

3.4. Gel permeation chromatography

Gel permeation chromatography (GPC) analysis was performed with pure PEO (7 M) samples and various processed F_1 formulations (PM, HME, and FDM) (Figure 5). The aim was to identify any changes in the M_w of PEO following thermal and mechanical stress due to processing conditions. Given that all formulations displayed a massive surge in release rate after the first thermal process (i.e., HME), we focused only on one formulation (i.e., F_1) for subsequent GPC studies to evaluate M_w changes in PEO.

Pure PEO 7 M exhibited a single peak with a retention time of 9.44 min in the chromatogram (black line in Figure 5a).

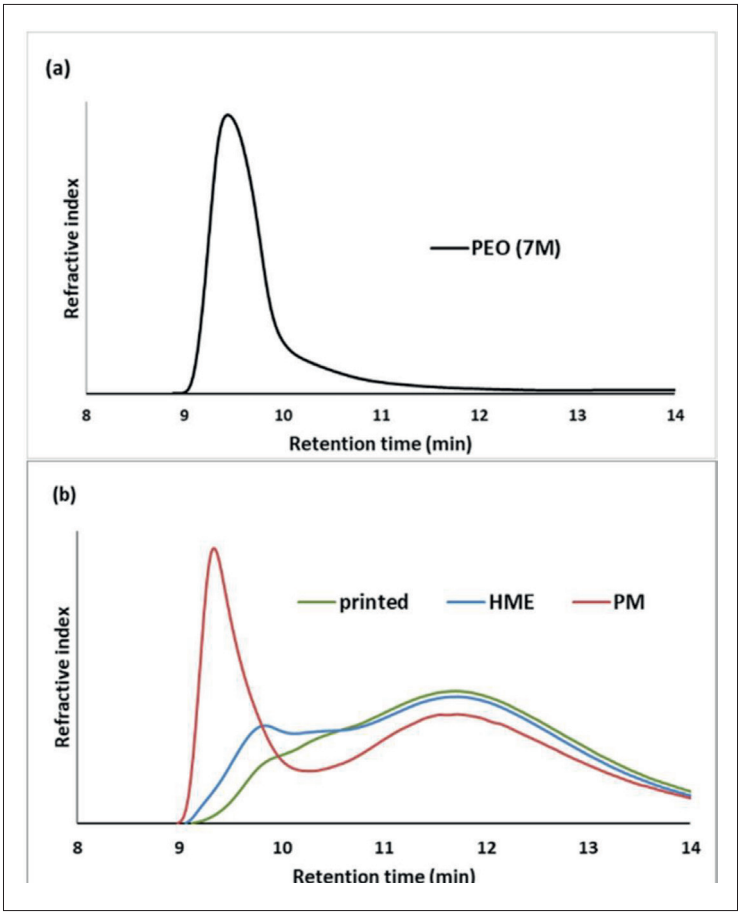


Figure 5. Gel permeation chromatography (GPC) chromatograms of (a) pure polyethylene oxide (PEO; 7M) and (b) physical mixture (PM), hot-melt extrudate (HME), and printed samples of F_1, displaying reduction and shifts in peak 1 due to PEO degradation after each thermal process.

PM samples (red line in Figure 5b) exhibited two signals; a sharp peak (peak 1) at the same retention time of PEO 7 M (~9.5 min) and a broader peak (peak 2) at 10–14 min, indicating HPC in the PM formulation. However, the intensity of the PEO 7 M signal at peak 1 in HME and printed samples decreased significantly compared to PM samples despite having the same starting composition and concentration. The relative intensity of each peak was calculated and reported in Table 3.

Chromatograms for HME and 3D-printed tablets (Figure 5) display a delayed peak 1 signal with obvious broadening. Moreover, the ratio of the intensity of the peaks (PEO to HPC; peak 1/peak 2) decreased in the order: PM > HME > 3D-printed samples. These observations can be explained by the reduction in PEO M_w during processing, resulting in smaller chains with higher retention time. The 3D-printed samples undergo two thermal processes: one in HME while making filament extrudates and another in the 3D printer; thus, these samples exhibit the highest reduction in the PEO 7 M signal (peak 1).

Table 3. Relative intensity of peaks 1 and 2 after each manufacturing process.

Sample	Relative intensity of peak 1/peak 2
PM	1.47
HME	0.9
Printed	0.45

Abbreviations: PM: Physical mixture; HME: Hot-melt extrudates.

3.5. Particle size analysis of ground filaments

Grinding the HME filaments of all the developed formulations in this study resulted in coarse, flake-shaped particles (Figure 6), whereas the PM powders were fine (<400 μm). The size distribution and arithmetic average particle size were determined using sieves.[20] Figure 7 displays the particle size distribution of ground filaments of all formulations. The plasticity of PEO results in coarse particles with irregular shapes upon grinding the filaments. For thermoplastic polymers, like PEO, it is challenging to obtain fine particles due to plastic deformation rather than



Figure 6. Flak-shaped powders after grinding filaments in the ball mill.

brittle fracture under conventional grinding methods,[33,34] such as ball-milling used in this study. Usually, cryogenic or wet grinding is employed to produce fine particles of plastic polymers.[33,34]

Regardless of the M_w of PEO, it is obvious that grinding the filaments containing EC (F_3 and F_4) produces considerably larger particles compared to those containing HPC (F_1 and F_2). The arithmetic average sizes of F_3 and F_4 ground filaments were 1352.69 and 1796.91 μm, respectively, while those for F_1 and F_2 were much smaller at 530.56 and 919.47 μm, respectively. The large particle size of EC-containing formulations can be attributed to the presence of DBS plasticizer in EC fractions. The addition of plasticizers can increase material ductility and reduce its brittleness, increasing the average particle size of the ground material.[35]

Regarding the M_w of PEO, formulations with PEO of a higher M_w (e.g., 7 M) produced finer particle sizes upon grinding the filaments. Ground filaments of F_1 containing HPC/PEO 7 M had a smaller average size than that of F_2 containing HPC/PEO 0.9 M (530.56 vs. 919.47 μm, respectively). Similarly, the average size of F_3

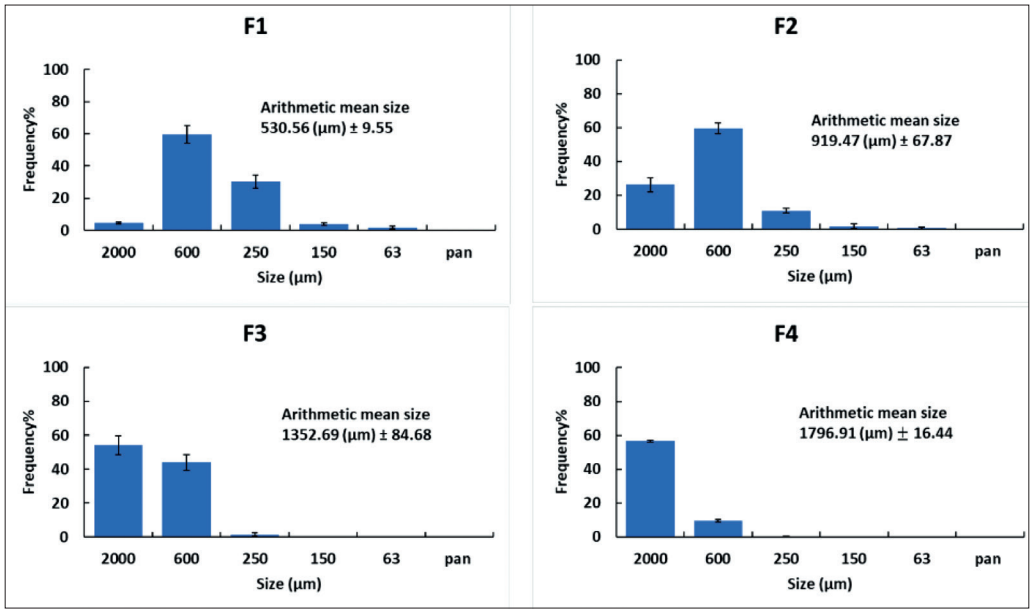


Figure 7. Size distribution based on the retained fraction (%) in each sieve for ground filaments of all formulations, presented as the mean ± *SD* for each formula. Abbreviation: pan: powder size <63 μm.

Table 4. Hardness of prepared tablets.

Formulation	Hardness, mean ± SD (N)		
	Printed	HME	PM
F_1	>300	216 ± 13	239 ± 6
F_2	>300	242 ± 19	236 ± 25
F_3	203 ± 10	170 ± 14	202 ± 7
F_4	256 ± 23	154 ± 7	211 ± 2

Note: *SD* is calculated from the mean of triplicates. Abbreviations: PM: Physical mixture; HME: Hot-melt extrudate.

ground filaments containing EC/PEO 7 M was smaller than F_4 containing EC/PEO 0.9 M (1352.69 vs. 1796.91 μm, respectively). Generally, high M_w PEO resins have relatively similar mechanical characteristics.[11] However, the inclusion of other materials can restrict the PEO polymer chain mobility and increase internal stress among formulations, resulting in stiffer formulations when compared to the use of lower M_w PEOs.[36] Having a brittle material can usually result in finer particle size.[33] Thus, the observed particle size reduction in ground F_1 vs. F_2 and ground F_3 vs. F_4 could be attributed to changes in PEO M_w.

3.6. Characterization of tablets

To rule out the effect of tablet weight and SA/V on the drug release profile, tablets from different processing methods were designed to have the same average weight (333.3 mg) and SA/V (0.8 mm^{-1}). The hardness, true density, apparent density, and porosity were measured for all the tablets (Tables 4–7). The results indicate that tablet hardness decreased in the order of 3D-printed > PM ≥ HME samples for most formulations. The 3D-printed tablets were the hardest (Table 4), probably due to the nature of the printing method, where tablets made of molten layers could produce stronger consolidation.[16] HME tablets appeared to be less hard than PM and printed tablets. For example, HME tablets of F_4 had a hardness of 154 N compared to 211 and 256 N for PM and printed tablets, respectively. These hardness results can be attributed to differences in particle size between PM powders and HME ground filaments. As previously discussed, HME ground filaments were much larger than PM.[37,38] Furthermore, PEO degradation, reported in GPC data, can reduce the mechanical strength of HME samples and the resulting tablets' hardness.

Notably, the formulation composition can impact the hardness of tablets. Tablets prepared from formulations containing PEO/HPC mixture (F_1 and F_2) are considerably harder than those prepared from EC/PEO (F_3 and F_4). For example, 3D-printed tablets of F_1 and F_2 had a hardness of over 300 N (beyond the detection limit of the hardness tester), while those of F_3 and F_4 had a hardness of 203–256 N. This can be due to the presence of DBS in F_3 and F_4, as the plasticizer can improve the flexibility of the polymer, making it less resistant to deformation.[35]

Since thermal processes can alter the specific volume of polymers,[39,40] the true density of the processed formulations will be affected. The results reported in Table 5 indicate a decrease in true density after 3D printing, which was significant for F_1 and F_2 but not for F_3 and F_4. Rapid heating/cooling occurs during 3D printing, where the materials' temperature fluctuates between room temperature and 220° within 4–5 min, affecting the formulations' true density.

Apparent density (Table 6) also featured a noticeable reduction after thermal processing, indicating the significant impact of the manufacturing method on density ($p < 0.05$). The apparent density of printed tablets was ~1 g/cm^3,

Table 5. True density of tablets for various formulations obtained via different manufacturing methods.

Formulation	True density, mean ± *SD* (g/cm^3)		
	Printed	HME	PM
F_1	1.215 ± 0.001	1.293 ± 0.001	1.282 ± 0.002
F_2	1.198 ± 0.001	1.294 ± 0.002	1.28 ± 0.002
F_3	1.245 ± 0.002	1.261 ± 0.003	1.264 ± 0.002
F_4	1.25 ± 0.002	1.27 ± 0.002	1.26 ± 0.002

Note: *SD* is calculated from the mean of triplicates. Abbreviations: PM: Physical mixture; HME: Hot-melt extrudate.

Table 6. Apparent density of tablets for various formulations obtained via different manufacturing methods.

Formulation	Apparent density, mean ± *SD* (g/cm³)		
	Printed	HME	PM
F_1	0.995 ± 0.015	1.184 ± 0.011	1.184 ± 0.011
F_2	1.001 ± 0.022	1.173 ± 0.017	1.166 ± 0.010
F_3	0.998 ± 0.020	1.147 ± 0.012	1.137 ± 0.011
F_4	1.017 ± 0.029	1.145 ± 0.019	1.133 ± 0.017

Note: *SD* is calculated from the mean of triplicates. Abbreviations: PM: Physical mixture; HME: Hot-melt extrudate.

much lower than that for PM and HME tablets (~1.18 g/cm³), indicating the high porosity of the printed tablets.

Porosity was calculated using the values of true and apparent densities, decreasing in the order: 3D-printed > HME ~ PM (Table 7). Since printed tablets of all formulations have significantly lower true and apparent densities, they are expected to be the most significantly porous compared to HME and PM ($p < 0.05$). This trend was also noticed in our previous work for 3D-printed tablets due to the layer-by-layer printing, forming gaps between the tablet layers.[16] Conversely, despite their high porosity, the printed tablets did not exhibit the lowest hardness compared to the other samples in this study, suggesting that the solidification of molten layers in 3D printing leads to stronger consolidation of tablet compartments, as previously observed.[16] Both HME and PM tablets have relatively similar porosities ($p > 0.05$), despite their significant differences in hardness. Therefore, hardness differences between HME and PM tablets are likely due to the impact of their particle size, manufacturing method, and formulation composition rather than the porosity.

3.7. *In vitro* dissolution studies

Dissolution profiles of tablets manufactured from the four formulations are displayed in Figures 8 and 9. DE% and similarity factors were calculated to compare the dissolution data. To elaborate on the dissolution profiles, tablets hardness, porosity, formulation composition, and M_w changes after thermal stress were considered. The effect of particle size on dissolution rate is not comparable between different manufacturing methods; in PM tablets, the particles of each material were mixed physically, whereas, in HME and 3D-printed tablets, the particles were mixed molecularly as a result of melting. Hence, the nature of particles is relatively different from each other. Moreover, in 3D-printed tablets, there were no particle sizes to be studied as they were made of molten layers.

Comparing the dissolution profiles displayed a considerable increase in DE% for all formulations as a result of the HME process (Figures 8 and 9). For example, the DE% of F_1 and F_2 increased from 26.48 and 49.58% for PM tablets to 75.05 and 73.79% for HME tablets, respectively. F_3 and F_4 also demonstrated similar patterns. These results corroborate the GPC findings, indicating a reduction in PEO M_w in HME samples, which can result in faster drug release. Moreover, HME tablets were less hard than PM tablets (Table 4), which can also be responsible for the faster theophylline release. Furthermore, the reduction in crystal size after HME, as observed from XRPD, can play a role in increasing DE%.[7] The f_2 between HME and PM tablets was in the range of 17.36–44.57%, which is an indication of a significant difference between the dissolution profiles of PM and HME tablets.

The GPC data displayed a further reduction in PEO M_w in printed tablets, and along with the increased porosity of these tablets should have increased the DE% for the 3D-printed tablets compared to HME tablets. However,

Table 7. Porosity of tablets for various formulations obtained via different manufacturing methods.

Formulation	Porosity, mean ± *SD* (%)		
	Printed	HME	PM
F_1	17.85 ± 1.195	8.399 ± 0.467	8.218 ± 0.841
F_2	16.685 ± 2.624	9.357 ± 1.296	8.919 ± 0.801
F_3	19.80 ± 1.627	9.045 ± 0.938	10.015 ± 0.908
F_4	18.492 ± 2.287	9.804 ± 1.476	10.083 ± 1.318

Note: *SD* is calculated from the mean of triplicates. Abbreviations: PM: Physical mixture; HME: Hot-melt extrudate.

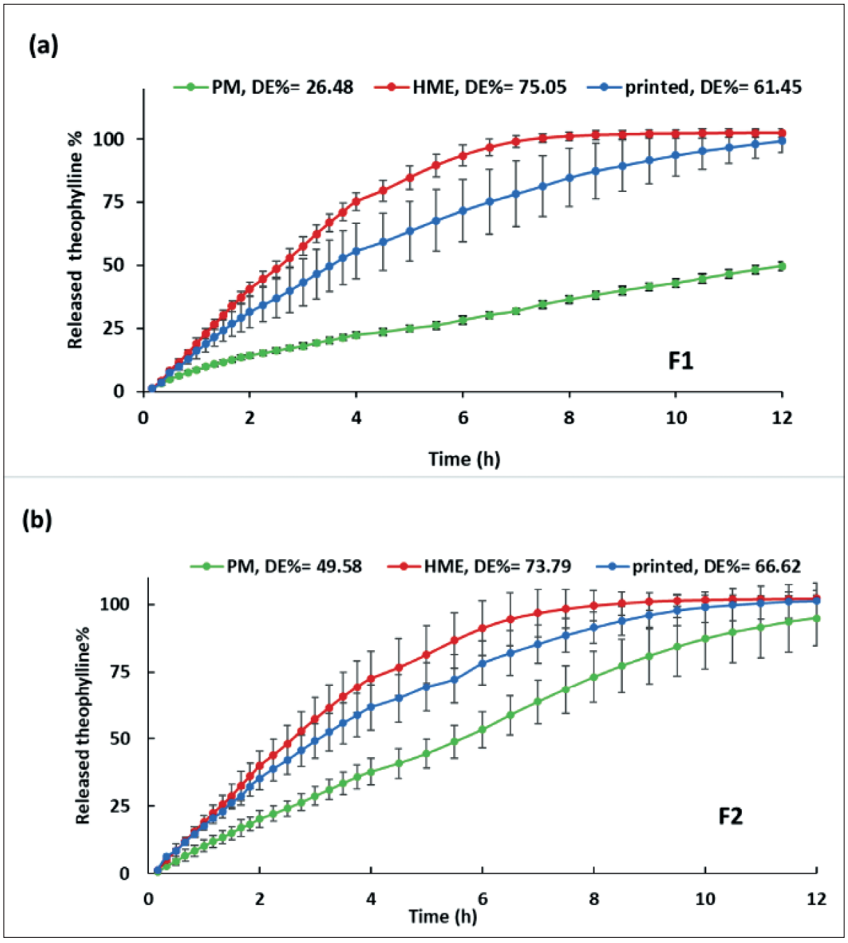


Figure 8. Dissolution curves of F_1 (a) and F_2 (b), presented with error bars and the dissolution efficiency (DE%) values for the physical mixture (PM), hot-melt extrudate (HME), and 3D-printed tablets.

this was not the case, and the DE% of printed tablets was less than that of HME tablets. For example, in F_1 and F_3, DE% decreased from 75.05 and 53.4% in HME tablets to 61.45 and 24.1% in 3D-printed tablets, respectively. Therefore, drug release from these tablets appeared to be more impacted by their significantly increased hardness rather than M_w reduction and porosity changes. Moreover, 3D-printed and HME tablets have dissimilar release behavior ($f_2 < 50$) in all tablet formulations except for F_2 ($f_2 = 56.53\%$). The f_2 values for dissolution profiles of HME compared to 3D-printed tablets of F_1–F_4 were 43.89, 56.53, 27.97, and 30.05%, respectively.

The printing method also improved the tablet's integrity when used for formulations containing EC, as printed tablets of F_3 and F_4 remained intact during the dissolution and did not disintegrate. In contrast, HME tablets were completely disintegrated during the dissolution test. The lack of disintegration of 3D-printed tablets results in low contact surface area with the dissolution medium, thus further delaying the dissolution process. For example, DE% of F_3 was 24.1% in printed tablets compared to 53.4% in HME tablets. This supports our previous findings and suggests that 3D printing can extend drug release when hydrophobic polymers, like EC, are incorporated into the formulation.[16,26] Notably, maintaining the integrity of 3D-printed tablets of F_3 and F_4 could prolong drug release compared to the tablets obtained via the PM method, despite the noticeable reduction in PEO M_w after printing. DE% of F_3 and F_4 was 24.1 and 25.77% for printed tablets compared to 28.05 and 38.7% for PM tablets, respectively.

Besides the manufacturing method, the type of materials used in formulations can also modulate drug release from tablets. For polymer mixtures, the dissolution behavior is determined by each polymer's contribution to the formulation, as well as the interaction of all the components with each other and the drug. This interplay between components is expected to be influenced by the tablet manufacturing method.[16]

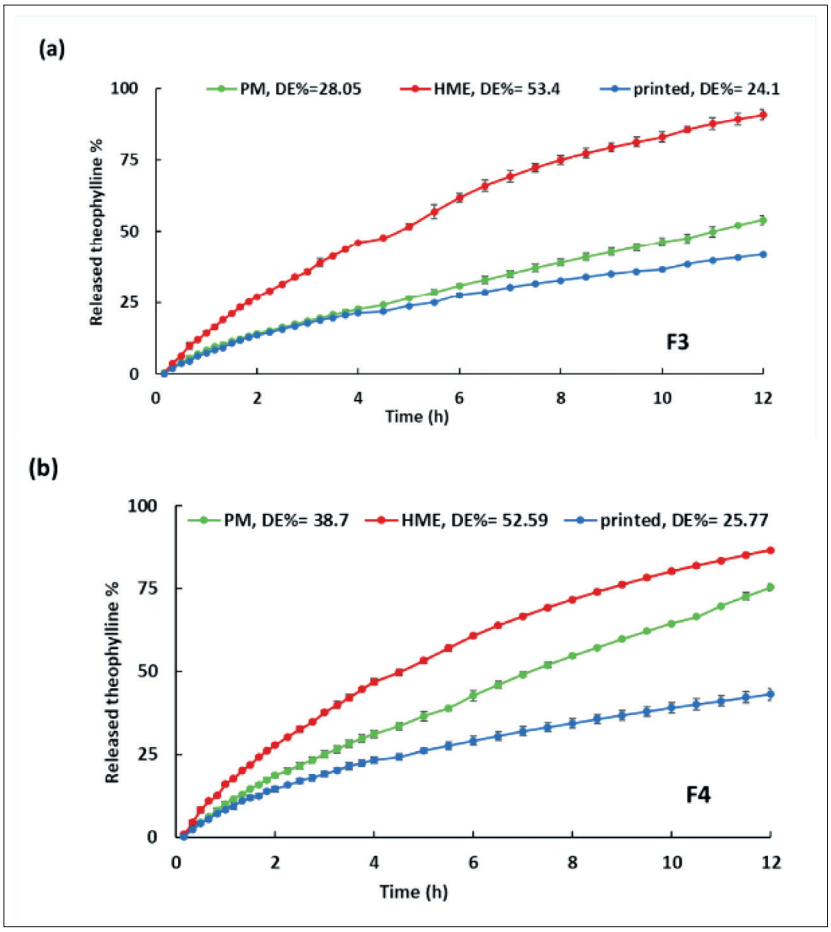


Figure 9. Dissolution curves of F_3 (a) and F_4 (b), presented with error bars and the dissolution efficiency (DE%) values for physical mixture (PM), hot-melt extrudate (HME), and 3D-printed tablets.

Figure 10 displays the dissolution profiles of the four formulations (F_1–F_4) made into PM tablets. The smaller standard deviation bars observed indicate that the dissolution behavior is more consistent in F_3 and F_4 tablets containing EC (as opposed to HPC in F_1 and F_2). An overall faster release for F_2 and F_4 containing 0.9 M PEO infers the impact of the M_w of PEO; formulations containing the 7 M PEO (F_1 and F_3) have a stronger gelling behavior and slower release. The strong gelling behavior of PEO 7 M appears to dominate the effects of HPC in F_1 and EC in F_3, as both formulations have similar dissolution profiles (f_2 = 84.86). However, the effect of HPC (hydrophilic) or EC (hydrophobic) on drug release was more noticeable in F_2 and F_4, and the release from F_2 (PEO/HPC) was significantly faster than that from F_4 (PEO/EC) (f_2 = 47.53).

When the formulations were thermally processed in HME and 3D printing, the pattern was reversed, and the dissolution profile followed the hydrophilic or hydrophobic nature of HPC or EC rather than the M_w of PEO (Figure 11). F_1 and F_2 (containing HPC) had a much faster release rate than F_3 and F_4 (containing EC) in both HME and 3D-printed tablets. Moreover, F_1 and F_2 had similar release profiles, i.e., f_2 = 88.08 and 65.28 for HME and 3D-printed tablets, respectively, despite having different M_w of PEO. Similarly, F_3 and F_4 had similar release behavior, i.e., f_2 = 83 and 86.45 for HME and 3D printed tablets, respectively. This pattern was also observed in other studies, where the dissolution profiles of different M_w PEOs were relatively similar after thermal processing.[1,13] Based on such findings and considering GPC-proven PEO degradation in heat-processed methods, it can be suggested that after a specific degradation in the M_w of PEO, gelling behavior becomes weak, and drug release becomes less sensitive to PEO M_w. A similar pattern was also noticed in a stability study of PEO tablets, where, after eight weeks of storage at high temperatures and humidity, all M_w exhibited similar release profiles.[8,9]

3.8. Release kinetics

Dissolution kinetics were also analyzed using four kinetic models (zero-order, first-order, Higuchi, and Korsmeyer-

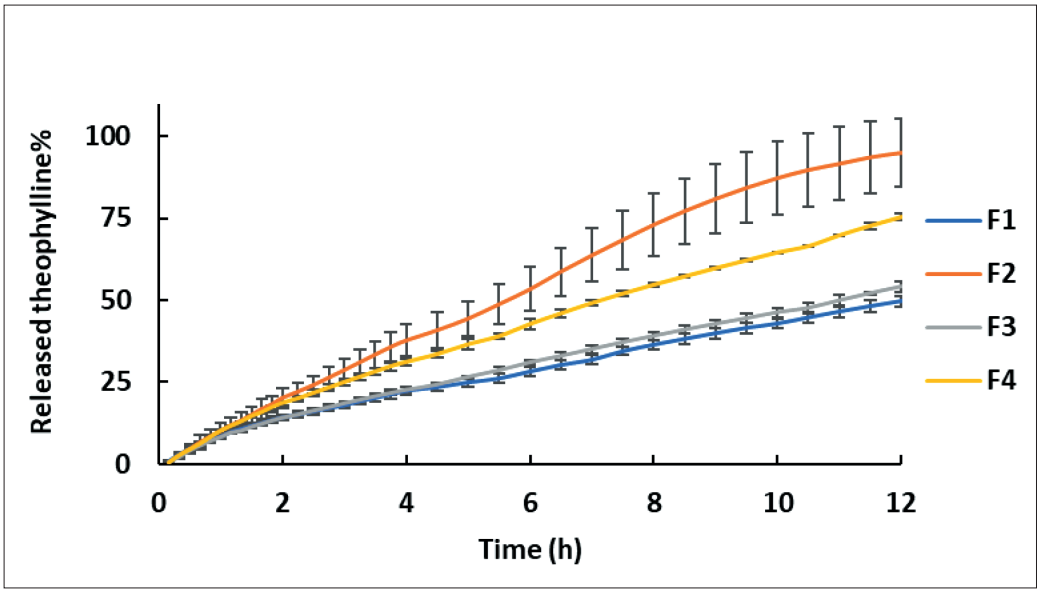


Figure 10. Comparison of dissolution behavior of the four formulations (F_1–F_4) prepared by physical mixture (PM) method.

Peppas) to investigate changes in the mechanism of drug release due to manufacturing methods. According to Table 8, the manufacturing method appears to impact the release kinetics of tablets. The drug release from PM tablets of F_1 and F_3 (containing high M_w PEO) fits best with the first-order mechanism ($R^2 > 0.99$), while the same formulations made by HME and 3D printing best follow the Higuchi model ($R^2 > 0.99$). Meanwhile, F_2 and F_4 tablets (containing low M_w PEO) made by the PM method follow a zero-order drug release ($R^2 > 0.99$), but the release mechanism changed to Higuchi ($R^2 \geq 0.99$) in HME and 3D-printed tablets.

For the release mechanism, n values from the Korsmeyer-Peppas model determine the drug release mechanism associated with each manufacturing method. All tablets displayed good fitting with the Korsmeyer-Peppas model ($0.84 < R^2 < 0.99$). F_2 and F_4 (containing lower M_w PEO, 0.9 M) have similar release mechanisms with $n > 0.85$, indicating diffusion in all manufacturing methods despite significant changes in DE%. However, formulations containing PEO 7 M exhibited different patterns. F_1 features an anomalous transport (diffusion and swelling) mechanism in PM tablets ($n = 0.766$). However, in HME and 3D-printed tablets, the mechanism is polymer relaxation ($n = 1.287$ and 1.157, respectively). F_3 also demonstrated the same pattern with n-values of 0.845, 1.282, and 0.939 for PM, HME, and printed tablets, respectively. Upon observation, PM tablets of F_1 and F_3 (with 7 M PEO) transformed into a thick gel ball at the end of the dissolution test, but this was absent in HME and printed tablets; this was also observed in other studies.[8,9] It is assumed that below a specific grade of M_w, the release mechanism and dissolution rate can be less sensitive to M_w changes.

Considering the dissolution profiles and mechanism of drug release, it can be concluded that FDM 3D printing can produce tablets with increased hardness and porosity, but lower density and crystallinity, compared to PM and HME methods. Although porosity and density can affect the release profile, their effect can be outweighed by the effect of hardness and formulation composition. Previous work indicates that increased hardness can extend the release profile of printed tablets when a considerable amount (>40%) of hydrophobic material is included in the formulation.[16,26,41] However, the delayed release effect of elevated hardness can be minimized when the formulation is completely hydrophilic.[16] PEO, as a polymer, can suffer from degradation and M_w reduction under thermal conditions of HME and 3D printing, subsequently reducing its gelling ability to extend drug release. Its crystallinity also decreases, which can increase DE%. Thus, an increase in DE% may be observed after heat processing, such as 3D printing, as observed for F_1 and F_2. Moreover, the impact of heat-induced PEO M_w reduction on drug release has its limitations. When high M_w PEO is used (7 M), M_w degradation in HME could significantly change DE% and its release mechanism, like in F_1. However, further degradation during the printing method (evidenced by GPC) displayed negligible impact on DE% or its release mechanisms. Similarly, variations in DE% of F_2, which contains a lower M_w of PEO (0.9 M), were minimal, and the release mechanism was consistent across PM, HME, and printed tablets.

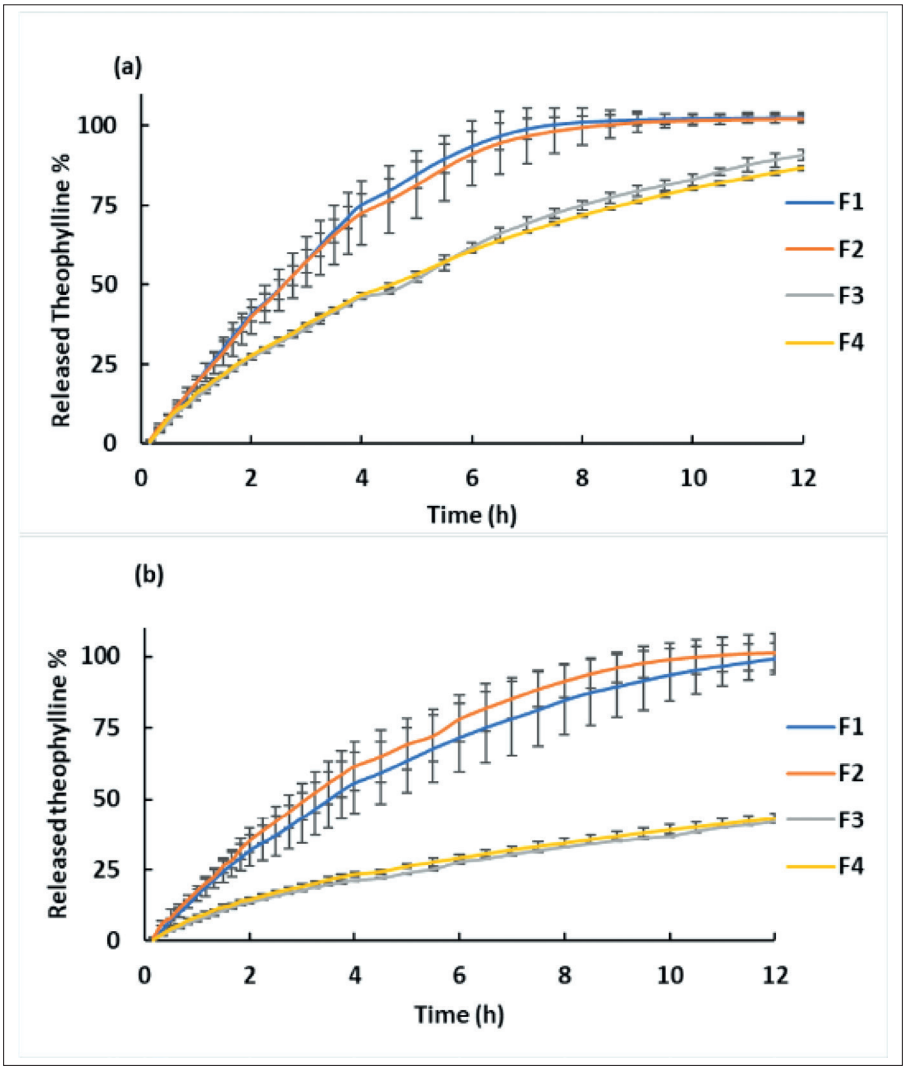


Figure 11. Comparison of dissolution behavior of the four formulations (F_1–F_4) prepared by the (a) hot-melt extrudate (HME) and (b) 3D-printing method.

Table 8. Kinetic parameters for F_1–F_4 prepared as a physical mixture (PM), hot-melt extrudates (HME), and by 3D printing.

Kinetic model	Parameter	F_1			F_2			F_3			F_4		
		PM	HME	Printed	PM	HME	Printed	PM	HME	Printed	PM	HME	Printed
Zero-order	R^2	0.991	0.97	0.951	0.992*	0.958	0.97	0.991	0.967	0.965	0.992*	0.957	0.957
First-order	R^2	0.996*	0.859	0.939	0.901	0.875	0.877	0.997*	0.990	0.986	0.989	0.998*	0.981
Higuchi	R^2	0.985	0.992*	0.994*	0.976	0.990*	0.996*	0.988	0.997*	0.999*	0.988	0.998*	1.00
Korsmeyer-Peppas	R^2	0.979	0.98	0.976	0.976	0.990*	0.969	0.959	0.845	0.877	0.939	0.935	0.869
	n	0.77	1.29	1.16	1.05	1.17	1.03	0.85	1.28	0.94	1.02	1.04	0.90

Note: *denotes Highest value of R^2. Abbreviations: PM: Physical mixture; HME: Hot-melt extrudate.

4. Conclusion

Two high M_w PEOs (7 M and 0.9 M) were used to produce extended-release tablets using direct compression of a PM of the formulation constituents or thermal processing of these mixtures via HME and FDM 3D printing. The studied formulations contained PEO mixed with theophylline (drug) and another polymer (HPC or EC). GPC studies demonstrated that PEO undergoes M_w reduction after thermal and mechanical stress in HME and FDM 3D printing, while XRPD displayed a reduction in crystallinity. These physical changes reduced the gelling behavior of PEO, resulting in faster drug release, which was more significant with higher M_w PEOs. As expected, HME and printed tablets exhibited significantly increased drug release compared to PM tablets. Conversely, the inclusion of hydrophobic materials in the formulation outweighs the impact of PEO degradation in 3D printing, leading to extended drug release. These hydrophobic polymers (like EC) are beneficial as they prevent the disintegration of tablets during dissolution and provide more control over dissolution behavior. Our findings and those of other studies suggest that printing methods appear to be more effective in extending drug release when hydrophobic materials are used. However, PEO remains a viable option for 3D printing, though it demands stringent process control to ensure consistent drug release and desired physicochemical properties.

Acknowledgments

None.

Funding

This research received no external funding.

Conflict of interest

The authors declare they have no competing interests.

Author contributions

Conceptualization: Matthew Lam, Taravat Ghafourian, Ali Nokhodchi

Formal analysis: Nour Nashed, Ali Nokhodchi, Taravat Ghafourian

Investigation: Nour Nashed, Mridul Majumder, Barnaby W. Greenland

Methodology: Nour Nashed, Barnaby W. Greenland, Mridul Majumder

Writing – original draft: Nour Nashed

Writing – review & editing: Matthew Lam, Taravat Ghafourian, Ali Nokodchi

Ethics approval and consent to participate

Not applicable.

Consent for publication

Not applicable.

Availability of data

Data used in this study are available from the corresponding author upon reasonable request.

References

1. Salem S, Byrn SR, Smith DT, et al. Impact assessment of the variables affecting the drug release and extraction of polyethylene oxide based tablets. *J Drug Deliv Sci Technol.* 2022;71:103337.
doi: 10.1016/j.jddst.2022.103337

2. Meruva S, Donovan MD. Polyethylene oxide (PEO) molecular weight effects on abuse-deterrent properties of matrix tablets. *AAPS PharmSciTech*. 2020;21: 1-10.
doi: 10.1208/s12249-019-1565-y

3. Pajander J, Rensonnet A, Hietala S, et al. The evaluation of physical properties of injection molded systems based on poly(ethylene oxide) (PEO). *Int J Pharm.* 2017;518 (1–2):203-212.
doi: 10.1016/j.ijpharm. 2016.12.050

4. Maggi L, Bruni R, Conte U. High molecular weight polyethylene oxides (PEOs) as an alternative to HPMC in controlled release dosage forms. *Int J Pharm.* 2000;195 (1–2):229-238.
doi: 10.1016/S0378-5173(99)00402-0

5. Malik P, Castro M, Carrot C. Thermal degradation during melt processing of poly(ethylene oxide), poly(vinylidenefluoride-co-hexafluoropropylene) and their blends in the presence of additives, for conducting applications. *Polym Degrad Stab.* 2006;91(4):634-640.
doi: 10.1016/j.polymdegradstab.2005.01.020

6. Crowley MM, Zhang F, Koleng JJ, et al. Stability of polyethylene oxide in matrix tablets prepared by hot-melt extrusion. *Biomaterials.* 2002;23(21):4241-428.
doi: 10.1016/S0142-9612(02)00187-4

7. Cantin O. *PEO Hot Melt Extrudates for Controlled Drug Delivery* (Doctoral dissertation, Université du Droit et de la Santé–Lille II). 2017.
https://tel.archives-ouvertes.fr/tel-01540630

8. Shojaee S, Asare-Addo K, Kaialy W, et al. An investigation into the stabilization of diltiazem HCl release from matrices made from aged polyox powders. *AAPS PharmSciTech*. 2013;14(3):1190-1198.
doi: 10.1208/s12249-013-0013-7

9. Shojaee S, Cumming I, Kaialy W, et al. The influence of vitamin E succinate on the stability of polyethylene oxide PEO controlled release matrix tablets. *Colloids Surf B Biointerfaces.* 2013;111:486-492. doi: 10.1016/j.colsurfb.2013.06.038

10 Vrandečić NS, Erceg M, Jakić M, et al. Kinetic analysis of thermal degradation of poly(ethylene glycol) and poly(ethylene oxide)s of different molecular weight. *Thermochim Acta.* 2010;498(1–2):71-80. doi: 10.1016/j.tca.2009.10.005

11. Smith KL, Van Cleve R. High molecular weight polymers of ethylene oxide plastic properties. *Indus Eng Chem.* 1958;50(1):12-16. doi: 10.1021/ie50577a024

12. Repka MA, McGinity JW. Influence of vitamin E TPGS on the properties of hydrophilic films produced by hot-melt extrusion. *Int J Pharm.* 2000;202(1–2):63-70. doi: 10.1016/S0378-5173(00)00418-X

13. Cantin O, Siepmann F, Danede F, et al. PEO hot melt extrudates for controlled drug delivery: importance of the molecular weight. *J Drug Deliv Sci Technol.* 2016;36:130-140. doi: 10.1016/j.jddst.2016.09.003

14. Isreb A, Baj K, Wojsz M, et al. 3D printed oral theophylline doses with innovative 'radiator-like' design: impact of polyethylene oxide (PEO) molecular weight. *Int J Pharm.* 2019;564:98-105. doi: 10.1016/j.ijpharm.2019.04.017

15. Ong JJ, Awad A, Martorana A, et al. 3D printed opioid medicines with alcohol-resistant and abuse-deterrent properties. *Int J Pharm.* 2020;579:119169. doi: 10.1016/j.ijpharm.2020.119169

16. Nashed N, Lam M, Ghafourian T, et al. An insight into the impact of thermal process on dissolution profile and physical characteristics of theophylline tablets made through 3D printing compared to conventional methods. *Biomedicines.* 2022;10(6):1-18. doi: 10.3390/biomedicines10061335

17. Quinten T. Evaluation of injection molding as a pharmaceutical production technology for sustained-release matrix tablets. *Ghent University.* 2010. http://library1.nida.ac.th/termpaper6/sd/2554/19755.pdf

18. Shodexhplc, Poly (Ethylene Oxide) Standards. Available from: shodexhplc.com/applications/poly-ethylene-oxide-standards/

19. Stringano E, Gea A, Salminen JP, et al. Simple solution for a complex problem: proanthocyanidins, galloyl glucoses and ellagitannins fit on a single calibration curve in high performance-gel permeation chromatography. *J Chromatogr A.* 2011;1218(43):7804-7812. doi: 10.1016/j.chroma.2011.08.082

20. Dishman KL. Sieving in particle size analysis. In: *Encyclopedia of Analytical Chemistry*. Wiley; 2000. doi: 10.1002/9780470027318.a1514.

21. Tan DK, Maniruzzaman M, Nokhodchi A. Development and optimisation of novel polymeric compositions for sustained release theophylline caplets (PrintCap) via FDM 3D printing. *Polymers.* 2020;12(1):1-18. doi: 10.3390/polym12010027

22. Anderson NH, Bauer M, Boussac N, et al. An evaluation of fit factors and dissolution efficiency for the comparison of *in vitro* dissolution profiles. *J Pharm Biomed Anal.* 1998;17 (4–5):811-822. doi: 10.1016/S0731-7085(98)00011-9

23. Zhang Y, Huo M, Zhou J, et al. DDSolver: an add-in program for modeling and comparison of drug dissolution profiles. *AAPS J.* 2010;12(3):263-271. doi: 10.1208/s12248-010-9185-1

24. Ritger PL, Peppas NA. A simple equation for description of solute release I. Fickian and non-fickian release from non-swellable devices in the form of slabs, spheres, cylinders or discs. *J Control Release.* 1987;5(1):23-36. doi: 10.1016/0168-3659(87)90034-4

25. Bruschi ML. Mathematical models of drug release. In: *Strategies to Modify the Drug Release from Pharmaceutical Systems.* Sawston, UK: Woodhead Publishing; 2015:63-86. doi: 10.1016/B978-0-08-100092-2.00005-9

26. Shi K, Slavage JP, Maniruzzaman M, et al. Role of release modifiers to modulate drug release from fused deposition modelling (FDM) 3D printed tablets. *Int J Pharm.* 2021;597:120315. doi: 10.1016/j.ijpharm.2021.120315

27. Ashland Inc. Klucel Hydroxypropylcellulose Physical and Chemical Properties (Datasheet). 2017. http://www.ashland.com/file_source/Ashland/Product/Documents/Pharmaceutical/PC_11229_Klucel_HPC.pdf

28 Homaee Borujeni S, Mirdamadian SZ, Varshosaz J, et al. Three-dimensional (3D) printed tablets using ethyl cellulose and hydroxypropyl cellulose to achieve zero order sustained release profile. *Cellulose.* 2020;27(3):1573–1589. doi: 10.1007/s10570-019-02881-4

29. Polaskova M, Peer P, Cermak R, et al. Effect of thermal treatment on crystallinity of poly(ethylene oxide) electrospun fibers. *Polymers.* 2019;11(9):1384. doi: 10.3390/polym11091384

30. PerkinElmer. Polymer crystallinity studies by DSC- Raman spectroscopy. 2009. https://perkinelmer.cl/wp-content/uploads/2018/05/Polymer-Crystallinity-by-DSC-Raman.pdf

31. Park MS, Kim JK. Phase behavior and crystallization of a poly(ethylene oxide)/cellulose acetate butyrate blend. *J Polym Sci B Polym Phys.* 2002;40(15):1673-1681.

doi: 10.1002/polb.10225

32. Leineweber A. Reflection splitting-induced microstrain broadening. *Powder Diffraction*. 2017;32(S1):S35-S39. doi: 10.1017/S0885715617000665

33 Bhagia S, Gallego NC, Hiremath N, et al. Fine grinding of thermoplastics by high speed friction grinding assisted by guar gum. *J Appl Polym Sci.* 2021;138(32):50797. doi: 10.1002/app.50797

34. Schmidt J, Plata M, Tröger S, et al. Production of polymer particles below 5μm by wet grinding. *Powder Technol.* 2012;228:84-90. doi: 10.1016/j.powtec.2012.04.064.

35. Jung H, Lee YJ, Yoon WB. Effect of moisture content on the grinding process and powder properties in food: a review. *Processes.* 2018;6(6):69. doi: 10.3390/pr6060069

36 Eckert A, Abbasi M, Mang T, et al. Structure, mechanical properties, and dynamics of polyethylenoxide/nanoclay nacre-mimetic nanocomposites. *Macromolecules.* 2020;53(5):1716-1725. doi: 10.1021/acs.macromol.9b01931

37. Xiao P, Guo Y, Wang J, et al. The effect of granules characters on mechanical properties of press-coated tablets: a comparative study. *Int J Pharm.* 2022;624:121986. doi: 10.1016/j.ijpharm.2022.121986

38. Vinayagamoorthy R. Effect of particle sizes on the mechanical behaviour of limestone-reinforced hybrid plastics. *Polym Polym Compos.* 2020;28(6): 410-420. doi: 10.1177/0967391119883163

39. Huang Y, Paul DR. Effect of temperature on physical aging of thin glassy polymer films. *Macromolecules.* 2005;38(24):10148-1054. doi: 10.1021/ma051284g

40. Greiner R, Schwarzl FR. Volume relaxation and physical aging of amorphous polymers I. theory of volume relaxation after single temperature jumps. *Colloid Polym Sci.* 1989;267(1):39-47. doi: 10.1007/BF01410147

41. Zhang J, Feng X, Patil H, et al. Coupling 3D printing with hot-melt extrusion to produce controlled-release tablets. *Int J Pharm*. 2016;519:186-197. doi: 10.1016/j.ijpharm.2016.12.049

ACCSCIENCE PUBLISHING

International Journal of Bioprinting

RESEARCH ARTICLE

Bioprinting with superelastic and fatigue-resistant bioinks for large-sized tissue delivery

Ruoyu Chen[1,2], Yijun Su[1], Dazhi Chen[1], Yinying Lu[1], Jinghua Zhao[3], Yali Zhang[3], Quan Yuan[3], Mingen Xu[4*], and Rui Yao[1,2*]

[1] Department of Mechanical Engineering, Tsinghua University, Beijing, China

[2] Institute of Zoology, Chinese Academy of Sciences, Beijing, China

[3] State Key Laboratory of Molecular Vaccinology and Molecular Diagnostics, National Institute of Diagnostics and Vaccine Development in Infectious Diseases, School of Public Health & School of Life Sciences, Xiamen University, Xiamen, Fujian, China

[4] Key Laboratory of Medical Information and 3D Bioprinting of Zhejiang Province, School of Automation, Hangzhou Dianzi University, Hangzhou, Zhejiang, China

(This article belongs to the *Special Issue: Advances in Bioprinting and Organ-on-a-chip and Applications for Precision Medicine*)

Abstract

3D bioprinting technology is advancing rapidly to construct multi-scale preformed architectures that satisfy the demands of tissue regeneration. However, challenges remain in accurately delivering large-sized preformed architectures to the defect sites without being damaged by the mechanical environment *in vivo*. In this study, we proposed a versatile bioprinting strategy to fabricate large-sized architectures with remarkable injection capacity for geometry-independent minimally invasive tissue delivery. We design a novel hydrogel by mixing gelatin methacryloyl with poly(ethylene glycol) diacrylate (PEGDA) and photocrosslinking the mixture under a white light source. The hydrogel forms a reinforced crosslinking network, exhibiting superelasticity and fatigue resistance. We infer that the flexible chains of high-molecular-weight PEGDA and interconnected macropores of hydrogel contribute to the reinforcement mechanisms. With a decoupled bioprinting strategy, the bioink can be 3D printed into large-sized architectures with different geometries and tunable Poisson's ratio. The printing architectures displayed excellent deformation and shape recovery capacity by compressing to less than 1% of the original size and fully recovering after injection. The injection capacity is geometry-independent, indicating the intrinsic properties of the hydrogel and allowing higher freedom for the structural design and geometry size of the architectures. The bioprinting process is compatible with genome-edited hepatic cells with high cell-bioprinting suitability, demonstrating high cell viability, a minimally altered transcriptomic profile after bioprinting, and a biocompatible microenvironment that supports cell survival and hepatic function maintenance. The cell-laden architectures express uncompromised injection capacity with unaffected cell viability after injection. This study presents a generalizable strategy for preparing and bioprinting with superelastic and fatigue-resistant bioinks into customized cell-laden architectures to facilitate minimally invasive large-sized tissue delivery.

Keywords: Tissue delivery; Bioprinting; Superelasticity; Fatigue resistance; Minimally invasive; Hepatic cells

***Corresponding authors:**
Rui Yao
(yaorui@ioz.ac.cn)

Mingen Xu
(xumingen@hdu.edu.cn)

Citation: Chen R, Su Y, Chen D, *et al*. Bioprinting with superelastic and fatigue-resistant bioinks for large-sized tissue delivery. *Int J Bioprint*. 2024;10(5):3898. doi: 10.36922/ijb.3898

Received: June 8, 2024
Accepted: July 11, 2024
Published Online: August 20, 2024

Copyright: © 2024 Authors. This is an Open Access article distributed under the terms of the Creative Commons Attribution License, permitting distribution, and reproduction in any medium, provided the original work is properly cited.

Publisher's Note: AccScience Publishing remains neutral with regard to jurisdictional claims in published maps and institutional affiliations.

1. Introduction

3D bioprinting is a versatile technique to construct cell-laden architectures for *in vivo* transplantation.[1] Bioprinting enables the creation of customized, large-sized architectures that match patients' specific defects. Recently, advanced printing techniques and functionalized bioinks have been developed to meet the translational challenges by fabricating advanced constructs with biomimetic heterogeneous structures or improved mechanical performance.[2] After *in vitro* culture, pre-formed architectures are commonly transplanted through open surgery methods, which can result in surgical trauma.[3] Injectable architectures offer one of the most viable options, allowing transplantation via minimally invasive methods. This approach can result in smaller wounds, less pain, and reduced post-surgical complications.[4] Minimally invasive tissue delivery holds promise for next-generation bioprinting architecture design and application, compatible with severe cases or patients of advanced age.[5] However, there is still a need to develop minimally invasive strategies for large-sized tissue delivery (delivered or injected with nozzles) to facilitate clinical application. Unlike cell therapy[6] and drug delivery,[7] which focus on dispersive therapeutic cells or nanoparticle drug carriers, large-sized tissue delivery emphasizes the efficient transplantation of engineered tissues with centimeter-scale size and complicated pre-formed 3D constructs. For clinical applications, pre-formed printed architectures should exhibit deformation and recovery capabilities to maintain structural integrity after tissue delivery. Moreover, the cyclic mechanical forces resulting from daily movement impose stringent requirements on the structural stability and fatigue resistance of architectures during long-term performance *in vivo*.

Microscale injectable scaffolds, also known as modular tissue engineering, and cell-laden injectable biomaterials[8] are widely used as bulk space fillers to transport therapeutic cells and cytokines. Yao *et al.* developed collagen/alginate microspheres with diameters in the hundreds of microns, demonstrating mechanical stability for subcutaneous injection and strong biological performance to support human vascularized adipose tissue regeneration.[9,10] For large-sized tissue delivery, stringent material requirements, including mechanical properties and fatigue resistance, pose challenges for breakthroughs in minimally invasive applications. 3D-printed cryogel scaffolds with high injection capacity have been fabricated using materials like chitosan or carboxymethylcellulose, leveraging their unique interconnected macroporous structure.[11,12] However, these strategies are limited in cell-laden applications due to the necessary lyophilization process. Recently, hydrogels that support cell survival and growth throughout their preparation and fabrication processes have attracted significant attention.[6] Ying *et al.* developed a gelatin methacryloyl (GelMA)-based hydrogel using a two-phase emulsion and an ultraviolet light (UV) exposure for bioprinting injectable, cell-laden hydrogel architectures.[13] However, the emulsion method is time-consuming and may result in limited pore connectivity, which affects long-term cell growth.[14] Tilton *et al.* proposed blue light-induced digital light processing (DLP) of GelMA/ poly(ethylene glycol) diacrylate (PEGDA) hydrogel to obtain injectable GelMA architectures under optimized geometrical designs, emphasizing the importance of structural designs in achieving desirable injection capacity, but at the expense of compatibility with customized geometries.[15] Besides injection capacity, fatigue resistance is another critical feature that affects the grafts' long-term performance *in vivo*. Tissues inside mammals undergo constant cyclic deformations due to daily movements. However, there is little research on the fatigue resistance of hydrogels that are compatible with living cells.

Herein, we propose a versatile bioprinting strategy to fabricate large-sized architectures with outstanding injection capacity using a novel bioink that features superelasticity and fatigue resistance for geometry-independent minimally invasive tissue delivery. We hypothesize that by using PEGDA (molecular weight [M_w]: 6000 Da) and a linear-chain structure, a reinforced crosslinking network containing flexible chains[16] can be introduced into the GelMA network. We utilized a white light source instead of commonly used UV or near-UV (typically blue) light, as white light is considered non-phototoxic.[17,18] The GelMA/PEGDA mixture (henceforth referred to as GP) with its specific composition and photocrosslinking under white light exhibits remarkable superelasticity and fatigue resistance, which are not observed in previous reports. A decoupled strategy of (i) micro-extrusion printing and (ii) photocrosslinking under white light enables independent control over the bioprinting and photocrosslinking processes, respectively. Large-sized architectures with different geometries, exhibiting tunable Poisson's ratios, are designed and successfully 3D printed using GP hydrogel. These printed architectures can be compressed to less than 1% of the original size, injected through syringe nozzles, fully recover their shape, and maintain intact 3D structures regardless of the geometrical designs. This behavior suggests that GP hydrogel is a distinct bioink that facilitates geometry-independent tissue delivery. Subsequently, large-sized cell-laden architectures were bioprinted using the cell-laden GP hydrogel, displaying excellent cell-bioprinting suitability with high cell viability and a minimally altered transcriptomic profile post-printing. The GP architectures provide a biocompatible microenvironment during

subsequent culture that supports hepatic cell aggregation and maintains cellular function. After a 16-day culture period, the cell-laden bioprinted architectures retained their injection capacity and were successfully compressed and injected without compromising cell viability (Figure 1). This study serves as a proof-of-concept for cell-laden bioprinting of injectable large-sized architectures, fostering potential advances in material development and applications in minimally invasive tissue delivery.

2. Materials and methods

2.1. Materials

Sterile GelMA powder with a 90% degree of substitution (BI-GM-p, R08020102) was purchased from Regenovo, China. GelMA was dissolved in phosphate-buffered saline (PBS; 02-024-1ACS; Biological Industries, Israel), heated to 70°C in an oven for 3 h to get a clear solution with 20% (w/v) concentration, and finally stored at 4°C for future use. PEGDA power (80020110, M_w: 6000 Da) was purchased from Tansh-Tech, China. PEGDA was dissolved in PBS at room temperature with 15% (w/v) final concentration, sterilized by 22 μm filter units (SLGPR33RB; Millipore, USA), and stored at 4°C. Eosin-Y (EY) disodium salt (E4382), triethanolamine (TEA; V900257), and 1-vinyl-2-pyrrolidinone (NVP; V3409) were purchased from Sigma-Aldrich, USA. Lithium phenyl-2,4,6-trimethylbenzoylphosphinate (LAP) powder was purchased from Regenovo, China.

2.2. Development and characterization of GP

2.2.1. Parameter optimization of GelMA

For parameter optimization, 20% (w/v) GelMA solution was mixed with the EY system to obtain final precursor solutions of 12.5% (w/v) GelMA with 1×, 2×, 3×, and 4× EY, respectively (e.g., 1×EY corresponds to 0.01 mM EY, 0.1% w/v TEA, and 37 nM NVP). The precursor solutions were cast in polydimethylsiloxane (PDMS) molds and exposed with a commercial tungsten halogen white light source (wavelength: 400–780 nm; light intensity: 12 mW/cm^2; HL250; NBet Company, China) for a gradient exposure period (2.5, 5, 7, and 10 min) (n = 4 per condition). Compared with arc or light-emitting diode lamps, this light source could provide a more stable output spectrum with no harmful UV emission or toxic ozone (Figure S1, Supporting Information). After light exposure, the PDMS molds were removed, leaving the GelMA samples. The crosslinking status (crosslinking, partial crosslinking, or no crosslinking) was evaluated via the mobility and shape integrity of GelMA samples. For the fabrication of PDMS molds, the elastomer base was mixed evenly with the curing agent (DOWSIL™ 184 Silicone Elastomer, 761036-5EA; Dow, USA) at a ratio of 10:1 and cured in an oven at 65°C for 100 min to reach total solidification. The solidified PDMS was then punched with a biopsy punch to obtain molds with a 5 mm diameter cylinder-shaped hollow. Before use, the surface of PDMS molds was plasma-treated with a plasma processor to alter the surface hydrophilicity. The stability of the GelMA cylinder was tested by adding 2

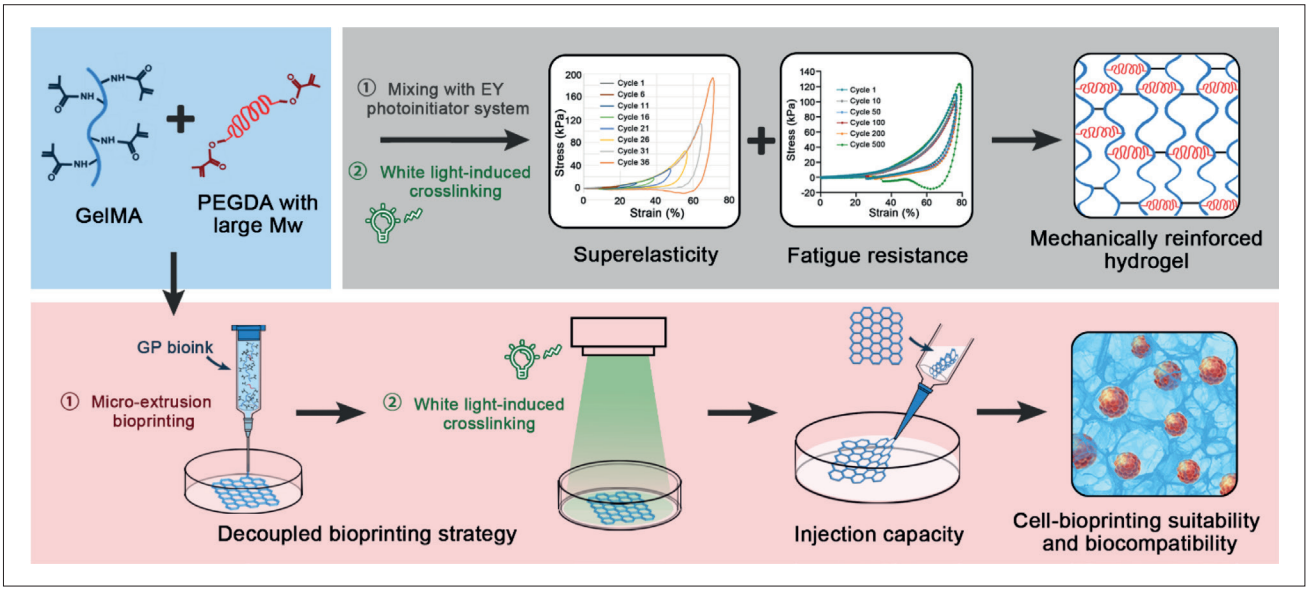


Figure 1. Schematic illustration of the workflow of this research. Abbreviations: GelMA: Gelatin methacryloyl; PEGDA: Poly(ethylene glycol) diacrylate; M_w: Molecular weight; EY: Eosin-Y; and GP: Gelatin methacryloyl/poly(ethylene glycol) diacrylate.

mL HepaRG culture medium to each sample and cultured in the incubator at 37°C and 5% CO_2. The stability of samples was observed and photographed with a camera and an inverted microscope (TS100; Nikon, Japan).

2.2.2. Development of GP hydrogel

For GP hydrogel development, the GP precursor was prepared by mixing 20% (w/v) GelMA, 15% (w/v) PEGDA, and the EY system to obtain final solutions of different material compositions, i.e., 12.5G (12.5% GelMA), 10G2.5P (10% GelMA and 2.5% PEGDA), 7.5G5P (7.5% GelMA and 5% PEGDA), and 6.25G6.25P (6.25% GelMA and 6.25% PEGDA), all containing 4×EY. GP precursors were then cast in PDMS molds and exposed to light (12 mW/cm^2) for a gradient period (2.5, 5, 7, 10, 12.5, 15, and 17.5 min) (n = 4 for each condition). The samples were observed and photographed using an inverted microscope to evaluate material uniformity and phase separation. The crosslinking status of samples was evaluated by the samples' mobility and shape integrity.

2.2.3. Cyclic compression and fatigue tests

The GelMA and GP samples were prepared, fully crosslinked, and punched using a biopsy punch to acquire cylindrical samples of 15 mm diameter and 2.5 mm height. Before testing, each sample's practical diameter and height were measured using a vernier caliper. For GelMA-LAP and GP-LAP samples, LAP powder (R08020102; Regenovo, China) was evenly dissolved in PBS in the dark to obtain a 40 mg/mL concentration solution. Material precursors were prepared by mixing 20% GelMA, 15% PEGDA, and 40 mg/mL LAP to reach a final solution of 10G2.5P and 12.5% GelMA with 0.5% (w/v) LAP. Material precursors were cast and crosslinked with a commercial UV light source (LS1601; Engineering for Life, China) for 30 s to achieve complete crosslinking. Fully crosslinked samples were punched using a biopsy punch to acquire cylindrical samples with 15 mm diameter and 2.5 mm height.

A dynamic mechanical testing device (Electroforce 3200 BioDynamic; Bose Company, USA) was used for the cyclic compression and fatigue tests. For cyclic compression tests, the cylindrical samples were loaded on the pressure head and subjected to deformation, increasing from 10% strain until the sample was damaged. Five repeated compressive cycles were performed for each strain. For fatigue tests, the samples were loaded and compressed to maximum strain (80% for GP-EY and GelMA-EY, 70% for GelMA-LAP, and 60% for GP-LAP) with a frequency of 1 Hz and 100 cyclic compressions. For 10G2.5P samples, 500 cyclic compressions were conducted. The real-time data of load and deformation was recorded during each compression cycle to plot the corresponding hysteresis curves. For each group, three independent samples were tested.

2.2.4. Scanning electron microscope analysis

The GP-EY samples were prepared and crosslinked as aforementioned. The samples were frozen at −80°C overnight and then lyophilized. Samples were fixed on the sample stage with conducting resin and platinum-coated to enhance surface electrical conductivity. The surface morphology was observed with a scanning electron microscope (SEM; JEOL, Japan). Semi-quantitative pore diameter and wall thickness were analyzed using Image J. Three independent random SEM images containing more than 60 macropores were calculated.

2.2.5. Rheological tests

Rheological properties of GP bioink were measured using a rotational rheometer (MCR301; Anton Paar, Austria) equipped with a cone plate featuring a 25 mm diameter, 2° cone angle, and 99 truncation gaps. The storage modulus (G'), loss modulus (G"), and viscosity (η) were recorded under the oscillatory model, with a strain (γ) of 1% and frequency (f) of 1 Hz, unless otherwise stated. The GP bioink (non-photocrosslinked GP precursor solution) was prepared as aforementioned. The bioink was incubated at 37°C before testing. For the temperature reduction sweep, the GP bioink was loaded on the test plate, and G' and G" were detected using a cooling platform process from 25 to 5°C, with 120 data points recorded. For temperature preservation testing, the plate's temperature was set at 19°C, and the G' and G" of samples were continuously measured for 20 min, with 60 data points recorded. The viscosity was measured with shear rate sweeps from 0 to 1000/s, with the temperature of the platform set to 25°C during the test.

2.3. 3D printing and injection experiments

2.3.1. Printing model design and decoupled 3D printing

All the printing models were designed using SolidWorks 2019 (Dassault Systèmes SOLIDWORKS Corporation, USA), G-code editing software IGcode Tool (Regenovo, China), and the built-in route planning functions of the printing control software, unless otherwise stated. Micro-extrusion bioprinting was conducted using a multi-nozzle bioprinter (Bioarchitect X; Regenovo, China). The GP solution was prepared, transferred into a 5 mL syringe, and loaded onto the printing device. A non-transparent syringe was used to avoid uncontrolled light exposure during extrusion. The syringe, nozzle, and baseplate temperatures were controlled at 21, 17, and 12°C, respectively, using a precise temperature-control module integrated within the bioprinter. The pre-designed models were then bioprinted with a pneumatic pump pressure of 0.14 MPa and an extrusion velocity of 5 mm/s. Unless otherwise stated, all the mentioned models were printed at dimensions of 15 × 15 × 1 mm (four layers). After printing, the 3D architectures

were photocrosslinked using white light for 10 min and washed with PBS to remove the residual photoinitiator. For bioprinting, various filling pattern architectures and biomimetic liver lobule architectures, red or blue dyes were evenly mixed to color the hydrogel and enhance the visualization of the filaments.

2.3.2. Shape fidelity assessment

Lattice architectures with 90° intersection angle were printed to determine the shape fidelity. Briefly, grid structures (10 × 10 × 1 mm) were 3D printed and photocrosslinked for 10 min under white light (12 mW/cm^2). The material preparation and bioprinting procedure were performed as aforementioned. The shape fidelity after printing was assessed by quantitative analysis of bioink printability (*Pr)* with the following equation:

$$Pr = \frac{L^2}{16A} \quad \text{(I)}$$

where L and A denote the perimeter and area of the hollow channels, respectively. The geometrical features of the channels within the grid structure were measured using Image J. Six independent images with more than 30 channels were calculated.

2.3.3. Degradation assessment

For the degradation test, 1.5 mL HepaRG culture medium was added to each sample and cultured for 16 days in the incubator. Every four days, optical images were captured using the microscope. For semi-quantitative statistics, the average width of filaments at each time point was measured using Image J and normalized to day 1. Four independent fields with more than 20 filaments were calculated for each time point.

2.3.4. Deformation behavior and injection capacity tests

Circular ring GP architectures with a diameter of 10 mm (two layers) were bioprinted into culture dishes and photocrosslinked under white light for 10 min. Samples were immersed in PBS buffer during the deformation procedure. For cyclic pinch, the two sides of the circular ring sample were pinched using a tweezer until the bilateral filaments were in contact and then loosened to enable free recovery. This deformation procedure was repeated for 30 cycles. For a cyclic stretch, the inner sides of the sample were clamped with tweezers, stretched to create large deformation, and loosened for recovery. The deformation cycle was repeated five times.

Complex models with disparate repetitive units were bioprinted inside culture dishes. After photocrosslinking, the GP-printed architectures were washed with PBS and incubated overnight with 2 mL of cell culture medium. The samples were immersed in PBS and injected through silicone tubes (inner diameter: 5, 4, and 3 mm) and dispensing needles (inner diameter: 2, 1.5, and 1 mm).

A fresh pork liver was used for the *in vivo* injection simulating experiment. Briefly, the sinusoidal mesh samples were collected and injected onto the surface of the pork liver via a dispensing needle with an inner diameter of 2 mm. PBS buffer was used as a carrier buffer. The injection and spreading process of samples were observed and recorded.

2.4. Cell-laden bioprinting and function assessments

2.4.1. Cell culture

HepaRG cells (HPRGC1) were purchased from Sigma-Aldrich, USA. M14A cells were established by Sleeping Beauty transposition. Briefly, hepatic determining transcription factor *HNF4A* and a cell proliferation regulatory factor *FoxM1* were cascaded on Sleeping Beauty transposons and transfected into HepaRG cells. The M14A clones were selected with 2 μg/mL puromycin (Gibco, A1113802) 24 h after transfection. M14A and HepaRG cells were cultured in an incubator at 37°C and 5% CO_2. The culture medium was composed of Dulbecco's Modified Eagle Medium (DMEM; 11995500BT; Gibco, USA), supplemented with 10% fetal bovine serum (11011-8615; Zhejiang Tianhang Biotech, China), 1% GlutaMAX (35050061; Gibco, USA), 1% minimum essential medium (MEM) non-essential amino acids solution (11140050; Gibco, USA), 0.05% insulin (PB180432; Procell, China), 5 × 10^{-5} mol/L hydrocortisone sodium succinate (Changzhou Siyao Pharm, China), and 1% penicillin-streptomycin (P1400; Solarbio, China). Cells were dissociated with 0.25% Typsin-EDTA (T1320; Solarbio, China) and passaged after reaching 85–90% confluence. The culture medium was changed every two days.

2.4.2. Cell viability assessment in the GP hydrogel

HepaRG cells were used to investigate the influence of exposure time on cell viability. HepaRG were collected from culture flasks using 0.25% Trypsin-EDTA, counted with a cell counter (Countstar, China), and then gently mixed with 20% GelMA solution, 15% PEGDA, and the EY system to obtain a final cell-laden GP precursor, consisting of 10% GelMA, 2.5% PEGDA, 4× EY and 3 × 10^6 cells/mL. The precursor was then cast in PDMS molds and exposed to 12 mW/cm^2 white light for a gradient period (5, 10, 15, and 20 min). After exposure, cell viability was assessed via live/dead straining. Briefly, calcein-AM and propidium iodide (PI) (Calcein-AM/PI Double Staining Kit, C346; Dojindo, Japan) were diluted with PBS to obtain

a final working solution containing 2 μmol/L calcein-AM and 4.5 μmol/L PI. Cell-laden GP samples without light exposure were used as the control group. All the samples were incubated in the live/dead staining working solution for 15 min in the dark to stain the live (green) and dead (red) cells. The samples were observed and recorded using a laser scanning confocal microscope (LSCM; Z2; Nikon, Japan). Quantitative analysis was performed using the count/size tool in Image J. Cell viability was calculated using the following equation:

$$\text{Cell viability} = \frac{\text{number of living cells}}{\text{total cell number}} \times 100\% \quad \text{(II)}$$

Three independent samples were analyzed for each group unless otherwise stated.

2.4.3. Uniaxial compression test

To determine the elastic modulus of GP hydrogel, we performed the uniaxial compression tests using the dynamic mechanical testing device. GP samples (10G2.5P with 10 min exposure) were loaded on the pressure head and compressed with a 25% deformation at a loading speed of 0.2 mm/s. The real-time data were recorded during the compression process to plot the stress–strain curve. The slope of the curve represents the compressive elastic modulus. The smoothed curve was generated from the treated data using the signal processing function in OriginPro 2018C (OriginLab Corporation, USA). Three independent samples were tested.

2.4.4. Cell-laden bioprinting and culture of the architectures

M14A cells were used to evaluate the cell-bioprinting suitability and biocompatibility of GP hydrogel. M14A cells were collected using 0.25% Trypsin-EDTA. Cells were counted and gently mixed to obtain a final cell-laden GP precursor consisting of 10% GelMA, 2.5% PEGDA, 4× EY, and 9×10^6 cells/mL. 3D architectures were bioprinted, photocrosslinked using white light for 10 min and washed with PBS to remove the residual photoinitiator. The cell-laden architectures were cultured in an incubator with the culture medium changed daily. The microscopic images of cell-laden architectures were captured on days 1, 5, 9, and 16. Semi-quantitative analysis was performed as described in **Section 2.3.3**.

2.4.5. Injection of cell-laden architectures

After 16 days of culture, the cell-laden architectures were injected using dispensing needles with an inner diameter of 1.5 mm. Cell viability before and after injection was assessed by live/dead staining. Semi-quantitative analysis of cell viability was performed using Image J as follows:

$$\text{Fluorescence intensity ratio} = \frac{\text{live cells}}{\text{live cells + dead cells}} \times 100\% \quad \text{(III)}$$

Three independent samples were analyzed for each group.

2.4.6. Immunofluorescence staining

Immunofluorescence staining was performed based on previously described protocols,[19] with slight modification. Briefly, planar cultured cells were fixed for 30 min using 4% paraformaldehyde (P1110; Solarbio, China), permeabilized by 0.3% Triton-X100 (T8200; Solarbio, China) for 20 min on ice, and blocked with 10% bovine serum albumin (BSA) (containing 0.1% Triton-X100) (9048-46-8; Yeasen Biotech Company, China) for 1 h at room temperature. The specimens were then incubated with primary antibodies (diluted with PBS buffer, containing 0.3% Triton-X and 1% BSA) at 4°C overnight, followed by incubation with the corresponding secondary antibodies for 2 h in the dark at room temperature. Cell nuclei were stained with DAPI (D9542; Sigma-Aldrich, USA) for 30 min in the dark. PBS was used to wash specimens between every step.

For the bioprinted architectures, samples were fixed for 4 h with 2.5% glutaraldehyde (G5882; Sigma-Aldrich, USA), permeabilized for 20 min on ice, and blocked for 2 h at room temperature. The specimens were washed three times with PBS and incubated with primary antibodies at 4°C overnight. The residual primary antibodies were washed out, and the specimens were incubated with secondary antibodies at 4°C overnight in the dark. The cell nucleus was then stained with DAPI for 30 min in the dark. The reagent and concentration of solutions used were similar to that for the 2D samples unless stated otherwise. Detailed information on the used antibodies is listed in **Table S1, Supporting Information**. A laser-scanning confocal microscope was used to capture immunofluorescence images. Images were captured using a 3D configuration with 100 μm total height for the printed specimens, and the maximum density projection images are presented accordingly.

2.4.7. Chemical staining

For planar cultured specimens, M14A and HepaRG cells were cultured in 35 mm culture dishes for 14 days, with the culture medium changed daily. Bioprinted architectures on day 16 were used for chemical staining. To assess glycogen storage functions, a glycogen periodic acid-Schiff (PAS) kit (G1360; Solarbio, China) was used for glycogen staining, following the manufacturer's instructions. To assess hepatocyte functions, indocyanine green (ICG) powder (S46424; Shanghai Yuanye Biotechnology Company, China) was completely dissolved in dimethyl sulfoxide

(100 mg/mL), added to the HepaRG culture medium, and mixed evenly to obtain a final concentration of 1 mg/mL. The samples were cultured with an ICG-containing medium to facilitate ICG uptake. Optical microscope images were captured using an optical microscope (BX51; Olympus, Japan) every 10 min until successful uptake of ICG by cells was observed. The ICG-containing medium was then replaced with a regular culture medium for ICG release. Cell release images were captured every 1 h until ICG was completely released.

2.4.8. RNA-seq analysis

For planar cultured HepaRG and M14A samples, cells were digested from culture flasks, centrifuged, and collected in TRIzol for RNA extraction (n = 3 per group). For cell-laden printed architectures, the samples were snap-frozen using liquid nitrogen and ground with mortar and pestle to fracture the materials and cell structures. RNA was then extracted using TRIzol (n = 2 per group). RNA isolation, complementary deoxyribonucleic acid library construction, sequencing, and basic analysis were performed at Novogene (China). For every sample, 1 μg of RNA was employed to establish sequencing libraries utilizing the NEBNext® UltraTM RNA Library Prep Kit for Illumina® (New England Biolabs, USA), and each sample was assigned an index code according to the attribute sequences. Before the library establishment, the integrity of sample RNA was analyzed using the RNA Nano 6000 Assay Kit of the Bioanalyzer 2100 system. Sequencing was performed using an Illumina NovaSeq 6000 platform, generating 150 bp paired-end reads. Reads were filtered and mapped to the reference genome sequence with HISAT2 (version 2.0.5). FeatureCounts v1.5.0-p3 was used to count the read numbers mapped to each gene. The Fragment Per Kilobase of transcript, per Million mapped reads (FPKM) method was used to calculate gene expression levels. Differentially expressed genes ($|\log2FoldChange| \geq 1.0$; false discovery rate [FDR] q-value < 0.05) were identified with the DESeq2 R package (version 1.16.1), and the resulting p values were adjusted Benjamini and Hochberg's approach for controlling the FDR q-value. The Gene Ontology (GO) dataset was used for gene set enrichment analysis (GSEA), which was performed using the local version of the GSEA tool (http://www.broadinstitute.org/gsea/index.jsp). The raw sequence datasets had been submitted to the Sequence Read Archive database with the GEO submission number GSE230068.

2.5. Statistical analysis

Statistical analysis was performed using IBM SPSS Statistics, using independent t-test (unpaired) and one-way analysis of variance (ANOVA) with a Tukey's honestly significant difference (HSD) post-hoc test. All data are presented as mean ± standard deviation. Statistical significance was defined as *p < 0.05, ** p < 0.01, *** p < 0.001 and **** p<0.0001. "N.S." denotes no statistical significance ($p \geq 0.05$). Unless otherwise stated, three independent experiments were performed, and repeated trends were observed.

3. Results and discussion

3.1. Development and characterization of GP hydrogel

The injection capacity of macroscale architectures depends on many factors, including the crosslinking mechanism, microstructure features, and the macrostructure design.[20,21] Compared to ionic, enzymatic, and thermal crosslinking, photocrosslinking forms a more stable covalent network that significantly enhances mechanical properties, including elastic deformation performance.[22] GelMA, a photocrosslinkable hydrogel with good biocompatibility, thermosensitivity, and low immunogenicity, is favorable for bioprinting and other biomedical applications.[23] To avoid the toxicity of UV or near-UV exposure on cells, we employed a white light-induced polymerization system utilizing the photosensitizer EY, which has an absorption peak of 510 nm (referred to as the EY system) (Figure S1, Supporting Information). The system also includes the photoinitiator TEA and co-monomer NVP. The latter was chosen to increase the abundance of vinyl groups for crosslinking with GelMA, enhance radical diffusion, and prevent free radicals from being scavenged by oxygen, thereby facilitating the photocrosslinking reaction.[24]

The hydrogel concentration, photoinitiator concentration, and light exposure time are important parameters for light-induced polymerization. We preliminarily optimized these parameters using GelMA hydrogel. As high concentrations of EY and TEA are toxic to cells during the light-induced reaction,[25,26] the upper limit of the EY system was set to 4× EY. As aforementioned, 1× EY corresponds to 0.01 mM EY, 0.1% (w/v) TEA, and 37 nM NVP. To prevent microbial contaminations, the lid of the petri dish was closed during photocrosslinking. We noticed that GelMA concentrations < 12.5% (w/v) would not trigger the crosslinking reaction. Considering that higher GelMA concentration can lead to higher viscosity, complicating experimental operations and potentially forming a compact crosslinking network that hinders cell proliferation and migration,[27] we set the GelMA concentration at 12.5% for this study and optimized the photoinitiator concentration and light exposure time accordingly. The crosslinking degree of GelMA increased with higher photoinitiator concentration and longer light exposure time (Figure 2A). Notably, 1× EY and 2× EY were insufficient to reach the crosslinking threshold, consistent

with the report by Bahney *et al.*[25] Likewise, 3× EY could not attain complete crosslinking, unless the exposure time was extended over 10 min. For GelMA containing 4× EY, the crosslinking reaction occurred within 7.5 min of light exposure, and the samples reached full crosslinking under 10 min of exposure. GelMA was then cast in cylindrical molds and cultured long-term to assess mechanical stability. After a 12-day culture period, severe material degradation and irregular edges were observed (Figure 2B), suggesting suboptimal mechanical behavior when using GelMA alone.

As an acrylate derivative of polyethylene glycol, PEGDA is a soft elastomer that can be crosslinked with GelMA to improve the degradation behavior.[28] Previous studies utilizing PEGDA (M_w < 1000 Da) (Table S2, Supporting Information) reported improved elastic modulus but decreased toughness.[15,29] Hence, linear-chained PEGDA with large M_w (6000 Da) was selected for this study. We hypothesize that the selected PEGDA will introduce flexible chains into the GelMA crosslinking network, thereby enhancing mechanical properties, including deformation capacity.

Based on the above optimization, we standardized the final concentration of GP prepolymer at 12.5% and the photoinitiator concentration at 4× EY. During the material mixture and photocrosslinking procedures, no signs of phase separation were observed (Figure S2, Supporting Information). We discovered a nonlinear relationship between PEGDA concentration and exposure time, with a minimum exposure time observed for 10% (w/v) GelMA and 2.5% (w/v) PEGDA (referred to as 10G2.5P) (Figure 2C). To assess the mechanical properties of GP hydrogel, we analyzed the mechanical behaviors of fully crosslinked GP under different prepolymer concentrations and compared them across different hydrogel types (GP and GelMA) and photoinitiator systems (EY system for white light-induced crosslinking and LAP system for UV-induced crosslinking) (Table S3, Supporting Information). LAP is widely used as a UV/near-UV photoinitiator with higher crosslinking efficiency and lower cytotoxicity compared to Irgacure 2959 (I2959).[30] In cyclic compression tests, all GP-EY and GelMA-EY groups displayed superior endurance when the strain increased from 10 to 80% (Figure S3A, Supporting Information; Video S1, Supporting Information), suggesting remarkable superelasticity. The corresponding stress–strain curves of 10G2.5P are presented in Figure 2D, indicating a maximum strain of 80% and a maximum stress of 192 kPa. Conversely, UV-induced crosslinking led to decreased elasticity, with GelMA-LAP fracturing at 70% strain (Figure S3B, Supporting Information) and GP-LAP fracturing at 60% strain (Figure S3C, Supporting Information).

Furthermore, the cyclic loading compression tests were conducted at 80% strain to characterize the mechanical fatigue features of GelMA and GP under white light-induced photocrosslinking (Figure 2E). The compressive stress of GelMA-EY rapidly decreased to 11% of the initial status after 50 deformation cycles, suggesting poor fatigue resistance (Figure 2F). However, all GP-EY samples endured 100 cyclic deformations without apparent fatigue or decrease in mechanical stress (Figure S4, Supporting Information), among which 10G2.5P samples could resist up to 500 cycles (Figure 2G). These results indicate significantly enhanced fatigue resistance upon incorporating the specific type of PEGDA into GelMA. In contrast, GelMA-LAP and GP-LAP exhibited no signs of fatigue resistance behavior and fractured rapidly after 5 cyclic compressions at 70% and 60% strain, respectively (Figure S5, Supporting Information).

The GP hydrogel expressed remarkable superelasticity and fatigue resistance. We hypothesized the reinforcement mechanism of the GP hydrogel from two aspects, i.e., (i) white light-induced crosslinking mechanism and (ii) microstructure features. Regarding the reaction mechanism, the EY system requires an extended crosslinking time of up to several minutes[22] for facilitating the full reaction of PEGDA with GelMA to form a hybrid crosslinking network. With the outstanding deformation capacity of PEGDA (M_w: 6000 Da),[31] flexible chains can be transformed into rigid crosslinking chains of acryl groups in GelMA, thus improving the deformation capacity and reinforcing the GP hydrogel (Figure 2I). Nevertheless, the LAP system is characterized by rapid photocrosslinking within tens of seconds,[30] which complicates achieving a complete reaction among long-chain PEGDA with the GelMA matrix, thereby compromising mechanical fatigue features. Similarly, He *et al.*[32] and Li *et al.*[33] have reported that long-chain PEGDA/GelMA mixtures exhibited enhanced toughness under the LAP photoinitiator system (Table S2, Supporting Information). However, neither superelasticity nor fatigue resistance was mentioned. For the microstructure features, SEM analysis displayed interconnected macroporous structures similar to cryogel scaffolds in the GP hydrogel, with an average pore diameter of 33.0 ± 9.0 μm and pore wall thickness of 4.2 ± 0.8 μm (Figures 2J and S6, Supporting Information). The macroporous structure with thin walls likely contributes to the reinforced mechanical behavior of GP. The large pores serve as deformation units to absorb and release elastic energy, while the thin walls provide sufficient stretchability under large deformations.[34]

At this stage, we conducted a comprehensive literature review on previous reports involving GP mixture in the PubMed database. To our knowledge, all the reports

presenting compressive stress–strain curves were included to compare with this study. GelMA is commonly used as a control group in these studies, and we highlighted the optimal conditions for GelMA (Figure 2H; Table S2, Supporting Information). Compared to previous studies, this is the first study to report on a GP mixture with superelasticity and fatigue resistance features. The preparation and crosslinking procedure of GP was versatile and did not require a complicated dispersion or freezing process, providing a generalized strategy for developing novel mechanically reinforced hydrogels for tissue delivery applications.

3.2. 3D printing, stability, and deformation behavior of GP architectures

3D printing technology is widely used to fabricate architectures with customized geometries. To fabricate large-sized architectures with high injection capacity using GP hydrogel, a decoupled strategy of micro-extrusion and photocrosslinking was utilized instead of commonly used DLP methods. The reversible thermal crosslinking of GelMA was employed to regulate the gelation status during cooling for smooth extrusion. Subsequently, the primary printed architectures were photocrosslinked by the white light source to establish a stable covalent network. This strategy enables independent regulation of bioprinting and photocrosslinking and is compatible with widely accessible bioplotting devices.

The rheological characteristics of the hydrogel matrix are vital for a stable extrusion process.[19] Upon rheological analysis, 10G2.5P without photocrosslinking displayed typical thermoresponsive characteristics and sol-gel phase transition with a gelation point at 19°C (Figure 3A). At a 20 min temperature preservation process at 19°C, 10G2.5P maintained a constant gel phase and exhibited stable viscoelasticity with G' of 306.6 Pa and G" of 9.7 Pa (Figure 3B), similar to that of gelatin/alginate bioink, thereby facilitating high cell viability after bioprinting.[35] The viscosity curve suggests that GP expresses a typical shear-thinning behavior under shear force (Figure 3C). These results indicate that GP is compatible with micro-extrusion printing, displaying suitable thermoresponsive and shear-shining properties. Using the multi-nozzle bioprinter with a precise temperature-control module (Regenovo, China), the gelation conditions of the bioink can be accurately controlled to facilitate continuous extrusion of smooth filaments (Figure 3C). Hence, the temperature of the syringe holder was set at 2°C higher than the gelation point to enhance bioink flow and cell survival. The temperature of the nozzle holder was set at 2°C lower than the gelation point to facilitate rapid gelation and filament formation.

The lattice architectures were first 3D printed and photocrosslinked (Figure S7A, Supporting Information) to assess the shape fidelity of GP hydrogel using equations previously established by our group.[36] The *Pr* was calculated to be 1.03 ± 0.02, suggesting good shape fidelity with a *Pr* value in the range of 0.9~1.1 (Figure S7B, Supporting Information). Thereafter, architectures with different filling patterns, i.e., sinusoidal, Hilbert, and zigzag curves, were designed and smoothly printed (Figure 3D). The decoupled strategy enables independent photocrosslinking with the culture dish lid closed, maintaining sterility and reducing water evaporation from the hydrogel (Figure S8, Supporting Information). The crosslinked architectures were then immersed in the culture medium at 37°C for 16 days to evaluate the material degradation under cell culture conditions. Semi-quantitative analysis displayed no significant differences in filament diameter after the 16-day culture (Figure 3E), suggesting good structural stability and potential for long-term cell culture. Next, the deformation behavior of circular ring-shaped printed architectures was assessed. The samples presented exemplary deformation capacity and fatigue resistance, enduring 30 pinch cycles and five stretch cycles, as well as recovering with intact structure (Figure 3F; Video S2, Supporting Information). This deformation behavior warranted further investigation into the injection capacity of large-sized printed architectures with more complex geometries.

3.3. 3D printing of large-sized architectures with high injection capacity

Repetitive units with different geometries exhibit tunable Poisson's ratios during deformation: honeycomb patterns display a positive Poisson's ratio (PPR); semi-re-entrant honeycomb repetitive patterns mostly display zero Poisson's ratio (ZPR); while re-entrant honeycombs, sinusoidal meshes, lozenge grids, and curved meshes demonstrate an auxetic effect, inducing a negative Poisson's ratio (NPR). In this study, the models mentioned above were designed (Figure 4A). The corresponding architectures were printed with a dimension of 15 × 15 × 1 mm for parallel studies (Figure 4B). A systematic evaluation of injection capacity was performed utilizing silicone tubes and dispensing needles with inner diameters ranging from 1 to 5 mm, comparable to the sizes of medical catheters or syringe needles widely used for clinical applications (Table S4, Supporting Information). After injection through the silicone tubes and needles, the injection capacity was evaluated via the integrity of geometric features and the fracture of filaments. Additionally, the injection capacity was semi-quantitatively calculated from the values of S_{inject} (minimum sectional area of the needle used) and $S_{architecture}$ (maximum sectional area of the architecture; i.e., 15 × 15 mm), using the equation listed below:

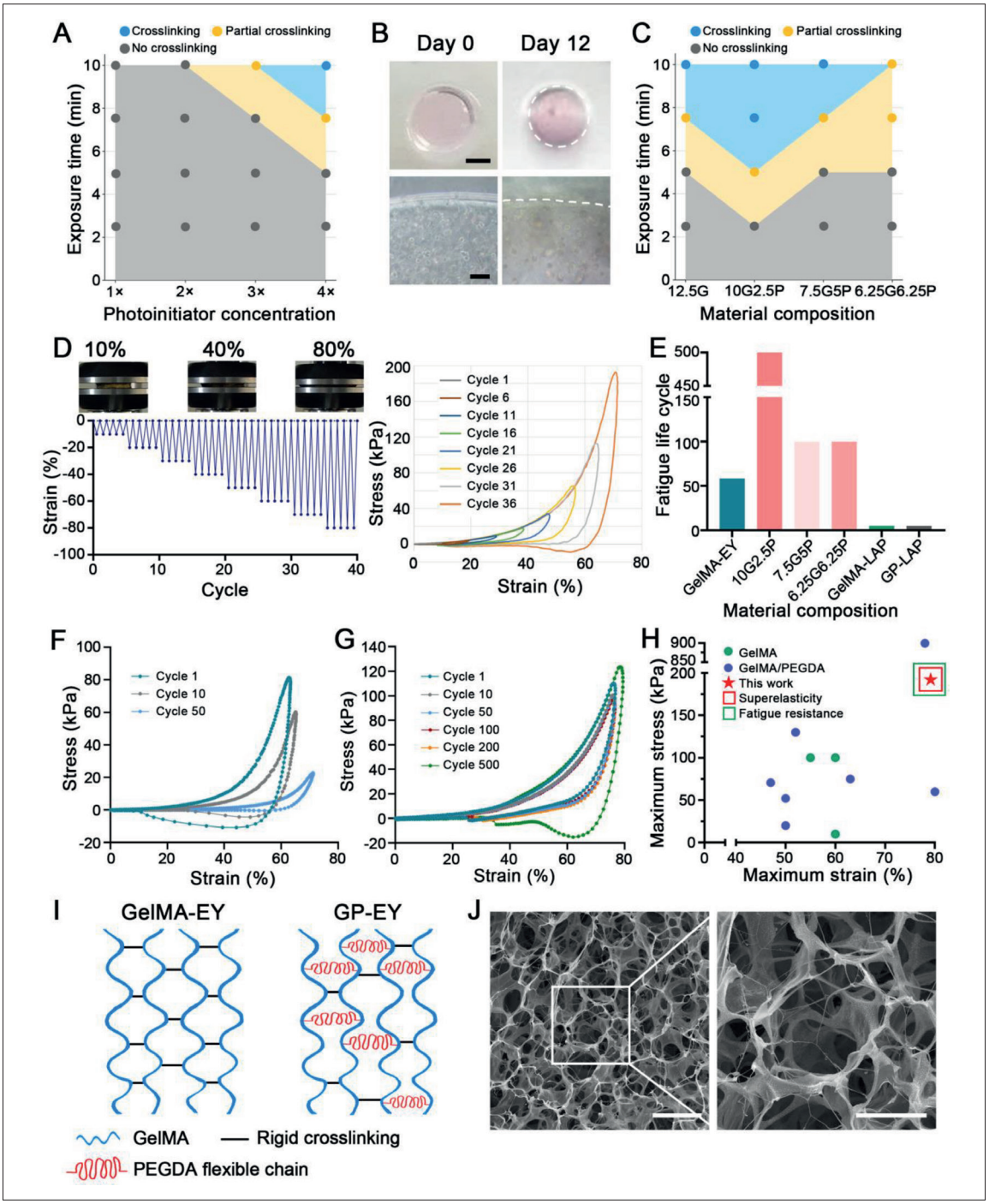


Figure 2. Development and characterization of the GP hydrogel. (A) Coupling optimization of exposure time and photoinitiator concentration (n = 4 for each condition). (B) Macroscopic (top row) and microscopic images (bottom row) of GelMA cylinders during mechanical stability evaluation, with dotted lines indicating the sample edges. (C) Optimization of GP exposure time with different material compositions under 12.5% final concentration and 4× EY (n = 4 for each condition). (D) Cyclic compression tests with increasing strain from 10% to 80% (left) and corresponding hysteresis curves (right) of 10G2.5P at 12.5 min light exposure. (E) Fatigue life cycles of different groups (n = 3). (F and G) Typical hysteresis curves of fatigue tests on GelMA (F) and 10G2.5P (G) at 10 min light exposure under the EY system, with 80% strain for each compression cycle. (H) Comparison of this work (red star) with previous reports on GelMA (green dots) and GP mixture (blue dots). (I) Schematic illustration of white light-induced reinforcement mechanism. (J) Low-magnification SEM image of photocrosslinked GP hydrogel (left) and a high-magnification image corresponding to the rectangular region (right). Magnification: 200,000× (J, left), 500,000× (J, right). Scale bars: 2 mm (B, top row); 100 μm (B, bottom row; J, left); 50 μm (J, right). Abbreviations: GelMA: Gelatin methacryloyl; PEGDA: Poly(ethylene glycol) diacrylate; GP: Gelatin methacryloyl/poly(ethylene glycol) diacrylate; and EY: Eosin-Y.

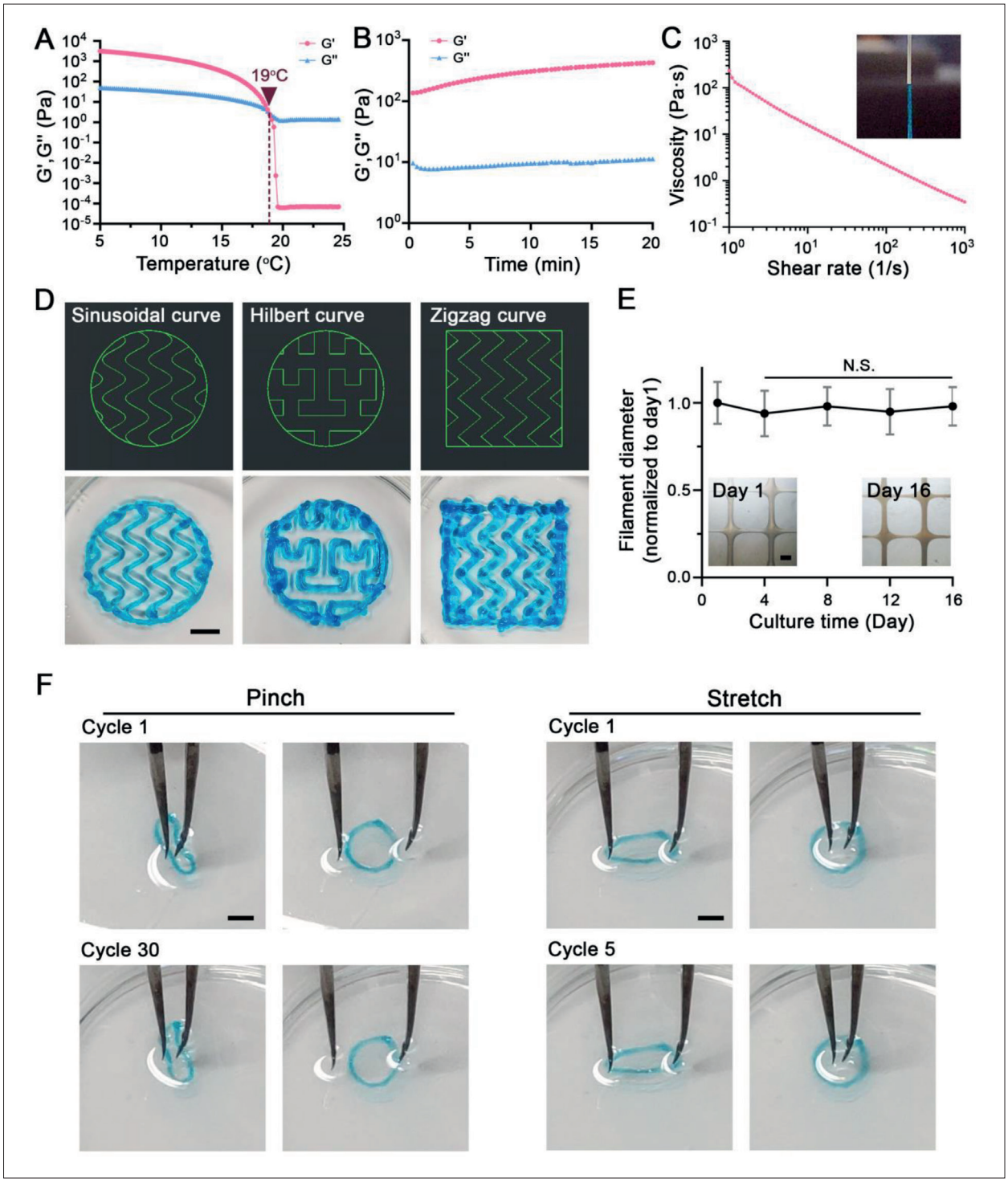


Figure 3. 3D printing, stability, and deformation behavior of GP architectures. (A) A temperature sweep from 5 to 25°C during the reduction process of GP hydrogel. (B) A 20-min time sweep at a constant temperature of 19°C. (C) Viscosity curve of GP hydrogel; smooth filament extrusion from the nozzle (inset). (D) The designed models and the corresponding printed architectures with different filling patterns. (E) Structural stability test of the printed architectures during long-term culture. Four independent fields with more than 20 filaments were calculated for each time point. (F) Cyclic pinch and (G) stretch of the bioprinted architectures with circular ring geometry. Statistical analysis in (E) is performed using ANOVA with Tukey's HSD post-hoc test. Scale bars: 5 mm (D); 500 μm (E–G). Abbreviations: N.S.: no statistical significance; GP: Gelatin methacryloyl/poly(ethylene glycol) diacrylate; G': Storage modulus; G": Loss modulus; ANOVA: one-way analysis of variance; and HSD: honestly significant difference.

$$\text{Injection capacity} = \frac{S_{inject}}{S_{architecture}} \times 100\% \quad \text{(IV)}$$

Interestingly, all large-sized architectures exhibited similar injection capacity, regardless of geometrical features and Poisson's ratios (Table S4, Supporting Information; Video S3, Supporting Information). These architectures could be consistently compressed to 0.79% of the original size, injected through needles with a minimum inner diameter of 1.5 mm (comparable to a 14G needle), and subsequently unfolded and restored to the original shape while maintaining structural integrity (Figure 4C; Video S4, Supporting Information). When the needle diameter decreased to 1 mm, all the samples were damaged, with fractured filaments (Figure S9, Supporting Information). These results revealed that the deformation and shape recovery behavior of large-scale architectures was versatile, depending on the inherent mechanical properties of GP, and compatible with different structural designs for injection procedures.

After assessing the injection capacity of large-sized architectures, a simulation experiment was conducted for *in vivo* injection. The sinusoidal mesh samples were injected via a dispensable syringe with an inner diameter of 2 mm onto the surface of a pork liver (Figure S10, Supporting Information). The printed architecture could be continuously injected and effectively spread on the surface of liver tissue, suggesting the potential for minimally invasive tissue delivery applications (Video S5, Supporting Information). Furthermore, biomimetic models of analogous liver lobules (radiation sinusoid model and hexagonal lobule model) were designed. The corresponding architectures were successfully printed using a multi-nozzle extrusion printer with temperature-control modules (Figure 4D). Taken together, we present a versatile bioprinting strategy for fabricating injectable large-sized architectures using GP hydrogel. Our findings highlight that the excellent injection capacity was dependent on the mechanical behavior of GP hydrogel and was compatible with various model designs featuring tunable Poisson's ratios. After injection, the samples were able to recover their original geometries. Hence, the versatility of GP hydrogel for bioprinting applications can be exploited to create intricate architectures with multiple materials and biomimetic designs.

3.4. Cell-laden GP hydrogel supports high cell-bioprinting suitability

Cells are living components in the bioink and are critically important for *in vitro* tissue/organ reconstruction. After printing, a high cell survival rate and unaffected phenotype are the prerequisites for subsequent cell assembly and function remodeling. Therefore, providing a comprehensive and scientific description of cell-bioprinting suitability is indispensable.

In this study, we evaluated the cell-bioprinting suitability of GP hydrogel using two cell types: HepaRG cell lines and genome-edited hepatocytes based on HepaRG. HepaRG is a human hepatoma cell line with bipotent hepatic progenitor-like characteristics and is readily used in artificial liver construction and drug testing applications.[37] The influence of light exposure time on HepaRG viability was tested to determine the optimal window for cell-laden bioprinting. Our findings indicate that 5 and 10 min of exposure did not significantly influence cell viability in the absence of added culture medium. However, long-term exposure (15 and 20 min) induced massive cell death, likely due to liquid evaporation and heat radiation from white light exposure (Figure 5A). A compressive test was then conducted on GP that was crosslinked for 10 min. The elastic modulus was determined to be 23.2 ± 1.6 kPa (Figure S11, Supporting Information), i.e., within the scope of human tissues and comparable to the natural liver.[38,39] Therefore, 10 min light exposure time was optimal for subsequent cell-laden bioprinting studies.

While cell viability is commonly used to assess the influence of the printing procedure,[35] we consider it a rough analysis because cell injury may alter cell phenotype, leading to unwanted variations in subsequent cell self-organization and morphogenesis.[40] Thus, we proposed a paradigm for assessing cell-bioprinting suitability by combining cell viability and transcriptome sequencing (RNA-sequencing analysis) to provide a full-scale evaluation of cellular alternations after printing.

We established a new genome-edited hepatic cell line based on HepaRG to assess the cell-bioprinting suitability of GP-bioprinted hydrogel. By transfecting two genes (*FoxM1* and *HNF4A*) using Sleeping Beauty transposon into HepaRG (Figure 5B), we obtained fluorescent-labeled HepaRG-M14A cells (henceforth referred to as M14A) that exhibit the typical polygonal morphology of hepatocytes (Figure 5C). Additionally, these cells could spontaneously differentiate into hepatocytes without a HepaRG induction medium. Immunofluorescence staining revealed that M14A expressed high levels of hepatic marker proteins, i.e., HNF4A and ALB (Figure 5D). Moreover, M14A expressed more glycogen storage and better ICG uptake capacity compared to HepaRG (Figure S12A, Supporting Information). RNA-sequencing analysis displayed a significantly different transcriptome for M14A compared to HepaRG (Figure S12B, Supporting Information). Multiple gene sets related to biosynthesis, metabolism, viral genome replication, and virus receptor

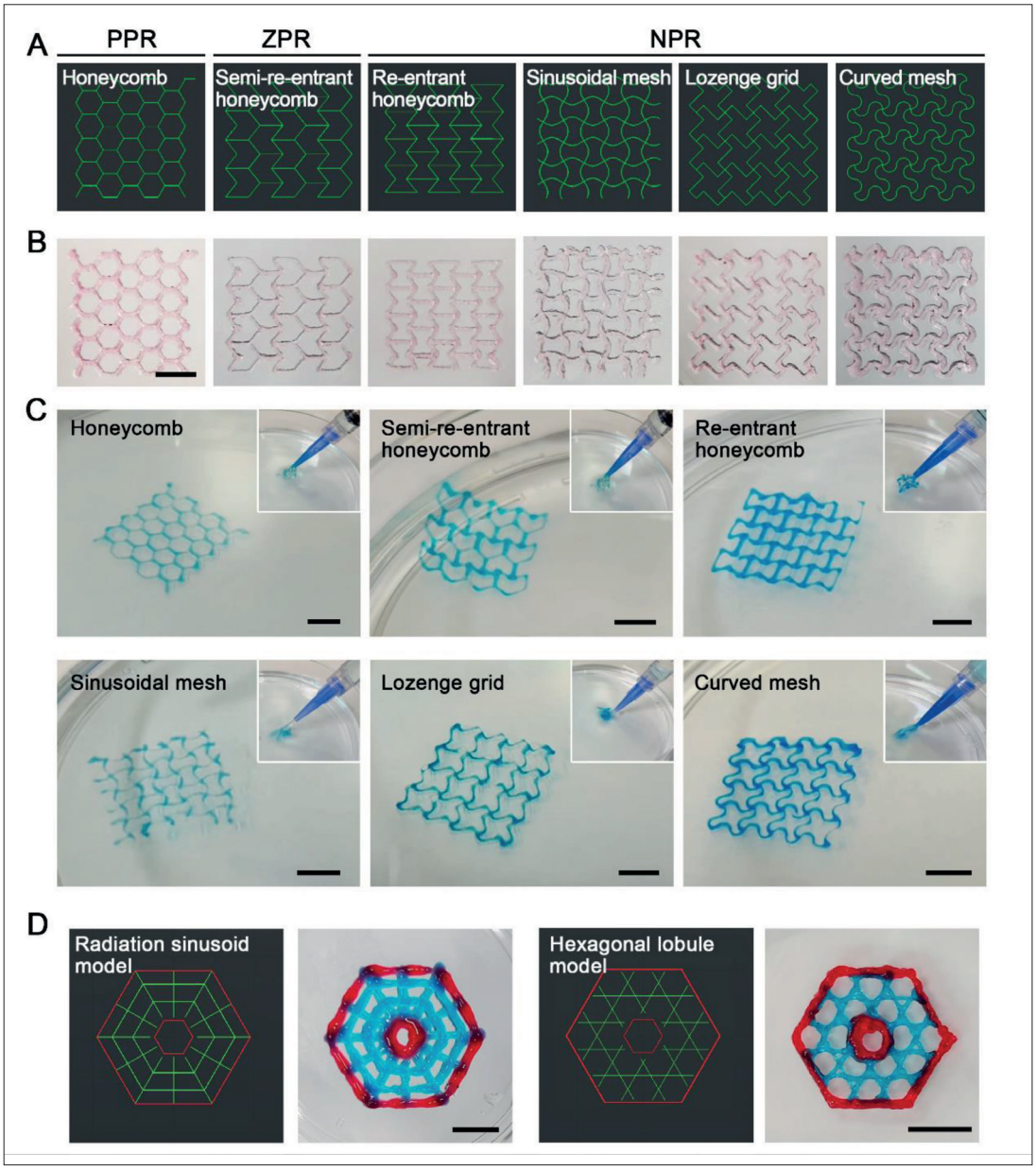


Figure 4. 3D printing of large-sized architectures with high injection capacity. (A) Design of complicated models and (B) corresponding printed architectures with disparate repetitive units and tunable Poisson's ratios. (C) The injection of large-sized architectures through dispensing needles with an inner diameter of 1.5 mm. (D) Design and corresponding printed architectures of the radiation sinusoid (radiation filling) and hexagonal lobule models (60° linear filling). GP bioink is colored with red and blue dyes to distinguish the filaments printed by different nozzles. Scale bars: 5 mm (B–D). Abbreviations: GP: Gelatin methacryloyl/poly(ethylene glycol) diacrylate; PPR: Positive Poisson's ratio; ZPR: Zero Poisson's ratio; and NPR: Negative Poisson's ratio.

activity were upregulated. In contrast, gene sets associated with the differentiation and development of non-hepatic lineages were downregulated (Figure S12C, Supporting Information), suggesting improved hepatic functions and heightened susceptibility to viral infection of M14A compared to HepaRG. Meanwhile, the genome-edited cells emerged as robust candidates for studying cell-bioprinting suitability, with greater sensitivity to environmental disturbances compared to immortalized or cancer cell lines.[41]

After decoupled bioprinting, M14A maintained a high cell viability of 95.3 ± 1.8%, indicating minor harm from bioprinting and photocrosslinking to cells (Figure 5E). RNA-sequencing analysis was conducted to compare

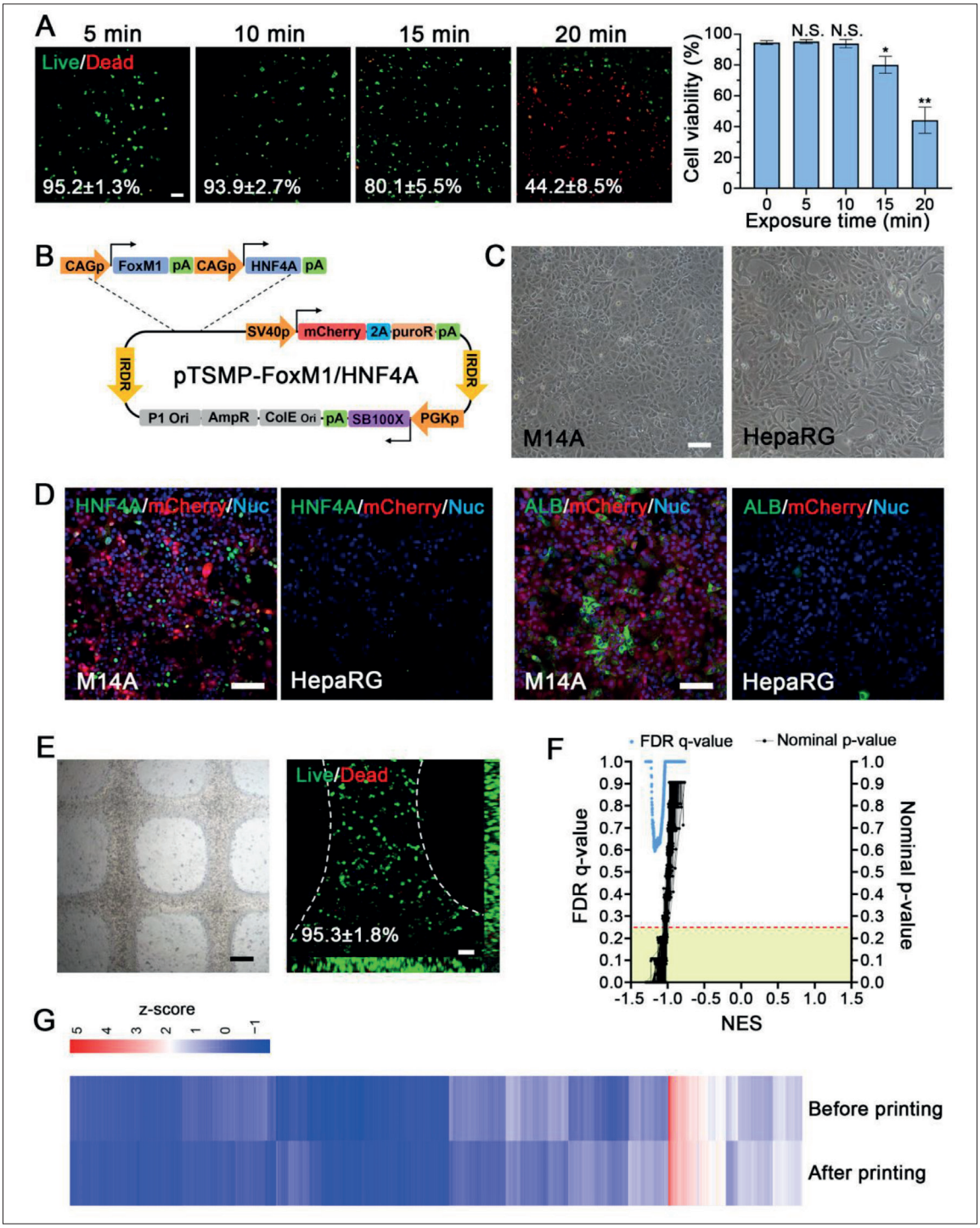


Figure 5. GP bioink supports high cell-bioprinting suitability. (A) Influence of exposure time (5, 10, 15, and 20 min) on HepaRG cell viability: fluorescence images of cells (left) and semi-quantitative analysis of cell viability (right). (B) Sleeping Beauty transposon genome-editing system for transferring targeted genes. (C) Morphology of M14A and HepaRG in planar culture. (D) The immunofluorescence images of hepatic markers HNF4A (left) and ALB (right) of M14A and HepaRG in planar culture; mCherry (red) represents the auto-fluorescence of M14A; cell nuclei are stained blue. (E) Microscope (left) and live/dead images (right) of the M14A-laden bioprinted architecture on day 0 ($n = 6$). (F) The NES-significance chart of M14A before and after bioprinting. All the gene sets with an absolute value of NES ≥ 1 display an FDR q-value > 0.25, indicating no significant difference. (G) Cluster heatmap of the whole transcriptome before and after printing. Statistical analysis was performed using an independent t-test (unpaired). Statistical significance is defined as $^*p < 0.05$; $^{**}p < 0.01$; N.S.: no statistical significance. Scale bars: 500 μm (E, left); 100 μm (A; C; D; and E, right). Abbreviations: GP: Gelatin methacryloyl/poly(ethylene glycol) diacrylate; FDR: False discovery rate; and NES: normalized enrichment score.

the M14A transcriptome before and after bioprinting. Surprisingly, GSEA indicated no significantly altered gene terms after printing (Figure 5F). The cluster heatmap of the whole transcriptome was minimally altered, suggesting that the gene expression profile was maintained after the bioprinting procedure (Figure 5G). Taken together, the cell viability test and RNA-seq analysis revealed the high cell-bioprinting suitability of the decoupled bioprinting strategy using GP bioink and white light-induced photocrosslinking, even for sensitive gene-edited cells.

3.5. Long-term culture and injection experiment of cell-laden bioprinted architectures

The M14A-laden bioprinted architectures were cultured for 16 days. During culture, the architectures maintained good structural stability with slight degradation and shrinkage of hydrogel filaments, suggesting the suitability for long-term cell culture with degradation time comparable to tissue regeneration (Figure 6A). More importantly, M14A cells embedded within GP hydrogel architectures maintained high cell viability and proliferation. We observed the formation of cellular aggregates around day 9, suggesting cell survival and growth (Figure 6B). Immunofluorescence staining on day 16 displayed positive expression of hepatic specific marker MRP2, suggesting that cells form tight junctions in aggregates (Figure 6C). Chemical staining was also performed to evaluate hepatic metabolic function. Glycogen PAS staining revealed that the cellular aggregates expressed high glycogen storage capacity (Figure 6D). ICG uptake and release experiments reported good endocytosis and exocytosis behavior of M14A within the GP hydrogel, with successful ICG uptake within 30 min and complete release after 8 h (Figure 6E). GP hydrogel proved to be a versatile candidate for bioprinting and long-term culture with mechanically reinforced behavior and acceptable biocompatibility. However, we found that the cell proliferation in GP-bioprinted architectures was significantly slower than the cells cultured in other biocompatible matrices (e.g., alginate and collagen), highlighting the need for improving material biofunctionality.

An injection test was performed on day 16. After injection via 1.5 mm dispensing needles, the samples did not exhibit any filament fracture and maintained the integrity of their geometric features (Figure S13, Supporting Information; Video S6, Supporting Information). Additionally, M14A cells displayed high viability compared to samples before injection, suggesting the little influence of the injection procedure on cell viability (Figure 6F). Taken together, cell-laden GP-bioprinted architectures could support long-term cell culture with good structural stability, providing a biocompatible microenvironment for cell aggregation and hepatic function maintenance with the potential for minimally invasive applications.

4. Conclusion

This study proposed a decoupled bioprinting strategy to fabricate large-sized architectures with outstanding deformation and shape recovery behavior using a novel bioink featuring superelasticity and fatigue resistance. The printed architectures presented geometry-independent injection capacity and potential applications for minimally invasive tissue delivery. The development of GP represents a paradigm shift from mechanically reinforced material development to biological performance. GelMA and PEGDA of large M_w formed a reinforced crosslinking network with improved mechanical properties, particularly superelasticity and fatigue resistance. We assume the unique mechanical properties were attributed to the incorporation of flexible chains during white light-induced photocrosslinking and the formation of macroporous structures. The superelastic GP hydrogel expressed remarkable printability for 3D printing to obtain customized off-the-shelf architectures with distinct features and tunable Poisson's ratios. The large-sized architectures can be compressed to less than 1% of their original sizes and injected through nozzles comparable to 14G syringe needles. This injection capacity is bioink-dependent and geometry-independent, offering greater freedom for structural design and architecture scale. The bioprinting of GP is compatible with cell-laden hydrogel. Additionally, a genome-edited hepatic cell line M14A was bioprinted and long-term cultured as a paradigm. A cell-bioprinting suitability test was proposed by combining live/dead staining with RNA-sequencing analysis to provide a full-scale visualization of the cellular alternations after printing. The decoupled bioprinting strategy using GP hydrogel demonstrated high cell-bioprinting suitability, high cell viability, and no significant alterations in the transcriptomic profile. During the 16-day culture, GP hydrogel expressed good structural stability and biocompatibility to support M14A cell survival and function maintenance. The cell-laden architectures could be successfully injected without structural fracture and with minimal impact on the cells. This proof-of-concept study provides an alternative approach for efficient tissue delivery in minimally invasive treatments.

Acknowledgments

The authors acknowledge Qiaobing Xu from Tufts University and Liqun Wang from Zhejiang University for their advice on the reinforcement mechanism investigation and assistance with manuscript writing.

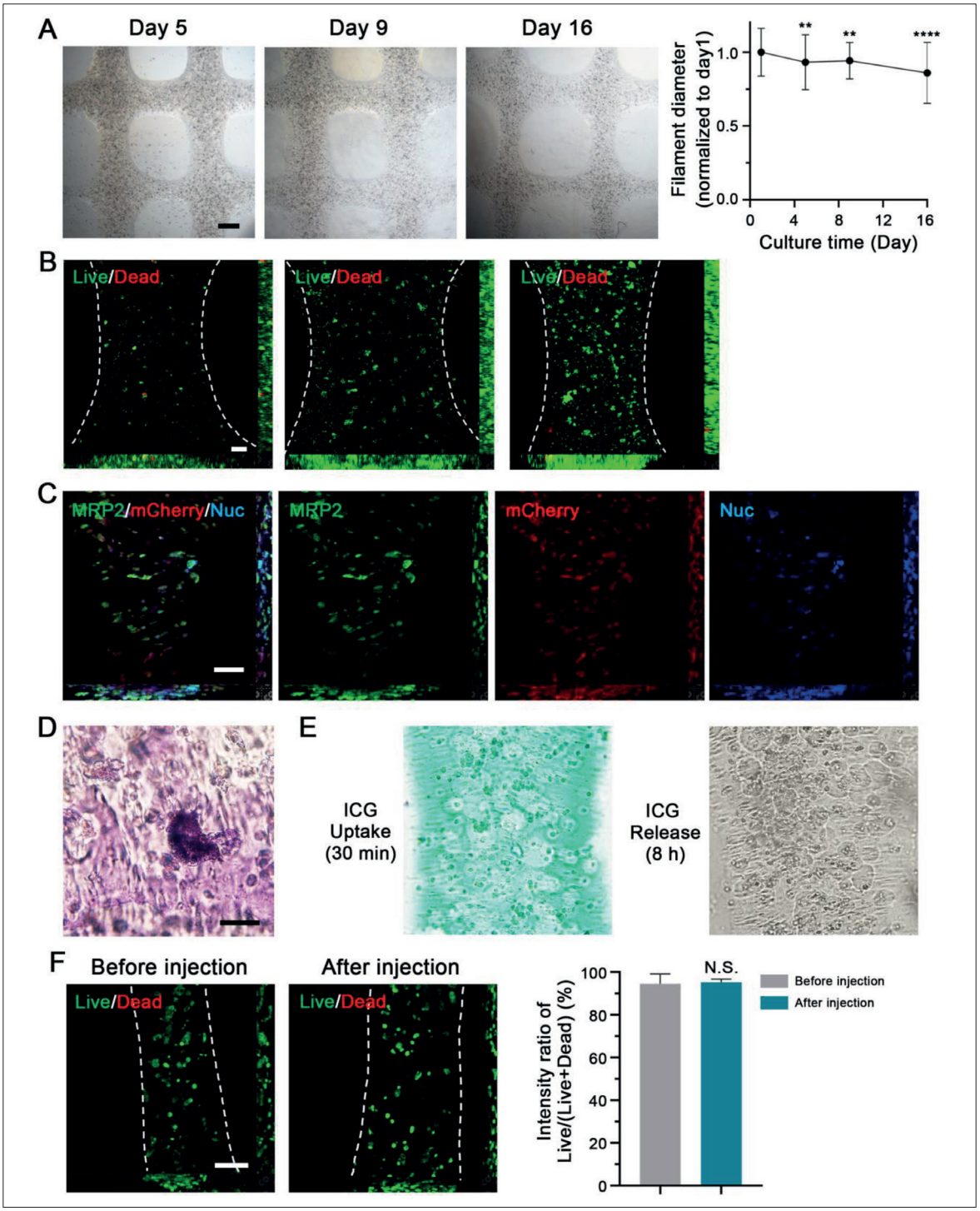


Figure 6. Phenotype and function evaluation of M14A-laden architectures. (A) Microscope images of M14A-laden bioprinted architectures (left) and the semi-quantitative analysis of structural stability during the 16-day culture (right). (B) Fluorescence images of live/dead staining on days 5, 9, and 16, respectively. (C) Immunofluorescence staining images of hepatic marker MRP2 (green) of M14A on day 16; mCherry (red) represents the auto-fluorescence of M14A; cell nuclei are stained blue. (D) Glycogen PAS staining of M14A within bioprinted architectures on day 16; cells with glycogen storage are stained red violet. (E) ICG uptake (left) and release (right) experiments. (F) Fluorescence images of live/dead staining (left) and the corresponding semi-quantitative analysis of M14A-laden architectures before and after injection (right) ($n = 3$). Statistical analyses were performed using an independent t-test (unpaired). Statistical significance is defined as $^{**}p < 0.01$; $^{****}p < 0.0001$; N.S.: no statistical significance. Scale bars: 500 μm (A); 100 μm (B, C, E, and F); 25 μm (D). Abbreviations: ICG: Indocyanine green; and PAS: Periodic acid-Schiff.

Funding

The authors are sincerely grateful for the funding from the National Key Research and Development Program of China (2022YFA1104600 and 2018YFA0109000).

Conflict of interest

Mingen Xu is a shareholder of Regenovo Biotechnology Co. Ltd, China. The other authors declare no competing financial interest.

Author contributions

Conceptualization: Rui Yao, Mingen Xu, Ruoyu Chen
Formal analysis: Ruoyu Chen, Rui Yao
Funding acquisition: Mingen Xu, Rui Yao
Investigation: Ruoyu Chen, Yijun Su, Jinghua Zhao, Yali Zhang, Yinying Lu, Quan Yuan
Methodology: Rui Yao, Ruoyu Chen, Jinghua Zhao, Yali Zhang, Quan Yuan
Project administration: Rui Yao, Mingen Xu
Visualization: Ruoyu Chen, Dazhi Chen, Yijun Su, Yali Zhang, Jinghua Zhao
Writing-original draft: Ruoyu Chen, Yinying Lu, Rui Yao
Writing-Review & Editing: Rui Yao, Mingen Xu

Ethics approval and consent to participate

Not applicable.

Consent for publication

Not applicable.

Availability of data

The raw sequence datasets of RNA-seq had been submitted to the Sequence Read Archive database with the GEO submission number GSE230068.

References

1. Zhang J, Eyisoylu H, Qin XH, Rubert M, Muller R. 3D bioprinting of graphene oxide-incorporated cell-laden bone mimicking scaffolds for promoting scaffold fidelity, osteogenic differentiation and mineralization. *Acta Biomater*. 2021;121:637-652.
doi: 10.1016/j.actbio.2020.12.026

2. Murphy SV, De Coppi P, Atala A. Opportunities and challenges of translational 3D bioprinting. *Nat Biomed Eng*. 2020;4(4):370-380.
doi: 10.1038/s41551-019-0471-7

3. Chen A, Wang W, Mao Z, et al. Multimaterial 3D and 4D bioprinting of heterogenous constructs for tissue engineering. *Adv Mater*. 2023:e2307686.
doi: 10.1002/adma.202307686

4. Eggermont LJ, Rogers ZJ, Colombani T, Memic A, Bencherif SA. Injectable cryogels for biomedical applications. *Trends Biotechnol*. 2020;38(4):418-431.
doi: 10.1016/j.tibtech.2019.09.008

5. Zarrintaj P, Khodadadi YM, Youssefi AM, et al. Injectable cell-laden hydrogels for tissue engineering: recent advances and future opportunities. *Tissue Eng Part A*. 2021; 27(11-12):821-843.
doi: 10.1089/ten.TEA.2020.0341

6. Chen R, Li L, Feng L, et al. Biomaterial-assisted scalable cell production for cell therapy. *Biomaterials*. 2020;230:119627.
doi: 10.1016/j.biomaterials.2019.119627

7. Huang X, Ma Y, Li Y, Han F, Lin W. Targeted drug delivery systems for kidney diseases. *Front Bioeng Biotechnol*. 2021;9:683247.
doi: 10.3389/fbioe.2021.683247

8. Ercan H, Durkut S, Koc-Demir A, Elcin AE, Elcin YM. Clinical applications of injectable biomaterials. *Adv Exp Med Biol*. 2018;1077:163-182.
doi: 10.1007/978-981-13-0947-2_10

9. Yao R, Zhang R, Lin F, Luan J. Biomimetic injectable HUVEC-adipocytes/collagen/alginate microsphere co-cultures for adipose tissue engineering. *Biotechnol Bioeng*. 2013;110(5):1430-1443.
doi: 10.1002/bit.24784

10. Yao R, Alkhawtani A, Chen R, Luan J, Xu M. Rapid and efficient in vivo angiogenesis directed by electro-assisted bioprinting of alginate/collagen microspheres with human umbilical vein endothelial cell coating layer. *Int J Bioprint*. 2019;5(2.1):194.
doi: 10.18063/ijb.v5i2.1.194

11. Chen TC, Wong CW, Hsu SH. Three-dimensional printing of chitosan cryogel as injectable and shape recoverable scaffolds. *Carbohydr Polym*. 2022;285:119228.
doi: 10.1016/j.carbpol.2022.119228

12. Beduer A, Piacentini N, Aeberli L, et al. Additive manufacturing of hierarchical injectable scaffolds for tissue engineering. *Acta Biomater*. 2018;76:71-79.
doi: 10.1016/j.actbio.2018.05.056

13. Ying G, Jiang N, Parra C, et al. Bioprinted injectable hierarchically porous gelatin methacryloyl hydrogel constructs with shape-memory properties. *Adv Funct Mater*. 2020;30(46):2003740.
doi: 10.1002/adfm.202003740

14. Porto ST, Cejas CM, Cunha RL. Microfluidics as a tool to assess and induce emulsion destabilization. *Soft Matter*. 2022;18(4):698-710.
doi: 10.1039/d1sm01588e

15. Tilton M, Camilleri ET, Astudillo PM, et al. Visible light-induced 3D bioprinted injectable scaffold for minimally invasive tissue regeneration. *Biomater Adv*. 2023;153:213539.
doi: 10.1016/j.bioadv.2023.213539

16. Jian X, Wang H, Jian X, et al. A flexible adhesive hydrogel dressing of embedded structure with pro-angiogenesis

activity for wound repair at moving parts inspired by commercial adhesive bandages. *Mater Today Adv*. 2024;21:100452.
doi: 10.1016/j.mtadv.2023.100452

17. Lewis JB, Wataha JC, Messer RL, Caughman GB, Yamamoto T, Hsu SD. Blue light differentially alters cellular redox properties. *J Biomed Mater Res B Appl Biomater*. 2005;72(2):223-229.
doi: 10.1002/jbm.b.30126

18. Zhang MD, Huang X, Li Z, et al. White-light-induced synthesis of injectable alginate-based composite hydrogels for rapid hemostasis. *Mil Med Res*. 2023;10(1):47.
doi: 10.1186/s40779-023-00483-7

19. Feng L, Liang S, Zhou Y, et al. Three-dimensional printing of hydrogel scaffolds with hierarchical structure for scalable stem cell culture. *Acs Biomater Sci Eng*. 2020;6(5):2995-3004.
doi: 10.1021/acsbiomaterials.9b01825

20. Kumar A, Lee Y, Kim D, et al. Effect of crosslinking functionality on microstructure, mechanical properties, and in vitro cytocompatibility of cellulose nanocrystals reinforced poly (vinyl alcohol)/sodium alginate hybrid scaffolds. *Int J Biol Macromol*. 2017;95:962-973.
doi: 10.1016/j.ijbiomac.2016.10.085

21. Joyce K, Fabra GT, Bozkurt Y, Pandit A. Bioactive potential of natural biomaterials: identification, retention and assessment of biological properties. *Signal Transduct Target Ther*. 2021;6(1):122.
doi: 10.1038/s41392-021-00512-8

22. Ghavaminejad A, Ashammakhi N, Wu XY, Khademhosseini A. Crosslinking strategies for 3D bioprinting of polymeric hydrogels. *Small*. 2020;16(35):e2002931.
doi: 10.1002/smll.202002931

23. Yue K, Trujillo-De SG, Alvarez MM, Tamayol A, Annabi N, Khademhosseini A. Synthesis, properties, and biomedical applications of gelatin methacryloyl (GelMA) hydrogels. *Biomaterials*. 2015;73:254-271.
doi: 10.1016/j.biomaterials.2015.08.045

24. Sharifi S, Sharifi H, Akbari A, Chodosh J. Systematic optimization of visible light-induced crosslinking conditions of gelatin methacryloyl (GelMA). *Sci Rep*. 2021;11(1):23276.
doi: 10.1038/s41598-021-02830-x

25. Bahney CS, Lujan TJ, Hsu CW, Bottlang M, West JL, Johnstone B. Visible light photoinitiation of mesenchymal stem cell-laden bioresponsive hydrogels. *Eur Cell Mater*. 2011;22:43-55.
doi: 10.22203/ecm.v022a04

26. Bryant SJ, Nuttelman CR, Anseth KS. Cytocompatibility of UV and visible light photoinitiating systems on cultured NIH/3T3 fibroblasts in vitro. *J Biomater Sci Polym Ed*. 2000;11(5):439-457.
doi: 10.1163/156856200743805

27. Slaughter BV, Khurshid SS, Fisher OZ, Khademhosseini A, Peppas NA. Hydrogels in regenerative medicine. *Adv Mater*. 2009;21(32-33):3307-3329.
doi: 10.1002/adma.200802106

28. Wang Z, Kumar H, Tian Z, et al. Visible light photoinitiation of cell-adhesive gelatin methacryloyl hydrogels for stereolithography 3D bioprinting. *ACS Appl Mater Interfaces*. 2018;10(32):26859-26869.
doi: 10.1021/acsami.8b06607

29. Wang Y, Ma M, Wang J, et al. Development of a photo-crosslinking, biodegradable GelMA/PEGDA hydrogel for guided bone regeneration materials. *Materials (Basel)*. 2018;11(8):1345.
doi: 10.3390/ma11081345

30. Nguyen AK, Goering PL, Reipa V, Narayan RJ. Toxicity and photosensitizing assessment of gelatin methacryloyl-based hydrogels photoinitiated with lithium phenyl-2,4,6-trimethylbenzoylphosphinate in human primary renal proximal tubule epithelial cells. *Biointerphases*. 2019;14(2):021007.
doi: 10.1116/1.5095886

31. Grigoryan B, Paulsen SJ, Corbett DC, et al. Multivascular networks and functional intravascular topologies within biocompatible hydrogels. *Science*. 2019;364(6439):458-464.
doi: 10.1126/science.aav9750

32. He B, Wang J, Xie M, et al. 3D printed biomimetic epithelium/stroma bilayer hydrogel implant for corneal regeneration. *Bioact Mater*. 2022;17:234-247.
doi: 10.1016/j.bioactmat.2022.01.034

33. Li W, Hu X, Liu H, et al. 3D light-curing printing to construct versatile octopus-bionic patches. *J Mater Chem B*. 2023;11(22):5010-5020.
doi: 10.1039/d3tb00590a

34. Qiu L, Liu JZ, Chang SLY, Wu Y, Li D. Biomimetic superelastic graphene-based cellular monoliths. *Nat Commun*. 2012;3:1241.
doi: 10.1038/ncomms2251

35. Zhao Y, Li Y, Mao S, Sun W, Yao R. The influence of printing parameters on cell survival rate and printability in microextrusion-based 3D cell printing technology. *Biofabrication*. 2015;7(4):45002.
doi: 10.1088/1758-5090/7/4/045002

36. Ouyang L, Yao R, Zhao Y, Sun W. Effect of bioink properties on printability and cell viability for 3D bioplotting of embryonic stem cells. *Biofabrication*. 2016;8(3):35020.
doi: 10.1088/1758-5090/8/3/035020

37. Gripon P, Rumin S, Urban S, et al. Infection of a human hepatoma cell line by hepatitis B virus. *Proc Natl Acad Sci USA*. 2002;99(24):15655–15660.
doi: 10.1073/pnas.232137699

38. Roulot D, Czernichow S, Le Clesiau H, Costes JL, Vergnaud AC, Beaugrand M. Liver stiffness values in apparently

healthy subjects: influence of gender and metabolic syndrome. *J Hepatol*. 2008;48(4):606-613.
doi: 10.1016/j.jhep.2007.11.020

39. Tringides CM, Vachicouras N, de Lazaro I, et al. Viscoelastic surface electrode arrays to interface with viscoelastic tissues. *Nat Nanotechnol*. 2021;16(9):1019-1029.
doi: 10.1038/s41565-021-00926-z

40. Han D, Dara L, Win S, et al. Regulation of drug-induced liver injury by signal transduction pathways: critical role of mitochondria. *Trends Pharmacol Sci*. 2013;34(4):243-253.
doi: 10.1016/j.tips.2013.01.009

41. Haapaniemi E, Botla S, Persson J, Schmierer B, Taipale J. CRISPR-Cas9 genome editing induces a p53-mediated DNA damage response. *Nat Med*. 2018;24(7):927-930.
doi: 10.1038/s41591-018-0049-z

42. Zhu W, Cui H, Boualam B, et al. 3D bioprinting mesenchymal stem cell-laden construct with core-shell nanospheres for cartilage tissue engineering. *Nanotechnology*. 2018;29(18):185101.
doi: 10.1088/1361-6528/aaafa1

43. Duan J, Cao Y, Shen Z, et al. 3D bioprinted GelMA/PEGDA hybrid scaffold for establishing an in vitro model of melanoma. *J Microbiol Biotechn*. 2022;32(4):531-540.
doi: 10.4014/jmb.2111.11003

44. Wang Z, Abdulla R, Parker B, Samanipour R, Ghosh S, Kim K. A simple and high-resolution stereolithography-based 3D bioprinting system using visible light crosslinkable bioinks. *Biofabrication*. 2015;7(4):45009.
doi: 10.1088/1758-5090/7/4/045009

ACCSCIENCE PUBLISHING

International Journal of Bioprinting

RESEARCH ARTICLE

3D-printed devices for optimized generation of cold atmospheric plasma to improve decontamination of surfaces from respiratory pathogens

Asma Bouazizi[1,2†], Klára Obrová[1†], Eva Vaňková[3,4†], Anna Machková[3], Josef Khun[3], Romana Hadravová[5], Jan Hodek[5], Lucie Ulrychová[5,6], Abdelhalim Trabelsi[2], Jan Weber[5], Leonardo Zampieri[7], Fabio Avino[8], Ivo Furno[8], Vladimír Scholtz[3*], and Thomas Lion[1,9*]

[1] St. Anna Children's Cancer Research Institute (CCRI), Vienna, Austria

[2] Research Laboratory of Epidemiology and Immunogenetics of Viral Infections (LR14SP02), Faculty of Pharmacy, University of Monastir, Tunisia

[3] Department of Physics and Measurements, University of Chemistry and Technology, Prague, Czech Republic

[4] Department of Biotechnology, University of Chemistry and Technology, Prague, Czech Republic

Institute of Organic Chemistry and Biochemistry of the Czech Academy of Sciences, Prague, Czech Republic

[6] Department of Genetics and Microbiology, Charles University, Faculty of Sciences, Czech Republic

[7] Department of Physics, University of Milano Bicocca, Milano, Italy

Ecole Polytechnique Fédérale de Lausanne (EPFL), Swiss Plasma Center (SPC), Lausanne, Switzerland

[9] Department of Pediatrics, Medical University of Vienna, Vienna, Austria

[†]These authors contributed equally to this work.

***Corresponding authors:**
Thomas Lion
(thomas.lion@ccri.at)

Vladimír Scholz
(Vladimir.Scholtz@vscht.cz)

Citation: Bouazizi A, Obrová K, Vaňková E, et al. 3D-printed devices for optimized generation of cold atmospheric plasma to improve decontamination of surfaces from respiratory pathogens. *Int J Bioprint*. 2024;10(5):3679. doi: 10.36922/ijb.3679

Received: May 16, 2024
Accepted: July 11, 2024
Published Online: August 15, 2024

Copyright: © 2024 Author(s). This is an Open Access article distributed under the terms of the Creative Commons Attribution License, permitting distribution, and reproduction in any medium, provided the original work is properly cited.

Publisher's Note: AccScience Publishing remains neutral with regard to jurisdictional claims in published maps and institutional affiliations.

Abstract

Three-dimensional (3D)-printing technology is instrumental in creating devices for biological applications, including the exploitation of cold atmospheric plasma (CAP). CAP, a partially ionized gas that functions at ambient temperatures, serves as a safe, inexpensive, and effective tool for the inactivation of various pathogens on different surfaces. In this study, we compared three different 3D-printed devices with respect to their ability to provide optimized CAP compositions effective against select respiratory viruses (SARS-CoV-2, influenza virus, adenovirus, and rhinovirus) and the bacterium *Pseudomonas aeruginosa*, which is associated with serious lung diseases. The transmission of respiratory pathogens via surface contamination may pose a serious health threat, thus highlighting the biological importance of the current study. The properties of a prototype 3D-printed CAP-generating device and two optimized versions were characterized by detecting reactive oxygen and nitrogen species (RONS) in a gaseous environment via infrared spectroscopy and analyzing the composition of the reactive compounds. The virucidal effects of CAP were examined by determining virus infectivity and particle integrity. The bactericidal effect was documented by viability testing and visualization via transmission electron microscopy. The findings indicate that optimization of the 3D-printed devices for CAP production yielded an environment with relatively high amounts of RONS (O_3, N_2O,

NO_2, and H_2O_2), reducing the exposure time required for inactivation of respiratory pathogens by approximately 50%. In addition to reducing infectivity and viability, CAP treatment led to the destruction of viral nucleic acids and physical damage to bacterial cells. Owing to its flexibility and easy implementation, optimized CAP generated by 3D-printed devices provides an attractive inactivation method adaptable for different biological applications, including surface decontamination from viral and bacterial pathogens.

Keywords: 3D-printed devices; Adenovirus; Disinfection; Influenza A; *Pseudomonas aeruginosa*; Reactive oxygen species; Rhinovirus; SARS-CoV-2

1. Introduction

Three-dimensional (3D)-printing technology is a powerful and readily implementable approach for creating devices for diverse biological applications. The moldability provided by 3D printing technology, with its highly flexible design of external and internal structures, allows for the optimization of the physical properties of cold atmospheric plasma (CAP) or nonthermal plasma (NTP). These properties are significantly influenced by the geometry of 3D-printed devices. The biological exploitation of CAP is an emerging technology for decontaminating various types of liquids, medical materials, devices, and even surfaces across diverse industries. Additionally, the antimicrobial effects of CAP are well documented.[1–7] Compared with conventional decontamination techniques, CAP has several advantages, such as on-demand operation (easy on/off switching), simple handling, low cost and maintenance, performance at ambient temperature and atmospheric pressure, and the ability to function in dry conditions. CAP has been applied in a wide range of fields, including physics, chemistry, biological sciences, life sciences, and medicine.[8–14]

Biomaterial-associated microbial contamination in biologically conducive 3D tissue-engineered constructs has greatly limited the clinical application of scaffold systems.[15,16] Although antimicrobial biomaterials are being developed to prevent such infections,[17,18] their use in bioprinting-based approaches for scaffold fabrication has not been thoroughly examined to date. Therefore, CAP may emerge as an alternative technical approach for surface decontamination of bioprinted materials in the future. The bactericidal effects of CAP are well established, but research on its effectiveness against pathogenic viruses remains relatively limited,[19–24] despite several reviews that have been published.[25–27] The virucidal mechanism of CAP is influenced by the characteristics of the plasma-generating devices, specifically their geometry, electric voltage and current applied, and several other application parameters.[28] CAP is produced by ionizing a neutral gas, e.g., ambient air, using a source of energy such as electric discharge.[29] The ionized gas is composed of reactive oxygen and nitrogen species (RONS; e.g., OH, H_2O_2, NO, and NO_2), radicals, free electrons, electric fields, heat, and other elements.[12] In propagating ionization waves, the gas draws particles out of the electrode area, forming a stream of (re)active particles that fills the entire reaction chamber (Figure 1).[29] Microbial inhibition by CAP is hypothesized to result from several processes. Some researchers discovered that active plasma particles target proteins, DNA, the cell wall, and membranes. For example, oxygen species, such as O (singlet oxygen) and O_3 (ozone), may physically affect the cell membrane and cause DNA damage.[30] O_3 has been reported as the main[24] or additional factor[31,32] involved in the inactivation of the bacteriophage MS2[33] and human adenovirus (HAdV).[34] Hydrogen peroxide (H_2O_2) has been suggested to be crucial for the inactivation of respiratory syncytial virus (RSV)[35] and influenza A virus (IAV)[36] but to play only a minor role in the inactivation of HAdV.[37] RONS can damage cells by reacting with various cellular biomacromolecules, such as proteins, lipids, and DNA.[38] As CAP components can enter cells, it is not surprising that cell organelles, such as mitochondria and nuclei, are affected.[39] Additionally, direct damage to nucleic acids and proteins has been reported.[40] These findings contribute to the reported effective disinfection of various microorganisms.[19] Pathogens can undergo oxidative damage from various RONS,[41] and the synergistic effect of combining these reactive species in CAP can increase their efficiency. A significant challenge lies in the precise control of CAP parameters. Surface decontamination may be more effective when physical parameters are optimized to produce specific concentrations of individual RONS.

Human respiratory pathogens, including viruses (e.g., severe acute respiratory syndrome coronavirus 2 [SARS-CoV-2], IAV, HAdV, and human rhinovirus [HRV]) and bacteria (e.g., *Pseudomonas aeruginosa*), can spread via different modes of transmission, and the control of contaminated surfaces is an important measure in different settings.[42–46] Human coronaviruses, such as

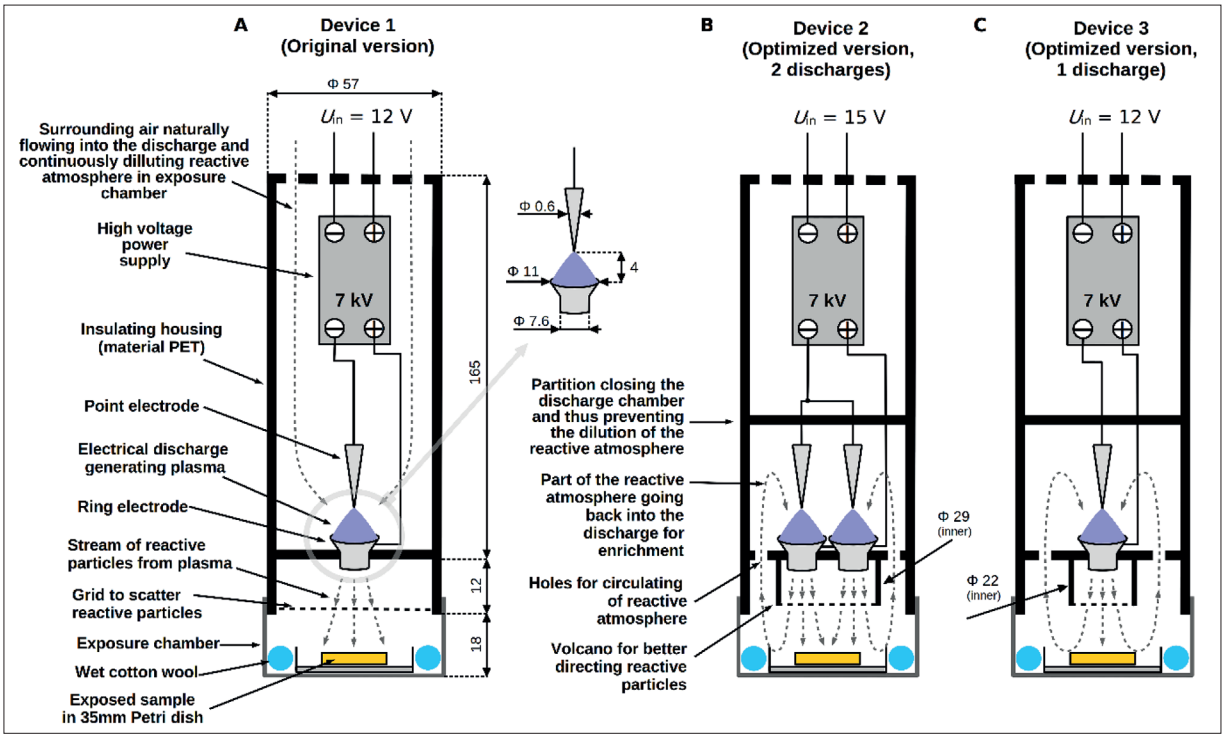


Figure 1. Schematic representation of 3D-printed cold atmospheric plasma (CAP)-generating devices: (A) Device 1: Original version with an opening for fresh air supply and ventilation; (B) Device 2: Optimized version enclosed in a chamber with a double discharge; (C) Device 3: Optimized version enclosed in a chamber with a single discharge. Abbreviations: PET: polyethylene terephthalate; U_{in}: input voltage; Φ: diameter.

SARS-CoV-2, frequently emerge globally because of their rapid evolution characterized by high rates of nucleotide substitution and recombination, as documented by the recent pandemic.[47] IAV infects a variety of species and mutates frequently, resulting in antigenic drift and shift. These processes contribute to repeated seasonal outbreaks and epidemics.[48] HAdV and HRV are highly contagious pathogens linked to a variety of respiratory diseases.[49,50] Although respiratory diseases caused by HAdV and HRV typically have moderate effects, they can cause substantial morbidity and economic impacts. *P. aeruginosa* is a frequently observed opportunistic pathogen that mainly infects the respiratory tract, with potentially severe disease, particularly in immunocompromised patients.[51,52] Owing to the potential role of fomites, such as doorknobs, utensils, and other commonly touched surfaces, in the transmission of these pathogens, the development of efficient surface disinfection strategies is crucial for infection control.

In the present study, we aimed to optimize the CAP technology generated by 3D-printed devices for the biological inactivation of respiratory pathogens. These were represented by four viruses with diverse features (SARS-CoV-2, IAV, HAdV, and HRV) and a clinically challenging bacterium (*P. aeruginosa*). The selected model microorganisms were included to encompass significant and widely encountered pathogens, each displaying distinct biological features that could affect the efficiency of decontamination. Our 3D-printed CAP devices are based on direct current (DC) corona discharge, which uses HV sources with low current outputs that are inherently safe (i.e., no risk of electric shock), and the devices are very cheap. Two optimized 3D-printed portable CAP-generating devices were also created, and their performance was compared to that of the original version used in previous investigations (Figure 1).[19] The detection of RONS produced by individual devices displayed obvious differences, which translated into enhanced virucidal and bactericidal effects. Unlike previous studies, we used a panel of human respiratory pathogens with epidemic potential and comprehensively investigated CAP efficiency, linking enhanced production of RONS species to improved efficiency. The flexibility and easy application of CAP decontamination via 3D-printed devices highlights the significant potential of this technology for pathogen inactivation, and the presented data pave the way for its further development and implementation in various applications.

2. Methods

2.1. CAP devices

Cold atmospheric plasma (CAP) was generated by corona discharges in three different 3D-printed devices (hereinafter referred to as devices 1, 2, and 3; Figure 1). The external appearance of the devices is displayed in Figure S1 (Supplementary File). The device bodies were fabricated via a Prusa i3 MK3 3D printer (Prusa Research, Czech Republic) from polyethylene terephthalate glycol-modified (PETG), which was selected for its superior chemical resistance, mechanical strength, and thermal stability. These properties ensure structural integrity under the thermal stresses encountered during plasma operations (Table 1).

These settings were meticulously selected to optimize the manufacturing process and enhance the functionality and durability of the CAP devices. Precise control of 3D -printing parameters, such as the nozzle temperature and print speed, plays a critical role in achieving the high-quality builds required for reliable plasma generation.

Devices with specific dimensions were developed to ensure plasma discharge and stability. The selection of PETG as the material was crucial because of its mechanical properties, ease of printing, and minimal warping tendencies, which are essential for maintaining the accuracy of the printed components. Furthermore, a 20% infill density was selected to provide a balance between structural integrity and material efficiency, ensuring that the devices remain lightweight yet strong enough to withstand operational stresses.

Table 1. Material specifications for 3D printing

Property	Specification
Printer model	Prusa i3 MK3
Material	Polyethylene terephthalate glycol-modified (PETG)
Layer resolution (mm)	0.05
Nozzle temperature (°C)	240–250
Bed temperature (°C)	75–85
Infill density (%)	20 (for a balance of lightness and durability)
Head printing speed (mm/s)	60 (optimized for precision)
Shell thickness	
Perimeter (mm)	0.4
Top/bottom (mm)	0.2
Filament flow (%)	95
Infill pattern	Linear grid (tilted by 45°)

The devices are robust and impact resistant and are thus appropriate for daily use in a variety of settings. The minimum force capable of damaging the functional properties of the device was assessed and demonstrated to require dropping the device from at least 1 m onto a hard surface. The device resisted a breaking force of up to 500 N on the 3D-printed package and a continuous force of 100 N on the mesh, protecting the electrode hole. At 150 N, the mesh was deformed but not destroyed.

2.1.1. Device 1

Device 1, referred to as the original device, was studied in our previous work[19] and served as a benchmark in the current study. CAP is generated by negative DC point-to-ring corona discharge, where the point electrode is a syringe needle (MEDOJECT 0.6 × 25 mm intramuscular injection needle; CHIRANA T. Injecta, Czech Republic) and the conical-shaped ring electrode consists of brass. The top of the ring electrode (~11 mm in diameter) is placed 3.3 mm below the tip of the needle and connected to the positive terminal of an HV source, whereas the needle electrode is connected to the negative terminal. The negative corona discharge is formed in the vicinity of the tip, whereas the positive corona discharge burns at the edge of the ring. This creates a bipolar corona discharge, where reactive species are carried with ions accelerated in the electric field between the electrodes. The discharge current was set at 150 μA, and the voltage was set at 7 kV, resulting in a power of 1.05 W, which was achieved through precise positioning of the tip of the needle relative to the ring. The discharge burns in pulse-less mode, as previously described.[53] The ion wind produced by the discharge draws air through the upper holes and directs it toward the sample. Cotton wool wetted with 10 mL of water was placed around the sample to increase the humidity, which reached over 90% in all the samples. Further details and dimensions are displayed in Figure 1A. To optimize the virucidal and microbicidal efficiency, two additional devices (devices 2 and 3) were developed.

2.1.2. Device 2

Device 2 is developed with the same type of discharge as device 1 but with two discharges. The discharge current and voltage were set identically to those of device 1 at 100 μA and 7 kV, respectively, resulting in a power of 1.4 W. The internal geometric arrangement was modified to prevent fresh air ventilation. The ions circulate from the discharge point toward the sample and back to the point electrode through the holes around the ring electrode. In addition, to improve the direction of the active particle stream from the discharge plasma to the exposed sample, a "volcano" design was incorporated into this device. The design features a tube with an internal diameter of 30 mm and a height of 10 mm attached to the outlet of the ring electrode. A fine metallic mesh (mesh size: 0.5 × 0.5

mm; wire thickness: 0.2 mm) is placed at the end of the "volcano" to ensure safety by preventing electrode contact and mediating a more homogeneous distribution of active particles within the chamber space. Further details on the arrangement and dimensions are displayed in Figure 1B.

2.1.3. Device 3

Device 3 has the same type of discharge as devices 1 and 3 but with a single discharge copy (power: 0.7 W). The internal arrangement is identical to that of device 2, except for the inner diameter of the "volcano," which surrounds only one discharge and thus has a smaller diameter of 22 mm. Further details on the arrangement and dimensions are displayed in Figure 1C.

2.2. Characterization of RONS

The production of RONS, which are known virucidal and microbicidal agents, can be monitored by detecting the long-lived final products NO, NO_2, and O_3. It is assumed that their concentrations are proportional to the concentrations of short-lived reactive particles.

The concentrations of NO and NO_2 were measured via chemiluminescence detection via a Serinus 40H NO_x analyzer (range: up to 1000 ppm; accuracy: 2%; ACOEM Ecotech, UK). Gas from the active region of the devices was led to the analyzer through a 1 m-long polytetrafluoroethylene (PTFE) tube with an inner diameter of 3 mm, and the measured values were recorded.

The concentrations of O_3 and N_2O were measured via Fourier transform infrared spectroscopy (FTIR; Vertex 80v spectrometer; Bruker, Germany). A custom cylindrical measurement cell (volume of circa (ca.): 1.7 L) was used. The cell features two potassium bromide windows on opposite sides to allow the passage of an infrared beam and a hole in the lid to insert the source. After preconditioning, the CAP device (turned on for 15 min) was inserted into the cell. After background determination, the source was turned on, and FTIR spectra were acquired every 15 s for 15 min. The same procedure was repeated for all three devices. The O_3 density was estimated from the main peak at approximately 1055 cm^{-1} and cross-checked with an overtone peak at 2120 cm^{-1} after the necessary baseline corrections were applied. Similarly, the concentration of N_2O was estimated from the main peak at 2240 cm^{-1}, and special care was taken to avoid interference with nearby CO_2 peaks. Additionally, O_3 was measured via an ozone analyzer (Figure S2 in Supplementary File).

2.3. Characterization of CAP-exposed saline

Viruses and bacteria were exposed to CAP in suspension. RONS production in an aqueous environment was also investigated by examining the presence of long-lived final products and monitoring the pH value in an exposed saline droplet. Drops of saline (30 µL; corresponding to the volume used for virus and bacteria testing) were placed on parafilm squares and treated with CAP for 120 min in triplicate. Approximate concentrations of nitrite (NO_2^-), nitrate (NO_3^-), and hydrogen peroxide (H_2O_2), as well as the pH, were semiquantitatively determined via indicator test strips (Quantofix nitrate/nitrite; Quantofix peroxide 100; and Lachner universal indicator strips for pH 0–12, respectively).

2.4. Bacteriology assessment

2.4.1. Assessment of P. aeruginosa viability

P. aeruginosa viability after CAP exposure was evaluated as previously described,[10] with slight modifications. Briefly, 1 × 1-cm parafilm squares were contaminated with a *P. aeruginosa* PAO1 strain suspension, which was adjusted to approximately 1×10^7 CFU/mL in 6 × 5-µL droplets. These squares were then placed in a Petri dish surrounded by two pieces of wet cotton wool to increase the humidity. The bacterial suspension was air-dried to stabilize the droplets on the parafilm surface for 15 min at room temperature and subsequently exposed to CAP for 1, 5, 10, and 30 min. The samples at each time point were tested in three technical and three independent biological replicates, along with the untreated control samples. Exposed *P. aeruginosa* cells (and untreated control samples) were collected from parafilm squares into 1 mL of saline in microtubes by vortexing. The counts (CFU/mL) were determined by decimal dilution of recovered suspensions inoculated directly on Luria–Bertani agar plates and incubated overnight at 37°C. The results were averaged and expressed as log CFU/mL with the standard error of the mean (SEM).

2.4.2. Visualization of P. aeruginosa cells via transmission electron microscopy

The morphology of *P. aeruginosa* PAO1 cells after CAP exposure was visualized via transmission electron microscopy (TEM), as previously reported,[54] with slight modifications. Briefly, bacterial cells exposed to CAP were visualized with negative staining via a JEOL JEM 1011 microscope (JEOL, Japan) operating at 80 kV. For negative staining, parlodion-carbon-coated grids were floated on 10 µL drops of each sample for 5 min. The grids were washed twice on a drop of water and negatively stained with 0.25% phosphotungstic acid (pH 7.4). The images are displayed in Figure 6 with scale bars of 500 nm.

2.4.3. Assessment of E. coli viability on 3D-printed objects

We also evaluated CAP-mediated surface decontamination via 3D-printed PETG that was exogenously contaminated with a wild-type *E. coli* suspension (~1×10^7 CFU/mL). As an additional control, the *E. coli* suspension was also

spotted on other materials, including parafilm and P3 R filter tissue, for comparison with measurements performed in our earlier studies.[18,19] The samples were processed and exposed to CAP generated by device 3, similar to that for *P. aeruginosa* (described in **Section 2.4.1.**).

2.5. Virologic assessment

The following virus strains and cell lines were used: (i) SARS-CoV-2 (hCoV-19/Czech Republic/NRL_6632_2/2020) was propagated in Vero E6 cells (ATCC CRL-1586) cultured in Dulbecco's modified Eagle medium (DMEM) supplemented with 2% fetal bovine serum (FBS); (ii) IAV (influenza A H1N1/California/07/2009; Diagnostic Hybrids, United States of America [USA]) was propagated in MDCK (ATCC CCL-34) cells cultured in influenza growth medium (DMEM supplemented with penicillin/streptomycin [Pen/Strep], 0.2% bovine serum albumin [BSA], 1 mM HEPES, 13.6 mM L-glutamine, 42 mg/L DEAE-Dextran, and 1 mg/L TPCK-Trypsin); (iii) HAdV (species C/type 2, ATCC VR-846) was propagated in A-549 cells (DSMZ ACC107) cultured in DMEM with 10% FBS and Pen/Strep; and (iv) HRV (species A/type 2, ATCC VR-482) was propagated in HeLa Ohio cells (both a kind gift of Heinrich Kowalski, Medical University of Vienna, Austria) cultured in DMEM with 10% FBS and Pen/Strep.

Parafilm squares (1 × 1 cm) inoculated with 30 µL of virus suspension (infectious dose: 10^3–10^6 IU/mL) were placed in a Petri dish surrounded by two pieces of wet cotton wool to increase the humidity. The virus-containing suspension was distributed across the parafilm surface in six droplets, air-dried for 15 min, and subsequently exposed to CAP for 10, 30, 90, and 120 min. Thereafter, the residual virus was recovered from the parafilm surface using 200 µL of phosphate-buffered saline (PBS), and the parafilm was thoroughly washed. To reduce the risk of bias, we implemented a control protocol for each sample, involving pipetting, 15 min of air-drying, mock exposure, and subsequent recovery. The recovered suspension was directly used for infecting permissive cells (specified above) to determine the infectious titer of each virus. All the data were generated from three biological replicates.

The SARS-CoV-2 titer was determined by diluting 20 µL of each sample in a 24-well plate containing 200 µL of cultivation medium in each well. The viral suspension was further diluted 1:10. Afterward, 300 µL of Vero E6 cells (2.5×10^5 per well) was added to the suspension and incubated for 4 h at 37°C and 5% CO_2. The mixture was subsequently overlaid with 500 µL of 3% carboxymethyl cellulose and incubated for 5 days at 37°C and 5% CO_2. The IAV titer was determined by pipetting 50 µL of each sample into a 24-well plate containing 300 µL of influenza growth medium (IGM) in each well. The viral suspension was further diluted 1:5. MDCK cells (1.8×10^5 per well, plated a day before the experiment) in a 24-well plate were washed once with PBS; 300 µL of IGM-containing serially diluted sample (1.5 µL of influenza A H1N1 virus in the first well) was added to the cells; the cells were then incubated for 1 h at 37°C and 5% CO_2. After 1 h, the cells were washed once with PBS; 300 µL of IGM was added to the cells; the medium was overlaid with 300 µL of 1.2% carboxymethyl cellulose; and the cells were incubated for 2 days at 37°C and 5% CO_2. For both SARS-CoV-2 and IAV, the infection was terminated by aspirating the medium. The cells were washed once with PBS, fixed, and stained with naphthalene black. After 45 min of incubation, the naphthalene black solution was aspirated, the cells were washed with water, and the resulting plaque-forming units (PFUs) were counted. The viral titer was expressed as PFU/mL. The 50% tissue culture infectious dose ($TCID_{50}$) of HAdV and HRV was determined by inoculating serially diluted (10-fold) samples (10 µL/well) in 96-well microtiter plates, in which A549 and HeLa Ohio cells were seeded, respectively. The infected cells were incubated at 37°C in a 5% CO_2 incubator for 5 (HRV) or 7 days (HAdV). The cytopathic effect (CPE) was visualized via a crystal violet assay as previously described.[20] The Spearman–Kärber method[21,22] was used to calculate the respective infectious titers (IU/mL).

Quantitative polymerase chain reaction (qPCR) was performed to determine the number of recovered virus genome copies. For SARS-CoV-2, a commercial kit (gb Sarbeco E, Cat. no. 3227--500; Generi Biotech, Czech Republic) was used in accordance with the manufacturer's instructions. IAV genome copies were determined via the Luna Universal Probe One-Step RT-qPCR Kit (New England Biolabs, USA), as previously described.[55] Recovered HAdV and HRV genome copies were measured via previously described protocols: HAdV (type C)[23,24] and HRV (multiplex).[28]

3. Results

3.1 CAP composition produced by the 3D-printed devices

The concentrations of NO and NO_2 in the gaseous environment of devices 1, 2, and 3 were measured during the generation of CAP over 120 min. While NO levels remained undetectable in all cases (data not disclosed), NO_2 levels displayed an obvious difference between optimized devices 2/3 and the original device 1, suggesting that the optimized devices are more efficient in producing NO_2 (Figure 2).

The concentrations of O_3 and N_2O obtained from the FTIR spectra are depicted in Figure 3 as a function of the source operating time. The gradual increase in the

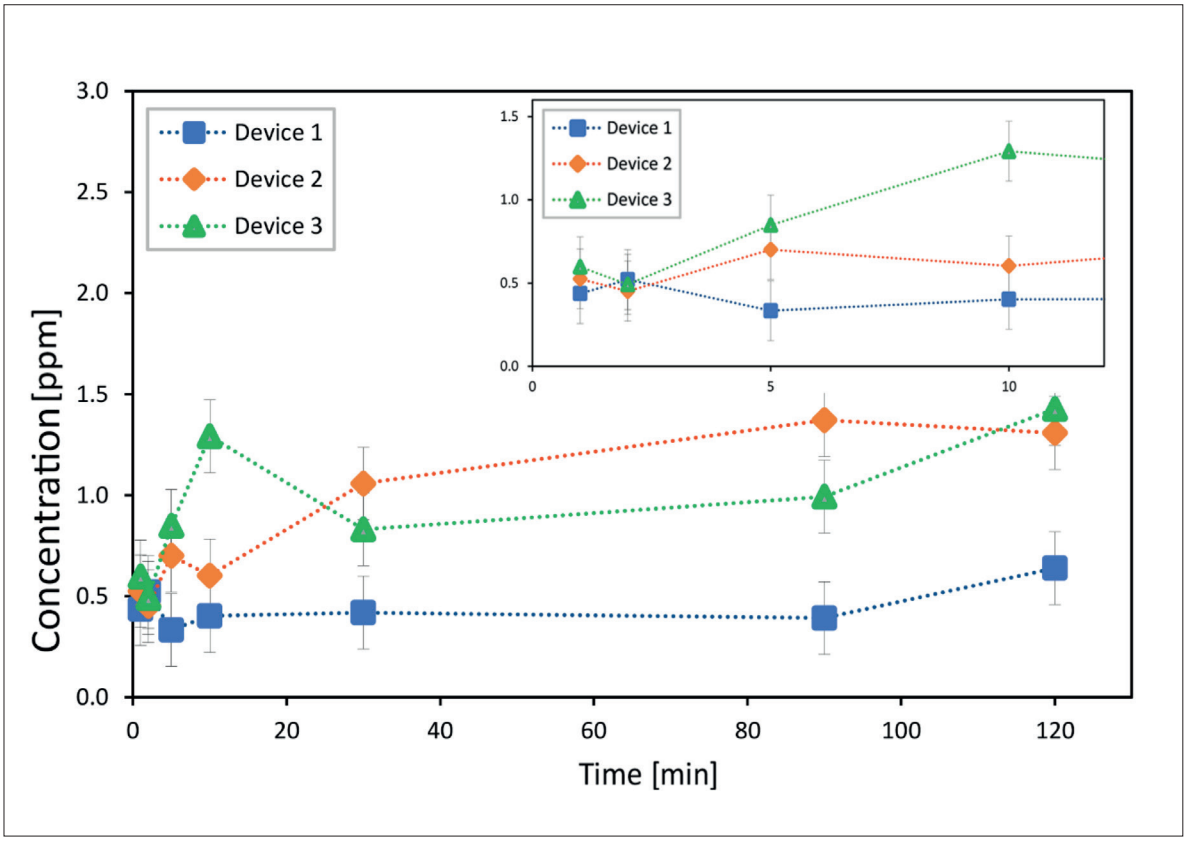


Figure 2. Concentration of NO_2 in the gaseous environment of devices 1, 2, and 3 measured over 120 min. Concentrations of NO_2 in devices 1, 2, and 3 in the first 10 min (inset). The concentration of NO_2 increases due to its accumulation in the gaseous environment of the devices, with the highest concentration noted for devices 2 and 3. The results are averaged from three independent measurements and depicted in ppm ± standard error of the mean.

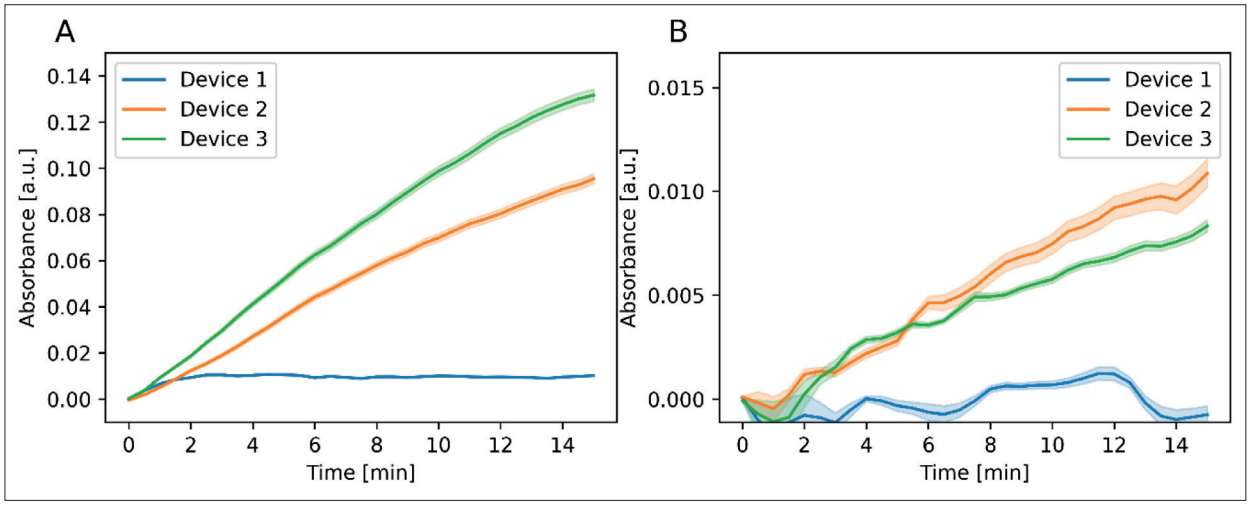


Figure 3. Concentration of O_3 (A) and N_2O (B) in the gaseous environment of devices 1, 2, and 3, measured over 15 min of operation in a closed reactor. Spectra were sampled every 30 s, and the concentration of gases was determined by integrating the area under the corresponding absorption peaks, after correcting for baseline drifting. Due to unavailable cross sections, the measure is reported in arbitrary units (a.u.), which are proportional to the actual density. The highlighted areas represent 1σ uncertainty, estimated from spectral analysis. The gradual increase reflects the production and accumulation of measured gases, with devices 2 and 3 producing more reactive species than device 1.

concentration measured inside the reactor suggested stable continuous production of O_3 and N_2O by the devices. Device 1 appeared to be less efficient in the production of both species, while the results of devices 2 and 3 were comparable (Figure 3). Similar results were obtained via an ultraviolet (UV)-100 ozone analyzer, whereby device 1 produced significantly less O_3 compared to the optimized devices (Figure S2 in Supplementary File).

To evaluate the CAP environment to which the pathogens were exposed, we assessed a drop of saline (representing the aqueous environment) exposed to CAP

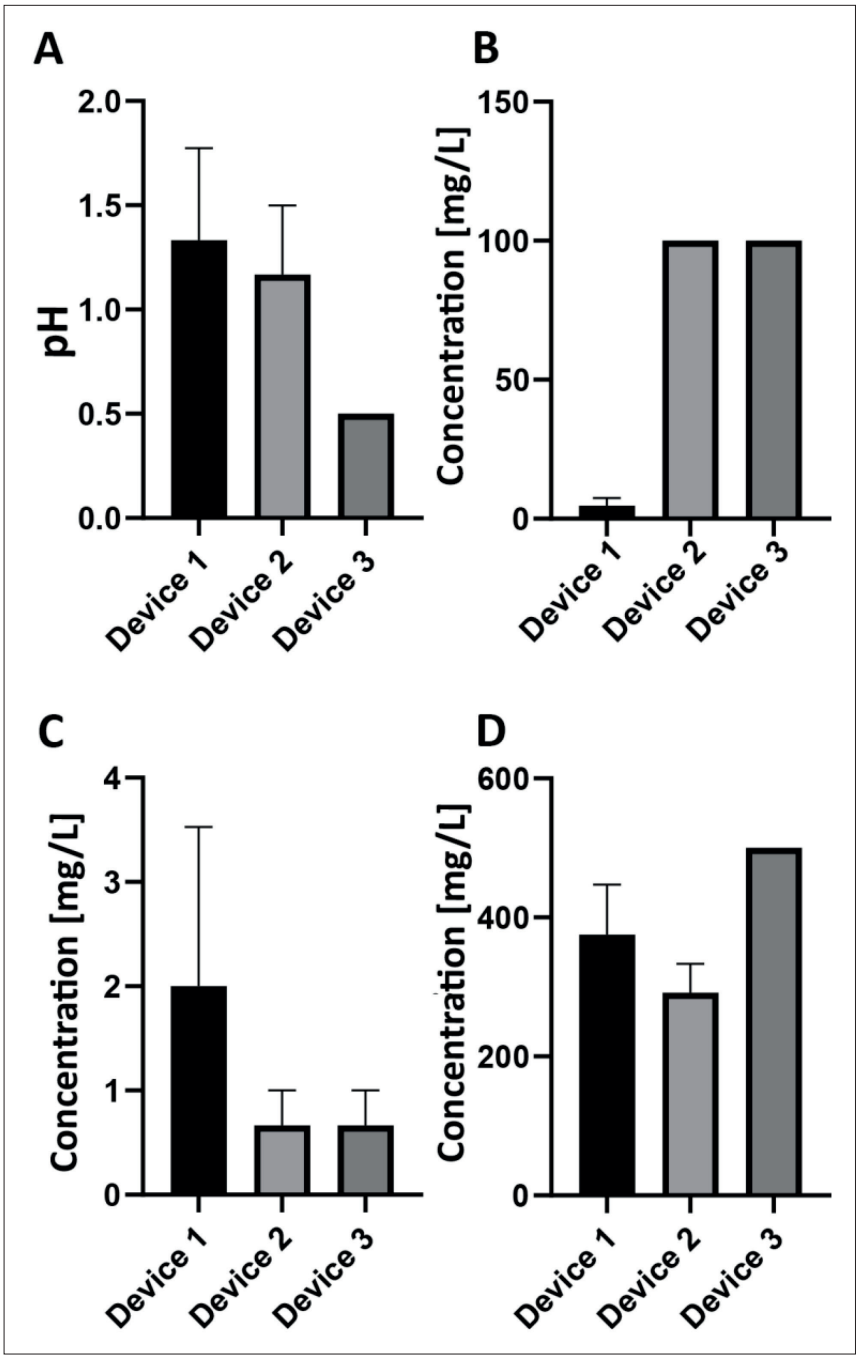


Figure 4. Reactive oxygen and nitrogen species (RONS) generated in saline after exposure (of 30 µL saline) to 3D-printed cold atmospheric plasma (CAP) in devices 1, 2, and 3 for 120 min. The pH (A) and concentrations of H_2O_2 (B), NO_2^- (C), and NO_3^- (D) were measured after 120 min of exposure. Results were averaged from three independent measurements and are presented as the mean and corresponding standard error of the mean. Values without depicted error bars were identical across all measurements (i.e., standard error of the mean = 0). Abbreviation: c: Concentration.

in the device chambers. The measured pH value indicated that the aqueous environment was highly acidic after treatment by all the devices. Specifically, device 1 reported a pH of approximately 1.3, whereas optimized devices 2 and 3 reported pH values of 1.2 and 0.5, respectively (Figure 4A). H_2O_2 was almost absent when the original device 1 was used, whereas optimized devices 2 and 3 reported H_2O_2 concentrations of up to 100 mg/L (Figure 4B). In general, the concentration of NO_2^- appeared to be relatively low (<4 mg/L) for all devices. The concentration of NO_2^- was, on average, the highest for device 1, approximately twice as high compared to the optimized devices 2 and 3. However, given the large SEM, the values obtained for all devices can be considered comparable (Figure 4C). NO_3^- levels were relatively high for all the tested devices (350–500 mg/L), with the highest value obtained for device 3 (500 mg/L) (Figure 4).

3.2. Viability of *P. aeruginosa* cells after exposure to CAP

P. aeruginosa PAO1 cells on parafilm squares were exposed to CAP from the three 3D-printed devices for 1, 5, 10, and 30 min. The results indicated that original device 1 exhibited a weaker microbicidal effect compared to optimized devices 2 and 3 (Figure 5). In contrast, devices 2 and 3, which were decontaminated with parafilm squares, displayed 100% efficiency after only 1 min of CAP exposure. Device 1 reduced *P. aeruginosa* contamination by approximately 1, 2, and 5 log CFU/L after 1, 5, and 10 min of CAP exposure, respectively, followed by complete decontamination of the parafilm squares only after 30 min of CAP exposure.

3.3. Morphology of *P. aeruginosa* cells after exposure to CAP

A visualization of *P. aeruginosa* PAO1 cells exposed to the three different CAP-generating devices via TEM is depicted in Figure 6. The control sample (Figure 6A) displayed intact rod-shaped cells with flagella. Device 1 did not cause any significant changes in cell morphology after 1 min of exposure (Figure 6B). However, after 5 min, visible dimming of the cell surface indicated incipient cell membrane damage (Figure 6C), which progressed to severely disturbed cell surface features after 10 min of exposure (Figure 6D). In contrast, 1 min of exposure to devices 2 and 3 (Figure 6E and H, respectively) resulted in changes in the cell surface; 5 min of exposure induced severe damage to the cell membrane, as indicated by thick dark demarcations (Figure 6F and I, respectively); and 10

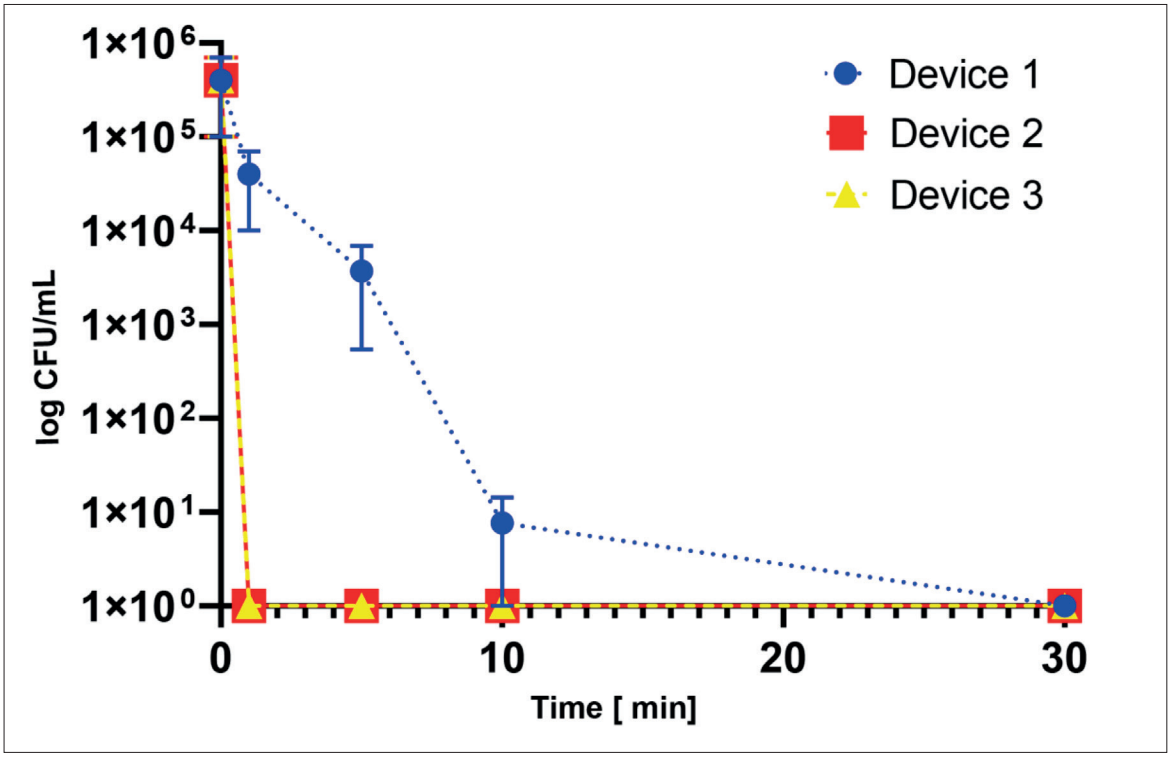


Figure 5. Effects of three 3D-printed cold atmospheric plasma (CAP)-generating devices on the viability of *P. aeruginosa* PAO1 cells. The bacteria were exposed to CAP for 1–30 min. Survival was determined by assessing the colony-forming units (CFUs) and plotting them as log CFU/mL.

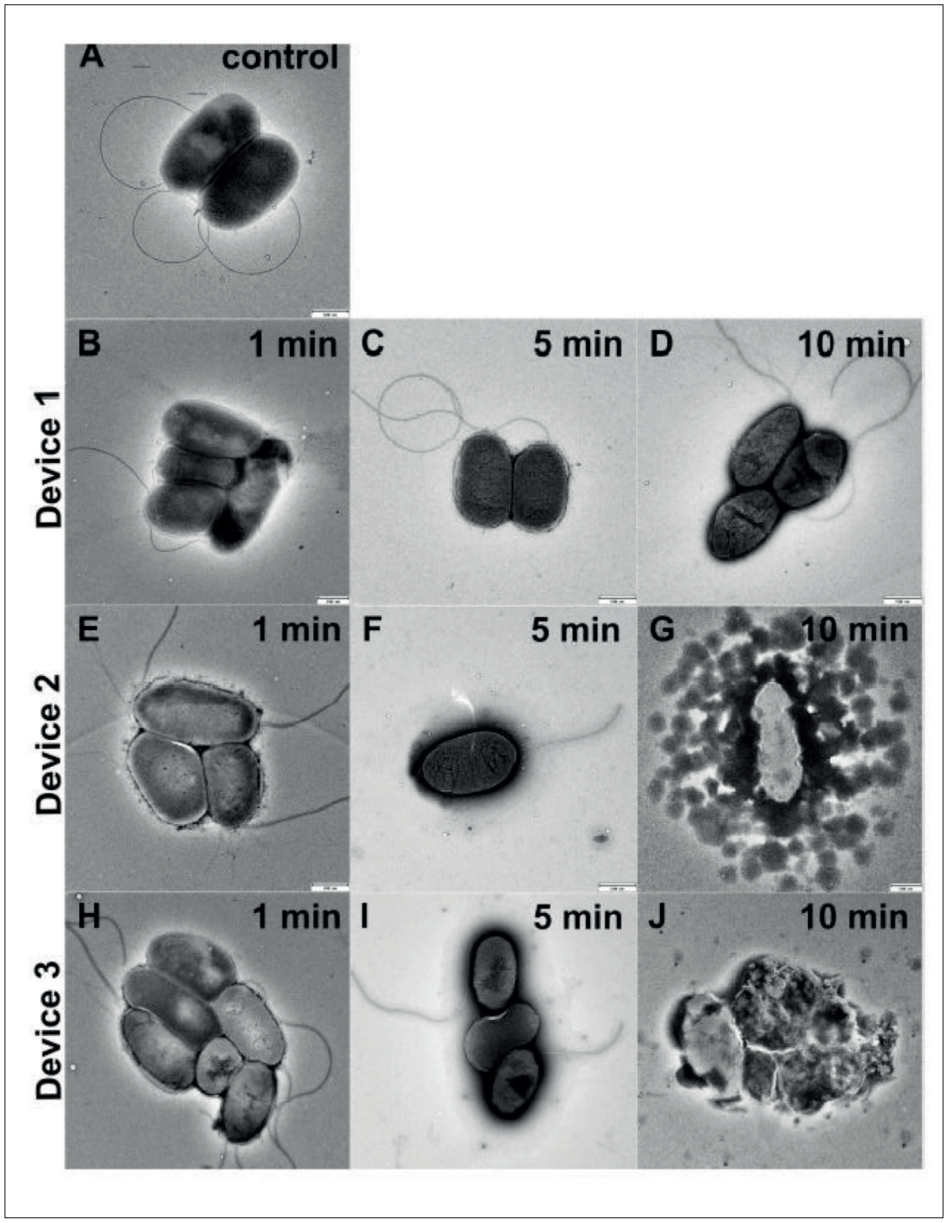


Figure 6. Differential effects of three different 3D-printed cold atmospheric plasma (CAP)-generating devices on the morphology of *Pseudomonas aeruginosa* PAO1 cells visualized by transmission electron microscopy (TEM). As observed, increasing the duration of exposure to CAP damages the cell membrane, leading to cell disruption and content leakage. TEM images of cells in (A) the unexposed control sample; (B) device 1, exposure for 1 min; (C) device 1, exposure for 5 min; (D) device 1, exposure for 10 min; (E) device 2, exposure for 1 min; (F) device 2, exposure 5 min; (G) device 2, exposure for 10 min; (H) device 3, exposure for 1 min; (I) device 3, exposure for 5 min; and (J) device 3, exposure for 10 min. Scale bars: 500 nm. Magnification: XXX.Will be done

min of exposure led to rupture of the cell membrane (Figure 6G and J, respectively). Notably, complete leakage of the cell contents was visible after 10 min of CAP exposure via device 2 (Figure 6G).

3.4. CAP exposure reduces viral infectivity and compromises particle integrity

We directly compared the virucidal effects of the three devices by exposing virus-contaminated parafilm squares to CAP for 10, 30, 90, and 120 min. SARS-CoV-2 infectivity in permissive cells was completely eliminated by optimized devices 2 and 3 after 90 min of exposure, whereas original device 1 required 120 min (Figure 7A; Table S1 in Supplementary File). Viral genome copy numbers determined by qPCR demonstrated that the optimized devices could effectively eliminate over 99.5% of SARS-CoV-2 RNA after 90 min, whereas the original device reduced the RNA level by 96% after only 120 min

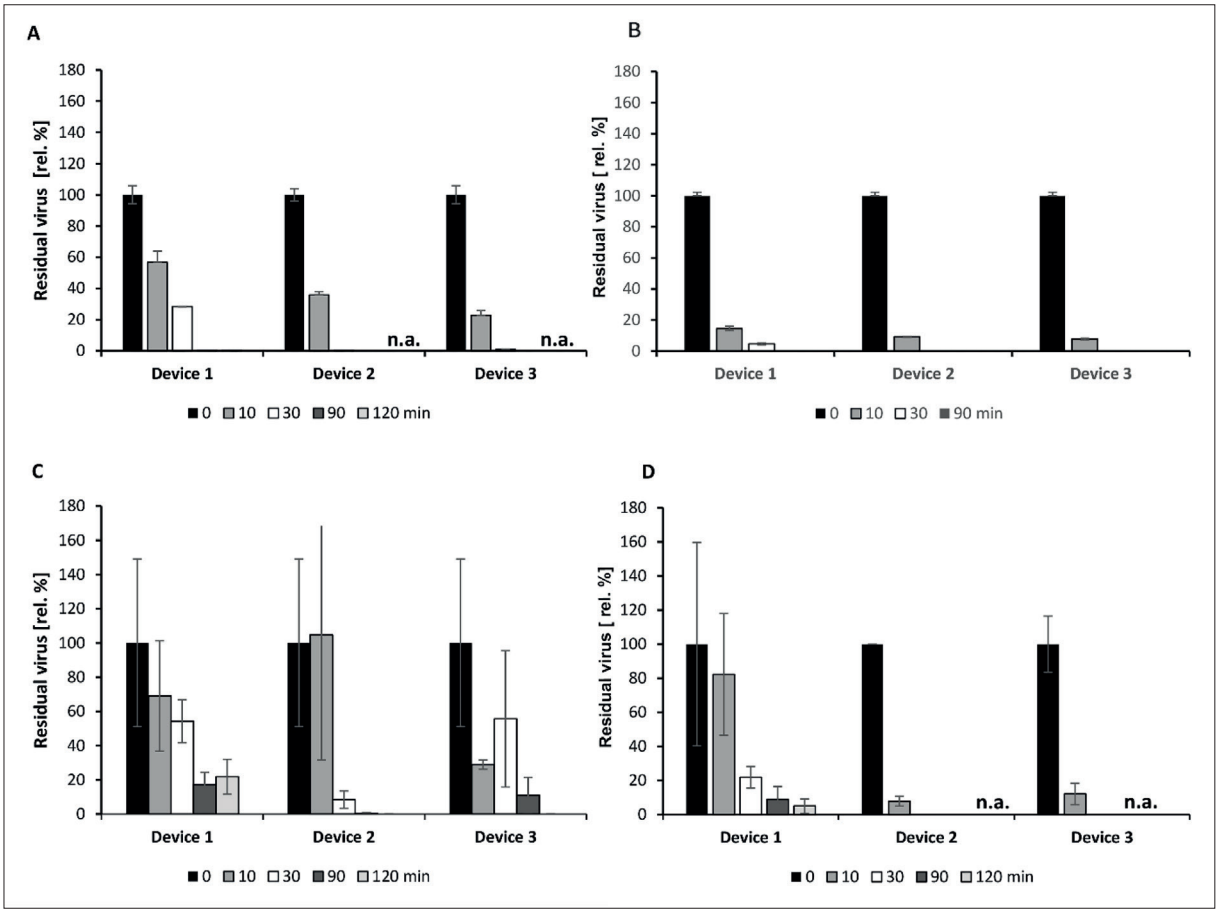


Figure 7. Virus infectivity reduction after cold atmospheric plasma (CAP) treatment for (A) SARS-CoV-2; (B) influenza A H1N1; (C) adenovirus; and (D) rhinovirus. The viral inoculum was spotted on parafilm, air-dried, and subsequently exposed to CAP for specific durations. The residual infectivity of the viruses was determined in cell culture, and the results are plotted as relative percentages to untreated control samples. The average of three biological replicates with the standard error of the mean are displayed for all the measurements. Increasing the duration of CAP exposure resulted in a progressive reduction in viral infectivity, and optimized devices 2 and 3 were superior to original device 1. If complete elimination of infectivity was achieved, residual infectivity was not analyzed at longer exposure times (n.a.).

(Figure 8A; Table S1 in Supplementary File). Hence, the virucidal effect of the optimized devices occurred more rapidly, with device 3 exhibiting slightly higher efficiency than device 2.

All the tested 3D-printed devices completely abrogated the infectivity of IAV. The original device required 90 min to completely eliminate the infectious capacity of IAV, whereas the optimized devices required only 30 min (Figure 7B; Table S2 in Supplementary File). Device 3 demonstrated significantly better performance in terms of particle destruction than did device 2 (Figure 8B; Table S2 in Supplementary File). The inferior performance of the original device was also documented by qPCR analysis.

Following CAP treatment using the optimized devices, HRV infectivity decreased over time, reaching complete elimination after 30 min of exposure, whereas the original device was unable to completely inactivate HRV even after 120 min (Figure 7D; Table S4 in Supplementary File). The number of viral genome copies decreased by approximately 75% after 30 min of treatment with devices 2 or 3, whereas device 1 produced similar results after only 120 min (Figure 8D; Table S4 in Supplementary File).

As expected, the HAdV samples were more resistant to treatment with CAP than the tested RNA viruses were and required longer exposures to decrease their infectivity. The optimized devices facilitated the complete elimination of the HAdV infectious capacity after 120 min, whereas the original device only reduced the infectivity by approximately 80% after the same exposure time (Figure 7C; Table S3). Viral genome

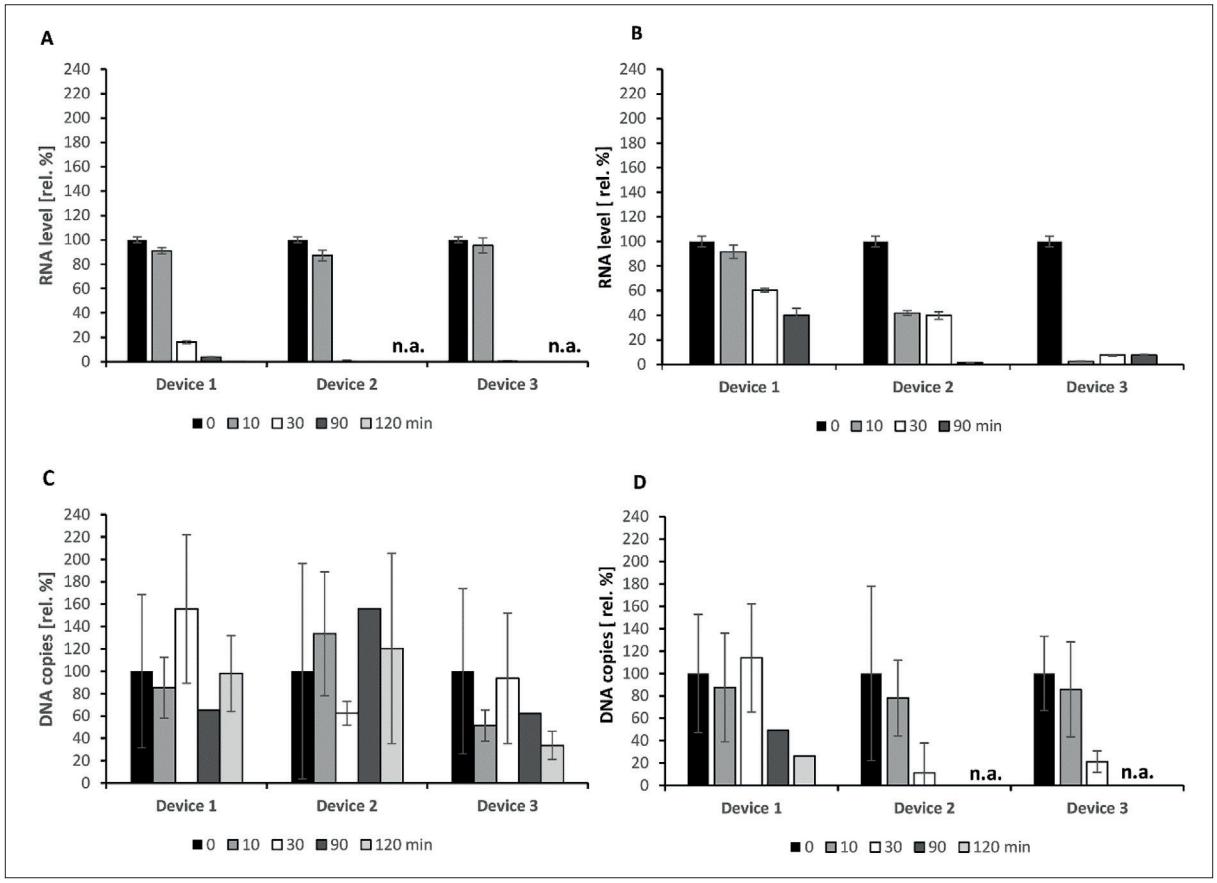


Figure 8. Viral genome copy reduction after cold atmospheric plasma (CAP) treatment for (A) SARS-CoV-2; (B) influenza A H1N1; (C) adenovirus; and (D) rhinovirus. The viral inoculum was spotted on parafilm, air-dried, and subsequently exposed to CAP for specific durations. Residual virus nucleic acid copies (genome equivalents) were determined via quantitative polymerase chain reaction (qPCR). The results are plotted as relative percentages to untreated control samples. The average of three biological replicates with the standard error of the mean are displayed for all the measurements. Increasing the duration of CAP exposure resulted in a progressive reduction of viral copy numbers, and optimized devices 2 and 3 were superior to original device 1. If complete elimination of infectivity was achieved, residual virus nucleic acid copies were not analyzed at longer exposure times (n.a.).

copies determined by validated qPCR[56] were reduced at a slower pace than infectivity (Figure 8C; Table S3). Additionally, the efficiency of device 3 was superior to that of device 2.

3.5. CAP-mediated decontamination of 3D-printed material

To assess the ability and efficacy of CAP in decontaminating 3D-printed materials, a proof-of-concept experiment was conducted in which 3D-printed PETG contaminated with *E. coli* was tested. Consistent with our earlier findings, exposure to CAP facilitated complete inactivation of the bacteria within 5 min (Figure S3).

4. Discussion

Cold atmospheric plasma (CAP) is regarded as a groundbreaking disinfection technology with vast potential for decontaminating various sensitive surfaces from pathogens. It features high effectiveness, nontoxic byproducts, minimal side effects, and operates under favorable conditions, including low temperatures. CAP can be used continuously and is amenable to human applications. The effects of CAP on biological samples depend on the plasma-generating device used, and 3D printing offers the required flexibility to facilitate the production of optimized instruments. Production is regulated by several critical factors, including construction (geometry) and technical parameters, such as applied power, voltage, and waveform. Furthermore, ambient conditions during application, such as the atmospheric composition, humidity, and pressure, influence the efficacy of CAP.[29] Hence, improving the design of 3D-printed devices, operating conditions, and parameters for the practical application of CAP is essential.

In this study, we examined the efficiency of three CAP devices for selecting enveloped and nonenveloped viruses and a clinically important gram-negative bacterium. The three devices were produced via a 3D printer and could be easily adjusted to the desired size, shape, and inner chamber geometry. Along with the original device used in earlier studies, we tested two optimized versions containing a closed chamber that produces a more densely concentrated particle environment. These versions incorporated a tubular "volcano" design, which accurately directs particle flow toward the sample. Another feature of potential improvement was the use of two electric discharges in parallel (Figure 1). All three devices demonstrated good performance in decontaminating surfaces from pathogens, but the devices displayed different efficiencies defined by the time of exposure to CAP required for inactivation. According to the parameters recorded, optimized devices 2 and 3 were superior to the original device 1 in all analyses performed, including the reduction in infectivity, nucleic acid degradation, and external membrane damage in relation to the duration of CAP exposure.

To characterize the CAP composition produced by individual devices, we analyzed the concentration of RONS accumulated in gaseous (Figures 2 and 3) and aqueous (Figure 4) environments. The optimized devices yielded relatively high concentrations of O_3, N_2O, and NO_2 in the gaseous environment and relatively high H2O2 concentrations in the saline solution. The pH of the exposed saline drop was generally low, with the lowest value generated by device 3 (pH 0.5). All the tested devices yielded comparable concentrations of NO_3^- and NO_2^- in the aqueous environment (based on SEM images). The results indicate that the use of closed-chamber formats (devices 2 and 3) led to changes in the CAP atmosphere, thereby increasing decontamination efficiency. Notably, the inclusion of an additional discharge electrode (device 2) had a minimal impact on decontamination efficiency.

The antibacterial properties of CAP apparently correlate with the concentration of RONS produced by the devices. This notion is reflected by the greater efficacy of optimized devices 2 and 3 in eliminating the viability of *P. aeruginosa* almost instantaneously, whereas device 1 required 30 min for the same effect (Figure 5). In this study, bacteria suspended in saline solution during CAP treatment suggested that RONS, specifically H2O2, may play a crucial role in antibacterial efficacy, especially in direct bacterial exposure to CAP.[56] This assumption is supported by the considerably greater H_2O_2 concentration in the CAP-exposed saline drop generated by devices 2 and 3 (Figure 4). The antimicrobial effect of RONS is well described in the literature,[57–59] and their presence has also been validated in a gaseous environment (Figures 2 and 3). However, H_2O_2 likely played a significant role in our analysis of bacterial inactivation in saline solution because of the low solubility of RONS in water. In contrast to the long CAP exposure times required for virus inactivation (up to 120 min; Figures 7 and 8), bacterial cells were inactivated by devices 2 and 3 within 1 min (Figure 5), where evaporation of the liquid is not expected to be a relevant factor. The antibacterial effect of CAP was also reflected by a greater degree of physical damage, including membrane impairment and cell content leakage, as visualized via TEM. This damage was more rapidly inflicted by devices 2 and 3 (Figure 6). CAP exposure damages the bacterial cell wall, leading to high levels of oxidative stress and cell membrane rupture, as well as bacterial cell death due to DNA damage.[60–64] Many studies have reported pronounced antibacterial effects of CAP generated in gaseous environments (i.e., containing a single RONS or a combination of RONS), which produces H_2O_2 and NO_2^- in aqueous environments.[58,65–69]

The antiviral efficiency exhibited a similar trend as described above, with devices 2 and 3 outperforming device 1 in all the assays performed (Figures 7 and 8; Tables S1–S4). Given the long exposure time required for viral inactivation (up to 120 min), significant evaporation of the liquid surrounding the viral particles is likely. Hence, both RONS detected in a gaseous environment and H_2O_2 detected at high concentrations in the aqueous environment upon treatment by devices 2 and 3 appear to play a relevant role in the virucidal effects observed. Viral infectivity decreased gradually over the CAP exposure time, and complete elimination was generally achieved more rapidly with the optimized devices. The reduction in viral genome copy number, which was analyzed to monitor the physical integrity of virus particles, exhibited the same trend, albeit more slowly, indicating that infectivity was diminished before complete particle disintegration. This trend was previously reported by us[19] and supports the notion that perfect virus fitness viability is required for infectivity but does not directly correlate with particle integrity. Repeated measurements often reveal fluctuating readouts, especially for HAdV and HRV, at shorter CAP exposure times. This was also the case for the control measurements before CAP exposure, thus reflecting the biological complexity of the experimental system. In line with previous observations,[70] enveloped RNA viruses (SARS-CoV-2 and IAV in the present study) and the nonenveloped virus HRV were more rapidly inactivated by CAP, whereas HAdV displayed a greater degree of stability. It has been previously reported that both enveloped and nonenveloped viruses can be inactivated by reactive plasma particles through oxidative damage to proteins, viral envelopes (if present), and nucleic acids.[71]

Various CAP experiments have suggested that O_3 might be the principal RONS responsible for viral inactivation.[72–74] whereas other observations highlighted the role of H_2O_2 and low pH[75] in the mechanism of CAP-mediated viral inactivation. Mentel et al.[76] examined the effects of H_2O_2 on different viruses at various concentrations and H_2O_2 exposure times. These findings indicate that all viruses tested (CoV strain 229E, influenza A and B viruses, HAdV, and HRV 1A, 1B, and type 7) were rendered inactive by 3% H_2O_2 within 1–30 min. In agreement with our data, the enveloped RNA viruses (SARS-CoV-2 and IAV) were most susceptible to the effects of H_2O_2, whereas HAdV was most resistant.[76] H_2O_2 is a powerful oxidizing agent that causes genetic damage, impairing the replicative capacity of both DNA and RNA viruses.[77] The mechanism of action of H_2O_2 involves attacking carbon double bonds in nucleosides or removing hydrogen atoms, leading to single- or double-strand breaks in DNA or RNA.[77,78] Additionally, CAP-derived RONS affect the receptor-binding region of the SARS-CoV-2 spike (S) protein, which is essential for its attachment to host cells and infectivity.[79,80] Consistent with published data, we observed a substantial improvement in both the microbicidal and virucidal efficiency of devices that produced O_3 and H_2O_2 at relatively high concentrations and more efficiently induced pH acidification.

The impact of the device on decontamination-related parameters is relevant not only from a scientific standpoint but also for its practical application in daily use. The device has the potential to be employed for decontaminating large areas and various sensitive materials and objects that are impossible or very difficult to disinfect via other methods. Specifically, one of our ongoing research objectives is to decontaminate children's plush toys, particularly for their use in stem cell transplant wards. Moreover, adapting the device for surface decontamination of 3D-bioprinted scaffolds for medical applications is also conceivable. In the present study, we demonstrated the basic applicability and efficacy of CAP for the decontamination of 3D-printed PETG, and the observations can expectedly be extended to a variety of other bioprinted materials.

In this context, safety is a concern due to the high voltages of several kVs used in the device. As outlined above, the device presented here is robust and mechanically resistant. The HV wires are well embedded in the device, and the separating air layer significantly exceeds the effective electrical strength. In addition, a significant advantage of the HV source used is its low current output. While capable of delivering HV, it generates only low currents on the order of 100 μA, well below the safety limit. In the event of direct contact with the HV wires, the voltage drops immediately, resulting in only a mild sensation of electrostatic charge for the person involved.

5. Conclusion

In summary, our observations indicate substantially enhanced CAP efficiency against all pathogens tested when using 3D-printed devices with closed reaction chambers and a "volcano" design to guide reactive particles. The optimized parameters facilitated complete inactivation with shorter CAP exposure times, potentially due to the increased accumulation of certain RONS in the gaseous environment or H_2O_2 in the aqueous environment. The findings highlight the potential of CAP as an easily applicable, inexpensive, and soft technique for decontaminating sensitive surfaces from viral and bacterial pathogens, particularly when other technical approaches based on heat exposure or antimicrobial liquids cannot be readily applied.

Acknowledgments

None

Funding

This study was supported by the FWF I 5293-B/GACR GF21-39019 L grant and by the National Institute Virology and Bacteriology project (Programme EXCELES; Project No. LX22NPO5103), funded by the European Union (EU) under the Next Generation EU initiative.

Conflict of interest

The authors declare that the research was conducted in the absence of any commercial or financial relationships that could be construed as potential conflicts of interest.

Author contributions

Conceptualization: Klára Obrová, Eva Vaňková

Formal analysis: Asma Bouazizi, Klára Obrová, Anna Machková, Josef Khun, Romana Hadravová, Jan Hodek, Lucie Ulrychová, Leonardo Zampieri, Fabio Avino

Funding acquisition: Klára Obrová, Abdelhalim Trabelsi, Jan Weber, Ivo Furno, Vladimír Scholtz, Thomas Lion

Investigation: Asma Bouazizi, Klára Obrová, Anna Machková, Josef Khun, Romana Hadravová, Jan Hodek, Lucie Ulrychová, Leonardo Zampieri, Fabio Avino

Methodology: Klára Obrová, Eva Vaňková

Project administration: Klára Obrová, Eva Vaňková

Supervision: Klára Obrová, Abdelhalim Trabelsi, Jan Weber, Ivo Furno, Vladimír Scholtz, Thomas Lion
Visualization: Asma Bouazizi, Klára Obrová, Anna Machková, Josef Khun, Romana Hadravová, Jan Hodek, Lucie Ulrychová, Leonardo Zampieri, Fabio Avino
Writing – original draft: Asma Bouazizi
Writing – review & editing: All authors

Ethics approval and consent to participate

Not applicable.

Consent for publication

Not applicable.

Availability of data

The data presented in this study are available upon request from the corresponding author.

References

1. Fernández A, Noriega E, Thompson A. Inactivation of *Salmonella enterica* serovar Typhimurium on fresh produce by cold atmospheric gas plasma technology. *Food Microbiol*. 2013;33(1):24-29. doi: 10.1016/j.fm.2012.08.007
2. Baier M, Görgen M, Ehlbeck J, Knorr D, Herppich WB, Schlüter O. Non-thermal atmospheric pressure plasma: Screening for gentle process conditions and antibacterial efficiency on perishable fresh produce. *Innov Food Sci Emerg Technol*. 2014;22:147-157. doi: 10.1016/j.ifset.2014.01.011
3. Hertwig C, Reineke K, Ehlbeck J, Knorr D, Schlüter O. Decontamination of whole black pepper using different cold atmospheric pressure plasma applications. *Food Control*. 2015;55:221-229. doi: 10.1016/j.foodcont.2015.03.003
4. Choi S, Puligundla P, Mok C. Corona discharge plasma jet for inactivation of *Escherichia coli* O157:H7 and *Listeria monocytogenes* on inoculated pork and its impact on meat quality attributes. *Ann Microbiol*. 2016;66(2):685-694. doi: 10.1007/S13213-015-1147-5
5. Oh YJ, Song AY, Min SC. Inhibition of *Salmonella typhimurium* on radish sprouts using nitrogen-cold plasma. *Int J Food Microbiol*. 2017;249:66-71. doi: 10.1016/J.IJFOODMICRO.2017.03.005
6. Van Gils CAJ, Hofmann S, Boekema BKHL, Brandenburg R, Bruggeman PJ. Mechanisms of bacterial inactivation in the liquid phase induced by a remote RF cold atmospheric pressure plasma jet. *J Phys D Appl Phys*. 2013;46(17):175203. doi: 10.1088/0022-3727/46/17/175203
7. Alkawareek MY, Algwari QT, Laverty G, et al. Eradication of *Pseudomonas aeruginosa* Biofilms by Atmospheric Pressure Non-Thermal Plasma. *PLoS One*. 2012;7(8):44289. doi: 10.1371/JOURNAL.PONE.0044289
8. Laroussi M. Low-temperature plasmas for medicine? *IEEE Trans Plasma Sci*. 2009;37(6 PART 1):714-725 doi: 10.1109/TPS.2009.2017267
9. Moreau M, Orange N, Feuilloley MGJ. Non-thermal plasma technologies: new tools for bio-decontamination. *Biotechnol Adv*. 2008;26(6):610-617. doi: 10.1016/j.biotechadv.2008.08.001
10. Kong MG, Kroesen G, Morfill G, et al. Plasma medicine: an introductory review. *New J Phys*. 2009;11(11):115012. doi: 10.1088/1367-2630/11/11/115012
11. Nosenko T, Shimizu T, Morfill GE. Designing plasmas for chronic wound disinfection. *New J Phys*. 2009;11(11):115013. doi: 10.1088/1367-2630/11/11/115013
12. Heinlin J, Isbary G, Stolz W, et al. Plasma applications in medicine with a special focus on dermatology. *J Eur Acad Dermatology Venereol*. 2011;25(1):1-11. doi: 10.1111/j.1468-3083.2010.03702.x
13. Von Woedtke T, Haertel B, Weltmann KD, Lindequist U. Plasma pharmacy - physical plasma in pharmaceutical applications. *Pharmazie*. 2013;68(7):492-498. doi: 10.1691/ph.2013.6521
14. von Woedtke T, Reuter S, Masur K, Weltmann KD. Plasmas for medicine. *Phys Rep*. 2013;530(4):291-320. doi: 10.1016/j.physrep.2013.05.005
15. Theus AS, Ning L, Kabboul G, et al. 3D bioprinting of nanoparticle-laden hydrogel scaffolds with enhanced antibacterial and imaging properties. *iScience*. 2022;25(9):104947. doi: 10.1016/j.isci.2022.104947
16. Liu H, Xing F, Yu P, et al. A review of biomacromolecule-based 3D bioprinting strategies for structure–function integrated repair of skin tissues. *Int J Biol Macromol*. 2024;268(Pt 2). doi: 10.1016/J.IJBIOMAC.2024.131623
17. Dubey A, Vahabi H, Kumaravel V. Antimicrobial and Biodegradable 3D Printed Scaffolds for Orthopedic Infections. *ACS Biomater Sci Eng*. 2023;9(7):4020-4044. doi: 10.1021/acsbiomaterials.3c00115
18. Vaňková E, Kašparová P, Khun J, et al. Polylactic acid as a suitable material for 3D printing of protective masks in times of COVID-19 pandemic. *PeerJ*. 2020;8:1-20. doi: 10.7717/peerj.10259
19. Obrová K, Vaňková E, Sláma M, et al. Decontamination of high-efficiency mask filters from respiratory pathogens including SARS-CoV-2 by non-thermal plasma. *Front Bioeng Biotechnol*. 2022;10(February):1-13. doi: 10.3389/fbioe.2022.815393

20. Aboubakr HA, Williams P, Gangal U, et al. Virucidal effect of cold atmospheric gaseous plasma on feline calicivirus, a surrogate for human norovirus. *Appl Environ Microbiol*. 2015;81(11):3612-3622. doi: 10.1128/AEM.00054-15

21. Ahlfeld B, Li Y, Boulaaba A, et al. Inactivation of a foodborne norovirus outbreak strain with nonthermal atmospheric pressure plasma. *MBio*. 2015;6(1). doi: 10.1128/MBIO.02300-14

22. Bae SC, Park SY, Choe W, Ha S Do. Inactivation of murine norovirus-1 and hepatitis A virus on fresh meats by atmospheric pressure plasma jets. *Food Res Int*. 2015;76: 342-347. doi: 10.1016/j.foodres.2015.06.039

23. Lacombe A, Niemira BA, Gurtler JB, et al. Nonthermal inactivation of norovirus surrogates on blueberries using atmospheric cold plasma. *Food Microbiol*. 2017;63:1-5. doi: 10.1016/j.fm.2016.10.030

24. Nayak G, Aboubakr HA, Goyal SM, Bruggeman PJ. Reactive species responsible for the inactivation of feline calicivirus by a two-dimensional array of integrated coaxial microhollow dielectric barrier discharges in air. *Plasma Process Polym*. 2018;15(1):1700119. doi: 10.1002/PPAP.201700119

25. Mohamed H, Nayak G, Rendine N, et al. Non-thermal plasma as a novel strategy for treating or preventing viral infection and associated disease. *Front Phys*. 2021;9(June):1-25. doi: 10.3389/fphy.2021.683118

26. Assadi I, Guesmi A, Baaloudj O, et al. Review on inactivation of airborne viruses using nonthermal plasma technologies: from MS2 to coronavirus. *Environ Sci Pollut Res*. 2022;29:4880-4892. doi: 10.1007/s11356-021-17486-3

27. Filipić A, Gutierrez-Aguirre I, Primc G, Mozetič M, Dobnik D. Cold Plasma, a new hope in the field of virus inactivation. *Trends Biotechnol*. 2020;38(11):1278-1291. doi: 10.1016/j.tibtech.2020.04.003

28. Scholtz V, Vaňková E, Kašparová P, Premanath R, Karunasagar I, Julák J. Nonthermal plasma treatment of ESKAPE pathogens: a review. *Front Microbiol*. 2021;12(October):1-20. doi: 10.3389/fmicb.2021.737635

29. Scholtz V, Julák J, Kříha V. The microbicidal effect of low-temperature plasma generated by corona discharge: comparison of various microorganisms on an agar surface or in aqueous suspension. *Plasma Process Polym*. 2010; 7(3-4):237-243. doi: 10.1002/ppap.200900072

30. Mai-Prochnow A, Murphy AB, McLean KM, Kong MG, Ostrikov K. Atmospheric pressure plasmas: infection control and bacterial responses. *Int J Antimicrob Agents*. 2014;43(6):508-517. doi: 10.1016/J.IJANTIMICAG.2014.01.025

31. Aboubakr HA, Mor SK, Higgins L, et al. Cold argon-oxygen plasma species oxidize and disintegrate capsid protein of feline calicivirus. *PLoS One*. 2018;13(3):e0194618. doi: 10.1371/journal.pone.0194618

32. Aboubakr HA, Nauertz A, Luong NT, et al. In vitro antiviral activity of clove and ginger aqueous extracts against feline calicivirus, a surrogate for human norovirus. *J Food Prot*. 2016;79(6):1001-1012. doi: 10.4315/0362-028X.JFP-15-593

33. Xu D, Ning N, Xu Y, et al. Effect of cold atmospheric plasma treatment on the metabolites of human leukemia cells. *Cancer Cell Int*. 2019;19(1):1-12. doi: 10.1186/s12935-019-0856-4

34. Zimmermann JL, Dumler K, Shimizu T, et al. Effects of cold atmospheric plasmas on adenoviruses in solution. *J Phys D Appl Phys*. 2011;44(50):505201. doi: 10.1088/0022-3727/44/50/505201

35. Sakudo A, Toyokawa Y, Imanishi Y, Murakami T. Crucial roles of reactive chemical species in modification of respiratory syncytial virus by nitrogen gas plasma. *Mater Sci Eng C*. 2017;74:131-136. doi: 10.1016/j.msec.2017.02.007

36. Sakudo A, Misawa T, Shimizu N, Imanishi Y. N_2 gas plasma inactivates influenza virus mediated by oxidative stress. *Front Biosci (Elite Ed)*. 2014;6(1):69-79. doi: 10.2741/E692

37. Sakudo A, Toyokawa Y, Imanishi Y. Nitrogen gas plasma generated by a static induction thyristor as a pulsed power supply inactivates adenovirus. *PLoS One*. 2016;11(6):e0157922. doi: 10.1371/JOURNAL.PONE.0157922

38. Alkawareek MY, Algwari QT, Gorman SP, Graham WG, O'Connell D, Gilmore BF. Application of atmospheric pressure nonthermal plasma for the in vitro eradication of bacterial biofilms. *FEMS Immunol Med Microbiol*. 2012;65(2):381-384. doi: 10.1111/j.1574-695X.2012.00942.x

39. Haertel B, Woedtke T von, Weltmann KD, Lindequist U. Non-thermal atmospheric-pressure plasma possible application in wound healing. *Biomol Ther*. 2014;22(6):477-490. doi: 10.4062/biomolther.2014.105

40. Guo L, Xu R, Gou L, et al. Mechanism of virus inactivation by cold atmospheric-pressure plasma and plasma-activated water. *Appl Environ Microbiol*. 2018;84(17):1-10. doi: 10.1128/AEM.00726-18

41. Dolezalova E, Lukes P. Membrane damage and active but nonculturable state in liquid cultures of *Escherichia coli* treated with an atmospheric pressure plasma jet. *Bioelectrochemistry*. 2015;103:7-14. doi: 10.1016/J.BIOELECHEM.2014.08.018

42. Haas M, Fürhacker P, Hodek J, et al. Detection of viable SARS-CoV-2 on the hands of hospitalized children with COVID-19. *Clin Microbiol Infect*. 2023;29(9):1211-1213.

doi: 10.1016/J.CMI.2023.06.012

43. Nogueira F, Obrova K, Haas M, et al. Intestinal shedding of SARS-CoV-2 in children: no evidence for infectious potential. *Microorganisms*. 2023;11(1):33. doi: 10.3390/microorganisms11010033

44. Lion T. Adenovirus persistence, reactivation, and clinical management. *FEBS Lett*. 2019;593(24):3571-3582. doi: 10.1002/1873-3468.13576

45. Lion T, Wold W. Adenoviruses. In: Knipe D, Howley P, eds. *Chapter in Fields Virology*, 7th ed. Wolters Kluver Health / Lippincott, Williams Wilkins 2022, 129-171. https://www.livres-medicaux.com/infectiologie-virologie-bacteriologie/23602-fields-virology-dna-viruses-vol-2-7th-ed.html. Accessed July 25, 2023.

46. Leung NHL. Transmissibility and transmission of respiratory viruses. *Nat Rev Microbiol*. 2021;19(8):528-545. doi: 10.1038/s41579-021-00535-6

47. Kirtipal N, Bharadwaj S, Gu S. From SARS to SARS-CoV-2, insights on structure, pathogenicity and immunity aspects of pandemic human coronaviruses. *Infect Genet Evol*. 2020;85(January):15. doi: 10.1016/j.meegid.2020.104502

48. Kumar V. Influenza in children. *Indian J Pediatr*. 2017;84(2):139-143. doi: 10.1007/s12098-016-2232-x

49. Lion T. Adenovirus infections in immunocompetent and immunocompromised patients. *Clin Microbiol Rev*. 2014;27(3):441-462. doi: 10.1128/CMR.00116-13

50. Piotrowska Z, Vázquez M, Shapiro ED, et al. Rhinoviruses are a major cause of wheezing and hospitalization in children less than 2 years of age. *Pediatr Infect Dis J*. 2009;28(1):25-29. doi: 10.1097/INF.0b013e3181861da0

51. Fazeli N, Momtaz H. Virulence gene profiles of multidrug-resistant *Pseudomonas aeruginosa* isolated from Iranian hospital infections. *Iran Red Crescent Med J*. 2014;16(10). doi: 10.5812/ircmj.15722

52. Ranjan Prasad R, Shree V, Kumar R, Kala K, Kumar P. Prevalence and antibiotic sensitivity of *Pseudomonas aeruginosa* isolated from CSOM in NMCH, Patna, India. *Int J Curr Microbiol Appl Sci*. 2017;6(6):2912-2916. doi: 10.20546/ijcmas.2017.606.345

53. Khun J, Machková A, Kašparová P, et al. Non-thermal plasma sources based on cometary and point-to-ring discharges. *Molecules*. 2022;27(1):238. doi: 10.3390/molecules27010238

54. Kašparová P, Vaňková E, Paldrychová M, et al. Nonthermal plasma causes *Pseudomonas aeruginosa* biofilm release to planktonic form and inhibits production of Las-B elastase, protease and pyocyanin. *Front Cell Infect Microbiol*. 2022;12(September):1-16. doi: 10.3389/fcimb.2022.993029

55. Ngaosuwankul N, Noisumdaeng P, Komolsiri P, et al. Research influenza A viral loads in respiratory samples collected from patients infected with pandemic H1N1, seasonal H1N1 and H3N2 viruses. *Virol J*. 2010;7(1):1-7. doi: 10.1186/1743-422X-7-75/TABLES/4

56. Machala Z, Tarabová B, Sersenová D, Janda M, Hensel K. Chemical and antibacterial effects of plasma activated water: correlation with gaseous and aqueous reactive oxygen and nitrogen species, plasma sources and air flow conditions. *J Phys D Appl Phys*. 2019;52(3):034002. doi: 10.1088/1361-6463/aae807

57. Kučerová K, Machala Z, Hensel K. Transient spark discharge generated in various N_2/O_2 gas mixtures: reactive species in the gas and water and their antibacterial effects. *Plasma Chem Plasma Process*. 2020;40(3):749-773. doi: 10.1007/s11090-020-10082-2

58. Lukes P, Dolezalova E, Sisrova I, Clupek M. Aqueous-phase chemistry and bactericidal effects from an air discharge plasma in contact with water: evidence for the formation of peroxynitrite through a pseudo-second-order postdischarge reaction of H_2O_2 and HNO_2. *Plasma Sources Sci Technol*. 2014;23(1):015019. doi: 10.1088/0963-0252/23/1/015019

59. Wang Z, Liu L, Liu D, et al. Combination of NO_x mode and O_3 mode air discharges for water activation to produce a potent disinfectant. *Plasma Sources Sci Technol*. 2022;31(5):05LT01. doi: 10.1088/1361-6595/ac60c0

60. Dasan BG, Onal-Ulusoy B, Pawlat J, Diatczyk J, Sen Y, Mutlu M. A New and Simple Approach for Decontamination of Food Contact Surfaces with Gliding Arc Discharge Atmospheric Non-Thermal Plasma. *Food Bioprocess Technol*. 2017;10(4):650-661. doi: 10.1007/S11947-016-1847-2

61. Belgacem Z Ben, Carre G, Charpentier E, et al. Innovative nonthermal plasma disinfection process inside sealed bags: Assessment of bactericidal and sporicidal effectiveness in regard to current sterilization norms. *PLoS One*. 2017;12(6):e0180183. doi: 10.1371/JOURNAL.PONE.0180183

62. Lunov O, Zablotskii V, Churpita O, et al. The interplay between biological and physical scenarios of bacterial death induced by nonthermal plasma. *Biomaterials*. 2016; 82:71-83. doi: 10.1016/J.BIOMATERIALS.2015.12.027

63. Scholtz V, Pazlarova J, Souskova H, Khun J, Julak J. Nonthermal plasma---a tool for decontamination and disinfection. *Biotechnol Adv*. 2015;33(6 Pt 2):1108-1119. doi: 10.1016/J.BIOTECHADV.2015.01.002

64. Alkawareek MY, Gorman SP, Graham WG, Gilmore BF. Potential cellular targets and antibacterial efficacy of atmospheric pressure nonthermal plasma. *Int J Antimicrob Agents*. 2014;43(2):154-160. doi: 10.1016/J.IJANTIMICAG.2013.08.022

65. Jablonowski H, Hänsch MAC, Dünnbier M, et al. Plasma jet's shielding gas impact on bacterial inactivation. *Biointerphases*. 2015;10(2):029506. doi: 10.1116/1.4916533

66. Machala Z, Tarabova B, Hensel K, Spetlikova E, Sikurova L, Lukes P. Formation of ROS and RNS in water electro-sprayed through transient spark discharge in air and their bactericidal effects. *Plasma Process Polym*. 2013;10(7):649-659. doi: 10.1002/PPAP.201200113

67. Oehmigen K, Hähnel M, Brandenburg R, Wilke C, Weltmann KD, Von Woedtke T. The role of acidification for antimicrobial activity of atmospheric pressure plasma in liquids. *Plasma Process Polym*. 2010;7(3-4):250-257. doi: 10.1002/PPAP.200900077

68. Liu Z, Xu D, Liu D, et al. Production of simplex RNS and ROS by nanosecond pulse N_2/O_2 plasma jets with homogeneous shielding gas for inducing myeloma cell apoptosis. *J Phys D Appl Phys*. 2017;50(19):195204. doi: 10.1088/1361-6463/aa66f0

69. Ke Z, Thopan P, Fridman G, et al. Effect of N_2/O_2 composition on inactivation efficiency of *Escherichia coli* by discharge plasma at the gas-solution interface. *Clin Plasma Med*. 2017;7-8:1-8. doi: 10.1016/j.cpme.2017.05.001

70. Thurston-Enriquez JA, Haas CN, Jacangelo J, Riley K, Gerba CP. Inactivation of Feline Calicivirus and Adenovirus Type 40 by UV Radiation. *Appl Environ Microbiol*. 2003;69(1):577-582. doi: 10.1128/AEM.69.1.577-582.2003

71. Von Woedtke T, Laroussi M, Gherardi M. Foundations of plasmas for medical applications. *Plasma Sources Sci Technol*. 2022;31(5):054002. doi: 10.1088/1361-6595/AC604F

72. Bisag A, Isabelli P, Laurita R, et al. Cold atmospheric plasma inactivation of aerosolized microdroplets containing bacteria and purified SARS-CoV-2 RNA to contrast airborne indoor transmission. *Plasma Process Polym*. 2020;17(10):1-8. doi: 10.1002/ppap.202000154

73. Kobza J, Geremek M, Dul L. Ozone concentration levels in urban environments—upper Silesia region case study. *Int J Environ Res Public Heal 2021, Vol 18, Page 1473*. 2021;18(4):1473. doi: 10.3390/IJERPH18041473

74. Wolfgruber S, Loibner M, Puff M, Melischnig A, Zatloukal K. SARS-CoV-2 neutralizing activity of ozone on porous and nonporous materials. *N Biotechnol*. 2022;66:36-45. doi: 10.1016/j.nbt.2021.10.001

75. Mileto D, Mancon A, Staurenghi F, et al. Inactivation of SARS-CoV-2 in the liquid phase: are aqueous hydrogen peroxide and sodium percarbonate efficient decontamination agents? *ACS Chem Heal Saf*. 2021;28(4):260-267. doi: 10.1021/acs.chas.0c00095

76. Mentel R, Schirrmacher R, Kewitsch A. Inactivation of viruses with hydrogen dioxide. *Vopr Virusol*. 1977;22(6):731-733. Accessed March 30, 2023. http://www.ncbi.nlm.nih.gov/pubmed/203115

77. Amanna IJ, Raué HP, Slifka MK. Development of a new hydrogen peroxide–based vaccine platform. *Nat Med 2012 186*. 2012;18(6):974-979. doi: 10.1038/nm.2763

78. Termini J. Hydroperoxide-induced DNA damage and mutations. *Mutat Res Mol Mech Mutagen*. 2000;450(1-2):107-124. doi: 10.1016/S0027-5107(00)00019-1

79. Wang H, Zhao T, Yang S, Zou L, Wang X, Zhang Y. Reactive force field-based molecular dynamics simulation of the interaction between plasma reactive oxygen species and the receptor-binding domain of the spike protein in the capsid protein of SARS-CoV-2. *J Phys D Appl Phys*. 2021;55(9):095401. doi: 10.1088/1361-6463/AC360E

80. Sahun M, Privat-Maldonado A, Lin A, et al. Inactivation of SARS-CoV-2 and other enveloped and non-enveloped viruses with non-thermal plasma for hospital disinfection. *ACS Sustain Chem Eng*. 2023;11(13):5206-5215. doi: 10.1021/acssuschemeng.2c07622

ACCSCIENCE PUBLISHING

International Journal of Bioprinting

RESEARCH ARTICLE

3D printing of retainer for post-otoplasty morphology preservation

Peixu Wang[1], Di Wang[1], Wenshuai Liu[2], Litao Jia[1], Bo Pan[1], Xiaobo Yu[1], Yiwen Deng[1], Xia Liu[2], Haiyue Jiang[1]* and Lin Lin[1]*

[1]Auricular Reconstruction Center, Plastic Surgery Hospital, Chinese Academy of Medical Sciences and Peking Union Medical College, Beijing, China

[2]Research Center of Plastic Surgery Hospital, Chinese Academy of Medical Sciences and Peking Union Medical College, Beijing, China

Abstract

Congenital external auricular anomalies necessitate surgical correction for normal ear appearance. Despite high success rates, recurrence is common due to the elasticity of ear cartilage. Postoperative support and stress on the anatomical structures can effectively maintain the surgical results. This study aims to develop a personalized, 3D-printed retainer for post-otoplasty support, utilizing structured light-scanning and stereolithography 3D printing to improve postoperative outcomes with greater accuracy and consistency. Retainers were designed using Rhinoceros software to fit and support the ear based on these models. BioMed Flex 80A Resin was employed for 3D printing the retainers, ensuring biocompatibility and mechanical strength. Mechanical testing was conducted to assess the cured resin's tensile and compressive properties, as well as its stress relaxation behavior. Finite element analysis (FEA) was performed to assess stress distribution and deformation for optimal support. Clinical validation was conducted involving 20 patients wearing the retainer for 8 h daily for a week, with satisfaction measured using the C-QUEST 2.0 scale. Clinical assessments were performed with 20 post-otoplasty patients treated with either a retainer or an external stretching device. The results indicated that high-precision, biocompatible, patient-specific retainers were successfully produced. BioMed Flex 80A Resin demonstrated strong performance under strain and good stress retention. FEA indicated uniform stress distribution and effective support in critical areas, ensuring structural stability. Clinical validation reported high satisfaction rates (85%), with minor issues in comfort and weight, suggesting a need for individualized adjustments. Clinical assessments demonstrated superior performance in maintaining auricular width and helix-mastoid (H-M) distance compared to the external stretching device. The personalized 3D-printed retainer offers a promising solution for post-otoplasty support, providing consistent, effective, and biocompatible results.

Keywords: 3D Printing; Biocompatible resin; Congenital auricular anomalies; Otoplasty complications; Post-surgery support

***Corresponding authors:**
Haiyue Jiang
(jianghaiyue@psh.pumc.edu.cn)

Lin Lin
(linlin@psh.pumc.edu.cn)

Citation: Wang P, Wang P, Liu W, et al. 3D printing of retainer for post-otoplasty morphology preservation. *Int J Bioprint*. 2024;10(5):3986. doi: 10.36922/ijb.3986

Received: June 19, 2024
Revised: July 23, 2024
Accepted: July 26, 2024
Published Online: July 29, 2024

Copyright: © 2024 Author(s). This is an Open Access article distributed under the terms of the Creative Commons Attribution License, permitting distribution, and reproduction in any medium, provided the original work is properly cited.

Publisher's Note: AccScience Publishing remains neutral with regard to jurisdictional claims in published maps and institutional affiliations.

1. Introduction

Congenital external ear anomalies include conditions such as microtia, prominent ears, and less frequent conditions like cryptotia, Stahl ear, constricted ear, and macrotia.[1,2]

Severe malformations, like microtia, are rare, occurring in 0.8–2.4 out of every 10,000 live births. However, simpler anomalies, such as pre-auricular tags and prominent ears, can affect > 5% of the population.[3] Given the complexity of auricular anomalies, there are various corrective surgery techniques to treat the wide variety of congenital auricular anomalies. Existing corrective surgeries for auricular deformities have a high success rate, potentially achieving 80–90% similarity to the corresponding normal ear appearance. However, there are some complications of otoplasty for congenital auricular anomalies, such as hematoma, hypertrophic scar, and recurrence of deformations. Among these, the loss of correction is more commonly seen in clinical practice, occurring in 12% of cases.[4] This is often attributed to the inherent elasticity of ear cartilage, causing the cartilage to gradually return to its initial shape over time. Other factors contributing to deformation recurrence include suture fatigue, subsequent edema, scarring, and the severity of the initial deformity.[5]

Ear molding techniques are widely used in neonatal patients to correct deformities.[6,7] It is a non-surgical intervention that gradually reshapes ear cartilage over several days to weeks by applying continuous tension. It can achieve satisfying results as ear cartilage is flexible in newborns.[3,8] The estrogen content in newborns gradually decreases as they grow, which causes the auricle cartilage to harden, increasing the elasticity of ear cartilage and the tendency to return to the original morphology after corrective surgery, especially in older patients.[9] Therefore, post-corrective surgery support for elder patients is essential, and postoperative molding is proven to be effective in some post-otoplasty cases using silicon supports.[10]

Stereolithography (SLA) 3D printing relies on the controlled solidification of a resin through photopolymerization. SLA can achieve very high resolution and precision in the printed parts, which is critical for fabricating detailed and accurate retainers. The process involves focusing an ultraviolet (UV) laser source onto the resin surface to induce photopolymerization according to a computer-aided design (CAD), resulting in resin solidification.[11] The layer-by-layer curing process enables fine control over the dimensions and intricate details of the final product, essential for ensuring a proper fit and effectiveness of the retainers. Besides, SLA provides a superior surface finish compared to other techniques like fused deposition modeling (FDM) or digital light processing (DLP). The smooth surface finish reduces the need for extensive post-processing, making the retainers more comfortable for patients to wear and enhancing their aesthetic appeal.[12]

Resins are raw materials for SLA additive manufacturing technology, and they solidify upon UV radiation exposure.[13–16] Due to its good biocompatibility, resins are widely used in 3D printing medical devices that come into direct contact with human tissue. Resins can also be printed with very smooth surfaces, reducing the need for post-processing and enhancing the comfort and functionality of the final product. Furthermore, resins can provide adequate strength and toughness, ensuring sufficient mechanical compressive strength.[17]

Currently, there are no widely used medical devices in clinical practice that can maintain the postoperative shape of the auricle. Given the significant individual differences in auricle structure, a personalized retainer design based on each patient's auricular data is crucial for maintaining the shape of the auricle. Additionally, since the retainer must adhere to the skin for an extended period, the material used needs to offer adequate support strength and good biocompatibility. Based on current clinical needs, we have developed a personalized postoperative auricle-shaped retainer utilizing structured light scanning data for the first time. Through innovative design, the retainer is easy to put on and take off while effectively securing around the auricle. In this study, we used a novel biocompatible elastomer BioMed Flex 80A to print the retainer, providing adequate elasticity and support for sub-anatomical units of the auricle. Furthermore, we performed mechanical tests to evaluate the performance of our material. After acquiring typical scanning data from one clinical case, we successfully designed and manufactured a retainer and its accessories. To further investigate the effect of the retainer, we utilized finite element analysis (FEA) to simulate the stress created by the retainer on the surface of the ear and mimic the biomechanical behaviors of both ear and retainer. Moreover, the prototype was successfully worn by the patient and achieved a satisfying result.

2. Methods

2.1. Data acquisition

A handheld structured light 3D scanner (Artec Spider Scanner; Artec Group, Luxembourg) was used to capture the structure of the outer ear from all angles. Prior to scanning, the 3D scanner was preheated, in accordance with the manufacturer's guidelines, to ensure optimal accuracy. Various angles were used in smooth motion to comprehensively capture the entire auricular area. Real-time fusion enabled visual monitoring of the scan's completeness during and immediately after the process. A range indicator displayed the distance between the scanner and the object in Artec Studio 11 (Artec Group, Luxembourg), consistently maintaining a working distance

of 0.2–0.3 m. Subsequently, the data was automatically imported and manually processed in the software. The point-clouds data were aligned and fused to construct a 3D digital model of the ear. The digital model was then refined with data smoothing and defect repairing. Excess points that were not functional in subsequent processes were removed to reduce the computational load. The final 3D scan was rendered by the software algorithm. The geometric model of the human ear structure obtained from 3D reconstruction is relatively rough, represented as a triangular mesh model. It may exhibit structural issues such as deformations, distortions, and overly rough surfaces. The human ear (in standard tessellation language [STL] file format) was imported into Geomagic Studio 2014 (Raindrop Company, United States of America [USA]), where it undergoes surface fitting and smoothing processes. Through processes like precise surfacing, additional structures such as ear retainers and 3D-printed hard shells are integrated. Finally, the finite element model of the ear retainer was assembled and exported (in STL file format) as a reference model.

2.2. Design of the retainer based on the 3D scanning

Corrective surgery for ear malformation and its morphological changes are closely related to the anatomical structures of the auricle (Figure 1A). A typical case of constricted ear deformity (cup ear) with mild resurgence one year after surgery is displayed in Figure 1B–D.

The digital model was designed using Rhinoceros (McNeel Europe, Spain). Based on the largest percentile of human ear dimensions, the main part of the retainer was designed with dimensions of 65 × 40 mm. The scanned digital model of the ear was placed within this range, and the ear and surrounding areas were trimmed. Along the outline of the outer ear helix and earlobe, a kidney-shaped surface was created. This surface was offset outward to the dimensions of 65 × 40 mm, creating a closed surface that forms the soft rubber shell model, which was printed with BioMed Flex 80A (Formlabs, USA) (Figure 1E).

Using Boolean tools, the ear model was subtracted from the main part of the model to obtain the preliminary completed soft rubber model. The resulting STL model was converted to a subdivided surface, and a flexible modification tool was subsequently employed to suitably raise the height, thereby accentuating key features like the concha and triangular fossa of the auricle. This adjustment was aimed at improving the retainer's performance in these deeper anatomical regions. Additionally, for ease of wearing, we divided the retainer into two parts at the auricular concha and fully aligned them using external fastening devices. To effectively secure the ear retainer, we have innovatively developed a 3D-printed positioning cover for the retainer to ensure proper alignment. The cover is connected to the outer shell (protective shell) using a fixture. Both the positioning cover and outer shell were printed using BioMed Clear Resin (Formlabs, USA). The restriction band was then tied around the patient's head to apply external pressure on the protective shell, effectively preventing movement. This device helps maintain the correct shape of the ear, ensuring the effectiveness of the corrective surgery.

2.3. 3D printing of post-otoplasty morphology retainer and relative constructs

The design of the maintainer was exported as an STL file and imported into PreForm software (3.21.0; Formlabs, USA). All prints were manufactured using a Form3B+ printer (Formlabs, USA) with a resin having a Shore hardnesses of 80 A (BioMed Flex 80A Resin; Formlabs, USA). The orientation, supportive material, and layout were automatically generated by the software. After printing, the part was removed from the platform using a scrapping tool and subjected to post-processing. The parts were immersed in 99% isopropyl alcohol (IPA) for 20 min, removed by gentle pulling, and washed again for 10 min. After washing, the parts were dried fully for 1 h at ambient temperature. The dry parts were then placed in a glass beaker and submerged in water to polymerize the parts for 30 min at 70° in a UV-polymerization unit (Form Cure; Formlabs, USA), according to the manufacturer's instructions. After the water had reduced to room temperature, the parts were dried with a paper towel. No additional post-processing procedures were performed.

2.4. Mechanical tests

To compare the mechanical properties of two biocompatible resins, BioMed Flex 80A Resin and BioMed Elastic 50A Resin, we conducted tensile, three-point bending, and compression tests on both materials using a universal testing machine (Instron 5967; Instron, USA).

To thoroughly assess the mechanical properties (i.e., resistance to deformation) of BioMed Flex 80A Resin, a series of tests were performed, including uniaxial tensile, equal biaxial tensile, plane tensile, and volumetric compression tests, to measure their response to tension and pressure.

For the uniaxial tensile test, the samples were processed into dumbbell-shaped with a length of 25 mm and a width of 2 mm in the middle narrow section. The samples used in the equal biaxial tensile test were round-shaped with a diameter of 60 mm and a thickness of 2 mm. The plane tensile test was performed using rectangular samples with a length of 150 mm, width of 10 mm, and thickness of 2 mm. The experiments utilized a slow cyclic time-strain

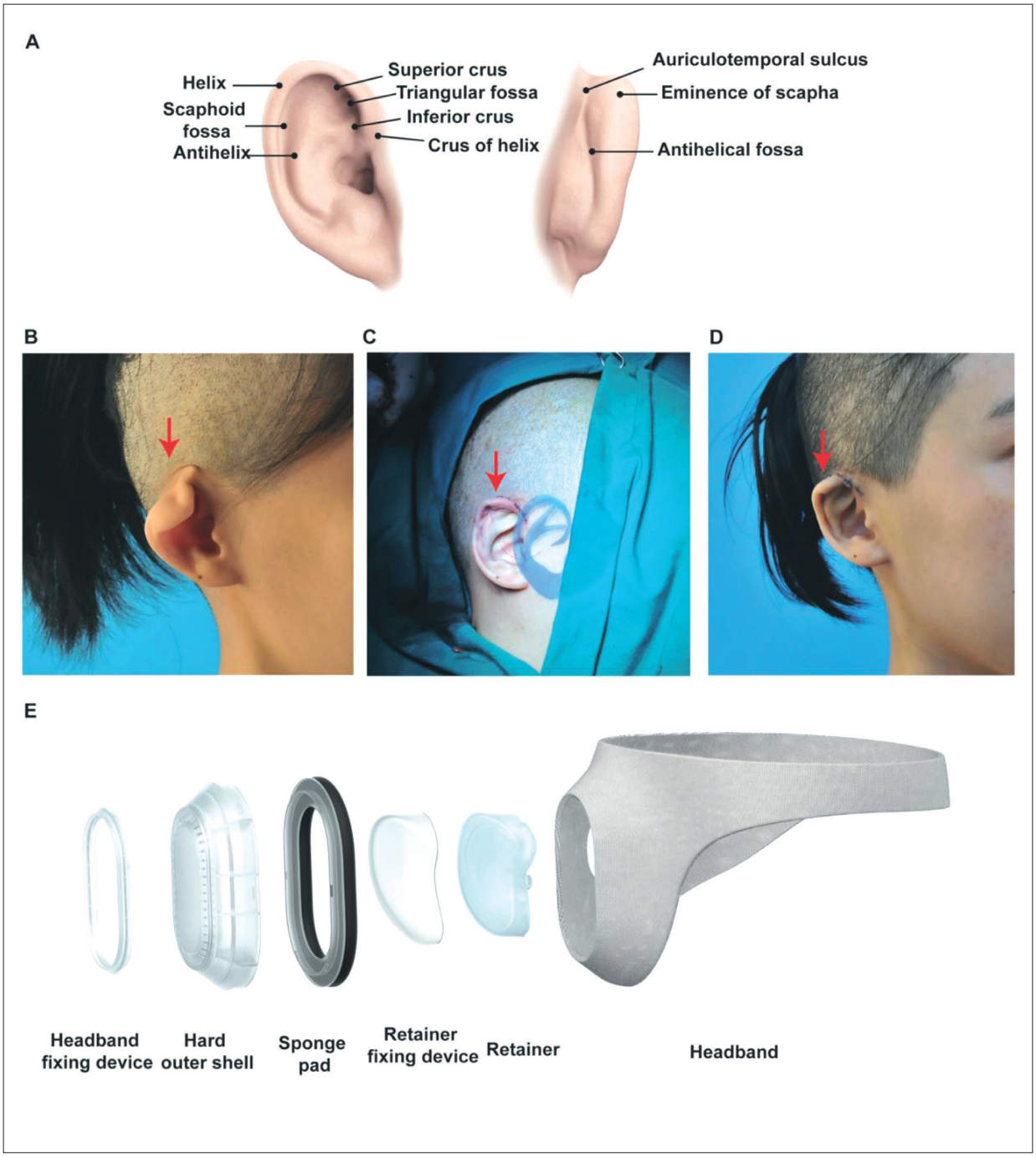


Figure 1. The background and design of postoperative ear retainer. (A) The auricular structures related to ear malformation corrective surgery: (A, left) anterior; (A, right) posterior, (B–D) a typical case of constricted ear deformity (cup ear) with mild resurgence one year after surgery. Photos were taken before (B), during (C), and one year after otoplasty (D). Red arrows indicate the transformation of the most severely deformed part of the constricted ear, and (E) design of the postoperative ear retainer: (from left to right) headband fixing device, hard outer shell, sponge pad, retainer fixing device, retainer, and headband.

loading-unloading method. Test samples were initially stretched from no stress to 20% strain and then unloaded back to no stress, the cycle of which was repeated five times. This procedure was then applied to 40% strain levels, repeated for five cycles, and subsequently extended to 60% and 100% strain levels. A 60% strain condition is acceptable for the part and was selected for stabilization. For each experiment, the fifth loading up to 60% strain was isolated from the broader data set, reset to zero stress and strain, and then utilized as a set of experiments to establish a material model.

The volumetric compression test was performed using cylindrical samples with a height of 2 mm and a diameter of 5 mm; a compression rate of 10 mm/min was used with indenters to compress the specimens. In their undeformed state, the nominal stress of the samples was calculated by dividing the applied force by the cross-sectional area.

To evaluate the decrease of stress over time, a stress-relaxation test was performed. The stress relaxation properties of a material cause the force acting on it to gradually weaken during use. The retention rate of stress directly reflects the material's corrective efficiency, making stress relaxation tests crucial. Stress relaxation tests were conducted using the ELF 3100 equipment at two strains in a 37°C water bath: 5% and 20% strains. Each test involved a three-part process: initially stretching the specimen by 1.25 mm over 15 s (equivalent to a tensile velocity of 5 mm/min and a total strain of approximately 5%); 5 s system stabilization and 3 h stretching at 5% strain for observing stress relaxation. For each material, three replicates were tested in both conditions. Stress values were recorded every 0.02 s. To reduce variations within the samples, stress relaxation curves were plotted using the percentile of residual stress.

2.5. Finite element analysis

The structural characteristics were determined by mechanical testing of the BioMed Flex 80A Resin, and these properties were then applied to the structure. Briefly, the model was refined to remove any inconsistencies or features that STP (Standard for the Exchange of Product Dat) could lead to computational errors, such as small fillets and sharp edges. The final assembled model, including the retainer and positioning cover, was completed to generate a geometric solid STP (Standard for the Exchange of Product Dat) STP model of the retainer. The STP file was subsequently imported into HyperMesh 14.0 software (Altair Company, USA) for mesh partitioning, and subsequently exported as a BDF (Boundary Data Format) file for finite element pre-processing using MSC. Patran2019 software (MSC Software Corporation, USA) and finite element post-processing using MSC Nastran 2019 software (MSC Software Corporation, USA).

The skull, 3D-printed shell, and internal cartilage of the ear are treated as isotropic, homogeneous, and continuously linear elastic materials. The facial skin, muscle, and soft tissue layers, as well as the soft retainer, are modeled as hyperelastic materials capable of large deformations and non-linear behavior.[18–20] The properties of the retainer are determined through experimental measurements involving planar tension, equibiaxial extension, and uniaxial tensile tests. Table 1 summarizes the properties used in FEA.

The boundary conditions for the finite element model of the ear mold retainer are assumed as follows: a fixed constraint is applied to the nodes on the lower surface of the model base, restricting movement in all six degrees of freedom; a pressure of 14 N was applied vertically to the outer surface of the hard shell using multi-point constraint (MPC) technology to simulate the pressure exerted on the ear structure when wearing the ear mold retainer. This setup allows for further observation of the impact of wearing the ear mold retainer on the biomechanical properties of the human ear. The constrained boundaries are illustrated in Figure S1, Supporting Information.

2.6. Clinical assessments

We conducted a clinical validation to investigate the feasibility of long-term retainer wear in 20 healthy patients. The patients were required to wear the retainers for 8 h per day for a week, and their satisfaction with the retainer was evaluated using the Chinese version of the Quebec Auxiliary Technology User Satisfaction Assessment Scale (C-QUEST 2.0).[21,22] C-QUEST 2.0 encompasses 12 subscales rated on a scale from 1 to 5, where higher

Table 1. Material properties used in finite element analysis.

Tissue/structure	Model	Elastic modulus (MPa)	Poisson's ratio
Auricular cartilage	Liner elastic	9	0.32
3D-printed positioning cover	Liner elastic	3500	0.30
Soft-gel retainer	Non-liner hyperelastic	Based on the mechanical tests	
Facial skin, muscle, and soft tissue	Hyperelastic (Mooney-Rivlin: C10 = 0.00165; C01 = 0.00335; D1 = 3.653)	0.7	0.45

scores indicate greater satisfaction and compliance. Our survey focused specifically on the device characteristics, evaluating eight items, including (i) dimension (size); (ii) weight; (iii) adjustments; (iv) safety; (v) durability; (vi) ease of use; (vii) comfort; and (viii) effectiveness.

Among the 20 patients who had undergone ear deformity corrective surgery, 10 of them wore personalized 3D-printed retainers after having their stitches removed two weeks post-surgery. For comparison, the other 10 patients used external stretching correctors, typically employed in the early non-surgical treatment of newborn ear deformities to maintain the ear shape (Figure S2, Supporting Information).[23] The patients were monitored weekly, and adjustments were made during treatment as needed. If any complications arose, the treatment was halted for two to three days to allow the ear to heal.

Before treatment and at the final follow-up, 3D scans of the craniofacial region were performed using the Spider handheld high-precision 3D scanner (resolution: 0.1 mm; accuracy: 0.05 mm; Artec, USA). The scan data were input into Artec Studio 10 software, where the ear morphology measurement points were determined, including the (i) anterior ear point, at the baseline of the auricle equal in height to the posterior ear point when the head maintains the eye-ear plane; (ii) posterior ear point, the most protruding point backward at the posterior edge of the helix when the head maintains the eye-ear plane; (iii) superior ear point, the highest point of the upper edge of the helix when the head maintains the eye-ear plane; and (iv) inferior ear point, the lowest point of the earlobe when the head maintains the eye-ear plane. The measurement function of the software was used to measure ear length, ear width, and the helix-mastoid (H-M) distance on the affected side before treatment and at the final follow-up. The ear length is the distance between the superior and inferior ear points; the ear width is the distance between the anterior and posterior ear points; and the H-M distance is the distance from the most protruding part of the helix to the mastoid in frontal view. These indices were measured three times by the same person, and the average was taken. The difference in these indices on the affected side before treatment and at the final follow-up was calculated.

2.7. Statistical analysis

Numerical data is presented as the mean ± standard deviation (*SD*). Differences among the groups were analyzed using Student's *t*-test. A p-value < 0.05 was considered significant. All analyses were conducted using Prism 10 (GraphPad Software, USA).

3. Results

3.1. 3D printing retainer and its accessories

For the first time, we developed a patient-specific post-otoplasty retainer using 3D printing technology with biocompatible material (Figure 2). The retainer was successfully assembled (Figure 3A–C) and worn by a patient without discomfort (Figure 3D–E).

3.2. Mechanical tests

The mechanical comparison between two biocompatible resins is displayed in Figure S3, Supporting Information. Previous research has indicated that Young's modulus of auricular cartilage is related to its anatomical location, ranging from 1.41 to 2.08 MPa. Therefore, we selected the mechanically superior BioMed Flex 80A Resin for subsequent experiments.

Figure 4 displays the mechanical tests conducted on the BioMed Flex 80A Resin. Figure 4A presents the stress-strain curves for the 3D-printed resin specimens used for FEA with different tensile tests. Figure 4B displays the stress-relaxation test with 5% and 20% strain at 37°, respectively. Figure 4C features the volumetric compression test of the resin used for the retainer. The BioMed Flex 80A Resin exhibited elevated stress at 5% strain over time, whereas the stress did not decrease at 20% strain. The results indicate the material exhibits high stress (that increases with time) at low strain (5%) and stable stress (over time) at high strain (20%).

3.3. Finite element analysis

Finite element analysis (FEA) was conducted on the ear-shaped retainer after being worn, examining the distribution patterns and peak values of different stress states (e.g., contact stress, von Mises stress, minimum principal stress, von Mises strain, and displacement) on the auricle, skin soft tissue, and retainer (Table 2).

The peak values for contact stress were 291 kPa for the skin and 394 kPa for the retainer (Figure 5). The peak values for von Mises equivalent stress were 93 kPa for the skin and 97 kPa for the retainer (Figure 6). The peak values for minimum principal stress were 94 kPa for the skin and 110 kPa for the retainer (Figure S4, Supporting Information). The peak values for von Mises equivalent strain were 0.052 for the skin and 0.042 for the retainer (Figure S5, Supporting Information). The maximum displacement for both the soft gel and the skin was 0.31 mm, with skin deformation around the contact area of the skin and soft gel retainer ranging from 0.10 to 0.16 mm (Figure S6, Supporting Information). The relatively

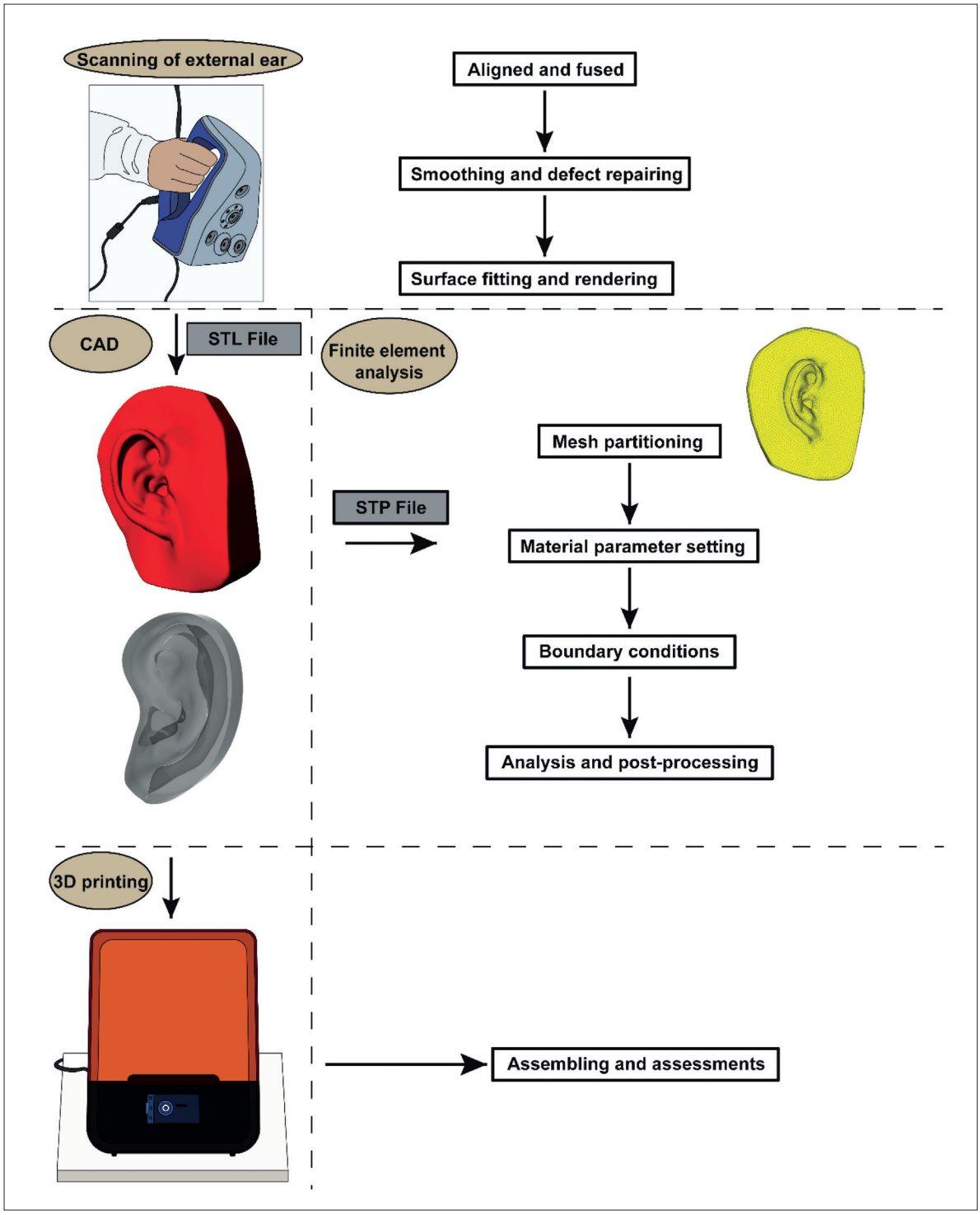


Figure 2. Flowchart of the design and manufacturing process of the 3D-printed retainer with finite element analysis and clinical assessments. Abbreviations: CAD: Computer-aided design; STL: Standard tessellation language; and STP: Standard for the exchange of product dat.

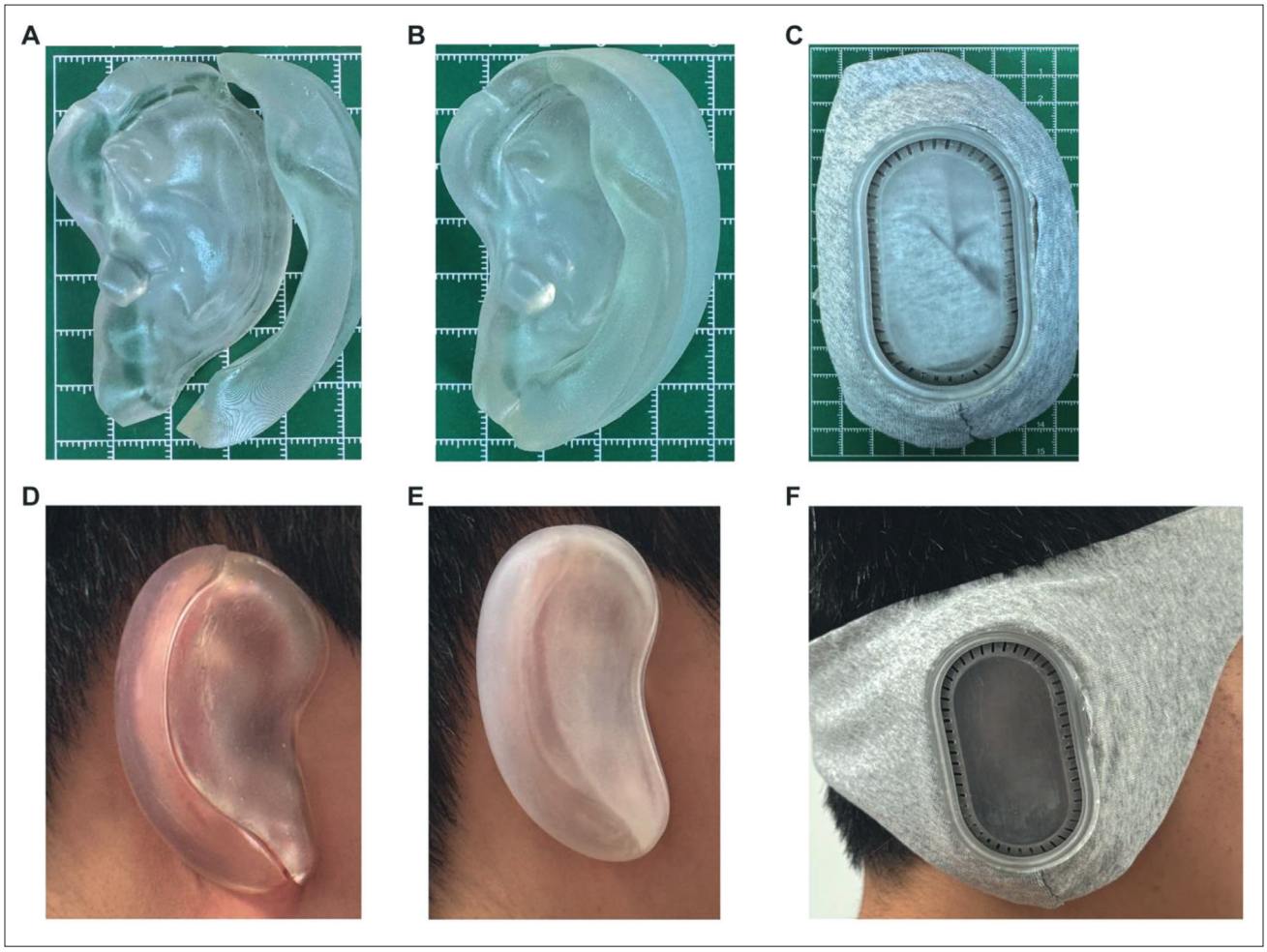


Figure 3. 3D-printed personalized ear retainer for post-ear correction surgery. (A and D) A 3D-printed BioMed Flex 80A retainer (A) that conforms to the patient's auricular morphology (D), (B and E) the positioning cover printed with BioMed Clear Resin (B) and attached with a split-type retainer on the patient's auricle (E), (C and F) an outer shell printed with BioMed Clear Resin (C) and equipped with a soft headband that is comfortably worn on the patient's auricle (F), effectively protecting the internal structure.

uniform distribution patterns from the contour map of both contact stress and von Mises stress indicate good contact between the retainer and the skin. Notably higher stress occurred near the helix, triangular fossa, antihelix, and the upper and lower legs of the ear skin; the surrounding ear skin exhibits relatively uniform stress distribution with lower stress values. The area behind the ear also demonstrated higher localized stress, with peak values higher than the surrounding skin stress. This suggests that after wearing the retainer, most of the force is transferred near the helix, triangular fossa, antihelix, and the superior crus and inferior crus, with stress diffusion around the ear being relatively uniform or lower. Moreover, the structure of the retainer also withstands the pressure to resist deformation towards the back of the ear, resulting in higher localized stress areas.

The results of FEA indicated that the overall structure has good stability when worn. Changes in stress and strain suggest that the retainer mechanically supports the structures post-otoplasty and should be constantly maintained. Otoplasty repairs the underdeveloped antihelix and obtuse concho-scaphal angle, and the postoperative mold for the scaphal and antihelical fossa on the back of the ear is essential for maintaining the morphology. In cryptotia corrective surgery, the upper part of the auricle (under the ear skin) and the auriculotemporal sulcus are restored, supporting the auriculotemporal sulcus.

3.4. Clinical validation

The satisfaction of patients wearing the retainer was assessed, and the findings are presented in Table 3. Most participants were "satisfied" or "very satisfied" with the retainer (n = 17; 85%). The highest satisfaction was reported for "safety"

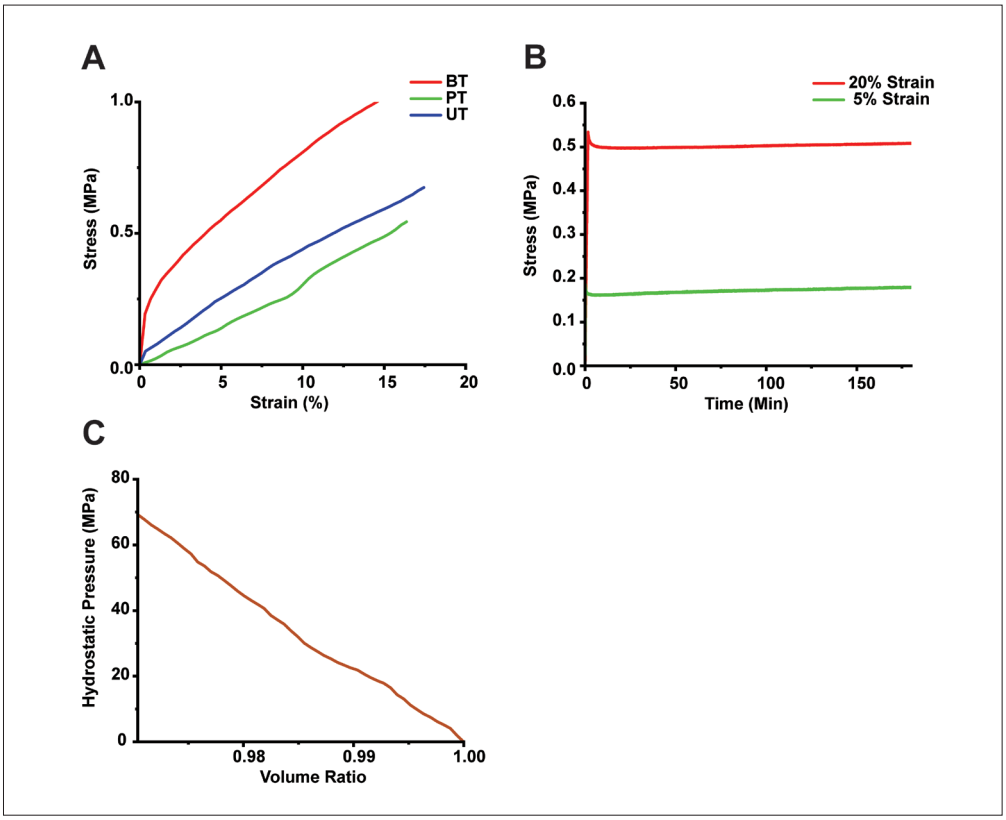


Figure 4. Results from mechanical tests performed at 37°. (A) Stress-strain curve from uniaxial tensile (UT; blue), equal biaxial tensile (BT; red), and plane tensile (PT; green) tests, (B) stress-relaxation test at 5% (green) and 20% (red) strain, and (C) volumetric compression test of the resin sample.

Table 2. Stress, strain, and deformation of auricular skin soft tissue and the soft gel retainer.

Parameter	Skin soft tissue	Retainer
Contact stress (kPa)	291	394
Von Mises stress (kPa)	93	97
Minimum principal stress (kPa)	94	110
Von Mises strain	0.052	0.042
Displacement (mm)	0.31 (Compression deformation of the surrounding skin upon contact is 0.10~0.16)	

(n = 19; 95%), followed by "adjustability" (n = 18; 80%), "weight" (n = 15; 75%), and "dimensions" (n = 17; 85%). Only several participants were not satisfied with the retainer, mostly attributed to "comfort" (n = 4; 20%). Two participants failed to finish the one-week experiment due to the retainer's "weight" and "discomfort," respectively. These two patients cannot be evaluated for durability and effectiveness because they did not consistently wear the retainer. These two patients did not comment (denoted as N/A) on the retainer's "durability" and "effectiveness." The two most reported answers were comfort (n = 4; 20%), simplicity of use (n = 3; 15%).

The discomfort from the retainer may be due to the over-fitness of the 3D-printing retainer, suggesting further personalized optimization for each individual in future designs. On the sixth day of evaluation, a patient expressed minor concerns about compliance, possibly due to the varying sensitivity levels of different patients to the retainer. None of the patients experienced pruritus after wearing the 3D-printed retainer, indicating that the material used has hypoallergenic properties after light-curing and post-processing and suggesting that the retainer is suitable for long-term wearing.

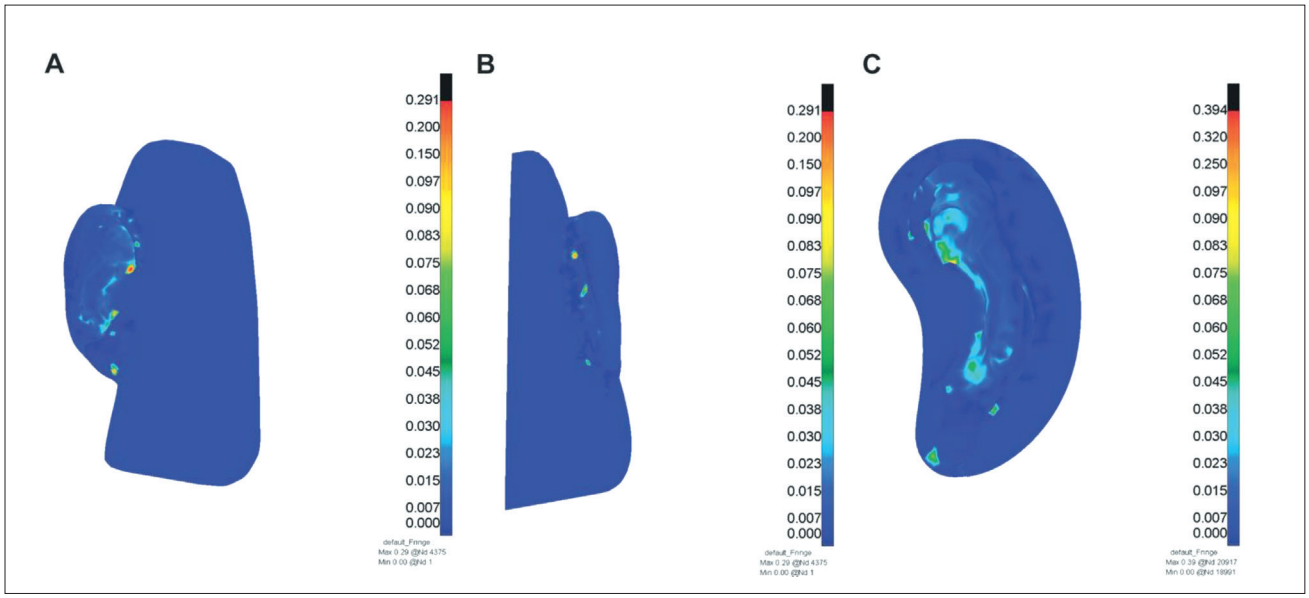


Figure 5. Contour plots of deformation and maximum contact stress on (A) the surface of the auricle, (B) the back of the auricle, and (C) the retainer.

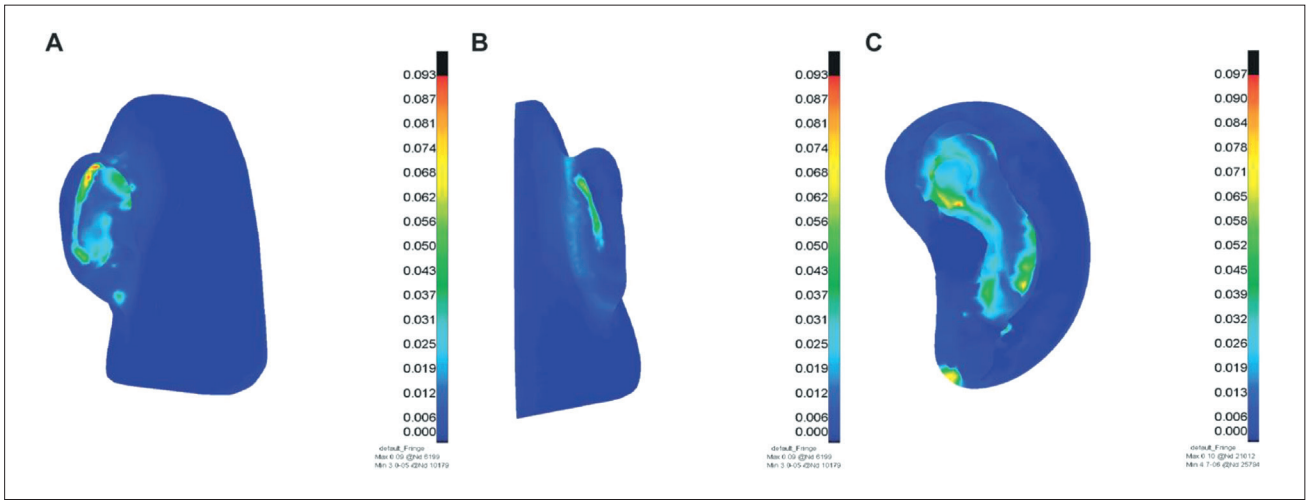


Figure 6. Contour plots of deformation and maximum von Mises stress on (A) the surface of the auricle, (B) the back of the auricle, and (C) the retainer.

A month after auricular corrective surgery, both the external stretching device and the 3D-printed personalized retainer demonstrated good performance in maintaining the ear shape (Figure 7). There was no significant difference in auricular length changes before and after treatment between the two, i.e., 1.905 ± 0.34 mm in the external stretching devices group vs. 1.520 ± 0.52 mm in the personalized retainer group (p = 0.07). However, in maintaining the postoperative auricular width, the 3D-printed personalized retainer displayed better shape retention (morphological difference: 1.96 ± 0.84 mm) compared to the external stretching device (morphological difference: 2.84 ± 0.84 mm) (p = 0.04). This may be due to the smaller contact area between the external stretching device and the scaphoid fossa at the transverse diameter of the auricle. In maintaining the postoperative H-M distance of the auricle, the 3D-printed personalized retainer also displayed better shape retention (morphological difference: 1.02 ± 0.54 mm) compared to the external stretching device (morphological difference: 1.72 ± 0.65 mm) (p = 0.02). The external stretching device's inferior performance in maintaining the cranio-auricular angle morphology could

Table 3. Satisfaction of patients wearing the retainer.

Parameter	Number of patients (%)			
	Very satisfied	Moderately satisfied	(Totally) not satisfied	N/A
Dimensions (size)	17 (85)	2 (10)	1 (5)	0 (0)
Weight	15 (75)	3 (15)	1 (10)	1(5)
Adjustability	18 (80)	2 (10)	0 (10)	0 (0)
Safety	19 (95) 1 (5)		0 (0)	0 (0)
Durability	13 (65)	4 (20)	1 (5)	2 (10)
Simplicity of use	14 (70)	3 (15)	3 (15)	0 (0)
Comfort	13 (65)	2 (10)	4 (20)	1 (5)
Effectiveness	14 (70)	4 (20)	0 (0)	2 (10)
General	17 (85)	2 (10)	1 (5)	0
Mean frequency (± *SD*), %	15 (± 2)	2 (± 1)	1 (± 1)	1 (± 1)

Note: The categories "not satisfied" and "totally not satisfied" were combined into a single category of "(totally) not satisfied." Abbreviation: N/A: Not applicable.

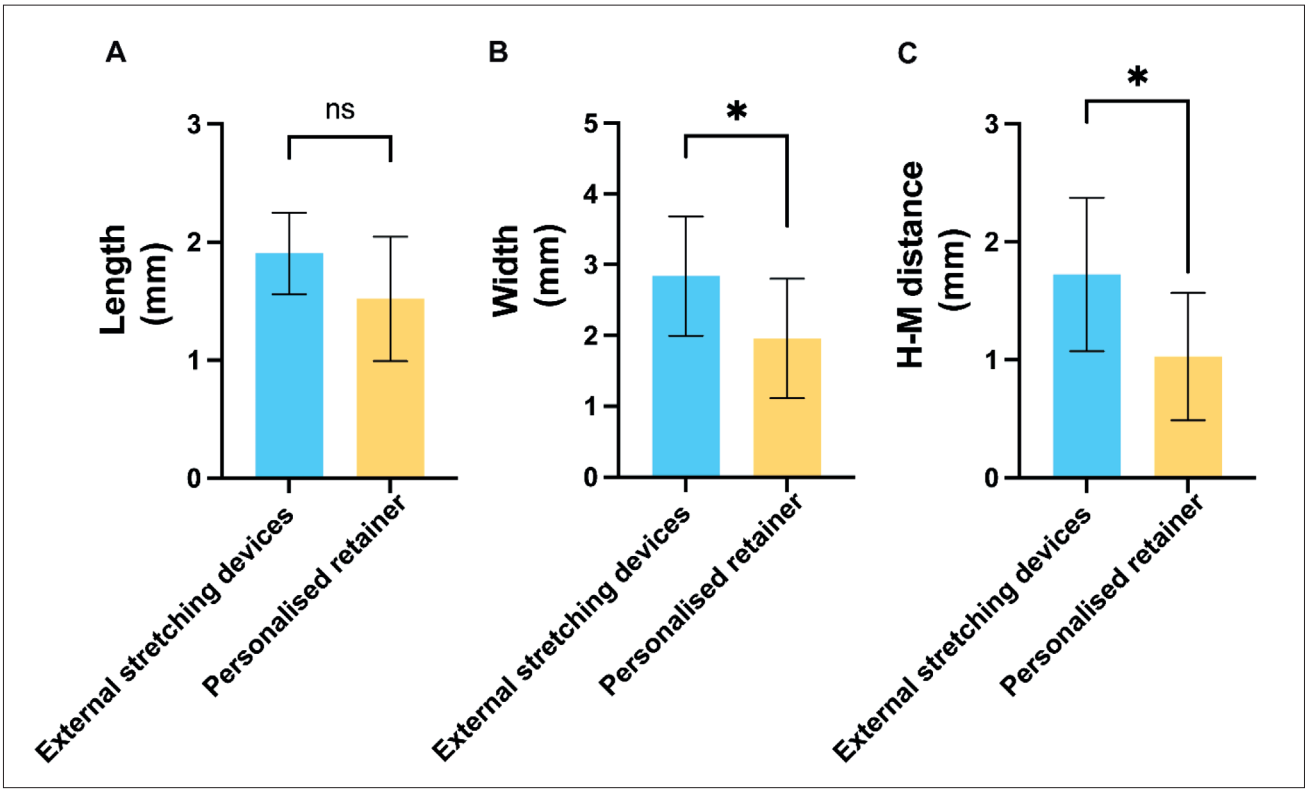


Figure 7. Changes in morphological parameters before and after treatment with external stretching devices and the personalized retainer. (A) Changes in the length of the ear one month after treatment, (B) changes in the width of the ear one month after treatment, and (C) changes in the helix-mastoid (H-M) distance of the ear one month after treatment. *$p < 0.05$. Abbreviation: ns: Non-significant.

be attributed to its inability to provide adequate support at the cranio-auricular groove. Although both devices can provide a certain level of shape retention after auricular surgery, the external stretching device, which functions to alter the shape of the auricle in infant patients with auricular deformities through the principle of stretching, has a good retention ability to maintain auricular length. However, it cannot offer personalized treatment for different individuals, leading to inferior performance in maintaining auricular width and H-M distance compared to the personalized 3D-printed retainer in some cases.

4. Discussion

In this study, we successfully developed a novel 3D-printed personalized ear-shaped retainer for post-surgical recovery. The printed material was tested for its properties and displayed good performance. The material can maintain effective stress under long-term strain and has certain self-recovery properties under low deformation, meeting the required performance for retainers. Additionally, the newly adopted material, BioMed Flex 80A Resin, has good biocompatibility, allowing for long-term contact with the patient's skin. Using the mechanical test data of the material, we conducted FEA of the retainer's contact with the ear. The results indicated good contact between the retainer and the skin, with relatively uniform stress distribution around it. Notable stress concentration was observed at parts of the ear that require shape maintenance after corrective ear surgery, such as the scapha, triangular fossa, antihelix, its superior and inferior crus, and the anti-helical fossa, providing good shape maintenance stress. The stress around the ear's skin was relatively uniform or lower, and the overall structural stability was good. The pattern of stress and strain changes suggests that wearing the retainer provides some mechanical protection for the post-surgical shape of the ear. Preliminary testing with 20 patients wearing the retainer for 8 h/day over a week did not result in any skin allergy incidents, demonstrating high patient acceptance and good compliance with the retainer design. Some patients reported odors from long-term wear, which will be improved in future designs by adding ventilation holes. To address pain from too-tight fit and prolonged wear, we will make corresponding improvements in subsequent designs. To better study the performance of the retainer, we compared its effectiveness in maintaining the auricle shape in postoperative patients to that of an external stretching device. The results indicated that the retainer achieved similar efficacy to the external stretching device in maintaining auricle length. Moreover, the personalized retainer demonstrated superior efficacy in maintaining auricle width and H-M distance.

3D printing technology is becoming increasingly significant in the field of medical devices due to its capabilities in printing and shaping a wide range of materials, its precision, and its ability to meet personalized and other customized requirements, as well as its high material utilization rate during the printing process.[24,25] Recently, 3D printing technology has been widely used for preoperative planning,[26,27] customizing surgical tools and prostheses,[28,29] patient education,[30,31] bioprinting, and tissue engineering.[32,33] The technology makes it possible for surgeons to customize medical devices with high-precision and complex structures based on specific patient anatomical data.[34] Postoperative shape retention devices in plastic surgery are widely used to stabilize and support the surgical area, thereby facilitating the healing process and maintaining the surgical results. Nasal splints and casts are typically made of thermoplastic and used after rhinoplasty to stabilize the nasal structure, reduce swelling, and prevent displacement.[35,36] A surgical binder is commonly used after breast surgeries (e.g., augmentation or reduction) to maintain breast shape, reduce swelling and pain, and prevent postoperative complications.[37,38] Likewise, ear molding techniques can be used to maintain or even change the morphology of the ear cartilage.[39,40] However, devices using metal retractors have limited effectiveness in maintaining the shape of large areas of ear cartilage. To our knowledge, there has yet to be a device for post-otoplasty shape retention in clinical practice. Hence, the combination of 3D printing and structured light technology now allows for the design and production of personalized ear-shaped retainers for post-otoplasty applications.

Photopolymer-based resins used in SLA contain various chemical components that may cause skin irritation or allergic reactions. Post-processes/cured resins are generally less likely to cause any irritation. BioMed Flex 80A Resin is a flexible, biocompatible material designed for medical applications that require long-term skin contact, i.e., over 30 days. This resin is produced in a United States (US) Food and Drug Administration (FDA)-registered, ISO 13485-certified facility and is certified according to the United States Pharmacopeia (USP) Class VI standards, indicating its safety for biocompatible applications. In our experiments, we did not observe any significant sensitization reactions caused by the retainer. There are no extensive studies specifically addressing long-term skin irritation from BioMed Flex 80A Resin. However, the certifications and standards of the resin imply that thorough testing for potential skin reactions was performed. The resin is designed to minimize risks associated with prolonged contact, including skin irritation and sensitization. Despite this, surgeons should

be aware of potential skin sensitization issues in clinical applications and advise patients to regularly monitor their skin condition.

Nonetheless, we plan to improve the design and performance of the 3D-printed retainer in future research. Detailed biomechanical parameter profiles will be used in FEA to optimize the retainer design. High-precision printing is the future of 3D printing development, as it can improve the accuracy of the retainer, enhance its fit with the patient's skin, and provide more effective support. Furthermore, hollow or lattice structures can be printed for future retainer designs to improve retainer performance, reduce its overall weight, and maintain the initial support strength.[41] Considering all associated costs, such as materials, machine maintenance, skilled labor, and additional operational expenses, an accurate cost-effectiveness analysis is necessary. A pilot study requires only a small number of patients to assess the clinical feasibility of 3D-printed retainers. Additionally, a clinical trial with a larger sample size and a multicenter, randomized, open-control design is required to validate the performance of the retainer.

Conclusion

In this study, we have successfully developed a personalized postoperative auricular retainer using SLA 3D printing technology and a biocompatible resin bioink. The personalized 3D-printed retainer offers a promising solution for post-otoplasty support, providing consistent, effective, and biocompatible results. Further research with a larger clinical sample size is warranted to validate its long-term efficacy and cost-effectiveness.

Acknowledgments

None.

Fundings

This work was supported by the Chinese Academy of Medical Science Innovation Fund for Medical Sciences (2021-I2M-052), Beijing Municipal Science & Technology Commission (No. Z221100007422084), Young Scientists Fund of the National Natural Science Foundation of China (Grant No. 8230092675), and Beijing Natural Science Foundation (No.7244400).

Conflict of interest

The authors declare no conflicts of interest.

Author contributions

Conceptualization: Peixu Wang, Lin Lin
Formal analysis: Yiwen Deng
Investigation: Di Wang, Litao Jia
Methodology: Bo Pan, Xiaobo Yu, Wenshuai Liu, Xia Liu
Writing – original draft: Peixu Wang
Writing – review & editing: Lin Lin, Haiyue Jiang

Ethics approval and consent to participate

Ethical approval for the study was obtained from the institutional review board of the Plastic Surgery Hospital of Chinese Academic of Medical Science and Peking Union Medical College, Beijing, China (approval no. 2022[183]). Written consent was obtained from each of the subjects to participate in the study.

Consent for publication

Written consent was obtained from each of the subjects to publish their data and images.

Availability of data

Data can be available for readers upon reasonable request.

References

1. Zhuang Q, Wei N, Zhou Q, et al. Efficacy and timing of neonatal ear correction molding. *Aesthetic Plast Surg*. 2020;44(3):872-878.
doi: 10.1007/s00266-019-01596-y

2. Lin J, Sclafani AP. Otoplasty for congenital auricular malformations. *Facial Plast Surg Clin North Am*. 2018;26(1):31-40.
doi: 10.1016/j.fsc.2017.09.003

3. Joukhadar N, McKee D, Caouette-Laberge L, Bezuhly M. Management of congenital auricular anomalies. *Plast Reconstr Surg*. 2020;146(2):205e-216e.
doi: 10.1097/PRS.0000000000006997

4. Handler EB, Song T, Shih C. Complications of otoplasty. *Facial Plast Surg Clin North Am*. 2013;21(4):653-662.
doi: 10.1016/j.fsc.2013.08.001

5. Basat SO, Askeroglu U, Aksan T, et al. New otoplasty approach: a laterally based postauricular dermal flap as an addition to Mustarde and Furnas to prevent suture extrusion and recurrence. *Aesthetic Plast Surg*. 2014;38(1):83-89.
doi: 10.1007/s00266-013-0269-z

6. Chen L, Li C, He A, et al. Long-term effectiveness of ear molding and factors affecting outcomes. *Plast Reconstr Surg*. 2024;153(4):905-913.
doi: 10.1097/PRS.0000000000010678

7. Zhang JL, Li CL, Fu YY, Zhang TY. Newborn ear defomities and their treatment efficiency with earwell infant ear correction system in China. *Int J Pediatr Otorhinolaryngol*. 2019;124:129-133.
doi: 10.1016/j.ijporl.2019.06.001

8. Sayadi JJ, Arora JS, Chattopadhyay A, Hopkins E, Quiter A, Khosla RK. A retrospective review of outcomes and complications after infant ear molding at a single institution. *Plast Reconstr Surg Glob Open*. 2023;11(8):e5133.
doi: 10.1097/GOX.0000000000005133

9. Xu H, Ding S, Yang H, et al. The treatment effect of non-surgical ear molding correction in children with mild cryptotia deformity. *Laryngoscope*. 2023;133(9):2122-2128.
doi: 10.1002/lary.30491

10. Aygit AC. Molding the ears after anterior scoring and concha repositioning: a combined approach for protruding ear correction. *Aesthetic Plast Surg*. 2003;27(1):77-81.
doi: 10.1007/s00266-002-0095-1

11. Triacca A, Pitzanti G, Mathew E, Conti B, Dorati R, Lamprou DA. Stereolithography 3D printed implants: a preliminary investigation as potential local drug delivery systems to the ear. *Int J Pharm*. 2022;616:121529.
doi: 10.1016/j.ijpharm.2022.121529

12. Ng WL, An J, Chua CK. Process, material, and regulatory considerations for 3D printed medical devices and tissue constructs. *Engineering*. 2024;36:146-166.
doi: 10.1016/j.eng.2024.01.028

13. Vidakis N, Petousis M, Michailidis N, et al. High-performance medical-grade resin radically reinforced with cellulose nanofibers for 3D printing. *J Mech Behav Biomed Mater*. 2022;134:105408.
doi: 10.1016/j.jmbbm.2022.105408

14. Ambrosio D, Gabrion X, Malécot P, Amiot F, Thibaud S. Influence of manufacturing parameters on the mechanical properties of projection stereolithography–manufactured specimens. *Int J Adv Manuf Technol*. 2020;106(1):265-277.
doi: 10.1007/s00170-019-04415-5

15. Aravind Shanmugasundaram S, Razmi J, Mian MJ, Ladani L. Mechanical anisotropy and surface roughness in additively manufactured parts fabricated by stereolithography (SLA) using statistical analysis. *Materials*. 2020;13(11):2496.
doi: 10.3390/ma13112496

16. Zhang S, Bhagia S, Li M, Meng X, Ragauskas AJ. Wood-reinforced composites by stereolithography with the stress whitening behavior. *Materials & Design*. 2021;206:109773.
doi: 10.1016/j.matdes.2021.109773

17. Keßler A, Dosch M, Reymus M, Folwaczny M. Influence of 3D-printing method, resin material, and sterilization on the accuracy of virtually designed surgical implant guides. *J Prosthet Dent*. 2022;128(2):196-204.
doi: 10.1016/j.prosdent.2020.08.038

18. Cai M, Shen S, Li H, Zhang X, Ma Y. Study of contact characteristics between a respirator and a headform. *J Occup Environ Hyg*. 2016;13(3):D50-60.
doi: 10.1080/15459624.2015.1116699

19. Tse KM, Tan LB, Lee SJ, Lim SP, Lee HP. Investigation of the relationship between facial injuries and traumatic brain injuries using a realistic subject-specific finite element head model. *Accid Anal Prev*. 2015;79:13-32.
doi: 10.1016/j.aap.2015.03.012

20. Chafi MS, Karami G, Ziejewski M. Biomechanical assessment of brain dynamic responses due to blast pressure waves. *Ann Biomed Eng*. 2010;38(2):490-504.
doi: 10.1007/s10439-009-9813-z

21. Lu P, Liao Z, Zeng Q, et al. Customized three-dimensional-printed orthopedic close contact casts for the treatment of stable ankle fractures: finite element analysis and a pilot study. *ACS Omega*. 2021;6(4):3418-3426.
doi: 10.1021/acsomega.0c06031

22. Chan SC, Chan AP. The validity and applicability of the Chinese version of the Quebec user evaluation of satisfaction with assistive technology for people with spinal cord injury. *Assist Technol*. 2006;18(1):25-33.
doi: 10.1080/10400435.2006.10131904

23. Wang D, Jiang H, Yang Q, et al. Non-surgical correction of cryptotia and the analysis of treatment time and other influence factors. *Int J Pediatr Otorhinolaryngol*. 2020;129:109771.
doi: 10.1016/j.ijporl.2019.109771

24. Palmara G, Frascella F, Roppolo I, Chiappone A, Chiado A. Functional 3D printing: approaches and bioapplications. *Biosens Bioelectron*. 2021;175:112849.
doi: 10.1016/j.bios.2020.112849

25. Wang S, Zhao S, Yu J, Gu Z, Zhang Y. Advances in translational 3D printing for cartilage, bone, and osteochondral tissue engineering. *Small*. 2022;18(36):e2201869.
doi: 10.1002/smll.202201869

26. He L, Liu X, Khatter NJ, Yu X, Washington KM, Shu M. Treatment of progressive hemifacial atrophy by cartilage graft and free adipofascial flap combined with three-dimensional planning. *Plast Reconstr Surg*. 2024;153(3):679-688.
doi: 10.1097/PRS.0000000000010585

27. Schwam ZG, Chang MT, Barnes MA, Paskhover B. Applications of 3-dimensional printing in facial plastic surgery. *J Oral Maxillofac Surg*. 2016;74(3):427-428.
doi: 10.1016/j.joms.2015.10.016

28. Li H, Fan W, Zhu X. Three-dimensional printing: the potential technology widely used in medical fields. *J Biomed Mater Res A*. 2020;108(11):2217-2229.
doi: 10.1002/jbm.a.36979

29. Pfaff MJ, Steinbacher DM. Plastic surgery applications using three-dimensional planning and computer-assisted design and manufacturing. *Plast Reconstr Surg*. 2016;137(3):603e-616e. doi: 10.1097/01.prs.0000479970.22181.53

30. Bernhard JC, Isotani S, Matsugasumi T, et al. Personalized 3D printed model of kidney and tumor anatomy: a useful tool for patient education. *World J Urol*. 2016;34(3):337-345. doi: 10.1007/s00345-015-1632-2

31. Andolfi C, Plana A, Kania P, Banerjee PP, Small S. Usefulness of three-dimensional modeling in surgical planning, resident training, and patient education. *J Laparoendosc Adv Surg Tech A*. 2017;27(5):512-515. doi: 10.1089/lap.2016.0421

32. Mishra A, Srivastava V. Biomaterials and 3D printing techniques used in the medical field. *J Med Eng Technol*. 2021;45(4):290-302. doi: 10.1080/03091902.2021.1893845

33. Zhu W, Ma X, Gou M, Mei D, Zhang K, Chen S. 3D printing of functional biomaterials for tissue engineering. *Curr Opin Biotechnol*. 2016;40:103-112. doi: 10.1016/j.copbio.2016.03.014

34. Wang Z, Yang Y. Application of 3D printing in implantable medical devices. *Biomed Res Int*. 2021;2021:6653967. doi: 10.1155/2021/6653967

35. Rohrich RJ, Mohan R. Male rhinoplasty: update. *Plast Reconstr Surg*. 2020;145(4):744e-753e. doi: 10.1097/PRS.0000000000006835

36. Boustany AN, Grover R, Alnaeem H, Seyidova N, Rohrich RJ, Lin SJ. Cosmetic rhinoplasty. *Plast Reconstr Surg*. 2023;151(2):315e-329e. doi: 10.1097/PRS.0000000000009874

37. Hidalgo DA, Spector JA. Breast augmentation. *Plast Reconstr Surg*. 2014;133(4):567e-583e. doi: 10.1097/PRS.0000000000000033

38. Xia Z, Xie J, Zhang W, Wang X, Zheng Y, Zeng A. Subfascial mini muscle-release dual plane technique: a modified procedure for breast augmentation. *Plast Reconstr Surg*. 2024. doi: 10.1097/PRS.0000000000011284

39. Roby BB, Woods T, Chinnadurai S. Update on congenital ear molding. *Curr Opin Otolaryngol Head Neck Surg*. 2023;31(4):215-218. doi: 10.1097/MOO.0000000000000895

40. Zou K, Fan Y, Jiang L, et al. Ear mold for congenital ear malformation: a randomized controlled trial. *Medicine (Baltimore)*. 2020;99(30):e21313. doi: 10.1097/MD.0000000000021313

41. Wang X, Liu J, Zhang Y, et al. Advances in precision microfabrication through digital light processing: system development, material and applications. *Virtual Phys Prototyp*. 2023;18(1):e2248101. doi: 10.1080/17452759.2023.2248101

ACCSCIENCE PUBLISHING

International Journal of Bioprinting

RESEARCH ARTICLE

Development of a biocompatible radiotherapy spacer using 3D printing and microcellular foaming process for enhanced prostate cancer treatment

DongHwan Lim[1], DoKun Yoon[2], JaeHoo Kim[3], KiHoon Sung[4], YoungEun Choi[4], HeeSoon Sheen[3], Han-Back Shin*[4], and Sung Woon Cha*[1]

[1]School of Mechanical Engineering, Yonsei University, Seoul, South Korea

[2]Department of Radiation Oncology, Gachon University Gil Medical Center, Incheon, Republic of Korea

[3]Department of Health Sciences and Technology, Samsung Advanced Institute for Health Sciences & Technology, Sungkyunkwan University, Seoul, Republic of Korea

[4]Department of Radiation Oncology, School/Faculty, Gachon University Gil Medical Center, Incheon, Republic of Korea

Abstract

In this study, a new active spacer was developed using three-dimensional (3D) printing technology and microcellular foaming process to overcome the limitations of current spacers used in prostate cancer treatment. In prostate cancer treatment, a spacer is inserted between the prostate and rectum to increase the distance between the two organs so as to reduce the radiation dose to the rectum. Radiotherapy spacer is widely used in particle therapy, such as proton and carbon beams, and X-ray radiation therapies, including intensity-modulated radiotherapy and stereotactic body radiation therapy. However, existing spacers have been reported to cause significant side effects. Therefore, this study introduces a 3D printing technique using polycaprolactone to develop a spacer that provides customized treatment and minimizes side effects. This technique utilizes the volume expansion that occurs when a 3D spacer printed to fit a patient's organs undergoes foaming through a supercritical carbon dioxide ($scCO_2$)-assisted microcellular foaming process. Additionally, the use of $scCO_2$ allows simultaneous gas absorption and sterilization, thereby reducing the number of process steps. This study confirms the potential of the newly developed spacer to provide effective and safe radiotherapy for prostate cancer, reduce patient discomfort, and minimize rectal side effects during radiation treatment.

Keywords: 3D printing; Prostate cancer treatment; Radiotherapy spacer; Microcellular foaming process; Biodegradable polymer

***Corresponding authors:**
Sung Woon Cha
(swcha@yonsei.ac.kr)

Han-Back Shin
(hbshin07@gmail.com)

Citation: Lim DH, Yoon DK, Kim JH, et al. Development of a biocompatible radiotherapy spacer using 3D printing and microcellular foaming process for enhanced prostate cancer treatment. *Int J Bioprint*. 2024;10(5):4252. doi: 10.36922/ijb.4252

Received: July 15, 2024
Revised: August 3, 2024
Accepted: August 5, 2024
Published Online: August 6, 2024

Copyright: © 2024 Author(s). This is an Open Access article distributed under the terms of the Creative Commons Attribution License, permitting distribution, and reproduction in any medium, provided the original work is properly cited.

Publisher's Note: AccScience Publishing remains neutral with regard to jurisdictional claims in published maps and institutional affiliations.

1. Introduction

The incidence of prostate cancer has been increasing worldwide. While radiotherapy (RT) is currently the most effective treatment available for prostate cancer, other

treatment techniques are constantly improving.[1] Despite the effectiveness in prostate cancer treatment, RT can cause radiation toxicity in surrounding organs and tissues, leading to complications in these regions.[2] Techniques such as three-dimensional conformal RT (3D-CRT), intensity-modulated RT (IMRT), and stereotactic body radiation therapy (SBRT) using X-rays and particles such as protons and carbon have been developed to minimize radiation exposure to healthy tissues and organs. Nevertheless, radiation toxicity from RT causes adverse side effects, such as diarrhea or bleeding, which may persist for years or even lifetime, potentially reducing the patient's quality of life.[3] Therefore, spacers have been developed to prevent the occurrence of radiation toxicity to healthy organs.

In April 2015, the U.S. Food and Drug Administration (FDA) approved the utilization of spacer devices, to further reduce radiation toxicity to normal tissues surrounding the prostate in patients with prostate cancer undergoing RT, prompting their increased usage in clinical settings since then.[4–7] Before implementing RT for prostate cancer, a spacer is surgically inserted between the rectum and prostate. This device physically separates the rectum from the prostate, thereby reducing the radiation exposure to the neighboring rectum during treatment.[8] Spacer types include endorectal balloons (ERBs), rectal hydrogel spacers, and rectal retractors (RR), all of which have been developed and are currently in use.[9–12] Despite the diverse types of spacers specifically designed for use in RT treatment, all of them serve a similar purpose—minimizing radiation exposure to the rectum,[13,14] but every spacer type has its own distinctive drawbacks. For instance, the ERB method requires the insertion of the device into the rectum before each RT session. This process takes approximately 3 min and can cause discomfort to the patients. In addition, achieving consistent placement at exactly the same position in each session can be challenging. The hydrogel method has the advantage of creating a 10 mm separation between the rectum and the prostate through a minimally invasive procedure, thereby minimizing radiation exposure to the rectum. This spacer remains in the body for the entire radiation treatment, which takes approximately 3 months, and then naturally dissolves and are excreted by the body through urine. However, owing to their polymerization characteristics, it can be difficult to reposition the hydrogels once placed, and achieving precise polymerization and placement can be challenging. Additionally, there are potential side effects such as rectal bleeding, abscesses, allergic reactions, and pain.[15]

Given the limitations of the available spacers, we developed an innovative spacer using an integration of three-dimensional (3D) printing technology and microcellular foaming process (MCP) in the current study. This technology combines 3D printing, specifically, fused deposition modeling (FDM), with MCP that involves dissolving gas into the polymer using supercritical carbon dioxide (scCO2) and inducing volume expansion through depressurization. The fusion of 3D printing and manufacturing process can transform the spacer in a pre-programmed manner in response to depressurization rate. Using the 3D printing technology, a spacer can be created to accurately match the unique shapes of each patient's prostate and rectum, ensuring precise positioning and effective functioning. Additionally, the use of $scCO_2$ allows both sterilization and volume expansion through gas absorption and foaming, thereby enabling the spacer to be produced and applied directly in the operating room for immediate use. Polycaprolactone (PCL) has been used as a 3D printing material. PCL is highly biocompatible and is suitable for biomedical applications. It is biodegradable and has no drawbacks when inserted into the human body. Since the degradation rate of PCL is controllable, there is a greater flexibility in manipulating when to dissolve the material in the body.[16] Recently, it has been reported that the size and density of microcells can be adjusted to control the degradation time within the body.[17] PCL is widely used as a material for low-temperature 3D printing, offering advantages such as low cost, easy availability, and simple manufacturing. Furthermore, it has the advantage of easily producing products using various 3D printing methods such as FDM and selective laser sintering.[18] Many drug delivery devices made from PCL have already received FDA approval and CE-mark certification, making them suitable for use as implantable medical devices in the human body.[19,20]

In this study, the MCP was used to implement 3D printing with PCL. MCP is a technology developed in the 1980s at the Massachusetts Institute of Technology. This process involves diffusing a blowing agent (such as CO_2 or nitrogen) in a supercritical fluid state into the amorphous polymer matrix, then inducing thermodynamic instability to create bubbles smaller than 100 μm at a high density of more than 10^9 bubbles/cm^3.[21,22] Microcellular foamed polymers are used in various industries, particularly in the automobile. Recently, they have also been introduced as a method for application in biomaterials, as an alternative to hydrogel. Additionally, they excel in their role as scaffolds, making them suitable for the generation of bone cells and vascular tissue engineering.[23] When neat polymer foams through MCP, numerous microcells are formed, leading to volume expansion. In this study, a spacer was created using the FDM method and foamed with MCP to achieve volume expansion and thickening. This is the first study to experimentally verify the feasibility of applying a PCL-

based 3D-printed, microcellular foamed spacer for prostate cancer RT.

2. Materials and methods

2.1. Materials

A PCL filament (eMate, eSUN, China) was prepared as the polymer matrix for the fabrication of spacers using 3D printing and MCP. PCL is a semi-crystalline polymer with a density of 1.16 g/cm^3, a glass transition temperature (T_g) of −60°C, and a melting temperature (T_m) of 60°C. PCL is readily available as a commercial or medical filament and has the advantage of being compatible with standard 3D printers. CO_2 (purity: 99.9%; 40 L; Samheung GasTech, Seoul, Republic of Korea) was used as a blowing agent in the MCP to achieve stable saturation and high solubility. Additionally, $scCO_2$ was selected because of its sterilization capability, making CO_2 a suitable blowing agent.

2.2. Microcellular foaming process

The spacer printed by the 3D printer was placed in a batch chamber, where scCO2 was generated at 40°C and 8 MPa, to allow CO_2 diffusion into the PCL for 15 min. For 3D-printed samples with 50% infill, we set the thickness of filaments extruded from the nozzle to less than 0.4 mm, allowing for full saturation within 15 min. Subsequently, depressurization was employed to induce thermodynamic instability, causing the CO_2 dissolved in the free volume of the amorphous regions of PCL to expand, resulting in foaming (Figure 1). Given that the T_g of PCL is approximately −60°C, microcellular foam is formed inside the chamber during depressurization.[24–26] The detailed experimental parameters for MCP are listed in Table 1.

2.3. Fabrication of 3D-printed sample

A 3D printer (X1-Carbon Combo; Bambu Lab, China) was used to create the biocompatible PCL spacer. The detailed 3D printing parameters for PCL included a nozzle temperature of 170°C and a bed temperature of 40°C. The nozzle diameter was set to 0.4 mm, with a printing speed of 15 mm/s. The layer thickness was 0.25 mm. The G-code was generated using a 3D printing open-source slicing program (Cura slicer program, Geldermalsen, the Netherlands). The infill pattern was set to a 50% grid pattern. 3D modeling was performed using a computer-aided design (CAD) software (Creo 4.0, PTC Inc., USA). Before designing the spacer, preliminary experiments were conducted to assess the volume expansion rate and cell morphology induced by the MCP. For these experiments, samples with dimensions of 20 mm × 20 mm × 5 mm were printed.

Table 1. Experimental parameters of microcellular foaming process

Property	Value
Saturation pressure (MPa)	8 ± 0.1
Saturation temperature (°C)	40 ± 1
Saturation time (min)	15
Depressurization ratio (MPa/s)	0.3

2.4. Length expansion along the *x*-, *y*-, and *z*-axes

After placing the 3D-printed spacer in a batch chamber, $scCO_2$ was diffused into the spacer for 15 min. Once the foaming process was completed through depressurization, the spacer achieved its final planned size and shape. Upon the completion of depressurization, the volume of the spacer expanded. The expanded spacer was then accurately positioned between the rectum and the prostate during the procedure, ensuring a separation of >10 mm between the two organs. After completion of the volume expansion using the MCP, the length expansion ratio (%) was measured to

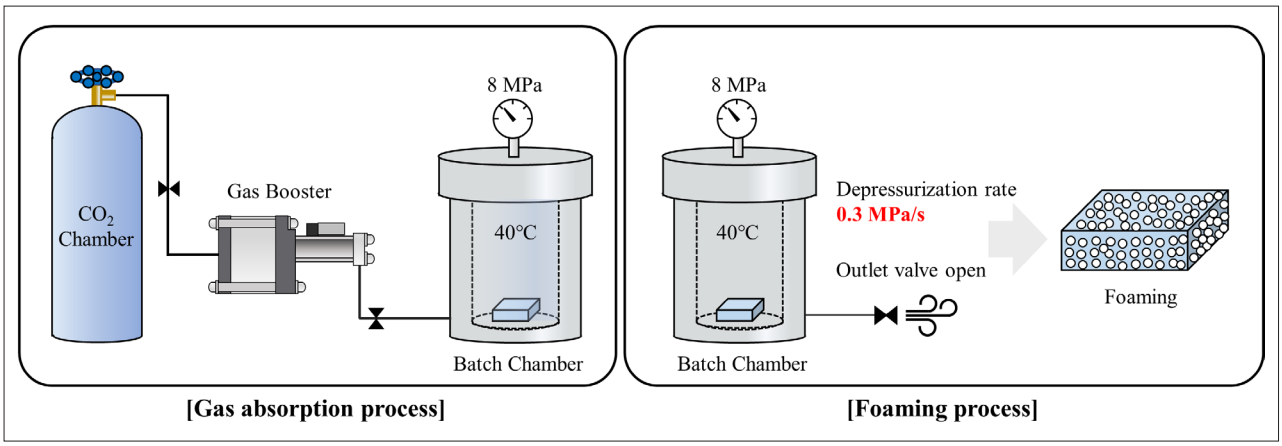


Figure 1. Schematic of the overall microcellular foaming process.

aid in accurate design of the initial 3D-printed sample. The length expansion ratio was calculated using Equation I:

$$\text{Length expansion ratio (\%)} = \frac{L_{after}\ (mm) - L_{before}\ (mm)}{L_{before}\ (mm)} \times 100 \quad (I)$$

where L_{after} is the length after foaming and L_{before} is the initial length of the 3D-printed sample before foaming. Considering the length expansion ratios along the *x*-, *y*-, and *z*-axes after foaming (Figure 2b), the length expansion ratio was set to be the same along the *x*- and *y*-axes because of the symmetric printing path (Figure 2a). Therefore, using these two length expansion ratios, the initial sample was designed to achieve the final size and shape necessary for insertion between the prostate and rectum.

2.5. Spacer pre-foam design

The length expansion ratio owing to foaming was measured along the *x*-, *y*-, and *z*-axes. Using these measurements, the final desired shape was reverse-engineered to create a 3D model for pre-foam 3D printing. Although the design should consider the shapes of the prostate, rectum, and surrounding organs of patients undergoing RT, the spacer was designed to match the shapes of the prostate and rectal wall of a phantom (053S, CIRS, USA), which was used for RT planning to verify the function of the spacer. To minimize radiation exposure to the rectum, the distance between the prostate and the rectum must be maintained at a minimum of 7.5 mm. Therefore, the initial pre-foam sample (Figure 3b and c) was designed to have a thickness of 5 mm to ensure that it expanded to more than 10 mm after foaming (Figure 3a). Additionally, to prevent the spacer from shifting within the body over time, it was designed to wrap around the prostate using CAD (Creo 4.0, PTC Inc., USA).

2.6. Sterilization

Surgical medical devices are commonly sterilized using steam, ethylene oxide (EtO), or gamma radiation. However, these methods could negatively impact the properties of the original materials. For spacers, EtO gas is typically used for sterilization, but the use of $scCO_2$ allows sterilization without affecting the material properties.[27] To achieve a supercritical state for CO_2, a pressure above 7.4 MPa and a temperature above 31°C are required. For sterilization, a 6-log reduction in the microbial count can be achieved by exposing bacteria to $scCO_2$ for 1 min and viruses for 15 min.[28] Conventionally, before performing surgery to insert a spacer for RT, a total of 10.5 h is required for sterilization—2.5 h for EtO treatment and 8 h for air bleeding.[29–31]. However, in this study, we reduced the sterilization time from 10.5 h to 15 min using $scCO_2$. This method allows for simultaneous sterilization of the spacer and gas absorption using a batch process. By doing so, the two separate processes of using EtO for 10.5 h sterilization and $scCO_2$ for foaming to create the spacer can be combined into a single 15-min process. This optimizes both the time and number of steps required to produce the spacer while simultaneously achieving sterilization and foaming. Therefore, it is anticipated that the shapes of the patient's prostate and rectum obtained from computed tomography (CT) results can be immediately captured, allowing for the

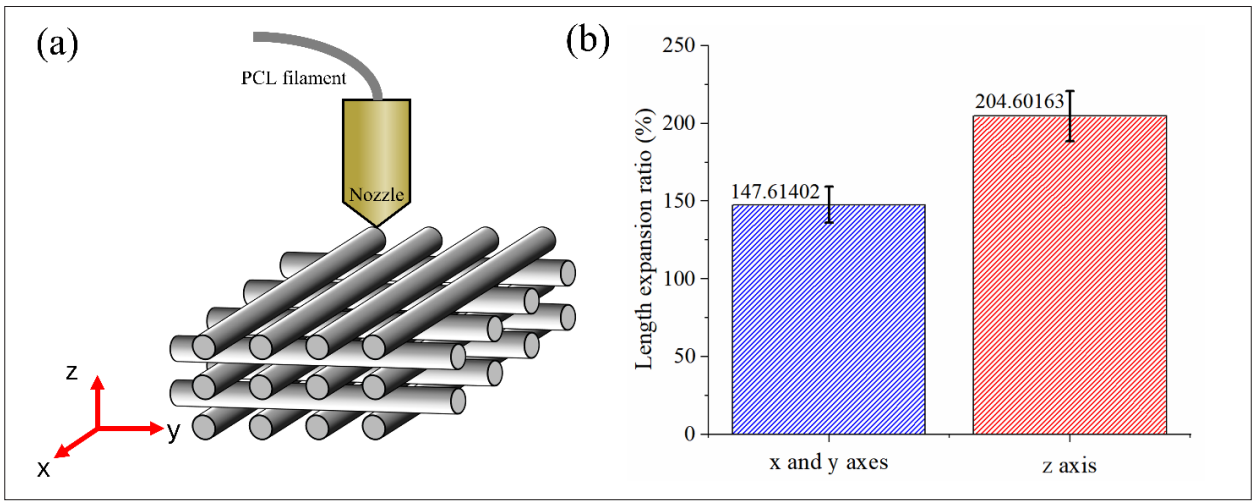


Figure 2. This figure demonstrates the expansion characteristics of the spacer, which are critical for achieving the desired final dimensions post-foaming for accurate placement between the prostate and rectum. (a) Design of the 3D-printed sample layer and printing path. (b) Measured length expansion ratio with respect to the axis. Abbreviations: PCL, polycaprolactone.

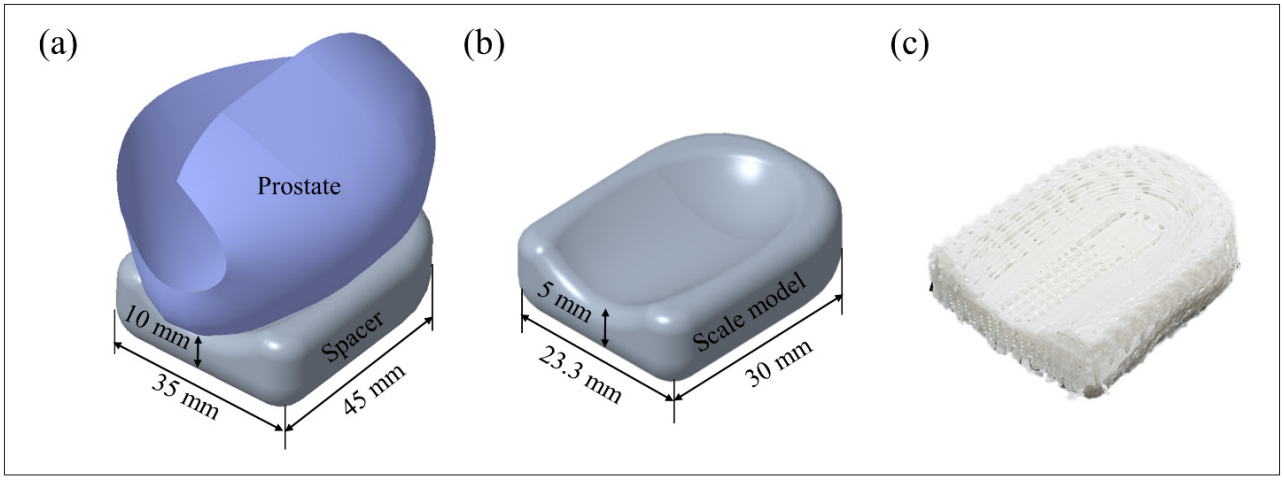


Figure 3. Design of the spacer that matches the contour of the phantom. (a) Final post-foam shape of the spacer to be inserted into the phantom. (b) CAD model and (c) the actual 3D-printed polycaprolactone (PCL) spacer of the scaled-down model before microcellular foaming actual printed polycaprolactone (PCL) pre-foam spacer of the scaled-down model for 3D printing.

production of a sterilized and foamed spacer within a short period of time and facilitating instant surgery.

2.7. Radiotherapy planning

The radiation dose for a prostate cancer phantom was calculated and optimized using the Eclipse treatment planning system (TPS) (Eclipse 17.0, Varian Medical Systems, Palo Alto, CA, USA). The prostate and rectum were delineated by a physician using a simulated CT. CT images were acquired using a 16-slice CT scanner (Sensation Open; Siemens Healthineers, Germany). The pixel resolution of scanned images was 1.5 × 1.5 mm^2, and the slice thickness of the images was fixed at 1.00 mm. The analytical anisotropic algorithm (AAA) was employed as the dose calculation algorithm, and a 2-arc volumetric modulated arc therapy was conducted using a Halcyon v3.0 (Varian Medical Systems, Palo Alto, CA, USA) coupled with a linear accelerator (Linac).

In this study, a dose regimen of 70.0 Gy in 28 fractions was adopted for a prostate cancer treatment scenario, and the prostate volume receiving >95% of the prescribed dose was 95%.[32] To evaluate the dosimetric effects in the presence of a spacer, three CT scans were acquired, as shown in Figure 4. The CT images included the original phantom (Figure 4a), the phantom with the spacer inserted between the rectum and prostate before expansion (Figure 4b), and after expansion of the spacer (Figure 4c). These images were captured at the same reference position using an external laser to ensure consistent positioning. Additionally, the acquired CT images were reconstructed using a 3D modeling software (Metasequoia 4, Tetraface v4.7.0, Tokyo, Japan), allowing precise verification of the spacer placement and orientation (Figure 4d).

3. Results and discussion

3.1. Foaming characteristics

Microcells were formed when foaming occurred through the MCP. To examine the morphology of these cells, it was necessary to evaluate cell density, cell size, and expansion ratio (ER). Field-emission scanning electron microscopy (FE-SEM; Nova Nano SEM200, FEI, USA) was used to examine the internal structure of the foam spacer. To make samples for FE-SEM measurement, the foamed samples were cryogenically fractured (liquid nitrogen, −196˚C). The samples were then coated with platinum in vacuum for 60 s using an ion sputter-coating machine (E1030, Hitachi, Japan). Based on the FE-SEM images, the cell diameter and density were calculated using **Equations II** and **III.**[33,34]

$$\text{Average cell diameter } (\mu m) = \frac{\sum d_i n_i}{\sum n_i} \quad \text{(II)}$$

$$\text{Cell density } (\text{cells/cm}^3) = \left(\frac{n_{bubble}}{A}\right)^{\frac{3}{2}} \times \psi \quad \text{(III)}$$

where d_i is the diameter of cell-type i; n_i is the number of cells of type i; n_{bubble} denotes the number of bubbles in the micrograph; A is the surface area of the micrograph; and ψ is the ER. ImageJ software was used to calculate the cell density and average cell diameter using the FE-SEM images (Figure 5a and b), and the results are plotted in Figure 5d. A cell distribution graph of the foamed PCL sample is shown in Figure 5e. To measure the ER of the spacer, the density of the PCL was measured using a densimeter

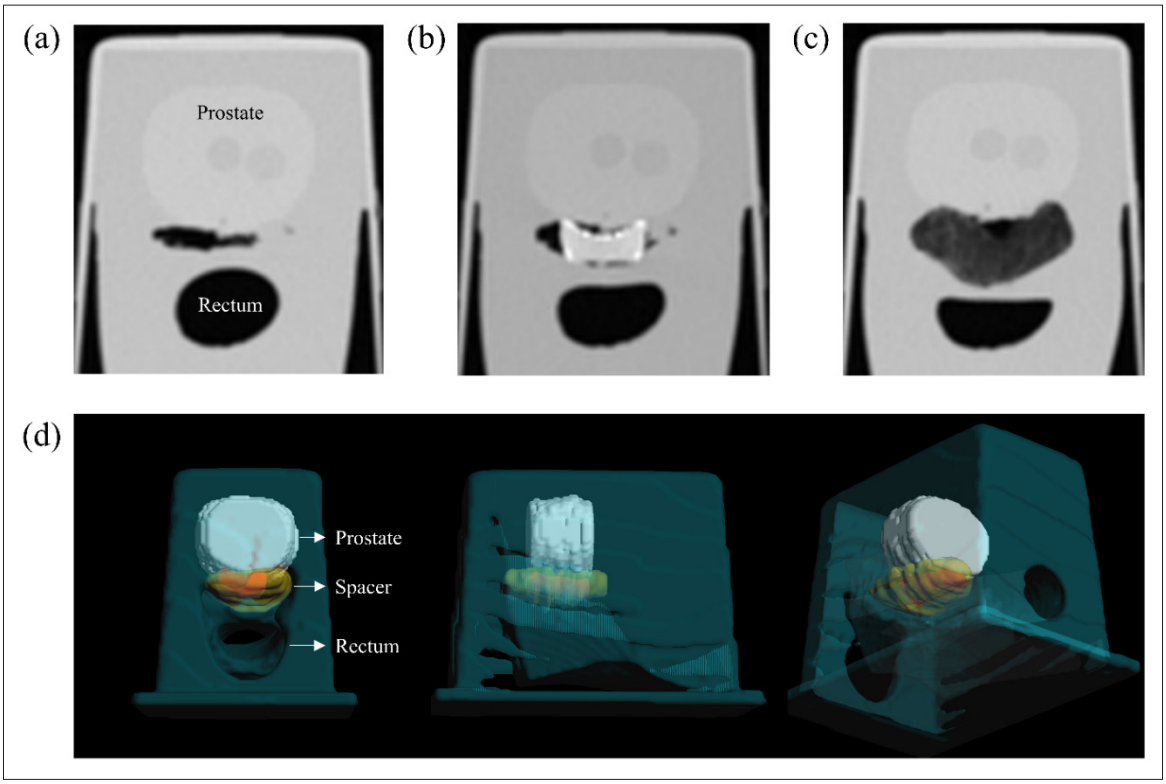


Figure 4. This figure demonstrates the effectiveness of the spacer in increasing the distance between the prostate and rectum. (a) Computed tomography (CT) scan images of original phantom without spacer. (b, c) Implantation of pre-foam (b) and post-foam (c) polycaprolactone (PCL) spacers. (d) 3D modeled phantom images with an implanted post-foam spacer.

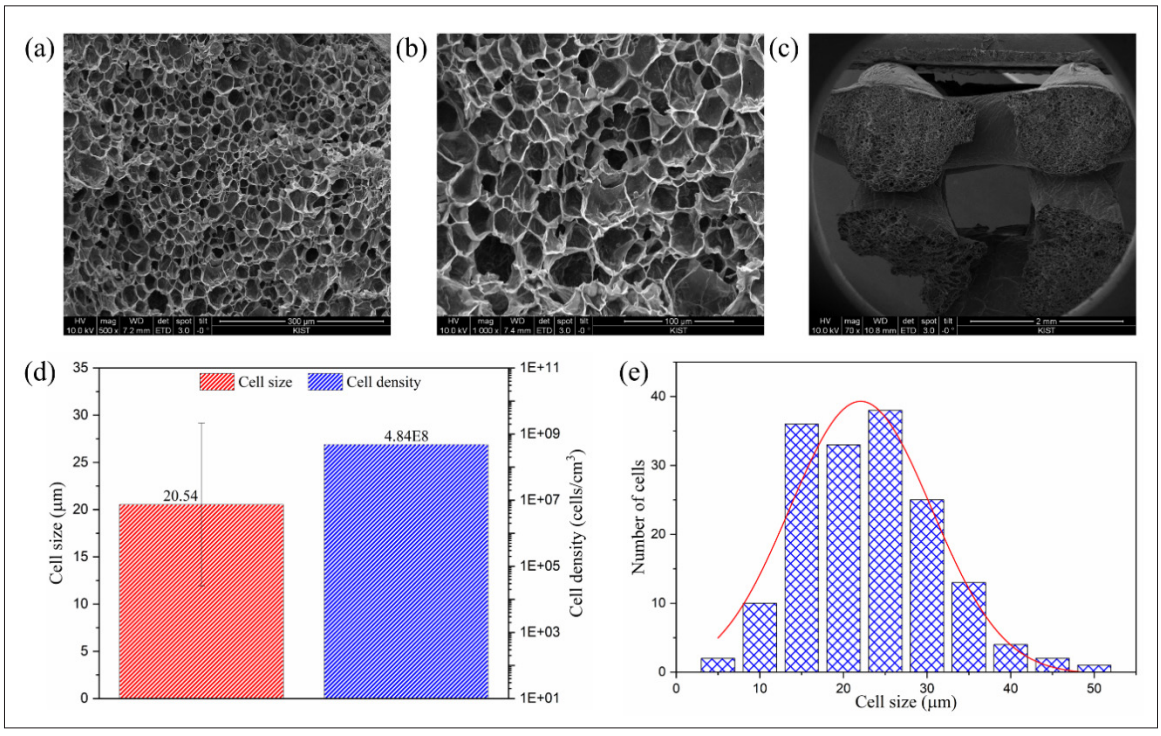


Figure 5. This figure provides detailed insight into the microstructure of the foamed spacer, which is important for understanding cell morphologies. (a, b) The FE-SEM images of foamed polycaprolactone (PCL) under the magnifications of 500× (a; scale bar: 300 μm) and 1000× (b; scale bar: 100 μm). (c) Section of foamed sample under the magnification of 70× (scale bar: 2mm). (d) Cell size and cell density. (e) Cell size distribution of foamed PCL sample.

(ALFAMIRAGE, MD-300S) in accordance with ASTM D792. The ER was then calculated using **Equation IV**.

$$\text{Expansion ratio} = \frac{\rho_{\text{unfoam}}\left(\text{g/cm}^3\right)}{\rho_{\text{foam}}\left(\text{g/cm}^3\right)} \quad \text{(IV)}$$

where ρ_{unfoam} is the density of the polymer before the MCP, and ρ_{foam} is the density of the polymer after the MCP. **Figure 5c** shows the cell morphology of the cross section of the foamed PCL sample.

By controlling the depressurization rate of the MCP, the porosity of the spacer can be precisely managed, allowing for the desired cell morphology in terms of cell density and cell size. This enables the adjustment of the spacer's rigidity to be maintained throughout the RT period for prostate cancer. In contrast, hydrogel spacers used in existing studies begin to degrade *in vivo* immediately after polymerization. However, a PCL spacer with controlled porosity, developed using the convergence of 3D printing technology and MCP, experiences minimal biodegradation for up to 36 weeks. This ensures the accurate maintenance of the distance between the prostate and rectum during the typical 36-week prostate cancer RT period, thereby minimizing treatment errors during RT.[35]

3.2. Dosimetric comparison with and without spacer

Figure 6 shows the dose distribution and dose-volume histogram (DVH) of the original phantom before and after spacer expansion. Table 2 lists the key dosimetric parameters of the rectum. The DVH indices for the prostate, such as the mean dose (D_{mean}) and the dose covering 95% of the volume ($D_{95\%}$), were compared. For the rectum, the maximum dose, mean dose, volume receiving 50 Gy ($V_{50\text{Gy}}$), and volume receiving 70 Gy ($V_{70\text{Gy}}$) were analyzed.[32] Ideally, there should be no difference in the dosimetric effect between the prostate and rectum in the original phantom and the phantom with a pre-foam spacer. However, as observed in the DVH (Figure 6b) and Table 2, there was a difference between the original phantom and the pre-foam spacer. This can be attributed to two main factors. First, as shown in Figures 4 and 6a, the space created for the insertion of the spacer in the original phantom was filled with air, which can introduce uncertainty during the dose calculation using the TPS.[36] Second, the distances between the prostate and rectum in the original phantom and the pre-foam spacer were not the same. In the CT images, the distances between the prostate and rectum before and after spacer expansion at the planned isocenter were 1.03, 1.38, and 2.05 cm, respectively. Because the measured distances from the original phantom and after inserting the pre-foam spacer

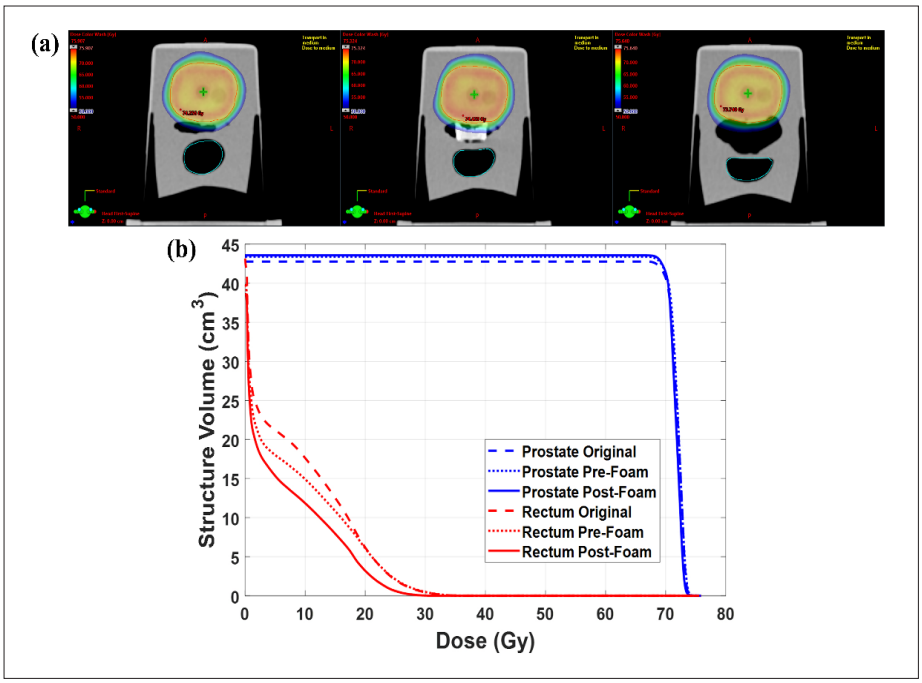


Figure 6. This figure shows the dosimetric impact on the rectum when no spacer, a pre-foam spacer, and a post-foam spacer are used, demonstrating that the dosimetric impact on the rectum is minimized when the post-foam spacer is implanted. (a) The dose distribution using the original phantom (left), pre-foam spacer (middle), and post-foam spacer (right). (b) Dose–volume histogram.

Table 2. Dosimetric parameters of the original phantom and phantoms using with pre-foam spacer and post-foam spacer.

Structure	Parameter	Original phantom	Phantom with pre-foam spacer	Phantom with post-foam spacer
Rectum	Max dose	36.5 Gy	36.0 Gy	30.9 Gy
	Mean dose	8.67 Gy	8.29 Gy	6.66 Gy
Prostate	Mean dose	71.9 Gy	71.7 Gy	71.7 Gy
	$D_{95\%}$	70.0 Gy	70.0 Gy	70.0 Gy

Abbreviation: $D_{95\%}$, dose covering 95% of the volume.

were not identical, it was not possible for the dosimetric parameters in the rectum to be the same. After inserting the pre-foam spacer, although the distance between the rectum and prostate increased, the mean and maximum doses in the rectum also increased owing to the influence of air. This limitation of this study indicates the need for further research using more sophisticated phantoms and animal experiments.

Comparing the results before and after the expansion of the spacer, it is clear that the distance between the prostate and rectum significantly increased. For the prostate, the results were normalized, indicating that the mean dose and $D_{95\%}$ remained nearly consistent. For the rectum, the maximum dose was below 50 Gy in all three scenarios, with V_{50Gy} and V_{70Gy} values being zero. The analysis of the rectum showed that the maximum dose decreased by approximately 15.3% and the mean dose decreased by 19.7%. This clearly demonstrated the efficacy of the spacer developed in this study in reducing the dose delivered to the rectum. Additionally, a larger planning target volume (PTV) for the prostate or the use of SBRT is expected to further enhance the dose-reduction effect.[32,37] However, a potential disadvantage of the post-foam spacer is that after expansion, its density is 0.12 g/cm^3, which could introduce uncertainty in dose calculation.

The developed spacer reduced radiation exposure to the rectum compared to when no spacer was used, which could potentially reduce radiation toxicity as a result of RT for prostate cancer. However, this was a feasibility study using a phantom, and further research involving small animal experiments and additional studies are needed for validating its application in clinical setting.

4. Conclusion

In this study, a completely new type of spacer that can replace the existing spacers was developed. Using 3D printing of biocompatible PCL resin with $scCO_2$ for sterilization and gas absorption, we developed a customized product that integrates all the advantages of current spacers. This study aimed to minimize radiation exposure to the organ at rick (rectum) during IMRT for prostate cancer treatment. To our knowledge, this is the first study to develop a medical device suitable for *in vivo* application using MCP, which has not been used in existing medical technologies. During the spacer placement procedure conducted before IMRT, the sterilized and foamed PCL spacer was expanded in the batch chamber and positioned correctly to increase the distance between the prostate and rectum. This method has the advantage of minimizing the side effects and drawbacks of existing spacers. However, the focus of this research was on the development and feasibility of spacer products, and not translating them into clinical applications. Therefore, additional validation experiments are warranted before clinical applications. By using 3D printing and MCP techniques, we developed a spacer for prostate cancer RT. By measuring DVH indices in the rectum, we demonstrated that the spacer created had sufficient clinical applicability; however, future clinical studies are required to validate its efficacy. Additionally, the biodegradation time of PCL can be adjusted based on the internal cell size and density, allowing it to remain in the body as needed. Therefore, future research should focus on selecting MCP conditions that can control cell size, thereby adjusting the duration that PCL can remain in the body. Moreover, research efforts will also be directed to exploring the construction of 4D-printed spacers that can expand upon body temperature changes to increase the distance between the prostate and rectum, in order to replace the conventional method of inserting a foamed spacer. Such 4D-printed spacers also will be validated using RT.

Acknowledgments

Graphical abstract was created with BioRender.com (agreement number VE276LCQ20).

Funding

This work was supported by National Research Foundation of Korea (NRF) grants funded by the Ministry of Education (RS-2023-00247348).

Conflict of interest

The authors declare they have no competing interests.

Author contributions

Conceptualization: DongHwan Lim, DoKun Yoon
Formal analysis: Han-Back Shin, DongHwan Lim
Investigation: DongHwan Lim
Methodology: JaeHoo Kim, KiHoon Sung, YoungEun Choi, HeeSoon Sheen
Writing – original draft: DongHwan Lim, Han-Back Shin
Writing – review & editing: DongHwan Lim, SungWoon Cha

Ethics approval and consent to participate

Not applicable.

Consent for publication

Not applicable.

Availability of data

Data will be made available from the corresponding author(s) upon reasonable request.

References

1. *American Cancer Society*. The cancer atlas: the burden: Europe [Internet]. Published Accessed at: December 9, 2020. https://canceratlas.cancer.org/the-burden/europe/
2. Datta NR, Stutz E, Rogers S, Bodis S. Conventional versus hypofractionated Radiation therapy for localized or locally advanced prostate cancer: a systematic review and meta-analysis along with therapeutic implications. *Int J Radiat Oncol Biol Phys*. 2017;99(3):573-589. doi: 10.1016/j.ijrobp.2017.07.021
3. Heemsbergen WD, Peeters STH, Koper PCM, Hoogeman MS, Lebesque JV. Acute and late gastrointestinal toxicity after radiotherapy in prostate cancer patients: Consequential late damage. *Int J Radiat Oncol Biol Phys*. 2006;66(1):3-10. doi: 10.1016/j.ijrobp.2006.03.055
4. Noel Rolon. *Letter to Noel Rolon*. Food and Drug Administration; 2015. Accessed December 2, 2020. https://www. accessdata.fda.gov/cdrh_docs/pdf14/DEN140030.pdf
5. Payne HA, Pinkawa M, Peedell C, Bhattacharyya SK, Woodward E, Miller LE. SpaceOAR hydrogel spacer injection prior to stereotactic body radiation therapy for men with localized prostate cancer: a systematic review. *Medicine (Baltimore)*. 2021;100(49):e28111. doi: 10.1097/MD.0000000000028111
6. Whalley D, Hruby G, Alfieri F, Kneebone A, Eade T. SpaceOAR hydrogel in dose-escalated prostate cancer radiotherapy: rectal dosimetry and late toxicity. *Clin Oncol*. 2016;28(10):e148-e154. doi: 10.1016/j.clon.2016.05.005
7. Babar M, Katz A, Ciatto M. Dosimetric and clinical outcomes of SpaceOAR in men undergoing external beam radiation therapy for localized prostate cancer: a systematic review. *J Med Imaging Radiat Oncol*. 2021;65(3):384-397. doi: 10.1111/1754-9485.13179
8. Sanei M, Ghaffari H, Ardekani M, et al. Effectiveness of rectal displacement devices during prostate external-beam radiation therapy: a review. *J Cancer Res Ther*. 2021;17(2):303-310. doi: 10.4103/jcrt.JCRT_841_19
9. Afkhami Ardekani M, Ghaffari H, Navaser M, Zoljalali Moghaddam SH, Refahi S. Effectiveness of rectal displacement devices in managing prostate motion: a systematic review. *Strahlenther Onkol*. 2021;197(2):97-115. doi: 10.1007/s00066-020-01633-9
10. Van Lin ENJT, Hoffmann AL, Van Kollenburg P, Leer JW, Visser AG. Rectal wall sparing effect of three different endorectal balloons in 3D conformal and IMRT prostate radiotherapy. *Int J Radiat Oncol Biol Phys*. 2005;63(2):565-576. doi: 10.1016/j.ijrobp.2005.05.010
11. Ghaffari H, Mehrabian A. Rectal retractor in prostate radiotherapy: pros and cons. *Radiat Oncol*. 2022;17(1):204. doi: 10.1186/s13014-022-02176-2
12. Shi S, Vissapragada R, Abi Jaoude J, et al. Evolving role of biomaterials in diagnostic and therapeutic radiation oncology. *Bioact Mater*. 2020;5(2):233-240. doi: 10.1016/j.bioactmat.2020.01.011
13. Armstrong N, Bahl A, Pinkawa M, et al. SpaceOAR hydrogel spacer for reducing radiation toxicity during radiotherapy for prostate cancer. A systematic review. *Urology*. 2021;156:e74-e85. doi: 10.1016/j.urology.2021.05.013
14. Mahdavi SR, Ghaffari H, Mofid B, Rostami A, Reiazi R, Janani L. Rectal retractor application during image-guided dose-escalated prostate radiotherapy. *Strahlenther Onkol*. 2019;195(10):923-933. doi: 10.1007/s00066-019-01445-6
15. Aminsharifi A, Kotamarti S, Silver D, Schulman A. Major complications and adverse events related to the injection of the spaceoar hydrogel system before radiotherapy for prostate cancer: review of the manufacturer and user facility device experience database. *J Endourol*. 2019;33(10):868-871. doi: 10.1089/end.2019.0431
16. Mohamed RM, Yusoh K. A review on the recent research of polycaprolactone (PCL). *Adv Mat Res*. 2015;1134:249-255. doi: 10.4028/www.scientific.net/amr.1134.249
17. Zhang Q, Jiang Y, Zhang Y, Ye Z, Tan W, Lang M. Effect of porosity on long-term degradation of poly (ε-caprolactone) scaffolds and their cellular response. *Polym Degrad Stab*. 2013;98(1):209-218. doi: 10.1016/j.polymdegradstab.2012.10.008

18. Yeong WY, Sudarmadji N, Yu HY, et al. Porous polycaprolactone scaffold for cardiac tissue engineering fabricated by selective laser sintering. *Acta Biomater*. 2010;6(6):2028-2034. doi: 10.1016/j.actbio.2009.12.033

19. Woodruff MA, Hutmacher DW. The return of a forgotten polymer - polycaprolactone in the 21st century. *Prog Polymer Sci (Oxf)*. 2010;35(10):1217-1256. doi: 10.1016/j.progpolymsci.2010.04.002

20. Malikmammadov E, Tanir TE, Kiziltay A, Hasirci V, Hasirci N. PCL and PCL-based materials in biomedical applications. *J Biomater Sci Polym Ed*. 2018;29(7-9):863-893. doi: 10.1080/09205063.2017.1394711

21. Dugad R, Radhakrishna G, Gandhi A. Recent advancements in manufacturing technologies of microcellular polymers: a review. *J Polymer Res*. 2020;27(7):182. doi: 10.1007/s10965-020-02157-7

22. Cha SW. *A Microcellular Foaming/Forming Process Performed at Ambient Temperature and a Super-Microcellular Foaming Process*. Mechanical Engineering Department; 1994. Ph D Thesis. Accessed June 9, 2023. https://cir.nii.ac.jp/crid/1572824498934882176.bib?lang=ja

23. Hou J, Jiang J, Guo H, et al. Fabrication of fibrillated and interconnected porous poly(ϵ-caprolactone) vascular tissue engineering scaffolds by microcellular foaming and polymer leaching. *RSC Adv*. 2020;10(17):10055-10066. doi: 10.1039/d0ra00956c

24. Wang H, Li W, Kumar V. *Solid-State Foaming Of Polycaprolactone (PCL)*; 2007. http://www.asme.org

25. Hatami T, Johner JCF, de Castro KC, Mei LHI, Vieira MGA, Angela M. New insight into a step-by-step modeling of supercritical CO2 foaming to fabricate poly(ε-caprolactone) scaffold. *Ind Eng Chem Res*. 2020;59(45):20033-20044. doi: 10.1021/acs.iecr.0c04372

26. Kosowska K, Krzysztoforski J, Henczka M. Foaming of PCL-based composites using scCO2: structure and physical properties. *Materials (Basel)*. 2022;15(3):1169. doi: 10.3390/ma15031169

27. Ribeiro N, Soares GC, Santos-Rosales V, et al. A new era for sterilization based on supercritical CO2 technology. *J Biomed Mater Res B Appl Biomater*. 2020;108(2):399-428. doi: 10.1002/jbm.b.34398

28. Soares GC, Learmonth DA, Vallejo MC, et al. Supercritical CO2 technology: the next standard sterilization technique? *Mater Sci Eng C*. 2019;99:520-540. doi: 10.1016/j.msec.2019.01.121

29. Matthews IP, Gibson C, Samuel AH. Sterilisation of implantable devices. *Clin Mater*. 1994;15(3):191-215. doi: 10.1016/0267-6605(94)90082-5

30. Tipnis NP, Burgess DJ. Sterilization of implantable polymer-based medical devices: a review. *Int J Pharm*. 2018;544(2):455-460. doi: 10.1016/j.ijpharm.2017.12.003

31. Rogers WJ. 2 - Steam and dry heat sterilization of biomaterials and medical devices. In: Lerouge S, Simmons A, eds. *Sterilisation of Biomaterials and Medical Devices*. Woodhead Publishing; 2012:20-55. doi: 10.1533/9780857096265.20

32. Li G, Li Y, Wang J, et al. Guidelines for radiotherapy of prostate cancer (2020 edition). *Precis Radiat Oncol*. 2021;5(3):160-182. doi: 10.1002/pro6.1129

33. Kuboki T. Foaming behavior of cellulose fiber-reinforced polypropylene composites in extrusion. *J Cell Plastics*. 2014;50(2):113-128. doi: 10.1177/0021955X13504775

34. Gong P, Taniguchi T, Ohshima M. Nanoporous structure of the cell walls of polycarbonate foams. *J Mater Sci*. 2014;49(6):2605-2617. doi: 10.1007/s10853-013-7959-4

35. Baker SC, Rohman G, Southgate J, Cameron NR. The relationship between the mechanical properties and cell behaviour on PLGA and PCL scaffolds for bladder tissue engineering. *Biomaterials*. 2009;30(7):1321-1328. doi: 10.1016/j.biomaterials.2008.11.033

36. Onizuka R, Araki F, Ohno T, et al. Accuracy of dose calculation algorithms for virtual heterogeneous phantoms and intensity-modulated radiation therapy in the head and neck. *Radiol Phys Technol*. 2016;9(1):77-87. doi: 10.1007/s12194-015-0336-z

37. Wang K, Mavroidis P, Royce TJ, et al. Prostate stereotactic body radiation therapy: an overview of toxicity and dose response. *Int J Radiat Oncol Biol Phys*. 2021;110(1): 237-248. doi: 10.1016/j.ijrobp.2020.09.054

ACCSCIENCE PUBLISHING

International Journal of Bioprinting

RESEARCH ARTICLE

3D bioprinting of in vitro full-thickness skin model with a rete ridge structure

Ilho Jang[1†], Jae-Hun Kim[2†], Misun Kim[3†], Paulo Andre Marinho[1], Younhwa Nho[3], Seunghyun Kang[3], Won-Soo Yun[1,4], Jin-Hyung Shim[1,4*], and Songwan Jin[1,4*]

[1] T&R Biofab Co., Ltd., Siheung-si, Gyeonggi-do, South Korea

[2] Department of Mechanical System Engineering, Graduate School of Convergence Technology and Energy, Tech University of Korea, Siheung-si, Gyonggi-do, South Korea

[3] Laboratory of Bio Technology, COSMAX BTI R&I Center, Seongnam-si, Gyeonggi-do, South Korea

[4] Department of Mechanical Engineering, Tech University of Korea, Siheung-si, Gyonggi-do, South Korea

Abstract

Rete ridges are undulating structures located between the epidermis and dermis that play a crucial role in maintaining the skin's barrier function, protecting the body from pollutants and ultraviolet (UV) radiation. This formation of rete ridges within *in vitro* skin models is essential for evaluating the efficacy and safety of pharmaceuticals or cosmetics, replacing the need for animal models. Micro-molding is a prominent technique for recreating the rete ridge structure in *in vitro* skin models. However, this method is characterized by high technical difficulty. Although 3D bioprinting technology has demonstrated potential for fabricating skin models with the rete ridge structure, it is also limited by the extended time required for structural implementation. In this study, we introduce a methodology for fabricating full-thickness skin equivalents with rete ridges using preset extrusion bioprinting. A polycaprolactone frame was 3D-printed, and the dermal layer was bioprinted in the frame. Subsequently, furrowing steps were undertaken to create a substrate for the stable anchoring of strands produced by the preset extrusion bioprinting, fabricating a dermis layer with a rete ridge structure. Keratinocytes were then seeded and differentiated, forming the stratum corneum. We observed that protein expression was preserved in the valleys of the rete ridge after UV irradiation of the rete ridge full-thickness skin equivalent, similar to that of human *ex vivo* skin models. Therefore, the rete ridge full-thickness skin equivalent generated using our method exhibits potential as a promising model to replace animal experiments and human *ex vivo* skin models.

Keywords: 3D bioprinting; Skin model; Rete ridge; Preset extrusion; Dermal-epidermal junction

1. Introduction

In vitro skin models offer a promising alternative to traditional animal-based and clinical studies for investigating skin biology and the effects of various compounds on

[†]These authors contributed equally to this work.

***Corresponding authors:**
Jin-Hyung Shim (happyshim@tukorea.ac.kr)

Songwan Jin (songwan@tukorea.ac.kr)

Citation: Jang I, Kim JH, Kim M, *et al.* 3D bioprinting of *in vitro* full-thickness skin model with a rete ridge structure. *Int J Bioprint.* 2024;10(5):3961. doi: 10.36922/ijb.3961

Received: June 17, 2024
Revised: July 22, 2024
Accepted: July 31, 2024
Published Online: August 1, 2024

Copyright: © 2024 Author(s). This is an Open Access article distributed under the terms of the Creative Commons Attribution License, permitting distribution, and reproduction in any medium, provided the original work is properly cited.

Publisher's Note: AccScience Publishing remains neutral with regard to jurisdictional claims in published maps and institutional affiliations.

the skin. Consequently, they are receiving considerable attention from researchers and the industry as a potential tool for advancing skin research and product development. The epidermis model is one of the most basic *in vitro* skin models, consisting of a monolayer of keratinocytes that form a stratified epithelium. This model can be used for a wide range of tests and experiments related to skin biology, including cell proliferation,[1] differentiation,[2] toxicity,[3] and barrier function.[4] Full-thickness skin equivalents (FTSEs) are 3D models that consist of both epidermis and dermis layers, offering a more physiologically relevant model of skin biology[5] and disease[6–8] than epidermis-only models. However, the use of FTSEs has some limitations, including variability, longer culture times, and lack of vasculature and a rete ridge structure.

Rete ridges are a series of downward projections that extend from the epidermis into the underlying dermis layer of the skin, enhancing the surface area of the epidermis and strengthening the bonding force between the dermis and epidermis.[9] As the rete ridge structure increases the surface area of the epidermis, it enables a greater number of keratinocytes to be compacted into a smaller area,[10] which is crucial for maintaining skin barrier function to protect the body from harmful environmental factors, such as ultraviolet (UV) radiation, pollutants, and pathogens. Moreover, the rete ridge structure is implicated in skin aging; one of the main alterations that occur with aging is a decrease in the number and height of the rete ridges.[11] This, in turn, can lead to a decrease in the surface area of the skin and its mechanical strength.[12] Consequently, the skin becomes more fragile and prone to wrinkling, sagging, and other signs of aging. Therefore, investigating the rete ridge structure can aid in understanding the mechanisms underlying skin aging and developing potential strategies for preventing or reversing these changes. However, as most *in vitro* skin models used in research do not fully recapitulate the architecture of the rete ridge structure, it is difficult to accurately assess the effects of aging on this structure and develop strategies for preventing or reversing these effects.

Ultraviolet (UV) radiation from the sun, specifically UVB and UVA with wavelengths above 280 nm, largely penetrates the Earth's ozone layer and inflicts damage to the skin. This exposure can lead to adverse skin effects, such as sunburn, photodermatoses, photoaging, and even skin cancer.[13] In particular, due to ozone layer depletion and climate anomalies resulting from environmental pollution, the level of UV exposure has increased. Consequently, there is active development of cosmetics and pharmaceuticals designed to prevent or treat UV-induced skin damage. During this development process, it is imperative to conduct safety and efficacy testing of developed medicines or substances, which often entails the use of animal testing. However, ethical concerns regarding animal testing arise and the rete ridge structure, unique to human or pig skin among mammals, poses limitations on the use of experimental animals. Therefore, there is a critical need for the development of *in vitro* tissue models that incorporate the rete ridge structure and can effectively evaluate UV-induced skin damage.

To address the limitations associated with the lack of rete ridge structure in advanced skin models, various tissue engineering techniques have been developed, including micro-molding,[14–17] laser micropatterning,[18] and 3D bioprinting.[19] The micro-molding technique is one of the most widely used techniques for creating skin models with inherent rete ridge structures. Recently, Nagarajan et al.[14] produced a stamp capable of replicating rete ridges using 3D printing and a silicone molding method and fabricated a full-thickness skin equivalent using atelocollagen and fibrin. However, this process requires a high-resolution 3D printing system to produce the microstructures and involves a lengthy and complex fabrication process, as the stamp for creating rete ridges was not directly produced using 3D printing. In contrast, 3D bioprinting is one of the most promising and rapidly developing techniques for establishing advanced skin equivalents. Bioprinting facilitates precise control over the spatial organization of cells and extracellular matrix (ECM) components, enabling the development of complex 3D structures that more closely mimic the architecture and function of native skin tissues. Bioprinting can also incorporate multiple cell types and biomaterials, which aids in creating more physiologically relevant skin models. Consequently, 3D bioprinting has been used to produce advanced skin equivalents with a complex structure, such as vasculature and rete ridge. However, a potential limitation of 3D-bioprinted skin equivalents is the time required for their manufacturing, especially when producing larger or more complex tissue structures.

We have previously introduced preset extrusion bioprinting that enabled us to create more precise patterns with higher speed.[20–23] In brief, a precursor cartridge is fabricated using 3D printing, filled with multiple bioinks, and then transferred to a syringe. Subsequently, when the bioinks are extruded through a nozzle, the cross-sectional pattern of the precursor cartridge is reproduced in a scaled-down form on the cross-section of extruded strands. By using this technology, we can easily print complex patterns, such as liver lobules, multilayered blood vessels, and capillaries. During the preset extrusion bioprinting process, the cross-sectional pattern of extruded strands

may not always match that of the precursor cartridge due to the complex flow path created by the precursor cartridge, syringe, and nozzle, as well as the non-Newtonian properties of the hydrogel. Therefore, achieving the desired cross-sectional shape required a trial-and-error process, which was time-consuming and unaffordable.

In this study, we fabricated FTSEs with a rete ridge structure using a preset extrusion bioprinting technique. To achieve this without an ineffective trial-and-error process, we used a computational fluid dynamics (CFD) method to design a precursor cartridge to print deep and narrow fissure structures. The dermal layer was bioprinted within the 3D-printed polycaprolactone (PCL) frame, which provides structural support until the bioink used in the dermal layer is fully gelled. This was followed by furrowing steps to establish a substrate for the stable anchoring of strands produced by the preset extrusion bioprinting process for creating a fissured structure. The epidermis was formed by differentiating keratinocytes on the surface of the dermis with fissure structures. We conducted histological and immunostaining analyses, followed by UV treatment, which confirmed differences between the rete ridge and conventional FTSEs using dermal-epidermal junction (DEJ), epidermal, and proliferation markers. These differences yield test results akin to those *in vivo*, suggesting that preset extrusion 3D bioprinting techniques can serve as a useful tool for fabricating structures that mimic *in vivo* environments.

2. Materials and methods

2.1. Preparation and characterization of hydrogels

Porcine skin-derived decellularized ECM (SdECM) was prepared as described in a previous study.[24] Briefly, dermal tissue was cut and immersed in phosphate-buffered saline (PBS; Welgene, Korea), containing 0.5% trypsin (Welgene, Korea) and 0.2% ethylene diamine tetra acetic acid (EDTA; Welgene, Korea), for 24 h. Subsequently, the treated dermal tissues were washed, followed by the addition of PBS containing 1% Triton X-100 (Samchun Pure Chemical Co., Ltd., Korea) for 24 h. Decellularized tissues were washed several times with distilled water and lyophilized. SdECM was solubilized through digestion with 0.5 M acetic acid (Sigma-Aldrich, United States of America [USA]) containing pepsin (1 mg/10 mg lyophilized SdECM). The SdECM was dissolved in 0.5 M acetic acid and neutralized to a concentration of 3.25% (w/v) for use in 3D bioprinting. Alginate (A2033; Sigma-Aldrich, USA) was dissolved in PBS at a concentration of 2.75% (w/v). As the hydrogels used in this study were non-Newtonian fluids, their shear viscosity profiles were obtained using a rheometer (Kinexus pro+; NETZSCH GmbH, Germany) with cone-plate geometry and a 1 mm gap, maintaining a controlled temperature of 4°C, consistent with the bioprinting temperature. Subsequently, the obtained shear viscosity data of SdECM were fitted to the power-law fluid model (**Equation I**):

$$\mu = K \cdot \dot{\gamma}^{m-1} \quad \text{(I)}$$

where K is the flow consistency index, $\dot{\gamma}$ is the shear rate and m is the flow behavior index. The shear viscosity data of the alginate solution were fitted to the Carreau model (**Equation II**):

$$\mu = \mu_0 \cdot [1 + (\lambda \dot{\gamma})^2]^{\frac{n-1}{2}} \quad \text{(II)}$$

where μ_0 is the viscosity value at zero shear rate, λ is the characteristic time, and n is the power index.

2.2. Computational simulation for the design of a precursor cartridge

To design a precursor cartridge for generating narrow fissures within extruded strands, CFD simulation was conducted. 3D computer-aided design (CAD) models of bioinks in the bioprinting process were created with dimensions matching those of the precursor cartridge, syringe, and nozzle using SolidWorks 2022 (Dassault System, France). The 3D CAD model was then imported to COMSOL Multiphysics 5.6 (COMSOL Inc., Sweden).

Initially, the physics module for the laminar flow of single-phase fluids was used to simulate the flow of bioinks during the bioprinting process. The viscosity of bioinks was based on rheological data. The inlet pressure was applied at the top of the precursor cartridge, corresponding to the actual bioprinting pressure, while the pressure at the end of the nozzle was set to zero relative pressure as an outlet. The other boundaries were considered as walls with a no-slip condition. Subsequently, the model was discretized to the tetrahedral solid mesh by an automatic mesh generator and then solved with the Navier-Stokes equation using a stationary solver.

To visualize the cross-sectional pattern at the outlet of the printing nozzle, particle tracing for the fluid flow interface was used in the solved result for the velocity field of laminar flow simulation.[25] The massless solid particles were released on the domain of alginate hydrogel, and all boundaries were set to the wall and conditioned as "Freeze." Subsequently, the simulation was performed with a time-dependent solver. Finally, the cross-section of the end of the nozzle was visualized by implementing the Poincaré map.

2.3. Fabrication of precursor cartridges

A 3D model of a precursor cartridge was created using SolidWorks 3D CAD. Subsequently, 3D CAD data were converted into an STL file. The STL file was loaded into a 3D printing system (ProJet 6000 HD; 3D Systems, USA) that uses United States Pharmacopeia (USP) Class VI certified polymer resin (VisiJet SL Clear; 3D Systems, USA) to fabricate precursor cartridges. After fabrication, the precursor cartridges were sterilized by immersing them in 70% ethanol for 5 min, followed by overnight exposure to UV light.

2.4. Cell culture

Normal human epidermal keratinocytes (NHEKs, 00192907) and normal human dermal fibroblast (NHDFs, CC2509) were purchased from Lonza (Switzerland). NHEKs were cultured using a keratinocyte growth medium (KGM; KGM-Gold bullet kit; Lonza, Switzerland). NHDFs were cultured in a fibroblast growth medium (FGM; FGM-2 Bullet Kit; Lonza, Switzerland) along with 10% fetal bovine serum (Gibco; Thermo Fisher Scientific, USA). NHEKs and NHDFs were used in the first or second passage and cultured at 37°C in 5% CO_2. The culture medium was changed every two days to ensure optimal growth conditions.

2.5. 3D printing of FTSEs

To fabricate skin equivalents, a 3D bioprinting system (3DXPrinter; T&R Biofab Co., Ltd., South Korea) with four microextrusion-based printing heads was used. This system featured three-axis precision stages and four pneumatic dispensers: three low-pressure dispensers for hydrogels and one high-pressure dispenser for thermoplastic polymer. PCL (Resomer C209; Evonik Inc., Germany) granules were loaded into a 10-mL metal syringe of the extruder, maintained at 80°C. After a 10 min heating period, molten PCL was extruded through a metal nozzle (500 μm diameter) at a pressure of 650 kPa and feed rate of 600 mm/min to fabricate a frame with dimensions of 10.5 × 9 × 3.5 mm. For preset extrusion bioprinting, SdECM containing NHDF (1×10^6 cells/mL) and alginate were each loaded into a precursor cartridge using a syringe and a needle. Subsequently, the precursor cartridges containing SdECM bioink and alginate were carefully transferred to a 10 mL plastic syringe and equipped with an 18-gauge tapered nozzle. Additionally, to print the dermis layer without the rete ridge structure, the SdECM bioink was transferred to a 10 mL plastic syringe and fitted with an 18-gauge straight nozzle. The syringes containing SdECM were mounted on a print head maintained at 4°C to prevent gelation during bioprinting. The applied pressure to extrude bioinks was 5–8 kPa and the feed rate was 450–750 mm/min. The printed dermis constructs were incubated at 37°C for 15 min for gelation and then washed three times with pre-warmed PBS at 37°C to remove sacrificial material. Subsequently, keratinocytes (1×10^6 cells/model) were seeded onto the dermis, and each skin model was cultured under air-liquid interface conditions for seven days.

2.6. Optical coherence tomography imaging

A spectral-domain optical cohesion tomography (OCT) imaging system (Lumedica Inc., USA) with 840 nm center wavelength was used to non-destructively observe the cross-sectional structure of printed FTSE. For observation, the printed rete ridge FTSE was transferred to a petri dish and images were captured at a size of 3547 × 2632 μm.

2.7. UV treatment

To confirm UV resistance, FTSEs were exposed to UVB using a UV irradiation system (UV Crosslinker; VWR International, France). Irradiation was performed for 30 min at intensities of 25 and 50 mJ/cm². Following UVB treatment, the samples were cultured for three days under standard conditions at 37°C in an atmosphere of 5% CO_2.

2.8 Tissue slide preparation

To perform hematoxylin & eosin (H&E) and immunofluorescence (IF) staining, the skin models were fixed overnight in 4% paraformaldehyde (PFA, 163-20145; Wako, Japan) at 4°C. Following fixation, the samples were dehydrated in a 30% sucrose solution. Once completely dehydrated, the samples were then immersed in optimal cutting temperature compound (FSC 22 Clear; Leica Microsystems, Germany) and frozen using liquid nitrogen for 15 min. Subsequently, tissue sections with a thickness of 8 μm were obtained using a cryotome.

2.9. Hematoxylin & eosin staining

The obtained tissue sections were mounted on glass slides, and the optimal cutting temperature compound was removed by washing the slides. H&E staining was performed using a commercially available H&E staining kit (HAE-1 kit; Scytek Laboratories Inc., USA), following the manufacturer's instructions. Briefly, the sections were treated with hematoxylin for 5 min to visualize nuclei, followed by a bluing reagent for 10 s. Subsequently, the sections were stained with eosin for 3 min to highlight cytoplasmic structures. Following each staining step, the samples were rinsed with distilled water and absolute ethanol.

2.10. Immunofluorescence staining

For IF staining, the samples were incubated with a 1× blocking buffer containing 0.2% Triton X-100 and 2.5% bovine serum albumin at room temperature (~23–25°C) for 1 h to minimize nonspecific antibody binding.

Subsequently, the slides were incubated at 4°C for 18 h with specific primary antibodies against proteins of interest, including collagen 17 (COL17, ab184996; Abcam, United Kingdom [UK]), integrin beta 1 (ITGB1, ab24693; Abcam, UK), integrin alpha 6 (ITGA6, ab181551; Abcam, UK), cytokeratin 10 (K10, ab9026; Abcam, UK) cytokeratin 14 (K14, ab7800; Abcam, UK), Kiel 67 (Ki67, ab16667; Abcam, UK), and filaggrin (FLG, 905804; Biolegend, USA). Following primary antibody incubation, the samples were washed thoroughly and then incubated with goat anti-mouse Alexa Fluor 488, (ab150113; Abcam, UK) and goat anti-rabbit lgG Alexa Fluor 594 (ab150080; Abcam, UK). Nuclei were counterstained with a nuclear marker, 4°C,6-diamidino-2-phenylindole. Finally, the stained samples were observed using an upright microscope (BX53; Olympus, Japan) equipped with a digital camera (DP73; Olympus, Japan).

2.11. Interdigitation index

The interdigitation index was calculated by analyzing H&E images using ImageJ (version 1.53t; National Institute of Health, USA). Briefly, using the segmented line tool, the boundary between the DEJ of the FTSEs was traced from one end of the image to the other and divided by a straight line connecting the same start and endpoints.

2.12. Statistical analysis

Statistical analysis was performed using Microsoft Excel. Two-tailed *t*-tests were used for comparisons, and $p < 0.05$ was considered significant. All data are presented as mean ± standard deviation.

3. Results

3.1. Precursor cartridge design

The cross-sectional design of the precursor cartridge determines the cross-sectional shape of the extruded strand. However, as aforementioned, the cross-sectional shape of the extruded strand may sometimes differ from that of the precursor cartridge. Therefore, to determine the optimal architecture of the precursor cartridge, we performed CFD simulations. Initially, using the non-Newtonian fluid model of the bioink described in Figure S2, Supporting Information and Table S1, Supporting Information, we validated the CFD method with a simple core-shell model (details are described in the Supporting Information). Briefly, alginate was loaded into the core compartment of the precursor cartridge, whereas the SdECM was loaded into the shell compartment, and a strand was generated by preset printing. Concurrently, CFD was conducted for the same model. A comparison between the experimental and CFD results regarding the proportion of the alginate within the cross-section of the strand indicated that the CFD method effectively predicted the experimental outcomes. Using the validated CFD method, we designed a precursor cartridge with a simple cross-sectional architecture capable of creating narrow fissures, and fluid flow simulations were performed. The detailed dimensions of the simulation model are illustrated in Figure 1A.

The simulation result indicated that the sacrificial bioink (indicated by red particles) in the printed strand would be over-extruded, leading to the formation of large fissures (Figure 1B). Therefore, we conducted further simulations by iterating the architecture of the precursor cartridge until achieving the desired structure size. Through this trial-and-error process in the simulation, a precursor cartridge was designed, as illustrated in Figure 1C, with the simulated width and depth of the fissure in the extruded strand being 164 and 594 μm, respectively. Finally, the simulation result was confirmed by comparison with the experimental result (Figure 1D). Figure 1E indicates that the width and depth of the fissure in the experimental results were similar to those obtained in the simulation results.

3.2. Printing process for rete ridge FTSEs

Figure 2A illustrates a schematic overview of the key steps in the printing process, offering a comprehensive insight into our methodology. To fabricate the rete ridge skin model, four printing heads were used in this step (Figure 2B). From left to right, the first and second heads were designated for dermis printing; however, the precursor cartridge, designed to create fissure structures in the extruded strand, was loaded only in the second printing head. Therefore, only the dermis bioink was loaded in the first head, whereas the dermis bioink and sacrificial bioink were loaded in the second head. The third head was equipped with a plow and used to form furrows on the dermis layer. The final head was a high-temperature printing head for PCL, responsible for constructing the frame of the model.

The PCL frame was initially printed onto the surface of the culture dish using the high-temperature printing head. Subsequently, the dermis bioink was extruded inside the PCL frame using the first head to construct a 2000 μm thick dermis layer. Preset extrusion printing to form fissures was then performed on the surface of the printed dermis layer. Figure 2C illustrates preset extrusion 3D bioprinting using a precursor cartridge, which was filled with bioink and sacrificial material. The cartridge was inserted into the barrel, and the bioink and sacrificial material were simultaneously extruded.

Fluid with a low Reynolds number can flow while maintaining a pattern of precursor cartridge; maintaining a strut shape with the bioink on a hydrophilic matrix is

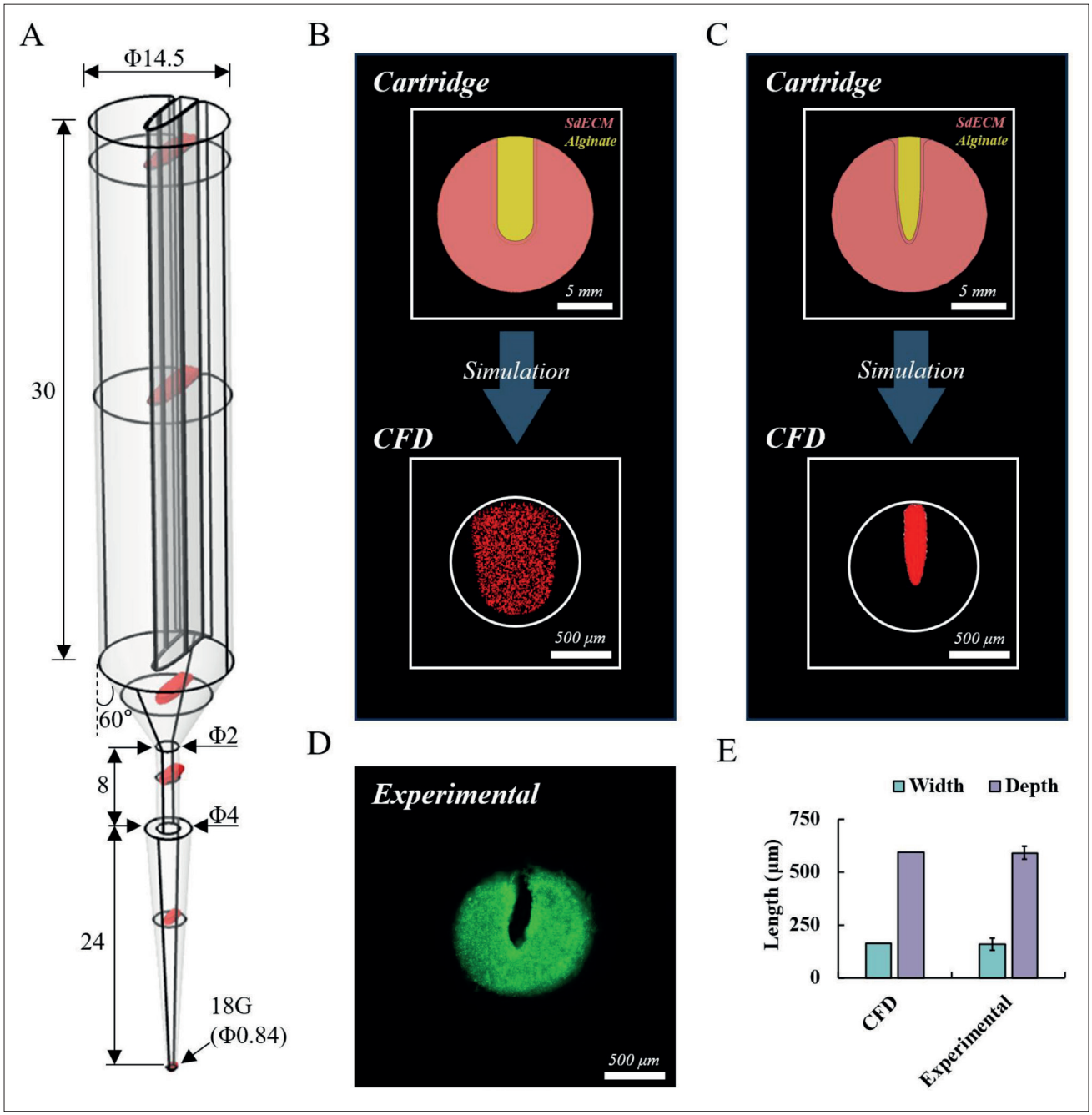


Figure 1. Computational fluid analysis for rete ridge structure precursor cartridge optimization. (A) A three-dimensional (3D) model with actual dimensions applied in the computational fluid dynamics (CFD) simulation, and the Poincaré map of the height direction for the fluid flow simulation results. Red marks indicate the sacrificial ink, i.e., alginate. (B) A precursor cartridge with a simple architecture capable of creating a fissure structure within extruded strands and the results of predicted fissure structure within the extruded strand using the CFD method (C) The final precursor cartridge architecture designed via the CFD method and the results of CFD. (D) The cross-sectional structure of extruded strands using a precursor cartridge is determined in (C). (E) Comparison between CFD-predicted and experimentally produced results for the width and depth of the fissure.

difficult.[20,26,27] Figure 2D displays the preset extruded strand with a fissure on the preprinted flat dermis layer. However, in this case, although the fissure was formed at the end of the printing nozzle (Figure 2C), the circular strand was rapidly flattened on the flat dermis layer owing to the surface tension, resulting in random distortion of the fissure. Therefore, before preset printing, we created semicircular furrows with a depth of 1000 μm on the

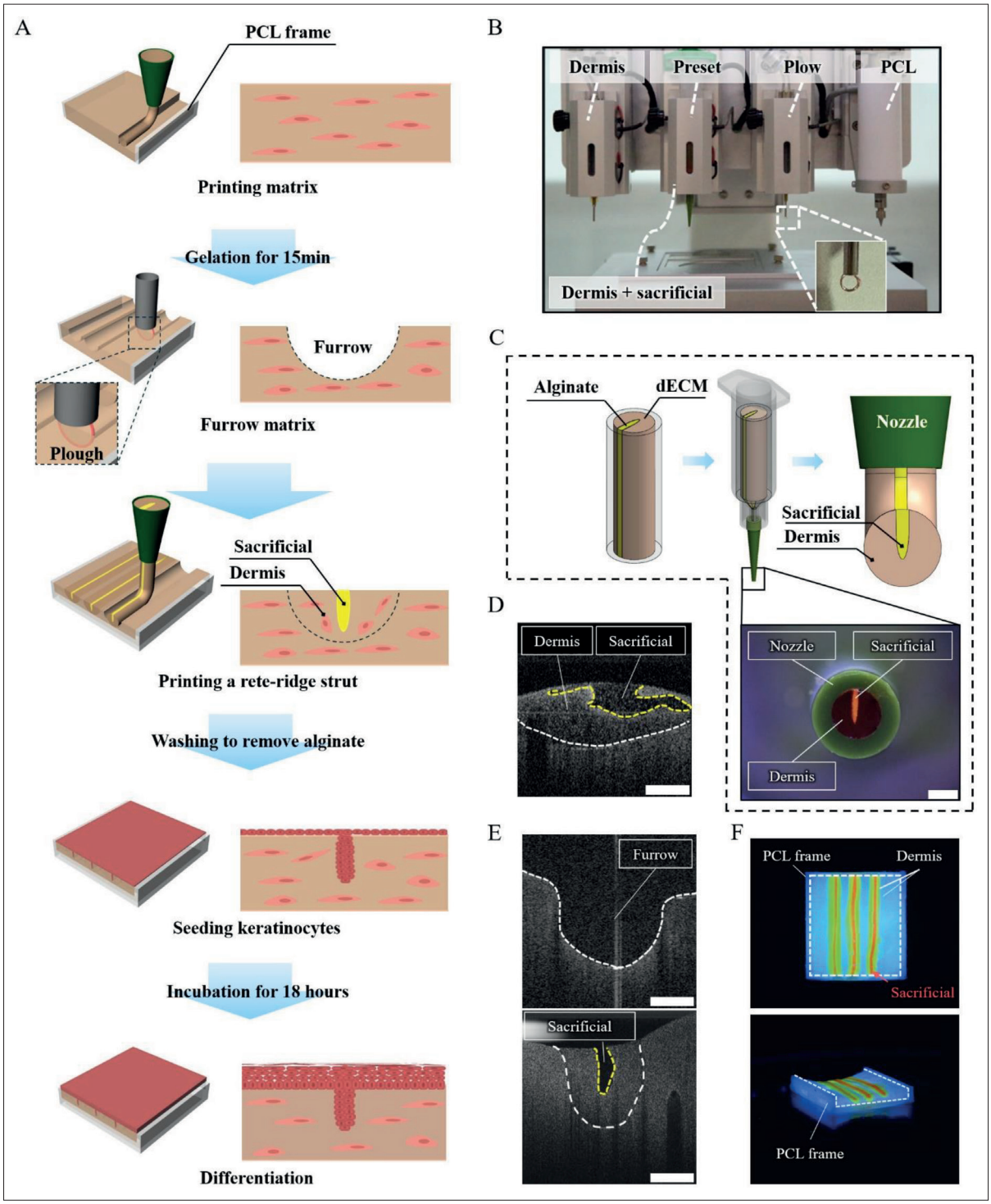


Figure 2. Fabrication of rete ridge full-thickness skin equivalents (FTSEs) using preset extrusion 3D bioprinting technology. (A) Schematic representation of key fabrication steps of rete ridge FTSEs. (B) A set-up of a 3D bioprinting system to fabricate rete ridge FTSEs. (C) Illustration of the precursor cartridge and preset extrusion bioprinting technique to fabricate a strand incorporating deep and narrow fissures. (D) Optical coherence tomography (OCT) image of the printed strut incorporating fissure by preset extrusion bioprinting on the unfurrowed, flat dermis layer. (E) Cross-sectional image of the furrowed dermis and a printed strand incorporating a fissured structure on the furrowed substrate. (F) The rete ridge FTSE was fabricated using the preset extrusion bioprinting-based technique introduced in this study. Red represents the sacrificial ink, i.e., alginate solution; green represents skin-derived decellularized extracellular matrix (SdECM) bioink printed via preset extrusion bioprinting; and blue represents the SdECM printed by bioprinting. Scale bars: 500 μm. Abbreviations: PCL: Polycaprolactone; dECM: Decellularized extracellular matrix.

surface of the dermis using the plow equipped in the third head (Figure 2B, inset). Subsequently, we preset-extruded a strand with a fissure along the furrow to ensure the maintenance of the fissure structure. Figure 2F presents the OCT photograph of the furrow (Figure 2E, upper panel) and the extruded stand with fissure along the furrow (Figure 2E, lower panel). The fissure printed along the furrow exhibited a deeper and narrower formation, closely resembling the cross-section of the strand at the exit of the nozzle. Notably, the fissure was maintained after washing out the sacrificial alginate. In this study, we created three fissures per model (Figure 2F).

3.3. Rete ridge FTSE analysis

Conventional and rete ridge FTSEs were fabricated by differentiating keratinocytes on the surface of the dermis. Keratinocytes were seeded onto the surface of each model and allowed to attach for one day before undergoing differentiation under air-liquid-interface (ALI) culture conditions. For conventional FTSEs, keratinocytes were uniformly distributed only on the surface of the dermis (Figure 3A, upper panels). In contrast, in the rete ridge skin model, cells were attached not only to the surface of the dermis but also to the narrow fissure. On day 3 of ALI culture (Figure 3A, middle panels), the model exhibited a progression in cellular organization, indicating the onset of differentiation and the formation of the epidermal tissue. We confirmed that the rete ridge FTSE was well-filled with keratinocytes extending into the fissure, whereas the conventional FTSE, lacking such a structure, maintained a flat shape. On day 7, distinct stratification of the cell layer suggested a successful response of both rete ridge and conventional FTSEs to ALI culture conditions. On day 7, the H&E results (Figure 3A, bottom panel) indicated significant differentiation, with a well-established stratified epidermal structure. Although there was no significant difference observed in the stratum corneum layer between the rete ridge and conventional FTSEs, intriguing distinctions emerged in the underlying layers. In the rete ridge region, the layers beneath the stratum corneum appeared noticeably thicker and well-organized. These features were quantified through the interdigitation index using the H&E results on day 7. Figure 3B displays the interdigitation index,[28] representing the ratio of DEJ length to straight line length, of rete ridge and conventional FTSEs. Owing to the narrow and deep fissure structure, the interdigitation index of rete ridge FTSEs exhibited a higher value than conventional FTSEs. However, the interdigitation index value of rete ridge FTSE decreased over time, though it still maintained the rete ridge structure compared to conventional FTSEs until day 7.

We investigated the protein expression in the skin model through IF staining (Figure 3C). COL17 was expressed at high levels at the bottom of the rete ridge region, indicating a localized enrichment of COL17 in the lowermost aspect of the rete ridge topography (Figure 3C, white dotted box). In addition, we explored the expression of ALPHA6 and BETA1 integrins in the rete ridge FTSE. We observed elevated expression of ALPHA6 and BETA1 integrins, precisely localized at the top corner of the rete ridges (Figure 3C, white arrowheads).

We investigated the cellular proliferation within the rete ridge FTSE by assessing the expression of the Ki67 marker. There was a notable difference in $Ki67^+$ cell density between the bottom of the rete ridge and the adjacent flat surface. The bottom of the rete ridge exhibited a higher density of $Ki67^+$ cells, indicating an area of increased cellular activity and proliferation (Figure 3C, red dotted box). Moreover, the higher $Ki67^+$ cell density at the bottom of the rete ridge further correlated with our earlier observation of thicker and well-stratified layers beneath the stratum corneum in this region (Figure 3A, bottom red dotted box). However, despite our rigorous analysis, we did not observe a significant difference in the expression of K10, K14, and filaggrin between the rete ridge region and adjacent flat region, suggesting that both regions exhibit comparable levels of epidermal differentiation and protein expression.

3.4. UV irradiation on FTSE

We irradiated UVB on rete ridge and conventional FTSEs and observed the histology and protein expression (Figure 4). In conventional FTSEs, we observed that the integrity of the stratum corneum was compromised and the expression levels of COL17, ITGA6, and ITGB1 decreased upon exposure to UV irradiation, regardless of its intensity. However, in rete ridge FTSEs, we observed different results based on the intensity of UV and the depth of the model. When exposed to 25 mJ/cm^2 of UV irradiation, the integrity of the stratum corneum located at the top of the skin model was compromised in a manner resembling that of conventional FTSEs. However, the structure of the stratum corneum within the rete ridge remained intact. Upon exposure to 50 mJ/cm^2 UV, we observed a more pronounced disruption of the stratum corneum integrity. Nevertheless, the stratum corneum in the valley part of the rete ridge remained intact. These differences were also observed in protein expression; although COL17, ITGA6, and ITGB1 expression decreased upon UV exposure in the adjacent flat region, it remained constant within the rete ridge structure.

We investigated the expression of K10 and Ki67 after UV irradiation. Figure 5A displays the results of IF staining for K10 and Ki67. UV exposure induced damage to K10 in both rete ridge and conventional FTSEs. However, under exposure to 25 mJ/cm^2 UV irradiation, preservation of

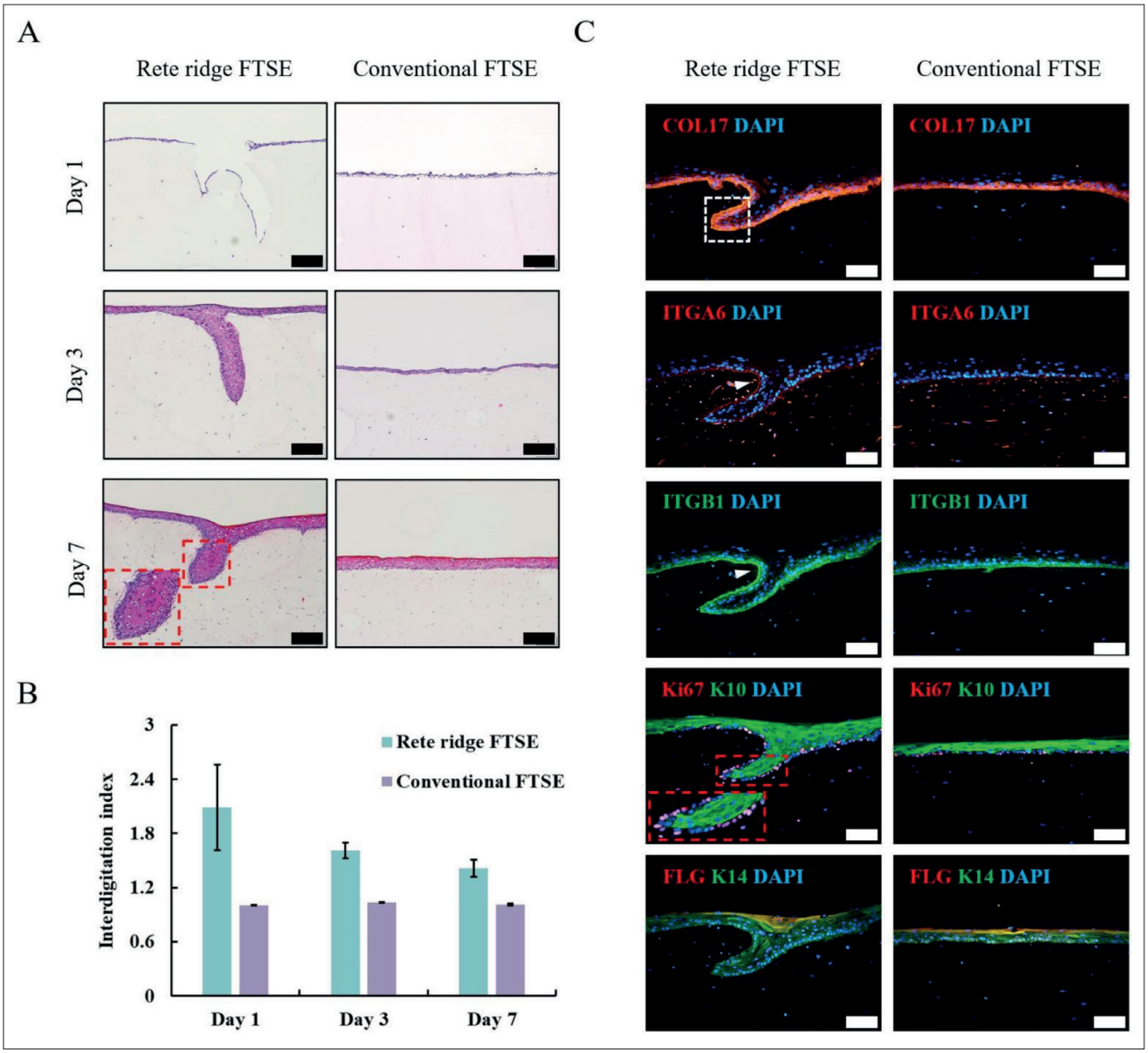


Figure 3. Histological and immunofluorescence staining analyses of full-thickness skin equivalents (FTSEs). (A) Hematoxylin & eosin (H&E) staining results of the rete ridge and conventional FTSEs. Red dotted boxes indicate well-differentiated keratinocytes at the rete ridge structure. Scale bars: 200 μm. (B) Difference in the interdigitation index between rete ridge and conventional FTSEs. The error bars indicate the standard deviation (n = 4). (C) Assessment of protein expression in the rete ridge and conventional FTSEs with immunofluorescence staining. High expression of COL17, ITGA6, and ITGB1 was observed in rete ridge FTSEs (white dotted box and white arrowhead). A higher expression of Kiel 67 (Ki67) was observed at the end of the rete ridge structure (red dotted box). Scale bars: 100 μm.

K10 was noted in the valleys of the rete ridge FTSE. As for Ki67, a discrepancy between rete ridge and conventional FTSEs was observed, with a higher number of Ki67+ cells being observed in rete ridge FTSEs (Figure 5B). Moreover, analysis based on the depth of the skin model (Figure 5C) revealed a comparable count of $Ki67^+$ cells between the flat and rete ridge FTSEs at a depth of 100 μm or less. However, at a depth exceeding 100 μm, a higher number of $Ki67^+$ cells were observed in rete ridge FTSEs.

4. Discussion

In this study, we explored the fabrication of advanced skin models that mimic the rete ridge structure of native skin, focusing on the discussion and implications of our

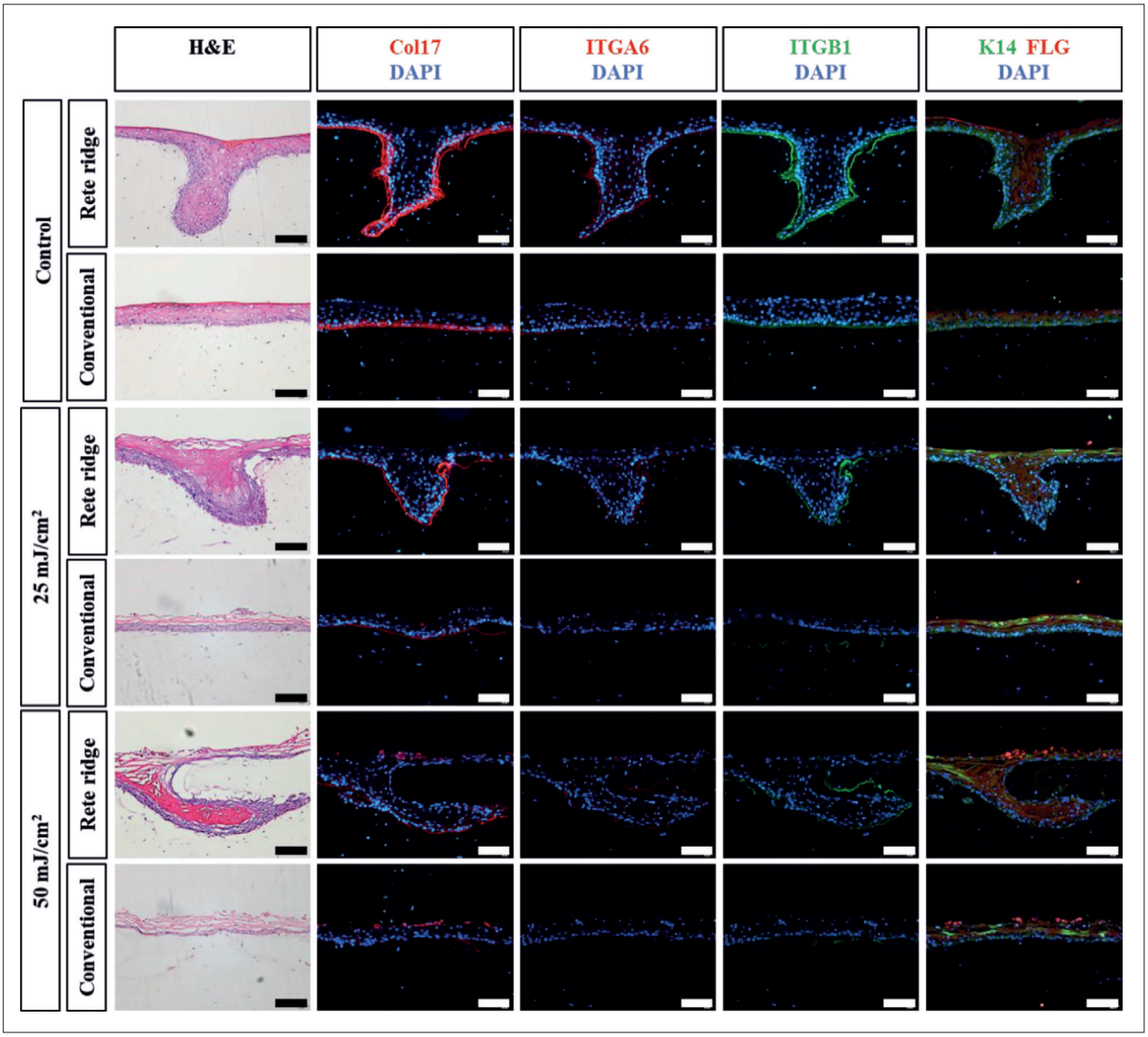


Figure 4. Observations of tissue sections to evaluate the influence of ultraviolet (UV) irradiation. Upon UV irradiation (25 and 50 mJ/cm^2), conventional full-thickness skin equivalents (FTSEs) exhibited notable stratum corneum collapse and a reduction in protein expression. Conversely, rete ridge FTSEs demonstrated preserved stratum corneum and protein expression, particularly within the valley of the rete ridge structure. Scale bars: 200 μm. Abbreviation: H&E: Hematoxylin & eosin.

discovery. Traditional skin research has primarily relied on epidermal models and FTSEs, which, despite their utility in initial investigations and understanding basic skin functions, are limited in their ability to accurately replicate the complex topographical features of native skin, particularly the rete ridges. These features are crucial for a realistic representation of skin, influencing cellular behaviors critical for skin health and disease. One major biological implication of the DEJ is its association with aging; certain tissues are prone to become flatter with age.[29] However, owing to technical limitations, most aging-related approaches have focused solely on short-term UV exposure of skin constructs[30] or skin reconstruction techniques that do not represent the histological profile of *in vivo* skin.[31] To address the limitations associated with conventional methods, we used a preset extrusion bioprinting technique, utilizing SdECM-based bioinks to fabricate skin models with detailed rete ridge structures. Unlike previous attempts that used molding or stamping techniques prone to damaging delicate biomaterials such as collagen, our method overcomes these challenges by incorporating a "furrow step" to achieve the desired

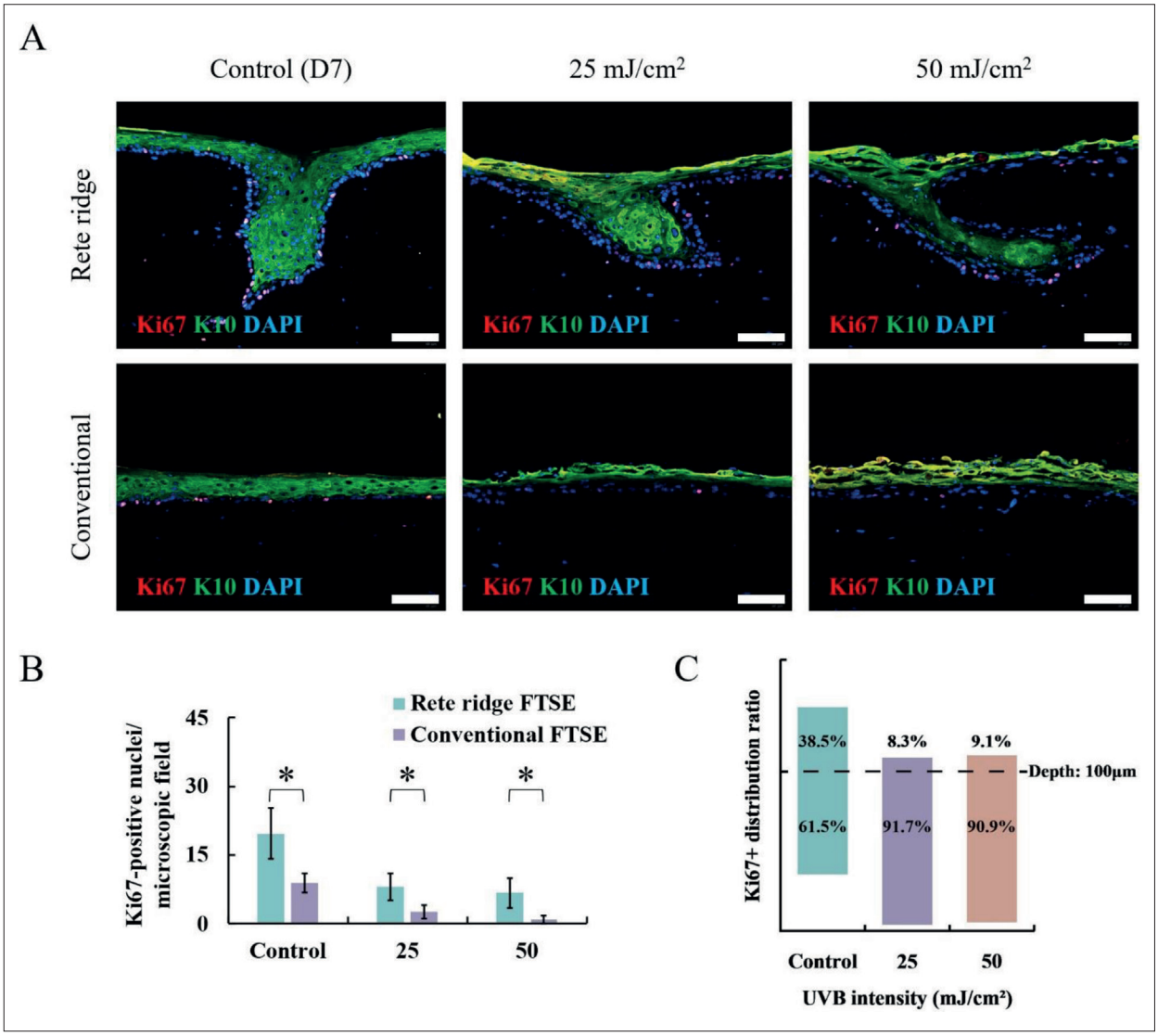


Figure 5. Assessment of the effect of ultraviolet (UV) irradiation on the cell proliferation marker, Ki67. (A) Immunofluorescence staining of the control and UV-irradiated (25 and 50 mJ/cm^2) rete ridge and conventional full-thickness skin equivalents (FTSEs). Red indicates Ki67, green indicates keratin 10 (K10), and blue indicates nuclei. (B–C) Quantitative analysis results of Ki67$^+$ cells are based on the presence of UV irradiation, cross-sectional structure (B), and depth (C) of rete ridge FTSEs. Scale bars: 100 μm. $^*p < 0.05$ ($n = 3$).

architecture. Furthermore, rather than depositing bioink, we successfully fabricated a skin model incorporating rete ridge structures through the application of preset extrusion bioprinting. In addition, our choice of SdECM as a bioink was motivated by its proven biological relevance and functionality, mirroring the native ECM of the skin. The SdECM not only supports cell adhesion, growth, and differentiation but also enhances the mechanical properties and structural integrity of the printed constructs.[24] The biological and structural fidelity of SdECM to native skin ECM underscores the potential of bioinks derived from specific tissues to improve the outcomes of 3D bioprinting. This approach highlights the importance of selecting appropriate biomaterials and fabrication techniques to accurately mimic the intricate features of native skin.

A significant finding in our study was the successful application of CFD to accurately predict the outcomes of the preset extrusion bioprinting process. The preset extrusion bioprinting technique is a type of multi-material bioprinting method. Important factors influencing the cross-sectional shape of the printed strands include fluid dynamic variables, such as the viscosity of the bioink and its flow path. Consequently, considerable effort is required

to achieve the production of the desired cross-sectional shape using preset extrusion bioprinting. Therefore, we applied CFD to predict the material location in printed strands through a preset extrusion, and the cross-sectional pattern was precisely predicted using the CFD method. The preset extrusion bioprinting technology utilizes the non-mixing property of low Reynolds number flow.[22] Moreover, the bioinks applied in this process are in a liquid phase, enabling the solution of the Navier-Stokes equation for single-phase laminar flow using the finite element analysis method to predict cross-sectional patterns of extruded strands with different bioinks. Particularly, by evaluating the rheological properties of different bioinks and applying non-Newtonian fluid viscosity models tailored to the unique characteristics of each bioink, the cross-sectional architecture of extruded strands can be accurately predicted. By employing the CFD method utilized in this study, it would be possible to print various intricate microstructures within the human body, in addition to the skin rete ridge or hepatic lobule structure explored in our previous research.[20]

The rete ridge FTSE produced using preset extrusion bioprinting displays improved characteristics in biological functionality compared to conventional models. We observed high levels of COL17, a critical component of the basement membrane zone that plays a crucial role in anchoring the epidermis to the underlying dermis,[32] at the base of the rete ridge. This observation suggests the reinforcement of adhesion structures in this region, likely essential for supporting the unique microarchitecture and structural integrity of the rete ridge features. Moreover, the localization of COL17 aligns with its physiological distribution in native human skin,[5] where it is essential for maintaining epidermal-dermal adhesion and promoting epidermal barrier function. The concentrated presence of COL17 at the bottom of the rete ridge reinforces the notion that the rete ridge topography is a pivotal region in shaping the functionality and complexity of the skin model. Furthermore, ITGA6 and ITGB1 were highly expressed at the top corner of the rete ridge, consistent with previous research results,[10] corroborating the spatial regulation of integrin expression within the specialized skin model. ALPHA6 and BETA1 integrins play a crucial role in skin physiology as members of the integrin family of receptors, mediating the attachment of cells to the surrounding ECM and specifically facilitating the stable adhesion of epidermal cells to the basement membrane. The differential expression of ALPHA6 and BETA1 integrins at the top corner of rete ridges suggests that these specific regions experience distinct mechanical and biochemical signals, possibly influencing the behavior and functionality of epidermal cells. Ki67 is a widely used protein marker that indicates active cellular proliferation during various phases of the cell cycle. The objective of this analysis was to elucidate the distribution and density of actively proliferating cells within the rete ridge and flat regions of the skin model on day 7 of ALI culture. $Ki67^+$ cells were observed at the bottom of the rete ridge. This result suggests that increased cellular proliferation contributes to the development of a more mature and functional epidermal tissue in the rete ridge area, closely resembling the *in vivo* characteristics of native human skin. Moreover, this finding is consistent with the results reported in previous studies.[17,33,34] This localized and enhanced cell proliferation in the rete ridge region suggests the role of the topographic features of the rete ridge in driving cellular turnover and differentiation within the skin model.

Ultraviolet (UV) irradiation accelerates wrinkle formation, pigmentation alterations, thinning of the stratum corneum, and skin aging. Aging also diminishes the skin's resistance to UV radiation, leading to a flattening of the rete ridge structure.[12,35,36] In the present study, the fabricated rete ridge FTSE exhibited a structural resemblance to young human skin, whereas the conventional FTSE resembled aged human skin models. The findings presented in this study could offer insights into the variations in UV resistance across different age groups using *in vitro* skin models. In addition, UV penetrates tissues to different depths depending on its wavelength. UVB radiation, which was utilized in our study, typically has a penetration depth of less than 150 μm.[37] Therefore, it can be speculated that the proteins located in the stratum corneum layer within the valley of the rete ridge structure and base membrane were not damaged by UV irradiation. Consequently, the effects of UV irradiation on the rete ridge FTSE revealed notable differences in damage between areas within the rete ridge structure. Moreover, reductions in the expression levels of COL17 and ITGB1 by UV irradiation were observed in the human *ex vivo* skin model similar to our rete ridge FTSE.[38,39] These findings highlight the sensitivity and potential of the rete ridge FTSE for studying skin responses to environmental stressors and offer new insights for studies focused on screening drugs or actives related to UV protection,[40,41] as the DEJ microstructures of the skin influence cell behavior. These insights demonstrate the advanced capabilities of our rete ridge FTSE over conventional models, thus potentially helping replace *ex vivo* skin models for future research applications.

However, our study also identified challenges in maintaining the integrity of the rete ridge structure over time, prompting the exploration of alternative techniques such as crosslinking the ECM post-bioprinting. Future research should explore the use of non-toxic crosslinking

agents, such as genipin, to preserve the initial structure, emphasizing the ongoing need for innovation in materials science to support the development of bioprinting technologies. Furthermore, as previously stated, the height of the rete ridge structure decreases as individuals age, resulting in a variable degree of UV damage to the skin depending on the extent of aging and the rate of aging progression. As demonstrated in our previous study,[23] the pattern of the extruded strands can be regulated by modifying the precursor cartridge or altering the viscosity of the applied bioink. Additionally, as illustrated in Figure S3, Supporting Information, the structure of the fabricated rete ridge exhibits a variety of architecture depending on the applied pressure during the preset extrusion bioprinting process. By leveraging these parameters, it will be possible to fabricate FTSEs with diverse structures of the rete ridge and to investigate the damage by UV irradiation on the width and depth of the rete ridge. Furthermore, it has been established that the skin is composed of heterogeneous microstructures, including the epidermis, dermis, capillaries, hypodermis, and other cells. Mimicking these heterogeneous microstructures in native tissue is crucial for the development of *in vitro* tissue models with high tissue functionality.[42] In addition to the rete ridge structure proposed in this study, further research is required to develop highly functional skin models that can serve as alternatives to *ex vivo* skin biopsy samples or animal experiments. This can be accomplished by implementing various heterogeneous tissue structures in the skin through the use of 3D bioprinting technology.

5. Conclusion

In this study, we introduced a technique for fabricating FTSEs with rete ridge, microstructures present in the dermal-epidermal interface of the human skin, using 3D bioprinting technology. Specifically, by employing the furrowing of printed dermis bioink and preset extrusion bioprinting technique in this rete ridge FTSE fabrication process, we successfully engineered a dermis layer featuring narrow and deep fissure structures. The design and optimization of the precursor cartridge for the preset extrusion bioprinting process were conducted through the CFD method, validating the predictive capability of this method in anticipating the cross-sectional structure of printed strands accurately. Subsequently, by seeding keratinocytes onto the dermis layer containing fissure structures and culturing them under ALI conditions, we achieved the successful fabrication of FTSE incorporating rete ridge structure. The rete ridge FTSE exhibited prominent formation of the stratum corneum and confirmed robust expression of key markers, including COL17, ITGA6, ITGB1, and Ki67. Furthermore, exposure of the rete ridge FTSE to UV radiation resulted in sustained protein expression in the valley owing to the structural characteristics of the rete ridge. Consequently, the proposed method for fabrication of FTSE with rete ridge structure in this study, based on preset extrusion bioprinting technology, indicates considerable promise for generating *in vitro* skin models that can serve as an alternative to animal experiments and *ex vivo* human skin models for physiological investigation and testing the safety and efficacy of drugs and cosmetics. By achieving a more accurate replication of the topographical complexity of the skin, more sophisticated studies on skin biology and drug testing can be conducted, thus advancing our efforts toward the goal of replicating human tissue structures in the laboratory.

Acknowledgments

None.

Funding

This research was supported by the National Research Foundation of Korea (NRF) grant funded by the Ministry of Education (NRF-2017R1A6A1A03015562) and the Tech University of Korea Sabbatical Year Research Grant (2023).

Conflict of interest

W.-S.Y., J.-H.S., P.A. Marinho, I.J., and S.J. are employed by and shareholders of T&R Biofab. The remaining authors declare no conflicts of interest.

Author contributions

Conceptualization: Songwan Jin, Paulo Andre Marinho
Formal analysis: Songwan Jin, Jae-Hun Kim
Funding acquisition: Won-Soo Yun
Investigation: Ilho Jang, Jae-Hun Kim, Misun Kim, Younhwa Nho, Seunghyun Kang
Methodology: Songwan Jin, Ilho Jang, Misun Kim, Jin-Hyung Shim
Project administration: Songwan Jin
Writing – original draft: Ilho Jang, Jae-Hun Kim, Paulo Andre Marinho
Writing – review & editing: Songwan Jin, Won-Soo Yun, Jin-Hyung Shim, Paulo Andre Marinho

Ethics approval and consent to participate

Not applicable

Consent for publication

Not applicable

Availability of data

Data will be made available upon reasonable request.

References

1. Malaisse J, Pendaries V, Hontoir F, et al. Hyaluronan does not regulate human epidermal keratinocyte proliferation and differentiation. *J Biol Chem.* 2016;291(12):6347-6358. doi: 10.1074/jbc.M115.661348.
2. Chamcheu JC, Afaq F, Syed DN, et al. Delphinidin, a dietary antioxidant, induces human epidermal keratinocyte differentiation but not apoptosis: studies in submerged and three-dimensional epidermal equivalent models. *Exp Dermatol.* 2013;22(5):342-348. doi: 10.1111/exd.12140.
3. Mini CA, Dorta DJ, Maria-Engler SS, Oliveira DP. Immortalized equivalent human epidermis as a platform to evaluation hair dyes toxicity: efficiency comparison between 3D and monolayer culture. *Chem Biol Interact.* 2020;330:109227. doi: 10.1016/j.cbi.2020.109227.
4. Jeong SH, Kim JH, Yi SM, et al. Assessment of penetration of quantum dots through *in vitro* and *in vivo* human skin using the human skin equivalent model and the tape stripping method. *Biochem Biophys Res Commun.* 2010; 394(3):612-615. doi: 10.1016/j.bbrc.2010.03.032.
5. Liu N, Matsumura H, Kato T, et al. Stem cell competition orchestrates skin homeostasis and ageing. *Nature.* 2019;568(7752):344-350. doi: 10.1038/s41586-019-1085-7.
6. Kim BS, Ahn M, Cho WW, Gao G, Jang J, Cho DW. Engineering of diseased human skin equivalent using 3D cell printing for representing pathophysiological hallmarks of type 2 diabetes *in vitro*. *Biomaterials.* 2021;272:120776. doi: 10.1016/j.biomaterials.2021.120776.
7. Liu X, Michael S, Bharti K, Ferrer M, Song MJ. A biofabricated vascularized skin model of atopic dermatitis for preclinical studies. *Biofabrication.* 2020;12(3):035002. doi: 10.1088/1758-5090/ab76a1.
8. Jang HJ, Lee JB, Yoon JK. Advanced *in vitro* three-dimensional skin models of atopic dermatitis. *Tissue Eng Regen Med.* 2023;20(4):539-552. doi: 10.1007/s13770-023-00532-1.
9. Langton AK, Graham HK, McConnell JC, Sherratt MJ, Griffiths CEM, Watson REB. Organization of the dermal matrix impacts the biomechanical properties of skin. *Br J Dermatol.* 2017;177(3):818-827. doi: 10.1111/bjd.15353.
10. Aleemardani M, Trikić MZ, Green NH, Claeyssens F. The importance of mimicking dermal-epidermal junction for skin tissue engineering: a review. *Bioengineering (Basel).* 2021;8(11):148. doi: 10.3390/bioengineering8110148.
11. Giangreco A, Goldie SJ, Failla V, Saintigny G, Watt FM. Human skin aging is associated with reduced expression of the stem cell markers beta1 integrin and MCSP. *J Invest Dermatol.* 2010;130(2):604-608. doi: 10.1038/jid.2009.297.
12. Liao YH, Kuo WC, Chou SY, et al. Quantitative analysis of intrinsic skin aging in dermal papillae by *in vivo* harmonic generation microscopy. *Biomed Opt Express.* 2014;5(9): 3266-3279. doi: 10.1364/BOE.5.003266.
13. Krystyna JGK, Anna PJ, Markiewicz-Żukowska R, Socha K. The impact of ultraviolet radiation on skin photoaging – review of *in vitro* studies. *J Cosmet Dermatol.* 2021;20(11):3427-3431. doi: 10.1111/jocd.14033.
14. Nagarajan MB, Ainscough AJ, Reynolds DS, et al. Biomimetic human skin model patterned with rete ridges. *Biofabrication.* 2023;16(1):015006. doi: 10.1088/1758-5090/acfc29.
15. Shen Z, Cao Y, Li M, et al. Construction of tissue-engineered skin with rete ridges using co-network hydrogels of gelatin methacrylated and poly(ethylene glycol) diacrylate. *Mater Sci Eng C Mater Biol Appl.* 2021;129:112360. doi: 10.1016/j.msec.2021.112360.
16. Bush KA, Pins GD. Development of microfabricated dermal epidermal regenerative matrices to evaluate the role of cellular microenvironments on epidermal morphogenesis. *Tissue Eng Part A.* 2012;18(21–22):2343-2353. doi: 10.1089/ten.TEA.2011.0479.
17. Viswanathan P, Guvendiren M, Chua W, et al. Mimicking the topography of the epidermal-dermal interface with elastomer substrates. *Integr Biol (Camb).* 2016;8(1):21-29. doi: 10.1039/c5ib00238a.
18. Blackstone BN, Malara MM, Baumann ME, McFarland KL, Supp DM, Powell HM. Fractional CO_2 laser micropatterning of cell-seeded electrospun collagen scaffolds enables rete ridge formation in 3D engineered skin. *Acta Biomater.* 2020;102:287-297. doi: 10.1016/j.actbio.2019.11.051.
19. Admane P, Gupta AC, Jois P, et al. Direct 3D bioprinted full-thickness skin constructs recapitulate regulatory signaling pathways and physiology of human skin. *Bioprinting.* 2019;15:e00051. doi: 10.1016/j.bprint.2019.e00051.
20. Kang D, Ahn G, Kim D, et al. Pre-set extrusion bioprinting for multiscale heterogeneous tissue structure fabrication. *Biofabrication.* 2018;10(3):035008. doi: 10.1088/1758-5090/aac70b.

21. Kang D, Hong G, An S, et al. Bioprinting of multiscaled hepatic lobules within a highly vascularized construct. *Small.* 2020;16(13):e1905505. doi: 10.1002/smll.201905505.

22. Hong G, Kim J, Oh H, et al. Production of multiple cell-laden microtissue spheroids with a biomimetic hepatic-lobule-like structure. *Adv Mater.* 2021;33(36):e2102624. doi: 10.1002/adma.202102624.

23. Kim JH, Park M, Shim JH, Yun WS, Jin S. Multi-scale vascularization strategy for 3D-bioprinted tissue using coaxial core-shell pre-set extrusion bioprinting and biochemical factors. *Int J Bioprint.* 2023; 9(4):726. doi: 10.18063/ijb.726.

24. Girardeau-Hubert S, Lynch B, Zuttion F, et al. Impact of microstructure on cell behavior and tissue mechanics in collagen and dermal decellularized extra-cellular matrices. *Acta Biomater.* 2022;143:100-114. doi: 10.1016/j.actbio.2022.02.035.

25. Samandari M, Alipanah F, Majidzadeh-A K, Alvarez MM, Trujillo-de Santiago G, Tamayol A. Controlling through designed 3D microcompartmentalization. *Appl Phys Rev.* 2021;8(2):021404. doi: 10.1063/5.0040732.

26. Ober TJ, Foresti D, Lewis JA. Active mixing of complex fluids at the microscale. *Proc Natl Acad Sci USA.* 2015;112(40):12293-12298. doi: 10.1073/pnas.1509224112.

27. Groisman A, Steinberg V. Efficient mixing at low Reynolds numbers using polymer additives. *Nature.* 2001;410(6831):905-908. doi: 10.1038/35073524.

28. Timár F, Soós G, Szende B, Horváth A. Interdigitation index – a parameter for differentiating between young and older skin specimens. *Skin Res Technol.* 2000;6(1):17-20. doi: 10.1034/j.1600-0846.2000.006001017.x.

29. Walton LA, Bradley RS, Withers PJ, et al. Morphological characterisation of unstained and intact tissue micro-architecture by X-ray computed micro- and nano-tomography. *Sci Rep.* 2015;5:10074. doi: 10.1038/srep10074.

30. Battie C, Jitsukawa S, Bernerd F, Del Bino S, Marionnet C, Verschoore M. New insights in photoaging, UVA induced damage and skin types. *Exp Dermatol.* 2014; 23(Suppl 1):7-12. doi: 10.1111/exd.12388.

31. Pageon H, Zucchi H, Rousset F, Monnier VM, Asselineau D. Skin aging by glycation: lessons from the reconstructed skin model. *Clin Chem Lab Med.* 2014;52(1):169-174. doi: 10.1515/cclm-2013-0091.

32. Nishie W, Kiritsi D, Nyström A, Hofmann SC, Bruckner-Tuderman L. Dynamic interactions of epidermal collagen XVII with the extracellular matrix: laminin 332 as a major binding partner. *Am J Pathol.* 2011;179(2):829-837. doi: 10.1016/j.ajpath.2011.04.019.

33. Clement AL, Moutinho TJ, Pins GD. Micropatterned dermal-epidermal regeneration matrices create functional niches that enhance epidermal morphogenesis. *Acta Biomater.* 2013;9(12):9474-9484. doi: 10.1016/j.actbio.2013.08.017.

34 Malara MM, Blackstone BN, Baumann ME, Bailey JK, Supp DM, Powell HM. Cultured epithelial autograft combined with micropatterned dermal template forms rete ridges *in vivo*. *Tissue Eng Part A.* 2020;26(21–22):1138-1146. doi: 10.1089/ten.TEA.2020.0090.

35. Tsatsou F, Trakatelli M, Patsatsi A, Kalokasidis K, Sotiriadis D. Extrinsic aging: UV-mediated skin carcinogenesis. *Dermatoendocrinol.* 2012;4(3):285-297. doi: 10.4161/derm.22519.

36. Newton VL, Bradley RS, Seroul P, et al. Novel approaches to characterize age-related remodelling of the dermal-epidermal junction in 2D, 3D and *in vivo*. *Skin Res Technol.* 2017;23(2):131-148. doi: 10.1111/srt.12312.

37. Meinhardt M, Krebs R, Anders A, Heinrich U, Tronnier H. Wavelength-dependent penetration depths of ultraviolet radiation in human skin. *J Biomed Opt.* 2008;13(4):044030. doi: 10.1117/1.2957970.

38. Bosset S, Bonnet-Duquennoy M, Barre P, et al. Decreased expression of keratinocyte β1 integrins in chronically sun-exposed skin *in vivo*. *Br J Dermatol.* 2003;148(4):770-778. doi: 10.1046/j.1365-2133.2003.05159.x.

39. Yaping X, Yingchun L, Yang Y, et al. Reduced expression of collagen 17A1 in naturally aged, photo aged, and UV-irradiated human skin *in vivo*: potential links to epidermal aging. *J Cell Commun Signal.* 2022;16(3):421-432. doi: 10.1007/s12079-021-00654-y.

40. Marionnet C, Tricaud C, Bernerd F. Exposure to non-extreme solar UV daylight: spectral characterization, effects on skin and photoprotection. *Int J Mol Sci.* 2014;16(1):68-90. doi: 10.3390/ijms16010068.

41. Marionnet C, de Dormael R, Marat X, et al. Sunscreens with the new MCE filter cover the whole UV spectrum: improved UVA1 photoprotection *in vitro* and in a randomized controlled trial. *JID Innov.* 2022;2(1):100070. doi: 10.1016/j.xjidi.2021.100070.

42. Riccardo L, Tomasz J, Ruben GS, et al. From shape to function: the next step in bioprinting. *Adv Mater.* 2020;32(12):1906423. doi: 10.1002/adma.201906423.

ACCSCIENCE PUBLISHING

International Journal of Bioprinting

RESEARCH ARTICLE

3D-bioprinted model of adult neural stem cell microenvironment in Alzheimer's disease

Natalia Dall'Agnol Ferreira[1,2], Paula Scanavez Ferreira[1,2], Cristina Pacheco Soares[3], Marimelia Aparecida Porcionatto[1,2*], and Geisa Rodrigues Salles[1,2,3*]

[1] Department of Biochemistry, Escola Paulista de Medicina, Universidade Federal de São Paulo, São Paulo, Brazil

[2] National Institute of Science and Technology in Modeling Human Complex Diseases with 3D Platforms (INCT Model 3D), São Paulo, Brazil

[3] Research & Development Institute, Universidade do Vale do Paraíba, São José dos Campos, São Paulo, Brazil

(This article belongs to the *Special Issue: Innovative Tissue and Diseases Models – Novelties in Bioprinting/3D bioprinting*)

Abstract

Neurogenesis plays a major role in neuroplasticity and memory. In adult human and mouse brains, neural stem cells (NSCs) are mainly distributed in two extensively characterized neurogenic niches: the subgranular zone (SGZ) of the hippocampus and the subventricular zone (SVZ) of the lateral ventricles. Impaired neurogenesis is one of the consequences of Alzheimer's disease (AD), contributing to cognitive decline and progressive memory loss. Developing new *in vitro* models that resemble this three-dimensional (3D) structure is fundamental for enhancing our understanding of the SVZ neurogenic niche dynamics in AD. Herein, we produced and characterized a 3D-bioprinted model of the adult SVZ neurogenic niche containing amyloid β (Aβ) oligomers, mimicking the NSC microenvironment in AD. In this model, Aβ oligomers induce oxidative stress and reduce the proliferative potential of NSCs, while stimulating neuronal differentiation. We hypothesize that these events are an early attempt of adult NSCs to compensate for neuronal death in AD pathogenesis. Our 3D model simulates the NSC niche physiology, reproducing an early response of NSCs in AD, strengthening the importance of studying the potential of neurogenesis in neurodegeneration.

Keywords: Bioprinting; Neurogenic niche; Alzheimer's disease; Amyloid beta; Neural stem cells; Subventricular zone

***Corresponding authors:**
Marimelia Aparecida Porcionatto (marimelia.porcionatto@unifesp.br)

Geisa Rodrigues Salles (geisa.salles@unifesp.br)

Citation: Ferreira NDA, Ferreira PS, Soares CP, Porcionatto MA, Salles GR. 3D-bioprinted model of adult neural stem cell microenvironment in Alzheimer's disease. *Int J Bioprint*. 2024;10(5):3751. doi: 10.36922/ijb.3751

Received: May 24, 2024
Accepted: July 19, 2024
Published Online: September 13, 2024

Copyright: © 2024 Author(s). This is an Open Access article distributed under the terms of the Creative Commons Attribution License, permitting distribution, and reproduction in any medium, provided the original work is properly cited.

Publisher's Note: AccScience Publishing remains neutral with regard to jurisdictional claims in published maps and institutional affiliations.

1. Introduction

Neurogenesis is defined as the process of generating neurons from neural stem cells (NSCs). In the adult brain, neurogenesis confers plasticity and neuronal replacement and occurs primarily in specialized regions known as neurogenic niches. The two main neurogenic niches of human and mouse brains are located in the subgranular zone (SGZ) of the hippocampus and the subventricular zone (SVZ) of lateral ventricles. As

the hippocampus is involved in memory and learning,[1] most studies involving neurogenesis in Alzheimer's disease (AD) primarily focus on this niche,[2–5] noting that neurogenesis decreases mainly due to amyloid beta (Aβ) aggregation and senile plaque formation.

However, recent studies have demonstrated that alterations in adult SVZ neurogenesis also play a crucial role in AD.[6–10] Transplantation of SVZ-derived newborn neurons can restore impaired neural circuits, which compensates for the reduced neuronal population found in AD,[11] playing a pivotal role in cognitive function and disease pathogenesis. Moreover, by undefined pathways, neurogenesis in the SVZ may be regulated and stimulated by Aβ in young adult animals.[12] Despite all evidence, there is a lack of studies focusing on the role of adult SVZ neurogenesis in AD.

The contribution of Aβ to AD initiation and progression is highly complex; it participates in different cellular events depending on the peptide's aggregation state, concentration, and the brain's developmental stage. Aβ can either impair the brain's homeostatic balance, as in AD, or play a role in normal brain development, by inducing NSC self-renewal and differentiation into neurons, astrocytes, and oligodendrocytes.[13] Aβ peptides are generated by enzymatic cleavage of amyloid precursor protein (APP) in the plasma membrane of neurons and glial cells. Two distinct pathways lead to APP cleavage: (i) the non-amyloidogenic pathway that results in the formation of a soluble form of APP (sAPPα), and (ii) the amyloidogenic pathway, which results in the formation of Aβ peptides that can form insoluble aggregates, a hallmark of AD. In the amyloidogenic pathway, APP is cleaved in distinct positions by two secretases (β and γ), producing different sizes of Aβ ($Aβ_{40}$ and $Aβ_{42}$), where $Aβ_{42}$ has more significant aggregation potential, resulting in senile plaques. Consequently, oxidative stress is observed during the formation of these plaques, inducing inflammatory responses, which enhances the aggregation of Aβ peptides and impairs synaptic plasticity.

As the brain is distinctly dynamic, the complexity of NSCs and Aβ oligomer interactions demands investigating AD using novel strategic models. Biotechnology and bioengineering have much to contribute, especially providing tools to develop biomaterials that may increase knowledge of pathophysiological mechanisms of the disease, in addition to reducing the number of animals used and highlighting specific pathways to be studied. Recently, valuable attention has been directed toward 3D models,[14–16] which create dynamic microenvironments that mimic the complexity of various tissues, including the brain.

Bioprinting has emerged as a highly promising tool for neurobiology, offering a technological approach to tailor 3D constructs effectively.[17–19] Moreover, bioprinting enables the creation of volumetric, biomimetic microenvironments that can emulate specific events of the central nervous system (CNS).[20] By designing specific combinations of cells and hydrogel that mimic the extracellular matrix environment, neurogenic niches, and other areas of the brain, specific microstructures can be potentially bioprinted.[17,21–25]

Therefore, bioprinting is at the forefront of elucidating NSC behavior by studying distinct areas, such as retina recreation by stem cell transplantation;[26] toxicological performance of compounds, such as cannabidiol, on neuroprogenitor cells;[27] modeling neural tissue using induced pluripotent stem cells (iPSCs) and iPSC-derived NSCs;[28] evaluation of neural regeneration;[29] and recapitulating areas of damaged CNS tissue.[30]

Although this technological tool is very promising, there is a lack of studies involving modeling and bioprinting neurodegenerative conditions, especially reproducing and biomimicking NSCs in AD. In this study, we developed and characterized a 3D model of the adult SVZ-NSC environment in AD by bioprinting NSC-derived neurospheres from six-week-old wild-type mice in a bioink containing Aβ oligomers. The biomaterial we produced and standardized may serve as a platform to further develop novel therapeutic strategies, also contributing to providing greater insights into underlying disease mechanisms.

2. Materials and methods

2.1. Study design

This study was designed to develop a 3D model of the adult SVZ-NSC microenvironment, representing a brain area, aside from the hippocampus, that can be a target for early events of neurodegeneration in AD. Briefly, SVZ-derived NSCs were isolated from six-week-old C57BL/6 mice, cultured as neurospheres, and bioprinted with or without $Aβ_{1–42}$ oligomers in the bioink composition. The constructs' physicochemical properties were characterized; the neurosphere areas were measured; and cell proliferation, oxidative stress, and cell differentiation were quantified.

2.2. Reagents and equipment

All reagents and equipment used in this work are described in Table 1.

2.3. Preparation of the hydrogel

The hydrogel (the polymeric base of the bioink) was composed of a homogenized combination of low-viscosity sodium alginate (ALG; molecular weight [M_W]: 30–100 kDa) and gelatin (GEL; M_W: ~ 50–100 kDa; type A from

Table 1. Reagents and equipment.

Reagent Or Resource	Source	Identifier
Reagents, antibodies, supplements, and other chemicals		
Accutase	Gibco, USA	A1110501
Alexa Fluor 488 Goat anti-Rabbit	Invitrogen, USA	A11008
Alexa Fluor 647 Goat anti-Chicken	Invitrogen, USA	A21449
Aβ-protein (Human, $A\beta_{1-42}$)	Peptide Institute, INC, Japan	4349-v
B-27 Supplement Minus Vitamin A	Gibco, USA	12587010
Calcium Chloride ($CaCl_2$)	Synth, Brazil	C201301AH
CellROX (Green Reagent)	Invitrogen, USA	C10444
DAPI	Sigma-Aldrich, USA	62248
Dimethyl sulfoxide (DMSO)	Sigma-Aldrich, USA	1003246030
Dulbecco's modified eagle medium/Nutrient mixture F-12 (DMEM/F12)	Gibco, USA	12400024
Fetal Bovine Serum (FBS)	Gibco, USA	12657-029
Gelatin from porcine skin (GEL)	Sigma-Aldrich, USA	G2500, 9000-70-8
Bovine sodium heparin	Kin Master, Brazil	50.1000.01
Human FGF-basic (FGF-2/bFGF)	Gibco, USA	PHG0026
L-glutamine	MP Biomedicals, USA	101806
LIVE/DEAD assay (Cell Imaging Kit 488/570)	Invitrogen, USA	R37601
Penicillin/streptomycin	Gibco, USA	15140-122
Phalloidin	Sigma-Aldrich, USA	49409
poly (2-hydroxyethylmethacrylate) (poly-hema)	Sigma-Aldrich, USA	P3932
Primary MAP-2 Antibody (Rb X MAP2)	Sigma-Aldrich, USA	ab5622
Primary Nestin Antibody (Chk pAb to Nestin)	Abcam, USA	ab134017
Recombinant Human EGF Protein	R&D System, USA	236-EG-01M
Resazurin powder	Sigma-Aldrich, USA	R7017
Sodium alginate (ALG, Alginic acid sodium salt from brown algae)	Sigma-Aldrich, Norway	A1112
Triton X-100	Sigma-Aldrich, USA	9002-93-1
Trypsin	Gibco, USA	15090046

Reagent Or Resource	Source	Identifier
Plastics and other non-perishable materials		
Cell culture dishes (100 mm)	Biofil, Brazil	TCD 000100
Cell culture flasks (25 cm^2 and 75 cm^2)	Corning, USA	430168
Cell culture plates (24 well)	Costar, USA	3524
Cell strainer (40μm nylon)	Falcon, USA	352340
Needles (25x0.70/0.60 22 G 1)	Injex, Brazil	25x0.70/0.60 22 G 1
Polypropylene conical tubes (15 mL and 50 mL)	Falcon, USA	352070 and 352095
Serological pipettes (1, 5, 10, and 25 mL)	Biofil, Brazil	GSP-010-005
Syringes (5 mL)	Descarpack, Brazil	
Equipment and Softwares		
3D Bioprinter	3D Biotechnology Solutions, Brazil (3DBS) Educational Starter, Brazil	http://www.3dbiotechnologiessolutions.com/educacional-starter/
ATR-FTIR spectrophotometer	Perkin Elmer FTIR Imaging System, USA	Spotlight-400
Centrifuge	Eppendorf, Germany	5702
Conductivity meter	Lactea, Brazil	
Confocal laser scanning microscope	Leica, Germany	TCS SP8
Electronic digital scale	Shimadzu, Brazil	AY220
Goniometer	KRUSS, Germany	EasyDrop DSA 100S
Hot plate magnetic stirrer	Kasvi, Brazil	
Humidifier incubator	Thermo Scientific, USA	Series 3 Water Jacketed
Microplate reader	Molecular Devices, USA	SpectraMax® M3
Microscope (Inverted fluorescent and phase contrast)	Olympus, USA	IX51 TH4-100
pHmeter	Kasvi, Brazil	K39-1420A
Pronterface software	Printrun, USA	Graphical User Interface host from Printrun
Rheometer	Thermo Scientific, Germany	Haake MARS 40/60
Scanning electron microscope	Zeiss, USA	EVO MA-10
Water bath	Novatecnica, Brazil	N1030T

porcine skin; and gel strength: ~300 g bloom). GEL (4% w/v) was first dissolved in sterile phosphate-buffered saline (PBS) on a hot plate magnetic stirrer at 72°C under constant agitation of 3 rcf. Once the powder was completely dissolved, ALG (6% w/v) was added to the solution and stirred for 30 min. The final solution was exposed to ultraviolet (UV) light for 30 min before printing.

2.4. Bioprinting and crosslinking the hydrogel

For bioprinting, 2 mL of the hydrogel was maintained in a water bath at 37°C, transferred to a 5 mL syringe with a 22-gauge blunt needle, and placed in the printhead of the 3D bioprinter. The bioprinting speed was set at 300 mm/min, at room temperature, and under G-code control, using two different extrusion codes in Pronterface software. The resulting constructs consisted of four deposited layers of cell-laden bioink (6 × 6 × 0.6 mm; Code 1) or six layers (6 × 6 × 1 mm; Code 2), as described in Table 2. Each construct was printed and deposited in a well of a 24-well plate, and the hydrogel was crosslinked in calcium chloride ($CaCl_2$) solution (2% w/v, diluted in distilled water, dH_2O) for 5–7 min.

2.5. Swelling degree

Constructs were weighed immediately after they were printed and crosslinked, before incubation in dH_2O or Dulbecco's modified eagle medium/nutrient mixture F-12 (DMEM/F12) (pH 7.2) at 37°C and 5% CO_2. They were weighed at different time points (0, 1, 2, 7, 14, 21, and 28 days). The percentage of swelling was calculated using **Equation I**:

$$Swelling\ (\%) = \frac{W_f - Wd_o}{Wd_o}\ x\ 100 \qquad (I)$$

where W_f is the final wet weight and Wd_o is the initial dry weight of constructs. Four constructs were weighed at each time point.

2.6. Degradation rate

The degradation rate of the constructs was determined by quantifying the weight loss of dry constructs. The printed constructs were weighed immediately after they were printed and crosslinked. They were then incubated in dH_2O or DMEM/F12 (pH 7.2) at 37°C and 5% CO_2. At different time points (0, 1, 2, 7, 14, 21, and 28 days), constructs were carefully blotted with filter paper to remove the excess liquid, maintained in a dry oven at 37°C for 20 min, and reweighed. The degradation percentage was calculated using **Equation II**:

$$Degradation\ (\%) = \frac{Wd_o - Wd_f}{Wd_o}\ x\ 100 \qquad (II)$$

Table 2. Bioprinting parameters.

Parameter	Code	
	1	2
Dimension (mm)		
X-axis	6	6
Y-axis	6	6
Z-axis	0.6	1
Number of layers	4	6
Individual layer height (mm)	0.2	0.2

where Wd_o is the initial dry weight and Wd_f is the final dry weight of constructs. Four constructs were weighed at each time point.

2.7. Wettability

The wetting of aqueous drops on the surface of constructs was characterized using a goniometer. Contact-angle measurements were based on the sessile drop method using aqueous drops at a volume of 5 µL placed on the top of the construct. Briefly, images of a single drop of deionized water deposited on the construct's surface were periodically acquired (every 2 min) by a custom setup with a charged-coupled device (CCD) camera. The first contact angle was measured 5 s after drop-casting to ensure the droplet reached equilibrium. Images were collected in triplicate, using different constructs, and contact angle values were measured. All measurements were conducted at a controlled temperature (25 ± 3°C) and humidified atmosphere (50 ± 10%).

2.8. Scanning electron microscopy

The surface observation of the constructs was performed by scanning electron microscopy (SEM). Right after crosslinking (day 0) and 14 days after dH_2O or DMEM/F12 incubation at 37°C and 5% CO_2, bioprinted constructs were dehydrated with a crescent sequence of acetone (30, 50, 70, and 100%) for 5 min in each solution. After that, samples were immersed in a 1:1 ratio of acetone: hexamethyldisilazane (HMDS) for 5 min, and finally in HMDS alone until the solution evaporated. Constructs were dried, sputter-coated with a thin layer of gold, and observed under a scanning electron microscope.

2.9. Attenuated total reflectance-Fourier transform infrared spectroscopy

The chemical structures of ALG, GEL, $CaCl_2$, crosslinked and non-crosslinked hydrogel, Aβ oligomers, and constructs with neurospheres (with and without Aβ oligomers) were analyzed using an attenuated total reflectance-Fourier transform infrared ATR-FTIR spectrophotometer at a range of 400–4000 cm^{-1} in transmittance mode.

2.10. Rheological characterization

The mechanical properties of the hydrogel were studied through rheological assessment using a stress-controlled rheometer with a parallel plate configuration (25 mm diameter; 200 μm gap). To determine the hydrogel's flow behavior and viscosity profile, samples were subjected to shear rates ranging from 0.01 to 100 s^{-1} and back with an interval of 30 s between curves. Next, oscillatory analyses were conducted to evaluate the viscoelastic properties of the hydrogels and constructs. Through amplitude sweep (1 Hz frequency; 0.1–100% strain) and frequency sweep (1% strain; 0.1–10 Hz) measurements, the values for storage modulus (G'), loss modulus (G"), and loss tangent (tan δ) were obtained. All measurements were performed at 25°C (room temperature), and each experiment was conducted in triplicate to ensure consistency. The rheograms are plotted based on the average of three replicates.

2.11. Electrical conductivity

The electrical conductivity of 5 mL of the hydrogel was determined using a conductivity meter.

2.12. Animals

All experiments using animals and their respective extracted cells were conducted with the approval of the Ethics Committee on the Use of Animals from the Universidade Federal de São Paulo (authorization number CEUA 2428100423). C57BL/6 wild-type male mice were dissected at six weeks of age. In detail, mice were divided into two groups and housed in standard cages (hardwood bedding) in a conventional animal facility (12 h light/dark cycle). Mice were monitored for health and welfare for the whole duration of the experiments. Only mice without signs of stress or discomfort (including hair loss and stereotype behaviors) were included in the study.

2.13. Neural stem cell extraction and neurosphere culture

Briefly, six-week-old mice were euthanized by decapitation, and their brains were removed. The SVZ was dissected, and cells were dissociated mechanically and enzymatically with 0.5% trypsin for 5 min at 37°C. After dissociation, cells were strained in a 40 μm mesh cell strainer and cultured in poly(2-hydroxyethylmethacrylate) (polyHEMA) pre-coated flasks, seeded in a complete medium (DMEM/F12 supplemented with 2% B-27 without vitamin A supplement, 20 ng/mL epidermal growth factor (EGF), 20 ng/mL fibroblast growth factor 2 (FGF2), 1% l-glutamine, 1% penicillin/streptomycin, and 5 μg/mL heparin) and maintained in a humidified incubator at 37°C and 5% CO_2 for three weeks. For propagation, neurospheres (100–200 μm in diameter) were subcultured by mechanical and enzymatic dissociation (described below), and the procedure was repeated on newly formed neurospheres. Half of the medium volume was replaced every 2–3 days.

2.14. Dissociation of neurospheres

Once the neurospheres reached approximately 100–200 μm in diameter, they were dissociated as follows. Briefly, cells were centrifuged at 200×g for 4 min and suspended in Accutase. Dissociation was performed mechanically and enzymatically with repeated up-and-down pipetting of neurospheres in Accutase. Then, the solution was incubated at 37°C for 10 min, and DMEM/F12 was added to the solution, which was then centrifuged at 200×g for 5 min. After discarding the supernatant, dissociated neurospheres were resuspended in the complete medium. Four days after dissociation, neurospheres were immersed into the hydrogel and bioprinted as described below.

2.15. Bioprinting the NSC microenvironment

The bioink was composed of 2×10^4 neurospheres mixed with 1 mL of the hydrogel with or without 1 μM Aβ oligomers. The bioink was transferred to a 5 mL syringe. Bioprinting and crosslinking were performed as described in **Section 2.4**. Thereafter, the constructs were transferred to 24-well plates and cultured with the complete medium at 37°C and 5% CO_2. The medium was changed every 2–3 days. Constructs were evaluated 2, 3, or 8 days after bioprinting.

2.16. Cellular proliferation and viability

The resazurin assay was used to assess cell proliferation at different time points (2, 3, and 8 days after bioprinting). Briefly, 24 h before the determined time point, the medium was substituted by 10% resazurin solution diluted in a complete medium. Samples were incubated at 37°C and 5% CO_2 for 24 h. Subsequently, the solution of each sample was transferred to a new plate for fluorescence measurement using a microplate reader (bottom-reading; excitation: 544 nm; emission: 590 nm). As a negative control, cell-free 10% resazurin solution was incubated for the same period under the same conditions. The results are presented as a percentage of the control.

To observe the distribution and localization of live and dead cells within the neurospheres cultured in the construct, viability was assessed using a Live/Dead assay kit two days after bioprinting. Constructs were incubated with a homogenized solution of calcein AM and ethidium homodimer-1 at room temperature for 15 min. Stained cells were imaged using a confocal laser scanning microscope.

2.17. Neurosphere area

On a phase contrast microscope, constructs were imaged on days 0, 1, 2, 3, 4, 7, and 8 after bioprinting. The area

of neurospheres in the constructs was measured using ImageJ software.

2.18. Morphological aspects

On day 2 after bioprinting, constructs without Aβ oligomers were fixed in 4% paraformaldehyde (PFA) and diluted in dH_2O for 40 min at room temperature. Samples were stained with phalloidin and 4′,6-diamino-2-phenylindole (DAPI) overnight and imaged using a confocal microscope to evaluate the shape and morphology of cells within the construct.

On day 3 after bioprinting, constructs were fixed in 4% PFA and diluted in dH_2O for 40 min at room temperature. Samples were dehydrated, sputter-coated with a thin layer of gold, and observed under a scanning electron microscope, as described in **Section 2.7**.

2.19. Oxidative stress

To evaluate the induction of oxidative stress, cytochemical analysis was performed using CellROX®. On days 2 and 3 after bioprinting, constructs were incubated with 5 μM CellROX® Green Reagent for 30 min at 37°C and 5% CO_2. Green fluorescent neurospheres were imaged using an inverted confocal laser scanning microscope. Fluorescence intensity quantification was performed with ImageJ software.

2.20. Cell differentiation

The differentiation of NSCs into neurons was investigated. Constructs were fixed in 4% PFA, diluted in dH_2O, and permeabilized with dH_2O-0.1% Triton X (dH_2O-T) for 5 min. After three washes, cells were incubated with blocking solution (5% fetal bovine serum in dH_2O-T) for 1 h at room temperature, followed by overnight incubation with anti-Nestin (1:250) and anti-microtubule-associated protein 2 (MAP-2) (1:500) and diluted in blocking solution at 4°C. Constructs were then washed with dH_2O and incubated overnight at 4°C with the corresponding secondary antibodies and fluorescence nuclear counterstain DAPI. Samples were imaged under an inverted confocal laser scanning microscope. Fluorescence intensity quantification was performed using ImageJ software.

2.21. Statistical analyses

Data are expressed as mean ± standard deviation. Statistical significance between groups was evaluated using one-way analysis of variance (ANOVA), followed by Bonferroni post hoc test for multiple comparisons using GraphPad Prism 5.0 (GraphPad Inc., USA). Statistical significance was set at $^{*}p < 0.05$, $^{**}p < 0.01$, $^{***}p < 0.001$, and $^{****}p < 0.0001$. Graphs were plotted in OriginPro 9 (OriginLab Corp, USA).

3. Results and discussion

Traditionally, 2D *in vitro* models cannot capture the complexity of the dynamic brain microenvironment. Therefore, 3D bioprinting offers an innovative platform to emulate the intricate cellular interactions within the NSC niche. NSCs cultured in a non-adherent condition proliferate and form clonal neurospheres that mimic the spatial arrangement and architecture of a neurogenic niche.[22,31] Here, we demonstrate that bioprinted NSCs-derived neurospheres from six-week-old C57BL/6 mice with 1 μM $Aβ_{1–42}$ oligomers could mimic the environmental conditions and cellular organization of neurogenic niche, establishing an innovative model to study SVZ-derived NSCs in AD.

3.1. Biomaterial production and characterization

Previous studies in the literature demonstrate the efficiency of ALG and GEL as a base for biomaterials[21,32–34] and bioprinting processes.[35,36] We tested several hydrogel compositions before selecting the one used in this study, including different concentrations of ALG-GEL, as well as adding agarose, Geltrex™, poly-L-lysine, and laminin (data not disclosed). The printability of the selected hydrogel composition was the most suitable for this study, promoting neurosphere encapsulation, survival, and growth, as well as retention of Aβ. Laminin, one of the main components of Geltrex™ and a potential component to facilitate cell spreading, is known to interact with Aβ[37–39], moreover, photocrosslinking with UV light could damage both cells and Aβ aggregates, consequently, we decided not to use them to produce our constructs.[40–42]

GEL, a collagen-derived protein, changes from gel to liquid state at 35–40°C, losing its ability to gel above such temperatures. It has attracted tremendous attention in bioprinting due to its high biocompatibility and hydrophilicity,[43] especially when mixed with other biomaterials to form double-network constructs with improved printability and cell functions.

In contrast, ALG, a biocompatible, biodegradable, and non-toxic polysaccharide, has better mechanical properties and represents the most commonly bioprinted material.[44] It is easily gelled when crosslinked with a divalent cation, e.g., Ca^{2+}, forming rigid hydrogels, ensuring long-term morphological stability and water retention. However, ALG alone has limited biological inertness, low cell attachment, adhesion properties, and biological activity.[45,46]

Since GEL solutions have desirable viscosity and tunable properties at temperatures lower than 25°C (depending on the polymer concentration and bloom value), blending GEL with ALG, a more viscous polymer, makes it possible to generate hydrogels with good flow and shape-retention

characteristics.[47,48] The presence of GEL facilitates rapid gelation of the construct during the bioprinting process at room temperature (compared to ALG-crosslinked with Ca^{2+} alone) and strengthens the ALG structure in a thermoresponsive manner, consequently improving the initial stability of the hydrogel.[36] Therefore, considering that the optimal polymeric concentration of a hydrogel should range from 10 to 20%,[49] our formulation consisted of 6% ALG + 4% GEL, leveraging the advantages of both polymers and displaying great promise for modeling the NSC environment (Figure S1, Supporting Information; Videos S1–S4, Supporting Information).[28,33]

Figures 1–3 present the characterization of both the hydrogel and the bioprinted construct. The polymeric blend was first printed without cells to determine the best design for printability and to measure wettability, surface roughness/porosity, degradation, and swelling rates. Furthermore, the mechanical and structural characteristics, as well as the electrical conductivity, were evaluated accordingly.

Code 2 (Figure 1A) was designed for the characterization assays. The wettability profile of the bioprinted hydrogel (crosslinked or not) is presented in Figure 1B, displaying snapshots and contact angle measurements every 2 min until complete absorption of a drop of water into the samples. The initial contact angle of the crosslinked hydrogel was 55.3 ± 0.2°, while that of the non-crosslinked hydrogel was 30.4 ± 0.4°. The crosslinked hydrogel fully absorbed the water droplet after 38 min, while the non-crosslinked hydrogel took less than 2 min, indicating that crosslinking is essential to harden the material while maintaining its hydrophilicity.

Hydrogel degradation was monitored for 28 days, with constructs immersed in dH_2O or DMEM/F12 at 37°C and 5% CO_2 (Figure 1E). In both conditions, the constructs maintained approximately 50% of their initial weight (49.6 ± 4.6% in DMEM/F12; 46.9 ± 4.2% in dH_2O) ($p < 0.001$ relative to their respective initial weight), suggesting that, despite the high degradability rate, constructs preserved their 3D structure for nearly a month. The sustained degradation over time might increase the construct's porosity and promote essential biological functions, as cells are more prone to migrate, proliferate, and differentiate when the surrounding network structure is less dense.[50]

Several factors may have influenced the degradability rate of the hydrogel, such as the concentration and duration of $CaCl_2$ crosslinking, the M_W of ALG, the concentration of both polymers, and the swelling rate[35,45,50–53]. Freeman and Kelly[51] reported that low-M_W ALG hydrogels (3.5%) had significant degradation over 21 days in culture, while high-M_W ALG hydrogels (3.5%) displayed little to no degradation. Additionally, Sonaye *et al.*[53] demonstrated that higher concentrations of ALG (8–12%) compared to GEL (6%), along with high crosslinking concentrations of $CaCl_2$ (300–500 mM), enhanced the swelling capacity and decreased the breakdown rate of hydrogels.

Considering the swelling profile (Figure 1F), when constructs were incubated in DMEM/F12 or dH_2O, the percentage of wet mass on day 2 was approximately 40% greater than the dry mass on day 0, demonstrating that constructs are easily tumefied by medium (or dH_2O) absorption. Over time, the swelling rate gradually decreased, as the structures degraded. Sonaye *et al.*[53] reported a similar phenomenon with their ALG-GEL hydrogels. Scaffolds with a greater ALG concentration swelled by 70%, peaking at day 4 to a saturation point, and started to disintegrate on day 8. As a result, their 3D model completely degraded within 14 days of incubation in DMEM. Kaliampakou and colleagues[50] also tested multiple blends of ALG-GEL hydrogels with varying $CaCl_2$ concentrations and crosslinking durations. They described that the best configuration (8% ALG+ 4% GEL; 248 mM $CaCl_2$; 15 min crosslinking) resulted in a hydrogel degradation time of ~20 days with a swelling ratio of 50%.

Unlike the constructs generated in the present study, none of the aforementioned materials was able to maintain their structure for the achieved benchmark duration of 28 days. Thus, the 6% ALG+ 4% GEL hydrogel produced constructs capable of retaining cell culture medium while also facilitating the diffusion of soluble components for supporting cellular growth within the core without entirely degrading the 3D structure in a short period.

The construct's morphology, analyzed by SEM, maintained a smooth and uniform surface for up to 14 days (Figure 1C). Polymeric homogeneity represents an important attribute of the hydrogel because heterogeneity in its structure can jeopardize cellular adhesion and survival due to the formation of polymeric clumps and cytotoxic aggregates.[54]

The size loss displayed in Figure 1D could be attributable to GEL thermal stability, as it can liquefy and release from the construct when incubated at 37°C.[52,55] Despite this, our hydrogel lasted longer than any ALG-GEL blend cited in this section, indicating that this composition delayed GEL release from the scaffolds by trapping it within the crosslinked ALG blocks.[55]

Rheological analysis was performed to investigate the fluidity and viscoelastic behavior of the hydrogel, as well as its viscosity under constant shear stress and strain (Figure 2). These assessments can provide key information about the printability of the hydrogel, the impact of forces

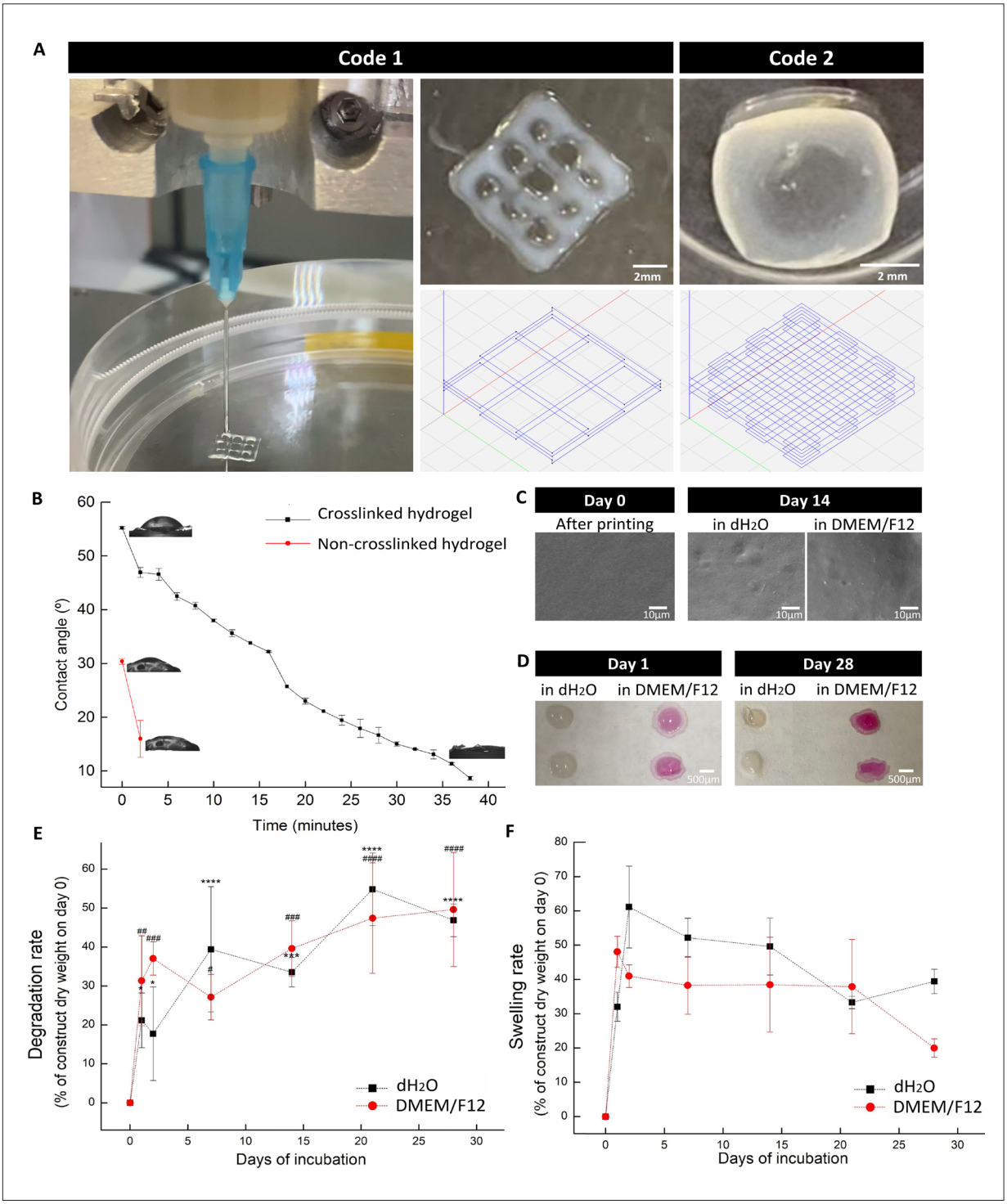


Figure 1. Characterization of the materials. (A) Codes 1 and 2 are designed by G-code and printed: macroscopic view of the bioprinting process, constructs, and G-code design. (B) Contact angle and wettability periodic scheme of crosslinked and non-crosslinked constructs (n = 3 per group). (C) SEM micrographs of the constructs immediately after printing and 14 days after immersion in dH_2O or DMEM/F12, respectively. (D) Macrographs of dried constructs after immersion in dH_2O or DMEM/F12 for 1 and 28 days, respectively. (E) Degradation rate of crosslinked constructs immersed in dH_2O or DMEM/F12 for up to 28 days (n = 4 per group, per period) ($^{*}p < 0.5$; $^{***}p < 0.001$; $^{****}p < 0.0001$; $^{\#\#}p < 0.1$; $^{\#\#\#}p < 0.001$; and $^{\#\#\#\#}p < 0.0001$, compared to the individual mass of the constructs after printing at day 0) (F) Swelling rate of crosslinked constructs immersed in dH_2O or DMEM/F12 for up to 28 days. Scale bars: 2µm (A); 10 µm (E); and 500 µm (F). Abbreviations: dH_2O: Distilled water; DMEM/F12: Dulbecco's modified eagle medium/nutrient mixture F-12; and SEM: scanning electron microscopy.

required for extrusion on its structure, and its ability to recover post-extrusion, maintaining the original shape of the 3D-bioprinted material.[56] Mechanical and rheological characterizations are also fundamental for understanding the influence of hydrogel network structures on the biological properties in the 3D-bioprinted model.[56,57] Nevertheless, according to a systematic review,[58] only 12.1% out of the 118 analyzed papers performed rheological characterization or detailed the viscosity of the hydrogels developed for 3D bioprinting.

A continuous shear rate sweep was performed to simulate the shear stress that the bioink undergoes in a 3D extrusion bioprinting process as it passes through the nozzle. The flow behavior and viscosity of the hydrogel obtained in this analysis are plotted as rheograms (Figure 2A and B). The ALG-GEL hydrogel behaved as a non-Newtonian fluid with pseudoplastic behavior and thixotropy. A pseudoplastic fluid (also called a shear-thinning material) exhibits a decrease in viscosity when the shear rate increases[59,60] which is crucial for 3D printing since the viscosity of the hydrogel decreases during extrusion. This viscosity reduction avoids excessive extrusion pressures that can negatively affect cell viability during the printing process.[61] The hydrogel also displayed minimal thixotropy with a narrow hysteresis loop, indicating that after extrusion, the hydrogel will recover its original structure at rest rather than continuing to flow as a fluid.[62]

The presence of yield stress, as depicted in Figure 2B, is another important component. Hydrogels composed of materials with solid-like properties typically have yield stress, making them promising candidates for 3D bioprinting.[63] The hydrogel behaves like a solid when it is at rest, e.g., when the bioink containing the cell suspension is in the syringe. It will not flow unless it is subjected to a specific stress, such as pressing the syringe plunger, that surpasses the yield stress. This behavior enables the hydrogel to be extruded in a controlled manner and rapidly recover its solid-like characteristics after the applied force is removed, right before crosslinking.[56,64]

Although the hydrogel demonstrated flow behavior and a viscosity profile that are critical for 3D bioprinting, the oscillatory studies yielded unexpected results. Figure 2D and E illustrates that the hydrogel behaves as a viscous material ($G'' > G'$) across a wide range of frequencies and strains. In both oscillatory sweeps, the loss modulus (G'') was greater than the storage modulus (G'), indicating that the hydrogel has a fluid structure and may be classified as a viscoelastic liquid.[65] Figure 2E also depicts the phase angle or loss tangent ($\tan \delta = G''/G'$), which confirms these results, where $\tan \delta < 1$ indicates a solid-like state of the hydrogel, and $\tan \delta > 1$ indicates a liquid-like state.[65,66] At low oscillatory strain, the ALG-GEL hydrogel reported $\tan \delta > 3$, which reduced with increasing strain stress but remained greater than 1. As the $\tan \delta$ value approached 1 (upon 60% strain), the hydrogel complex viscosity increased, indicating a potential transition from a liquid-like to a solid-like state (where G' dominates G'' and $\tan \delta < 1$) (Figure 2F).

To assess the mechanical strength of the hydrogel composition before and after crosslinking with 2% $CaCl_2$ solution (construct), the storage modulus and phase angle of the hydrogel and the construct were determined at 1 Hz frequency and 1% strain, respectively. Figure 2G and H indicates that constructs had G' values nearly tenfold higher than the hydrogel (10 kPa), suggesting that the presence of an ionic crosslinker promoted the formation of a harder/stiffer structure with elastic character ($\tan \delta < 1$), most likely due to interactions between Ca^{2+} ions and ALG chains.[67] Although the presence of GEL may enhance the biological and physicochemical properties of ALG due to the tripeptide Arg-Gly-Asp (RGD) sequence that facilitates cell attachment,[68,69] the uncrosslinked hydrogel did not present viscoelastic solid-gel behavior ($G' < 10$ Pa; $\tan \delta > 1$), possibly due to weak internal chemical bonds between the two biopolymers.

The hydrogel developed in the present study exhibited viscoelastic characteristics ($G' < G''$ $\tan \delta > 1$) that differ from other ALG-GEL hydrogels reported in the literature. Several studies characterize these hydrogels as having gel-like behavior and elastic mechanical characteristics.[70–73] However, when comparing these results, various aspects must be considered, the most important of which is the GEL: ALG ratio. Blending GEL with ALG boosts the hydrogel's viscosity and elastic behavior, as the ideal mechanical characteristics of ALG hydrogels are heavily influenced by the polymer's molecular weight and concentration, as well as the ionic crosslinker used.[72,74,75] Furthermore, some researchers noted that cooling the hydrogels before printing could result in overall gel properties that are more suitable for higher print resolution due to GEL's thermoresponsive qualities.[76]

Chung *et al.*[76] described that GEL hydrogels with low ALG concentration (2%) behave like fluids ($G'' > G'$) at room temperature (25°C) or higher, consistent with our findings. Maihemuti *et al.*[77] demonstrated that when fish GEL is blended with ALG, the printability is determined by the concentration of ALG rather than the GEL itself, the finding of which supports our results. In their study, hydrogels were only printable and stable when they included 6% ALG, which kept the viscosity within a printable range that was neither too high to extrude nor too low to maintain the shape.

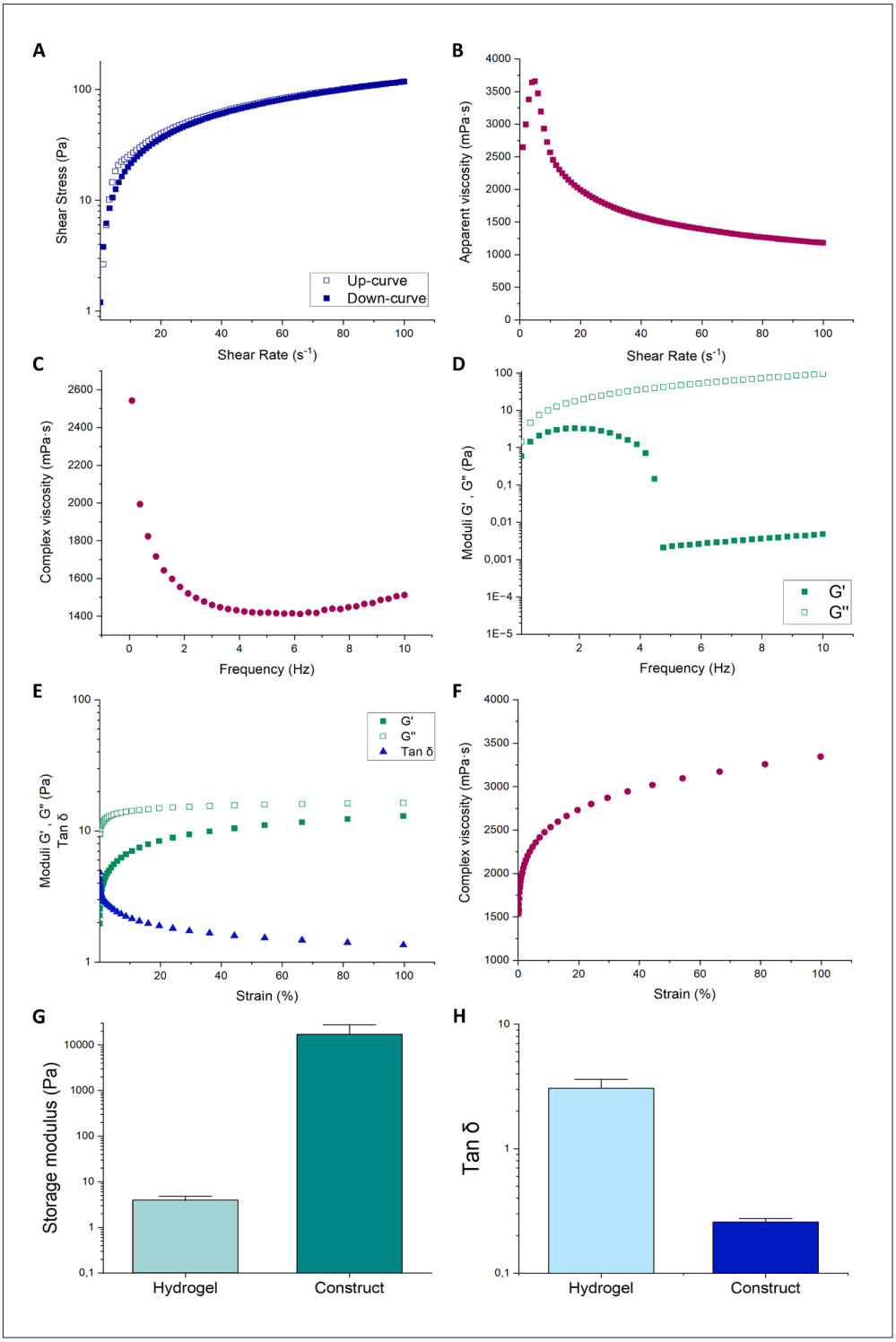


Figure 2. Rheological characterization of the materials. (A) Flow curves of the hydrogel display minimal thixotropy. Filled symbols indicate an upward curve; empty symbols indicate a downward curve. (B) Viscosity as a function of increasing shear rate reveals the shear-thinning behavior of the hydrogel. (C) Complex viscosity vs. frequency. (D and E) Storage modulus (G'; filled symbols) and loss modulus (G"; empty symbols) obtained from a frequency sweep test (D) and an amplitude sweep test (E) demonstrated the hydrogel's viscous behavior. (E) Oscillatory analysis also revealed that, upon increasing strain stress, the loss factor (tan δ) declined but remained greater than one (tan $\delta > 1$), emphasizing how the hydrogel behaves as a viscous liquid. (F) On the other hand, the complex viscosity rose. (G and H) The storage modulus (G) and loss factor (H) of both hydrogel and construct at frequency = 1 Hz and strain = 1%. All rheological measurements were performed at 25°C. Data are plotted as the mean values from three replicates.

Given that GEL liquefies at 37°C, a hydrogel containing more GEL than ALG would gradually deteriorate during incubation and disintegrate within a few days, shortening the time for cell culture. Therefore, we utilized a hydrogel with greater ALG content to prevent such drawbacks. Although our hydrogel exhibited viscoelastic-liquid behavior throughout our oscillatory rheological measurements, it could still be printed and maintain its original shape post-extrusion, indicating a promising profile for use as a bioink for cellular culture in a 3D environment.

The chemical structure composition of the bioprinted hydrogel (crosslinked or not), the crosslink agent $CaCl_2$, and the polymeric components of the hydrogel, ALG, and GEL, were analyzed by ATR-FTIR spectroscopy (Figure 3A). In the ALG spectrum, the transmission bands at 1600 and 1410 cm^{-1} represent the asymmetric and symmetric vibrations of COO^-, respectively, while the bands at 1090 and 1030 cm^{-1} are attributed to C-O and C-O-C bonds.[78,79] In GEL, the bands observed at 1630, 1543, and 1238 cm^{-1} are attributed to the amide I, II, and III vibration peaks, respectively. The crosslinked hydrogel exhibited all the bands mentioned above. However, the amide I band of GEL is obscured by the strong absorption band at 1600 cm^{-1} of ALG, attributed to the asymmetric stretching of the COO^- vibration, and shifted to a discretely lower wavelength, suggesting that there was an interaction between the positive charges of the amino group of GEL and the negative charges of the terminal COO^- groups of ALG. Additionally, as there was more ALG than GEL in the hydrogel, the characteristic bands of GEL diffused with reducing chain order. Notably, crosslinking with $CaCl_2$ did not modify the main structures of the hydrogel.

As our primary goal is to develop a 3D model for AD, we investigated whether the presence of Aβ in the hydrogel composition would affect its structure. In Figure 3B and C, we present the characterization of the Aβ structure alone and the structure after incorporation into the hydrogel with neurospheres as oligomeric/fibrillary structures. The main amide I band (1700–1600 cm^{-1}) of the Aβ peptide backbone is correlated with oligomer size, where larger oligomers are associated with lower wavenumbers.[80] The amide I band of Aβ was at 1625 cm^{-1}, representing Aβ oligomeric arrangement.[81–83] This is an important feature once monomeric Aβ is found in healthy brains. However, oligomers and fibrils are toxic and are the components of amyloid plaques, one of the AD hallmarks.[12,84,85] The amyloid or senile plaques are responsible for increasing oxidative stress, contributing to neuronal dysfunction, disruption of synaptic function, compromising neuroplasticity, decreasing memory formation, and inducing neuroinflammation.

The electrical conductivity of the hydrogel was also evaluated. This parameter is essential for understanding the physicochemical relationship between biological and artificial systems,[86] mimicking physiological electrical processes. *In vivo*, electrical conductivity facilitates neuronal communication[87,88] and directs NSC maturation into functional neuronal networks.[89] Even without externally applied electric fields, conductive hydrogels promote neurite outgrowth and NSC differentiation, efficiently contributing to the native CNS support for neural cells.[90] At room temperature, the hydrogel we produced has an electrical conductivity of 27.46 mS/cm. Conductivity measurements for native CNS tissues (matrix and cells) ranged from 2 to 7 mS/cm,[89] indicating a closer conductivity of the bioink to the brain tissue. High-conductive biomaterials for neural applications could reach up to 17 S/cm[91] to specifically electro-stimulate NSCs and up to 7500 S/cm for further biomedical applications.[92]

3.2. Aβ oligomers incorporated into the bioink induce a decrease in cell viability and an increase in oxidative stress

Neurospheres are free-floating populations derived from neural stem and progenitor cells isolated from the neurogenic niches (dentate gyrus of the hippocampus or the SVZ).[93] In the constructs we produced, Aβ was incorporated into the bioink rather than inside the neurospheres, aiming at mimicking senile plaques distributed within the neurogenic niches and in the brain parenchyma of AD patients as extracellular deposits. The neurosphere structure was maintained in the bioink, and Aβ oligomers were retained within the hydrogel, simulating one of the pathological features of AD, i.e., the deposition and accumulation of Aβ in the extracellular microenvironment.

Simpson *et al.*[94] demonstrated that Aβ aggregates more readily in a 3D environment of collagen hydrogel than in 2D, suggesting that a 3D environment may increase Aβ-Aβ interactions, accelerating aggregation and shifting Aβ organization from oligomers to fibril. According to the authors, Aβ aggregation kinetics is fundamentally different in 3D structures compared to a 2D environment.

A critical issue in modeling the neural tissue is optimizing cell density to ensure that they will be properly preserved within the construct and viable after printing.[95] Moreover, to achieve optimal printability and provide a proper 3D matrix, cells must be compatible with the hydrogel to proliferate and/or differentiate within it. It is recognized that cytoviability can be reduced by extrusion-based bioprinting due to the high shear force exerted on the cells by the printing nozzles.[96] Using code 1 (Table 2; Figure 1A), we demonstrate that the total area of the neurospheres

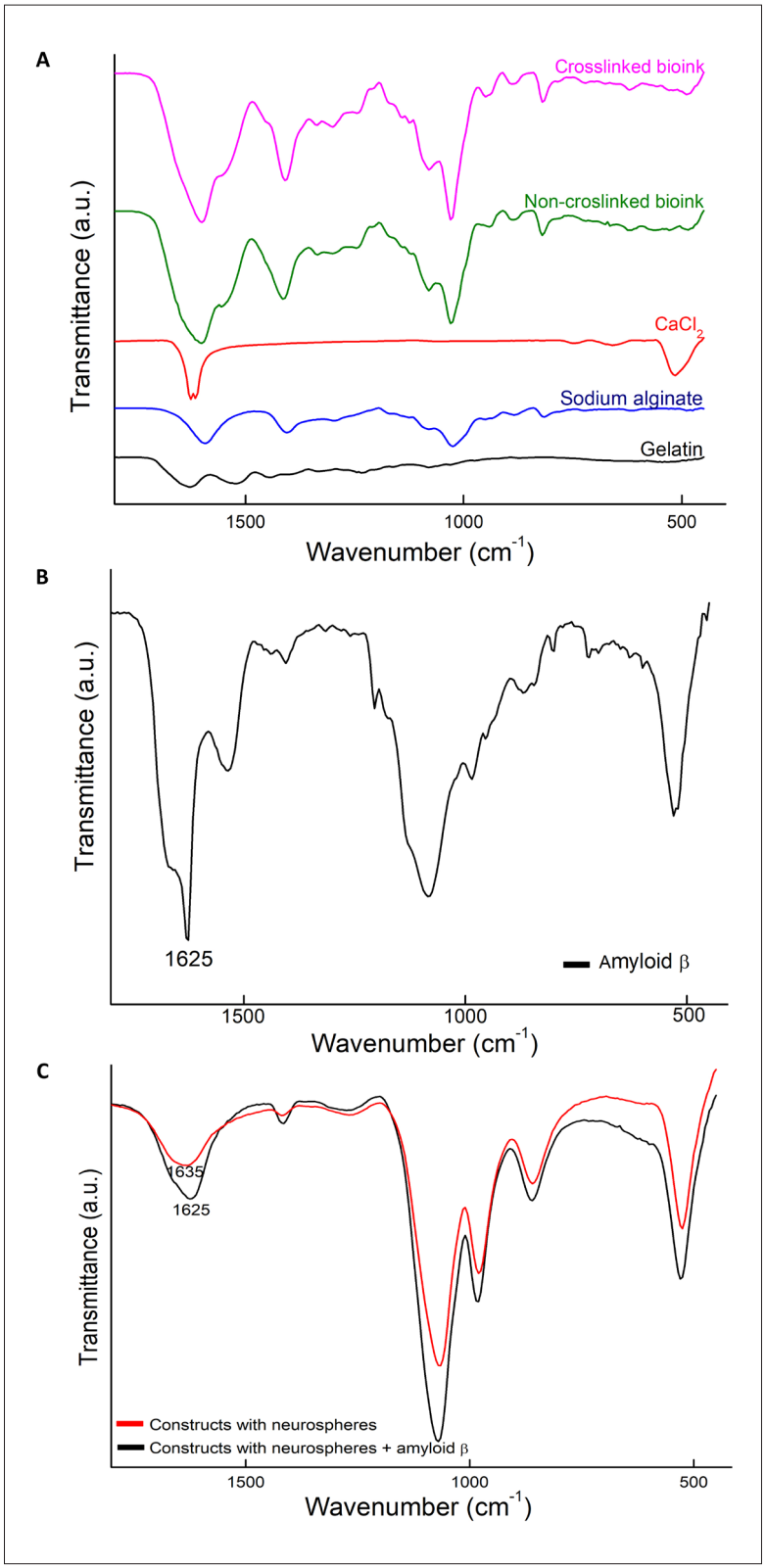


Figure 3. Attenuated total reflectance-Fourier transform infrared (ATR-FTIR) spectra of (A) constructs crosslinked (magenta) and non-crosslinked (green) with $CaCl_2$, $CaCl_2$ alone (red), and hydrogel components sodium alginate (ALG; blue) and gelatin (GEL; black); (B) oligomerized amyloid β (Aβ); and (C) constructs with neurospheres with and without Aβ oligomers.

bioprinted in the absence of Aβ oligomers increased up to eight days after bioprinting ($p < 0.0001$; day 8 vs. day 0 [immediately after bioprinting]) (Figure 4A and B). This growth in the neurosphere area corresponded to increased cell proliferation (379.8 ± 7.7%) on day 8 compared to day 0 ($p < 0.0001$; immediately after bioprinting) (Figure 4C).

Although a recent study has emphasized the great potential of neurospheres from transgenic animals for evaluating familial AD,[97] in this study, we prioritized the Aβ extracellular oligomers in the 3D model in the NSC environment. This decision was based on the fact that over 95% of AD cases are sporadic instead of familial,[98,99] and *in vitro* models for this form of AD are scarce.

The area of the neurospheres bioprinted in the hydrogel containing Aβ oligomers did not increase over time (Figure 4B). Although there were smaller neurospheres on day 8 compared to day 0 (Figure 4A), the average size did not statistically change. A pronounced negative effect on cell proliferation/viability was observed in neurospheres bioprinted in the hydrogel containing Aβ oligomers (52.7 ± 16.5% for day 3; 8.02 ± 3.1% for day 8; $p < 0.0001$, compared with constructs bioprinted in the hydrogel

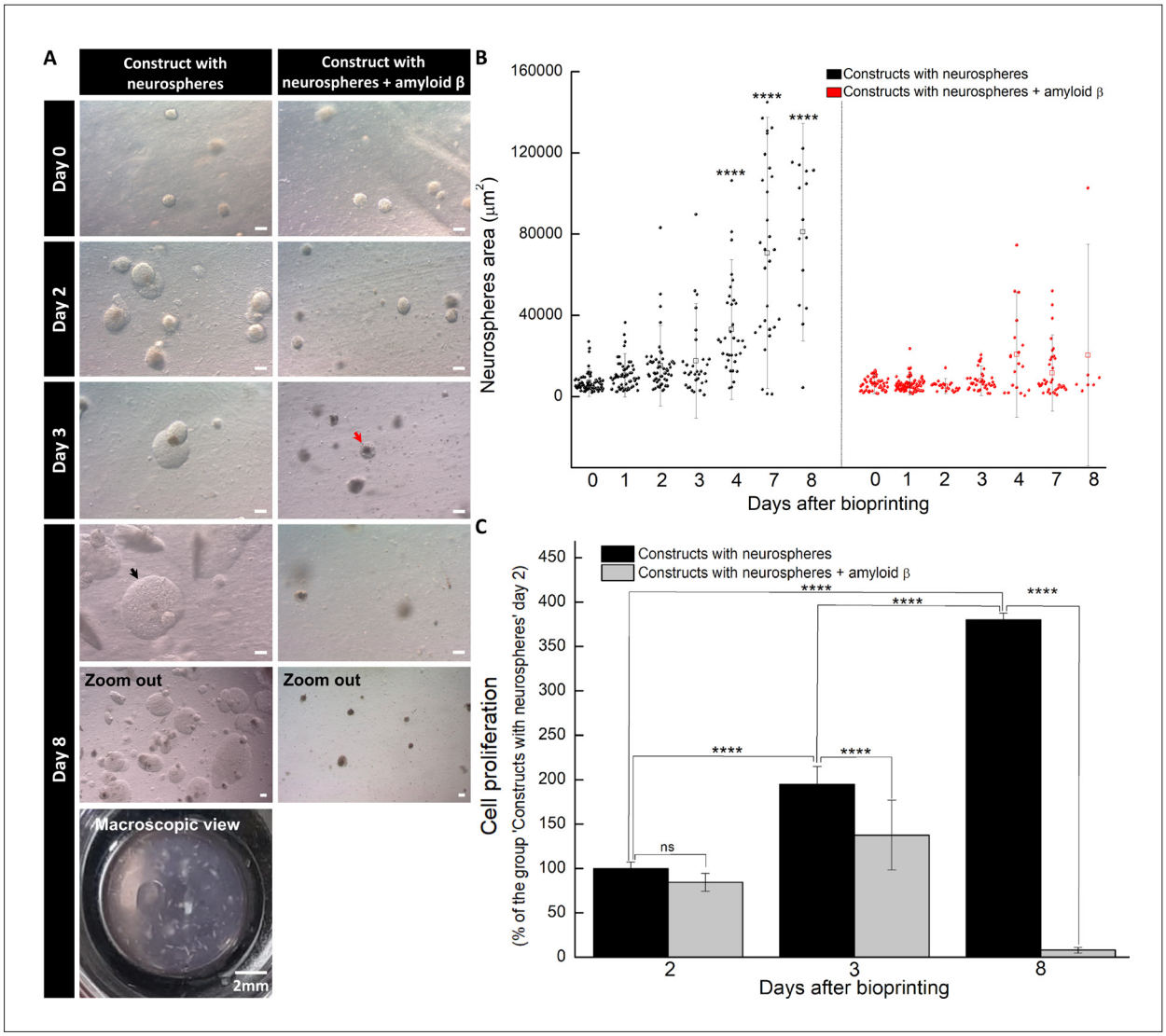


Figure 4. Amyloid β (Aβ) oligomers impact neurosphere area and proliferation in the 3D constructs. (A) Light microscope micrographs of constructs with neurospheres from the subventricular zone (SVZ) of six-week-old C57bl/6 mice, bioprinted with or without 1 μM Aβ oligomers. The black arrow indicates the well-delimited and spheroidal surface of the neurosphere, even eight days after bioprinting. The red arrow demonstrates the necrotic core and small neurospheres three days after bioprinting. Scale bars: 100 μm. (B) Area of neurospheres in constructs with and without Aβ oligomers ($^{****}p < 0.0001$, compared with neurospheres area from day 0). (C) Cell proliferation in constructs with and without Aβ oligomers ($^{****}p < 0.0001$; and ns: non-significant).

without Aβ oligomers and cultured for the same periods) (Figure 4C). These results corroborate a recent study by Esteve *et al.*, which demonstrated that an Aβ-induced increase in reactive oxygen species (ROS) levels led to DNA damage and subsequently induced cell cycle arrest with an increase in cadherin-1 (Cdh1) and a decrease in cyclin B1 and cyclin-dependent kinase 5 (Cdk5)/p35 expression.[100] Moreover, it was demonstrated that exposing neurospheres from prenatal rat cerebral cortical regions to Aβ decreases cell viability and induces degeneration of neurites and apoptosis.[101] Bernabeu-Zornoza *et al.*[102] reported that 1 μM $Aβ_{40}$, the same concentration we used, induced cell death in the human NSC cell line hNS1.

As the neurosphere area and proliferative assay demonstrated small and lowly proliferative cells on day 8 in constructs with Aβ oligomers, the following assays were performed 2–3 days after bioprinting. On day 2 after bioprinting, the live/dead assay demonstrated that cells in the neurospheres within the constructs are viable, and phalloidin staining revealed that the neurospheres have a well-structured spheroid shape and a complex and dense cytoskeleton arrangement (Figure 5A).

Oxidative stress is one of the main pathological events in AD, causing damage to biomolecules, such as neuronal membrane proteins and lipids, affecting their integrity, contributing to neuronal death, and directly impairing NSC proliferation and survival.[103] Aβ oligomers may trigger the generation of ROS, which impairs neurogenesis. There is a vicious cycle whereby Aβ oligomers induce increased ROS levels and oxidative stress, consequently raising Aβ production and leading to AD.[104,105] ROS can cause DNA damage, leading to genomic instability in NSCs. As displayed in Figure 5B and C, oxidative stress significantly increased in constructs containing Aβ oligomers in the bioink as early as 2 days after bioprinting. The same increase in oxidative stress in NSCs exposed to Aβ oligomers was observed by Chiang *et al.*[105], and the oxidative stress also increased the expression of pro-inflammatory cytokines TNF-α and IL-1β. Consequently, the ability of NSCs to proliferate and generate functional neurons may be compromised, contributing to cognitive decline.

Interestingly, oxidative stress can be transiently generated by neurogenesis,[106,107] which could explain the increased ROS production and enhanced neurogenesis in constructs containing Aβ oligomers (Figures 5 and 6). Some evidence indicates that NSCs are well-adapted to protect their host environment from oxidative stress,[108] leading to a synergistic effect between ROS and neurogenesis when the brain is trying to protect or compensate for neuronal loss.

3.3. Exposing cells to Aβ oligomers induces morphological changes and neurogenesis

Three days after bioprinting, an evident morphological change was observed on the surface of constructs with and without Aβ oligomers (Figure 5D). SEM images revealed that constructs without neurotoxic aggregates presented a homogeneous and smooth surface, whereas adding 1 μM Aβ oligomers made the constructs' surface rougher.

A reduction of NSCs (Figure 6; $Nestin^+$ cells, stained in red) and an increase of mature neurons (Figure 6; $MAP\text{-}2^+$ cells, stained in green) within the neurospheres in constructs with Aβ oligomers is presented in Figure 6C ($p < 0.0001$, compared with constructs without Aβ oligomers). The 3D reconstitution of a stained neurosphere displays more mature neurons in the constructs with Aβ oligomers than NSCs, compared to constructs without Aβ oligomers (Figure 6A and B). $Nestin^+$ cells represent 42.4 ± 9.9% of the total stained area of neurospheres in constructs without Aβ oligomers, while in the presence of the aggregates, the percentage decreases to 26.8 ± 9.6% (Figure 6C). Conversely, mature neurons correspond to 14.8 ± 8.6% of the stained area of constructs without Aβ aggregates, while in constructs with Aβ oligomers, mature neurons represent 29.6 ± 9.3% (Figure 6C).

It is important to emphasize that NSCs in the neurospheres were not stimulated to differentiate by adding a differentiation medium, which can also modulate neurogenesis and neurosphere morphology (Figures S2 and S3, Supporting Information). Neurogenesis observed in Figure 6 is mainly induced by the 3D bioink environment or the presence of Aβ. *In vivo*, as AD progresses, the neurotoxicity of Aβ increases, and when coupled with other elements, such as glucose uptake imbalance[9] and dysregulated insulin signaling, adult neurogenesis is increasingly inhibited. Notably, bioprinting Aβ oligomers instead of incorporating them into the neurospheres allowed our model to mimic the extracellular deposit of Aβ aggregates that surround the neurogenic niches in the brain of patients with AD.

Neurospheres used in this study are derived from six-week-old mice, representing adult but not aged conditions. In adults, Aβ oligomers distributed in the 3D environment may stimulate neuronal differentiation as a mechanism to overcome future impairment in AD progression. By increasing oxidative stress, autophagy is induced to meet high energy demands.[109,110] Consequently, neurogenesis is increased as a response to NSC impairment caused by the disease. Another hypothesis is that in earlier stages of AD, Aβ oligomers can activate a compensatory mechanism to replace lost or damaged cells by increasing the differentiation of neuronal progenitors into new neurons. However, as

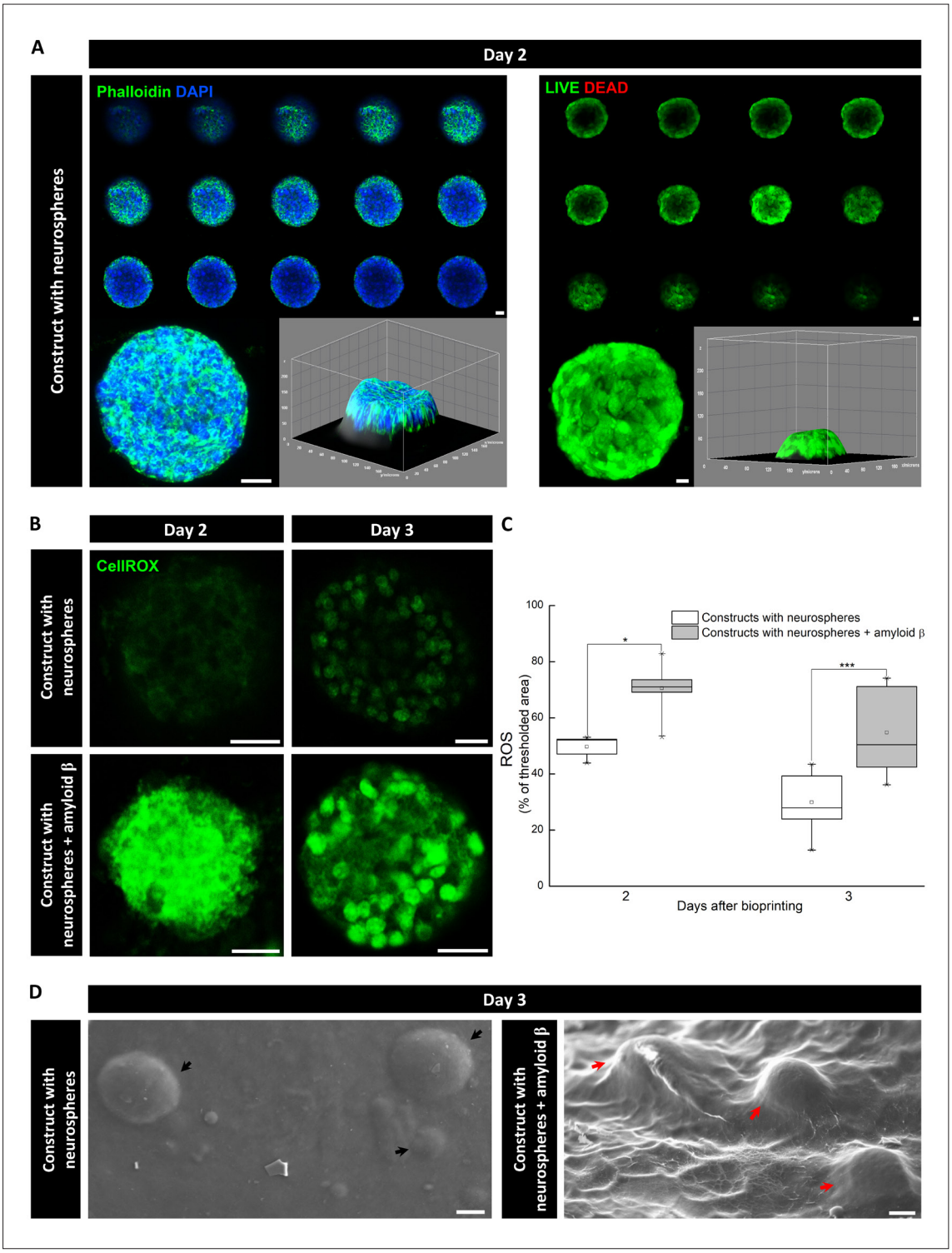


Figure 5. Amyloid β (Aβ) oligomers modify the morphological aspects and induce oxidative stress in the 3D constructs. (A) Montage of stained Z-projection, followed by 3D-plot reconstitution of one representative neurosphere stained with phalloidin/DAPI and LIVE/DEAD kit assay, respectively, two days after bioprinting. (B) Oxidative stress assay in the neurospheres, using the CellROX reagent, on days 2 and 3 after bioprinting. (C) Quantification of reactive oxygen species (ROS) in the neurospheres of the constructs, on days 2 and 3 after bioprinting ($^{*}p < 0.5$; $^{***}p < 0.001$). (D) Scanning electron microscopy (SEM) micrographs of the surface morphology of constructs without and with Aβ oligomers three days after printing. Black arrows indicate neurospheres immersed in a smooth construct surface. Red arrows indicate neurospheres within a rough construct under Aβ oligomers exposure. Scale bars: 20 μm.

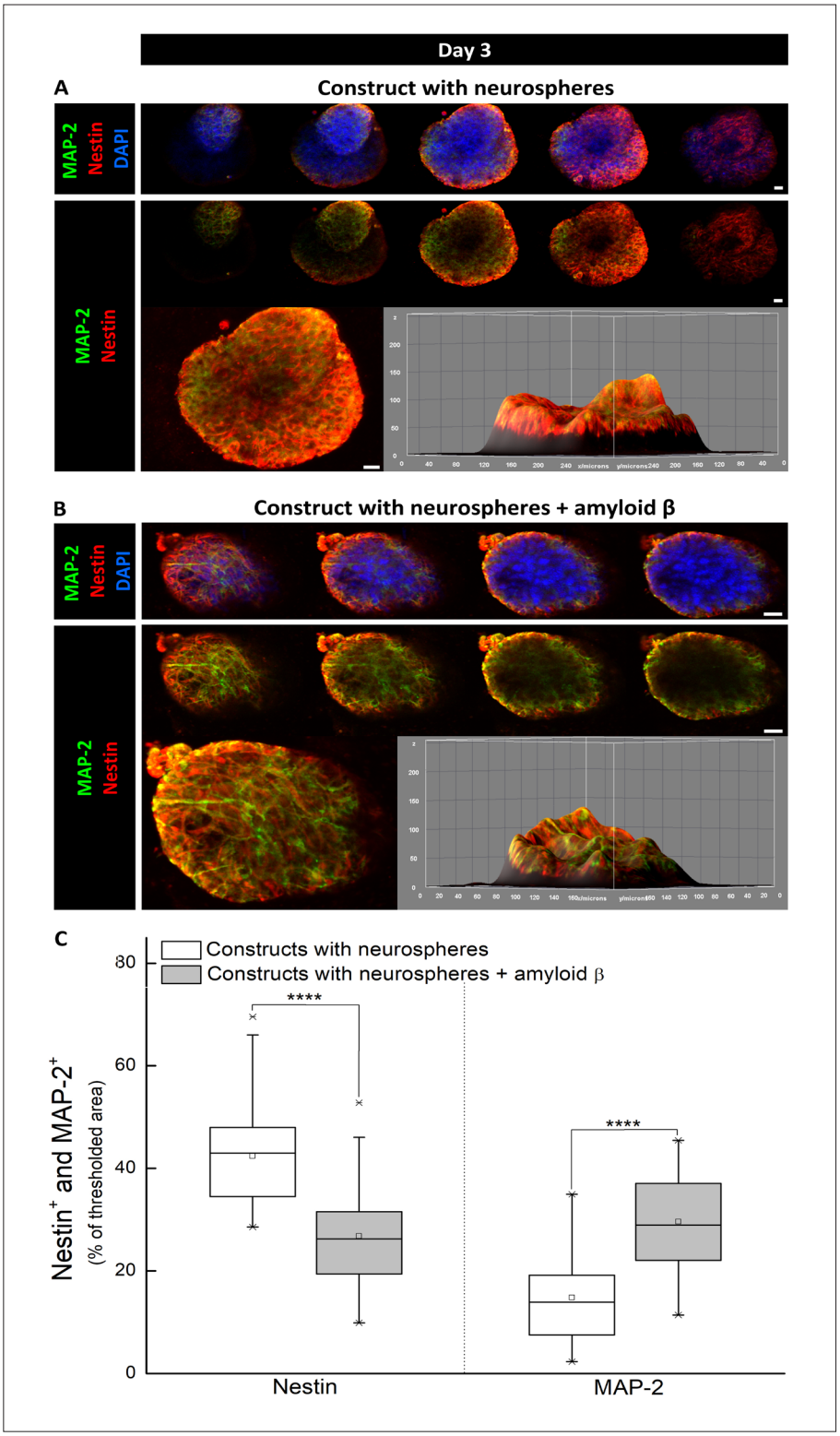


Figure 6. Amyloid β (Aβ) oligomers in 3D constructs induce neural stem cell (NSC) differentiation three days after bioprinting. (A) Construct with neurospheres. (B) Construct with neurospheres + Aβ oligomers. The micrographs indicate a sequence of neurosphere staining, where blue: DAPI (nuclei), green: MAP-2$^+$ (mature neurons), and red: Nestin$^+$ (NSCs), followed by a Z-projection of MAP-2$^+$ and Nestin$^+$ cells. Scale bars: 20 μm. The 3D plots reconstitute the surface of the constructs, where stained cell distribution can be observed from a 3D perspective. (C) Quantification of Nestin$^+$ and MAP-2$^+$ cells in constructs with and without Aβ oligomers ($^{****}p < 0.0001$; × indicates maximum or minimum values; and ◘ indicates the mean).

time passes and senile plaques are formed, the imbalance creates an increasingly neurotoxic environment.[111]

Studies in the literature corroborated the effects of Aβs in promoting gliogenesis[112] or neurogenesis[102] in human NSCs and NSCs from rat hippocampus,[111] impairing NSC proliferation and stimulating microglial proliferation.[8–10,12,113] Another *in vitro* study demonstrated that exosomes secreted from NSCs, but not mature neurons, may confer resistance to the dysfunctional impact of Aβ oligomers,[114] indicating the possible neuroprotective potential of NSCs.[115]

Once incorporated into the 3D microenvironment of our bioprinted neurospheres, Aβ oligomers and other secreted factors may be effectively retained within the matrix environment, mimicking the NSCs environment. Our findings are in accordance with previous reports which indicate that Aβ oligomers promote neurogenesis and neuronal differentiation[85,111] even in the hippocampus of humans with AD.[116] Sotthibundhu *et al.*[12] also observed that Aβ stimulates adult neurogenesis in neurospheres derived from NSCs extracted from the SVZ of two-month-old mice.

Although it has been demonstrated that higher levels of Aβ monomers, oligomers, and fibrils in the brain microenvironment of individuals with amyloidosis-β-induced oxidative stress have a negative effect on endogenous neurogenesis,[117] AD is a progressive and dynamic disease. It is plausible that an increase in neuronal differentiation is followed by an overall decline as Aβ aggregates and loses its neurogenic-inducer functions.[109] Consequently, neurogenesis is differentially regulated throughout the disease, possibly contributing to its progression.

While most AD studies focus on hippocampal neurogenesis in older mice (2–10 months) with AD genotype and demonstrate impaired neurogenesis,[3] it is essential to explore diverse brain regions. In this regard, engineering adult NSCs niche is a valuable tool.[118] Here, we fabricated a 3D model of the adult SVZ-NSCs environment in AD. Although cell viability is impaired and oxidative stress is raised, NSCs differentiate more into neurons when exposed to Aβ oligomers, and we presume this could be a compensatory mechanism of the neurogenic niche, which can be further investigated and tested using the bioprinted model we developed.

4. Conclusion

The constructs we fabricated and characterized successfully reproduced the NSC environment of AD with Aβ oligomer modulation, subsequently decreasing cell viability, increasing oxidative stress, and inducing neuronal differentiation of NSCs. We explored the application of 3D bioprinting to engineer a physiologically relevant model that mimics the cellular composition and dynamic interactions observed in the adult neurogenic niche, highlighting the different pathways of AD.

Acknowledgments

The authors would like to thank Clara Pompeu Ferreira (Universidade Federal de São Paulo) for providing the neurospheres, and MSc. Henrique Correa and Prof. Dr. Beatriz O. Monteiro (Universidade Federal de São Paulo) for providing Aβ oligomers. We are grateful to the technicians, MSc. Priscila M. S. C. M. Leite and Dr. Angela A. M. Vieira (Instituto de Pesquisa e Desenvolvimento, IP&D, Universidade do Vale do Paraíba), for their assistance with SEM and FTIR. We are grateful to Prof. Dr. Fabiana Perrechil Bonsanto (Laboratory of Biotechnology and Natural Products, BioNat, Universidade Federal de São Paulo), for providing the rheometer for our rheological analysis. We thank the technicians, Elizabeth N. Kanashiro and Carolina Z. Romera, for their assistance with the confocal microscope (Universidade Federal de São Paulo).

Funding

This study was supported by grants from (i) the São Paulo Research Foundation (FAPESP): Grants 2022/08664-4 (GRS), 2023/08040-3 (NDF), and 2018/12605-8 (MAP); and (ii) the Brazilian National Council for Scientific and Technological Development (CNPq): 406258/2022-8, INCT Model 3D, and 152384/2024-3 (GRS).

Conflict of interest

The authors declare that they have no conflicts of interest. The research was conducted without any commercial or financial relationship.

Author contribution

Conceptualization: Marimelia Aparecida Porcionatto, Geisa Rodrigues Salles
Formal analysis: Geisa Rodrigues Salles
Investigation: All authors
Methodology: Geisa Rodrigues Salles, Natalia Dall'Agnol Ferreira, Paula Scanavez Ferreira
Writing – original draft: All authors
Writing – review & editing: All authors

Ethics approval and consent to participate

The Ethics Committee on the Use of Animals from the Universidade Federal de São Paulo (CEUA/UNIFESP;

Authorization number 2428100423) approved all experimental procedures in this study.

Consent for publication

Not applicable.

Availability of data

Data are available from the corresponding authors upon reasonable request.

References

1. Moreno-Jiménez EP, Flor-García M, Terreros-Roncal J, et al. Adult hippocampal neurogenesis is abundant in neurologically healthy subjects and drops sharply in patients with Alzheimer's disease. *Nat Med*. 2019;25(4):554-560. doi: 10.1038/s41591-019-0375-9
2. Selkoe DJ. Alzheimer's disease: genes, proteins, and therapy. *J Physiol Rev*. 2001;81(2):741-766. doi: 10.1152/physrev.2001.81.2.741
3. Li Puma DD, Piacentini R, Grassi C. Does impairment of adult neurogenesis contribute to pathophysiology of Alzheimer's disease? A still open question. *J Front Mol Neurosci*. 2021;13:578211. doi: 10.3389/fnmol.2020.578211
4. Kim HS, Shin SM, Kim S, Nam Y, Yoo A, Moon M. Relationship between adult subventricular neurogenesis and Alzheimer's disease: pathologic roles and therapeutic implications. *Front Aging Neurosci*. 2022;14:1002281. doi: 10.3389/fnagi.2022.1002281
5. Selkoe DJ. Alzheimer's disease. *Cold Spring Harb Perspect Biol*. 2011;3:a004457. doi: 10.1101/cshperspect.a004457
6. Culig L, Chu X, Bohr VA. Neurogenesis in aging and age-related neurodegenerative diseases. *Ageing Res Rev*. 2022;78:101636. doi: 10.1016/j.arr.2022.101636
7. Scopa C, Marrocco F, Latina V, et al. Impaired adult neurogenesis is an early event in Alzheimer's disease neurodegeneration, mediated by intracellular Aβ oligomers. *Cell Death Differ*. 2020;27(3):934-948. doi: 10.1038/s41418-019-0409-3
8. Salles GN, Calió ML, Afewerki S, et al. Prolonged drug-releasing fibers attenuate Alzheimer's disease-like pathogenesis. *ACS Appl Mater Interfaces*. 2018;10(43):36693-36702. doi: 10.1021/acsami.8b12649
9. Salles GN, Calió ML, Hölscher C, Pacheco-Soares C, Porcionatto M, Lobo AO. Neuroprotective and restorative properties of the GLP-1/GIP dual agonist DA-JC1 compared with a GLP-1 single agonist in Alzheimer's disease. *Neuropharmacology*. 2020;162:107813. doi: 10.1016/j.neuropharm.2019.107813
10. Calió ML, Mosini AC, Marinho DS, et al. Leptin enhances adult neurogenesis and reduces pathological features in a transgenic mouse model of Alzheimer's disease. *Neurobiol. Dis*. 2021;148:105219. doi: 10.1016/j.nbd.2020.105219
11. Diaz Brinton R, Ming Wang J. Therapeutic potential of neurogenesis for prevention and recovery from Alzheimer's disease: allopregnanolone as a proof of concept neurogenic agent. *Curr Alzheimer Res*. 2006;3(3):185-190. doi: 10.2174/156720506777632817
12. Sotthibundhu A, Li Q-X, Thangnipon W, Coulson EJ. Aβ1–42 stimulates adult SVZ neurogenesis through the p75 neurotrophin receptor. *Neurobiol Aging*. 2009;30(12):1975-1985. doi: 10.1016/j.neurobiolaging.2008.02.004
13. Bernabeu-Zornoza A, Coronel R, Palmer C, Monteagudo M, Zambrano A, Liste I. Physiological and pathological effects of amyloid-β species in neural stem cell biology. *Neural Regen Res*. 2019;14(12):2035-2042. doi: 10.4103/1673-5374.262571
14. Walus K, Beyer S, Willerth SM. Three-dimensional bioprinting healthy and diseased models of the brain tissue using stem cells. *Curr Opin Biomed Eng*. 2020; 14:25-33. doi: 10.1016/j.cobme.2020.03.002
15. de Melo BAG, Jodat YA, Cruz EM, Benincasa JC, Shin SR, Porcionatto MA. Strategies to use fibrinogen as bioink for 3D bioprinting fibrin-based soft and hard tissues. *Acta Biomater*. 2020;117:60-76. doi: 10.1016/j.actbio.2020.09.024
16. de Melo BAG, Benincasa JC, Cruz EM, Maricato JT, Porcionatto MA. 3D culture models to study SARS-CoV-2 infectivity and antiviral candidates: From spheroids to bioprinting. *Biomed J*. 2021;44(1):31-42. doi: 10.1016/j.bj.2020.11.009
17. Cruz EM, Machado LS, Zamproni LN, et al. A gelatin methacrylate-based hydrogel as a potential bioink for 3D bioprinting and neuronal differentiation. *Pharmaceutics*. 2023;15(2):627. doi: 10.3390/pharmaceutics15020627
18. Knowlton S, Anand S, Shah T, Tasoglu S. Bioprinting for neural tissue engineering. *Trends Neurosci*. 2018; 41(1):31-46. doi: 10.1016/j.tins.2017.11.001
19. Cadena M, Ning L, King A, et al. 3D bioprinting of neural tissues. *Adv Healthc Mater*. 2021;10(15):2001600. doi: 10.1002/adhm.202001600
20. Parra-Cantu C, Li W, Quiñones-Hinojosa A, Zhang YS. 3D bioprinting of Glioblastoma model. *J 3D Print Med*. 2020;4(2):113-125. doi: 10.2217/3dp-2019-0027
21. Gao T, Gillispie GJ, Copus JS, et al. Optimization of gelatin–alginate composite bioink printability using rheological

parameters: A systematic approach. *Biofabrication*. 2018;10(3):034106.
doi: 10.1088/1758-5090/aacdc7

22. Ioannidis K, Angelopoulos I, Gakis G, et al. 3D reconstitution of the neural stem cell niche: connecting the dots. *Front Bioeng Biotechnol*. 2021;9:705470.
doi: 10.3389/fbioe.2021.705470

23. Centeno EGZ, Cimarosti H, Bithell A. 2D versus 3D human induced pluripotent stem cell-derived cultures for neurodegenerative disease modelling. *Mol Neurodegener*. 2018;13:1-15.
doi: 10.1186/s13024-018-0258-4

24. Ioannidis K, Danalatos RI, Champeris Tsaniras S, et al. A custom ultra-low-cost 3D bioprinter supports cell growth and differentiation. *Front Bioeng Biotechnol*. 2020;8:580889.
doi: 10.3389/fbioe.2020.580889

25. Benwood C, Walters-Shumka J, Scheck K, Willerth SM. 3D bioprinting patient-derived induced pluripotent stem cell models of Alzheimer's disease using a smart bioink. *Bioelectron Med*. 2023;9(1):10.
doi: 10.1186/s42234-023-00112-7

26. Bovi dos Santos G, de Lima-Vasconcellos TH, Móvio MI, Birbrair A, Del Debbio CB, Kihara AH. New perspectives in stem cell transplantation and associated therapies to treat retinal diseases: from gene editing to 3D bioprinting. *Stem Cell Rev Rep*. 2024;20(3):722-737.
doi: 10.1007/s12015-024-10689-4

27. Romariz SAA, Sanabria V, da Silva KR, et al. High concentrations of cannabidiol induce neurotoxicity in neurosphere culture system. *Neurotox Res*. 2024; 42(1):14.
doi: 10.1007/s12640-024-00692-5

28. Fantini V, Bordoni M, Scocozza F, et al. Bioink composition and printing parameters for 3D modeling neural tissue. *Cells*. 2019;8(8):830.
doi: 10.3390/cells8080830

29. Zhou X, Cui H, Nowicki M, et al. Three-dimensional-bioprinted dopamine-based matrix for promoting neural regeneration. *ACS Appl Mater Interfaces*. 2018;10(10):8993-9001.
doi: 10.1021/acsami.7b18197

30. Joung D, Truong V, Neitzke CC, et al. 3D printed stem-cell derived neural progenitors generate spinal cord scaffolds. *Adv Funct Mater*. 2018;28(39):1801850.
doi: 10.1002/adfm.201801850

31. Suslov ON, Kukekov VG, Ignatova TN, Steindler DA. Neural stem cell heterogeneity demonstrated by molecular phenotyping of clonal neurospheres. *Proc Natl Acad Sci USA*. 2002;99(22):14506-14511.
doi: 10.1073/pnas.212525299

32. Othman SA, Soon CF, Ma NL, et al. Alginate-gelatin bioink for bioprinting of hela spheroids in alginate-gelatin hexagon shaped scaffolds. Polym Bull. 2021;78:6115-6135.
doi: 10.1007/s00289-020-03421-y

33. Li Z, Huang S, Liu Y, et al. Tuning alginate-gelatin bioink properties by varying solvent and their impact on stem cell behavior. *Sci Rep*. 2018;8(1):8020.
doi: 10.1038/s41598-018-26407-3

34. Cheng L, Yao B, Hu T, et al. Properties of an alginate-gelatin-based bioink and its potential impact on cell migration, proliferation, and differentiation. *Int J Biol Macromol*. 2019;135:1107-1113.
doi: 10.1016/j.ijbiomac.2019.06.017

35. Giuseppe MD, Law N, Webb B, et al. Mechanical behaviour of alginate-gelatin hydrogels for 3D bioprinting. *J Mech Behav Biomed Mater*. 2018;79:150-157.
doi: 10.1016/j.jmbbm.2017.12.018

36. Łabowska MB, Cierluk K, Jankowska AM, Kulbacka J, Detyna J, Michalak I. A review on the adaption of alginate-gelatin hydrogels for 3D cultures and bioprinting. *Materials (Basel, Switzerland)*. 2021;14(4):858.
doi: 10.3390/ma14040858

37. Morgan C, Inestrosa NC. Interactions of laminin with the amyloid ß peptide: implications for Alzheimer's disease. *Braz J Med Biol Res*. 2001;34:597-601.
doi: 10.1590/S0100-879X2001000500006

38. Bronfman FC, Garrido J, Alvarez A, Morgan C, Inestrosa NC. Laminin inhibits amyloid-beta-peptide fibrillation. *Neurosci Lett*. 1996;218(3):201-203.
doi: 10.1016/s0304-3940(96)13147-5

39. Rodin S, Kozin SA, Kechko OI, Mitkevich VA, Makarov AA. Aberrant interactions between amyloid-beta and alpha5 laminins as possible driver of neuronal disfunction in Alzheimer's disease. *Biochimie*. 2020;174: 44-48.
doi: 10.1016/j.biochi.2020.04.011

40. Zhang Z, Wang J, Song Y, Wang Z, Dong M, Liu L. Disassembly of Alzheimer's amyloid fibrils by functional upconversion nanoparticles under near-infrared light irradiation. *Colloids Surf B Biointerfaces*. 2019;181: 341-348.
doi: 10.1016/j.colsurfb.2019.05.053

41. Almenar-Queralt A, Falzone TL, Shen Z, et al. UV irradiation accelerates amyloid precursor protein (APP) processing and disrupts APP axonal transport. *J Neurosci*. 2014;34(9):3320-3339.
doi: 10.1523/jneurosci.1503-13.2014

42. Measey TJ, Gai F. Light-triggered disassembly of amyloid fibrils. *Langmuir*. 2012;28(34):12588-12592.
doi: 10.1021/la302626d

43. Gómez-Guillén MC, Giménez B, López-Caballero MEa, Montero MP. Functional and bioactive properties of collagen and gelatin from alternative sources: a review. *Food Hydrocolloids*. 2011;25(8):1813-1827.
doi: 10.1016/j.foodhyd.2011.02.007

44. Mancha Sánchez E, Gómez-Blanco JC, López Nieto E, et al. Hydrogels for bioprinting: a systematic review of hydrogels

synthesis, bioprinting parameters, and bioprinted structures behavior. *Front Bioeng Biotechnol*. 2020;8:776. doi: 10.3389/fbioe.2020.00776

45. Lee KY, Mooney DJ. Alginate: properties and biomedical applications. *Prog Polym Sci*. 2012;37(1):106-126. doi: 10.1016/j.progpolymsci.2011.06.003
46. Ishiwata R, Iwasa M. Cellular inertia. *Sci Rep*. 2021;11(1):23799. doi: 10.1038/s41598-021-02384-y
47. Derkach SR, Voron'ko NG, Kuchina YA, Kolotova DS. Modified fish gelatin as an alternative to mammalian gelatin in modern food technologies. *Polymers*. 2020;12(12):3051. doi: 10.3390/polym12123051
48. Kokol V, Pottathara YB, Mihelčič M, Perše LS. Rheological properties of gelatine hydrogels affected by flow-and horizontally-induced cooling rates during 3D cryo-printing. *Colloids Surf A Physicochem Eng Asp*. 2021;616:126356. doi: 10.1016/j.colsurfa.2021.126356
49. Liu S, Yang H, Chen D, et al. Three-dimensional bioprinting sodium alginate/gelatin scaffold combined with neural stem cells and oligodendrocytes markedly promoting nerve regeneration after spinal cord injury. *Regen Biomater*. 2022;9:rbac038. doi: 10.1093/rb/rbac038
50. Kaliampakou C, Lagopati N, Pavlatou EA, Charitidis CA. Alginate–gelatin hydrogel scaffolds; an optimization of post-printing treatment for enhanced degradation and swelling behavior. *Gels*. 2023;9(11):857. doi: 10.3390/gels9110857
51. Freeman FE, Kelly DJ. Tuning alginate bioink stiffness and composition for controlled growth factor delivery and to spatially direct MSC fate within bioprinted tissues. *Sci Rep*. 2017;7(1):17042. doi: 10.1038/s41598-017-17286-1
52. Chung JHY, Naficy S, Yue Z, et al. Bio-ink properties and printability for extrusion printing living cells. *Biomater Sci*. 2013;1(7):763-773. doi: 10.1039/C3BM00012E
53. Sonaye SY, Ertugral EG, Kothapalli CR, Sikder P. Extrusion 3D (bio) printing of alginate-gelatin-based composite scaffolds for skeletal muscle tissue engineering. *Materials*. 2022;15(22):7945. doi: 10.3390/ma15227945
54. Hazur J, Detsch R, Karakaya E, et al. Improving alginate printability for biofabrication: establishment of a universal and homogeneous pre-crosslinking technique. *Biofabrication*. 2020;12(4):045004. doi: 10.1088/1758-5090/ab98e5
55. Kim J, Choi YJ, Gal CW, Sung A, Park H, Yun HS. 142Development of an alginate-gelatin bioink enhancing osteogenic differentiation by gelatin release. *Int J Bioprint*. 2023;9(2):660. doi: 10.18063/ijb.v9i2.660
56. Cooke ME, Rosenzweig DH. The rheology of direct and suspended extrusion bioprinting. *APL Bioeng*. 2021;5(1):011502. doi: 10.1063/5.0031475
57. Chimene D, Kaunas R, Gaharwar AK. Hydrogel bioink reinforcement for additive manufacturing: a focused review of emerging strategies. *Adv Mater*. 2020;32(1):e1902026. doi: 10.1002/adma.201902026
58. Mancha Sánchez E, Gómez-Blanco JC, López Nieto E, et al. Hydrogels for bioprinting: a systematic review of hydrogels synthesis, bioprinting parameters, and bioprinted structures behavior. *Front Bioeng Biotechnol*. 2020;8:776. doi: 10.3389/fbioe.2020.00776
59. O'Connell C, Ren J, Pope L, et al. Characterizing bioinks for extrusion bioprinting: printability and rheology. *Methods Mol Biol*. 2020;2140:111-133. doi: 10.1007/978-1-0716-0520-2_7
60. Semba JA, Mieloch AA, Tomaszewska E, Cywoniuk P, Rybka JD. Formulation and evaluation of a bioink composed of alginate, gelatin, and nanocellulose for meniscal tissue engineering. *Int J Bioprint*. 2023;9(1):621. doi: 10.18063/ijb.v9i1.621
61. Schwab A, Levato R, D'Este M, Piluso S, Eglin D, Malda J. Printability and shape fidelity of bioinks in 3D bioprinting. *Chem Rev*. 2020;120(19):11028-11055. doi: 10.1021/acs.chemrev.0c00084
62. Cui R, Li S, Li T, et al. Natural polymer derived hydrogel bioink with enhanced thixotropy improves printability and cellular preservation in 3D bioprinting. *J Mater Chem B*. 2023;11(17):3907-3918. doi: 10.1039/D2TB02786K
63. Mouser VH, Melchels FP, Visser J, Dhert WJ, Gawlitta D, Malda J. Yield stress determines bioprintability of hydrogels based on gelatin-methacryloyl and gellan gum for cartilage bioprinting. *Biofabrication*. 2016;8(3):035003. doi: 10.1088/1758-5090/8/3/035003
64. Venkata Krishna D, Ravi Sankar M. Persuasive factors on the bioink printability and cell viability in the extrusion-based 3D bioprinting for tissue regeneration applications. *Eng Regener*. 2023;4(4):396-410. doi: 10.1016/j.engreg.2023.07.002
65. Herrada-Manchón H, Fernández MA, Aguilar E. Essential guide to hydrogel rheology in extrusion 3D printing: how to measure it and why it matters? *Gels*. 2023;9(7):517. doi: 10.3390/gels9070517
66. Tuladhar S, Clark S, Habib A. Tuning shear thinning factors of 3D bio-printable hydrogels using short fiber. *Materials (Basel, Switzerland)*. 2023;16(2):572. doi: 10.3390/ma16020572
67. Malektaj H, Drozdov AD, deClaville Christiansen JJP. Mechanical properties of alginate hydrogels cross-linked with multivalent cations. *Polymers (Basel)*. 2023;15(14):3012. doi: 10.3390/polym15143012

68. Łabowska MB, Cierluk K, Jankowska AM, Kulbacka J, Detyna J, Michalak IJM. A review on the adaption of alginate-gelatin hydrogels for 3D cultures and bioprinting. *Materials (Basel)*. 2021;14(4):858. doi: 10.3390/ma14040858

69. Shams E, Barzad MS, Mohamadnia S, Tavakoli O, Mehrdadfar AJJoBA. A review on alginate-based bioinks, combination with other natural biomaterials and characteristics. *J Biomater Appl*. 2022;37(2):355-372. doi: 10.1177/08853282221085690

70. Ioannidis K, Danalatos RI, Champeris Tsaniras S, et al. A custom ultra-low-cost 3D bioprinter supports cell growth and differentiation. *Front Bioeng Biotechnol*. 2020;8:580889. doi: 10.3389/fbioe.2020.580889

71. Leonardo M, Prajatelistia E, Judawisastra HJB. Alginate-based bioink for organoid 3D bioprinting: a review. *Bioprinting*. 2022;28:e00246. doi: 10.1016/j.bprint.2022.e00246

72. Mondal A, Gebeyehu A, Miranda M, et al. Characterization and printability of Sodium alginate-gelatin hydrogel for bioprinting NSCLC co-culture. *Sci Rep*. 2019; 9(1):19914. doi: 10.1038/s41598-019-55034-9

73. Hiller T, Berg J, Elomaa L, et al. Generation of a 3D liver model comprising human extracellular matrix in an alginate/gelatin-based bioink by extrusion bioprinting for infection and transduction studies. *Int J Mol Sci*. 2018;19(10):3129. doi: 10.3390/ijms19103129

74. Di Giuseppe M, Law N, Webb B, et al. Mechanical behaviour of alginate-gelatin hydrogels for 3D bioprinting. *J Mech Behav Biomed Mater*. 2018;79:150-157. doi: 10.1016/j.jmbbm.2017.12.018

75. Freeman FE, Kelly DJJSr. Tuning alginate bioink stiffness and composition for controlled growth factor delivery and to spatially direct MSC fate within bioprinted tissues. *Sci Rep*. 2017;7(1):17042. doi: 10.1038/s41598-017-17286-1

76. Chung JH, Naficy S, Yue Z, et al. Bio-ink properties and printability for extrusion printing living cells. *Biomater Sci*. 2013;1(7):763-773. doi: 10.1039/C3BM00012E

77. Maihemuti A, Zhang H, Lin X, et al. 3D-printed fish gelatin scaffolds for cartilage tissue engineering. *J Bioact Mater*. 2023;26:77-87. doi: 10.1016/j.bioactmat.2023.02.007

78. Derkach SR, Voron'ko NG, Sokolan NI, Kolotova DS, Kuchina YA. Interactions between gelatin and sodium alginate: UV and FTIR studies. *J Dispers Sci Technol*. 2020;41(5):690-698. doi: 10.1080/01932691.2019.1611437

79. Costa HdS, Dias MR. Alginate/bioactive glass beads: synthesis, morphological and compositional changes caused by SBF immersion method. *Mater Res*. 2021;24(4): e20200587. doi: 10.1590/1980-5373-MR-2020-0587

80. Vosough F, Barth A. Characterization of homogeneous and heterogeneous amyloid-β42 oligomer preparations with biochemical methods and infrared spectroscopy reveals a correlation between infrared spectrum and oligomer size. *ACS Chem Neurosci*. 2021;12(3):473-488. doi: 10.1021/acschemneuro.0c00642

81. Fraser PE, Nguyen JT, Inouye H, et al. Fibril formation by primate, rodent, and Dutch-hemorrhagic analogues of Alzheimer amyloid beta-protein. *Biochemistry*. 1992;31(44):10716-10723. doi: 10.1021/bi00159a011

82. Zandomeneghi G, Krebs MR, McCammon MG, Fändrich M. FTIR reveals structural differences between native beta-sheet proteins and amyloid fibrils. *Protein Sci*. 2004;13(12):3314-3321. doi: 10.1110/ps.041024904

83. Sarroukh R, Goormaghtigh E, Ruysschaert J-M, Raussens V. ATR-FTIR: A "rejuvenated" tool to investigate amyloid proteins. *Biochim Biophys Acta*. 2013;1828(10):2328-2338. doi: 10.1016/j.bbamem.2013.04.012

84. Yankner BA, Duffy LK, Kirschner DA. Neurotrophic and neurotoxic effects of amyloid beta protein: reversal by tachykinin neuropeptides. *Science (New York, NY)*. 1990;250(4978):279-282. doi: 10.1126/science.2218531

85. Mazur-Kolecka B, Golabek A, Nowicki K, Flory M, Frackowiak J. Amyloid-beta impairs development of neuronal progenitor cells by oxidative mechanisms. *Neurobiol Aging*. 2006;27(9):1181-1192. doi: 10.1016/j.neurobiolaging.2005.07.006

86. Wang X, Sun X, Gan D, et al. Bioadhesive and conductive hydrogel-integrated brain-machine interfaces for conformal and immune-evasive contact with brain tissue. *Matter*. 2022;5(4):1204-1223. doi: 10.1016/j.matt.2022.01.012

87. Pettikiriarachchi JTS, Parish CL, Shoichet MS, Forsythe JS, Nisbet DR. Biomaterials for brain tissue engineering. *Aust J Chem*. 2010;63(8):1143-1154. doi: 10.1071/CH10159

88. Sadeghi A, Afshari E, Hashemi M, Kaplan D, Mozafari M. Brainy biomaterials: latest advances in smart biomaterials to develop the next generation of neural interfaces. *Curr Opin Biomed Eng*. 2023;25:100420. doi: 10.1016/j.cobme.2022.100420

89. Bierman-Duquette RD, Safarians G, Huang J, et al. Engineering tissues of the central nervous system: interfacing conductive biomaterials with neural stem/progenitor cells. *Adv Healthc Mater*. 2022;11(7):2101577. doi: 10.1002/adhm.202101577

90. Modulevsky DJ, Cuerrier CM, Pelling AE. Biocompatibility of subcutaneously implanted plant-derived cellulose biomaterials. *PloS One*. 2016;11(6):e0157894. doi: 10.1371/journal.pone.0157894

91. Sordini L, Garrudo FFF, Rodrigues CAV, et al. Effect of electrical stimulation conditions on neural stem cells differentiation on cross-linked PEDOT: PSS films. *Front Bioeng Biotechnol*. 2021;9:591838. doi: 10.3389/fbioe.2021.591838

92. Kaur G, Adhikari R, Cass P, Bown M, Gunatillake P. Electrically conductive polymers and composites for biomedical applications. *RSC Adv*. 2015;5(47):37553-37567. doi: 10.1039/C5RA01851J

93. Jensen JB, Parmar M. Strengths and limitations of the neurosphere culture system. *Mol Neurobiol*. 2006;34(3): 153-161. doi: 10.1385/mn:34:3:153

94. Simpson LW, Szeto GL, Boukari H, Good TA, Leach JB. Collagen hydrogel confinement of Amyloid-β (Aβ) accelerates aggregation and reduces cytotoxic effects. *Acta Biomater*. 2020;112:164-173. doi: 10.1016/j.actbio.2020.05.030

95. Li YE, Jodat YA, Samanipour R, et al. Toward a neurospheroid niche model: optimizing embedded 3D bioprinting for fabrication of neurospheroid brain-like co-culture constructs. *Biofabrication*. 2020;13:015014. doi: 10.1088/1758-5090/abc1be

96. Sears NA, Seshadri DR, Dhavalikar PS, Cosgriff-Hernandez E. A review of three-dimensional printing in tissue engineering. *Tissue Eng Part B Rev*. 2016;22(4):298-310. doi: 10.1089/ten.TEB.2015.0464

97. Pillat MM, Ayupe AC, Juvenal G, et al. Differentiated embryonic neurospheres from familial Alzheimer's disease model show innate immune and glial cell responses. *Stem Cell Rev Rep*. 2023;19(6):1800-1811. doi: 10.1007/s12015-023-10542-0

98. Gaugler J, James B, Johnson T, et al. Alzheimer's disease facts and figures. *Alzheimers Dement*. 2022;18(4):700-789. doi: 10.1002/alz.12638

99. Andrade-Guerrero J, Santiago-Balmaseda A, Jeronimo-Aguilar P, et al. Alzheimer's disease: an updated overview of its genetics. *Int J Mol Sci*. 2023;24(4):3754. doi: 10.3390/ijms24043754

100. Esteve D, Molina-Navarro MM, Giraldo E, et al. Adult neural stem cell migration is impaired in a mouse model of Alzheimer's disease. *Mol Neurobiol*. 2022;59(2): 1168-1182. doi: 10.1007/s12035-021-02620-6

101. Choi YJ, Park J, Lee SH. Size-controllable networked neurospheres as a 3D neuronal tissue model for Alzheimer's disease studies. *Biomaterials*. 2013;34(12):2938-2946. doi: 10.1016/j.biomaterials.2013.01.038

102. Bernabeu-Zornoza A, Coronel R, Palmer C, Martín A, López-Alonso V, Liste I. Neurogenesis is increased in human neural stem cells by Aβ40 peptide. *Int J Mol Sci*. 2022;23(10):5820. doi: 10.3390/ijms23105820

103. Cheignon C, Tomas M, Bonnefont-Rousselot D, Faller P, Hureau C, Collin F. Oxidative stress and the amyloid beta peptide in Alzheimer's disease. *Redox Biol*. 2018;14:450-464. doi: 10.1016/j.redox.2017.10.014

104. Li F, Gong Q, Dong H, Shi J. Resveratrol, a neuroprotective supplement for Alzheimer's disease. *Curr Pharm Des*. 2012;18(1):27-33. doi: 10.2174/138161212798919075

105. Chiang MC, Nicol CJB, Lin CH, Chen SJ, Yen C, Huang RN. Nanogold induces anti-inflammation against oxidative stress induced in human neural stem cells exposed to amyloid-beta peptide. *Neurochem Int*. 2021;145:104992. doi: 10.1016/j.neuint.2021.104992

106. Walton NM, Shin R, Tajinda K, et al. Adult neurogenesis transiently generates oxidative stress. *PloS One*. 2012;7(4):e35264. doi: 10.1371/journal.pone.0035264

107. Pérez Estrada C, Covacu R, Sankavaram SR, Svensson M, Brundin L. Oxidative stress increases neurogenesis and oligodendrogenesis in adult neural progenitor cells. *Stem Cells Dev*. 2014;23(19):2311-2327. doi: 10.1089/scd.2013.0452

108. Madhavan L, Ourednik V, Ourednik J. Grafted neural stem cells shield the host environment from oxidative stress. *Ann NY Acad Sci*. 2005;1049:185-188. doi: 10.1196/annals.1334.017

109. Fonseca MB, Solá S, Xavier JM, Dionísio PA, Rodrigues CM. Amyloid β peptides promote autophagy-dependent differentiation of mouse neural stem cells: Aβ-mediated neural differentiation. *Mol Neurobiol*. 2013;48(3):829-840. doi: 10.1007/s12035-013-8471-1

110. Vázquez P, Arroba AI, Cecconi F, de la Rosa EJ, Boya P, de Pablo F. Atg5 and Ambra1 differentially modulate neurogenesis in neural stem cells. *Autophagy*. 2012;8(2):187-199. doi: 10.4161/auto.8.2.18535

111. López-Toledano MA, Shelanski ML. Neurogenic effect of beta-amyloid peptide in the development of neural stem cells. *J Neurosc*. 2004;24(23):5439-5444. doi: 10.1523/jneurosci.0974-04.2004

112. Bernabeu-Zornoza A, Coronel R, Palmer C, et al. Aβ42 peptide promotes proliferation and gliogenesis in human neural stem cells. *Mol Neurobiol*. 2019;56(6):4023-4036. doi: 10.1007/s12035-018-1355-7

113. Baglietto-Vargas D, Sánchez-Mejias E, Navarro V, et al. Dual roles of Aβ in proliferative processes in an amyloidogenic model of Alzheimer's disease. *Sci Rep*. 2017;7(1):10085. doi: 10.1038/s41598-017-10353-7

114. Micci MA, Krishnan B, Bishop E, et al. Hippocampal stem cells promotes synaptic resistance to the dysfunctional impact of amyloid beta oligomers via secreted exosomes. *Mol Neurodegener*. 2019;14(1):25. doi: 10.1186/s13024-019-0322-8

115. Wander CM, Song J. The neurogenic niche in Alzheimer's disease. *Neurosci Lett*. 2021;762:136109. doi: 10.1016/j.neulet.2021.136109

116. Jin K, Peel AL, Mao XO, et al. Increased hippocampal neurogenesis in Alzheimer's disease. *Proc Natl Acad Sci USA*. 2004;101(1):343-347. doi: 10.1073/pnas.2634794100

117. Porayette P, Gallego MJ, Kaltcheva MM, Bowen RL, Vadakkadath Meethal S, Atwood CS. Differential processing of amyloid-beta precursor protein directs human embryonic stem cell proliferation and differentiation into neuronal precursor cells. *J Biol Chem*. 2009;284(35): 23806-23817. doi: 10.1074/jbc.M109.026328

118. Matta R, Gonzalez AL. Engineered biomimetic neural stem cell niche. *Curr Stem Cell Rep*. 2019;5(3):109-114. doi: 10.1007/s40778-019-00161-2

ACCSCIENCE PUBLISHING

International Journal of Bioprinting

RESEARCH ARTICLE

Mechanism study of structural functional dual biomimetic composite bone scaffold for repair of mandibular defects in rabbits

Jiaqi Hu[1†], Hong Zhu[1†], Chongqing He[1], Xiaochuan Liu[1], Kenny Man[2,3], Shanqin Liang[1*], and Jingying Zhang[1*]

[1] Center for Oral Medicine, The First Dongguan Affiliated Hospital, Guangdong Medical University, Dongguan, Guangdong, China

[2] Department of Oral and Maxillofacial Surgery & Special Dental Care, University Medical Center Utrecht, Utrecht, The Netherlands

[3] Regenerative Medicine Center Utrecht, Utrecht, The Netherlands

Abstract

The present study aims to explore the potential mechanisms of bone tissue-engineered triply periodic minimal surfaces (TPMS) scaffolds containing injectable platelet-rich fibrin and stromal cell-derived factor-1 (in short, SIT scaffolds) in promoting angiogenesis in mandibular defects. Surface structures with a 70% porosity were created using the Matlab R2020a program. SIT scaffolds were fabricated using digital laser processing. Histological structures on SIT scaffolds inoculated with rabbit bone marrow mesenchymal stem cells (BMSCs) were observed using alkaline phosphatase (ALP) immunohistochemical staining, Alcian blue staining, and Masson-Goldner staining. Double-end sequencing in PE150 mode was performed using the Illumina NovaSeq™ 6000. Analyses such as Gene Ontology (GO), Kyoto Encyclopedia of Genes and Genomes (KEGG), protein-protein interactions, and gene set enrichment analysis (GSEA) were conducted to delineate the gene functions. RT-qPCR was performed to confirm the expression of genes of interest. Finally, cells on different samples were examined by confocal laser scanning microscopy to observe c-Jun expression. Confocal imaging and quantitative analysis showed that BMSCs supported by the SIT scaffold had a greater tendency to differentiate into osteoblasts than those supported by the TPMS scaffold or the control group. The SIT group exhibited the most intense ALP staining. The expression of angiogenesis-related factors VEGFA was significantly upregulated in T and SIT groups. Expression of osteogenic gene *RUNX2* and c-Fos/c-Jun pathway genes *FOS/JUN* was significantly upregulated in the SIT group. GSEA revealed that the WNT signaling pathway and MAPK signaling pathway were more active in the SIT group. Immunofluorescence showed that the c-Jun is highly expressed in newly formed capillaries in the SIT group. In conclusion, both TPMS and SIT scaffolds promote angiogenesis in mandibular defects.

Keywords: TPMS scaffold; Mechanism; Mandibular defect; 3D printer; Additive manufacturing; RNA sequencing

†These authors contributed equally to this work.

***Corresponding authors:**
Shanqin Liang
(29090731@qq.com)

Jingying Zhang
(zhangjy@gdmu.edu.cn)

Citation: Hu J, Zhu H, He C, et al. Mechanism study of structural functional dual biomimetic composite bone scaffold for repair of mandibular defects in rabbits. *Int J Bioprint*. 2024;10(5):4147. doi: 10.36922/ijb.4147

Received: July 4, 2024
Revised: August 14, 2024
Accepted: August 15, 2024
Published Online: August 16, 2024

Copyright: © 2024 Author(s). This is an Open Access article distributed under the terms of the Creative Commons Attribution License, permitting distribution, and reproduction in any medium, provided the original work is properly cited.

Publisher's Note: AccScience Publishing remains neutral with regard to jurisdictional claims in published maps and institutional affiliations.

1. Introduction

Mandibular defects refer to missing or damaged portions of the mandible, or lower jawbone, resulting from various causes such as trauma, surgical removal of tumors, congenital abnormalities, infections, and osteoradionecrosis.[1,2] These defects can significantly impact a person's ability to chew, speak, and maintain normal facial aesthetics, leading to both functional and psychological issues.[3,4] Autologous bone grafting and allogeneic bone transplantation are the primary clinical treatment methods for bone defects; however, they have inherent limitations related to cost and integration with the host bone.[5,6] A major focus in recent research on bone defect repair and regeneration is the application of triply periodic minimal surface (TPMS) scaffolds in bone tissue engineering, which holds great promise. TPMS can be divided into Gyroid (G), Diamond (D), and Schwarz Primitive (P) surfaces.[7] The G surface, with its relatively large specific surface area and porosity, can significantly induce osteoblast differentiation.[8,9] Previously, we demonstrated that TPMS-G surface scaffolds with 70% porosity exhibited the best compressive strength and superior cell proliferation and adhesion in a mandibular defect model.[10]

Biphasic calcium phosphate (BCP) consists of hydroxyapatite and tricalcium phosphate (TCP).[11,12] Studies have demonstrated that 85% β-TCP and 15% hydroxyapatite exhibit excellent properties, such as biocompatibility, mechanical strength, and osteoconductivity, and have been widely used in bone scaffolds.[13–16] Additive manufacturing methods are commonly employed for fabricating calcium phosphate-based bioceramics.[17] Our scaffolds feature complex structures with delicate details, containing pores on the side walls with a maximum diameter of 0.87 mm.[10] Compared to other printing strategies, such as stereolithography (SLA), digital light processing (DLP) offers higher resolution and accuracy, making it more suitable for constructing intricate geometries.[18–20] By harnessing the low viscosity of BCP ceramic particles and the high-resolution capabilities of DLP, the scaffolds achieve optimal mechanical performance.[17,21] This study employed 85% β-tricalcium phosphate and 15% hydroxyapatite to fabricate TPMS bone scaffolds through DLP.

Recent studies by Dong and Zhao (2021) have highlighted the potential of TPMS scaffolds in promoting bone regeneration, emphasizing that through optimized design and manufacturing processes, these scaffolds can provide improved solutions for bone defect repair.[22] Shi et al. developed a novel gradient porous scaffold by integrating TPMS with the sigmoid function method to facilitate the repair of mandibular bone defects by mimicking the natural gradient between cortical and cancellous bones.[23] Toosi et al. explored the use of scaffolds based on TPMS geometries to emulate the hierarchical structure of human bones, proposing a patient-specific 3D printing solution.[24] These studies indicate a trend toward personalized and refined research in TPMS, demonstrating significant potential. However, the design of scaffolds should not only promote osteogenesis but also support angiogenesis to ensure the blood supply to the newly formed bone tissue. Further research is required on how to enhance the osteogenic efficiency of TPMS scaffolds and promote angiogenesis through design optimization and functionalization strategies.

One promising strategy for improving osteogenic efficiency and angiogenesis is using composites rich in growth factors. In our previous studies, we loaded injectable platelet-rich fibrin (I-PRF) and stromal cell-derived factor-1 (SDF-1) into the TPMS scaffold and demonstrated that the SIT scaffold showed good biocompatibility and promoted cell migration, proliferation, and osteogenesis.[25] Case studies have shown that using bone grafts with advanced platelet-rich fibrin (A-PRF), I-PRF, and leukocyte- and platelet-rich fibrin (L-PRF) can enhance the quality of the bone graft material in both maxilla and mandible.[26–28] Many studies supported the role of the SDF-1/CXCR4 axis in angiogenesis through the ERK/MAPK pathway activation.[29–31] However, there is limited knowledge on the underlying mechanisms of TPMS scaffold loaded with I-PRF and SDF-1 (SIT scaffold) in osteogenesis as well as angiogenesis and interaction between cells and scaffold materials.

In the present study, we aim to verify the impact of SIT scaffolds on bone marrow mesenchymal stem cells (BMSCs) in bone defect and examine whether SDF-1 and I-PRF in SIT scaffolds can influence bone repair through the MAPK pathway. Using reference-guided RNA sequencing, which is widely utilized to comprehensively delineate gene expression levels in response to treatment, we analyzed the potential of SIT scaffold in mandible reconstruction. Additionally, we evaluated the expression and localization of significantly different protein c-Jun in a New Zealand white rabbit model of mandibular defect. The results of this research will enhance our understanding of the molecular processes involved in the SIT composite scaffold and contribute to the advancement of bone tissue engineering.

2. Materials and methods

2.1. Design and preparation of SIT scaffolds

Matlab R2020a was used to design G-surface scaffolds with a porosity of 70%. The scaffolds were intended to have a cylindrical shape, measuring 8 mm in diameter and 4 mm in height, with a wall thickness of 0.25 mm. Cylindrical scaffolds were constructed with an 8 mm base diameter, 4 mm thickness, and 200 μm wall thickness. Our bone

scaffold was manufactured using a digital laser process and was composed of 85% β-tricalcium phosphate and 15% hydroxyapatite. The 3D printing process parameters for the AUTOCERA-M (Beijing Shiwei Technology Co. Ltd, China) include a light wavelength of 405 nm, a spot size of 50 μm, an exposure time of 6 seconds, an exposure power of 30 mW/cm², and a layer thickness of 25 μm. After the scaffold was cleaned with distilled water, it was sterilized in an autoclave at 121°C for 30 minutes, followed by drying at 37°C for 12 hours.

To prepare SIT scaffolds, I-PRF was obtained by collecting and centrifuging blood from the central artery of a rabbit's ear. We mixed 500 μL of 200 ng/mL SDF-1 solution with 200 μL of I-PRF solution and used a pipette to repeatedly aspirate and dispense the mixture onto the scaffold, ensuring even distribution throughout the scaffold.

2.2. Preparation of critical mandibular bone defect model of rabbits

Nine male New Zealand white rabbits (Guangzhou Xinhua Animal Farm, China), all healthy and 6 months old, were chosen based on their weight of 3.0±0.5 kg. The participants were randomly divided into three groups: control, TPMS, and SIT (n = 3 per group). Following the administration of anesthesia, the skin in the right submandibular area was prepared in the usual manner, sterilized, covered with sterile sheets, and then a 2–3 cm cut was made alongside the lower border of the rabbit's jaw from the back. An 8 mm circular bone drill was utilized to create a defect in the center of the mandibular body. Cold physiological saline was then applied to lower the temperature, resulting in a cylindrical bone defect measuring 8 mm in diameter and 4 mm in depth. Various scaffold materials with varying levels of porosity were inserted into the injury site based on pre-defined groups, followed by the sequential suturing of the muscle membrane, fascia, and skin. Following the procedure, a 30000-unit dose of penicillin was administered intramuscularly every three days, with the wound disinfected using iodophor to reduce the risk of infection after surgery.

2.3. Confocal microscopy and image analysis

Microscopy imaging was performed using Zeiss LSM 780 and Olympus SD-OSR. Rabbit BMSCs were seeded onto the SIT scaffolds. Cells were fixed with 4% paraformaldehyde (PFA; 30525-89-4, Wako, Japan) at room temperature for 10 minutes, followed by washing, and permeabilization with 0.1% Triton X-100 (Sigma, Germany) in phosphate-buffered saline (PBS) for 15 minutes. Cells were then washed twice with Dulbecco's phosphate-buffered saline (DPBS) and incubated with ActinGreen (Alexa-Fluor-488-conjugated phalloidin; R37110, Invitrogen, USA) at room temperature for 15 minutes. Before imaging, cells were washed with DPBS. Subsequently, single-cell morphological changes were captured under a confocal microscope at 60× magnification, and quantitative analysis was performed using ImageJ software (NIH, Germany).

2.4. Analysis of differentially expressed genes

DESeq2 software was used to analyze differential gene expression between two distinct groups (and edgeR was used for two samples). Genes meeting the criteria of false discovery rate (FDR) <0.05 and absolute fold change ≥2 were identified as differentially expressed genes (DEGs). Genes with varying expression levels were subsequently analyzed for Gene Ontology (GO) enrichment and Kyoto Encyclopedia of Genes and Genomes (KEGG) pathway enrichment.

2.5. GO enrichment analysis

Gene Ontology is a globally recognized system for categorizing gene functions, providing a constantly updated set of terms and clear definitions to fully characterize the attributes of genes and their products across all organisms. GO consists of three ontologies: molecular function, cellular component, and biological process. GO term is the fundamental building block of GO. Every GO term is associated with a specific ontology category. First, all DEGs were mapped to the GO terms available in the Gene Ontology database (http://www.geneontology.org/). Then, the number of genes associated with each term was calculated. To identify significantly enriched GO terms among the DEGs, a hypergeometric test was performed, comparing the DEG-associated terms against the genome background.

2.6. KEGG pathway enrichment analysis

Genes typically collaborate with one another to fulfill specific biological functions. Analyzing pathways aids in gaining a deeper comprehension of the biological roles of genes. The KEGG is a publicly available, primary pathway-related database. Through the KEGG pathway enrichment analysis, metabolic pathways or signal transduction pathways that were significantly enriched in DEGs compared to the entire genome could be revealed.

2.7. Protein-protein interaction analysis

Protein-protein interactions were analyzed using the STRING database (version 12.0) with a confidence threshold of 0.7. Interactions were limited to *Homo sapiens* and visualized using Cytoscape (version 3.10.2). Key hub proteins were identified using plugin "cytoHubba."

2.8. Gene set enrichment analysis

Gene set enrichment analysis (GSEA) was conducted utilizing GSEA (v4.1.0) software and MSigDB. Enrichment

scores and *p*-value were calculated in default parameters. GO terms and KEGG pathways (DO terms, Reactome) meeting the following criteria: |NES|>1, NOM p-val<0.05, and FDR q-val<0.25, were considered to be different in two groups.

2.9. Real-time quantitative polymerase chain reaction

Following a 14-day co-culture of rabbit BMSCs with TPMS scaffolds, the medium in each well was removed. After being washed 3 times with 1× PBS solution, 1 mL of Trizol solution was added to each well. Total RNA was extracted from the cells on the scaffolds using a standard RNA extraction protocol, which included cell lysis and homogenization steps followed by purification. The extracted RNA (1 μg of total RNA) was subjected to cDNA synthesis using the PrimeScript Reverse Transcription kit (Takara, Japan). Following this, a real-time quantitative polymerase chain reaction (RT-qPCR) was carried out. The PCR reaction conditions included an initial denaturation at 95°C for 5 seconds, followed by denaturation at 95°C for 15 seconds, annealing for 40 cycles at 60°C for 1 minute, and extension at 72°C for 30 seconds. The levels of gene expression were determined using the $2^{-\Delta\Delta Ct}$ method for quantification.

2.10. Immunofluorescence staining

Immunofluorescence staining was carried out to assess the bone-forming potential of rabbit BMSCs. Rabbit jawbone tissue samples were sectioned and the cells were treated with 4% neutral formaldehyde for 15 minutes, followed by permeabilization and incubation in Quick BlockBlock™ blocking buffer (Beyotime, China) for 15 minutes prior to immunostaining. After incubating the tissue sections overnight at 4°C with a primary antibody against c-Jun (1:500; Invitrogen, USA), they were then treated with a secondary goat anti-mouse IgG antibody (a secondary goat anti-mouse IgG antibody (A-11005; Invitrogen, USA); Invitrogen, USA) at room temperature for 1 hour following PBS washing. DAPI (blue; Solarbio, China) was used to stain cell nuclei for 15 minutes at room temperature, and then gentle washing with PBS was performed. Finally, cells on different samples were observed for c-Jun expression using confocal laser scanning microscopy.

2.11. Immunohistochemical staining

Alkaline phosphatase (ALP) staining was conducted to assess osteogenic activity in tissue samples. Briefly, the samples were fixed in 4% paraformaldehyde and rinsed with PBS. The samples were then incubated with the ALP substrate solution at room temperature to allow color development. After staining, the samples were dehydrated and mounted. Staining was imaged using an inverted phase contrast microscope (Leica, Germany).

2.12. Alcian blue staining and Safranin O-fast green staining

Alcian blue staining was performed using a 1% Alcian blue solution for 8–10 minutes to detect glycosaminoglycans in tissue samples. Following this, the samples were counterstained with 1% nuclear fast red for 1 minute. The samples were initially fixed in 4% paraformaldehyde and embedded in paraffin. After deparaffinization and rehydration, the staining procedure was carried out. The stained sections were then washed, dehydrated, and mounted.

We employed the Safranin O-fast green staining method to distinguish collagen fibers from other tissue components. The sections were stained using a Modified Safranine O-Fast Green FCF Cartilage Stain Kit (Salarbio, China). The experimental procedure was carried out according to the manufacturer's instructions.

2.13. Masson-Goldner staining

Masson–Goldner staining was used to differentiate collagen fibers from other tissue components. The tissue samples were initially fixed in 4% paraformaldehyde and embedded in paraffin. After deparaffinization and rehydration, staining was performed using the Masson–Goldner staining kit (Beyotime, China), following the manufacturer's protocol. Finally, the tissue sections were sequentially dehydrated in 70, 80, and 90% ethanol solutions, followed by absolute ethanol, with each step lasting 10 seconds, and then cleared in xylene three times for 1–2 minutes in each round.

2.14. Statistical analysis

Data are presented as mean ± standard deviation (SD). The normality of the data was assessed using the Shapiro–Wilk test. For normally distributed data, differences between groups were analyzed using the one-way analysis of variance (ANOVA) followed by Tukey's post hoc test for multiple comparisons. Non-normally distributed data were analyzed using the Kruskal–Wallis test followed by Dunn's post hoc test. A *p*-value of less than 0.05 was considered statistically significant.

3. Results and discussion

3.1. Effectiveness and structural properties of SIT scaffold

Previously, we demonstrated that the SIT scaffold can effectively repair critical mandibular defects.[25] It has an elastic modulus of 627.188±31.823 MPa and a compressive strength of 11.571±2.069 MPa. The substances loaded on the scaffold are released at an average rate of 7.56% per day and are completely released after 10 days. Scanning electron microscopy showed that the scaffold significantly

enhances the adhesion of mouse pre-osteoblast cells (MC3T3) after being loaded with I-PRF and SDF-1. The SIT scaffold exhibits excellent mechanical properties and biocompatibility and promotes the osteogenic differentiation of MC3T3 cells.

In this study, BMSCs were used as experimental cells, and New Zealand white rabbits served as experimental animals to investigate the effects of SIT scaffolds loaded with mesenchymal stem cells on bone defect areas and the potential mechanisms of mandibular bone repair. The detailed experimental procedure is shown in Figure 1.

3.2. Confocal microscopy and cell morphology analysis

The image of the printed scaffold is shown in Figure 2A. In the microscopic examination, BMSCs within the control group were observed to be comparatively smaller in size, with their nuclei exhibiting a flattened ellipsoidal shape. In contrast, the BMSCs associated with both the TPMS and SIT scaffold groups were noticeably larger, assuming a more polygonal morphology (Figure 2B). The smaller size and flattened ellipsoidal shape of nuclei in the control group's BMSCs suggest a baseline or quiescent state of these cells. Contrastingly, increases in cell size, prominent cell projections, and enhanced cell–cell contacts in the SIT group are considered significant indicators of osteoblast differentiation and promotion of bone formation.[32] These changes are consistent with the findings of Li et al., who reported similar morphological alterations as indicators of early osteogenic differentiation.[33]

The selection of fields of view in confocal microscopy can be subjective, and images from a single field of view may lack statistical significance. Therefore, we used ImageJ to measure the mean fluorescence intensity, average cell area, and perimeter/area ratio of all cells observed under the electron microscope (Figure 2C–E). Results revealed that the TPMS group had significantly higher average fluorescence intensity than the control group, while the SIT group showed even greater intensity than the TPMS group. The marked increase implies an increase in the viability of BMSCs, which could be attributed to the specific scaffolding and treatment conditions used in the SIT group, aligning with the conclusions drawn by Shi et al. regarding the impact of scaffold properties on BMSC differentiation.[34] The perimeter-to-area ratio of the SIT group was significantly greater than that observed in both the control and TPMS groups. These findings suggest the SIT scaffold has an exceptional ability to support stem cell proliferation and differentiation into osteoblasts.

3.3. Differential gene expression results based on RNA sequencing analysis

RNA sequencing analysis was conducted on mesenchymal stem cells cultured in the SIT scaffolds for 2 weeks to

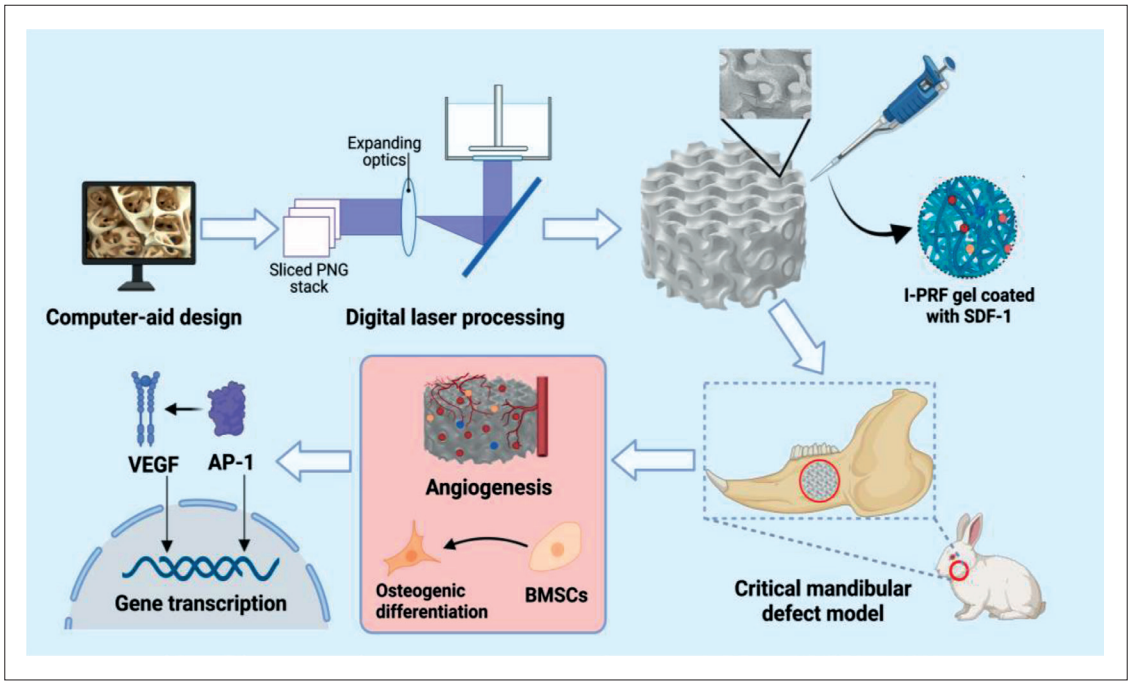


Figure 1. General overview of the study. Schematic created with BioRender.com.

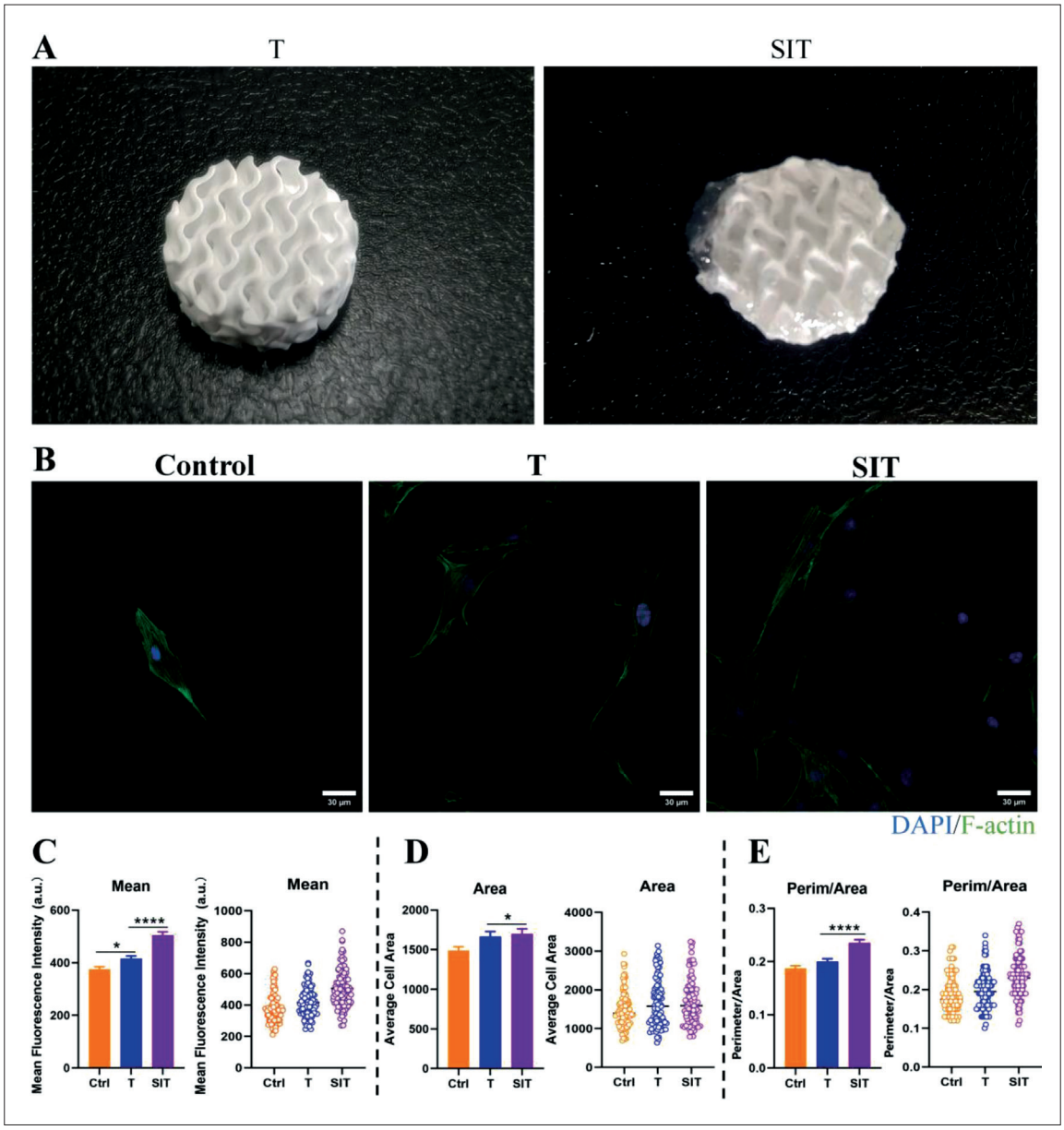


Figure 2. Scaffold appearance and morphology of bone marrow mesenchymal stem cells (BMSCs) observed via confocal microscopy. (A) The image of actual 3D-printed TPMS and SIT scaffolds. (B) Fluorescence staining of rabbit BMSCs. The cytoplasm is stained green and the nucleus is stained blue. Scale bars: 30 μm. Magnification: 63×. (C) Mean fluorescence intensity of BMSCs. (D) Average cell area of BMSCs. (E) Perimeter/area (Perim/Area) ratio of BMSCs. Abbreviations: T: TPMS scaffolds; SIT: TPMS scaffolds loaded with SDF-1 and I-PRF.

investigate how the scaffold affects bone repair mechanisms. Volcano maps of DEGs revealed that the transcriptomic expression of the SIT scaffold group samples exhibits greater differences compared to that of the TPMS scaffold group (Figure 3A and B). Filtering with the criteria applied in this study, we pinpointed 413 DEGs from the TPMS group and 853 DEGs from the SIT group, with 316 overlapping DEGs shared by both groups (Figure 3C). Figure 3D illustrates the overall mRNA expression trend differences among the three groups. Several genes showed increased expression in both the TPMS and SIT scaffold groups. Specifically, the genes associated with osteoblasts (*RUNX2*, *COL1A1*, *COL1A2*, and *Osx*) and factors related to angiogenesis (*VEGFA*, *VEGFC*, and *FGF2*) showed a notable increase in expression in the scaffold groups (Figure 3E and F). Interestingly, as one of the key components of

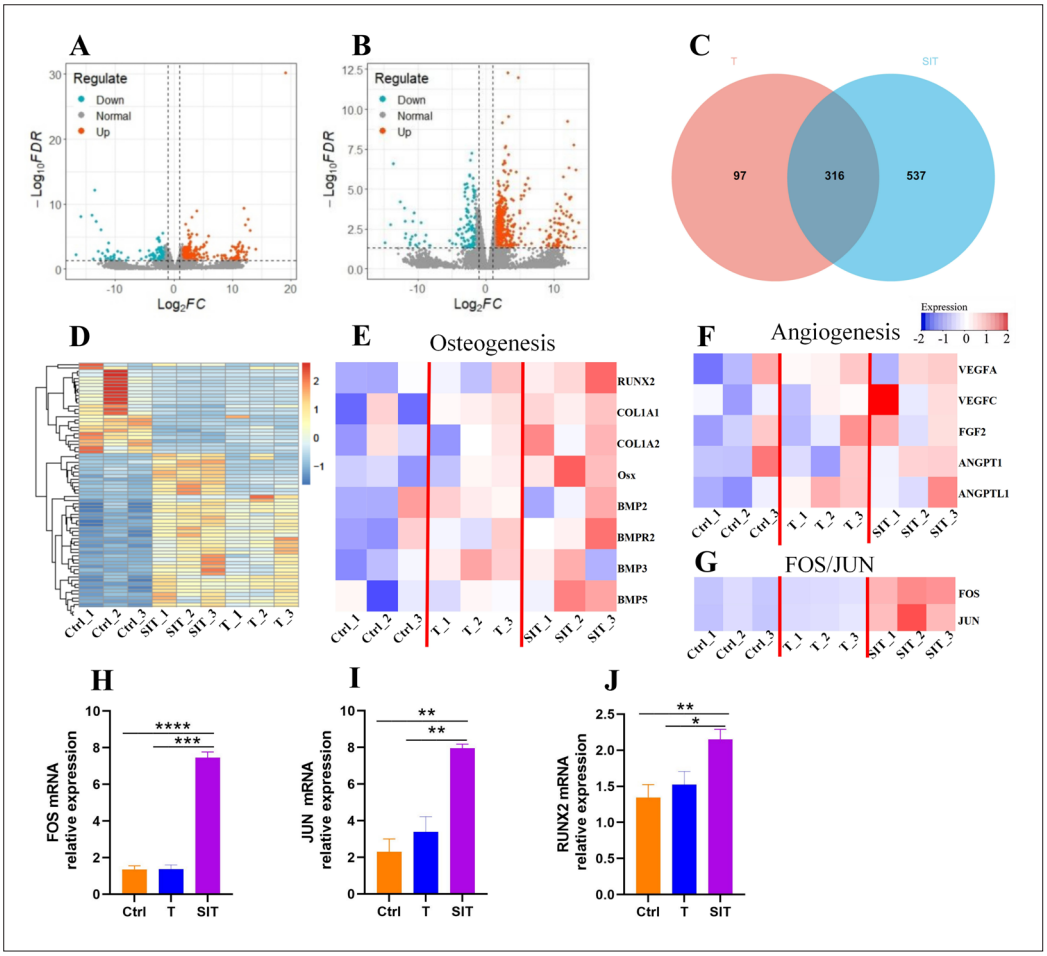


Figure 3. RNA sequencing analysis and qPCR reveal differential gene expression in the SIT scaffold influencing bone repair mechanisms. (A, B) Volcano maps of TPMS scaffold (A) and SIT scaffold (B) versus control group. $p < 0.05$, log2FC ≥1.5. (C) Intersection Venn diagram of differentially expressed genes (DEGs) between TPMS and SIT scaffold groups. (D) Heat maps of DEGs for control, TPMS and SIT groups. (E–G) Heat maps of osteogenesis-related genes, angiogenesis-related factors and FOS/JUN pathway genes expression after implanting the control, TPMS and SIT scaffolds, respectively, for 2 weeks (red: high expression; blue: low expression). (H) RT-qPCR result of FOS. (I) RT-qPCR result of JUN. (J) RT-qPCR result of RUNX2. Abbreviations: T: TPMS scaffolds; SIT: TPMS scaffolds loaded with SDF-1 and I-PRF.

the MAPK signaling pathway, *FOS/JUN* exhibited specific upregulation in the SIT scaffold group (Figure 3G). RT-qPCR confirmed the specific upregulation of *FOS*, *JUN*, and *RUNX2* in the SIT scaffold group (Figure 3H–J). Shen et al. found that bioceramic scaffolds significantly increased the expression of the osteogenic gene *RUNX2* in BMSCs.[8,35] Li et al. demonstrated that high expression of VEGFA is associated with enhanced angiogenesis.[36] Therefore, the observed upregulation of *RUNX2* and *VEGFA* in the SIT group is consistent with these findings, highlighting the effectiveness of our scaffold in supporting both angiogenesis and osteogenesis.

To investigate the potential pathway mechanisms of SIT and distinguish them from pure TPMS scaffolds, we conducted an enrichment analysis. The GO enrichment analysis revealed that the genes with altered expression in the SIT scaffold group are mainly involved in cellular macromolecule biosynthetic process, cell differentiation, animal organ development, *etc.* (Figure 4A). The KEGG pathway enrichment analysis highlighted the AGE-RAGE signaling pathway and axon guidance, with the MAPK signaling pathway exhibiting the largest difference (with the smallest p-value) compared to the control group (Figure 4B). Furthermore, gene set enrichment analysis (GSEA) more directly demonstrated that the SIT scaffold not only exhibited significant differences in multiple pathways from the control group but also obtained higher enrichment scores compared to the TPMS group. This further validates the unique differences of the SIT scaffold group in the

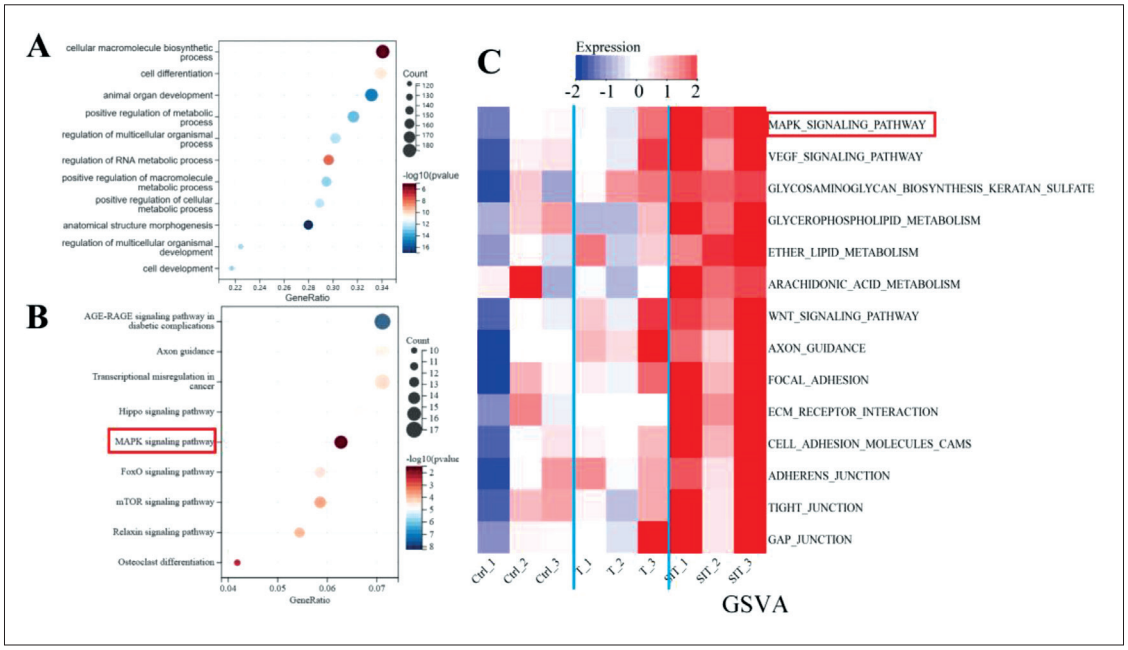


Figure 4. Enrichment analysis reveals the mechanisms by which the scaffold promotes bone regeneration. (A) GO enrichment analysis of differentially expressed genes (DEGs) in SIT scaffolds. (B) KEGG pathway analysis of DEGs in SIT scaffolds. (C) Gene set variation analysis of control, TPMS and SIT groups. Abbreviations: T: TPMS scaffolds; SIT: TPMS scaffolds loaded with SDF-1 and I-PRF.

MAPK and VEGF signaling pathways (Figure 4C). GSEA analysis found that the SIT group could promote bone development, osteoclast differentiation, angiogenesis, the positive regulation of MAPK cascade, and the WNT signaling pathway (Figure 5A–F). To explore protein-protein interactions, we inputted DEGs into the STRING database and investigated the top 20 key genes using the cytoHubba in Cytoscape, including *JUN*, *FOS,* and *RUNX2* (Figure 5G). These results together revealed the important role of SIT scaffold in BMSCs behaviors and bone repair.

I-PRF has been utilized for regenerative applications in the field of dentistry. Wang et al. co-cultured I-PRF with human primary osteoblasts and found that I-PRF significantly promoted osteogenic differentiation, with higher mRNA levels of *ALP*, *RUNX2*, and osteocalcin in the I-PRF group.[37] Combined with our results, this indicates that I-PRF remains unaffected and continues to exert its reparative potential when loaded onto TPMS scaffolds. The MAPK/ERK pathway is a vital connection between cell surface and nuclear control of growth, development, movement, and cell demise, interacting with various molecular pathways and having a key function in bone creation.[38,39] Previous studies have demonstrated that SDF-1 significantly influences the expression of early- and mid-stage osteogenic markers by activating the Smad and MAPK signaling pathways, and I-PRF can regulate the osteogenic differentiation of human BMSCs by activating the MAPK/ERK signaling pathway.[37,40] ERK1/2, a member of MAPK, can be promoted by SDF-1 and plays a key role in angiogenesis.[41] Previous studies found that ERK1/2 induces osteogenic differentiation by promoting the phosphorylation of Runx2 and inducing the activation ability of Runx2.[42–44] Taken together, this suggests that SIT scaffolds promote mandibular defect repair *in vivo*, possibly via the MAPK pathway.

Notably, FOS/JUN exhibited higher expression in the SIT group and serves as a key hub in the protein interaction network. Activator protein 1 (AP-1), a transcriptional regulator consisting of members from the Fos and Jun families, plays a vital role in bone development.[45,46] The c-Jun protein directly promotes angiogenesis, indicating the potential importance of c-Fos/c-Jun heterodimers in SIT-mediated angiogenesis.[47,48]

3.4. Rabbit mandible section staining

In this study, mandibular defect modeling in New Zealand white rabbits was observed for two months, by means of tissue section staining, to explore the effectiveness of bone tissue regeneration (Figure 6). Staining results revealed the presence of new bone formation (indicated by yellow asterisks) around the defect periphery, with the injury site mainly occupied by connective tissue and muscle fibers. Higher levels of new bone formation were observed around and within the implanted TPMS and SIT scaffolds.

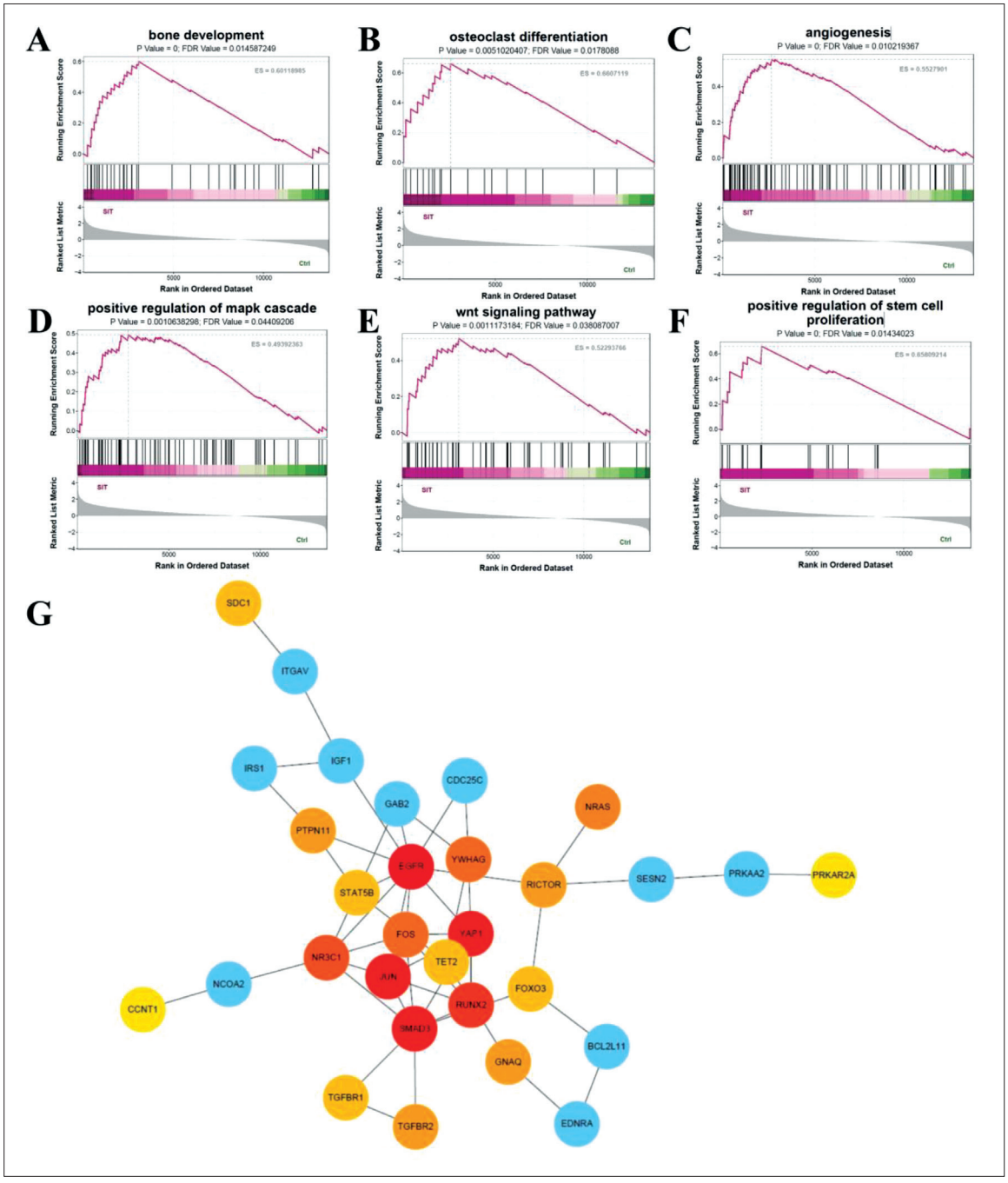


Figure 5. Gene set enrichment analysis (GSEA) and protein-protein interaction network. (A–F) GSEA of differentially expressed genes in SIT scaffolds. (G) Top 20 protein interaction networks screened by cytoHubba in the Cytoscape.

Osteoblasts in the TPMS and SIT scaffold groups were mainly concentrated at the interface between the scaffold and newly formed bone. Additionally, staining of both T and SIT scaffold groups indicated the presence of new blood vessels (indicated by arrows) distributed within the scaffold pores, suggesting that the scaffolds possessed appropriate porosity conducive to cell attachment and vascular formation. Compared to the control group, the TPMS and SIT scaffold groups loaded with I-PRF and SDF-1 showed significantly increased new bone tissue and neovascularization within the scaffold structure, with more evident bone lacunae, osteoblasts, and vascular networks observed within the scaffolds (Figure 6A).

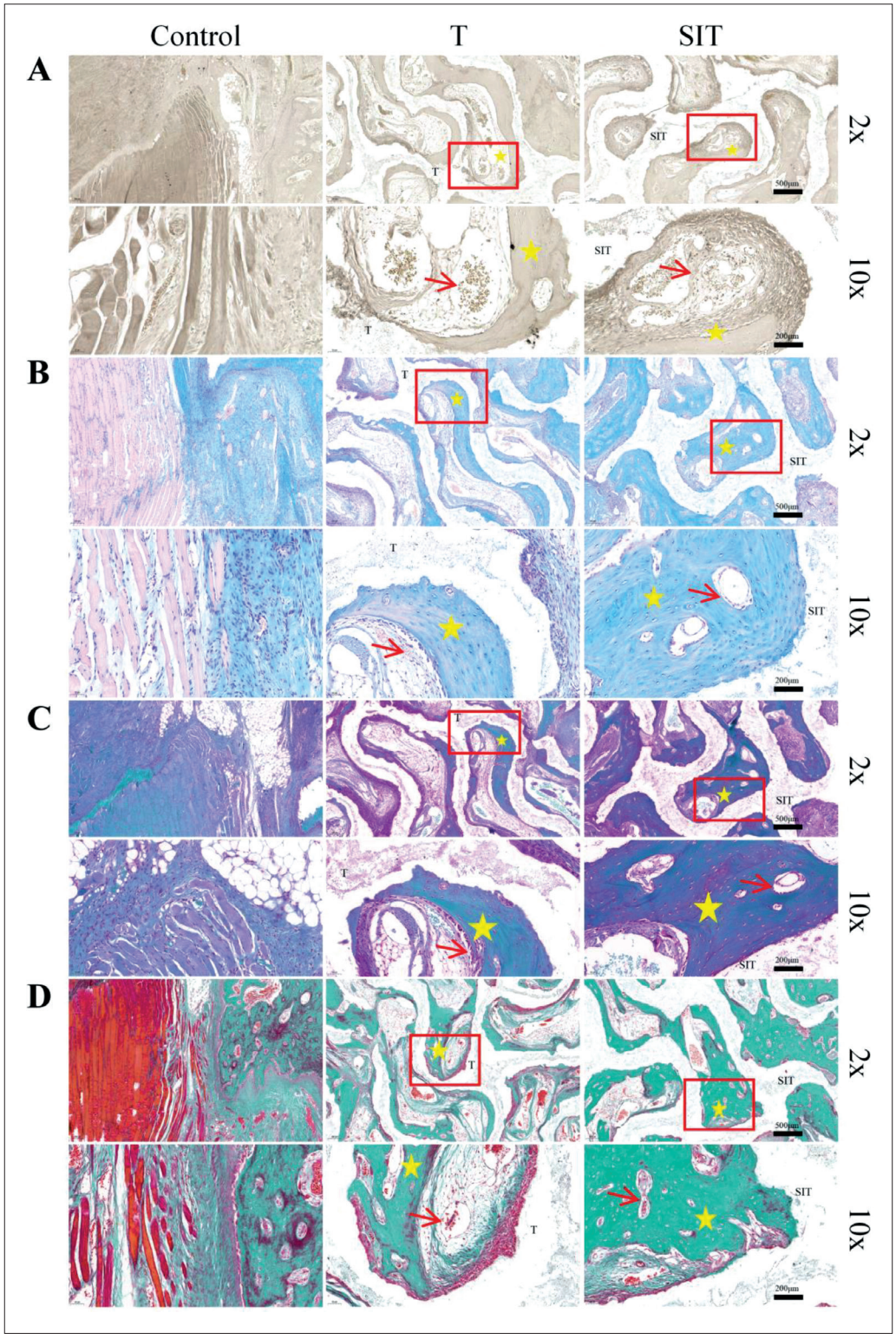


Figure 6. Immunohistochemical analysis of bone regeneration induced by TPMS scaffold and SIT scaffold. (A) Alkaline phosphatase (ALP) staining of mandibular defect model: ALP protein is stained brown. (B) Alcian blue staining: bone is stained light blue. (C) Safranin O-fast green staining results: bone is stained green or blue, while proteins and collagen fibers are dyed pink. (D) Masson-Goldner staining results: mineralized bone is stained green, while non-mineralized bone is dyed orange-red. The yellow asterisk indicates mature bone tissue, while the red arrow indicates new blood vessels. Abbreviations: T: TPMS scaffolds; SIT: TPMS scaffolds loaded with SDF-1 and I-PRF.

Alcian blue staining results demonstrated more active cartilage tissue generation in both the TPMS and SIT groups, with the SIT group exhibiting more neovascularization, indicating potential additional advantages of SIT scaffolds in bone repair (Figure 6B). Safranin O-fast green staining results showed pink-stained collagen fibers and proteins at the junction between the scaffold and newly formed bone compared to the control group, indicating the presence of bone collagenization (Figure 6C). Figure 6D illustrates that the control group exhibited abundant muscle tissue at the site of bone defect, while the TPMS and SIT groups showed no muscle tissue due to the supportive role of the scaffold, suggesting the positive effect of SIT scaffolds in maintaining the stability of surrounding tissue structure. Mineralized bone tissue was observed in all three groups, represented by green coloration, indicating that the bone tissue scaffolds did not significantly inhibit the physiological mineralization of bone repair.

These results suggested that single TPMS scaffolds promote osteogenesis and provide support and attachment in the defect area, consistent with our previous studies.[10] SIT scaffolds retain the aforementioned advantages in promoting repair, with an especially better effect on promoting angiogenesis. Previous studies have demonstrated that SDF-1 possesses angiogenic properties, mediating angiogenesis by stimulating human vascular endothelial cells to form microvessels.[49,50] SDF-1/CXCR4 exerts a regulatory effect on the JNK/c-Jun pathway, enhancing the expression of c-Jun, which promotes blood vessel formation.[51,52] These indications suggest that the superior angiogenic effect of SIT is likely due to SDF-1. SDF-1 promotes angiogenesis by upregulating the expression of c-Jun. Dense bone tissue and adequate blood supply are crucial for the effective repair of mandibular defects, and I-PRF containing various growth factors and SDF-1 with chemotactic and recruitment functions play significant roles in stimulating the uniform formation of dense bone tissue and vascular regeneration within the scaffold. Furthermore, no signs of infection or inflammation were observed in any of the scaffold groups or control groups.

3.5. Immunofluorescence staining of c-Jun

To further investigate whether the SIT scaffold exerts its role in promoting bone defect repair through the regulation of c-Fos/c-Jun, we conducted c-Jun protein-specific immunofluorescence staining on mandibular bone tissue from New Zealand rabbits. We observed that under DAPI staining, the nuclei of mandibular bone tissue cells in all three groups exhibited typical blue fluorescence, while the cytoplasmic regions showed weaker or no fluorescence (Figure 7A). As shown in Figure 7B, the TPMS scaffold exhibited obvious tissue ingrowth but few visible microvascular networks, while the SIT scaffold showed newly formed bone tissue within the pores and extensive microvascular networks (Figure 7C). Within the pores of the SIT scaffold, particularly under 20× magnification, there was a stronger c-Jun protein fluorescence signal concentrated within the newly formed microvessels, whereas, the overall c-Jun fluorescence intensity in the control and TPMS groups was significantly lower. Numerous studies have suggested that c-Jun plays a direct or indirect role in angiogenesis.[47,53,54] These clues confirm our previous conjecture that the SIT scaffold promotes the generation of extensive microvascular networks by regulating the expression of c-Jun protein, and these vascular networks may facilitate the delivery of oxygen and nutrients, promoting the healing and repair of bone defects.

Angiogenesis is the most effective and rapid method for creating new blood vessels in tissue repair, like bone regeneration, to provide essential nutrients and oxygen for cell function at the site of injury. The clinical translation of various bone scaffolds made from different materials has been primarily impeded by inadequate vascularization within the scaffolds and poor osteogenic activity resulting from the differentiation of osteogenesis-related precursor cells, despite extensive *in vitro* and *in vivo* studies.[55–57] We enhanced angiogenesis through 3D porous structure design and the delivery of angiogenic-related factors. c-Jun plays a significant role in the AP-1 transcription factor, interacting with and stimulating the transcription of TRE/AP-1 sequences. We found it to be highly expressed in new blood vessels. Studies have shown that AP-1 subsequently increases vascular endothelial growth factor (VEGF), promoting endothelial cell proliferation and affecting angiogenesis.[58] In human umbilical vein endothelial cells, c-Jun protein can induce the expression of downstream genes such as *VEGF*.[59] Since angiogenesis strategies can enhance bone resorption and formation,[55,60,61] we infer that the superior angiogenic effect of SIT scaffolds indirectly facilitate osteogenic repair in the defect area.

4. Conclusion

Both TPMS and SIT scaffolds promote angiogenesis in mandibular defects. TPMS scaffolds loaded with I-PRF and SDF-1, also known as SIT scaffolds, are more effective at promoting angiogenesis than pure TPMS scaffolds, solving the problem of insufficient scaffold vascularization. The enhanced osteogenic efficiency and angiogenesis observed with the SIT scaffolds may be related to the MAPK pathway and the c-Fos/c-Jun (AP-1) complex.

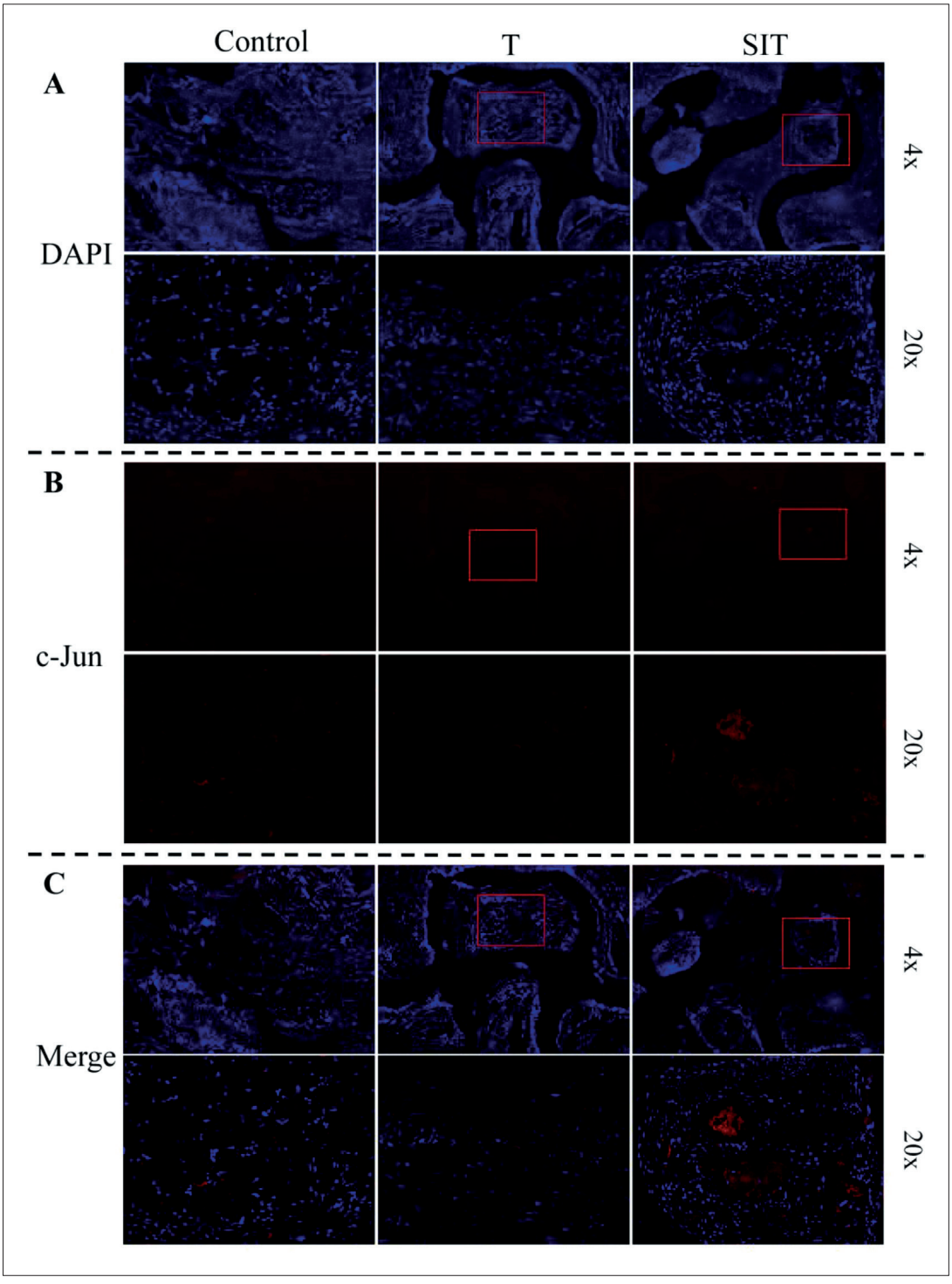


Figure 7. Immunofluorescence results of tissue sections from New Zealand white rabbits. (A) DAPI fluorescence staining. (B) Immunofluorescence staining of c-Jun protein. (C) Merged images.

Acknowledgments

We are grateful to the Intelligent Soft Matter Team at the Songshan Lake Materials Laboratory for providing the laser scanning confocal microscope used for capturing cell morphology.

Funding

The study was supported by the Dongguan Science and Technology of Social Development Program (20231800940152), Talent Development Foundation of the First Dongguan Affiliated Hospital of Guangdong Medical University (GCC2023013), Guangdong Medical University Undergraduate Innovation Experiment Project (FYDS001, FYDS002, FYDS003), Guangdong University Student Innovation Project (S202310571068, S202310571069), and 2024 Special Funds for Science and Technology Innovation Strategy of Guangdong Province (Cultivation of Science and Technology Innovation for University Students) (pdjh2024b185).

Conflict of interest

The authors declare no conflicts of interest.

Author contributions

Conceptualization: Jiaqi Hu, Hong Zhu, Shanqin Liang, Xiaochuan Liu
Data curation: Jiaqi Hu, Hong Zhu
Formal analysis: Jiaqi Hu, Shanqin Liang
Funding acquisition: Jingying Zhang, Shanqin Liang
Investigation: Hong Zhu, Chongqing He
Writing–original draft: Jiaqi Hu, Hong Zhu
Writing–review & editing: Jingying Zhang, Kenny Man, Shanqin Liang, Xiaochuan Liu
All authors have reviewed and approved the final version of the manuscript.

Ethics approval and consent to participate

All animal surgical protocols were approved by the Institutional Animal Care and Use Committee at Guangdong Medical University (GDY2204012).

Consent for publication

Not applicable.

Availability of data

All data needed to validate the conclusions of this study are presented in the paper.

References

1. Brown JS, Barry C, Ho M, Shaw R. A new classification for mandibular defects after oncological resection. *Lancet Oncol*. 2016;17(1):e23-30.
doi: 10.1016/S1470-2045(15)00310-1

2. Miljanovic D, Seyedmahmoudian M, Stojcevski A, Horan B. Design and fabrication of implants for mandibular and craniofacial defects using different medical-additive manufacturing technologies: a review. *Ann Biomed Eng*. 2020;48(9):2285-2300.
doi: 10.1007/s10439-020-02567-0

3. Sivaraman K, Chopra A, Venkatesh SB. Clinical importance of median mandibular flexure in oral rehabilitation: a review. *J Oral Rehabil*. 2016;43(3):215-225.
doi: 10.1111/joor.12361

4. Pickrell BB, Serebrakian AT, Maricevich RS. Mandible fractures. *Semin Plast Surg*. 2017;31(2):100-107.
doi: 10.1055/s-0037-1601374

5. García-Lamas L, Lozano D, Jiménez-Díaz V, et al. Enriched mesoporous bioactive glass scaffolds as bone substitutes in critical diaphyseal bone defects in rabbits. *Acta Biomater*. 2024;180:104-114.
doi: 10.1016/j.actbio.2024.04.005

6. Stahl A, Yang YP. Regenerative approaches for the treatment of large bone defects. *Tissue Eng Part B Rev*. 2021;27(6):539-547.
doi: 10.1089/ten.TEB.2020.0281

7. Zheng X, Fu Z, Du K, Wang C, Yi Y. Minimal surface designs for porous materials: from microstructures to mechanical properties. *J Mater Sci*. 2018;53(14):10194-10208.
doi: 10.1007/s10853-018-2285-5

8. Shen M, Li Y, Lu F, et al. Bioceramic scaffolds with triply periodic minimal surface architectures guide early-stage bone regeneration. *Bioact Mater*. 2023;25:374-386.
doi: 10.1016/j.bioactmat.2023.02.012

9. Wang C, Lai J, Li K, et al. Cryogenic 3D printing of dual-delivery scaffolds for improved bone regeneration with enhanced vascularization. *Bioact Mater*. 2021;6(1):137-145.
doi: 10.1016/j.bioactmat.2020.07.007

10. Zhu H, Wang J, Wang S, et al. Additively manufactured bioceramic scaffolds based on triply periodic minimal surfaces for bone regeneration. *J Tissue Eng*. 2024;15:20417314241244997.
doi: 10.1177/20417314241244997

11. Ahn J-H, Kim J, Han G, et al. 3D-printed biodegradable composite scaffolds with significantly enhanced mechanical properties via the combination of binder jetting and capillary rise infiltration process. *Addit Manufactur*. 2021;41:101988.
doi: 10.1016/j.addma.2021.101988

12. LeGeros RZ, Lin S, Rohanizadeh R, Mijares D, LeGeros JP. Biphasic calcium phosphate bioceramics: preparation, properties and applications. *J Mater Sci Mater Med*. 2003;14(3):201-209. doi: 10.1023/A:1022872421333

13. Ishack S, Mediero A, Wilder T, Ricci JL, Cronstein BN. Bone regeneration in critical bone defects using three-dimensionally printed β-tricalcium phosphate/hydroxyapatite scaffolds is enhanced by coating scaffolds with either dipyridamole or BMP-2. *J Biomed Mater Res B Appl Biomater*. 2017;105(2):366-375. doi: 10.1002/jbm.b.33561

14. Witek L, Shi Y, Smay J. Controlling calcium and phosphate ion release of 3D printed bioactive ceramic scaffolds: an *in vitro* study. *J Adv Ceramics*. 2017;6(2):157-164. doi: 10.1007/s40145-017-0228-2

15. Liu B, Lun DX. Current application of β-tricalcium phosphate composites in orthopaedics. *Orthop Surg*. 2012;4(3):139-144. doi: 10.1111/j.1757-7861.2012.00189.x

16. Fariña NM, Guzón FM, Peña ML, Cantalapiedra AG. *In vivo* behaviour of two different biphasic ceramic implanted in mandibular bone of dogs. *J Mater Sci Mater Med*. 2008;19(4):1565-1573. doi: 10.1007/s10856-008-3400-y

17. Wang Y, Chen S, Liang H, Liu Y, Bai J, Wang M. Digital light processing (DLP) of nano biphasic calcium phosphate bioceramic for making bone tissue engineering scaffolds. *Ceram Int*. 2022;48(19, Part A):27681-27692. doi: 10.1016/j.ceramint.2022.06.067

18. Chen Z, Li Z, Li J, et al. 3D printing of ceramics: a review. *J Euro Ceram Soc*. 2019;39(4):661-687. doi: 10.1016/j.jeurceramsoc.2018.11.013

19. Melchels FPW, Feijen J, Grijpma DW. A review on stereolithography and its applications in biomedical engineering. *Biomaterials* 2010;31(24):6121-6130. doi: 10.1016/j.biomaterials.2010.04.050

20. Zhang J, Hu Q, Wang S, Tao J, Gou M. Digital light processing based three-dimensional printing for medical applications. *Int J Bioprint*. 2020;6(1):242. doi: 10.18063/ijb.v6i1.242

21. Monfared MH, Nemati A, Loghman F, et al. A deep insight into the preparation of ceramic bone scaffolds utilizing robocasting technique. *Ceram Int*. 2022;48(5):5939-5954. doi: 10.1016/j.ceramint.2021.11.268

22. Dong Z, Zhao X. Application of TPMS structure in bone regeneration. *Eng Regeneration*. 2021;2:154-162. doi: 10.1016/j.engreg.2021.09.004

23. Shi J, Zhu L, Li L, Li Z, Yang J, Wang X. A TPMS-based method for modeling porous scaffolds for bionic bone tissue engineering. *Sci Rep*. 2018;8(1):7395. doi: 10.1038/s41598-018-25750-9

24. Toosi S, Javid-Naderi MJ, Tamayol A, Ebrahimzadeh MH, Yaghoubian S, Mousavi Shaegh SA. Additively manufactured porous scaffolds by design for treatment of bone defects. *Front Bioeng Biotechnol*. 2023;11:1252636. doi: 10.3389/fbioe.2023.1252636

25. Zhu H, Lin Z, Luan Q, et al. Angiogenesis-promoting composite TPMS bone tissue engineering scaffold for mandibular defect regeneration. *Int J Bioprint*. 2023;10(1):0153. doi: 10.36922/ijb.0153

26. Thanasrisuebwong P, Kiattavorncharoen S, Deeb GR, Bencharit S. Implant site preparation application of injectable platelet-rich fibrin for vertical and horizontal bone regeneration: a clinical report. *J Oral Implantol*. 2022;48(1):43-50. doi: 10.1563/aaid-joi-D-20-00031

27. Chenchev IL, Ivanova VV, Neychev DZ, Cholakova RB. Application of platelet-rich fibrin and injectable platelet-rich fibrin in combination of bone substitute material for alveolar ridge augmentation – a case report. *Folia Medica*. 2017;59(3):362-366. doi: 10.1515/folmed-2017-0044

28. Lorenz J, Al-Maawi S, Sader R, Ghanaati S. Individualized titanium mesh combined with platelet-rich fibrin and deproteinized bovine bone: a new approach for challenging augmentation. *J Oral Implantol*. 2018;44(5):345-351. doi: 10.1563/aaid-joi-D-18-00049

29. Dong Y, Zhou X, Zhang N. CCN1 inhibition affects the function of endothelial progenitor cells under high-glucose condition. *Adv Clin Exp Med*. 2024;33(6):619-631. doi: 10.17219/acem/170998

30. Pan C, Hu T, Liu P, et al. BM-MSCs display altered gene expression profiles in B-cell acute lymphoblastic leukemia niches and exert pro-proliferative effects via overexpression of IFI6. *J Transl Med*. 2023;21(1):593. doi: 10.1186/s12967-023-04464-1

31. Gonçalves TL, de Araújo LP, Pereira Ferrer V. Tamoxifen as a modulator of CXCL12-CXCR4-CXCR7 chemokine axis: A breast cancer and glioblastoma view. *Cytokine*. 2023;170:156344. doi: 10.1016/j.cyto.2023.156344

32. Olmo N, Martín AI, Salinas AJ, Turnay J, Vallet-Regí M, Lizarbe MA. Bioactive sol–gel glasses with and without a hydroxycarbonate apatite layer as substrates for osteoblast cell adhesion and proliferation. *Biomaterials* 2003;24(20):3383-3393. doi: 10.1016/S0142-9612(03)00200-X

33. Li Y, Dai X, Bai Y, et al. Electroactive BaTiO3 nanoparticle-functionalized fibrous scaffolds enhance osteogenic differentiation of mesenchymal stem cells. *Int J Nanomedicine*. 2017;12:4007-4018. doi: 10.2147/IJN.S135605

34. Shi W, Sun M, Hu X, et al. Structurally and functionally optimized silk-fibroin-gelatin scaffold using 3d printing to repair cartilage injury *in vitro* and *in vivo*. *Adv Mater (Deerfield Beach, Fla)*. 2017;29(29):10.1002/adma.201701089. doi: 10.1002/adma.201701089

35. Li Y, Li J, Jiang S, et al. The design of strut/TPMS-based pore geometries in bioceramic scaffolds guiding osteogenesis and angiogenesis in bone regeneration. *Mater Today Bio*. 2023;20:100667. doi: 10.1016/j.mtbio.2023.100667

36. Li M, Jiang J, Liu W, et al. Bioadaptable bioactive glass-β-tricalcium phosphate scaffolds with TPMS-gyroid structure by stereolithography for bone regeneration. *J Mater Sci Technol*. 2023;155:54-65. doi: 10.1016/j.jmst.2023.01.025

37. Wang J, Li W, He X, Li S, Pan H, Yin L. Injectable platelet-rich fibrin positively regulates osteogenic differentiation of stem cells from implant hole via the ERK1/2 pathway. *Platelets*. 2023;34(1):2159020. doi: 10.1080/09537104.2022.2159020

38. Majidinia M, Sadeghpour A, Yousefi B. The roles of signaling pathways in bone repair and regeneration. *J Cell Physiol*. 2018;233(4):2937-2948. doi: 10.1002/jcp.26042

39. Daigang L, Jining Q, Jinlai L, et al. LPS-stimulated inflammation inhibits BMP-9-induced osteoblastic differentiation through crosstalk between BMP/MAPK and Smad signaling. *Exp Cell Res*. 2016;341(1):54-60. doi: 10.1016/j.yexcr.2016.01.009

40. Liu C, Weng Y, Yuan T, et al. CXCL12/CXCR4 signal axis plays an important role in mediating bone morphogenetic protein 9-induced osteogenic differentiation of mesenchymal stem cells. *Int J Med Sci*.2013;10(9):1181-1192. doi: 10.7150/ijms.6657

41. Mousavi A. CXCL12/CXCR4 signal transduction in diseases and its molecular approaches in targeted-therapy. *Immunol Lett*. 2020;217:91-115. doi: 10.1016/j.imlet.2019.11.007

42. Xiao G, Jiang D, Thomas P, et al. MAPK pathways activate and phosphorylate the osteoblast-specific transcription factor, Cbfa1. *J Biological Chem*. 2000;275(6): 4453-4459. doi: 10.1074/jbc.275.6.4453

43. Ge C, Xiao G, Jiang D, et al. Identification and functional characterization of ERK/MAPK phosphorylation sites in the Runx2 transcription factor. *J Biological Chem*. 2009;284(47):32533-32543. doi: 10.1074/jbc.M109.040980

44. Fu L, Peng S, Wu W, Ouyang Y, Tan D, Fu X. LncRNA HOTAIRM1 promotes osteogenesis by controlling JNK/AP-1 signalling-mediated RUNX2 expression. *J Cell Mol Med*. 2019;23(11):7517-7524. doi: 10.1111/jcmm.14620

45. Zenz R, Wagner EF. Jun signalling in the epidermis: from developmental defects to psoriasis and skin tumors. *Int J Biochem Cell Biol*. 2006;38(7):1043-1049. doi: 10.1016/j.biocel.2005.11.011

46. Zenz R, Eferl R, Scheinecker C, et al. Activator protein 1 (Fos/Jun) functions in inflammatory bone and skin disease. *Arthritis Res Ther*. 2008;10(1):201. doi: 10.1186/ar2338

47. Vleugel MM, Greijer AE, Bos R, van der Wall E, van Diest PJ. c-Jun activation is associated with proliferation and angiogenesis in invasive breast cancer. *Hum Pathol*. 2006;37(6):668-674. doi: 10.1016/j.humpath.2006.01.022

48. Folkman J. Angiogenesis and c-Jun. *J Natl Cancer Inst*. 2004;96(9):644. doi: 10.1093/jnci/djh148

49. Liekens S, Schols D, Hatse S. CXCL12-CXCR4 axis in angiogenesis, metastasis and stem cell mobilization. *Curr Pharm Des*. 2010;16(35):3903-3920. doi: 10.2174/138161210794455003

50. Mirshahi F, Pourtau J, Li H, et al. SDF-1 activity on microvascular endothelial cells: consequences on angiogenesis in *in vitro* and *in vivo* models. *Thromb Res*. 2000;99(6):587-594. doi: 10.1016/s0049-3848(00)00292-9

51. He C, Zhang H, Wang B, He J, Ge G. SDF-1/CXCR4 axis promotes the growth and sphere formation of hypoxic breast cancer SP cells by c-Jun/ABCG2 pathway. *Biochem Biophys Res Commun*. 2018;505(2):593-599. doi: 10.1016/j.bbrc.2018.09.130

52. Lue H, Dewor M, Leng L, Bucala R, Bernhagen J. Activation of the JNK signalling pathway by macrophage migration inhibitory factor (MIF) and dependence on CXCR4 and CD74. *Cell Signal*. 2011;23(1): 135-144. doi: 10.1016/j.cellsig.2010.08.013

53. Strassheim D, Karoor V, Nijmeh H, et al. c-Jun, Foxo3a, and c-Myc transcription factors are key regulators of ATP-mediated angiogenic responses in pulmonary artery vasa vasorum endothelial cells. *Cells*. 2020;9(2):416. doi: 10.3390/cells9020416

54. Ma J, Zhang L, Han W, et al. Activation of JNK/c-Jun is required for the proliferation, survival, and angiogenesis induced by EET in pulmonary artery endothelial cells. *J Lipid Res*. 2012;53(6):1093-1105. doi: 10.1194/jlr.M024398

55. Huang J, Han Q, Cai M, et al. Effect of angiogenesis in bone tissue engineering. *Ann Biomed Eng*. 2022;50(8):898-913. doi: 10.1007/s10439-022-02970-9

56. Chia HN, Wu BM. Recent advances in 3D printing of biomaterials. *J Biol Eng*. 2015;9:4. doi: 10.1186/s13036-015-0001-4

57. Eftekhari H, Jahandideh A, Asghari A, Akbarzadeh A, Hesaraki S. Assessment of polycaprolacton (PCL) nanocomposite scaffold compared with hydroxyapatite (HA) on healing of segmental femur bone defect in rabbits. *Artif Cells Nanomed Biotechnol*. 2017;45(5):961-968. doi: 10.1080/21691401.2016.1198360

58. Wang S, Lu J, You Q, Huang H, Chen Y, Liu K. The mTOR/AP-1/VEGF signaling pathway regulates vascular endothelial cell growth. *Oncotarget*. 2016;7(33):53269-53276. doi: 10.18632/oncotarget.10756

59. Lee C-C, Chen S-C, Tsai S-C, et al. Hyperbaric oxygen induces VEGF expression through ERK, JNK and c-Jun/AP-1 activation in human umbilical vein endothelial cells. *J Biomed Sci*. 2006;13(1):143-156. doi: 10.1007/s11373-005-9037-7

60. Shin M, Pandya M, Espinosa K, et al. Istradefylline mitigates age-related hearing loss in C57BL/6J mice. *Int J Mol Sci*. 2021;22(15):8000. doi: 10.3390/ijms22158000

61. Mercado-Pagán ÁE, Stahl AM, Shanjani Y, Yang Y. Vascularization in bone tissue engineering constructs. *Ann Biomed Eng*. 2015;43(3):718-729. doi: 10.1007/s10439-015-1253-3

ACCSCIENCE PUBLISHING

International Journal of Bioprinting

RESEARCH ARTICLE

Methacrylic anhydride-assisted one-step *in situ* extrusion 3D bioprinting of collagen hydrogels for enhanced full-thickness skin regeneration

Xiaxia Yang[1,2], Linyan Yao[1,2], Wenhua Li[1,2], Xiaodi Huang[1,2], Na Li[1,2], and Jianxi Xiao[1,2]*

[1] State Key Laboratory of Applied Organic Chemistry, College of Chemistry and Chemical Engineering, Lanzhou University, Lanzhou, Gansu, China

[2] Gansu Engineering Research Center of Medical Collagen, Lanzhou, Gansu, China

Abstract

Full-thickness skin injuries cause extended inflammation, compromised angiogenesis, and protracted wound healing, presenting considerable health risks. Herein, we introduce an innovative technique utilizing methacrylic anhydride (MA)-enhanced, one-step *in situ* extrusion 3D bioprinting of collagen hydrogels, specifically engineered for the effective repair of full-thickness skin injuries. This method capitalizes on the inherent bioactivity of collagen, surmounting its mechanical constraints via a streamlined, one-step extrusion process enabled by MA. The resultant biomaterial ink, an optimized mix of collagen, MA, and photoinitiator, demonstrates superior printability, mechanical robustness, and stability, making it an ideal candidate for direct application to wound sites. The bioprinted collagen scaffolds exhibit improved mechanical strength, reduced swelling, and enhanced resistance to enzymatic degradation, providing a durable matrix for cell proliferation and tissue in-growth. *In vitro* assessments reveal that the scaffolds support human foreskin fibroblast adhesion, proliferation, and migration, creating a conducive environment for skin regeneration. *In vivo* evaluations, conducted using a rat full-thickness skin injury model, further validate the scaffold's efficacy in promoting rapid and orderly tissue repair, characterized by accelerated re-epithelialization and organized collagen deposition. This MA-enhanced, *in situ* extrusion 3D bioprinting technique generates collagen hydrogel scaffolds that significantly accelerate wound healing, offering promising advancements in tissue engineering and regenerative medicine.

Keywords: Collagen; Extrusion 3D bioprinting; Full-thickness skin regeneration

***Corresponding author:**
Jianxi Xiao (xiaojx@lzu.edu.cn)

Citation: Yang X, Yao L, Li W, Huang X, Li N, Xiao J. Methacrylic anhydride-assisted one-step *in situ* extrusion 3D bioprinting of collagen hydrogels for enhanced full-thickness skin regeneration. *Int J Bioprint*. 2024;10(5):4069. doi: 10.36922/ijb.4069

Received: June 28, 2024
Revised: August 5, 2024
Accepted: August 7, 2024
Published Online: August 9, 2024

Copyright: © 2024 Author(s). This is an Open Access article distributed under the terms of the Creative Commons Attribution License, permitting distribution, and reproduction in any medium, provided the original work is properly cited.

Publisher's Note: AccScience Publishing remains neutral with regard to jurisdictional claims in published maps and institutional affiliations.

1. Introduction

The skin, as the body's primary protective barrier and largest organ, is highly susceptible to external damage.[1-4] Full-thickness skin injuries are particularly vulnerable to infections from environmental bacteria, leading to prolonged inflammatory responses, diminished angiogenesis, and delayed wound healing.[5,6] Existing approaches, such as autologous and allogeneic transplantation, seek to improve wound healing, but

clinical applications face challenges, including infection risks, potential harm to soft tissues, and the possibility of immune rejection.[7–9] Tissue engineering for skin repair is an emerging technology that aims to establish personalized microenvironments for wound healing, offering promising solutions to the complexities associated with full-thickness skin injuries.[10–12]

Collagen, the primary component of the dermal layer of the skin, is widely utilized as a scaffold in skin tissue engineering due to its excellent biocompatibility, low immunogenicity, flexibility, and biodegradability.[13–16] Collagen is utilized in various forms (e.g., sponges, films, and hydrogels) for skin repair. Its pivotal roles in hemostasis, inflammation, proliferation, and maturation during wound healing contribute to its effectiveness in promoting skin regeneration.[17–23] Initially, collagen hydrogels provide temporary structural support and create a 3D environment for dermal fibroblasts and keratinocytes, promoting tissue formation and integration.[24,25] As skin regeneration progresses, the hydrogels gradually degrade into biocompatible products. Ideally, the degradation rate should match the tissue regeneration rate for optimal healing. However, traditional tissue engineering techniques face challenges in precisely fabricating highly conformable hydrogels tailored to wound demands.[26]

As a cutting-edge technology in biomanufacturing, 3D bioprinting can produce personalized biomimetic scaffolds tailored to specific wound shapes.[27–29] Extrusion-based 3D printing, the most widely used technique in 3D bioprinting, has been employed to fabricate various tissues such as skin, bone, heart valves, corneas, and more.[30,31] However, current strategies in extrusion-based bioprinting, including support bath,[32,33] temperature[34,35] and pH regulation,[36,37] and post-extrusion crosslinking agents,[38–41] encounter several issues. These include residual support baths, rapid temperature and pH changes causing collagen denaturation, toxic side effects from crosslinking agents, and complex operational procedures, limiting their effectiveness for *in situ* printing directly applicable to wound repair.[42–45] Consequently, there is an urgent need to develop a new, simple, and efficient method for the 3D printing of active collagen with enhanced efficacy.

Herein, we introduce, for the first time, an approach employing methacrylic anhydride (MA)-assisted one-step *in situ* extrusion 3D bioprinting of collagen, which significantly enhances full-thickness skin regeneration (Figure 1). The stable extrusion collagen-based biomaterial ink, consisting of collagen, trace amounts of MA, and the photoinitiator lithium phenyl-2,4,6-trimethylbenzoylphosphinate (LAP), was obtained and efficiently facilitated *in situ* 3D bioprinting of the biomaterial ink through a one-step method. The resulting collagen scaffold exhibited micron-scale resolution, substantial mechanical strength, and robust resistance to swelling and degradation. Demonstrating commendable biocompatibility, these collagen scaffolds supported the proliferation, adhesion, migration, and differentiation of human foreskin fibroblasts (HFF-1 cells). In a rat full-thickness skin injury model, the collagen scaffold exhibited outstanding biological activity, significantly enhancing the regeneration of full-thickness skin injuries. This innovative *in situ* 3D bioprinting method for collagen-based biomaterial ink holds immense potential for applications in tissue regenerative engineering and clinical medicine.

2. Materials and methods

2.1. Materials

Methacrylic anhydride (MA) was procured from Hebei Bailingwei Hyperfine Material Co., Ltd. (China). LAP was obtained from Shanghai Aladdin Biochemical Technology Co., Ltd. (China). Other reagents used were analytically pure.

2.2. Preparation of collagen-based biomaterial ink

Yak tendons are an excellent collagen source due to their high collagen content, constituting 65–80% of their dry weight, predominantly as collagen type I (Col-I). Their superior quality (healthier, purer collagen with fewer contaminants) is attributed to the yaks' high-altitude, pollution-free environments. Additionally, sourcing collagen from yaks is more sustainable and ethical compared to industrial farming, as yaks are often raised in traditional, extensive farming systems that have a lower environmental impact and are more aligned with natural animal behaviors.

The yak tendons were washed with ultra-pure water to remove surface impurities and then cut into small pieces of tendon tissue. These small tissue pieces were soaked overnight in a 20% (w/v) NaCl solution, followed by treatment with a 0.1% (w/v) chlorhexidine solution and a 5% (w/v) hydrogen peroxide solution. Subsequently, they were successively immersed in a 10% (w/v) n-butyl alcohol solution, a 0.1 M NaOH solution, and a 0.5 M HCl solution with shaking.[46] Finally, collagen was extracted from the treated tendon tissue using an acetic acid solution containing pepsin.[47] The extracted yak collagen underwent purification through salting out, redissolving, and dialysis. It was then freeze-dried and stored at −20 °C.

The 100 mg freeze-dried yak collagen was dissolved in 10 mL acetic acid solution (1 M). The solution was stirred until fully dissolved before being transferred to a dialysis bag with a molecular weight cutoff range of 8000–14000 Da. Dialysis was carried out first in a 0.5 M acetic acid solution for 12 hrs, followed by dialysis in a 0.1 M acetic acid solution

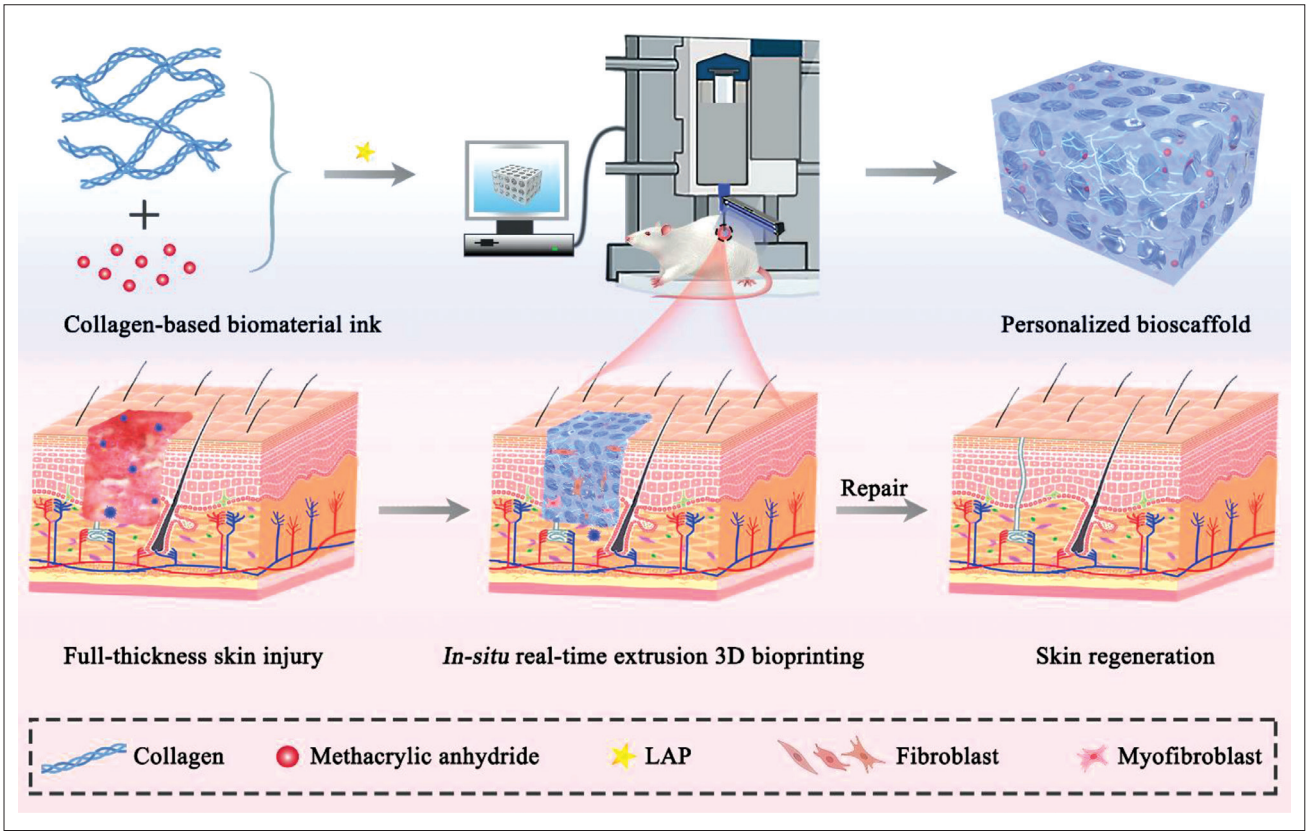


Figure 1. Schematic representation of an *in situ* extrusion 3D-bioprinted collagen scaffold. Abbreviation: LAP: Lithium phenyl-2,4,6-trimethylbenzoylphosphinate.

for another 12 hrs, and finally in ultra-pure water for three days. After achieving neutrality through dialysis, 40 µL MA was added to the collagen solution. After thorough mixing, LAP was added to achieve a final concentration of 0.2% (w/v), obtaining the collagen-based biomaterial ink (CML-Ink) for extrusion-based 3D printing.

2.3. Characterization of CML-Ink

2.3.1. Selection of CML-Inks

The dialyzed 10 mg/mL collagen was mixed uniformly with 0.2–0.5% (v/v) MA and 0.1–0.4% (m/v) LAP solutions to prepare different ratios of CML-Inks.

The CML-Inks were loaded into 5 mL injection syringes, each equipped with a needle featuring an inner diameter of 0.25 mm. This setup was utilized to examine the extrusion states of the CML-Inks. Rheological tests were conducted to assess the mechanical strength of the dynamic mechanical properties of these CML-Inks before and after illumination.

Using a collagen solution (Col) as a reference is crucial for evaluating the properties and performance of the CML-Ink. It provides a consistent baseline for comparing the CML-Ink's gum-forming properties, extrudability, dynamic viscosities, and mechanical strength. This comparison allows for an accurate assessment of how the addition of MA and LAP affects the collagen's behavior, ensuring that any observed changes are attributable to the ink's modifications. This systematic approach helps in understanding the effectiveness of crosslinking and the biomaterial's suitability for various applications.

2.3.2. Evaluation of gelation performance

Both Col and CML-Ink, each at a concentration of 10 mg/mL, were placed in separate vials. The gelation status was observed using the inverted vial method both before and after 10 s of 405 nm light irradiation.

2.3.3. Extrudable properties of CML-Ink

A needle with an inner diameter of 0.6 mm was chosen as the standard for extrusion testing of the CML-Ink. The CML-Ink was loaded into a 5 mL syringe and extruded to spell the word "Col," and the extrusion process was conducted under 405 nm blue light irradiation, with accompanying photographic documentation.

To further verify the stability and uniformity of CML-Ink, Orange G (Aladdin Biochemical Technology Co., Ltd., China) was added and mixed with CML-Ink to extract the shape of a "butterfly" and "sun," accompanied by 405 nm blue light irradiation.

To evaluate the extrudability of Col and CML-Ink, they were loaded into a 5 mL syringe with a needle inner diameter of 0.25 mm. A needle tester (BosinTech, China) was employed to measure the time-dependent extrusion force required for Col and CML-Ink over 30 s. The materials, Col and CML-Ink, were loaded into sterile syringes, which were then connected to the needle device. The extrusion was performed at a constant speed of 10 mm/min, and the thrust magnitude was measured continuously over 30 s at room temperature.

2.3.4. Rheological test

Rheological tests were performed utilizing a modular compact rheometer (MCR 302; Anton Paar, Germany) equipped with a 25 mm stainless steel parallel plate geometry. A multi-step rheological test was carried out to assess the dynamic mechanical properties of both Col and CML-Ink before and after illumination.[48] The changes in the storage modulus (G′) and loss modulus (G″) of Col and CML-Inks were evaluated before, after 30 s, and following 405 nm illumination. These measurements were performed at 25 °C under an angular frequency of 1 rad/s and a strain of 1%.

To explore the shear-thinning properties of Col and CML-Ink, viscosity as a function of shear rate (at $\omega = 1$ rad/s and $\gamma = 1\%$) was measured over a range of 0.01–100 s^{-1}. The dynamic step strain amplitude test, conducted at both low strain ($\gamma = 1.0\%$) and high strain ($\gamma = 300\%$) conditions for three cycles, aimed to investigate the sol–gel transition properties of Col and CML-Ink.

2.4. Extrusion 3D bioprinting of CML-Ink

3D models were designed and generated in SolidWorks CAD software, and subsequently saved in STL file format.[49] 3D bioprinting was conducted using a 3D bioprinter (BIOMAKER2i; Shangpu Boyuan Biotechnology Co., LTD., China) equipped with a modular electric sprinkler head compatible with a disposable standard 5 mL BD syringe. The CML-Ink was loaded into a 5 mL syringe for 3D printing, utilizing a 25 G needle with an inner diameter of 0.25 mm.

A computer-aided design (CAD) model featuring a grid pattern (8.00 × 8.00 × 2.00 mm) was selected, with a line distance set at 500 μm. The model was sectioned, and the printing parameters were configured as follows: a printing speed of 3 mm/s, extrusion speed of 0.3 mm^3/s, and immediate irradiation of the extruded contours with a 405 nm light source upon the start of extrusion printing. After printing the first layer, observations were made through photographs. Subsequently, a two-layer structure was printed to examine the impact of accumulated printed layers on the printing size.

Pentagonal and heart-shaped models were 3D printed using CML-Ink, followed by photographic observation. Finally, a 3D model of a rabbit's head and ears, featuring a complex structure, was designed and introduced for 3D printing.

2.5. Characterization of 3D-printed collagen-based scaffold

2.5.1. Scanning electron microscopyv

The CML-Ink was extrusion-based 3D printed into porous scaffolds, named CML-scaffold, with a pore size of 1.00 mm under the aforementioned 3D printing conditions. The CML-scaffold was then subjected to freeze-drying.

Scanning electron microscopy (SEM) was employed to analyze the microscopic dimensions of the lyophilized CML-scaffold. The scaffold underwent gold spraying treatment for 5 mins inside an ion sputtering machine (Hitachi, Japan). A field emission scanning electron microscope (Hitachi S-4800; Hitachi, Japan) was used to observe the size and microstructural features of the scaffold at a voltage of 5.0 kV.

2.5.2. Mechanical characteristics

Rotational rheological measurements were performed on Col and CML-scaffold with an angular frequency of 1 rad/s, covering a strain range of 1–100%. Additionally, a constant shear strain of 1% was maintained, and frequency scanning was carried out on the Col and CML-scaffold in the range of 0.1–100 Hz.

Compression tests were employed to assess the alterations in mechanical strength of both Col and CML-scaffold at 25 °C using a universal testing machine (AGX-V 500 N; Shimadzu, Japan). Cylindrical CML-scaffold structures, with a height of 2 mm and a diameter of 15 mm, were fabricated using 3D printing. Similarly, Col was placed in a mold of the same size to create the cylinder. The cylindrical hydrogels were positioned on the lower pressure plate, and the upper pressure plate was set to move at 10 mm/min until rupture. Force and displacement were recorded in each case.

The mechanical properties of the CML-scaffold were further verified through tensile measurements. A universal mechanical tester (AGX-V 500 N; Shimadzu, Japan) was employed to assess the tensile properties of the CML-scaffold. Rectangular CML-scaffold samples (25 × 5 ×1.5 mm) were fabricated via 3D printing. The tensile test was

conducted at a speed of 10 mm/min. The elastic modulus was determined by calculating the slope of the stress–strain curve within an elongation range of 25–30%.

2.5.3. Swelling properties

The swelling properties of the CML-scaffold were evaluated by immersing it in deionized water at 25 °C to determine the swelling ratio (SR; %). The initial weight of the CML-scaffold (W_0; g) was recorded prior to immersion. At intervals of 1, 2, 4, 8, 18, 24, 30, 39, and 48 hrs, the scaffold was removed; excess water on its surface was removed by suction using filter paper, and the scaffold was reweighed (W_1; g). The swelling ratio of the hydrogel was calculated using **Equation I**:

$$SR\ (\%) = W_1/W_0 \times 100\% \quad (I)$$

2.5.4. Degradation characteristics

The degradation behavior of the freeze-dried CML-scaffold was assessed in a 5 U/mL collagenase solution, with an equivalent mass of freeze-dried Col serving as a reference. The samples were accurately weighed (W_0; mg) and immersed in 1 mL of collagenase solution at 37 °C. The collagenase solution was refreshed daily to maintain enzyme activity. On days 1, 3, 5, 7, 9, 11, 13, and 15, the samples were withdrawn from the enzyme solution, thoroughly rinsed three times with ultra-pure water, subjected to centrifugation, and the supernatant was removed. The remaining weight (W_t; mg) of the samples was measured after freeze-drying. The degradation rate (MD; %) of the sample was calculated using **Equation II**:

$$MD\ (\%) = (W_0\text{-}W_t)/W_0 \times 100\% \quad (II)$$

Concurrently, the degradation behavior of wet CML-scaffold and ColMA hydrogels, both at the same concentration, was evaluated in a 5 U/mL collagenase solution following the aforementioned method.

2.6. *In vitro* biocompatibility and bioactivity

2.6.1. Cell culture

Human foreskin fibroblasts (HFF-1 cells) were sourced from Procell Life Science & Technology Co., Ltd (China) and cultured in complete cell culture medium, i.e., high-glucose DMEM medium (PM150312; Procell, China) supplemented with 15% fetal bovine serum (FBS; Gibco, Thermo Fisher Scientific, United States of America [USA]) and 1% penicillin-streptomycin antibiotics (Antibiotic-Antimycotic; Hyclone, USA). The cells were maintained at 37˚C in a 5% CO_2 atmosphere.

2.6.2. Cytotoxicity test

The CML-scaffold extracts were obtained by immersing the CML-scaffold in 1 mL of DMEM at 37 °C for seven days. The cytotoxicity of CML-scaffold extract on HFF-1 cells was evaluated using the Cell Counting Kit-8 (CCK-8) assay. A 100 μL suspension of HFF-1 cells, with a density of 1×10^5 cells/mL, was added to a 96-well plate. Following a 24-hour incubation period in a cell incubator (37 °C, 5% CO_2), 100 μL of both DMEM and CML-scaffold extract were separately introduced into the corresponding wells. After an additional 24-hour incubation under the same conditions, the supernatant was removed, and 10 μL of CCK-8 reagent, diluted with 90 μL of DMEM, was added to each well to assess cell viability. The 96-well plate was placed in the dark and incubated for 1 hrs at 37 °C. Subsequently, the optical density (OD) values at 450 nm for the pure DMEM (DMEM), DMEM-treated cells (Blank), and CML-scaffold extract-treated cells (CML-scaffold) were measured using a Tecan Infinite F200/M200 multifunction microplate reader (Tecan, Switzerland). The cell viability of each well was then calculated using **Equation III**:

$$\text{Cell viability}\ (\%) = \frac{(OD_{\text{CML-scaffold}}\text{-}OD_{\text{DMEM}})}{(OD_{\text{Blank}}\text{-}OD_{\text{DMEM}}) \times 100\%} \quad (III)$$

2.6.3. Cell proliferation assay

Cell proliferation was assessed by the CCK-8 assay to evaluate the bioactivity of the CML-scaffold. The HFF-1 cells were seeded onto the CML-scaffold hydrogel and incubated at 37 °C for 1, 3, and 5 days. At each time point, the experimental procedures were conducted following the same protocol used in the cytotoxicity test. Cell activity was calculated using **Equation III**. The OD value of DMEM-treated cells on day 1 served as the blank (OD_{Blank}) for the calculations.

2.6.4. Live/dead staining

The viability of HFF-1 cells on CML-scaffold hydrogels was assessed through live/dead cell staining. HFF-1 cell suspensions at a density of 1×10^5 cells/mL were seeded onto CML-scaffold in laser confocal dishes (diameter: 15 mm) and incubated in a cultivation chamber (37 °C, 5% CO_2). On days 1, 4, and 7, live and dead cells were stained with calcein AM and propidium iodide using the live/dead cell staining reagent kit (CA1630; Solarbio, China). The staining process was performed at 37 °C for 1 hrs, and cellular viability was examined with laser confocal microscopy (FV3000; Olympus, Japan).

2.6.5. Immunofluorescence staining

HFF-1 cells (1×10^5 cells/mL) were seeded onto the CML-scaffold in laser confocal dishes (diameter: 15 mm)

and incubated at 37 °C with 5% CO_2. Cell adhesion was observed on days 1, 4, and 7. At each time point, CML-scaffold-containing cells were fixed sequentially in 4% paraformaldehyde for 10 mins, permeabilized with 0.1% triton X-100 for 5 mins, and then blocked with a 1% bovine serum albumin (BSA) solution for 30 mins at room temperature. Subsequently, the actin cytoskeleton was stained in the dark using phalloidin-tetramethyl rhodamine isothiocyanate (Solarbio, China) for 60 mins at room temperature. Nuclei were stained by incubating with Hoechst 33258 (Solarbio, China) for 20 mins at 37 °C in the dark. Subsequently, a laser confocal microscope (FV3000; Olympus, Japan) was used to capture the fluorescence images.

2.6.6. Cell migration

The capacity of the CML-scaffold to enhance cell migration was evaluated by quantifying changes in the scratched cell area over time. HFF-1 cells at a density of 1×10^5 cells/mL were cultured in 6-well plates with 2 mL of medium. After 24 hrs of incubation in a CO_2 incubator (37 °C, 5% CO_2), a blank area was artificially created at the bottom of the well plate using a white tip. Following a 24-hour incubation with the CML-scaffold, the migration of cells in the well plates was observed using inverted fluorescence microscopy (IX53; Olympus, Japan) and quantitatively analyzed using ImageJ software.

2.6.7. Cell differentiation

HFF-1 cells, at a density of 1×10^5 cells/mL, were cultured in 6-well plates containing 2 mL of medium. Following 24 hrs of incubation in a CO_2 incubator (37 °C, 5% CO_2), the CML-scaffold was placed in 6-well plates with adherent HFF-1 cells for seven days. Subsequently, cell differentiation was assessed by extracting total RNA using an RNA isolation kit (AG21101; Accurate Biology, China). RNA samples' concentration and purity were initially determined with a spectrophotometer (Implant, Germany). Subsequently, cDNA was synthesized using the PrimeScript RT reagent Kit with gDNA Eraser (Takara, Japan) and analyzed with TB Green Premix Ex Taq II (Takara, Japan). Reverse-Transcription Quantitative Polymerase Chain Reaction (RT-qPCR) experiments were conducted using a qPCR system (Mx 3005P; Agilent, USA) to assess the expression of differentiation-related genes in HFF-1 cells. The $2^{-\Delta\Delta CT}$ method, normalized to the housekeeping gene (β-actin) expression levels, was employed to determine the relative expression levels of target genes. The primer sequences for myofibroblast genes are provided in Table 1.

2.7. *In situ* extrusion with a 3D bioprinter of CML-scaffold for full-thickness skin regeneration

2.7.1. Animal model construction

Sprague-Dawley (SD) rats were selected for full-thickness skin regeneration due to their larger size, which facilitates more extensive surgical procedures and handling of larger wound areas, allowing for a more accurate assessment of wound healing and biomaterial interactions. Their size also enhances the evaluation of printability and performance of multi-layer printed scaffolds, enabling better visualization and effectiveness in wound repair. Additionally, the use of SD rats is well-established in similar studies, providing a reliable foundation for comparison and validation of the findings. This approach has offered valuable insights into both the wound-healing process and the performance of the biomaterials.

Sixty male SD rats, weighing between 150 and 200 g, were sourced from the Lanzhou Veterinary Research Institute (China). They were fed a standard laboratory diet. All surgical procedures were performed following the guidelines approved by the Ethics Committee of the College of Chemistry and Chemical Engineering at Lanzhou University (No. G09, 20220711). Prior to the modeling procedure, rats underwent anesthesia via intraperitoneal injection of 10% sodium pentobarbital (0.3 mL/100 g). Subsequently, the rats' dorsal fur was shaved, and the area was cleaned with 0.9% NaCl solution before being sterilized with iodophor. A circular region with a 1.0 cm diameter was delineated on the back. Using surgical scissors, the upper skin tissue was entirely excised to create a circular full-thickness skin defect wound, reaching deep into the fascia. Hemostasis procedures were then carried out.

2.7.2. In situ 3D printing of CML-scaffold

The rats were randomly divided into the control and CML-scaffold groups. The wounds in the control group were left

Table 1. Primer sequence of myofibroblast genes for quantitative reverse transcription polymerase chain reaction (RT-qPCR).

Gene	Sequence	
	Forward (5′–3′)	Reverse (5′–3′)
α-SMA	CTGCTGAGCGTGAGATTGTC	CTCAAGGGAGGATGAGGATG
Vimentin	GGCTCGTCACCTTCGTGAAT	GAGAAATCCTGCTCTCCTCGC
Col-I	TTCACCTACAGCACGCTTGT	TTGGGATGGAGGGAGTTTAC
Col-III	GGTCACTTTCACTGGTTGACGA	TTGAATATCAAACACGCAAGGC

untreated, while the CML-scaffold group first established a consistent-sized STL model of the wound. Subsequently, an *in situ* real-time 3D printing of a CML-scaffold hydrogel scaffold was performed to cover the entire wound area. To prevent material detachment and control a single variable, the wounds of the two groups were covered with sterilized Vaseline gauze and ordinary sterilized gauze, respectively, and secured with elastic bandage and zinc oxide polyethylene (PE) tape.

2.7.3. Macroscopic assessment

Material shedding and wound healing of the rats were observed every day, and samples were collected on days 4, 7, 14, 21, and 28 post-operation. Six rats in each group were euthanized each time. The wound edge tissue and granulation tissue were completely excised and fixed in 10% formaldehyde fixative for more than three days before conventional paraffin embedding. Before each sampling, the corresponding wound was photographed to observe its healing, and ImageJ was used to visualize the skin defect area and overlay it to display the degree of skin repair. Simultaneously, the wound area was calculated by ImageJ, and the wound healing rate was calculated.

2.7.4. Histological analysis

The samples were initially fixed in 4% formaldehyde solution for more than 48 hrs. Subsequently, the samples underwent gradient dehydration using different concentrations of ethanol, followed by embedment in paraffin.[50] The paraffin-embedded samples were sectioned with a thickness of 6 μm. The sections were stained using hematoxylin and eosin (H&E, G1120; Solarbio, China) and Masson's trichrome stain (Masson, G1120; Solarbio, China) to assess the healing status of the full-thickness skin defect. Histological images of the tissues were captured using a vertical microscope (BX63; Olympus, Japan). ImageJ was employed to measure the epithelial regeneration rate and collagen deposition.

2.8. Statistical analysis

The data is presented as the mean ± standard deviation based on the results of three independent experiments. Statistical significance was assessed using Student's *t*-test for the quantitative analysis of various parameters between two independent groups, with significance determined by a *p*-value less than 0.05. Statistical significance is defined as follows: $^{*}p < 0.05$, $^{**}p < 0.01$, $^{***}p < 0.001$, and $^{****}p < 0.0001$.

3. Results

3.1. Characterization of collagen-based biomaterial ink

Printability was assessed by examining the extrusion state of the ink at the needle tip and determining whether the ink promptly gelled after extrusion to maintain shape and structural stability in extrusion-based bioprinting.[51] The concentration of MA and LAP, as constituents of the CML-Ink, significantly influenced its extrudability and structural stability after extrusion and photocuring (Figure 2A). In the triangular region (LAP ≥ 0.4% m/v; MA ≥ 0.5% v/v, LAP ≥ 0.2% m/v), the CML-Ink formed droplets at the needle tip. Meanwhile, in the rectangular area (LAP ≤ 0.1% m/v, MA ≤ 0.4% v/v), the CML-Ink faced challenges in extrusion, leading to nozzle blockages, difficulty in printing, and poor curing, thereby hindering scaffold support. Conversely, the CML-Ink in the circular area facilitated uniform filamentous extrusion with favorable curing properties, making it suitable for extrusion 3D printing. Under varying LAP concentrations, the G′ of CML-Ink reached its maximum after the addition of 0.4% MA (Figure S1, Supporting Information), indicating the optimal concentration for effective optical crosslinking. Likewise, 0.2% LAP was selected to ensure effective photoinitiation while minimizing potential cytotoxicity. Prioritizing safety with biological materials, we selected 0.2% (m/v) LAP and 0.4% (v/v) MA for subsequent experiments.

The CML-Ink was prepared by thoroughly mixing collagen with a small quantity of MA and LAP. The gum-forming properties of Col and CML-Ink were assessed using the inverted vial method both before and after exposure to 405 nm light (Figure 2B). Prior to light exposure, both Col and CML-Ink displayed a milky-white appearance. Following 10 s of light exposure, Col demonstrated no discernible alterations and retained its fluid state, whereas CML-Ink underwent solidification, forming a stable hydrogel. These findings indicate that CML-Ink undergoes crosslinking upon exposure to blue light irradiation.

The extrudability of the CML-Ink was investigated by loading it into a 5 mL syringe (Figure 2C). Upon extrusion, the CML-Ink formed the word "Col" and promptly solidified, demonstrating its ability to be extruded into a desired shape with excellent extrudability. Furthermore, shape stability was maintained after extrusion. To validate the stability and uniformity of the CML-Ink, it was blended with Orange G and extruded into predetermined shapes (Figure 2D). The outcomes revealed that the CML-Ink remained stable even after mixing with Orange G, enabling continuous extrusion of uniform "butterfly" and "sun" shapes. This indicates that the CML-Ink is a stable ink for uniform 3D bioprinting.

A multi-step rheological test was conducted to measure the variation in mechanical strength between Col and CML-Ink before and after illumination (Figure 2E). Prior to illumination, the CML-Ink displayed consistent values of G′ and G″. After 30 s of illumination, both G′and G″

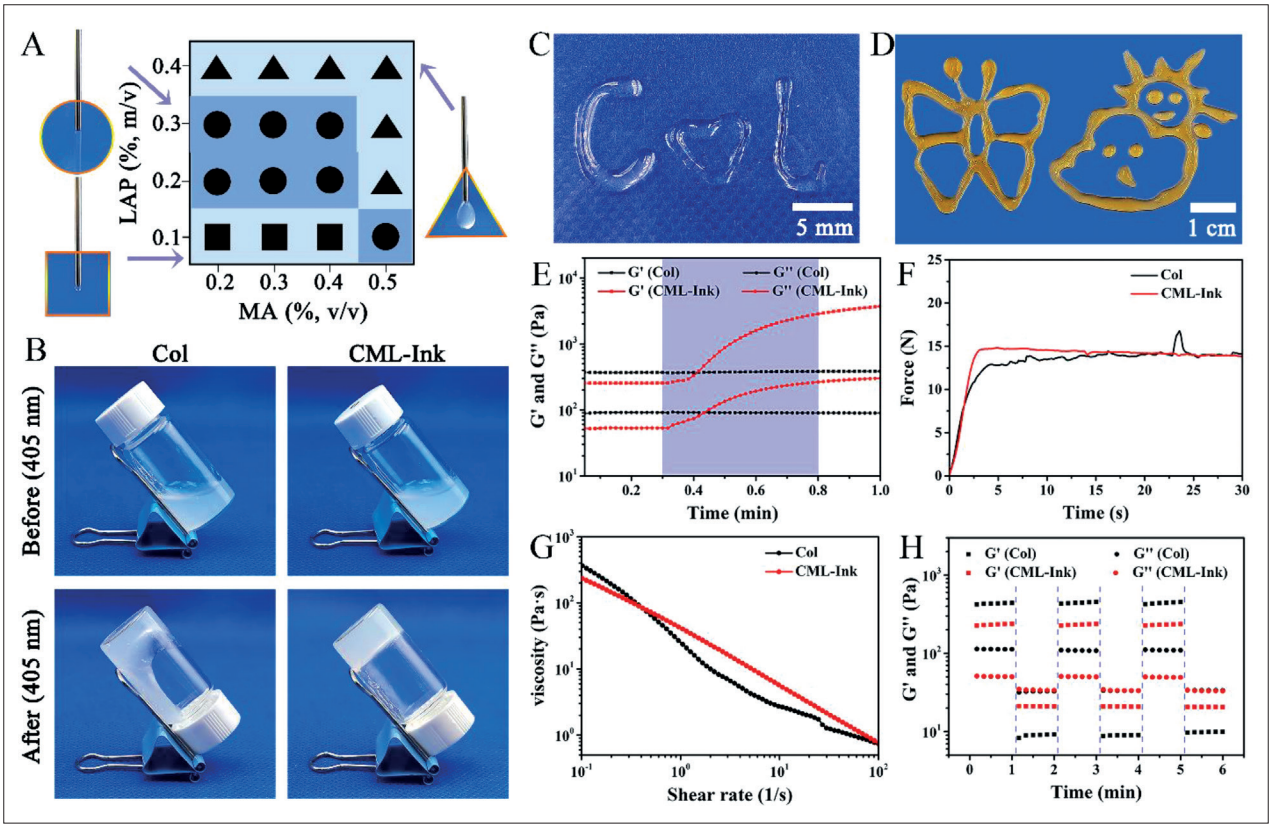


Figure 2. Characterization of the collagen biomaterial ink (CML-Ink). (A) Printability zone of the CML-Ink. (B) Gum-forming properties of the collagen solution (Col) and CML-Ink. (C) Extrudability of the CML-Ink. (D) Stability and uniformity of the CML-Ink. (E) A multi-step rheological test of Col and the CML-Ink. (F) Extrudable performance of Col and the CML-Ink. (G) Viscosity of Col and the CML-Ink at different shear rates. (H) Dynamic step strain amplitude test of Col and the CML-Ink. Abbreviations: MA: Methacrylic anhydride; LAP: Lithium phenyl-2,4,6-trimethylbenzoylphosphinate; G′: Storage modulus; G″: Loss modulus.

increased significantly, with G′ rising by 14 times compared to its pre-illumination level. In contrast, Col maintained constant values of G′ and G″ before and after illumination. These findings indicate that the mechanical strength of the CML-Ink substantially improved following illumination at 405 nm.

The Col and CML-Ink were loaded into the syringe used for 3D printing, with consistent extrusion speed and needle size, adhering to the printing conditions. The extrusion pressure experiment was carried out at room temperature to determine the extrudable performance of the prepared ink (Figure 2F). Col exhibited noticeable fluctuations in the pushing force required during the extrusion process. In contrast, the CML-Ink could be consistently extruded as a uniform fine filament with a pushing force of approximately 15 N, indicating its stable extrudable performance and suitability for 3D printing.

The dynamic viscosities of Col and the CML-Ink were measured at 25 °C across shear rates of 0.1–100 s^{-1} (Figure 2G). The viscosity of both Col and the CML-Ink decreased as the shear rate increased. The CML-Ink exhibited a linear decrease, suggesting stable shear thinning behavior across the tested range and suitability for extruded 3D printing.

A dynamic step strain amplitude test (γ = 1.0 or 300%) was carried out at 25 °C to replicate the extrusion process of Col and the CML-Ink in a syringe through continuous step changes of oscillating strain (Figure 2H). Upon application of high strain (300%), the internal structure of both Col and the CML-Ink was immediately disrupted, leading to a decrease in G′ to approximately 9 and 21 Pa, respectively, with G′ becoming lesser than G″ and exhibiting a sol-like appearance. However, upon reduction to low strain (1%), the G′ and G″ of both materials almost fully recovered within a few seconds, with G′ surpassing G″ and displaying a gel-like appearance. Both Col and CML-Ink demonstrated rapid sol-gel conversion ability during the three rupture and reforming cycles, indicating their ability to swiftly transition to a sol state during syringe extrusion and return to the pre-extrusion gel state immediately afterward.

3.2. Real-time 3D printing of the CML-Ink

A CAD model with a grid structure (8.00 × 8.00 × 2.00 mm) was selected, with the line distance set at 500 μm, to evaluate the real-time 3D printing performance of the CML-Ink. After printing the first layer, photographs were taken to observe and measure the size of the printed structure (Figure 3A). The CML-Ink could be uniformly extruded and cured immediately after illumination. The line distance of the printed structure, calculated by ImageJ, was 500.30 ± 10.42 μm, and the width of the extruded linear scaffold was 262.63 ± 3.50 μm, consistent with the printing settings. Double-layer printing was utilized to investigate the effect of layer count on printing accuracy (Figure 3B). The double-layer printing structure maintained micrometer-level precision without structural collapse, indicating no impact between the printed layers in the 3D printing of CML-Ink.

Complex CAD models were employed for extrusion-based 3D printing to investigate the printability of the CML-Ink. Printing pentagonal and heart-shaped patterns with a certain thickness demonstrated the efficient 3D printing of 3D structures using the CML-Ink (Figure 3C). The precise 3D printing of complex rabbit patterns and organ-like ear models indicated CML-Ink's capability for accurately manufacturing intricate 3D structures (Figure 3D). These findings highlight the broad printing capabilities of the CML-Ink.

3.3. Physicochemical characterization of CML-scaffold

The CML-Ink was extrusion-based 3D printed into porous scaffolds, named CML-scaffold, with a pore size of 1.00 mm, and then freeze-dried (Figure 4A). Scanning electron microscopy (SEM) was used to characterize the microscopic dimensions of the freeze-dried CML-scaffold (Figure 4B), revealing a grid pattern with each side length

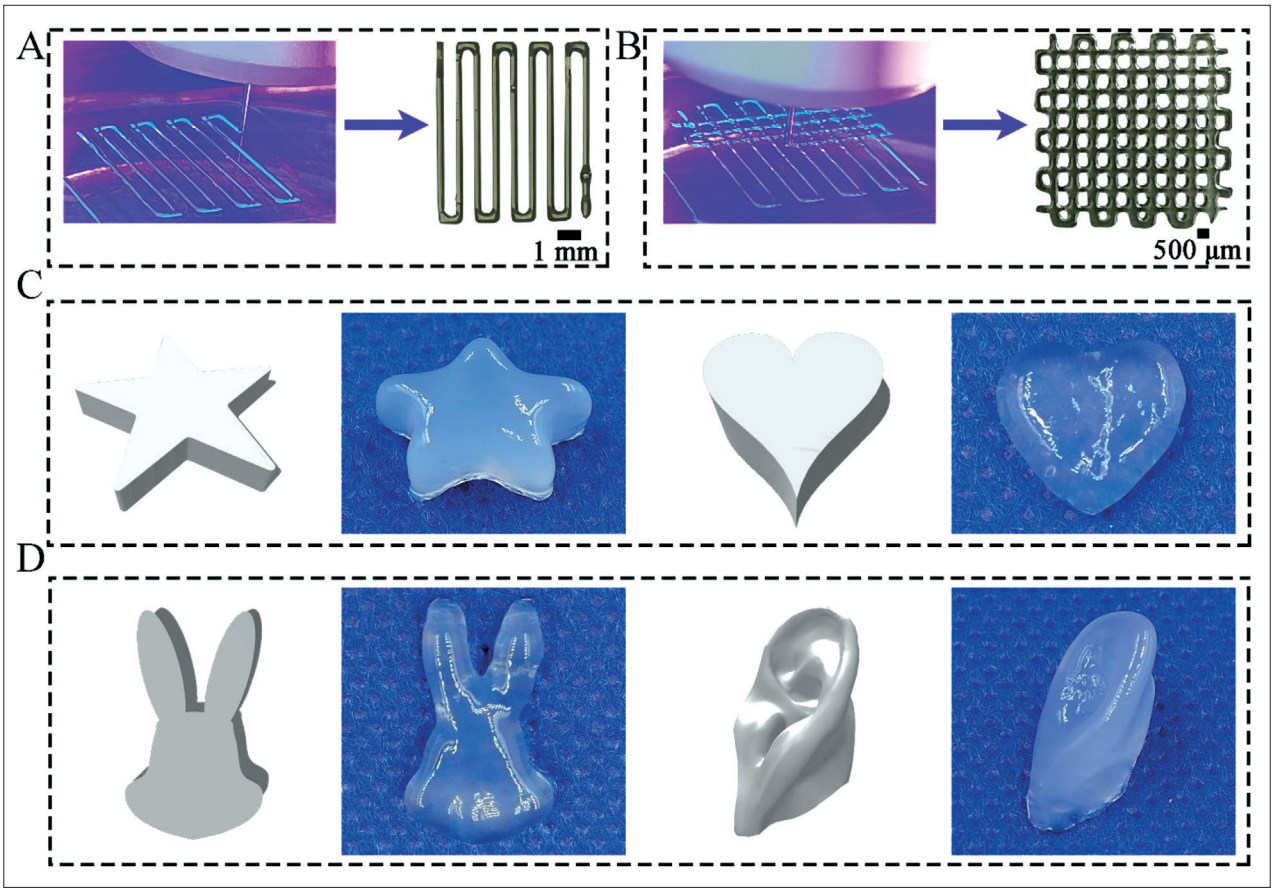


Figure 3. Real-time 3D printing of the collagen biomaterial ink (CML-Ink). Single-layer 3D printing (A) and double-layer 3D printing (B) of the grid structure. (C) 3D-printed five-pointed star- and heart-shaped models. (D) 3D-printed complex rabbit- and ear-shaped structures. Scale bars: 1 mm (A); 500 μm (B).

measuring 1.00 ± 0.05 mm, consistent with the grid model size. The structure exhibited a well-defined mesh with interconnected pores, and the average pore size was 33.28 ± 7.57 μm (Figure S2, Supporting Information).

Rheological testing was performed to investigate the mechanical characteristics of Col and the CML-scaffold. The amplitude scan curves revealed that the CML-scaffold exhibited a wider linear viscoelastic region (LVR) compared to Col, with G′ being higher than Col's G′ at both LVRs. At a strain of 1%, the CML-scaffold had a G′ of 3974 Pa, while Col had a G′ of 467 Pa (Figure 4C). The results indicate that both Col and the CML-scaffold exhibit a viscoelastic solid state within the LVR range, with the CML-scaffold notably possessing significantly higher hardness than Col. The frequency scan curves revealed that the G′ of both Col and the CML-scaffold remained consistently higher than the G″ within the frequency range of 1–100 rad/s (Figure 4D). The CML-scaffold exhibited minimal variations in G′ across different frequencies, indicating its ability to maintain a stable gel state under both short- and long-timescale stress. In contrast, the strength of Col was notably influenced by the timescale, suggesting temporal sensitivity. Consequently, the mechanical strength of Col was significantly lower compared to that of the CML-scaffold.

Compression tests were conducted on Col and the CML-scaffold to further assess changes in mechanical strength. The compressive stress–strain curves revealed that when the strain of the CML-scaffold reached 44.99%, its ultimate fracture strength was 216.68 kPa, while the compressive strength of Col under this strain was 4.21 kPa (Figure 4E). In the elastic phase (0–20%), the compressive moduli were

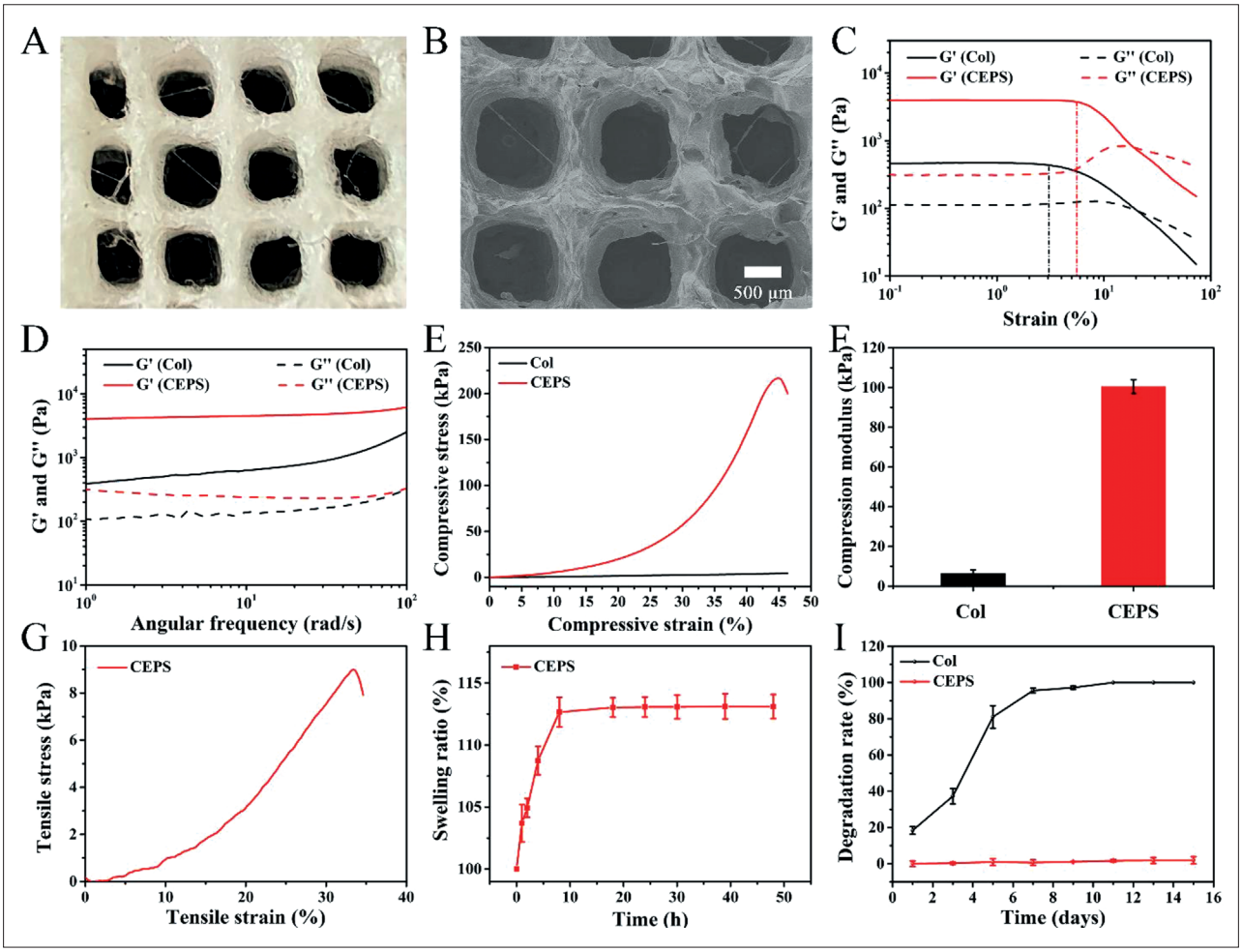


Figure 4. Physicochemical characterization of the collagen biomaterial scaffold (CML-scaffold). (A) Freeze-dried CML-scaffold. (B) Scanning electron microscopic (SEM) image of the CML-scaffold. (C and D) The amplitude (C) and frequency (D) scan curves of the collagen solution (Col) and CML-scaffold. (E and F) The compressive stress–strain curves (E) and the compressive moduli (F) of Col and the CML-scaffold (n = 3). (G and H) The tensile curve (G) and swelling characteristics (H) of the CML-scaffold (n = 3). (I) Degradation of Col and the CML-scaffold (n = 3). Abbreviations: G′: Storage modulus; G″: Loss modulus.

100.49 ± 3.46 kPa and 6.37 ± 1.88 kPa, respectively (Figure 4F). The findings emphasized that the CML-scaffold was significantly stronger mechanically than Col.

The mechanical properties of the CML-scaffold were further investigated through tensile measurements. The maximum tensile stress recorded for the CML-scaffold was 9.07 kPa, with a corresponding strain of 33.72% (Figure 4G). The elastic modulus was determined to be 45.49 ± 2.50 kPa. These findings collectively indicate that the CML-scaffold possesses excellent mechanical strength.

The CML-scaffold was submerged in deionized water to assess its swelling ratio (SR) at various time points (Figure 4H). The swelling of the CML-scaffold reached equilibrium within 8 hrs, achieving an SR of approximately 113%, and no macroscopic alterations were detected in the scaffold structure. The result highlights that the CML-scaffold exhibited a nearly constant expansion rate and demonstrated outstanding structural stability.

The degradation characteristics of the freeze-dried CML-scaffold, along with an equivalent mass of Col, were assessed in a 5 U/mL collagenase solution (Figure 4I). Col degraded by 81.06, 95.60, and 97.20% on days 5, 7, and 9, respectively, and completely degraded by day 11. In contrast, the CML-scaffold demonstrated a degradation rate of only 1.91% on day 15, highlighting its robust resistance to degradation. Additionally, the degradation rates of ColMA and the CML-scaffold hydrogels post-polymerization were compared (Figure S3, Supporting Information). Both hydrogels exhibited progressive degradation over time. By day 15, the ColMA hydrogel had degraded by 47.08%, whereas the CML-scaffold hydrogel displayed a slower degradation rate of 28.16%, indicating enhanced stability.

3.4. *In vitro* biocompatibility and bioactivity of CML-scaffold

The CCK-8 assay was employed to assess the cytotoxicity of CML-scaffold extract *in vitro* (Figure 5A). In comparison to the blank group, the viability of HFF-1 cells cultured in the CML-scaffold extract was 100%, indicating that the CML-scaffold exhibited no cytotoxic effects and demonstrated excellent cytocompatibility. The biological activity of the CML-scaffold was evaluated through a cell proliferation assay. The proliferation of HFF-1 cells in the CML-scaffold was assessed using the CCK-8 assay on days 1, 3, and 5 (Figure 5B). On day 1 of culture, the relative proliferation rates for the blank and CML-scaffold groups were 100.00 and 104.98%, respectively. By day 3, the proliferation rates increased to 104.12 and 111.78%, respectively. On day 5, the levels further rose to 106.73 and 119.56%, respectively, indicating that the CML-scaffold could enhance the proliferation of HFF-1 cells.

Live/dead cell staining was further employed to assess the cell survival status on the CML-scaffold (Figure 5C). The laser confocal scanning microscopy images displayed that the original structure of the CML-scaffold remained intact after seven days of culture. HFF-1 cells were uniformly distributed on the scaffold and thriving throughout its entirety, with no dead cells observed on day 7. These results suggest that the CML-scaffold demonstrated outstanding biological activities, promoting cell growth both around and within the scaffold.

Immunofluorescence staining was utilized to observe the adhesion of HFF-1 cells on the CML-scaffold (Figure 5D). Fluorescence images captured by the laser confocal microscope revealed that HFF-1 cells adhering to the CML-scaffold were uniformly distributed in a spindle shape, displaying a complex actin cytoskeleton structure. These observations indicate that the biological scaffold offered by the CML-scaffold substantially promoted the adhesion and spreading of HFF-1 cells.

The ability of the CML-scaffold to enhance cell migration was evaluated by measuring the change in cell scratch area (Figure 5E). The inverted fluorescence microscopy results demonstrated that the CML-scaffold markedly enhanced the migration of HFF-1 cells, as quantitatively analyzed, revealing a migration rate of 80.29%, in contrast to the blank group, which exhibited a rate of only 26.86% (Figure 5F). Statistical analysis revealed a notable disparity in the cell migration rate between the two groups.

Reverse-transcription quantitative polymerase chain reaction (RT-qPCR) was employed to assess the expression of differentiation-related genes in HFF-1 cells cultured on the CML-scaffold (Figure 5G). In comparison to the blank group, the CML-scaffold markedly enhanced the expression of α-smooth muscle actin (α-SMA), vimentin, Col-I, and collagen type III (Col-III) in HFF-1 cells. These findings indicated that the CML-scaffold significantly promoted the differentiation of fibroblasts into myofibroblasts.[52] In summary, the CML-scaffold provided a highly bioactive scaffold for HFF-1 cell adhesion, migration, and differentiation.

3.5. *In situ* extrusion of CML-scaffold for full-thickness skin regeneration

The rat full-thickness skin injury model was employed to assess the reparative effects of the CML-scaffold on full-thickness skin injuries. The CML-scaffold was precisely 3D printed *in situ* by extrusion onto the site of full-thickness skin defects (Figure 6A). The decision to apply *in situ* printing instead of using pre-fabricated printed scaffolds was based on several key advantages. *In situ* printing enables direct deposition of biomaterials at the injury site, promoting better integration with surrounding tissue

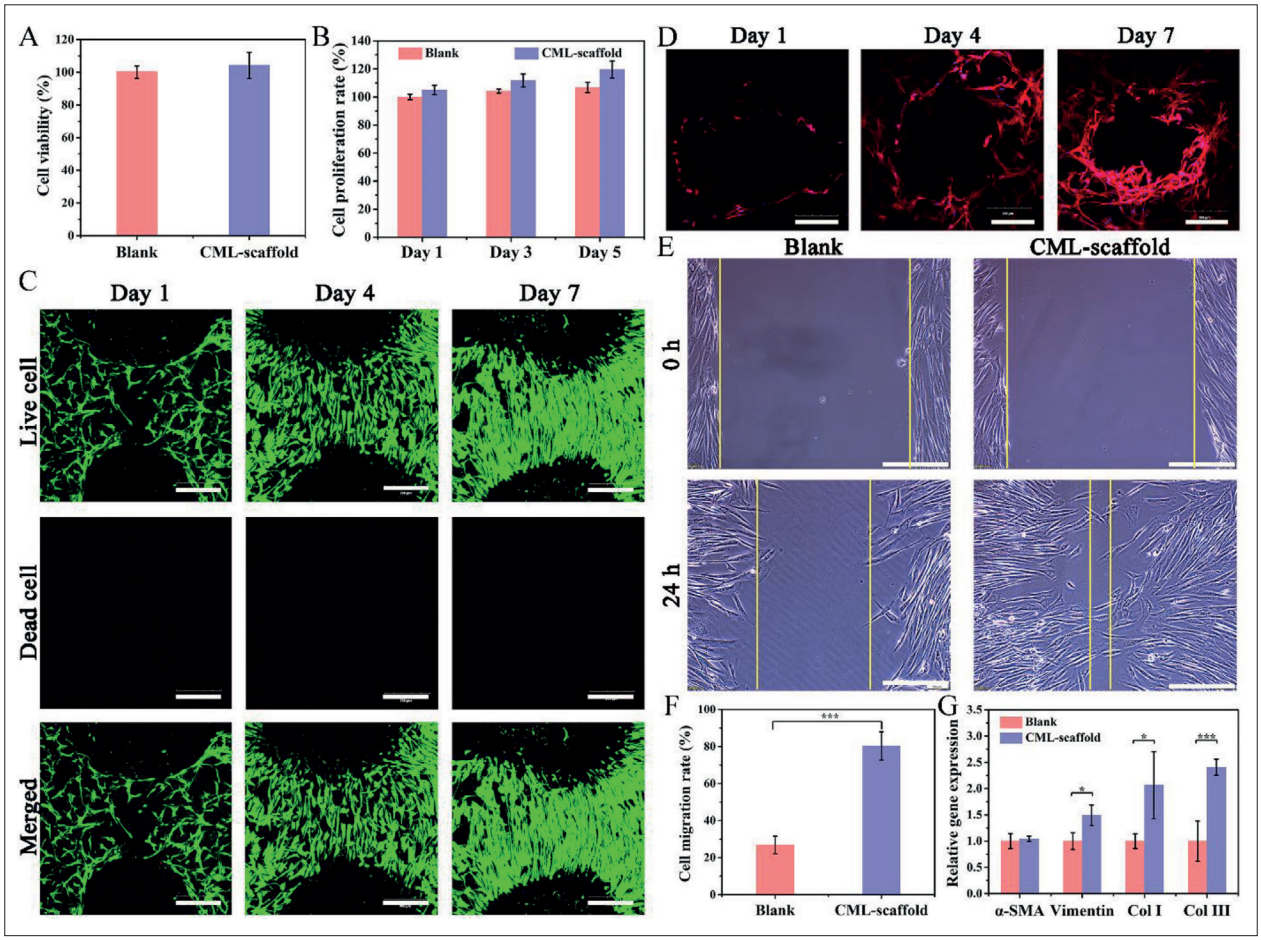


Figure 5. *In vitro* biocompatibility and bioactivity of the collagen biomaterial scaffold (CML-scaffold): (A) cytotoxicity, (B) cell proliferation rate, (C) live/dead cell staining, (D) immunofluorescence staining, (E) cell migration, (F) cell migration rate, and (G) expression of differentiation-related genes of HFF-1 cells cultured on the CML-scaffold. Data is expressed as mean ± standard deviation (n = 3); $^{*}p < 0.05$, $^{***}p < 0.001$. Scale bars: 300 μm (C–E). Abbreviations: α-SMA: Alpha smooth muscle actin; Col: Collagen.

and customization to fit the damaged area's unique needs. This method also reduces risks of contamination and complications associated with handling, sterilization, and implantation of pre-fabricated scaffolds. Additionally, *in situ* printing allows for real-time adjustments during the printing process, accommodating changes in the surgical environment or tissue characteristics that are not possible with pre-fabricated scaffolds. This approach enhances the efficiency and effectiveness of the treatment.

Photographs of the wounds were captured before each sampling to monitor their healing progress for gross observation. The skin injury areas were visualized using ImageJ and superimposed to depict the extent of skin repair (Figure 6B). The wound area was quantitatively analyzed using ImageJ to calculate the wound healing rate (Figure 6C). In both the control and CML-scaffold groups, wound contraction began on day 4, with wound healing rates of 25.77 and 47.74%, respectively. By day 7, a portion of the scab naturally fell off in the CML-scaffold group, resulting in a wound healing rate of 62.58% compared to 82.38% in the control group. On day 14, scabs fell off in both groups, with wound healing rates of 82.38 and 98.07%, respectively. By day 21, the wound closure rates for the control and CML-scaffold groups were 90.42 and 99.07%, respectively. On day 28, the wounds in the CML-scaffold group were entirely replaced by regenerated skin, whereas there was still a 1.40% residual wound in the control group. The findings indicate that the CML-scaffold had a notable capability to promote wound healing significantly.

Hematoxylin and eosin (H&E) staining was performed to evaluate the extent of epithelialization and tissue regeneration in the injuries of both groups (Figure 7A and C). On day 4 post-modeling, granulation tissue

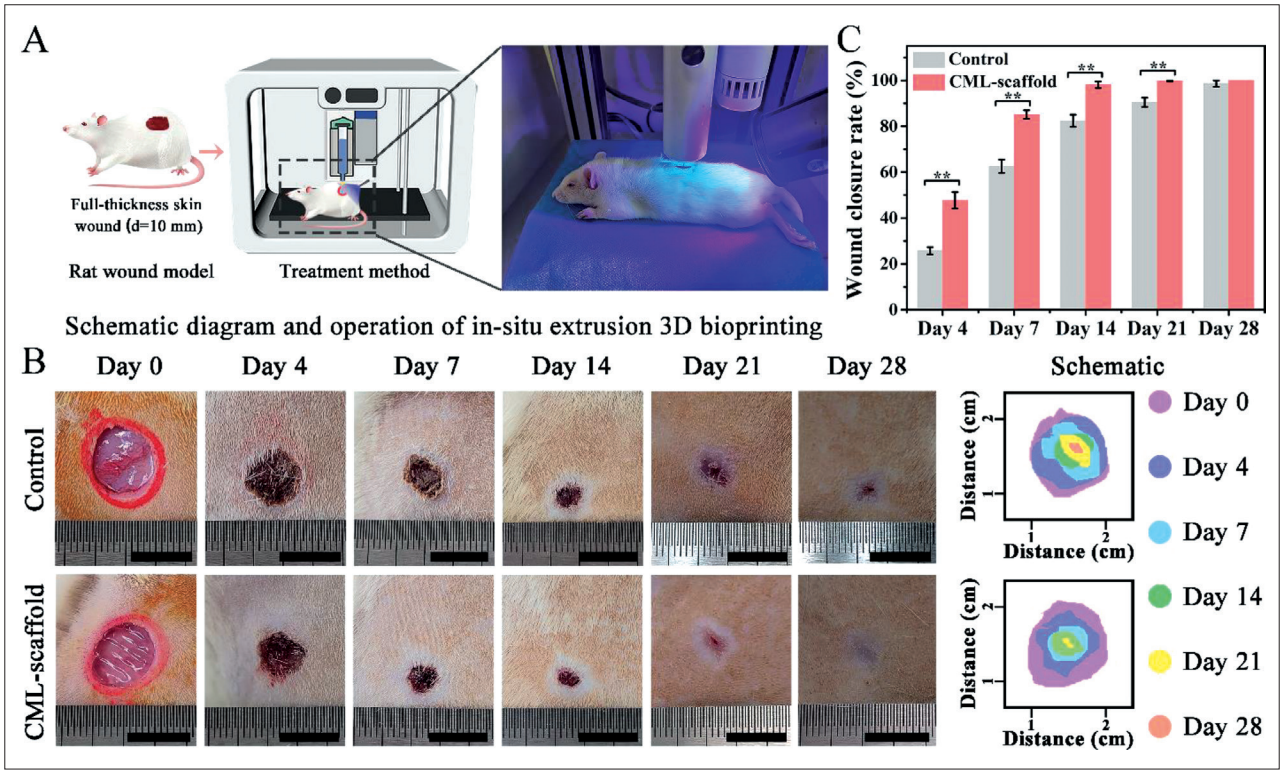


Figure 6. *In situ* extrusion 3D bioprinting of the collagen biomaterial scaffold (CML-scaffold) for full-thickness skin regeneration. (A) Schematic diagram of the rat full-thickness skin injury model and treatment method. (B) Gross observation photographs of the wound healing process and the extent of skin repair. (C) Wound healing rate. Data is expressed as mean ± standard deviation ($n = 6$); $^{**}p < 0.01$. Scale bars: 10mm. Abbreviation: d: Diameter.

appeared in the CML-scaffold group, and epithelial cells began to migrate. The epithelial regeneration rates for the control and CML-scaffold groups were 25.14 and 48.01%, respectively. By day 7, both groups exhibited a significant amount of granulation tissue, with epithelial regeneration rates of 67.77% for the control group and 83.90% for the CML-scaffold group. On day 14, epithelial tissue had formed on the wound surface of the CML-scaffold group, with a regeneration rate of 98.76%, compared to 84.35% in the control group. On day 21, reticular epithelium began growing in the CML-scaffold group, reaching a regeneration rate of 99.45%. Conversely, the control group exhibited delayed wound healing, with an epidermal regeneration rate of 91.64%. By day 28, the CML-scaffold group achieved complete re-epithelialization, resembling normal epidermis. In the control group, the central part of the wound was still not completely covered by the epidermis, resulting in an epithelial regeneration rate of 97.79%. These experimental results confirmed that the CML-scaffold had a significant reparative effect on full-thickness skin injuries, yielding newly formed regenerated skin with dense and orderly characteristics similar to normal skin.

Masson's trichrome staining was utilized to visualize the deposition of regenerated collagen fibers in the skin (Figure 7B and D). On day 4, sporadic collagen fibers appeared in the skin wounds of both the control and CML-scaffold groups, accounting for 1.15 and 7.39%, respectively. By day 7, the presence of new collagen fibers in the CML-scaffold group significantly increased to 31.30%, while the collagen fibers in the control group remained less prominent at 4.79%. At day 14, the collagen fiber proportions for each group were 30.84 and 68.90%, respectively. On day 21, a substantial number of newly formed collagen fibers were observed in both the control and CML-scaffold groups, constituting 49.84 and 85.71%, respectively. By day 28, the regenerated collagen fibers in the CML-scaffold group were densely arranged, accounting for 95.11%, while the collagen fibers in the control group were sparsely distributed, accounting for 71.15%. These observations suggest that the CML-scaffold promotes skin regeneration by enhancing granulation tissue development, accelerating re-epithelialization, and guiding the orderly deposition of collagen fibers.

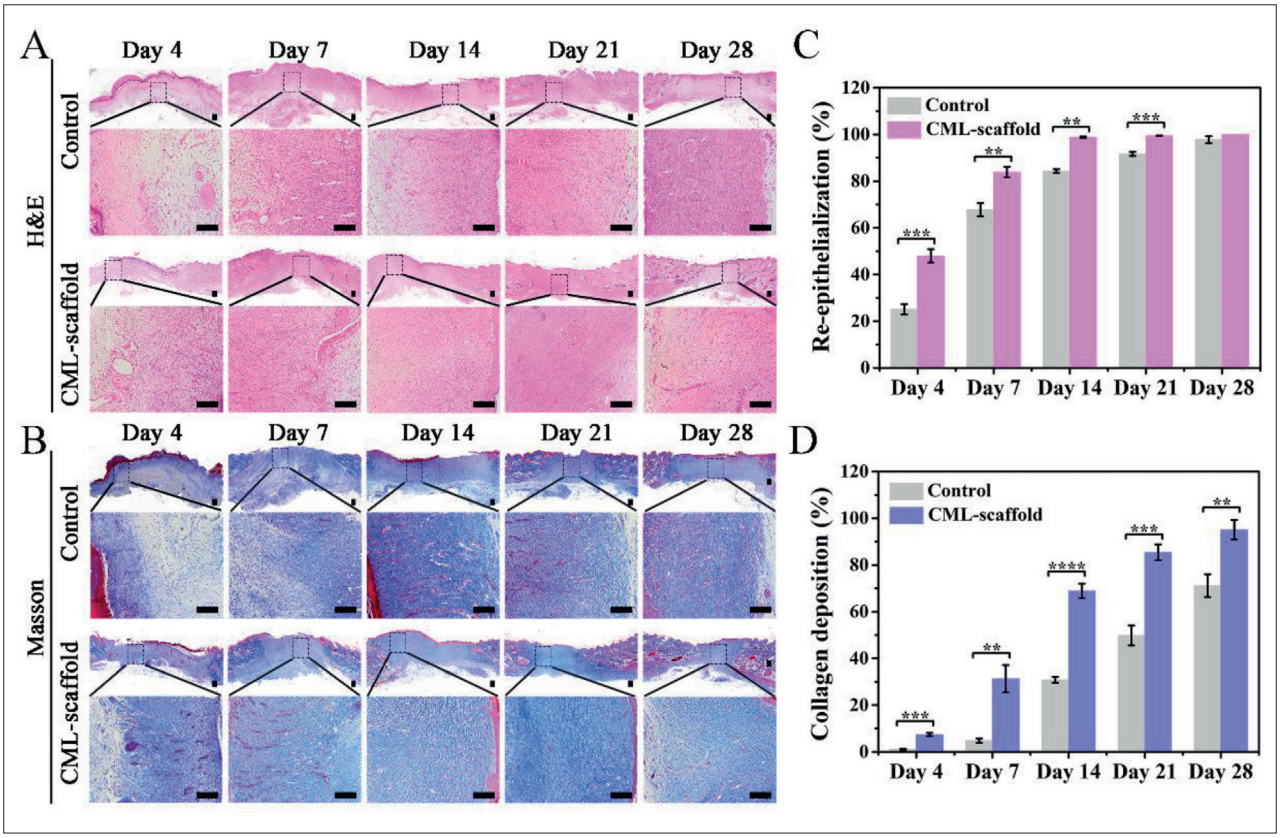


Figure 7. Histological evaluation of the rat full-thickness skin injury: (A) hematoxylin and eosin (H&E) staining, (B) Masson's trichrome staining, (C) extent of epithelialization, and (D) deposition of regenerated collagen fibers of skin regeneration on days 4, 7, 14, 21, and 28 after modeling and collagen biomaterial scaffold (CML-scaffold) implantation. Data is expressed as mean ± standard deviation ($n = 6$); $^{**}p < 0.01$, $^{***}p < 0.001$, $^{****}p < 0.0001$. Scale bars: 200 μm.

4. Discussion

Skin damage requires timely intervention to prevent complications and promote healing. Traditional treatments, such as skin transplantation, pose risks including infection and rejection. In contrast, 3D bioprinting can create personalized bionic skin, enhancing wound healing.[53,54] Compared to gelatin and dextran, collagen is the primary component of skin and possesses a complete triple helix structure, making it more suitable for 3D printing biomaterials. This structural integrity better mimics the natural extracellular matrix, which is crucial for enhancing cell adhesion, proliferation, and differentiation in 3D printing applications, thereby improving the performance and efficacy of the printed scaffolds.[13–16] However, current 3D printing methods face challenges, such as complex procedures and standalone application difficulties, limiting their clinical use. *In situ* bioprinting, which deposits biomaterials directly at the injury site, offers a solution by allowing real-time adjustments and better tissue integration.

In this study, we successfully printed scaffolds *in situ* on full-thickness skin lesions in rats by combining collagen with MA and LAP in a single-step process. The printability of the CML-Ink was evaluated based on its gelatinization, extrudability, and rheological properties. The gelatinous collagen, obtained by dialysis to neutral pH, gains colloidal properties through the addition of trace amounts of MA and LAP.[55] This crosslinking allows the CML-Ink to be cured immediately after extrusion from the print needle, eliminating the need for a support bath or secondary treatment.[32–41] The CML-Ink exhibits shear-thinning behavior, and its G′ is significantly greater than its G″. These properties make the ink well-suited for direct extrusion 3D printing.[56]

The physical and chemical properties of 3D-printed biological scaffolds significantly impact their biomedical applications. Sufficient mechanical strength of the biological scaffold is crucial for simulating the properties of normal skin and accelerating the healing of full-thickness skin wounds.[57] Notably, the CML-scaffold exhibits a higher compression modulus compared to 3D-printed scaffolds

with high collagen concentrations.[58] Additionally, its aperture size is conducive to cell growth,[59] rendering it more appropriate for applications necessitating enhanced strength and cellular proliferation. To effectively promote skin regeneration, the printed scaffold must possess an appropriate degradation rate.[60]

The CML-scaffold significantly enhances the proliferation, adhesion, migration, and differentiation of HFF-1 cells, demonstrating its excellent biocompatibility and biological activity. This suggests that the CML-scaffold is a promising material for supporting cellular functions essential for effective tissue regeneration. During the *in situ* printing process, the animal is positioned within the bioprinter, which facilitates the direct deposition of the scaffold onto the wound site. This method improves the integration of the scaffold with the surrounding tissue, thereby enhancing binding efficiency and functional recovery. Additionally, it allows for the precise customization of the scaffold to match the unique geometry of the damaged tissue, reducing the risk of contamination and complications associated with handling, disinfection, and implantation. *In situ* bioprinting also permits real-time adjustments to accommodate changes in the surgical environment or tissue properties, thereby simplifying the treatment process and increasing overall efficiency.

The CML-scaffold, characterized by its excellent biocompatibility and mechanical properties, in conjunction with the precision and adaptability of *in situ* bioprinting, demonstrates significant potential for advancing tissue regeneration and skin tissue engineering. Future research will focus on incorporating cells into the scaffold to enhance its regenerative capabilities and overall treatment efficacy.[61] This approach aims to investigate the potential improvements in scaffold performance in supporting tissue repair and regeneration through cellular integration.

5. Conclusion

The skin, the body's primary barrier, is prone to damage, especially in full-thickness injuries, which can lead to prolonged inflammation, compromised angiogenesis, and delayed wound healing, posing significant health risks.[62] Conventional methods, like transplantation, aim to enhance the healing process; however, they encounter challenges such as the risk of infections and immune rejection. Tissue engineering for skin, an emerging technology, strives to establish a personalized microenvironment to enhance wound healing. Collagen, as a critically important biomaterial, holds extensive potential applications in tissue engineering processes. However, achieving precise tailoring for skin wounds remains a challenge in traditional tissue engineering. 3D bioprinting, a cutting-edge technique, offers automated precision for intricate biomimetic tissue structures using collagen. Presently, extrusion-based 3D printing of collagen presents challenges such as complex operation, residual support bath, and the risk of collagen denaturation.

In this study, we have presented an innovative approach involving MA-assisted one-step *in situ* extrusion 3D bioprinting of collagen to significantly improve full-thickness skin regeneration. We prepared collagen-based biomaterial ink for extruded 3D printing by directly mixing a trace amount of MA and the photoinitiator LAP with collagen. This method is straightforward, enabling *in situ* 3D bioprinting of collagen through a one-step process, without the need for secondary crosslinking steps, thereby minimizing the risk of collagen denaturation. The resulting collagen scaffolds from 3D printing exhibited micron-scale resolution, significant mechanical strength, and stable anti-swelling and anti-degradation properties. The scaffolds demonstrated good cell compatibility, promoting the proliferation, adhesion, migration, and differentiation of human foreskin fibroblasts. In a rat full-thickness skin injury model, the collagen scaffold exhibited excellent biological activity, significantly enhancing epidermal regeneration and orchestrating collagen deposition in the injured skin. This one-step *in situ* 3D printing of collagen-based biomaterial ink represents a novel strategy for the regeneration of damaged skin, providing vast potential for applications in tissue engineering and clinical medicine.

Acknowledgments

None

Funding

This work was supported by grants from the National Natural Science Foundation of China (grant nos. 22074057 and 22205089), the Natural Science Foundation of Gansu Province (grant no. 20YF3FA025), and the Fundamental Research Funds for the Central Universities (grant no. lzujbky-2021-it15).

Conflict of interest

The authors declare no competing interest.

Author contributions

Conceptualization: Xiaxia Yang, Linyan Yao, Jianxi Xiao
Data curation: Xiaxia Yang, Jianxi Xiao
Formal analysis: Xiaxia Yang, Jianxi Xiao
Funding acquisition: Jianxi Xiao
Investigation: Xiaxia Yang, Xiaodi Huang
Methodology: Xiaxia Yang, Jianxi Xiao

Project administration: Xiaxia Yang, Jianxi Xiao
Resources: Xiaxia Yang, Wenhua Li, Na Li
Supervision: Linyan Yao, Jianxi Xiao
Validation: Xiaxia Yang, Xiaodi Huang, Linyan Yao, Jianxi Xiao
Visualization: Xiaxia Yang
Writing – original draft: Xiaxia Yang
Writing – review & editing: Linyan Yao, Jianxi Xiao

Ethics approval and consent to participate

All surgical procedures were performed following the guidelines approved by the Ethics Committee of the College of Chemistry and Chemical Engineering at Lanzhou University (No. G09, 20220711).

Consent for publication

Not applicable.

Availability of data

Data are available from the corresponding author upon reasonable request.

References

1. Park H, Patil TV., Dutta SD, *et al*. Extracellular matrix-bioinspired anisotropic topographical cues of electrospun nanofibers: a strategy of wound healing through macrophage polarization. *Adv. Healthcare Mater.* 2024;13:2304114. doi: 10.1002/adhm.202304114
2. Todorova K, Mandinova A. Novel approaches for managing aged skin and nonmelanoma skin cancer. *Adv. Drug Delivery Rev.* 2020;153:18-27. doi: 10.1016/j.addr.2020.06.004
3. Eyerich S, Eyerich K, Traidl-Hoffmann C, Biedermann T. Cutaneous barriers and skin immunity: differentiating a connected network. *Trends Immunol.* 2018;39:315-327. doi: 10.1016/j.it.2018.02.004
4. Cao X, Lin X, Li N, Zhao X, Zhou M, Zhao Y. Animal tissue-derived biomaterials for promoting wound healing. *Mater. Horiz.* 2023;10:3237-3256. doi: 10.1039/D3MH00411B
5. Zhou C, Sheng C, Chen J, *et al*. Gradual hydrogel degradation for programable repairing full-thickness skin defect wound. *Chem. Eng. J.* 2022;450:138200. doi: 10.1016/j.cej.2022.138200
6. Wang Y, Luo M, Li T, Xie C, Li S, Lei B. Multi-layer-structured bioactive glass nanopowder for multistage-stimulated hemostasis and wound repair. *Bioact. Mater.* 2023;25:319-332. doi: 10.1016/j.bioactmat.2023.01.019
7. Luo Y, Yi X, Liang T, *et al*. Autograft microskin combined with adipose-derived stem cell enhances wound healing in a full-thickness skin defect mouse model. *Stem Cell Res. Ther.* 2019;10:279. doi: 10.1186/s13287-019-1389-4
8. Cuono C, Langdon R, McGuire J. Use of cultured epidermal autografts and dermal allografts as skin replacement after burn injury. *Lancet.* 1986;327:1123-1124. doi: 10.1016/S0140-6736(86)91838-6
9. Moore TC, Schayer RW. Histidine decarboxylase activity of autografted and allografted rat skin. *Transplantation.* 1969;7:99-104. doi: 10.1097/00007890-196902000-00002
10. Priya SG, Jungvid H, Kumar A. Skin tissue engineering for tissue repair and regeneration. *Tissue Eng., Part B.* 2008;14:105-118. doi: 10.1089/teb.2007.0318
11. Tottoli EM, Rossella D, Genta I, Chiesa E, Pisani S, Conti B. Skin wound healing process and new emerging technologies for skin wound care and regeneration. *Pharmaceutics.* 2020;12:735. doi: 10.3390/pharmaceutics12080735
12. Chouhan D, Dey N, Bhardwaj N, Mandal BB. Emerging and innovative approaches for wound healing and skin regeneration: current status and advances. *Biomaterials.* 2019;216:119267. doi: 10.1016/j.biomaterials.2019.119267
13. Liu H, Dong J, Du R, Gao Y, Zhao P. Collagen study advances for photoaging skin. *Photodermatol. Photoimmunol. Photomed.* 2024;40:e12931. doi: 10.1111/phpp.12931
14. Yang W, Meyers MA, Ritchie RO. Structural architectures with toughening mechanisms in nature: a review of the materials science of Type-I collagenous materials. *Prog. Mater. Sci.* 2019;103:425-483. doi: 10.1016/j.pmatsci.2019.01.002
15. Amirrah IN, Lokanathan Y, Zulkiflee I, Wee MFMR, Motta A, Fauzi MB. A comprehensive review on Collagen Type I development of biomaterials for tissue engineering: from biosynthesis to bioscaffold. *Biomedicines.* 2022;10:2307. doi: 10.3390/biomedicines10092307
16. Lin K, Zhang D, Macedo MH, Cui W, Sarmento B, Shen G. Advanced Collagen-based biomaterials for regenerative biomedicine. *Adv. Funct. Mater.* 2019;29:1804943. doi: 10.1002/adfm.201804943
17. Ruszczak Z. Effect of collagen matrices on dermal wound healing. *Adv. Drug Delivery Rev.* 2003;55:1595-1611. doi: 10.1016/j.addr.2003.08.003
18. Gajbhiye S, Wairkar S. Collagen fabricated delivery systems for wound healing: a new roadmap. *Biomater. Adv.* 2022;142:213152. doi: 10.1016/j.bioadv.2022.213152

19. Sharma S, Rai VK, Narang RK, Markandeywar TS. Collagen-based formulations for wound healing: a literature review. *Life Sci.* 2022;290:120096. doi: 10.1016/j.lfs.2021.120096

20. Mathew-Steiner SS, Roy S, Sen CK. Collagen in wound healing. *Bioengineering.* 2021;8:63. doi: 10.3390/bioengineering8050063

21. Wang Y, Wang Z, Dong Y. Collagen-based biomaterials for tissue engineering. *ACS Biomater. Sci. Eng.* 2023;9: 1132-1150. doi: 10.1021/acsbiomaterials.2c00730

22. Shi S, Wang L, Song C, Yao L, Xiao J. Recent progresses of collagen dressings for chronic skin wound healing. *Collagen Leather.* 2023;5:31. doi: 10.1186/s42825-023-00136-4

23. Chattopadhyay S, Raines RT. Collagen-based biomaterials for wound healing. *Biopolymers.* 2014;101:821-833. doi: 10.1002/bip.22486

24. Bacakova M, Pajorova J, Broz A, et al. A two-layer skin construct consisting of a collagen hydrogel reinforced by a fibrin-coated polylactide nanofibrous membrane. *Int. J. Nanomed.* 2019;14:5033-5050. doi: 10.2147/IJN.S200782

25. Wang Y, Zhang Y, Li T, *et al.* Adipose mesenchymal stem cell derived exosomes promote keratinocytes and fibroblasts embedded in collagen/platelet-rich plasma scaffold and accelerate wound healing. *Adv. Mater.* 2023;35:2303642. doi: 10.1002/adma.202303642

26. Liu J, Garcia J, Leahy L, *et al.* 3D printing of multifunctional conductive polymer composite hydrogels. *Adv. Funct. Mater.* 2023;33:2214196. doi: 10.1002/adfm.202214196

27. Boyer C, Blasco E, Ke C. Unleashing the potential of 3D printing: bridging chemistry and applications. *Small.* 2023;19:2309837. doi: 10.1002/smll.202309837

28. Vijayavenkataraman S, Lu WF, Fuh JYH. 3D bioprinting of skin: a state-of-the-art review on modelling, materials, and processes. *Biofabrication.* 2016;8:032001. doi: 10.1088/1758-5090/8/3/032001

29. Shapira A, Noor N, Asulin M, Dvir T. Stabilization strategies in extrusion-based 3D bioprinting for tissue engineering. *Appl. Phys. Rev.* 2018;5:041112. doi: 10.1063/1.5055659

30. Donderwinkel I, Hest JCMv, Cameron NR. Bio-inks for 3D bioprinting: recent advances and future prospects. *Polym. Chem.* 2017;8:4451. doi: 10.1039/C7PY00826K

31. Mu X, Agostinacchio F, Xiang N, *et al.* Recent advances in 3D printing with protein-based inks. *Prog. Polym. Sci.* 2021;115:101375. doi: 10.1016/j.progpolymsci.2021.101375

32 Lee A, Hudson AR, Shiwarski DJ, *et al.* 3D bioprinting of collagen to rebuild components of the human heart. *Science.* 2019;365:482-487. doi: 10.1126/science.aav9051

33. Guo C, Wu J, Zeng Y, Li H. Construction of 3D bioprinting of HAP/collagen scaffold in gelation bath for bone tissue engineering. *Regener. Biomater.* 2023;10:rbad067. doi: 10.1093/rb/rbad067

34. Liu Y, Luo X, Wu W, *et al.* Dual cure (thermal/photo) composite hydrogel derived from chitosan/collagen for *in situ* 3D bioprinting. *Int. J. Biol. Macromol.* 2021; 182:689-700. doi: 10.1016/j.ijbiomac.2021.04.058

35. Suo H, Zhang J, Xu M, Wang L. Low-temperature 3D printing of collagen and chitosan composite for tissue engineering. *Mater. Sci. Eng. C.* 2021;123:111963. doi: 10.1016/j.msec.2021.111963

36. Stepanovska J, Otahal M, Hanzalek K, Supova M, Matejka R. pH modification of high-concentrated collagen bioinks as a factor affecting cell viability, mechanical properties, and printability. *Gels.* 2021;7:252. doi: 10.3390/gels7040252

37. Yoon H, Lee J, Yim H, Kim G, Chun W. Development of cell-laden 3D scaffolds for efficient engineered skin substitutes by collagen gelation. *RSC Adv.* 2016;6:21439. doi: 10.1039/C5RA19532B

38. Kim W, Kim GH. An innovative cell-printed microscale collagen model for mimicking intestinal villus epithelium. *Chem. Eng. J.* 2018;334:2308-2318. doi: 10.1016/j.cej.2017.12.001

39. Yeo MG, Kim GH. A cell-printing approach for obtaining hASC-laden scaffolds by using a collagen/polyphenol bioink. *Biofabrication.* 2017;9:025004. doi: 10.1088/1758-5090/aa6997

40. Lee J, Yeo M, Kim W, Koo Y, Kim GH. Development of a tannic acid cross-linking process for obtaining 3D porous cell-laden collagen structure. *Int. J. Biol. Macromol.* 2018;110:497-503. doi: 10.1016/j.ijbiomac.2017.10.105

41. Lee J, Kim G. 3D hierarchical nanofibrous collagen scaffold fabricated using fibrillated collagen and pluronic F-127 for regenerating bone tissue. *ACS Appl. Mater. Interfaces.* 2018;10:35801–35811. doi: 10.1021/acsami.8b14088

42. Lee HJ, Kim YB, Ahn SH, *et al.* A new approach for fabricating Collagen/ECM-based bioinks using preosteoblasts and human adipose stem cells. *Adv. Healthcare Mater.* 2015;4:1359-1368. doi: 10.1002/adhm.201500193

43. Chen C, Xu H, Liu X, *et al.* 3D printed collagen/silk fibroin scaffolds carrying the secretome of human umbilical mesenchymal stem cells ameliorated neurological

dysfunction after spinal cord injury in rats. *Regener. Biomater.* 2022;9:rbac014.
doi: 10.1093/rb/rbac014

44. Stepanovska J, Supova M, Hanzalek K, Broz A, Matejka R. Collagen bioinks for bioprinting: a systematic review of hydrogel properties, bioprinting parameters, protocols, and bioprinted structure characteristics. *Biomedicines.* 2021;9:1137.
doi: 10.3390/biomedicines9091137

45. Lee JM, Suen SKQ, Ng WL, Ma WC, Yeong WY. Bioprinting of Collagen: considerations, potentials, and applications. *Macromol. Biosci.* 2021;21:2000280.
doi: 10.1002/mabi.202000280

46. Matinong AME, Chisti Y, Pickering KL, Haverkamp RG. Collagen extraction from animal skin. *Biology.* 2022;11:905.
doi: 10.3390/biology11060905

47. Fauzi MB, Lokanathan Y, Aminuddin BS, Ruszymah BHI, Chowdhury SR. Ovine tendon collagen: extraction, characterisation and fabrication of thin films for tissue engineering applications. *Mater. Sci. Eng. C.* 2016;68:163-171.
doi: 10.1016/j.msec.2016.05.109

48. Diamantides N, Wang L, Pruiksma T, *et al.* Correlating rheological properties and printability of collagen bioinks: the effects of riboflavin photocrosslinking and Ph. *Biofabrication.* 2017;9:034102.
doi: 10.1088/1758-5090/aa780f

49. Mondy WL, Cameron D, Timmermans J, *et al.* Computer-aided design of microvasculature systems for use in vascular scaffold production. *Biofabrication.* 2009;1:035002.
doi: 10.1088/1758-5082/1/3/035002

50. Logan ME, Zaim MT. Histologic stains in dermatopathology. *J. Am. Acad. Dermatol.* 1990;22:820-830.
doi: 10.1016/S0190-9622(08)81173-5

51. Fu Z, Naghieh S, Xu C, Wang C, Sun W, Chen X. Printability in extrusion bioprinting. *Biofabrication.* 2021;13:033001.
doi: 10.1088/1758-5090/abe7ab

52. Suess PM, Smith SA, Morrissey JH. Platelet polyphosphate induces fibroblast chemotaxis and myofibroblast differentiation. *J. Thromb. Haemostasis.* 2020;18: 3043-3052.
doi: 10.1111/jth.15066

53. Zhao M, Wang J, Zhang J, *et al.* Functionalizing multi-component bioink with platelet-rich plasma for customized *in-situ* bilayer bioprinting for wound healing. *Mater. Today Bio.* 2022;16:100334.
doi: 10.1016/j.mtbio.2022.100334

54. Ding X, Yu Y, Li W, Zhao Y. *In situ* 3D-bioprinting MoS_2 accelerated gelling hydrogel scaffold for promoting chronic diabetic wound healing. *Matter.* 2023; 6:1000-1014.
doi: 10.1016/j.matt.2023.01.001

55. Santefort AL, Yuya PA, Shipp DA. Dynamic covalent exchange induced cyclization in poly (methacrylic anhydride). *Polym. Chem.* 2022;13:4502-4510.
doi: 10.1039/D2PY00488G

56. Cavallo A, Kayal T, Mero A, *et al.* Marine Collagen-based bioink for 3D bioprinting of a Bilayered skin model. *Pharmaceutics.* 2023;15:1331.
doi: 10.3390/pharmaceutics15051331

57. Kang D, Wang W, Li Y, Ma Y, Huang Y, Wang J. Biological macromolecule hydrogel based on recombinant Type I Collagen/Chitosan scaffold to accelerate full-thickness healing of skin wounds. *Polymers.* 2023;15:3919.
doi: 10.3390/polym15193919

58. Osidak EO., Karalkin PA., Osidak MS, *et al.* Viscoll collagen solution as a novel bioink for direct 3D bioprinting. *J. Mater. Sci.: Mater. Med.* 2019;30:31.
doi: 10.1007/s10856-019-6233-y

59. Yannas I, Tzeranis D, So PT. Surface biology of collagen scaffold explains blocking of wound contraction and regeneration of skin and peripheral nerves. *Biomed. Mater.* 2016;11:014106.
doi: 10.1088/1748-6041/11/1/0A14106

60. Ma L, Gao C, Mao Z, Zhou J, Shen J. Biodegradability and cell-mediated contraction of porous collagen scaffolds: the effect of lysine as a novel crosslinking bridge. *J. Biomed. Mater. Res., Part A.* 2004;71A:334–342.
doi: 10.1002/jbm.a.30170

61. Albanna M, Binder KW, Murphy SV, *et al. In situ* bioprinting of autologous skin cells accelerates wound healing of extensive excisional full-thickness wounds. *Sci. Rep.* 2019;9:1856.
doi: 10.1038/s41598-018-38366-w

62. Wei Q, Wang Y, Wang H, *et al.* Photo-induced adhesive carboxymethyl chitosan-based hydrogels with antibacterial and antioxidant properties for accelerating wound healing. *Carbohydr. Polym.* 2021;278:119000.
doi: 10.1016/j.carbpol.2021.119000

ACCSCIENCE PUBLISHING

International Journal of Bioprinting

RESEARCH ARTICLE

Machine learning-generated compression modulus database for 3D printing of gelatin methacryloyl

Shiue-Luen Chen[1,2†], Manisha Senadeera[3†], Kalani Ruberu[4], Johnson Chung[4], Santu Rana[3], Svetha Venkatesh[3], Chong-You Chen[1,2], Guan-Yu Chen[1,2,5,6*], and Gordon Wallace[4*]

[1] Institute of Biomedical Engineering, College of Electrical and Computer Engineering, National Yang Ming Chiao Tung University, Hsinchu, Taiwan

[2] Department of Electronics and Electrical Engineering, College of Electrical and Computer Engineering, National Yang Ming Chiao Tung University, Hsinchu, Taiwan

[3] Applied Artificial Intelligence Institute (A^2I^2), Deakin University, Geelong, Victoria, Australia

[4] Intelligent Polymer Research Institute, ARC Centre of Excellence for Electromaterial Science, AIIM Facility, Innovation Campus, University of Wollongong, New South Wales, Australia

[5] Department of Biological Science and Technology, College of Biological Science and Technology, National Yang Ming Chiao Tung University, Hsinchu, Taiwan

[6] Center for Intelligent Drug Systems and Smart Bio-devices (IDS^2B), National Yang Ming Chiao Tung University, Hsinchu, Taiwan

(This article belongs to the *Special Issue: Bioprinting of in vitro tissue and disease models*)

Abstract

3D bioprinting enables the fabrication of printable tissues, including those for neural, cartilage, and skin repair. The mechanical properties, especially stiffness, of 3D-bioprinted scaffolds are crucial for modulating cell adhesion, growth, migration, and differentiation. The stiffness of a scaffold can be adjusted post-printing by modifying the hydrogel concentration, crosslinker concentration, light intensity during photocrosslinking, and duration of crosslinking. The optimization of these conditions to produce the desired scaffold stiffness for a particular cell type or application is a time-consuming and rigorous process. This study developed an innovative approach to predict the compression modulus of 3D-printed gelatin methacryloyl (GelMA) scaffolds using the Bayesian optimization (BO) algorithm. Through just 10 iterations (75 experimental data points), the model was able to predict > 13,000 possible compression modulus values in a search space comprising four independent variables (GelMA concentration, crosslinker concentration, ultraviolet light [UV] distance, and UV exposure time). This approach can be utilized in other photocrosslinkable bioinks for 3D printing that have a myriad of pre- or post-printing parameters that can affect scaffold stiffness.

Keywords: 3D bioprinting; Scaffold stiffness; Compression modulus; Bayesian optimization; Gelatin methacryloyl

†These authors contributed equally to this work.

***Corresponding authors:**
Guan-Yu Chen (guanyu@nycu.edu.tw)

Gordon Wallace (gwallace@uow.edu.au)

Citation: Chen SL, Senadeera M, Ruberu K, et al. Machine learning-generated compression modulus database for 3D printing of gelatin methacryloyl. *Int J Bioprint*. 2024;10(5):3814. doi: 10.36922/ijb.3814

Received: May 31, 2024
Accepted: July 19, 2024
Published Online: September 20, 2024

Copyright: © 2024 Author(s). This is an Open Access article distributed under the terms of the Creative Commons Attribution License, permitting distribution, and reproduction in any medium, provided the original work is properly cited.

Publisher's Note: AccScience Publishing remains neutral with regard to jurisdictional claims in published maps and institutional affiliations.

1. Introduction

3D bioprinting can fabricate cell constructs that closely mimic the 3D cytoarchitecture of native tissues *in vitro*. The physicochemical characteristics of the biomaterial and the mechanical properties of the scaffold are paramount for supporting the targeted cell line, providing a temporary environment until the tissue-specific extracellular matrix is produced.[1,2] With the growing number of biomaterials and composite bioinks in tissue engineering,[3–5] there remains a substantial gap in knowledge to precisely determine the optimal mechanical properties for these biomaterials to enhance cell-matrix interactions and promote cell maturation and function.

In tissue engineering, the mechanical properties (especially stiffness) of 3D-printed scaffolds have been highlighted as a crucial element in modulating cell adhesion, growth, migration, and differentiation for tissue development.[6–8] Hence, simulating the substrate rigidity or softness of the native tissue target would constitute a promising strategy in 3D biofabrication for tissue engineering and regenerative medicine. The quantification of biomaterial stiffness of tissue scaffolds is widely performed using elastic, shear, and bulk moduli.[8,9] Among these, many studies focus primarily on the elastic modulus as the preferred technique to analyze substrate stiffness.[10]

The stiffness of a scaffold can be modulated in the manufacturing and processing stages,[11,12] oftentimes by varying the reactant concentrations,[12–16] blending biomaterials,[13,17] and modifying the crosslinker concentration, ultraviolet light (UV) intensity (i.e., for photocrosslinking), and the duration of crosslinking in the post-printing stage.[13,14,18,19] However, the optimization of these parameters to attain a specific scaffold stiffness is an extensive and time-consuming process.

With recent advancements, machine learning methods have been applied to fast-track and fine-tune the 3D bioprinting process.[20–25] In this study, we utilized the Bayesian optimization (BO) algorithm with a Gaussian process (GP) probabilistic model to predict scaffold stiffness, i.e., compression modulus based on bioink concentration, crosslinker concentration, UV exposure time, and the distance from the UV source (Figure 1). Gelatin methacryloyl (GelMA) was used as our model bioink as it is currently the most prevalent bioink for tissue engineering applications.[5,15] An active sampling method was applied to iteratively select experimental points for system modeling, with BO driving the active sampling process and GP constructing the system model. Our experimentation and fine-tuning of the model continued until the model achieved a pre-specified degree of certainty. Within the BO algorithm, an acquisition function was used to select data points for experimentation; the function is reportedly biased toward selecting data points that maximize information gain about the model, indicated by the relatively high levels of uncertainty (standard deviation) in its predictions.[26] To improve the data collection efficiency in the physical experiments, recommendations for each iteration are provided in batches. These batches are conditioned such that all recommendations have the same GelMA concentration but allow for a broad range of values for other variables. This is a valuable tool for predicting the compression modulus of a selected bioink to determine its optimal biological requirements, while significantly reducing the time needed for testing each variable individually.

2. Materials and methods

2.1. Preparation of GelMA bioink

Gelatin methacryloyl (GelMA), blended from 300-bloom gelatin type A (synthesized as described previously in O'Connell et al.[19]), was used to prepare 5, 7.5, and 10% (w/v) solutions. Appropriate amounts of freeze-dried GelMA (degree of functionalization: 57%) were dissolved in cell culture grade phosphate-buffered saline (PBS; Sigma-Aldrich, USA), containing 100 U/mL penicillin and 100 μg/mL streptomycin (Gibco, USA), in a laminar flow cabinet. The bioinks were heated at 37°C with intermittent vortexing to expedite dissolution.

2.2. Addition of photoinitiator/crosslinker to the bioinks

Lithium phenyl-2,4,6-trimethylbenzoylphosphinate (LAP; TRICEP, Australia) was selected as the photoinitiator for crosslinking GelMA at 405 nm (UV). An 8.5% (w/v) LAP stock solution was prepared in sterile PBS and diluted into the GelMA bioink as required. The final LAP concentration range used in this study was 0.01–1% (w/v). The photoinitiator-containing bioink was then transferred to 10 cc printer reservoirs (Nordson EFD, USA) for printing using the GeSiM BioScaffolder (GeSiM, Germany).

2.3. GelMA scaffold printing

Extrusion printing was performed using BioScaffolder 3.2 (GeSiM, Germany). Lattice structures of 10 × 10 × 1.5 mm with 130 μm slicing were fabricated using 27-gauge smooth-flow tapered nozzles (200 μm; Nordson EFD, USA). Reservoir temperature was optimized for 5% (w/v), 7.5% (w/v), and 10% (w/v) GelMA bioinks. The printed scaffolds with variable LAP concentrations were exposed to 405 nm UV (Omnicure Lx400+; (Excelitas Technologies, USA) at the specified distance and time as per values predicted by the BO framework (described in

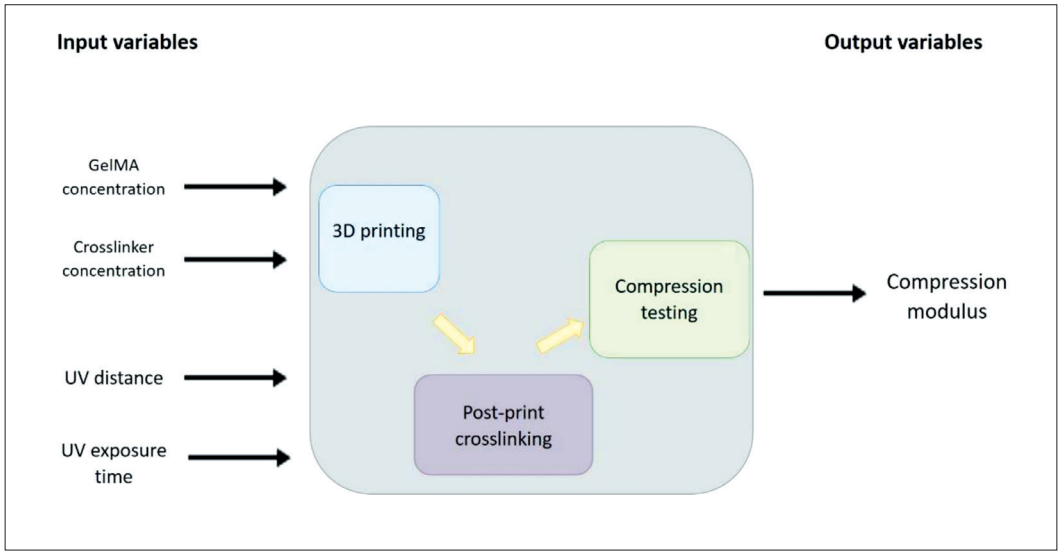


Figure 1. The input and output variables of the system to be optimized. Abbreviations: GelMA: Gelatin methacryloyl; UV: Ultraviolet light.

Section 2.5). Four replicates of each experimental condition were printed to improve reliability. Printed scaffolds were placed in Petri dishes, immersed in cell culture medium, and incubated overnight at 37°C.

2.4. Compression testing

The scaffolds were subjected to mechanical stress testing using a uniaxial EZ-L testing machine (Shimadzu, Japan) (Figure 2). This equipment allows for the calculation of stress and stiffness of the material, which can be used for theoretical calculations of pressure. A 10 N kit was used for the testing in this experiment. After overnight incubation in the cell culture medium, each GelMA scaffold was removed and placed on the testing platform. The thickness of the scaffold was approximately 1.5 mm. The compression interval was set to 1 mm, achieving 67% strain, with the corresponding pressure at 30–50% strain selected for calculating the compression modulus (Figure 2).

2.5. Bayesian optimization framework

The algorithm used in this study was a BO-based framework[27] with GP as the probabilistic model.[28] We used BO to guide the sampling of experimental settings, improving the accuracy of the GP model in predicting scaffold strength, as indicated by the compression modulus value. Within the BO framework, an acquisition function tailored toward uncertainty reduction recommended experimental settings for the system. This is automatically performed by the framework using the variable search space to assess previous experiments, thereby improving the system based on the key findings. Figure 3 illustrates the machine learning search algorithm used to concurrently (i) select experimental settings at which scaffolds should be photo-crosslinked and tested, and (ii) use these results to update the GP model in the system. The process can be understood as follows:

(i) Initialization: Random experimental settings (a random set at each of the three GelMA concentrations) are chosen, and testing of the scaffolds is conducted. The resulting compression modulus was then pre-processed, where the experimental settings (X variables) are scaled (to a range of 0–1), and the compression modulus values (Y) are standardized (to have a mean of 0 and standard deviation of 1).

(ii) GP model fitting: The pre-processed data from (i) are used to fit the GP model. Once fitted, the maximum uncertainty of the system is checked against the "uncertainty threshold." If found to be within the uncertainty threshold, experimentation is halted. Otherwise, the process continues with (iii).

(iii) Acquisition function optimization: The predicted standard deviation of the GP model was utilized as the acquisition function, and a batch of experiments was sampled for the next iteration. Following each sample added to the batch, the GP is updated temporarily and only partially (i.e., only predictive variance computation is updated) to determine the experiments suitable for this batch. This process continues until the batch number is filled up. Additionally, this batch selection process is constrained, such that all settings in the batch have the same GelMA concentration.

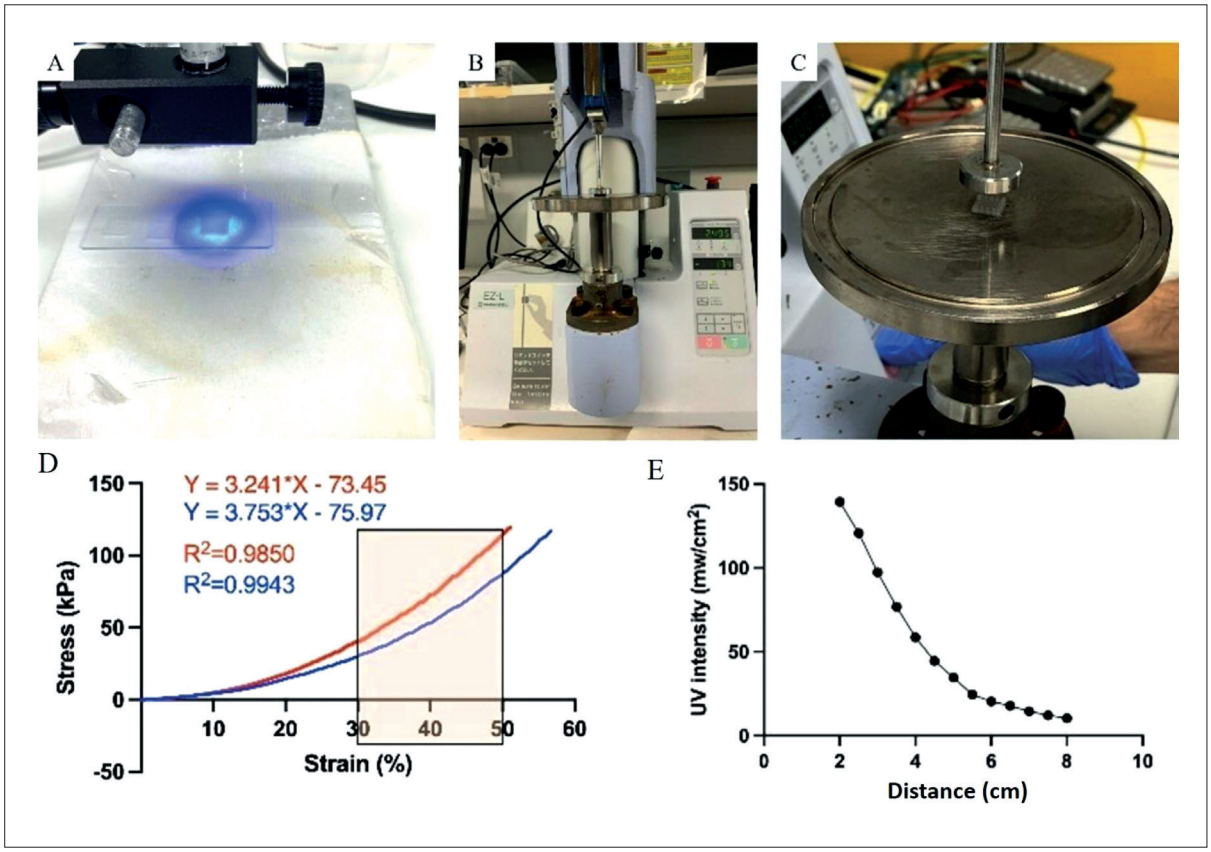


Figure 2. Mechanical stress testing of printed scaffolds. (A–C) Printed scaffolds subjected to (A) ultraviolet light (UV)-crosslinking at 405 nm; and B. Photo of the printed scaffold during compression testing on the uniaxial EZ-L testing machine and C. after the compression testing. (D)The stop limit at 1 mm corresponds to 30–50% strain. The red group displays the value of the printed scaffold immediately following preparation, with the blue group showing the value after a day of immersion in the medium. The stop limit at 1 mm corresponds to 30–50% strain. (E) Relationship between distance and intensity of UV source.

(iv) Experimentation: A batch of experiments is returned to the experimenter, and laboratory (real-world) experiments are conducted. The resulting compression modulus values are obtained and pre-processed to update the GP model. The entire process restarts at (ii).

Further details of each component are discussed below.

2.5.1. Search space

Table 1 details the range and the discretized step size of post-print crosslinking parameters for GelMA used throughout the experiment, i.e., 10 iterations. From the initial recommendations, it was evident that adjustments to the crosslinker concentration and UV exposure time were required due to constraints during experimentation. The addition of high photoinitiator concentration resulted in immediate crosslinking of the bioink, hindering its extrusion from the printing nozzle. Hence, the search space for the crosslinker concentration was reduced to 0.01–1% (w/v) in the second iteration. Moreover, scaffolds that were exposed to UV for a short period (e.g., 10–20 s) were observed to have disintegrated into the media overnight due to insufficient crosslinking of the bioink. This initiated the second search space alteration from the third iteration onwards.

2.5.2. Gaussian process model fitting

A GP model was fitted to the data to represent the system. In any experimental setting, the model provides a prediction for the compression modulus along with the associated uncertainty (standard deviation), reflecting the confidence of the model in its prediction.

Equations I and II correspond to determining the mean and variance of the model, where $y = f + \epsilon$ is the noisy system response (i.e., the compression modulus) and x is the vector form of the experiment settings. We assume the noise of each sample is normally distributed by $\epsilon \sim N\left(0, \sigma_n^2\right)$. We use the average variance of samples to represent this noise (more details are provided in Section 3.4). The relationship between points within the experimental space is governed by a kernel function, which is parameterized by a length scale vector ($l \in \mathbb{R}^4$),

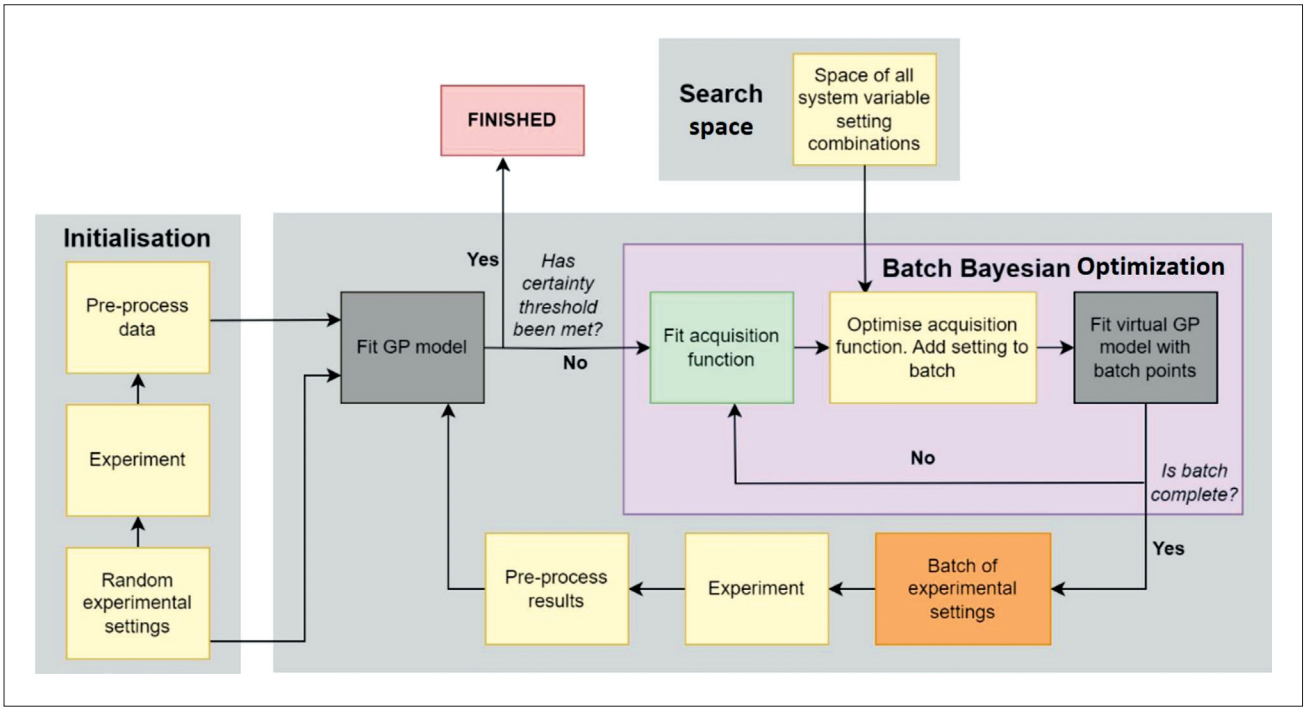


Figure 3. Batch Bayesian optimization framework. Abbreviation: GP: Gaussian process.

Table 1. Range and step size of each experimental variable at various iterations.

Round of iterations	GelMA concentration (% w/v)		UV distance (cm)		UV exposure time (s)		Crosslinker concentration (% w/v)	
	Range	Step	Range	Step	Range	Step	Range	Step
1	5–10	2.5	2–8	0.5	10–180	10	0.01–2	0.05
2	5–10	2.5	2–8	0.5	10–180	10	0.01–1	0.05
3–10	5–10	2.5	2–8	0.5	30–180	10	0.01–1	0.05

Note: Abbreviations: GelMA: Gelatin methacryloyl; UV: Ultraviolet light.

where each element is the length scale in each input parameter dimension (n). A popular choice of the kernel is the squared exponential kernel, the form of which is displayed in Equation III. The squared exponential kernel is also known as a universal kernel, i.e., its use in a GP model enables the GP to model any smooth function, making it a suitable choice for a wide range of function modeling. The value of the length scale is often estimated based on data, making the GP model fully data-driven. It is noted that when updating the variance, information about the system responses (the compression modulus values in the case of our system) is not needed, as the variance and subsequent standard deviation reflect the variance of the true mean of the system and are independent of the values of the compression modulus.

$$\mu\left(\boldsymbol{x}_{t+1}\right)=\boldsymbol{k}^{T}\left(\boldsymbol{K}+\sigma_{n}^{2}\boldsymbol{I}\right)^{-1}y_{1:t} \quad \text{(I)}$$

where $y=f+\epsilon$

$$\sigma^{2}\left(\boldsymbol{x}_{t+1}\right)=k\left(\boldsymbol{x}_{t+1},\boldsymbol{x}_{t+1}\right)-\boldsymbol{k}^{T}\left(\boldsymbol{K}+\sigma_{n}^{2}\boldsymbol{I}\right)^{-1}\boldsymbol{k} \quad \text{(II)}$$

where:

$$k\left(\boldsymbol{x},\boldsymbol{x}'\right)=\exp\left(-\frac{1}{2}\sum_{n=1}^{4}\frac{1}{l_{n}^{2}}\left(x_{n}-x_{n}^{'}\right)^{2}\right) \quad \text{(III)}$$

$$\boldsymbol{K}=\begin{bmatrix}k\left(\boldsymbol{x}_{1},\boldsymbol{x}_{1}\right) & \cdots & k\left(\boldsymbol{x}_{1},\boldsymbol{x}_{t}\right)\\ \vdots & \ddots & \vdots\\ k\left(\boldsymbol{x}_{t},\boldsymbol{x}_{1}\right) & \cdots & k\left(\boldsymbol{x}_{t},\boldsymbol{x}_{t}\right)\end{bmatrix}$$

$$\boldsymbol{k} = \left[k\left(\boldsymbol{x}_{t+1}, \boldsymbol{x}_1\right) \quad \ldots \quad k\left(\boldsymbol{x}_{t+1}, \boldsymbol{x}_t\right) \right]$$

2.5.3. Acquisition function

An acquisition function is optimized to select the next experimental settings. As our study focuses on reducing the epistemic (predictive) uncertainty in the GP model, our acquisition function refers to the predicted standard deviation of the GP.

2.5.4. Constrained batch sampling

When filling the batch of up to 10 experimental settings for the next iteration, the first point of the batch is determined by optimizing the acquisition function from the usual GP (Figure A1). After selecting this point, all experimental points in the batch (initially 1) are used to update the predicted standard deviation (Equation II) by fitting a temporary GP that updates its model for predictive variance. The updated model of predictive variance is further optimized to determine the next experimental setting for the batch. This process is continued (using all points in the batch so far) until the batch is full.

2.5.5. Manual values

In some instances, the experimental settings returned to the experimenter resulted in scaffolds that disintegrated in the cell culture medium and the compression modulus could not be measured. In these situations, the compression modulus value was manually coded as 0 before fitting the GP model.

3. Results

3.1. Scaffold printing optimization

The reservoir temperature was optimized for the GeSiM BioScaffolder to ensure a continuous filament was produced during bioink extrusion from the needle tip and that square pores were formed on layer stacking of the 3D scaffold (Figure 4). Optimized reservoir temperatures for 5, 7.5, and 10% (w/v) GelMA bioinks were 19, 21, and 23°C, respectively. Printing pressure and speed were fine-tuned accordingly (Table 2) to fabricate 3D structures with good shape fidelity.

3.2. Maximum uncertainty

Sampling was stopped when at least 90% of the GP model's prediction had a standard deviation within the user-specified threshold of 40 kPa. This was determined by predicting the standard deviation at each of the experimental settings. Figure 5 features the percentage of points, at each iteration, which have a predicted standard deviation within 40 kPa. Experimentation ceased after iteration 10 when the percentage of points meeting this criterion reached 91.3% (Figure A2). Figure 6 presents the maximum standard deviation within the system. This plot illustrates the changes in overall uncertainty and highlights the reduction in uncertainty in the most uncertain areas of the search space. Figure 7 displays the distribution of the predicted standard deviation at iteration 10 when experimentation ended. By then, 91.3% of points in the search space were below the 40 kPa criteria, with the highest uncertainty remaining within the system at 52.8 kPa.

3.3. Length scale of experimental variables

In each iteration, a new GP model is fitted based on the latest data available. In doing so, the length scale hyperparameter is tuned via maximization of the log-likelihood.[28] The length scale reflects the sensitivity of the change in compression modulus values to changes in the experimental variables. A larger length scale indicates a system that is less sensitive to changes in the given variable, while a smaller length scale indicates greater sensitivity. Our experiment consisted of respective constant length scale values associated with each of the four experimental variables. Figure 8 displays the adjusted length scale value for each experimental variable at each iteration. In early iterations, the limited data resulted in more fluctuations in the length scales between iterations; in later iterations, when more data is available, more stable estimates can be made. After iteration 8, the length scale was observed to have stabilized, and further adjustments were not made henceforth.

The final length scale for each of the input parameters was 0.25 for GelMA concentration, 0.475 for crosslinker concentration, 0.25 for UV exposure time, and 0.3 for UV distance (Figure 8). These values reveal that GelMA concentration and UV exposure time are major contributing

Table 2. Printing parameters for gelatin methacryloyl (GelMA) in the 3D BioScaffolder.

GelMA concentration (%)	Printing pressure (kPa)	Printing speed (mm/s)	Reservoir temperature (°C)	Platform temperature (°C)
5	80–110	9	19	10
7.5	90–120	8	21	10
10	200–220	7	23	10

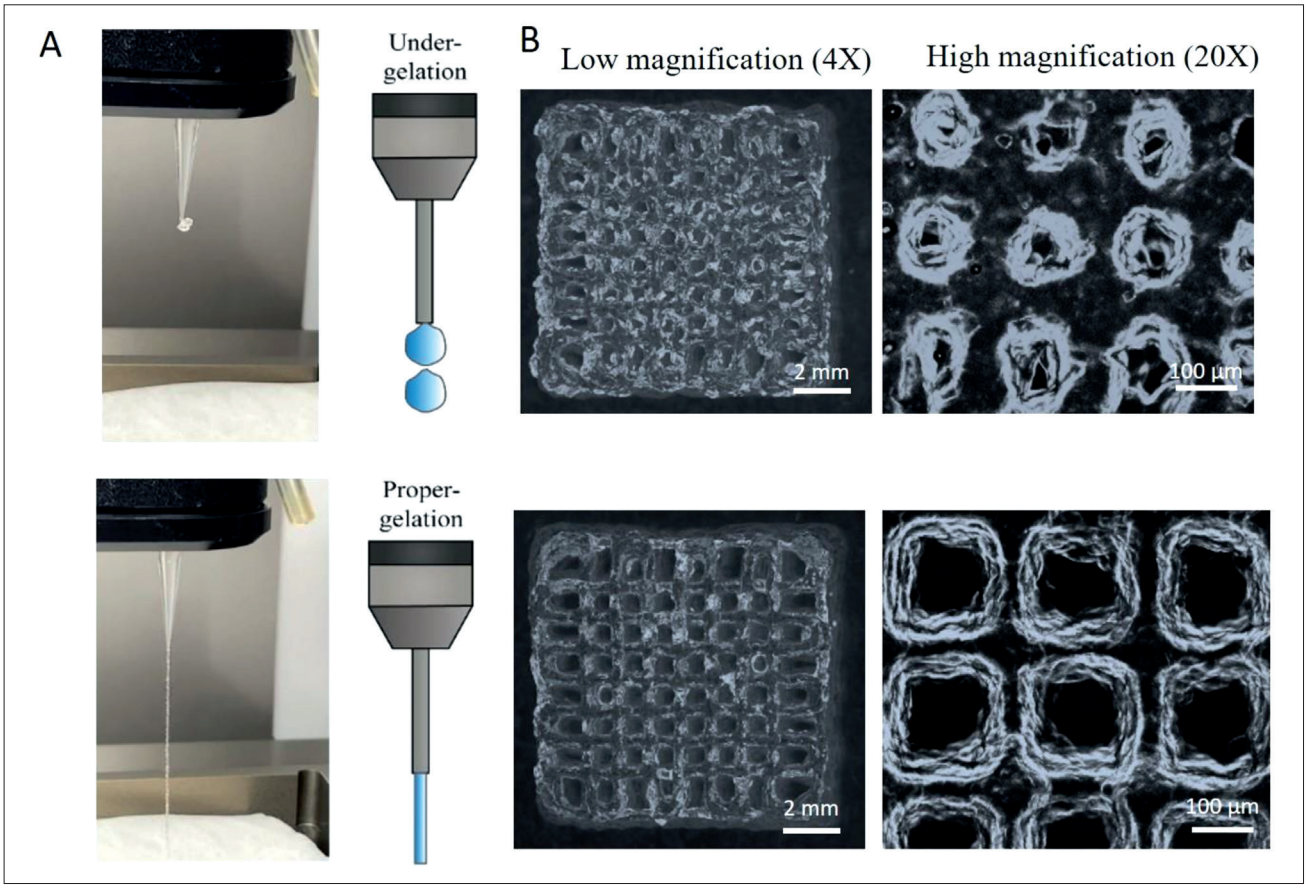


Figure 4. Scaffold printing optimization in the GeSiM BioScaffolder. (A) Filament formation during bioink extrusion from the printer nozzle. (B) Microscopic images of pore architecture of the printed scaffold under low and high magnification.

factors influencing the stiffness of the printed scaffolds, followed by UV distance and crosslinker concentration.

3.4. System noise

For each batch of experiments returned to the experimenter, 3–5 samples at each setting were tested to capture variation in the compression modulus. The average sample variances were used as the noise variance in the GP model (σ_n^2). Figure 9 displays the average noise in the system across iterations. We assume constant noise throughout our GP model, as the noise estimate from the average of the sample variances was fairly consistent as sampling continued, i.e., iteration 5 onwards.

3.5. Validation of machine learning framework

Validation of 5, 7.5, and 10% (w/v) GelMA scaffolds was performed after iteration 10 by comparing the BO-predicted compression modulus with the experimental values of nine randomly selected photocrosslinking conditions across the three GelMA concentrations. Our BO model demonstrated 89% accuracy (Table 3) between predicted and experimental values, displaying an ideal fit for attaining the required compression modulus of GelMA bioinks for bioprinting applications.

3.6. Comparison with experimental values

When reviewing the GP predictions against the experimental data used to train the model (as a sense check), two points fell outside of the 95% confidence interval constructed with the GP-predicted mean and standard deviation. The experimental setting of these two points (Table 4) is relatively close within the search space, differing only by their crosslinker concentration value. Upon close inspection, the under and overshooting in the GP predictions can be attributed to the inability of the GP model to capture the significant variation in compression modulus values between these two points. Although the points are close in the experimental space, the GP model lacked the flexibility to change rapidly from the first point to the second point (Figure 10). The flexibility of the model is determined by the length scale of the GP, but as the length scale is assumed to be constant across the whole dimension (in this case, a

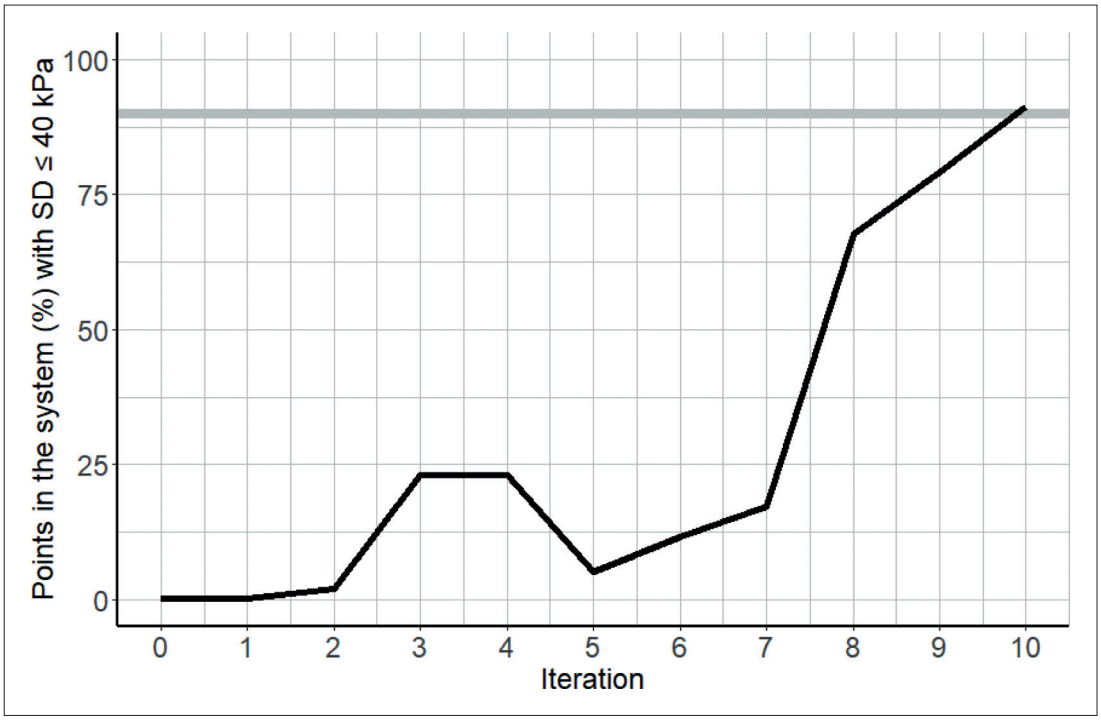


Figure 5. Points in the system (%) with a standard deviation (*SD*) ≤ 40 kPa. By iteration 10, the 90%-point threshold (grey line) was met.

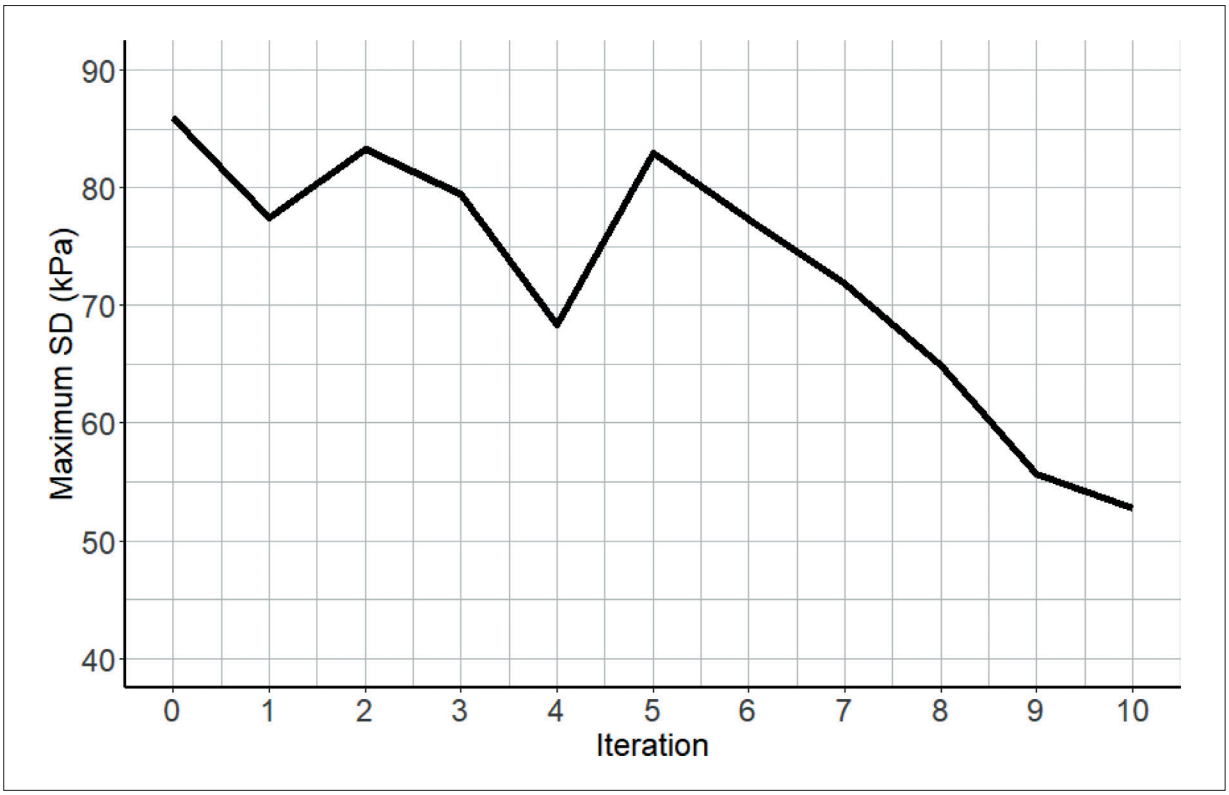


Figure 6. Maximum standard deviation (SD) remaining within the system.

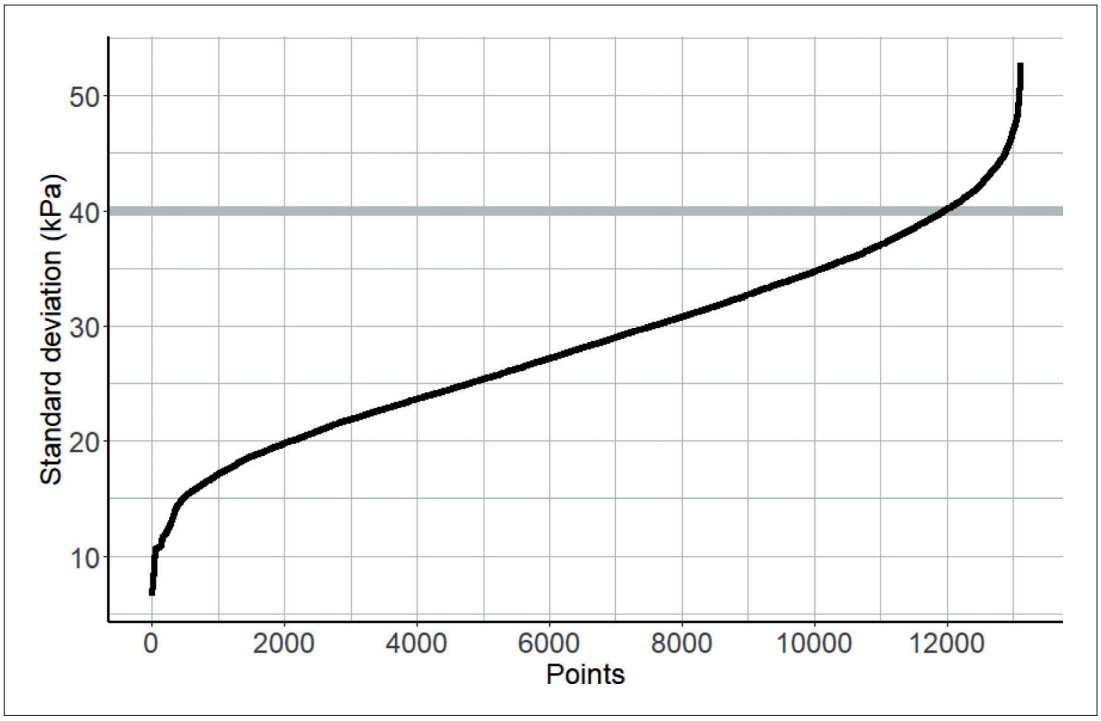


Figure 7. Distribution of standard deviation in the system after the final iteration (i.e., iteration 10). The standard deviation threshold (40 kPa) is indicated by a solid grey line. The objective was to continue Bayesian optimization (BO) sampling until ≥ 90% of the Gaussian process (GP) model predictions were within the standard deviation threshold, which was achieved after iteration 10.

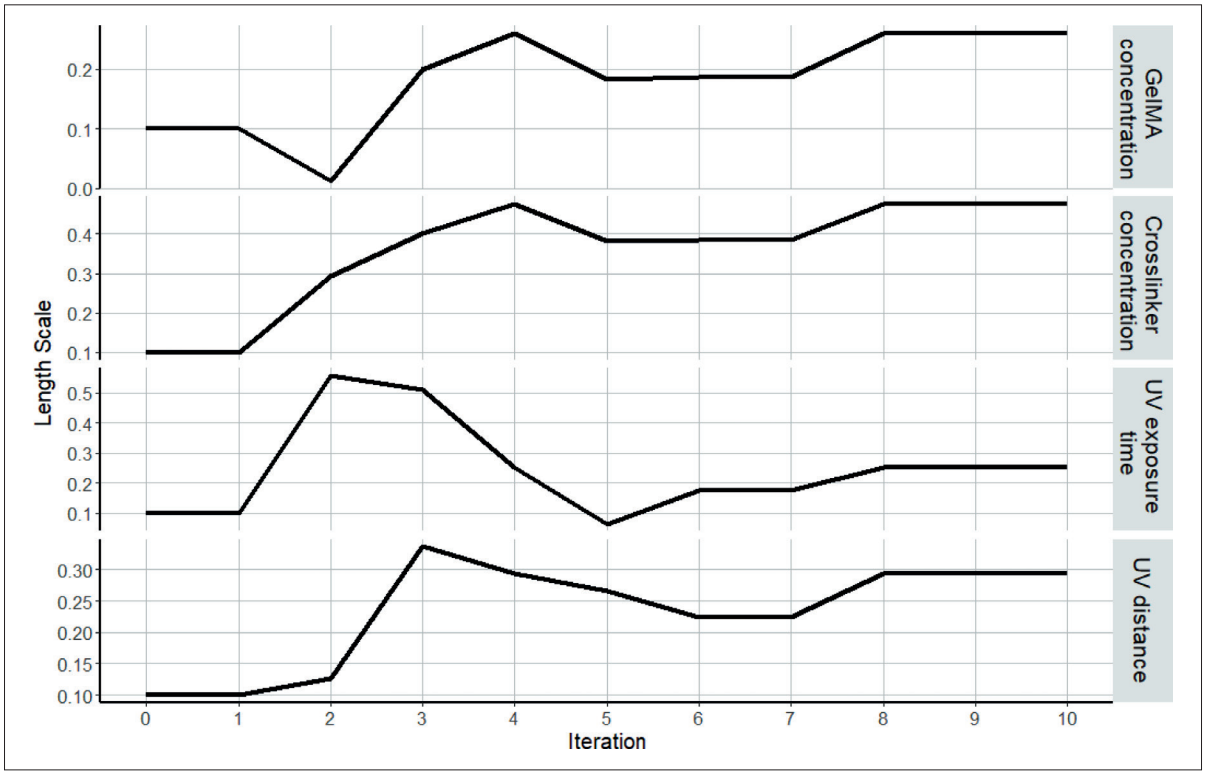


Figure 8. Optimized length scale for each experimental variable after each iteration. The length scale was stabilizing toward iteration 8 for each of the experimental variables; no changes in the length scale were observed at iterations 9 and 10. Hence, the conditions corresponding to the length scale from iteration 8 were used. Abbreviations: GelMA: Gelatin methacryloyl; UV: Ultraviolet light.

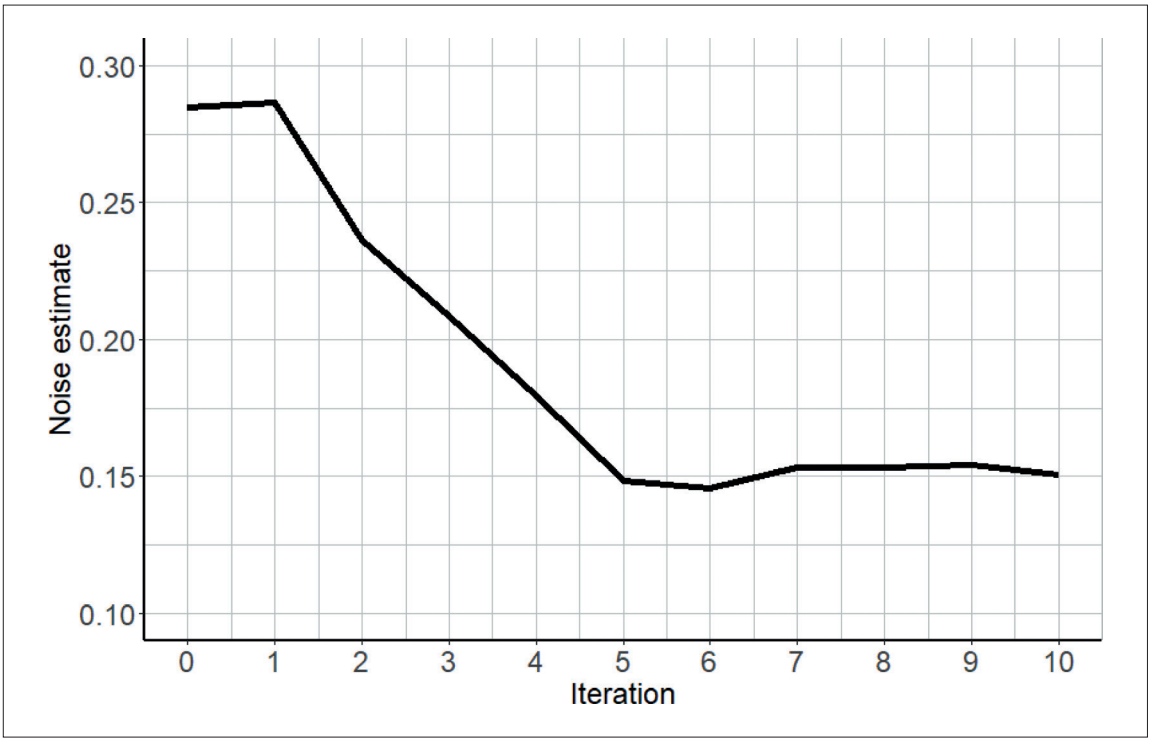


Figure 9. The average noise of the system estimated from the experimental data. Over time (number of iterations), the noise estimate stabilizes to a lower value.

Table 3. Validation of experimental results vs. Bayesian optimization (BO)-predicted values.

Sample number	Input variables				Av compression modulus/output (kPa)	Predicted value from GP (kPa)
	GelMA concentration (w/v%)	Crosslinker concentration (w/v%)	UV exposure time (s)	UV distance (cm)		
1*	5	0.46	170	4	88.66 ± 7.8	86.93 ± 17.81
2*	5	0.46	160	5.5	84.18 ± 3.31	79.91 ± 37.86
3*	5	1.01	50	4	64.66 ± 3.1	68.36 ± 30.30
4#	7.5	0.01	30	6.5	Degradation in media	16.01 ± 46.20
5*	7.5	0.66	60	3	104.8 ± 13.5	134.45 ± 44.92
6*	7.5	0.71	80	2	102.83 ± 5.21	145.66 ± 49.87
7*	10	0.06	160	6.5	22.89 ± 1.55	5.50 ± 28.30
8*	10	0.21	30	4.5	106.66 ± 0.48	96.21 ± 26.05
9*	10	0.96	100	2	87.72 ± 4.37	97.47 ± 11.02

Note: *Correctly predicted values; #Incorrectly predicted values. Abbreviations: GP: Gaussian process; GelMA: Gelatin methacryloyl; UV: Ultraviolet light; Av: Average.

Table 4. Two settings where experimental value mismatched with the Gaussian process (GP) predicted mean and standard deviation.

Setting	GelMA concentration (w/v%)	Crosslinker concentration (w/v%)	UV exposure time (s)	UV distance (cm)	Experimental value (kPa)	Lower 95% bound	Upper 95% bound
1	5	0.12	180	2	142.60	99.68	137.50
2	5	0.21	180	2	57.41	68.39	103.01

Abbreviations: GelMA: Gelatin methacryloyl; UV: Ultraviolet light.

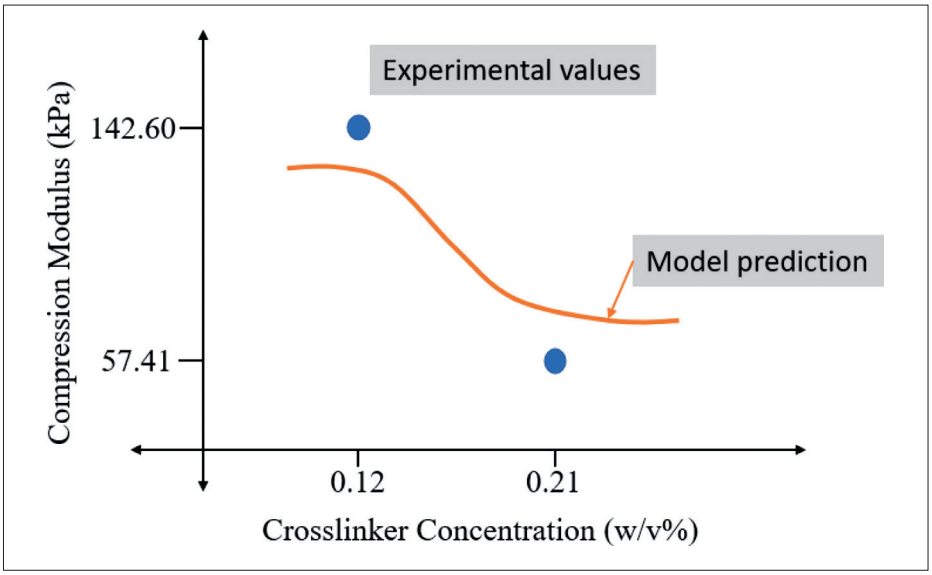


Figure 10. Illustration of the model prediction error for two closely positioned experimental settings. Experimental conditions, i.e., gelatin methacryloyl (GelMA) concentration, ultraviolet light (UV) exposure, and UV distance, were kept the same for both experimental settings.

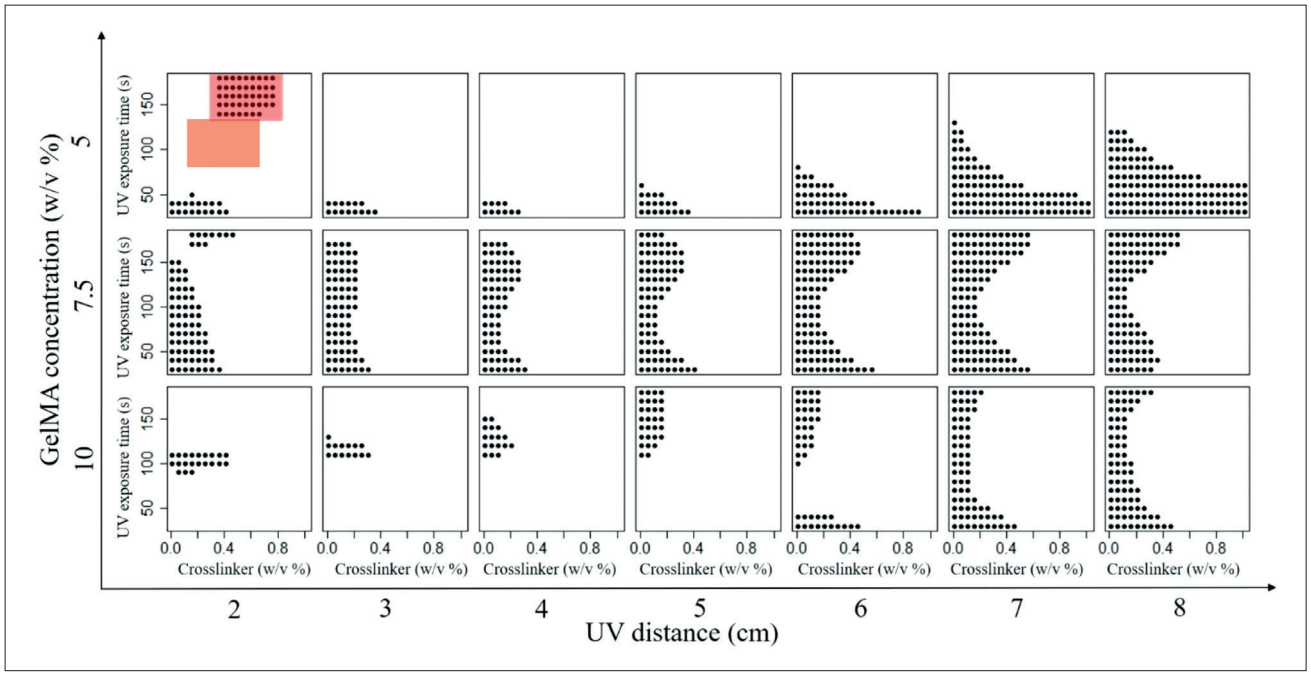


Figure 11. Scatter plots of compression modulus data (< 50 kPa) obtained from the Gaussian process (GP) model. For example, the region highlighted in red has a compression modulus < 50 kPa when gelatin methacryloyl (GelMA) concentration is 5% w/v, ultraviolet light (UV) exposure time is 150–180 s, UV distance is 2 cm, and the crosslinker concentration is 0.5-0.7% (w/v).

constant length scale across the crosslinker concentration dimension), the adjusted length scale (using all data) was on average too large to capture the sudden change in this particular location of the experimental variable space. This could be improved in future works by utilizing a variable length scale along each parameter dimension.

3.7. Scatter plots of compression modulus values

After iteration 10 was complete, the GP model was able to predict 13,104 compression modulus values in our search space of 5–10% (w/v) GelMA concentration, 0.01–1% (w/v) crosslinker concentration, 2–8 cm distance from the UV source, and 30–180 s UV exposure time. Figure 11

displays a representative scatter plot displaying the GelMA and crosslinker concentrations, as well as the post-print crosslinking parameters required to achieve a compression modulus of < 50 kPa. Instead of using the model to predict the compressive modulus (output) based on sample processing and printing parameters (concentration, distance, crosslinker, and time), the GP model can also be utilized inversely to predict the input parameters based on a particular compression modulus of interest. This demonstrates the versatility of using the GP model for bioink design when a particular compression modulus is desired, without the need for rigorous trial and error in sample preparation and post-printing parameters.

4. Discussion

Numerous studies have investigated the effect of biomaterial stiffness on regulating cell viability in 2D and 3D platforms. In a pioneering study, Engler and co-workers demonstrated matrix stiffness drives mesenchymal stem cell (MSC) differentiation in an elastically tunable gel system. Naive MSCs predominantly differentiate into neuronal cells when grown on soft gels, myogenic cells when grown on relatively stiff matrices, and osteogenic cell lineage when grown on stiff gels.[29] This observation correlating substrate stiffness with cell proliferation has been further corroborated by numerous studies utilizing different cell lines.[18,30,31] Hence, the importance of determining the scaffold stiffness in the bioprinting space is evident.

A machine learning model was employed in this study to predict the stiffness of the GelMA scaffolds by varying several input parameters with realistic lower and upper limits for cell printing. The BO framework utilized in this study demonstrated high accuracy in predicting scaffold stiffness via compression modulus values of GelMA scaffolds based on numerous input parameters, namely GelMA concentration, photoinitiator concentration, UV-crosslinking time, and distance. By using an uncertainty reduction approach with the acquisition function as the standard deviation, the BO method can build the GP model by efficiently collecting data points from regions of the search space where prediction uncertainty is high. Additionally, by employing batch BO, multiple experiments can be conducted within a single iteration, saving time to complete the study. Batch BO is also flexible enough to have constraints applied to the batch to cater to experimenter requirements (e.g., all samples of the batch need to have the same GelMA concentration). A comparison to the BO approach employed in the study is conducting grid search sampling. However, this method has limitations: (i) the experimenter must predefine the appropriate spacing between experimental points, and (ii) determine whether the spacing between points should be uniform or varied across different parameters. Using our BO approach, these decisions are avoided, as the algorithm can flexibly adapt its sampling choices to the system information received during the study, i.e., the length scale parameter which produces a rough measure of the distance between samples.

The length scale of our GP model provides insights into the influence of each parameter on scaffold properties, i.e., significantly affected by the GelMA concentration and UV exposure time, followed by UV distance and the crosslinker concentration. Further research is warranted to increase the flexibility of the length scale, thereby allowing variations in the length scale for each parameter. Further research could also explore the potential of this model to optimize various cell lines for their proliferation, differentiation, and function.

5. Conclusion

This study developed a machine learning model to predict the compression modulus values of 5, 7.5, and 10% (w/v) GelMA scaffolds by varying post-print photocrosslinking parameters within realistic upper and lower limits for cell printing. Ten iterations with a total of 75 experiments resulted in a library of 13,000 compression modulus values for GelMA bioink to be predicted with the aid of the BO algorithm. The ability to predict the stiffness or the compressive modulus of a 3D scaffold is a valuable tool in bioengineering, as it can enhance cell-matrix biomechanical crosstalk and direct cells toward maturation and proper function.

Acknowledgments

None.

Funding

The authors acknowledge funding from the Australian Research Council (ARC) (CE140100012) and (FL170100006), and support from the Australian National Fabrication Facility (ANFF) – Materials Node. G.-Y.C. would like to acknowledge funding from The National Science and Technology Council (NSTC113-2321-B-A49-021, NSTC113-2628-B-A49-008-MY3, NSTC113-2823-8-A49-003, NSTC112-2321-B-A49-015, NSTC 112-2321-B-A49-016), Center for Intelligent Drug Systems and Smart Bio-devices (IDS^{2}B) from the Featured Areas Research Center Program within the framework of the Higher Education Sprout Project by the Ministry of Education (MOE) (113W30305), and the Higher Education Sprout Project of the National Yang Ming Chiao Tung University and MOE, Taiwan (113W020211, 113W020211, 113W020214).

Conflict of interest

The authors declare that they have no known competing financial interests or personal relationships that could have appeared to influence the work reported in this article.

Author Contributions

Conceptualization: Johnson Chung, Kalani Ruberu, Manisha Senadeera

Data curation: Shiue-Luen Chen, Manisha Senadeera

Funding acquisition: Svetha Venkatesh, Guan-Yu Chen, Gordon Wallace

Methodology: Shiue-Luen Chen, Johnson Chung, Kalani Ruberu, Manisha Senadeera, Santu Rana

Resources: Svetha Venkatesh, Guan-Yu Chen, Gordon Wallace

Supervision: Svetha Venkatesh, Guan-Yu Chen, Gordon Wallace

Writing – original draft: Shiue-Luen Chen, Manisha Senadeera, Johnson Chung, Kalani Ruberu

Writing – review & editing: Chong-You Chen, Johnson Chung, Guan-Yu Chen, Gordon Wallace

Ethics approval and consent to participate

Not applicable.

Consent for publication

Not applicable.

Availability of data

Data are available from the corresponding author upon reasonable request.

References

1. Hashizume R, Fujimoto KL, Hong Y, et al. Morphological and mechanical characteristics of the reconstructed rat abdominal wall following use of a wet electrospun biodegradable polyurethane elastomer scaffold. *Biomaterials*. 2010;31(12):3253-3265. doi: 10.1016/j.biomaterials.2010.01.051
2. Simmons CA, Alsberg E, Hsiong S, Kim WJ, Mooney DJ. Dual growth factor delivery and controlled scaffold degradation enhance *in vivo* bone formation by transplanted bone marrow stromal cells. *Bone*. 2004;35(2): 562-569. doi: 10.1016/j.bone.2004.02.027
3. Chung JHY, Kade JC, Jeiranikhameneh A, et al. 3D hybrid printing platform for auricular cartilage reconstruction. *Biomed Phys Eng Express*. 2020;6(3):035003. doi: 10.1088/2057-1976/ab54a7
4. Daikuara LY, Yue Z, Skropeta D, Wallace GG. *In vitro* characterisation of 3D printed platelet lysate-based bioink for potential application in skin tissue engineering. *Acta Biomater*. 2021;123:286-297. doi: 10.1016/j.actbio.2021.01.021
5. Hospodiuk M, Dey M, Sosnoski D, Ozbolat IT. The bioink: a comprehensive review on bioprintable materials. *Biotechnol Adv*. 2017;35(2):217-239. doi: 10.1016/j.biotechadv.2016.12.006
6. Floren M, Bonani W, Dharmarajan A, Motta A, Migliaresi C, Tan W. Human mesenchymal stem cells cultured on silk hydrogels with variable stiffness and growth factor differentiate into mature smooth muscle cell phenotype. *Acta Biomater*. 2016;31:156-166. doi: 10.1016/j.actbio.2015.11.051
7. Macri-Pellizzeri L, De-Juan-Pardo EM, Prosper F, Pelacho B. Role of substrate biomechanics in controlling (stem) cell fate: implications in regenerative medicine. *J Tissue Eng Regene Med*. 2018;12(4):1012-1019. doi: 10.1002/term.2586
8. Yi B, Xu Q, Liu W. An overview of substrate stiffness guided cellular response and its applications in tissue regeneration. *Bioact Mater*. 2022;15:82-102. doi: 10.1016/j.bioactmat.2021.12.005
9. Lv H, Wang H, Zhang Z, et al. Biomaterial stiffness determines stem cell fate. *Life Sci*. 2017;178:42-48. doi: 10.1016/j.lfs.2017.04.014
10. Querceto S, Santoro R, Gowran A, et al. The harder the climb the better the view: the impact of substrate stiffness on cardiomyocyte fate. *J Mol Cell Cardiol*. 2022;166:36-49. doi: 10.1016/j.yjmcc.2022.02.001
11. Huang Y, Xu K, Liu J, Dai G, Yin J, Wei P. Promotion of adrenal pheochromocytoma (PC-12) cell proliferation and outgrowth using Schwann cell-laden gelatin methacrylate substrate. *Gels*. 2022;8(2):84. doi: 10.3390/gels8020084
12. Nichol JW, Koshy ST, Bae H, Hwang CM, Yamanlar S, Khademhosseini A. Cell-laden microengineered gelatin methacrylate hydrogels. *Biomaterials*. 2010;31(21):5536-5544. doi: 10.1016/j.biomaterials.2010.03.064
13. Fan Y, Yue Z, Lucarelli E, Wallace GG. Hybrid printing using cellulose nanocrystals reinforced GelMA/HAMA hydrogels for improved structural integration. *Adv Healthc Mater*. 2020;9(24):2001410. doi: 10.1002/adhm.202001410
14. Sharifi S, Sharifi H, Akbari A, Chodosh J. Systematic optimization of visible light-induced crosslinking conditions of gelatin methacryloyl (GelMA). *Sci Rep*. 2021;11(1):23276. doi: 10.1038/s41598-021-02830-x
15. Wu Y, Xiang Y, Fang J, et al. The influence of the stiffness of GelMA substrate on the outgrowth of PC12 cells. *Biosci Rep*. 2019;39(1): BSR20181748. doi: 10.1042/BSR20181748

16. Yin J, Yan M, Wang Y, Fu J, Suo H. 3D bioprinting of low-concentration cell-laden gelatin methacrylate (GelMA) bioinks with a two-step cross-linking strategy. *ACS Appl Mater Interfaces*. 2018;10(8):6849-6857. doi: 10.1021/acsami.7b16059

17. Chung JHY, Naficy S, Yue Z, et al. Bio-ink properties and printability for extrusion printing living cells. *Biomater Sci*. 2013;1(7):763-773. doi: 10.1039/c3bm00012e

18. Her GJ, Wu H-C, Chen M-H, Chen M-Y, Chang S-C, Wang T-W. Control of three-dimensional substrate stiffness to manipulate mesenchymal stem cell fate toward neuronal or glial lineages. *Acta Biomater*. 2013;9(2):5170-5180. doi: 10.1016/j.actbio.2012.10.012

19. O'Connell CD, Zhang B, Onofrillo C, et al. Tailoring the mechanical properties of gelatin methacryloyl hydrogels through manipulation of the photocrosslinking conditions. *Soft Matter*. 2018;14(11):2142-2151. doi: 10.1039/c7sm02187a

20. Freeman S, Calabro S, Williams R, Jin S, Ye K. Bioink formulation and machine learning-empowered bioprinting optimization. *Front Bioeng Biotechnol*. 2022;10:913579. doi: 10.3389/fbioe.2022.913579

21. Ruberu K, Senadeera M, Rana S, et al. Coupling machine learning with 3D bioprinting to fast track optimisation of extrusion printing. *Appl Mater Today*. 2021;22:100914. doi: 10.1016/j.apmt.2020.100914

22. Shin J, Lee Y, Li Z, Hu J, Park SS, Kim K. Optimized 3D bioprinting technology based on machine learning: a review of recent trends and advances. *Micromachines*. 2022;13(3):363. doi: 10.3390/mi13030363

23. Sun J, Yao K, An J, Jing L, Huang K, Huang D. Machine learning and 3D bioprinting. *Int J Bioprint*. 2023;9(4):717. doi: 10.18063/ijb.717

24. Yu C, Jiang J. A perspective on using machine learning in 3D bioprinting. *Int J Bioprint*. 2020;6(1):253. doi: 10.18063/ijb.v6i1.253

25. An J, Chua CK, Mironov V. Application of machine learning in 3D bioprinting: focus on development of big data and digital twin. *Int J Bioprint*. 2021;7(1):342. doi: 10.18063/ijb.v7i1.342

26. Tian S, Stevens R, McInnes BT, Lewinski NA. Machine assisted experimentation of extrusion-based bioprinting systems. *Micromachines*. 2021;12(7):780. doi: 10.3390/mi12070780

27. Brochu E, Cora VM, Freitas ND. A tutorial on Bayesian optimization of expensive cost functions, with application to active user modeling and hierarchical reinforcement learning. *ArXiv*. 2010;1012:2599 doi: 10.48550/arXiv.1012.2599

28. Bishop CM, Nasrabadi NM. Pattern recognition and machine learning. *J Electronic Imaging*. 2007;16(4):049901. doi: 10.1117/1.2819119

29. Engler AJ, Sen S, Sweeney HL, Discher DE. Matrix elasticity directs stem cell lineage specification. *Cell*. 2006;126(4):677-689. doi: 10.1016/j.cell.2006.06.044

30. Aregueta-Robles UA, Martens PJ, Poole-Warren LA, Green RA. Tissue engineered hydrogels supporting 3D neural networks. *Acta Biomater*. 2019;95:269-284. doi: 10.1016/j.actbio.2018.11.044

31. Chatterjee K, Lin-Gibson S, Wallace WE, et al. The effect of 3D hydrogel scaffold modulus on osteoblast differentiation and mineralization revealed by combinatorial screening. *Biomaterials*. 2010;31(19):5051-5062. doi: 10.1016/j.biomaterials.2010.03.024

International Journal of Bioprinting

Special Issue Alerts

Invitation for Special Issue Proposals



Organizing and editing for a Special Issue helps Guest Editors gain editorial experience and improve academic profile, in addition to being a part of organizing scientific communication of contemporary topics.

If you are published researcher and have an idea for a Special Issue, please write in via email to our Managing Editor (ijb.office@accscience.sg). Please provide your CV, professional profile page and a topic of interest in your email. Our colleague will guide you in the process of writing a Special Issue proposal.

Visit Special Issues site for the list of Special Issues featured in *International Journal of Bioprinting*.

Frequently Asked Questions

1. **Are Special Issue submissions processed in the same way how Regular Issue papers are being pre-screened and reviewed?**
   Yes, all full-length article submissions to a Special Issue will go through the same editorial and peer-review process. The distinct difference here is that the Guest Editors will replace the usual editors and get involved in the making professional decisions on papers after peer review. Note that the specific roles of a Guest Editor could vary across Special Issues.

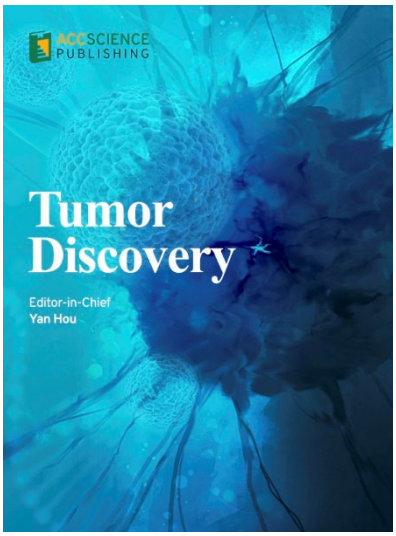
2. **How many Guest Editors are required to organize a Special Issue?**
   There is no fixed number; however, we suggest no more than 4 Guest Editors per Special Issue. More importantly, all Guest Editors should have excellent publication track records and demonstrated expertise in the topic(s) being proposed.

3. **Is the Special Issue governed by important deadlines?**
   Yes.

Benefits of Being A Guest Editor

- A chance to get involved in the conception and development of a specialty, contemporary topic that is of interest to the readers
- A chance to expand your professional network to the scholars and researchers who are similarly involved in the research of specialty topic
- A chance to hone your editorial skills
- A chance to gain first-hand experience of editing a thematic issue publication, which is a very valuable experience for those who aspire to edit their own journal in future
- A chance to improve your academic profile and help establish your academic influence within your discipline

Our Journals

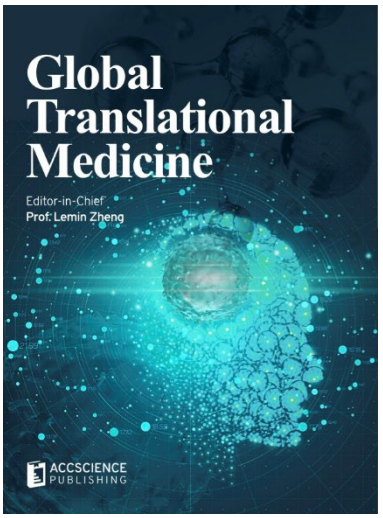


Tumor Discovery is a peer-reviewed and open-access journal that aims to present new cancer research with strong emphasis on fundamental and translational studies. *Tumor Discovery* covers topics, including but not limited to the following:

- Etiology and pathogenesis of cancer
- Mechanisms and molecular pathways underlying cancer initiation and progression
- Tumor metastasis
- Tumor evolution and heterogeneity
- Tumor microenvironment and tumor-host interactions
- Cancer genetics and genomics
- Cancer characterization using omics approaches
- Discovery and validation of cancer biomarker
- Discovery of new therapeutic targets
- New approaches of diagnostic and treatment modalities
- Statistical methods in cancer research

Global Translational Medicine is a quarterly journal that focuses on medicine, biological sciences, and biomaterials engineering. The goal of *Global Translational Medicine* is to provide a platform to researchers for showcasing their latest research works in translational medicine so as to advance the field towards the betterment of human health. Despite the advancement of omics and new technologies, the process of transforming these technologies and scientific research results into effective therapies and putting them into clinical use still has a long way to go. *Global Translational Medicine* provides a platform to fill the gaps in preclinical and inter-disciplinary research, to promote clinical translation of scientific research results, and to contribute to the conception of new and improved preventive measures as well as diagnostic and therapeutic techniques of diseases.

Global Translational Medicine covers the following themes: cardiovascular disease, metabolism/diabetes/obesity, neuroscience/neurology, cancer, biomaterials and their applications in medicine, proteomics/metabolomics, pharmacogenomics, biomarkers, bioinformatics and data mining, animal and clinical research, and medical methods arising from interdisciplinary crossover.



Start a new journal

Write to us via email if you are interested to start a new journal with AccScience Publishing. Please attach your CV, professional profile page and a brief pitch proposal in your email. We shall inform you of our decision whether we are interested to collaborate in starting a new journal.

Contact: info@accscience.com

ACCSCIENCE PUBLISHING

ACCSCIENCE PUBLISHING

Publishing Office:
8 Burn Road, #15-03 Trivex, Singapore 369977.
Editorial Office:
30-2, Jalan BS 1/2, Olive Hill Business Park, 43300 Seri Kembangan, Selangor. Malaysia.

Editorial Office: editor.ijb@accscience.com
General Inquires: info@accscience.com

https://accscience.com/journal/IJB